# IIUM ENGINEERING JOURNAL

Volume 26 Number 1

January 2025

IIUM Press

INTERNATIONAL ISLAMIC UNIVERSITY MALAYSIA

ISSN: 1511-788X E-ISSN: 2289-7860

http://journals.iium.edu.my/ejournal

IIUM ENGINEERING JOURNAL

Volume 26, Issue 1, January 2025

https:/doi.org/10.31436/iiumej.v26i1

# Copyright Notice

**Consent to publish**: The Author(s) agree to publish their articles with IIUM Press.

**Declaration**: The Author(s) declare that the article has not been published before in any form, that it is not concurrently submitted to another publication, and that it does not infringe on anyone's copyright. The Author(s) holds the IIUM Press and Editors of the journal harmless against all copyright claims.

**Transfer of copyright**: The Author(s) hereby agree to transfer the article's copyright to IIUM Press, which shall have the non-exclusive and unlimited right to publish the article in any form, including in electronic media. For articles with more than one author, the corresponding author confirms that he/she is authorized by his/her co-author(s) to grant this copyright transfer.

**The IIUM Engineering Journal follows the open access policy**.

All articles published for open access will be immediately and permanently free for everyone to read, download, copy, and distribute for noncommercial purposes.

IIUM Engineering Journal at https://journals.iium.edu.my/ejournal is licensed under a Creative Commons Attribution-NonCommercial 4.0 International License.

# IIUM ENGINEERING JOURNAL EDITORS

**CHIEF EDITOR**
Ahmad Faris Ismail, IIUM, Malaysia

**TECHNICAL EDITOR**
Khairul Azami Sidek, IIUM, Malaysia

**EXECUTIVE EDITOR**
Teddy Surya Gunawan, IIUM, Malaysia

**ASSOCIATE EDITOR**
Nor Farahidah Za'bah, IIUM, Malaysia

**LANGUAGE EDITOR**
Lynn Mason, Malaysia

**COPY EDITOR**
Aliza 'Aini Md Ralib, IIUM, Malaysia
Suriza Ahmad Zabidi, IIUM, Malaysia

**MALAY TRANSLATOR**
Nurul Arfah Che Mustapha, IIUM, Malaysia

**EDITORIAL BOARD MEMBERS**

Abdullah Al-Mamun, IIUM, Malaysia
Abdumalik Rakhimov, IIUM, Malaysia
Aishah Najiah Dahnel, IIUM, Malaysia
Alya Naili Rozhan, IIUM, Malaysia
Ani Liza Asnawi, IIUM, Malaysia
Hanafi Ani, IIUM, Malaysia
Hanafy Omar, Saudi Arabia
Huda Adibah Mohd. Ramli, IIUM, Malaysia
Konstantin Khanin, University of Toronto, Canada
Ma'an Al-Khatib, IIUM, Malaysia
Meftah Hrairi, IIUM, Malaysia
Mohamed B. Trabia, United States
Mohammad S. Alam, Texas A&M University-Kingsville, United States
Mohd Sultan Ibrahim Shaik Dawood, IIUM, Malaysia
Mustafizur Rahman, National University Singapore, Singapore
Noorasikin Samat, IIUM, Malaysia
Nor Fadhillah Mohamed Azmin, IIUM, Malaysia
Norsinnira Zainul Azlan, IIUM, Malaysia
Ossama Abdulkhalik, Michigan Technological University, United States
Waqar Asrar, IIUM, Malaysia

**AIMS & SCOPE OF IIUMENGINEERING JOURNAL**

The **IIUM Engineering Journal**, published biannually (January and July), is a carefully refereed international publication of the International Islamic University Malaysia (IIUM). Contributions of high technical merit within the span of engineering disciplines covering the main areas of engineering: Electrical and Computer Engineering; Mechanical and Manufacturing Engineering; Automation and Mechatronics Engineering; Material and Chemical Engineering; Environmental and Civil Engineering; Biotechnology and Bioengineering; Engineering Mathematics and Physics; and Computer Science and Information Technology are considered for publication in this journal. Contributions from other areas of engineering and applied science are also welcome. The IIUM Engineering Journal publishes contributions under *Regular papers and Invited review papers*. It also welcomes contributions that address solutions to the specific challenges of the developing world, as well as science and technology issues, from an Islamic and multidisciplinary perspective.

**REFEREES' NETWORK**

All papers submitted to the IIUM Engineering Journal will be subjected to a rigorous reviewing process through a worldwide network of specialized and competent referees. Each accepted paper should have at least two positive referees' assessments.

**SUBMISSION OF A MANUSCRIPT**

A manuscript should be submitted online to the IIUM-Engineering Journal website at https://journals.iium.edu.my/ejournal. The journal website can also be used for further correspondence on the paper's status.

## INTERNATIONAL ADVISORY COMMITTEE

A. Anwar, United States
Abdul Latif Bin Ahmad, Malaysia
Farzad Ismail, USM, Pulau Pinang, Malaysia
Hanafy Omar, Saudi Arabia
Hany Ammar, United States
Idris Mohammed Bugaje, Nigeria
K.B. Ramachandran, India
Kunzu Abdella, Canada
Luis Le Moyne, ISAT, University of Burgundy, France
M Mujtaba, United Kingdom
Mohamed AI-Rubei, Ireland
Mohamed B Trabia, United States
Syed Kamrul Islam, United States
Tibor Czigany, Budapest University of Technology and Economics, Hungary
Yiu-Wing Mai, The University of Sydney, Australia.

Published by:

IIUM Press

**IIUM Press**,
International Islamic University Malaysia
Jalan Gombak, 53100 Kuala Lumpur, Malaysia
Phone (+603) 6421-5014, Fax: (+603) 6421-6298

Whilst every effort is made by the publisher and editorial board to see that no inaccurate or misleading data, opinion or statement appears in this Journal, they wish to make it clear that the data and opinions appearing in the articles and advertisement herein are the responsibility of the contributor or advertiser concerned. Accordingly, the publisher and the editorial committee accept no liability whatsoever for the consequence of any such inaccurate or misleading data, opinion, or statement.

ISSN 1511 - 788X

9 771511 788008

**IIUM Engineering Journal**
**ISSN: 1511-788X E-ISSN: 2289-7860**

https://doi.org/10.31436/iiumej.v26i1.3564

# EDITORIAL MESSAGE

The IIUM Engineering Journal, Vol. 26 No. 1, showcases a diverse array of pioneering research that pushes the boundaries of engineering and technology. This issue reflects a commitment to addressing critical challenges, exploring innovative solutions, and advancing sustainable practices across various disciplines. This edition captures the essence of interdisciplinary collaboration and ingenuity, from air pollution modeling and flood mapping to groundbreaking healthcare and renewable energy applications.

Environmental sustainability is a recurring theme in this issue. Researchers have tackled pressing global issues such as air pollution, water purification, and waste management with novel solutions. Developing deep, sparse autoencoder models for predicting the Air Pollution Index in Malaysia exemplifies how artificial intelligence can guide impactful environmental decisions. Similarly, advancements in green cementless mortar and geopolymer technology utilizing waste paper sludge ash highlight engineering's role in reducing carbon footprints and repurposing industrial by-products.

Solar-driven innovations also take center stage, with the introduction of PVA-Chitosan/PANi hydrogels demonstrating a leap forward in solar vapor generation efficiency. This research addresses freshwater scarcity and opens new avenues for sustainable material development.

Healthcare and safety remain pivotal in this issue, with studies delving into early autism screening using federated learning and diabetic retinopathy detection leveraging deep convolutional neural networks. These works underscore the transformative potential of artificial intelligence in improving diagnostic accuracy and protecting sensitive medical data.

Another noteworthy contribution is a study on lightning protection systems for large-scale solar photovoltaic plants in Malaysia. This study provides critical insights into safeguarding renewable energy infrastructures in lightning-prone regions. Such research bridges the gap between technological advancement and safety, ensuring resilience in natural adversities.

This issue also highlights the integration of AI and machine learning in optimizing engineering systems. From a fuzzy logic-based indoor navigation system to an energy management system for standalone microgrids, these innovations demonstrate AI's capability to enhance decision-making, reduce costs, and improve system reliability. For instance, using a Model Predictive Control-based EMS for microgrids presents a tangible solution to balancing renewable energy intermittency and load demands.

Interdisciplinary efforts shine through research on 4D radar imaging and its fusion with deep learning for road-crossing classification, emphasizing the role of technology in creating safer urban environments. Similarly, the application of fuzzy logic for vehicle speed control and the development of SolatExo—a passive exoskeleton for individuals with physical disabilities—illustrate how engineering transcends traditional boundaries to address societal needs.

This volume stands as a testament to the vital role of engineering research in shaping a sustainable, inclusive, and technologically advanced future. The diversity of topics and the depth of innovation presented in this issue underline the IIUM Engineering Journal's dedication to advancing knowledge and fostering impactful solutions to global challenges.

We extend our gratitude to the authors, reviewers, and editorial board for their unwavering commitment to excellence. Your contributions ensure that this journal continues to thrive as a beacon of scholarly inquiry and practical impact. Let us embrace these breakthroughs as stepping stones to a brighter, more sustainable future.

Prof. Dr. Teddy Surya Gunawan

*Executive Editor*

**IIUM Engineering Journal**

# IIUM ENGINEERING JOURNAL

Volume 26, Issue 1, January 2025
https:/doi.org/10.31436/iiumej.v26i1

## Table of Contents

**Copyright** ..... i
**Editorial Board** ..... ii
**Editorial Message** ..... iv

**Chemical and Biotechnology Engineering**

2818: Autoencoder Artificial Neural Network Model for Air Pollution Index Prediction ..... 1
*Nor Irwin Basir, Kathlyn Kaiyun Tan, Danny Hartanto Djarum, Zainal Ahmad, Dai-Viet N. Vo, Zhang Jie*

3173: Effects of Fermentation Time and Extraction Solvent on Antioxidant Activity and Total Phenolic and Flavonoid Content of Phenolic Extract from Orange (Citrus reticulata) Peel ..... 22
*Khalilan Lambangsari, Agnesia Gita Regita, Laely Munawaroh, Elen Etha Yulinar Simanjuntak, Nadia Delfi Zafira, Muhammad Yusuf Abduh*

**Civil and Environmental Engineering**

2998: Machine Learning Models for Predicting the Compressive Strength of Concrete with Shredded PET Bottles and M-Sand as Fine Aggregate ..... 42
*Altamashuddinkhan Nadimalla, Siti Aliyyah Masjuki, Abdullah Gubbi, Anjum Khan, Imran Mokashi*

3015: Physical and Mechanical Properties of Green Cementless Mortar Incorporating Waste Paper Sludge Ash ..... 57
*Aida Nabila Jamaluddin, Siti Asmahani Saad, Siti Aliyyah Masjuki, Wan Nur Firdaus Wan Hassan, Siti Noratikah Che Deraman, Nadiah Md Husain*

3244: Bentonite-Amended Geo-Polymerised Fly Ash-GGBS Mixture for Waste Containment Applications ..... 69
*Sagiri Sivasai Saranya, Maya Naik, Puvvadi Sivapullaiah*

3321: Factors Influencing the Elastic Stiffness Factor in Reinforced Concrete Structures of Dual Systems Using Pushover Analysis ..... 84
*Shahram Jkhsi, Saya Saber*

**Electrical, Computer and Communications Engineering**

3157: Map Floodwater Radar Imagery using Machine Learning Algorithms ..... 97
*Thanh-Nghi Doan, Duc-Ngoc Le-Thi*

3186: Enhanced Early Autism Screening: Assessing Domain Adaptation with Distributed Facial Image Datasets and Deep Federated Learning ..... 113
*Shafiul Alam, Muhammad Mahbubur Rashid*

3194: Retinopathy Disease Detection and Classification Using a Coordinate Attention Module-Based Convolutional Neural Network with Leaky Rectified Linear Unit ..... 129
*Pravin Balaso Chopade, Prabhakar N. Kota, Bhagvat D. Jadhav, Pravin Marotrao Ghate, Shriram Sadashiv Kulkarni*

3221: Wearable Textile Patch DSSRS Antenna for Body Tumors Detection with Reduced SAR ..... 148
*M.M. Hasan Mahfuz, Md Rafiqul Islam, Norun Farihah Abdul Malek, Mohamed Hadi Habaebi, Nazmus Sakib, Elham Baladi*

3230: Model Predictive Control-Based Energy Management System with Load Curtailment for Standalone Microgrid ..... 169
*Muhammad Sharir Fathullah Mohd Yunus, Siti Hajar Yusoff, Siti Nadiah Mohd Sapihie, Mohd Shahrin Abu Hanifah, Teddy Surya Gunawan, Suriza Ahmad Zabidi*

3238: A Novel Induced Current Protection Scheme for Large-Scale Solar Photovoltaic Systems Using Early Streamer Emissions ..... 187
*Nurul 'Aini Mohamad Zakaria, Mohd Najib Mohd Hussain, Kanendra Naidu Vijyakumar, Intan Rahayu Ibrahim, Nor Salwa Damanhuri, Nur Fadzilah Ahmad*

3255: Comprehensive Analysis of a Bridged-T Pre-Equalizer Circuit for High-Speed Visible Light Communications ..... 205
*Siti Hajar Ab Aziz, Norhanis Aida Mohd Nor, Suriza Ahmad Zabidi*

3268: 4D Radar Imaging and Camera Fusion for Road Crossing Detection and Classification Using Deep Learning ..... 217
*Liyaana Shahirah Wan Abd Aziz, Farah Nadia Mohd Isa, Faridah Abd Rahman, Arvind Hari Narayanan, Ahmad Reza Alghooneh, George Shaker*

3328: Optimizing FPGA Resource Allocation for SHA-3 Using DSP48 and Pipelining Techniques ..... 240
*Agfianto Eko Putra, Oskar Natan, Jazi Eko Istiyanto*

3337: Design of Intelligent Feature Selection Technique for Phishing Detection ..... 254
*Sharvari Sagar Patil, Narendra M. Shekokar, Sridhar C. Iyer*

3386: Global-Local Self-Attention-Based Long Short-Term Memory with Optimization Algorithm for Speaker Identification ..... 278
*Pravin Marotrao Ghate, Bhagvat D. Jadhav, Shriram Sadashiv Kulkarni, Pravin Balaso Chopade, Prabhakar N. Kota*

3392: Electrochemical Sensing of Nicotine Using Laser-Induced Graphene Screen-Printed Electrode ..... 293
*Balqis Nurnadia Badrol Hisham, Rosminazuin Ab. Rahim, Anis Nurashikin Nordin, Aliza Aini Md Ralib, Nor Farahidah Za'bah, Lun Hao Tung, Zainiharyati Mohd Zain*

3407: Development of 3D-Printed Serpentine Fluidic Channel Integrated with Heating Element for Loop-Mediated Isothermal Amplification (LAMP) Process ..... 308
*Muhammad Khairul Faisal Muhamad Atan, Rosminazuin Ab. Rahim, Anis Nurashikin Nordin, Aliza Aini Md Ralib, Teddy Surya Gunawan, Zainiharyati Mohd Zain*

3411: Utilizing MFCCs and TEO-MFCCs to Classify Stress in Females Using SSNNA ..... 324
*Nur Aishah Zainal, Ani Liza Asnawi, Siti Noorjannah Ibrahim, Nor Fadhillah Mohamed Azmin, Norharyati Harum, Nora Mat Zin*

3446: Modified COST-235 Empirical Pathloss Model for Agricultural WSN Using Particle Swarm Optimization ..... 336
*Syahfrizal Tahcfulloh, Etty Wahyuni, Dwi Santoso, Rizkyandi Juliannanda*

3455: Design and Implementation of a Deep Learning-Based Hand Gesture Recognition System for Rehabilitation Internet-of-Things (RIoT) Environments Using MediaPipe . 353
*Nurul Hanis Mohd Dhuzuki, Ahmad Anwar Zainuddin , Nur Anis Sofea Kamarul Zaman, Alin Nur Maisarah Ahmad Razmi, Wonderful Shammah Kaitane, Asmarani Ahmad Puzi, Mohd Naqiuddin Johar, Maslina Yazid, Nor Azlin Mohd Nordin, Shahrul Naim Sidek, Hasan Firdaus Mohd Zaki*

3531: Integration of LoRa IoT with Cloud Platform in a Stingless Beehive Remote Monitoring System ..... 373
*Yasser Asrul Ahmad, Nurul Salshabila Mustapa, Anis Hannani Razaman, Muhammad Nasrin Aqil Abdul Hamid, Noreha Abdul Malik, Mohd Faizal Jamlos*

3537: Optimizing N-1 Contingency Rankings Using a Nature-Inspired Modified Sine Cosine Algorithm ..... 398
*Irnanda Priyadi, Novalio Daratha, Teddy Surya Gunawan, Kalamullah Ramli, Febrian Jalistio, Hazlie Mokhlis*

3547: Improving Model Performance for Predicting Exfiltration Attacks Through Resampling Strategies ..... 420
*Arif Rahman Hakim, Kalamullah Ramli, Muhammad Salman, Esti Rahmawati Agustina*

**Engineering Mathematics and Applied Science**

3259: Analysis of Brain Tissue Poroelastic Properties Using Multiscale Modelling ..... 437
*Abbas Shabudin, Mohd Jamil Mohamed Mokhtarudin, Nik Abdullah Nik Mohamed, Mohd Akramin Mohd Romlay*

**Materials and Manufacturing Engineering**

3236: Solar-Driven Water Purification: Advancing PVA-Chitosan/PANI Hydrogel to Enhance Solar Vapor Generation for Freshwater Treatment ..... 450
*Flora Serati, Syazwani Mohd Zaki, Ahmad Akid Zulkifli, Siti Rabizah Makhsin*

3239: Application of Kansei Engineering in Various Train Compartment Designs to Determine the User's Affective Response ..... 466
*Dinda Karina Yohanny, Lu'Lu' Purwaningrum, Ambar Mulyono*

3397: Sheet Metal Manual Handling Aids: Effects of Design Differences on Muscle Activity and Subjective Assessment ..... 480
*Nadiah Ahmad, Radin Zaid Radin Umar, Isa Halim, Dian Mardi Safitri*

3430: Development and Evaluation of Passive Exoskeleton (SolatExo) for Assisting Muslims with Physical Disability in Salah ..... 495
*Isa Halim, Muhammad Nadzirul Izzat Mahadzir, Zulkeflee Abdullah, Muhammad Haikal Sidek, Mariam MD Ghazaly, Adi Saptari*

**Mechanical and Aerospace Engineering**

3379: Bilateral Ground Reaction Force Prediction Using Deep Learning Models and Custom Force Plate ..... 524
*Ying Heng Yeo, Muhammad Fauzinizam Razali, Zaidi Mohd Ripin, Nur-Akasyah J., Mohamad Ikhwan Zaini Ridzwan, Alexander Wai Teng Tan, Jia Yi Tay*

**Mechatronics and Automation Engineering**

3189: Fuzzy Logic-Based Arrival Time Estimation for Indoor Navigation Using Augmented Reality ..... 549
*Muhammad Hidayat Mohammed Sohif, Muhammad Imran Mardzuki, Azhar Mohd Ibrahim, Ahmad Jazlan*

3436: Optimized Type-2 Fuzzy Logic Control for Low-Speed Vehicle Pedal Pressing Automation Using Hybrid Spiral Sine Cosine Algorithm ..... 563
*Azrul Azim Abdullah Hashim, Nor Maniha Abdul Ghani, Salmiah Ahmad, Mohd Ruzaini Hashim, Noor Zirwatul Ahlam Naharuddin, Addie Irawan*

*Blank page.*

https://doi.org/10.31436/iiumej.v26i1.2818

# AUTOENCODER ARTIFICIAL NEURAL NETWORK MODEL FOR AIR POLLUTION INDEX PREDICTION

**NOR IRWIN BASIR[1], KATHLYN KAIYUN TAN[1], DANNY HARTANTO DJARUM[1], ZAINAL AHMAD[1*], DAI-VIET N. VO[1], JIE ZHANG[2]**

*[1]School of Chemical Engineering, Universiti Sains Malaysia, Engineering Campus, Seri Ampangan, 14300, Nibong Tebal, Penang, Malaysia*

*[2]School of Engineering, Merz Court, Newcastle University, Newcastle upon Tyne NE1 7RU, United Kingdom*

**Corresponding author: chzahmad@usm.my*

*(Received: 3 April 2024; Accepted: 4 September 2024; Published online: 10 January 2025)*

***ABSTRACT:*** Air pollution, a significant global challenge driven by industrialization, urbanization, and population growth, is caused by the emission of harmful gases, particulates, and biological molecules into the atmosphere, posing serious risks to health and the environment. Key sources include power plants, industrial activities, vehicles, and residential heating. Thus, effective air quality monitoring and forecasting are crucial to mitigating the adverse impacts of pollution. This paper presents shallow and deep sparse autoencoder artificial neural network models to improve the prediction of the Air Pollution Index (API) in Perak Darul Ridzuan, Malaysia, as a case study. The results show that the deep sparse autoencoder achieves better prediction accuracy with $\boldsymbol{MSE}$ and $\boldsymbol{R^2}$ values of 0.1474 and 0.8331, respectively, compared to 0.1515 and 0.8300 for the shallow sparse autoencoder. The performance of these autoencoder models is also compared with other models, such as feedforward artificial neural networks (FANN) and principal component analysis (PCA). The findings confirm that both autoencoder models enhance API prediction accuracy, with the deep sparse autoencoder emerging as the optimal model, highlighting the potential of deep learning in improving air quality prediction.

***ABSTRAK:*** Pencemaran udara, merupakan satu cabaran global yang didorong oleh perindustrian, urbanisasi pesat, dan pertumbuhan populasi, adalah disebabkan oleh pelepasan gas, partikel, dan molekul biologi merbahaya ke atmosfera, menimbulkan risiko serius kepada kesihatan dan alam sekitar. Sumber utama termasuk loji janakuasa, aktiviti industri, kenderaan, dan pemanasan kediaman. Oleh itu pemantauan dan ramalan kualiti udara penting bagi mengurangkan kesan buruk pencemaran. Kajian ini membentangkan model rangkaian neural tiruan pengauto kod jarang 'cetek' dan pengauto kod jarang 'dalam' memperbaiki ramalan Indeks Pencemaran Udara (API) di negeri Perak Darul Ridzuan, Malaysia sebagai kes kajian. Dapatan kajian menunjukkan bahawa pengautokod jarang 'dalam' mencapai ketepatan ramalan lebih baik, dengan nilai MSE dan R2 masing-masing sebanyak 0.1474 dan 0.8331, berbanding 0.1515 dan 0.8300 bagi pengautokod jarang 'cetek'. Prestasi model pengautokod ini juga dibandingkan dengan model lain, seperti rangkaian neural tiruan suapan hadapan (FANN) dan analisis komponen utama (PCA). Hasil kajian mengesahkan bahawa kedua-dua model pengautokod meningkatkan ketepatan ramalan API, dengan pengautokod jarang 'dalam' muncul sebagai model paling optimum, menonjolkan potensi pembelajaran mendalam 'dalam' meningkatkan ramalan kualiti udara.

***KEYWORDS:*** *Air pollution index, Shallow sparse autoencoder, Deep sparse autoencoder, Prediction.*

https://doi.org/10.31436/iiumej.v26i1.2818

# 1. INTRODUCTION

Research on environmental quality assessment and prediction-related fields can be generally categorized into two main groups: deterministic methods and statistical methods [1]. Deterministic methods incorporate statistical methods and meteorological theoretical principles in representing the processes of diffusion, dispersion, elimination, emanation, and transformation of air pollutants fundamentally based on atmospheric physical and chemical reactions. This method is considered model-based since its architecture is predefined with theoretical assumptions; the output/target data can be calculated with precise knowledge of the model parameters prior. On the other hand, statistical methods utilize statistic-based techniques, such as autoregressive moving average (ARMA) [2], multiple linear regression (MLR) [3], support vector regression (SVR) [4] and artificial neural network (ANN), in predicting or forecasting air quality instead of employing complex theoretical techniques.

Artificial neural network (ANN) is a topic of great interest in the research world in its development to be used in air quality model prediction due to its ability and capability to handle a high dimensionality of real data and its self-adaptivity in performing dimensionality reduction, features representation, and relationship learning between the input data and the output/target data. In a typical ANN, the raw input data is remodeled into new interpretable data with smaller dimensions; thus, this process is called 'dimensionality reduction.' This process is essential to preserve significant information of the input data (features extraction) for further analysis of the data, whereby in this paper, it is for Air Pollution Index (API) prediction purposes. Air pollution is detrimental to health. It is caused by industrialization, rapid urbanization, and population growth. It is a common problem faced on a worldwide scale. In particular, power plant energy production, industrial processes, fuel-burning vehicles, residential heating, and natural catastrophes are the usual causes of the problem. The effects of air pollution can be generally categorized into two groups: short-term consequences and long-term consequences. Among the short-term consequences, human health-related effects are the utmost significant concerns, specifically at the metropolises; on the other hand, the long-term consequences encompass global climate-related effects such as the greenhouse effect and global warming. In conjunction with the escalation of air pollution issues, enhanced public awareness concerning air quality has resulted in both developed and developing countries.

The air quality monitoring and forecasting tools are indeed essential so that precautionary measures can be taken by minimizing the potential negative effects of predicted pollution peaks on the surrounding ecosystem and habitat. In general, the monitoring of the air quality is conducted in a manual manner continuously to detect the ambient air quality variations that may pose adverse effects to human health and the environment. The Department of Environment (DOE), Malaysia, carries out ambient air quality monitoring through a network that consists of 51 monitoring stations. All the aforementioned stations are situated strategically in residential, industrial, and heavy-traffic areas for air pollution control purposes. The Air Pollution Index (API) is used to describe and report the ambient air quality in Malaysia instead of utilizing the actual air pollutant concentration due to the simplicity in terms of presentation of the former. API not only reflects the intensity of the air pollution effects on human health, which ranges from hazardous to good, but also can be categorized in terms of the action criteria in accordance with the National Haze Action Plan. In this paper, sparse autoencoder ANN with both shallow and deep architecture models are proposed to improve API prediction performance. In this study, both proposed types of architecture are modeled using the same training data.

An autoencoder has various applications in various disciplines, as validated and proven by other researchers. An autoencoder (formerly known as an auto-associator) functions as a robust

https://doi.org/10.31436/iiumej.v26i1.2818

device with self-supervised learning [5]. It aims to transform input data to output data with a minimum degree of distortion. It is trained autoassociatively using its three main components (see Figure 1), i.e., encoder, bottleneck, and decoder [6, 7]. It learns to encode and compress the input into a latent space representation, which preserves significant information of the input to be stored in the bottleneck layer with smaller dimensions as features. It then learns to decode and reconstruct the input information at the output layer. Backpropagation is employed in the learning algorithm of an autoencoder [8, 9]. The autoencoder learning algorithm is able to generate a significant range of behaviors that are psychologically related, such as distortion, generalization, inferencing, recalling, and recognition [10]. A shallow autoencoder that employs a linear activation function is equivalent to a principal component analysis (PCA) model [11]. One of the significant differences between the two models is that an autoencoder is capable of learning both linear and nonlinear feature representation, while a traditional PCA model is capable of learning linear feature representation only. Thus, an autoencoder has become one of the highly considered artificial neural network models in constructing a statistical model based on a set of training data.

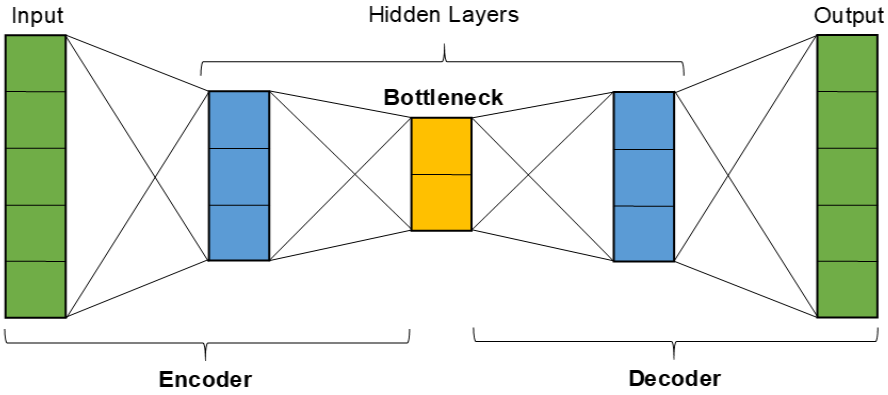


Figure 1. A typical autoencoder ANN architecture

Due to the high dimensionality of real data, a deep architecture approach is often employed in developing an autoencoder from a shallow autoencoder into a deep autoencoder. An autoencoder with one hidden layer of bottleneck is known as a shallow autoencoder. A deep autoencoder is technically an extension of a shallow autoencoder with more than a single hidden layer. Figure 1 illustrates a deep autoencoder with three hidden layers: one bottleneck hidden layer and one hidden layer each in its encoder and decoder. The additional hidden layers in the architecture of a deep autoencoder allow the ANN to learn the underlying features of the input data with higher complexity. The first hidden layer may learn the first-order features, while the second hidden layer may learn the second-order features. A deep autoencoder with a hierarchy of hidden layers tends to learn higher-order features and capture unknown data structures but takes longer training time.

Research on the application of autoencoders for prediction via relationship learning between the input data and the output/target data has been proven to be valid and successful by other researchers in a wide range of disciplines. It has been proposed for use as a structural condition monitoring tool [12]. The relationship between the modal information, such as mode shapes and frequencies, and the structural stiffness parameters is significant for structural damage detection in order to assess the safety conditions of a civil infrastructure under certain operating conditions. Excellent structural stiffness prediction was achieved using the autoencoder via a nonlinear dimensionality reduction of the modal information (input data) features followed by a nonlinear regression against the structural stiffness parameters for relationship learning purposes between the input modal information (concatenated feature

vector) and the output structural stiffness parameters. A similar approach was taken by proposing an autoencoder for use in the estimation of sea state bias (SSB) according to radar altimeter data [13]. SSB is defined as an altimeter-ranging error due to the presence of ocean waves on the surface of the sea. Relationship learning has been carried out between the input data (automatic gain control, backscatter coefficient, sea surface height, significant wave height, and wind speed) and the output data (SSB) using an autoencoder. It is presented that the proposed autoencoder model yields both higher prediction accuracy and operational efficiency compared to the conventional parametric model and nonparametric model.

Apart from that, the application of autoencoders for prediction through relationship learning in the climate-related discipline, which is closely related to our target model, has also been proven to be valid for weather forecasting [14]. Being inspired by successful applications of autoencoder for prediction purposes, it is, thus, believed that autoencoder ANN is able to solve practical nonlinear environmental modelling problems, improving API prediction performance with proper tuning and optimization as proposed in this paper. In recent years, research on air pollution modeling has been conducted with significant efforts. There are several types of ANN being applied in the development of air quality prediction models, such as feedforward artificial neural network (FANN) [15, 16], combined all multiple neural network (MNN), forward selection (FS) aggregated multiple neural network (MNN) and backward elimination (BE) aggregated multiple neural network (MNN) [16], and principal component analysis – feedforward artificial neural network (PCA-FANN) [17]. These ANN models, which have been trained, might sometimes fail to predict the target data with significant accuracy when being applied to test/unseen data due to the learning models converging to non-desirable local minima and/or overfitting of the noise present in the training data [18]. Thus, in this paper, an autoencoder with proper tuning and optimization is proposed for modeling an API predictor based on real data with the fundamental objective of enhancing the prediction accuracy and reliability of the air quality prediction model.

This study is significant and beneficial as it enhances air quality forecasting by introducing a more precise and dependable model. It can guide individuals, communities, or relevant entities interested in air quality control and forecasting. The search for enhanced prediction accuracy can aid in more effective planning and decision-making related to air quality management. This research can be a noteworthy contribution to the existing knowledge in the field of air quality forecasting using artificial intelligence methodologies.

This paper is organized as follows: the Materials and Methods section describes the case study, including the air quality data sampling location in Malaysia and the proposed shallow, sparse autoencoder and deep sparse autoencoder with the predictor. The Results and Discussions section presents the proposed autoencoder's results and discussions, and the last section concludes this paper.

## 2. MATERIALS AND METHODS

Please refer to Figure 2 for a detailed flowchart illustrating the various stages of the research process, from problem identification to conclusion. Each stage provides a comprehensive overview of the methodology employed in this study. As an overview, the research process starts with identifying the air pollution problem and understanding the need for accurate prediction models. Relevant air quality data is collected and prepared for modeling. The proposed artificial neural network models are then developed, trained, and tested to enhance prediction performance. The models are evaluated using specific metrics, and the results are analyzed to validate their effectiveness. The research concludes by summarizing the

findings and suggesting future work. This process ensures a thorough and significant contribution to air quality prediction.

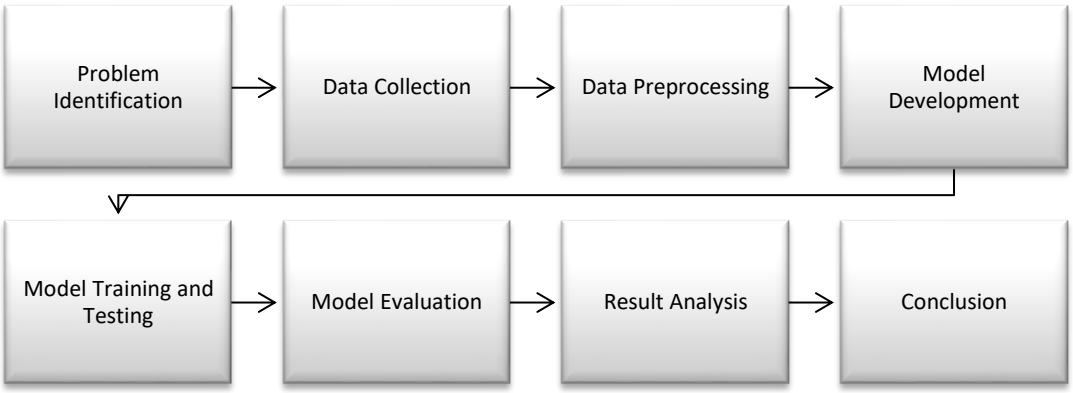


Figure 2. Overall Process Flow Diagram of the Research Processes

### 2.1. Case Study: Perak Darul Ridzuan State Air Monitoring Station, Malaysia

Most air quality data was acquired directly from the air quality monitoring stations or via the remote sensing instruments. In this study, the air quality data was collected by the Department of Environment (DOE), Malaysia, from 4 monitoring stations around Perak that are situated at CA0020, CA0041, CA0045, and CA0046, as shown in Figure 3 and described in Table 1. Reference [19] stated that the continuous air quality monitoring (CAQM) stations are strategically located in residential, industrial, and traffic areas to detect any significant changes in the air quality that may threaten the surrounding ecosystem and habitat.

In this study, the air quality data comprises data recorded for 5 years (from the 1st of January 2006 till the 31st of December 2010) with 8 input variables and 1 output/target variable. For API prediction modeling, the input variables involved include meteorological variables (air temperature, relative humidity, and wind speed) and air pollutants (carbon monoxide (CO), nitrogen dioxide ($NO_2$), ozone ($O_3$), particulate matter $PM_{10}$ and sulfur dioxide $SO_2$) concentration variables. In contrast, the output/target variable is API.

Table 1. Locations of Perak air monitoring stations [19]

| Station ID | Air Monitoring Station | Alternate Name | Latitude (N) | Longitude (E) |
|---|---|---|---|---|
| CA0020 | Sekolah Kebangsaan Ayer Puteh | Taiping | 4°89.881 | 100°67.912 |
| CA0041 | Pejabat Daerah Manjung | Manjung | 4°12.020 | 100°39.800 |
| CA0045 | Universiti Pendidikan Sultan Idris | Tanjung Malim | 3°68.758 | 101°52.438 |
| CA0046 | Sekolah Menengah Pegoh | Ipoh | 4°55.330 | 101°08.017 |

Table 2. Input and output/target variables for API prediction modeling.

| Input Variables | Output/Target Variable |
|---|---|
| Wind Speed (km/hr) | API |
| Air Temperature (°C) | |
| Relative Humidity (%) | |
| $O_3$ concentration (mg/L) | |
| CO concentration (mg/L) | |
| $PM_{10}$ concentration (µg/m$^3$) | |

https://doi.org/10.31436/iiumej.v26i1.2818

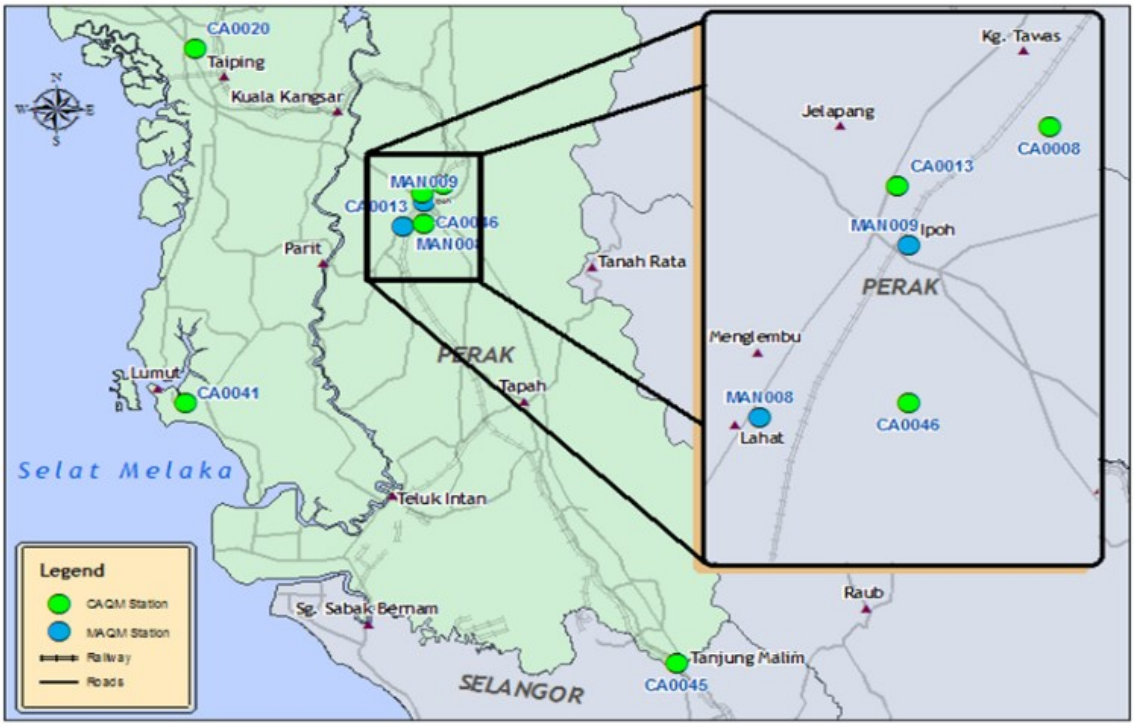


Figure 3. Perak air monitoring stations

As the $SO_2$ and NO2 concentrations displayed infinitesimal change throughout the 5 years, the involvement of both variables in API prediction modeling would yield a negligible effect on the proposed model performance. Thus, to increase the efficiency and effectiveness of the proposed model and develop a parsimonious model (a model that depends on a few input variables as necessary), the number of predictor input variables is reduced without losing important information. In this study, only 6 input variables were selected for the API prediction modeling, as summarized in Table 2. In this study, a total of 1826 samples are used for modeling and analysis, while the missing data is denoted as Not a Number (NaN).

## 2.2. Sparse Autoencoder Artificial Neural Network (ANN) with Predictor Model Development

In this case study, 1826 sampling instances were obtained from the DOE, Malaysia database from the 1st of January 2006 to the 31st of December 2010. MATLAB® was used for the API prediction modeling. All data was normalized on the same scale to zero mean ($\mu \approx 0$) and unit standard deviation ($\sigma \approx 1$) to cope with the difference in magnitude across the variables, introducing a common ground for the equal treatment of the features extracted after this during the ANN learning process. The time series data was transposed from a matrix of 1826 samples × 7 elements into a matrix form where the proposed and developed ANN model can process 7 elements × 1826 samples; it is noted that the first 6 elements represent the 6 input variables, respectively while the 7th element represents the output/target variable. Then, the scaled data was divided randomly into 2 sets of data: 85 % for training (1552 samples) and the remaining 15 % for testing (274 samples). Static time series data was applied in the API prediction modeling where the output/target data was a function of the input data, as shown in Eq. (1):

$$y_i(t) = f\left(x_{i1}(t), x_{i2}(t), \cdots, x_{in}(t)\right) \quad (1)$$

where $y_i(t)$ is the output/target data $y$ (API) at time $t$ in $i^{\text{th}}$ sample, $x_i(t)$ is the input data $x$ at time $t$ in $i^{\text{th}}$ sample where the subscripts 1 and 2 denote the first and second input variables,

https://doi.org/10.31436/iiumej.v26i1.2818

respectively, and $n$ represents the total number of model input variables. In this case study, the model input variables consist of air temperature, relative humidity, wind speed, CO concentration, $O_3$ concentration, and $PM_{10}$ concentration, making up a total number of 6 ($n$ = 6).

### 2.3. Sparse Autoencoder Artificial Neural Network (ANN)

As mentioned in Section 1, an autoencoder is a type of ANN that encodes and compresses the input into its latent space representation for reconstruction and decodes the input information as the output [20]. The most important part of the learning process is to preserve the important information from the input. In this study, a sparse autoencoder with 2 architectural models is proposed to extract significant features of the input data, which contains the data from the 6 input variables as mentioned in Table 2.

### 2.4. Shallow Sparse Autoencoder Artificial Neural Network (ANN)

A shallow autoencoder is an autoencoder with a single input layer, a single hidden layer (bottleneck), and a single output layer. The proposed shallow autoencoder architecture in this study is shown in Figure 4.

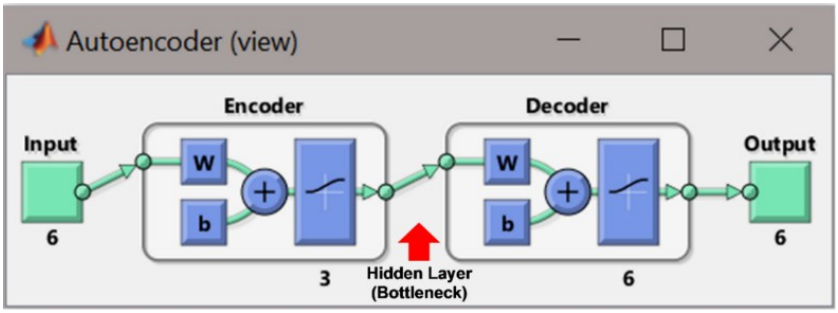


Figure 4. Shallow autoencoder architecture

An autoencoder is an ANN that implements 2 major transformations; the encoder transforms $d$ dimensional input into $r$ dimensional latent representation ($encode(x)$: $R^d \rightarrow R^r$) and the decoder transforms $r$ dimensional latent representation back into $d$ dimensional reconstructed input ($decode(h)$: $R^r \rightarrow R^d$). A set of training samples is given as $\{x_1, x_2, \cdots, x_m\}$ where, in this case, $x$ is the input data sample whereby each sample contains 6 input variable data, the subscripts 1 and 2 denote the first and second training input samples, respectively, and m represents the total number of model training input samples, whereby in this case $m = 1552$, such that $x_i \in R^d$ where the subscript $i = 1, 2, \cdots, m$. Firstly, in general, an autoencoder encodes and compresses the input vector $x$ into the hidden layer as the representation $h$ whose computational function is expressed as Equation 2; then, the representation $h$ is decoded back to the $x$ dimension as reconstruction $z$ whose computational function is described in Equation 3 as follows;

$$h = encode(x) = \Phi(W_1 x + b) \quad (2)$$

$$z = decode(h) = \Phi(W_2 h + c) \quad (3)$$

where $W_1$ is the weight matrix for the optimization process, $b$ is the encoding bias vector, $W_2$ is the weight matrix for the decoding process, $c$ is the decoding bias vector, and $\Phi$ is the activation/transfer function. In this study, $\Phi$ was set to be a logistic sigmoid function, as shown in Eq. (4), for both encode ($x$) and decode ($h$) to allow the developed autoencoder to learn nonlinear feature representation.

https://doi.org/10.31436/iiumej.v26i1.2818

$$\Phi(x) = \frac{1}{1+e^{-x}} \tag{4}$$

An autoencoder is trained by minimizing the reconstruction error, which is the difference between the original and reconstruction outputs. The autoencoder model parameters of $W_1$, $b$, $W_2$ and $c$ are optimized to minimize the average reconstruction error whose computational equation is shown in Eq. (5), where the loss function $L(x_{ij}, z_{ij})$ The traditional squared error function, shown in Eq. (6), was employed in this study. For optimization purposes, the scaled conjugate gradient descent algorithm was employed to train the autoencoder.

$$[W_1^*, b^*, W_2^*, c^*] = arg\ min_{W_1,b,W_2,c}\ \frac{1}{m}\sum_{i=1}^{m}\sum_{j=1}^{n} L(x_{ij}, z_{ij}) \tag{5}$$

$$L(x_{ij}, z_{ij}) = (x_{ij} - z_{ij})^2 \tag{6}$$

An ideal autoencoder balances two main reconstruction criteria: sensitive enough to capture significant features of the input to reconstruct the encoded data as the output with high accuracy and minimum distortion and insensitive enough to prevent memorizing and overfitting of the noise present in the training data [21]. Thus, to force the autoencoder to preserve only the important and useful variations present in the input essential for reconstruction without holding onto the redundancies present in the input, the sparsity constraint method was applied, transforming the autoencoder model into a sparse autoencoder model [22]. In order to obtain sparse representation, Eq. (5) was optimized and modified by embedding a sparsity constraint into it, as expressed in Eq. (7).

$$[W_1^*, b^*, W_2^*, c^*] = arg\ min_{W_1,b,W_2,c}\left[\frac{1}{m}\sum_{i=1}^{m}\sum_{j=1}^{n}(x_{ij} - z_{ij})^2 + (\alpha \times \Omega_{weights}) + (\beta \times \Omega_{sparsity})\right] \tag{7}$$

$$\Omega_{weights} = \frac{1}{2}\sum_{k=1}^{p}\sum_{i=1}^{m}\sum_{j=1}^{n}\left(W_{ij}^{(k)}\right)^2 \tag{8}$$

$$\Omega_{sparsity} = \sum_{l=1}^{r} KL(\rho \,||\, \widehat{\rho_l}) \tag{9}$$

$$KL(\rho \,||\, \widehat{\rho_l}) = \rho \log\left(\frac{\rho}{\widehat{\rho_l}}\right) + (1-\rho)\log\left(\frac{1-\rho}{1-\widehat{\rho_l}}\right) \tag{10}$$

$$\widehat{\rho_l} = \frac{1}{m}\sum_{i=1}^{m}(h_l \times x_i) \tag{11}$$

where $\alpha$ is the coefficient for the $L_2$ regularization term $\Omega_{weights}$ whose mathematical equation is expressed in Equation 8, $\beta$ is the coefficient for the sparsity regularization term $\Omega_{sparsity}$ whose mathematical equation is expressed in Eq. (9), $p$ is the number of hidden layers, $W$ is the weight matrix, $r$ is the number of hidden units, $KL$ is the Kullback-Leibler divergence between two Bernoulli random variables with the means equal to $\rho$ and $\widehat{\rho_l}$, respectively as defined in Eq. (10), $\rho$ is the desired sparsity parameter whose value defines the desired proportion of training samples a hidden unit reacts to, and $\widehat{\rho_l}$ is the average output activation value of the hidden unit l over the training data set, as expressed in Eq. (11).

The sparsity enforce constraint, as expressed mathematically in Eq. (12), was applied. Typically, $\rho$ is a small value close to 0. In this case, with shallow architecture, $\rho$ was set to 0.05 for the logistic sigmoid activation/transfer function. The setting enforces $\widehat{\rho_l}$ to be as close to 0.05 as possible, leading to the activation value of the hidden unit mostly nearing 0. Kullback-Leibler divergence was employed as it fastens the sparsity constraint during the coding process, penalizing $\widehat{\rho_l}$ from diverging away from $\rho$ significantly $KL(\rho \,||\, \widehat{\rho_l}) \approx 0$ if $\widehat{\rho_l} \approx \rho$.

$$\widehat{\rho_l} \approx \rho \tag{12}$$

https://doi.org/10.31436/iiumej.v26i1.2818

The list of significant shallow, sparse autoencoder ANN training parameters for the API prediction model is shown in Table 3. The features captured in the bottleneck hidden layer of the proposed and developed shallow sparse autoencoder, which contains significant representative information of the input data, were then utilized for successive API prediction via the relationship learning process.

Table 3. Shallow sparse autoencoder ANN training parameters for API prediction model

| Training Parameter | Description/Value (MATLAB® Code) |
|---|---|
| Number of hidden nodes (bottleneck hidden layer) | 3 |
| Activation/Transfer function for encoder | Logistic sigmoid (logsig) |
| Activation/Transfer function for decoder | Logistic sigmoid (logsig) |
| Maximum number of training epochs/iterations | 2000 |
| $L_2$ weight regularizer coefficient, $\boldsymbol{\alpha}$ | 0.001 |
| Desired sparsity parameter, $\boldsymbol{\rho}$ | 0.05 |
| Sparsity regularizer coefficient, $\boldsymbol{\beta}$ | 1 |
| Training algorithm | Scaled conjugate gradient descent (trainscg) |

## 2.5. Deep Sparse Autoencoder Artificial Neural Network (ANN)

A deep autoencoder is technically the extension of a shallow autoencoder with a single input layer, more than one hidden layer, and a single output layer. The proposed deep autoencoder architecture in this study is shown in Figure 5. It is noted that Figure 5 depicts the encoding architecture of the proposed deep autoencoder but not the generic structure of the whole deep autoencoder architecture, which includes the decoding part.

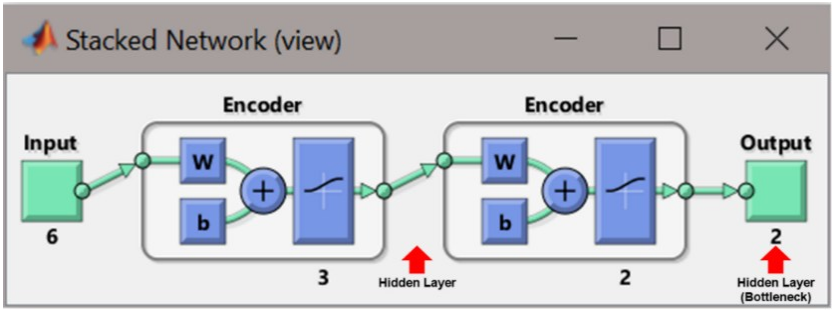


Figure 5. Deep autoencoder encoding architecture

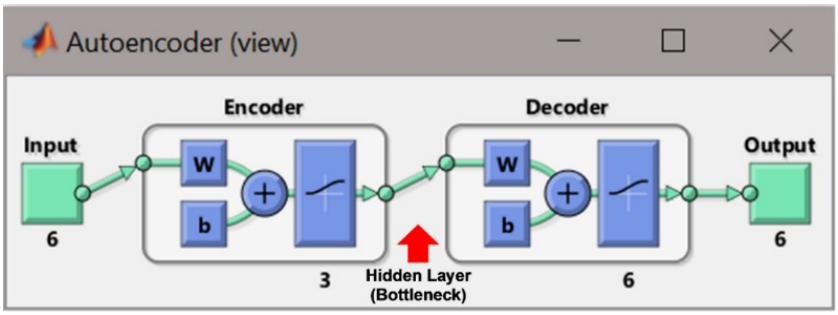


Figure 6. First shallow autoencoder architecture (encoding hidden layer of deep autoencoder)

During the construction of the proposed deep autoencoder for this study, 2 shallow sparse autoencoder models were first developed, each using similar computational approaches and functions as described in Section 2.4. In order to train a deep autoencoder effectively, pretraining of one of the hidden layers at a time sequentially (layer-wise training) was

https://doi.org/10.31436/iiumej.v26i1.2818

performed. The first shallow sparse autoencoder model architecture with the input data x as the model input is shown in Figure 6, and the second shallow sparse autoencoder model architecture with the features extracted from the first shallow sparse autoencoder h as the model input is shown in Figure 7. Then, these developed shallow sparse autoencoder models were stacked together to create a deep architecture, as illustrated in Figure 5, forming a deep sparse autoencoder.

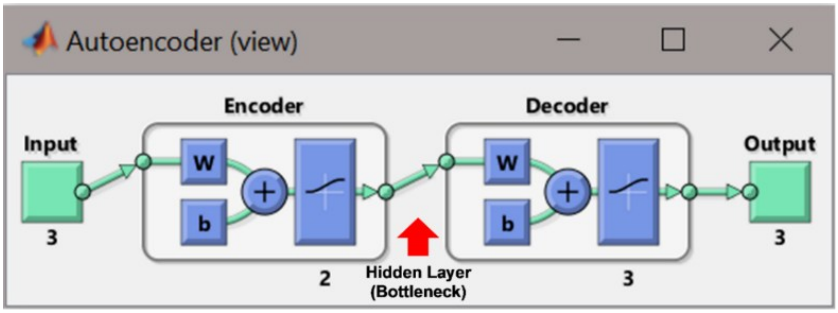


Figure 7. Second shallow autoencoder architecture (bottleneck hidden layer of deep autoencoder)

Table 4. First and second shallow sparse autoencoder ANN training parameters for deep architectural model

| **First shallow autoencoder (encoding hidden layer of deep autoencoder)** | |
|---|---|
| **Training Parameter** | **Description/Value (MATLAB® Code)** |
| Number of hidden nodes (bottleneck hidden layer) | 3 |
| Activation/Transfer function for encoder | Logistic sigmoid (logsig) |
| Activation/Transfer function for decoder | Logistic sigmoid (logsig) |
| Maximum number of training epochs/iterations | 2000 |
| $L_2$ weight regularizer coefficient, $\boldsymbol{\alpha}$ | 0.001 |
| Desired sparsity parameter, $\boldsymbol{\rho}$ | 0.05 |
| Sparsity regularizer coefficient, $\boldsymbol{\beta}$ | 1 |
| Training algorithm | Scaled conjugate gradient descent (trainscg) |
| **Second shallow autoencoder (bottleneck hidden layer of deep autoencoder)** | |
| **Training Parameter** | **Description/Value (MATLAB® Code)** |
| Number of hidden nodes (bottleneck hidden layer) | 2 |
| Activation/Transfer function for encoder | Logistic sigmoid (logsig) |
| Activation/Transfer function for decoder | Logistic sigmoid (logsig) |
| Maximum number of training epochs/iterations | 1000 |
| $L_2$ weight regularizer coefficient, $\boldsymbol{\alpha}$ | 0.00001 |
| Desired sparsity parameter, $\boldsymbol{\rho}$ | 0.025 |
| Sparsity regularizer coefficient, $\boldsymbol{\beta}$ | 0.9 |
| Training algorithm | Scaled conjugate gradient descent (trainscg) |

In the proposed and developed deep sparse autoencoder architecture, as illustrated in Figure 5, the first hidden layer is the bottleneck hidden layer indicated by the middle arrow in Figure 6 (first shallow sparse autoencoder), while the second hidden layer is the bottleneck hidden layer indicated by the middle arrow in Figure 7 (second shallow sparse autoencoder). In the deep sparse autoencoder architecture, as shown in Figure 5, the first hidden layer (encoding hidden layer) performs a feature fusion process on the 6 input variables of air temperature, relative humidity, wind speed, CO concentration, $O_3$ concentration, and $PM_{10}$ concentration via nonlinear dimensionality reduction, while the second hidden layer (bottleneck hidden layer) performs further feature extraction on the low dimensional features representation learned in the first hidden layer. Stated generically, for a deep autoencoder with

$p$ hidden layers and $k = (1, 2, \cdots, p)^{th}$ hidden layer, training of the first ($k = 1^{st}$) hidden layer is conducted with the training data set as its input; then, training of the successive $(k + 1)^{th}$ hidden layer is carried out with the output of the $k^{th}$hidden layer as its input. Sequential autoencoder models are stacked hierarchically depending on the depth (number of hidden layers) of the desired deep autoencoder.

The list of significant first and second shallow sparse autoencoder ANN training parameters for deep sparse autoencoder model development is shown in Table 4. It is noted that the value for each training parameter of the second shallow autoencoder is relatively smaller than the one listed under the first shallow autoencoder; this is because the dimensionality of the model input whose features representation is to be learned by the second shallow autoencoder is relatively lower compared to the first shallow autoencoder. The bottleneck hidden layer of the proposed and developed deep sparse autoencoder contains more feature abstraction than the encoding hidden layer. The features captured in the bottleneck hidden layer that contain significant representative information of the input data were then utilized for successive API prediction via the relationship learning process.

### 2.6. Relationship Learning

The primary objective of this process is to learn the relationship between the feature extracted h by the sparse autoencoder ANN models that have been developed and the output/target API values. This study embedded a 2 layered shallow feedforward neural network model into the developed sparse autoencoder for API prediction purposes via supervised relationship learning. A shallow feedforward neural network was used as the predictor due to its robustness in relationship learning to fit practical functions and its simplicity in utilization and architectural development. The proposed model consists of 3 layers: an input layer (features extracted h by sparse autoencoder ANN), a hidden layer, and an output layer (predicted API), as illustrated in Figure 8.

$$a = \frac{2}{1+e^{-2h}} - 1 \tag{13}$$

$$\hat{y} = a \tag{14}$$

The feedforward neural network predictor was pretrained with a hyperbolic tangent sigmoid activation/transfer function, as mathematically expressed in Equation 13, to learn the nonlinear relationship and linear activation/transfer function as mathematically expressed in Equation 14 in the output layer where a is the output of hidden layer and $\hat{y}$ is the network's predicted data (predicted API). The network was trained using a scaled conjugate gradient backpropagation training function.

The list of significant feedforward neural network training parameters for API prediction is shown in Table 5. It is noted that the sparsity constraint was enforced in the dimensionality reduction (features extraction) component (autoencoder) only and not in the relationship learning component (feedforward neural network) due to its proven effectiveness in dimensionality reduction and its inability and poor performance in learning efficient mapping [23]. The feedforward neural network was adapted with weight and bias learning rules.

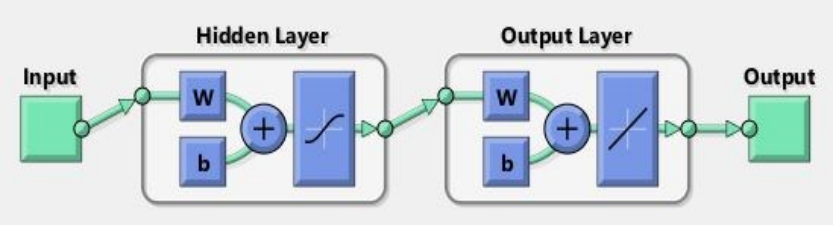


Figure 8. Shallow feedforward neural network architecture (relationship learning)

Table 5. Shallow feedforward neural network training parameters for API prediction model

| Training Parameter | Description/Value (MATLAB® Code) |
|---|---|
| Number of hidden nodes (hidden layer) | 11 |
| Activation/Transfer function (hidden layer) | Hyperbolic tangent sigmoid (tansig) |
| Activation/Transfer function (output layer) | Linear (purelin) |
| Maximum number of training epochs/iterations | 2000 |
| Training function | Scaled conjugate gradient backpropagation (trainscg) |

## 2.7. Fine Tuning of Sparse Autoencoder Artificial Neural Network (ANN) with Predictor Model

In this study, the dimensionality reduction (features extraction) component (sparse autoencoder) and the relationship learning component (feedforward neural network) were combined as a deep ANN, as shown in Figure 9, for API prediction. All of the constructed layers were pretrained in a layer-wise manner with a scaled conjugate gradient descent backpropagation algorithm being employed throughout the API prediction ANN model for optimization of each layer purpose. However, it is studied that the application of the aforementioned approach in training deep ANN may yield relatively poor performance [24-26]. This is because a deep ANN with small initial weights tends to generate tiny gradients at the bottom layers, reducing the applicability of the training ANN with numerous hidden layers; on the other hand, a deep ANN with large initial weights tends to generate relatively poor local minima [27]. Due to the complexity of the algorithm underlying the deep ANN architecture in nature, it is often challenging to preserve the relevancy between the parameters across the layers. To tackle this issue, a fine-tuning procedure was employed on the developed full sparse autoencoder ANN-based API prediction model for final joint optimization to further train the deep ANN more effectively with the fundamental goal of minimizing the prediction error [28, 29].

https://doi.org/10.31436/iiumej.v26i1.2818

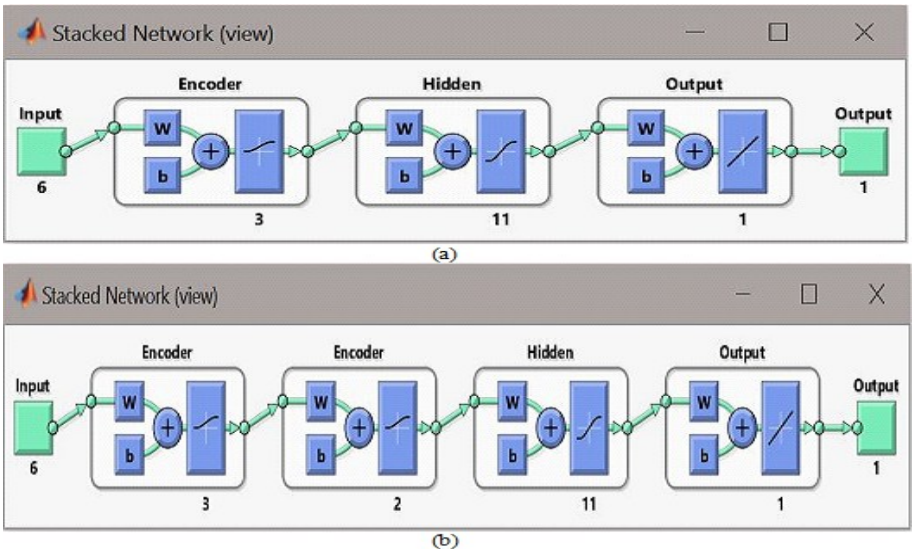


Figure 9. API prediction model architecture with: (a) shallow sparse autoencoder, (b) deep sparse autoencoder

The principal idea of this technique consists of 2 stages; the first stage is to conduct pretraining of the full deep ANN layer-wise in a bottom-up manner, and the subsequent stage is to carry out fine-tuning (updating) of the entire deep ANN parameters in a top-down fashion via a backpropagation algorithm whereby, in this study, it is the scaled conjugate gradient descent backpropagation algorithm. During the second stage, the developed deep ANN was fine-tuned by retraining the entire architecture on the training data in a supervised manner, adjusting the weights of the trained model from the final layer to optimize all the constructed layers.

### 2.8. Model Performance Evaluation

The performance of the proposed and developed sparse autoencoder ANN-based API prediction model was evaluated in terms of mean squared error $MSE$ and coefficient of determination $R^2$ between observed true API $y$ and predicted API $\hat{y}$. $MSE$ and $R^2$ are mathematically expressed as Equation 15 and Equation 16, respectively.

$$MSE = \frac{1}{m}\sum_{i=1}^{m}(y_i - \hat{y}_i)^2 \tag{15}$$

$$R^2 = 1 - \frac{\sum_{i=1}^{m}(y_i - \hat{y}_i)^2}{\sum_{i=1}^{m}\hat{y}_i^2 - \frac{\sum_{i=1}^{m}\hat{y}_i^2}{m}} \tag{16}$$

where $m$ is the total number of evaluation samples, $y_i$ is the observed true target variable data (API) of the $i^{th}$ sample, and $\hat{y}_i$ is the predicted target variable data (API) of the $i^{th}$ sample by the model. The smaller the $MSE$ and the closer the $R^2$ to the value of 1 ($R^2 \leq 1$) obtained from the model, the higher the model's performance in terms of prediction accuracy. A critical comparative analysis was performed in terms of $MSE$ and $R^2$ among FANN by [15] and PCA-FANN by [16], as proposed in previous research.

## 3. RESULTS AND DISCUSSION

The full architecture of the developed sparse autoencoder ANN-based API prediction model with shallow, sparse autoencoder and deep sparse autoencoder is shown in Figure 9(a) and Figure 9(b), respectively. The input for the API prediction model consists of the data from 6 variables: air temperature, relative humidity, wind speed, CO concentration, $O_3$

https://doi.org/10.31436/iiumej.v26i1.2818

concentration, and $PM_{10}$ concentration. The shallow sparse autoencoder was constructed with one bottleneck hidden layer, while the deep sparse autoencoder was developed with one encoding hidden layer and one bottleneck hidden layer. They played a role in dimensionality reduction (features extraction) on the input and were both connected with a shallow feedforward neural network, each for relationship learning purposes between the features captured in the bottleneck hidden layer of the respective autoencoder and the output/target variable data (API). The encoder part of the sparse autoencoder was trained with a scaled conjugate gradient descent algorithm and logistic sigmoid activation/transfer function. The hidden layer and the output layer of the feedforward neural network were both trained with scaled conjugate gradient backpropagation function and were trained with hyperbolic tangent sigmoid activation/transfer function and linear activation/transfer function, respectively.

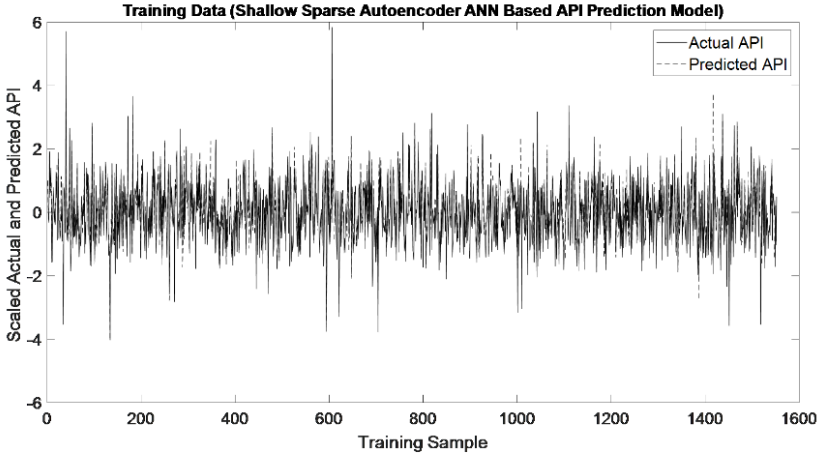


(a)

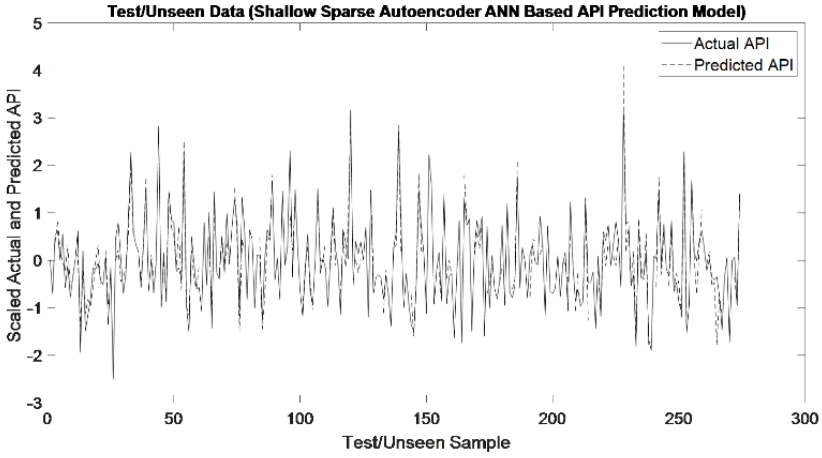


(b)

Figure 10. Actual and predicted API of (a) training sample and (b) test/unseen sample with shallow sparse autoencoder

The shallow sparse autoencoder was developed with 3 hidden nodes in its bottleneck hidden layer, while the deep sparse autoencoder was developed with 3 hidden nodes in its encoding hidden layer and 2 hidden nodes in its bottleneck hidden layer. The shallow feedforward neural network was constructed with 11 hidden nodes in its hidden layer and 1 node in its output layer. The output for the API prediction model is the predicted target variable data (API). The model was first trained with the training data set to determine the optimum model parameter values and algorithms by applying theoretical knowledge and employing trial

https://doi.org/10.31436/iiumej.v26i1.2818

and error methods. The trained model was then tested with the test/unseen data set. The API prediction model performance was evaluated in terms of $MSE$ and $R^2$ Two critical comparative analyses are being conducted: a comparative analysis between the observed true API and predicted API for both training and test/unseen data sets and a comparative analysis between the developed sparse autoencoder ANN-based API prediction model and the other prediction models proposed in previous research. Figure 10 shows the API prediction performance of the developed shallow, sparse autoencoder ANN-based model on both training and test/unseen data sets in graphical form. The x-axis is the sample number, and the y-axis is the scaled actual and predicted API.

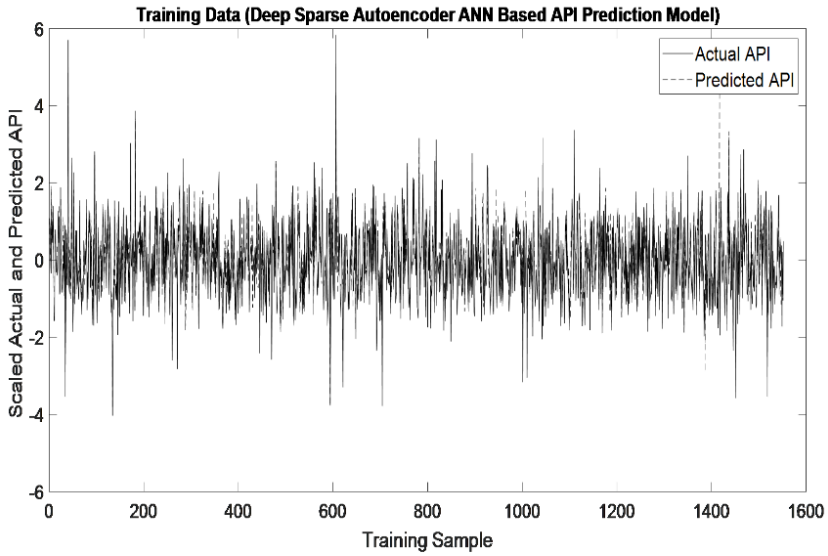


(a)

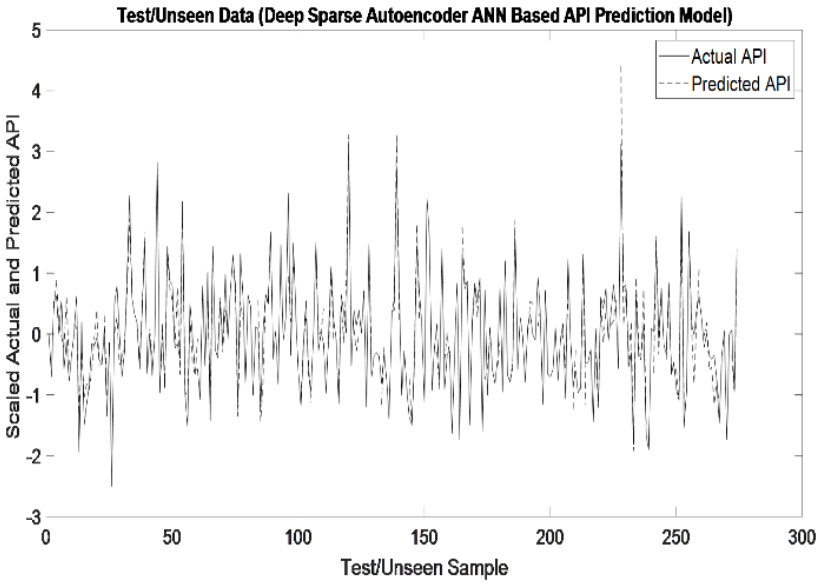


(b)

Figure 11. Actual and predicted API of (a) training sample and (b) test/unseen sample with deep sparse autoencoder

Figure 11 shows the API prediction performance of the developed deep sparse autoencoder ANN-based model on both training and test/unseen data sets in a graphical form where the x-

axis is the sample number, and the y-axis is the scaled actual and predicted API. Based on Figure 10 and Figure 11, it is clearly observed that the API prediction of the proposed shallow/deep sparse autoencoder ANN-based model emulates the actual API behavioral pattern relatively well for both training and test/unseen data.

To further evaluate the API prediction performance from a statistical point of view, the $MSE$ and $R^2$ are computed between the actual API and the predicted API on both training and test/unseen data sets to the architecture (shallow/deep) of the sparse autoencoder, which serves as the base of the proposed API prediction model as tabulated in Table 6 and illustrated in Figure 12. Based on Table 6 and Figure 12, it is observed that the predicted API values are relatively close to the actual API values of both training and test/unseen samples regardless of shallow sparse autoencoder or deep sparse autoencoder as the base of the API prediction model with low $MSE (MSE < 0.1800)$ and $R^2$ which is close to 1 $(0.8000 < R^2 < 1)$. In other words, the degree of discrepancy between the actual and predicted data by both architectures is very small. Thus, the proposed and developed sparse autoencoder ANN-based model in API prediction is proven to be valid due to the ability of the model to generalize and model the problem effectively with significantly high relevancy in target variable data prediction.

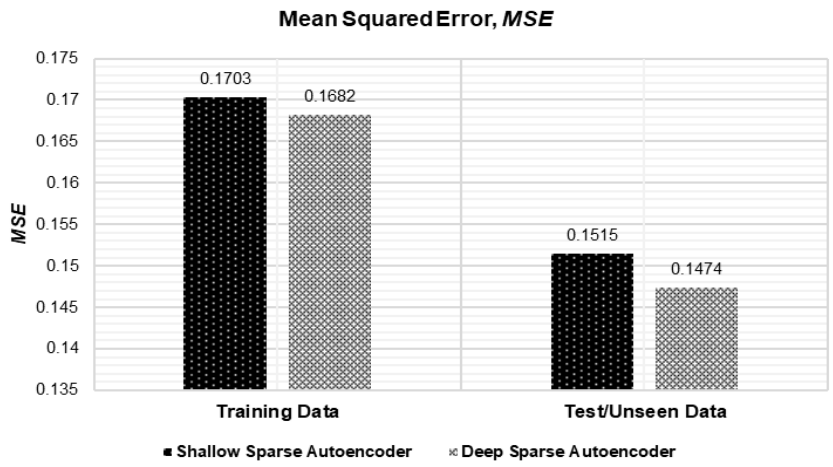


(a) MSE

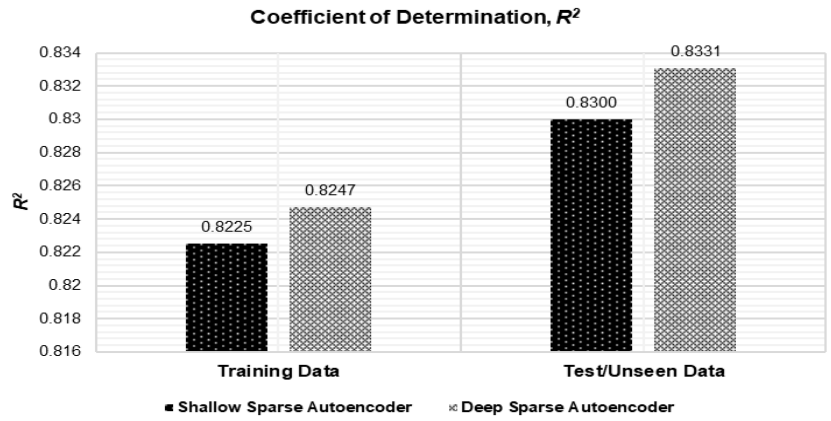


(b) $R^2$

Figure 12. Statistical analysis of the API prediction model performance

https://doi.org/10.31436/iiumej.v26i1.2818

Table 6. Statistical analysis of the API prediction model performance

| Architecture of Sparse Autoencoder | Training Data | | Test/Unseen Data | |
|---|---|---|---|---|
| | $MSE$ | $R^2$ | $MSE$ | $R^2$ |
| Shallow | 0.1703 | 0.8225 | 0.1515 | 0.8300 |
| Deep | 0.1682 | 0.8247 | 0.1474 | 0.8331 |

Besides, it is observed that the API prediction model with deep sparse autoencoder achieves higher prediction performance with higher prediction accuracy due to lower MSE and closer $R^2$ to the value of 1 obtained compared to the API prediction model with shallow sparse autoencoder. The results and findings obtained in this study are in accordance with the theoretical studies where numerous hidden layers in the deep sparse autoencoder architecture allow the ANN to learn higher-order features of the input and capture unknown data structure, further increasing the model generalization performance and effectiveness. Thus, the proposed and developed sparse autoencoder ANN-based API prediction model is further validated.

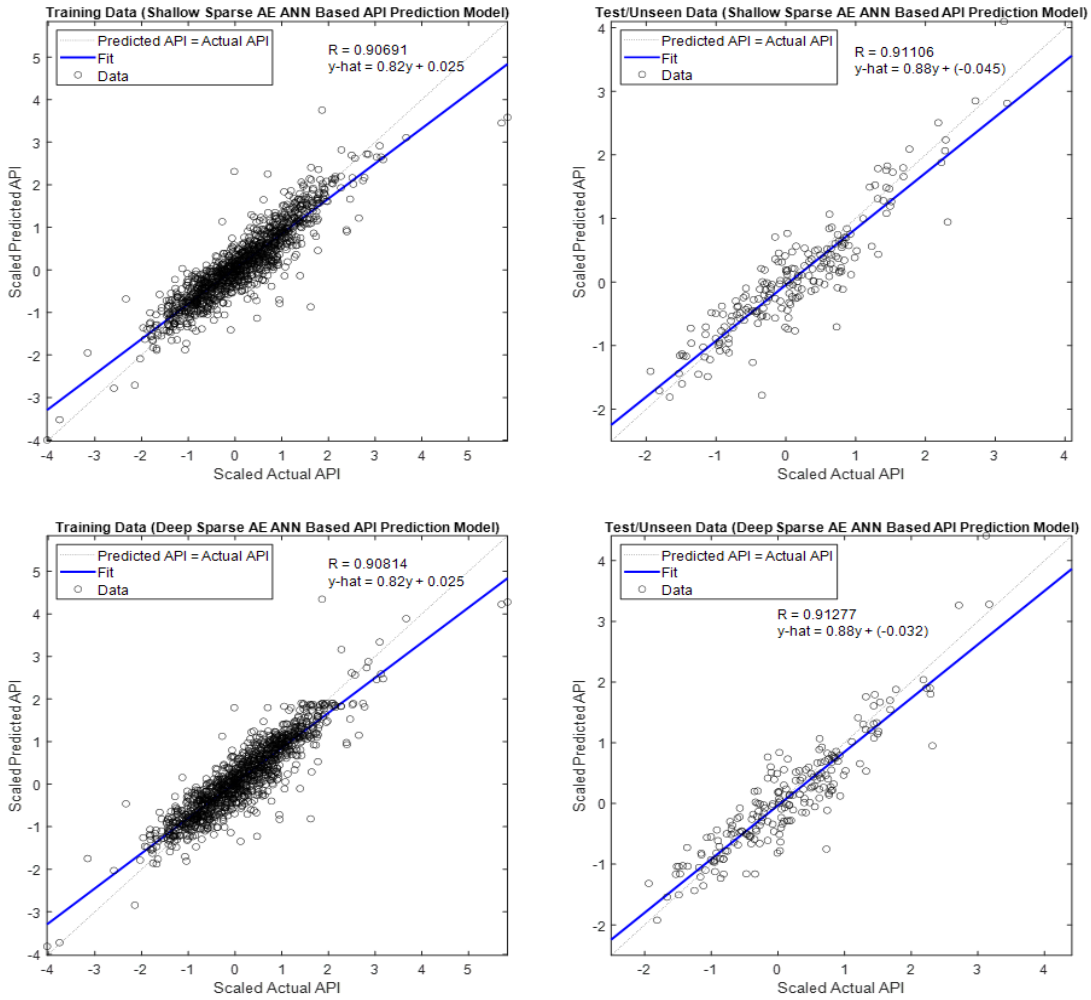


Figure 13. Linear regression plot of actual API relative to predicted API, where AE stands for 'autoencoder'

A linear regression of actual API relative to predicted API is plotted as shown in Figure 13 on both training and test/unseen data sets, each with respect to the architecture (shallow/deep) of the sparse autoencoder, which serves to be the base of the proposed API prediction model. A comparative analysis between the developed shallow/deep sparse

https://doi.org/10.31436/iiumej.v26i1.2818

autoencoder ANN-based API prediction model and other proposed API prediction models in previous research, which are feedforward artificial neural network (FANN) and principal component analysis – feedforward artificial neural network (PCA-FANN), is conducted further to validate the proposed API prediction model in this study. Table 7 presents the overall statistical analysis of the performance of all the API prediction models in terms of $MSE$ and $R^2$ on unseen data.

Table 7. Overall statistical analysis of the API prediction model performance on unseen data

| **API Prediction-Based Model** | ***MSE*** | $\boldsymbol{R^2}$ |
|---|---|---|
| Shallow sparse autoencoder | 0.1515 | 0.8300 |
| Deep sparse autoencoder | 0.1474 | 0.8331 |
| FANN from [16] | 0.1856 | 0.7950 |
| PCA from [17] | 7.5620 ($RMSE$) | 0.7360 |

Based on Table 7, it is observed that the proposed sparse autoencoder ANN-based API prediction model, regardless of shallow or deep sparse autoencoder, has the highest performance on the unseen data among the other proposed models in previous research, with $MSE$ value of 0.1515 and $R^2$ value of 0.8300 for shallow sparse autoencoder, and $MSE$ value of 0.1474 and $R^2$value of 0.8331 for deep sparse autoencoder. It is evidently clear that the proposed API prediction model in this study further improves the accuracy of API prediction. Hence, the proposed model in this study is further validated once again. the smallest $MSE$ and the largest $R^2$(closest to 1) are both achieved by the developed deep sparse autoencoder ANN-based API prediction model; thus, the model is determined to be the best model in API prediction and selected as the final model structure in this study.

The research paper demonstrated the flexible application of shallow and deep sparse autoencoder artificial neural network models, presenting a novel alternative method in the field of API prediction. The deep sparse autoencoder model, in particular, demonstrates improved prediction performance, making it a promising tool for API prediction. However, there are several limitations to this research that need to be addressed for this model to be considered the best for API prediction. Firstly, the model's training and testing are based on data from specific monitoring stations in Perak, which may limit its applicability to other regions. Secondly, the study only considers six input variables, potentially overlooking other relevant factors that could influence API prediction. Thirdly, the model uses data from 2006 to 2010, which may not reflect more recent trends or changes in air pollution patterns. Lastly, the deep sparse autoencoder, while effective, is a complex model that requires longer training times compared to simpler models. Addressing these limitations in future research could enhance the model's performance and its utility in API prediction.

## 4. CONCLUSION

This study proposed data-driven modeling for API prediction using autoencoder ANN with the fundamental objective of improving the API prediction performance. Two API prediction models were developed. One used a shallow sparse autoencoder, while the other used a deep sparse autoencoder. The model with shallow sparse autoencoder could predict the API with promising accuracy, with an $MSE$ value of 0.1515 and $R^2$ value of 0.8300 on the test/unseen data. However, the shallow sparse autoencoder may lack robustness due to the presence of only one single hidden layer in the representation of learning features. When

applied to test/unseen data, it may face difficulties and challenges. To further improve the model generalization and prediction accuracy, an API prediction model with a deep sparse autoencoder was proposed. Based on the results and findings, it is concluded that the model with the deep sparse autoencoder does improve the prediction performance compared to the model with the shallow sparse autoencoder, with $MSE$ value of 0.1474 and $R^2$ value of 0.8331 on the test/unseen data. Nevertheless, both proposed architectures are concluded to be valid as they both show significant improvement in API prediction performance with relatively small values of $MSE$ and $R^2$ values that are relatively close to 1 as compared to other API prediction models proposed in previous research. Since the proposed and developed deep sparse autoencoder ANN-based API prediction model achieved the smallest $MSE$ value with a $R^2$ value significantly close to 1, the model is, thus, determined to be the best model in API prediction and selected as the final model structure in this study.

## ACKNOWLEDGEMENT

This work was supported by Kementerian Pendidikan Malaysia (KPM) through the Fundamental Research Grant Scheme (FRGS) grant number FRGS/1/2022/TK05/USM/01/5. Special gratitude to the Department of Environmental (DOE) Malaysia for providing the air quality data for this study and Universiti Sains Malaysia (USM) for the support.

## REFERENCES

[1] Li X, Peng L, Yao X, Cui S, Hu Y, You C, Chi T (2017) Long short-term memory neural network for air pollutant concentration predictions: Method development and evaluation. Environmental Pollution 231:997-1004. https://doi.org/10.1016/j.envpol.2017.08.114

[2] Box GEP, Jenkins GM, Reinsel GC, Ljung GM (2015) Time series analysis: Forecasting and control, 5th edn. Wiley, Hoboken.

[3] Li C, Hsu NC, Tsay S-C (2011) A study on the potential applications of satellite data in air quality monitoring and forecasting. Atmospheric Environment 45:3663-3675. https://doi.org/10.1016/j.atmosenv.2011.04.032

[4] García Nieto PJ, Combarro EF, del Coz Díaz JJ, Montañés E (2013) A SVM-based regression model to study the air quality at local scale in Oviedo urban area (Northern Spain): A case study. Applied Mathematics and Computation 219(17):8923-8937. https://doi.org/10.1016/j.amc.2013.03.018.

[5] McClelland JL, Rumelhart DE (1986) A distributed model of human learning and memory. In: McClelland JL, Rumelhart DE, the PDP Research Group (eds) Parallel distributed processing: Explorations in the microstructure of cognition, Vol 2: Psychological and biological models. MIT Press, Cambridge, 170-215.

[6] Anderson JA, Silverstein JW, Ritz SA, Jones RS (1977) Distinctive features, categorical perception, and probability learning: Some applications of a neural model. Psychological Review 84(5):413-451. https://doi.org/10.1037/0033-295X.84.5.413

[7] Kohonen T (1977) Associative memory: A system-theoretical approach. Springer-Verlag, New York.

[8] Rumelhart DE, Hinton GE, Williams RJ (1986) Learning internal representations by error propagation. In: Rumelhart DE, McClelland JL (eds) Parallel distributed processing: Explorations in the microstructure of cognition, Vol 1: Foundations. MIT Press, Cambridge, 318-362.

[9] Rumelhart DE, Durbin R, Golden R, Chauvin Y (1996) Backpropagation: The basic theory. In: Smolensky P, Mozer MC, Rumelhart DE (eds) Mathematical perspectives on neural networks. Lawrence Erlbaum Associates, Mahwah, 533-566.

[10] Rumelhart DE (1989) Toward a microstructural account of human reasoning. In: Vosniadou S, Ortony A (eds) Similarity and analogical reasoning. Cambridge University Press, New York, 298-312.

[11] Baldi P, Hornik K (1989) Neural networks and principal component analysis: Learning from examples without local minima. Neural Networks 2:53-58. https://doi.org/10.1016/0893-6080(89)90014-2.

[12] Pathirage CSN, Li J, Li L, Hao H, Liu W (2018) Application of deep autoencoder model for structural condition monitoring. Journal of Systems Engineering and Electronics 29(4):873-880. https://doi.org/10.21629/JSEE.2018.04.22.

[13] Miao X, Miao H, Jia Y, Guo Y (2018) Using a stacked-autoencoder neural network model to estimate sea state bias for a radar altimeter. PLoS ONE 13(12): e0208989. https://doi.org/10.1371/journal.pone.0208989.

[14] Liu JNK, Hu Y, He Y, Chan PW, Lai L (2015) Deep neural network modeling for big data weather forecasting. In: Pedrycz W, Chen S-M (eds) Information granularity, big data, and computational intelligence. Springer, Heidelberg, 389-408.

[15] Rahim NA, Ahmad Z (2017) Graphical user interface application in Matlab environment for water and air quality process monitoring. Chemical Engineering Transactions 56:97-102. https://doi.org/10.3303/CET1756017.

[16] Ahmad Z, Rahim NA, Bahadori A, Zhang J (2017) Air pollution index prediction using multiple neural networks. International Islamic University Malaysia Engineering Journal 18(1):1-12. https://doi.org/10.31436/iiumej.v18i1.684

[17] Azid A, Juahir H, Latif MT, Zain SM, Osman MR (2013) Feed-forward artificial neural network model for air pollutant index prediction in the southern region of Peninsular Malaysia. Journal of Environmental Protection 4:1-10. https://doi.org/10.4236/jep.2013.412A1001

[18] McLoone S, Irwin GW (2001) Improving neural network training solutions using regularisation. Neurocomputing 37(1-4):71-90. https://doi.org/10.1016/S0925-2312(00)00314-3.

[19] Department of Environment, Malaysia (2012) Malaysia environmental quality report 2012. Enviro Knowledge Management Center (EKMC). https://enviro2.doe.gov.my/ekmc/digital-content/86803/. Accessed 2 January 2021.

[20] Xu G, Fang W (2016) Shape retrieval using deep autoencoder learning representation. In: Proceedings of the 13th international computer conference on wavelet active media technology and information processing (ICCWAMTIP),227-230. Institute of Electrical and Electronics Engineers. https://doi.org/10.1109/ICCWAMTIP.2016.8079843

[21] Vincent P, Larochelle H, Lajoie I, Bengio Y, Manzagol P-A (2010) Stacked denoising autoencoders: Learning useful representations in a deep network with a local denoising criterion. Journal of Machine Learning Research 11:3371-3408.

[22] Olshausen BA, Field DJ (1997) Sparse coding with an overcomplete basis set: A strategy employed by V1?. Vision Research 37(23):3311-3325. https://doi.org/10.1016/S0042-6989(97)00169-7.

[23] Pathirage CSN, Li J, Li L, Hao H, Liu W, Wang R (2019) Development and application of a deep learning-based sparse autoencoder framework for structural damage identification. Structural Health Monitoring 18(1):103-122. https://doi.org/10.1177/1475921718800363.

[24] Drucker H, Schapire R, Simard P (1993) Improving performance in neural networks using a boosting algorithm. In: Hanson SJ, Cowan JD, Giles CL (eds) Advances in neural information processing systems 5. Morgan Kaufmann Publishers, San Francisco, 42-49.

[25] Kambhatla N, Leen TK (1997) Dimension reduction by local principal component analysis. Neural Computation 9:1493-1516. https://doi.org/10.1162/neco.1997.9.7.1493

[26] Tenenbaum JB, de Silva V, Langford JC (2000) A global geometric framework for nonlinear dimensionality reduction. Science 290(5500):2319-2323. https://doi.org/10.1126/science.290.5500.2319

[27] Hinton GE, Salakhutdinov RR (2006) Reducing the dimensionality of data with neural networks. Science 313(5786):504-507. https://doi.org/10.1126/science.1127647.

[28] Hinton GE, Osindero S, Teh Y-W (2006) A fast learning algorithm for deep belief nets. Neural Computation 18(7):1527-1554. https://doi.org/10.1162/neco.2006.18.7.1527

[29] Bengio Y, Lamblin P, Popovici D, Larochelle H (2007) Greedy layer-wise training of deep networks. In: Schölkopf B, Platt J, Hofmann T (eds) Advances in neural information processing systems 19. MIT Press, Cambridge, 153-160.

https://doi.org/10.31436/iiumej.v26i1.3173

# EFFECTS OF FERMENTATION TIME AND EXTRACTION SOLVENT ON ANTIOXIDANT ACTIVITY AND TOTAL PHENOLIC AND FLAVONOID CONTENT OF PHENOLIC EXTRACT FROM ORANGE (*Citrus reticulata*) PEEL

**KHALILAN LAMBANGSARI, AGNESIA GITA REGITA, LAELY MUNAWAROH, ELEN ETHA YULINAR SIMANJUNTAK, NADIA DELFI ZAFIRA, MUHAMMAD YUSUF ABDUH***

*School of Life Sciences and Technology, Institut Teknologi Bandung (ITB)*
*Jalan Ganesha No. 10 Bandung 40132 Indonesia*

**Corresponding author: yusuf@sith.itb.ac.id*

*(Received: 18 January 2024; Accepted: 6 March 2024; Published online: 10 January 2025)*

***ABSTRACT***: The rise in consumption of oranges worldwide causes an increase in orange peel, which accounts for 30 – 35% of the orange's weight. Phenolic compounds found in orange peel are conjugated with the cell wall components. The utilization of solid-state fermentation by *Aspergillus niger* can release bound phenolic compounds from the cell wall, thereby hence increases phenolic compounds extraction. This study aims to determine the effects of the fermentation time of orange peel using *A. niger* and extraction solvents (methanol, ethanol, acetone) on the yield of orange peel extract, total phenolic content, total flavonoid content, antioxidant activity, and hesperidin content of orange peel extract. The results showed that all the parameters performed best after 3 days of fermentation. The extract yield, total phenolic content, and total flavonoid content were 34.1% (dry weight), 51.01 mg GAE/g extract, and 14.75 mg QE/g extract, respectively. Moreover, the highest antioxidant activity ($IC_{50}$ value) and hesperidin content found in orange peel were 184.32 ppm and 27.47 mg/g (dry weight) using 80% ethanol. Furthermore, the utilization of deep eutectic solvent as a biodegradable and environmentally benign substitute for organic solvents was investigated, proving that the alternative mixture of choline chloride and ethylene glycol is competitive.

***ABSTRAK:*** Peningkatan penggunaan oren di seluruh dunia menyebabkan peningkatan sisa dalam bentuk kulit oren, iaitu 30 – 35% daripada beratnya. Sebatian fenolik yang terdapat dalam kulit oren berkonjugasi dengan komponen dinding sel. Penggunaan penapaian keadaan pepejal oleh *Aspergillus niger* boleh membebaskan sebatian fenolik terikat dari dinding sel dan seterusnya meningkatkan hasil pengekstrakan sebatian fenolik. Kajian ini bertujuan untuk mengetahui pengaruh variasi dalam masa penapaian dan pemilihan pelarut terhadap hasil ekstrak kulit oren, jumlah kandungan fenolik, jumlah kandungan flavonoid, aktiviti antioksidan, dan kandungan hesperidin ekstrak kulit oren. Hasil menunjukkan bahawa selepas 3 hari penapaian semua parameter menunjukkan prestasi terbaik. Hasil ekstrak, jumlah kandungan fenolik dan jumlah kandungan flavonoid masing-masing adalah 34.1% (berat kering), 51.01 mg ekstrak GAE/g dan 14.75 mg ekstrak QE/g. Selain itu, aktiviti antioksidan tertinggi (nilai $IC_{50}$) dan kandungan hesperidin yang terdapat dalam kulit oren ialah 184.32 ppm dan 27.47 mg/g menggunakan 80% etanol. Tambahan pula, penggunaan *deep eutectic solvent* sebagai plearut yang mesra alam dan dapat terdegradasi telah dikenalpasti dan terbukti bahawa campuran alternatif kolin klorida dan etilena glikol adalah kompetitif.

***KEYWORDS:*** *Antioxidant activity, Aspergillus niger, hesperidin, orange peel, solid-state fermentation*

https://doi.org/10.31436/iiumej.v26i1.3173

# 1. INTRODUCTION

Citrus is an annual plant that bears fruit throughout the year and can grow in both tropical and subtropical climates. The most common type of citrus variety sold in the market is the orange (*Citrus reticulata*), and the total worldwide production is 104 million tons per year [1]. The food industry generally uses oranges to produce canned fruit, jam, jellies, and juice, which results in significant by-product production that accounts for around 50% of the overall weight. The percentage of peel in one orange is around 30 – 35%, making it one of the major wastes generated throughout this production [2]. The proper utilization of fruit waste is a critical issue since the amount produced each year threatens to contaminate the soil, water, and ecosystem. This waste is a significant problem for the environment because the acidic nature of the orange peel will lower the soil pH [3] causing a reduction in the solubility of oxygen in the soil, which can reduce soil fertility.

Numerous studies have been conducted to investigate approaches for increasing the value of the productive chain through the valorization of agro-industrial residue and acquiring marketable products [4-8]. Valorization of these wastes becomes attractive since the waste composition may be a source of bioactive substances, including polyphenols, sugars, essential oils, pigments, enzymes, and pectin [9]. These compounds could potentially be utilized in the agriculture sector, flavor and fragrance companies, food and beverage companies, and pharmacies as nutraceuticals. Orange (Citrus reticulata) is a popular fruit as it has significant effects such as antimutagenic, anti-inflammatory, antioxidant, antitumor, anti-atherosclerotic, and antibacterial [10]. As a result, the conversion of orange peel waste into value-added products has recently drawn more attention [2, 9, 11, 12]. Orange peel consists of an outer part (flavedo), which is rich in essential oils and carotenoids, and an inner part (albedo), which is rich in lignocellulose, pectin, and phenolics [13]. Phenolics are compounds mostly found in plants that have hydroxyl groups and are produced in response to environmental stress to counter its effects. As a result, phenolic compounds function as antioxidants, antimicrobials, and anti-inflammatory [14, 15]. The total phenolic content of orange peel ranges from 1.39 to 1.85 mg GAE/100 g dry biomass [16, 17].

Orange peel contains lignocellulose, which is the main ingredient in plant cell walls consisting of hemicellulose, cellulose, and lignin [18]. Phenolic compounds generally exist in a conjugated form with cell wall components. Extracts of phenolic compounds can be obtained by providing pre-treatment in fermentation. Solid state fermentation is an alternative method that can release cell-wall bound bioactive compounds by degrading the components of the cell wall to facilitate contact of the solvent with the compound to be isolated [19]. Aspergillus niger is one of the fungi that can be utilized in the fermentation process. This is because A. niger produces the enzymes cellulase, xylanase, and ligninase, which break down lignocellulosic materials to facilitate the release of phenolic chemicals [20, 21]. In recent studies, no initial treatment was given in the form of fermentation. Therefore, in this study, fermentation was carried out using A. niger to degrade lignocellulose in orange peel to increase extraction yield, total phenolic content, total flavonoid content, antioxidant activity, and hesperidin content in orange peel extract.

Extraction is an important step in isolating, identifying, and quantifying phenolic compounds in plants. In this study, the maceration extraction method used ethanol, methanol, and acetone as organic solvents. Maceration is the simplest extraction method for isolating polyphenolic compounds from plant materials [22]. Many previous studies reported the content of phenolic compounds in orange peel from different origins and varieties. In the study of Safdar et al. [23], the yield of Kinnow orange peel (C. reticulata L.) phenolic compound

https://doi.org/10.31436/iiumej.v26i1.3173

extracts using ethanol, methanol, and acetone was 18.46%, 14.5%, and 8% respectively. Whereas in the study of Hegazy & Ibrahium [24], the yield of orange peel phenolic compound extracts using ethanol, methanol, and acetone solvents was 27.96%, 28.32%, and 18.21%, respectively.

However, large-scale consumption of organic solvents can harm the environment and pose health risks to humans [25]. Thus, the idea of extracting valuable molecules from biomass using green solvents is increasingly being considered. Deep eutectic solvent (DES) is a promising alternative for organic solvents as they are low cost, renewable, environmentally friendly, non-toxic, and biodegradable [26]. A previous study by Xu et al. [27] showed that choline chloride: levulinic acid: n-methyl urea outperformed several organic solvents such as methanol, ethanol, and n-butanol in polyphenols extraction from citrus peel waste. This study aims to use various solvents, ranging from organic solvents to choline chloride-based DES to extract and recover phenolic compounds from orange peel waste. The extraction capabilities of different types of solvents are examined.

## 2. MATERIALS AND METHODS

### 2.1. Materials

Fresh oranges (*Citrus reticulata*) used in this study were obtained from plantations in Ciwidey, West Bandung, West Java, Indonesia. The commercial culture of *A. niger* was obtained from the Nanobio Laboratory. Analytical grade hesperidin (98%) used as a standard compound in this study was obtained from Markherb. Ethanol, methanol, acetone, ethylene glycol, lactic acid, sodium hydroxide (NaOH), potassium sulfate ($K_2SO_4$), copper (II) sulfate ($CuSO_4$), hydrochloric acid (HCl), boric acid ($H_3BO_3$), aluminum chloride ($AlCl_3$), sulfuric acid ($H_2SO_4$), nitric acid ($HNO_3$), acetic acid ($CH_3COOH$), sodium carbonate ($Na_2CO_3$), Folin-Ciocalteu reagent, and gallic acid were obtained from Merck, while DPPH reagent (2,2-diphenyl-1-picrylhydrazyl) was from Sigma. Choline chloride was from MaxLab, Quercetin was from Nitrakimia, magnesium sulfate ($MgSO_4$) was from Pudak Scientific, potassium phosphate ($KH_2PO_4$) was from Kimia Market, yeast extract was from HiMedia, and calcium chloride ($CaCl_2$) was from Pharmapreneur store.

### 2.2. Preparation of orange peel

The fresh oranges were peeled off, and the peel was washed with water and divided into tiny (1×1 cm) pieces. The whole orange peel was then dried in an oven at 60°C for 24 hours until the moisture content was 15%, followed by crushing using a dry miller (Miyako blender BL-152GF 300 W) and then sieved using a 60-mesh sieve to obtain a size of 0.25 mm [28].

### 2.3. Proximate analysis of orange peel

Proximate analysis was applied to determine the moisture, protein, lipid, carbohydrate, and ash content of orange peel samples used in this study. The proximate analysis of the samples was performed with three repetitions, and a gravimetric approach was applied to measure the moisture content. The protein content was determined using the Kjeldahl method, whereas the lipid content was assessed using the Soxhlet method. The samples were dried in a furnace at 600°C for 6 hours to determine the ash content, while the carbohydrate content was determined using the by-difference approach.

### 2.4. Solid-state fermentation of orange peel using *A. niger*

The solid-state fermentation was carried out under aseptic conditions using trays, with each tray containing 250 g orange peel mixed with a salt solution containing 3.4 g yeast extract, 0.09 g $CaCl_2.2H_2O$, 1.3 g $KH_2PO_4$, 6.6 g glucose, and 3.3 g $MgSO_4.7H_2O$ in 100 g of orange peel. Subsequently, distilled water was added to the mixture with a ratio of 1:2 (v/w) [20, 21]. Following that, a 3:20 fungus-to-substrate ratio was used to inoculate *A. niger*, which had a cell count of 4 x $10^8$ CFU/g, and the fermentation was carried out for 7 days at 27°C, 76% humidity, and 0 W/$m^2$ light intensity [29].

### 2.5. Determination of *A. niger* growth curve

The growth curve of *A. niger* was determined based on the daily measured dry weight of the biomass [30]. Approximately 7 g ($m_1$) of a fresh fermented mixture was dried at 60°C for 4 hours, and after that, the dried biomass was weighed again ($m_2$). A mixture of acetic acid solution (80%) and pure nitric acid reagent was then added to the fermented mixture with a ratio of 1:10 and then incubated for 30 minutes in a water bath at a temperature of 55°C and a stirring speed of 120 rpm followed by treatment with acid and then dried once more in an oven set at 60°C for 4 hours ($m_3$). The dry biomass and specific growth rate of *A. niger* were calculated using Eq. (1) and Eq. (2), respectively.

$$\text{Dry biomass } \left(\frac{g}{g}\right) = \frac{m_3\,(g) - m_2\,(g)}{m_1(g)} \quad (1)$$

$$\mu = \frac{lnX_t - lnX_0}{\Delta t} \quad (2)$$

where μ is the growth rate (hour-1), $X_t$ is the amount of dry biomass at the end of the exponential phase (g), $X_0$ is the amount of dry biomass at the beginning of the exponential phase (g), and Δt is the difference in observation time or the length of the logarithmic phase.

### 2.6. Determination of lignocellulosic content

The lignocellulosic content in the biomass was determined using the method of Chesson-Datta [31]. Approximately 4 g of dried orange peel sample ($m_1$) were mixed with 200 mL of distilled water, followed by 2 hours of refluxing at 100°C before filtration. The filtrate was then washed using 300 mL of hot water and dried in an oven at 105ºC for approximately 2 hours, and the weight remained constant ($m_2$). After that, the residue was added to 300 mL of 1 N $H_2SO_4$ and refluxed for 2 hours at 100°C, followed by filtration. The residue was then washed with 300 mL of hot water, dried in an oven at 105ºC for 2 hours, and then weighed ($m_3$). Next, the dry residue was soaked in 10 mL of 72% $H_2SO_4$ for 4 hours at room temperature (27ºC). After that, 300 mL of 1 N $H_2SO_4$ was added, followed by reflux at 100°C for 2 hours before being filtered. The residue was washed again with 300 mL of hot water, dried in an oven at 105ºC for 2 hours, and then weighed ($m_4$). Lastly, the residue was placed in a furnace set at 600ºC to measure the amount of ash ($m_5$). The determination of lignocellulosic content was carried out 3 times for each fermentation time. The levels of hemicellulose, cellulose, and lignin can be determined by Eq. (3), (4), and (5).

$$Hemicellulose(\%) = \frac{m_2\,(g) - m_3(g)}{m_1(g)} \times 100 \quad (3)$$

$$Cellulose(\%) = \frac{m_3(g) - m_4(g)}{m_1(g)} \times 100 \quad (4)$$

$$Lignin(\%) = \frac{m_4(g) - m_5(g)}{m_1(g)} \times 100 \quad (5)$$

https://doi.org/10.31436/iiumej.v26i1.3173

where $m_1$ is the initial mass of dried orange peel, $m_2$ is the mass of dried orange peel after refluxing using distilled water, $m_3$ is the mass of dried orange peel using reflux using 1 N $H_2SO_4$, $m_4$ is the mass of dried orange peel after immersion using 72% $H_2SO_4$ and reflux using 1 N $H_2SO_4$ N, $m_5$ is the ash of orange peel. The lignocellulose content of orange peel was calculated on the first, third, fifth, and seventh days of fermentation.

### 2.7. Preparation of Deep Eutectic Solvent

Three different DES were prepared following the procedure described by Dai [32]. Choline chloride was used as a hydrogen bond acceptor (HBA), while glycerol, ethylene glycol, or lactic acid were used as hydrogen bond donors (HBD). The compounds were weighed using an analytical balance (New Classic MS, Mettler Toledo) with an accuracy of ± 0.0001 g according to the required molar ratio. Subsequently, HBA and HBD mixtures at appropriate ratios were stirred and heated at 50ºC until a homogeneous transparent liquid was formed. The complete list of DES abbreviations and organic solvents utilized in this study is provided in Table 1.

Table 1. Deep Eutectic Solvents and organic solvents used for orange peel extraction

| Solvent | Molar ratio | Water content (%) | Abbreviation |
|---|---|---|---|
| Choline chloride: Glycerol | 1:2 | 10 | ChCl: Gly |
| Choline chloride: Lactic acid | 1:1 | 10 | ChCl: LA |
| Choline chloride: Ethylene glycol | 1:2 | 10 | ChCl: EG |
| Acetone | - | 20 | Acetone |
| Ethanol | - | 20 | Ethanol |
| Methanol | - | 20 | Methanol |

### 2.8. Extraction of orange peel

10 grams of dried orange peel were placed inside an Erlenmeyer flask and added to each organic solvent and DES sample with a solid-liquid ratio of 1:10 (w/v). Extractions were conducted in three replicates at 60ºC with 400 rpm stirring speed for 2 hours using an incubator shaker. An ultrasound-assisted extraction at room temperature **(**27°C**)** for 30 minutes with a sample-solvent ratio of 1:20 (w/v) was carried out as an initial screening step to select the DES for further experimentation [27]. The empty flask was weighed using an analytical balance (m1) to calculate the yield extract. Subsequently, the organic solvents were evaporated using a rotary vacuum evaporator to obtain a crude extract. The flasks containing the orange peel extract were weighed to determine the orange peel extract ($m_2$). The yield of the orange peel extract was determined 3 times for each fermentation time. The yield of the orange peel extract was calculated using Eq. (6). Following that, the samples were filtered using Whatman No. 1 paper and stored at 4°C in dark tubes for further analysis.

$$Yield\ extract\ (\%) = \frac{m_2(g) - m_1(g)}{m_3(g)} \times 100 \quad (6)$$

### 2.9. Determination of hesperidin content

The hesperidin content in the orange peel extract was identified using high-performance liquid chromatography (HPLC). An Agilent 1100 LC system (Agilent, Santa Clara, CA, USA) equipped with a Zorbax SB-C18 reversed-phase column (150 × 4.6 mm, 5 µm) was used. The mobile phase consisted of isocratic elution with a low-pressure gradient using double-distilled water HPLC grade and methanol HPLC grade (65:35). The flow rate was set at 1.0 mL/min, and the column temperature was maintained at 40°C. The injection volume was 20 µl, and peaks were monitored at 280 nm. As much as 6 points dilutions of the standard solution were

made by diluting the hesperidin standard compound in HPLC methanol with a range of 2.5 – 100 ppm. Before any injection, both the standard and samples were filtered through a 0.22 µm membrane filter. To quantify hesperidin content, retention times of hesperidin were 98% as the standard was considered, and extracts were identified based on the retention times and order of elution with respect to standards [33].

### 2.10. Determination of Total Phenolic Content

The Folin-Ciocalteu method was used to calculate the total phenolic content of the extracts, and gallic acid was chosen as the reference standard for the calibration curve. Briefly, 100 mg of gallic acid was dissolved in 1 L of 80% ethanol before being diluted to produce solutions with concentrations of 2, 8, 20, 32, 64, and 90 ppm. After establishing the standard curve, the mixture containing 2.5 mL of 10% Folin-Ciocalteau reagent and 2.5 mL of 7.5% $Na_2CO_3$ was added to 0.5 mL of extracts. The mixture was then vortexed until uniform and incubated for 30 minutes in the dark. A UV/Vis spectroscopy with a 765 nm wavelength was used to measure the absorbance, and the results were represented as mg of gallic acid equivalent (GAE) per gram of orange peel [23].

### 2.11. Determination of Total Flavonoid Content

The total flavonoid content in this study was measured using the calorimetry test adapted from Chandra [27]. The quercetin solution was made by weighing 5 mg of quercetin that had been dissolved in 1 mL of ethanol (5000 ppm). With the quercetin solution diluted, concentrations of 5, 10, 15, 20, 25, 30, and 40 ppm were obtained. Approximately 2 mL of the dilution solution was then added to 2 mL of 2% $AlCl_3$ prior to incubation for 60 minutes at room temperature. The analysis was done using UV-Vis spectroscopy, with the wavelength used to measure absorbance 420 nm. Then, 2 mL of a 5000-ppm orange extract and 2 mL of 2% $AlCl_3$ were incubated at room temperature **(**27°C**)** for 60 minutes. The value of the total flavonoid content was calculated using the standard curve equation that had been obtained, and the results were expressed in mg QE/g extract [34].

### 2.12. Determination of antioxidant activity

The DPPH free radical scavenging capacity of the orange peel extract was determined as described by Molyneux [35]. A solution of 50 µM DPPH was prepared in ethanol. The mixture containing 1 mL of the diluted sample and 4 mL of 50 µM DPPH solution was then homogenized using a vortex and incubated for 30 minutes in a dark room. The absorbance was measured using a UV-Vis spectrophotometer at a wavelength of 514 nm for each solvent extraction. The antioxidant activity was determined by Eq. (7).

$$Antioxidant\ activity = DPPH\ Scavenging\ activity\ (\%) = \frac{A_{blank} - A_{sample}}{A_{blank}} \times 100 \quad (7)$$

### 2.13. Statistical analysis

Statistical analysis carried out in this study included one-way ANOVA, post-hoc testing through Duncan's test, and correlation testing between research parameters through Pearson Coefficient Correlation and P-values using SPSS Statistics 26 software. The one-way ANOVA test ($P < 0.05$) aimed to determine the significance of the results obtained from the extraction of phenolic compounds, whereas post-hoc testing aimed to determine whether there were significant differences between data from one group to another. The correlation testing aimed to determine the level of closeness of the relationship between research parameters [30].

https://doi.org/10.31436/iiumej.v26i1.3173

# 3. RESULTS AND DISCUSSIONS

## 3.1. Proximate analysis of orange peel and growth of *A. niger*

The proximate analysis was carried out to determine the moisture, ash, protein, lipid, and carbohydrate contents of the orange peel, and the results are shown in Table 2.

Table 2. Moisture, ash, protein, lipid, and carbohydrate content of orange peel

| Content | This study | References |
|---|---|---|
| Moisture (%) | 84.63 ± 0.75 | 75 – 90 [10] |
| Ash (%) | 2.23 ± 0.03 | 2 – 4 [31] |
| Protein (%) | 6.27 ± 0.97 | 6 – 9 [31] |
| Lipid (%) | 2.43 ± 0.15 | 2 – 6 [31] |
| Carbohydrate (%) | 4.43 ± 0.43 | 7.13 [29] |

The moisture, ash, protein, and lipid content of the orange peel investigated in the study are within the range of previous values reported by de la Torre et al. [36] and Bruinhorst et al. [37]. Slight variations in the carbohydrate content may be due to the differences in geographical locations and meteorological conditions [38].

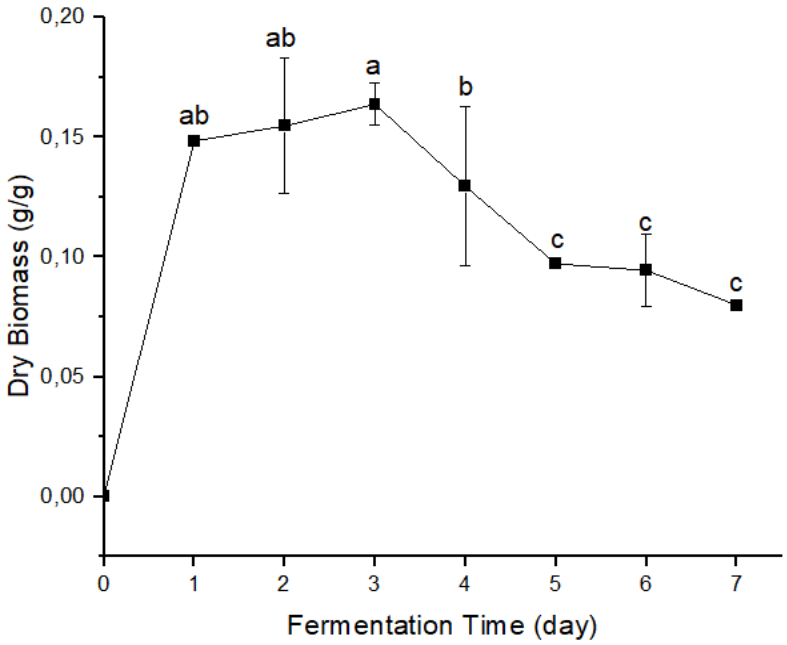


Figure 1. Growth curve of *A. niger* based on dry weight.

The specific growth rate of A. niger found in this study was 0.002 hour-1. From the growth curve of A. niger as shown in Figure 1, it can be observed that the growth increased considerably from the first day up to the third day of fermentation before then slowed down throughout the remaining fermentation period due to the decrease in nutrients supporting the growth of A. niger present in the fermentation medium [38]. These results are in line with the results obtained by Kuivanen et al. [39], which found that A. niger grew best on an orange peel substrate between 2 to 4 days.

https://doi.org/10.31436/iiumej.v26i1.3173

### 3.2. Effects of fermentation on biodegradation of lignocellulose

The lignocellulose content of the orange peel investigated in this study is shown in Table 3. A. niger is capable of decomposing cellulose and hemicellulose into saccharides to be used as an organic carbon source for metabolic growth [19]. Consequently, there is a clear relationship between the decrease in lignocellulosic content and the increase in fungal biomass. The weight of the dry biomass increased during the exponential phase while the lignocellulosic content sharply dropped. According to Augustine et al. [40], the fungus was particularly active in manufacturing its extracellular enzymes throughout the early to late exponential phases. This indicates that A. niger actively grew and produced many cellulolytic enzymes from day 1 to day 3 to digest complex polysaccharides like lignocellulose and use them as a source of organic carbon [41]. The percentage of degradation during the fermentation period is shown in Table 4 and Figure 2.

Table 3. Lignocellulose content of orange peel without fermentation treatment

| Component | Content (%) |
|---|---|
| Hemicellulose | 27.67 ± 0.84 |
| Cellulose | 11.43 ± 1.25 |
| Lignin | 7.19 ± 0.57 |

Table 4. Lignocellulose degradation of orange peel during fermentation

| Fermentation time (day) | Percentage of degradation (%) | | |
|---|---|---|---|
| | Hemicellulose | Cellulose | Lignin |
| 1 | 28.17 | 3.76 | 16.79 |
| 3 | 40.34 | 5.09 | 35.97 |
| 5 | 49.53 | 9.94 | 11.23 |
| 7 | 62.56 | 46.63 | 39.97 |

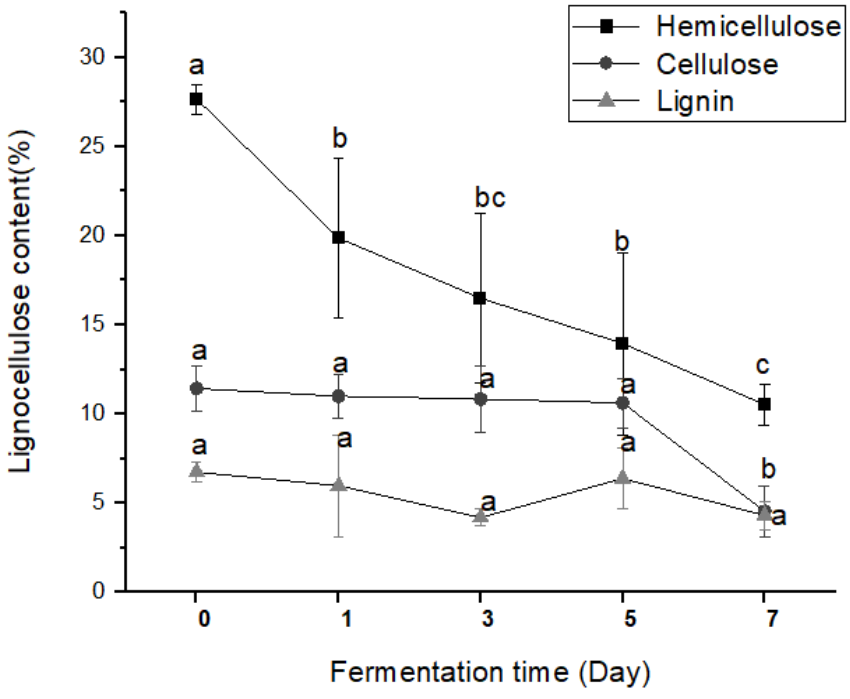


Figure 2. Lignocellulose content of orange peel on variations in fermentation time.

https://doi.org/10.31436/iiumej.v26i1.3173

Initially, the hemicellulose, cellulose, and lignin content were 27.67 ± 0.84, 11.43% ± 1.25, and 7.19% ± 1.25, respectively. All components exhibited a decreasing profile, and after 7 days of fermentation, the hemicellulose, cellulose, and lignin eventually dropped to 62.56%, 46.63%, and 39.97%, respectively. This may highlight that A. niger is able to degrade lignocellulose due to the presence of xylanase, cellulase, α-amylase, and β-glucosidase that can selectively and efficiently hydrolyze the lignocellulosic matrix in plant cell walls [42].

### 3.3. Effects of fermentation time and extraction solvent on the yield of orange peel extract

Unfermented (day 0) and fermented orange peel samples (1, 3, 5, and 7 days) were extracted using different organic solvents (80% ethanol, 80% methanol, and 80% acetone), and the results are shown in Figure 3. The yield of orange peel extract following A. niger fermentation tends to be higher than the yield of orange peel extracts without fermentation. For unfermented biomass, the highest yield (33.1%, dry weight) of orange peel extract was obtained when the extraction was carried out using 80% methanol, followed by 80% ethanol and 80% acetone. This value is higher than the orange peel extract of 27.3% for 30 minutes using alkaline hot water [43].

The maximum yield of 34.1% was achieved on the third day of fermentation using 80% methanol, while the lowest yield (17.1%, dry weight) was obtained when the extraction was carried out using 80% acetone. Santos da Silveira, et al. [44] assert that the conjugate bonds between phenolic chemicals and polysaccharides in plant cell walls can be broken by the cellulolytic enzyme complex produced by A. niger, and that this can boost the yield of phenolic extracts. As a result, phenolic compounds may become more soluble in the organic solvents used in the extraction process. The quantity of orange peel extract did, however, start to decline after the third day of fermentation. This is a result of A. niger biomass's diminished capacity to release enzymes because of its slower growth after the fourth day of fermentation.

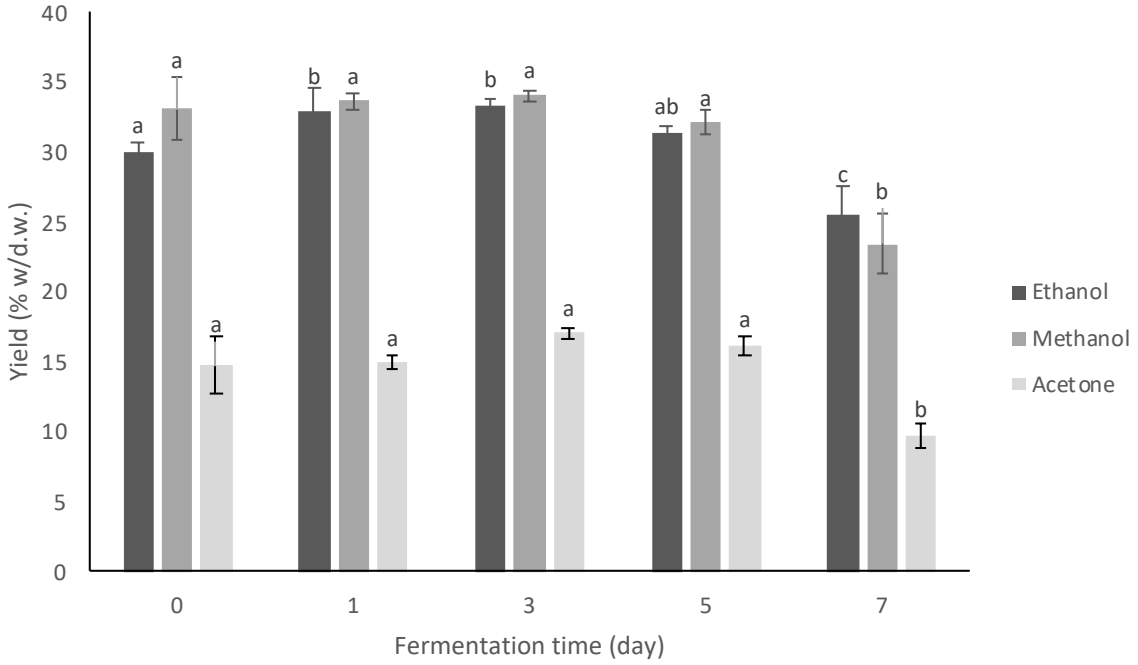


Figure 3. Yield of orange peel extract with variations of solvent ethanol 80%, methanol 80%, and acetone 80%.

The degree of polarity of the solvent plays an important role in determining the yield of orange peel extract. Since phenolic compounds are polar, they tend to dissolve in polar solvents

https://doi.org/10.31436/iiumej.v26i1.3173

[45]. At 20oC, methanol has a dielectric constant of 32.35, and ethanol has a dielectric constant of 25.00; both values are larger than the dielectric constant of acetone, which is 19.56 [46]. Accordingly, methanol is more polar than ethanol and acetone. The gain will rise in proportion to the solvent's polarity level. Because methanol has greater polar characteristics than ethanol and acetone, the yield of orange peel extract extracted using methanol solvent is higher.

### 3.4. Effects of fermentation time and extraction solvent on hesperidin content of orange peel extract

Figure 4 illustrates that the hesperidin content reached its highest point after three days of fermentation. The obtained value of the extraction yield, which peaks on the third day of fermentation, is in line with this result. These findings indicate that pre-treating orange peel extract with solid-state fermentation increases the amount of hesperidin by 1.67 times. These findings align with [47], who obtained hesperidin compound in the Geotrichum candidum fermented extract by 1.96 times greater than without fermentation when extracting flavonoids from orange peel. Meanwhile, the decrease in hesperidin content after the third to seventh day of fermentation may be caused by the conversion of hesperidin to hesperetin after the third day of fermentation [48]. Lee et al. [49] reported that Aspergillus sp. produces mannosidase, which releases the rhamnose sugar group from hesperidin and converts it into hesperetin-7-O-glucosidase which is then converted to hesperidin by the enzyme β-glucosidase.

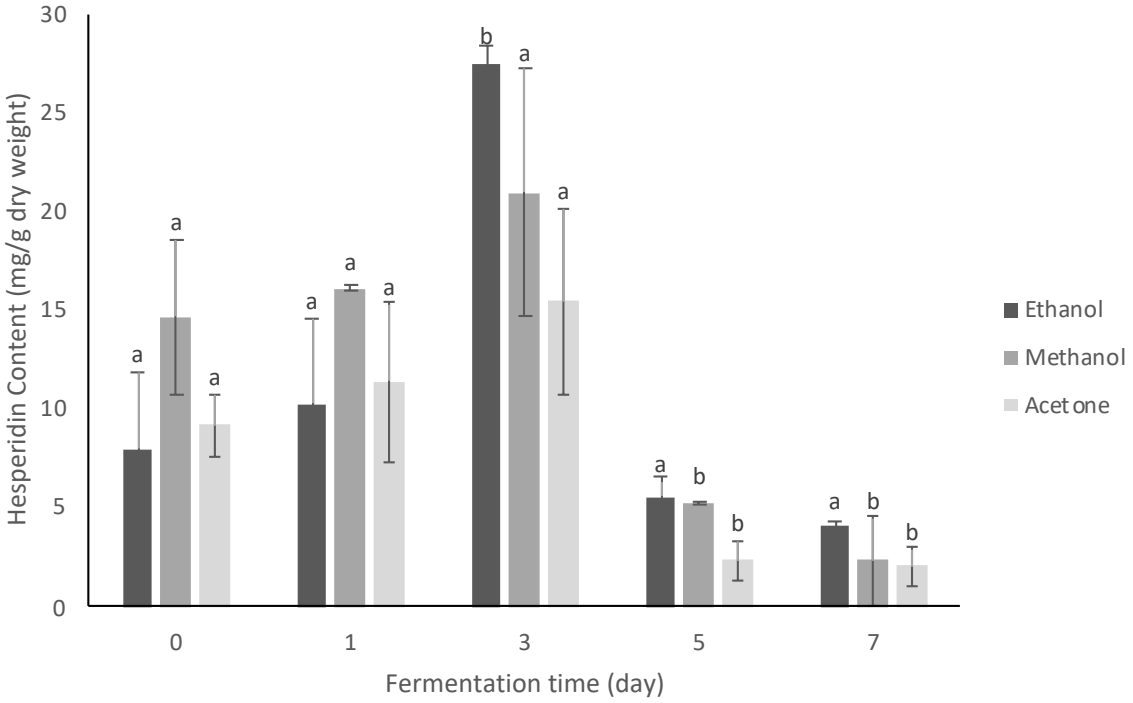


Figure 4. Hesperidin content in C. reticulata peel extract using ethanol 80%, methanol 80%, and acetone 80%.

Compared to methanol and acetone, the hesperidin content with ethanol as an extraction solvent has the highest value. This result is confirmed by Kim and Lim [50], which demonstrated that orange pomace (Citrus unshiu) extracted with ethanol had the highest hesperidin level, followed by acetone and methanol. In contrast, Samota, et al. [51] found that hesperidin content in orange peel extract (C. reticulata) using methanol as the solvent is higher than when ethanol was used. Different orange varieties, solvent concentrations, and extraction parameters such as temperature and time can all contribute to different results. In general,

https://doi.org/10.31436/iiumej.v26i1.3173

ethanol is a suitable extraction solvent for flavonoids and their glycosides, catechol, and tannins; methanol for phenolic acids and catechins; and acetone for high molecular weight polyphenols such as proanthocyanidins and tannins.

This study also carried out preliminary studies on utilizing deep eutectic solvents as a sustainable alternative to organic solvents. The initial step involved screening for glycerol, lactic acid, and ethylene glycol as three different sources of hydrogen bond donors of DES. In this screening, fermented orange peel from day 3 of fermentation was used for the DES extraction as the best result. Figure 5 depicts the results of the hesperidin content analysis.

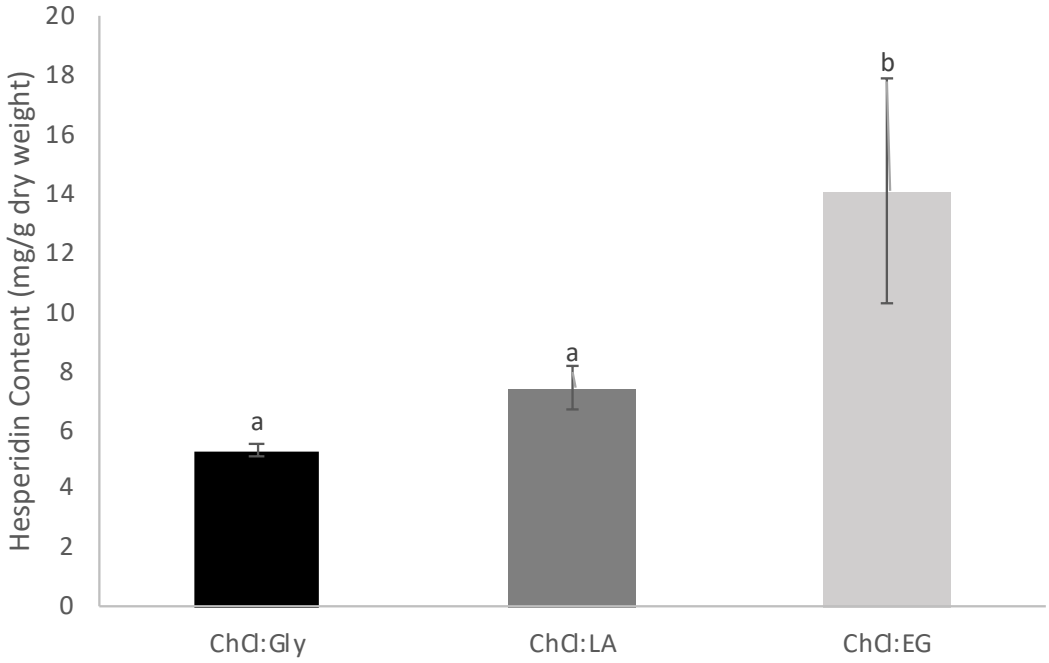


Figure 5. Screening of deep eutectic solvent for extraction of hesperidin from C. reticulata.

The DES produced the highest amount of hesperidin consisting of choline chloride and ethylene glycol, at 14.08 mg/g of dried fermented orange peel. As ChCl was used as HBA in all DES systems, the ultimate physicochemical properties of the used DES depend on the chemical structures of the HBD. In this study, the viscosity of ChCl: Gly, ChCl: LA, and ChCl: EG at 30ºC were 188 mPa.s, 508.17 mPa.s, and 35 mPa.s, respectively [27, 52, 53]. DES consists of ethylene glycol, creating a solvent with lower viscosity than lactic acid and glycerol as hydrogen bond donors. Low-viscosity DES is regarded as an effective extractants because low viscosities can facilitate the mass transfer of target chemicals to the DES solution [54]. These findings align with the previous results obtained by Xu et al. [27] all three types of DES followed the same trend when extracting freeze-dried orange peel. Hence, DES, which consists of choline chloride and ethylene glycol, was selected and further used to compare its performance with previously used organic solvents.

The extraction of hesperidin was conducted at 60°C for 120 minutes using an organic solvent. 80% ethanol extracted 27.47 mg/g of hesperidin under these conditions. In contrast, ChCl: EG could only extract 12.5 mg/g of the sample under the same conditions. However, using DES at a higher temperature of 70, the hesperidin yield continued to climb, reaching 17.6 mg/g, as indicated in Figure 6. A previous study [55] showed the potential of choline chloride-based DES utilization, which proved more effective than ethanol in extracting polyphenols

https://doi.org/10.31436/iiumej.v26i1.3173

from orange waste. Therefore, further optimization studies are necessary to explore the capacity of ChCl further: EG to extract hesperidin

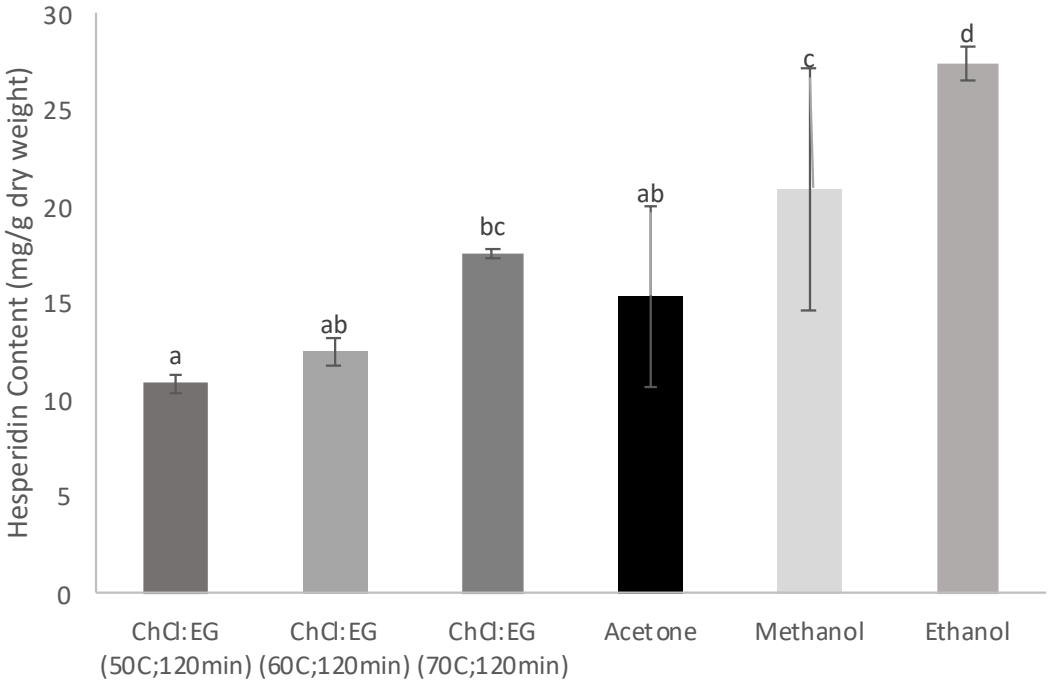


Figure 6. Comparison of hesperidin content using DES and organic solvents after three days of fermentation

### 3.5. Effects of fermentation time and extraction solvent on total phenolic and flavonoid content of orange peel extract

Figure 7 illustrates the effects of fermentation time and extracting solvent on the orange peel extract's total phenolic content and flavonoid content. The orange peel extract with 80% methanol, 80% ethanol, and 80% acetone for unfermented samples had a total phenolic content of 25.61 ± 1.77 mg GAE/g extract, 20.11 ± 2.04 mg GAE/g extract, and 38.23 ± 3.49 mg GAE/g and total flavonoid content of 3.63 ± 0.124 mg QE/g extract, 3.78 ± 0.22 mg QE/g extract, and 6.1 ± 0.97 mg QE/g extract, respectively. The trend of total phenol content during the fermentation period is strongly associated with the total flavonoid content, as shown in Figures 7(a) and 7(b). The overall concentration of flavonoids and phenols increased from the first to the third day of fermentation, then decreased from the fourth to the seventh day. The total phenol concentration and the total flavonoid content were highest on the third day of fermentation. Table 5 displays each solvent's TPC and TFC values, including the DES.

https://doi.org/10.31436/iiumej.v26i1.3173

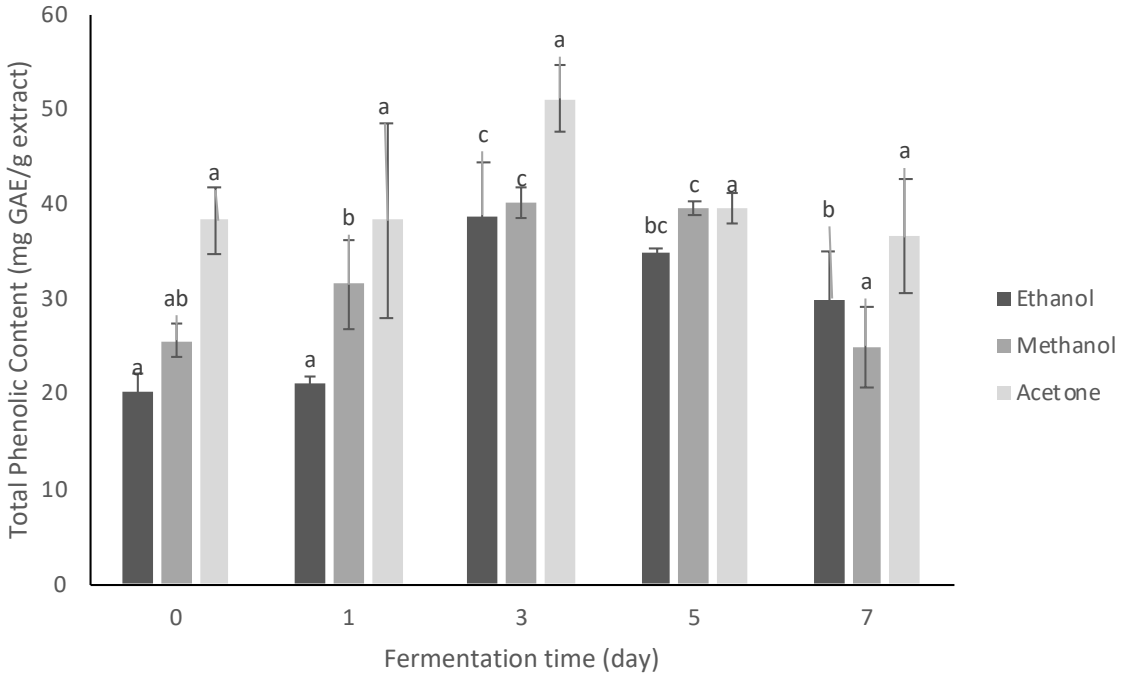


(a)

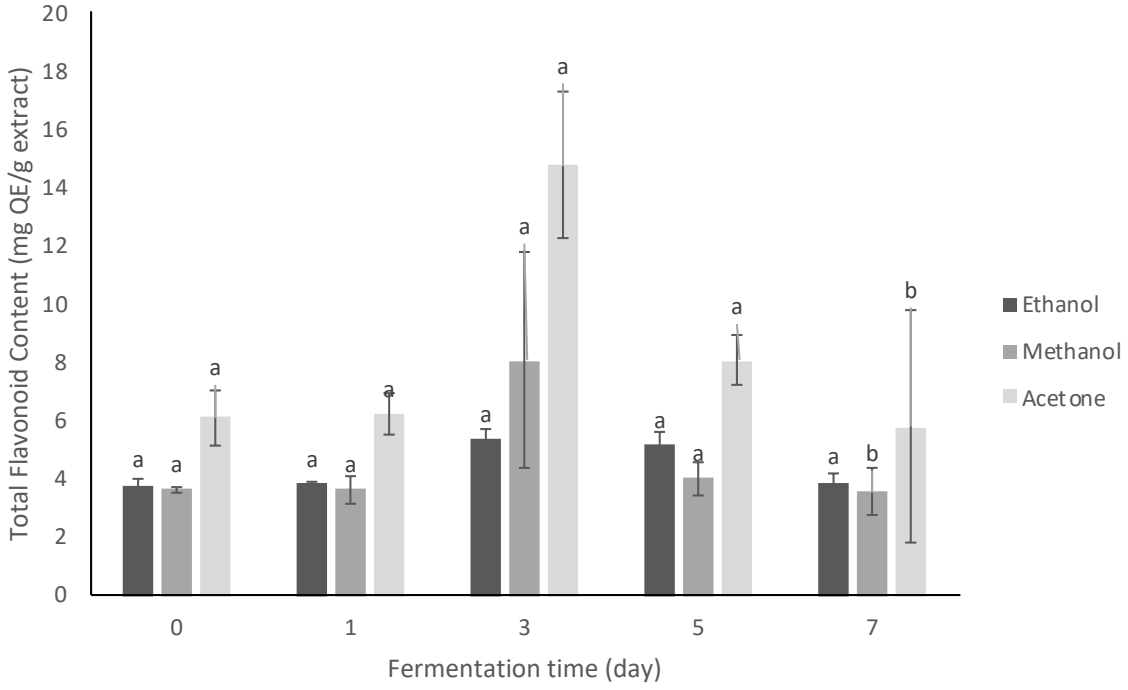


(b)

Figure 7. Total phenolic content (a) and total flavonoid content (b) of C. reticulata peel extract using different solvents.

Most phenols are in the conjugated form in plants, where one or more sugar residues are joined to hydroxyl groups. The amount of free phenolic in the orange peel, which was utilized as a substrate in the fermentation process, could be increased through the enzymatic hydrolysis of phenolic conjugated with enzymes that break down carbohydrates generated by filamentous fungal strains during solid-state fermentation. Cellulolytic enzymes that may break down cell

https://doi.org/10.31436/iiumej.v26i1.3173

walls containing recalcitrant such as lignocellulose are naturally produced by A. niger [56]. As a result, more phenolic compounds may be mobilized for solvent extraction, and more antioxidant compounds may be synthesized. The exponential phase was demonstrated in this study from day zero to its peak, the third day of fermentation. The fungus actively produces its extracellular enzymes and reproduces throughout the exponential phase. The fungal biomass grew at its maximum rate on the third day of fermentation, indicating that this is also the day when the fungi are actively establishing extracellular enzymes. The ability of β-glucosidase enzyme produced by Aspergillus sp. to hydrolyze phenolic glycosides and release free phenolic compounds can improve the extraction of phenolic compounds [57].

From the fourth to the seventh day of fermentation, the total phenolic and flavonoid content decreased, similar to that observed in a study by Torres-León, et al. [58] in which they used A. oryzae to brew barley for seven days. Due to the exponential phase of the fermentation process, the overall phenolic and flavonoid concentration may decrease. Following the exponential phase, the *A.niger* started to exhibit a decline in self-replication activity and a reduction in the synthesis of the enzyme β-glucosidase, which slowed the process of hydrolyzing phenolic glycosides to liberate phenolic compounds. The findings of this study are consistent with those of a study by Gulo, et al. [59], which found that orange peel extract contains more total flavonoids and phenolics in acetone than in ethanol or methanol. This demonstrates that acetone solvents are more effective than ethanol and methanol for extracting phenolic compounds. However, less polar aglycones such as isoflavones, flavonones, flavones, and flavonols tend to be more soluble in semi-polar solvents [60], while flavonoids that are attached to sugar prefer to dissolve in polar solvents.

Table 5. Total phenolic and flavonoid content on the third day of fermentation

| Solvent | Total phenolic content (mg GAE/g) | Total flavonoid content (mg QE/g) |
|---|---|---|
| Ethanol | 38.66 | 5.34 |
| Methanol | 40.02 | 8.08 |
| Acetone | 51.01 | 14.75 |
| ChCl: EG | 25.79 | 3.40 |

### 3.6. Effects of fermentation time and extraction solvent on antioxidant activity of orange peel extract

In this study, the antioxidant activity in orange peel extract samples was determined by determining the percentage of DPPH inhibition in the sample to determine the IC50 value. The IC50 value can indicate the sample concentration required to counteract 50% of the free radical content [61]. Figure 8 illustrates the effects of fermentation time and extracting solvent on the antioxidant activity of the orange peel extract. Without being given pre-treatment, the antioxidant activities of the orange peel extract using 80% ethanol, 80% methanol, and 80% acetone were 508.52, 828.73 ppm, and 371.41 ppm, respectively. The IC50 value decreased on the first and third day of fermentation and then increased on the fifth and seventh day. The lower the IC50 value, the lower the sample concentration needed to inhibit as much as 50% of the percent DPPH inhibition. The lower the IC50 value in an extract sample, the better the antioxidant activity of the sample because the dose or concentration required to inhibit 50% of the percent DPPH inhibition is smaller [62]. This trend shows consistency between antioxidant activity and total flavonoid, phenolic, and hesperidin content [57].

https://doi.org/10.31436/iiumej.v26i1.3173

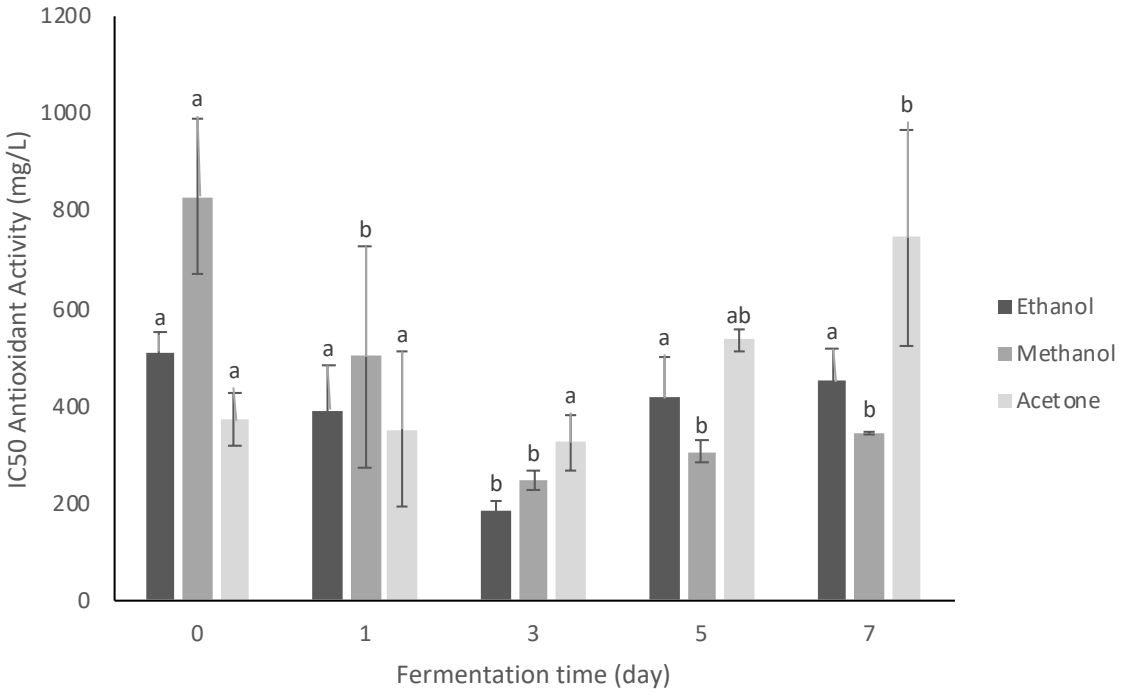


Figure 8. Antioxidant activity of C. reticulata peel extract using different solvents.

Phenolic compounds found in orange peel extract can act as antioxidant compounds so that they can increase the antioxidant activity of the extract [63] due to the presence of aromatic rings in the phenolic compound containing one or two hydroxyl groups, which can donate their hydrogen atoms to free radicals so that the product formation is more stable [64]. However, on the fifth and seventh days of fermentation, the IC50 value of the orange peel extract indicated that its antioxidant activity decreased. This was due to the decrease in extract yield on those days, so the phenolic compounds released were also reduced, thereby reducing the antioxidant activity produced.

Table 6 demonstrates that the orange peel extract utilizing 80% ethanol had the lowest value of IC50 among all the solvents, indicating that the antioxidant activity of the extract is stronger than that of the other solvents. This aligns with the research of Truong, et al. [65], where the ethanol and methanol extracts of S. buxifolia twigs exhibited a stronger antioxidant activity than acetone extracts. Flavonoids have the potential as antioxidants. However, the flavonoids in the acetone extract may be glycosides, making them less effective as antioxidant agents compared to their aglycone forms. This results in the antioxidant activity of the acetone extract being weaker than that of the ethanol extract and methanol extract.

Table 6. Antioxidant activity of orange peel extract on the third day of fermentation

| Solvent | Antioxidant activity ($IC_{50}$, ppm) |
|---|---|
| Ethanol | 184.32 |
| Methanol | 247.24 |
| Acetone | 323.95 |
| ChCl: EG | 269.30 |

## 4. CONCLUSION

The extraction of phenolic compounds using various solvent types was evaluated to extract phenolic compounds from orange peel waste. Hemicellulose, cellulose, and lignin content in the orange peel decreased due to the solid-state fermentation using A. niger. The yield of orange peel extract increased as the lignocellulose level decreased. The third day of fermentation with 80% methanol resulted in the highest yield of orange peel extract (34.1%). The total phenolic content, total flavonoid content, and antioxidant activity of the extract all increased due to the solid-state fermentation of orange peel using A. niger. The third day of fermentation led to the highest hesperidin content of orange peel extract, 27.47 mg/g dried fermented orange peel using 80% ethanol. In this study, hesperidin extraction was also performed using DES as a more sustainable alternative for organic solvents. The experiment showed that HBD in DES and ethylene glycol may extract hesperidin as effectively as organic solvents. A further study to explore the capacity of ChCl: EG as a green solvent for hesperidin extraction should also be investigated.

## REFERENCES

[1] M. Agustí, C. Mesejo, C. Reig, and A. Martínez-Fuentes, "Citrus Production," in *Horticulture: Plants for People and Places, Volume 1*, 2014, ch. Chapter 6, pp. 159-195.

[2] M. Ortiz-Sanchez, J. C. Solarte-Toro, C. E. Orrego-Alzate, C. D. Acosta-Medina, and C. A. Cardona-Alzate, "Integral use of orange peel waste through the biorefinery concept: an experimental, technical, energy, and economic assessment," *Biomass Conversion and Biorefinery,* vol. 11, no. 2, pp. 645-659, 2020, doi: 10.1007/s13399-020-00627-y.

[3] T. A. Sial *et al.*, "Evaluation of orange peel waste and its biochar on greenhouse gas emissions and soil biochemical properties within a loess soil," *Waste Manag,* vol. 87, pp. 125-134, Mar 15 2019, doi: 10.1016/j.wasman.2019.01.042.

[4] D. C. M. Ferreira, P. N. dos Santos, F. H. Santos, G. Molina, and F. M. Pelissari, "Sustainability approaches for agrowaste solution: Biodegradable packaging and microbial polysaccharides bio-production," (in English), *Sci. Total Environ.,* Article vol. 886, 2023, Art no. 163922, doi: 10.1016/j.scitotenv.2023.163922.

[5] K. O. Omeje, N. E. Nnolim, B. O. Ezema, J. N. Ozioko, E. C. Ossai, and S. O. O. Eze, "Valorization of agro-industrial residues for pectinase production by Aspergillus aculeatus: Application in cashew fruit juice clarification," (in English), *Clean. Circ. Bioeconomy.,* Article vol. 4, 2023, Art no. 100038, doi: 10.1016/j.clcb.2023.100038.

[6] S. Shokrollahi, A. Shavandi, O. Valentine Okoro, J. F. M. Denayer, and K. Karimi, "Sustainable biorefinery development for valorizing all wastes from date palm agroindustry," (in English), *Fuel,* Article vol. 358, 2024, Art no. 130291, doi: 10.1016/j.fuel.2023.130291.

[7] J. D. Sosa-Martínez, J. Montañez, J. C. Contreras-Esquivel, N. Balagurusamy, S. K. Gadi, and L. Morales-Oyervides, "Agroindustrial and food processing residues valorization for solid-state fermentation processes: A case for optimizing the co-production of hydrolytic enzymes," (in English), *J. Environ. Manage.,* Article vol. 347, 2023, Art no. 119067, doi: 10.1016/j.jenvman.2023.119067.

[8] J. D. Sosa-Martínez *et al.*, "Sustainable Co-Production of Xylanase, Cellulase, and Pectinase through Agroindustrial Residue Valorization Using Solid-State Fermentation: A Techno-Economic Assessment," (in English), *Sustainability,* Article vol. 16, no. 4, 2024, Art no. 1564, doi: 10.3390/su16041564.

[9] M. Boukroufa, C. Boutekedjiret, L. Petigny, N. Rakotomanomana, and F. Chemat, "Bio-refinery of orange peels waste: a new concept based on integrated green and solvent free extraction processes using ultrasound and microwave techniques to obtain essential oil, polyphenols and pectin," *Ultrason Sonochem,* vol. 24, pp. 72-9, May 2015, doi: 10.1016/j.ultsonch.2014.11.015.

[10] M. F. Abbas, A. M. Jasim, and H. A. Al-Taha, "Effect of exogenous proline on protein pattern changes in Citrus sinensis (L.) Osbeck under in vitro salt stress," *Advances in Agriculture & Botanics - International Journal of the Bioflux Society,* vol. 4, no. 2, 2012.

[11] F. Rizzioli, V. Benedetti, F. Patuzzi, M. Baratieri, D. Bolzonella, and F. Battista, "Valorization of orange peels in a biorefinery loop: recovery of limonene and production of volatile fatty acids and activated carbon," (in English), *Biomass Conversion and Biorefinery,* Article vol. 14, no. 8, pp. 9793-9803, 2024, doi: 10.1007/s13399-023-03738-4.

[12] A. F. Ramos and A. P. Kempka, "Bioinformatics for circular economy research decision-making: A case study in obtaining bioactive peptides from Citrus sinensis peels via limonene synthase analysis," (in English), *Sustain. Chem. Environ.,* Article vol. 6, 2024, Art no. 100101, doi: 10.1016/j.scenv.2024.100101.

[13] N. M'hiri, I. Ioannou, M. Ghoul, and N. M. Boudhrioua, "Extraction Methods of Citrus Peel Phenolic Compounds," *Food Reviews International,* vol. 30, no. 4, pp. 265-290, 2014, doi: 10.1080/87559129.2014.924139.

[14] K. Ghasemi, Y. Ghasemi, and M. A. Ebrahimzadeh, "Antioxidant Activity, Phenol and Flavonoid Contents of 13 Citrus Species Peels and Tissues," *Pak. J. Pharm. Sci.,* vol. 22, no. 3, pp. 277-281, 2009.

[15] A. Bocco, M.-E. Cuvelier, H. Richard, and C. Berset, "Antioxidant Activity and Phenolic Composition of Citrus Peel and Seed Extracts," *J. Agric. Food Chem,* vol. 46, p. 2123−2129, 1998.

[16] A. Kammoun Bejar, N. Ghanem, D. Mihoubi, N. Kechaou, and N. Boudhrioua Mihoubi, "Effect of Infrared Drying on Drying Kinetics, Color, Total Phenols and Water and Oil Holding Capacities of Orange (Citrus Sinensis) Peel and Leaves," *International Journal of Food Engineering,* vol. 7, no. 5, 2011, doi: 10.2202/1556-3758.2222.

[17] C. Morel-Salmi, J.-M. Souquet, M. Bes, and V. Cheynier, "Effect of Flash Release Treatment on Phenolic Extraction and Wine Composition," *J. Agric. Food Chem.,* vol. 54, p. 4270−4276, 2006, doi: 10.1021/jf053153k

[18] J. R. Ayala *et al.*, "Characterization of Orange Peel Waste and Valorization to Obtain Reducing Sugars," *Molecules,* vol. 26, no. 5, Mar 3 2021, doi: 10.3390/molecules26051348.

[19] A. K. Chandel, S. S. da Silva, and O. V. Singh, "Detoxification of Lignocellulose Hydrolysates: Biochemical and Metabolic Engineering Toward White Biotechnology," *BioEnergy Research,* vol. 6, no. 1, pp. 388-401, 2012, doi: 10.1007/s12155-012-9241-z.

[20] P. Bergquist *et al.*, "Expression of xylanase enzymes from thermophilic microorganisms in fungal hosts," *Extremophiles,* vol. 6, no. 3, pp. 177-84, Jun 2002, doi: 10.1007/s00792-001-0252-5.

[21] G. Najafpour, A. Ideris, S. Salmanpour, and M. Norouzi, "Acid Hydrolysis of Pretreated Palm Oil Lignocellulosic Wastes," *IJE Transactions B: Applications,* vol. 20, no. 2, 2007.

[22] J. E. Cacace and G. Mazza, "Optimization of Extraction of Anthocyanins from Black Currants with Aqueous Ethanol," *JOURNAL OF FOOD SCIENCE,* vol. 68, no. 1, pp. 240-248, 2003.

[23] M. N. Safdar, T. Kausar, S. Jabbar, A. Mumtaz, K. Ahad, and A. A. Saddozai, "Extraction and quantification of polyphenols from kinnow (Citrus reticulate L.) peel using ultrasound and maceration techniques," *J Food Drug Anal,* vol. 25, no. 3, pp. 488-500, Jul 2017, doi: 10.1016/j.jfda.2016.07.010.

[24] A. E. Hegazy and M. I. Ibrahium, "Antioxidant Activities of Orange Peel Extracts," *World Applied Sciences Journal,* vol. 18, no. 5, pp. 684-688, 2012, doi: 10.5829/idosi.wasj.2012.18.05.64179.

[25] F. Pena-Pereira, A. Kloskowski, and J. Namieśnik, "Perspectives on the replacement of harmful organic solvents in analytical methodologies: a framework toward the implementation of a generation of eco-friendly alternatives," *Green Chemistry,* vol. 17, no. 7, pp. 3687-3705, 2015, doi: 10.1039/c5gc00611b.

[26] S. C. Cunha and J. O. Fernandes, "Extraction techniques with deep eutectic solvents," *TrAC Trends in Analytical Chemistry,* vol. 105, pp. 225-239, 2018, doi: 10.1016/j.trac.2018.05.001.

[27] M. Xu, L. Ran, N. Chen, X. Fan, D. Ren, and L. Yi, "Polarity-dependent extraction of flavonoids from citrus peel waste using a tailor-made deep eutectic solvent," *Food Chem,* vol. 297, p. 124970, Nov 1 2019, doi: 10.1016/j.foodchem.2019.124970.

[28] S. Yatnatti, D. Vijayalakshmi, and R. Chandru, "Processing and Nutritive Valu e of Mango Seed Kernel Flour," *Current Research in Nutrition and Food Science Journal,* vol. 2, no. 3, pp. 170-175, 2014, doi: 10.12944/crnfsj.2.3.10.

[29] M. Y. Abduh, R. Yulianto, D. Avima, A. K. Widianto, and R. Alfianny, "Solid-State Fermentation of Cinnamon Bark using Aspergillus Awamori to Increase Cinnamon Oil Yield Extracted using Hydrodistillation, Maceration, and Soxhlet Extraction," *Natural Volatiles and Essential Oils,* vol. 8, no. 6, pp. 1575-1588, 2021.

[30] D. M. Updegraff, "Semimicro Determination of Cellulose in Biological Materials," *Analytical Biochemistry,* vol. 32, pp. 420-424, 1969.

[31] M. Y. Abduh, E. Nababan, F. Ginting, J. Juliati, and H. Nugrahapraja, "Biodelignification of Lemon Peels Using Aspergillus Sp. to Improve Yield and Composition of Extracted Lemon Oil," *IIUM Engineering Journal,* vol. 21, no. 2, pp. 55-66, 2020, doi: 10.31436/iiumej.v21i2.1320.

[32] Y. Dai, G. J. Witkamp, R. Verpoorte, and Y. H. Choi, "Tailoring properties of natural deep eutectic solvents with water to facilitate their applications," *Food Chem,* vol. 187, pp. 14-9, Nov 15 2015, doi: 10.1016/j.foodchem.2015.03.123.

[33] C. R. *et al.*, "Development and Validation of Hesperidin from Orange Peel Citrus Aurantium by RP-HPLC Method " *Journal of Global Trends in Pharmaceutical Sciences,* vol. 11, no. 4, pp. 8657 - 8664, 2020.

[34] S. Chandra *et al.*, "Assessment of total phenolic and flavonoid content, antioxidant properties, and yield of aeroponically and conventionally grown leafy vegetables and fruit crops: a comparative study," *Evid Based Complement Alternat Med,* vol. 2014, p. 253875, 2014, doi: 10.1155/2014/253875.

[35] P. Molyneux, "The use of the stable free radical diphenylpicryl- hydrazyl (DPPH) for estimating antioxidant activity," *Songklanakarin J. Sci. Technol.,* vol. 26, no. 2, pp. 211-219, 2004.

[36] I. de la Torre, V. Martin-Dominguez, M. G. Acedos, J. Esteban, V. E. Santos, and M. Ladero, "Utilisation/upgrading of orange peel waste from a biological biorefinery perspective," *Appl Microbiol Biotechnol,* vol. 103, no. 15, pp. 5975-5991, Aug 2019, doi: 10.1007/s00253-019-09929-2.

[37] V. d. Bruinhorst A, K. Pd, T. Jmk, d. C. Mhjm, and K. Mc, "Exploring Orange Peel Treatment with Deep Eutectic Solvents and Diluted Organic Acids," *Natural Products Chemistry & Research,* vol. 04, no. 06, 2016, doi: 10.4172/2329-6836.1000242.

[38] P. Vrabl, C. W. Schinagl, D. J. Artmann, B. Heiss, and W. Burgstaller, "Fungal Growth in Batch Culture - What We Could Benefit If We Start Looking Closer," *Front Microbiol,* vol. 10, p. 2391, 2019, doi: 10.3389/fmicb.2019.02391.

[39] J. Kuivanen *et al.*, "Conversion of orange peel to L-galactonic acid in a consolidated process using engineered strains

of Aspergillus niger," *AMB Express,* vol. 4, no. 33, pp. 1-8, 2014.

[40] Asha-Augustine, Imelda-Joseph, and R. P. Raj, "Biomass estimation of Aspergillus niger S,4 a mangrove fungal isolate and A. oryzae NCIM 1212 in solid-state fermentation," *J. Mar. Biol. Ass. India,* vol. 48, no. 2, pp. 139 - 146, 2006.

[41] P. Alves de Castro *et al.*, "The Aspergillus fumigatus SchA(SCH9) kinase modulates SakA(HOG1) MAP kinase activity and it is essential for virulence," *Mol Microbiol,* vol. 102, no. 4, pp. 642-671, Nov 2016, doi: 10.1111/mmi.13484.

[42] K. Haryani, "Studi Kinetika Pertumbuhan Aspergillus Niger pada Fermentasi Asam Sitrat dari Kulit Nanas dalam Reaktor Air-Lift External Loop," *Momentum,* vol. 7, no. 1, pp. 48 – 52, 2011.

[43] X. M. Chen, A. R. Tait, and D. D. Kitts, "Flavonoid composition of orange peel and its association with antioxidant and anti-inflammatory activities," *Food Chem,* vol. 218, pp. 15-21, Mar 1 2017, doi: 10.1016/j.foodchem.2016.09.016.

[44] J. Santos da Silveira *et al.*, "Solid-state fermentation as a sustainable method for coffee pulp treatment and production of an extract rich in chlorogenic acids," *Food and Bioproducts Processing,* vol. 115, pp. 175-184, 2019, doi: 10.1016/j.fbp.2019.04.001.

[45] A. Chahyadi and Elfahmi, "The influence of extraction methods on rutin yield of cassava leaves (Manihot esculenta Crantz)," *Saudi Pharm J,* vol. 28, no. 11, pp. 1466-1473, Nov 2020, doi: 10.1016/j.jsps.2020.09.012.

[46] G. Åkerlöf, "Dielectric Constants of Some Organic Solvent-Water Mixture at Various Temperatures," *The Journal of The American Chemical Society,* vol. 54, no. 11, pp. 4125-4139, 1932.

[47] R. L. Curto, M. M. Tripodo, U. Leuzzi, D. Giuffrè, and C. Vaccarino, "Flavonoids Recovery and SCP Production from Orange Peel," *Bioresource Technology,* vol. 42, pp. 83-87, 1992.

[48] R. Liu *et al.*, "Antioxidant activity increased due to dynamic changes of flavonoids in orange peel during Aspergillus niger fermentation," *International Journal of Food Science & Technology,* vol. 58, no. 6, pp. 3329-3336, 2023, doi: 10.1111/ijfs.16239.

[49] Y. S. Lee, J. Y. Huh, S. H. Nam, S. K. Moon, and S. B. Lee, "Enzymatic bioconversion of citrus hesperidin by Aspergillus sojae naringinase: enhanced solubility of hesperetin-7-O-glucoside with in vitro inhibition of human intestinal maltase, HMG-CoA reductase, and growth of Helicobacter pylori," *Food Chem,* vol. 135, no. 4, pp. 2253-9, Dec 15 2012, doi: 10.1016/j.foodchem.2012.07.007.

[50] D. S. Kim and S. B. Lim, "Extraction of flavanones from immature Citrus unshiu pomace: process optimization and antioxidant evaluation," *Sci Rep,* vol. 10, no. 1, p. 19950, Nov 17 2020, doi: 10.1038/s41598-020-76965-8.

[51] M. K. Samota *et al.*, "Hesperidin from citrus peel waste: extraction and its health implications," *Quality Assurance and Safety of Crops & Foods,* vol. 15, no. 2, pp. 71-99, 2023, doi: 10.15586/qas.v15i2.1256.

[52] A. Yadav, S. Trivedi, R. Rai, and S. Pandey, "Densities and dynamic viscosities of (choline chloride+glycerol) deep eutectic solvent and its aqueous mixtures in the temperature range (283.15–363.15)K," *Fluid Phase Equilibria,* vol. 367, pp. 135-142, 2014, doi: 10.1016/j.fluid.2014.01.028.

[53] C. D'Agostino, R. C. Harris, A. P. Abbott, L. F. Gladden, and M. D. Mantle, "Molecular motion and ion diffusion in choline chloride based deep eutectic solvents studied by 1H pulsed field gradient NMR spectroscopy," *Phys Chem Chem Phys,* vol. 13, no. 48, pp. 21383-91, Dec 28 2011, doi: 10.1039/c1cp22554e.

[54] M. H. Zainal-Abidin, M. Hayyan, A. Hayyan, and N. S. Jayakumar, "New horizons in the extraction of bioactive compounds using deep eutectic solvents: A review," *Anal Chim Acta,* vol. 979, pp. 1-23, Aug 1 2017, doi: 10.1016/j.aca.2017.05.012.

[55] B. Ozturk, C. Parkinson, and M. Gonzalez-Miquel, "Extraction of polyphenolic antioxidants from orange peel waste using deep eutectic solvents," *Separation and Purification Technology,* vol. 206, pp. 1-13, 2018, doi: 10.1016/j.seppur.2018.05.052.

[56] I. da Costa Maia *et al.*, "Effect of solid-state fermentation over the release of phenolic compounds from brewer's spent grain revealed by UPLC-MSE," *Lwt,* vol. 133, 2020, doi: 10.1016/j.lwt.2020.110136.

[57] D. Mamy, Y. Huang, N. D. K. Akpabli-Tsigbe, M. Battino, and X. Chen, "Valorization of Citrus Reticulata Peels for Flavonoids and Antioxidant Enhancement by Solid-State Fermentation Using Aspergillus niger CGMCC 3.6189," *Molecules,* vol. 27, no. 24, Dec 15 2022, doi: 10.3390/molecules27248949.

[58] C. Torres-León *et al.*, "Solid-state fermentation with Aspergillus niger to enhance the phenolic contents and antioxidative activity of Mexican mango seed: A promising source of natural antioxidants," *Lwt,* vol. 112, 2019, doi: 10.1016/j.lwt.2019.06.003.

[59] K. N. Gulo, Suhartomi, A. D. Saragih, M. A. Raif, and R. Ikhtiari, "Antioxidant Activity of Flavonoid Compounds in Ethanol and Ethyl Acetate Extract from Citrus Sinensis," presented at the 2021 International Conference on Artificial Intelligence and Mechatronics Systems (AIMS), 2021.

[60] M. Jimenez, I. Castillo, E. Azuara, and C. I. Beristain, "Antioxidant and Antimicrobial Activity of Capulin (*Prunus Serotina Subsp Capuli*) Extracts," *Revista Mexicana de Ingeniería Química,* vol. 10, no. 1, pp. 29-37, 2011.

[61] J. H. Park, M. Lee, and E. Park, "Antioxidant activity of orange flesh and peel extracted with various solvents," *Prev Nutr Food Sci,* vol. 19, no. 4, pp. 291-8, Dec 2014, doi: 10.3746/pnf.2014.19.4.291.

[62] J. F. Rivero-Cruz *et al.*, "Phytochemical Constituents, Antioxidant, Cytotoxic, and Antimicrobial Activities of the Ethanolic Extract of Mexican Brown Propolis," *Antioxidants (Basel),* vol. 9, no. 1, Jan 13 2020, doi: 10.3390/antiox9010070.

[63] H. Myo, N. Nantarat, and N. Khat-Udomkiri, "Changes in Bioactive Compounds of Coffee Pulp through Fermentation-Based Biotransformation Using Lactobacillus plantarum TISTR 543 and Its Antioxidant Activities," *Fermentation,* vol. 7, no. 4, 2021, doi: 10.3390/fermentation7040292.

[64] R. A. *et al.*, "Determination of antioxidant activity in methanolic and chloroformic extracts of Momordica charantia," *African Journal of Biotechnology,* vol. 10, no. 24, pp. 4932-4940, 2011, doi: 10.5897/AJB10.1972.

[65] D.-H. Truong, D. H. Nguyen, N. T. A. Ta, A. V. Bui, T. H. Do, and H. C. Nguyen, "Evaluation of the Use of Different Solvents for Phytochemical Constituents, Antioxidants, and In Vitro Anti-Inflammatory Activities of Severinia buxifolia," *Journal of Food Quality,* vol. 2019, pp. 1-9, 2019, doi: 10.1155/2019/8178294.

https://doi.org/10.31436/iiumej.v26i1.2998

# MACHINE LEARNING MODELS FOR PREDICTING THE COMPRESSIVE STRENGTH OF CONCRETE WITH SHREDDED PET BOTTLES AND M-SAND AS FINE AGGREGATE

**ALTAMASHUDDINKHAN NADIMALLA[1,2], SITI ALIYYAH MASJUKI[1*], ABDULLAH GUBBI[3], ANJUM KHAN[4], IMRAN MOKASHI[5]**

[1]*Department of Civil Engineering, International Islamic University Malaysia), Gombak, Malaysia*
[2]*Department of Civil Engineering, Bearys Institute of Technology, Mangalore, India*
[3]*Department of Electronics and Communication, Bearys Institute of Technology, Mangalore, India*
[4]*Department of Basic Science, Bearys Institute of Technology, Mangalore, India*
[5]*Department of Mechanical Engineering, Bearys Institute of Technology, Mangalore, India*

**Corresponding author: aliyyah@iium.edu.my*

*(Received: 8 September 2023; Accepted: 24 September 2024; Published online: 10 January 2025)*

***ABSTRACT:*** Machine Learning (ML) and Artificial Intelligence (AI) are closely intertwined and represent the latest cutting-edge technologies that facilitate the development of intelligent prototypes. Machine learning is a critical subset of AI that deliberates the development of self-trained algorithms that use previous databases and analysis for result predictions. By leveraging past data, machine learning empowers computers to make predictions and decisions. This study investigates the use of ML algorithms to predict the compressive strength of grade 30 concrete, incorporating shredded PET bottles and M-sand as fine aggregates. The experimental setup involved preparing concrete specimens with shredded PET bottle aggregates, varying the volume from 0% to 2% in increments of 0.5%. Different percentages of M-sand were incorporated at 25%, 50%, 75%, and 100%. The mixing proportions adhered to the standards defined by the Department of Environment (DOE). Cubic specimens were cast and cured for 7, 28, and 90 days. The study employs Multiple Linear Regression (MLR), Artificial Neural Network (ANN), and Decision Tree (DT) models, using the experimental data for predictive analysis. The evaluation of the three models for predicting compressive strength yielded interesting results: The Decision Tree (DT) model demonstrated the best performance, with a relatively low Mean Squared Error (MSE) of 5.125 and Mean Absolute Error (MAE) of 1.642 and a high $R^2$ value of 0.918, indicating that the model explains approximately 91.8% of the variance in the target variable. The DT model's ability to handle complex, non-linear data relationships made it particularly effective in evaluating concrete strength. The Multiple Linear Regression (MLR) model provided reasonable predictions but showed higher errors compared to the DT model, with MSE and MAE values of 26.663 and 4.298, respectively, and an $R^2$ score of 0.571, demonstrating a moderate ability to explain the variance in the data. Conversely, the Artificial Neural Network (ANN) model exhibited the least accuracy, with the highest errors (MSE of 112.33 and MAE of 8.52) and a negative $R^2$ score (-0.64), indicating poor model training and an inability to capture the relationships between parameters effectively, partly due to the relatively small dataset. The study highlights the potential of DT models in sustainable construction practices, emphasizing the importance of comprehensive datasets and further exploration of alternative algorithms. The findings advocate for using ML in concrete strength prediction, contributing to advancements in sustainable engineering and material science.

***ABSTRAK:*** Pembelajaran Mesin (ML) dan Kecerdasan Buatan (AI) saling berkait rapat dan mewakili teknologi canggih terkini yang membantu pembangunan prototaip pintar.

Pembelajaran mesin adalah subset kritikal AI yang menumpukan pada pembangunan algoritma dilatih sendiri menggunakan pangkalan data dan analisis terdahulu bagi meramal hasil. Dengan memanfaatkan data masa lalu, pembelajaran mesin memberi kuasa kepada komputer bagi membuat ramalan dan keputusan. Kajian ini menyelidik penggunaan algoritma ML bagi meramalkan kekuatan mampatan konkrit gred 30, menggabungkan botol PET yang dicincang dan pasir-M sebagai agregat halus. Susunan eksperimen melibatkan penyediaan spesimen konkrit dengan agregat botol PET yang dicincang, memvariasikan isipadu dari 0% hingga 2% dalam kenaikan 0.5%. Peratusan berbeza bagi pasir-M telah digabungkan pada 25%, 50%, 75%, dan 100%. Nisbah campuran mematuhi piawaian yang ditetapkan oleh Jabatan Alam Sekitar (DOE). Spesimen kubik dipadatkan dan diawetkan selama 7, 28, dan 90 hari. Kajian ini menggunakan model Regresi Linear Berganda (MLR), Rangkaian Neural Buatan (ANN), dan Pokok Keputusan (DT), manakala data eksperimen digunakan bagi analisis ramalan. Penilaian terhadap tiga model bagi meramal kekuatan mampatan menghasilkan keputusan yang menarik: Model Pokok Keputusan (DT) menunjukkan prestasi terbaik, dengan Ralat Kuasa Dua Min (MSE) yang agak rendah iaitu 5.125 dan Ralat Mutlak Min (MAE) 1.642, serta nilai $R^2$ yang tinggi iaitu 0.918, menunjukkan bahawa kira-kira 91.8% daripada model varian ini dalam pemboleh ubah sasaran. Keupayaan model DT bagi mengurus data kompleks dan tidak linear menjadikannya sangat berkesan dalam menilai kekuatan konkrit. Model Regresi Linear Berganda (MLR) memberi ramalan munasabah tetapi menunjukkan ralat lebih tinggi berbanding model DT, dengan nilai MSE dan MAE masing-masing 26.663 dan 4.298, dan skor $R^2$ 0.571, menunjukkan keupayaan sederhana bagi menjelaskan varians data. Sebaliknya, model Rangkaian Neural Buatan (ANN) menunjukkan ketepatan paling rendah, dengan ralat tertinggi (MSE 112.33 dan MAE 8.52) dan skor $R^2$ negatif (-0.64), yang menunjukkan latihan model yang lemah dan ketidakmampuan menangkap hubungan antara parameter dengan berkesan, sebahagiannya disebabkan oleh dataset yang kecil. Kajian ini menekankan potensi model DT dalam amalan pembinaan lestari, menekankan kepentingan dataset yang komprehensif dan penerokaan lanjut mengenai algoritma alternatif. Dapatan kajian menyokong penggunaan ML dalam ramalan kekuatan konkrit, menyumbang kepada kemajuan dalam kejuruteraan lestari dan sains bahan.

***KEYWORDS:*** *M-sand, PET Bottles, Multiple Linear Regression (MLR), Decision Tree (DT) and Artificial Neural Network (ANN)*

# 1. INTRODUCTION

Plastic waste, particularly polyethylene terephthalate (PET) bottles, poses serious environmental challenges related to accumulating in landfills and pollution when incinerated. Recently, interest has grown in incorporating recycled PET particles as aggregates within concrete mixtures, giving rise to a sustainable construction material. In the construction industry, PET bottle aggregates serve as an efficient substitute for sand and conversely develop comparable compressive strength of concrete. By reducing plastic waste and conserving natural sand resources, this approach offers substantial environmental benefits [1, 2]. Moreover, PET aggregates can result in lighter concrete with improved insulation properties, enhancing sustainability. If PET-based concrete demonstrates adequate compressive strength, it unlocks potential applications in non-structural elements, low-rise construction, and sustainable building projects. Additionally, repurposing PET waste could offer economic benefits in terms of material costs [3, 4]. This research direction contributes to developing innovative construction materials that promote a circular economy, address environmental challenges, and offer potential advantages in both cost and material properties.

The exploration of alternative materials for construction purposes has been a significant area of research in the civil engineering domain, aiming to address the environmental concerns

and resource scarcity associated with traditional materials. The use of M-sand as an alternative to river sand has been employed for a considerable period in concrete production [5].

M-Sand is produced by crushing specific types of rocks, and its physical and chemical properties can significantly differ from those of natural sand. Research studies indicate that concrete made with M-Sand exhibits a comparable or even superior compressive strength to that of concrete made with natural river sand. This can be attributed to the angular shape and rougher texture of M-Sand particles, which enhance the interlocking and bonding with cement paste in the concrete mix [5, 6].

Researchers have conducted a thorough study showing that substituting M-sand for natural sand can increase the strength of concrete. This is due to the particle size distribution of M-sand, which is often well-graded and falls within the specified limits for fine aggregate. This contributes to a denser packing of the concrete matrix, reducing the voids in the concrete and increasing its strength. The improved strength is a result of increased friction among the concrete ingredients attributed to the texture of M-sand [6, 7, 8].

The increasing popularity of M-sand is also attributed to its environmental benefits. Excessive sand mining has led to the depletion of riverbeds, raising environmental concerns and driving the search for sustainable alternatives. M-sand, made from abundant rock sources, provides a more sustainable option, reducing reliance on natural sand and lessening environmental impact. This sustainability, along with the potential for improved compressive strength, makes M-sand an appealing alternative for concrete production. [5].

A correlation exists between ML and AI, and they are the most recent trending technologies that are used in building smart systems. People are still confused with these two terms, but the fact is that both function differently. Artificial intelligence concerning building programs can think similarly to human beings, where the techniques developed are to enable computers to mimic human behaviors and thinking. Machine learning is a subset of artificial intelligence, and the primary concern is establishing algorithms that allow computers to learn without being explicitly programmed by using past data and experiences. The scenario is similar to constantly teaching a group of amateurs by providing complete training tools. As the training process increases, the experience gained also increases. Machine learning allows computers to predict and make decisions based on historical data [1, 2]. ML algorithms are usually used for forecasting and estimation purposes. The segregation of parameters under categories is termed classification. Conversely, the estimation of variables based on relationships between the dependent and independent parameters is referred to as regression [9].

Chopra et al. (2016) conducted research to predict concrete compressive strength using a machine-learning model [10]. The study included predictions for duration of 28, 56, and 91 days. The ML algorithm was developed using R software. A comparative study of the estimated values using various models was performed by using Root Mean Square Error (RMSE) and coefficient of determination (R2). The ML techniques used in the study included Artificial Neural Networks (ANN), random forests, Genetic Programming (GP), and decision trees [11]. The results indicated that the Neural Network (NN) machine learning model provided more accurate predictions for concrete compressive strength.

In a study by Dantaset. et. al. (2013), the researchers analyzed the debris from construction and demolition mixed in concrete to determine its strength. They utilized a machine learning algorithm using artificial neural networks (ANN) and conducted a phase study over 3, 7, 28, and 91 days. The results of the ML model were compared with experimental results obtained from the existing literature. The training set comprised of 1178 samples, with 77.76% used for

training and 22.24% for testing. The ANN model was employed to predict the concrete strength based on the testing and training results [12].

The concrete strength evaluation has been reported [13]. The researchers utilized ANN and Multiple Regression analysis as prediction tools. The additives used in concrete cement were nanosilica and copper slag. The curing times considered were 1, 3, 7, 28, 56 and 90 days. The research demonstrated that the ANN machine-learning model achieved high accuracy [13]**.** Meanwhile, Silva et al. (2020) employed ANN, RF, and SVM machine-learning algorithms to forecast concrete strength. Experimental data from previous studies from the literature was incorporated for prediction analysis, whereas Random Forest (RF) indicated more accurate predictions [14]. In addition, the prediction models of RF, LR, DT, and SVR were also used by Cherickal et al. (2021) to calculate the strength of concrete for a set of assumed data. The application regression techniques revealed accurate prediction for the random forest ML algorithm [15].

The properties of concrete were studied by Bhanu P. Koyaa (2001). The mechanical properties such as Poisson's ratio, Elasticity Modulus, Compressive strength, coefficient of expansion, and splitting strength were investigated. Machine Learning models were used, including DT, linear regression, SVM, gradient boosting, and RF. The study utilized a sample set obtained from the Wisconsin concrete mix data. The error correction methods of $R^2$ and RMSE indicated that the results produced by the SVM were more accurate than other models [16].

The technique of partial replacement of cement was incorporated by Mohammed Majeed Hameed et al. (2022) to evaluate hybrid models in order to estimate the concrete strength. The study proposed two predictive models: Support Vector Regression - Particle Swarm Optimization (SVR-PSO) and Support Vector Regression - Genetic Algorithm (SVR-GA). These models combined support vector regression (SVR) with improved particle swarm optimization (PSO) and genetic algorithm (GA), respectively. Additionally, an extreme learning machine (ELM) model was compared for evaluation using various statistical parameters. The SVR-PSO model displayed a high rate of accuracy, surpassing the SVR-GA and ELM models. The study also included sensitivity analysis to identify influential parameters affecting CS. The models considered for the study revealed improvised results of concrete compressive strength for partial cement substitution, thereby overriding the earlier studies undertaken for such models [17].

El-Mir et al. (2023) conducted a study focusing on the use of data-driven forecasting models for determining concrete strength. The main aim was to reduce the time and costs associated with laboratory tests. The study involved examining changes in the rebound hammer repeatability index for various concrete mixtures. Additionally, the study proposed new models for simplified strength prediction. To achieve this, the researchers built an experimental database and utilized machine learning models, including MMR, GPR, SVM, and DT. The findings showed that incorporating the water-to-powder ratio and concrete age improved prediction accuracy. Notably, models such as SVM/ GPR and RT outperformed others in predicting compressive strength. The study also suggested potential areas for future research, such as integrating rebound hammer tests with self-improving AI and exploring AI-based models for precise and rapid strength assessment [18].

Concrete strength estimation studies have been conducted by many researchers employing ML techniques. The research studies include usage of regression techniques such as Decision Trees (DT), k-Nearest Neighbors (kNN), Linear Regression (LR), Random Forests (RF) and

https://doi.org/10.31436/iiumej.v26i1.2998

Support Vector Machines (SVM). However, it was observed that these models have not been applied specifically to predict the strength of M-sand and fine aggregates of SPB (PET bottles).

The present study is focused on the prediction of strength when concrete is mixed with PET bottle shreds and M-sand. The estimation of compressive strength is done using ML models. This is a novel and sustainable technique to reuse waste resources and lower the environmental impact of concrete production. Concrete compressive strength is an important attribute that influences structural design, performance, and durability. As a result, it is essential to create precise and trustworthy models that can estimate the concrete strength depending on various proportion combinations and other criteria. The relevant study incorporates ML models of DT, LR, and ANN. The ML algorithm that was developed provides a cost- and time-effective solution for predicting the mechanical performance of concrete. This technique holds promise for large construction sites where traditional testing and evaluation methods can be time-consuming. The ML model facilitates precise prediction of the concrete properties relevant to experimental data.

The following are three machine learning techniques utilized in this research.

### 1.1. Multiple Linear Regression

This model uses a set of independent variables to predict the dependent variable statistically, assuming linear variation among the dependent and independent parameters. The model equation is $Y = \beta_0 + \beta_1 X_1 + \beta_2 X_2 + \ldots + \beta_n X_n + \varepsilon$, where $Y$ is the dependent variable, $X^1, X^2, \ldots, X_n$ are the independent variables, $\beta_0$ is the intercept term, $\beta^1, \beta^2, \ldots, \beta_n$ are the coefficients and $\varepsilon$ is the error term.

### 1.2. Decision Tree

A decision tree serves as a non-parametric algorithm in supervised learning, employed for tasks involving classification and regression. This algorithm functions by recursively dividing the feature space according to the values of input features. When making predictions, it follows a path from the root to a leaf node in the tree. Each internal node in the tree represents a decision rule, while each leaf node indicates the expected outcome. For regression tasks, the predicted values are the average or median of the target variable values within the training samples of a leaf node. This approach, using a tree-like structure instead of a single equation, is what sets decision trees apart in making predictions. $Y = \alpha_1 w_1 + \alpha_2 w_2 + \cdots + \alpha_n w_n$. In this equation, $\alpha_1, \alpha_2, \ldots, \alpha n$ represent the weights assigned to each feature and $w_1, w_2, \ldots, w_n$ represent the corresponding feature values.

### 1.3. Neural Network

The NN model draws similarities to the human neural system of the brain. The ML algorithm configures layered interconnected junctions (nodes) called neurons. The preceding layers provide each neuron with an input, which was evaluated based on the weighted sum through a governing function resulting in an output. This prediction model has diverse fields of application namely image recognition, natural language processing, and predictive modeling.

The regression equation for a neural network involves forward propagation. In a simple neural network with one hidden layer, the equation can be written as:

https://doi.org/10.31436/iiumej.v26i1.2998

$$\begin{aligned} Z_h &= W_{ih}X + b_h \\ A_h &= f(Z_h) \\ Z_o &= W_{oh}A_h + b_o \\ A_o &= Z_o \end{aligned} \tag{1}$$

Here, $X$ is the input, $W_{ih}$ and $W_{oh}$ are weight matrices, $b_h$ and $b_o$ are biased terms, and $f(\ )$ is an activation function applied to the hidden layer activations. Note that actual equations and network architectures vary. Different activation functions and network structures can be used to model complex relationships and improve performance.

### 1.4. Contribution to the Research

The research makes significant contributions to the field, as outlined below:

- *Comparative Analysis*: The study presents a comprehensive comparison among three distinct predictive models: Decision Tree, MLR, and NN. The forecasting model assessment deliberates its effectiveness for strength prediction and shortcomings. This analysis provides a basic reference for academicians and researchers in the selection of appropriate models for relevant applications.
- *Performance Evaluation*: The research presents a comprehensive evaluation of the predictive models using various evaluation metrics, including MSE, MAE, and $R^2$. By reporting these metrics for each model, the research provides a quantitative assessment of their accuracy, precision, and ability to explain the variance in the target variable. The assessment develops the model characteristic for effective and accurate prediction of concrete strength.
- *Model Comparison*: The comparative analysis reveals DT model to provide better estimation relative to other models. The MSE and MAE for DT are low signifying precise output. Additionally, it obtains a higher $R^2$ score, indicating a greater ability to explain the variance in the target variable. Thus, the study shows the DT strength characteristic required for relevant parametric predictions.
- *Practical Implications*: The research has practical implications for industries and organizations involved in predicting compressive strength. The determination of DT as the effective prediction model contributes to achieving a practical solution in the estimation of concrete compressive strength. This finding can assist construction companies, civil engineers, and material scientists in optimizing their processes, improving quality control, and ensuring structural integrity.
- *Future Research Directions*: The research opens avenues for future investigations. It suggests further exploration of alternative machine learning algorithms or advanced neural network architectures that could potentially improve the predictive performance for compressive strength. Additionally, the research encourages the examination of additional input features or data sources that might enhance the accuracy of predictions. These future research directions can contribute to advancing the field of predictive modeling for material properties.

Overall, the research contribution lies in its comparative analysis, performance evaluation, model comparison, practical implications, and suggestions for future research. By shedding light on the predictive models' performance for compressive strength prediction, the research provides valuable insights and guidance for researchers, practitioners, and industry professionals working in the field of material science and construction engineering.

https://doi.org/10.31436/iiumej.v26i1.2998

## 2. OBJECTIVES

This study aimed to predict the concrete strength for varying proportions of M-sand and PET aggregates. The value estimation is done using ML models such as DT, ANN, and MLR. The models were tested using available data, and their accuracy was evaluated using experimental results. The model accuracy determined the precise estimation of the strength and thereby facilitated the researchers' decision of which model to incorporate for their study. The current work is a consolidated study of prediction model applications for concrete strength determination and their effectiveness in estimating the compressive strength for different proportions of M-sand and PET shreds.

## 3. METHODOLOGY

The methodology followed in this research involved the following steps in the estimation of compressive and flexural strength of concrete composite mixture using ML models:

- *Experimental Setup*: Concrete specimens were prepared using shredded PET bottle aggregates as an alternative to conventional aggregates. The PET bottle aggregate volume varied from 0% to 2% in increments of 0.5%. Different percentages of M-sand were incorporated for 25%, 50%, 75% and 100%. The mixing proportions adhered to the standards defined by the Department of Environment (DOE). Cubic specimens were cast and cured for 7, 28, and 90 days.
- *Data Collection*: The necessary data for model development was collected from the experimental data, including the proportions of river sand, PET bottle aggregates, M-sand, and the curing duration. The output parameter measured was the concrete compressive strength.
- *Python Programming*: Python, specifically the Anaconda Navigator platform, was utilized for model development. The ML algorithms of DT, ANN, and MLR were implemented using appropriate libraries and frameworks.
- *Data Preparation*: The data cluster was segregated into 80% training dataset and 20% test dataset. This process helped in evaluating the model performance and reliability of implementing new datasets.
- *Model Training*: The training set was used to train the decision tree, MLR, and ANN models. These models were trained to establish the relationship between the input parameters (river sand, PET bottle aggregates, M-sand, and curing duration) and the output variables (compressive and flexural strengths).
- *Error Definition and Model Evaluation*: The assessment of model accuracy and predictive performance involved the utilization of error definition techniques, including MAE, MSE, and RMSE. These metrics quantified the disparities between predicted values and actual values. The model exhibiting the smallest error values was deemed the most proficient for forecasting purposes.

The model estimation accuracy was tested using a set of unseen test data. The obtained values of the compressive and flexural strength were compared with the experimental values to evaluate the model's ability to predict strength for different proportional mixtures of concrete.

The research aims to develop an accurate predictive model using machine learning techniques to estimate the compressive strengths of various concrete composites. The methodology involved data collection, model training, error analysis, and validation to identify

the most effective forecasting model. This study contributes to the field of concrete strength predictions.

In this research, Anaconda, an open-source software distribution, was used to create the required software environment. Jupyter Notebook, an interactive computing platform, facilitated code development, data exploration, and documentation. The model was trained on 80% of the dataset, and its performance was evaluated using 20% of the test dataset. The model was trained for the relationship approximation among different parameters. The appropriateness of the relations trained was tested using a 20% test dataset.

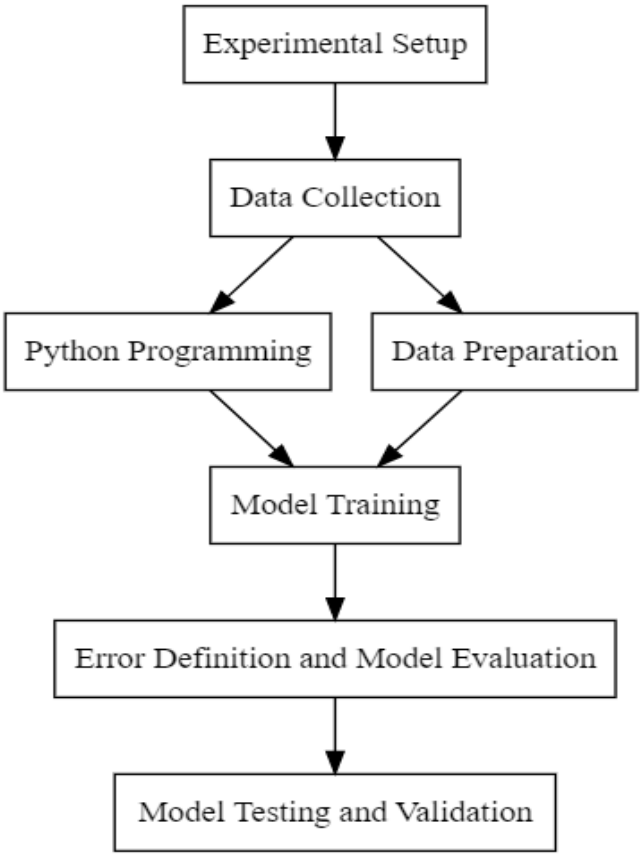


Figure 1. Flow Chart of Machine Learning Model Methodology

## 4. ERRORS

Machine learning (ML) algorithms are designed to make predictions based on a training dataset where the desired outcomes are already known. After being trained on this dataset, the model is then tested using a separate dataset to predict results, which are subsequently compared to the actual outcomes. Any discrepancies between the desired and predicted results are referred to as errors, and they serve as a measure of the accuracy of the ML algorithm.

It is important to note that ML models may encounter unknown variables or factors that can affect their accuracy, resulting in irreducible errors. These errors are inherent and cannot be eliminated or reduced. This variation between desired and predicted output can be minimized to enhance the model's performance effectiveness.

In summary, ML algorithms are trained to predict outcomes using known data, and their accuracy is assessed by comparing their predictions to actual outcomes. Irreducible errors can

arise from unknown variables. Nevertheless, model optimization techniques can be applied to minimize the differences between desired and predicted results.

### 4.1. Mean Absolute Error (MAE)

The accuracy of estimating data can be evaluated using MAE. It provides absolute mean value, indicating an appropriate scale of deviation between model prediction and actual value. The absolute values obtained are unaffected by outliers [19-21]. MAE is calculated by Eq. (2).

$$MAE = \frac{1}{N}\sum_{i=1}^{N}\left|f\left(\hat{\phi}\right)_i - f(\phi)_i\right| \quad (2)$$

### 4.2. Mean Squared Error (MSE)

Mean Squared Error (MSE) serves as a metric utilized to gauge the average of the squared discrepancies between predicted values and actual values. This metric offers an assessment of the extent to which the model's predictions correspond with the genuine values. By calculating the average of these squared differences, MSE accentuates larger errors, thereby assisting in quantifying the comprehensive accuracy of the model's predictions [20-22].

$$MSE = \frac{1}{N}\sum_{i=1}^{N}\left(f\left(\hat{\phi}\right)_i - f(\phi)_i\right)^2 \quad (3)$$

### 4.3. R-squared Score $R^2$

R-squared ($R^2$) functions as a statistical indicator that signifies the portion of the variability in the dependent variable explained by the independent variables within a regression model. This metric is determined using the equation:

$$R^2 = 1 - \frac{\sum_{i=1}^{N}\left(f(\phi)_i - f\left(\hat{\phi}\right)_i\right)^2}{\sum_{i=1}^{N}(f(\phi)_i - \bar{f}(\phi)_i)^2} \quad (4)$$

Here, $\sum$ represents summation, $f(\phi)$ is the actual value of the dependent variable, $\bar{f}(\phi)$ is the mean of the dependent variable, and $f\left(\hat{\phi}\right)$ is the predicted value based on the regression model. The numerator represents the sum of squared differences between the actual values and the mean, while the denominator represents the sum of squared differences between the actual values and the predicted values.

R-squared ranges from 0 to 1, where 1 indicates a perfect prediction, and 0 indicates that the model doesn't explain any variability in the dependent variable. However, R-squared alone doesn't provide information about prediction accuracy or precision, so it should be used alongside other evaluation metrics for a comprehensive assessment of the regression model [21, 22].

## 5. RESULTS AND DISCUSSION

Table 1 depicts the MSE, MAE, and $R^2$ scores for each model. The prediction accuracy is good for low values of MSE and MAE. Conversely, the variance for the value target is dependent on the $R^2$ value. These parameters determine that the DT model has better performance than the ANN and MLR, with ANN being the least accurate. The evaluation of the three models for predicting compressive strength yielded interesting results.

The Decision Tree model demonstrated the best performance, with a relatively low MSE of 5.125 and MAE of 1.642. Additionally, it achieved a high $R^2$ of 0.918, indicating that the model explains around 91.8% of the variance in the target variable. It is evident that the DT model predicts the concrete strength more accurately.

https://doi.org/10.31436/iiumej.v26i1.2998

The Multiple Linear Regression model also provided reasonable predictions, although it showed higher errors compared to the Decision Tree model. The MSE and MAE values were 26.663 and 4.298, respectively, while the $R^2$ score was 0.571. Although this model performs less accurately than the Decision Tree model, it still demonstrates a moderate ability to explain the variance in the data, as presented in Fig.2.

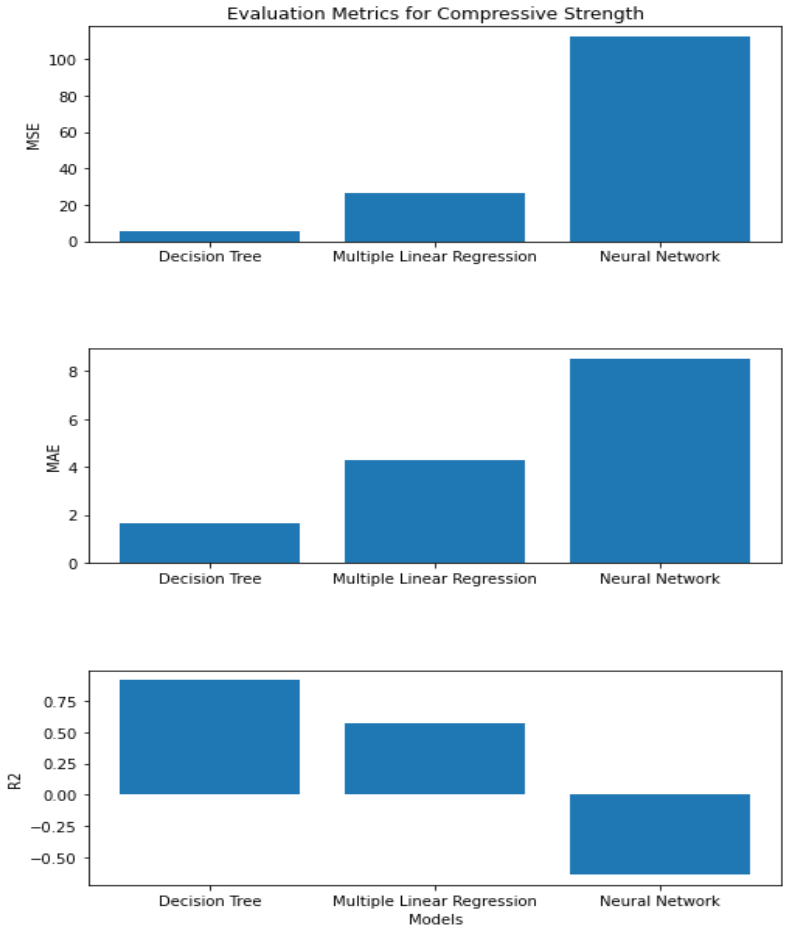


Figure 2. Regression Evaluation Metrics for Compressive Strength

The NN model exhibited the least accuracy among the three models. It exhibited the highest errors, with an MSE of 112.33 and an MAE of 8.52. Furthermore, the $R^2$ score was negative (-0.64), specifying that the model training for capitalizing on the relations between parameters did not yield, which is also evident in Fig.5. The obtained outputs infer that the DT model is highly suited for concrete strength prediction, which can also be deduced from Fig.4., followed by the Multiple Linear Regression model. However, further analysis and experimentation might be necessary to improve the performance of the Neural Network model. Nadimalla et al. (2022) developed machine learning models to predict the workability of concrete mixes containing manufactured sand (M-sand), shredded PET bottles, and river sand. Workability was measured by the slump, VeBe time (using a vibration densitometer), and compaction factor. The authors created MLR and DTR models using experimental data on these concrete properties. The DTR model, which handles nonlinear relationships better, proved superior at predicting all three workability measures with lower errors compared to MLR [23].

https://doi.org/10.31436/iiumej.v26i1.2998

Table 1. Error Evaluation Metrics

| Machine Learning Models | Mean Squared Error (MSE) | Mean Absolute Error (MAE) | R-squared Score ($R^2$) |
|---|---|---|---|
| Decision Tree | 5.13 | 1.64 | 0.92 |
| Multiple Linear Regression | 26.66 | 4.30 | 0.57 |
| Neural Network | 112.33 | 8.52 | -0.64 |

The multiple linear regression equation for calculating the compressive strength can be expressed as:

$$CompressiveStrength = \beta_0 + \beta_1 \times sand + \beta_2 \times PET + \beta_3 \times Msand + \beta_4 \times curing\ days \quad (5)$$

Where:

$\beta_0$ = 34.45 (intercept or constant term)

$\beta_1$ = -0.00 (coefficient associated with the "sand" input feature)

$\beta_2$ = 0.01 (coefficient associated with the "PET" input feature)

$\beta_3$ = -0.00 (coefficient associated with the "M sand" input feature)

$\beta_4$ = 0.11 (coefficient associated with the "curing days" input feature)

This equation calculates the compressive strength based on the weighted sum of the input features: sand, PET, M sand, and curing days, along with the intercept term $\beta_0$. The multiple linear regression algorithm determines the optimal values of the coefficients through the learning process, considering the relationships between the input features and the target variable (compressive strength) in the training data.

The proposed equation by the decision tree for calculating the compressive strength can be expressed as:

$$CompressiveStrength = \alpha_1 \times sand + \alpha_2 \times PET + \alpha_3 \times Msand + \alpha_4 \times curing\ days \quad (6)$$

Where:

$\alpha_1$ = 0.15 (weight or coefficient associated with the "sand" input feature)

$\alpha_2$ = 0.13 (weight or coefficient associated with the "PET" input feature)

$\alpha_3$ = 0.28 (weight or coefficient associated with the "M sand" input feature)

$\alpha_4$ = 0.44 (weight or coefficient associated with the "curing days" input feature).

In this analysis, we compare the performance of three prediction methods—Multiple Linear Regression (MLR), Decision Tree (DT), and Artificial Neural Network (ANN)—using the provided data and graph. The DT method demonstrates the highest correlation with actual values, showing an $R^2$ of 0.9318. This suggests that the DT method captures the relationship between variables effectively, making it the most reliable method for this dataset. The MLR method shows a moderate correlation ($R^2$ = 0.705), indicating reasonably good predictive accuracy, but it remained less effective than DT. This method struggles with non-linear relationships and extreme values, leading to more significant prediction errors. In contrast, the ANN method demonstrates poor predictive performance with an $R^2$ of 0.0435. The predictions are widely scattered and do not align well with the actual values.

The DT model outperforming the MLR and ANN models in concrete strength estimation is attributed to the following.

- Decision Trees are non-linear models that can capture complex relationships in the data. In the case of predicting compressive strength, there might be non-linear interactions among input features that are better captured by a Decision Tree than a linear model like MLR [13] [24].
- The Artificial Neural Network model did not perform well as compared to the DT model and MLR Model because it is a more complex model that requires more data to train. The dataset used in the experiment was small, which may not have been enough to train the ANN model effectively [24].

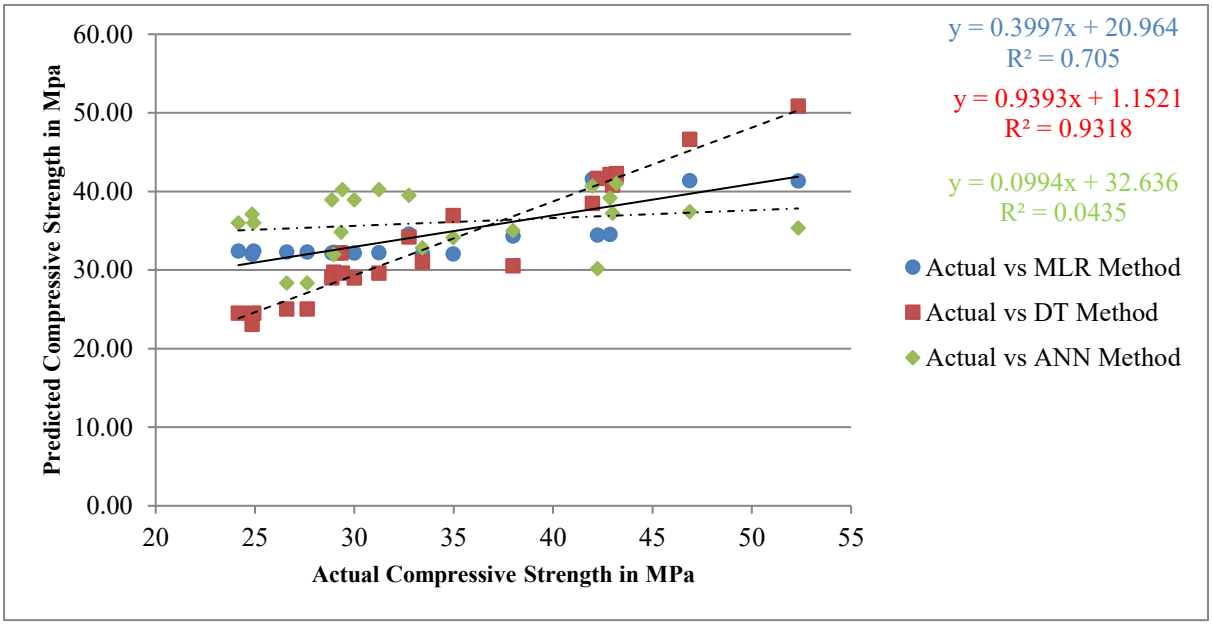


Figure 3. Actual vs Predicted Compressive Strength

## 6. CONCLUSION

The results show that the DT model provides an accurate prediction compared to MLR and ANN. The MAE and MSE values are low for the DT model, which indicates good accuracy. Additionally, the Decision Tree model has the highest R-squared score, implying that it explains a significant portion of the variance in the compressive strength.

The Decision Tree model outperforming the MLR and ANN models in predicting compressive strength can be attributed to several factors:

- Decision Trees are non-linear models that can capture complex relationships in the data. In the case of predicting compressive strength, there might be non-linear interactions among input features that are better captured by a Decision Tree than a linear model like MLR.
- The ANN model did not perform as well as the Decision Tree model because it is a more complex model that requires more data to train effectively. The dataset used in the experiment was relatively small, which may not have been enough to train the Artificial Neural Network model effectively.

In contrast, the Multiple Linear Regression model demonstrates moderate performance with higher MSE and MAE values and a lower R-squared score. Unfortunately, the Neural Network model emerges as the poorest performer, yielding the highest MSE and MAE values along with a negative R-squared score, suggesting its ineffectiveness in explaining the variance

in the compressive strength. Overall, the Decision Tree model stands out as the most accurate and reliable option for predicting compressive strength based on the given evaluation metrics.

## 7. LIMITATIONS

While this research work explores the estimation of compressive strength in concrete using ML algorithms, it is important to acknowledge some potential limitations:

- *Data availability and quality*: The accuracy of ML models heavily depends on the quality and quantity of data used for training. Limited or insufficient data may result in less reliable predictions. Additionally, the data quality, such as measurement errors or inconsistencies, can impact the accuracy of the models.
- *Generalizability*: The research focuses on a specific concrete mixture composed of M-sand and PET fine aggregates. The findings may not be directly applicable to different concrete mixtures or compositions. Generalizing the results to a broader context may require further validation and experimentation.
- *Feature selection*: The choice of features or variables used in the ML models can influence their performance. It is crucial to ensure that all relevant factors affecting compressive strength are considered and appropriately included in the models. Failure to include important features or incorporating irrelevant ones can lead to inaccurate predictions.
- *Model selection and performance*: The research employs three ML algorithms: decision tree, multiple linear regression, and ANN. However, there might be other ML algorithms that could potentially yield better results. The performance comparison may not include all possible algorithms, limiting the understanding of the best-performing model for this specific task.
- *Interpretability*: While ML algorithms provide accurate predictions, they often lack interpretability. Understanding the underlying reasons or relationships behind the predictions made by the models can be challenging. In domains where interpretability is crucial, such as engineering or construction, this limitation might restrict the practical application of the models.

These limitations should be considered when interpreting the results of the research and its potential application in real-world scenarios. Further studies and validations are necessary to address these limitations and enhance the reliability and applicability of the proposed ML models.

## REFERENCES

[1] Saikia, N., & De Brito, J. (2012). Use of plastic waste as aggregate in cement mortar and concrete preparation: A review. Construction and Building Materials, 34, 385-401. https://doi.org/10.1016/j.conbuildmat.2012.02.066

[2] Shahidan, S., Ranle, N. A., Zuki, S. S. M., Khalid, F. S., Ridzuan, A. R. M., &Nazri, F. M. (2018). Concrete incorporated with optimum percentages of recycled polyethylene terephthalate (PET) bottle fiber. International Journal of Integrated Engineering, 10(1), 1-8.

[3] Ochi, T., Okubo, S., & Fukui, K. (2007). Development of recycled PET fiber and its application as concrete-reinforcing fiber. Cement and Concrete Composites, 29(6), 448-455. https://doi.org/10.1016/j.cemconcomp.2007.02.002

[4] Alqahtani, F. K., Ghataora, G., Khan, M. I., &Dirar, S. (2017). Novel lightweight concrete containing manufactured plastic aggregate. Construction and Building Materials, 148, 386-397. https://doi.org/10.1016/j.conbuildmat.2017.05.011

[5] Manju, M., & K, A. N. (2016). Durability Studies on Concrete by Replacing Natural Sand with M-Sand-A Review. International Journal of Emerging Technology and Advanced Engineering, 6(3), 3-7.

[6] Cheah, C. B., Lim, J. S., &Ramli, M. B. (2019). The mechanical strength and durability properties of ternary blended cementitious composites containing granite quarry dust (GQD) as natural sand replacement. Construction and Building Materials, 197, 291-306. https://doi.org/10.1016/j.conbuildmat.2018.11.194

[7] Meisuh, B. K., Kankam, C. K., &Buabin, T. K. (2018). Effect of quarry rock dust on the flexural strength of concrete. Case Studies in Construction Materials, 8(July 2017), 16-22. https://doi.org/10.1016/j.cscm.2017.12.002

[8] Shen, W., et. al. (2018). Influence of manufactured sand's characteristics on its concrete performance. Construction and Building Materials, 172(May), 574-583. https://doi.org/10.1016/j.conbuildmat.2018.03.139

[9] Cihan, M. T. (2019). Prediction of Concrete Compressive Strength and Slump by Machine Learning Methods. Advances in Civil Engineering, 2019. https://doi.org/10.1155/2019/3069046

[10] Heath, N. (2020). What is machine learning? Everything you need to know. Retrieved from https://www.zdnet.com/article/what-is-machine-learning-everything-you-need-to-know/

[11] Chopra, P., Sharma, R. K., & Kumar, M. (2016). Prediction of Compressive Strength of Concrete Using Artificial Neural Network and Genetic Programming. Advances in Materials Science and Engineering, 2016. https://doi.org/10.1155/2016/7648467

[12] Dantas, A. T. A., Leite, M. B., &Nagahama, K. D. J. (2013). Prediction of compressive strength of concrete containing construction and demolition waste using artificial neural networks. Construction and Building Materials, 38, 717-722. https://doi.org/10.1016/j.conbuildmat.2012.09.026

[13] Chithra, S., Kumar, S. R. R. S., Chinnaraju, K., &Ashmita, F. A. (2016). A comparative study on the compressive strength prediction models for High Performance Concrete containing nano silica and copper slag using regression analysis and Artificial Neural Networks. Construction and Building Materials, 114, 528-535. https://doi.org/10.1016/j.conbuildmat.2016.03.214

[14] Silva, P. F. S., Moita, G. F., &Arruda, V. F. (2020). Machine learning techniques to predict the compressive strength of concrete. RevistaInternacional de MétodosNuméricos para Cálculo y DiseñoenIngeniería, 1-14. https://doi.org/10.23967/j.rimni.2020.09.008

[15] Cherickal, P. J., Kumar, V. V., Philipose, R. M., Shailesh, S., & Thomas, T. (2021). Compression Strength Prediction Using Machine Learning Techniques. International Journal of Advanced Trends in Computer Science and Engineering, 10, 301-307. https://doi.org/10.30534/ijatcse/2021/431012021

[16] Koyaa, R. G., &Bhanu, C. V., &Aneja, S., P. (2021). Comparative analysis of different machine learning algorithms to predict mechanical properties of concrete. Mechanics of Advanced Materials and Structures.

[17] Hameed, M. M., Abed, M. A., Al-Ansari, N., & Alomar, M. K. (2022). Predicting Compressive Strength of Concrete Containing Industrial Waste Materials: Novel and Hybrid Machine Learning Model. Advances in Civil Engineering, 2022. https://doi.org/10.1155/2022/5586737

[18] El-Mir, A., El-Zahab, S., Sbartaï, Z. M., Homsi, F., Saliba, J., & El-Hassan, H. (2023). Machine learning prediction of concrete compressive strength using rebound hammer test. Journal of Building Engineering, 64(July 2022), 105538. https://doi.org/10.1016/j.jobe.2022.105538

[19] Wang, W., & Lu, Y. (2018). Analysis of the Mean Absolute Error (MAE) and the Root Mean Square Error (RMSE) in Assessing Rounding Model. IOP Conference Series: Materials Science and Engineering, 324(1), 012049. https://doi.org/10.1088/1757-899X/324/1/012049

[20] Chai, T., &Draxler, R. R. (2014). Root mean square error (RMSE) or mean absolute error (MAE)? – Arguments against avoiding RMSE in the literature. Geoscientific Model Development, 7(3), 1247-1250. https://doi.org/10.5194/gmd-7-1247-2014

[21] Agrawal. (2021). Know The Best Evaluation Metrics for Your Regression Model!. Retrieved from https://www.analyticsvidhya.com/blog/2021/05/know-the-best-evaluation-metrics-for-your-regression-model/

[22] Varshini, A. G. P., Kumari, K. A., Janani, D., &Soundariya, S. (2021). Comparative analysis of Machine learning and Deep learning algorithms for Software Effort Estimation. Journal of Physics: Conference Series, 1767(1), 012019. https://doi.org/10.1088/1742-6596/1767/1/012019

[23] Nadimalla, A. ., Masjuki, S. ., Saad, S. ., & Ali, M. (2022). Machine Learning Model to Predict Slump, VEBE and Compaction Factor of M Sand and Shredded Pet Bottles Concrete. IOP Conference Series: Materials Science and Engineering, 1244(1), 012023. https://doi.org/10.1088/1757-899x/1244/1/012023

[24] Chopra, P., Sharma, R. K., Kumar, M., & Chopra, T. (2018). Comparison of Machine Learning Techniques for the Prediction of Compressive Strength of Concrete. Advances in Civil Engineering, 2018. https://doi.org/10.1155/2018/5481705

https://doi.org/10.31436/iiumej.v26i1.3015

# PHYSICAL AND MECHANICAL PROPERTIES OF GREEN CEMENTLESS MORTAR INCORPORATING WASTE PAPER SLUDGE ASH

**AIDA NABILA JAMALUDDIN, SITI ASMAHANI SAAD*, SITI ALIYYAH MASJUKI, WAN NUR FIRDAUS WAN HASSAN, SITI NORATIKAH CHE DERAMAN, NADIAH MD HUSAIN**

*Department of Civil Engineering, International Islamic University Malaysia, Gombak, Malaysia*

**Corresponding author: asmahanisaad@iium.edu.my*

*(Received: 14 September 2023; Accepted: 3 August 2024; Published online: 10 January 2025)*

***ABSTRACT:*** As an alternative to conventional construction material such as normal concrete, waste paper sludge ash (WPSA) based geopolymer is seen as a promising and viable option in construction material selection due to its high amount of aluminum (Al) and silicon (Si) content. This research aims to determine the microstructure and mechanical characteristics of WPSA in geopolymers. The alkaline solution that contains 6 M of sodium hydroxide (NaOH) and sodium silicate ($Na_2SiO_3$) was used to activate the geopolymer. The hardened 50 mm-sized mortars were prepared and underwent a heat-cured process for 1 day at various temperatures at 24 ℃, 60 ℃, and 90 ℃, respectively. Then, the mortar cubes were placed in the laboratory until the testing days. A compression test was conducted to identify the strength development of the WPSA-based geopolymer mortar at 7, 14, and 28 days, respectively. Chemical composition was analyzed using X-ray fluorescence (XRF). Furthermore, Fourier-transformed infrared spectroscopy (FTIR) was conducted to ascertain the structural elucidation and scanning electron microscope (SEM) analysis was done to provide microstructural observations of the geopolymer. Based on the XRF analysis, the WPSA has the highest amount of calcium oxide (CaO) instead of aluminum oxide ($Al_2O_3$) and silicon dioxide ($SiO_2$), and it reduces the performance of WPSA as a cement replacement material. The ratio of $SiO_2$ and $Al_2O_3$ is recorded as 1.1:1. Therefore, it is suitable for bricks and ceramics production instead of concrete production. As for the curing process, the heat-cured method is evident in accelerating strength development in the WPSA-based geopolymer mortar compared to the ambient curing method due to the rapid polymerization process in the geopolymer system. It is proven that 60 ℃ is the optimum temperature for the curing process for geopolymer mortar.

***ABSTRAK:*** Sebagai salah satu alternatif kepada bahan binaan konvensional seperti konkrit biasa, geopolimer berasaskan abu enap cemar kertas (WPSA) adalah dilihat sebagai pilihan yang baik kerana bahan ini mempunyai kandungan aluminium (Al) and silika (Si) yang tinggi. Penyelidikan ini bertujuan untuk menentukan struktur mikro dan ciri mekanikal WPSA dalam geopolimer. Larutan alkali yang mengandungi 6 M natrium hidroksida (NaOH) dan natrium silikat ($Na_2SiO_3$) digunakan untuk mengaktifkan geopolimer. Mortar yang bersaiz 50 mm telah disediakn dan ia melalui proses pengawetan haba selama 1 hari pada suhu yang berza-beza, iaitu 24 ℃, 60 ℃, and 90 ℃. Kemudian, kiub mortar tersebut diletakkan di dalam makmal sehingga hari ujian. Ujian mampatan dijalankan untuk mengenal pasti perkembangan kekuatan mortar geopolimer apabila mencapai 7, 14, dan 28 hari. Komposisi kimia dalam sampel telah dianalisa menggunakan pendarfluor sinar-X (XRF). Tambahan pula, Spektroskopi inframerah fourier transformasi (FTIR) untuk memastikan sifat bahan dan analisis pengimbasan mikroskop elektron (SEM) untuk menyediakan pemerhatian struktur mikro geopolimer. Berdasarkan data dari analisa XRF, WPSA mempunyai jumlah kalsium oksida (CaO) tertinggi berbanding aluminium oksida ($Al_2O_3$) dan silikon dioksida ($SiO_2$), dan

ia mengurangkan prestasi WPSA sebagai bahan gantian simen. Nisbah $SiO_2$ dan $Al_2O_3$ direkodkan sebagai 1.1:1. Oleh itu, ia sesuai digunakan untuk pengeluaran batu bata dan seramik berbanding pengeluaran konkrit. Bagi proses pengawetan, kaedah pengawetan haba terbukti mempercepat perkembangan kekuatan geopolimer berasaskan WPSA berbanding pengawetan pada suhu ambien disebabkan berlakunya proses pempolimeran yang sangat pantas dalam sistem geopolimer tersebut. Telah terbukti bahawa suhu 60 °C adalah suhu optimum bagi proses pengawetan mortar geopolimer berasaskan WPSA ini.

***KEYWORDS:*** *Geopolymer, Waste Paper Sludge Ash, NaOH, $Na_2SiO_3$.*

# 1. INTRODUCTION

Nowadays, ordinary Portland cement (OPC) is widely used as a construction material worldwide [1–3]. Cement production is one of the largest sources of CO2 emitted into the atmosphere than deforestation and fossil fuels [4], [5]. The high demand for cement production is rising rapidly day by day because of the increased need for building construction materials. Cement manufacturing is the source of harmful gas outflow to the earth's atmosphere, which is assessed at around 1.5 billion tons every year [3]. However, the expected value is greater than 4.8 billion tons of CO2 production in 2020 [6].

On the other hand, waste materials generated from rapid industrial activities continue to expand each day [7]. Managing the disposal of these waste materials requires proper landfilling techniques. The amount of waste generation per capita in Malaysia is about 1.1kg/day [8]. The per capita generation of municipal waste is from 0.5 to 0.8 kg/ person/ day [7]. In addition, 166 landfills have been operated to dump more than 26,500 tons of waste every day in the country [8]. Among the commonly generated waste is paper waste. This type of waste is the most frequently found in almost all areas. The paper can only be recycled six to ten times because of the decreasing strength of the cellulose fiber of the paper. After the recycling process, the rest of the waste paper will be dumped into landfills. Paper production industries contribute a significant amount of waste materials since the material can only be recycled a few times, which is before its fiber becomes weak to produce the high-quality end product such as paper tissue [9]. Therefore, exploring the potential to use this waste material in the construction industry is seen as one green solution to address the issue accordingly.

In this regard, geopolymer is an environment-friendly construction material that utilizes industrial or agricultural waste materials mixed with an alkaline activator as the binder to bind sand instead of OPC [10]. Examples of waste materials used in geopolymer are fly ash, slag, silica fume, bagasse ash, clay, rice husk ash, and metakaolin [11], [12]. Waste paper sludge ash (WPSA) that consists of high amount of alumina-siliceous material can be a possible cement substitution in the construction industry [13], [14]. The alumina-siliceous is crucial in geopolymer technology, as it enhances good physical and chemical characteristics. $SiO_2$ and $Al_2O_3$ presented in the WPSA react with an alkaline-activated solution to produce an excellent geopolymer with a high alumina-siliceous material [15]. This reaction is known as the geopolymerization process, involves the dissolution of silicate and aluminate substances and polycondensation reaction [6]. The end product of this process is silicon oxo aluminates, which look like a three-dimensional (3D) polymeric ring structure. Thus, the WPSA enhances the performance of geopolymer [16], [17]. Contrasting to the OPC, the binder is calcium-silicate-hydrates to develop strength [18]. A geopolymer required an aluminosilicate to cohere the aggregates and enhance the strength [16].

Using geopolymer innovation is one of the feasible strategies to lessen the utilization of OPC in concrete, which causes environmental contamination and expands the measurement of

https://doi.org/10.31436/iiumej.v26i1.3015

waste materials. Therefore, the best way to ensure that the concrete industry is more competitive is by using waste and natural materials. Geopolymer is a new green concrete concept that uses eco-friendly materials in cement production. Geopolymer is an excellent substitute for cement to reduce pollution. Geopolymer cement can contribute considerably to the carbon dioxide discharges in the atmosphere compared to OPC. In addition, many researchers [9], [14], [20], [21] have stated that WPSA can be used as cement replacement material as well. Therefore, an effort has been made to optimize the usage of recycled waste materials as beneficial alternative materials for cement [17]. The geopolymer is the best way to replace OPC in concrete.

In this regard, this research used WPSA as the main constituent in the geopolymer. Thus, the research aimed to find the mechanical properties through a compressive strength test and microstructure properties through X-ray fluorescence (XRF) analysis, scanning electron microscopy (SEM) analysis, and Fourier-transformed infrared spectroscopy (FTIR) analysis of WPSA-based geopolymer.

## 2. MATERIALS AND METHODS

### 2.1. Material Selection

#### *2.1.1. Waste Paper Sludge Ash (WPSA)*

As shown in Fig. 1, WPSA is waste material directly taken from the local paper milling factory, Malaysian Newsprint Sdn Bhd, located in Mentakab, Pahang. The WPSA is light grey and a by-product of the paper milling process. The percentage of WPSA used as a binder in geopolymer mortar is 100% to replace cement.

Figure 1. Waste Paper Sludge Ash

https://doi.org/10.31436/iiumej.v26i1.3015

### *2.1.2. Fine Aggregates*

For this study, a sieve analysis test was done to determine the grain size distribution of fine aggregate particles (sand). Commonly, the grading of fine aggregates is defined as the proportions of particle size less than 5 mm. The sieve analysis produced a grading curve for fine aggregate according to ASTM C136/C136-19. The grading curve is plotted in the percent passing (%) graph versus sieve size (mm), also known as the particle size distribution graph for fine aggregates.

Gradation and size distribution of the fine aggregates affect the mechanical and microstructure properties of the produced geopolymer mortar. Commonly, well-graded aggregates contribute towards compressive strength increment for the mortar. From the data in Table 1, the total weight of the fine aggregate was 5200.00 g, while the total weight was calculated at 5004.20 g. Thus, there was a 195.80 g loss of fine aggregates. Therefore, some errors might affect the experiment's accuracy, such as the fine aggregates that have been used may contain unwanted materials such as dust and stone.

Table 1. Sieving analysis of aggregates

| Sieve size (mm) | Weight of sieve (g) | Weight of sieve + sample (g) | Weight of sample (g) | Cumulative weight sample (g) | Cumulative % retained (%) | % passing (%) |
|---|---|---|---|---|---|---|
| **5.00** | 0.00 | 0.00 | 0.00 | 0.00 | 0.00 | 100.00 |
| **2.36** | 503.20 | 754.30 | 251.10 | 251.10 | 5.02 | 94.98 |
| **1.18** | 704.40 | 1390.00 | 685.60 | 936.70 | 18.72 | 76.26 |
| **0.60** | 903.80 | 2206.30 | 1302.50 | 2239.20 | 44.75 | 31.52 |
| **0.30** | 908.90 | 2610.00 | 1701.10 | 3940.30 | 78.74 | 24.00 |
| **0.15** | 1223.90 | 1931.40 | 707.50 | 4647.80 | 92.88 | 10.00 |
| **pan** | 748.10 | 1104.50 | 356.40 | 5004.20 | 100.00 | 0.00 |

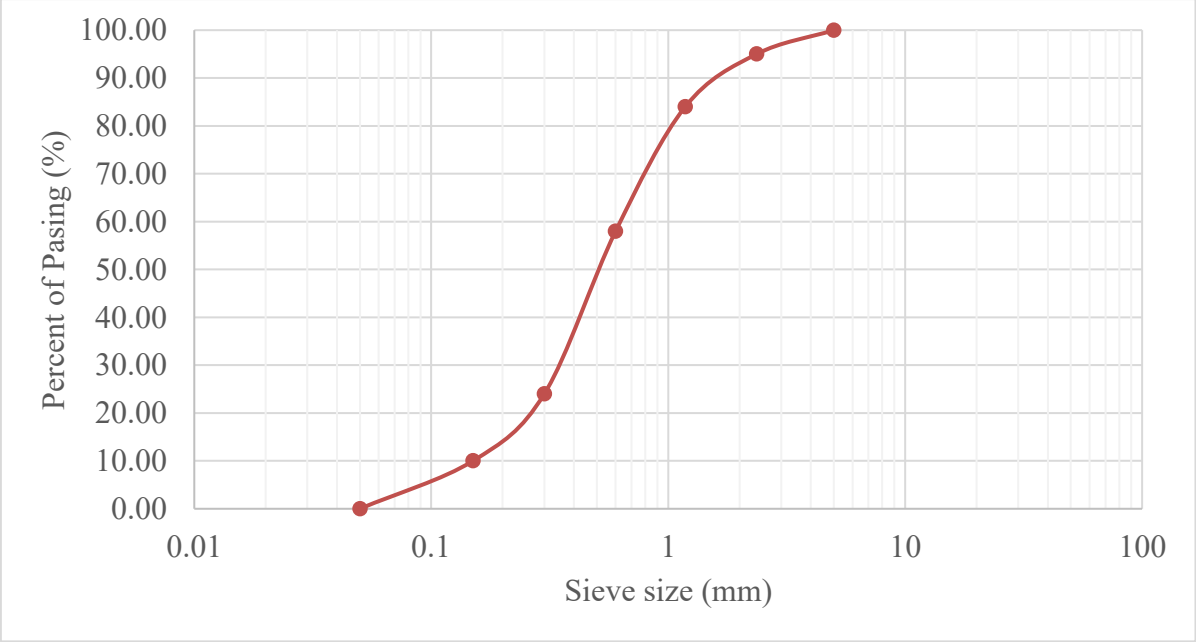


Figure 2. Particle size distribution of fine aggregates.

Fig. 2 shows the grading curve of the particle distribution of sand for the geopolymer mortar obtained from sieve analysis. According to the standard ASTM C136/C136-19, it is a well-graded aggregate containing sand particles retained on each sieve stack that is less than 5 mm. Steven et al. [22] Describe how well-graded aggregates give great workability and durability. The gap between aggregate particles that paste must fill is reduced when they are well-graded aggregates. A good bond between WPSA and sand is created since the sand can be compacted to reduce the geopolymer mortar's air void and porosity.

### *2.1.3. Alkaline Solution*

An alkaline solution is a combination of (sodium hydroxide) NaOH solution and (sodium silicate) $Na_2SiO_3$ solution. 6 M of NaOH solution was used in this research. $Na_2SiO_3$ solution combined with NaOH solution to form an alkaline solution. The chemical composition of the $Na_2SiO_3$ solution adopted was $Na_2O$ = 16.5 %, $SiO_2$ = 50.60%, and water = 32.90% by mass, respectively. The density of $Na_2SiO_3$ is 1.350-1.380 units.

## 2.2. Mix Proportions

30 samples of geopolymer mortars were prepared in this research. The ratio of WPSA to sand (W/S) is 1: 2.75 based on ASTM C109/C109M. (W/S) adopted was constant for all samples. 6 M of NaOH solution and $Na_2SiO_3$ activated the geopolymer mortar. The ratio of $Na_2SiO_3$ and NaOH was fixed and applied as 4:1 to all samples to produce an alkali activator, as reported by other researchers as well [20]. The ratio is considered an optimum value for producing high aluminosilicate in geopolymer to bind aggregates and develop strength. NaOH is less than $Na_2SiO_3$ because enormous NaOH can disturb the end product properties. However, an adequate amount of $Na_2SiO_3$ ensures sufficient silica is available for network formation. Adding $Na_2SiO_3$ solution to NaOH solution significantly enhances the reaction between the waste material and the alkaline solution [23]. NaOH diffuses aluminosilicate material, while $Na_2SiO_3$ helps NaOH act as a binder in the mortar composition [24]The ratio of water to material (W/M) is 0.25. The material is a combination of sand and WPSA.

To prepare WPSA-based geopolymer mortar samples, a similar procedure of conventional cement-based mortar production in accordance with ASTM C451 is implemented. The aim is to observe the effect of various curing temperatures on the properties of geopolymer containing WPSA and the compressive strength conducted on the hardened specimens. Table 1 shows the proportions of the geopolymer mixture. From Table 2, the polymeric mortar mixtures were mixed with the same amount of WPSA and sand.

Table 2. The proportion of the mixture of geopolymer (kg/m$^3$)

| Mix Code | WPSA | Sand | Alkaline solution/ material ratio (L/M) | NaOH | Na2SiO3 | Total water/materials ratio (W/M) |
|---|---|---|---|---|---|---|
| WPSA-T24 | 300 | 825 | 0.6 | 135 | 540 | 0.25 |
| WPSA-T60 | 300 | 825 | 0.6 | 135 | 540 | 0.25 |
| WPSA-T90 | 300 | 825 | 0.6 | 135 | 540 | 0.25 |

## 2.3. Curing Method

This study determines the effect of WPSA-based geopolymer at three different curing temperatures. Table 3 shows various curing temperatures for the specimens. The curing method is the most important process that has to be properly conducted to develop the strength of the specimens. The size of the test specimens was 50 mm x 50 mm x 50 mm, and they went through heat-cured in an oven at various temperatures for 1 day. Cubes that underwent a heat-cured

https://doi.org/10.31436/iiumej.v26i1.3015

process were placed in a drying oven, as shown in Fig. 3. After the curing process, the specimens were left for about 1 hour to cool down and then placed in the laboratory until the testing day.

Table 3. Curing temperature of geopolymer mortar

| Mix Code | No of samples | Curing temperature (°C) |
|---|---|---|
| WPSA-T24 | 10 | 24 |
| WPSA-T60 | 10 | 60 |
| WPSA-T90 | 10 | 90 |

Figure 3. Heat-cured process.

## 2.4. Geopolymer Testing Method

### *2.4.1. Characterization Properties Test*

For this research, three analyses were conducted for the physical properties test of WPSA. Firstly, the X-ray fluorescence (XRF) Analysis is used to determine the chemical composition of geopolymer mortar. XRF analysis defines the arrangement and types of chemical substances in the geopolymer. This research used a 5-gram WPSA powder sample. Next, the morphologies of WPSA images are shown through Scanning Electron Microscopy (SEM) analysis according to ASTM C1723-16. The magnifications of SEM images of WPSA are at 170 and 500 times. This study used 5 grams of WPSA to undergo this test. Lastly, the geopolymer pastes were prepared for Fourier Transformed Infrared Spectroscopy (FTIR) analysis. The FTIR analysis conducted for the age of geopolymer pastes reached 7 and 28 days based on ASTM E168.

### *2.4.2. Compressive Strength Test*

A compressive strength test was conducted to measure the hardened mortar's compressive strength development and analyze the impact of WSPA-based geopolymer. After the 50 mm ×

50 mm × 50 mm cubes had aged 7, 14, and 28 days, the compressive strength of each geopolymer mortar was measured according to ASTM C109/C109M.

# 3. RESULT AND DISCUSSION

## 3.1. Characterization Properties of Waste Paper Sludge Ash (WPSA)

### *3.1.1. Chemical Composition and Morphology of Waste Paper Sludge Ash (WPSA)*

The chemical composition of WPSA was determined through XRF analysis and tabulated in Table 4. From the XRF observation, the WPSA contains calcium oxide (CaO) as a major composition. WPSA as a cement replacement material depends on the ratio of Si: Al. The ratio of $SiO_2$ and $Al_2O_3$ is 1.1:1 and is unfavorable for geopolymer use. Newman et al. [17] stated that the ratio of Si: Al is 1.1:1, which is suitable for producing bricks and ceramics. Many past researchers stated that the ratio of $SiO_2$ and $Al_2O_3$ should be 2:1 in geopolymer [13], [15]. The presence of high CaO in geopolymer affected the cations, caused a rapid stiffening, and altered the output of the polymerization [20]. Thus, Rahman et al. [20] concluded that the high amount of CaO in WPSA could disturb the polymerization process, causing changes in the microstructure of geopolymer mortar. This is because a geopolymer is not similar to normal concrete with 100% OPC, which requires the calcium-silicate hydrates to be involved in the polymerization process to develop strength [14]. Despite the low presence of $SiO_2$ and $Al_2O_3$ in WPSA, further mechanical tests, namely compressive strength tests, need to be conducted to confirm the trend.

Table 4. Chemical composition of WPSA

| Chemical oxide | $SiO_2$ | MgO | $Al_2O_3$ | $P_2O_5$ | $K_2O$ | $Na_2O$ | $Fe_2O_3$ | $SO_3$ | TiO | CaO |
|---|---|---|---|---|---|---|---|---|---|---|
| Chemical content (%) | 17.14 | 5.54 | 15.00 | 0.24 | 0.58 | 0.64 | 0.44 | 0.09 | 0.18 | 60.15 |

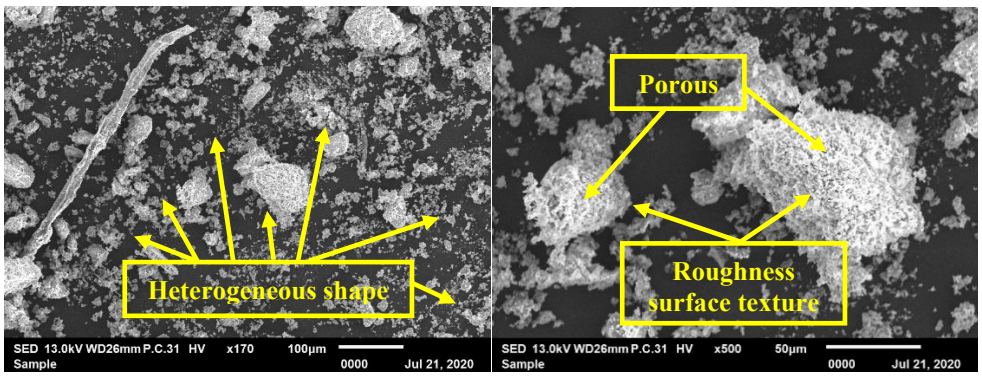


Figure 4. SEM images of WPSA, (a) Magnification 170 times, (b) Magnification 500 times.

Fig. 4 (a) and Fig. 4 (b) are the SEM images of WPSA at magnification 170 and 500 times. The SEM images of WPSA showed a highly porous structure and agglomerated particles. So, it causes problems with the workability of geopolymer mortar and geopolymer paste. The same observations were made by past researchers regarding the WPSA powder [17–19] [20]–[22]. All the authors observed that the WPSA has porous and agglomerated particles. Mamat et al. [21] stated that the agglomeration of isolated mineral grains results from the burning process. SEM observations show that the WPSA particles do not have a consistent pattern and shape, such as irregular and non-uniform shapes. The pattern and shape inconsistency of WPSA

showed a large range of particle sizes that created a good interlocking with aggregates and then enhanced the strength of geopolymer [25]. Fig. 3 (b) shows a close view of the rough surface texture of WPSA particles. The rough surface of WPSA particles created high friction between aggregates and produced strong bonds.

### *3.1.2. Structural Elucidation of Geopolymer*

Then, the paste composition of a geopolymer undergoes the Fourier-transformed infrared spectroscopy (FTIR) at a wavenumber of 4000 – 500 $cm^{-1}$. This analysis aims to find the functional groups of the chemical compound in the WPSA-based geopolymer. The geopolymer pastes at the age of 7 and 28 days were used for this analysis.

Based on Fig. 5, the wave number of the O-H is recorded between 3500 and 4000cm-1. Other researchers similarly report this finding [13]. In addition, the Si-O-Si and Al-O-Si stretching vibrations were detected at the wavenumber 1200-950$cm^{-1}$. The degree of polymerization is related to Si-O-Si and Al-O-Si stretching [26]. This increase in the Si-O-Si and Al-O-Si stretching band increases the polymerization process. However, the increase of C-O stretching at the wavenumber of 1400 - 1450 $cm^{-1}$ indicated the $CaCO_3$ because of the high calcite in WPSA [26].

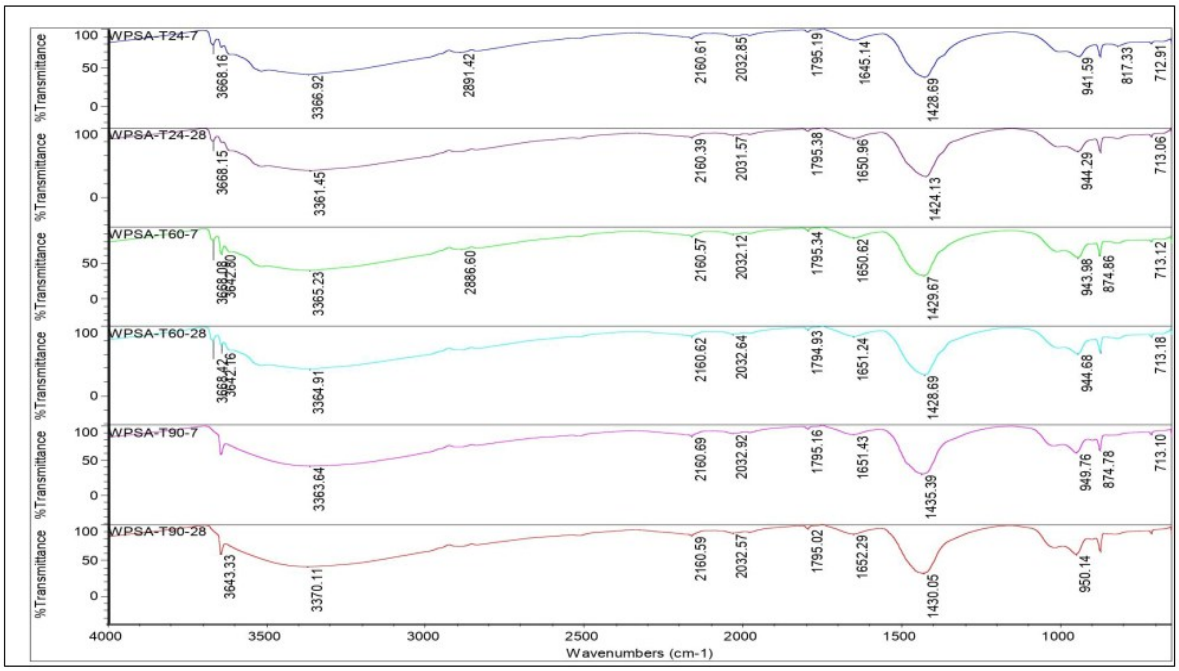


Figure 5. FTIR analysis for geopolymer pastes at 7 and 28 days.

## 3.2. Compressive Strength Results of Geopolymer Mortar

Based on Fig. 5, the geopolymer mortar cured at 60ºC has 4.65 MPa strength as the highest compressive strength at seven days. After that, the compressive strength of all geopolymer mortars shows an increasing pattern in the following seven days. For 14 days of compressive strength results, the geopolymer mortar cured at 60ºC still has the highest strength, 6.25 MPa. On the other hand, the geopolymer mortar samples cured at 24ºC gave the lowest strength, which is 4.24 MPa. Then, all geopolymer mortars' strength are expected to increase at 28 days based on the trend shown at 7 and 14 days, respectively. The geopolymer mortar cured at 60ºC still has the highest strength, 6.54 MPa, while the geopolymer mortar samples cured at 24ºC are the least.

https://doi.org/10.31436/iiumej.v26i1.3015

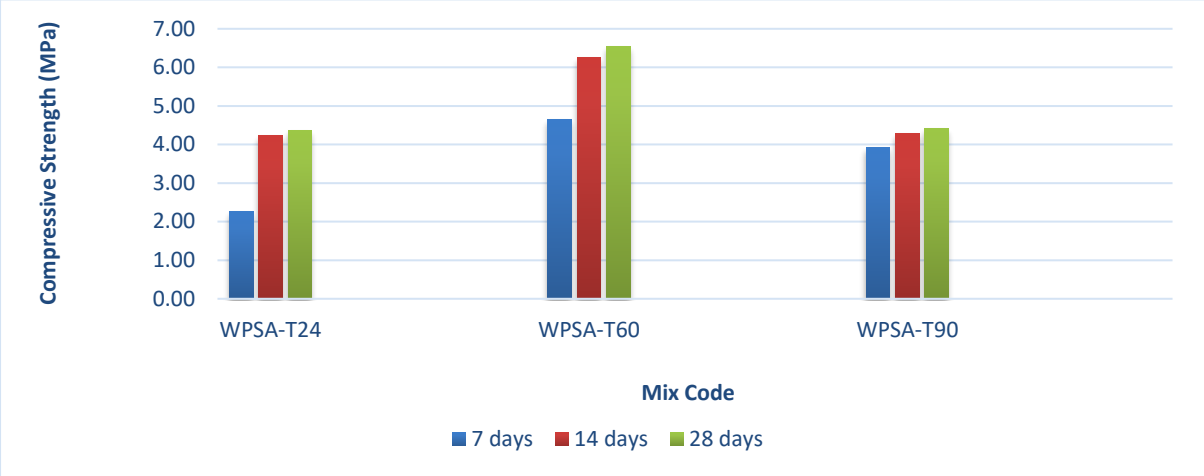


Figure 5. The comparison of compressive strength of mortar cubes at 7, 14, and 28 days.

Table 5. Observation of WPSA at 24ºC, 60ºC and 90ºC at 28 days

| Specimens | Compressive Strength Test | |
|---|---|---|
| | Before | After |
| WPSA-T24 | | 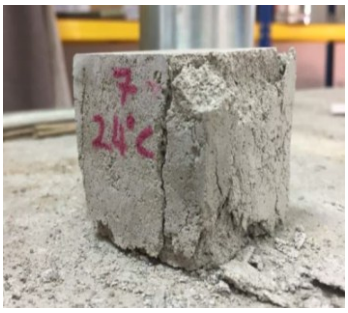 |
| WPSA-T60 | | 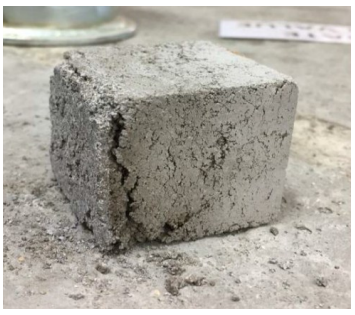 |
| WPSA-T90 | | |

In addition, Table 5 shows specimens cured at 24ºC, 60ºC, and 90ºC at 28 days before the compression test and after being set under the compressive load during the test until it reached

failure. From the observation of images in Table 5, the geopolymer mortar cured at 60ºC had a few cracks appearing on the surface of the specimen after the test. Overall, the geopolymer mortar sample cured at 24 ºC has the lowest compressive strength for 7, 14, and 28 days of the curing process. Adam and Horianto [27] stated that heat-cured curing is more favorable than normal curing. The polymerization process occurred rapidly and developed more than 50% of the geopolymer mortar strength in the first four hours of heat curing. A geopolymer had a high development strength at an early cured period [28]. The geopolymer concrete cured at 24 ºC has poor development of compressive strength [29].

The findings show that the geopolymer mortar cured at 60 ºC has the highest strength throughout 28 days of the curing process. This finding agrees with Bhushan Jindal [29], who also summarized the optimum temperature and duration of the curing process for fly ash-based geopolymer suggested by past researchers, which is 60 ºC for 24 hours. In addition, Rajan and Ramujee [30] suggested that the optimum curing temperature is 60 ºC for the size of the geopolymer mortar 50 mm cube. The 50 mm cube is small and cannot undergo a high curing temperature. The smaller size of the cube is more vulnerable and loses moisture content toward high curing temperature.

## 4. CONCLUSION

This research concludes that the Waste Paper Sludge Ash (WPSA) powder contains a higher amount of CaO compared to $SiO_2$ and $Al_2O_3$, which disrupts the polymerization process and slows the strength development of geopolymer mortar. The SiO2 to $Al_2O_3$ ratio of 1.1:1 is not ideal as a geopolymer mortar binder, where the optimal ratio for producing geopolymer is 2:1; however, the 1.1:1 ratio is suitable for brick and ceramic production. The preferred curing method for WPSA-based geopolymer mortar is heat curing, which significantly accelerates the polymerization process and strength development, with 60°C identified as the optimum temperature for curing. For future research, using WPSA as a sole binder is not recommended. Further studies should investigate the mechanical properties of the geopolymer mortar after 90 days of curing, as the strength would be fully developed by then. Additionally, conducting flexural and tensile tests is suggested to understand better the effects of these properties on the performance of geopolymer mortar.

## ACKNOWLEDGEMENT

The author would like to express the highest gratitude to the Ministry of Higher Education Malaysia (MoHE) under the Fundamental Research Grant Scheme, project ID FRGS/1/2019/TK06/UIAM/03/1 for project funding allocation and technicians of the Civil Engineering Department, International Islamic University Malaysia (IIUM), for facilitating adequate facilities and supports for the accomplishment of this study.

## REFERENCES

[1] P. Abhilash, C. Sashidhar, and I. V. Ramana Reddy, “Strength properties of fly ash and GGBS based geo-polymer concrete,” Int. J. ChemTech Res., vol. 9, no. 3, pp. 350–356, 2016.
[2] B. Nagashree, V. Kishore, and M. Malathi, “Studies on geopolymerisation Reaction using synthesised activators,” Int. J. Innov. Res. Sci. Eng. Technol., vol. 6, no. 11, 2017.
[3] G. Lavanya and J. Jegan, “Durability Study on High Calcium Fly Ash Based Geopolymer Concrete,” Adv. Mater. Sci. Eng., vol. 2015, 2015, doi: 10.1155/2015/731056.
[4] S. Ahmad, “Study of Concrete Involving Use of Waste Paper Sludge Ash as Partial Replacement of Cement,” IOSR J. Eng., vol. 3, no. 11, pp. 06–15, 2013, doi: 10.9790/3021-031130615.
[5] B. Singh, G. Ishwarya, M. Gupta, and S. K. Bhattacharyya, “Geopolymer concrete: a review of

some recent developments," Constr. Build. Mater., vol. 85, pp. 78–90, 2015, doi: 10.3390/su11164394.
[6] N. B. Singh and B. Middendorf, "Geopolymers as an alternative to portland cement: an overview," Constr. Build. Mater., vol. 237, p. 117455, 2020, doi: 10.1016/j.conbuildmat.2019.117455.
[7] Z. M. Zahib, K. Kamaruddin, and H. Saman, "Strength performance of blended ash based geopolymer mortar," in E3S Web of Conferences, 2018, vol. 34, p. 01016, doi: 10.1051/e3sconf/20183401016.
[8] M. A. Kamaruddin, M. S. Yusoff, L. M. Rui, A. M. Isa, M. H. Zawawi, and R. Alrozi, "An overview of municipal solid waste management and landfill leachate treatment: Malaysia and Asian perspectives," Environ. Sci. Pollut. Res., vol. 24, no. 35, pp. 26988–27020, 2017, doi: 10.1007/s11356-017-0303-9.
[9] C. Aciu, D. A. I. Varvara, N. Cobirzan, and A. Balog, "Recycling of Paper Waste in the Composition of Plastering Mortars," Procedia Technol., vol. 12, pp. 295–300, 2014, doi: 10.1016/j.protcy.2013.12.489.
[10] H. Y. Zhang, J. C. Liu, and B. Wu, "Mechanical properties and reaction mechanism of one-part geopolymer mortars," Constr. Build. Mater., vol. 273, 2021, doi: 10.1016/j.conbuildmat.2020.121973.
[11] G. U. Alaneme, K. A. Olonade, and E. Esenogho, Eco-friendly agro-waste based geopolymer-concrete: a systematic review, vol. 3, no. 1. Springer International Publishing, 2023.
[12] Z. Podolsky, J. Liu, H. Dinh, J. H. Doh, M. Guerrieri, and S. Fragomeni, "State of the art on the application of waste materials in geopolymer concrete," Case Stud. Constr. Mater., vol. 15, no. July, p. e00637, 2021, doi: 10.1016/j.cscm.2021.e00637.
[13] R. A. Antunes Boca Santa, A. M. Bernardin, H. G. Riella, and N. C. Kuhnen, "Geopolymer synthetized from bottom coal ash and calcined paper sludge," J. Clean. Prod., vol. 57, pp. 302–307, 2013, doi: 10.1016/j.jclepro.2013.05.017.
[14] S. Yan and K. Sagoe-Crentsil, "Evaluation of fly ash geopolymer mortar incorporating calcined wastepaper sludge," J. Sustain. Cem. Mater., vol. 5, no. 6, pp. 370–380, 2016, doi: 10.1080/21650373.2016.1174962.
[15] B. V. Rangan et al., "Properties of wastepaper sludge in geopolymer mortars for masonry applications," Constr. Build. Mater., vol. 53, no. 1, pp. 275–279, 2018, doi: 10.3390/su11164394.
[16] M. A. Faris et al., "Assessment of alkali activated geopolymer binders as an alternative of portlant cement," Mater. Plast., vol. 54, no. 1, pp. 145–154, 2017.
[17] A. Newman, N. I. Halim, M. N. Muhd Sidek, H. Mohd Saman, and A. Alisibramulisi, "Enhancement of High Strength Concrete Performance By Utilising Nano Waste Paper Sludge Ash," Sci. Res. J., vol. 18, no. 2, pp. 89–101, 2021, doi: 10.24191/srj.v18i2.11398.
[18] R. P. Venkatesan and K. C. Pazhani, "Strength and durability properties of geopolymer concrete made with ground granulated blast furnace slag and black rice husk ash," KSCE J. Civ. Eng., vol. 20, no. 6, pp. 2384–2391, 2016, doi: 10.1007/s12205-015-0564-0.
[19] Chand, M.V.L.G., "Experimental Investigation on Geo Polymer," vol. 5, no. 8, pp. 164–173, 2020.
[20] N. Rahman, A. Kusbiantoro, N. Mamat, K. Muthusamy, and M. M. A. B. Abdullah, "Roles of calcium in geopolymer containing paper mill sludge ash," Mater. Sci. Forum, vol. 917 MSF, no. 2013, pp. 311–315, 2018, doi: 10.4028/www.scientific.net/MSF.917.311.
[21] N. Mamat, A. Kusbiantoro, and N. Rahman, "Hydrochloric acid based pre-treatment on paper mill sludge ash as an alternative source material for geopolymer," Mater. Today Proc., vol. 5, no. 10, pp. 21825–21831, 2018, doi: 10.1016/j.matpr.2018.07.038.
[22] H. K. Steven, Beatrix.K, and C. P. William, Design and Control Design and Control of concrete mixtures. 2002.
[23] F. A. Shilar, S. V. Ganachari, V. B. Patil, T. M. Y. Khan, and S. Dawood Abdul Khadar, "Molarity activity effect on mechanical and microstructure properties of geopolymer concrete: A review," Case Stud. Constr. Mater., vol. 16, no. March, p. e01014, 2022, doi: 10.1016/j.cscm.2022.e01014.
[24] S. Y. Kwek, H. Awang, and C. B. Cheah, "Influence of liquid-to-solid and alkaline activator

(Sodium silicate to sodium hydroxide) ratios on fresh and hardened properties of alkali-activated palm oil fuel ash geopolymer," Materials (Basel)., vol. 14, no. 15, 2021, doi: 10.3390/ma14154253.

[25] Y. Zhang, H. Li, A. Abdelhady, J. Yang, and H. Wang, "Effects of specimen shape and size on the permeability and mechanical properties of porous concrete," Constr. Build. Mater., vol. 266, 2021, doi: 10.1016/j.conbuildmat.2020.121074.

[26] A. Wongsa, K. Boonserm, C. Waisurasingha, V. Sata, and P. Chindaprasirt, "Use of municipal solid waste incinerator (MSWI) bottom ash in high calcium fly ash geopolymer matrix," J. Clean. Prod., vol. 148, pp. 49–59, 2017, doi: 10.1016/j.jclepro.2017.01.147.

[27] A. A. Adam and Horianto, "The effect of temperature and duration of curing on the strength of fly ash based geopolymer mortar," Procedia Eng., vol. 95, no. Scescm, pp. 410–414, 2014, doi: 10.1016/j.proeng.2014.12.199.

[28] D. D. Sakthidoss and T. Senniappan, "A Study on High Strength Geopolymer Concrete with Alumina-Silica Materials Using Manufacturing Sand," Silicon, vol. 12, no. 3, pp. 735–746, 2020, doi: 10.1007/s12633-019-00263-w.

[29] B. Bhushan Jindal, "Development of High Strength Fly Ash based Geopolymer Concrete with Alccofine," IOSR J. Mech. Civ. Eng., vol. 01, no. 01, pp. 55–58, 2016, doi: 10.9790/1684-15010010155-58.

[30] B. R. Rajan and K. Ramujee, "Strength & Development of Fly ash and GGBS Based Geopolymer Mortar," vol. 07, no. 03, pp. 42–45, 2015.

https://doi.org/10.31436/iiumej.v26i1.3244

# BENTONITE-AMENDED GEO-POLYMERISED FLY ASH-GGBS MIXTURE FOR WASTE CONTAINMENT APPLICATIONS

**SAGIRI SIVASAI SARANYA[1*], MAYA NAIK[1], P.V. SIVAPULLAIAH[2]**

[1]*Department of Civil Engineering, BMS College of Engineering, Bangalore, Karnataka, India*
[2]*Research Advisor, Adichunchanagiri University, BGS Nagara, Karnataka, India*

**Corresponding author: saranya@bmsce.ac.in*

*(Received: 28 March 2024; Accepted: 1 August 2024; Published online: 10 January 2025)*

***ABSTRACT*:** The reuse of Fly Ash (FA) with the optimum amount of Ground Granulated Blast Furnace Slag (GGBS) polymerized with an alkali solution for the construction of barriers for waste containment and vertical cutoff walls for the contaminated ground is explored in this study. For this, detailed strength and permeability tests have been conducted on different ratios of FA and GGBS compacted and cured for up to 28 days. Compacted samples of FA and GGBS mixtures, at an optimal ratio of 40:60, were polymerized with sodium hydroxide alkali solution up to 5 molar concentration, as the effectiveness of polymerization varies with alkali concentration. The significant increase in compressive strength is attributed to pozzolanic reactions, whereas the increase in tensile strength is due to the polymerization of the components of the mixtures. Geopolymerisation is done through the incorporation of alkali and is known to enhance pozzolanic activity by converting part of silica to reactive silica, producing more pozzolanic compounds and part modification of pozzolanic reaction compounds. To optimize the increase in compressive strength and the percent reduction in tensile strength, the maximum concentration of alkali is restricted to 5 M. To reduce the permeability for their application in the construction of the barrier, a 5% bentonite, in addition to the optimum FA-GGBS mixture, is considered, as its high specific surface and negative charges can retain ionic contaminants such as heavy metals. Both compressive and tensile strength increased over curing, and permeability decreased. The retention capacity of selected heavy metal (lead and nickel) ions is due to their precipitation in the voids of the barrier materials.

***ABSTRAK*:** Penggunaan semula Abu Terbang (FA) dengan jumlah optimum Lebihan Pasir Kisar Relau Bagas (GGBS) yang dipolimerkan dengan larutan alkali bagi pembinaan penghalang pembendungan sisa dan dinding titik potong menegak bagi tanah tercemar diterokai dalam kajian ini. Bagi tujuan ini, ujian kekuatan dan kebolehtelapan terperinci telah dijalankan pada nisbah berbeza FA dan GGBS yang dipadatkan dan diawet selama 28 hari. Sampel padat campuran FA dan GGBS, pada nisbah optimum 40:60, digeopolimerkan dengan larutan alkali natrium hidroksida sehingga 5 kepekatan molar, kerana keberkesanan pempolimeran berbeza dengan kepekatan alkali. Peningkatan ketara dalam kekuatan mampatan adalah disebabkan oleh tindak balas pozzolanik, manakala peningkatan dalam kekuatan tegangan adalah disebabkan oleh pempolimeran komponen campuran. Geopolimerisasi adalah melalui penggabungan alkali dan diketahui dapat meningkatkan aktiviti pozzolanik melalui penukaran sebahagian silika kepada silika reaktif, menghasilkan lebih banyak sebatian pozzolanik dan sebahagian pengubahsuaian sebatian tindak balas pozzolanik. Bagi mengoptimumkan peningkatan kekuatan mampatan dan pengurangan peratus kekuatan tegangan, kepekatan maksimum alkali dihadkan kepada 5 M. Bagi

mengurangkan kebolehtelapan penggunaannya dalam pembinaan halangan, bentonit 5% sebagai tambahan kepada campuran optimum FA-GGBS dipertimbangkan, kerana permukaan spesifiknya yang tinggi dan cas negatif boleh mengekalkan bahan cemar ionik seperti logam berat. Kedua-dua kekuatan mampatan dan tegangan meningkat berbanding pengawetan, dan kebolehtelapan berkurangan. Kapasiti pengekalan ion logam berat (plumbum dan nikel) terpilih adalah disebabkan oleh pemendakannya di dalam lompang bahan penghalang.

***KEYWORDS:*** *alkali, bentonite, fly ash, ground granulated blast furnace slag, permeability*

# 1. INTRODUCTION

To meet the increasing energy demand worldwide, coal is combusted in thermal power plants to generate electricity. Fly ash (FA) is a by-product generated from these plants, and its characteristics and properties vary depending on the type of coal and combustion conditions. Class C fly ash is generated by combusting lignite or sub-bituminous coal, whereas anthracite or bituminous coal combustion generates Class F fly ash. Most FA in India is Class F due to the abundance of bituminous coal reserves. FA is utilized in various applications such as concrete production, the construction industry, soil stabilization, roads, and embankments to a limited extent, and excess FA is generally disposed of, which consumes cost, land, and environmental hazards [1]. Studies have shown that Class F fly ash alone as a source material results in less strength over curing at ambient temperature due to its reduced pozzolanic nature [2]. Utilization of Class F fly ash is highly desirable as it is considered a negative-cost material. ASTM C618-22 classified fly ashes mainly based on their calcium content. Class C fly ash with a higher amount of calcium is pozzolanic in nature besides being cementitious, whereas Class F fly ash with a lower amount of calcium is less pozzolanic or not pozzolanic but can become sufficiently pozzolanic if it contains reactive silica or more silica becoming soluble in the presence of alkali.

The restricted suitability of class F FA is due to its slow early strength gain, longer setting time, and higher water absorption. Materials rich in calcium (Ca) can be added to FA to enhance the mechanical properties. In the present work, Ground Granulated Blast Furnace Slag (GGBS) is added to increase the efficiency of FA. In addition, FA alone produced cementitious compounds by lime and reactive silica if available or becomes available in the presence of alkali. This pozzolanic reaction is time-dependent, and strength development can be slow. GGBS with higher reactive silica can react fast and produce cementitious materials to develop strength. Improper combination can also lead to decreased efficiency, and the optimum proportions of the mixture need to be evaluated [3]. Therefore, FA is amended to match the right proportion of GGBS.

Another approach for mobilizing the strength of the FA and GGBS is through alkaline polymerization. Geopolymers are gaining attention as they offer various benefits like high early and long-term compressive strength, high tensile strength, sorption capacity, sufficient durability, low $CO_2$ emissions, and limited drying shrinkage, which make them sustainable as landfill liner materials [4]. The eco-friendly construction materials are formed by activating source materials rich in silica ($SiO_2$) and alumina ($Al_2O_3$) like FA, GGBS, kaolinite, metakaolin, etc. with alkaline activators like sodium hydroxide, sodium silicate, and a combination of both [5]. Studies on the effect of alkaline activators in the polymerization process revealed that sodium hydroxide is preferred to sodium silicate as an activator as it leaves a smaller carbon footprint, and the precursors can be activated with NaOH solution without resorting to alkali silicate. Earlier studies have noticed an effective polymerization with

sodium hydroxide and without sodium silicate [6]. The use of an appropriate amount of alkali needs to be determined through laboratory testing.

One of the promising uses for alkali polymerized FA-GGBS mixtures is as a component of barriers for landfills and in constructing vertical cut-off walls to protect adjacent sites and groundwater from potential sources of pollution. Besides forming pozzolanic compounds, polymerization enhances tensile strength, a major advantage in the present application [7]. Generally, pozzolanic compounds bind particles, which can increase mostly UCS only. The enhancement in the tensile strength is only through polymerization. This is the major advantage of polymerization of the material with alkali. However, alkali inclusion also enhances pozzolanic reactions by dissolving crystalline silica and partially modifying pozzolanic compounds to N-A-S-H and C-S-H [8].

The desirable properties of any barrier materials and impoundments are good strength, low permeability, adsorption, and/or retention of contaminants contained in the leachate generated [9]. These properties also become important for constructing cut-off walls for contaminated grounds to isolate them from the surrounding environment. Relatively high strength is required for cut-off walls compared to constructing barriers for landfills, and lower permeability is more desirable for landfills than for cut-off walls. The upper limit of permeability of vertical cut-off walls is 10-6 cm/s, whereas the same is 10-7 cm/s for bottom liners [10] since cut-off walls are not constructed for hazardous waste landfills to minimize contaminant migration. The pozzolanic materials have low settlement and shrinkage properties. Being highly alkaline, they can precipitate most metal ions and make them immobile [11].

Initial tests have shown that fly ash with 60% GGBS develops optimum strength. Later, FA-GGBS mixtures were polymerized with different concentrations of sodium hydroxides in the range of 1 to 5 molar (M), which further improved their properties, particularly their applications in barriers. To further improve the tensile strength, lower hydraulic conductivity, and enhance the sorption of contaminants in the migrating leachates, the addition of about 5% calcium bentonite is considered [12]. Bentonite is known to swell on hydration in the presence of water and block the voids, reducing the hydraulic conductivity. Bentonite with high negative surface charges can also absorb ionic species present in the system, which will be an added advantage in retaining ionic contaminants such as heavy metals when they are trying to migrate through the barrier system. This swelling and blocking of the pores will be maximum when the ionic species is monovalent sodium. The initial divalent cation ions, such as calcium, are used for pozzolanic reactions, and bentonite will tend to become increasingly monovalent sodium bentonite. The alkaline conditions of the material precipitate any ionic metal ions, making them immobile and trapping them within the barrier system, apart from reducing the effective void ratio for the conduction of the contaminated leachate generated in the landfill disposal or contaminated grounds [13].

## 2. MATERIALS AND METHODS

### 2.1. Materials Used

Pozzolanic materials used in the production of geopolymers include FA and GGBS. Polymerization of these admixtures was attempted using sodium hydroxide as an alkali activator. Bentonite (B) is added to enhance cohesiveness and reduce permeability. FA was collected from the Raichur thermal power plant in Karnataka. Commercially available GGBS, bentonite, and sodium hydroxide pellets were used in the study.

The materials used in the study were characterized for specific gravity as per ASTM D792, grain size distribution (ASTM, 2007a), and compaction characteristics (including the maximum dry unit weight and optimum moisture content; ASTM, 2007b). The details are given in Table 1. Grain size distribution shows that FA and GGBS are sand and silt-sized particles, with coarse sand-sized particles being more common in FA and silt-sized particles being more prevalent in GGBS. Additionally, bentonite contains almost equal amounts of silt and clay-sized particles. Thus, a mixture of FA-GGBS amended with bentonite results in a well-packed composite with fewer voids.

Table 1. Physical properties of materials

| Properties | FA | GGBS | B |
|---|---|---|---|
| Specific Gravity (G) | 2.14 | 2.80 | 2.70 |
| Grain Size distribution (%) | | | |
| Coarse sand (4.75- 0.075mm) | 58.55 | 25.51 | 0.90 |
| Silt size (0.075- 0.002mm) | 39.82 | 70.49 | 57.80 |
| Clay size (<0.002mm) | 0.63 | 4.00 | 41.30 |
| Liquid Limit. % | 27 | 30 | 233 |
| Compaction parameters | | | |
| MDD (kN/m$^3$) | 14.00 | 15.90 | - |
| OMC (%) | 15.60 | 22.70 | - |

The oxide compositions of $SiO_2$, $Al_2O_3$, and CaO of FA, GGBS, and bentonite are obtained through Figure 1. Based on the oxide composition, FA can be categorized as Class F fly ash, a low-calcium precursor, as the calcium content of FA is less than 18%, according to ASTM C618-22 [14].

The ternary diagram shows that FA, GGBS, and bentonite used in the study contain silicon, aluminum, and CaO oxides. A mixture of FA and GGBS is advantageous for optimally utilizing both available reactive silica and CaO. It was found that FA and GGBS, in a ratio of 40:60, can achieve optimal amounts of cementitious compounds and possess better strength.

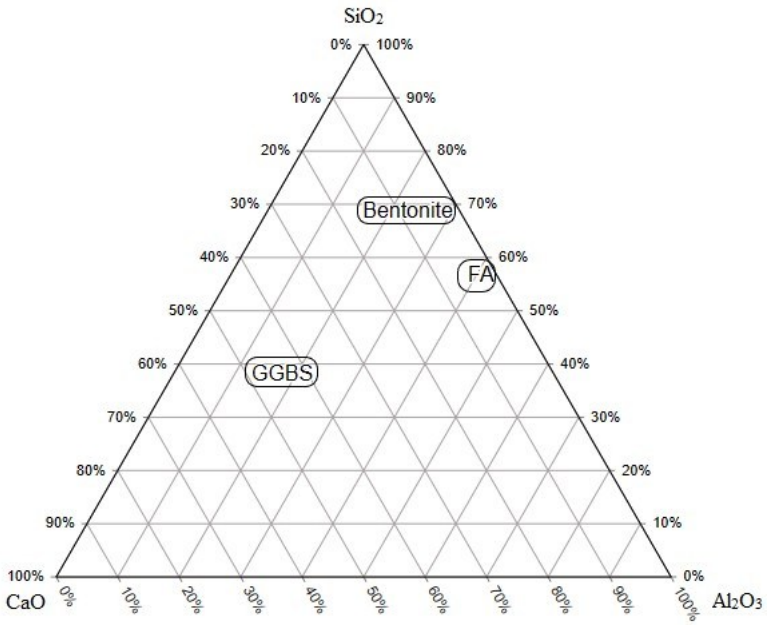


Figure 1. Composition of major FA, GGBS, and Bentonite oxides in a ternary diagram.

### 2.2. Alkali Activator

As an alkali, sodium hydroxide (NaOH) is dissolved in a calculated amount of distilled water, depending upon the required concentration as per IS 10262-2009 standards. For example, the alkaline activator was prepared by dissolving 40 g of sodium hydroxide pellets in 1 liter of water to make a 1 molar concentration solution [15].

### 2.3. Preparation of Solution with Heavy Metal Ions

The required amount of lead nitrate was dissolved in 1 liter of distilled water to make a 1000-ppm lead solution. Similarly, the required quantity of nickel nitrate is dissolved in 1000 ml of distilled water to get a 1000 ppm solution. 50 ppm solutions of lead and nickel were obtained by diluting the stock solutions.

### 2.4. Test Methods

Compaction parameters for the following four FA: GGBS mixtures were evaluated by a minicompaction test apparatus [16]. i) 20 FA:80 GGBS; ii) 40 FA:60 GGBS; iii) 60 FA:40 GGBS; and iv) 80 FA:20 GGBS. FA and GGBS were dry mixed initially until a homogeneous mixture was obtained, and then, depending on the molar concentration, sodium hydroxide solution was added as an activator. The influence of bentonite on FA-GGBS-based geopolymers with respect to strength and permeability has been investigated in the present study.

### 2.5. Preparation of Test Specimen

The mixtures were prepared on a dry-weight basis by adding the requisite quantity of water. Compacted samples of standard size (3.8 cm x 7.6 cm) for Unconfined Compressive Strength (UCS) were prepared so that the same impact energy is maintained per unit volume for each sample. Then, the extruded samples were sealed in airtight bags, and the effect of time was investigated by curing the samples in a desiccator while maintaining 100% relative humidity at room temperature for 3, 14, and 28 days [16]. During their respective curing periods, the samples were unwrapped from polythene bags and tested per ASTM-D5102 standards. The effect of the curing period and concentration of sodium hydroxide on different combinations of FA and GGBS mixtures was studied. Later, the influence of bentonite on the optimized FA-GGBS mixture in terms of strength is examined. The percentage addition of 5% bentonite was selected from the literature [17].

The optimized FA-GGBS mixture with the highest compressive strength is considered for tensile strength analysis. Specimens were cast and cured for 28 days by adding 5% bentonite to the optimized FA-GGBS mixture, with dimensions of 100 mm in diameter and 200 mm in height under molar concentrations of 1 to 5. The stiffness or tensile strength is studied by testing the specimens using a digital compression testing machine per IS 5816 (1999) standards.

Cubic specimens of 100 mm size were cast and cured for 28 days. Then, they were permeated with water and tested for permeability in terms of penetration depth as per IS 516-Part 2-Sec1.

Batch equilibrium experiments were performed by adding 5% Bentonite to a polymerized 40% FA- 60% GGBS mixture. 50 ppm of lead (Pb) and nickel (Ni) solutions were used in batch equilibrium studies. 10 grams of adsorbent collected from the tested UCS samples were added to 100 ml of solution and kept in a rotary shaker, maintaining a contact time of 8 hours. Later, the samples were filtered and tested for heavy metals using Atomic Absorption Spectroscopy (AAS).

A representative sample from the tested specimens was collected to analyze the microstructural studies using SEM. Moisture in the collected powdered sample is eliminated by oven drying it for 24 hours and maintaining a temperature of less than 40°C [18].

## 3. RESULTS AND DISCUSSION

### 3.1. UCS of FA-GGBS Mixtures After Curing for Different Periods

Figure 2 presents the variation in UCS of FA-GGBS mixtures after curing for different periods. An increase in UCS with curing is observed in all FA-GGBS mixtures, where the strength increment is greater from 3 to 14 days when compared to the increment observed between 14 and 28 days of curing.

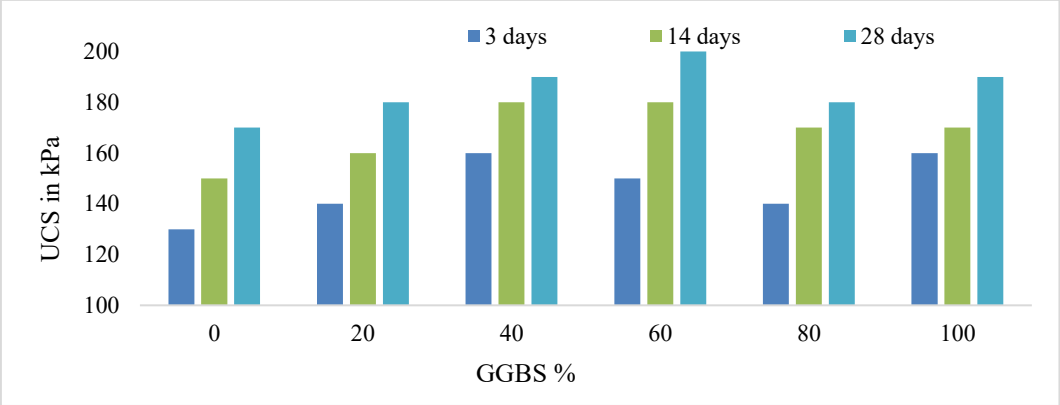


Figure 2. Influence of curing on UCS of FA-GGBS mixtures.

Among all the mixtures, the mix with 80% GGBS gave the lowest UCS after curing for 3 days but increased with further curing. Interestingly, mixtures with a GGBS content of 40 to 60% showed higher compressive strength at any curing period. It is seen from Figure 1 that GGBS has a higher calcium content compared to FA. Cementitious compounds such as CSH are produced better when calcium and silica (reactive) are in the desired proportion. This ideal ratio is achieved with 40% FA and 60% GGBS. The formation of pozzolanic reaction compounds increased gradually over time and probably reached their maximum after 28 days of curing. At the optimum percentage, a calcium-to-reactive silica ratio reaches the ideal proportion for maximum production of calcium silicate hydrates, as evident from earlier studies [19].

### 3.2. Compaction Behavior

From the unconfined compressive strength studies of different FA-GGBS mixtures compacted at their respective OMC and MDD and cured for 28 days, a mixture of 40% FA and 60% GGBS exhibited the highest strength at all molar concentrations at the 28-day curing time. So, this is considered the optimized mix in the present work. 5% bentonite is added to the optimized mixture, and its OMC and MDD were calculated using a mini-compaction test apparatus, as shown in Figure 3.

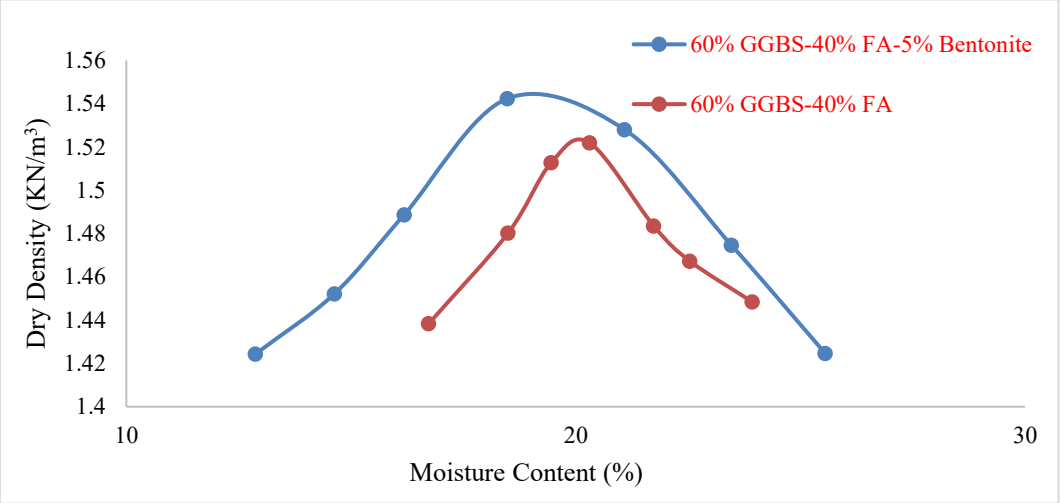


Figure 3. Compaction behavior of FA-GGBS-Bentonite mixtures.

It is known that bentonite is a highly swelling clay, and a decrease in MDD and a higher OMC are expected due to its high water-holding capacity. On the contrary, it is observed that the addition of 5% bentonite to the optimized FA-GGBS mixture resulted in an increase in MDD and a decrease in OMC. This reversal effect of bentonite on compaction behavior might be due to a reduction in swell capacity and water adsorption capacity in the presence of FA and GGBS due to the higher calcium content, which reduces its ability to swell. With the reduced swell capacity of bentonite, its finer particles get accommodated within the voids of the FA-GGBS matrix, increasing its density and decreasing its ability to hold water.

### 3.3. UCS of 40% FA-60% GGBS Mixture with 5% Bentonite After Curing

When FA or GGBS is in higher proportions, the formation of pozzolanic compounds is not ideal. Thus, the effect of adding alkali and bentonite to this combination is considered.

The mixture with 40% FA and 60% GGBS is considered an optimized mix (O) as it gave the highest compressive strength after 28 days of curing at all molar concentrations. To this, 5% bentonite is added, and the specimens are compacted for standard dimensions of UCS at their respective OMC and MDD, cured for different aging periods, and then tested.

Figure 4 shows that when 5% bentonite is added to the optimized mix with varying alkali concentrations, a gradual increase in UCS is observed with both an increase in curing and also the alkali concentration. At any alkali concentration, the strength increase is considerable after 3 days of curing, which further increases with 4 to 5 M concentrations. The increase in compressive strength with the curing period shows that the enhanced strength is mainly due to pozzolanic activity by reactions between calcium from GGBS and FA.

https://doi.org/10.31436/iiumej.v26i1.3244

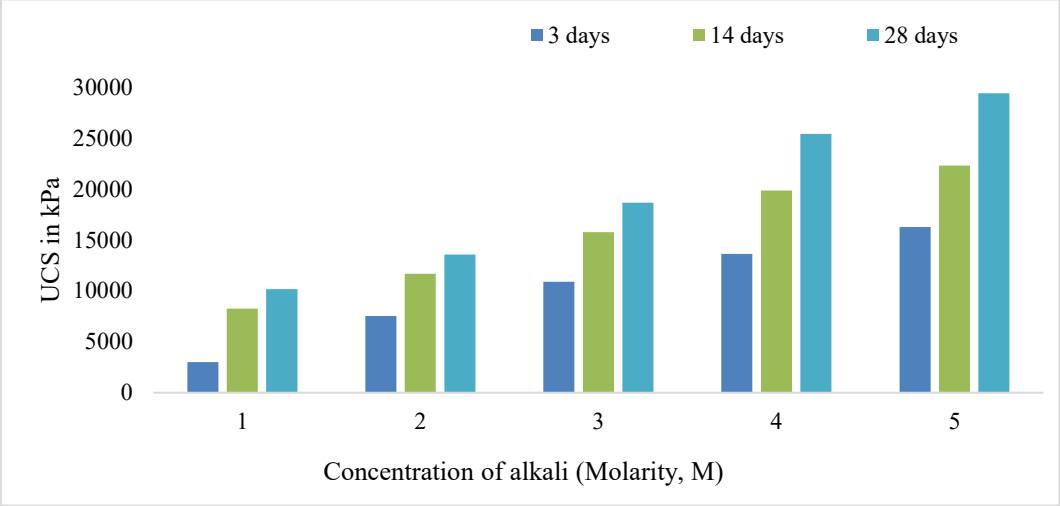


Figure 4. Effect of alkali concentration on 5% Bentonite on 40% FA-60% GGBS mixture

Apart from FA and GGBS, the added bentonite also participates in pozzolanic reactions with the available calcium hydroxide. If it were only due to polymerization, there would not have been such a significant increase in strength with an alkali solution. However, the increase in strength with increasing concentrations of alkali might also be due to the modification of the pozzolanic compounds of FA and GGBS, which produce more voluminous calcium aluminate silicate hydrate (C-A-S-H) than calcium silicate hydrate (C-S-H) alone. The effect of polymerization with alkali may not be substantial on compressive strength. This is seen more clearly by comparing the strength of the material with and without bentonite after curing for 28 days in Figure 5.

The increase in strength of FA and GGBS mixtures is low up to 3M alkali concentration when cured beyond 14 days. However, the strength is significantly higher up to 28 days of curing with a higher alkali concentration of 4 and 5 M. This will ensure that the strength reduction will not occur with higher concentrations. The UCS achieved is about 13 MPa with 4 M, which further increases with 5 M to 16 MPa after curing for 3 days. In practice, the strength required for most landfills of more than 20 feet in height is about 200 kPa. The strength achieved with the 4 or 5 M solution is more than adequate for their use as components of any barrier systems, even at lower curing periods. Thus, for these mixtures, alkali activation is sufficient with 3 to 4M alkali concentrations for enhancing the compressive strength.

### 3.4. Comparison of UCS in FA-GGBS Mixtures with the Effect of Bentonite

A comparison is made between the UCS of the 40% FA-60% GGBS mixture under varying molar concentrations with and without 5% bentonite after 28 days of curing. Figure 5 shows that at all curing periods, the 40% FA-60% GGBS mixture with 5% bentonite gave a higher compressive strength than the normal 40% FA-60% GGBS mixture. It is noticed that until 3 molar concentration, the increase in UCS for the mix having 5% bentonite is less when compared with the increase in UCS beyond 3 M alkali. This can be because of the presence of bentonite in the pozzolanic reaction with free lime to increase strength.

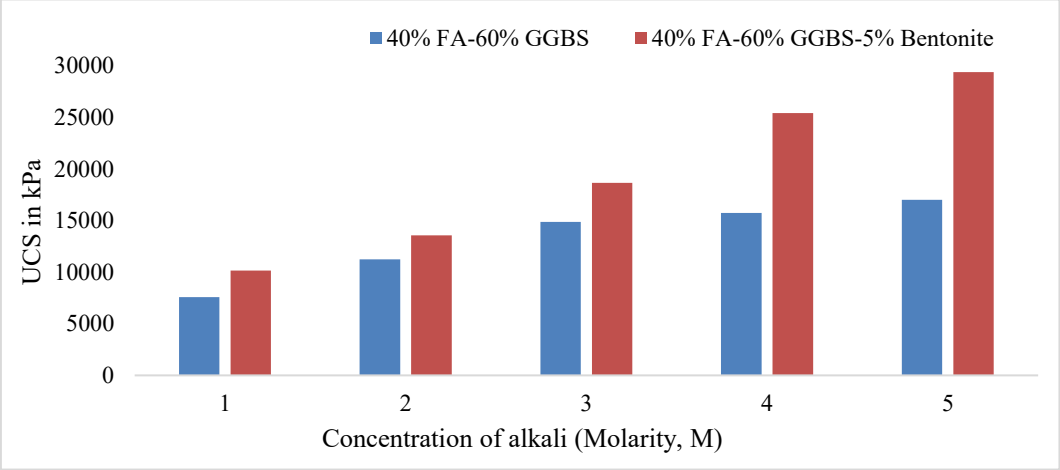


Figure 5. UCS of 40% FA-60% GGBS mixture with 5% Bentonite at 28 days curing.

### 3.5. Effect of Bentonite on Tensile Strength of FA-GGBS Mixtures at Different Alkali Concentrations

After 28 days of curing, a study was conducted on the 40% FA-60% GGBS mixture with 5% Bentonite for tensile strength. Figure 6 shows that the tensile strength is gradually increasing with an increase in alkali concentration after 28 days of curing. However, the 40% FA-60% GGBS mixture with a 5% Bentonite addition exhibited less tensile strength when compared to the optimized mixture (40% FA-60% GGBS). This contrasts the trend obtained in UCS, where mixtures with bentonite exhibited more UCS than the normal FA-GGBS mixture. The increase in tensile strength concerning alkali is due to the polymerization effect. In contrast, the reason behind the reduction in tensile strength compared to mixtures without bentonite is the dominance of pozzolanic compounds over polymerization. Additionally, bentonite possesses sufficient tensile strength due to its cohesive nature in its unreacted part.

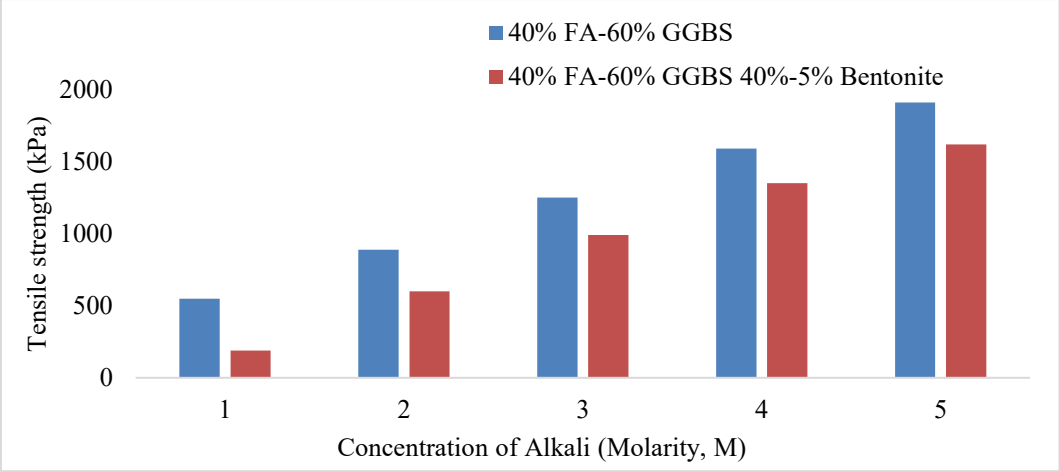


Figure 6. Effect of alkali on Tensile strength of 40%FA-60%GGBS mixture with Bentonite.

Also, bentonite is an ultrafine material with a large specific surface and adsorption capacity, which might favorably affect the development of tensile strength. Thus, bentonite can have higher cohesion than higher friction resistance, contributing more to the tensile strength. Other researchers have observed similar behaviour.

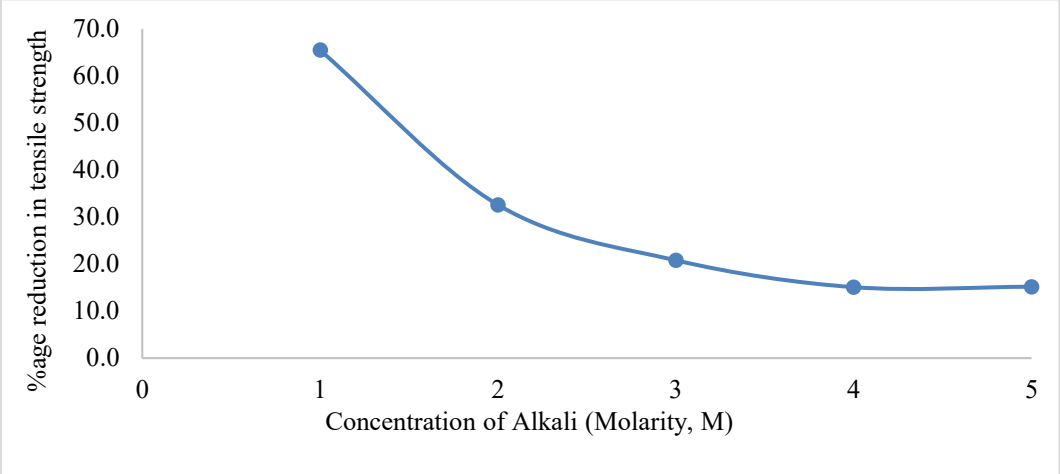


Figure 7. Reduction in tensile strength in 40% FA-60% GGBS due to Bentonite.

From Figure 7, it is evident that the percent reduction in the tensile strength gradually reduces with an increase in the alkali concentration up to 4M and remains unaffected with a further increase in the alkali concentration. This confirms that the initial effect of the presence of alkali is to reduce tensile strength. Still, with effective polymerization and increased alkali concentration, the reduction is countered by polymeric bonding. It is evident that the reduction in tensile strength is lowest with a concentration of alkali greater than 3 M. Thus, the concentration of alkali is restricted to 5 M. Higher concentrations of alkali may cause very high compressive strength, leading to brittleness, which in some cases leads to unnecessary complications.

### 3.6. Permeability

As shown in Figure 8, the permeability of the mixture of 40% FA and 60% GGBS cured for 28 days meets the criteria of a hazardous waste landfill, which should be less than $1\times10^{-7}$ cm/s.

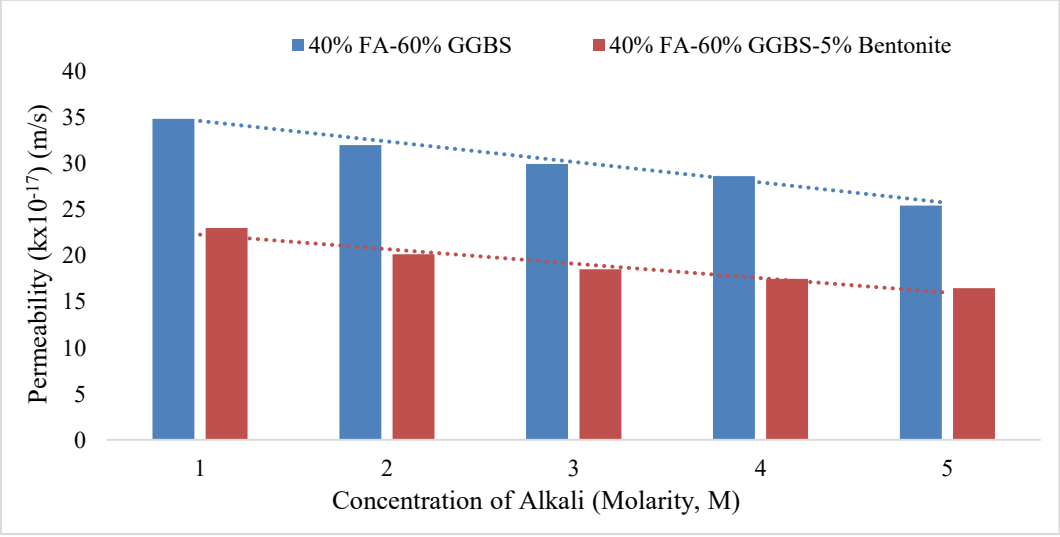


Figure 8. Effect of Bentonite on the permeability of 40% FA-60% GGBS mixture with alkali concentration.

The addition of 5% bentonite further reduced the hydraulic conductivity by about 30 to 40%, irrespective of the alkali concentration. The decrease is almost linear with the

concentration of alkali. This is due to the formation of more cementitious compounds with the addition of bentonite, which blocks the voids in FA-GGBS mixtures. Thus, an increase in alkali concentration may further reduce the permeability. From the overall consideration of strength and permeability, the concentration is restricted to 5 molars. Thus, this impermeable material overcomes the situation where leachate interaction might increase the permeability and adversely affect its long-term performance.

### 3.7. Batch adsorption investigation

Batch adsorption experiments were performed by adding an optimized FA-GGBS mixture with 5% bentonite as an adsorbent to a synthetic solution prepared in a laboratory at a known initial concentration of 50 ppm. Lead (Pb) and nickel (Ni) were the selected heavy metals for these studies. 10 grams of adsorbent are added to 100 ml of synthetic solution and kept in a rotary shaker, maintaining a contact time of 8 hours. Later, the samples were filtered and tested for heavy metals using Atomic Absorption Spectroscopy (AAS), as shown in Table 2.

Table 2. Heavy metal analysis

| Concentration of alkali | Lead (Pb), mg/l | Nickel (Ni), mg/l |
|---|---|---|
| 1M | BDL | 1.4 |
| 2M | BDL | BDL |
| 3M | BDL | BDL |
| 4M | BDL | BDL |
| 5M | 0.2 | BDL |

The concentration of Pb and Ni was very low or not detectable in the filtered solution, confirming good removal or retention efficiency of heavy metals in the barrier material. The concentration of Pb in the leachate/filtrate was Below Detectable Level (BDL) at all alkali concentrations of 1 to 4 M. In contrast, it was slightly observed when a 5 M solution was used. However, in the case of Ni, a very low concentration is observed with 1 M concentration but not detectable at all other concentrations of Ni used. This confirms that Ni is completely precipitated at a higher concentration of alkali.

### 3.8. Micro Structural Investigations

An attempt is made to support the above comparative study's findings regarding variations in UCS and tensile strength with varying GGBS content, bentonite content, and alkali concentration.

A noticeable alteration in the FA-GGBS structure is evidenced after geopolymerization and is studied through microstructural studies using scanning electron microscopy. Imposed changes in FA-GGBS mixtures due to polymerization were detected. Evaluation of surface morphology using SEM images of FA-GGBS mixtures at 28 days of curing on the optimized mix with and without 5% bentonite at 5M of alkali concentration shows that a major percentage of FA and GGBS particles reacted and resulted in gel formation. While the role of bentonite in gel formation is limited, the predominant mechanism is silica reactions with lime of FA and GGBS. At an alkali concentration of 5 molars, when a comparison is made between the optimized mixture (60% GGBS-40% FA) and the optimized mixture with 5% bentonite (60% GGBS-40% FA-5% B), the SEM images reveal the formation of more cementitious compounds in bentonite mixtures, which results in more compressive strength and also makes the specimen more flexible. The mineralogical formation is shown in Figure 9.

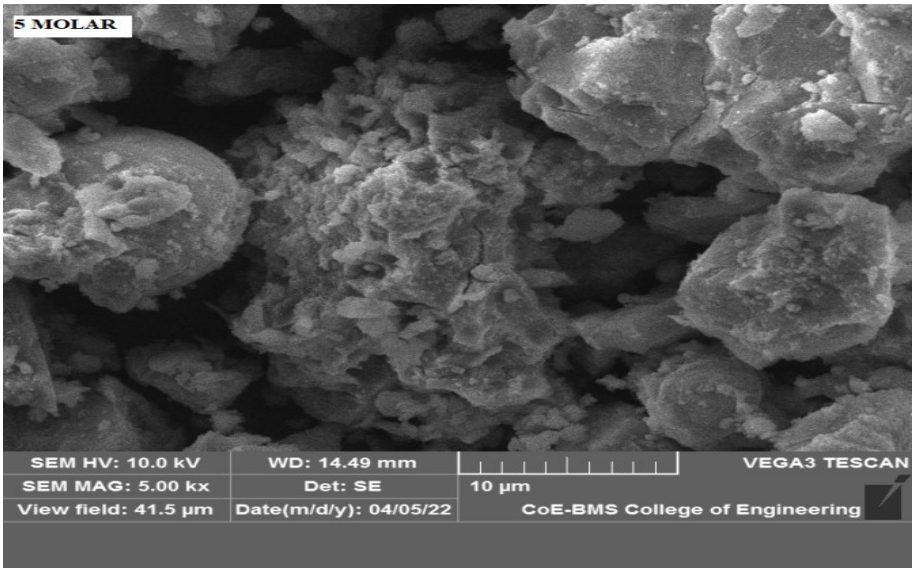


(a) Without Bentonite

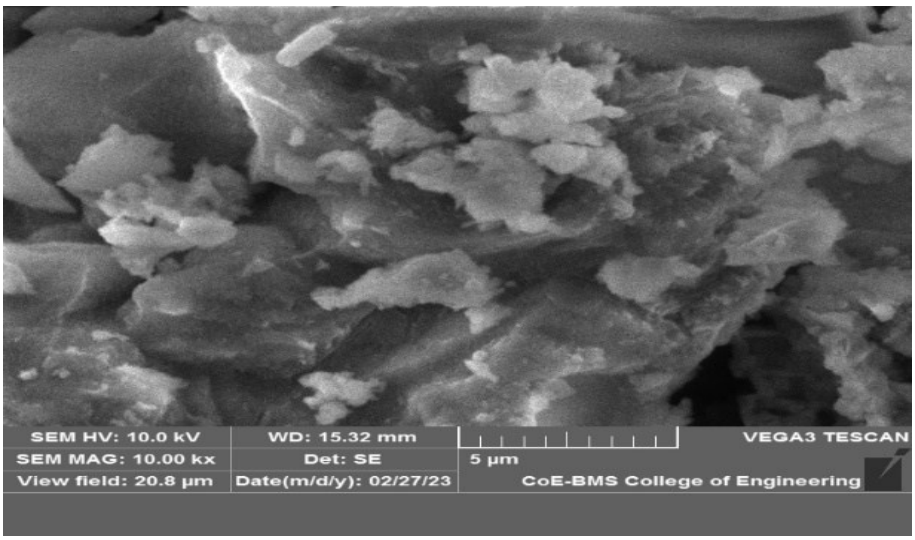


(b) With Bentonite

Figure 9. SEM image for 60% GGBS- 40% FA at 5 M concentration cured for 28 days

## 4. MECHANISM PROPOSED FOR THE STRENGTH AND PERMEABILITY OF THE IMPROVED POLYMERIZED MIXTURES

Based on the available literature on the studies by various investigators and the data presented in this paper, as explained above, the summary of the mechanism proposed for variations in the strength forms and permeability has been illustrated.

### 4.1. Pozzolanic Reactions

The main pozzolanic reaction between reactive silica and lime of FA and GGBS is described as:

$$Ca^{++} + 2\,(OH)^{-} + SiO_2 \rightarrow CSH \quad (1)$$

These reactions, which produce CSH gel, are mainly responsible for binding particles and developing strength, particularly compressive strength.

#### *4.1.1. Enhancement of pozzolanic reaction in the presence of alkali*

Alkali presence can enhance the available silica for pozzolanic reactions by dissolving reactive silica, producing more pozzolanic compounds. Also, it is possible that modification of pozzolanic reaction compounds could enhance the cementation of the barrier material.

#### *4.1.2. Modification of the pozzolanic reactions*

With various combinations of FA and GGBS, the amount of reactive silica and lime varies, producing maximum pozzolanic reaction compounds at an optimum ratio of FA and GGBS.

$$Ca^{++} + Na^{+} + 2\,(OH)^{-} + SiO_2 \rightarrow NCSH \quad (2)$$

Part conversion/formation of CSH to more voluminous NCSH can also enhance the strength.

#### *4.1.3. Polymerization of FA and GGBS*

Both FA and GGBS can get polymerized as per the general equation or formula:

$$Na_n\{—(SiO_2)_r—AlO_2—\}_n \quad (3)$$

where Na is a sodium ion, n is the degree of polycondensation, and r is the Si/Al ratio [20]. $SiO_2$ and $AlO_2$ are from FA and GGBS. This polymerization can enhance the tensile strength of the FA-GGBS mixture.

#### *4.1.4. Role of Bentonite*

Bentonite is a fine, swelling, cohesive material that swells in the presence of water and blocks the voids of the barrier system, effectively reducing the voids and hydraulic conductivity. It can also absorb ionic contaminants, leading to the adsorption and retention of the contaminants.

#### *4.1.5. Precipitation of Heavy Metals in the Presence of Alkaline Barriers*

Heavy metals such as Pb and Ni can precipitate and get trapped, making them immobile and also reducing the void ratio, leading to lower hydraulic conductivity.

## 5. CONCLUSIONS

This study has clearly shown that the properties of the FA-GGBS mixture in the presence of alkali and bentonite were improved in terms of increased strength and reduced permeability, along with the retention of heavy metal ions, making it a good barrier material for landfills and cut-off walls.

The detailed conclusions include:

- The compacted FA and GGBS mixture in the proportion of 40:60 develops good strength, which further increases with the incorporation of an alkali solution in the range of 1 to 5 M. The increase in strength with alkali solution has been attributed to enhanced pozzolanic reactions in compressive strength and polymerization in tensile strength. While a lower alkali concentration, up to 3 M, does not significantly increase the strength beyond 14 days, a higher concentration of alkali, 4 or 5 M, increases the strength beyond 14 days. Further, the reduction in percent tensile strength becomes negligible with a higher concentration of 5M alkali solution, and the alkali concentration is restricted to a maximum of 5M. Thus, an alkali solution effectively enhances the pozzolanic reaction and polymerization effect.

- Incorporating 5% bentonite steeply reduces the permeability of the compacted FA-GGBS mixture. This is due to the occupation of bentonite particles within the polymerized FA-GGBS mixture, confirmed through SEM.
- Batch equilibrium studies revealed effective retention of ionic metal contaminants by precipitation at high alkaline conditions prevailing in the barrier system.

## REFERENCES

[1] Raj K, Das A. P (2023). Lead pollution: Impact on environment and human health and approach for a sustainable solution. Environmental Chemistry and Ecotoxicology, 5, 79–85. doi: 10.1016/j.enceco.2023.02.001

[2] Phoo-Ngernkham T, Maegawa A, Mishima N, Hatanaka S, Chindaprasirt P (2015). Effects of sodium hydroxide and sodium silicate solutions on compressive and shear bond strengths of FA–GBFS geopolymer. Construction and Building Materials, 91, 1–8 doi: 10.1016/j.conbuildmat.2015.05.001

[3] Deka A, Sreedeep S (2016). Contaminant retention characteristics of fly ash–bentonite mixes. Waste Management & Research, 35(1), 40–46. doi: 10.1177/0734242x16670002

[4] Hui X, Wan Y, He X, Li J, Huang X, Liu L, Xue Q (2023). Using alkali-activated dredge sludge ash-bentonite for low permeability cutoff walls: The engineering properties and micromechanism. Environmental Technology and Innovation, 30, 103060. doi: 10.1016/j.eti.2023.103060

[5] Cristelo N, Glendinning S. G, Fernandes L, Pinto A. T (2012). Effect of calcium content on soil stabilisation with alkaline activation. Construction and Building Materials, 29, 167–174. doi: 10.1016/j.conbuildmat.2011.10.049

[6] Bernabeu, J. P., Monzó, J., Borrachero, M. V., Soriano, L., Tashima, M. M. (2022a). Activadores alternativos para cementos de activación alcalina. Revista Alconpat, 12(1), 16–31. https://doi.org/10.21041/ra.v12i1.568

[7] Gupt, C. B., Bordoloi, S., Sahoo, R. K., Sreedeep, S. (2021). Mechanical performance and micro-structure of bentonite-fly ash and bentonite-sand mixes for landfill liner application. Journal of Cleaner Production, 292, 126033. https://doi.org /10.1016/ j.jclepro. 2021.126033

[8] Amran, Y. M., Alyousef, R., Alabduljabbar, H., El-Zeadani, M. (2020). Clean production and properties of geopolymer concrete; A review. Journal of Cleaner Production, 251, 119679. https://doi.org/10.1016/j.jclepro.2019.119679

[9] Prashanth J, Sivapullaiah P. V, Sridharan A (2001). Pozzolanic fly ash as a hydraulic barrier in land fills. Engineering Geology, 60(1–4), 245–252. doi: 10.1016/s0013-7952(00)00105-8

[10] Bagheri, A., Alibabaie, M., Babaie, M. (2008). Reduction in the permeability of plastic concrete for cut-off walls through utilization of silica fume. Construction and Building Materials, 22(6), 1247–1252. https://doi.org/10.1016/j.conbuildmat.2007.01.024

[11] Azhar U, Ahmad H, Shafqat H, Babar M, Munir H. M. S, Sagir M, Arif M, Hassan A, Rachmadona N, Rajendran S, Mubashir M, Khoo K. S (2022). Remediation techniques for elimination of heavy metal pollutants from soil: A review. Environmental Research, 214, 113918. doi: 10.1016/j.envres.2022.113918

[12] Devarangadi M, M U. S (2019). Use of ground granulated blast furnace slag blended with bentonite and cement mixtures as a liner in a landfill to retain diesel oil contaminants. Journal of Environmental Chemical Engineering, 7(5), 103360. doi: 10.1016/j.jece.2019.103360

[13] Consoli N. C, Heineck K. S, Carraro J. A. H (2010). Portland Cement Stabilization of Soil–Bentonite for vertical cutoff walls against diesel oil contaminant. Geotechnical and Geological Engineering, 28(4), 361–371. doi: 10.1007/s10706-009-9297-5

[14] ASTM C 618, "Standard Specification for Coal Fly Ash and Raw or Calcined Natural Pozzolan for Use as a Mineral Admixture in Concrete," ASTM International, West Conshohocken, Pa., 2001, 4 pp

[15] Anuradha, R., Sreevidya, V., Venkatasubramani, R., Rangan, B. V. (2012). Modified Guidelines For Geopolymer Concrete Mix Design Using Indian Standard. Asian Journal Of Civil Engineering (Building And Housing), 13(3),357– 68.

[16] Devarangadi M, M U. S. (2020). Correlation studies on geotechnical properties of various industrial byproducts generated from thermal power plants, iron and steel industries as liners in a landfill- a detailed review. Journal of Cleaner Production, 261, 121207. doi: 10.1016 /j.jclepro.2020.121207

[17] Fan, R.-D, Yang Y, Liu S (2021b). Impact of in situ soil in Soil-Bentonite cutoff wall backfill on compressibility and hydraulic conductivity. Advances in Civil Engineering, 2021, 1–12. doi: 10.1155/2021/9350604

[18] Su, J., Huang, Z., Ren, L. (2007). High compact melamine-formaldehyde microPCMs containing n-octadecane fabricated by a two-step coacervation method. Colloid & Polymer Science, 285(14), 1581–1591. https://doi.org/10.1007/s00396-007-1729-2

[19] Grace, M. A., Clifford, E., Healy, M. G. (2016). The potential for the use of waste products from a variety of sectors in water treatment processes. Journal of Cleaner Production, 137, 788–802. https://doi.org/10.1016/j.jclepro.2016.07.113

[20] M, B., Sudhir, Chen, S., Rai, S., Jain, D. (2022). An empirical model for geopolymer reactions involving fly ash and GGBS. Advances in Materials Science and Engineering, 2022, 1–13. https://doi.org/10.1155/2022/8801294

https://doi.org/10.31436/iiumej.v26i1.3321

# FACTORS INFLUENCING THE ELASTIC STIFFNESS FACTOR IN REINFORCED CONCRETE STRUCTURE OF DUAL SYSTEM USING PUSHOVER ANALYSIS

**SHAHRAM JKHSI*, SAYA ABDULLAH SABER**

*Department of Civil Engineering, Near East University, Nicosia, Northern Cyprus*

**Corresponding author: shahram.jkhsi@gmail.com*

*(Received: 10 June 2024; Accepted: 20 November 2024; Published online: 10 January 2025)*

***ABSTRACT:*** Stiffness is one of the most critical characteristics of a building, which is considered for public safety against earthquake loads and refers to displacement resistance. Buildings must be built with proper strength and stiffness. This study uses pushover analysis to evaluate the parameters influencing the stiffness of the RC Dual system. The research used ASCE 7-10 and ACI 318-08 codes to design 24 two-dimensional buildings. Pushover analysis is conducted in the models using the ETABS software. Factors, including the number of stories, span length, thickness of the shear walls, and compressive strength, were considered while evaluating the stiffness and base shear of the designed buildings. The highest stiffness factor is (149.30) found in low-rise buildings with smaller span lengths, higher shear wall thickness, and higher compressive strength. In comparison, the lowest stiffness factor of (27.88) appeared in high-rise buildings with longer span lengths, lower shear wall thickness, and lower compressive strength. This study analyzed a dual system consisting of a moment-resisting frame and a shear wall. In further studies, other structural systems can be considered. By increasing the span length from 5.5m to 6.5m, the stiffness factor decreases by 8%. While by increasing shear wall thickness, the stiffness factor increased by 4.5%. Since every sample consists of two-dimensional dual systems, the influence of torsion is avoided. Future work should take torsional impacts into account since they have the potential to impact the design.

***ABSTRAK:*** Untuk menyediakan keselamatan umum terhadap daya gempa, salah satu ciri bangunan yang paling penting ialah kekakuan, yang menerangkan tentangan terhadap anjakan. Bangunan mesti dibina dengan kekuatan dan kekakuan yang betul. Kajian ini menggunakan analisis pushover untuk menilai parameter yang mempengaruhi kekukuhan sistem RC Dual. Penyelidikan menggunakan kod ASCE 7-10 dan ACI 318-08 untuk mereka bentuk 24 bangunan dua dimensi. Analisis pushover dijalankan dalam model menggunakan perisian ETABS. Beberapa faktor, termasuk bilangan tingkat, panjang rentang, ketebalan dinding ricih, dan kekuatan mampatan, diambil kira semasa menilai kekukuhan dan ricih asas bangunan yang direka bentuk. Faktor kekukuhan tertinggi yang diukur dengan membahagikan ricih asas kepada anjakan (149.30) muncul di bangunan bertingkat rendah dengan panjang rentang yang lebih kecil, ketebalan dinding ricih yang lebih tinggi, dan kekuatan mampatan yang lebih tinggi. Manakala faktor kekakuan terendah (27.88) terdapat pada bangunan bertingkat tinggi dengan panjang rentang yang lebih panjang, ketebalan dinding ricih yang lebih rendah, dan kekuatan mampatan yang lebih rendah. Hanya kerangka tahan momen dengan dinding ricih yang dipanggil model (sistem dwi) telah dianalisis dalam kajian ini; sistem struktur lain boleh dipertimbangkan dalam kajian lanjut. Dengan meningkatkan panjang rentang daripada 5.5m kepada 6.5m, faktor kekakuan berkurangan sebanyak 8%. Manakala dengan meningkatkan ketebalan dinding ricih, faktor kekakuan meningkat sebanyak 4.5%. Memandangkan setiap sampel terdiri daripada sistem dwi dua

https://doi.org/10.31436/iiumej.v26i1.3321

dimensi, pengaruh kilasan dielakkan, kerja masa hadapan harus mengambil kira kesan kilasan kerana ia berpotensi memberi kesan kepada reka bentuk.

***KEYWORDS***: *reinforced concrete structure, pushover analysis, dual system, base shear, elastic stiffness factor*

# 1. INTRODUCTION

In reinforced concrete structures, earthquakes can result in various damages like concrete bursting, cracking, and failure of nonductile parts. The degree of damage is determined by several factors, including the type of seismic event, building design, and construction materials. Structures are designed to withstand earthquakes and built according to specific criteria to improve human life stability during severe seismic events [1, 2]. A moment-resistant frame combined with a shear wall makes the structure stiff and capable of withstanding lateral loads [3]. Dual systems, such as structural reinforced concrete (RC) with shear walls, were widely employed as structural resistance against attraction and lateral forces [4]. The pushover analysis method determines the maximum load a structure can withstand, indicating its capability to endure earthquakes [5].

In pushover analysis (nonlinear static method), a push is applied to the top level of the structure until it collapses. The collapse of the structure is represented by the relationship between maximum load and displacement in the ETABS pushover analysis [6]. Static inelastic analysis determines the strength requirement and displacement of the structure during the seismic period. The main objective of pushover analysis is to assess the desired quality level of the structure [7]. The objective of the elastic stiffness factor of a building is the ability to resist loads applied to the structure without causing plastic hinges, and it can be used to determine the building's natural period. The pushover curve can be used to determine this component by dividing the base shear by the lateral displacement at the first appearance of the plastic hinge [8]. Stiffness is the capacity of a beam or column to resist deformation when load is applied. One purpose of building design is to ensure that no part of the structure is exposed to damage or cracking that may cause its collapse after construction [9]. The capability curves, also known as pushover curves, are base shear load-deformation curves that point in the direction of the lateral deformation of the building and show the nonlinear characteristic of the structure. The pushover curve provides an expression of structural capabilities. The most effective way to map the load-deformation curves was to follow the base shear by considering both roof displacement and the base shear [10]. It is known that stiffness increases with increases in compressive strength and shear wall thickness. Conversely, extending the span length or adding stories from low to high causes the stiffness factor to decrease.

Each reinforced concrete element is classified into two types: B-regions (Bernoulli regions), which have a uniform distribution of stresses and no substantial turbulence in stress line contours. The flexural analytical concept can be employed in this region. The second type of region is the D-region (Discontinuity region), which occurs when there is a discontinuity in the distribution of stresses or when contour lines are disturbed [11]. The D-region (disturbed region) in reinforced concrete (RC) constructions refers to locations around discontinuities, like openings, heavy loads, or abrupt shifts in geometry, where stress distribution differs from a standard beam or column behavior. The D-region gets non-uniform stress distributions. It may become a weak point if it is not properly reinforced or accurately calculated, reducing the elastic stiffness factor. The stiffness of the dual system depends on the D-region's integrity, which requires material qualities and stress transfer mechanisms. D-regions can be caused by changes in geometry, like pile caps, openings, beam-column joints, and non-prismatic beams.

https://doi.org/10.31436/iiumej.v26i1.3321

Due to the significant stresses in the D-regions, the cross-section of the members will not remain plane after deflection [12].

Jamnani et al. [13] evaluated the energy distribution in reinforced concrete shear walls and structural frames when subjected to multiple earthquakes by determining the stability of the structures. The paper investigated the nonlinear action and strength distribution of RC shear wall composite frames. Reliable predictions can be made when comparing the impacts of several earthquakes on structures using a single wave analysis. Generally, repetitive building earthquakes lead to fading inelastic strength. Benaied et al. [14] investigated the reaction of inelastic reinforced concrete structures with mass and stiffness irregularities to seismic activity. By incorporating vertical irregularities into various designs of a ten-story building, the responses of key parameters are analyzed and quantified. Stiffness irregularities were shown to have a more significant influence than mass irregularities on the seismic response, which were discovered to have a negligible effect on the building's seismic behavior. The outcome demonstrates that irregular structures must be built to reduce seismic effects and cannot satisfy seismic design standards.

Bertagnoli et al. [15] present a software study of the reinforced concrete structure. The structure under explanation is a combination of beams and columns that provides part of the structural building frame of ten-story RC structures. It is also subjected to lateral forces and a progressively increasing longitudinal displacement of the central column to simulate the column removal scenario. In urban areas of India, mid-rise residence reinforced concrete buildings with several stories that range from 8 to 10 or 12 will become ordinary. Shear walls were provided in mid-rise reinforced concrete frames for lateral force tolerances. Considering the shear walls were also provided via openings, in addition to the drifting floor stiffness, moment, and shear, it is essential to look into how these openings impact the stresses in the shear walls. A three-dimensional analysis was conducted to design the shear wall across the building structure. This study emphasizes the significance of the locations and sizes of each of those openings [16].

Birzhandi et al. [17] present a new approach to the design of one-way asymmetrical plan reinforced concrete wall structures. The modified modal pushover design method (MMPD) is the name given to this approach. Three eight-story structures have been planned accordingly to evaluate the impact of two distinct reinforcement area distributions on the NRHA requirements for each level. The elastic jagged response spectrum has higher mode contributions in responses of all structures. The mean-matched smoothed displacement response spectrum standard deviation curve is also applied to evaluate the shear and torsional stresses indicated by these two response spectra for stories. In conclusion, MMPD offers a safe design for the flexural capacity of shear walls on both the stiff and flexible sides of the plan. This highly reliable and cost-effective approach uses the structure’s responses over time to adapt and optimize the design for future needs. The outcomes demonstrate how accurately the MMPD approach calculates the stiffness and strength of shear walls that resist earthquakes. Ahmad [18] used twelve two-dimensional reinforced concrete frames with various span lengths, and the number of stories, with shear walls and without shear walls, were subjected to pushover analysis to determine the impact of these factors on the elastic stiffness factor. The study’s findings demonstrated that the stiffness factor reduces as the number of stories increases, and the elastic stiffness factor increases when the span length increases. Frames with shear walls are much stiffer compared to frames without shear walls. Using a shear wall in a building will effectively reduce the displacement of the structure and story drift. It would reduce the damage caused by lateral forces like earthquakes. Depending on the study, the

https://doi.org/10.31436/iiumej.v26i1.3321

highest performance that reduces displacement and story drift is achieved by evenly placing the shear wall of the structures in the middle span of the building [19].

The suitability of pushover analysis for the seismic assessment of mid-rise and high-rise buildings is examined. Pushover analysis overestimates the highest displacements and underestimates story drifts, especially those occurring on the tallest floors of structural buildings. The shear wall's optimal location for a multiple-story structural building has been investigated. Nonlinear structural analysis is performed for various shear wall locations inside building structures. An eight-story building structure was given. A pushover curve was compared with several models by using the ETABS program. The results show that having a shear wall at a suitable location is more critical when base shear and displacement are present in building structures [20].

Elements that affect long-term stiffness, including creep, shrinkage, and concrete, should be considered. The advantages of the pushover method include handling nonlinear behavior, simulating progressive collapse, supporting performance-based design, identifying weaknesses in structure, developing hinge properties, and ensuring code compliance. Exploring how the height and slenderness of a building affect its elastic stiffness, particularly in very tall buildings, is an essential area of study. This research can lead to new insights into designing super-tall structures that remain stable and resilient under lateral loads. Further investigation is necessary about the influence of new materials (such as fiber-reinforced polymers and high-performance concrete) on the stiffness factor of dual systems.

# 2. METHODOLOGY

The study studied reinforced concrete dual systems (moment-resisting frame with shear wall) to determine the base shear and elastic stiffness factors. Twenty-four two-dimensional models with different shear wall thicknesses, story numbers, span lengths, and compressive strengths were designed to identify stiffness. Various models have been used by adapting each parameter to each other, and each model contributes to identifying and evaluating the effect of these variables. ASCE 7-10 and ACI 318-08 codes have been used in this investigation. Pushover analysis is applied to the models using the ETABS computer program.

## 2.1. Assumed Material Properties

Materials that were used in this article are shown in Table 1.

Table 1. Material Properties

| Materials | Properties |
|---|---|
| **Compressive strength ($f'c$)** | 250 $kgf/cm^2$ and 280 $kgf/cm^2$ |
| ***Fy* of reinforcement steel** | 420 $N/mm^2$ |
| **Modulus of elasticity of steel** | 200,000 $N/mm^2$ |
| **Concrete modulus of elasticity** | 23500 and 25743 $N/mm^2$ |

* $Fy$: Yield Strength

*ACI: American Concrete Institute

*ASCE: American Society for Civil Engineering

## 2.2. Description of Models

Details of the models that were used are shown in Figure 1.

https://doi.org/10.31436/iiumej.v26i1.3321

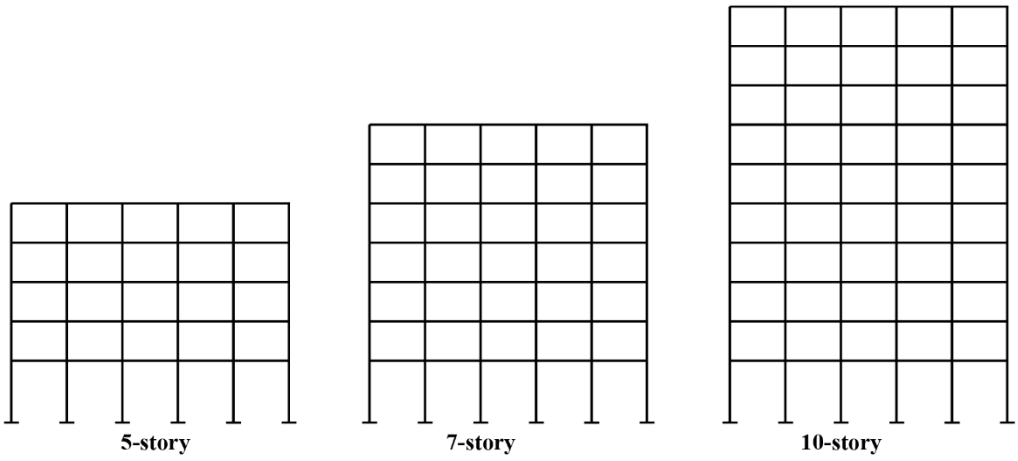


(a) Number of stories

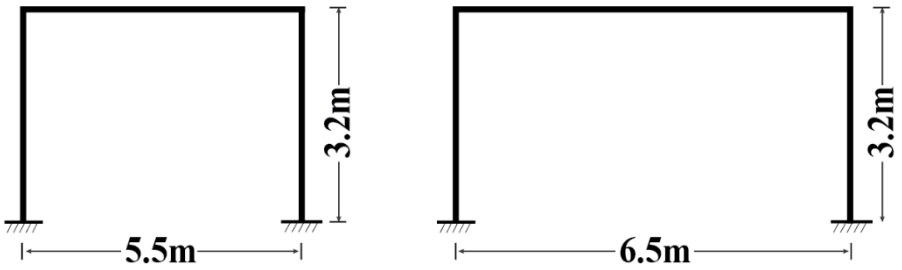


(b) Span lengths and story height

(c) Number of spans (5)

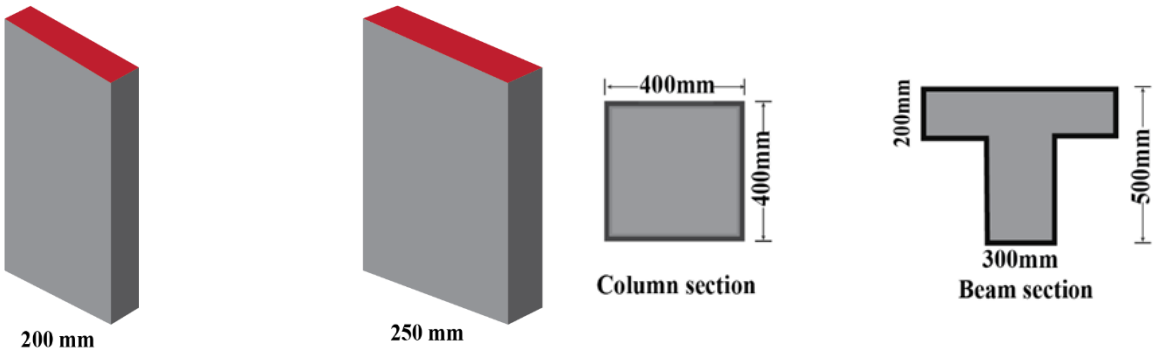


(d) Shear wall thickness (e) Column and beam section sizes

Figure 1. Details of the models.

https://doi.org/10.31436/iiumej.v26i1.3321

### 2.3. Elastic Stiffness Factor Analysis

Pushover analysis is a valuable technique for analyzing the behavior of the building, recording yielding and cracking when the base shear rate increases. Static analysis displays the degree of performance, the collapse mechanism, and the behavior of elements in the structure [21]. Static analysis shows the relationship between base shear and displacement. Figure 2 shows the building when the lateral load adds a push.

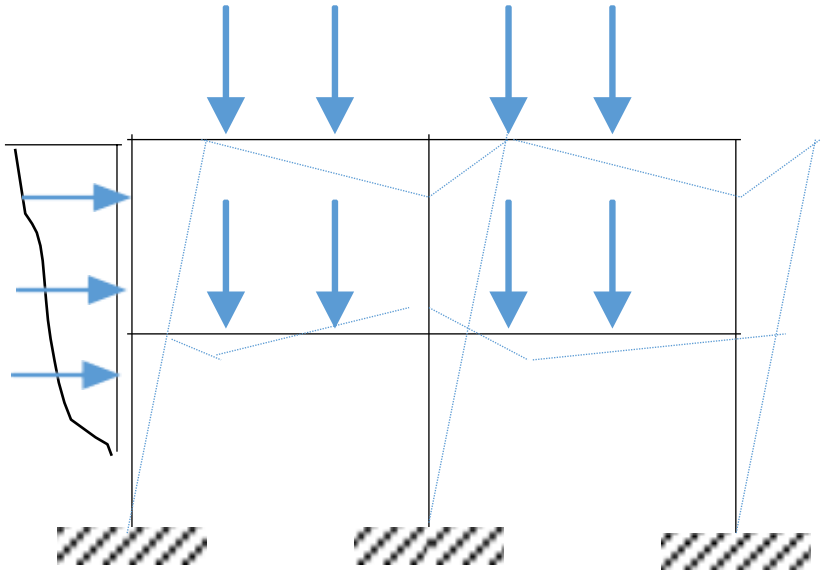

Figure 2. Pushover illustration [22]

The two-dimensional mathematical models of the dual systems are first built and designed, with hinges given to the frames. Pushover analysis is then stated, and the load patterns of pushover analysis have been assigned to a direction. All the models are pushed up to rupturing displacement at the dictated joint. This research looks at the acceleration pattern of lateral load, which draws a pushover curve up to the point where the structure collapses. In this acceleration pattern, the lateral load is increased until the structure reaches the system's maximum capacity. Following pushover analysis, a curve shows the structure's lateral displacement and base shear. An example of the elastic stiffness factor calculation process via a pushover curve can be observed in the sample below.

The stiffness factor is found by dividing the base shear by the lateral displacement at the occurrence of the first plastic hinge. After constructing the pushover curve, the base shear is taken from the curve, and the elastic stiffness factor is determined [23]. Figure 3 illustrates extracting the highest base shear strength from the pushover curve and calculating the elastic stiffness factor.

https://doi.org/10.31436/iiumej.v26i1.3321

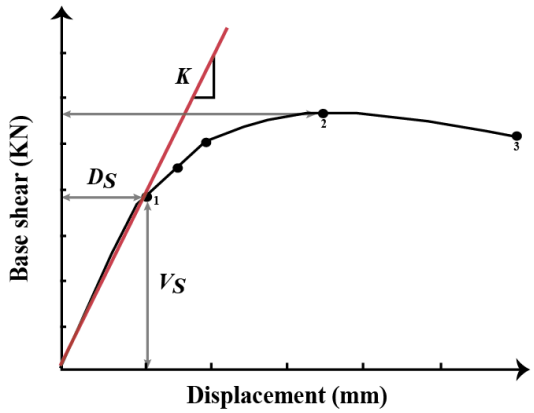


Vs - Base shear
Ds - Displacement at first plastic hinge formation
K - Elastic stiffness factor

Figure 3. States of pushover curve [21].

The equation for finding the elastic stiffness factor:

$$K = \frac{V_S}{D_S} \tag{1}$$

where $V_s$ is the base shear (first hinge formation in $kN$, $D_s$ is the displacement at the first plastic hinge formation (in $mm$), and $K$ is the elastic stiffness factor in $kN/mm$.

## 3. RESULTS AND DISCUSSION

In this section, the analysis results of 24 2D models of reinforced concrete dual systems, as well as their ease of operation and graphical user interface, are compared and discussed in graphs and tables for different parameters that affect the elastic stiffness factor, as shown in Table 2, including different shear wall thickness, different number of stories, different span length, and different compressive strength. Comparison and assessment of the reinforced concrete structure with the shear wall is established based on the elastic stiffness factor and the base shear of the dual system.

Table 2. Results of elastic stiffness factor for all of the models

| Model No. | Shear wall thickness (mm) | Compressive strength *(f'c)* $kgf/cm^2$ | Number of stories | Span length (m) | Stiffness factor $KN/mm$ |
|---|---|---|---|---|---|
| **1** | 200 | 250 | 5 | 5.5 | 138.73 |
| **2** | 200 | 250 | 5 | 6.5 | 127.21 |
| **3** | 200 | 250 | 7 | 5.5 | 59.33 |
| **4** | 200 | 250 | 7 | 6.5 | 55.14 |
| **5** | 200 | 250 | 10 | 5.5 | 29.31 |
| **6** | 200 | 250 | 10 | 6.5 | 27.88 |
| **7** | 200 | 280 | 5 | 5.5 | 140.82 |
| **8** | 200 | 280 | 5 | 6.5 | 132.05 |
| **9** | 200 | 280 | 7 | 5.5 | 64.33 |
| **10** | 200 | 280 | 7 | 6.5 | 61.09 |
| **11** | 200 | 280 | 10 | 5.5 | 33.76 |
| **12** | 200 | 280 | 10 | 6.5 | 30.19 |
| **13** | 250 | 250 | 5 | 5.5 | 145.37 |
| **14** | 250 | 250 | 5 | 6.5 | 136.91 |
| **15** | 250 | 250 | 7 | 5.5 | 69.04 |
| **16** | 250 | 250 | 7 | 6.5 | 67.17 |
| **17** | 250 | 250 | 10 | 5.5 | 36.44 |
| **18** | 250 | 250 | 10 | 6.5 | 33.20 |
| **19** | 250 | 280 | 5 | 5.5 | 149.30 |

| | | | | | |
|---|---|---|---|---|---|
| **20** | 250 | 280 | 5 | 6.5 | 139.01 |
| **21** | 250 | 280 | 7 | 5.5 | 70.14 |
| **22** | 250 | 280 | 7 | 6.5 | 68.29 |
| **23** | 250 | 280 | 10 | 5.5 | 38.74 |
| **24** | 250 | 280 | 10 | 6.5 | 35.31 |

### 3.1. The Effect of the Number of Stories on the Elastic Stiffness Factor

The following chart illustrates how the stiffness factor varies across the stories of 5-, 7-, and 10-story buildings with different span lengths. Figure 4 illustrates that the highest stiffness factor, 140.82 $KN/mm$, was observed in the shorter span length of the 5-story building, while the lowest stiffness factor, 30.19 $KN/mm$, was observed in the 10-story building with a longer span length. Elastic stiffness decreases by 55% when the number of stories in a building increases from low to mid-rise and by 50% as the building type changes from mid-rise to high-rise. Ngenge et al. [3] showed that increasing the number of stories from 4 to 10 decreased the elastic stiffness factor by 63%. Factors used in this section: Shear wall thickness= 200mm, and compressive strength (f'c)= 280 $kgf/cm^2$.

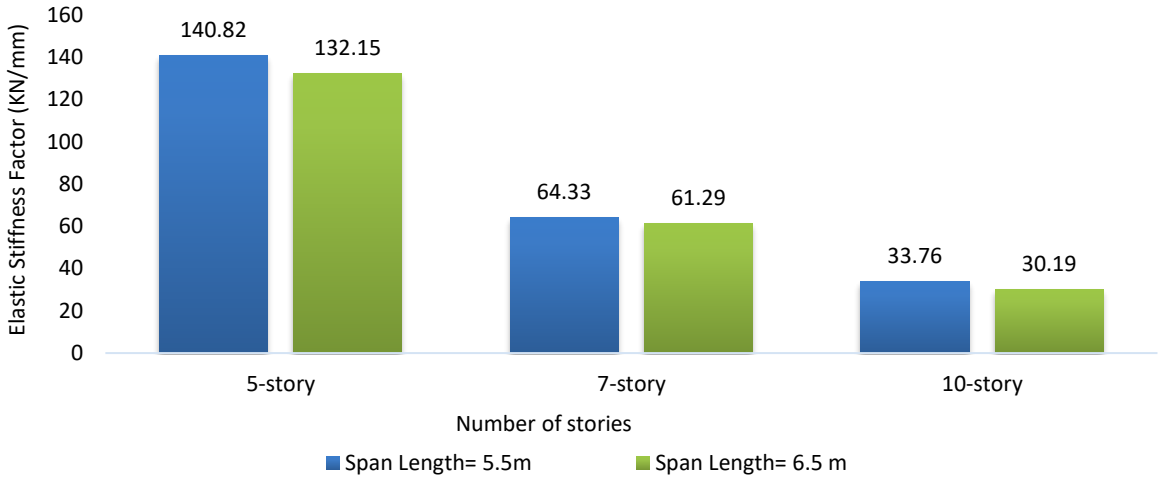


Figure 4. Elastic stiffness factor versus number of stories

### 3.2. The Effect of Span Length on the Elastic Stiffness Factor

The span length is one of the factors that impact stiffness value. Differences in span length are an appropriate means to show how the stiffness and seismic behavior of the building are affected. Figure 5 illustrates the highest stiffness factor of 138.73 $KN/mm$ appeared in low-rise buildings with span lengths of 5.5 m. On the other hand, the lowest stiffness factor of 27.88 $KN/mm$ appeared in high-rise buildings with span lengths of 6.5 m. Increasing the span length from 5.5 to 6.5 meters in low-rise buildings decreases the elastic stiffness factor by 5%. AlHassan et al. [5] showed that by increasing the span length from 5.5 to 6.5 m, the elastic stiffness factor decreased by 16% for the lowest building. Factors used in this section: Shear wall thickness= 200mm, and compressive strength (f'c)= 250 $kgf/cm^2$.

https://doi.org/10.31436/iiumej.v26i1.3321

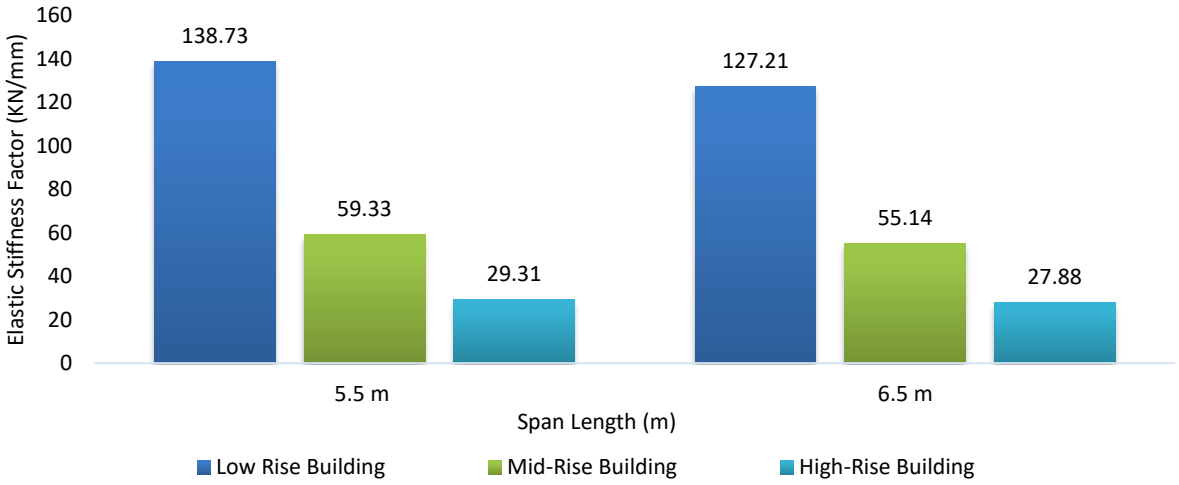


Figure 5. Elastic stiffness factor versus Span length

### 3.3. The Effect of Compressive Strength on the Elastic Stiffness Factor

Compressive strength ($f'c$) is one of the essential factors that can determine the stiffness of the building. Changes in compressive strength have a positive or negative effect on the stiffness factor. Figure 6 shows how increasing the compressive strength from 250 $kgf/cm^2$ to 280 $kgf/cm^2$ increases the stiffness factor from (145.37 to 149.31 $KN/mm$) equal to a 2.5% increment for a span length of 5.5m. Additionally, when the span length is increased to 6.5 meters, the stiffness factor rises from 136.91 $KN/mm$ to 139.01 KN/mm, representing a 1.5% increase. Factors used in this section: Story number = 5 (low-rise buildings), and shear wall thickness= 250mm.

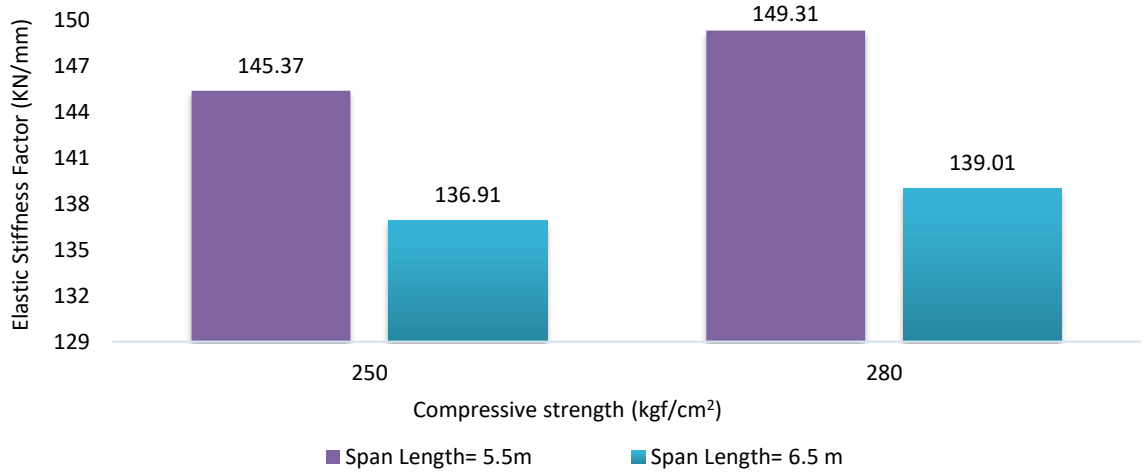


Figure 6. Elastic stiffness factor versus Compressive strength

### 3.4. The Effect of Shear Wall Thickness on the Elastic Stiffness Factor

This section presents the results of an experiment into how different shear wall thicknesses affect the stiffness factor at different span lengths. The founded stiffness factors with 200 mm shear wall thickness are (140.82 and 132.15 $KN/mm$) for span lengths of (5.5m and 6.5m), while with a shear wall thickness of 250 mm, the stiffness factors are (149.31 and 139.01 $KN/mm$) for span lengths of (5.5m and 6.5m). Figure 7 illustrates how the stiffness factor increases with increasing shear wall thickness from 200 to 250 mm. Specifically, it increases

https://doi.org/10.31436/iiumej.v26i1.3321

by 7% for span lengths of 5.5m and 6% for span lengths of 6.5 m. Factors used in this section: Story number = 5 (low-rise buildings), and compressive strength (f'c) = 280 kgf/cm$^2$.

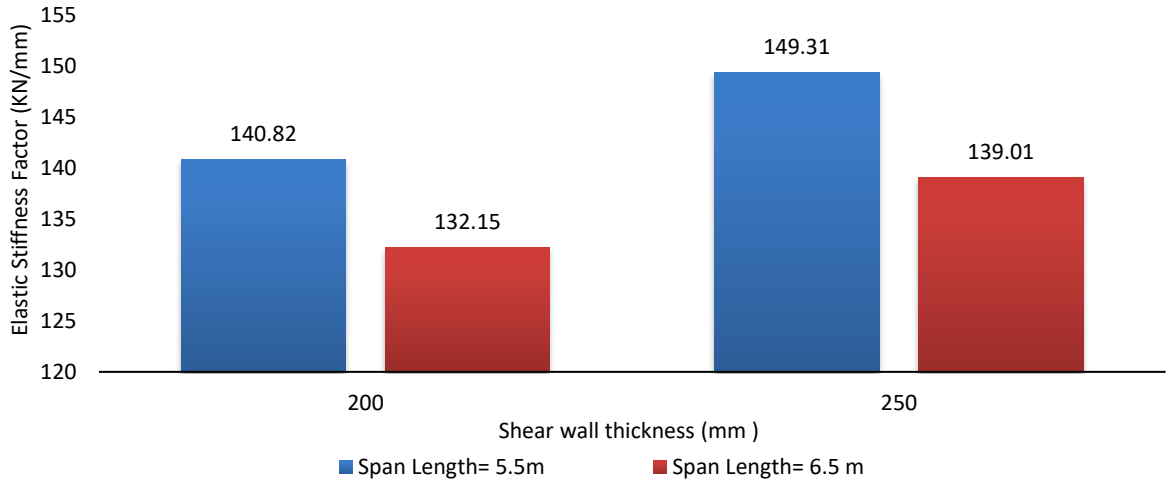


Figure 7. Elastic stiffness factor versus shear wall thickness

### 3.5. The Effect of Span Length and Number of Stories on Base Shear

This section indicates how the base shear of a dual system varies depending on the number of stories and span length. Figure 8 illustrates how base shear rapidly decreases from (1903 to 774 and then to 580 KN) as stories increase from (5 to 7 and then to 10 stories) for a span length of 5.5 m. The base shear decreases from (1752 to 701 and 490KN) as the number of stories increases from (5 to 7 and then to 10 stories) for a 6.5m span length. When the span length increases from 5.5 to 6.5 meters, the base shear decreases by 8% in low-rise buildings, 9.5% in mid-rise buildings, and 15.5% in high-rise buildings. Maximum base shear was achieved in fewer stories and smaller span lengths. Factors used in this section: Shear wall thickness= 200mm, and compressive strength (f'c)= 250 kgf/cm$^2$.

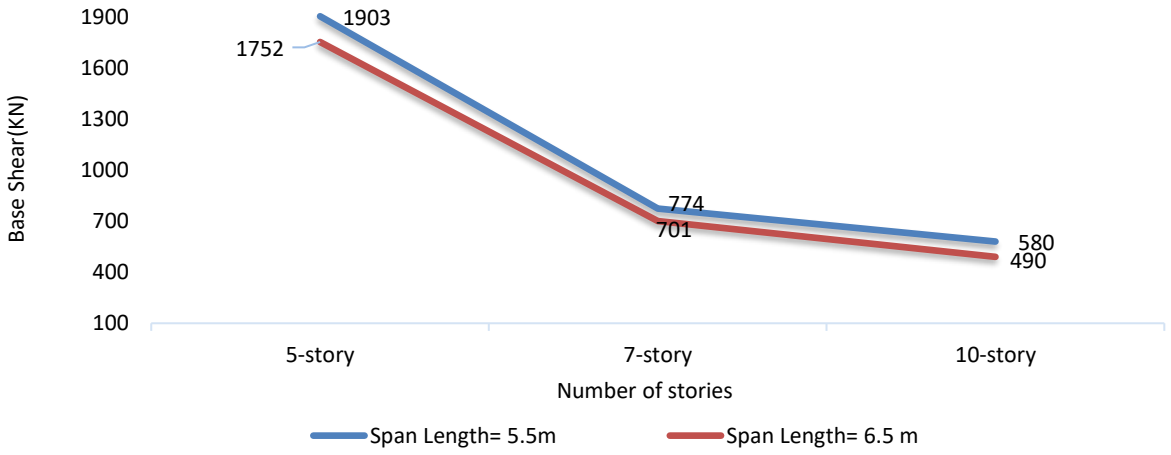


Figure 8. Relation between story number and span length vs base shear

The results achieved in this study are from only buildings with shear walls, and the number of stories used is expected in the study area.

# 4. CONCLUSION

This study evaluates the elastic stiffness factor and base shear of a two-dimensional reinforced concrete structure with a shear wall (dual system) for various parameters affecting stiffness using a non-linear static (pushover) analysis approach. To determine the impact of the number of stories, span length, compressive strength, and shear wall thickness on the elastic stiffness factor and base shear, 24 ETABS models were analyzed and designed using the equivalent lateral force procedure. Each model's results were compared and assessed. The following is a summary of the study's outcome:

- Studying the parameters that influence stiffness in RC buildings with dual systems is critical for assuring the building's reliability and performance, particularly under seismic and wind loads. Stiffness directly impacts the structure's ability to withstand lateral forces and control deflections, lowering the risk of extreme deformation or collapsing.
- Implementing dual systems in reinforced concrete (RC) structures, combining moment-resisting frames with shear walls, improves flexibility and strength. The moment-resisting frames provide ductility and dissipated energy, whereas shear walls give stiffness and lateral load resistance. This combination increases the structure's performance under gravity and seismic stresses, resulting in more outstanding durability and resistance. Dual systems are wildly successful in high-rise buildings and seismically active areas, where flexibility and strength are required for structural stability.
- Pushover analysis is a fundamental approach to evaluating buildings' non-linear properties.
- Using the pushover method helps to identify story displacement in each story.
- Pushover analysis finds weak points in the building with the help of plastic hinge location.
- Compared to mid-rise and high-rise buildings, the low-rise building was stiffer.
- By changing the number of stories from a low-rise building to a mid-rise building, the stiffness factor decreases by 55%, and by changing the number of stories from a mid-rise building to a high-rise building, the stiffness factor decreases by 50%.
- The span length and stiffness have been observed to be inversely proportionate to each other.
- By raising the span length from 5.5m to 6.5m, the stiffness factor decreases approximately by % 5 for all story numbers.
- The stiffness factor increases by 2% by increasing compressive strength from 250 $kgf/cm^2$ to 280 $kgf/cm^2$.
- Increasing the shear wall thickness from 200 mm to 250 mm increases the stiffness factor by 7%.
- When the number of stories increases from 5 to 7 and 7 to 10, base shear immediately reduces. Similarly, base shear reduces when the span length increases from 5.5m to 6.5m.

# REFERENCES

[1] Behera B, Datta AK, Pal A.(2024). Earthquake resistant design of framed reinforced concrete building using artificial intelligence model. Asian Journal of Civil Engineering. Apr 16:1-4. http://dx.doi.org/10.1007/s42107-024-01051-7

[2] Furtado A, Rodrigues H, Arêde A, Varum H, Grubišić M, Šipoš TK.(2018). Prediction of the earthquake response of a three-storey infilled RC structure. Engineering Structures. Sep 15;171:214-35. https://doi.org/10.1016/j.engstruct.2018.05.054

[3] Ngenge JP, Wafi AM.(2020). Assessment of plastic hinge in RC structures with and without shear walls applying pushover analysis. International Journal of Advanced Engineering, Sciences and Applications. Jan 30;1(1):11-8. https://doi.org/10.47346/ijaesa.v1i1.27

[4] Resatoglu R, Jkhsi S.(2022). Evaluation of Ductility of Reinforced Concrete Structures with Shear Walls having Different Thicknesses and Different Positions. IIUM Engineering Journal. Jul 4;23(2):32-44. https://doi.org/10.31436/iiumej.v23i2.2070

[5] AlHassan M, Abdelrahim M.(2020). Plastic hinge assessment of RC moment-resisting frames. International Journal of Advanced Engineering, Sciences and Applications. Jul 15;1(3):37-41. https://doi.org/10.47346/ijaesa.v1i3.29

[6] Kamath K, Hirannaiah S, Noronha JC.(2016). An analytical study on performance of a diagrid structure using nonlinear static pushover analysis. Perspectives in Science. Sep 1;8:90-2. https://doi.org/10.1016/j.pisc.2016.04.004

[7] Wang Z, Martinez-Vazquez P, Zhao B.(2020). Pushover analysis of structures subjected to combined actions of earthquake and wind. Engineering structures. Oct 15; 221:111034. https://doi.org/10.1016/j.engstruct.2020.111034

[8] Sarhan O, Raslan M.(2020). Study of the elastic stiffness factor of steel structures with different lateral load resisting systems. International Journal of Advanced Engineering, Sciences and Applications. Apr 30;1(2):6-11. https://doi.org/10.47346/ijaesa.v1i2.26

[9] Das S, Choudhury S.(2019). Influence of effective stiffness on the performance of RC frame buildings designed using displacement-based method and evaluation of column effective stiffness using ANN. Engineering Structures. Oct 15; 197:109354. https://doi.org/10.1016/j.engstruct.2019.109354

[10] Ghasemi Jouneghani H, Haghollahi A, Moghaddam H, Sarvghad Moghadam A.(2016). Study of the seismic performance of steel frames in the elliptic bracing. Journal of Vibroengineering. Aug 15;18(5):2974-85. https://doi.org/10.21595/jve.2016.16858

[11] Shakir QM, Alliwe R. (2020). Upgrading of deficient disturbed regions in precast RC beams with near surface mounted (NSM) steel bars. Journal of Materials and Engineering Structures «JMES», 7(2), 167-184.

[12] Shakir QM, Hanoon HK. (2023). New models for reinforced concrete precast hybrid deep beams under static loads with curved hybridization. In Structures; 54,1007-1025). https://doi.org/10.1016/j.istruc.2023.05.084

[13] Jamnani HH, Amiri JV, Rajabnejad H.(2018). Energy distribution in RC shear wall-frame structures subject to repeated earthquakes. Soil Dynamics and Earthquake Engineering. Apr 1; 107:116-28. https://doi.org/10.1016f/j.soildyn.2018.01.010

[14] Benaied B, Hemsas M, Benanane A, Hentri M.(2023). Seismic analysis of RC building frames with vertical mass and stiffness irregularities using adaptive pushover analysis. Revista de la construcción. Dec;22(3):597-612. https://doi.org/10.7764/RDLC.22.3.597

[15] Bertagnoli G, Giordano L, La Mazza D, Mancini G.(2016). Reinforced concrete frame structures.Procedia engineering .Jan1;161:1013-7. https://doi.org/10.1016/j.proeng.2016.08.841

[16] Varma VN, Kumar UP.(2021). Seismic response on multi-storied building having shear walls with and without openings. Materials Today: Proceedings. Jan 1;37:801-5. https://doi.org/10.1016/j.matpr.2020.05.827

[17] Birzhandi MS, Mirzakhani D.(2023). Modified Modal Pushover Design for Asymmetric-Plan RC Shear-Wall Structures. Advances in Civil Engineering. Apr 17;2023. https://doi.org/10.1155/2023/5627191

[18] Ahmad O.(2021). Evaluation of elastic stiffness factor of 2D reinforced concrete frame system with different parameters. International Journal of Advanced Engineering, Sciences and Applications. Jul 31;2(2):26-31. https://doi.org/10.47346/ijaesa.v2i2.69

[19] Tarigan J, Manggala J, Sitorus T.(2018). The effect of shear wall location in resisting earthquake. InIOP Conference Series: Materials Science and Engineering. Feb 1;309(1): 012077. IOP Publishing. https://doi.org/10.1088/1757-899X/309/1/012077

[20] Sattar S, Liel AB.(2016). Seismic performance of nonductile reinforced concrete frames with masonry infill walls—II: Collapse assessment. Earthquake Spectra. May;32(2):819-42. https://doi.org/10.1193/091514eqs141m

[21] Ambhaikar, S. S., Patil S. D., & Kognole, R. S. (2018). performance-based seismic analysis of building. International Journal of Trend in Scientific Research and Development, 2(3), 249-255. https://doi.org/10.31142/ijtsrd9684

[22] Pierre AJ, Hidayat I.(2020). Seismic performance of reinforced concrete structures with pushover analysis. InIOP Conference Series: Earth and Environmental Science. Feb 1; 426(1): 012045. https://doi.org/10.1088/1755-1315/426/1/012045

[23] Youcef M, Abderrahmane K, Benazouz C.(2018) Seismic performance of RC building using spectrum response and pushover analyses. InFacing the Challenges in Structural Engineering: Proceedings of the 1st GeoMEast International Congress and Exhibition, Egypt 2017 on Sustainable Civil Infrastructures 1 (pp. 158-169). Springer international publishing. https://doi.org/10.1007/978-3-319-61914-9_13

https://doi.org/10.31436/iiumej.v26i1.3157

# MAP FLOODWATER RADAR IMAGERY USING MACHINE LEARNING ALGORITHMS

**THANH NGHI DOAN[1,2], DUC-NGOC LE-THI[1]**

[1]*Faculty of Information Technology, An Giang University, An Giang, Vietnam*

[2]*Vietnam National University, Ho Chi Minh City, Vietnam*

**Corresponding author: dtnghi@agu.edu.vn*

*(Received: 7 January 2024; Accepted: 10 October 2024; Published online: 10 January 2025)*

***ABSTRACT:*** Flooding is a widespread and costly natural disaster around the world. Accurately assessing the extent of flooding in near real-time is crucial for governments and humanitarian organizations. This information strengthens early warning systems, evaluates risks, and guides effective relief efforts. Therefore, precise flood mapping is essential for saving lives through improved early warning systems and targeted emergency responses. In this study, radar imagery available on the Planetary Computer Data was utilized to train a U-Net model specifically designed to label flood-affected pixels in an image from a flood event. Different blocks of the U-Net encoder architecture were fine-tuned to identify the most efficient fine-tuned model, and their results were compared. As a result, the model with blocks 1 and 2 being fine-tuned demonstrated the highest Intersection over Union (IoU) score of 78.904%, an increase of 8.663% over the baseline methods.

***ABSTRAK***: Banjir merupakan bencana alam yang meluas dan mahal di seluruh dunia. Penilaian yang tepat terhadap skala banjir secara hampir masa nyata adalah penting bagi kerajaan dan organisasi kemanusiaan. Maklumat ini memperkukuhkan sistem amaran awal, menilai risiko, dan membimbing usaha bantuan yang lebih berkesan. Oleh itu, pemetaan banjir yang tepat adalah penting untuk menyelamatkan nyawa melalui sistem amaran awal yang lebih baik dan respons kecemasan yang disasarkan. Dalam kajian ini, imej radar yang tersedia pada Planetary Computer Data digunakan untuk melatih model U-Net yang direka khas untuk melabelkan piksel yang terjejas oleh banjir dalam imej daripada kejadian banjir. Bagi mengenal pasti model ditala-halus yang paling cekap, blok-blok berlainan dalam arkitektur pengekod U-Net telah ditala-halus, dan hasilnya dibandingkan. Hasilnya, model dengan blok 1 dan 2 yang ditala-halus menunjukkan skor Intersection over Union (IoU) tertinggi sebanyak 78.904%, iaitu peningkatan sebanyak 8.663% berbanding kaedah asas.

***KEYWORDS:*** *Flood mapping, Fine-tunning, Radar imagery, U-Net*

## 1. INTRODUCTION

Floods are natural disasters when large amounts of water temporarily submerge land. According to [1], strategies to mitigate the effects of floods can be broadly categorized into two types: prevention measures and complementary solutions. Prevention measures focus on infrastructure and physical interventions to control water flow and reduce water accumulation [2]. Complementary solutions, which work in tandem with prevention efforts, aim to enhance flood management [3]. These include flood monitoring, early warning systems, emergency response protocols, and public awareness campaigns. Among these, early warning systems are particularly effective, as they provide timely and accurate information about the extent of the

affected area in advance. This enables better damage assessment and mapping, aiding crisis management and recovery.

Various methods have been explored for mapping floods and assessing flood risks. Traditional approaches, such as those mentioned in [4], have been commonly used to address these challenges. While high-resolution hydrologic models are effective at smaller scales, their application to community-level urban flooding is limited by high computational and data input requirements [5]. This underscores the need for innovative techniques to predict flooding accurately without demanding extensive computational resources.

Remote sensing, particularly Synthetic Aperture Radar (SAR), provides an efficient and cost-effective solution for large-scale flood mapping without the need for highly accurate or resource-intensive processes. Unlike traditional methods that often face challenges in addressing the complexities of urban flooding, SAR offers a more robust alternative. A detailed examination of remote sensing techniques, including SAR and multi-frequency Polarimetric SAR for terrain classification, is presented in [6]. As an active sensor, SAR excels at capturing detailed images of the Earth's surface, regardless of time of day or cloud cover. Its capabilities have greatly improved flood detection and monitoring.

For instance, in [7], innovative multi-temporal COSMO-SkyMed data from Northern Italy were utilized to develop a classification algorithm for mapping flood progression. The authors in [3] demonstrated the successful use of RADARSAT-2 SAR images and flood stage data to monitor the 2011 Richelieu River flood. Additionally, the study in [8] combined TerraSAR-X with high-resolution aerial imagery to capture the complex flooding dynamics along the River Severn in England.

Recently, significant advancements have been made in supervised machine learning algorithms, particularly in deep learning techniques and Convolutional Neural Networks (CNNs) [9]Unlike traditional pixel-based learning methods, CNNs exploit the spatial structure of target segments, enabling more effective feature extraction. Additionally, automatic feature representation within CNNs partitions the feature space, reducing uncertainties in the data. Due to these capabilities, CNNs have emerged as powerful tools in various fields, with recent successes in flood mapping being a prime example.

In 2019, the authors of [10] investigated using CNNs for flood detection from high-resolution unmanned aerial vehicle (UAV) images. They employed a VGG-based fully convolutional network (FCN-16s). They demonstrated that CNNs outperformed traditional classification methods, such as fully convolutional networks (FCNs) and support vector machines (SVMs), in identifying flooded regions. In another study, the authors of [11] developed a CNN-based approach specifically for extracting flooded areas from Sentinel-1 SAR data. Their method involved generating flood masks through classical semi-automatic techniques, followed by manual cleaning and visual inspections, while exploring different CNN architectures. This approach significantly reduced the time needed to produce flood maps. The CNN models used in the study achieved impressive F1 scores of 91% and 92% on the test dataset.

Nevertheless, training a deep convolutional neural network from scratch presents substantial challenges, particularly in fields like medical imaging, where annotated data is often limited and expensive to obtain. A promising alternative is transfer learning, which involves fine-tuning a pre-trained network for a specific application. This approach adapts a network trained on a large, general dataset to a new task. When working with a small dataset, it is typically recommended to retain the initial layers of the pre-trained network and fine-tune only the final layers for the new application [12]. The authors in [13] propose a deep learning-based

flood detection system using semantic segmentation with a U-Net architecture to analyze aerial and satellite images, detecting flood-affected regions at the pixel level. Trained on a diverse set of annotated flood images, the model achieves an IoU score of 0.85, surpassing existing methods in accuracy. This system offers real-time flood mapping, enhancing disaster response by providing timely, accurate data, which helps emergency responders assess the extent of the disaster, plan rescue operations, and manage resources more effectively.

The authors in [14] provides a reasoned overview of flood detection using SAR imaging. The main detection mechanisms, such as thresholding and machine learning-based algorithms, and the usual performance measures used to assess the reliability of demarcation maps have been reviewed. The presentation included publicly accessible SAR datasets with accompanying reference labeled data that may be utilized for both performance assessment and ML algorithm training. Situations where SAR-based flood detection remains difficult, such as in the presence of vegetation, terrain, or metropolitan areas, have been considered. They finish this assessment by discussing future viewpoints on the subject.

The U-Net model [15], widely recognized for its speed and accuracy in medical image segmentation, has also been successfully applied to SAR image segmentation [16], [17]. In particular, the study by [18] demonstrated that the U-Net model outperforms the X-Net model in flood detection using radar imagery from both polarizations. For Vertical-Horizontal (VH) polarization, the U-Net model achieved an Intersection over Union (IoU) score of 64.46%, surpassing the X-Net model's score of 62.54%. Similarly, for Vertical-Vertical (VV) polarization, the U-Net model achieved an IoU score of 67.35%, outperforming the X-Net model's 64.38%. These results underscore the U-Net model's effectiveness in flood detection using radar imagery. However, it is essential to note that the U-Net model architecture used in [18] has not been altered. This raises the question of whether this specific U-Net architecture is the most appropriate choice for segmentation applications. A more thorough analysis is warranted in the context of SAR image segmentation, which presents unique complexities that necessitate specialized handling.

Based on the brief review of deep learning segmentation methods discussed earlier, this study aims to develop a robust CNN model for mapping floodwater. Specifically, it investigates the effects of fine-tuning different layers within a U-Net encoder as applied to SAR image segmentation. This paper presents a comprehensive investigation into enhancing floodwater mapping using machine learning techniques. The study employs a fine-tuned U-Net model to label flood-affected pixels in SAR imagery accurately. The results reveal that fine-tuning the first two blocks of the U-Net encoder achieved a remarkable IoU score of 78.904%, representing an improvement of 8.663% over baseline methods. This study demonstrates the proposed approach's efficacy in flood mapping and contributes valuable insights into the potential of machine learning for disaster management and climate resilience. Therefore, the main contributions of this paper are as follows:

- Exploring the impact of block-level fine-tuning in the encoder architecture of the U-Net model.
- Introducing an efficient SAR image segmentation approach for improved flood mapping.
- Providing foundational knowledge in remote sensing for flood mapping.
- Offering practical insights for future radar-based flood monitoring.
- Enhancing flood detection methods for improved climate resilience and disaster management.

https://doi.org/10.31436/iiumej.v26i1.3157

# 2. MATERIALS AND METHODS

## 2.1. Synthetic-Aperture Radar Imagery

Synthetic Aperture Radar images are produced by an active system that uses microwave signals transmitted to the ground and received back by a sensor platform, which can be either airborne (via planes) or satellite-based [17]. This process entails signal transmission, reception, and the application of specific filters, as illustrated in Figure 1.

In Vertical-Horizontal (VH) polarization, the transmitted signal's electric field is vertical, while the received signal is measured in both vertical and horizontal orientations. Vertical-vertical (VV) polarization, in which both the transmitted and received signals are oriented vertically.

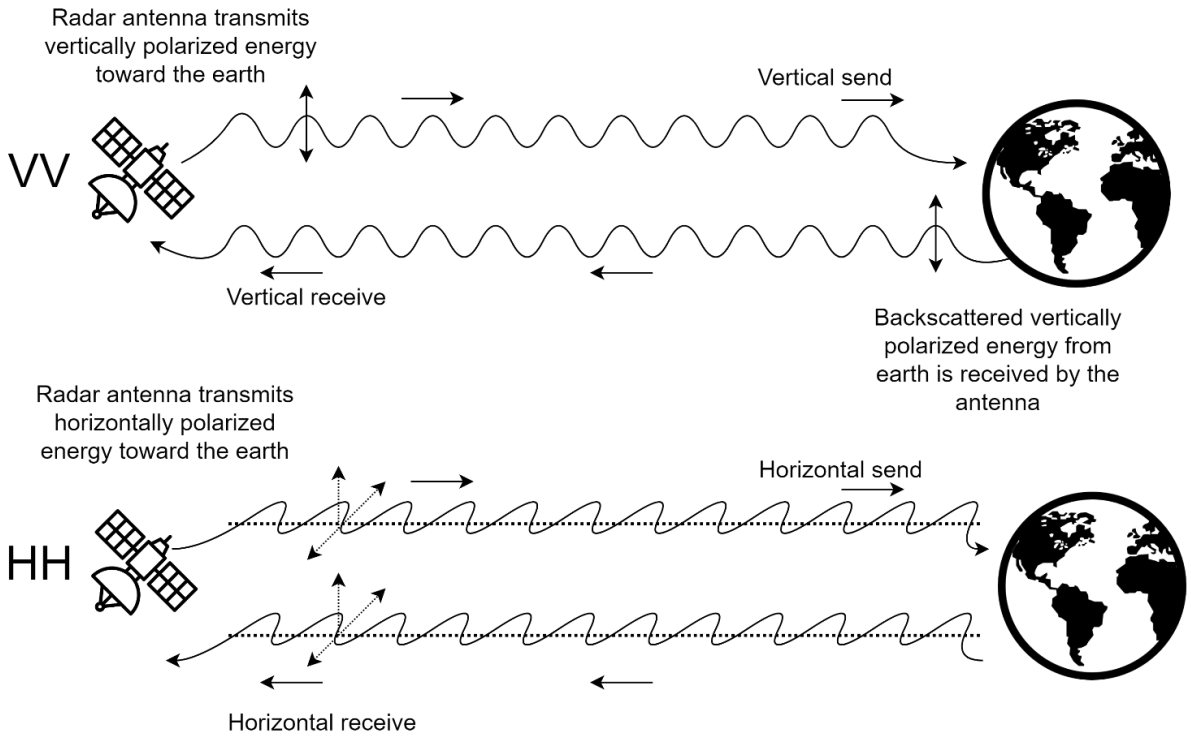


Figure 1. The first symbol indicates the direction of signal transmission, and the second indicates the direction of signal reception.

The complex interplay between transmitted signals and the terrain influences the distribution and reception of VH and VV data. Visual aids, such as figures, depict these interactions, illustrating how VH and VV signals interact with various surface features and water bodies. These visuals highlight signal fluctuations resulting from different polarization modes and surface characteristics, such as open water, vegetation, or urban environments. The advantages of SAR imagery include:

- Operation in various weather conditions, ensuring uninterrupted monitoring.
- Penetration of obstacles like clouds and vegetation, reflecting diverse surface features for insightful analysis.
- Provision of high-resolution images for precise flood area identification and land feature differentiation.

https://doi.org/10.31436/iiumej.v26i1.3157

### 2.2. Planetary Computer Data

The dataset for model training is accessed via the Planetary Computer, a platform hosted on Microsoft's Azure cloud infrastructure that provides a wide range of geospatial and environmental datasets. This platform provides a suite of cloud computing services for deploying, managing, and scaling applications and services globally, as detailed in [19]. The datasets available on this platform are freely accessible through the Data Catalog and come with accompanying metadata and code examples to facilitate their effective use.

Raw data from upstream data providers is initially transmitted to Azure Blob Storage, from which users can easily retrieve the data via HTTP requests. The Planetary Computer enhances accessibility by creating cloud-optimized data variants, including converting data into Cloud-optimized GeoTIFF format. Data exploration is facilitated through the STAC API, while a tile server visualizes data on maps using the Explorer tool. For a visual representation of the relationship between upstream data providers and the Planetary Computer, please refer to Figure 2.

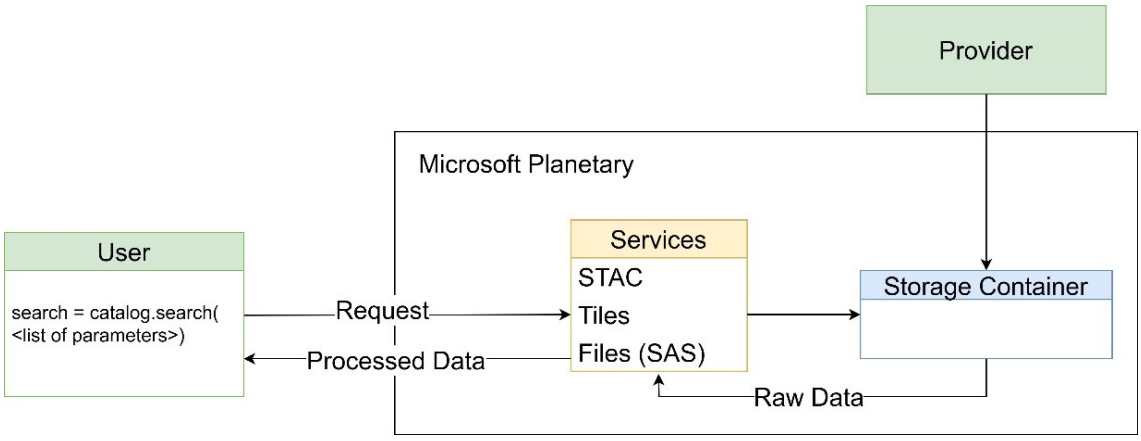


Figure 2. Relationship between upstream data providers, Planetary Computer and users.

### 2.3. Data Preprocessing

Accurate predictions hinge on the critical step of data preprocessing. Various data preprocessing strategies were employed to enhance classification performance and generate additional training data. The quality and utility of the training dataset were optimized through meticulous processes such as masking, augmentation, channel combination, and scaling.

#### *2.3.1. Step 1 - Pixel Masking: Improving Data Quality*

In the context of satellite imagery, pixel values indicate the energy reflected to the satellite. In some regions outside the satellite's coverage, missing data points may exist within the dataset's images. Each image in this dataset is associated with a GeoTIFF label, essentially serving as a binary mask. In these masks, a pixel value of 1 clearly indicates the presence of water, while a value of 0 signifies its absence. Notably, any missing or erroneous data is marked with a pixel value of 255. During the image loading phase for training, this issue is intelligently handled by converting any pixels labeled as missing data to represent the absence of water.

#### *2.3.2. Step 2 - Data Normalization*

Normalization involves scaling pixel values to achieve a standard scale and distribution. This technique enables the model to converge more quickly during training, often resulting in improved predictive performance. Pixel z-score normalization is carried out using Eq. (1):

https://doi.org/10.31436/iiumej.v26i1.3157

$$z = \frac{X-\mu}{\sigma} \quad (1)$$

where $X$ represents the original pixel value while $\mu$ and $\sigma$ denote the mean and standard deviation values of the pixel values across the entire image.

### 2.4. Data Augmentation

Utilizing data augmentation is a crucial machine-learning strategy aimed at mitigating overfitting during model training, as highlighted by [20]. In the field of computer vision, image augmentation methods have become a prominent implicit regularization technique for reducing overfitting in deep convolutional networks. These approaches are widely used to enhance performance, as emphasized in previous studies [20], [21], [22]. The necessity of data augmentation becomes clear in our efforts to develop a robust machine-learning model for radar-based flood mapping. This technique introduces variability into the training dataset, reflecting real-world complexities. This study applies various image data augmentation techniques, including random resized crops, horizontal and vertical flipping, rotations, and blurring, to the dataset. Augmentor, an image augmentation library for machine learning [23], is utilized to enhance radar imagery and its corresponding masks, thereby improving the accuracy of flood mapping. Figure 3 presents a visual representation of the data augmentation process.

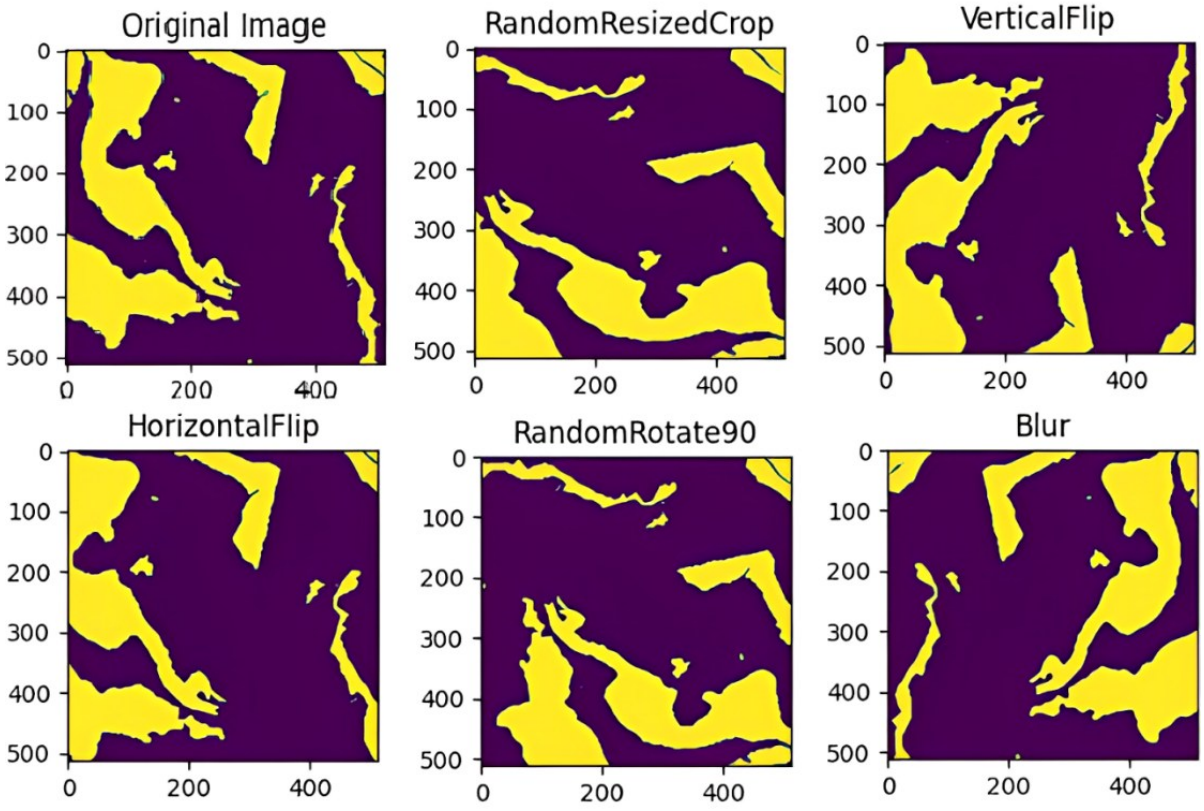


Figure 3. Visual representation of data augmentation results.

**Random Resized Crop:** The Random Resized Crop technique was incorporated to diversify the size and scale of radar images. This method randomly crops and resizes images to dimensions of 512x512 pixels, with scaling factors ranging from 0.75 to 1.0. By doing so, variations in the field of view of radar sensors are simulated, enhancing the model's adaptability to different spatial contexts.

https://doi.org/10.31436/iiumej.v26i1.3157

**Vertical and Horizontal Flips:** Vertical and horizontal flips were implemented to expose the model to variations in orientation. These augmentations create mirror images of the radar data, effectively doubling the dataset. They simulate different perspectives and orientations that radar sensors may encounter in real-world flood mapping scenarios.

**Random 90-Degree Rotations:** Random 90-degree rotations add rotational diversity to the training data. Flood events can manifest at *varIoUs* angles relative to the radar sensor. By incorporating these rotations, our model learns to recognize flood patterns from different orientations, bolstering its ability to map floods accurately under varied conditions.

**Blurring:** The blurring augmentation adds complexity to the dataset by mimicking radar imagery affected by adverse weather conditions or natural interference. Training on these blurred images makes the model more robust, improving its ability to identify flood-affected regions in radar images with lower clarity.

### 2.5. U-Net Architecture

In this study, the influential U-Net architecture [15] was utilized to facilitate the task of flood mapping. While the core architecture closely follows the original U-Net framework proposed in the seminal paper [18], specific adaptations were implemented to optimize its performance for radar-based flood mapping. The U-Net architecture comprises blocks, each containing two 3x3 convolutional layers with ReLU activation. These convolutional layers are essential for feature extraction and mapping. The network is organized into a series of blocks, each connected to the next through either a max-pooling or an upsampling operation (Figure 4). Transitioning from one block to the next involves scaling and compression operations. The final layer of our U-Net architecture consists of a 1x1 convolutional layer with a sigmoid activation function. This layer is crucial in mapping the feature vector to a continuous range between 0 and 1. During the evaluation phase, a threshold value of 0.5 was applied, allowing us to categorize pixels as follows:

- Pixels with values above 0.5 were designated as 1, indicating flood-affected regions.
- Pixels with values below 0.5 were classified as 0, signifying non-flood areas.

Notably, traditional transposed convolutional layers were replaced with a hybrid approach that combines bilinear upsampling followed by 2x2 convolutions. This method of upsampling with bilinear interpolation allows for improved capture of fine features [24]. Additionally, in the blocks designated for fine-tuning, 64 filters were incorporated, with their count doubled after each max-pooling operation to better capture complex patterns [25]. Conversely, after each upsampling operation, the number of filters was halved, leading to a more efficient computational process. This technique enhances the model's ability to capture intricate features while minimizing computational overhead.

https://doi.org/10.31436/iiumej.v26i1.3157

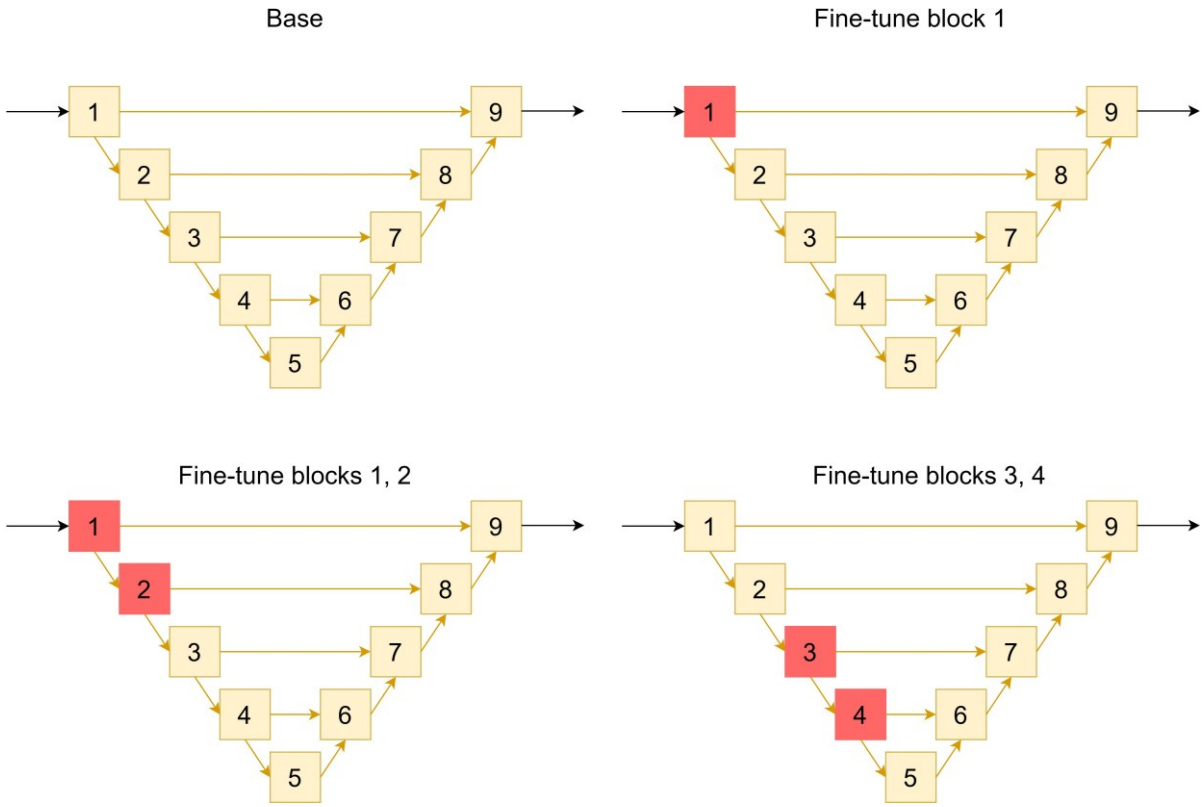


Figure 4. Schematic of the U-Net [18] and the fine-tuning strategies. Red blocks are the blocks included in fine-tuning, and yellow ones are frozen.

### 2.6. Stratified K-Fold Cross Validation

To ensure a robust evaluation of the models, Stratified K-Fold Cross-Validation (SKCV) was employed, an advanced technique that provides a fair and unbiased assessment of model performance [26]. SKCV meticulously divides our floodwater radar imagery dataset into K subsets, ensuring that each fold maintains a proportional representation of the various classes present in the data. This stratification is essential, particularly when dealing with imbalanced datasets where certain classes may be underrepresented. By preserving the class distribution in each fold, SKCV helps mitigate biases arising from uneven class proportions. The SKCV process involves the following steps:

Step 1 - *Dataset Division*: The floodwater radar imagery dataset, denoted as $X$, is divided into $K$ subsets: $X_1, X_2, \ldots X_K$.

Step 2 - *Iterative Evaluation*: For each iteration $i$ from 1 to $K$:

- Validation and Training Sets: One subset, $X_i$, is used as the validation set, while the remaining subsets are merged to form the training set.
- Model Training: Our machine learning models are trained on the training set, allowing them to learn patterns and relationships within the data.
- Model Evaluation: The trained models are evaluated on the validation set, providing specific performance metrics for each fold.

Overall model performance is assessed by averaging evaluation metrics across iterations. This is done by calculating the average performance metric $P_{avg}$, derived by summing

performance metrics $P_i$ from each fold and dividing by the number of folds $K$, as shown in Eq. (2):

$$P_{avg} = \frac{1}{K}\sum_{i=1}^{K} P_i \quad (2)$$

This approach ensures that each class is evenly distributed across the $K$-folds, maintaining the sample distribution ratio among the classes within SKCV. It provides an unbiased evaluation of model performance by accurately representing the target class distribution in each fold.

### 2.7. Evaluation Metric: Intersection over Union

For precise model assessment, the Jaccard Index, also known as the Generalized Intersection over Union (IoU), was utilized. This metric is crucial for comparing ground truth and predicted segmentations in supervised segmentation models [27]. It measures label similarity, indicating the overlap between segmentations. Higher values indicate better alignment, while lower values signify less accurate segmentations. The mathematical formulation of the Jaccard Index is presented in Eq. (3):

$$IoU = \frac{|A \cap B|}{|A \cup B|} = \frac{|A \cap B|}{|A|+|B|-|A \cap B|} \quad (3)$$

where, $A$ represents the set of flood pixels in the label, while $B$ corresponds to the set of predicted flood pixels.

## 3. EXPERIMENTS

### 3.1. Dataset

In our study, the dataset used for both training and testing was sourced from the project described in [28]. This project provides a global catalog of flood maps for major historical events, accessible via Microsoft's Planetary Computer platform. The dataset used for flood detection in this study consists of high-resolution radar images captured by the Sentinel-1 satellite, which employs SAR technology. SAR is particularly effective for flood monitoring as it can capture images through clouds day and night, making it ideal for use in adverse weather conditions. The dataset contains images processed in dual polarization (VV and VH), which helps capture the flood extent more accurately. The thirteen most severe floods, determined by their peak water levels, were specifically selected, as shown in Table 1.

Table 1. List of the ten most severe flood events selected from a total of 156 simulated historic surge events documented in [28].

| Name | Country | Date | Lat | Lon | Peak Water Level |
|---|---|---|---|---|---|
| Rosita | AU | 21/04/2000 | -18.2 | 122.26 | 8.42 |
| Ingrid | AU | 17/03/2005 | -12.78 | 135.29 | 8.42 |
| Chris | AU | 07/02/2002 | -19.85 | 120.41 | 8.19 |
| Annette | AU | 19/12/1994 | -19.7 | 120.81 | 7.82 |
| Orson | AU | 24/04/1989 | -20.66 | 116.7 | 6.45 |
| Glenda | AU | 31/03/2006 | -20.76 | 116.62 | 6.38 |
| Ian | AU | 03/03/1992 | -20.71 | 115.46 | 6.34 |
| Vance | AU | 24/03/1999 | -21.8 | 114.74 | 6.2 |
| Katrina | US | 29/08/2005 | 27.7 | -85.21 | 6.09 |
| Connie | AU | 20/01/1987 | -20.31 | 118.58 | 5.99 |
| Bobby | AU | 27/02/1995 | -20.78 | 116.67 | 5.91 |
| Rachel | AU | 08/01/1997 | -20.31 | 118.57 | 5.85 |
| John | AU | 16/12/1999 | -20.31 | 118.58 | 5.75 |

https://doi.org/10.31436/iiumej.v26i1.3157

The training dataset comprises 542 chips, totaling 1,084 images (each image paired with a corresponding label), facilitating supervised learning techniques. For a visual example of a chip and its corresponding water labels, refer to Figure 5. The radar images in the dataset are stored as GeoTIFF files, each containing 512x512 pixels. These images are measured in decibels (dB) and are acquired using the Sentinel-1 system, which employs a dual-polarization SAR technique. The SAR data is collected in both VV and VH polarizations, as shown in Figure 6. Depending on the specific flood detection requirements, one or both polarization bands are selectively used for analysis.

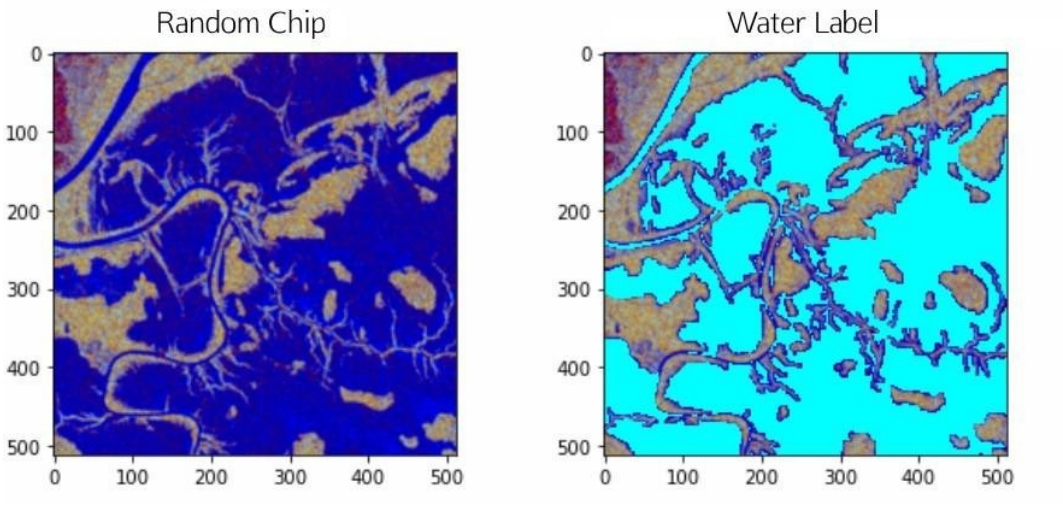


Figure 5. Visual representation of a random chip with its water labels.

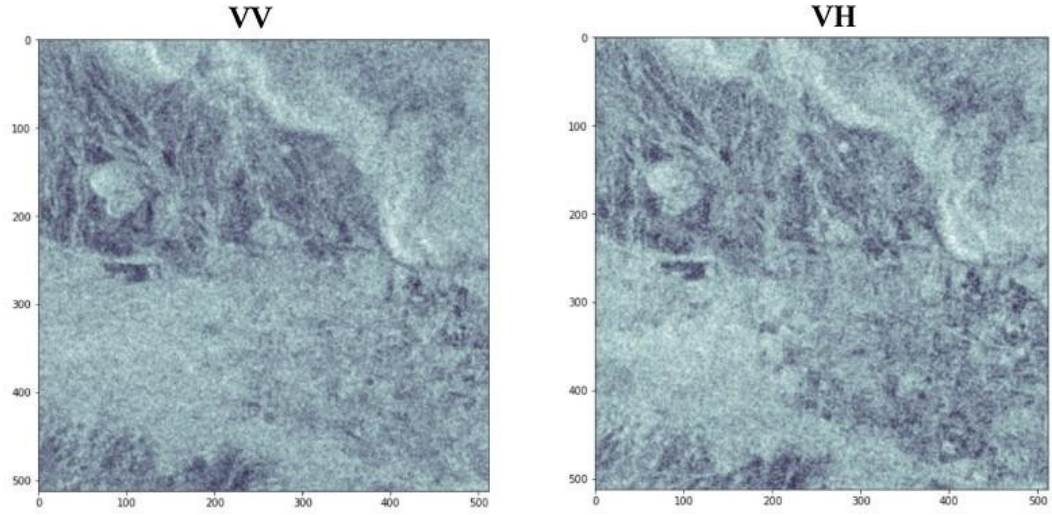


Figure 6. Visual comparison of VV and VH bands for polarization distinctions.

### 3.2. Experimental Design

It is important to note that including skip connections in the U-Net architecture complicates the conventional distinction between shallow and deep layers, necessitating a thorough investigation to determine the most effective fine-tuning strategy.

The U-Net encoder was divided into several subdivisions to tackle this challenge, each encompassing layers of varying depths. This division strategy is crucial for determining which network segments are most relevant for fine-tuning. The subdivisions are illustrated in Figure 4 and outlined as follows:

- Fine-Tuning the First Block (1): This experiment involved fine-tuning only the U-Net encoder's initial block.
- Fine-Tuning the First Two Blocks (1, 2): This experiment explored the impact of fine-tuning the encoder's first and second blocks.
- Fine-Tuning the Second Half of the Encoder (3, 4): This experiment focused on fine-tuning the latter part of the encoder, specifically blocks 3 and 4.

### 3.3. Experimental Setup

The experimental setup is the cornerstone of our research, detailing key elements such as the operating system, hardware, and software. The experiments were conducted on Ubuntu 20.04.1 LTS, utilizing an Intel Core i7 processor and an NVIDIA GeForce RTX 2080 Ti for high-performance computation. The exact package versions used are outlined in Table 2, ensuring accuracy and reproducibility. This carefully curated setup ensures seamless interactions, boosting reliability. Strategic environment configurations were applied to optimize efficiency and effectiveness, providing a solid foundation for comprehensive flood detection model evaluations.

Table 2. Imported packages and their descriptions

| Package | Version | Description |
|---|---|---|
| albumentations | 1.3.1 | Image augmentation library for machine learning tasks. |
| catboost | 1.2 | Gradient boosting library optimized for categorical data. |
| gdal | 3.4.1 | Geospatial Data Abstraction Library for raster data manipulation. |
| matplotlib | 3.6.2 | Visualization library for creating static, animated, and interactive plots. |
| numpy | 1.24.0 | Fundamental package for scientific computing with Python. |
| pandas | 1.5.2 | Data manipulation and analysis library providing data structures and functions. |
| rasterio | 1.3.8 | Library for reading and writing geospatial raster data. |
| sklearn | 1.2.0 | Machine learning library with tools for classification, regression, and more. |
| tqdm | 4.64.1 | Library for reading and writing geospatial raster data. |

### 3.4. Model Training

During the training process, the early stopping technique was applied. This technique halts training once the minimum loss is reached on the validation set and no improvement is observed for 20 consecutive epochs. The model that performed best on the validation set was saved for further evaluation on the test set. If early stopping did not occur within 200 epochs, the training was deemed unsuccessful, ensuring that resources were not wasted on unproductive runs.

The training was carried out using the configuration detailed in Table 3. All experiments employed the same folds to facilitate a meaningful comparison of different fine-tuning scenarios. The network's performance was consistently evaluated using the same test set, representing the entire held-out fold.

Table 3. Model training configuration

| Parameters | Value |
|---|---|
| Optimization algorithm | ADAM optimizer |
| Loss function | Binary Cross-Entropy |
| Batch size | 32 |
| Learning rate | 10−4 |

https://doi.org/10.31436/iiumej.v26i1.3157

## 4. RESULTS AND DISCUSSIONS

The results of the study reveal an interesting phenomenon. When comparing different fine-tuning strategies for the U-Net encoder, it was consistently observed that training the shallow path while freezing the deep path produced superior results (Figure 7). Notably, the shallow path contains significantly fewer parameters (Table 4), with approximately less than half the number found in the deep path (comparing the Blocks 1 and 2 scheme to Blocks 3 and 4). Despite this substantial difference in parameter count, training fewer parameters still improved performance.

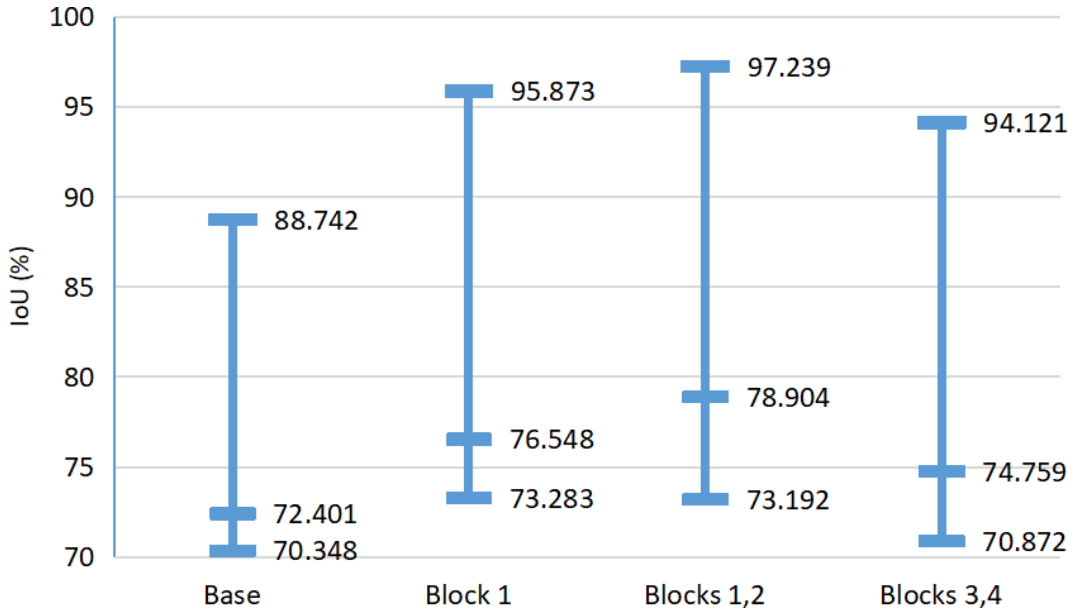


Figure 7. IoU scores for different fine-tuning schemes

Table 4. Mean IoU scores and number of parameters of different fine-tuning schemes

| U-Net Model | Baseline | Block 1 | Blocks 1,2 | Blocks 3,4 |
|---|---|---|---|---|
| Number of Parameters | 3.1e+7 | 3.7e+5 | 2.5e+6 | 4.3e+7 |
| Mean IoU (%) | 70.241 | 76.548 | 78.904 | 74.759 |

As demonstrated in Table 4, our findings provide important insights into the efficiency of fine-tuning various blocks within the U-Net architecture for floodwater mapping. The maximum Intersection over Union (IoU) score of 78.904% obtained by fine-tuning the first two blocks of the encoder architecture is especially remarkable because it represents an 8.663% improvement above baseline approaches. This increase demonstrates the effectiveness of intentional model fine-tuning in enhancing performance for specific applications like flood detection. Several elements contribute to the U-Net model's performance:

*Layer-Specific Fine-Tuning*: By concentrating on fine-tuning only the first two blocks, these layers' extensive feature extraction capabilities were leveraged while preserving the stability of the deeper levels. This strategy lowered the danger of overfitting, which is common when fine-tuning deeper layers, while allowing for more efficient training with fewer parameters. The network's short route (with fewer parameters) produced better results, demonstrating that effective feature learning may occur without too complicated model designs.

*Data Preprocessing and Augmentation*: Preprocessing processes such as pixel masking, normalization, and other data augmentation approaches considerably enhanced the quality and variability of the training dataset. This variety enabled the model to generalize more well across various flood conditions, increasing its resilience in real-world applications.

*Application of SAR Imagery*: SAR imagery, recognized for its ability to pierce cloud cover and produce high-resolution data, enabled accurate flood mapping even in difficult climatic circumstances. The model's dependence on SAR data highlights the value of remote sensing in flood control, especially in locations where traditional ground-based surveillance is restricted.

*Implications for Disaster Management*: Our technique's improved mapping accuracy has important implications for disaster management and climate resilience. Improved flood mapping helps governments and humanitarian groups respond more quickly and precisely, allowing for improved resource allocation and focused relief operations. This expertise is critical for reducing the human and economic toll of flooding occurrences.

*Future Directions*: While the findings are encouraging, more studies are needed to investigate the use of the U-Net model in various flood situations and geographic locations. Furthermore, additional data sources, such as meteorological and hydrological information, may improve the model's forecasting powers. The possibility of real-time flood monitoring and evaluation might be a useful path for future research, leading to a more proactive approach to disaster management.

Our findings show that fine-tuning the U-Net architecture is a potent technique for floodwater mapping, with considerable gains in accuracy and efficiency. The findings provide a solid platform for future advances in remote sensing applications, underlining the importance of machine learning in solving global concerns such as climate change and natural catastrophes.

Figure 8 provides a comparison of segmentation results from several fine-tuning procedures used on a U-Net model for flood detection. Flood maps generated using the fine-tuning of Block 1 and Blocks 3, 4 techniques achieved IoU scores exceeding 74%, with the resulting flood maps showing similar patterns. However, the flood maps produced by the fine-tuned Blocks 1, 2 approach demonstrated greater precision, capturing finer details and aligning more closely with the ground truth labels, leading to the highest overall score.

The input data in the VH column comprises vertical-horizontal polarization (VH) from radar pictures, which were most likely collected using Synthetic Aperture Radar (SAR) devices. SAR data is very useful in flood mapping since it can pierce clouds and collect photos in all weather, making it excellent for estimating flood extents. This serves as the starting point for model projections.

The Label column depicts the ground truth, the manually labeled flood extent. It shows flooded areas in yellow and dry sections in deep purple, serving as a baseline for assessing the model's accuracy. The Base column displays the results of the base U-Net model with no fine-tuning. While the basic model covers the general flood size, the forecasts are less precise, with insufficient accuracy in identifying smaller features, which might be essential in flood detection jobs.

The subsequent columns, Block 1 and Blocks 1 and 2 display the results of fine-tuning various areas of the U-Net encoder. Fine-tuning Block 1 (the shallow layers) significantly increases accuracy, capturing more specific flood extents than the baseline model. Further fine-tuning using Blocks 1 and 2 further improves the findings, catching precise details of flood boundaries and producing the most accurate predictions. This strategy is most likely associated

with the greatest IoU score described before, highlighting the need for shallow layers for detailed flood mapping.

Finally, the findings in Blocks 3 and 4 demonstrate the effect of fine-tuning the U-Net encoder's deeper layers. While this method captures wider flood patterns, it ignores the fine-grained intricacies apparent in forecasts from fine-tuning superficial layers. These findings indicate that deeper layers are less successful at recording accurate flood limits than shallow ones. Overall, the comparison shows that focusing on fine-tuning the shallower regions of the network results in more accurate flood extent identification, especially when collecting finer details.

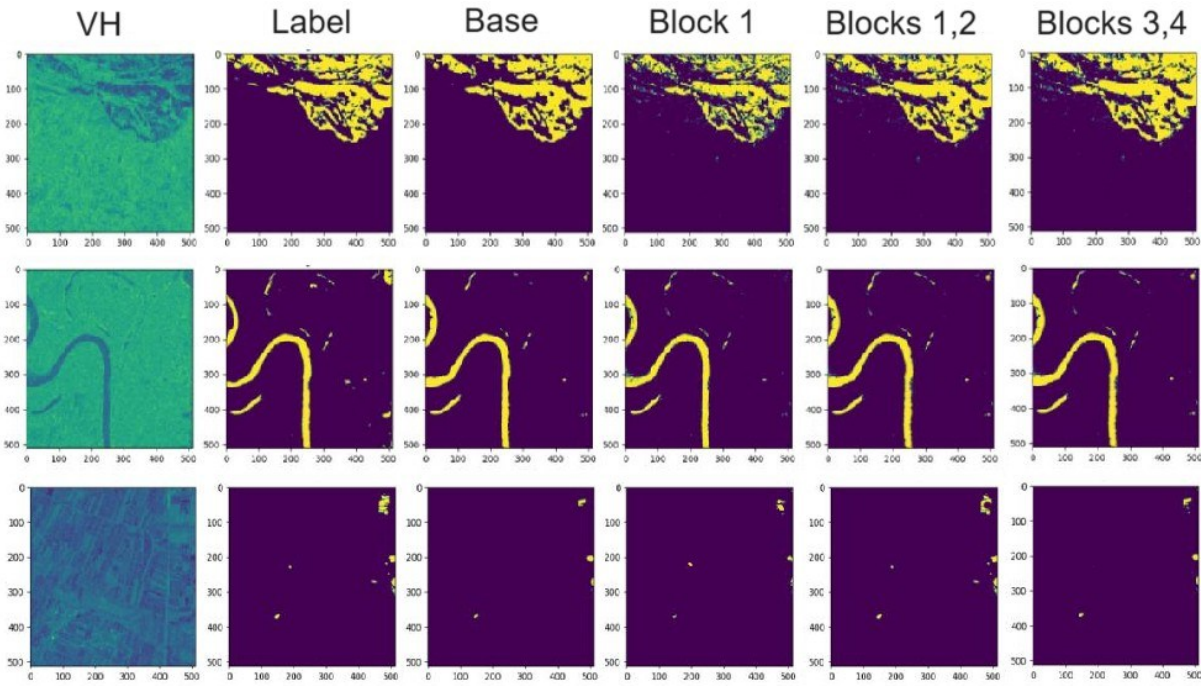


Figure 8. Visual comparisons of flood detection results for the different fine-tuning schemes are shown, with yellow representing flood extents and deep purple indicating dry areas.

## 5. CONCLUSION, LIMITATIONS AND FUTURE WORKS

This paper has presented a comprehensive comparative analysis of fine-tuning various blocks within the U-Net encoder framework for flood extent detection. Our findings demonstrate that fine-tuning Blocks 1 and 2 outperformed other methods, yielding a more robust and efficient solution for flood mapping, with the highest IoU score of 78.904%. This systematic approach shows significant potential for improving flood mapping accuracy. Despite the promising results, limitations exist, including the reliance on a relatively small dataset of 13 flood events and the exclusive use of Sentinel-1 radar data, which may limit the model's generalization and real-time applicability in regions with less frequent data availability. Future research should concentrate on increasing the dataset, including other data sources like optical or LiDAR imaging, and investigating more complex structures like transformers or hybrid models. Furthermore, real-time implementation on cloud platforms and cooperation with disaster management organizations might increase the model's practical influence in real-world disaster response situations, boosting worldwide flood preparedness and mitigation.

# REFERENCES

[1] L. P. Hoang et al., "Managing flood risks in the Mekong Delta: How to address emerging challenges under climate change and socioeconomic developments," Ambio, vol. 47, pp. 635–649, 2018, [Online]. Available: https://api.semanticscholar.org/CorpusID:3508948.

[2] M. Marchand, D. Pham, and T. Le, "Mekong Delta: Living with Water, But for How Long?," Built Environ., vol. 40, 2014, doi: 10.2148/benv.40.2.230.

[3] M. Tanguy, K. Chokmani, M. Bernier, J. Poulin, and S. Raymond, "River flood mapping in urban areas combining Radarsat-2 data and flood return period data," Remote Sens. Environ., vol. 198, pp. 442–459, 2017, doi: 10.1016/j.rse.2017.06.042.

[4] M. J. Hammond, A. S. Chen, S. Djordjević, D. Butler, and O. Mark, "Urban flood impact assessment: A state-of-the-art review," Urban Water J., vol. 12, no. 1, pp. 14–29, 2015, doi: 10.1080/1573062X.2013.857421.

[5] F. Dottori, G. Di Baldassarre, and E. Todini, "Detailed data is welcome, but with a pinch of salt : Accuracy, precision, and uncertainty in flood inundation modeling," Water Resour. Res., vol. 49, no. 9, pp. 6079–6085, 2013, doi: 10.1002/wrcr.20406.

[6] L. C. Smith, "Satellite remote sensing of river inundation area, stage, and discharge: a review," Hydrol. Process., vol. 11, pp. 1427–1439, 1997, [Online]. Available: https://api.semanticscholar.org/CorpusID:46008875.

[7] L. Pulvirenti, M. Chini, N. Pierdicca, L. Guerriero, and P. Ferrazzoli, "Flood monitoring using multi-temporal COSMO-SkyMed data: Image segmentation and signature interpretation," Remote Sens. Environ., vol. 115, pp. 990–1002, 2011, doi: 10.1016/j.rse.2010.12.002.

[8] L. Giustarini, R. Hostache, P. Matgen, G. J.-P. Schumann, P. D. Bates, and D. C. Mason, "A Change Detection Approach to Flood Mapping in Urban Areas Using TerraSAR-X," IEEE Trans. Geosci. Remote Sens., vol. 51, no. 4, pp. 2417–2430, 2013, doi: 10.1109/TGRS.2012.2210901.

[9] Y. Jia et al., "Caffe: Convolutional Architecture for Fast Feature Embedding," Proc. 22nd ACM Int. Conf. Multimed., 2014, [Online]. Available: https://api.semanticscholar.org/CorpusID:1799558.

[10] A. Gebrehiwot, L. H. Beni, G. Thompson, P. Kordjamshidi, and T. E. Langan, "Deep Convolutional Neural Network for Flood Extent Mapping Using Unmanned Aerial Vehicles Data," Sensors (Basel)., vol. 19, 2019, [Online]. Available: https://api.semanticscholar.org/CorpusID:91187268.

[11] E. Nemni, J. Aylett-Bullock, S. Belabbes, and L. Bromley, "Fully Convolutional Neural Network for Rapid Flood Segmentation in Synthetic Aperture Radar Imagery," Remote. Sens., vol. 12, p. 2532, 2020, [Online]. Available: https://api.semanticscholar.org/CorpusID:221980528.

[12] J. Yosinski, J. Clune, Y. Bengio, and H. Lipson, "How transferable are features in deep neural networks?" 2014.

[13] M. Divya, V. Chandran, D. J. Anitha, M. Anusree, and M. G. Nair, "Deep Learning-Based Flood Detection System Using Semantic Segmentation," 2024 7th Int. Conf. Circuit Power Comput. Technol., vol. 1, pp. 1584–1592, 2024, [Online]. Available: https://api.semanticscholar.org/CorpusID:272711335.

[14] D. Amitrano, G. Di Martino, A. Di Simone, and P. Imperatore, "Flood Detection with SAR: A Review of Techniques and Datasets," Remote Sens., vol. 16, no. 4, pp. 1–38, 2024, doi: 10.3390/rs16040656.

[15] O. Ronneberger, P. Fischer, and T. Brox, "U-Net: Convolutional Networks for Biomedical Image Segmentation," ArXiv, vol. abs/1505.0, 2015, [Online]. Available: https://api.semanticscholar.org/CorpusID:3719281.

[16] K. Sarra and A. Boulmerka, "Semantic segmentation of remote sensing images using U-net and its variants : Conference New Technologies of Information and Communication (NTIC 2022)," 2022 2nd Int. Conf. New Technol. Inf. Commun., 2022, doi: 10.1109/ntic55069.2022.10100581.

[17] R. K. Vincent, "RADAR | Synthetic Aperture Radar (Land Surface Applications)," null, 2015,

doi: 10.1016/b978-0-12-382225-3.00331-5.
[18] M. Abbasi, R. Shah-Hosseini, and M. Aghdami-Nia, "Sentinel-1 Polarization Comparison for Flood Segmentation Using Deep Learning," Proceedings, vol. 87, no. 1, 2023, doi: 10.3390/IECG2022-14069.
[19] P. Herath, "Azure Cloud Security for Absolute Beginners: Enabling Cloud Infrastructure Security with Multi-Level Security Options," Azur. Cloud Secur. Absol. Beginners, 2022, [Online]. Available: https://api.semanticscholar.org/CorpusID:244780408.
[20] C. Shorten and T. M. Khoshgoftaar, "A survey on Image Data Augmentation for Deep Learning," J. Big Data, vol. 6, no. 1, 2019, doi: 10.1186/s40537-019-0197-0.
[21] A. Mikołajczyk and M. Grochowski, "Data augmentation for improving deep learning in image classification problem," 2018 Int. Interdiscip. PhD Work., pp. 117–122, 2018, [Online]. Available: https://api.semanticscholar.org/CorpusID:49348179.
[22] S. Yang, W.-T. Xiao, M. Zhang, S. Guo, J. Zhao, and S. Furao, "Image Data Augmentation for Deep Learning: A Survey," ArXiv, vol. abs/2204.0, 2022, [Online]. Available: https://api.semanticscholar.org/CorpusID:248240105.
[23] M. D. Bloice, C. Stocker, and A. Holzinger, "Augmentor: An Image Augmentation Library for Machine Learning," CoRR, vol. abs/1708.0, 2017, [Online]. Available: http://arxiv.org/abs/1708.04680.
[24] L. Xu, J. Xu, Q. Zheng, J. Yuan, and J. Liu, "A miniature U-net for k -space-based parallel magnetic resonance imaging reconstruction with a mixed loss function," Quant. Imaging Med. Surg., vol. 12, no. 9, 2022, [Online]. Available: https://qims.amegroups.org/article/view/96423.
[25] W. Shang, K. Sohn, D. Almeida, and H. Lee, "Understanding and Improving Convolutional Neural Networks via Concatenated Rectified Linear Units," in Proceedings of The 33rd International Conference on Machine Learning, 2016, vol. 48, pp. 2217–2225, [Online]. Available: https://proceedings.mlr.press/v48/shang16.html.
[26] S. Widodo, H. Brawijaya, and S. Samudi, "Stratified K-fold cross validation optimization on machine learning for prediction," Sink. J. dan Penelit. Tek. Inform., 2022, doi: 10.33395/sinkron.v7i4.11792.
[27] D. Ogwok and E. M. Ehlers, "Jaccard Index in Ensemble Image Segmentation: An Approach," in Proceedings of the 2022 5th International Conference on Computational Intelligence and Intelligent Systems, 2023, pp. 9–14, doi: 10.1145/3581792.3581794.
[28] "Planetary computer and Deltares global data," 2021.

# ENHANCED EARLY AUTISM SCREENING: ASSESSING DOMAIN ADAPTATION WITH DISTRIBUTED FACIAL IMAGE DATASETS AND DEEP FEDERATED LEARNING

**MOHAMMAD SHAFIUL ALAM[1,2], MUHAMMAD MAHBUBUR RASHID[1*]**

[1]*Department of Mechatronics Engineering, IIUM, Kuala Lumpur, Malaysia*
[2]*Department of Electrical and Electronic Engineering, Northern University Bangladesh (NUB), Dhaka, Bangladesh*

**Corresponding author: mahbub@iium.edu.my*

*(Received: 27 January 2024; Accepted: 30 September 2024; Published online: 10 January 2025)*

***ABSTRACT:*** This study offers a significant advancement in the area of early autism screening by offering diverse domain facial image datasets specifically designed for the detection of Autism Spectrum Disorder (ASD). It stands out as the pioneering effort to analyze two facial image datasets – Kaggle and YTUIA, using federated learning methods to adapt domain differences successfully. The federated learning scheme effectively addresses the integrity issue of sensitive medical information and guarantees a wide range of feature learning, leading to improved assessment performance across diverse datasets. By employing Xception as the backbone for federated learning, a remarkable accuracy rate of almost 90% is attained across all test sets, representing a significant enhancement of more than 30% for the different domain test sets. This work is a significant and remarkable contribution to early autism screening research due to its unique novel dataset, analytical methods, and focus on data confidentiality. This resource offers a comprehensive understanding of the challenges and opportunities in the field of ASD diagnosis, catering to both professionals and aspiring scholars.

***ABSTRAK:*** Kajian ini menawarkan kemajuan yang ketara dalam bidang saringan awal autisme dengan menyediakan pelbagai set data imej wajah yang direka khusus untuk pengesanan Gangguan Spektrum Autisme (ASD). Kajian ini menonjol sebagai usaha perintis untuk menganalisis dua set data imej wajah – Kaggle dan YTUIA, menggunakan kaedah pembelajaran teragih untuk menyesuaikan perbezaan domain dengan jayanya. Skim pembelajaran teragih ini berkesan menangani isu integriti maklumat perubatan sensitif dan menjamin pembelajaran ciri yang meluas, yang membawa kepada prestasi penilaian yang lebih baik merentas set data yang berbeza. Dengan menggunakan Xception sebagai tunjang pembelajaran teragih, kadar ketepatan yang luar biasa hampir 90% dicapai merentas semua set ujian, mewakili peningkatan ketara lebih daripada 30% untuk set ujian domain yang berbeza. Hasil kerja ini merupakan sumbangan penting dan luar biasa dalam penyelidikan saringan awal autisme kerana set data yang unik dan baharu, kaedah analisis yang digunakan, serta tumpuan kepada kerahsiaan data. Sumber ini menawarkan pemahaman yang menyeluruh mengenai cabaran dan peluang dalam bidang diagnosis ASD, sesuai untuk para profesional dan sarjana yang berminat.

***KEYWORDS:*** *Autism Spectrum Disorder (ASD), Artificial Intelligence, Deep Learning, Data Federation, Domain Adaptation*

## 1. INTRODUCTION

Rapid Autism spectrum disorder (ASD) is a neurological condition that leads to challenges in activities of daily living and communication skills for the affected person. It results from an

impairment in the development of the human brain and is characterized by a predominance of repetitive behavioral patterns and an inability to speak or communicate. The World Health Organization reports that ASD impacts 1% of babies, or one in every one hundred [1]. Unfortunately, there is presently no conclusive biomarker that can be used to diagnose ASD, nor are there any specific medications available for treating ASD[2]. However, the diagnosis is dependent on a set of standardized questionnaires and behavioral evaluations administered by experienced professionals, while the therapy is based on effective intervention and support[3]. Furthermore, current studies show that individuals diagnosed with ASD can experience substantial enhancements in cognitive and daily functioning through specific interventions and therapies before reaching the age of two. This is attributed to the ongoing development of the brain during this period, allowing for potential recovery and an increase in IQ levels up to 20 points [4].

In these circumstances, early diagnosis is essential for ASD patients to initiate appropriate intervention and cognitive therapy despite the uncertain etiology of autism in children. Preliminary study indicates that genetic factors exert a substantial influence on the likelihood of developing ASD. Research has discovered multiple genes linked to ASD, and having a family history of the illness raises the probability of its manifestation. Instead of genetic variables, researchers have investigated a limited number of prenatal and perinatal factors as potential influences on ASD. These risks include difficulties during pregnancy, exposure to specific medicines or chemicals, and maternal illnesses. In addition, scientists are studying the involvement of the immune system and gut-brain axis in the formation of ASD. The process of conventional diagnosis is quite stringent, requiring patients, together with their parents or caregivers, to undergo a series of standardized questionnaires. This can be tedious for both the patients and their guardians. This process may be biased by human expertise, age window, and parental attitudes toward their children [5].

Conversely, artificial intelligence can play a crucial function in this matter in the present era. Machine learning and deep learning, which are primary artificial intelligence techniques, can significantly automate the screening of ASD [6]. Deep learning (DL) is an algorithm created by humans that uses solid mathematical principles to identify intricate patterns in various forms of data, such as sound, images, and text, to generate precise insights and predictions. Utilizing the capacity for pattern recognition, deep learning algorithms can accurately predict autism based on specific patterns seen in brain neuroimaging data. As ASD is a neurodevelopmental disorder, these images can serve as an effective tool for identifying autism in children[7]. Deep learning models can be trained using many modalities of neuroimaging data, such as MRI and EEG thus, this model can further recognize the patterns in future samples, aiding the ASD detection process. While these brain scans show promise in detecting ASD, obtaining these samples necessitated clinical environments, sophisticated technology, and skilled physicians, all connected with significant expenses and human resources. It would be beneficial if a convenient and readily available method could be implemented for the initial assessment of ASD. Screening for ASD using face image datasets has shown significant potential as a valuable resource in numerous applications, particularly in the field of deep learning [8]. Given that the face is a direct reflection of the brain, it is reasonable to use facial traits to forecast neurological disorders such as autism [9]. Facial images offer significant advantages, including easy accessibility and the requirement for minimal preprocessing before using deep learning techniques for early screening of autism.

Deep learning relies on expansive and diverse datasets, which is crucial for training accurate models. Moreover, diverse datasets are essential for mitigating biases in machine learning, ensuring fairness and equity in applications like facial image-based pattern

recognition. While medical data sharing is essential for research, safeguarding identities remains a priority, emphasizing the delicate balance between data availability and privacy in the ever-evolving landscape of deep learning. The regulations enforced by different regulatory bodies, such as the Health Insurance Portability and Accountability Act (HIPAA) in the U.S. and the General Data Protection Regulation (GDPR) in Europe, impose additional responsibilities on data operators concerning data management and prevent the centralization of data [10]. Federated learning (FL) can serve as a solution in this context, enabling AI models to be trained utilizing decentralized datasets that are not public. Google pioneered FL, which is a decentralized machine-learning methodology that allows multiple institutions to collaborate on deep-learning projects without the need to share client data [11]. An illustrative instance of federated learning occurs when the training data is stored on the individual users' devices (nodes) instead of being sent to a central data center, which carries out computations using a local dataset to update a global model.

When utilizing several facial image datasets on separate client sites, domain differences may likely arise due to variations in imaging settings, sources, demographics, and modalities. These differences often make it challenging to create a model that is both generalizable and robust[12]. When the features of multiple datasets are not shared, accuracy is reduced across locally trained models that are isolated and applied to separate domain datasets. The federated learning system guarantees feature sharing globally and aggregates the model weight to increase accuracy among different clients; hence, it can handle multiple domain data. This study proposes an early autism screening scheme that utilizes multiple facial image datasets to train Deep CNN models. It also applies federated learning techniques for domain adaptation tasks while ensuring the security and confidentiality of individuals' crucial private information.

Table 1 presents a comparative analysis of several deep-learning models applied to a facial image dataset to detect ASD. Ying Li et al. (2023) [13] utilized an enhanced version of MobileNetV2 to identify ASD from facial images with an astounding 90.50 percent accuracy. M.F. Rabbi et al. (2023) [14] obtained an accuracy of 85 percent for ASD prediction using VGG19. H. Kang et al. (2023) [15] achieved noteworthy levels of accuracy, 85%, through the training of Xception. The AlexNet model utilized by T. M. Ghazal et al. (2023) [16] demonstrated an accuracy of 87.70 percent. All of the aforementioned studies were conducted using a single dataset, thus eliminating any potential for domain variation among the samples.

Table 1. Recent research on ASD screening using facial image dataset

| Ref | Author | Algorithm | Accuracy | Dataset | Federated Learning | Domain Adaptation |
|---|---|---|---|---|---|---|
| [13] | Ying Li et al. | MobileNetV2 | 90.50 | Kaggle | No | Not Required |
| [14] | M.F Rabbi et al. | VGG 19 | 85.00 | Kaggle | No | Not Required |
| [15] | H. Kang et al. | Xception | 85.00 | Kaggle | No | Not Required |
| [16] | T. M. Ghazal et al. | AlexNet | 87.70 | Kaggle | No | Not Required |

A new facial image dataset, YTUIA, is introduced in this study to investigate the domain adaptation efficacy over multiple source datasets. The chosen method for domain adaptation is a federated learning scheme using deep CNN in the backbone. The main contributions are

1. Introduced a new and innovative facial dataset for the purpose of comparing and investigating the impact of multiple dataset environments on ASD detection.
2. Pioneering effort in analyzing various domain datasets for domain adaptation tasks for ASD detection.

3. It innovatively employs federated learning for improved ASD screening, ensuring domain adaptation and data privacy for real-life scenarios.

The first section of the study covers an Introduction that examines contemporary research, identifies gaps in the said research, and delineates potential noteworthy contributions. The following section provides an in-depth analysis of the methodology employed in diagnosing ASD. It consists of a detailed description of the newly synthesized facial image dataset for ASD, the application of the federated learning scheme, and the domain adaptation accomplished by deploying this technique as well as maintaining data safety. Following this, the subsequent section assesses various performance indices derived from the training and testing stages of deep CNN models, as well as domain adoption, which yields more accurate predictions in scenarios involving multiple domains. Section 4 closes by providing an overview of potential future research directions and summarizing the key findings of the present study.

## 2. METHOD

The research study presented a suitable approach for leveraging sensitive medical datasets from different servers to improve the accuracy of ASD detection while maintaining the confidentiality of personal information. Additionally, the research endeavored ingeniously to create a new facial image dataset to examine the efficacy of domain adaptation across numerous decentralized datasets for distinct servers. The “server” is a computational node situated in different hospitals, clinics, or healthcare centers.

### 2.1. Datasets

#### *2.1.1. Dataset 1 (Kaggle)*

The first dataset was named "Kaggle"[1], which is compiled utilizing facial images of children with autism [17]. This dataset was readily available and easily accessible on the Kaggle repository. The dataset comprises 2D RGB images and encompasses individuals from 2 to 14 years of age, specifically focusing on toddlers between the ages of 2 and 8. The data set illustrates a male-to-female ratio of approximately 3:1, with the ratio near 1:1 for the autistic and normal control (NC) groups. Train, test, and validation sets contain 86.38%, 10.22%, and 3.41% of the sample size, respectively. Gerry Piosenka compiled the dataset exclusively from online sources, excluding demographic information, including ethnicity, clinical history, and severity of ASD.

#### *2.1.2. Dataset 2 (TYUIA)*

The second facial image dataset is called YTUIA[2] (The dataset was developed at UIA – Universiti Islam Antarabangsa). It is developed from the widely recognized video dataset named the Self-Stimulatory Behaviours dataset (SSBD) [18]. Initially, the SSBD comprised seventy-five videos. To meet the quota of one hundred videos for frame extraction, an additional fifty videos were incorporated from therapists or specialized institutions that were readily accessible on YouTube, as specific videos of the SSBD dataset were unavailable on YouTube. Following the age group, YouTube videos depicting elementary school activities were chosen as NC samples. Each frame from the videos was extracted into a distinct folder, and facial detection was performed on each frame using the MTCNN algorithm in order to eliminate frames without faces.

[1] https://github.com/mm909/Kaggle-Autism
[2] https://drive.google.com/drive/u/2/folders/1g8iyO2Q0jnWLj6w6l5Nb8vm7GogTzK0J

Following that, a rigorous preprocessing pipeline was implemented, encompassing operations such as cropping, resizing, and aligning. The "Normal control" group comprised 173 distinct members, of which 117 were male and 56 were female. The participants' age was dispersed across a range of 1 to 11 years. There were 123 individuals in the "ASD" category in the dataset; 30 were female, and 93 were male. The participants comprised an age group from 3 to 11 years. A total of 1068 samples were used in the training set, while 100 samples were used in the testing set, and a 1:1 ratio of individuals with ASD to NC was preserved.

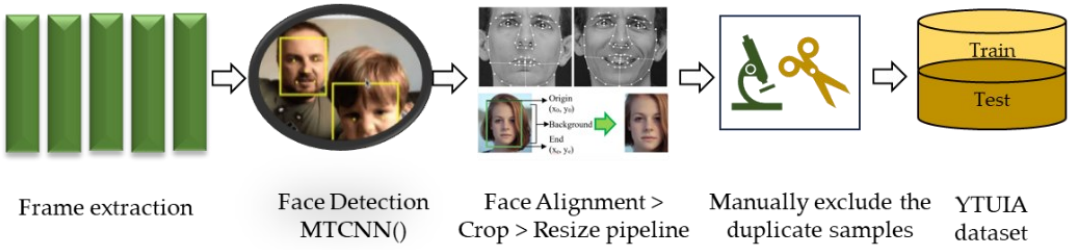


Figure 1. The process flow to develop the YTUIA dataset from video files

## 2.2. Domain Adaptation

Federate learning, which enables feature learning from the number of local clients remotely, has been implemented as a domain adaptation strategy to aid in the early detection of autism using facial image datasets. Domain adaptation refers to the process through which a machine learning model, trained initially on a dataset called the "source domain," is adjusted to function most effectively on a target domain dataset comprising unique characteristics. The dissimilarity between the source and target domains in facial images can be attributed to imaging apparatus and configuration variations. Transductive transfer learning is necessary to guarantee task consistency when source and target domains diverge. By facilitating the smooth transfer of features between models, this methodology guarantees the efficient adaptation of the feature space.

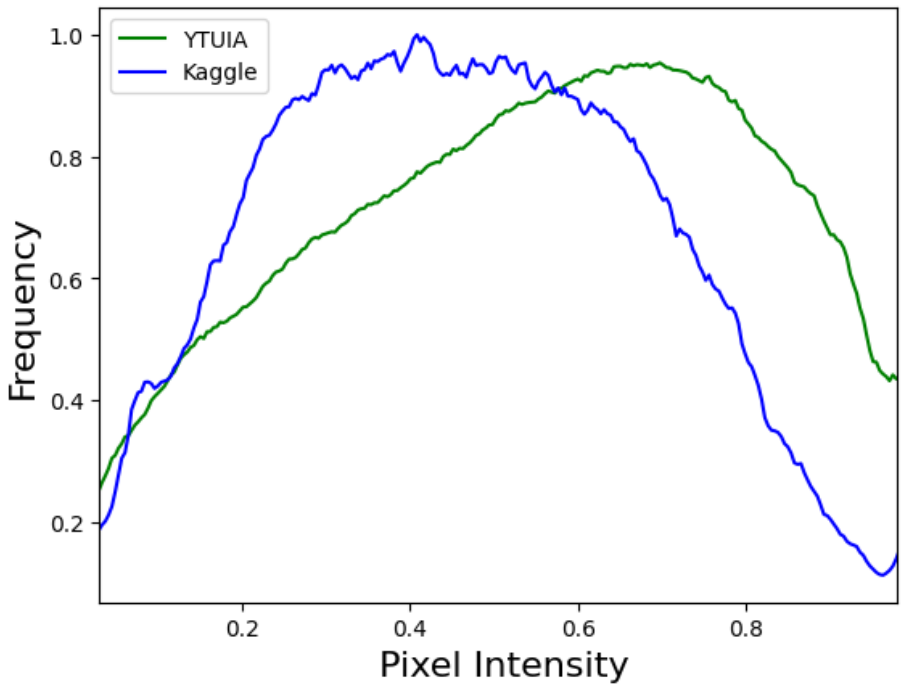


Figure 2. The domain shift in the two different facial image datasets for ASD detection

The datasets employed in this research are labeled Kaggle and YTUIA, and the corresponding test sets are denoted as T1 and T2, as described in the previous section. The normalized intensity distribution of both datasets is achieved by converting the pixel intensities of the facial images that make up the datasets, as depicted in Figure 2.

The variation in intensity distribution, indicative of a distinction in the field, leads to confusion for models when performing classification tasks. In addition, the T-statistic yields a p-value of 0.15 and a T-value of 3.10, providing strong evidence for the differentiation between the samples of the Kaggle and YTUIA datasets.

### 2.3. CNN Models

Convolutional Neural Networks (CNNs) have been applied to image recognition and classification in recent research. CNNs originated from investigations into the visual cortex of the brain. In recent years, CNNs have demonstrated exceptional performance on difficult visual tasks due to advancements in computing capacity and the availability of many images to train DNN. The primary function of the object classification model is to obtain features of an object, thereby enabling the binary classification of faces into two distinct classes—ASD and NC through feature learning from the facial image dataset. To derive features of both autistic and normal faces, CNN-based models that were trained using ImageNet previously can utilize the core convolutional layers. Additionally, the classification layers are adjusted to perform binary classification. MobileNetV2, ResNet50V2, and Xception models have been identified as the most effective in recent studies and are utilized here [3].

#### *2.3.1. MobileNetV2*

MobileNetV2 is an advanced algorithm that employs inverted residuals and a linear bottleneck. It is a basic module that expands for utilization in applications installed in hand phones. The algorithm has the capability to handle input with fewer dimensions, hence reducing the computational workload and memory usage while still retaining a higher accuracy level. This model employs depth-wise separable convolution, and the convolution operation is divided into two separate layers. The initial layer consists of depth-wise convolution, which is very efficient as it performs a single filtering operation. The second layer obtains new properties that are proportional to the inputs. This model greatly reduced the computational expense of typical layers of the model, where k2 acts as a multiplication factor, resulting in a savings of 8 or 9 times the computing capacity needed for 3×3 depth-wise separable convolution compared to other traditional CNNs.

#### *2.3.2. ResNet50V2*

This model consists of many bi-directional propagating residual units via identity mapping. Propagation can take place with high precision regarding classification performance between blocks. These residual mappings will greatly facilitate and enhance the training process, making it more streamlined and applicable to various scenarios. ResNet models often have a depth of over 100 layers and demonstrate outstanding performance using ImageNet.

#### *2.3.3. Xception*

This module is derived from the Inception model of Google and features a direct and modular nature. This is structured into three main components: entry, center, and exit. Each component utilizes a separable convolutional layer with activation functions Relu. The convolution layer's output has been subjected to max-pooling, with residual connections implemented at the end of each compartment. The input image with dimensions 299×299×3 is

processed by the entry flow to obtain the desired result. As a result, the output will consist of feature maps of dimensions 19×19×728. Despite undergoing nine iterations in the segment, the size of the image's features remains consistent after the middle flow. The final component produces a result with 2048 features for an input image of standard size. Finally, the prediction layer acquires the features via a fully connected (FC) layer, which is not depicted in the diagram. The ultimate layers will undergo alterations to facilitate binary categorization, as elucidated in the subsequent section.

### 2.4. Federated Learning

The primary concept behind employing the Federated learning scheme is to incorporate many datasets into the ASD detection process while ensuring remote operation and preserving the security and confidentiality of the data. When datasets are obtained from distinct environments, they may exhibit domain discrepancies due to variations in the equipment used and the processing pipelines employed. Therefore, it is necessary to implement an aggregated feature learning protocol to tackle this domain shift and accurately forecast the object classes for the varied domain dataset. According to Figure 3, an aggregator is required to combine the acquired features from the local client. Assume there are n diagnosis centers labeled as $C_1, C_2, \dots, C_n$, that are collecting data for ASD screening. The data samples and models are stored on local servers. Each center possesses a locally stored dataset, referred to as $\mathbf{D}l_i$. In this particular scenario, two datasets, Kaggle and YTUIA, are saved on the servers of $C_1$ and $C_2$, respectively. Each center conducts local training by training their respective datasets. For example, Center 1 trains dataset $\mathbf{D}l_1$, while Center 2 trains dataset $\mathbf{D}l_2$. Consequently, the weights obtained from local training are stored on the local server, as in Eq. (1) [19]:

$$M_i = \sum_{i,k=1}^{i,k=m} W_{i,k} F_i \tag{1}$$

where $M_i$ is the local DL algorithm $W_{1,1}, W_{1,2}, \dots, W_{1,n}$ are the weights and $F_1, F_2, \dots, F_n$ are the features learned by $m$ number of local models.

The process of developing a global model requires a global server and aggregator to calculate the overall weight of the DL models of the local client servers. There is no data sharing between the local clients $C_1$ and $C_2$ with the global center $C_g$, but the weights $W_{1,1}, W_{1,2}$ of the DL models $M_1$ and $M_2$ are shared with the global server to aggregate the weight globally and sent back to the local servers. In the end, the global aggregator makes the $FedAvg$ expressed as

$$GM = \sum_{i=1}^{i=m} h_i F_i \tag{2}$$

where $GM$ is the averaged weight calculated by the global server considering all the features learned by the local algorithms and can be given by

$$h_i = \frac{\sum_{i=1}^{m} w_i}{n} \tag{3}$$

where $n$ is the total number of centers in our specific case, which is 2.

### 2.5. Experimental Setup

The model is trained on the Kaggle platform using the TensorFlow library. Two clients for the two different domain datasets are considered two assessment centers for ASD screening. Local models‘ are trained on the two separate datasets, Kaggle and YTUIA. The test set for Kaggle will be identified as T1, and the test set for YTUIA will be named as T2. The details of the datasets are given in Table 2, where it is evident the data for the two clients is unbalanced

as the number of samples is different for the two datasets and as the datasets are collected from different persons thus, the nature of the data is not Independently and Identically Distributed (non-IID). So, the effect of the unbalanced non-IID dataset on this method can also be investigated with the domain adaptation task. Local hyperparameter was set based on the best result of the recent ablation study on these datasets [3]. The LR is set to 0.001, Adagrad is used as an optimizer, and the batch size is 32. As we work on binary classification, the loss function is set as categorical_crossentropy.

Table 2. The details of two facial image datasets

| Split | Kaggle | YTUIA | Binary Class |
|---|---|---|---|
| Train set | 2654 | 1068 | 0 - non-ASD<br>1 - ASD |
| Test set | 280 | 100 | |
| Valid set | 80 | - | |

The deep CNN models were trained for 50 epochs and evaluated on both T1, T2, and the combined test set (T1+T2). The weights are then shared with the global server, and the model aggregator generates the global model using FedAvg. The weight of the global models is shared with each of the clients. The evaluation for T1, T2, and the combined test set was done using the global model with the federated weight from each client. To compare the evaluation performance of the federated learning approach, we commence by juxtaposing its performance with that of a conventional learning method that employs centralized and shared data to train the identical network architecture.

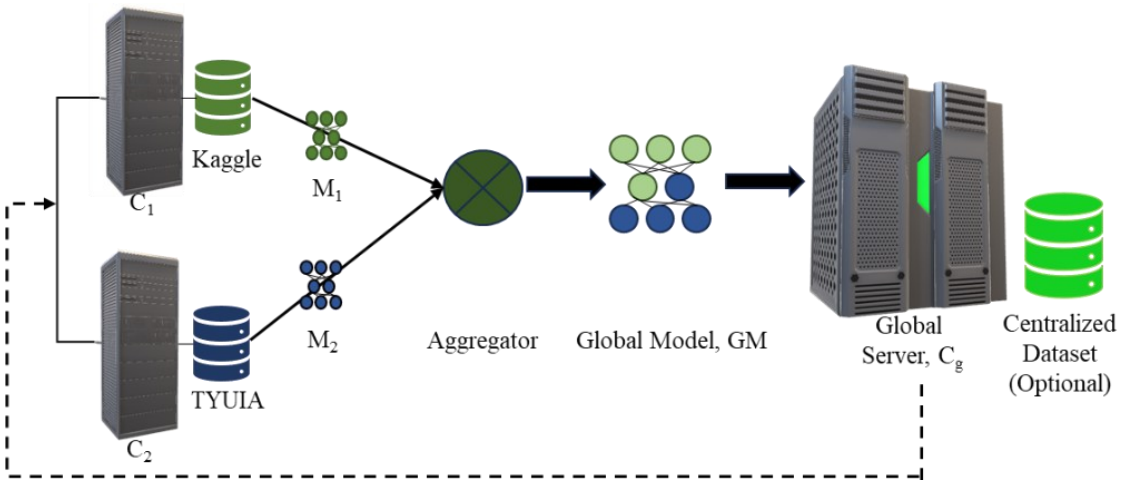


Figure 3. Process flow for federated learning for ASD detection with facial images

## 2.6. Evaluation Metrics

We employed several parameters to assess the performance of models. The most popular metric was the accuracy of classification, commonly referred to as 'accuracy' in this body of research. As done in earlier studies, the assessment of the model's precision also included using AUC, which stands for area under the curve. Derived from the ROC curve, this area under the curve (AUC) is a more valid measure than accuracy for illustrating the model's performance. The remaining two matrices, precision and recall, indicate the capacity to forecast the intended classes accurately. The F1-score is a metric utilized in statistical analysis of information

retrieval and binary classification systems to assess their predictive performance. The mathematical equations for accuracy, precision, and recall are as follows:

$$Accuracy = \frac{T_p + T_n}{T_p + T_n + F_n + F_p} \tag{4}$$

$$Precision = \frac{T_p}{T_p + F_p} \tag{5}$$

$$Recal = \frac{T_p}{T_p + F_n} \tag{6}$$

$$F1score = 2 \times \frac{Precision \times Recall}{Precision + Recall} \tag{7}$$

## 3. RESULTS AND DISCUSSION

The code was executed on the Kaggle platform, whereas the Python programming language was employed during the code development phase. Following the conclusion of the model training process, the acquired results underwent examination utilizing a variety of data analysis tools. The performance assessment in this research entailed the computation of accuracy, precision, recall, and F1-score, utilizing Equations (4) to (7).

### 3.1. Performance Evaluation at Local Centers

A comprehensive evaluation of three models, Xception, ResNet50V2, and MobileNetV2, trained on the Kaggle dataset, is presented in Table 3. The assessment provides critical performance matrices per the equations (4) to (7). Every model undergoes a comprehensive evaluation on two separate sets, denoted as T1 and T2, to demonstrate their efficacy under different domain scenarios. The Xception model achieved a maximum accuracy of 95% and an AUC value of 98% on T1. The ResNet50V2 and MobileNetV2 models demonstrate nearly identical evaluation performance, reaching an accuracy of 94% and 92%, respectively.

Table 3. Performance evaluation at $C_1$ model trained with the Kaggle dataset

| Models | $M_{kaggle}$ evaluated on T1 | | | | | $M_{kaggle}$ evaluated on T2 | | | | |
|---|---|---|---|---|---|---|---|---|---|---|
| | **Acc** | **Prec** | **Recall** | **F1** | **AUC** | **Acc** | **Prec** | **Recall** | **F1** | **AUC** |
| Xception | **0.95** | 0.95 | 0.95 | 0.94 | 0.98 | 0.49 | 0.49 | 0.49 | 0.48 | 0.50 |
| ResNet50V2 | 0.94 | 0.94 | 0.94 | 0.94 | 0.96 | **0.53** | 0.53 | 0.53 | 0.53 | 0.55 |
| MobileNetV2 | 0.92 | 0.92 | 0.92 | 0.92 | 0.96 | 0.44 | 0.44 | 0.44 | 0.44 | 0.43 |

The $C_1$ models were evaluated on the YTUIA test set (T2), which is from a different domain, to identify the research gap. The evaluation performance has experienced a reduction of approximately 50 percent. The highest accuracy achieved was 53 percent for ResNet50V2; however, for MobileNetV2, the reported accuracy is just 44 percent, indicating a significant decrease. The result indicates a substantial disparity in performance between the two sets of tests, highlighting the need for domain adaptation when testing among various dataset samples.

Table 4 illustrates the scenario at $C_2$, where the local models are trained using the YTUIA dataset. As the models were evaluated on the same domain test set T2, just as $C_1$, their performance is quite good. ResNet50V2 obtained the highest accuracy and AUC of 95 and 97, respectively. The substantial decline in accuracy to 74% for MobileNetV2 suggests that the feature extraction by the model is unsuitable for the YTUIA dataset.

Table 4. Performance evaluation at $C_2$ model trained with the YTUIA dataset

| Models | $M_{YTUIA}$ evaluated on T1 | | | | | $M_{YTUIA}$ evaluated on T2 | | | | |
|---|---|---|---|---|---|---|---|---|---|---|
| | Acc | Prec | Recall | F1 | AUC | Acc | Prec | Recall | F1 | AUC |
| Xception | **0.57** | 0.57 | 0.57 | 0.49 | 0.60 | **0.95** | 0.95 | 0.95 | 0.95 | 0.97 |
| ResNet50V2 | 0.56 | 0.56 | 0.56 | 0.46 | 0.57 | 0.93 | 0.93 | 0.93 | 0.93 | 0.95 |
| MobileNetV2 | 0.56 | 0.56 | 0.56 | 0.48 | 0.59 | 0.74 | 0.74 | 0.74 | 0.74 | 0.83 |

While testing on T1, a dataset obtained from Kaggle that belongs to a different domain, the assessment metrics show a significant decrease in accuracy for the Xception and ResNet50V2 models, reaching 57% and 56%, respectively.

Table 5. Performance evaluation on combined test sets locally at $C_1$ and $C_2$

| Models | $M_{kaggle}$ evaluated on T1+T2 | | | | | $M_{YTUIA}$ evaluated on T1+T2 | | | | |
|---|---|---|---|---|---|---|---|---|---|---|
| | Acc | Prec | Recall | F1 | AUC | Acc | Prec | Recall | F1 | AUC |
| Xception | **0.83** | 0.83 | 0.83 | 0.83 | 0.90 | 0.64 | 0.64 | 0.64 | 0.64 | 0.66 |
| ResNet50V2 | 0.81 | 0.81 | 0.81 | 0.81 | 0.87 | **0.66** | 0.66 | 0.66 | 0.66 | 0.69 |
| MobileNetV2 | 0.82 | 0.82 | 0.82 | 0.82 | 0.86 | 0.60 | 0.60 | 0.60 | 0.60 | 0.64 |

Table 5 displays the assessment outcome conducted on the combined test set T1+T2. The results fall short of the values obtained while testing the models on the same domain test sets. The highest accuracy achieved on the combined test was 83% at $C_1$ while getting 66% at $C_2$. This issue arises due to the unbalanced number of samples in the combined test set from Kaggle and YTUIA. Due to the threefold increase in the amount of samples from Kaggle in the combined test set, the accuracy at $C_1$ is higher. This happens only because the models have learned features exclusively from the Kaggle dataset. For this reason, the evaluation accuracy is lower on the combined test set at $C_2$, where models are trained on the YTUIA dataset only.

### 3.2. Performance Evaluation after Federated Learning

After the training at the local servers, model weights are sent to the aggregators to update the global model, GM, as per equation (2). The global server updates the local servers with the global aggregated models. Table 6 displays the thorough performance assessment of various models, such as Xception, ResNet50V2, and MobileNetV2, utilizing global model weights on separate test sets, T1 and T2. The Xception model scored an accuracy, precision, recall, F1-score of 91%, and AUC of 99% when evaluated on T1, indicating its reliable performance. Similarly, the assessment on T2 produced slightly lower but still praiseworthy outcomes, with an accuracy of 89% and other metrics remaining consistently good.

Table 6. Performance evaluation on different test sets with global model weights

| Models | $M_{Federated}$ evaluated on T1 | | | | | $M_{Federated}$ evaluated on T2 | | | | |
|---|---|---|---|---|---|---|---|---|---|---|
| | Acc | Prec | Recall | F1 | AUC | Acc | Prec | Recall | F1 | AUC |
| Xception | **0.91** | 0.91 | 0.91 | 0.91 | 0.99 | 0.89 | 0.89 | 0.89 | 0.89 | 0.98 |
| ResNet50V2 | 0.90 | 0.90 | 0.90 | 0.90 | 0.96 | **0.92** | 0.92 | 0.92 | 0.92 | 0.99 |
| MobileNetV2 | 0.82 | 0.82 | 0.82 | 0.82 | 0.91 | 0.84 | 0.84 | 0.84 | 0.84 | 0.90 |

The ResNet50V2 model demonstrated better performance, attaining an accuracy of 92% while evaluated on T2 than evaluation on T1, which is 90 percent. All the performance matrices consistently demonstrated the model's reliability across both test sets. Despite a slightly reduced accuracy of 82% on T1, MobileNetV2 exhibited significant precision, recall, F1-score,

and AUC values. At T2, the accuracy increased to 84 percent, confirming the model's adaptive capacity to adjust effectively, predicting various test scenarios. The variability in performance across different test sets indicates that data characteristics between T1 and T2 likely influenced the models' results, underscoring the importance of considering data heterogeneity when developing robust and generalizable models. This finding validates that the model's effectiveness is enhanced following domain adaptation, regardless of the dataset utilized for evaluation.

Moreover, when evaluating real-time unseen datasets with trained models, feature extraction and generalization are notably more adaptive after federated learning, as the model weights are averaged following training on diverse and unique datasets from different health centers.

Figure 4 shows the graphs of the proposed federated learning vs. centralized learning techniques. The results for centralized learning are the average value accumulated from both training with the Kaggle and YTUIA datasets and evaluated on the own domain dataset. The same process can also be experienced by storing the shared combined dataset in the optional global database. At first, the accuracy of the federated technique is lower than that of the centralized training data for both the Xception and ResNet50V2 models. However, after a specific number of epochs, the accuracy of the federated strategy approaches the accuracy of the centralized training data.

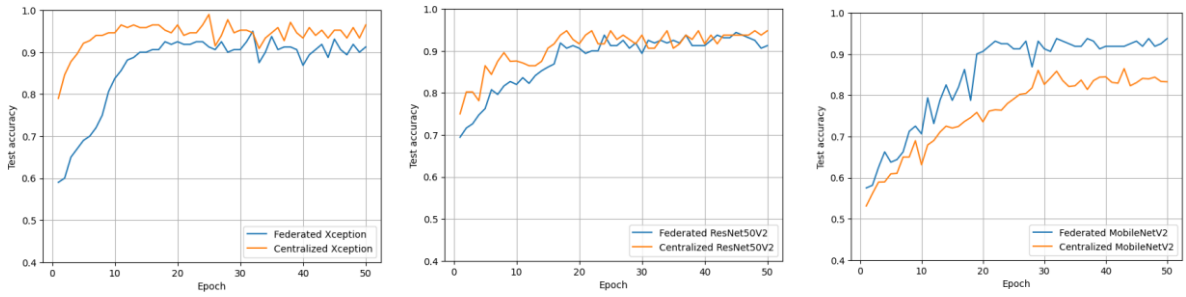


(a) Xception (b) ResNet50V2 (c) MobileNetV2

Figure 4. Comparison of the Centralized and Federated Learning

While the accuracy achieved with federated learning may not exceed the values obtained from training on a centralized dataset hosted on a global server, the results are consistent across all clients and test sets. The test accuracy curve obtained via federated learning surpasses shared or centralized training for MobileNetV2. The outcome from $C_2$, as presented in Table 4, unexpectedly demonstrates a decrease in value. This decrease has contributed to the decline of the MobileNetV2 model in the centralized training scheme.

Table 7. Performance comparison of Centralized and Federated learning on the combined set

| **Models** | **$M_{centralized}$ (avg) evaluated on T1+T2** | | | | | **$M_{Federated}$ evaluated on T1+T2** | | | | |
|---|---|---|---|---|---|---|---|---|---|---|
| | **Acc** | **Prec** | **Recall** | **F1** | **AUC** | **Acc** | **Prec** | **Recall** | **F1** | **AUC** |
| Xception | 0.950 | 0.950 | 0.950 | 0.950 | 0.975 | 0.901 | 0.901 | 0.901 | 0.901 | 0.959 |
| ResNet50V2 | 0.935 | 0.935 | 0.935 | 0.935 | 0.955 | 0.891 | 0.891 | 0.891 | 0.891 | 0.951 |
| MobileNetV2 | 0.830 | 0.830 | 0.830 | 0.830 | 0.895 | 0.887 | 0.887 | 0.887 | 0.887 | 0.904 |

Table 7 compares the evaluation matrices for the centralized and Federated training strategy when tested on the combined test set of the Kaggle and YTUIA datasets. Training models using a shared training set from all clients guarantees smooth feature learning from the training data, but it compromises the confidentiality of medical information and violates patients' privacy.

The centralized training for Xception achieves a high accuracy of 95 percent, mostly because of the open sharing of medical information. Federated learning guarantees data security and allows us to achieve up to 90 percent accuracy using the Xception model. ResNet50V2 exhibited consistent behavior throughout both schemes, while MobileNetV2 produced contrasting outcomes, which can be attributed to a lack of proper feature learning during the training phase at $C_2$ using the YTUIA dataset.

### 3.3. Discussion

The preceding discourse constitutes a research endeavor that introduces a unique dataset of facial photos specifically designed for detecting ASD. This research also pioneers the analysis of two datasets from different domains to improve the effectiveness of domain adaptation tasks. Federated learning algorithms improve ASD screening and prioritize domain adaptability while maintaining medical information confidentiality. There are many potential challenges to employing deep federated learning for domain adaptation, and this study can contribute a few significant insights. Figure 4 displays the graph depicting the two primary performance metrics, AUC and accuracy, for different evaluation criteria. Figure 5 (a) and (b) show the performance of local models trained on a single-domain dataset.

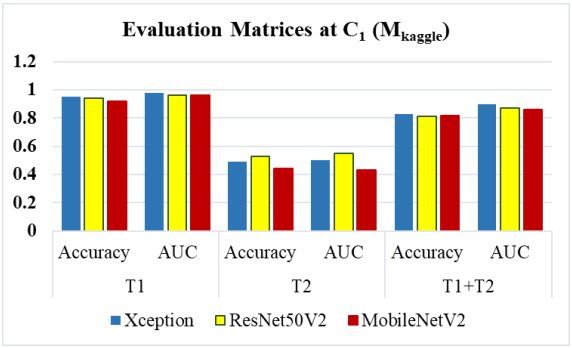


(a) Local models trained with Kaggle

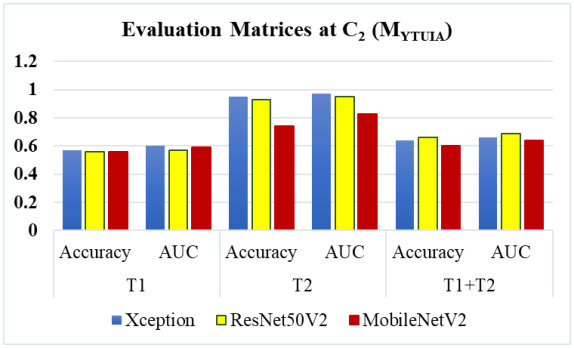


(b) Local models trained with YTUIA

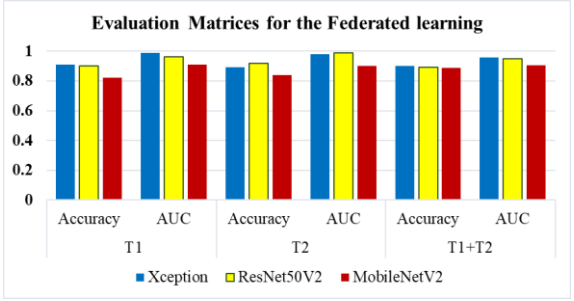


(c) Federated global model

Figure 5. Evaluation matrices after testing with different test sets

However, when assessed on diverse test sets, the performance deteriorates. Observing the impact of an unbalanced training dataset at both centers, $C_1$ and $C_2$ are important. The evaluation result on the combined test set is better at $C_1$ due to using models trained on the Kaggle dataset. The combined test set has three times as many test samples from the Kaggle

test set as it does from YTUIA. Consequently, training using YTUIA leads to a decrease in performance on the combined dataset at $C_2$. Therefore, the prediction job is at stake when working at any of the local centers due to the presence of distinct features in the different samples, as opposed to the local training set. On the other hand, freely sharing personal medical information with every server is not a prudent strategy. The federated learning scheme addresses the challenges of data security through the use of certain methodologies. It also ensures diversity in feature learning by aggregating common features from local models, resulting in improved evaluation performance for test samples from different domains. Figure 5(c) shows the evaluation of the global aggregated model on all the test sets. The accuracy values for all test configurations and models are nearly identical and consistently remain near to or above 90 percent. While it may not exceed the evaluation performance of centralized training, it significantly enhances performance across all testing settings. These global models are accessible to local clients, allowing specialists from anywhere to utilize the ASD screening facility for diverse samples.

There is a lack of research on federated learning for ASD diagnosis that utilizes facial images as a tool to train the deep learning algorithm. However, this study is the first attempt to utilize federated learning to adapt a domain difference for ASD screening. Therefore, it is challenging to compare with the previous studies due to the lack of appropriate criteria that are directly relevant. Table 8 provides a concise overview of the current studies relevant to diagnosing Autism Spectrum Disorder (ASD). Only one research paper addressing facial images utilizing federated learning was in the Scopus database. However, the purpose of this paper does not involve achieving domain adaptation. In this research, a core component of federated learning is the CNN, which achieves a maximum accuracy of 60% with a 13% improvement compared to the benchmark [19]. The other two studies utilize a questionnaire-based CSV dataset. One specific research [20] employs Logistic Regression (LR), a shallow approach, while the other[21] utilizes FCNN-LSTM. Both researchers claimed a 99% accuracy rate. However, no minimum floor value for enhancement is specified. The data size is 200 for the shallow approach [20], though the subsequent study [21] does not explicitly specify the dataset size. However, Z. Fan et al. (2021) [22] employed ResNet as the backbone model for Federated learning in order to train MRI images for the purpose of ASD screening. They achieved an accuracy of 61.91%, which represents a 4% enhancement compared to the baseline value.

Table 8. Comparison with the recent research

| Ref | Backbone | Algorithm | Accuracy | Improve (%) | Dataset Type | Dataset Size |
|---|---|---|---|---|---|---|
| **Federated learning** | | | | | | |
| [20] | LR | - | 99 | NA | Interview Based | 200 |
| [21] | FCNN-LSTM | - | 99 | NA | Interview Based | NA |
| [19] | Own CNN | FedAVg | 60 | 13 | Facial images | 2940 |
| [22] | ResNet | FedAVg | 61.92 | 4 | Neuroimage | 2131 |
| **Domain adaptation** | | | | | | |
| [23] | DCNN | MSDA | 58.8 | 45 | Neuroimage | 409 |
| [12] | MLP | FedAVg | 84.9 | 26 | Neuroimage | 390 |
| **The proposed method for domain adaptation by Federated Learning** | | | | | | |
| | Xception | FedAVg | 90.1 | 36 | Facial images | 3726 |

Regarding domain adaptation, J. Wang et al. (2020) [23] utilize neuroimaging data to train deep CNN models and employ the MSDA approach for domain adaptation. The research findings indicate an accuracy rate of 58.8%, representing a significant improvement of 45%

compared to the benchmark. The subsequent study [12] utilized a federated learning approach to attain domain similarity, resulting in an 84.9% accuracy rate, representing a 26% enhancement compared to the minimum benchmark. The sole distinction in our suggested approach lies in using facial pictures to train the deep CNNs' backbones. The utilization of Xception as the backbone framework in federated learning yielded an impressive accuracy rate of nearly 90% across all test sets, exhibiting a remarkable improvement of over 30% compared to the baseline values. Moreover, incorporating deep federated learning methods paves the way for a detailed examination of ethical concerns and for creating stronger and more secure solutions that benefit both researchers and individuals engaged in ASD screening fields.

## 4. CONCLUSION

This research presents a groundbreaking contribution to early autism screening by introducing a unique collection of facial image datasets specifically for detecting ASD. The innovative research of various domain datasets and the utilization of federated learning methods represent a revolutionary approach to improving domain adaptation tasks. The federated learning scheme is a reliable method that effectively tackles data security concerns and guarantees a wide range of features, resulting in enhanced assessment performance on diverse datasets. This study fills a gap in research by exploring the use of facial images for federated learning in the diagnosis of ASD. By employing Xception as the backbone of the federated learning approach, an accuracy rate of nearly 90% was achieved across all test sets. This represents a significant improvement of over 30% compared to the baseline values. However, the study does not explore explainable AI, which could offer insights into the neural network's decision-making. Future research should integrate explainable AI to improve model transparency and clinician trust. Despite this limitation, the study's distinctive dataset, methodological innovations, and ethical considerations make it a significant contribution to early autism screening research. It offers a comprehensive perspective on the challenges and opportunities in the field, serving as a valuable resource for practitioners and future researchers.

## ACKNOWLEDGMENT

The authors would like to express their deepest gratitude to the International Islamic University Malaysia for its support of M.S.A through the Tuition Fee Waiver Scheme (2021).

## CODE REPOSITORY

https://github.com/gmshafiuliium/ASD-Federated-Shafi

## REFERENCES

[1] Autism (2023).World Health Organization. Available: https://www.who.int/news-room/fact-sheets/ detail/autism-spectrum-disorders
[2] Rashid, M. M., & Alam, M. S. (2024). Power of Alignment: Exploring the effect of face alignment on ASD diagnosis using facial images .IIUM Engineering Journal, 25(1):317–327. https://doi.org/10.31436/iiumej.v25i1.2838
[3] Alam, M. S., Rashid, M. M., Roy, R., Faizabadi, A. R., Gupta, K. D., & Ahsan, M. M. (2022). Empirical Study of Autism Spectrum Disorder Diagnosis Using Facial Images by Improved Transfer Learning Approach. Bioengineering, 9(11):1–18. https://doi.org/10.3390/bioengineering9110710
[4] Kojovic, N., Natraj, S., Mohanty, S. P., Maillart, T., & Schaer, M. (2021). Using 2D video-based pose estimation for automated prediction of autism spectrum disorders in young children. Scientific Reports, 11(1):15069. https://doi.org/10.1038/s41598-021-94378-z

[5] Khodatars, M., Shoeibi, A., Sadeghi, D., Ghaasemi, N., Jafari, M., Moridian, P., Khadem, A., Alizadehsani, R., Zare, A., Kong, Y., Khosravi, A., Nahavandi, S., Hussain, S., Acharya, U. R., & Berk, M. (2021). Deep learning for neuroimaging-based diagnosis and rehabilitation of Autism Spectrum Disorder: A review. Computers in Biology and Medicine, 139:104949. https://doi.org/10.1016/j.compbiomed.2021.104949

[6] Mohammad Shafiul Alam, Zabina Tasneem, Sher Afghan Khan, & Muhammad Mahbubur Rashid. (2023). Effect of Different Modalities of Facial Images on ASD Diagnosis using Deep Learning-Based Neural Network. Journal of Advanced Research in Applied Sciences and Engineering Technology, 32(3):59–74. https://doi.org/10.37934/araset.32.3.5974

[7] Uddin, M. Z., Shahriar, M. A., Mahamood, M. N., Alnajjar, F., Pramanik, M. I., & Ahad, M. A. R. (2024). Deep learning with image-based autism spectrum disorder analysis: A systematic review. Engineering Applications of Artificial Intelligence, 127:107185. https://doi.org/10.1016/j.engappai.2023.107185

[8] Alam, M. S., Rashid, M. M., Faizabadi, A. R., Mohd Zaki, H. F., Alam, T. E., Ali, M. S., Gupta, K. D., & Ahsan, M. M. (2023). Efficient Deep Learning-Based Data-Centric Approach for Autism Spectrum Disorder Diagnosis from Facial Images Using Explainable AI. Technologies, 11(5):115. https://doi.org/10.3390/technologies11050115

[9] Vuilleumier, P., & Pourtois, G. (2007). Distributed and interactive brain mechanisms during emotion face perception: Evidence from functional neuroimaging. Neuropsychologia, 45(1): 174–194. https://doi.org/10.1016/j.neuropsychologia.2006.06.003

[10] Vizitiu, A., Nita, C. I., Puiu, A., Suciu, C., & Itu, L. M. (2019). Towards Privacy-Preserving Deep Learning based Medical Imaging Applications. 2019 IEEE International Symposium on Medical Measurements and Applications (MeMeA), 1–6. https://doi.org/10.1109/MeMeA.2019.8802193

[11] Feki, I., Ammar, S., Kessentini, Y., & Muhammad, K. (2021). Federated learning for COVID-19 screening from Chest X-ray images. Applied Soft Computing, 106:107330. https://doi.org/10.1016/j.asoc.2021.107330

[12] Li, X., Gu, Y., Dvornek, N., Staib, L. H., Ventola, P., & Duncan, J. S. (2020). Multi-site fMRI analysis using privacy-preserving federated learning and domain adaptation: ABIDE results. Medical Image Analysis, 65:101765. https://doi.org/10.1016/j.media.2020.101765

[13] Li, Y., Huang, W.-C., & Song, P.-H. (2023). A face image classification method of autistic children based on the two-phase transfer learning. Frontiers in Psychology, 14. https://doi.org/10.3389/fpsyg.2023.1226470

[14] Rabbi, M. F., Zohra, F. T., Hossain, F., Akhi, N. N., Khan, S., Mahbub, K., & Biswas, M. (2023). Autism Spectrum Disorder Detection Using Transfer Learning with VGG 19, Inception V3 and DenseNet 201, Communications in Computer and Information Science, Springer, Cham, 1704:190–204. https://doi.org/10.1007/978-3-031-23599-3_14

[15] Kang, H., Yang, M., Kim, G.-H., Lee, T.-S., & Park, S. (2023). DeepASD: Facial Image Analysis for Autism Spectrum Diagnosis via Explainable Artificial Intelligence. 2023 Fourteenth International Conference on Ubiquitous and Future Networks (ICUFN), 2023:625–630. https://doi.org/10.1109/ICUFN57995.2023.10200203

[16] M. Ghazal, T., Munir, S., Abbas, S., Athar, A., Alrababah, H., & Adnan Khan, M. (2023). Early Detection of Autism in Children Using Transfer Learning. Intelligent Automation & Soft Computing, 36(1):11–22. https://doi.org/10.32604/iasc.2023.030125

[17] Musser, M. (2020). Detecting Autism Spectrum Disorder in Children With Computer Vision. Towards Data Science. Available: https://github.com/mm909/Kaggle-Autism

[18] Rajagopalan, S. S., & Goecke, R. (2014). Detecting self-stimulatory behaviours for autism diagnosis. 2014 IEEE International Conference on Image Processing (ICIP), 2014:1470–1474. https://doi.org/10.1109/ICIP.2014.7025294

[19] Shamseddine, H., Otoum, S., & Mourad, A. (2022). On the Feasibility of Federated Learning for Neurodevelopmental Disorders: ASD Detection Use-Case. GLOBECOM 2022 - 2022 IEEE Global Communications Conference, 1121–1127. https://doi.org/10.1109/GLOBECOM48099.2022.10001248

[20] Farooq, M. S., Tehseen, R., Sabir, M., & Atal, Z. (2023). Detection of autism spectrum disorder

(ASD) in children and adults using machine learning. Scientific Reports, 13(1): 9605. https://doi.org/10.1038/s41598-023-35910-1

[21] Lakhan, A., Mohammed, M. A., Abdulkareem, K. H., Hamouda, H., & Alyahya, S. (2023). Autism Spectrum Disorder detection framework for children based on federated learning integrated CNN-LSTM. Computers in Biology and Medicine, 166:107539. https://doi.org/10.1016/j.compbiomed.2023.107539

[22] Fan, Z., Su, J., Gao, K., Hu, D., & Zeng, L.-L. (2021). A Federated Deep Learning Framework for 3D Brain MRI Images. 2021 International Joint Conference on Neural Networks (IJCNN), 1–6. https://doi.org/10.1109/IJCNN52387.2021.9534376

[23] Wang, J., Zhang, L., Wang, Q., Chen, L., Shi, J., Chen, X., Li, Z., & Shen, D. (2020). Multi-Class ASD Classification Based on Functional Connectivity and Functional Correlation Tensor via Multi-Source Domain Adaptation and Multi-View Sparse Representation. IEEE Transactions on Medical Imaging, 39(10): 3137–3147. https://doi.org/10.1109/TMI.2020.2987817

https://doi.org/10.31436/iiumej.v26i1.3194

# RETINOPATHY DISEASE DETECTION AND CLASSIFICATION USING COORDINATE ATTENTION MODULE BASED CONVOLUTIONAL NEURAL NETWORK WITH LEAKY RECTIFIED LINEAR UNIT

**PRAVIN BALASO CHOPADE[1*], PRABHAKAR N. KOTA[1], BHAGVAT D. JADHAV[2], PRAVIN MAROTRAO GHATE[2], SHRIRAM SADASHIV KULKARNI[3]**

[1]*Dept. of Electronics &Telecommunications, M.E.S. College of Engineering, Pune, India*
[2]*Dept. of Electronics & Telecommunications, JSPM's Rajarshi Shahu College of Engineering, Pune, India*
[3]*Dept. of Information Technology, Sinhgad Academy of Engineering, Pune, India*

**Corresponding author: pbchopade@mescoepune.org*

*(Received: 1 February 2024; Accepted: 30 October 2024; Published online: 10 January 2025)*

***ABSTRACT:*** The detection of Diabetic Retinopathy (DR) is an emergent research topic in recent decades, where DR is a primary cause of vision loss in humans. The existing techniques have limitations such as neuron death issues, vanishing gradient, and output offset. To overcome these issues, this paper proposes a Deep Learning (DL)-based technique for early and accurate DR detection. The Coordinate Attention Module (CAM) based Convolutional Neural Network (CNN) with Leaky Rectified Linear Unit (LReLU) is proposed for early and accurate detection of DR. The MESSIDOR dataset is preprocessed through the median filter to eliminate noise, and Contrast-Limited Adaptive Histogram Equalization (CLAHE) is utilized to increase the contrast level in an input image. The preprocessed images are given to Mayfly Optimization Algorithm-based Region Growing (MOARG) for image segmentation. Then, the features are extracted using ResNet50 and SqueezeNet, which extract deep learning features. The extracted features are given to CAM-based CNN with LReLU to detect DR, which overcomes the dead issues of neurons and minimizes the probability of inactive neurons. The proposed model achieves better results on the MESSIDOR datasets on the metrics of accuracy, precision, recall, specificity, f1-score, and Area Under Curve (AUC) values of about 99.72%, 99.46%, 99.25%, 99.61%, 99.37% and 99.14%, correspondingly, proving to be superior to the existing method, Capsule Network and Hybrid Adaptive DL based DR (HADL-DR).

***ABSTRAK*:** Pengesanan Retinopati Diabetik (DR) merupakan topik penyelidikan yang semakin mendapat perhatian dalam dekad-dekad kebelakangan ini, di mana DR merupakan punca utama kehilangan penglihatan pada manusia. Teknik sedia ada mempunyai beberapa kekangan seperti isu kematian neuron, vanishing gradient, dan output offset. Untuk mengatasi isu-isu ini, kertas ini mencadangkan teknik berasaskan Pembelajaran Mendalam (DL) untuk pengesanan awal dan tepat bagi DR. Modul Coordinate Attention Module (CAM) berasaskan Convolutional Neural Network (CNN) dengan Leaky Rectified Linear Unit (LReLU) dicadangkan untuk pengesanan awal dan tepat bagi DR. Dataset MESSIDOR diproses melalui penapis median yang digunakan untuk menghapuskan hingar, dan Contrast-Limited Adaptive Histogram Equalization (CLAHE) digunakan untuk meningkatkan tahap kontras pada imej input. Imej yang telah diproses diberikan kepada Algoritma Pengoptimuman Mayfly berasaskan Region Growing (MOARG) untuk segmentasi imej. Kemudian, ciri-ciri diekstrak menggunakan ResNet50 dan SqueezeNet yang mengekstrak ciri-ciri pembelajaran mendalam. Ciri-ciri yang diekstrak ini diberikan kepada CNN berasaskan CAM dengan LReLU untuk pengesanan DR, yang mengatasi isu kematian neuron dan meminimumkan

kebarangkalian neuron tidak aktif. Model yang dicadangkan mencapai keputusan yang lebih baik pada dataset MESSIDOR berdasarkan metrik ketepatan, ketepatan, panggilan semula, kekhususan, skor f1, dan nilai Kawasan di Bawah Lengkung (AUC) iaitu sekitar 99.72%, 99.46%, 99.25%, 99.61%, 99.37% dan 99.14%, masing-masing, membuktikan keunggulannya berbanding kaedah sedia ada, Capsule Network dan Hybrid Adaptive DL berasaskan DR (HADL-DR).

***KEYWORDS:*** *Area Under Curve, Convolutional Neural Network, Coordinate Attention Module, Leaky Rectified Linear Unit, Mayfly Optimization Algorithm.*

# 1. INTRODUCTION

Retinopathy refers to a group of eye conditions that affect the retina and the light-sensitive tissue at the back of the eye [1]. Diabetic Retinopathy (DR) is the most common type of disease that occurs in people with diabetes, leading to vision impairment or blindness if not identified and detected at an early stage [2]. DR detection utilizes various medical image techniques to identify abnormalities in the retina [3]. Blurriness, dark areas of vision, floaters, difficulty perceiving colors, and vision loss are early symptoms of DR [4]. According to the World Health Organization (WHO), the prevalence of DR-related is approximately 4.8% among 37 million cases worldwide [5]. Therefore, individuals with DR require regular retinal screening to detect DR at an early stage, manage its progression, and prevent blindness [6]. Statistical analysis indicates that DR affects individuals over 18 and is increasing daily [7]. DR risk factor is separated into modifiable risks, such as smoking, blood pressure, and glucose levels, and non-modifiable risks, like age, genetic predisposition, and disease duration [8].

The severity of DR is classified into 5 stages: no DR, mild Non-Proliferative (NP) DR, moderate NPDR, severe NPDR, and proliferative DR based on the extent of damage to the retinal blood vessels [9]. In the No DR stage, the retina appears normal during an eye examination. In mild NPDR, there are small areas of swelling in blood vessels of the retina, but they do not cause vision issues, which is Van's early stage of DR [10] [11]. In moderate NPDR, severe changes occur in retinal blood vessels that contain blockages in vessels and decreased blood supply to the retina [12]. In severe NPDR, there is a substantial reduction in blood supply to the retina, which results in the growth of new blood vessels that compensate for the lack of blood flow [13]. Proliferative DR occurs when new, abnormal blood vessels start growing on the retina's surface, leading to retinal detachment and vision loss [14]. Several researchers have utilized DL techniques for the detection of DR, such as CNN and long short-term memory (LSTM), because they provide high accuracy [15]. Most of the research has utilized image patching and deep network architectures for DR detection [16]. The neuron death issue occurs when the ReLU activation function, which is observed in various neural networks, is applied to the MESSIDOR dataset. The traditional approach with ReLU leads to inactive neurons when gradients turn to zero during training, impacting the model's learning ability. The vanishing gradient issue occurs mainly in deeper networks where the activation functions compress gradients to smaller values, making it difficult for the network to propagate meaningful data to previous layers. The output offset rises when the predicted score deviates from its correct targets, occurring in networks that fail to converge optimally. The main contributions of the research are given below:

- The MOARG is used for segmentation, utilizing the global search capability of MOA to adapt intricate shapes in retinal images, such as lesions, abnormal regions, and blood vessels. This ensures that this model is capable and precise enough to deal with difficult variations in retinal structures, which is significant for accurate DR detection.

https://doi.org/10.31436/iiumej.v26i1.3194

- The CAM assists in visualizing the input image regions, enabling the model to highlight significant retinal regions that denote DR, thereby enhancing interpretability and performance.
- The LReLU function addresses the issue of dead neurons in traditional ReLU by introducing a small negative slope for negative input scores. It enables neurons to stay active even while receiving negative inputs, reducing inactive neuron issues and ensuring the model learns efficiently, enhancing its overall performance in DR detection.

The remaining parts of the paper are arranged as follows: Section 2 provides a literature review, Section 3 explains the proposed methodology in detail, Section 4 provides the results and discussion, and Section 5 gives the conclusion.

## 2. LITERATURE REVIEW

This section describes some recent literature on retinopathy detection using Machine Learning (ML) and deep learning (DL) techniques.

Parthiban and Kamarasan [17] introduced an Intelligent Coyote Optimization Algorithm with DL-based DR Detection (ICOA-DLDRD) on fundus images. The model contained Gabor Filtering (GF)-based noise elimination and optimum region growing for segmentation. Lastly, COA with Deep Extreme Learning Machine (DELM) utilized cross-validation that assisted invisible data for DR. The developed model easily handled high-dimensional data, making it suitable for solving complex problems. However, this model was prone to overfitting issues, particularly when dealing with noisy data.

Palaniswamy and Vellingiri [18] developed an Internet of Things DL-DR Diagnosis (IoTDL-DRD) through Retinal Fundus Images (RFI). Initially, the RFI was preprocessed to eliminate noise and enhance contrast. Then, the optimum region growing segmentation was utilized to detect the lesion region in an image. Next, the DenseNet-based feature extraction and LSTM-based classification were utilized for efficient DR detection. The developed model was capable of handling long-term dependencies and sequential input data. However, it struggled with learning certain features and the inability to handle temporal dependencies, making the model complex to train.

Kalyani et al. [19] presented a Capsule Network (CapsNet) for DR detection and classification. The features were extracted from the fundus image using the convolutional and primary capsule layers. Subsequently, the class capsule and SoftMax layer were utilized to assign the image to a precise class, where the created CapsNet accurately identified the issues at every stage. The developed model outperformed individual transfer learning and numerous ensemble approaches. Nevertheless, it could not manage complex data due to its vanishing gradient problems.

Islam et al. [20] suggested Supervised Contrastive Learning (SCL) for DR detection and classification of severity levels from images. A dual-stage training method with a loss function was developed in SCL to recognize DR and classify its severity levels. The CLAHE was used to enhance image quality, and Xception CNN was developed as an encoder. The developed model learned discriminative and meaningful features in the input data, which made the model more effective. However, the model was sensitive to noisy data and attempted to identify the optimal hyperplane.

Hemanth and Alagarsamy [21] implemented a HADL-DR through optimal feature extraction and classification. Initially, an enhanced Multichannel-based Generative Adversarial

https://doi.org/10.31436/iiumej.v26i1.3194

Network (MGAN) with semi-maintenance was employed to detect blood vessel segmentation. Scale Invariant Feature Transform (SIFT) was used for feature extraction, and the best solution was selected through an enhanced Sequential Approximation Optimization (SAO). Then, the hybrid Recurrent Neural Network with LSTM (RNN-LSTM) was used to classify DR. The developed model was used to prevent the network from overfitting issues, enhancing the training data. However, it is computationally exhaustive and struggles with noisy data.

Das and Saha [22] developed a CNN-tuned Genetic Algorithm (GA) for DR detection and classification. The developed CNN contained a series of convolutional and pooling layers that were utilized for feature extraction. Then, the Support Vector Machine (SVM) was used for classification. By using GA, hyperparameters like the number of kernels, pooling, and convolutional layers were determined. According to the dimensions of an input image, minimum and maximum kernel sizes needed to be generated. It efficiently captured spatial hierarchies and enabled the detection of significant structures at different levels, thereby leading to overfitting issues when dealing with limited data.

Zhang et al. [23] presented DR grading through the Deep Graph Correlation Network (DGCN) without Manual Annotations. The DGCN comprised the Graph Convolutional Network (GCN) to progress automatic DR grading without annotations. The DGCN included GCN for exploiting intrinsic correlations from autonomous images learned through CNN. The presented model designed three loss functions of pseudo-contrastive, transformation-invariant constraint, and graph-center to optimize the DGCN. The developed model efficiently learned long short-term spatiotemporal dependencies but failed to capture the spatial correlations.

Abbood et al. [24] introduced a hybrid image enhancement technique for DR diagnosis through ResNet50. The introduced model included two stages: cropping the image to eliminate irrelevant content and applying Gaussian blurring and shape crop for noise elimination and enhancing contrast. The ResNet50 was used to extract a feature set to aid the classification process. The introduced model was evaluated using the MESSIDOR and EyePACS datasets, which provided effective solutions in terms of accuracy. Nonetheless, it encountered issues related to high running time and computational costs.

## 3. PROPOSED METHODOLOGY

This research proposes a CAM-based CNN with LReLU for early and accurate DR detection. The MESSIDOR dataset used comprises 1800 fundus images with five classes. The preprocessing is done using a median filter to eliminate noise, and CLAHE is used to enhance the contrast level in an input image. The preprocessed images are fed to MOARG for image segmentation. Then, the features are extracted using ResNet50 and SqueezeNet, which extract deep learning features. The extracted features are given to CAM-based CNN with LReLU for detection and classification. It overcomes neuron death issues by allowing negative values for certain neurons and reducing the likelihood of inactive neurons. Figure 1 illustrates the process of the proposed methodology.

https://doi.org/10.31436/iiumej.v26i1.3194

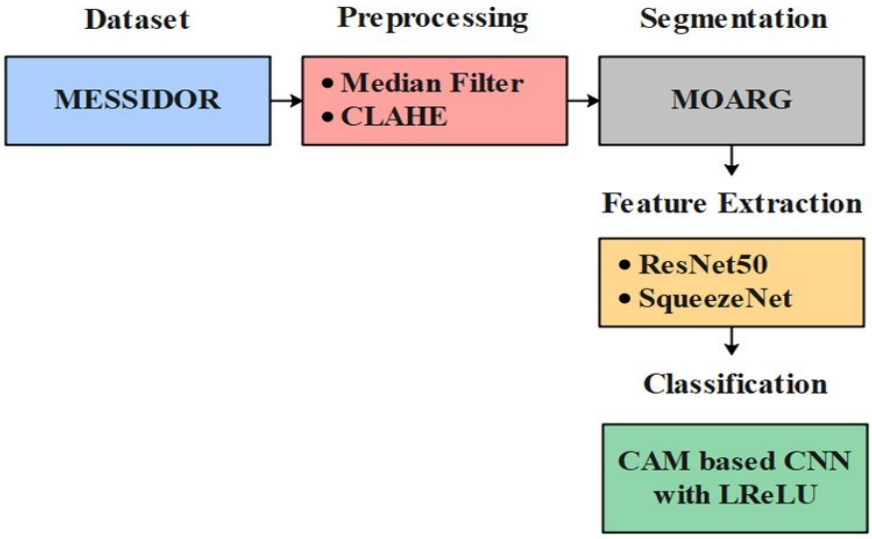


Figure 1. Process of the proposed methodology

### 3.1. Dataset

The dataset utilized in this manuscript is the MESSIDOR dataset [25], which consists of 1800 fundus images categorized into five different classes. Each class contains 360 images, and all images have been cropped and resized to 300×300. The classes of the dataset are listed below, and sample images are shown in Figure 2.

0: No DR

1: Mild Non-Proliferative DR (NPDR)

2: Moderate NPDR

3: Severe NPDR

4: Proliferative DR

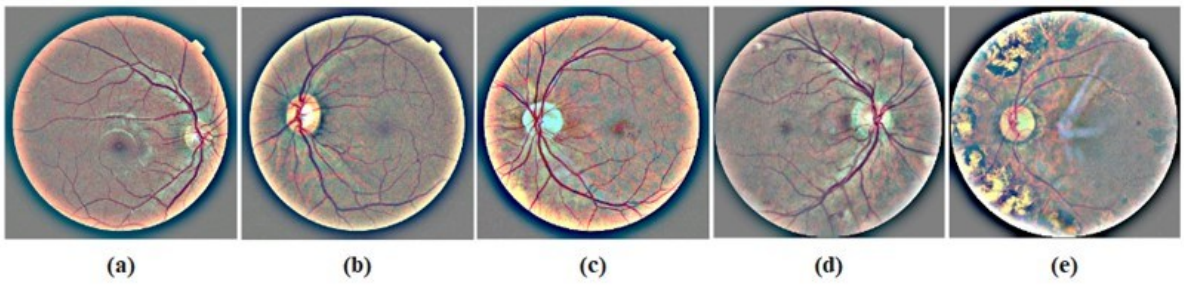


Figure 2. Dataset sample images (a) No DR (b) Mild NPDR (c) Moderate NPDR (d) Severe NPDR (e) Proliferative DR

### 3.2. Preprocessing

Preprocessing is a crucial phase in image processing because it improves the quality of the images from the MESSIDOR dataset. The median filter and CLAHE are applied to preprocess the MESSIDOR dataset. The median filter is applied to remove noise by replacing every pixel value with median intensity values in the adjacent pixels. The CLAHE is utilized to enhance the visibility of the retinal feature to improve the important regions for segmentation and feature extraction.

https://doi.org/10.31436/iiumej.v26i1.3194

### *3.2.1. Median Filter*

The MESSIDOR dataset is preprocessed using a median filter, which removes noise in the MESSIDOR dataset. It is processed through shifting image pixels, adapting each score by the median value of the nearest pixel. The pixel is calculated by separating the entire pixel values from the nearest patterns in an arithmetic way and adapting the pixel measured as the average pixel value. It eliminates noise without minimizing image sharpness, and the mathematical formula is presented in Eq. (1).

$$\hat{f}(x,y) = median\{g(s,t)\},\ where\ (s,t) \in S_{xy} \tag{1}$$

where, $S_{xy}$ denotes the coordinate groups in a rectangular image window, which has a center at $(x,y)$. The $\hat{f}(x,y)$ is the reestablished image and $g(s,t)$ is estimated and corrupted region in $S_{xy}$. A median filter removes noise from an input image, which replaces each pixel with a median value in its local adjacent area.

### *3.2.2. CLAHE*

The CLAHE is utilized to increase the contrast level, and the histogram of the resultant image is estimated based on the local window placed on every pixel in an adjacent region. Then, it is fixed through the limit value, and the region is mapped. However, reducing the number of histogram bars is unable to create a substantial variance, which results in pixels in the intermediate histogram and diminishing contrast among tissues—the output image after CLAHE is presented in Eq. (2).

$$CL = fZ_m(x,y) | \forall Z_m(x,y) \in Z_m \tag{2}$$

where, $(x,y)$ represents the coordination of image pixels, $fZ_m$ represents a transformation function based on density. By utilizing CLAHE, the contrast level is enhanced in an input image, helping to avoid saturation and clipping issues, which improves the image visibility without significantly amplifying noise. The preprocessed images are given as input to the segmentation process. The preprocessed (CLAHE) sample images are presented in Figure 3.

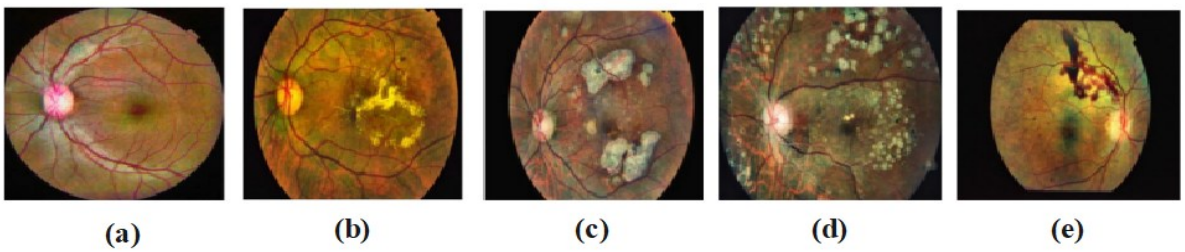


Figure 3. Preprocessed (CLAHE) sample images (a) No DR (b) Mild NPDR (c) Moderate NPDR (d) Severe NPDR (e) Proliferative DR

### 3.3. Segmentation

The preprocessed images are given as input to the Mayfly Optimization Algorithm-based Region Growing (MOARG) for image segmentation. Segmentation is identifying the particular region or structures in a fundus image. The optimization helps adjust the model's parameters to align with image features, which reduces communication and computational complexity. The RG is a pixel-based segmentation comprising similarity restrictions of intensity and texture, which are utilized to integrate pixels into the region. Primarily, the groups of pixels are incorporated with the assistance of iterations, and then the seed pixel is selected with regions. The group is carried out by incorporating equivalent, adjacent pixels to enhance the region size.

https://doi.org/10.31436/iiumej.v26i1.3194

The RG is completed if the adjacent pixel does not satisfy the similarity restriction and selects the other seed pixels. This process is repeated unless every pixel in an image corresponds to specific regions. The threshold and seed point selection are considered in this paper due to the increased segmentation accuracy. The MOARG is used for segmentation, utilizing the global search capability of the MOA to adapt complex shapes in the retinal images, including lesions, abnormal regions, and blood vessels. It ensures that this process is proficient and precise in dealing with complex variations in retinal structures essential for accurate DR detection. The process of region growth is presented as follows:

1. Provide the abnormal image as input.
2. Consider $t$ as an optimum threshold produced through MOA.
3. Consider $t$ as a seed point for the RG approach.
4. Include 4 adjacent pixels.
5. Evaluate the distance among adjacent pixels and the average region intensity.
6. Compute RG if $d \leq t$ on 4 neighboring pixels and save a coordinate point of new pixels.
7. Novel region mean is stored and returned to step 2 and RG is repeated until each pixel is integrated.

The MOA is a meta-heuristic optimization algorithm [26] for resolving difficult nonlinear issues that are motivated by the behavior of mayflies. The MOA location in 2D search space is defined by $a = (a_1, \dots, a_d)^T$ and $b = (b_1, \dots, b_d)^T$ respectively, and the velocity of $v = (v_1, \dots, v_d)^T$ is assigned to each mayfly. In each repetition, it maintains the global position ($gbest$) and best personal ($pbest$). The mayfly search is based on two populations, considering their position and speed with respect to specific rules. The male individual's speed and position are mathematically presented in Eq. (3) and (4).

$$x_i^{t+1} = x_i^t + v_i^{t+1} \tag{3}$$

$$v_i^{t+1} = v_i^t + a_1 e^{-\beta r_p^2}(pbest_i - x_i^t) + a_2 e^{-\beta r_g^2}(gbest - x_i^t) \tag{4}$$

where, $x_i^t$ and $v_i^t$ are the respective position and speed of $i$th the mayfly at $k$th iteration, $pbest_i$ is the best position of $i$th mayfly reached, and $a_2$ are coefficients of positive attractions and $r_p$ is the Cartesian distance between mayfly and individuals' optimum positions. The female flies to the male for breeding to facilitate the mating approach, while the female is attracted to the male. The female mayflies and position are described in Eq. (5), (6), and (7).

$$v_i^{t+1} = v_i^t + a_2 e^{-\beta r_{mf}^2}(x_i^t - y_i^t),\ f(y_i) > f(x_i) \tag{5}$$

$$v_i^{t+1} = v_i^t = fl \times r,\ f(y_i) \leq f(x_i) \tag{6}$$

$$y_i^{t+1} = y_i^t + v_i^{t+1} \tag{7}$$

where, $v_i^t$ and $y_i^t$ are the speed and position of $i$th female mayfly at $k$th iteration, $r_{mf}$ is the speed of a female from a male mayfly, and $fl$ is a coefficient for random movement. Based on the above rule, the crossover is influenced by two population locations. The crossover is illustrated in Eq. (8) and (9).

$$offspring\ 1 = L \times male + (1 - L) \times female \tag{8}$$

$$offspring\ 2 = L \times female + (1 - L) \times male \tag{9}$$

https://doi.org/10.31436/iiumej.v26i1.3194

where, $offspring$ is an individual's offspring mayfly, $L$ is a random value in a particular range, $male$ and $female$ is an individual male and female mayfly. Based on population size, if the new generation obtains the best fitness value, it will replace the respective variable of the previous generation. Otherwise, the previous generation will remain unchanged. At this stage, the objective function $f(x)$ is utilized to estimate and select the target population. Integrating MOA with RG explores the global search spaces that adapt to complex shapes in the segmentation process.

### 3.4. Feature Extraction

After segmentation, features are extracted using ResNet50 and SqueezeNet. By using this technique, the MESSIDOR dataset is much more informative. The ResNet50 extracts high-level features from the segmented regions to capture the significant patterns based on the abnormal blood vessels and lesions. The SqueezeNet focuses on low-level features, such as textures and edges in early layers, and higher-level features like patterns in deeper layers. Using both ResNet50 and SqueezeNet provides the corresponding set of deep features, thereby enhancing the overall feature extraction performance.

#### *3.4.1. ResNet50-based Feature Extraction*

ResNet50 has a residual block to resolve CNN's vanishing gradient and degradation issues. It can produce better classification results, and the residual function is given in Eq. (10).

$$y = F(x, W) + x \tag{10}$$

Here, $x$, $y$, and $W$ are residual block input, output, and weight. It has different residual blocks in the different convolution layer filter sizes.

#### *3.4.2. SqueezeNet-based Feature Extraction*

SqueezeNet comprises fire modules containing squeeze and expand layers 1 convolutional (conv) layer, 8 fire modules, and 3 max-pooling layers. This layer has $1 \times 1$ conv and expand layers comprising an integration of $1 \times 1$ and $3 \times 3$ conv. In the expanded layer, the feature map of conv outputs is integrated into the channel of the fire module. The number of conv filters in the squeeze and expand layer is presented in Eq. (11).

$$X < Y_1 + Y_2 \tag{11}$$

where $X$ is the number of 1×1 conv filters in the squeeze layer, and $Y_1$ and $Y_2$ are the number of 1×1 and 3×3 conv filters in the expand layer. Figure 4 represents the architecture of feature extraction methods. In the framework of detecting and classifying retinopathy diseases, SqueezeNet's approach captures significant low-level features like edges and textures to determine the fine-grained information in retinal images. This low-level information contains microaneurysms and vascular structures, which provide accurate diagnoses. While ResNet50 effectively captures high-level features, its deeper layers generate finer information because of the abstraction process. Even ResNet50 also extracts low-level features, but SqueezeNet is applied to obtain comparable accuracy with fewer parameters and smaller model sizes, making extraction effective. This hierarchical approach enables SqueezeNet to manage the fine-grained information, whereas ResNet50 increases the representation by focusing on high-level patterns. This approach ensures that no primary low-level characteristics are missed, enhancing classification performance in retinopathy detection. Therefore, combining each network utilizes a complementary benefit for a further process. The ResNet and SqueezeNet is combined by concatenating the extracted feature maps (2048 from ResNet50 and 1024 from SqueezeNet) into a unified feature vector. The final layer of ResNet50/SqueezeNet is Global

https://doi.org/10.31436/iiumej.v26i1.3194

Average Pooling (GAP). Overall, the output extracted no. of features is $N \times 3072$, which are fed as input to the classification process, where $N$ is represented as the number of samples.

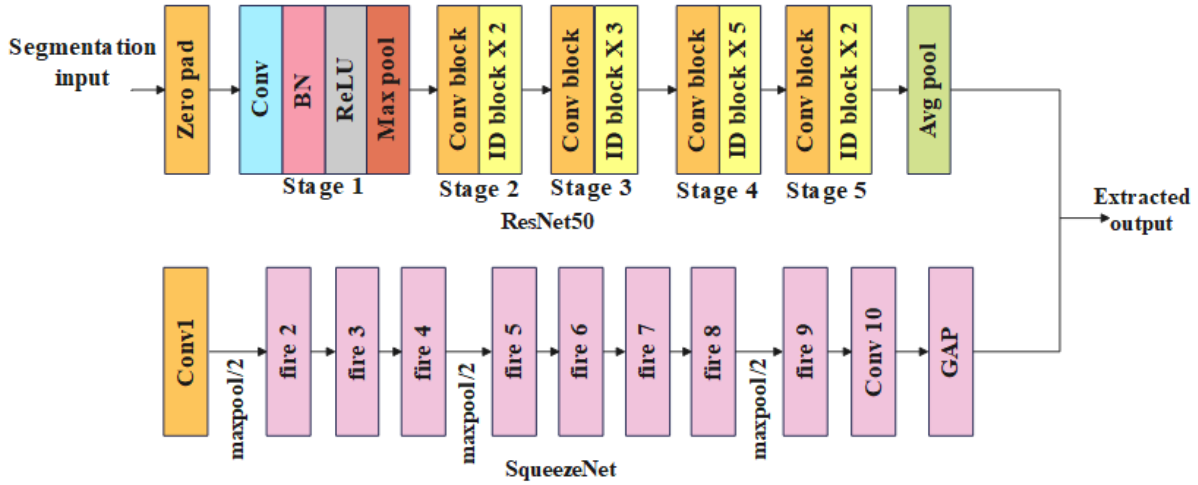


Figure 4. Architecture of feature extraction methods

### 3.5. Classification

The extracted features are classified through CAM-based CNN with LReLU, which is utilized to improve the model's capability to learn spatial relationships and focus on relevant features in an image. The CAM helps visualize the input image regions to highlight the important retinal regions, which further denotes that the DR helps enhance performance and interpretability. The LReLU addresses the issue of dead neurons in traditional ReLU by introducing a small negative slope for negative input scores. It allows neurons to stay active even when receiving negative inputs. It reduces inactive neuron issues and ensures the model learns efficiently, enhancing overall performance in DR detection. CNN is utilized to classify and identify large amounts of data. The advantage of CNN is that it automatically extracts and learns features from the training images, although existing techniques require manual feature extraction. The CNN contains 3 different conv, pooling, and Fully Connected (FC) layers. The conv is the initial and main element of CNN, extracting features from the input and containing fewer arrays named filters, which are used throughout the input and produce outputs of the feature maps. Different conv kernels are applied to extract various features. Numerous conv layers are based on the input image size. Then, pooling is used to reduce the dimension of the conv feature map. It produces down-sampling operations by reducing feature maps, which reduces computational complexity. Different pooling operations, such as max, min, and average pooling, are employed. The feature map outputs of the conv or pooling layer are altered to a 1D vector in which every input is combined through each result with weights and is named a dense layer. Lastly, it has FC layers; the last FC layer comprises an output number equivalent to many classes. The CNN approach employs the LeakyReLU activation function in all layers after convolution. The LeakyReLU's slope parameter is represented as $\alpha$ which manages the negative slope and has a default value of 0.01.

#### *3.5.1. Coordinate Attention Module*

The attention mechanism in deep neural networks (DNN) focuses on relevant elements and removes irrelevant ones. The Coordinate Attention Module (CAM) is an efficient attention module that can be easily integrated into DNN [27]. It supports maximizing the feature extraction ability without incurring significant computational overhead. It uses an efficient

https://doi.org/10.31436/iiumej.v26i1.3194

technique for obtaining data location and channel for better feature extraction. Figure 5 presents the structure of CAM.

The CAM input is represented as $C \times H \times W$, where $C$ is an input channel, $H$ and $W$ are the feature map's height and width. The CAM process is formulated below:

- The CAM festers 2D to dual 1D global pooling operations horizontally and perpendicularly. The 1D pooling operation outputs are $C \times 1 \times W$ and $C \times H \times 1$, correspondingly.
- Results of dual 1D pooling are integrated and managed to utilize $1 \times 1$ conv, batch norm, and non-linear layer. The output is $C/r \times 1 \times (W + H)$, here $r$ is a compression ratio.
- The previous stage output is separated into dual sets ($C \times 1 \times W$ *and* $C \times H \times 1$), which are calculated to achieve weight in the horizontal and perpendicular ways.
- Lastly, input feature $C \times H \times W$ is reevaluated through the third stage results.

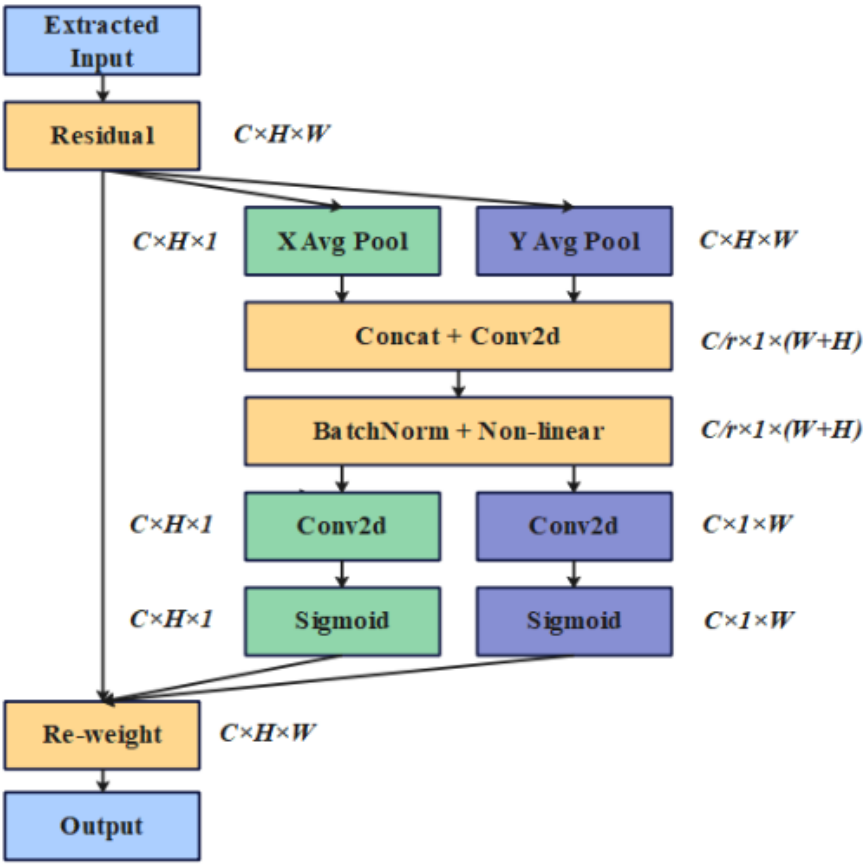


Figure 5. Structure of CAM

Assume the input of CAM is a vector presented in Eq. (12).

$$X = [x_1, x_2, \dots, x_c] \in R^{C \times H \times W} \tag{12}$$

It is calculated through dual 1D pooling in the horizontal and vertical ways. The channel $c$ result at height $h$ is presented in Eq. (13).

$$z_c^h(h) = \frac{1}{W} \sum_{0 \le i \le W} x_c(h, i) \tag{13}$$

https://doi.org/10.31436/iiumej.v26i1.3194

The channel $c$ result at width $w$ is presented in Eq. (14).

$$z_c^w(w) = \frac{1}{H}\sum_{0\le i\le H} x_c(j,w) \tag{14}$$

After producing feature maps, the concatenation operation is accomplished on a spatial dimension, and feature maps are integrated to $1 \times 1$ conv alteration function $F_1$ is presented in Eq. (15).

$$f = \delta\left(F_1(z^h, z^w)\right) \tag{15}$$

where, $[.,.]$ is an addition operation through geometric dimension, $\delta$ denotes non-linear activation function, $f \in R^{C/r\times(H+W)}$ presents the separating of feature map that encodes geometric data in vertical and horizontal directions and $r$ is the reduction ratio to manage the block size. The $f$ separates the geometric dimension into dual different tensors $f \in R^{C/r\times H}$ and $f \in R^{C/r\times W}$. The remaining two $1 \times 1$ conv alteration functions $F_h$ $and$ $F_w$ are applied to separate transform $f^h$ and $f^w$ into tensors by the same input channel $X$, as is presented in Eq. (16) and (17).

$$g^h = \delta\left(F_h(f^h)\right) \tag{16}$$

$$g^w = \delta\left(F_w(f^w)\right) \tag{17}$$

The results of $g^h$ and $g^w$ in 2D are extended and utilized as attention weights. The result of CAM is presented in Eq. (18).

$$y_c(i,j) = x_c(i,j) \times g_c^h(i) \times g_c^w(j) \tag{18}$$

where, $y_c$ is the output of the CAM module, and the weights of $g^h$ and $g^w$ in 2D are fused with the input $X$ to obtain the coordinate attention module output. Integrating CNN with CAM improves the model's capability to learn spatial relationships and focus on relevant features in an image.

### *3.5.2. Leaky Rectified Linear Unit*

The drawbacks of ReLU and other activation functions lead to neuron death, vanishing gradient, and output offset. To overcome these issues, this paper proposes an LReLU that is a non-monotonic constant function that preserves an equal binary format. LReLU is used to reduce the dead neuron problem that occurs with ReLU, and LReLU also provides a smoother gradient flow for negative inputs. It contributes to increased model stability for retinopathy detection and classification in this research. The nature of activation functions is a bivariate function $b(x, g(x))$, where, $x$ is an unfiltered pre-activation given as input to the final bivariate function, which is numerically presented in Eq. (19).

$$f(x) = \begin{cases} x & x \ge 0 \\ \alpha \times x \times \sigma(x) & x < 0 \end{cases} \tag{19}$$

where $\sigma(x)$ is a sigmoid function that is equivalent to $\frac{1}{1+e^{-x}}$ and $\alpha$ is a hyperparameter within the range of [0.1, 1]. As an output, the LReLU resolves the problems of non-zero gradients and saturation to speed up the learning procedure. The absence of a sigmoid function minimizes the power operations, which leads to faster processing. The Leaky approach makes the negative function area adaptable through a single input. The LReLU delivers a negative bump for small inputs that resolve the neuron death issues. The LReLU derivative function is presented in Eq. (20).

https://doi.org/10.31436/iiumej.v26i1.3194

$$f'(x) = \begin{cases} 1 & x \geq 0 \\ \alpha\left[\frac{1}{1+e^{-x}} + \frac{xe^{-x}}{(1+e^{-x})^2}\right] & x < 0 \end{cases} \quad (20)$$

where, $\alpha$ manages the depth of the negative dump for non-zero inputs, whereas the derivative is one in a positive region. The negative region is a combination of two functions, requiring a partial derivative to attain a gradient during backpropagation. By utilizing LReLU, the neuron death, vanishing gradient, and output offset are addressed, leading to early and accurate DR detection.

## 4. EXPERIMENTAL RESULT

The CAM-based CNN with LReLU is implemented in Python with the following configuration: Intel Core i7 processor, 16 GB RAM, and Windows 10 OS. The metrics, including accuracy, precision, recall, specificity, f1-score, AUC, Dice Score Coefficient (DSC), Intersection-Over-Union (IoU), Structural Similarity Index (SSIM), and Mean IoU (MIoU), are considered to calculate CAM-based CNN with LReLU, as shown mathematically in Eqs. (21)-(30).

$$Accuracy = \frac{TP+TN}{TP+TN+FP+FN} \quad (21)$$

$$Precision = \frac{TP}{TP+FP} \quad (22)$$

$$Recall = \frac{TP}{TP+FN} \quad (23)$$

$$Specificity = \frac{TN}{TN+FP} \quad (24)$$

$$F1-score = 2 \times \frac{Precision \times recall}{Precision+recall} \quad (25)$$

$$AUC = \frac{\sum R_i(I_I) - I_I(I_I+I)/2}{I_I+I_f} \quad (26)$$

$$DSC = \frac{2 \times TP}{(TP+FP)+(TP+FN)} \quad (27)$$

$$IoU = \frac{TP}{TP+FP+FN} \quad (28)$$

$$SSIM = \frac{(2\mu_x\mu_y+c_1)(2\sigma_{xy}+c_2)}{(\mu_x^2+\mu_y^2+c_1)(\sigma_x^2+\sigma_y^2+c_2)} \quad (29)$$

$$MIOU = \frac{1}{k+1}\sum_{i=0}^{k} \frac{TP}{FN+FP+TP} \quad (30)$$

where, $R_i$ is the rate of $i$th image, $I_I$ and $I_f$ is the number of positive and negative images, $\mu_x$ and $\mu_y$ are the average values of $x$ and $y$, $\sigma_x^2$ and $\sigma_y^2$ are the variances of $x$ and $y$, $\sigma_{xy}$ is the covariance of $x$ and $y$, $TP$, $TN$, $FP$ and $FN$ are the True Positive, True Negative, False Positive and False Negative values, correspondingly.

### 4.1. Quantitative and Qualitative Analysis

The quantitative and qualitative analysis of CAM-based CNN with LReLU is given in this section based on accuracy, precision, recall, specificity, F1-score, and AUC. The Long-Short Term Memory (LSTM) needs higher training data and is slowly trained on large datasets. The Recurrent Neural Network (RNN) cannot handle huge amounts of data due to the vanishing gradient issue. The proposed CAM-based CNN with LReLU overcomes the problem of neuron

https://doi.org/10.31436/iiumej.v26i1.3194

death by allowing negative values for some neurons and minimizing the probability of inactive neurons.

Table 1. Performance of segmentation

| Method | DSC | IoU | SSIM | MIOU |
|---|---|---|---|---|
| WOA | 0.9079 | 0.9062 | 0.9068 | 0.9071 |
| GOA | 0.9261 | 0.9258 | 0.9247 | 0.9253 |
| MOA | 0.9358 | 0.9347 | 0.9353 | 0.9341 |
| **MOARG** | **0.9574** | **0.9566** | **0.9571** | **0.9559** |

Figure 6. Performance of segmentation

Table 1 and Figure 6 present the performance of MOARG on the MESSIDOR dataset. The performance of the Whale Optimization Algorithm (WOA), Grasshopper Optimization Algorithm (GOA), and MOA are evaluated and compared with MOARG. The results indicate that MOARG achieves better results by utilizing DSC, IoU, SSIM, and MIOU, with respective values of 0.9574, 0.9566, 0.9571, and 0.9559, which is superior to the existing techniques.

Table 2. Performance of optimization in segmentation

| Method | DSC | IoU | SSIM | MIOU |
|---|---|---|---|---|
| CSO | 0.8964 | 0.8953 | 0.8949 | 0.8926 |
| WOA | 0.9079 | 0.9062 | 0.9068 | 0.9071 |
| GOA | 0.9261 | 0.9258 | 0.9247 | 0.9253 |
| **MOA** | **0.9358** | **0.9347** | **0.9352** | **0.9341** |

https://doi.org/10.31436/iiumej.v26i1.3194

Figure 7. Performance of optimization in segmentation

Table 2 and Figure 7 present the performance of MOA in segmentation on the MESSIDOR dataset. The performance of Cat Swarm Optimization (CSO), WOA, and GOA is measured and compared with MOA. The obtained results prove that MOA achieves superior outcomes by utilizing DSC, IoU, SSIM, and MIOU with respective values of 0.9358, 0.9347, 0.9352, and 0.9341, thereby yielding higher results compared to existing techniques.

Table 3. Performance of feature extraction

| Method | Accuracy (%) | Precision (%) | Recall (%) | Specificity (%) | F1-score (%) | AUC (%) |
|---|---|---|---|---|---|---|
| ResNet18 | 91.82 | 91.66 | 91.74 | 91.61 | 91.55 | 91.47 |
| ResNet50 | 93.68 | 93.54 | 93.65 | 93.59 | 93.46 | 93.38 |
| SqueezeNet | 94.73 | 94.61 | 94.68 | 94.62 | 94.58 | 94.51 |
| **ResNet50+ SqueezeNet** | **96.56** | **96.48** | **96.51** | **96.43** | **96.37** | **96.33** |

Figure 8. Performance of feature extraction

https://doi.org/10.31436/iiumej.v26i1.3194

Table 3 and Figure 8 display the outcomes of ResNet50+SqueezeNet on the MESSIDOR dataset. ResNet18, ResNet50, and SqueezeNet are measured and matched with ResNet50+SqueezeNet. The outcomes demonstrate the ResNet50+SqueezeNet's commendable performance in terms of accuracy, precision, recall, specificity, f1-score, and AUC, with values of 96.56%, 96.48%, 96.51%, 96.43%, 96.37%, and 96.33%, surpassing the previous techniques.

Table 4. Performance of activation functions

| Method | Accuracy (%) | Precision (%) | Recall (%) | Specificity (%) | F1-score (%) | AUC (%) |
|---|---|---|---|---|---|---|
| ReLU | 94.57 | 94.43 | 94.51 | 94.39 | 94.35 | 94.27 |
| PReLU | 95.83 | 95.62 | 95.78 | 95.56 | 95.43 | 95.38 |
| SGReLU | 97.76 | 97.48 | 97.63 | 97.51 | 97.25 | 97.29 |
| **LReLU** | **98.69** | **98.51** | **98.55** | **98.42** | **98.36** | **98.31** |

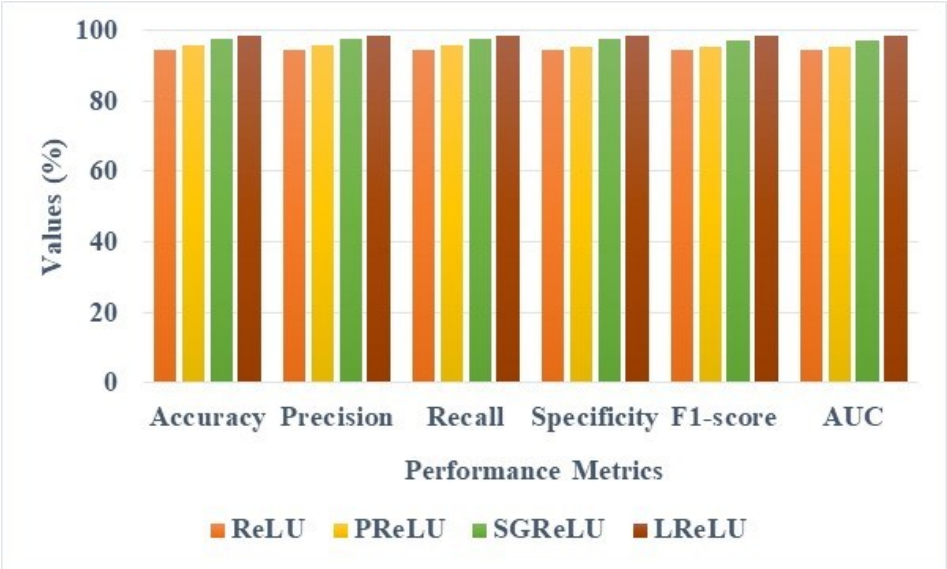


Figure 9. Performance of activation functions

Table 4 and Figure 9 showcase the performance of LReLU on the MESSIDOR dataset. ReLU, PReLU, and SGReLU are measured and matched against LReLU. The results indicate that LReLU outperforms with a commendable display of findings with 98.69% accuracy, 98.51% precision, 98.55% recall, 98.42% specificity, 98.36% f1-score, and 98.31% AUC value. This exemplifies the exceptional performance of the proposed method.

Table 5. Performance of classification

| Method | Accuracy (%) | Precision (%) | Recall (%) | Specificity (%) | F1-score (%) | AUC (%) |
|---|---|---|---|---|---|---|
| LSTM | 93.55 | 93.48 | 93.37 | 93.51 | 93.24 | 95.08 |
| RNN | 95.89 | 95.61 | 95.56 | 95.62 | 95.16 | 95.36 |
| CNN | 97.68 | 97.24 | 97.13 | 97.54 | 97.45 | 97.21 |
| **CAM based CNN with LReLU** | **99.72** | **99.46** | **99.25** | **99.61** | **99.37** | **99.14** |

https://doi.org/10.31436/iiumej.v26i1.3194

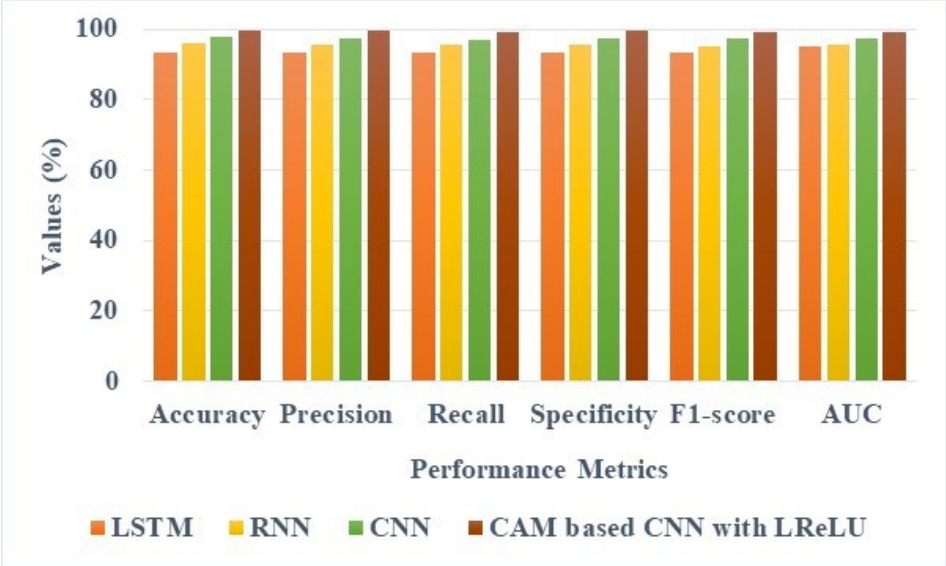


Figure 10. Performance of classification

Table 5 and Figure 10 reveal the performance of the proposed CAM-based CNN with LReLU on the MESSIDOR dataset. The LReLU activation function with LSTM, RNN, and CNN is utilized, and their performance is measured and compared with CAM-based CNN with LReLU. The obtained result speaks for the CAM-based CNN with LReLU's exemplary outcomes in terms of accuracy, precision, recall, specificity, f1-score, and AUC values of about 99.72%, 99.46%, 99.25%, 99.61%, 99.37%, and 99.14%, respectively, and in doing so, eclipses the previous methods.

### 4.2. Comparative Analysis

A comparative analysis of CAM-based CNN with LReLU performance based on six metrics is shown in Table 6. Existing techniques such as ICOA-DLDRD [17], IoTDL-DRD [18], CapsNet [19], SCL [20], and RNN-LSTM [21] are used to evaluate the classifier capability. The CAM-based CNN with LReLU is trained, tested, and validated on the MESSIDOR dataset. The obtained outcomes imply that CAM-based CNN with LReLU achieves superior results in terms of accuracy, precision, recall, specificity, f1-score, and AUC values of about 99.72%, 99.46%, 99.25%, 99.61%, 99.37%, and 99.14%, respectively, which takes over the other classifiers.

Table 6. Comparative Analysis Using the MESSIDOR Dataset

| Method | Accuracy (%) | Precision (%) | Recall (%) | Specificity (%) | F1-score (%) | AUC (%) |
|---|---|---|---|---|---|---|
| ICOA-DLDRD [17] | 99.65 | 99.18 | 99.01 | 99.76 | N/A | N/A |
| IoTDL-DRD [18] | 99.08 | N/A | 94.28 | 99.34 | N/A | 94.84 |
| CapsNet [19] | 97.65 | 97.54 | 94.18 | N/A | 95.85 | N/A |
| SCL [20] | 80.52 | 77.64 | 93.63 | N/A | 84.89 | 84.60 |
| RNN-LSTM [21] | 98.29 | 96.45 | 95.78 | 94.03 | N/A | 97.37 |
| **Proposed CAM-based CNN with LReLU** | **99.72** | **99.46** | **99.25** | **99.61** | **99.37** | **99.14** |

### 4.3. Discussion

This section discusses the advantages of CAM-based CNN with LReLU and the drawbacks of existing methods. The ICOA-DLDRD [17] requires highly labeled data, which consumes more time for training. The IoTDL-DRD [18] was not adapted to manage long-term dependencies and sequential input data. The CapsNet [19] could not manage complex data because of a vanishing gradient issue. The SCL [20] was sensitive to noisy data and tried to identify the optimum hyperplane. The RNN-LSTM [21] was computationally exhaustive and struggled with noisy data. The proposed CAM-based CNN with LReLU overcomes these existing models' limitations, including dead neurons, vanishing gradient, output offset issues, and the probability of inactive neurons. The MOARG enhances segmentation accuracy by exploring the global search space and adopting complex shapes, resulting in a more prominent segmentation performance than traditional algorithms, namely CSO, WOA, and GOA. The CAM-based CNN with LReLU model performs commendably, outperforming the other techniques with improved accuracy, precision, recall, specificity, F1-score, and AUC values of about 99.72%, 99.46%, 99.25%, 99.61%, 99.37%, and 99.14%. These values are superior to the existing models, namely ICOA-DLDRD [17], IoTDL-DRD [18], CapsNet [19], SCL [20], and RNN-LSTM [21], as shown in Table 6. This display of conduct deduces its capability to generate accurate and reliable DR detection and classification.

## 5. CONCLUSION

This research proposes a CAM-based CNN with LReLU for early and accurate detection of Diabetic Retinopathy. The MESSIDOR dataset is preprocessed through the median filter to remove noise, while CLAHE is deployed to increase the contrast level in an input image. The preprocessed images are given as input to the MOARG for image segmentation. Then, the features are extracted using ResNet50 and SqueezeNet, which extract deep learning features. The extracted features are provided to CAM-based CNN with LReLU for the detection and classification of Diabetic Retinopathy. It overcomes the issue of dead neurons by allowing negative values for some neurons and minimizing the probability of inactive neurons. The CAM-based CNN with LReLU obtains commendable findings on the MESSIDOR dataset in terms of metrics of respective accuracy, precision, recall, specificity, F1-score, and AUC values of about 99.72%, 99.46%, 99.25%, 99.61%, 99.37%, and 99.14%. This delivery of such outputs confirms the high-quality, superior capabilities of the suggested method over the existing methods. In the future, hyperparameter tuning will further enhance Diabetic Retinopathy performance.

## REFERENCES

[1] Özbay E. (2023) An active deep learning method for diabetic retinopathy detection in segmented fundus images using artificial bee colony algorithm. Artif. Intell. Rev., 56:3291-3318. https://doi.org/10.1007/s10462-022-10231-3

[2] Raiaan MAK, Fatema K, Khan IU, Azam S, ur Rashid MR, Mukta MSH, Jonkman M, De Boer F. (2023) A Lightweight Robust Deep Learning Model Gained High Accuracy in Classifying a Wide Range of Diabetic Retinopathy Images. IEEE Access, 11:2169-3536. https://doi.org/10.1109/ACCESS.2023.3272228

[3] Usman TM, Saheed YK, Ignace D, Nsang A. (2023) Diabetic retinopathy detection using principal component analysis multi-label feature extraction and classification. Int. J. Cognit. Comput. Eng., 4:78-88. https://doi.org/10.1016/j.ijcce.2023.02.002

[4] Erciyas A, Barışçı N, Ünver HM, Polat H. (2023) Improving detection and classification of diabetic retinopathy using CUDA and Mask RCNN. Signal, Image Video Process., 17(4):1265-1273. https://doi.org/10.1007/s11760-022-02334-9

[5] Luo X, Wang W, Xu Y, Lai Z, Jin X, Zhang B, Zhang D. (2024) A deep convolutional neural network for diabetic retinopathy detection via mining local and long-range dependence. CAAI Trans. Intell. Technol., 9(1):153-166. https://doi.org/10.1049/cit2.12155
[6] Feng M, Wang J, Wen K, Sun J. (2023) Grading of Diabetic Retinopathy Images Based on Graph Neural Network. IEEE Access, 11:98391-98401. http://dx.doi.org/10.1109/ACCESS.2023.3312709
[7] Saranya P, Umamaheswari KM. (2024) Detection of exudates from retinal images for non-proliferative diabetic retinopathy detection using deep learning model. Multimedia Tools Appl., 83(17), pages 52253-52273. https://doi.org/10.1007/s11042-023-17462-8
[8] Fatima, Imran M, Ullah A, Arif M, Noor R. (2022) A unified technique for entropy enhancement based diabetic retinopathy detection using hybrid neural network. Comput. Biol. Med., 145:105424. https://doi.org/10.1016/j.compbiomed.2022.105424
[9] Nanda P, Duraipandian N. (2022) A Novel Optimizer in Deep Neural Network for Diabetic Retinopathy Classification. Computer Systems Science & Engineering, 43(3), 1099-1110. DOI: 10.32604/csse.2022.024695
[10] Kasim Ö. (2023) Ensemble classification based optimized transfer learning feature method for early stage diagnosis of diabetic retinopathy. J. Ambient Intell. Hum. Comput., 14(8):11337-11348. https://doi.org/10.1007/s12652-023-04648-z
[11] Rachapudi V, Rao KS, Rao TSM, Dileep P, Roy TLD. (2023) Diabetic retinopathy detection by optimized deep learning model. Multimedia Tools Appl., 82(18):27949-27971. https://doi.org/10.1007/s11042-023-14606-8
[12] Butt MM, Iskandar DNFA, Abdelhamid SE, Latif G, Alghazo R. (2022) Diabetic Retinopathy Detection from Fundus Images of the Eye Using Hybrid Deep Learning Features. Diagnostics, 12(7):1607. https://doi.org/10.3390/diagnostics12071607
[13] Mustafa H, Ali SF, Bilal M, Hanif MS. (2022) Multi-stream deep neural network for diabetic retinopathy severity classification under a boosting framework. IEEE Access, 10:113172-113183. https://doi.org/10.1109/ACCESS.2022.3217216
[14] Vinayaki VD, Kalaiselvi R. (2022) Multithreshold image segmentation technique using remora optimization algorithm for diabetic retinopathy detection from fundus images. Neural Process. Lett., 54:2363-2384. https://doi.org/10.1007/s11063-021-10734-0
[15] Murugappan M, Prakash NB, Jeya R, Mohanarathinam A, Hemalakshmi GR, Mahmud M. (2022) A novel few-shot classification framework for diabetic retinopathy detection and grading. Measurement, 200:111485. https://doi.org/10.1016/j.measurement.2022.111485
[16] Jagadesh BN, Karthik MG, Siri D, Shareef SKK, Mantena SV, Vatambeti R. (2023) Segmentation Using the IC2T Model and Classification of Diabetic Retinopathy Using the Rock Hyrax Swarm-Based Coordination Attention Mechanism. IEEE Access, 11:124441-124458. https://doi.org/10.1109/ACCESS.2023.3330436
[17] Parthiban K, Kamarasan M. (2023) Diabetic retinopathy detection and grading of retinal fundus images using coyote optimization algorithm with deep learning. Multimedia Tools Appl., 82(12):18947-18966. https://doi.org/10.1007/s11042-022-14234-8
[18] Palaniswamy T, Vellingiri M. (2023) Internet of Things and Deep Learning Enabled Diabetic Retinopathy Diagnosis Using Retinal Fundus Images. IEEE Access, 11:27590-27601. https://doi.org/10.1109/ACCESS.2023.3257988
[19] Kalyani G, Janakiramaiah B, Karuna A, Prasad LVN. (2023) Diabetic retinopathy detection and classification using capsule networks. Complex Intell. Syst., 9(3):2651-2664. https://doi.org/10.1007/s40747-021-00318-9
[20] Islam MR, Abdulrazak LF, Nahiduzzaman M, Goni MOF, Anower MS, Ahsan M, Haider J, Kowalski M. (2022) Applying supervised contrastive learning for the detection of diabetic retinopathy and its severity levels from fundus images. Comput. Biol. Med., 146:105602. https://doi.org/10.1016/j.compbiomed.2022.105602
[21] Hemanth SV, Alagarsamy S. (2023) Hybrid adaptive deep learning classifier for early detection of diabetic retinopathy using optimal feature extraction and classification. J. Diabetes Metab. Disord., 22(1):881-895. https://doi.org/10.1007/s40200-023-01220-6
[22] Das S, Saha SK. (2022) Diabetic retinopathy detection and classification using CNN tuned by

genetic algorithm. Multimedia Tools Appl., 81(6):8007-8020. https://doi.org/10.1007/s11042-021-11824-w

[23] Zhang G, Sun B, Chen Z, Gao Y, Zhang Z, Li K, Yang W. (2022) Diabetic retinopathy grading by deep graph correlation network on retinal images without manual annotations. Front. Med., 9:872214. https://doi.org/10.3389/fmed.2022.872214

[24] Abbood SH, Hamed HNA, Rahim MSM, Rehman A, Saba T, Bahaj SA. (2022) Hybrid retinal image enhancement algorithm for diabetic retinopathy diagnostic using deep learning model. IEEE Access, 10:73079-73086. https://doi.org/10.1109/ACCESS.2022.3189374

[25] Dataset link: https://www.kaggle.com/datasets/mohammadasimbluemoon/diabeticretinopathy-messidor-eyepac-preprocessed

[26] Hu A, Deng Z, Yang H, Zhang Y, Gao Y, Zhao D. (2021) An Optimal Geometry Configuration Algorithm of Hybrid Semi-Passive Location System Based on Mayfly Optimization Algorithm. Sensors, 21(22):7484. https://doi.org/10.3390/s21227484

[27] Xu T, Yuan Z. (2022) Convolution neural network with coordinate attention for the automatic detection of pulmonary tuberculosis images on chest x-rays. IEEE Access, 10:86710-86717. https://doi.org/10.1109/ACCESS.2022.3199419

https://doi.org/10.31436/iiumej.v26i1.3221

# WEARABLE TEXTILE PATCH DSSRS ANTENNA FOR BODY TUMORS DETECTION WITH REDUCED SAR

**M.M. HASAN MAHFUZ[1], MD RAFIQUL ISLAM[2*], NORUN FARIHAH ABDUL MALEK[2], MOHAMED HADI HABAEBI[2], NAZMUS SAKIB[3], ELHAM BALADI[4]**

[1]*Department of Electrical and Computer Engineering, Concordia University, Montreal, QC, Canada*
[2]*Department of Electrical and Computer Engineering, International Islamic University Malaysia*
[3]*Graduate School of Science and Technology, Gunma University, Japan*
[4]*Department of Electrical Engineering, Polytechnique Montréal, QC, Canada*

**Corresponding author: rafiq@iium.edu.my*

*(Received: 12 March 2024; Accepted: 6 September 2024; Published online: 10 January 2025)*

***ABSTRACT***: The purpose of this study is to present a lightweight wearable (jeans) monopole antenna configuration for body area network (BAN) communication, breast and head tumors detections with back lobe reduction (i.e., low SAR), and it does so without introducing any special methodologies like as, AMC, EBG, HIS. The planned antenna has dual symmetrical slots as well as a ring-shaped slot (DSSRS) at the top, and it is in the form of a radiating rectangular patch with a ground plane. The design procedure has been finished with the help of CST MWS, and the next step will be to fine-tune the parameters of the antenna structure to achieve resonance at the ISM band (5.79 GHz). Testing for BAN, breast, and brain tumor detection was done using this prototype. With the proper impedance matching, the antenna achieves an operational bandwidth of 5.798 GHz (5.739–5.865 GHz), 5.77 GHz (5.715–5.838 GHz), 5.77 GHz (5.718–5.843 GHz) and 5.78 GHz (5.725–5.834 GHz), with an overall peak gain of 8.18 dBi, 7.69 dBi, 5.73 dBi, and 4.59 dBi; when proposed antenna placed on the free space, on the body, on the breast, and the head respectively. The suggested antenna meets the specific absorption rate (SAR) standards given by the FCC (1 gm) and the ICNIRP (10 gm).

***ABSTRAK***: Kajian ini bertujuan untuk membentangkan konfigurasi antena monopole ringan boleh pakai (jenis jeans) untuk komunikasi rangkaian kawasan badan (BAN), pengesanan tumor payudara dan kepala dengan pengurangan lobus belakang (iaitu, SAR rendah), tanpa menggunakan metodologi khas seperti AMC, EBG, atau HIS. Antena yang dicadangkan mempunyai dua slot simetri (dual symmetrical slots) serta slot berbentuk cincin (DSSRS) di bahagian atas, dan berbentuk patch segi empat tepat yang memancar dengan satah tanah. Prosedur reka bentuk telah diselesaikan dengan bantuan perisian CST MWS, dan langkah seterusnya adalah untuk menyesuaikan parameter struktur antena bagi mencapai resonans pada jalur ISM (5.79 GHz). Ujian untuk BAN, pengesanan tumor payudara, dan tumor otak telah dijalankan menggunakan prototaip ini. Dengan padanan impedans yang betul, antena ini mencapai lebar jalur operasi sebanyak 5.798 GHz (5.739–5.865 GHz), 5.77 GHz (5.715–5.838 GHz), 5.77 GHz (5.718–5.843 GHz), dan 5.78 GHz (5.725–5.834 GHz), dengan pencapaian keuntungan puncak keseluruhan sebanyak 8.18 dBi, 7.69 dBi, 5.73 dBi, dan 4.59 dBi; apabila antena yang dicadangkan diletakkan di ruang bebas, pada badan, pada payudara, dan pada kepala masing-masing. Antena yang dicadangkan memenuhi piawaian kadar penyerapan spesifik (SAR) yang ditetapkan oleh FCC (1 gm) dan ICNIRP (10 gm).

***KEYWORDS:*** Antenna, Microwave, Wideband, Cancer, Breast phantom, Tumor detection

https://doi.org/10.31436/iiumej.v26i1.3221

# 1. INTRODUCTION

In order to collect data about the user's personal health or, more broadly, to interface with the user, wearable technology includes gadgets that consumers can easily wear and use for lengthy periods of time inconspicuously, such as clothing or accessories [1]. At present, smart accessories like smartwatches, wristbands, smart glasses, and other garments clip-on account for the vast majority of the market share held by wearable devices [2]. Wearable gadgets like these often incorporate preexisting small sensors and electronics into compact packages [3]. As a result of their inflexible and nonflexible construction, they are not well suited to the creation of increasingly sophisticated wearable devices, which call for increased skin-to-device contact and an enhanced user interface. Micro and nano-electronics integrated into textile substrates are useful in creating smart materials with improved ergonomics or "smart textiles" [4]. Smart textile technology has the potential to enable the development of a broad range of capabilities on a textile substrate, previously only possible in rigid and nonflexible electronic goods [3], [5]. Many people became curious about electronic textiles because of this promising prospect [6], [7]. Rapid advances in technology, small gadgets, and mobile computing are fueling a market for wearable technologies that are predicted to continue growing at a compound annual growth rate of 15.5%. Recent market forecasts predict that the wearable devices industry will grow to more than USD 155 billion by 2027, in large part due to the participation of many large companies that are increasing their research efforts to switch from uncomfortable wearable electronics hardware to more comfortable smart textile [8].

Manufacturers are being encouraged by the rising consumer demand to create and commercialize billions of wearable electronics devices in a variety of market segments, such as health and wellness, military and defense, space exploration, fashion, and entertainment [9], [10]. Healthcare is one of the most promising markets, propelled by customers' growing desire to continuously monitor their health or be monitored by healthcare professionals who need to have more health data available to them so they may more thoroughly analyze a wider cohort of patients [11]. Smart biomedical clothing's comfort and accessibility could be crucial components of ongoing, long-term clinical monitoring. These cutting-edge devices can be integrated into Internet of Things (IoT) networks, utilizing straightforward but effective wireless solutions to create smart systems for remote health monitoring, allowing patients to continue living at home instead of spending money on expensive healthcare facilities. Having continuous, noninvasive, and seamless surveillance of health and physical well-being allows people to live independently and actively in their own houses, which is one of the key functions of wearable health monitoring devices [12]. This is a huge benefit, especially for people dealing with long-term medical conditions or having trouble moving around. The use of wearable monitoring systems highlights two additional benefits for users: first, it lessens the influence and stress that the clinical environment exerts on patient performance, and second, the massive amount of data gathered with this system can be processed by AI algorithms to detect a possible worsening of a patient's clinical situation [13]Smart wearable biomedical systems have the potential to offer advanced services to patients from the perspective of the public health system by combining frequently worn material with the most technologically advanced sensing, processing, and communicating capabilities. They can also support health cost reduction through the facilitation of early hospital discharges.

The essential criteria for comfortable wearing materials are compact size, flexibility, resilience, low SAR, and low power requirements [14], [15]. The SAR measures how much energy is transmitted through human tissue. The absorption of electromagnetic energy could potentially be harmful to human health. So, it's crucial to consider SAR when designing wearable antennas. The SAR must be significantly lower than the minimum allowed level. To

https://doi.org/10.31436/iiumej.v26i1.3221

safeguard the public from excessive exposure to EM fields, many organizations, such as the IEEE, ICNIRP, and the FCC, have proposed limitations on the radiation released by these devices. The FCC and ICNIRP require a SAR of less than 2 W/kg averaged over 10 gm and less than 1.6 W/kg averaged over 1 gm of human tissue [1], [16-17]. However, the battery life of ISM (Industrial, Scientific, and Medical) equipment is increased, and it does not require a lot of energy to send a signal to the receiver. Fabrics intended for use as clothing are a particularly promising option for developing flexible antennas. This is because fabric antennas can be readily sewn into the fabric. A highly effective, highly gain-flexible antenna can be conceived and fabricated by fusing ISM (2.4 & 5.8 GHz) and textile technologies. For BAN applications, the bending performance of the wearable textile antenna is typically a significant consideration. However, the bending effects are less significant for tumor detection in areas such as the breast or head. This is because the garments used in these applications, such as a female bra or a head cap, are more stable and consistent in shape compared to regular clothing worn on other parts of the body [18], [19]. The stretchy antenna might be concealed within the fabric of jeans. This approach has been followed in microwave scattered technology for tumor detection. When the tumors are present inside the human body (breast, head) model, the $S_{11}$ response of the antenna system is successfully altered.

### 1.1. Specific Absorption Rate (SAR)

SAR measures the rate at which energy is absorbed by the human body when exposed to a radio frequency (RF) electromagnetic field. It's commonly used to quantify the exposure levels from devices. SAR is expressed in watts per kilogram (W/kg) and indicates how much RF energy is absorbed per unit mass of tissue. There are some key points for SAR:

- **Measurement:** SAR values are determined through laboratory testing using standardized procedures. These tests simulate the human body's exposure to RF energy.
- **Regulatory Limits:** In the United States, the Federal Communications Commission (FCC) limits SAR to 1.6 W/kg, averaging over 1 gm of tissue. In Europe, the limit is 2.0 W/kg, averaging over 10 gm of tissue, as per the International Commission on Non-Ionizing Radiation Protection (ICNIRP) guidelines.
- **Health and Safety:** Regulatory agencies set SAR limits to ensure that exposure stays within safe levels, minimizing potential health risks. Ongoing research investigates the long-term effects of RF exposure to ensure that the guidelines remain current with scientific findings. SAR can be calculated using the following formula:

$$SAR = \frac{\sigma E^2}{\rho} \quad (1)$$

where $\sigma$ is the electrical conductivity of the tissue (measured in Siemens per meter, S/m), $E$ is the root mean square (RMS) electric field strength (measured in volts per meter, V/m), and $\rho$ is the mass density of the tissue (measured in kilograms per cubic meter, kg/m³).

### 1.2. Motivation

Recent research has focused on using $S_{11}$ for tumor detection, whereas AMC and UWB antennas have been used for skin cancer detection [20]. The scattering parameter ($S_{11}$) was used in this paper to evaluate the difference between cancerous and normal skin tissues. Those research works in [19-23] have focused on antenna design for breast and skin cancer detection. The work in [26] has also focused on the use of $S_{11}$ for the detection of cancer cells. It uses a flexible antenna design and microwave scattering parameters for tumor detection. Brain tumor detection using an antenna was also studied in [27] and [28], utilizing changes in the $S_{11}$

https://doi.org/10.31436/iiumej.v26i1.3221

parameter as an indicator. The references in these above-cited works also present previous studies on the use of changes in $S_{11}$ as an indicator for several types of cancer. The work in this field is still in progress and has neither been finalized nor clinically approved or adopted for detection, but it is a research area. Combining the $S_{11}$ changes with other techniques may help in more accurate diagnosis and detection procedures. Hence, the work in this manuscript is motivated.

### 1.3. Novelty and Contribution

A new patch configuration comprising a circular slot with two parallel adjacent rectangular slots was designed, and its performance details were evaluated using simulation models. The contribution of this work is as follows:

- A motivation for using a flexible patch antenna for jeans fabrication and the change in $S_{11}$ to detect the presence of breast cancer is presented.
- A novel patch design comprising a circular slot with two parallel rectangular slots resonating at the ISM band is presented.
- A sweep parametric study was conducted to achieve optimal results at resonance.
- The parameters like $S_{11}$, VSWR, gain, and radiation pattern were evaluated and presented.

The following is the research article's structure. The first part of this article provided a high-level overview of potential uses for wearable antennas. In Section 2, the various types of recent wearable antennas, together with their performance characteristics and prospective applications, are presented to the reader. Section 3 illustrated the DSSRS antenna's design, simulated results, and bending effect on different radii. Section 4 shows the DSSRS antenna's performance on the different parts of the human body, such as the body, breast, and head. This section also discussed the SAR values during breast and head tumor detection. Finally, section 5 shows the conclusion part of this research article.

## 2. RECENT RELATED WORKS

Recently published articles related to the suggested work are mentioned here. Wearable applications of coplanar keyhole antenna, including the design of novel antenna on fabric substrates for interfacing with internal and external sensors, are described [29]. The process of designing the fabrication method of screen printing on fabric substrates is explained using conductive inks available for purchase on the market. Antenna resonance at 5.8 GHz is discussed, as well as the impacts of wash durability and the inks' resistance to deterioration over time when used as interface layers between conductive elements and fabric substrates of coplanar keyhole fabric antenna. This research [30] introduces a compact AMC wearable textile antenna optimized for 5.8 GHz band Wireless Body Area Network (WBAN) applications in the ISM band. For these reasons, better antenna performance and shielding from harmful back radiation Artificial Magnetic Conductor (AMC) structure was implemented. The antenna with the built-in AMC has a measured gain of 8.92 dBi, efficiency of 80%, impedance bandwidth of 1.4 GHz (24.1%), and SAR values of 0.00103 W/Kg for 10 gm and 0.00034 W/Kg for 1 gm tissues. Wearable on-body scenarios using the suggested antenna were investigated with a multi-layer computational model of the human body. Each human tissue layer's thickness and its potential impact were studied. Antenna performance was maintained, consistent gain was achieved, and SAR values were below IEEE recommendations for wearer safety.

https://doi.org/10.31436/iiumej.v26i1.3221

To boost the antenna's impedance bandwidth, this study proposes a rectangular eight-shaped Electromagnetic Band Gap (EBG) structure operating in the 5.8 GHz ISM band for wearable applications [31]. Ansys HFSS High-Frequency Structure Simulator's Eigenmode solution simulates the eight-shaped EBG unit cell. An inverted E-shape monopole antenna operating at 5.8 GHz is also used to show the successful use of the proposed EBG. As a result of the band stop property of EBG construction, surface waves are reduced, and a wearable antenna's back lobe also experiences a reduction. The Internet of Things (IoT) gives a boost to the latest generation of wearable devices. Textile antennas are developed, and they can be completely integrated into garments. An on-body single patch and multiple-input multiple-output (MIMO) textile (Taffeta fabric) antenna was presented in this study [32]. The findings confirmed the constructed antenna's viability at the specified frequency (5.8 GHz). Frequency shifts and other performance issues, such as those caused by the pressure used during the eyelet attachment procedure, are possible consequences of making textile antennas by hand. For use in medical telemetry, the suggested antenna [33] has been optimized for design and construction. A rising area of study, biocompatible antenna design is essential in pollution-controlled environments for telemetry systems used in patient monitoring, elderly health monitoring, children's safety, and firefighter's safety. Denim is offered as the substrate for a unique E-shaped textile antenna to be used in patient telemetry. Biocompatibility, miniaturization, and operation in the ISM band at 2.45 GHz.

On the other hand, by simulating a common scenario for WBAN applications, this research [34] measures the influence of mechanical curvature on a textile inset-fed microstrip patch antenna placed above a human head phantom. Therefore, this study evaluates how operational properties, including resonance frequency, bandwidth, and radiation pattern, are affected by body proximity and antenna curvature. In addition, the SAR of the cranium was determined and compared to global safeguarding requirements. Computational studies reveal that when the antenna is applied to a human head, the curvature of the antenna produces a significant change in the resonant frequency. Therefore, the antenna's bandwidth must be sufficiently high in the first place to compensate for this negative effect. The developed antenna achieved a front-to-back ratio of 19 dB to reduce brain radiation exposure. This research [35] suggested using an AMC-backed leather antenna that operates in the ISM 5.8 GHz band. Leather substrate allows the antenna and AMC to be worn with casual attire. The suggested antenna has good impedance matching within the ISM band at 5.8 GHz, and its reflection coefficient was unaffected by crumpling and bending. The suggested antenna has a 90% reduction in SAR value compared to the antenna alone, making it acceptable for use by the general public. The design's return loss and SAR performance also degrades very little when the human body is loaded. The proposed AMC-supported wearable antenna is a viable option for use in the medical field. As a wearable antenna for use in the ISM band at a central frequency of 2.45 GHz, this study [36] introduces an antenna based on the Mercedes-Benz insignia, with a metal plate placed at an optimized distance from the suggested antenna. To optimize the radiation performance of the suggested design, decrease the back radiation, and lower the SAR when loaded on a human body, a metal plate is integrated with the antenna to serve as an isolator and reflector. The suggested antenna, coplanar waveguide-fed, was printed on a Rogers 4003C substrate and has dimensions of 35 mm × 35 mm × 0.508 mm. Its impedance bandwidth is (2.20–2.56) GHz, and its gain was 7.3 dB at 2.45 GHz. The SAR was lower than the criteria the FCC and the ICNIRP set.

An easily transportable asymmetric coplanar strip-fed comb-shaped patch (CSP) antenna made of textile was presented [37] and investigated for use in the Medical Body Area Network and the ISM band. Denim has been implanted with a thin piece of highly conductive fabric to create a flexible, conductive, wearable antenna. The CSP antenna has been tested in open areas

and worn. The proposed CSP antenna has a free space resonance frequency of 2.49 GHz (2.27–3.42) GHz and an operating frequency range of 1150 MHz. When worn on the body, the antenna has a 900 MHz bandwidth and 2.44 GHz (1.9–2.8) GHz resonance frequency. In open space, the gain is measured at 4.67 dBi, which drops to –4.82 dBi when used on a human body. The CSP antenna has been crumpled and bent without affecting its performance. For use in the ISM band, a unique, miniature implantable antenna has been proposed [38]. The suggested antenna was a circular patch antenna with a shape; it was designed using information from existing studies, and its smaller size was accomplished using various downsizing methods. The radiating structure was patched with a circular shape and features square fillet edges. The ground plane was extended to cover the entire plane, eliminating the back reflections. This antenna structure operates at 2.45 GHz with the preferred omnidirectional pattern to maximize compatibility with other in-body devices. Within the ISM band, modeling, designing, and fabrication of a wearable pentagon microstrip patch antenna were carried out [39]. Its medical uses include diagnosing diseases like brain cancer and examining images of the head. In order to choose, simulate, and carry out the design most effectively, it is necessary to compute the patch's physical dimensions, including the matching circuits. The simulation tool utilizes a human head model to calculate SAR. This study will provide preliminary results that can be used for future development of technologies involving wearable antennas, and it will also make it easier to design additional innovative detecting methods.

## 3. DESIGN, SIMULATION, AND PARAMETRIC ANALYSIS OF DSSRS ANTENNA

Typically, microstrip patch antennas are the best option for wearable applications due to their flexibility and ease of incorporation [1]. The wearable antenna design must be simple and use flexible, versatile building materials. A variety of material characteristics affect an antenna's performance [40]. The rectangular patch antenna is often used due to its superior layout compared to other patch antennas [41]. Due to their compact size and adaptability, microstrip and patch antennas are widely used. Fabric construction means it is lightweight and compact design is ideal for human use [42]. The developed antenna has significant utility for investigating health-related parameters. The simulation processes are performed using the CST MWS. The antenna substrate is a piece of denim fabric (jeans). Jeans fabric is an attractive substrate for textile antennas due to its durability, stiffness, low density, and low cost [43]. On a jeans substrate, dual symmetrical slots and a ring-shaped slot (DSSRS) top on the radiating patch antenna were developed with a height of 1 mm, relative permittivity of 1.7, and loss tangent of 0.025. Copper material is used for the conducting patch and the ground plane, and each of these components has a thickness of 0.035 mm. Eqs. (2) to (9) were utilized to design initial circular slot rectangular slots. The optimized values of width ($W_p$ = 45 mm), patch length ($L_p$ = 46.1 mm), feedline width ($W_f$ = 3.6 mm), and ring-shape slot diameter ($R$ = 12 mm) are obtained through simulation. Figure 1 shows a representation of the simulated antenna.

$$W_p = \frac{c}{2f_r\sqrt{\frac{\varepsilon_r+1}{2}}} \tag{2}$$

$$\varepsilon_{eff} = \frac{\varepsilon_r+1}{2} + \frac{\varepsilon_r-1}{2}\left[1 + 12\frac{h}{W_p}\right]^{-\frac{1}{2}} \tag{3}$$

$$L_{eff} = \frac{c}{2f_r\sqrt{\varepsilon_{ff}}} \tag{4}$$

https://doi.org/10.31436/iiumej.v26i1.3221

$$\Delta L = 0.412h\frac{(\varepsilon_{eff}-0.3)\left(\frac{W_p}{h}+0.264\right)}{(\varepsilon_{eff}-0.258)\left(\frac{W_p}{h}+0.8\right)} \quad (5)$$

$$L_p = L_{eff} - 2\Delta L \quad (6)$$

$$W_f = \frac{7.48h}{e^{z_0\frac{\sqrt{\varepsilon_r+1.41}}{87}}} - 1.25t \quad (7)$$

$$R = F\left\{1+\frac{2h}{\pi\varepsilon_r F}\left[\ln\left(\frac{\pi F}{2h}\right)\right]+1.7726\right\}^{-\frac{1}{2}} \quad (8)$$

$$F = \frac{8.791\times10^9}{f_r\sqrt{\varepsilon_r}} \quad (9)$$

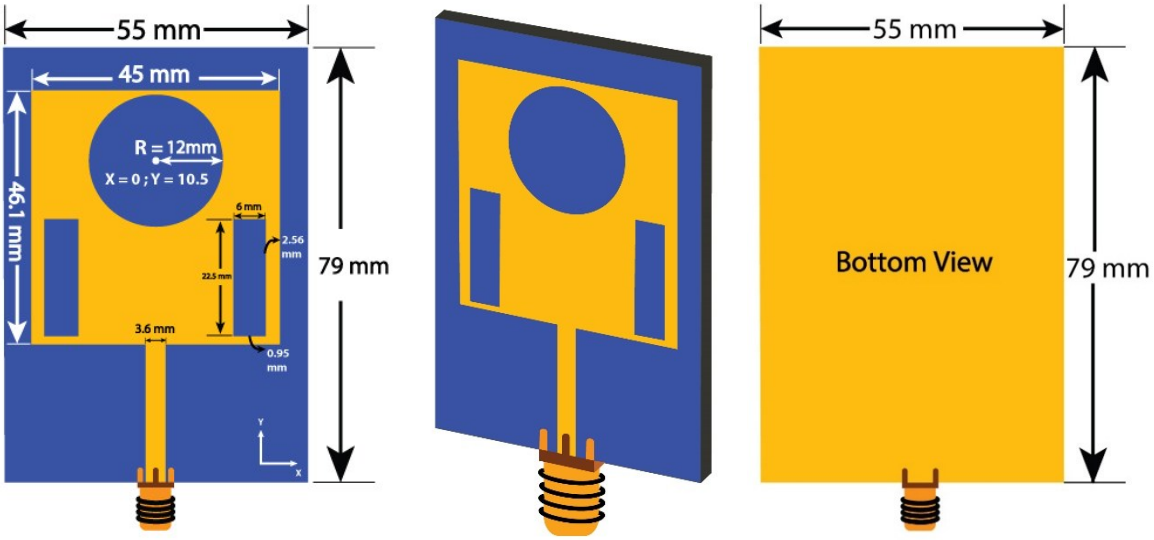


(a) Front View (b) Side View (c) Bottom View

Figure 1. The proposed DSSRS antenna

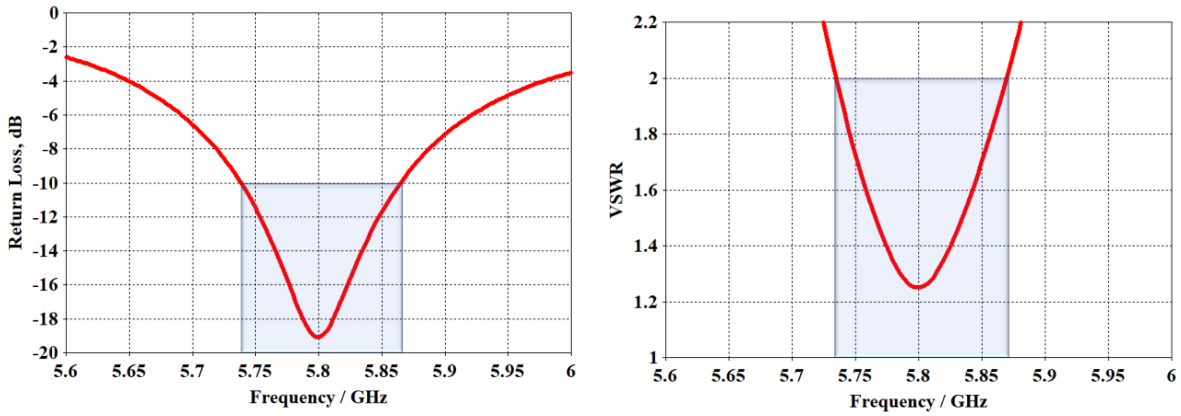


(a) (b)

Figure 2. The simulated (a) return loss & (b) VSWR of the DSSRS antenna

The return loss can refer to the reflection coefficient, which can be represented by the symbol $S_{11}$. Specifically, it is the ratio of incident power to reflected power. The reflection coefficient must be high (or at least satisfactory). An antenna needs $S_{11}$ of at least –10 dB and preferably more than –15 dB [44]. As shown in Figure 2(a), the simulated antenna has a return

https://doi.org/10.31436/iiumej.v26i1.3221

loss of –19.068 dB at 5.798 GHz while maintaining a respectable level of bandwidth (5.739–5.865 GHz). Another name for it is the voltage standing wave ratio (written as VSWR). It is put to use in the process of determining matches. The magnitude of the mismatch increases proportionately with the VSWR value. The suggested antenna has a VSWR ratio of 1.251 at 5.798 GHz, as illustrated in Figure 2(b).

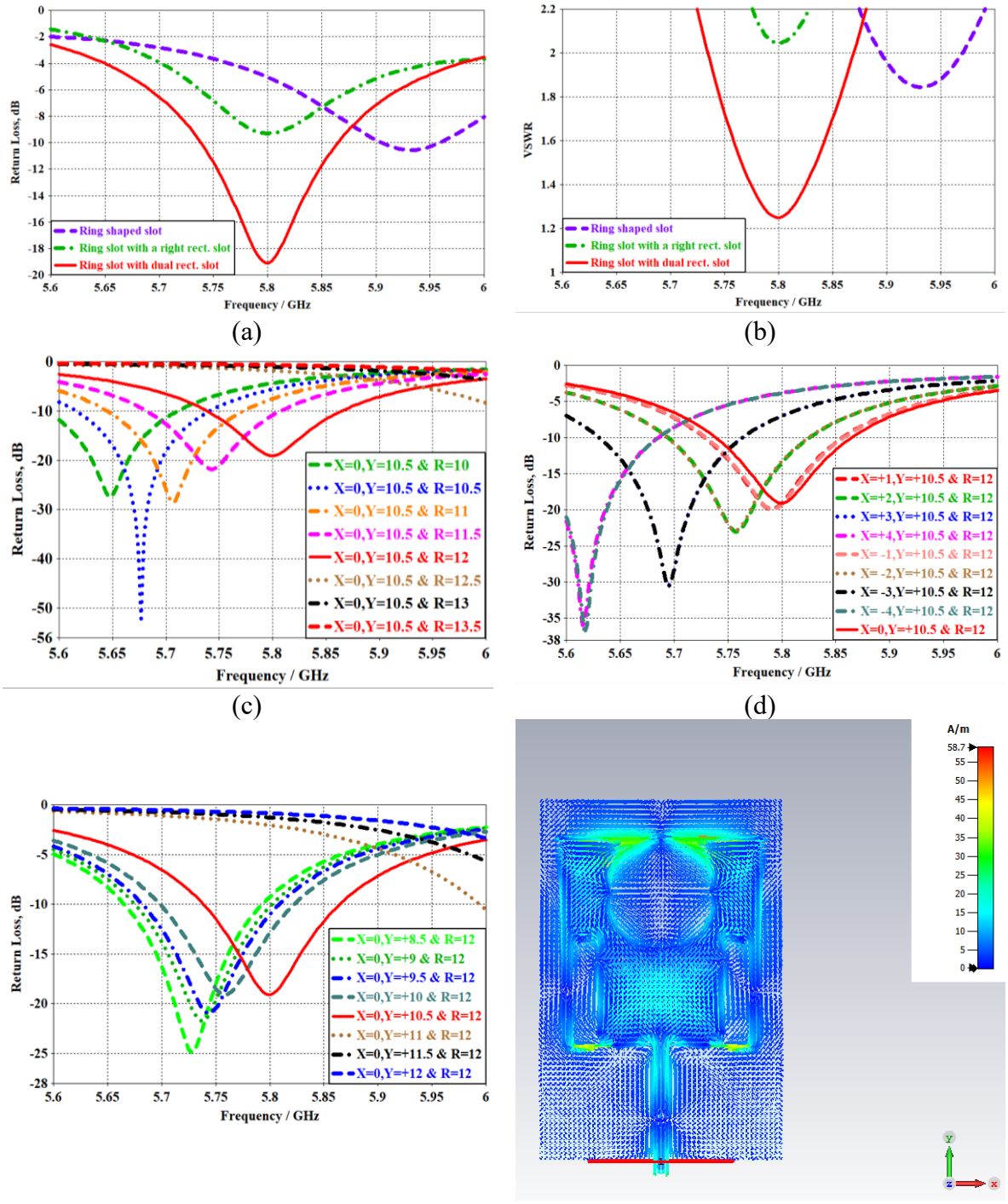


Figure 3. The parametric studies of (a, b) ring-shaped slots with dual symmetrical rectangular slots $S_{11}$, VSWR and $S_{11}$ of (c) altering the radius of the ring-shaped slot, (d) altering the X-axis values, (e) altering the Y-axis values & (f) surface current (58.7 A/m) at 5.798 GHz

https://doi.org/10.31436/iiumej.v26i1.3221

Figures 3(a) and (b) show the $S_{11}$ and VSWR of the ring-shaped slots with dual symmetrical rectangular slots parametric studies. This study clearly shows that the DSSRS proposed antenna operates at 5.79 GHz. Figure 3(c)(d)(e) is sufficient proof that $X$=0, $Y$=10.5 mm, and $R$=12 mm have an excellent performance of the proposed antenna. However, Figure 3(c) shows the $S_{11}$ study while the $X$, $Y$-axis constant just altering $R$ values. Figure 3(d)(e) illustrates the changing of $X$, $Y$-axis values. The remaining parameters ($Y$, $X$-axis, $R$) values are constant. The surface current accumulating of 58.7 A/m at 5.798 GHz, as shown in Figure 3(f), which supports that the DSSRS, the antenna resonates at 5.798 GHz and it exhibits high magnitude at the edges and maximum current distribution at the center of the patch at the resonant frequency. This distribution strongly depends on the height of the substrate, which is crucial for determining the antenna size. However, due to the DSSRS, the antenna resonates at a frequency $f_r$ =5.798 GHz. From the surface current, as shown in Figure 3(f), it is clear that the DSSRS significantly impacts the entire bandwidth.

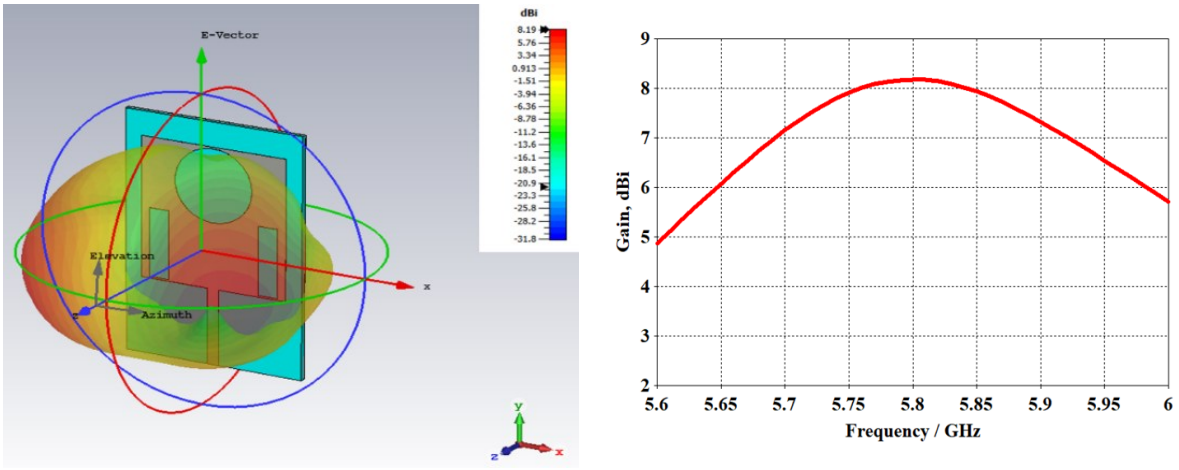


(a) (b)

Figure 4. The simulated (a) 3-D radiation pattern and (b) Gain

Figure 4(a)(b) shows the simulated 3D radiation pattern and gain (8.19 dBi at 5.798 GHz), respectively. An important performance metric is the antenna gain, calculated by adding the directivity to the antenna's radiation efficiency. The amount of input power an antenna can successfully convert into radio frequency that travels in a certain direction is called its gain. It has been determined that the proposed antenna has a gain of 8.18 dBi at resonant frequency = 5.798 GHz. To determine the radiated power level, it is necessary to observe the radiation pattern. For wearable antennas to be useful, they must be able to resist performance degradation when bent or stretched.

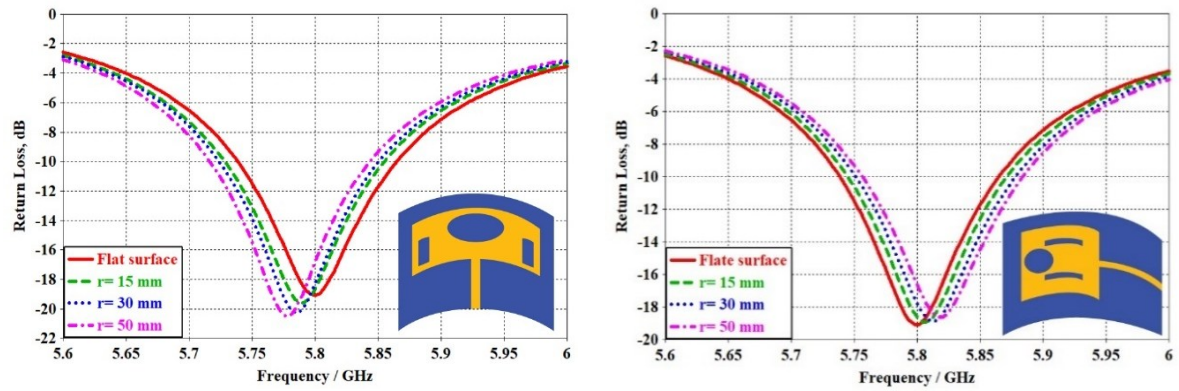


(a) E-plane (b) H-plane

https://doi.org/10.31436/iiumej.v26i1.3221

Figure 5. Comparisons of return loss for the antenna at varying bending radii

Figure 5 shows the simulated return loss of the proposed antenna in the E and H planes, respectively, for three alternative radii (15, 30 & 50 mm). The suggested antenna has improved impedance matching, as seen in Figure 5(a), with a return loss of less than –10 dB for all E-plane bending radii. With a return loss for the H-plane below –10 dB, Figure 5(b) illustrates that the suggested antenna exhibits a superior impedance-matching response. It is important to note that both the antenna's E and H-plane resonant frequencies are slightly delayed left and right (compared to the flat counterpart). Despite this, the fractional bandwidths of the bent antenna vary from 128 MHz to 130 MHz, which can be considered almost the same regardless of all bending (15, 30 & 50 mm) circumstances. The slot combination was chosen to exploit complementary effects on electromagnetic properties, resulting in a compact design suitable for various body configurations. It minimized the bending effects, as shown in Figure 5.

## 4. PERFORMANCE EVALUATION OF DSSRS ANTENNA FOR BODY APPLICATIONS

### 4.1. On Body

Since the human body has lossy properties, the antenna's performance changes as it gets closer to a person's body. A human phantom with four layers evaluates the antenna's performance. Figure 6 shows that the four layers of the human phantom are composed of dry skin, fat, muscles, and cortical bone, with corresponding thicknesses of 2 mm, 3.5 mm, and 10 mm [45]. As can be seen in Figure 6, the proposed antenna’s performance simulation on the human body.

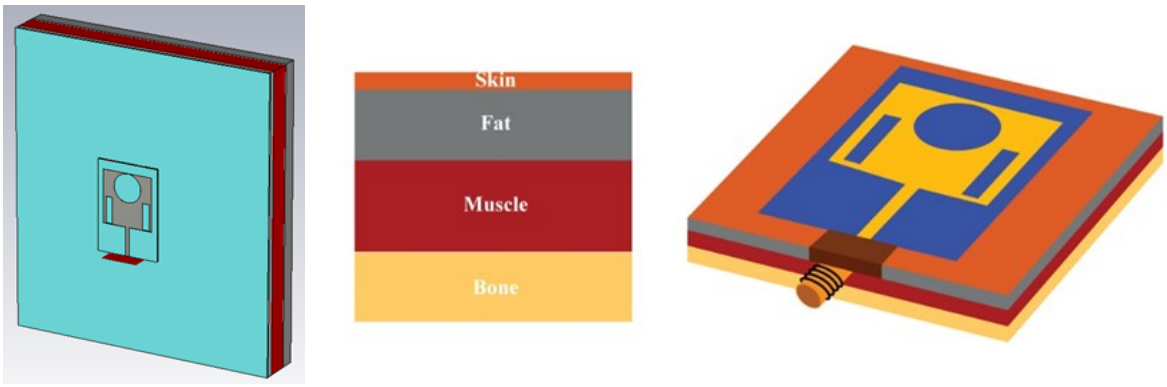


(a) (b)

Figure 6. Prototype (a, b) of the proposed antenna mounted on the human body

Figure 7(a)(b) displays the simulated return loss and VSWR obtained by fastening the antenna to a human body, and the resonant frequency lightly shifted from 5.798 GHz to 5.77 GHz. An excellent impedance match is achieved with minimal frequency shift when the antenna is placed on a human body, as seen by the fractional bandwidth of 2.146%. Figure 7(c) illustrates the 3-D radiation pattern performed at 5.77 GHz (5.715–5.838 GHz) on the human body. Because of the pattern's form, the antenna exhibits Z-plane directional radiation and a maximum gain of 7.69 dBi (Figure 7d), making it suitable for on-body communications. When the antenna was placed for realistic on-body applications, it was supposed to be incorporated into a suit, and then it would be subject to bending.

https://doi.org/10.31436/iiumej.v26i1.3221

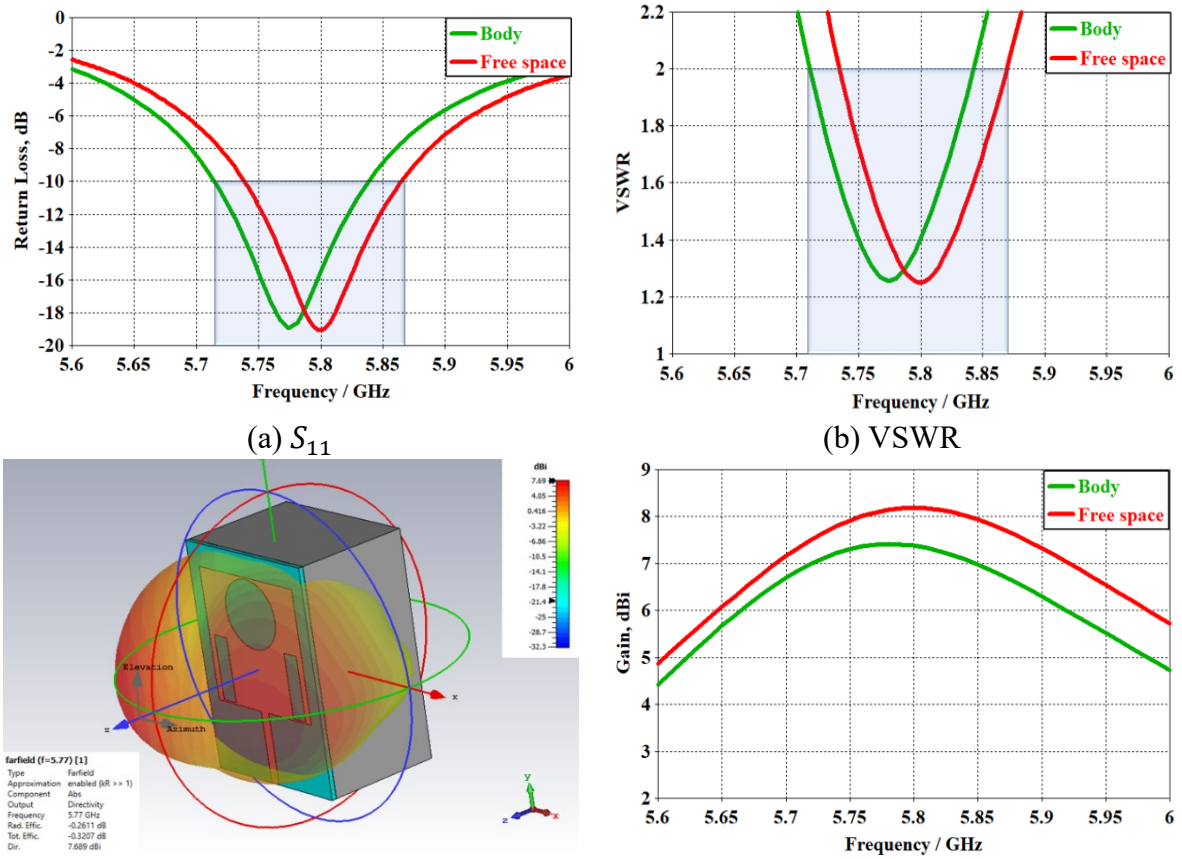


(a) $S_{11}$ (b) VSWR

(c) 3D Radiation Pattern at 5.77 GHz (d) Gain

Figure 7. The simulated results of the DSSRS antenna

Thus, the consequences of bending on the human body have been studied for the E and H-plane in different radii (15, 30, 50 mm) and illustrated in Figure 8. As can be seen in Figure 8, when the antenna is bent, the detuning of the resonant frequency is accentuated. The fractional bandwidths of the bent antenna vary from 128 MHz to 130 MHz for all bending (15, 30 & 50 mm) circumstances, which are similar, as shown in Figure 5, without a body.

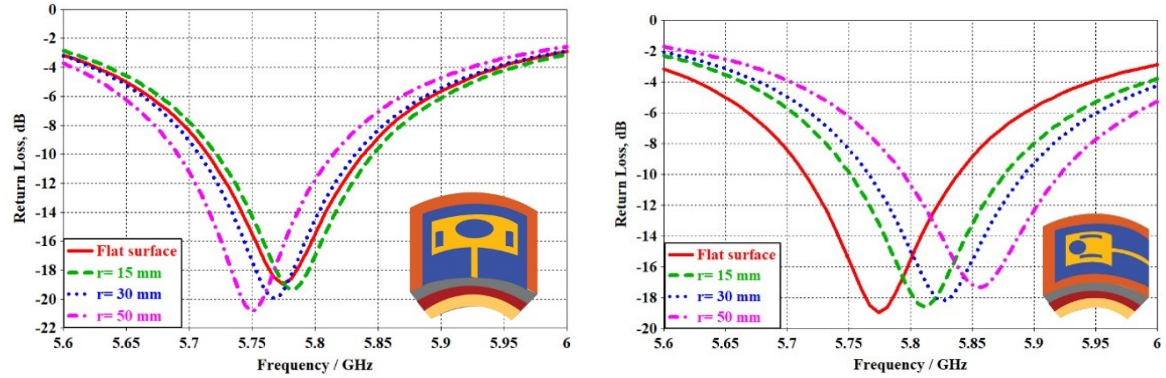


(a) E-plane (b) H-plane

Figure 8. Comparisons of $S_{11}$ for the antenna on the body at varying bending radii

Figure 9 depicts a simulation of the SAR at 5.77 GHz, performed following the FCC (1 gm) and ICNIRP (10 gm) regulations. Maximum SAR values were 0.00000662 W/kg for 1 gm of tissue and 0.0000027 W/kg for 10 gm. As a result, the completed design was compatible

https://doi.org/10.31436/iiumej.v26i1.3221

with both the United States and the European Union's SAR criteria, and it can be suggested as a wearable antenna for ISM band applications.

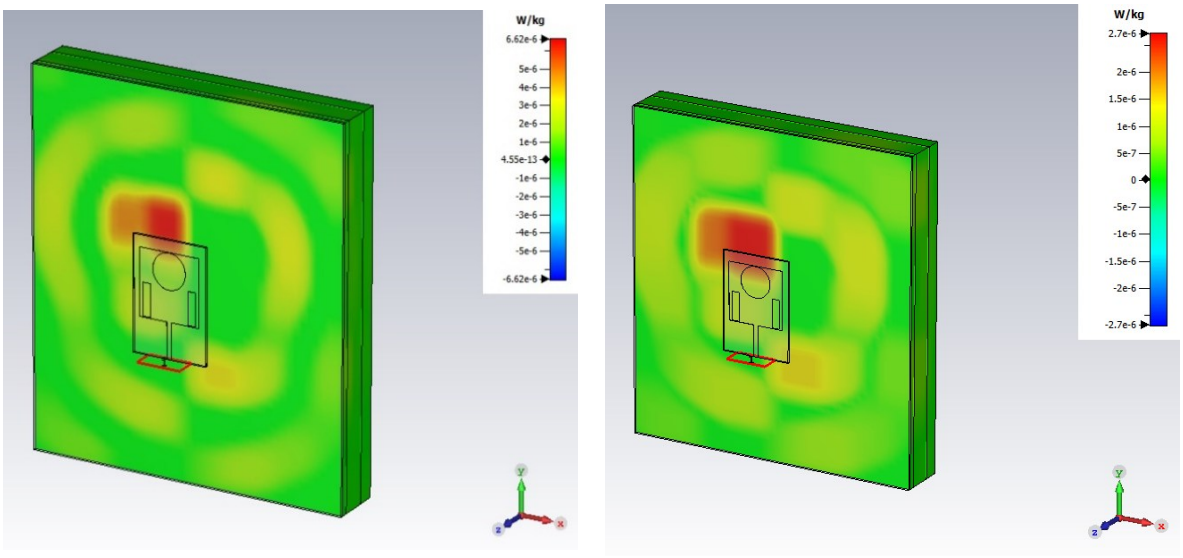


(a) 1 gm (0.00000662 W/kg) (b) 10 gm (0.0000027 W/kg) tissue

Figure 9. The SAR evaluation at 5.77 GHz

### 4.2. On Breast

Female breast cancer is increasingly common, making early detection crucial for prompt treatment. Conventional methods of tumor detection are both costly and time-consuming [46]. Because of the dispersed $S_{11}$ values, it has been determined that tumors alter the relative permittivity and conductivity of the tissues in the vicinity of tumors. The identification of breast tumors was the primary objective of the antenna. Specific dielectric and thermal properties ($\varepsilon_r$=5.08, σ=0.13 [S/m], thermal conductivity, δ=0.33 [W/(m*K)], specific heat, θ=[2550J/(kg*K)], density, d=1041[kg/m$^3$] were associate with the breast phantom [47]. This study aimed to examine the relationship between return loss and the condition of a breast phantom. A simulation was run using CST MWS with the textile (jeans) antenna placed on the normal breast phantom, as illustrated in Figure 10.

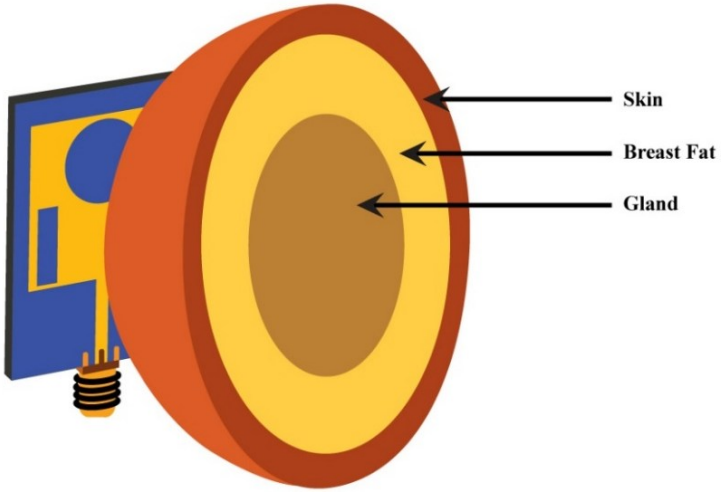


Figure 10. The 3-D model of a healthy breast phantom

https://doi.org/10.31436/iiumej.v26i1.3221

There was a –19.128 dB attenuation for a healthy breast's reflection coefficient at 5.77 GHz, as shown in Figure 11(a), and the VSWR in Figure 11(b). The VSWR<2 means the proposed antenna has excellent impedance matching on the breast phantom environment. Figure 11(c)(d) illustrates the 3-D radiation pattern and gain. Gain has been achieved at 5.73 dBi in breast phantom at 5.77 GHz, with a z-axis directional.

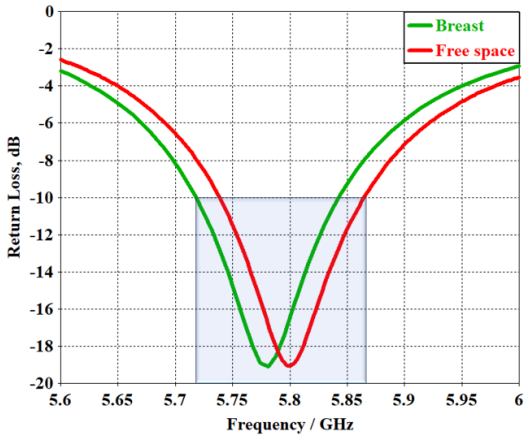


(a) $S_{11}$

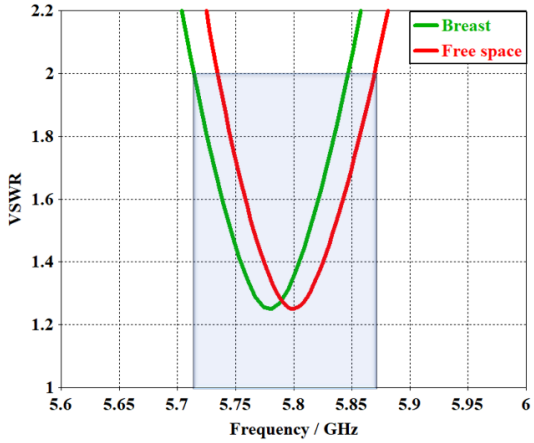


(b) VSWR

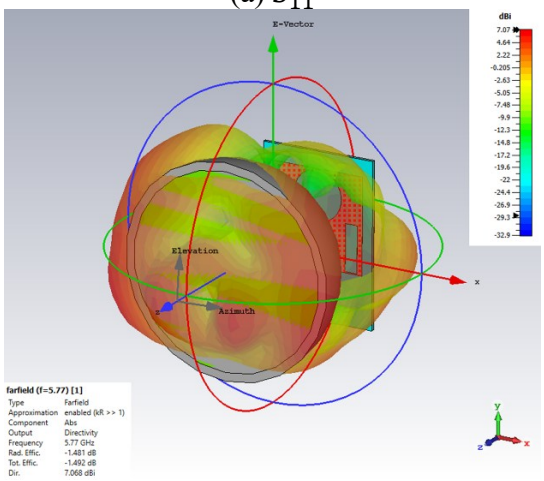


(c) 3D Radiation Pattern at 5.78 GHz

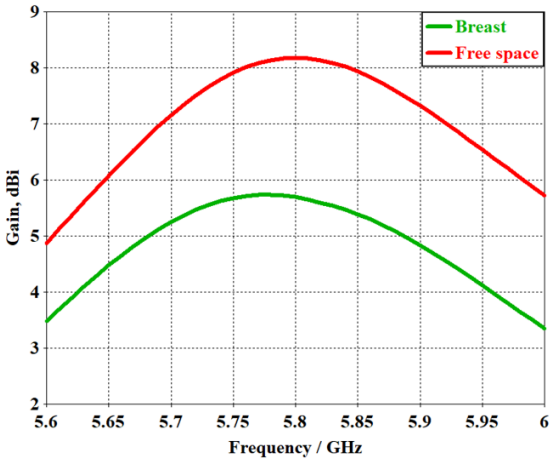


(d) Gain

Figure 11. The textile antenna was placed on a phantom of a healthy breast

The SAR value was 0.651 W/Kg for 1 gm of tissue and 0.419 W/Kg for 10 gm of tissue, as shown in Figure 12. This value was quite low compared to the necessary maximum level. The characteristics of fictitious tumors in the breast are shown in Figure 13(a) ($\varepsilon_r$=59.06, σ=3[S/m], δ=0.5[W/(m*K)]). The unhealthy breast tissue is augmented using those values. Figure 13(b) displays the simulated $S_{11}$, which is attenuated by –18.283 dB, –17.967 dB & –18.349 dB to 10, 20 and 30 mm radii tumor sizes. These simulations aim to test the antenna's performance in the presence of tumors in a breast phantom. The return loss value is slightly higher than in normal tissues, and the resonance frequencies are shifted towards the left as tumor sizes increase in breast tumors, as shown in Figure 13(b).

https://doi.org/10.31436/iiumej.v26i1.3221

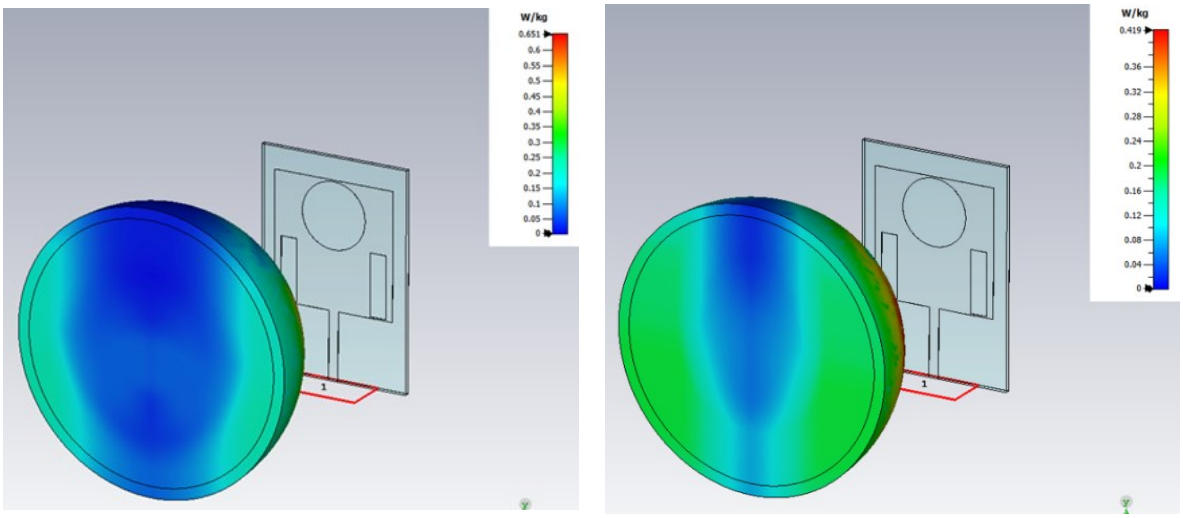


(a) 1 gm (0.651 W/Kg) (b) 10 gm (0.419 W/Kg) tissue

Figure 12. The simulated SAR value

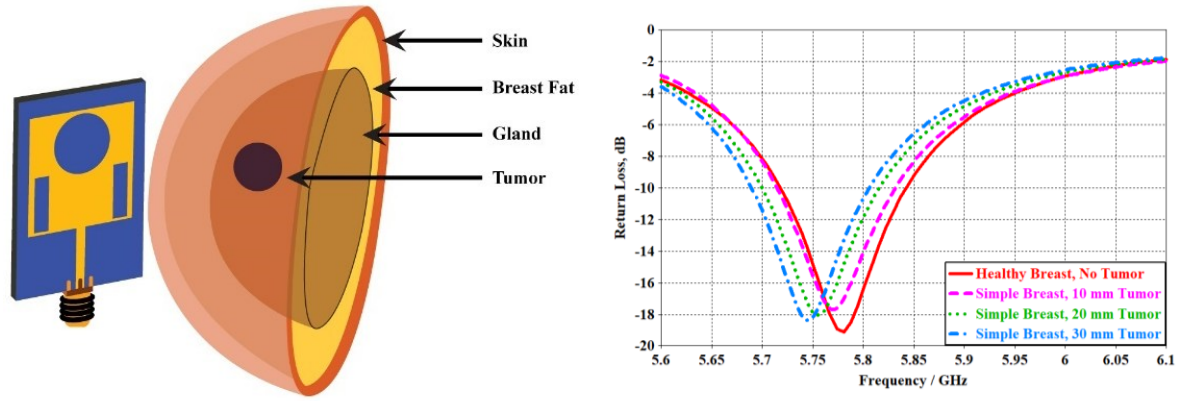


(a) tumor (b) $S_{11}$

Figure 13. A 3-D view of breast phantom of different radii tumors

### 4.3. On Head

Computed tomography (CT), positron emission tomography (PET), magnetic resonance imaging (MRI), ultrasound, and x-ray imaging are common medical diagnostic imaging techniques used to detect cancer, stroke, tumors, and other malignant elements in the human head. Negative aspects of computed tomography (CT) and X-ray imaging include exposure to harmful radiation, a high rate of false negatives, decreased susceptibility, and an increased risk of cancer due to both the duration and intensity of exposure [46], [47]. While the MRI method aids doctors in investigating the human body for the presence of specific disorders, it is more costly and less effective than alternative methods. Additionally, ultrasound is superior for some disorders but cannot provide an accurate picture. Although PET scanning technology can differentiate between malignant and noncancerous cells (i.e., tumors), its main drawback is that it may create severe complications for pregnant women [48]. Numerous studies have been conducted in recent years to develop imaging systems of the human body utilizing microwave technology for the early detection and diagnosis of a wide range of disorders, such as cancer, tumors, strokes, and internal bleeding in the brain [39-41]. There are six types of tissue in a human head: skin, fat, muscle, bone, or skull, CSF (cerebrospinal spinal fluid), and dura. The

https://doi.org/10.31436/iiumej.v26i1.3221

suggested antenna was designed and run through the CST simulator. The phantom human head was placed next to the antenna, modeled in free space, and illustrated in Figure 14.

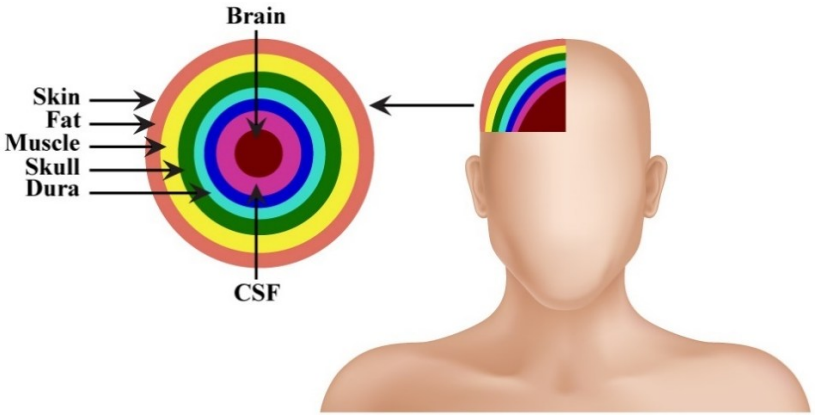


Figure 14. A 3-D view of the human head phantom

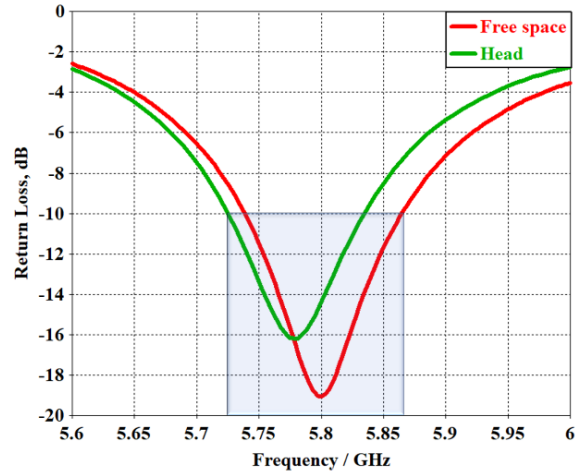


(a) $S_{11}$

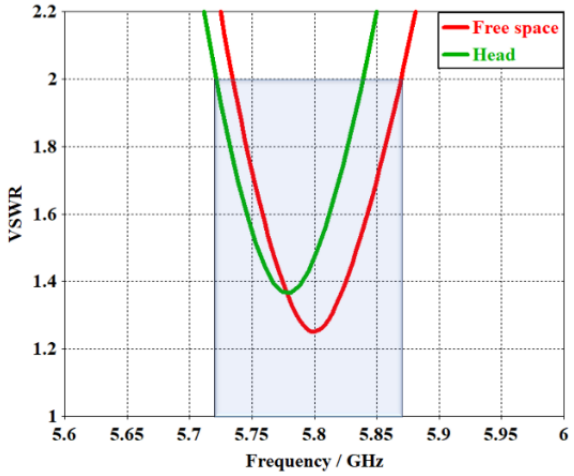


(b) VSWR

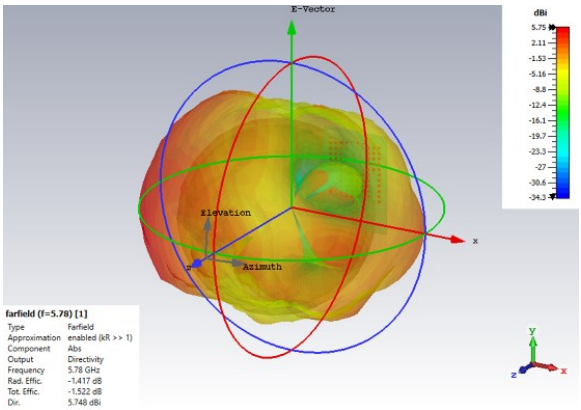


(c) 3D Radiation Pattern at 5.78 GHz

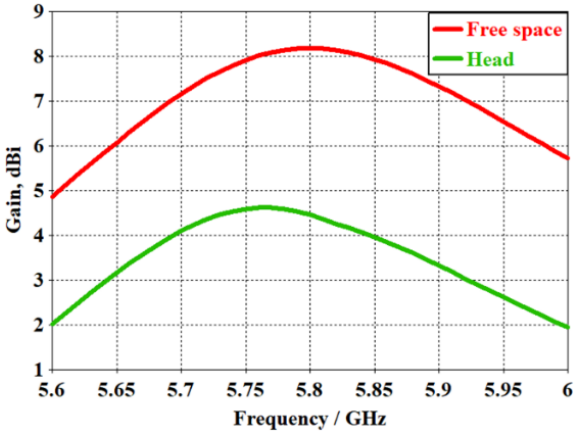


(d) Gain

Figure 15. The simulated results of the human head phantom

A simulation performed on a human head phantom revealed respectable values of the reflection coefficient and VSWR with satisfactory impedance matching from the antenna at 5.78 GHz, as shown in Figure 15(a)(b). The DSSRS antenna has achieved (5.725–5.834) GHz bandwidth of resonant frequency 5.78 GHz on the human head phantom. Figure 15(c)(d)

https://doi.org/10.31436/iiumej.v26i1.3221

illustrates the 3-D radiation pattern and gain. It has been observed that the 3-D radiation pattern is directed toward the Z-axis; on the other hand, the 4.59 dBi gain was achieved at 5.78 GHz on the human head phantom. The SAR can gauge an antenna's suitability for biomedical applications. It was found that from Figure 16, the suggested antenna had a maximum average SAR of 0.0635 W/kg for 1 gm of tissue and 0.0344 W/kg for 10 gm of tissue. There will be no harmful effects from having the values so close to the head. The identification of head tumors is the primary objective of the proposed antenna.

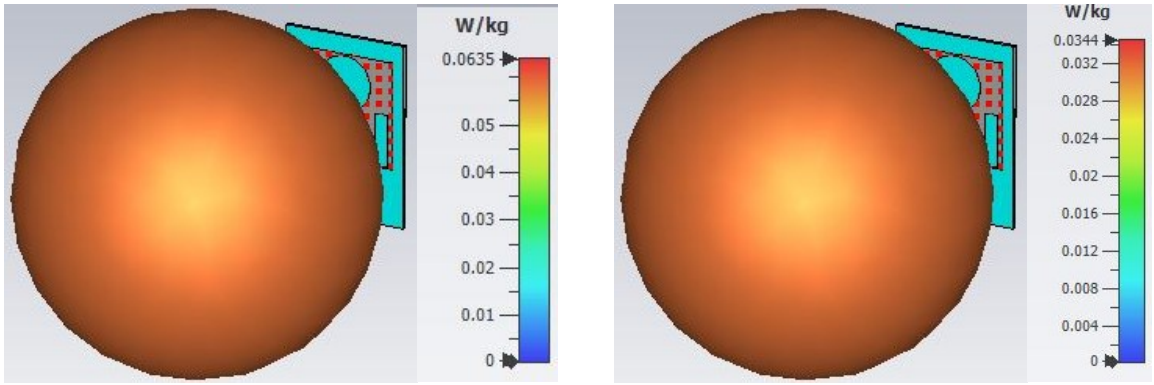


(a) 1 gm (0.0635 W/Kg) (b) 10 gm (0.0344 W/Kg)

Figure 16. The SAR evaluation at 5.78 GHz

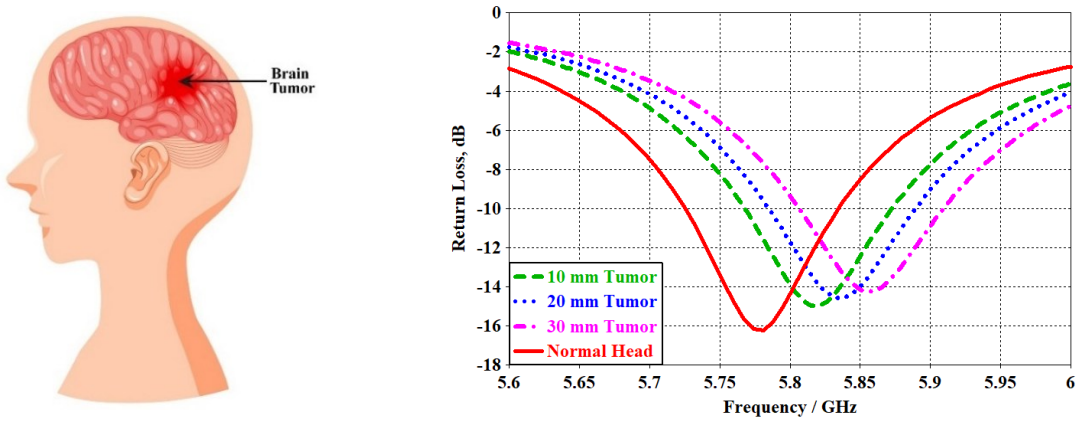


(a) tumor (b) $S_{11}$

Figure 17. A 3-D view of the head phantom of different radii tumors

The characteristics of fictitious tumors in the head are shown in Figure 17(a) ($\varepsilon_r$=68, σ =0.13[S/m], δ=5.46[W/(m*K)]). Figure 17(b) shows the simulated $S_{11}$ with attenuation of $f_r$=5.82GHz, –14.973 dB; $f_r$=5.84GHz, –14.572 dB, and $f_r$=5.86 GHz, –14.237 dB for tumors with 10, 20, and 30 mm radii, respectively. These simulations aim to test the antenna's performance while a head phantom has a tumor. The value of return loss is slightly higher than it would be in the case of normal tissues, and the resonance frequencies are shifted towards the right as the sizes of the tumor increase, as shown in Figure 17(b). This is demonstrated by the fact that it exhibits the presence of tumors. The distinct characteristics of breast and head tumors result in changes in resonant frequencies, decreases in breast tumors, and increases in head tumors, respectively. This different behavior may be caused by the dielectric and thermal properties of tumors in the breast and head being different in nature. Hence, for accurate detection of the tumors in different body parts, their dielectric and thermal properties and impacts on resonance frequencies must be known earlier. Table 1 summarizes the results achieved with previously developed jeans substrate antenna designs, respectively.

https://doi.org/10.31436/iiumej.v26i1.3221

Table 1. In-depth analysis of the proposed DSSRS antenna versus existing antenna models with the operating frequency in ISM band (GHz)

| Ref. | Antenna Design | Substrate | h (mm) | $\varepsilon_r$ | Max. Gain (dBi) | SAR (W/kg) | | | | | |
|---|---|---|---|---|---|---|---|---|---|---|---|
| | | | | | | Body | | Breast | | Head | |
| | | | | | | 1gm | 10gm | 1gm | 10gm | 1gm | 10gm |
| [27] | Coplanar keyhole antenna | Nylon blend | --- | 1.50 | 2.76 | --- | --- | --- | --- | --- | --- |
| [28] | AMC structure | Polyester textile | 4.58 | 2.20 | 8.92 | 0.00103 | 0.000349 | --- | --- | --- | --- |
| [29] | 8-shaped EBG structure | Denim | 0.8 | 1.70 | --- | 0.6 | 0.056 | --- | --- | --- | --- |
| [30] | Single patch MIMO antenna | Taffeta fabric | 0.98 | 1.30 | --- | --- | --- | --- | --- | --- | --- |
| [32] | RPA | Jeans fabric | 1.34 | 1.78 | --- | --- | --- | --- | --- | --- | 0.9555 |
| [33] | AMC embedded antenna | Leather | 2 | 2.75 | 7.47 | 3.0 | --- | --- | --- | 6.28 | --- |
| [34] | Mercedes Benz logo | Rogers 4003C | 0.508 | 3.38 | 7.3 | 0.17 | 0.09 | --- | --- | --- | --- |
| [35] | Comb-shape patch antenna | Denim textile | --- | 1.7 | 4.67 | 1.4 | --- | --- | --- | --- | --- |
| [36] | Slotted circular patch antenna | ROGER 3010 | 1.6 | 10.2 | --- | 1.8 | 0.3 | --- | --- | --- | --- |
| [37] | Pentagon patch antenna | RT/Duroid 5880 | 1.524 | 2.2 | 6.71 | --- | --- | --- | --- | 0.69 | 0.26 |
| **This work** | **DSSRS antenna** | **Jeans textile** | **1** | **1.7** | **8.18** | **0.00000662** | **0.0000027** | **0.651** | **0.419** | **0.0635** | **0.0344** |

Table 2. Comparison with recent jeans substrate antenna

| Ref. | Type of Material | Simulated $S_{11}$ (GHz) | Measured $S_{11}$ (GHz) | Simulated Gain (dBi) | Measured Gain (dBi) | SAR (W/kg) | |
|---|---|---|---|---|---|---|---|
| | | | | | | 1 gm | 10 gm |
| [41] | Jeans | 0.9–6, –25 | 0.85–6.5, –23.50 | 2.44 | --- | --- | --- |
| [49] | Jeans | 2.2–2.53, –37 | 2.1–2.54, –36 | --- | --- | --- | --- |
| [50] | Jeans | 2.42–2.484, 5.5–6.3, –12.80 | 1.72–2.9, 5.73–5.85, –12.50 | --- | --- | --- | --- |
| [51] | Denim | 2.4–2.48, –40 | 2.42–2.47, –33 | 7.1 | --- | --- | --- |
| [52] | Jeans | 2.42–2.49, –34 | 2.44–2.51, –23.30 | 7.47 | --- | Chest:0.0257; Arm:0.0358 | --- |
| [53] | Jeans | 2.96–12, –50 | 2.96–11, –23 | 6.2 | 5.47 | --- | Body: 1.6018 |
| **This work** | **Jeans** | **5.79–5.87, –19.07** | **---** | **8.18** | **---** | **Breast: 0.651; Head: 0.0635** | **Breast:0.419; Head: 0.0344** |

# 5. CONCLUSION

This work presents an illustration of the design of the DSSRS wearable textile monopole antenna for BAN and tumors (breast & head) detection. The structure of the DSSRS antenna, which enables it to operate at the ISM band, makes it appropriate for tumor detection. Tumor detection in areas such as the breast and head operates on the same principle, where the backscatter from the $S_{11}$ parameter provides data for microwave imaging. This study utilized the same antenna for observing tumors in both the breast and head, demonstrating that the

proposed antenna performs very well in both applications, irrespective of gain variation. The proposed antenna is compact in size and has good impedance matching, radiation pattern, and gain while maintaining lower SAR values, making it suitable for use in applications involving wearable devices and breast and brain tumors. In addition, the antenna is tested (by simulation) in various bending scenarios. The antenna has almost the same agreement as the flat surface antenna in bending mode. Findings suggest that the developed compact textile antenna operating in the ISM band is a promising candidate for wearable applications. To validate this work, we conducted a benchmarking study comparing our results with similar studies in the literature. Tables 1 and 2 summarize comparisons based on material, gain, frequency band, and SAR values. Most studies provided simulated SAR readings, while measurements focused on VSWR, $S_{11}$, and gain. The results presented in this manuscript through simulation are consistent with those in the tables.

## ACKNOWLEDGMENT

The authors are very thankful to the International Islamic University Malaysia (IIUM) for the research group program under grant FRGS/1/2024/TK08/UIAM/02/1.

## REFERENCES

[1] M. M. H. Mahfuz *et al.*, "Wearable Textile Patch Antenna: Challenges and Future Directions," *IEEE Access*, vol. 10, pp. 38406–38427, 2022.

[2] S. Noor, N. Ramli, and N. Liyana Hanapi, "A Review of the Wearable Textile-Based Antenna using Different Textile Materials for Wireless Applications," *Open J. Sci. Technol.*, vol. 3, no. 3, Art. no. 3, Oct. 2020.

[3] K. N. Paracha, S. K. Abdul Rahim, P. J. Soh, and M. Khalily, "Wearable Antennas: A Review of Materials, Structures, and Innovative Features for Autonomous Communication and Sensing," *IEEE Access*, vol. 7, pp. 56694–56712, 2019.

[4] S. G. Kirtania *et al.*, "Flexible Antennas: A Review," *Micromachines*, vol. 11, no. 9, Art. no. 9, Sep. 2020.

[5] M. U. Ali Khan, R. Raad, F. Tubbal, P. I. Theoharis, S. Liu, and J. Foroughi, "Bending Analysis of Polymer-Based Flexible Antennas for Wearable, General IoT Applications: A Review," *Polymers*, vol. 13, no. 3, Art. no. 3, Jan. 2021.

[6] D. N. Elsheakh, R. A. Mohamed, O. M. Fahmy, K. Ezzat, and A. R. Eldamak, "Complete Breast Cancer Detection and Monitoring System by Using Microwave Textile Based Antenna Sensors," *Biosensors*, vol. 13, no. 1, p. 87, 2023.

[7] A. R. Chishti *et al.*, "Optically Transparent Antennas: A Review of the State-of-the-Art, Innovative Solutions and Future Trends," *Appl. Sci.*, vol. 13, no. 1, Art. no. 1, Jan. 2023.

[8] K. Ghaffarzadeh and J. Hayward, "Stretchable and Conformable Electronics: Heading Toward Market Reality," *Inf. Disp.*, vol. 33, no. 6, pp. 28–31, Nov. 2017.

[9] K. S, N. R, and K. Venusamy, "Recent Trends in Microstrip Patch Antenna Using Textile Applications," Computer-Assisted Learning for Engaging Varying Aptitudes: From Theory to Practice. Accessed: Jan. 13, 2023.

[10] T. Nahar and S. Rawat, "A Survey on Wearable Antenna Used for Defense Applications," in *Flexible Electronics for Electric Vehicles*, S. Dwivedi, S. Singh, M. Tiwari, and A. Shrivastava, Eds., in Lecture Notes in Electrical Engineering. Singapore: Springer Nature, 2023, pp. 121–130.

[11] N. Vikram, R. S. Sabeenian, M. Nandhini, and V. Visweeshwaran, "Design and Implementation of Microstrip Patch Antenna for Biomedical Application," in *International Conference on Innovative Computing and Communications*, D. Gupta, A. Khanna, S. Bhattacharyya, A. E.

Hassanien, S. Anand, and A. Jaiswal, Eds., in Lecture Notes in Networks and Systems. Singapore: Springer Nature, 2023, pp. 613–620.

[12] S. Merugu, A. Kumar, and G. Ghinea, "Real-Time Health Monitoring Using Wearable Devices," in *Track and Trace Management System for Dementia and Intellectual Disabilities*, S. Merugu, A. Kumar, and G. Ghinea, Eds., in Advanced Technologies and Societal Change. , Singapore: Springer Nature, 2023, pp. 119–122.

[13] F. Amitrano, A. Coccia, L. Donisi, G. Pagano, G. Cesarelli, and G. D'Addio, "Gait Analysis using Wearable E-Textile Sock: an Experimental Study of Test-Retest Reliability," in *2021 IEEE International Symposium on Medical Measurements and Applications (MeMeA)*, Jun. 2021, pp. 1–6.

[14] M. M. Mahfuz, M. Islam, M. Habaebi, and J. Chebil, "Design of Wearable Textile Patch Antenna Using C-Shape Etching Slot," *Int. J. Interact. Mob. Technol. IJIM*, p. 2022, Apr. 2022.

[15] K. Guido and A. Kiourti, "Wireless Wearables and Implants: A Dosimetry Review," *Bioelectromagnetics*, vol. 41, no. 1, pp. 3–20, Jan. 2020.

[16] "ICNIRP." Accessed: Jan. 25, 2024. [Online]. Available: https://www.icnirp.org/en/differences.html

[17] A. M. Tripathi, P. K. Rao, and R. Mishra, "An AMC Inspired Wearable UWB Antenna for Skin Cancer Detection," in *2020 International Conference on Electrical and Electronics Engineering (ICE3)*, Feb. 2020, pp. 475–480.

[18] G. K. Soni, D. Yadav, and A. Kumar, "Design consideration and recent developments in flexible, transparent and wearable antenna technology: A review," *Trans. Emerg. Telecommun. Technol.*, vol. 35, no. 1, p. e4894, 2024.

[19] T. A. Karthikeyan, M. Nesasudha, S. Saranya, and B. Sharmila, "A review on fabrication and simulation methods of flexible wearable antenna for industrial tumor detection systems," *J. Ind. Inf. Integr.*, vol. 41, p. 100673, Sep. 2024.

[20] T. Saeidi *et al.*, "Miniaturized Spiral UWB Transparent Wearable Flexible Antenna for Breast Cancer Detection," in *2020 International Symposium on Networks, Computers and Communications (ISNCC)*, Oct. 2020, pp. 1–6.

[21] N. Narang, "Compact Wideband Microstrip Patch Antenna Design for Breast Cancer Detection," *Def. Sci. J.*, vol. 71, p. 352, May 2021.

[22] S. Bhavani and T. Shanmuganantham, "Wearable Antenna for Bio Medical Applications," in *2022 IEEE Delhi Section Conference (DELCON)*, Feb. 2022, pp. 1–5.

[23] N. Jebali, "Textile Ultra-Wide Band Antenna With X Band For Breast Cancer Detection," *Indian J. Sci. Technol.*, vol. 13, no. 11, pp. 1232–1242, Mar. 2020.

[24] Y. Rahayu and R. Saputra, "Design Strategy on Medical Wearable Antenna for Tumor Detection," in *2020 International Symposium on Antennas and Propagation (ISAP)*, Jan. 2021, pp. 105–106.

[25] S. Sinha, T.-S. R. Niloy, R. R. Hasan, Md. A. Rahman, and S. Rahman, "A Wearable Microstrip Patch Antenna for Detecting Brain Tumor," in *2020 International Conference on Computation, Automation and Knowledge Management (ICCAKM)*, Jan. 2020, pp. 85–89.

[26] A. T. Baklezos, C. D. Nikolopoulos, and C. N. Capsalis, "A Planar On-Body Antenna System for Cancerous Tumor Detection through Microwave Transmission Sensing," *J. Electr. Eng.*.

[27] U. Hasni, M. E. Piper, J. Lundquist, and E. Topsakal, "Screen-Printed Fabric Antennas for Wearable Applications," *IEEE Open J. Antennas Propag.*, vol. 2, pp. 591–598, 2021.

[28] W. Bouamra, I. Sfar, A. Mersani, L. Osman, and J. M. Ribero, "A Low-Profile Wearable Textile Antenna Using AMC for WBAN Applications at 5.8GHz," *Eng. Technol. Appl. Sci. Res.*, vol. 12, no. 4, pp. 9048–9055, Aug. 2022.

[29] V. R. Keshwani, P. P. Bhavarthe, and S. S. Rathod, "Eight shape electromagnetic band gap structure for bandwidth improvement of wearable antenna," *Prog. Electromagn. Res. C*, vol. 116, pp. 37–49, 2021.

[30] C. Loss, T. M. Silveira, P. Pinho, R. Salvado, and N. B. de Carvalho, "Design and Analysis of the Reproducibility of Wearable Textile Antennas," in *2020 12th International Symposium on Communication Systems, Networks and Digital Signal Processing (CSNDSP)*, Jul. 2020, pp. 1–5.

[31] P. Balaji and R. Narmadha, "Wearable E-shaped Textile Antenna for Biomedical Telemetry," in *2021 International Conference on Advances in Electrical, Computing, Communication and Sustainable Technologies (ICAECT)*, Feb. 2021, pp. 1–5.

[32] R. S. Campos and F. D. R. Henriques, "Performance evaluation of a microstrip wearable antenna considering on-body curvature," *Int. J. Eng. Sci.*, vol. 11, no. 10, pp. 8–19, 2021.

[33] P. Saha, D. Mitra, and S. K. Parui, "Control of Gain and SAR for Wearable Antenna Using AMC Structure," *Radioengineering*, vol. 30, no. 1, pp. 81–88, Apr. 2021.

[34] S. Kiani, P. Rezaei, and M. Fakhr, "A CPW-fed wearable antenna at ISM band for biomedical and WBAN applications," *Wirel. Netw.*, vol. 27, no. 1, pp. 735–745, Jan. 2021.

[35] D. Gopi, P. V. Kokilagadda, S. Gupta, and V. R. K. R. Dodda, "Asymmetric coplanar strip-fed textile-based wearable antenna for MBAN and ISM band applications," *Int. J. Numer. Model. Electron. Netw. Devices Fields*, vol. n/a, no. n/a, p. e2920.

[36] G. Narmadha, M. Malathi, S. A. Kumar, T. Shanmuganantham, and S. Deivasigamani, "Performance of implantable antenna at ISM band characteristics for biomedical base," *ICT Express*, vol. 8, no. 2, pp. 198–201, Jun. 2022.

[37] S. Alhuwaidi and T. Rashid, "A Novel Compact Wearable Microstrip Patch Antenna for Medical Applications," in *2020 International Conference on Communications, Signal Processing, and their Applications (ICCSPA)*, Mar. 2021, pp. 1–6.

[38] G. S. Deepthy and M. Nesasudha, "Analysis of substrate materials in microstrip antenna for biomedical applications," *Mater. Today Proc.*, Jan. 2023.

[39] C. A. Balanis, *Antenna Theory: Analysis and Design*. John Wiley & Sons, 2016.

[40] D. M. G. Preethichandra, L. Piyathilaka, U. Izhar, R. Samarasinghe, and L. C. De Silva, "Wireless Body Area Networks and Their Applications – A Review," *IEEE Access*, pp. 1–1, 2023.

[41] F. Khajeh-Khalili and Y. Khosravi, "A novel wearable wideband antenna for application in wireless medical communication systems with jeans substrate," *J. Text. Inst.*, vol. 112, no. 8, pp. 1266–1272, Aug. 2021.

[42] M. Faisal, A. Gafur, S. Z. Rashid, Md. O. Shawon, K. I. Hasan, and Md. B. Billah, "Return Loss and Gain Improvement for 5G Wireless Communication Based on Single Band Microstrip Square Patch Antenna," in *2019 1st International Conference on Advances in Science, Engineering and Robotics Technology (ICASERT)*, Dhaka, Bangladesh: IEEE, May 2019, pp. 1–5.

[43] V. Karthik and T. Rama Rao, "Investigations on SAR and Thermal Effects of a Body Wearable Microstrip Antenna," *Wirel. Pers. Commun.*, vol. 96, no. 3, pp. 3385–3401, Oct. 2017.

[44] N. Sharma, A. Kumar, A. De, and R. K. Jain, "Design of compact hexagonal shaped multiband antenna for wearable and tumor detection applications," *Prog. Electromagn. Res. M*, vol. 105, pp. 205–217, 2021.

[45] J. E. Lara, A. Vera, and L. Leija, "Proposal for the application of microwave ablation as a treatment for breast cancer using interstitial applicators: Antenna design and FEM modeling," in *2016 Global Medical Engineering Physics Exchanges/Pan American Health Care Exchanges (GMEPE/PAHCE)*, Apr. 2016, pp. 1–6.

[46] K. Kerlikowske, C. C. Gard, B. L. Sprague, J. A. Tice, and D. L. Miglioretti, "One versus Two Breast Density Measures to Predict 5- and 10-Year Breast Cancer Risk," *Cancer Epidemiol. Biomarkers Prev.*, vol. 24, no. 6, pp. 889–897, Jun. 2015.

[47] H. Been Lim, N. Thi Tuyet Nhung, E.-P. Li, and N. Duc Thang, "Confocal Microwave Imaging for Breast Cancer Detection: Delay-Multiply-and-Sum Image Reconstruction Algorithm," *IEEE Trans. Biomed. Eng.*, vol. 55, no. 6, pp. 1697–1704, Jun. 2008.

[48] A. Alikhassi *et al.*, "False-positive incidental lesions detected on contrast-enhanced breast MRI: clinical and imaging features," *Breast Cancer Res. Treat.*, Feb. 2023.

[49] A. Ashyap *et al.*, "Inverted E-Shaped Wearable Textile Antenna for Medical Applications," *IEEE Access*, vol. PP, pp. 1–1, Jun. 2018.

[50] K. Wang and J. Li, "Jeans Textile Antenna for Smart Wearable Antenna," in *2018 12th International Symposium on Antennas, Propagation and EM Theory (ISAPE)*, Dec. 2018, pp. 1–3.

[51] P. M. Potey and K. Tuckley, "Design of wearable textile antenna for low back radiation," *J. Electromagn. Waves Appl.*, vol. 34, no. 2, pp. 235–245, Jan. 2020.

[52] A. Y. I. Ashyap *et al.*, "Fully Fabric High Impedance Surface-Enabled Antenna for Wearable Medical Applications," *IEEE Access*, vol. 9, pp. 6948–6960, 2021.

[53] A. Yadav, V. Kumar Singh, A. Kumar Bhoi, G. Marques, B. Garcia-Zapirain, and I. de la Torre Díez, "Wireless Body Area Networks: UWB Wearable Textile Antenna for Telemedicine and Mobile Health Systems," *Micromachines*, vol. 11, no. 6, Art. no. 6, Jun. 2020.

https://doi.org/10.31436/iiumej.v26i1.3230

# MODEL PREDICTIVE CONTROL-BASED ENERGY MANAGEMENT SYSTEM WITH LOAD CURTAILMENT FOR STANDALONE MICROGRID

**MUHAMMAD SHARIR FATHULLAH BIN MOHD YUNUS[1], SITI HAJAR YUSOFF[1], SITI NADIAH MOHD SAPIHIE[2], MOHD SHAHRIN BIN ABU HANIFAH[1], TEDDY SURYA GUNAWAN[1], SURIZA AHMAD ZABIDI[1]**

*[1]Department of Electrical and Computer Engineering, Kulliyyah of Engineering, International Islamic University Malaysia, Kuala Lumpur, Malaysia*
*[2]Petronas Research Sdn Bhd, Bandar Baru Bangi, Malaysia*

**Corresponding author: fathullah.sharir@gmail.com*

*(Received: 19 March 2024; Accepted: 16 September 2024; Published online: 10 January 2025)*

***ABSTRACT:*** The standalone microgrid emerges as an economical solution for providing electricity to remote areas disconnected from the main grid. However, the intermittent nature of renewable energy sources (RES) and unpredictable load demands can disrupt its balance. Diesel generators are commonly used to supply auxiliary power and serve as a backup for the microgrid. Nevertheless, inefficient utilization of diesel generators can lead to high operational costs, shortened lifespan, and environmental pollution. An energy management system (EMS) is implemented to optimize the operational cost and reliability of the microgrid by incorporating model predictive control (MPC), which has grown in popularity in recent years due to its ability to support multiple inputs and multiple outputs. The MPC-based EMS is developed using MATLAB/Simulink software, with the optimization problem formulated using mixed integer quadratic programming (MIQP). A comparative analysis is conducted between the MPC-based EMS with and without load curtailment capability, revealing a significant improvement of 52.21% in diesel fuel cost savings with the inclusion of load curtailment capability.

***ABSTRAK:*** Grid mikro berdiri sendiri muncul sebagai penyelesaian ekonomi untuk menyediakan perkhidmatan elektrik kepada kawasan terpencil yang jauh daripada grid utama. Walau bagaimanapun, ciri-ciri ketidaktentuan sumber tenaga boleh diperbaharui (RES) dan permintaan beban yang tidak dapat diramalkan boleh mengganggu keseimbangan dalam grid mikro. Jentera diesel selalunya digunakan untuk menyediakan kuasa tambahan dan berfungsi sebagai sandaran untuk grid mikro. Namun begitu, penggunaan jentera diesel yang tidak cekap boleh menyebabkan kos operasi yang berlebihan, pengurangan jangka hayat dan pencemaran alam sekitar. Pengurusan tenaga (EMS) dilaksanakan untuk mengoptimumkan kos operasi grid mikro dan kebolehpercayaan dengan menggunakan kawal perkiraan model (MPC) yang semakin popular kerana keupayaannya dalam menyokong input dan output yang pelbagai. EMS berasaskan MPC dibangunkan menggunakan perisian MATLAB/Simulink, dengan masalah pengoptimuman diformulasikan menggunakan pengaturcaraan kuadratik berbilangan campuran (MIQP). Analisis perbandingan dijalankan antara EMS berasaskan MPC dengan dan tanpa keupayaan pemangkasan beban, yang mendedahkan pengurangan yang signifikan sebanyak 52.21% dalam penjimatan kos bahan api diesel dengan penambahan keupayaan pemangkasan beban.

***KEYWORDS:*** *Model Predictive Control (MPC), Energy Management System (EMS), Microgrid, Mixed Integer Quadratic Programming (MIQP), Load Curtailment*

https://doi.org/10.31436/iiumej.v26i1.3230

# 1. INTRODUCTION

Increased energy demand, environmental pollution, and high costs are some reasons why renewable energy sources (RES), such as solar photovoltaics (PV), wind energy, and others, have emerged in popularity to replace the traditional energy generation sources [1]. RES has become the first choice to replace the infeasible traditional energy sources due to their clean nature, abundance availability, and low cost. However, RES is heavily dependent on environmental conditions. Hence, RES poses some uncertainties in the energy generation. Microgrid is introduced to properly manage the RES to overcome the impact of these uncertainties [2-4].

A microgrid is a structure that incorporates distributed energy resources (DER), either renewable or non-renewable energy sources, with other components such as energy storage systems (ESS) to meet the load demand [2]. The Department of Energy of the United States of America defines a microgrid as " a group interconnected loads and distributed energy resources (DERs) within clearly defined electrical boundaries that act as a single controllable entity with respect to the grid and can operate in grid-connected and island mode" [5]. Microgrids can be categorized into grid-connected and islanded modes. The difference between these two modes is the connection or disconnection of the microgrid from the grid through the point of common coupling [1, 2]. The islanded microgrid can also be considered a standalone or isolated microgrid due to the unavailability of the main grid.

The intermittent nature of RES and the unpredictable nature of load can cause instability in the microgrid. In addition, the inefficient usage of non-renewable energy sources such as diesel generators can cause immediate wear and tear, shorten the life span, and pollute the environment [6]. Hence, an energy management system (EMS) is introduced for efficient DER management in the microgrid. According to [7], EMS can help maintain the supply and demand in the microgrid, improve reliability, and reduce energy production costs, especially for non-renewable energy sources such as diesel generators. While researchers have developed various EMS techniques for microgrids, model predictive control (MPC) has emerged as a particularly popular approach within the research community [8]. This is due to its capability to forecast the dynamic of the system, thus reducing the uncertainty in managing the microgrid [1, 9]. This will improve the overall operation of the microgrid in terms of operational cost and efficiency.

MPC does not relate to a specific control strategy but rather a group of control approaches that take full use of the system model under certain constraints to generate control signals or directives by minimizing predetermined cost functions [10]. Some advantages of MPC are the ability to handle multiple inputs and multiple outputs (MIMO) and allow the plant constraints to be defined explicitly, unlike other control approaches. However, MPC needs the control system designer to understand the system to create an accurate model thoroughly. In addition, MPC requires powerful processing since it is computationally expensive [8].

Demand Side Management (DSM) is a part of the branches under the EMS. DSM is important for EMS in microgrids since it helps relax the tightness of an optimization problem, improving the load patterns and reducing the peak load demand in the microgrid [11]. DSM is important, especially in standalone microgrids, since it relies only on the energy sources available in the microgrid. Figure 1 shows some of the side management techniques [12]. Load shedding or curtailment is one of the famous techniques under DSM, and it can help in reducing the operational cost in the microgrid [13]. Many papers have been observed focusing on developing MPC-based EMS for standalone microgrids.

https://doi.org/10.31436/iiumej.v26i1.3230

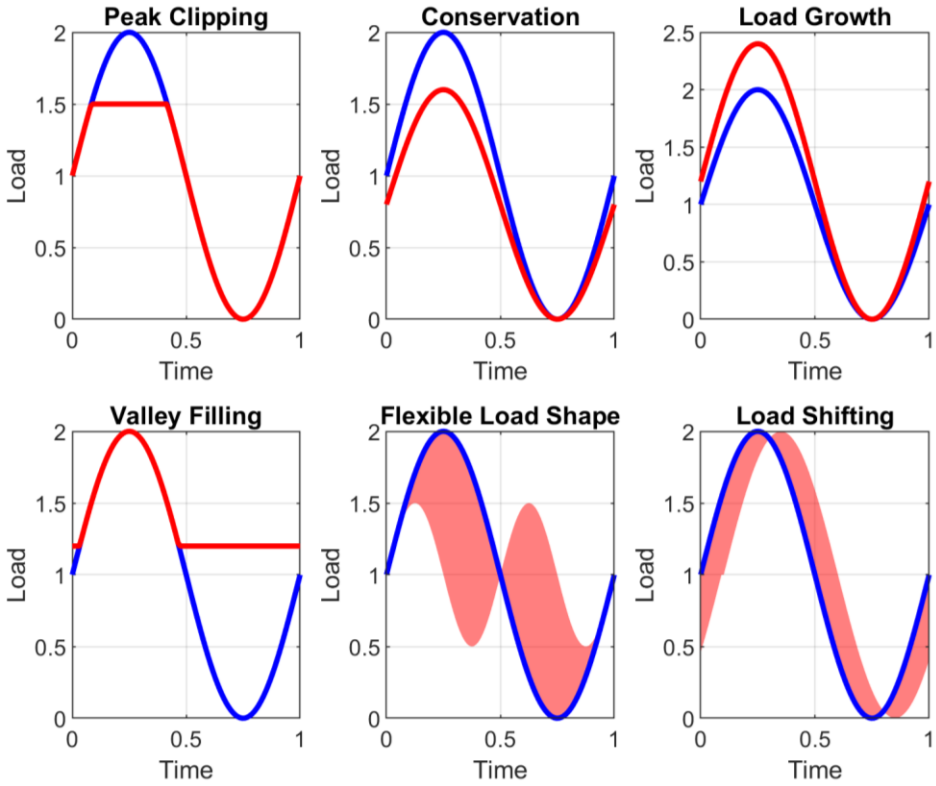


Figure 1. Demand Side Management Techniques

Several research, such as [14] and [15] has been observed implementing load curtailment in the standalone microgrid. [14] utilized MPC in their EMS to implement load curtailment to minimize the operation cost of the diesel generator. On the other hand, load curtailment is utilized in [15] to manage power balance by decreasing the reliance on diesel generators. However, these two papers focus on industrial microgrid and electric vehicle applications. In contrast, studies [6], [16], [17], [18] and [19] stated that a standalone residential microgrid indicates no load curtailment is implemented. Authors in [20] while not implementing load curtailment, the authors penalized the unmet demand and curtailed the PV power output. According to [6], this move defeats the microgrid's purpose, where the RES's power consumption should be maximized. Properly sizing the microgrid at the design stage helps prevent unmet demand and RES curtailment. Correctly sizing the microgrid components ensures that energy can be delivered to meet demand effectively in all situations [21].

This paper simulates MPC-based EMS with load curtailment for a standalone microgrid using MATLAB/Simulink. The standalone microgrid comprises solar PV, battery ESS, diesel generators, and loads for residential applications. The MPC-based EMS is intended to reduce the fuel cost of the diesel generator through load curtailment and ensure the power balance in the standalone residential microgrid. A comparison is made between MPC-based EMS without load curtailment and load curtailment under residential usage.

## 2. METHODOLOGY

### 2.1. Microgrid Design

In this paper, a standalone AC/DC microgrid is considered. Figure 2 shows the standalone microgrid. Solar PV is the primary energy generation source and is set in maximum power point tracking (MPPT) mode. This ensures that the maximum power is extracted from the solar

https://doi.org/10.31436/iiumej.v26i1.3230

PV. A diesel generator will be acting as a backup energy generation source. Its usage should be minimized to reduce operational costs and protect the environment. The BESS is used to store the excess energy produced by solar PV and release the energy when the solar PV is unable to meet the demand. When solar PV and BESS are unable to meet the demand, diesel generators will be turned on to aid in ensuring the power balance is met.

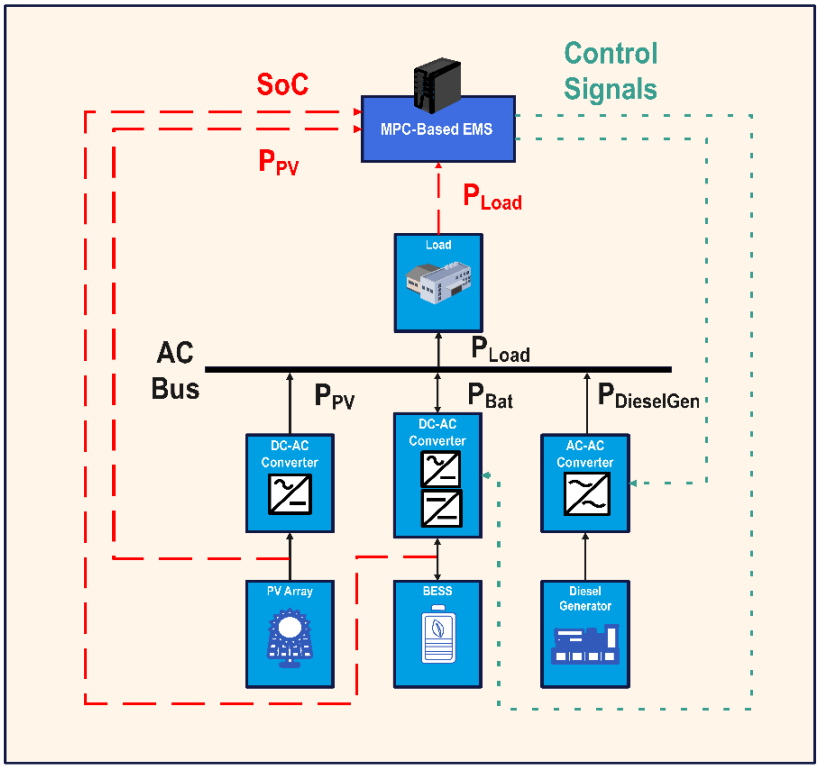


Figure 2. Proposed Standalone Microgrid

From Figure 2, MPC-based EMS collects information such as the current power output of solar PV, $P_{PV}$, current BESS power, $P_{Bat}$, current load, $P_{Load}$ and the BESS's current state of charge (SoC). This information will be processed to generate the optimal control signals for the BESS, diesel generator, and load.

## 2.2. System Modelling

The BESS considered in this paper is a Lithium-ion (Li-Ion) battery. The dynamic model of the BESS can be represented as the SoC of the BESS. There are many ways to model the SoC of the BESS. One of the methods is the Coulomb Counting method. The dynamic model of BESS is shown in Eq. (1) [22, 23].

$$SoC(k+1) = SoC(k) + \frac{P_{Bat}^{discharging}(k).T_s}{C_{Bat}^{max}} - \frac{P_{Bat}^{charging}(k).T_s}{C_{Bat}^{max}} \quad (1)$$

where $SoC(k+1)$ is the SoC of the BESS at the next time step, $SoC(k)$ is the current SoC of the BESS, $P_{Bat}^{discharging}(k)$ and $P_{Bat}^{charging}(k)$ are the current discharging and charging battery power in watts, respectively, $T_s$ is the sampling time in hours and $C_{Bat}^{max}$ is the maximum capacity of the battery in watt-hours. The efficiency of the power converter, as well as the charging and discharging efficiency, need to be considered in the model. Furthermore, the dynamic model can be divided to show the SoC of the BESS when charging and discharging mode. This is shown in Eq. (2).

https://doi.org/10.31436/iiumej.v26i1.3230

$$SoC(k+1) = \begin{cases} SoC(k) - \frac{P_{Bat}(k).T_S.\eta_{charging}}{C_{Bat}^{max}} & if\ P_{Bat}(k) < 0 \\ SoC(k) - \frac{P_{bat}(k).T_S}{C_{Bat}^{max}.\eta_{discharging}} & if\ P_{Bat}(k) \geq 0 \end{cases} \quad (2)$$

where $\eta_{charging}$ and $\eta_{discharging}$ represents the product of BESS charging and discharging efficiency and power converter efficiency, respectively. Eq. (2) is a hybrid dynamical model where the system's dynamic changes according to the power flow from and to the BESS and cannot be used directly in the optimization problems [6]. It needs to be converted into a mixed logical dynamic (MLD) where a particular model form can be represented using the Boolean variable. The MLD model of the BESS Is shown in Eq. (3) [6].

$$oC(k+1) = SoC(k) + \frac{T_S}{C_{Bat}^{max}}.Z_{Bat}(k).\left(\eta_{charging} - \frac{1}{\eta_{discharging}}\right) - \frac{T_S.\eta_{charging}}{C_{Bat}^{max}}P_{Bat}(k) \quad (3)$$

where $Z_{Bat}(k)$ is an auxiliary variable, which $Z_{Bat}(k) = \delta_{Bat}(k).P_{Bat}(k)$. $\delta_{bat}(k)$ is the Boolean variable, and $\delta_{Bat}(k) \in \{0,1\}$. When $[\delta_{Bat}(k) = 1] \leftrightarrow [P_{Bat}(k) < 1]$. The BESS will be set to charging mode when $\delta_{Bat}(k)$ is equal to 1 and vice versa. The auxiliary variable is introduced to ensure the formulation is linear. The constraints for BESS model are listed in equation (4) – (9) [6].

$$-P_{Bat}^{min}.\delta_{Bat} \leq P_{Bat} - P_{Bat}^{min} \quad (4)$$

$$-P_{Bat}^{max}.\delta_{Bat} \leq -P_{Bat} \quad (5)$$

$$Z_{Bat} \leq P_{Bat}^{max}.\delta_{Bat} \quad (6)$$

$$Z_{Bat} \geq P_{Bat}^{min}.\delta_{Bat} \quad (7)$$

$$Z_{Bat} \leq P_{Bat} + P_{Bat}^{max}.(1 - \delta_{Bat}) \quad (8)$$

$$Z_{Bat} \geq P_{Bat} + P_{Bat}^{min}.(1 - \delta_{Bat}) \quad (9)$$

This paper does not consider the detailed model of the diesel generator. The diesel generator is assumed to be fast-acting and has low start-up time. The constraint of the diesel generator is defined as the minimum and maximum power output that can be generated by the diesel generator. The constraints are shown in Eq. (10) and Eq. (11) [6].

$$P_{DiseselGen}^{min}\delta_{DieselGen} \leq P_{DieselGen} \quad (10)$$

$$P_{DieselGen} \leq P_{DieselGen}^{max}\delta_{DieselGen} \quad (11)$$

where $\delta_{DieselGen}(k)$ is the Boolean variable, and $\delta_{DieselGen}(k) \in \{0,1\}$. The diesel generator is ON and OFF when $\delta_{DieselGen}(k) = 1$ and when $\delta_{DieselGen}(k) = 0$ respectively. The diesel generator can operate by generating output power ranging from $P_{DieselGen}^{min}$ until $P_{DieselGen}^{max}$ when in ON mode while output none when in OFF mode.

The constraint for the load curtailment is shown in Eq. (12) [15]. The load curtailment cannot exceed a specified value.

$$P_{Curtail}^{min} \leq P_{Curtail}(k) \leq P_{Curtail}^{max} \quad (12)$$

https://doi.org/10.31436/iiumej.v26i1.3230

where $P_{Curtail}^{min}$ and $P_{Curtail}^{max}$ are the minimum and maximum power that can be curtailed by the EMS, respectively.

The power balance in the microgrid should always be met and cannot be violated. The equality equation in Eq. (13) shows the power balance equation for the microgrid.

$$P_{PV}(k) + P_{Bat}(k) + P_{Dieselgen}(k) = P_{Load}(k) - P_{Curtail}(k) \quad (13)$$

$P_{PV}(k)$ is the PV output power, $P_{Bat}(k)$ is the BESS output power, $P_{DieselGen}(k)$ is the diesel generator output power, $P_{Load}(k)$ is the load consumption power and $P_{Curtail}(k)$ is the load curtailment power. The power flow considered is that power is positive when flowing into the grid while negative when flowing out from the grid.

### 2.3. Objective Functions

The first objective function is to minimize the fuel cost of the diesel generator. For this, the fuel consumption of the diesel generator needs to be reduced by efficiently using the diesel generator. The fuel cost function of the diesel generator can be represented by the quadratic cost curve (QCC) [24]. Equation (14) shows the fuel cost function equation of the diesel generator.

$$J_{DG} = C_{DieselGen}.[a.P_{DieselGen}(k)^2 + b.P_{DieselGen}(k) + c] \quad (14)$$

where $P_{DieselGen}(k)$ is diesel generator power output. $a, b$ and $c$ are the fuel cost coefficients. $C_{DieselGen}$ is the cost of the diesel. The QCC is illustrated in Figure 3.

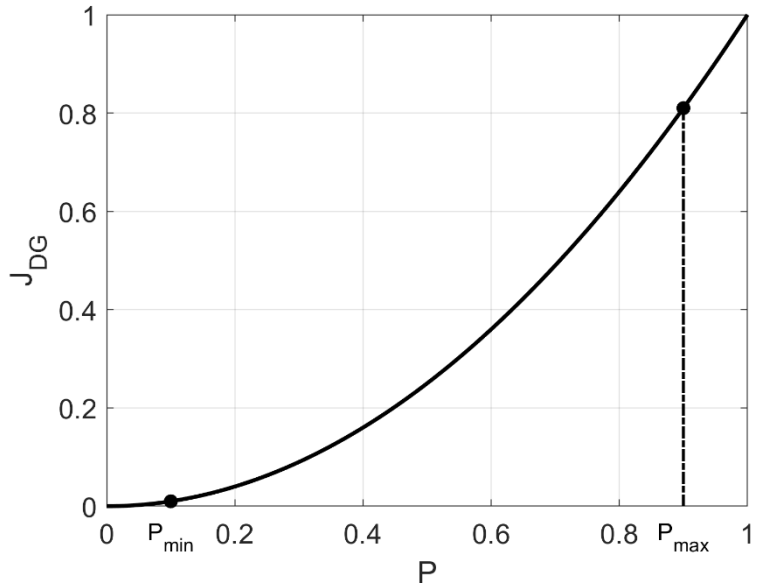


Figure 3. Quadratic Cost Curve

Figure 3 illustrates that when the diesel generator power delivered to the grid decreases, the fuel cost required while the generator runs also decreases. If the diesel generator is not supplying power to the grid, the fuel cost is zero. It is advisable to either switch off the diesel generator most of the time or to provide the grid with less electricity.

Next, the second objective is to guarantee that the BESS's SoC always follows the reference SoC value. This ensures that there will always be reserved energy in the BESS. The

https://doi.org/10.31436/iiumej.v26i1.3230

SoC reference value is recommended to be between the minimum and maximum SoC. The objective function is shown in Eq. (15).

$$J_{Bat} = \left[SoC\ (k+1) - SoC_{ref}\right]^2 \tag{15}$$

where $SoC\ (k+1)$ is the future or predicted SoC value and $SoC_{ref}$ is the reference SoC value. Lastly, the third objective is to reduce greenhouse gas emissions due to the burning of diesel fuel [25]This is represented in Eq. (16). Burning diesel fuel from the diesel generator releases greenhouse gases into the atmosphere. Reducing the microgrid's diesel generator usage can reduce this.

$$J_{GHG} = \left[\alpha_{NO_x}\mu_{NO_x} + \alpha_{CO_2}\mu_{CO_2} + \alpha_{CO}\mu_{CO} + \alpha_{SO_2}\mu_{SO_2}\right].P_{DieselGen}(k) \tag{16}$$

where $\alpha$ is the emission factor of a greenhouse gas expressed in $kg/kWh$. $\mu$ is the environmental damage cost due to the gas emission expressed in $RM/kg$. $P_{DieselGen}(k)$ is DG power output. $NO_x$, $CO_2$, $CO$ and $SO_2$ are nitric oxide, nitrogen dioxide, carbon dioxide, carbon monoxide, and sulfur dioxide.

The overall objective functions can be formulated as in Eq. (17). It can be observed that the cost function of the BESS, $J_{Bat}$, is the only cost function defined with error square optimization, while other cost functions, $J_{DieselGen}$ and $J_{GHG}$ are not. The $J_{Bat}$ is intended to ensure that the EMS always maintains the SoC of the BESS according to the reference. In contrast, the other cost functions can vary if their constraints are not violated. However, depending on the weights assigned to each cost function, the optimization might focus on a specific cost function instead of balancing all of them [26].

$$J_{Global} = J_{DieselGen} + J_{Bat} + J_{GHG} \tag{17}$$

### 2.4. Optimization Using Mixed Integer Quadratic Programming (MIQP) under MPC Framework

The overall optimization problem can be formulated by combining the system model, constraints, and objective functions discussed in previous sections.

| | |
|---|---|
| **Minimize** | Eq. (17) |
| **Subject to** | BESS Model: Eq. (3) |
| | BESS Constraints: Eq. (4) – Eq. (9) |
| | Diesel Generator Constraints: Eq. (10) – Eq. (11) |
| | Load Curtailment Constraint: Eq. (12) |
| | Power Balance: Eq. (13) |

https://doi.org/10.31436/iiumej.v26i1.3230

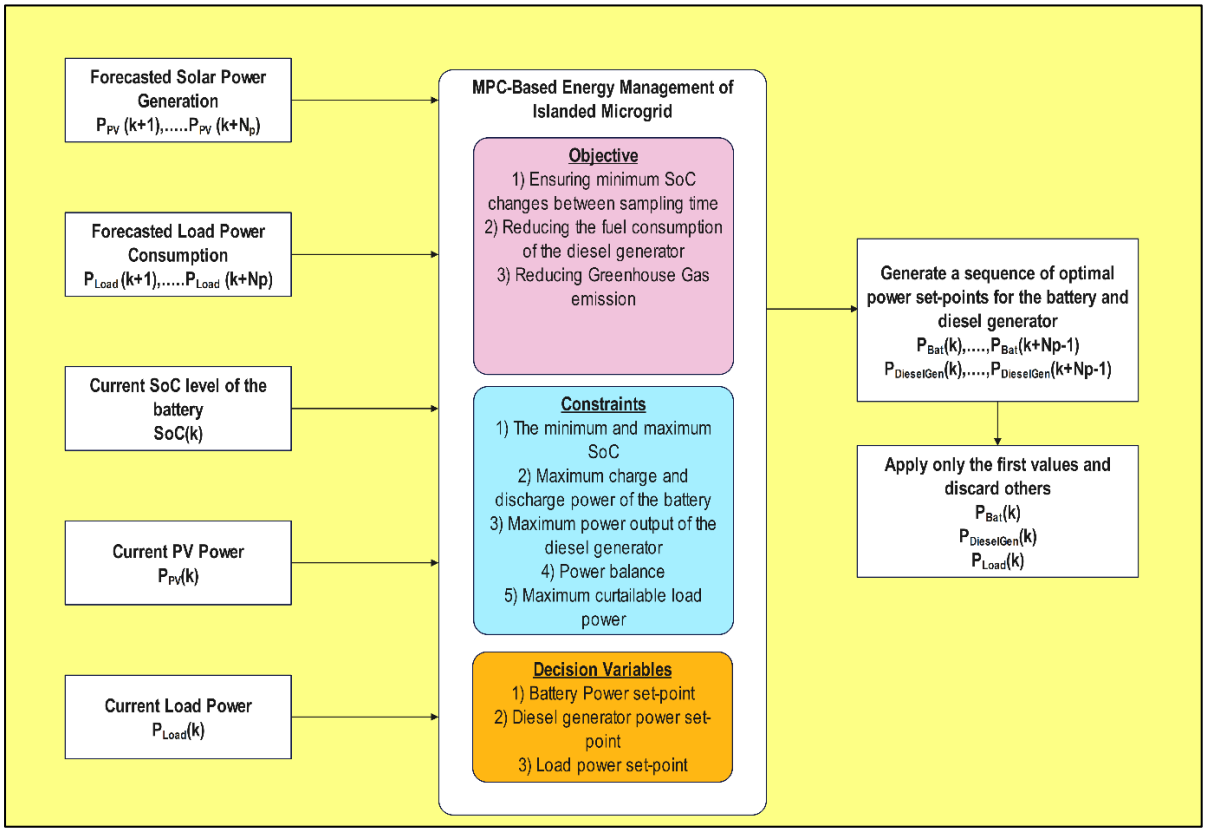


Figure 4. MPC-Based EMS of Islanded Microgrid

From Figure 4, the optimization problem is solved, and the optimal input sequence for the prediction horizon $N_p$ is obtained. Although a complete sequence of $N_p$ is computed, only the first element is sent to the system, and the remaining optimal values are discarded. The prediction horizon is shifted at the following sample time, and the optimization problem is solved again with EMS collecting a new information value from the microgrid.

In this paper, MPC-based EMS is developed by using MATLAB software. CPLEX is utilized to solve the energy management optimization problem. CPLEX is a mathematical optimization software package developed by IBM, and CPLEX version 12.10 is employed, which is the most recent version to support MATLAB integration. CPLEX is used to solve the MIQP optimization problem due to the unavailability of the MIQP solver in MATLAB. Multiple commercial solvers, such as CPLEX, Gurobi, etc., are available. CPLEX is chosen due to its extensive documentation and easy integration [6].

### 2.5. Solar PV Generation Forecasting and Load Forecasting

In this paper, future solar PV generation and the load demand are certainly known. With this, solar PV generation forecasting and load demand forecasting are perfect with no uncertainty. The MPC-based EMS may not be able to be tested for its robustness due to the absence of uncertainty, especially in real-time systems. However, according to [27], the MPC-based EMS can perform excellently with or without uncertainty factors in forecasting generation and load demand.

https://doi.org/10.31436/iiumej.v26i1.3230

## 3. RESULT AND DISCUSSION

The microgrid, cost, and simulation parameters are listed in Tables 1, 2, and 3. The solar PV generation and load demand data are obtained from [28]. The dataset consists of residential load and PV systems with a 1-minute resolution. This paper resamples the dataset into a 1-hour interval for 72 hours. Figures 5 and 6 show the profile of solar PV generation and load demand.

Table 1. Microgrid Parameters

| Microgrid Parameters | Value |
|---|---|
| $C_{bat}^{max}$ | 9 $kWh$ |
| $P_{bat}^{min}$, $P_{bat}^{max}$ | -3 $kW$, 3 $kW$ |
| $SoC_{initial}, SoC_{min}, SoC_{max}, SoC_{ref}$ | 50%, 10%, 80%, 50% |
| $\eta_{charge}, \eta_{discharge}$ | 0.95, 0.95 |
| $P_{DG}^{min}$, $P_{DG}^{max}$ | 1 $kW$, 5 $kW$ |
| $P_{CURTAIL}^{min}$, $P_{CURTAIL}^{max}$ | 0 $kW$, 30% of load demand of that interval $(kW)$ |

Table 2. Cost Functions Parameters

| Cost Parameters | Value |
|---|---|
| Weight of BESS Cost Function, $\lambda_1$ | 1 |
| Weight of Fuel Consumption Cost Function, $\lambda_2$ | 70 |
| Weight of Greenhouse Emission Cost Function, $\lambda_3$ | 475.17 |
| $a$ | 2.5 $\frac{L}{kWh^2}$ |
| $b$ | -1.375 $\frac{L}{kWh}$ |
| $c$ | 0.7813 $\frac{L}{h}$ |
| $C_{DG}$ | 2.05 $\frac{RM}{L}$ |
| $\alpha_{CO_2}$ | 0.232037 $\frac{kg}{kWh}$ |
| $\alpha_{NO_x}$ | 0.00431 $\frac{kg}{kWh}$ |
| $\alpha_{CO}$ | 0.00233 $\frac{kg}{kWh}$ |
| $\alpha_{SO_2}$ | 0.00464 $\frac{kg}{kWh}$ |
| $\mu_{NO_x}$ | 1.27 $\frac{RM}{kg}$ |
| $\mu_{CO_2}$ | 0.0057 $\frac{RM}{kg}$ |
| $\mu_{CO}$ | 0.10 $\frac{RM}{kg}$ |
| $\mu_{SO_2}$ | 0.57 $\frac{RM}{kg}$ |

Table 3. Simulation Parameters

| Simulation Parameters | Value |
|---|---|
| Sampling Time, $T_s$ | 1 Hour |
| Simulation Duration | 72 Hours |
| Prediction Horizon, $N_P$ | 24 Hours |

https://doi.org/10.31436/iiumej.v26i1.3230

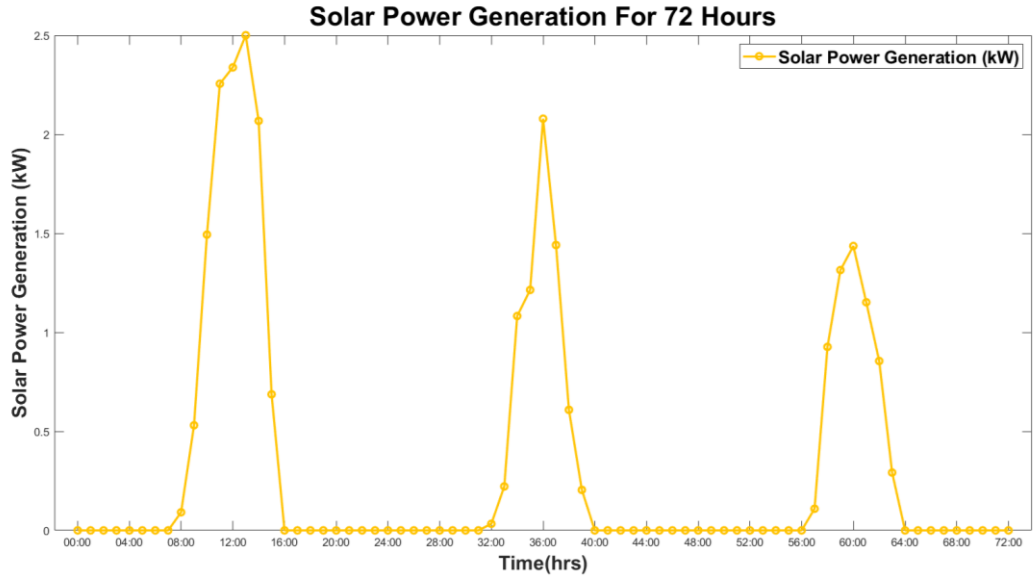


Figure 5. Solar PV Generation Profile

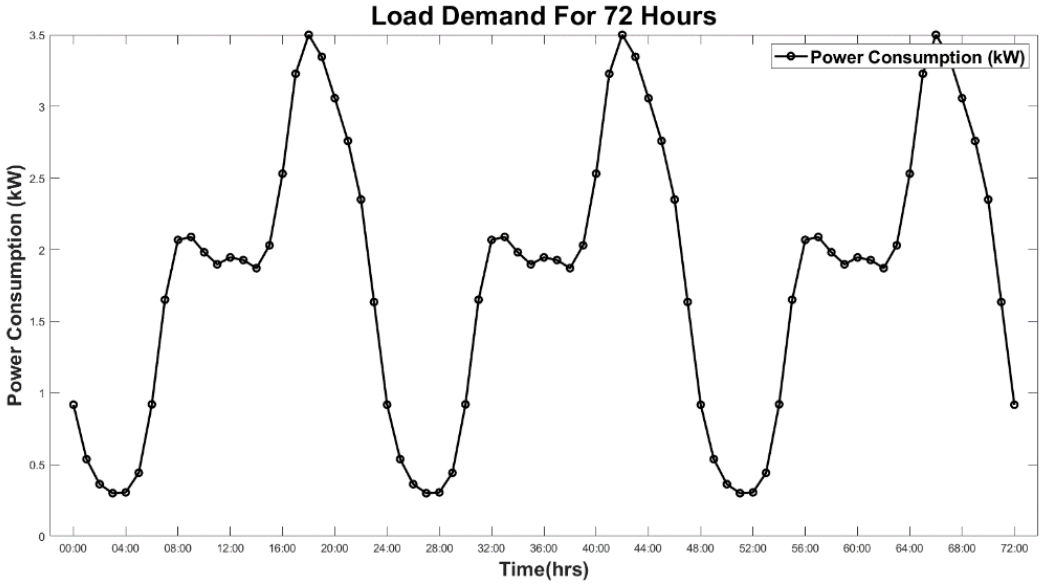


Figure 6. Load Demand Profile

The BESS cost function is assigned a weight of 1, while the fuel consumption cost function and greenhouse gas emission cost function are given weights of 70 and 475.17, respectively. This allocation of weights aims to balance the final cost value, accounting for the difference between the fuel cost and greenhouse gas emission cost, which are 2.05 $\frac{RM}{L}$ and 0.302 $\frac{RM}{kWh}$ respectively.

https://doi.org/10.31436/iiumej.v26i1.3230

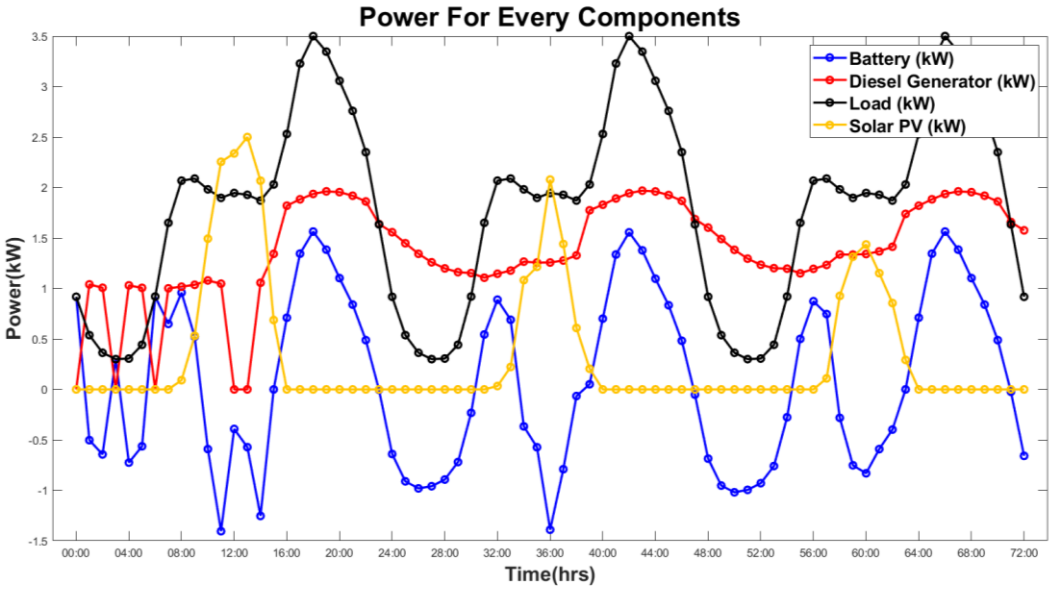


Figure 7. Energy Profile for All Components for MPC-Based EMS Without Load Curtailment

Table 2. Power Set-Point for Every Component for MPC-Based EMS Without Load Curtailment for the first 24 hours

| Time (h) | $P_{PV}$ $(kW)$ | $P_{DG}$ $(kW)$ | $P_{BESS}$ $(kW)$ | $P_{Loads}$ $(kW)$ |
|---|---|---|---|---|
| 00:00 | 0 | 0 | 0.9176 | 0.9176 |
| 01:00 | 0 | 1.0403 | -0.5027 | 0.5375 |
| 02:00 | 0 | 1.0069 | -0.6438 | 0.3631 |
| 03:00 | 0 | 0 | 0.3 | 0.3 |
| 04:00 | 0 | 1.0306 | -0.7249 | 0.3057 |
| 05:00 | 0 | 1.0057 | -0.5636 | 0.4422 |
| 06:00 | 0 | 0 | 0.9202 | 0.9202 |
| 07:00 | 0 | 1.0012 | 0.6492 | 1.6505 |
| 08:00 | 0.0916 | 1.0179 | 0.9587 | 2.0681 |
| 09:00 | 0.5307 | 1.0365 | 0.5216 | 2.0888 |
| 10:00 | 1.4934 | 1.0795 | -0.5911 | 1.9818 |
| 11:00 | 2.2552 | 1.0471 | -1.4047 | 1.8976 |
| 12:00 | 2.3377 | 0 | -0.3919 | 1.9458 |
| 13:00 | 2.5 | 0 | -0.5723 | 1.9277 |
| 14:00 | 2.0676 | 1.0566 | -1.2534 | 1.8708 |
| 15:00 | 0.6872 | 1.3433 | 0 | 2.0305 |
| 16:00 | 0 | 1.8203 | 0.7103 | 2.5306 |
| 17:00 | 0 | 1.8832 | 1.3450 | 3.2281 |
| 18:00 | 0 | 1.9363 | 1.5637 | 3.5 |
| 19:00 | 0 | 1.9619 | 1.3846 | 3.3465 |
| 20:00 | 0 | 1.9544 | 1.1030 | 3.0575 |
| 21:00 | 0 | 1.9188 | 0.8402 | 2.7590 |
| 22:00 | 0 | 1.8619 | 0.4880 | 2.35 |
| 23:00 | 0 | 1.6387 | -0.0040 | 1.6347 |
| 00:00 | 0 | 1.5574 | -0.6398 | 0.9176 |

https://doi.org/10.31436/iiumej.v26i1.3230

Figure 7 shows the energy profile for all components in MPC-based EMS without load curtailment, while Table 2 shows the power set-point for every component in MPC-based EMS without load curtailment for the first 24 hours. It shows that the MPC-based EMS effectively manages energy within the islanded microgrid. The constraints for all components, particularly the BES and diesel generator, are adhered to. The BESS maintains its charging and discharging power within the limits of 3 kW and -3 kW, respectively. Similarly, the diesel generator's output does not exceed the 5 kW threshold. The power balance is consistently maintained, as demonstrated in Table 2. Figure 8 illustrates the SoC of the BESS over 72 hours, showing that the SoC remains within the prescribed limits to prevent deep charging and discharging, as indicated in Table 4.5

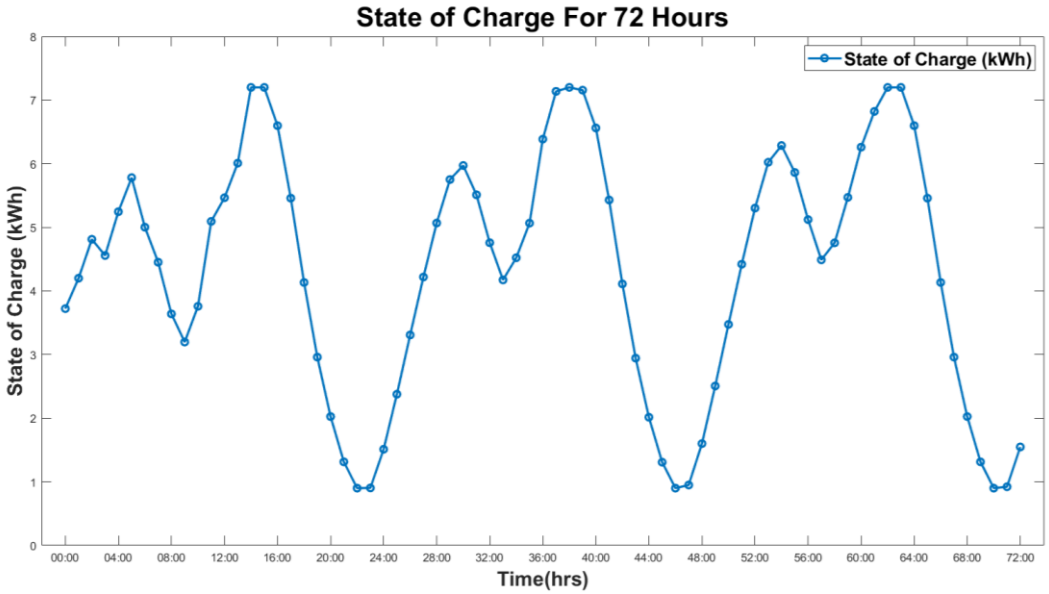


Figure 8. SoC of the BESS for MPC-Based EMS Without Load Curtailment

Figure 8 shows that the BESS charges whenever the solar PV generates power, typically between 8:00 AM and 3:00 PM. During this period, the EMS directs the BESS to store the excess energy, and the diesel generator either remains inactive or outputs minimal power, especially on subsequent days. The stored energy is utilized from 3:00 PM onwards, when the solar PV ceases power generation, causing the BESS to discharge alongside the diesel generator to meet the energy demand.

Additionally, the BESS charges after midnight when the load demand decreases, utilizing power from the diesel generator. The diesel generator's output during this time also supplies the loads. However, this extensive use of the diesel generator results in high fuel consumption, leading to increased operational costs. Figure 9 shows the energy profile for all components for MPC-based EMS with load curtailment, while Table 3 shows the power set-point for every component for MPC-based EMS with load curtailment for the first 24 hours.

https://doi.org/10.31436/iiumej.v26i1.3230

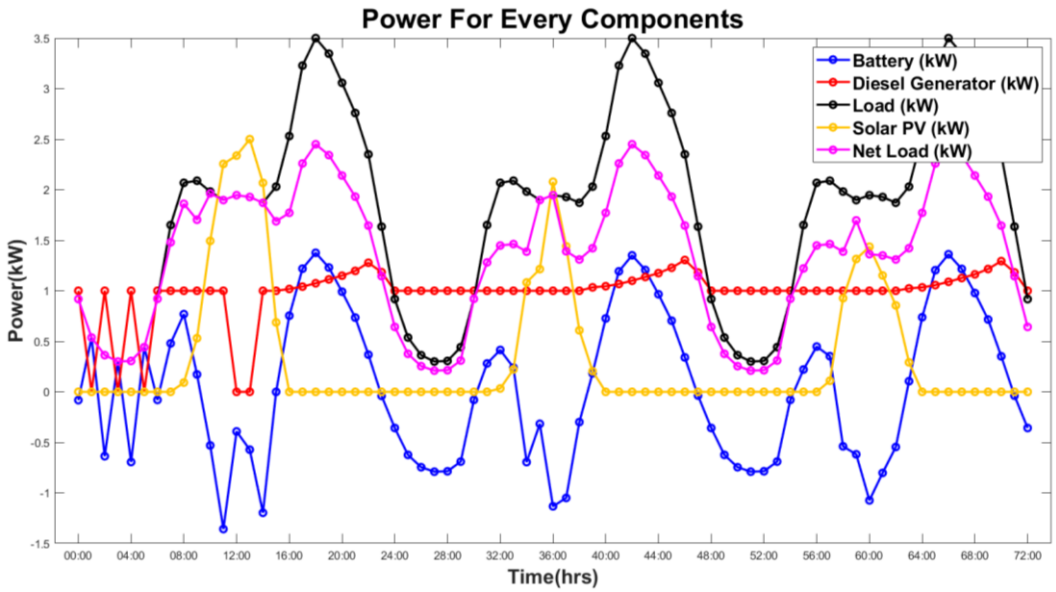


Figure 9. Energy Profile for All Components for MPC-Based EMS With Load Curtailment

Table 3. Power Set-Point for Every Component for MPC-Based EMS With Load Curtailment for the First 24 hours

| Time (h) | $P_{PV}$ $(kW)$ | $P_{DG}$ $(kW)$ | $P_{BESS}$ $(kW)$ | $P_{Loads}$ $(kW)$ | $P_{CURTAIL}$ $(kW)$ |
|---|---|---|---|---|---|
| 00:00 | 0 | 1 | -0.0824 | 0.9176 | 0 |
| 01:00 | 0 | 0 | 0.5375 | 0.5375 | 0 |
| 02:00 | 0 | 1 | -0.6369 | 0.3631 | 0 |
| 03:00 | 0 | 0 | 0.3 | 0.3 | 0 |
| 04:00 | 0 | 1 | -0.6943 | 0.3057 | 0 |
| 05:00 | 0 | 0 | 0.4422 | 0.4422 | 0 |
| 06:00 | 0 | 1 | -0.0798 | 0.9202 | 0 |
| 07:00 | 0 | 1 | 0.4793 | 1.6505 | 0.1712 |
| 08:00 | 0.0916 | 1 | 0.7689 | 2.0681 | 0.2076 |
| 09:00 | 0.5307 | 1 | 0.1722 | 2.0888 | 0.3859 |
| 10:00 | 1.4934 | 1 | -0.5302 | 1.9818 | 0.0186 |
| 11:00 | 2.2552 | 1 | -1.3576 | 1.8976 | 0 |
| 12:00 | 2.3377 | 0 | -0.3919 | 1.9458 | 0 |
| 13:00 | 2.5 | 0 | -0.5723 | 1.9277 | 0 |
| 14:00 | 2.0676 | 1 | -1.1968 | 1.8709 | 0 |
| 15:00 | 0.6872 | 1 | 0 | 2.0305 | 0.3433 |
| 16:00 | 0 | 1.0180 | 0.7535 | 2.5306 | 0.7592 |
| 17:00 | 0 | 1.0411 | 1.2186 | 3.2281 | 0.9684 |
| 18:00 | 0 | 1.0743 | 1.3757 | 3.5 | 1.05 |
| 19:00 | 0 | 1.1123 | 1.2302 | 3.3465 | 1.0039 |
| 20:00 | 0 | 1.1494 | 0.9909 | 3.0575 | 0.9172 |
| 21:00 | 0 | 1.1965 | 0.7348 | 2.7590 | 0.8277 |
| 22:00 | 0 | 1.2772 | 0.3678 | 2.35 | 0.7050 |
| 23:00 | 0 | 1.1841 | -0.0397 | 1.6347 | 0.4904 |
| 00:00 | 0 | 1 | -0.3577 | 0.9176 | 0.2753 |

Figure 9 demonstrates that the proposed MPC-based EMS effectively manages energy within the islanded microgrid while adhering to the constraints of all components, particularly the BES and diesel generator. The BESS operates within its charging and discharging limits of

https://doi.org/10.31436/iiumej.v26i1.3230

3 kW and -3 kW, respectively, while the diesel generator's output remains below the 5-kW threshold. The power balance is consistently maintained, as outlined in Table 3. Additionally, Figure 9 illustrates the SoC of the BESS over a 72-hour period, showing that it stays within the prescribed boundaries, thereby protecting the BESS from deep charging and discharging.

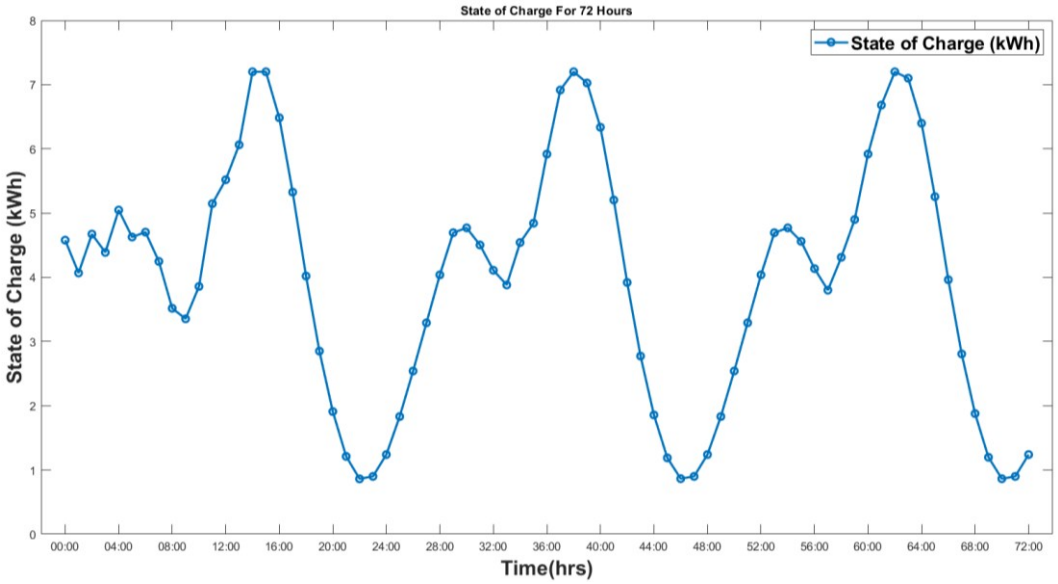


Figure 10. SoC of the BESS for MPC-Based EMS With Load Curtailment

It is observed that the MPC-based EMS applied load curtailment, as shown in Figure 9. Load curtailment occurred from morning until noon and from evening until night, consistently staying within 30% of the original loads. While the EMS aimed to curtail all loads by 30%, it did not always achieve this level. For example, during 6:00 AM, 7:00 AM, and 8:00 AM, the curtailment ranged from 10% to 20% of the original loads, likely due to the availability of solar PV power, which provided additional energy to meet demand. In contrast, during the evening and night, when there was little to no sunlight and solar PV could not generate power, load curtailment increased. Table 3 indicates that from 3:00 PM until midnight, load curtailment was generally around 30% of the original loads. During this period, the BESS discharged to help supply the load alongside the diesel generator. Figure 9 shows that the diesel generator's output remained constant throughout the 72-hour period, suggesting that load curtailment effectively reduced the supply and demand gap between the solar PV, diesel generator, BESS, and loads.

From these results, it can be concluded that the MPC-based EMS effectively and efficiently manages the microgrid's components in both scenarios. The power balance is maintained, and the power output constraints are respected, as shown in Table 2 and Table 3. Additionally, in both cases, the SoC of the BESS is kept within the specified range, as depicted in Figure 8 and Figure 10. The fluctuating SoC of the BESS is attributed to the weight assignments in the optimization process, which prioritize reducing fuel consumption and greenhouse gas emissions.

In the scenario without load curtailment, the diesel generator is used excessively to meet the high demand, especially during the evening and night. Conversely, with load curtailment, the diesel generator exhibits an almost constant low power output. This reduction is attributed to load curtailment, which helps minimize the gap between generation and demand. Table 4 compares diesel fuel consumption and fuel costs between the MPC-based EMS with and

https://doi.org/10.31436/iiumej.v26i1.3230

without load curtailment, further highlighting the benefits of incorporating load curtailment into the energy management strategy.

Table 4. Fuel Consumption and Fuel Cost Comparison

| | **Case 1: MPC-based EMS Without Load Curtailment** | **Case 2: MPC-based EMS With Load Curtailment** |
|---|---|---|
| **Diesel Fuel Consumption** | 309.50 Litres | 147.88 Litres |
| **Diesel Fuel Cost** | RM 665.43 | RM 317.95 |

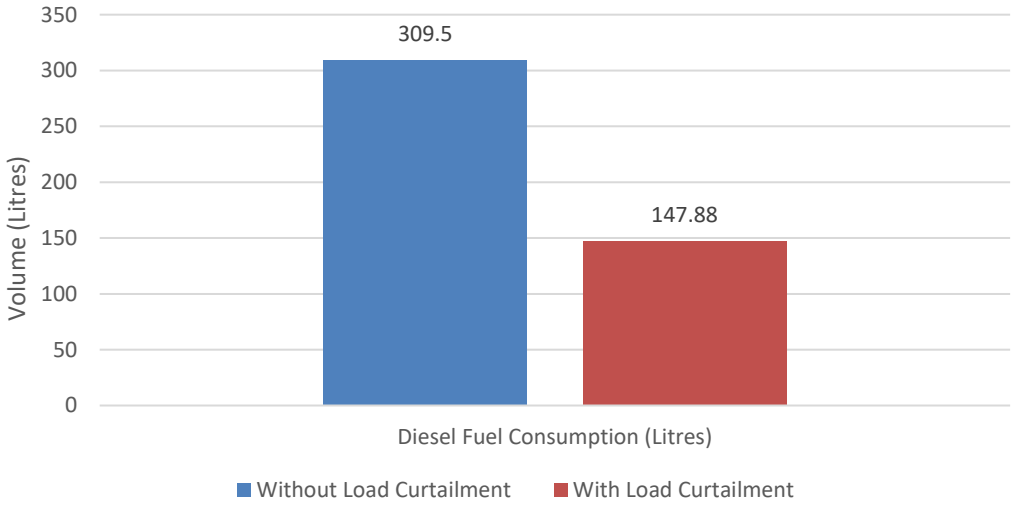


Figure 11. Diesel Fuel Consumption Comparison

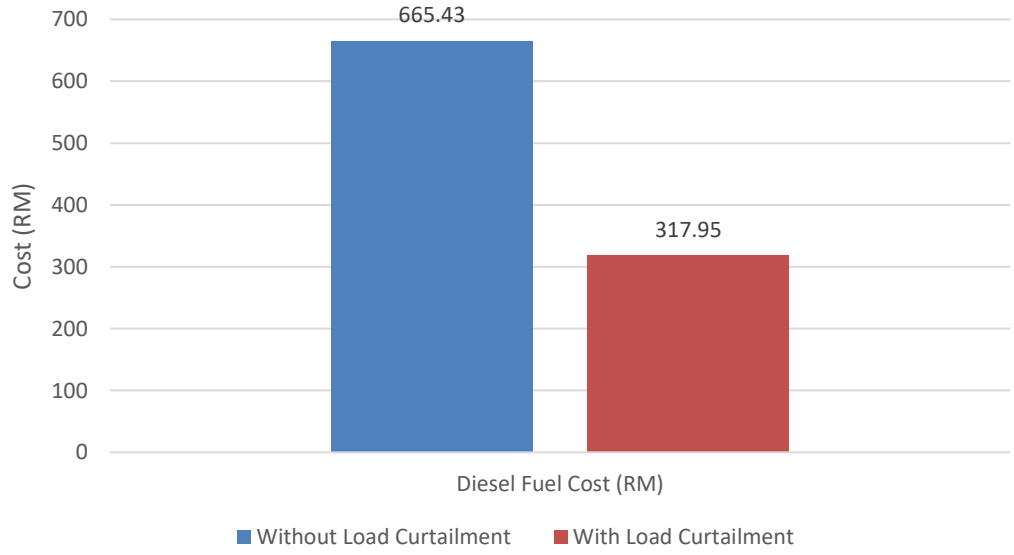


Figure 12. Diesel Fuel Cost Comparison

Figures 11 and 12 illustrate a significant reduction in diesel fuel consumption and expenses achieved by implementing load curtailment in an islanded microgrid. Diesel fuel consumption

decreased drastically from 309.50 liters to 147.88 liters, representing a remarkable reduction of 52.21%. Correspondingly, diesel fuel expenses dropped from RM 665.43 to RM 317.95, highlighting the economic benefits of integrating load curtailment within the MPC-based EMS. This substantial improvement underscores the effectiveness of load curtailment in optimizing resource utilization and reducing operational costs.

The results strongly demonstrate that the proposed MPC-based EMS, equipped with load curtailment capabilities, minimizes diesel generator operation costs within an islanded microgrid. The 52.21% reduction in fuel consumption and expenses underscores the system's efficiency and indicates its potential for further cost savings. Beyond cost reductions, the MPC-based EMS ensures efficient microgrid component management by maintaining power balance and adhering to predefined constraints. This capability highlights the robustness and practicality of the system for real-world applications, making it a highly viable solution for enhancing the performance and sustainability of islanded microgrids.

## 4. CONCLUSION

This paper presents the implementation of an MPC-based EMS for a standalone microgrid, focusing on integrating load curtailment to optimize diesel generator fuel consumption. The results demonstrate the system's ability to manage microgrid components while adhering to predefined constraints effectively. With load curtailment, the MPC-based EMS achieved a remarkable 52.21% reduction in diesel fuel consumption, saving 161.52 liters of diesel, valued at RM347.80, compared to operations without load curtailment. These findings highlight the dual benefits of enhanced economic efficiency and environmental sustainability, as the significant reduction in diesel usage minimizes greenhouse gas emissions, paving the way for more eco-friendly microgrid operations. The integration of load curtailment within the MPC framework enhances resource efficiency and ensures a more sustainable and cost-effective energy management strategy for standalone microgrids. However, recognizing the potential discomfort to users caused by curtailed loads, future work should explore penalizing load curtailment to balance operational efficiency with user satisfaction. Future developments can further refine the MPC-based EMS to deliver even more robust, user-friendly, and sustainable energy management solutions by addressing this trade-off.

## ACKNOWLEDGMENTS

Petronas Research Sdn. Bhd. partially supported this work under grant number SPP22-124-0124.

## REFERENCES

[1] J. M. Raya-Armenta, N. Bazmohammadi, J. G. Avina-Cervantes, D. Sáez, J. C. Vasquez, and J. M. Guerrero (2021). Energy management system optimization in islanded microgrids: An overview and future trends. Renewable and Sustainable Energy Reviews, 149: 111327. https://doi.org/10.1016/j.rser.2021.111327

[2] Y. Zahraoui, I. Alhamrouni, S. Mekhilef, M. R. Basir Khan, M. Seyedmahmoudian, A. Stojcevski, and B. Horan, (2021). Energy Management System in Microgrids: A Comprehensive Review. Sustainability, 13(19). https://doi.org/10.3390/su131910492

[3] A. Badawi, N. Hasbullah, S. Yusoff, and A. Hashim (2019). Energy and power estimation for three different locations in Palestine. Indonesian Journal of Electrical Engineering and Computer Science, 14: 1049-1056. https://doi.org/10.11591/ijeecs.v14.i3.pp1049-1056

[4] A. Badawi, A. Zyoud, S. Khan, A. Hashim, and N. Hasbullah (2019). Evaluation of Wind Power for Electrical Energy Generation in the Mediterranean Coast of Palestine for 14 Years.

International Journal of Electrical and Computer Engineering, 9: 2212-2219. https://doi.org/10.11591/ijece.v9i4.pp2212-2219

[5] M. F. Zia, E. Elbouchikhi, and M. Benbouzid (2018). Microgrids energy management systems: A critical review on methods, solutions, and prospects. Applied Energy, 222: 1033-1055. https://doi.org/10.1016/j.apenergy.2018.04.103

[6] U. R. Nair and R. Costa-Castelló (2020). A Model Predictive Control-Based Energy Management Scheme for Hybrid Storage System in Islanded Microgrids. IEEE Access, 8: 97809-97822. https://doi.org/10.1109/ACCESS.2020.2996434

[7] S. Rathor and D. Saxena (2020). Energy management system for smart grid: An overview and key issues. International Journal of Energy Research, 44. https://doi.org/10.1002/er.4883

[8] K. S. Joshal and N. Gupta, (2023). Microgrids with Model Predictive Control: A Critical Review. Energies, 16(13). https://doi.org/10.3390/en16134851

[9] S. K. Rathor and D. Saxena (2020). Energy management system for smart grid: An overview and key issues. International Journal of Energy Research, 44(6): 4067-4109.

[10] J. Hu, Y. Shan, J. M. Guerrero, A. Ioinovici, K. W. Chan, and J. Rodriguez (2021). Model predictive control of microgrids – An overview. Renewable and Sustainable Energy Reviews, 136: 110422. https://doi.org/10.1016/j.rser.2020.110422

[11] C. Essayeh, M. Raiss El-Fenni, H. Dahmouni, and M. A. Ahajjam (2021). Energy Management Strategies for Smart Green MicroGrid Systems: A Systematic Literature Review. Journal of Electrical and Computer Engineering, 2021: 6675975. https://doi.org/10.1155/2021/6675975

[12] A. M. Jasim, B. H. Jasim, B.-C. Neagu, and B. N. Alhasnawi, (2023). Efficient Optimization Algorithm-Based Demand-Side Management Program for Smart Grid Residential Load. Axioms, 12(1). https://doi.org/10.3390/axioms12010033

[13] S. Ahmad, M. Shafiullah, C. B. Ahmed, and M. Alowaifeer (2023). A Review of Microgrid Energy Management and Control Strategies. IEEE Access, 11: 21729-21757. https://doi.org/10.1109/ACCESS.2023.3248511

[14] H. He, S. Huang, Y. Liu, and T. Zhang (2021). Robust Model Predictive Control for Energy Management of Isolated Microgrids Based on Interval Prediction. Discrete Dynamics in Nature and Society, 2021: 2198846. https://doi.org/10.1155/2021/2198846

[15] K.-S. Ryu, D.-J. Kim, H. Ko, C.-J. Boo, J. Kim, Y.-G. Jin, and H.-C. Kim (2021). MPC Based Energy Management System for Hosting Capacity of PVs and Customer Load with EV in Stand-Alone Microgrids. Energies, 14(13). https://doi.org/10.3390/en14134041

[16] T. Pippia, J. Sijs, and B. D. Schutter (2020). A Single-Level Rule-Based Model Predictive Control Approach for Energy Management of Grid-Connected Microgrids. IEEE Transactions on Control Systems Technology, 28(6): 2364-2376. https://doi.org/10.1109/TCST.2019.2945023

[17] I. Novickij and G. Joós, (2019). Model Predictive Control Based Approach for Microgrid Energy Management. IEEE: 1-4. https://doi.org/10.1109/CCECE.2019.8861781

[18] P. K. Ndwali, J. G. Njiri, and E. M. Wanjiru (2021). Economic Model Predictive Control of Microgrid Connected Photovoltaic-Diesel Generator backup Energy System Considering Demand side Management. Journal of Electrical Engineering & Technology, 16(5): 2297-2312. https://doi.org/10.1007/s42835-021-00801-w

[19] A. Salazar, D. Arcos-Aviles, J. Llanos, D. Ortiz, M. Rodríguez, E. Motoasca, and W. Martinez, (2021). Model predictive control-based energy management system for isolated electro-thermal microgrids in rural areas of Ecuador. IEEE: 1-10. https://doi.org/10.23919/EPE21ECCEEurope50061.2021.9570196

[20] S. Polimeni, L. Meraldi, L. Moretti, S. Leva, and G. Manzolini (2021). Development and experimental validation of hierarchical energy management system based on stochastic model predictive control for Off-grid Microgrids. Advances in Applied Energy, 2: 100028. https://doi.org/10.1016/j.adapen.2021.100028

[21] M. Abbasi, E. Abbasi, L. Li, R. P. Aguilera, D. Lu, and F. Wang, (2023). Review on the Microgrid Concept, Structures, Components, Communication Systems, and Control Methods. Energies, 16(1). https://doi.org/10.3390/en16010484

[22] M. A. Alarcón, R. G. Alarcón, A. H. González, and A. Ferramosca, (2021). Economic model predictive control for energy management in a hybrid storage microgrid. IEEE: 1-6. https://doi.org/10.1109/RPIC53795.2021.9648465

[23] S. U. Ali, A. Waqar, M. Aamir, S. M. Qaisar, and J. Iqbal (2023). Model predictive control of consensus-based energy management system for DC microgrid. PLoS One, 18(1): e0278110. https://doi.org/10.1371/journal.pone.0278110

[24] M. Ajani (2020). Model Predictive Control Approach to Microgrid Operation. Master Thesis. McGill University (Canada).

[25] M. S. Taha, H. H. Abdeltawab, and Y. A. R. I. Mohamed (2018). An Online Energy Management System for a Grid-Connected Hybrid Energy Source. IEEE Journal of Emerging and Selected Topics in Power Electronics, 6(4): 2015-2030. http://doi.org/10.1109/JESTPE.2018.2828803

[26] G. S. Thirunavukkarasu, M. Seyedmahmoudian, E. Jamei, B. Horan, S. Mekhilef, and A. Stojcevski (2022). Role of optimization techniques in microgrid energy management systems—A review. Energy Strategy Reviews, 43: 100899. https://doi.org/10.1016/j.esr.2022.100899

[27] A. Elmouatamid, R. Ouladsine, M. Bakhouya, N. E. Kamoun, K. Zine-Dine, and M. Khaidar, (2019). A Model Predictive Control Approach for Energy Management in Micro-Grid Systems. IEEE: 1-6. https://doi.org/10.1109/SEST.2019.8848995

[28] J. L.-L. X. A. L. R. B. G. M. D. J. Morrow (2021). Annual timeseries (1-minute resolution) of per-unit profiles of residential electric load and 8 PV systems: a case study in Northern Ireland, UK.). https://doi.org/10.21227/edzt-vh05

https://doi.org/10.31436/iiumej.v26i1.3238

# A NOVEL INDUCED CURRENT PROTECTION SCHEME FOR LARGE-SCALE SOLAR PHOTOVOLTAIC SYSTEMS USING EARLY STREAMER EMISSIONS

**NURUL 'AINI MOHAMAD ZAKARIA[1*], MOHD NAJIB MOHD HUSSAIN[1], KANENDRA NAIDU VIJYAKUMAR[2], INTAN RAHAYU IBRAHIM[2], NOR SALWA DAMANHURI[2], NUR FADZILAH AHMAD[2]**

*[1]School of Electrical Engineering, College of Engineering, Universiti Teknologi MARA, Cawangan Pulau Pinang, 13500, Permatang Pauh, Penang, Malaysia*
*[2]School of Electrical Engineering, College of Engineering, Universiti Teknologi MARA, 40450 Shah Alam, Malaysia*

**Corresponding author: ainizakaria95@gmail.com*

*(Received: 27 March 2024; Accepted: 30 June 2024; Published online: 10 January 2025)*

***ABSTRACT:*** The reliability and safety of large-scale solar photovoltaic systems (LSSPV) is paramount in harnessing renewable energy sources effectively. Given the increasing adoption of solar energy in Malaysian regions prone to lightning strikes, understanding and enhancing protection mechanisms is imperative. This study investigated an induced current protection system for LSSPV using an early streamer emission (ESE) air terminal in Malaysia. Two systems (ESE and Franklin lightning rod types) were employed in a 50 MWp PV power plant spanning 260 acres and were installed on the lightning arrester to ensure adequate protection. The Franklin rod type comprised 763 pieces and was constructed following the Council of Engineer standards (Thailand) standard. Meanwhile, the ESE lightning rod contained 68 pieces and was built following the NFC17102 standard (France). A 150 kA direct lightning impact was then simulated on the PV power plant using MATLAB/Simulink. Consequently, the ESE lightning protection system (LPS) effectively protected and prevented the lightning strike. The Franklin rod type's shading effects and installation costs (USD 10,026,800 vs. USD 8,026,800) were also more significant than the ESE rod type. These outcomes demonstrated that the ESE LPS was suitable for the PV power plant implementation. The findings of this study could also assist in optimizing the lightning protection technology for large-scale PV power plants.

***ABSTRAK:*** Kebolehpercayaan dan keselamatan sistem fotovoltan suria berskala besar (LSSPV) adalah penting dalam memanfaatkan sumber tenaga boleh diperbaharui dengan berkesan. Memandangkan penggunaan tenaga suria yang semakin meningkat di kawasan Malaysia yang terdedah kepada panahan kilat, pemahaman dan meningkatkan mekanisme perlindungan adalah penting. Kajian ini menyiasat sistem perlindungan arus teraruh untuk LSSPV menggunakan terminal udara pelepasan aliran awal (ESE) di Malaysia. Dua sistem (jenis rod kilat ESE dan rod Franklin) telah digunakan dalam loji kuasa PV 50 MWp seluas 260 ekar dan dipasang pada penangkap kilat untuk memastikan perlindungan yang mencukupi. Jenis rod Franklin terdiri daripada 763 keping dan dibina mengikut piawaian Majlis Jurutera (Thailand). Sementara itu, rod kilat ESE mengandungi 68 keping dan dibina mengikut piawaian NFC17102 (Perancis). Kesan kilat langsung 150 kA kemudiannya disimulasikan pada jana kuasa PV menggunakan MATLAB/Simulink. Akibatnya, sistem perlindungan kilat (LPS) ESE melindungi dan menghalang serangan kilat dengan berkesan. Kesan teduhan dan kos pemasangan (USD 10,026,800 lwn. USD 8,026,800) jenis rod Franklin juga lebih ketara daripada jenis rod ESE. Hasil ini menunjukkan bahawa LPS ESE

https://doi.org/10.31436/iiumej.v26i1.3238

sesuai untuk pelaksanaan jana kuasa PV. Penemuan kajian ini juga boleh membantu dalam mengoptimumkan teknologi perlindungan kilat untuk jana kuasa PV berskala besar.

***KEYWORDS:*** *Early Streamer Emission, Lightning protection, Induced current, Solar Photovoltaic farm, Lightning effect*

# 1. INTRODUCTION

Malaysia is increasingly turning to solar energy to diversify energy sources, reduce reliance on fossil fuels, and promote sustainable development. Notably, the Malaysian government has implemented various programs and measures to encourage the expansion of solar energy. The Feed-in Tariff (FiT) mechanism is the main program, which provides solar energy producers with long-term contracts and enticing tariffs. This mechanism has aided the industry's development and investment in large-scale solar projects [1]. Despite the increasing use of solar energy in Malaysia, several issues are still encountered. These issues include intermittency, energy storage, and grid integration. Nonetheless, the Malaysian solar energy industry is anticipated to continue expanding and contribute to the nation's renewable energy goals through ongoing investments and government support.

Malaysia receives plenty of sunlight throughout the year due to its proximity to the equator. The nation gets a high solar irradiation level, rendering it conducive to producing solar energy. Typically, the solar irradiation of Malaysia from 4 to 5 kWh/m2/day annually makes it a desirable location for solar power generation [2]. Multiple large-scale solar projects have also been established in Malaysia, including grid-connected solar farms and power plants. These initiatives significantly improve the country's energy mix while assisting in lowering greenhouse gas emissions. Meanwhile, the interest in residential and commercial solar installations is rising alongside large-scale initiatives. This outcome is attributed to the Malaysian government promoting the installation of solar panels on rooftops through various incentives, such as the Net Energy Metering (NEM) program. Hence, solar energy enables consumers to decrease their total electricity consumption and potentially sell surplus electricity to the grid through NEM [1].

Malaysia is investing in research and development to enhance solar energy technology and improve efficiency further. Academic institutions and research organizations collaborate with business partners to create inventive solutions, such as advanced solar panels and energy storage systems. Therefore, Malaysia's transition to a cleaner and more sustainable energy system relies significantly on solar energy. This system can enhance energy security, lower carbon emissions, and reduce reliance on fossil fuels [3]. Nonetheless, grid-connected solar PV farm systems are costly due to the expensive equipment (PV modules and inverters). Hence, various studies have utilized different experimental methodologies and data analysis approaches to address these issues [4]. These studies aim to sustain the performance and efficiency of solar PV farms while preventing downtime for the investors, ensuring that they receive a return on their investment over a reasonable period.

Malaysian solar PV farms are usually exposed to direct and indirect lightning strikes due to their construction in an open area, resulting in high induced currents. This scenario occurred in Kuala Ketil Solar PV farm two years ago, when a 50 MW solar PV farm was damaged by lightning. Nevertheless, no official damage data was recorded. Generally, a lightning strike can cause interruption and damage the equipment in a solar PV system [5]. The damage to a grid-connected solar PV system from lightning is influenced by the strike location and the type of lightning protection equipment [6,7]. Additionally, the lightning striking point is inversely

related to the distance of the lightning strike impact [8]. For example, the solar PV farm at Tucson Electric Power in Tucson, Arizona, encountered lightning strikes during its operations, resulting in substantial equipment replacement costs [9]. Hence, direct and indirect lightning strikes can demonstrate significant damage and repair expenses [10,11].

Considering that designers often overlook the necessity of lightning protection systems (LPSs) or underestimate their significance, many solar PV farms are vulnerable to lightning strikes due to insufficient protection systems [12]. The lack of an LPS puts solar PV farms at risk of significant equipment damage and system destruction. Certain designers also overlook that replacing or fixing equipment damaged by a strike can surpass the cost of installing an LPS [13]. Therefore, the design and installation of an LPS for a solar PV farm is necessary. A solar panel mounted on a large surface area is more exposed to intense sunlight, resulting in a higher induced current. Lightning strikes can then cause damage to solar PV farms, leading to significant replacement costs, repair expenses, and inconvenience for electricity consumers. Given that an open area-based solar PV farm increases solar radiation and air humidity, this area is more susceptible to lightning strikes. The correlation between solar radiation, air humidity, and lightning discharge frequency produces these lightning strikes [14].

Numerous studies have investigated a suitable LPS for large-scale solar photovoltaic systems (LSSPV) to prevent interruptions during operations while minimizing the repair and replacement cost of the damaged equipment. The improvement of suitable LPS for LSSPV is still being researched. These studies have primarily examined the lightning protection of a solar PV system either theoretically (using simulation tools) [15,16,17,18] or experimentally (laboratory or field tests). Large-scale solar photovoltaic systems (LSSPVs) are typically vulnerable to damage caused by lightning-induced stroke-induced currents (SICs). These SICs cause harmful voltages and currents in PV arrays, inverters, and other electrical equipment, potentially producing equipment failure, system outages, and safety risks. Hence, current lightning protection measures may not adequately reduce the risk of SICs, necessitating the development of a specific induced current protection system for LSSPVs.

The layout and configuration of LSSPVs involving large areas and complex electrical designs pose challenges for implementing effective induced current protection schemes. Therefore, numerous factors (spacing between solar panels, electrical cable routing, and inverter placements) should be considered to reduce the impact of SICs on system performance and reliability. This study investigated an induced current protection system for LSSPV using an early streamer emission (ESE) air terminal in Malaysia. Two systems (ESE and Franklin lightning rod types) were employed in a 50 MWp PV power plant.

## 2. MATERIALS AND METHODS

### 2.1. Study Area and the Proposed Methodology

This section validates the calculation approach used to obtain design parameters, power results, and plant-associated efficiency to measure plant performance. The modeling of the solar PV system in the MATLAB/Simulink software covering the solar PV modules, solar PV array, inverter, transformer, grid, and cable were discussed in detail. Alternatively, the ESE for LPS was modelled based on the datasheet of the manufacturer for Level III ESE, which was designed for the grid-connected solar PV system. The grid-connected solar PV farm system and ESE implementation were validated by comparing this system to the Franklin Rod-based LPS. Subsequently, the solar PV farm data from a 50 MW solar PV farm in Malaysia was acquired as a reference for the case study. This data included all parameter specifications of the components (power, current, voltage, rating, and size) for the solar PV modules, solar PV

https://doi.org/10.31436/iiumej.v26i1.3238

array, inverter, transformer, grid, and cable. A direct lightning strike was then simulated and applied to the solar PV farm using a lightning amplitude current to measure the voltage and current values at different points. This study also provided recommendations on ESE's appropriate number, rating, and position for protective purposes.

Figure 1 displays the flowchart of this study, while Figure 2 depicts the block diagram of a 50 MW solar PV system without a lightning protection scheme. Figure 3 portrays the current solar PV system study model created using MATLAB. The model consisted primarily of an inductor-capacitor-inductor (LCL) filter, a boost converter, a three-phase inverter with (IGBT), and a PV array model. Moreover, the MATLAB PV array icon was created to produce 50 MW using 34 series-connected modules per string containing 1000 parallel strings. The temperature and the irradiance were also set to 25°C and 1000 W/m$^2$ following the standard test conditions (STC). A boost converter was then employed to increase the variable voltage of the solar panel to a higher and steady (direct current) DC voltage. This converter used voltage feedback to maintain a constant output voltage. The IGBT changed the DC output to an (alternating current) AC output. These IGBT firing pulses were generated using the Sinusoidal Pulse Width Modulation (SPWM) technique, which involved comparing three sinusoidal modulating waves to a triangular carrier wave.

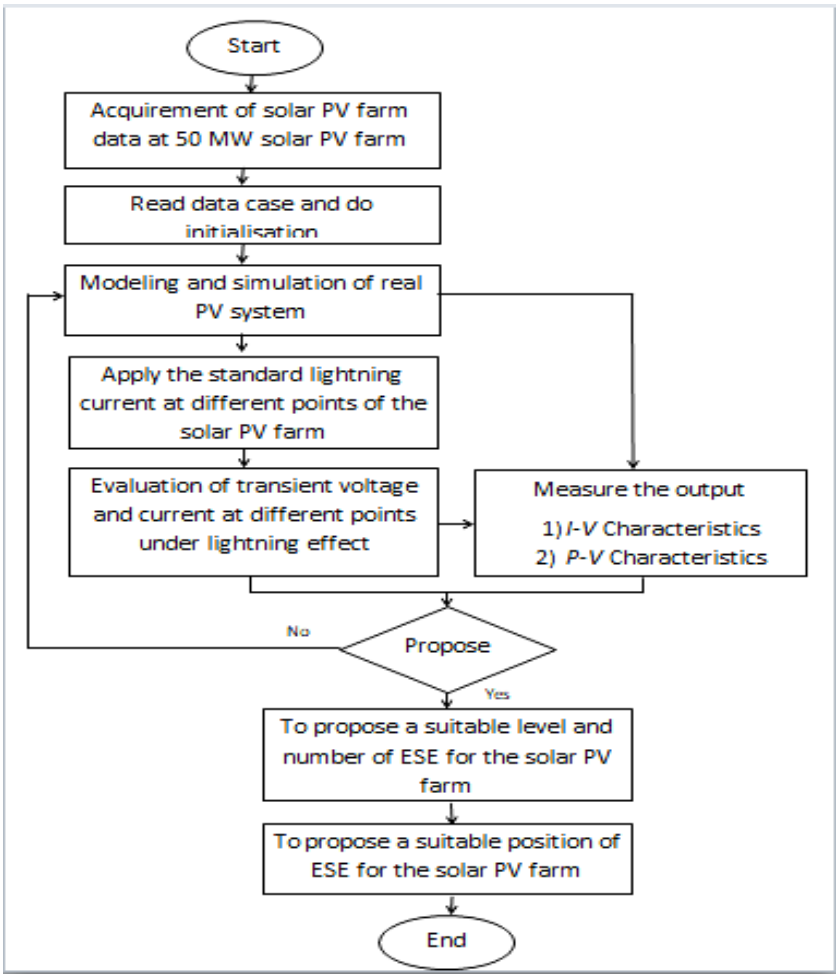


Figure 1. Flowchart of research.

The minimum capacity for the LSS must be 30 MWac to connect to the transmission network. The LSSPV required approval by the Commission at one Interconnection Point [Point of Common Coupling (PCC)] (see Fig. 2). Although a link could be established at any point

https://doi.org/10.31436/iiumej.v26i1.3238

on the grid system to export power generated by the transmission-connected LSS, the power output of an LSS coupled to a gearbox determined its dependency. Likewise, the PV cell employed a series-parallel architecture to establish the basis for simulating solar PV modules. A solar PV array was created by combining these solar PV modules.

The minimum capacity for the LSS must be 30 MWac to connect to the transmission network. The LSSPV required approval by the Commission at one Interconnection Point [Point of Common Coupling (PCC)] (see Figure 2). Although a link could be established at any point on the grid system to export power generated by the transmission-connected LSS, the power output of an LSS coupled to a gearbox determined its dependency. Likewise, the PV cell employed a series-parallel architecture to establish the basis for simulating solar PV modules. A solar PV array was created by combining these solar PV modules.

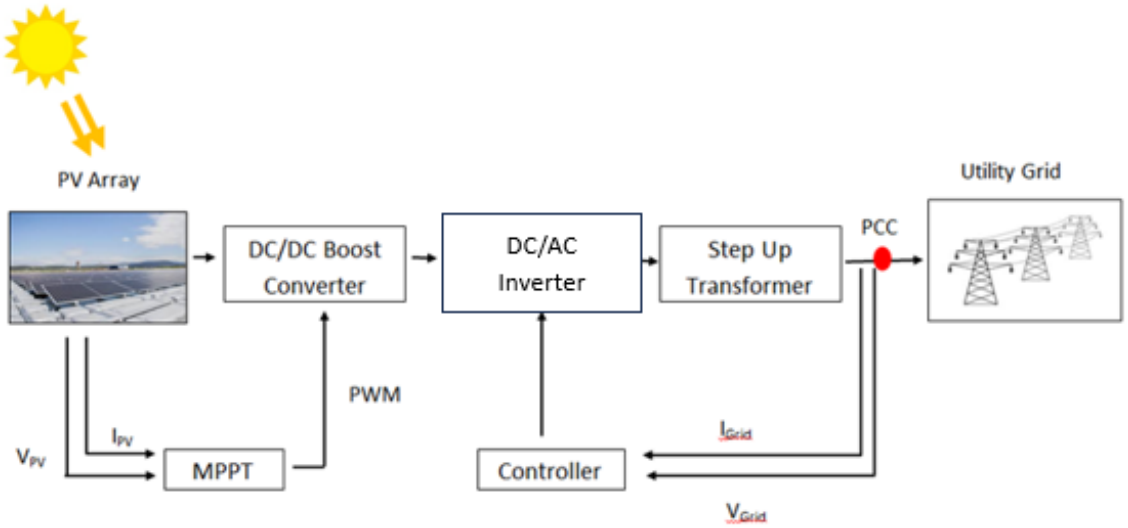


Figure 2. The 50 MW solar farm system block diagram

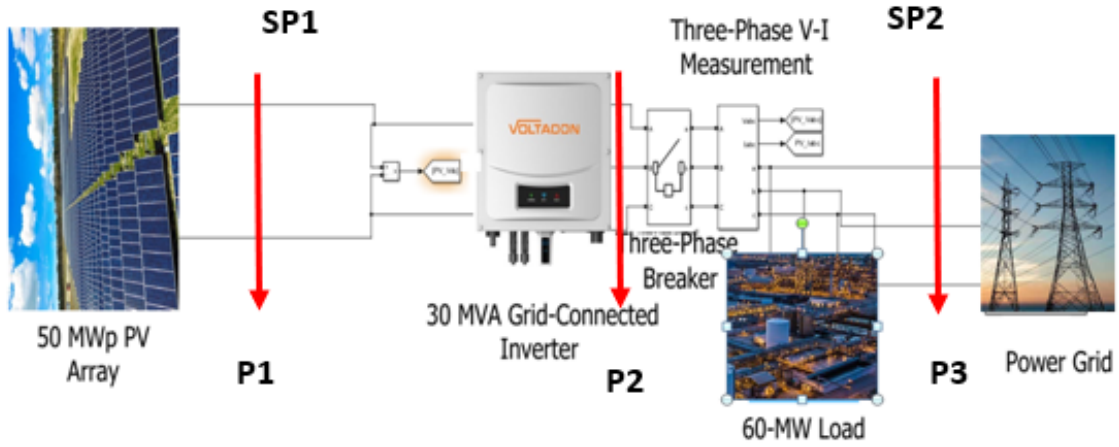


Figure 3. The 50 MW solar farm system

The standard lightning current was applied at different points: the PV array Point 1 (P1), before the inverter Point 2 (P2), and at the utility grid Point 3 (P3). After simulating the PV system, the transient current was examined at these points under the impact of the lightning effect. The measurement output of the current and voltage (I-V) characteristic was then recorded. This study involved creating a highly intricate model of a PV module to examine the correlation between induced current and the solar PV system. The model serves as the

https://doi.org/10.31436/iiumej.v26i1.3238

foundation for electromagnetic simulations replicating the adjacent lightning strike effects on the induced currents in a PV module as follows:

- The location of the lightning strike at different angles concerning the module.
- The current and voltage short circuits between the output terminals of the PV module.
- The interconnections within a four-module array and the functional distinctions between subpar and superior wiring techniques.

### 2.2. Theoretical Background

The grid-connected solar PV farm system was modeled using MATLAB/Simulink based on an actual application solar PV farm (50 MW). The solar PV farm system with a grid connection consisted of solar PV modules, inverters, cables, transformers, and a grid. Before the PV plant design calculations were initiated, suitable PV modules and their corresponding specifications were selected. Thus, the Canadian Solar Inc. CS3U-375P module was chosen for the PV plant design. Table 1 tabulates the main characteristics of these PV modules.

Table 1. Characteristic summary of the proposed PV module

| Parameter | Value |
|---|---|
| Type of Technology | Monocrystalline |
| Maximum open circuit voltage | 47.6 V |
| Maximum short circuit current | 9.93 A |
| Peak power | 375.314 W |

Table 2 lists the details of each component in the solar PV farm modeled in the power systems computer-aided design/electromagnetic transients with DC (PSCAD/EMTDC). Generally, the effectiveness of LPSs (Franklin rods or ESE) mainly depends on their spacing from one another. Therefore, the closer an LPS is placed to the structure it protects, the better it can efficiently redirect the energy from a lightning strike to the ground.

Table 2. A detailed summary of the components in the solar PV farm

| Component | Quantity | Specification |
|---|---|---|
| Solar Module | 136,000 | 72 multi-crystalline solar cells<br>Power solar PV modules = 375 W<br>Voltage of solar PV modules = 47.6 V<br>Current of solar PV modules = 9.93 A |
| Inverter | 100 | Nominal AC Power per inverter = 500 kW |
| Sub Distribution Board (SDB) | 6 | Maximum output aggregated at SDB is 140 kW |
| Main Distribution Board (MSB) | 2 | Maximum output aggregated at MSB is 500 kW |
| Transformer | 1 | 70MVA step-up transformer, 440 V/11 kV |
| Grid | - | 11 kV |

The magnitude of induced currents during a lightning strike largely depended on the separation between LPSs (lightning rods or ESE). Hence, the following are the crucial components:

1. Maximization of lightning protection radius:

   i. The lightning protection radius provided a low-resistance path for the lightning discharge to reach the ground to reduce the likelihood of structural damage.
   ii. To maximize the protected radius, the distance between the LPS and the structure it was protecting must be kept to a minimum. The closer the LPS was to the structure, the better it was at intercepting and safely conducting a lightning strike to the ground.
2. Zone of protection:
   i. The separation distance surrounding the LPS was the protection zone. This system conducted and intercepted lightning strikes within this zone.
   ii. The zone of protection expanded as the separation distance increased. Nonetheless, the LPS and the features of the building should be considered when optimizing this distance.
3. Reduction of induced voltages:
   i. Lightning strikes could change electromagnetic fields, inducing currents and voltages in conductive materials. Thus, an effective LPS minimizes induced voltages.
   ii. Enhancing the overall efficiency of the LPS involved minimizing induced currents and voltages in the protected structure by optimizing the separation distance.
4. Risk of side flashes:
   i. Side flashes could occur when lightning current leaps from the LPS to other conductive pathways (such as metal structures or utilities) due to insufficient separation distance. This process put the occupants of the protected structure in danger.
   ii. Proper separation distances were required to minimize side flashes and ensure that the lightning discharge followed the intended path to the earth.
5. Compliance with standards and guidelines:
   i. Separation distance guidelines for LPSs were included in national and international standards, such as the National Fire Protection Association (NFPA) and the International Electrotechnical Commission (IEC).
   ii. Adhering to these criteria ensured that the separation distance was based on scientific considerations and provided a uniform protection level.

Overall, separation distance primarily affected induced currents by affecting the efficiency of the LPS. Therefore, this distance must be optimized to maximize protection, minimize induced voltages, and lower the occurrences of side flashes during a lightning strike.

### 2.3. LPS Validation and Mathematical Modelling

This section validates the LPSs (ESE and Franklin Rod) using MATLAB/SIMULINK with the manufacturer-provided data. The design process used two systems (conventional and ESE) to define the external lightning concept. Thus, the lightning protection design consisted of the separator distance and air termination system. In contrast, this design neglected the down conductors, earth termination, and lightning equipotential bonding. The validation process is as follows:

1. The (IEC/EN 32305) standard defined the conventional system and was a design reference for three different methods to protect the PV power plant.
2. The angle under the shade concept and the height level of the lightning rod defined the protective angle method. Given that the height level could affect the PV power plant, this parameter must be specified as the separation distance clearance.

https://doi.org/10.31436/iiumej.v26i1.3238

3. The rolling sphere method or electro-geometric model was utilized using the protective angle method to protect PV power plants. The air terminator rod position for installation is determined by expressing a radian of an equation as follows:

$$r = 10 \times I^{0.65} \quad (1)$$

where $I$ is the current strike magnitude, and $r$ is the rolling sphere radian. Alternatively, the four lightning protection classes were connected through the $r$ value calculation. Table 3 summarizes the lightning rod positions computed using the $r$ value.

Table 3. Calculation summary of the lightning radius protection

| Class of Lighting Protection Zone (LPS) | Radius of the Rolling Sphere (r) |
|---|---|
| I | 20 m |
| II | 30 m |
| III | 45 m |
| IV | 60 m |

4. The mesh approach was used to develop lightning protection for a building or infrastructure with a complicated and flat geometry. Therefore, the mesh dimensions defined the mesh method, which was connected to the degree of lightning protection.

5. The French NFC17102 standard on the ESE rods was applied to define the ESE system. This method utilized the rolling sphere concept by including a rolling sphere and an upward streamer to determine the radius measurement. The height then identified the protection radius of the ESE about the surface or region. Table 3 demonstrates the calculation of the protected zone using the following equations:

$$R_p(h) = \sqrt{2rh - h^2 + \Delta(2r + \Delta)}\,; \in \mathrm{h} \geq 5\ \mathrm{m} \quad (2)$$

$$R_p(h) = h \times R_p(5)/5;\ \in 2\mathrm{m} \leq \mathrm{h} \leq 5\ \mathrm{m} \quad (3)$$

where $R_p(h)$ is the rolling sphere radian at a given height, $h$ is the height of the ESE over the protection zone, is the radius of the rolling sphere, $\Delta$ is the earlier upward streamer with a simple rod by adding $\Delta$T that equals $\Delta = \Delta T \times 106$. On the contrary, a new method was proposed to enhance the efficiency of the current measurement output to decrease the induced current in LSSPV. The equation was a combination of Equations (2) with (3), the vertical spacing between the conductor, i.e., Eq. (4), and the height of the conductor, i.e., Eq. (5), as follows:

$$L = 5.08 + 1.814 \times V + \left[\frac{I}{27.8}\right] \quad (4)$$

$$\varphi_n - \varphi_m = R_{ii}I_i + \sum jwL_{ij}I_jV_n = \sum P_{nm}I_{qm} \quad (5)$$

where $R_{ii}$ is the resistance of segment $i$, and $L_{ij}$ and $p_{ij}$ are the inductance and coefficient of potential between segments $i$ and $j$, nodes inductive cell $n$ and inductive cell $m$. Note that lightning return stroke currents contain high-frequency components. The current in a segment at high frequency was not uniformly distributed over its cross-section due to the eddy current effect. Both resistance and internal inductance then varied significantly with frequency. These values could be determined by surface impedance.

Therefore, the new expression of LPS ESE is as follows:

$$ESE = R_p(h) + L + (\phi_n - \phi_m) \quad (6)$$

https://doi.org/10.31436/iiumej.v26i1.3238

where $R_p(h)$ is the lightning protection radius, $L$ is the spacing between a conductor in meters, $(\phi_n - \phi_m)$ is the conductor segment, and $V$ is the system voltage in kV.

Considering that the source current was known, the contribution from the external current source was divided in Eq. (4). The scalar potentials at the center of its two neighboring potential cells ($n$ and $m$) were also denoted by $\phi_n$ and $\phi_m$. Meanwhile, a scalar Green's function $Gq$ could express the scalar potential $\phi$ for a vertical wire.

Table 4. Summary of the IEC/EN 32305 class for various protection levels

| Lightning Radius Protection | | | |
|---|---|---|---|
| **Lightning Protection Level, h (m)** | **1 (D = 20 m)** | **2 (D = 45 m)** | **3 (D = 60 m)** |
| 2 | 32 | 39 | 43 |
| 3 | 48 | 59 | 65 |
| 4 | 64 | 78 | 86 |
| 5 | 79 | 97 | 107 |
| 10 | 79 | 99 | 109 |
| 15 | 80 | 101 | 111 |
| 20 | 80 | 102 | 113 |
| 45 | 80 | 105 | 119 |
| 60 | 80 | 105 | 120 |

## 2.4. The External Lightning Protection Design for the PV Power

This study assessed the field installation connected with the economics of the PV power plant. The power generated by the PV power plant immediately affected solar PV farms. Thus, examining the quantity of conventional and ESE lightning rods was essential to evaluate the ideal circumstances and capital costs. Fig. 4 depicts the PV power plant location in this study, which is within a 50 MW solar PV farm in Malaysia. A polling sphere method was used within the PV power plant area to design the LPS.

Figure 4. The location of the PV power plant in this study at the Kuala Ketil Solar Farm

https://doi.org/10.31436/iiumej.v26i1.3238

# 3. RESULTS

This section analyses the lightning strike effect from various perspectives without any LPS. Typically, a conductor produces a traveling wave of voltage and current related to surge impedance at the speed of light when lightning hits. Therefore, three different measurement points were utilized after the lightning strike: P1 (which was used to determine the transient at solar PV modules), P2 (the transient at the inverter), and P3 (the transient at the transformer) (see Fig. 3). This process identified the traveling waves of the transient voltage and current causing damage to the components of the grid-connected solar PV farm system.

## 3.1. Effect of Different Lightning Striking Point

This section describes the simulation to study the effects of different lightning striking points. Consequently, two points were observed to possess significant possibilities of being struck by lightning in the solar PV farm: between the solar PV array and inverter (SP1) and between the inverter and substation (SP2) (see Fig. 3.). The lightning struck two independent points, first at SP1 and then moving to SP2. Considering that the solar PV farm was installed in an open area, the 150 kA peak current was applied to SP1 and SP2. Tables 5 to 7 tabulate the lightning strike results of these two different points before the LPS implementation.

Table 5. Lightning strike summary at two different points before the LPS implementation at P1

| **Lightning Amplitude (kA)** | **P1 (PV Array)** | |
|---|---|---|
| | **$V_{pv}$ (kV)** | **$I_{pv}$ (kA)** |
| **SP1** | 3.005 | 1.948 |
| **SP2** | 3 | 4.709 |

Table 6. Lightning strike summary at two different points before the LPS implementation at P2

| **Lightning Amplitude (kA)** | **P2 (After Inverter)** | | | | | |
|---|---|---|---|---|---|---|
| | **$V_{in}$ DC (kV)** | | | **$I_{in}$ Dc (kA)** | | |
| | **Phase A** | **Phase B** | **Phase C** | **Phase A** | **Phase B** | **Phase C** |
| **SP1** | -0.02804 | 0.03894 | $-5.328\times10^{-8}$ | $1.4210^{-6}$ | $-1.95210^{-6}$ | $-1.84510^{-5}$ |
| **SP2** | 0 | 0 | 0 | 1.138 | -1.432 | 0 |

Table 7. Lightning strike summary at two different points before the LPS implementation at P3

| **Lightning Amplitude (kA)** | **P3 (Before Transformer)** | | | | | |
|---|---|---|---|---|---|---|
| | **$V_{in}$ DC (kV)** | | | **$I_{in}$ Dc (kA)** | | |
| | **Phase A** | **Phase B** | **Phase C** | **Phase A** | **Phase B** | **Phase C** |
| **SP1** | 0.09867 | 0.03749 | 0.055 | 3.339 | 1.346 | 2.371 |
| **SP2** | 0.01063 | 0.03751 | 0.03376 | -3423 | 1431 | 2287 |

## 3.2. Effect of Different Cable Lengths

The cables chosen for the solar PV farm inverter were crucial, particularly the DC cable length between the solar PV array and the string inverter. Hence, this section analyses the

https://doi.org/10.31436/iiumej.v26i1.3238

impact of lightning strikes on solar PV array and string inverter (DC side) based on various cable lengths. Different cable lengths ranging from 5 to 20 km were set, and the transient voltage and current results were documented (see Tables 8 to 10). The lightning current of 150 kA peak current was also employed in this analysis.

When different cable lengths were applied to connect the solar PV array and the string inverter, voltage and current traveling waves on the AC side were almost similar. Slight differences between the measured voltage and current on the DC side were still observed, specifically in solar PV modules. Thus, the simulation findings demonstrated a higher correlation between the transient voltage and current with higher cable length. Meanwhile, a higher resistivity value of the core material decreased the maximum overvoltage on the cable. This outcome was attributed to an increased attenuation coefficient, causing the voltage peak value of a voltage wave transmitted along the cable to be reduced. Overall, the effect of a lightning strike on different cable lengths in this study could be employed to determine the LPS installation placement. The cable length connecting the solar PV array and the string inverter should be as short as possible to minimize damage to the solar PV modules.

The findings in this section indicated that a lightning surge could cause damage to the solar PV array and inverter, both of which were costly to replace. Therefore, various voltage and current readings behaviors could be monitored at the solar panel (before and after the inverter) and the main panel connected to the grid. These results were useful in facilitating decisions regarding the LPS placement and identifying the relevant ratings aligning with the objectives of this study.

Table 8. Effect of different cable lengths before the LPS implementation at P1

| Cable Length (km) | P1 (PV Array) | |
|---|---|---|
| | $V_{pv}$ (kV) | $I_{pv}$ (kA) |
| **2** | 3.005 | 1.348 |
| **5** | 7.786 | 1.777 |
| **10** | 2.885 | 2.566 |

Table 9. Effect of different cable lengths before the LPS implementation at P2

| Cable Length (km) | P2 (After Inverter) | | | | | |
|---|---|---|---|---|---|---|
| | $V_{in}$ DC (kV) | | | $I_{in}$ Dc (kA) | | |
| | **Phase A** | **Phase B** | **Phase C** | **Phase A** | **Phase B** | **Phase C** |
| **2** | -0.02804 | 0.03894 | $-5.328\times10^{-8}$ | $1.42\times10^{-6}$ | $-1.952\times10^{-6}$ | $-1.845\times10^{-5}$ |
| **5** | -0.02238 | 0.02639 | $-1.043\times10^{-8}$ | $2.08\times10^{-6}$ | $-2.427\times10^{-6}$ | $-3.612\times10^{-6}$ |
| **10** | -0.01928 | 0.02185 | $-5.126\times10^{-9}$ | $1.86\times10^{-6}$ | $-2.984\times10^{-6}$ | $-1.775\times10^{-6}$ |

Table 10. Effect of different cable lengths before the LPS implementation at P3

| Cable Length (km) | P3 (Before Transformer) | | | | | |
|---|---|---|---|---|---|---|
| | $V_{in}$ DC (kV) | | | $I_{in}$ Dc (kA) | | |
| | **Phase A** | **Phase B** | **Phase C** | **Phase A** | **Phase B** | **Phase C** |
| **2** | 0.09867 | 0.03749 | 0.055 | 3.339 | 1.346 | 2.371 |
| **5** | 0.07135 | (-0.0386) | 0.03797 | (-2.115) | 9.112 | 1.343 |
| **10** | 0.06107 | 0.03823 | 0.03815 | (-1.719) | 7.538 | 1.054 |

### 3.3. Protection Scheme for Solar PV Farm

The ESE lightning protection rod type used in the selected PV power plant was designed according to the standard reference. Notably, the distance pole of the ESE lightning protection rod acquired a radius of lightning protection of 45 m Level III. This system was validated using

https://doi.org/10.31436/iiumej.v26i1.3238

another LPS, Franklin Rod protection, which was created to compare its location distance with ESE lightning protection. A MATLAB simulation was then employed to simulate the effects of LPSs on the PV power plants. This study simulated two forms of lightning protection in a 50 MWp PV power plant. The simulation consisted of the ESE and the Franklin lightning protection types. Subsequently, the case study was performed using the grid-connected solar PV farm system implemented in the 50 MW solar PV farm. The lightning struck SP1 (DC side) and then moved to SP2 (AC side) in the grid-connected solar PV farm system. This lightning strike produced a high transient voltage and current to the nearest point.

The LPS model used in this simulation was verified by comparing it with two different LPS types based on the datasheet of the manufacturer. Several parameters were then analyzed, including cable length, LPS placement, and LPS rating. The ESE lightning protection simulation used 68 rods with a height of 10 m. This design was based on Level III for protection according to the NFC17102 standard, in which the distance length of the ESE lightning type was approximately 44.8999 m. Likewise, the Franklin lightning protection simulation utilized 763 rods with a height of 10 m.

### 3.4. Installation of LPS at 50 MW Solar PV System

This section investigates the installation of LPS ESE Level III on the DC and AC side of the solar PV farm, while Franklin Rod is Level IV. Tables 11 to 13 list the current measurements resulting from a lightning strike applied to SP1 and SP2 with installing an ESE system on the DC and AC sides. The lightning strike possessed a peak current of 150 kA and was conducted through a 2 km cable length with ESE conductors at 5 m, 10 m, and 20 m. Meanwhile, Tables 14 to 16 display the current measurements from a lightning strike applied to SP1 and SP2 by installing an ESE on the DC and AC sides. The lightning strike possessed a peak current of 150 kA and involved a 2 km length of wire with Franklin Rod conductors at heights of 5 m, 10 m, and 20 m.

Table 11. Lightning strike at two different points after ESE implementation at P1

| Lightning Amplitude (kA) | P1 (PV Array) | | |
|---|---|---|---|
| | ESE (5m) | ESE (10m) | ESE (20m) |
| SP1 | -2.54 | -2.61 | -2.45 |
| SP2 | 4,6 | 4.6 | 4.6 |

Table 12. Lightning strike at two different points after ESE implementation at P2

| Lightning Amplitude (kA) | P2 (After Inverter) | | | | | | | | |
|---|---|---|---|---|---|---|---|---|---|
| | ESE (5m) | | | ESE (10m) | | | ESE (20m) | | |
| | Phase A | Phase B | Phase C | Phase A | Phase B | Phase C | Phase A | Phase B | Phase C |
| SP1 | 0.000845 | -0.001956 | -0.001763 | $-8.47\times10^{-4}$ | -0.001814 | -0.001908 | 0.000847 | -0.00181 | -0.001913 |
| SP2 | 3.664 | -1432 | -2231 | 3.664 | -1432 | -2231 | 3.664 | -1432 | -2231 |

Table 13. Lightning strike at two different points after ESE implementation at P3

| Lightning Amplitude (kA) | P3 (before Transformer) | | | | | | | | |
|---|---|---|---|---|---|---|---|---|---|
| | ESE (5m) | | | ESE (10m) | | | ESE (20m) | | |
| | Phase A | Phase B | Phase C | Phase A | Phase B | Phase C | Phase A | Phase B | Phase C |
| SP1 | -3.643 | 1.326 | 2.281 | -3.643 | 1.326 | 2.281 | -3.643 | 1.326 | 2.281 |
| SP2 | -3.66 | 1.433 | 2.231 | -3.66 | 1.433 | 2.231 | -3.66 | 1.433 | 2.231 |

https://doi.org/10.31436/iiumej.v26i1.3238

Table 14. Lightning strike summary at two different points after Franklin Rod implementation at P1

| Lightning Amplitude (kA) | P1 (PV Array) | | |
|---|---|---|---|
| | Franklin Rod (5m) | Franklin Rod (10m) | Franklin Rod (20m) |
| **SP1** | -1.100 | -1,747 | -1.539 |
| **SP2** | 4.595 | 4.595 | 4.599 |

Table 15. Lightning strike summary at two different points after Franklin Rod implementation at P2

| Lightning Amplitude (kA) | P2 (After Inverter) | | | | | | | | |
|---|---|---|---|---|---|---|---|---|---|
| | Franklin Rod (5m) | | | Franklin Rod (10m) | | | Franklin Rod (20m) | | |
| | Phase A | Phase B | Phase C | Phase A | Phase B | Phase C | Phase A | Phase B | Phase C |
| **SP1** | 0.002402 | 0.00181 | -0.000899 | 0.002269 | 0.001383 | -0.00769 | 0.002337 | 0.001284 | -0.0007374 |
| **SP2** | 3.664 | -1.432 | -2.231 | 3664 | -1432 | -2.231 | 3.664 | -1.432 | -2.231 |

Table 16. Lightning strike summary at two different points after Franklin Rod implementation at P3

| Lightning Amplitude (kA) | P3 (before Transformer) | | | | | | | | |
|---|---|---|---|---|---|---|---|---|---|
| | Franklin Rod (5m) | | | Franklin Rod (10m) | | | Franklin Rod (20m) | | |
| | Phase A | Phase B | Phase C | Phase A | Phase B | Phase C | Phase A | Phase B | Phase C |
| **SP1** | -3.643 | 1.326 | 2.281 | -3.643 | 1.326 | 2.281 | -3.643 | 1.326 | 2.281 |
| **SP2** | -3.664 | 1.433 | 2.231 | -3.664 | 1.433 | 2.231 | -3.664 | 1.433 | 2.231 |

Tables 17 to 19 summarize the current measurements when a lightning strike is applied to cables of varied lengths, with ESE installations on the DC and AC sides. The lightning strike possessed a 150 kA peak current with 5 m, 10 m, and 20 m height conductors of ESE. Similarly, Tables 20 to 23 tabulate the current measurements when a lightning strike is applied to cables of varied lengths, with ESE on the DC and AC sides. The lightning strike possessed a 150 kA peak current with 5 m, 10 m, and 20 m height conductors of Franklin Rod.

Table 17. Effect of different cable lengths after ESE implementation at P1

| Cable Length (km) | P1 (PV Array) | | |
|---|---|---|---|
| | ESE (5m) | ESE (10m) | ESE (20m) |
| **2** | -2.452 | -2.51 | -2.459 |
| **5** | -2.12 | -2.08 | -2.08 |
| **10** | -2.22 | -2.093 | -2.09 |

Table 18. Effect of different cable lengths after ESE implementation at P2

| Cable Length (km) | P2 (After Inverter) | | | | | | | | |
|---|---|---|---|---|---|---|---|---|---|
| | ESE (5m) | | | ESE (10m) | | | ESE (20m) | | |
| | Phase A ($\times10^{-4}$) | Phase B ($\times10^{-4}$) | Phase C ($\times10^{-4}$) | Phase A ($\times10^{-4}$) | Phase B ($\times10^{-3}$) | Phase C ($\times10^{-3}$) | Phase A ($\times10^{-4}$) | Phase B ($\times10^{-4}$) | Phase C ($\times10^{-3}$) |
| **2** | 8.45 | -18.14 | -19.08 | -8.47 | -1.814 | -1.908 | 8.47 | -18.1 | -1.913 |
| **5** | -8.4467 | -8.4467 | -8.4467 | -8.229 | 1.538 | 2.099 | -8.32 | 1.59 | 2.056 |
| **10** | 7.13 | 7.13 | 7.13 | 6.45 | -1.032 | -2.476 | 6.65 | -1.076 | -2.452 |

https://doi.org/10.31436/iiumej.v26i1.3238

Table 19. Effect of different cable lengths after ESE implementation at P3

| Cable Length (km) | P3 (Before Transformer) | | | | | | | | |
|---|---|---|---|---|---|---|---|---|---|
| | ESE (5m) | | | ESE (10m) | | | ESE (20m) | | |
| | Phase A | Phase B | Phase C | Phase A | Phase B | Phase C | Phase A | Phase B | Phase C |
| **2** | -3.643 | 1.326 | 2.281 | -3.643 | 1.326 | 2.281 | -3.643 | 1.326 | 2.281 |
| **5** | -2.947 | 1.156 | 1.791 | -2.947 | 1.156 | 1.791 | -2.947 | 1.156 | 1.791 |
| **10** | -2.234 | 0.9184 | 1.315 | -2.234 | 0.9184 | 1.315 | -2.234 | 0.9184 | 1.315 |

Table 20. Effect of different cable lengths after ESE implementation at P3

| Cable Length (km) | P3 (Before Transformer) | | | | | | | | |
|---|---|---|---|---|---|---|---|---|---|
| | ESE (5m) | | | ESE (10m) | | | ESE (20m) | | |
| | Phase A | Phase B | Phase C | Phase A | Phase B | Phase C | Phase A | Phase B | Phase C |
| **2** | -3.643 | 1.326 | 2.281 | -3.643 | 1.326 | 2.281 | -3.643 | 1.326 | 2.281 |
| **5** | -2.947 | 1.156 | 1.791 | -2.947 | 1.156 | 1.791 | -2.947 | 1.156 | 1.791 |
| **10** | -2.234 | 0.9184 | 1.315 | -2.234 | 0.9184 | 1.315 | -2.234 | 0.9184 | 1.315 |

Table 21. Effect of different cable lengths after Franklin Rod implementation at P1

| Cable Length (km) | P1 (PV Array) | | |
|---|---|---|---|
| | Franklin Rod (5m) | Franklin Rod (10m) | Franklin Rod (20m) |
| **2** | -1.700 | -1.747 | -1.539 |
| **5** | -1.62 | -1.608 | -1.611 |
| **10** | -1.522 | -1.527 | -1.525 |

Table 22. Effect of different cable lengths after Franklin Rod implementation at P2

| Cable Length (km) | P2 (After Inverter) | | | | | | | | |
|---|---|---|---|---|---|---|---|---|---|
| | Franklin Rod (5m) | | | Franklin Rod (10m) | | | Franklin Rod (20m) | | |
| | Phase A ($\times10^{-4}$) | Phase B ($\times10^{-3}$) | Phase C ($\times10^{-4}$) | Phase A ($\times10^{-4}$) | Phase B ($\times10^{-3}$) | Phase C ($\times10^{-3}$) | Phase A ($\times10^{-4}$) | Phase B ($\times10^{-3}$) | Phase C ($\times10^{-4}$) |
| **2** | 24.02 | 1.81 | -8.99 | 22.69 | 1.383 | -7.69 | 23.37 | 1.284 | -7.374 |
| **5** | -8.4467 | 1.709 | 19.53 | -8.229 | 1.538 | 2.099 | -8.32 | 1.59 | 20.56 |
| **10** | 7.13 | -1.191 | -23.84 | 6.45 | -1.032 | -2.476 | 6.65 | -1.076 | -4.52 |

Table 23. Effect of different cable lengths after Franklin Rod implementation at P3

| Cable length (km) | P3 (Before Transformer) | | | | | | | | |
|---|---|---|---|---|---|---|---|---|---|
| | Franklin Rod (5m) | | | Franklin Rod (10m) | | | Franklin Rod (20m) | | |
| | Phase A | Phase B | Phase C | Phase A | Phase B | Phase C | Phase A | Phase B | Phase C |
| **2** | -3.643 | 1.326 | 2.281 | -3.643 | 1.326 | 2.281 | -3.643 | 1.326 | 2.281 |
| **5** | -2.947 | 1.156 | 1791 | -2.947 | 1.156 | 1.791 | -2.947 | 1.156 | 1.791 |
| **10** | -2.234 | 0.9184 | 1315 | -2.234 | 0.9184 | 1.315 | -2.234 | 0.9184 | 1.315 |

# 4. DISCUSSION

When lightning hits a conductor, it produces a traveling wave of voltage and current related to surge impedance at the speed of light. Therefore, three different points of measurement were used after the lightning strike to identify the traveling waves of the transient voltage and current that can damage the components of the grid-connected solar PV farm system. The three points include P1, which was used to determine the transient at solar PV modules; P2, the transient at the inverter; and P3, the transient at the transformer.

The separation distance between components in LSSPVs could significantly impact induced currents, particularly during lightning or electromagnetic disturbances [6]. Generally, individual solar panels (modules) are arranged in arrays with specific spacing between them. The separation distance between modules can affect the induced currents during lightning strikes or electromagnetic interference. Thus, greater separation between modules reduced the coupling effects between adjacent modules, potentially minimizing induced currents in neighboring modules during transient events [7]. Alternatively, the separation distance between cabling and conduits within a solar PV system also significantly influenced induced currents. Therefore, proper spacing between cables, conduits, and communication signals could reduce electromagnetic interference and induced currents, maintaining system reliability and performance.

The layout and separation distance between equipment and components within a solar PV system significantly influence induced currents. Thus, proper spacing and arrangement of the equipment could help minimize electromagnetic coupling and induced currents between components, ensuring optimal system operation and reliability during transient events.

The ESE type of lightning protection rod was utilized in the chosen PV power plant. The ESE lightning protection rod was created using the standard as a guide. The PV power plant employed the positioning design of the ESE lightning protection rod type. The ESE lightning protection rod's distance pole offers a 45 m Level III radius of lightning protection. The system was validated using another LPS, Franklin Rod protection. The Franklin lightning protection rod type simulation's positioning distance was created to be compared to the ESE lightning protection.

The generated currents diminished rapidly as the distance from the current impulse increased for the cable length. This outcome was anticipated for the short-circuited bypass diodes, in which the induced currents were more significant in the conductive loops closer to the current impulse than those farther away. Specifically, the induced currents for the 2 km and 10 km separation distances increased by 150 kA with the addition of a short-circuit loop between the output terminals of the model. Subsequently, an investigation was conducted using ESE with LPS installation following the accepted practices and standards. The analysis was divided into two cases: LPS ESE Level III and LPS Franklin Rod Level IV. Consequently, LPS ESE Level III was installed with a cable length of 2 km. The length of conductor LPS ESE was also 10 m, sufficient to safeguard the equipment (solar PV modules and string inverters).

Separation distance standards must be followed for PV systems to minimize induced currents, guarantee safety, maximize performance, abide by regulations, and support certification and warranty requirements. By adhering to standard guidelines, PV installations can be designed, installed, and operated with confidence, reducing risks and increasing system reliability.

There are several ways in which separation distance affects induced currents in large-scale solar PV systems. In particular, during lightning events and electromagnetic disturbances,

proper spacing between modules, cables, and electrical components helps to minimize electromagnetic coupling, reduce induced currents, and ensure the safety and reliability of the PV system.

## 5. CONCLUSION

This study successfully compared the simulated installation of LPS ESE and LPS Franklin Rod for lightning protection in a PV power plant. A lightning strike produced high transient voltage and current that could severely damage solar PV modules, inverters, and other electronic components. Therefore, a template model of a grid-connected solar PV farm system was developed to evaluate the LPS. An analysis of the lightning effect on the solar PV farm without any installation of LPS was conducted to study the consequences if the engineers neglected the LPS installation. This analysis was performed based on two crucial perspectives: striking points and different cable lengths. Meanwhile, the new ESE technique was used to replicate the lightning-induced current in the PV system. Consequently, significant induced current was observed, which might potentially damage the PV systems if appropriate protection measures were not implemented. Certain scenarios also demonstrated that the simulated results matched the field observations recorded in other studies.

The PV system's lightning-induced current was simulated using the new ESE technique. Considerable induced current was seen, which could harm the PV systems if proper protective measures were not taken. In certain instances, the simulation resultswere in line with the field observations documented in Tables 11 to 23.

It was discovered that the induced currents quickly attenuate as the distance from the current impulse increases for the length of the cable. As expected, in the case of the short-circuited bypass diodes, the induced currents were higher in the conductive loops that were closer to the current impulse than in the conductive loops that were farther away. For both the 2 km and 10 km separation distances, the induced currents increased by 150 kA by adding a short-circuit loop between the model's output terminals.

Although the LPS Franklin Rod Level IV provided sufficient protection equipment, this system required more rod amounts installation than LPS ESE. The performance of using this LPS Franklin Rod slightly increased, requiring more installation costs. Thus, the LPS ESE Level III was more suitable for a direct lightning strike than the LPS Franklin Rod Level IV. This outcome was attributed to the capability of the LPS ESE Level III to handle the high energy of LPS for solar PV farms for a long duration. Overall, the LPS ESE Level II was required to be installed between electronic parts connected in series for protection from direct lightning strikes

## ACKNOWLEDGEMENT

The authors would like to acknowledge the Journal Support Fund, Universiti Teknologi MARA, for supporting this article.

## REFERENCES

[1] Wong, J., Lim, Y.S., Tang, J.H., and Morris, E. (2014) Grid-connected photovoltaic system in Malaysia: A review on voltage issues. *Renewable and Sustainable Energy Reviews*, *29*, 535–545. https://doi.org/10.1016/j.rser.2013.08.087.

[2] Zhang, P.,Jin,Q. (2022) Evolution, status, and trends of exergy research: a systematic analysis during 1997–2020. *Environ Sci Pollut Res 29*, *30*(2), 73769-73794, https://doi.org/10.1007/s11356-022-22915-y.
[3] Azhari, A.W., Sopian, K., Zaharim, A., and Al Ghoul, M. (2008) A new approach for predicting solar radiation in tropical environment using satellite images - Case study of Malaysia," *WSEAS Transactions on Environment and. Development*, *4*(4), 373–378.
[4] Soares, A.P. (2013) Investigation of Typical Problems of PV-Inverters. *Journal of Chemical Information and Modelling*, *53*(9), 1689–1699.
[5] Shahsavari, A., Farajollahi, M., Stewart, E., Roberts, C., and Mohsenian-Rad, H. (2017, 17-19 September) A data-driven analysis of lightning-initiated contingencies at a distribution grid with a PV farm using Micro-PMU data. North American Power Symposium (NAPS). Morgantown, USA. https://doi.org/10.1109/NAPS.2017.8107307.
[6] Coetzer, K.M., Gideon Wiid, P., and Rix, A.J. (2019, November) Investigating lightning induced currents in photovoltaic modules. *International Symposium on Electromagnetic Compatibility* - EMC Europe, pp 261–266, https://doi.org/10.1109/EMCEurope.2019.8871890.
[7] Ren, H., and Zhang, Y. (2021) Research on induced current and induced voltage of 500 kV double circuit transmission line. *Energy Reports*, *7*(1), 216–223. https://doi.org/10.1016/j.egyr.2021.01.077.
[8] Hernández, J.C., Vidal, P.G., and Jurado, F. (2008) Lightning and surge protection in photovoltaic installations. *IEEE Transactions on Power Delivery*, *23*(4), 1961–1971. https://doi.org/10.1109/TPWRD.2008.917886.
[9] Muller, B., Hardt, L., Armbruster, A., Kiefer, K., and Reise, C. (2015) Yield predictions for photovoltaic power plants: Empirical validation, recent advances and remaining uncertainties. *Progress in Photovoltaics, 24*(4), 570–583, https://doi.org/10.1002/pip.2616.
[10] Belik, M. (2014, 12-14 May) PV panels under lightning conditions. Proceedings of the 2014 15th International Scientific Conference on Electric Power Engineering (EPE), pp. 367–370. https://doi.org/10.1109/EPE.2014.6839446.
[11] Phanthuna, N., Thongchompoo, N., Plangklang, B., and Bhumkittipich, K. (2010, November) Model and experiment for photovoltaic lightning effects. International Conference on Power System Technology (POWERCON), *2*. https://doi.org/10.1109/POWERCON.2010.5666054
[12] Ittarat, S., Hiranvarodom, S., and Plangklang, B. (2013) A computer program for evaluating the risk of lightning impact and for designing the installation of lightning rod protection for photovoltaic system. *Energy Procedia*, *34*, 318–325. https://doi.org/10.1016/j.egypro.2013.06.760.
[13] Sueta, H.E., Mocelin, A., Zilles, R., Obase, P.F., and Boemeisel, E. (2013, 7-11 October) Protection of photovoltaic systems against lightning experimental verifications and techno-economic analysis of protection. 2013 International Symposium on Lightning Protection (XII SIPDA), pp. 354–359, https://doi.org/10.1109/SIPDA.2013.6729233.
[14] Sobolewski, K., and Sobieska, E. (2022) Analysis of the effectiveness of lightning and surge protection in a large solar farm. *71*(2), 523–542. https://doi.org/10.24425/aee.2022.140726.
[15] Radulović, V., Miljanić, Z. (2020). Determination of Effective Protection Distance in Front of Surge Protective Devices in Low Voltage Systems. In: Avdaković, S., Mujčić, A., Mujezinović, A., Uzunović, T., Volić, I. (eds) Advanced Technologies, Systems, and Applications IV - Proceedings of the International Symposium on Innovative and Interdisciplinary Applications of Advanced Technologies (IAT 2019). IAT 2019. Lecture Notes in Networks and Systems, vol 83. Springer, Cham. https://doi.org/10.1007/978-3-030-24986-1_6.
[16] J. He, Z. Yuan, S. Wang, J. Hu, S. Chen, and R. Zeng, (2009) Effective protection distances of low-voltage SPD with different voltage protection levels," *IEEE Transactions on Power Delivery*, *25*(1), 187–195. https://doi.org/10.1109/TPWRD.2009.2035297.
[17] Pons, E., and Tommasini, R. (2013, 6-8 June) Lightning protection of PV systems. *4th International Youth Conference on Energetics (IYCE)*, Hungary, pp. 1–5, https://doi.org/10.1109/IYCE.2013.6604209.
[18] Formisano, A., Petrarca, C., Hernández, J.C., and Munõz-Rodríguez, F.J. (2019) Assessment of induced voltages in common and differential-mode for a PV module due to nearby lightning

strikes. *IET Renewable Power Generation, 13*(8), 1369–1378. https://doi.org/10.1049/iet-rpg.2018.6033.

[19] Ahmad, N.I., Ali, Z., Kadir, M.Z.A.A., Osman, M., Zaini, N.H., and Roslan, M.H. (2021) Analysis of lightning-induced voltages effect with SPD placement for sustainable operation in hybrid solar PV-battery energy storage system. *Sustainability, 13*(12). https://doi.org/10.3390/su13126889.

https://doi.org/10.31436/iiumej.v26i1.3255

# COMPREHENSIVE ANALYSIS OF A BRIDGED-T PRE-EQUALIZER CIRCUIT FOR HIGH-SPEED VISIBLE LIGHT COMMUNICATIONS

**SITI HAJAR AB AZIZ[1,2], NORHANIS AIDA MOHD NOR[3*], SURIZA AHMAD ZABIDI[2]**

[1]*Communication Technology Section, Universiti Kuala Lumpur – British Malaysian Institute, Selangor, Malaysia*
[2]*Department of Electrical and Computer Engineering, Kulliyyah of Engineering, International Islamic University Malaysia, Kuala Lumpur, Malaysia*
[3]*Department of Science in Engineering, Kulliyyah of Engineering, International Islamic University Malaysia, Kuala Lumpur, Malaysia*

**Corresponding author: norhanis_aida@iium.edu.my*

*(Received: 9 April 2024; Accepted: 21 August 2024; Published online: 10 January 2025)*

***ABSTRACT:*** This paper presents a comprehensive analysis of a bridged-T equalizer circuit (BTEC) designed for a high-speed visible light communications (VLC) system. The circuit is proposed to overcome the bandwidth limitation of light-emitting diodes (LEDs) in the VLC system. The advanced design system (ADS) and MATLAB were integrated to analyze the behavior of the BTEC in terms of transfer functions and scattering parameters $S11$, $S12$, $S21$, and $S22$. The results indicate a good correlation between the two tools, with the center frequency being 786 MHz. The 3-dB lower and upper cut-off frequencies are 501 MHz and 1.23 GHz, respectively. The impedance point is at magnitude 1 and 0 phase degrees on the Smith chart. This precise point ensures optimal matching to 50 Ω of source and load impedance. This simulation proves that the bridged-T pre-equalizer circuit is a symmetric and reciprocal network since $S11 = S22$ and $S12 = S21$. This work combines the computational capabilities of MATLAB with the circuit simulation capabilities of ADS, which satisfied the pre-equalizer circuit experimental stage.

***ABSTRAK:*** Kertas kerja ini membentangkan analisis komprehensif bagi litar penyama T terjepit (BTEC) yang direka untuk sistem komunikasi cahaya nampak (VLC) berkelajuan tinggi. Litar ini dicadangkan untuk mengatasi had lebar jalur diod pemancar cahaya (LED) dalam sistem VLC. Sistem reka bentuk lanjutan (ADS) dan MATLAB telah disepadukan untuk menganalisis kelakuan BTEC dari segi fungsi pemindahan dan parameter serakan $S11$, $S12$, $S21$, dan $S22$. Keputusan menunjukkan korelasi yang baik antara kedua-dua alat, dengan frekuensi tengah ialah 786 MHz. Frekuensi potong bawah dan atas 3-dB ialah 501 MHz dan 1.23 GHz, masing-masing. Titik impedans adalah pada magnitud 1 dan 0 darjah fasa pada carta Smith. Titik tepat ini memastikan padanan optimum kepada 50 Ω sumber dan galangan beban. Dalam simulasi ini, terbukti bahawa litar pra-penyamaan bridged-T adalah rangkaian simetri dan timbal balik sejak $S11 = S22$ dan $S12 = S21$. Kerja ini menggabungkan keupayaan pengiraan MATLAB dengan keupayaan simulasi litar ADS, yang memenuhi peringkat percubaan litar pra-penyamaan.

***KEYWORDS:*** *Bridged-T circuit, Pre-equalizer, VLC, Scattering parameter, Two-port networks, and ADS/ MATLAB*

https://doi.org/10.31436/iiumej.v26i1.3255

# 1. INTRODUCTION

Visible light communications (VLC) have been recognized as one of the enablers that could revolutionize the future of wireless communications. The extensive deployment of light-emitting diodes (LEDs) provides dual illumination and communication functionality, particularly in indoor environments [1], [2]. The LED-based VLC system complements radio frequency (RF) wireless systems due to its low cost, energy efficiency, and reliable wireless connectivity solution to meet the infrastructure trends of the 6G networks. However, VLC suffers severely from the limited modulation bandwidth of LEDs, $B_{\mathrm{LED}}$ (less than 5MHz for commercial white LEDs) [3], which is lower than the current wireless-fidelity (WIFI) data throughput [4]. Researchers are trying to improve the $B_{\mathrm{LED}}$ by employing various techniques in hardware and algorithms, including blue filtering at the receiver (Rx) to filter out the yellow element [5], micron-sized LEDs [6], and advanced modulation schemes, such as orthogonal frequency division multiplexing (OFDM) [7], and pulse amplitude modulation (PAM) [8], and carrier-less amplitude phase (CAP) modulation [9]. However, most mitigation techniques have the limitations of higher implementation complexity, larger fabrication size, higher power consumption, and high costs [3], [10].

Equalization techniques have been employed in various fields, such as audio systems [10], communication systems [11], optical fiber communication [12], and optical wireless communications (OWC) [13]. Equalization is an approach to adjust the balance between the frequency components of a signal, achieved by amplifying or attenuating specific frequency components within an electronic signal [1]. The equalization technique may be performed either at the transmitter (Tx) (i.e., pre-equalization) or the Rx (i.e., post-equalization) using software and hardware approaches. Theoretically, pre-equalization aims to diminish low-frequency components and amplify high-frequency components, achieving a more uniform distribution of the entire received spectrum to enhance system performance [14]. In contrast, post-equalization is performed at the Rx to compensate for other channel losses and mitigate linear/nonlinear distortions [4].

A bridged-T pre-equalizer circuit (BTEC) is used in communication systems to compensate or equalize the frequency-dependent attenuation or distortion introduced by transmission channels. The circuit is typically employed in high-speed data communication, wired or wireless communication systems, audio and video transmission systems, and RF communication systems. The BTEC comprises passive components connected in a specific configuration, including resistors ($R$), capacitors ($C$), and inductors ($L$). The circuit shapes the system's frequency response power booster and attenuates specific frequency components to achieve desired signal characteristics [1].

Huang et al. [15] were the first to demonstrate that a single bridged T network exhibits constant characteristic impedance and consistent response for high-speed and high-frequency applications such as fiber optic communication systems, digital video broadcasting, and voice-over IP (VoIP). The research was then continued by [16] cascading two constant resistance symmetrical bridged-T networks to give more precise channel compensation, which proved that the 3-dB bandwidth was extended from 12 MHz to 235 MHz and subsequently [17] extended from 17 MHz to 366 MHz using a differential output PIN Rx and a blue filter. Next, Nan Chi et al. [9] investigated cascaded homogeneous and heterogeneous BTEC to enhance transmission data rates in a high-speed LED-based VLC system. They found that a 2-cascaded heterogeneous equalizer provides a larger, more significant gain area than a 2-cascaded homogeneous equalizer. The gain values were 21 and 31 dB for heterogeneous and homogeneous designs, respectively. It shows that increasing the gain area affects the magnitude response due to the amplification of the signal. Moreover, Haiqi et al. [18] extended the $B_{\mathrm{LED}}$

https://doi.org/10.31436/iiumej.v26i1.3255

used in the VLC system from 14 MHz to 520 MHz with a cascaded BTEC in a real-time indoor environment. Aiming for a simpler single circuit, Ziying et al. [7] achieved 879.2 MHz and 765.2 MHz for the forward transmission parameter *S*21 in simulation and measurement, respectively. Recently, Chengyu et al. [5] demonstrated a novel hybrid pre-equalization circuit to extend the bandwidth of the VLC system from 30 MHz to 600 MHz using a single commercially available phosphorescent white LED. The equalization circuit was based on four cascaded BTECs, an impedance-matching network, and an active RC frequency-selecting network. However, the circuit complexity contributes to higher costs due to high power consumption. In [19], Yufen et al. combined the folded equalization circuit and the bridged-T equalizer, without using blue filters to extend from a few megahertz to 893 MHz. They designed an AC-coupled drive circuit to provide a constant current of 350 mA to the 1 W LED. This VLC system achieved 1.9 Gb/s using OOK-NRZ modulation over a distance of 7 meters, with a bit error rate (BER) of $3 \times 10^{-5}$.

While there have been several reports in the literature on enhancing the data rates of VLC systems using BTEC, fewer researchers have analyzed the circuit design in terms of the circuit transfer function and scattering parameters (*S*-parameters). Furthermore, simple circuits with no active component have lower power dissipation, making them more energy efficient [10]. Hence, this paper focuses on designing a low-complexity pre-equalizer based on a BTEC to enhance the 3-dB bandwidth of the VLC system using the circuit transfer function and *S*-parameters. The study also aims to optimize the $B_{\text{LED}}$ system design while minimizing the circuit complexity using bridged-T networks in pre-equalization circuits for VLC applications.

## 2. THE BRIDGED-T PRE-EQUALIZER CIRCUIT (BTEC)

A BTEC is an electronic circuit component that is widely used in telecommunications and RF systems. The BTEC consists of a *T*-network configuration, a type of circuit with a fourth branch connecting the two series arms from input to output terminal ports. Equalization is a well-known method that modifies the stability between the frequency components of a signal by strengthening or weakening, which modifies the amplitude or phase response of specific frequency ranges [1]. Specifically, a pre-equalizer circuit attenuates low-frequency components and amplifies high-frequency components to flatten the entire receiving spectrum, thereby improving the system's performance [14].

### 2.1. Principles of the Bridged-T Network

Fig. 1 shows the proposed single BTEC, which consists of four equivalent impedances, $Z_1$, $Z_2$, $Z_3$, and $Z_4$. Referring to Fig. 1(a), $Z_1$ is the equivalent impedance of $C_1, L_1\, R_1$ whereas the Fig. 1(b) is the equivalent impedance of $C_2, L_2\, R_4$. In order to match the impedance of the input and output ports, this branch bridges the two impedances of $Z_2$ and $Z_3$, which corresponds to the desired iterative impedance of the network, $R_o$ = 50 Ω. The input and output voltages are $V_{in}$ and $V_{out}$, respectively. The circuit was benchmarked by Huang et al. [1]. However, the parameter values and the locations of resistors, in particular $R_1$ and $R_4$ exhibit crucial variations that significantly affect the BTEC frequency and phase responses. These variations have led to noteworthy research discoveries.

https://doi.org/10.31436/iiumej.v26i1.3255

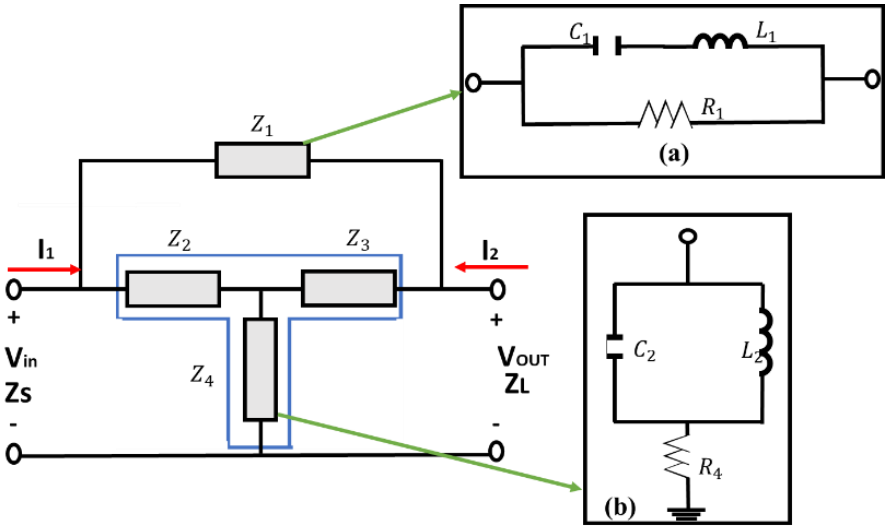


Figure 1. The proposed single bridged- T pre-equalizer circuit.

Additionally, based on Eq. (1) in [15], it can be observed that the transfer function of a single bridged-T network, $H_{EQ}$ which is expressed as:

$$H_{EQ} = \frac{Z_3Z_2 + Z_1Z_4 + Z_3Z_4 + Z_4Z_2}{Z_1Z_2 + Z_3Z_2 + Z_4Z_2 + Z_1Z_4 + Z_3Z_4}, \tag{1}$$

Then, to design a constant resistance amplitude equalizer, the equivalent impedance product of $Z_1$ and $Z_4$ must equal $R_o^2$, which can be expressed as:

$$Z_1 = \frac{R_1\,(Z_c + Z_L)}{R_1 + Z_c + Z_L}, \tag{2}$$

$$Z_4 = R_4 + \frac{Z_c\,Z_L}{Z_c + Z_L}, \tag{3}$$

$$Z_1 \times Z_4 = R_0^2, \tag{4}$$

where $Z_L = j\omega L$, $Z_c = \frac{1}{j\omega C}$, and $\omega$ is the angular frequency.

### 2.2. *S*-parameters in a Two-port Networks

Two-port networks consist of four terminals. A pair of terminals across which a current ($I$) may enter or exit a network is known as a port. $I$ enter one terminal and exit through the other terminal, so the net current entering the port equals zero. Fig. 2 shows the two-port circuits to describe the circuit performance in terms of the voltage ($V$) and $I$ at both input and output ports. $I_1$ current enters terminal 'a' and exits terminal 'b' of the input ports 'a and b.'

https://doi.org/10.31436/iiumej.v26i1.3255

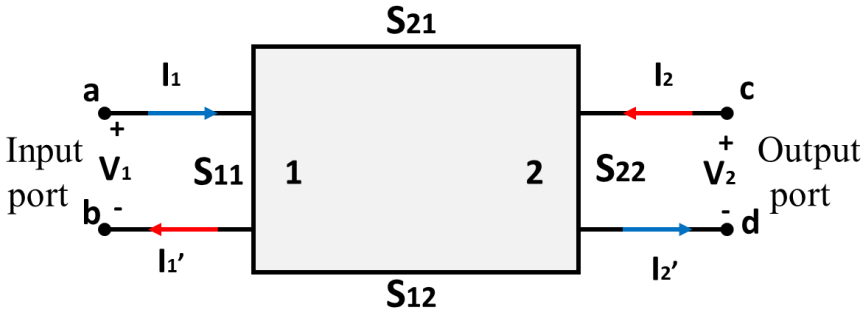


Figure 2. A two-port networks

Fundamentally, *S*11 is the input reflection coefficient, *S*12 is the reverse transmission coefficient, *S*21 is the forward transmission coefficient, and *S*22 is the output reflection coefficient. $V_1$ is the input voltage from port a-b, while $V_2$ is the output voltage from port c-d.

The two-port networks describe the circuit's *V* and *I* at each port. Hence, it allows us to describe its operation when connected to a more extensive and complex network. The four most prominent parameters are *S*-parameters, which define the relationship between the incident wave and reflected wave at both ports 1 and 2, *Z*-parameters (impedance parameters), *ABCD*-parameters (transmission parameters), *Y*-parameters (admittance parameters), and *H*-parameters (hybrid parameters).

At high frequencies, which are larger than 300 MHz, such as microwaves, radar waves, and up to GHz frequencies, Ohm's Law is unsuitable for analysing circuit behaviours. Instead, the transmission line theory is preferable due to the causal relationship between the transfer function and *S*-parameter analysis [20]. The *S*-parameters knowledge is vital in describing circuit behaviours in high-speed applications, especially in RF and microwave filter design, circuitry and systems, semiconductor device characterization, and high-speed digital systems.

This work calculates the *S*-parameters with MATLAB and simulates them with ADS software. The default source and load impedances in ADS are 50 Ω. Additionally, the proposed design is derived by analysing the parallel interconnection of two port networks in terms of the *S*-parameters, including *S*11, *S*12, *S*21, and *S*22.

The BTEC was considered as a parallel interconnection of the two port networks, represented using *Y*-parameters as shown in Fig. 1. The input and output ports are $Z_s$ and $Z_L$, respectively, and concurrently $Z_s$ represents the output impedance of the vector network analyser (VNA) and $Z_L$ represents the load of the circuit. The network admittance, $Y_1$ is solely for $Z_1$, can be expressed as:

$$Y_1 = \begin{bmatrix} \frac{1}{Z_1} & -\frac{1}{Z_1} \\ -\frac{1}{Z_1} & \frac{1}{Z_1} \end{bmatrix}, \tag{5}$$

The T-shape configuration of $Z_2$, $Z_3$, and $Z_4$ , the network admittance $Y_2$ , is expressed as:

$$Y_2 = \begin{bmatrix} \frac{Z_3 + Z_4}{Z_2Z_3 + Z_2Z_4 + Z_3Z_4} & -\frac{Z_4}{Z_2Z_3 + Z_2Z_4 + Z_3Z_4} \\ -\frac{Z_4}{Z_2Z_3 + Z_2Z_4 + Z_3Z_4} & \frac{Z_2 + Z_4}{Z_2Z_3 + Z_2Z_4 + Z_3Z_4} \end{bmatrix}, \tag{6}$$

https://doi.org/10.31436/iiumej.v26i1.3255

The total admittance, $Y_T$ can be expressed as:

$$Y_T = Y_1 + Y_2\,, \tag{7}$$

where $Z_1$ and $Z_4$ same as in Eqs (1) and (2), while $Z_2 = Z_3 = R_o$.

The *S*-parameters and the normalized *Y*-parameters with $Z_s$ and, $Z_L$ can be expressed as [21]

$$S11 = \frac{\left[1 - Y_{11n}\left(\frac{Z_S^*}{Z_S}\right)\right](1 + Y_{22n}) + Y_{12n}Y_{21n}\left(\frac{Z_S^*}{Z_S}\right)}{(1 + Y_{11n})(1 + Y_{22n}) - Y_{12n}Y_{21n}}, \tag{8}$$

$$S12 = \frac{-2Y_{21n}}{(1 + Y_{11n})(1 + Y_{22n}) - Y_{12n}Y_{21n}}, \tag{9}$$

$$S21 = \frac{-2Y_{21n}}{(1 + Y_{11n})(1 + Y_{22n}) - Y_{12n}Y_{21n}}, \tag{10}$$

$$S22 = \frac{(1 + Y_{11n})\left[(1 - Y_{22n})\left(\frac{Z_L^*}{Z_L}\right)\right] + Y_{12n}Y_{21n}\left(\frac{Z_L^*}{Z_L}\right)}{(1 + Y_{11n})(1 + Y_{22n}) - Y_{12n}Y_{21n}}, \tag{11}$$

where the normalized admittance parameters are denoted as:

$$Y_{11n} = \frac{Y11}{Z_s};\ Y_{12n} = Y_{12}\sqrt{Z_s \times Z_L};\ Y_{21n} = Y_{21}\sqrt{Z_s \times Z_L};\ \text{and}\ Y_{22n} = \frac{Y22}{Z_L}.$$

### 2.3. Relationship of Transfer Function and S-parameter

The transfer function and S-parameters are crucial mathematical models for comprehending the systems and network performance. Although both models serve the same purpose, they provide distinct information about the system's response. The transfer function characterizes the system's input-output relationship, specifically in the frequency domain. Whereas S-parameters describe the power transfer and scattering characteristics of a network or device[20].The $S21$ of a single equalizer circuit can be expressed as:

$$S21 = 2 \times \mathrm{H_{EQ}}\,, \tag{12}$$

where $\mathbf{H_{EQ}}$ is the frequency response of a single equalizer.

In this paper, both MATLAB and ADS results are then compared for validation. The comparison of the obtained output with the theoretical model ascertains the validity of the proposed design and ensures its practicality and feasibility.

## 3. RESULTS AND DISCUSSION

This section describes the simulation results of the pre-equalizer circuit through cross-validation analysis using MATLAB and ADS. The analysis compares the frequency response of the transfer function and *S*-parameter analysis for validation purposes. The process was initiated by adjusting the component values using Eq. (4) through MATLAB simulation. Following this adjustment, the circuit was constructed using ADS software using the identified optimal values. Upon identifying the optimal values in ADS software, the closest available

https://doi.org/10.31436/iiumej.v26i1.3255

component values were selected in our laboratory. In this work, the component values are set to $R_1 = 500\ \Omega$, $R_4 = 5\ \Omega$, $L = 10$ nH, $C = 4.1$ pF, $Z_2$ and $Z_3 = 50\ \Omega$. The value of $R_1$ is obtained from ADS simulation, and $R_4$ is calculated from Eq (3). Additionally, to maintain the impedance stability of the two-port circuit, the values of $C_1 = C_2$ and $L_1 = L_2$.

### 3.1. The Frequency Response of the Transfer Function

Fig. 3 presents the transfer function responses versus frequency from both MATLAB and the ADS simulation tools. The MATLAB result is based on the calculation using Eq (1), whereas the ADS simulation result is obtained from the output voltage to input voltage ratio in the proposed design.

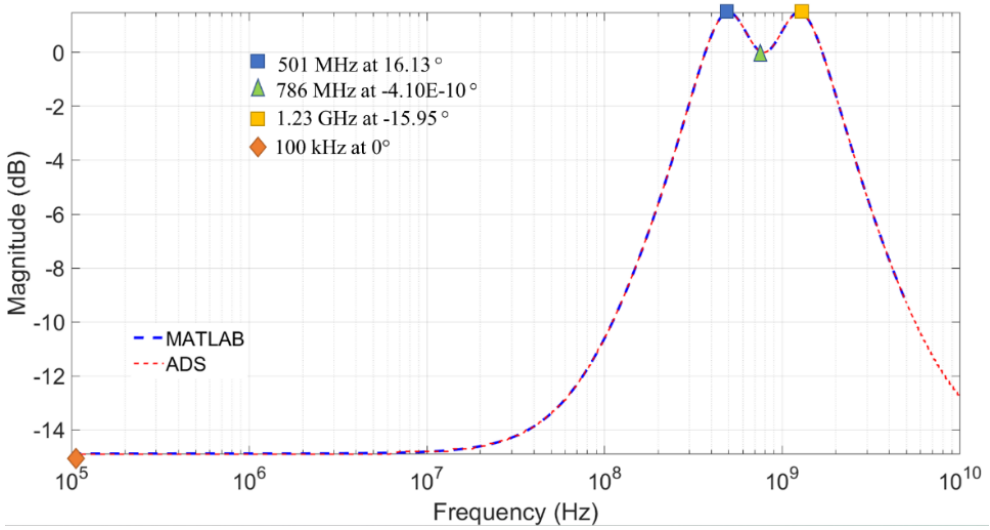


(a) The magnitude response

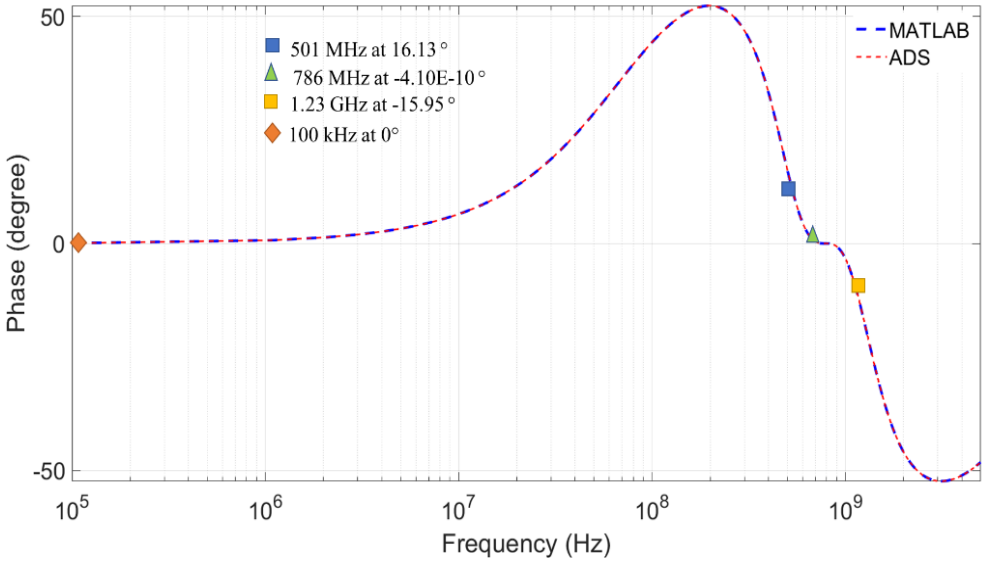


(b) The phase response

Figure 3. Comparison of (a) magnitude response and (b) phase response of the pre-equalizer circuit using MATLAB and ADS.

Fig. 3 (a) shows the frequency response result, which shows the maximum amplitude of 1.48 dB gain at double peak responses of 501 MHz and 1.23 GHz. The presence of a double

https://doi.org/10.31436/iiumej.v26i1.3255

peak in the frequency response curve resulting from the resonant circuit configuration of $R$, $L$, and $C$, each at $Z_1$ and $Z_4$, enhances the selectivity and precision of filtering in the passband. The center frequency was 786 MHz at 0 dB, indicating that the input signal was neither amplified nor attenuated. This allowed for the preservation of the original signal strength at the center frequency while attenuating the lower and upper cut-off frequencies. The minimum attenuation was -14.9 dB at 100 kHz, demonstrating that the BTEC attenuates frequencies outside the passband by at least -14.9 dB. Fig. 3 (b) shows that the phase response of both the calculated and simulated results was identical, providing evidence of the circuit design accuracy and consistency of the simulation tools and mathematical methods.

### 3.2. Scattering Parameter Analysis

To investigate the proposed BTEC's performance in the frequency domain, the start and end sweep frequencies were set to 100 MHz and 5 GHz, respectively, with 1 MHz increment for both calculation and simulation. Fig. 5. illustrates the S–parameters in terms of magnitude and phase response calculated using MATLAB and simulated with the ADS tool, respectively.

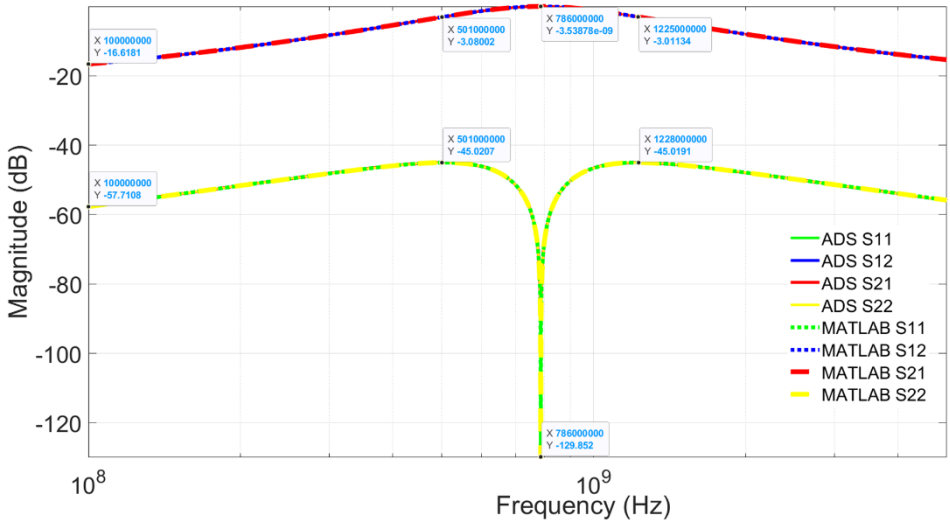


(a) Magnitude responses

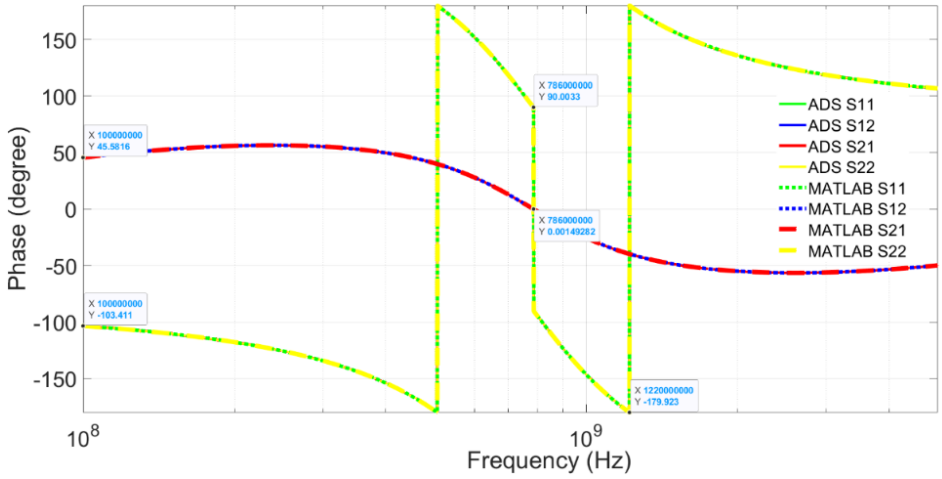


(b) Phase responses

Figure 4. Simulated ADS and calculated MATLAB in terms of (a) magnitude response and (b) phase response over frequency.

https://doi.org/10.31436/iiumej.v26i1.3255

In Fig. 4 (a), the obtained center frequency was 786.1 MHz at -16.62 dB with a 3-dB lower cut-off frequency of 501 MHz and a 3-dB upper cut-off frequency of 1.23 GHz, which resulted in a bandwidth of 729 MHz. In Fig. 4 (b), it can be observed that the phase angle was 0 degrees at the center frequency in calculation and simulation, which indicates that the BTEC did not introduce any additional phase shift. This means that the output signal was in phase with the input signal. The calculated and simulated results confirmed that the S11 and S22 responses were identical, while the S12 response was identical to S21. The similarity of ADS and MATLAB results proved that BTEC is a symmetric and reciprocal network. This finding validated that the circuit was investigated correctly through calculation and simulation.

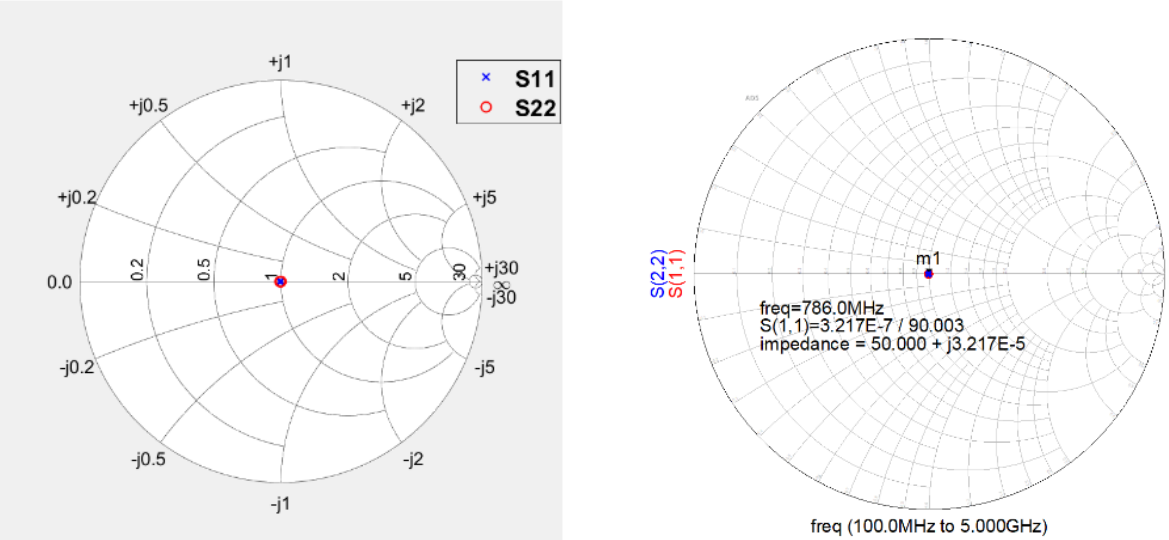


(a) MATLAB (b) ADS

Figure 5. S11 and S22 on the Smith chart

The BTEC input and output reflection coefficients, S11 and S22 parameters, were plotted on the Smith chart using MATLAB and ADS, as shown in Fig. 5 (a) and (b), respectively. The circuit demonstrated highly effective matching of the source and load impedances, as evidenced by the plots produced in both software. The center point of the Smith chart, with a magnitude of 1 and 0 degrees, clearly indicates that BTEC delivers excellent impedance matching. Moreover, the calculated and simulated results showed good agreement in matching the source and load impedance to the standard 50 Ω.

Table 1 summarizes the proposed circuit with the bridged-T circuit in the VLC system. Remarkably, for a single BTEC method, our designed pre-equalizer circuit outperformed the research presented in [15] and [7]. The proposed BTEC and the work in [15] shared the same total number of passive components: 2 inductors, 2 capacitors, and 4 resistors, with a peak response of 175 MHz. In contrast, the work presented in [7] utilizes a lesser number of passive components, but the simulation and measurement results were significantly higher, at 879.2 MHz and 765.2 MHz, respectively. However, it is noted that neither work validated the circuit transfer function through analytical and simulation modeling. The discussion in both works was limited to the presentation of the S21 and S22 scattering parameters, as obtained through simulation and measurement.

https://doi.org/10.31436/iiumej.v26i1.3255

Table 1. Comparison of the BTEC employed in pre-equalization in the VLC system

| Papers | Light device | BTEC Methods | $f_c$ (MHz) | $H_{EQ}$ | *S*-param | 3-dB VLC |
|---|---|---|---|---|---|---|
| [15] | RGB (Cree) | single | 175 MHz | Derived, no validation | *S*21; *S*22 (both) | - |
| [16] | white LED (OSRAM) | 2- cascaded | 353 MHz | Derived, no validation | *S*21 (M) | 12MHz to 235 MHZ |
| [17] | white LED (OSRAM) | 2- cascaded | 352 MHz | Derived, no validation | *S*21 (M) | 17MHz to 366MHz |
| [9] | RGB (Engine) | 2- cascaded | 400 MHz | - | *S*21 (S) | - |
| [18] | white LED (OSRAM) | RC-series parallel cascaded | - | Derived, no validation | - | 1 MHz to 520 MHz |
| [7] | HV-Blue LED | single | 879.2 MHz (S) 765.2 MHz (M) | Derived, no validation | *S*21; *S*22 (both) | 45 MHz to 750 MHz S21 (air)/ to 850 MHz (underwater) |
| [5] | white LED (OSRAM) | 4- cascaded | - | Yes | *S*21 (M) | 30 MHz to 600 MHz |
| [19] | white LED (OSRAM) | 2- cascaded | - | Derived, no validation | - | 893 MHz |
| This paper | white LED (OSRAM) | single | 786 MHz (S) | Yes | *S*11; *S*12; *S*21; *S*22 (both) | Expected to reach 800 MHz |

*S* = simulation; *M* = measurement; $f_c$=center frequency; *S*-param = scattering parameter; RGB = red, green, blue.

In this work, the frequency-domain characterization of the circuit's behavior is well described through the analytical and simulation models of the S11, S21, S21, and S22 scattering parameters. This comprehensive analysis ensures good impedance matching, stability, and overall validation of the circuit's performance in high-frequency applications.

## 4. CONCLUSION

In this paper, we analyzed the performance of a pre-equalizer circuit based on a bridged-T network. The findings demonstrate an excellent alignment between the calculated and simulated results, which were performed using MATLAB and ADS software. We successfully achieved a center frequency of 786 MHz, designed with a single bridged-T circuit configuration. The 3-dB lower and upper cut-off frequencies obtained were 501 MHz and 1.23 GHz, respectively. Besides, we have demonstrated that *S*11=*S*22 and, likewise, *S*12 = *S*21, indicating that the circuit is a symmetric and reciprocal network. The circuit is designed to support a port impedance of 50 Ω port, making it compatible with a range of devices, including amplifiers, RF connectors, and cables. In comparison to previous works, our findings show a significant improvement in terms of center frequency $f_c$ and 3-dB cut-off frequencies. Notably, the utilization of a single bridged-T circuit has resulted in reduced circuit complexity and lower fabrication cost. Additionally, both *S*-parameters and frequency response analysis are essential parameters in comprehending the system's frequency-related behavior despite their fundamental disparities. These findings are critical for validating the proposed design and ensuring its efficacy during the experimental stage.

## ACKNOWLEDGEMENT

The author wishes to thank International Islamic University Malaysia (IIUM) and to Universiti Kuala Lumpur - British Malaysian Institute (BMI) for supporting the dissemination of this research.

## REFERENCES

[1] R. Zhang, J. Xiong, M. Li, and L. Lu. (2024) Design and Implementation of Low-Complexity Pre-Equalizer for 1.5 GHz VLC System. IEEE Photonics Journal, vol. 16, pp 1–10. https://doi: 10.1109/JPHOT.2024.3351192.

[2] X. Li, Z. Ghassemlooy, S. Zvanovec, R. Perez-Jimenez, and P. A. Haigh. (2020) Should Analogue Pre-Equalisers be Avoided in VLC Systems? IEEE Photonics Journal, vol. 12, pp 1–14. https://doi: 10.1109/JPHOT.2020.2966875.

[3] S. Chaudhary, X. Tang, and X. Wei (2020) Experimental demonstration of 62.5 Mbps VLC link for healthcare infrastructures by incorporating limiting amplifier as an amplification scheme. Microelectronics Journal, vol. 108. https://doi: 10.1016/j.mejo.2020.104971.

[4] A. Thao, X. Kang, and G. H. Lee. (2021) Implementation of an optical wireless communication system deploying a novel post-equalization circuit for indoor application. Microwave Optical Technology Letter, vol. 63, pp 13–18. https://doi: 10.1002/mop.32556.

[5] C. Min et al. (2020) A novel method for constructing VLC equalizer with active-passive hybrid network. IEEE Photonics Journal, vol. 12, no. 2. https://doi: 10.1109/JPHOT.2020.2969413.

[6] Wei-Ta Huang, Chun-Yen Peng, Hsin Chiang, Yu-Ming Huang, Konthoujam James Singh, Wei-Bin Lee, Chi-Wai Chow, Shih-Chen Chen, and Hao-Chung Kuo. (2022) Toward high-bandwidth yellow-green micro-LEDs utilizing nanoporous distributed Bragg reflectors for visible light communication. Photonics Research, Res. 10, pp 1810-1818. https://doi.org/10.1364/PRJ.462519

[7] Z. Zhang et al. (2019) Over 700 MHz -3 dB Bandwidth UOWC System Based on Blue HV-LED with T-Bridge Pre-Equalizer. IEEE Photonics Journal, vol. 11. https://doi: 10.1109/JPHOT.2019.2910090.

[8] L. Wang, X. Wang, J. Kang, and C. Patrick Yue. (2021) A 75-Mb/s RGB PAM-4 Visible Light Communication Transceiver System with Pre- and Post-Equalization. Journal of Lightwave Technology, vol. 39, pp 1381–1390. https://doi: 10.1109/JLT.2020.3034227.

[9] N. Chi, Y. Zhou, S. Liang, F. Wang, J. Li, and Y. Wang. (2018) Enabling Technologies for High-Speed Visible Light Communication Employing CAP Modulation. Journal of Lightwave Technology, vol. 36, pp 510–518. https://doi: 10.1109/JLT.2017.2783906.

[10] D. Yan, X. Mao, S. Xie, J. Cong, and H. Chen. (2019) Design Fully Integrated Driver Circuit for Phosphorescent White Light-Emitting-Diode High Speed Real-Time Wireless Communication. IEEE Photonics Journal, vol. 11, no. 2. https://doi: 10.1109/JPHOT.2019.2904607.

[11] R. Martinek, L. Danys, and R. Jaros. (2020) Adaptive software defined equalization techniques for indoor visible light communication. Sensors (Switzerland), vol. 20, no. 6. https://doi: 10.3390/s20061618.

[12] C. Jin et al. (2022) High-Speed Long-Haul Multi-Channel Nonlinear Optical Communication Systems Influenced by Equalization Enhanced Phase Noise. IEEE 14th International Conference on Advanced Infocomm Technology, pp 103–106. https://doi: 10.1109/ICAIT56197.2022.9862695.

[13] N. Liu, C. Ju, D. Wang, D. Wang, and P. Xie. (2023) Multi-Aperture Coherent Digital Combining Based on Complex-Valued MIMO 2N × 2 Adaptive Equalizer for FSO

Communication. Journal of Lightwave Technology, vol. 41, pp 5983–5990. https:// doi: 10.1109/JLT.2023.3276637.

[14] D. Silveira, W. Wijekoon, and G. H. Lee. (2018) Demonstration of an optical wireless communication link with pre-emphasis circuit for high-speed application. Microwave Optical Technology Letter, vol. 60, no. 11, pp 2613–2618. https://doi: 10.1002/mop.31491.

[15] X. Huang, J. Shi, J. Li, Y. Wang, and N. Chi. (2015) A Gb/s VLC transmission using hardware preequalization circuit. IEEE Photonics Technology Letters, vol. 27, no. 18, pp 1915–1918. https://doi: 10.1109/LPT.2015.2445781.

[16] X. H. Xingxing Huang, S. C. Siyuan Chen, Z. W. Zhixin Wang, Y. W. Yiguang Wang, and N. C. Nan Chi. (2015) 1.2 Gbit/s visible light transmission based on orthogonal frequency-division multiplexing using a phosphorescent white light-emitting diode and a pre-equalization circuit. Chinese Optics Letters, vol. 13, pp 100602–100606. https:// doi: 10.3788/col201513.100602.

[17] X. Huang, Z. Wang, J. Shi, Y. Wang, and N. Chi. (2015) 16 Gbit/s phosphorescent white LED based VLC transmission using a cascaded pre-equalization circuit and a differential outputs PIN receiver. Optical Express, vol. 23, no. 17, pp 22034. https:// doi: 10.1364/oe.23.022034.

[18] H. Zhang, A. Yang, L. Feng, and P. Guo. (2018) Gb/s Real-Time Visible Light Communication System Based on White LEDs Using T-Bridge Cascaded Pre-Equalization Circuit. IEEE Photonics Journal, vol. 10, no. 2. https:// doi: 10.1109/JPHOT.2018.2812759.

[19] Y. Wang, X. Chen, and Y. Xu. (2023) Transmitter for 1.9 Gbps phosphor white light visible light communication without a blue filter based on OOK-NRZ modulation. Optical Express, vol. 31, no. 5, pp 7933. https:// doi: 10.1364/oe.476911.

[20] S. H. Hashim and R. Kwok. (2011) Network Techniques: Conversion between Filter Transfer Function and Filter Scattering (S-Matrix) Parameters.

[21] D. A. Frickey. (1999) Conversions between S, Z, Y, H, ABCD, and T parameters which are valid for complex source and load impedances. IEEE Transactions on Microwave Theory and Techniques, vol. 42, pp. 205-211. https:// doi: 10.1109/22.275248.

https://doi.org/10.31436/iiumej.v26i1.3268

# 4D RADAR IMAGING AND CAMERA FUSION FOR ROAD CROSSING DETECTION AND CLASSIFICATION USING DEEP LEARNING

**LIYAANA SHAHIRAH WAN ABD AZIZ[1*], FARAH NADIA MOHD ISA[1], FARIDAH ABD RAHMAN[1], ARVIND HARI NARAYANAN[2], AHMAD REZA ALGHOONEH[3], GEORGE SHAKER[4]**

[1]*Department of Electrical and Computer Engineering, Kulliyyah of Engineering, International Islamic University Malaysia, 53100, Jalan Gombak, Kuala Lumpur, Malaysia*

[2]*Emrail Sdn. Bhd., 19-8 Block C1 Dataran Prima, Jalan PJU 1/41, 47301, Petaling Jaya, Selangor, Malaysia*

[3]*Department of Mechanical and Mechatronics Engineering, University of Waterloo, Waterloo, ON N2L 3G1, Canada*

[4]*Department of Electrical and Computer Engineering, University of Waterloo, Waterloo, ON N2L 3G1, Canada*

**Corresponding author: yaanashira97@gmail.com*

*(Received: 19 April 2024; Accepted: 6 October 2024; Published online: 10 January 2025)*

***ABSTRACT:*** This paper presents the development of an object detection and classification system for road crossing areas, integrating 4D radar imaging and a mono-camera dataset with a deep-learning neural network. The system utilizes deep neural networks implemented via Keras and TensorFlow to detect and classify multiple targets, including pedestrians, cars, buses, and trucks. At the core of this work is Retina-4F, a multi-chip radar imaging system developed by Smart Radar System, which offers high-resolution object detection and localization capabilities. Retina-4F provides real-time 4D information on detected objects, operating in a cascading architecture with three transmitters and four receivers per chip. Two road-crossing scenes were simulated to collect data, generating a point cloud dataset labeled with target classes for neural network training and testing. Data from two main sensors—Retina-4F and a mono-camera—were pre-processed using DBSCAN and YOLOv7 for enhanced accuracy. Operating at 77 GHz, Retina-4F was tested in two road environments, generating a dataset with approximately 10,000 frames. The deep learning model demonstrated an accuracy of 84% in classifying multiple targets, including cars, pedestrians, buses, and trucks. The fusion of radar point cloud data with visual sensor data proved effective, showing strong results in distinguishing target types.

***ABSTRAK:*** Kertas ini membentangkan pembangunan sistem pengesanan dan pengelasan objek untuk kawasan lintasan jalan raya, menggabungkan pengimejan radar 4D dan set data mono-kamera dengan rangkaian neural pembelajaran mendalam. Sistem ini menggunakan rangkaian neural mendalam yang dilaksanakan melalui *Keras* dan *TensorFlow* untuk mengesan dan mengelaskan pelbagai sasaran, termasuk pejalan kaki, kereta, bas, dan trak. Inti daripada kajian ini adalah *Retina-4F*, sistem pengimejan radar berbilang cip yang dibangunkan *oleh Smart Radar System*, yang menawarkan keupayaan pengesanan objek dan penentuan lokasi resolusi tinggi. *Retina-4F* menyediakan maklumat 4D masa nyata mengenai objek yang dikesan, beroperasi dengan tiga pemancar dan empat penerima bagi setiap cip dalam seni bina kaskad. Dua adegan lintasan jalan disimulasikan untuk mengumpul data, menghasilkan set data awan titik yang dilabel dengan kelas sasaran untuk latihan dan ujian

rangkaian neural. Data daripada dua sensor utama—*Retina-4F* dan mono-kamera—dipra-proses menggunakan *DBSCAN* dan *YOLOv7* untuk meningkatkan ketepatan. Beroperasi pada 77 GHz, *Retina-4F* diuji dalam dua persekitaran jalan yang berbeza, menghasilkan set data dengan kira-kira 10,000 bingkai. Model pembelajaran mendalam menunjukkan ketepatan sebanyak 84% dalam mengelaskan pelbagai sasaran, termasuk kereta, pejalan kaki, bas, dan trak. Penggabungan data awan titik radar dengan data sensor visual terbukti berkesan, menunjukkan hasil yang kuat dalam membezakan antara jenis sasaran.

***KEYWORDS:*** *4D Radar Imaging, sensors fusion, deep learning, YOLOv7, Keras and TensorFlow.*

# 1. INTRODUCTION

The number of projects conducted in recent years involving automotive radar imaging is growing drastically. This is due to the demands in the automotive industry to move towards Adaptive driver-assistance systems (ADAS). The number of road accidents and incidents is very high as vehicles on the road have increased. Thus, this has led to a global safety issue, as these problems are commonly seen in high-income and low- and middle-income countries. According to the World Health Organization (WHO), 1.3 million people have died because of road accidents around the world, and about 20 to 50 million have suffered road accident injuries [1]. Hence, to improve the safety of road users, researchers and manufacturers have begun to support the automotive radar imaging technology [2] in autonomous vehicles, where the technology offers much higher reliability in providing high accuracy in object detection, road lane warning, blind spot detection, and an early potential crash warning system [3].

The advancement of radar for autonomous vehicles is provided by Complementary Metal-Oxide-Semiconductor (CMOS) technology, which has been integrated with automotive radar imaging and offers a much lower cost of radar on-chip and antenna on-chip mass production [4]. Moreover, CMOS technology plays a vital role in radar systems by providing low power consumption and increased data processing capacity [5]. This has enabled radar manufacturers to improve their radar chipset solutions for the automotive market [3]. Today, radar imaging systems implement the cascading of multiple chips to enhance sensor technology. Based on [6], compared to a single chip, a radar system cascaded with multiple chips allows the radar to operate with multiple transmit and receive antennas, which improves object detection.

Multiple Input Multiple Output (MIMO) radar has proven to be a reliable radar system, and the concept is mostly used in many types of radar applications. MIMO systems are used in radar imaging technology to improve angular resolution and accuracy, slow-moving target detection, and the percentage of object detection [2, 6]. For this purpose, the presence of this MIMO system led to high-resolution 4D radar imaging, resulting in a denser point cloud output [7]. The concept of 4D radar imaging is to provide high-resolution azimuth, elevation, range, and Doppler information of a target [8]. However, a single sensor system is insufficient with today's radar technology to achieve highly advanced automated driving. ADAS implementation on automated vehicles combines several sensor technologies known as Lidar, Camera, and Ultrasound [5]. Even so, radar still plays a vital role [9] in automated driving, especially with 4D radar imaging systems that enable high accuracy of distance measurement, Doppler velocity, and independence in weather conditions and lighting exposure [2].

There has been much ongoing research on radar systems using RF chips for automotive 4D radar imaging to use MIMO-based radar with frequency-modulated continuous wave (FMCW) waveform. In [10], a parking monitoring system was estimated using 77-GHz MIMO

FMCW radar to detect vacant parking spaces. The radar's performance is demonstrated by adopting radar image properties to improve the performance of radar imaging processing. Moreover, in [11], the authors demonstrated the measurement of curbstone height estimation, drain cover detection, and parking lot detection as part of safety applications in autonomous vehicles. Furthermore, as demonstrated in [12], the authors work on the performance of the MIMO FMCW automotive radar under adverse weather conditions. Using 77 GHz radar platforms, the MIMO FMCW radars are tested for snowy and foggy weather conditions.

To classify 3D radar point clouds, deep neural networks are employed as 4D radar imaging has established its credibility in the market [13-15]. Several active projects investigate the classification of human activities using Convolutional Neural Networks (CNN). Some methods for classifying human activity use CNN as the training model, which produces a point cloud image of the target when utilizing FMCW MIMO-based 4D radar image [14-16]. Recurrent Neural Network (RNN) usage is another common method for target classification [17]. In order to achieve denser point cloud features of a target, RNN is primarily used in the application of identifying moving targets [18].

Among the work done in classifying point cloud data for any application, the classification of radar point clouds faces several challenges. For example, in [14][15], radar point clouds are insufficient for classifying human activity, which requires understanding the pattern of human activity, such as sitting or standing. To overcome these obstacles, the authors determined how to merge point cloud data to produce a denser point cloud. By doing so, the distinctive signatures of each human activity can be identified and classified more easily. Training a classifier with aggregated radar point cloud data requires more computational effort than training it with a single radar data frame.

To simplify classification work, we propose a point cloud classification method using sensor fusion with a mono camera and 4D radar image. In this paper, the radar sensor used is Retina-4F, developed by Smart Radar Systems. Based on the Smart Radar system, Retina-4F is designed and developed for automotive applications [19]. With its capability of providing real-time raw data, users can work on data processing for various purposes, such as collecting datasets for deep learning and object recognition.

A study utilized a Retina-4F radar module to estimate vehicle orientation for autonomous driving [20]. Their work focuses on estimating the vehicle's orientation using three machine learning methods: Principal Component Analysis (PCA), decision tree, and Convolutional Neural Network (CNN). The radar provides the data, and the point cloud output of the vehicle is used to process the orientation estimation. Based on the authors' work, Retina-4F provides dense point cloud data, which offers a sufficient point cloud image to process the orientation angle further.

Millimeter-wave radar has the potential to provide a highly accurate location, Doppler velocity, and angular resolution of the desired target [21]. However, concerning object classification, radar point cloud sparsity could affect the recognition system due to the presence of a significant number of reflection points originating from the background. Hence, we can observe the trend of research work moving towards sensor fusion. As mentioned in [22], the authors enhance the system for detecting and tracking objects in autonomous vehicles by fusing camera data and radar 3D object detection. Therefore, combining this technology can enhance the object's visual recognition and the system's tracking capability.

In obtaining a dataset for developing a neural network point cloud classifier, only a few datasets are available in radar point cloud target classification. Hence, a point cloud dataset

with target labeling is needed before developing a neural network classifier. We proposed a sensor fusion that combined radar point cloud data and image data to create a custom dataset. Many studies adopt this method in combining sensor fusion for higher efficiency in target detection and classification [23-25], especially for fully autonomous applications.

Our paper aims to develop target detection and classification using the deep learning method by performing measurements using a 77 GHz automotive radar image system for object detection by varying targets commonly seen on road crossings, like pedestrians, cars, buses, and trucks. With the aid of the 4D radar image and mono camera, we obtained the target's data information and used the Python environment and YOLOv7 for data processing and manipulation. Based on the information obtained, like target point cloud data and image data, it is used for data fusion to associate the sensor data for object classification. Based on this data fusion, we obtained a dataset of targets with their point cloud features and class labels.

The rest of the paper is organized as follows: Section 2 describes the materials and methodology used in this work, along with a brief workflow discussion. Section 3 discussed the processing involved after obtaining data from the sensors and the medium used for processing the data. Section 4 focuses mainly on sensor data fusion, preparing datasets for neural network training, and discussing the development of neural network models. In Section V, we discussed the performance of the neural network classifier and the analysis of the results obtained. In the last section, we share the conclusion of this work and future improvement areas.

## 2. MATERIALS AND METHOD

### 2.1. Retina-4F

For this work, we employed Retina-4F FMCW-MIMO millimeter-wave imaging radar from the Smart Radar System. This radar operates in medium-range mode, with a maximum detectable distance of 100 m for cars and 40 m for pedestrians. Table 1 lists the radar specifications.

Table 1. Retina-4F Specifications

| Parameter | Value |
|---|---|
| Number of chips cascading | TI AWR2243 x 4 |
| Number of Tx/Rx | 12 Tx / 16 Rx |
| Frequency | 77 GHz |
| Bandwidth | 3.8 GHz |
| Range resolution | 0.5 m |
| Azimuth angle resolution | 2.0° |
| Azimuth field of view | 100° ± 50° |
| Elevation angle resolution | 2.0° |
| Elevation field of view | 24° ± 12° |
| Point cloud output | Max 6, 144 per frame |

Four Texas Instruments (TI) AWR2243 chips have been integrated into this radar system, enabling RETINA-4F to differentiate several objects without experiencing a significant loss in detection and localization accuracy. The radar uses four cascade chips, each of which has patch

https://doi.org/10.31436/iiumej.v26i1.3268

antennas with four transmitters (Tx) and three receivers (Rx), for a total of 12 transmitter antennas, 16 receiver antennas, and 192 virtual channels.

### 2.2. Experimental Setup and Workflow

Pedestrians, cars, buses, and trucks are the items of interest for classification in the experiment that involves gathering data at road crossings since they are the most frequent types of objects at these locations. The experimental setup for data collection at a road crossing is shown in Figure 1, with the distance between the crossing and the radar set to be roughly 50m. All measurements were made outside at two different road crossings. Due to the radar's azimuth field of view, which is 100° ± 50°, and its location approximately 50 meters from the crossing, it is possible to observe and measure the motions of various objects, including pedestrians, before and after they cross the road. Many more actions can be collected by having a much wider view than when the radar image is focused exclusively on the crossing. For example, a car waiting for pedestrians to cross will have a very low, approaching zero, Doppler velocity value. This information is useful for training the classifier to recognize that cars have Doppler features with different ranges of Doppler velocity.

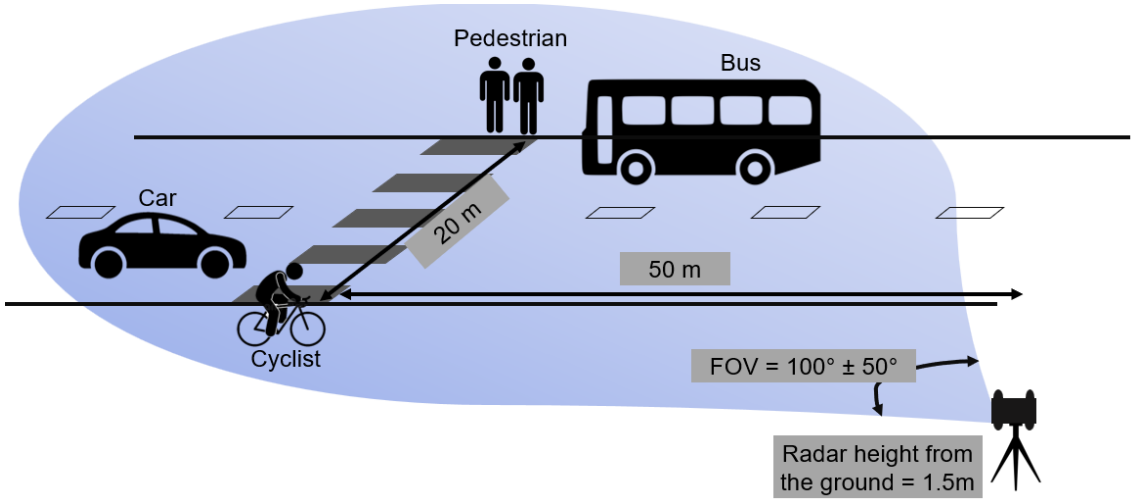


Figure 1. Experimental setup data collection.

Based on Figure 2, 4D Radar Imaging and a monocular camera are used for the measurement. Due to the unavailability of datasets currently available for radar point clouds at road crossing areas, gathering data to train a deep neural network for classification is necessary. This data must include the objects' features as well as their labels. The camera and radar are combined only for deep neural network training. The robotic operating system (ROS) environment in which Retina-4F operates makes data collection easier since it allows for simultaneous control over radar and camera nodes. As a result, the timestamp can be used to synchronize the radar point cloud data and camera images.

Referring to Figure 2, the mounting arrangement between the radar and camera is made for the simple data fusion process. In this case study, the data obtained from the camera is passed through the You Only Look Once version 7 (YOLOv7) object detection algorithm to produce bounding box predictions of objects present in the image. Meanwhile, radar data from Retina-4F are being preprocessed using density-based spatial clustering of applications with noise (DBSCAN) for point cloud clustering.

https://doi.org/10.31436/iiumej.v26i1.3268

Figure 2. Camera and radar sensors setup.

Based on the bounding box and cluster data obtained from the preprocessing, the next step is to associate both sensors' data using the data fusion method. The sensor data fusion provides a complete dataset of point clouds with class labels. This dataset is utilized to train a deep learning model for object classification and is divided into two subsets: the training set and the test set. The entire experimental workflow is illustrated in Figure 3.

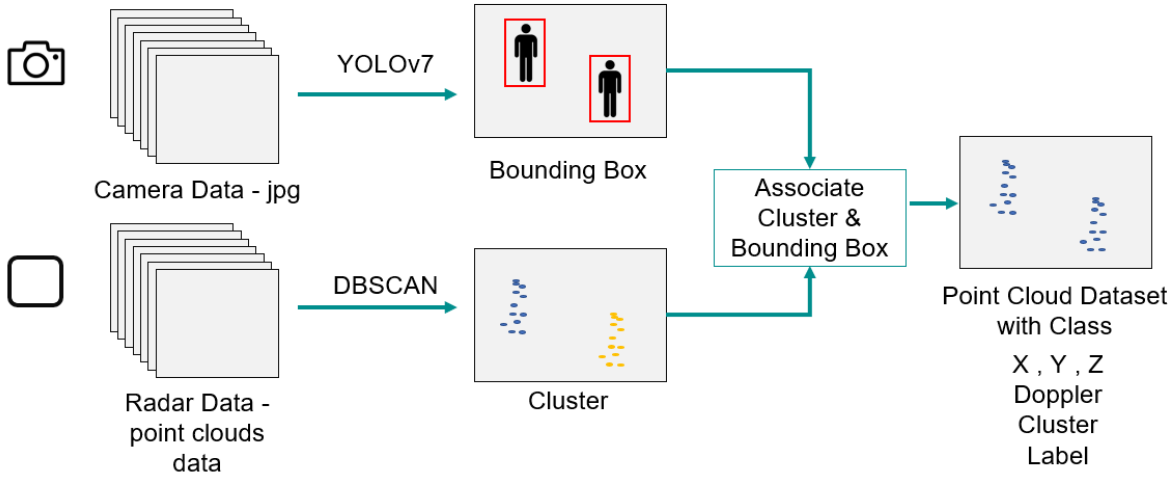


Figure 3. Experimental workflow for point cloud dataset preparation.

## 3. MEASURED DATA PROCESSING

Both sets of data require different processing approaches to prepare the point cloud data and camera data gathered from the measurement. Referring to the experimental workflow block

https://doi.org/10.31436/iiumej.v26i1.3268

diagram, the data fusion commences after processing the sensor data. The point cloud data from the radar sensor undergoes clustering through DBSCAN. Image data captured by a mono camera is processed using YOLOv7 for object classification and recognition.

### 3.1. DBSCAN

Retina-4F point cloud data output has the following information: timestamp, Cartesian coordinates (X, Y, and Z), Doppler, and Power Intensity. Lidar point cloud clustering is usually used for segmentation to distinguish different segments of the point cloud features, for instance, to segment the car point cloud between the tires and body of the car. However, in this project, the clustering process focuses on grouping the point cloud solely based on the type of objects. This means that the point cloud of each object belongs to different clusters. The point cloud segmentation is unnecessary for the fusion process with image data. Moreover, the sparsity of the radar point cloud is still too large compared to the lidar point cloud, which makes it very complex for segmentation.

One commonly known method for clustering non-linear data is DBSCAN [26]. The algorithm used in DBSCAN finds the nearest neighbor around each point of the point cloud and defines the cluster by connecting the points that are within the range. The region can be defined by adjusting DBSCAN parameters known as Epsilon and minimum points. Epsilon defines the radius around a point, and the algorithm will use that radius to search for neighboring points. Any points within the radius region will be part of the same cluster. Minimum points refer to the minimum number of points within a core point's radius to form a cluster. This is where the algorithm defines noise's presence in the point cloud. By identifying a core point and having a minimum number of points within the radius to form a cluster, it will be considered noise if the minimum number of points is not satisfied.

In this experiment, the optimal values for epsilon and minimum point chosen were 1.5 and 5, respectively. Next, the point cloud data can be processed for clustering after defining the epsilon and minimum point values. For clustering, four features of the point cloud data are passed to DBSCAN: the Cartesian coordinates of the point (x, y, and z) and Doppler velocity.

DBSCAN's point cloud clustering produces a cluster of points; hence, preparing the dataset for neural network classification algorithm training and testing is insufficient. To aid the neural network in recognizing and predicting the type of class a point cloud belongs to, a further step is required to provide a class label for the point cloud data. Therefore, YOLOv7 is incorporated into the workflow to create a dataset of point clouds with a class label.

### 3.2. YOLO-V7

The mono-camera's image data must be processed with an object detection algorithm to get the bounding box information for labeling the point cloud to its class. In this experiment, we use YOLOv7, a real-time object detection known for its high-speed processing and accuracy [27]. The YOLOv7 model is pre-trained using the Microsoft COCO dataset [28] and has around 90 classes of objects. Hence, objects that are of interest, such as cars, pedestrians, trucks, and buses, can be easily acquired from this model. By performing the object detection task on the image collected by the mono-camera, it gives information on bounding boxes, type of class, and class probability for all the objects recognized in the image. Most users used YOLOv7 after its release due to its high accuracy and efficiency in processing up to 160 frames per second of real-time data.

https://doi.org/10.31436/iiumej.v26i1.3268

The neural network in YOLOv7 uses the forward propagation method compared to another neural network, which normally uses both forward and backward propagation to perform predictions. The algorithm will first find and locate objects in the frame based on the input, either image or video. This process is usually called object detection. Correspondingly, the algorithm will generate bounding box predictions as well as the labels and confidence thresholds of the objects. This process is called object recognition. However, these two processes happen together as YOLOv7 is based on a one-stage architecture. As seen in Figure 4, the YOLO network architecture consists of 24 convolutional layers and 2 fully linked layers.

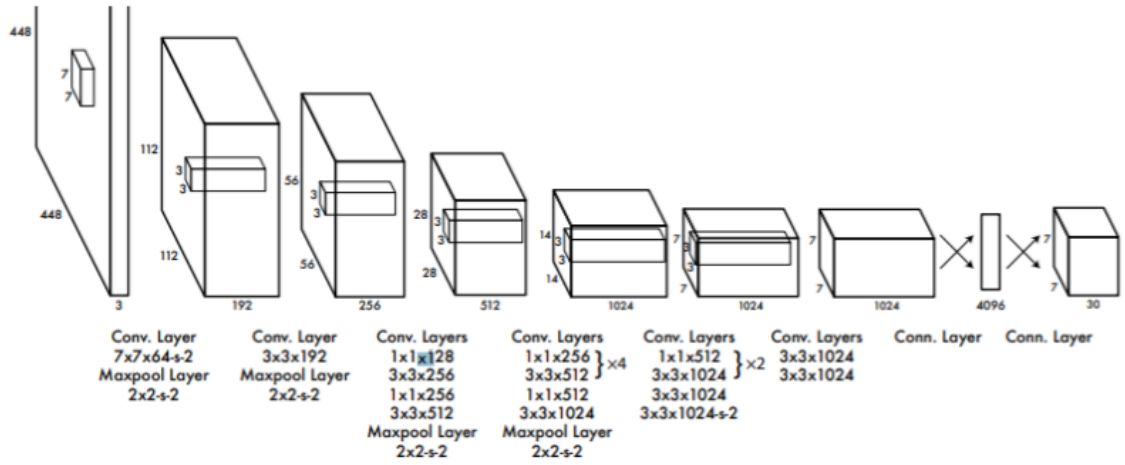


Figure 4. YOLO network architecture comprising Convolutional Neural Network (CNN) [29].

Based on the input, YOLO divides the image into grid cells, and a grid cell is in charge of detecting an object if its center falls within that grid cell. YOLO then predicts the bounding box and confidence scores of the box that encloses the object detected in the grid cell. The network defines the bounding boxes given by the center coordinate of the bounding box (x, y), the width (w), and the height (h). The confidence score is defined by the probability of an object with respect to the class label that is present inside the bounding box. To get the prediction, the YOLO network predicts the class label in each grid cell as the YOLO model is already pre-trained with many types of objects that allow the neural network to be able to classify objects in the input image into its specific labels.

Due to the prediction done by the YOLO network for each grid cell, multiple bounding boxes are generated. The network needs to assign just one bounding box predictor to handle each object during training. Based on whose prediction has the highest current intersection over union (IOU) with the ground truth, YOLO designates one predictor for predicting an object. Using the IOU method allows the network to improve its accuracy in detecting objects with different proportions. Another approach that YOLO uses to tackle the multiple bounding box generation is by implementing a post-processing step known as Non-Maximum Suppression (NMS). NMS is used mainly to eliminate redundant and overlapping bounding boxes by suppressing the bounding that has the largest IOU with the current highest probability bounding box. This guarantees that each object is only detected once, and one bounding box is obtained. As a result, YOLO produces information about the object's presence in an image, including details about the object's bounding box location and size, class label, and confidence score.

https://doi.org/10.31436/iiumej.v26i1.3268

# 4. PROJECTION AND CLASSIFICATION USING DEEP NEURAL NETWORK

We propose using point cloud projection onto an image to classify the point cloud data after clustering. This part of the work involves the fusion of the camera and radar data. The first step of this work is to calibrate the camera and radar before taking measurements at the road crossings. Calibration is crucial as we want accurate position and orientation of both sensors with respect to the measurement scene. From here, the intrinsic and extrinsic parameters of the sensors can be acquired to help in the projection process; this calibration method is usually known as Extrinsic Calibration. The significance of the calibration lies mainly in the misalignment between the camera data and radar data. A more detailed explanation of the projection work will be further discussed below.

## 4.1. Point Cloud Projection

Figure 5 shows the block diagram of the steps taken to project point cloud data onto the image. The point cloud data must be transformed from radar Cartesian coordinates (XR, YR, ZR) into a camera coordinate system (XC, YC, ZC) and then to image coordinates. The coordinate system between the radar coordinate and camera coordinate system is significantly different, as presented in Figure 6. The X-axis of the camera and the radar coordinate system remain the same; however, it is observed that the Y-axis of the radar coordinate system is facing the same axis as the z-axis in the camera coordinate system. To transform the Z-axis of the radar coordinate system into a camera coordinate, it is facing downwards with respect to the camera's principal axis.

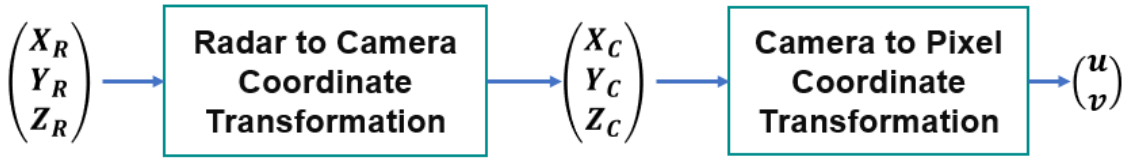


Figure 5. Radar to pixel coordinate system transformation.

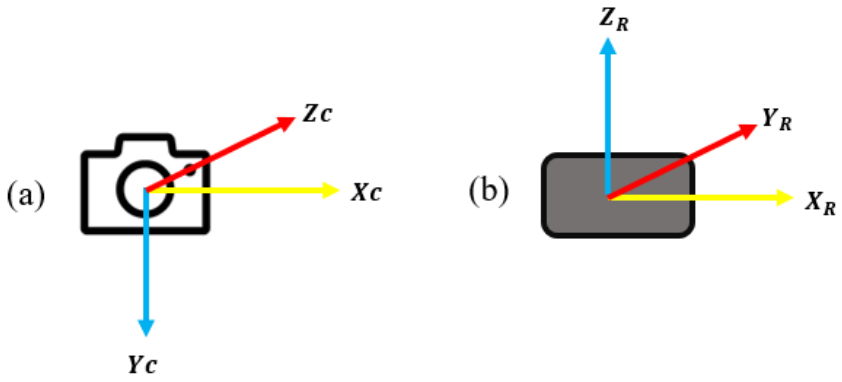


Figure 6. Difference between camera and radar coordinate system. (a) Camera coordinate system. (b) Radar coordinate system.

From here on, the intrinsic matrix (K), rotation matrix (R), and translation matrix (t) are the main parameters to construct the camera projection matrix [30]. Assuming that a scatterer point exists in an image coordinate given by $(X_C, Y_C, Z_C)$, we want to project the point into a 2D

https://doi.org/10.31436/iiumej.v26i1.3268

image plane. Hence, there is a need to transform from image coordinate to pixel known as $[u, v]$. The transformation matrix can be obtained from the camera-radar calibration and represented as

$$[u, v, w]^T = K[R|t][x, y, z, 1]^T \quad (1)$$

where $K$ is the intrinsic parameter of the camera obtained by camera-radar calibration represented as

$$K = \left[f_x, 0, c_x, 0, f_y, c_y, 0,0,1\right] \quad (2)$$

where $f_x$ and $f_y$ are the camera's focal length along the $x$-axis and $y$-axis. This focal length determines the camera's zoom level and horizontal field of view. Moreover, cx and cy represent the principal points of the x-axis and y-axis, where the optical axis and image plane intersect. This point is presented in pixels. Note that the Rotation and Translation, $[R|t]$ matrix is concatenated, where it is known as an extrinsic parameter obtained after calibration. The Rotation matrix is represented as:

$$\begin{gathered} R = R_x R_y R_z \\ R_x = [1,0,0,0, \cos\theta\ , -\sin\theta\ , 0, \sin\theta\ , \cos\theta] \\ R_y = [\cos\theta\ , 0, \sin\theta\ , 0,1,0, -\sin\theta\ , 0, \cos\theta] \\ R_z = [\cos\theta\ , -\sin\theta\ , 0, \sin\theta\ , \cos\theta\ , 0,0,0,1] \end{gathered} \quad (3)$$

and the translation matrix is represented as:

$$t = \left[t_x, t_y, t_z\right]^T \quad (4)$$

Point cloud projection onto an image can be made after calibrating the camera-radar sensor using the Extrinsic Calibration method and converting the 3D point cloud coordinate into the 2D image coordinate. Figure 9 (left) – Figure 16 (left), which shows the 3D point cloud projected onto a 2D image, demonstrates this. From here on, the point cloud cluster that is contained inside the bounding box may be retrieved using the bounding box information that we obtained using the YOLOv7 technique. The center coordinate of the bounding box shows the location of the bounding box in 2D image coordinates, along with the width and height.

Through simple data processing using Python, after transforming the 3D point cloud onto the image, any point cloud cluster within the bounding box can be extracted. At this stage, the point cloud cluster will be labeled according to the type of class of target in the image included within the bounding box. After a few processing steps, this produces a custom dataset of radar point clouds with class labels, which can be used for neural network classification training and testing.

The custom dataset comprises radar data containing point cloud clusters, target labels, Doppler velocity, and power intensity. The entire dataset is subsequently divided into two subsets, which are the training set and the testing set. This division allocates 80% of the dataset for training purposes and leaves the remaining 20% for testing. The distribution of data points for each class for both subsets is presented in Table 2 and shown in Figure 7. It can be observed that the pedestrian class makes up around 28% of the dataset. In comparison, cars and big vehicles (such as buses and trucks) constitute approximately 25% and 13% of the dataset, respectively. The clutter class comprises 34% of the dataset.

https://doi.org/10.31436/iiumej.v26i1.3268

Table 2. Number of Data Points for Each Classes

| | Training | Testing | Total |
|---|---|---|---|
| Person | 203 341 | 51 108 | 254 449 |
| Car | 183 126 | 45 632 | 228 758 |
| Big Vehicle | 93 085 | 23 248 | 116 333 |

Figure 7. Illustration of the custom dataset distribution.

The imbalance in class frequencies observed in the point cloud dataset, which includes people, cars, buses, and trucks, can be linked to two primary sources. To begin with, it is common for the distribution of these classes in real-world scenarios to display a natural imbalance. In road crossing settings, there is often a greater majority of pedestrians and cars than buses and trucks. As a result, the imbalanced representation of the custom dataset may effectively reflect the real-world condition. Furthermore, it is important to acknowledge that data-gathering processes have the potential to induce bias, which might subsequently result in class imbalance. This potential bias may arise due to several factors related to the data-gathering process, including the selection of the timing of data collection. However, the overall custom dataset is satisfactory enough to train and test deep neural networks.

### 4.2. Deep Learning Model Using TensorFlow and Keras

In this work, we develop a deep learning model using an open-source machine learning library known as Keras. To be more specific, Keras is a neural network library that is built on top of TensorFlow [31]. Keras uses the Python programming language, which makes it a more popular choice for an application programming interface (API) than any other neural network library, such as PyTorch. The integration between Keras and TensorFlow makes this open-source machine-learning library more advantageous. TensorFlow works as the backend, providing low-level computational complexity on either CPUs or GPUs to train neural networks, while Keras is the frontend, which offers a high-level and user-friendly API.

The network architecture of Keras as a deep neural network model is called a Feedforward Neural Network (FNN) [32], as presented in Figure 8. The network is made up of several layers

https://doi.org/10.31436/iiumej.v26i1.3268

consisting of neurons in each layer and fully connected to each neuron in the following layers. In other words, the neurons in the first layer are connected to adjacent neurons in the following layers, but they are not connected to the neurons within the same layer. This explains why this network architecture is known as a feedforward neural network since it goes from the input layer to the output layer in a single direction.

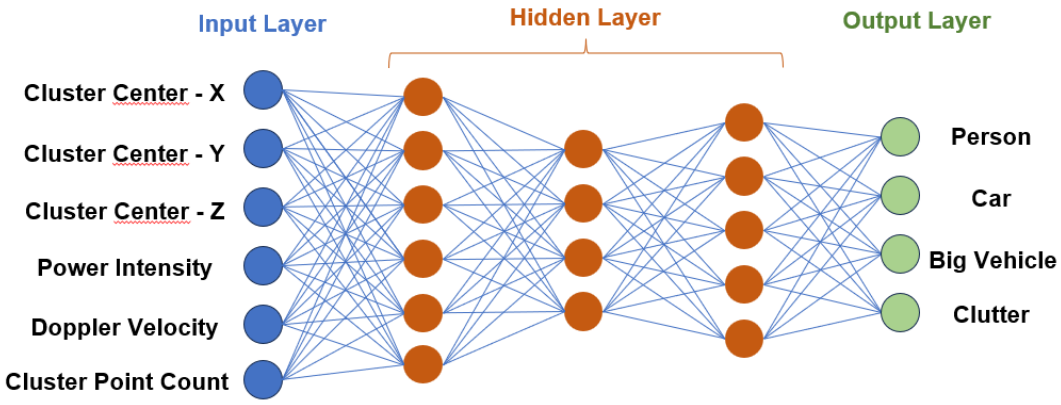


Figure 8. Feedforward neural network architecture.

The feedforward neural network has three main layers: the input, hidden, and output layers. As the name suggests, the input layer will receive the input data the user passes. In this work, we pass point cloud features to the input layer, which is the point cloud's cluster center coordinates: $X$, $Y$, and $Z$, Doppler velocity, power intensity, and cluster point count. The presence of neurons in the input layer depends on the dimension of the input. For instance, in this work, the dimension size is 6; hence, there are 6 neurons in the input layer. The hidden layer refers to the layers between the input and output layers, which perform computational tasks and nonlinear transformations of the input data.

The neural network's final layer, the output layer, focuses mostly on providing the network's final prediction. The neurons in this layer are determined by the user's desired prediction for the network's final result. Binary classification tasks and multi-class classification are the two categories into which it is typically split. In the output layer of a binary classification task, there is often simply one neuron that provides the likelihood that the input belongs to one of the two classes. More than one neuron is often included in the output layer of a multi-class classification task to determine which specific class the input data would belong to from more than two classes [33].

To handle the numerous kinds of classes, we want the neural network to learn and predict in this study; we employ multi-class classification. As a result, our model's final output includes four classes: person, car, big vehicles, and clutter. Since there are four classes that need to be distinguished, the final layer of the neural network will consist of four nodes for each class, as was previously stated.

The fundamental component of the neural network is the activation function within the hidden layers. The deep neural network designed utilizes ReLU (Rectified Linear Unit) activation functions in this study. The Rectified Linear Unit (ReLU) is a commonly employed activation function recognized for its straightforwardness and efficiency in deep learning. The network integrates non-linearity by enabling positive values to remain undisturbed while assigning a value of zero to negative values [34]. This characteristic assists in reducing the issue of vanishing gradients and helps the development of the neural network during the

https://doi.org/10.31436/iiumej.v26i1.3268

training process. In short, this is how feedforward neural networks work: the user passes on the data features to the layers, and each neuron in each layer of the neural network completes its task by weighing the inputs, applying activation functions, and sending the output that has been transformed to the following layer.

## 5. RESULTS AND ANALYSIS

This study collects and processes images and radar point clouds for target classification. We trained the model with the dataset obtained after the data fusion processing. Two road-crossing scenes are used for data collection, and the dataset is randomly divided into a training and testing set. The combination of both scenes gives a dataset consisting of approximately 10,000 frames.

In our Python data processing system, each target has been labeled using distinct colors representing different classes. In this context, people are associated with the color blue on the plot, cars are represented by the color red, orange denotes buses, and trucks are represented by the color purple on the plot. In addition, aside from the point cloud associated with the targets, all other point clouds of the background and uninterested targets are now assumed to be cluttered and colored grey.

Figures 9 to 16 display the outcomes from the data fusion, including 3D point cloud projection onto a 2D image and plotting point cloud data with labeling of several targets. Figure 9 (left) to Figure 16 (left) display targets, bounding boxes, and point clouds. Based on the projection process of the point cloud onto the 2D image, the point cloud that is inside the bounding box is extracted using simple Python processing and labeled as the target according to the label of the bounding box. We now have a point cloud dataset with points relevant to the target being labeled appropriately due to the processing. This can be observed by the point cloud labeled as several targets in Figure 9 (right) to Figure 16 (right). The point cloud related to the targets is accurately mapped when plotted along the X-Y axis.

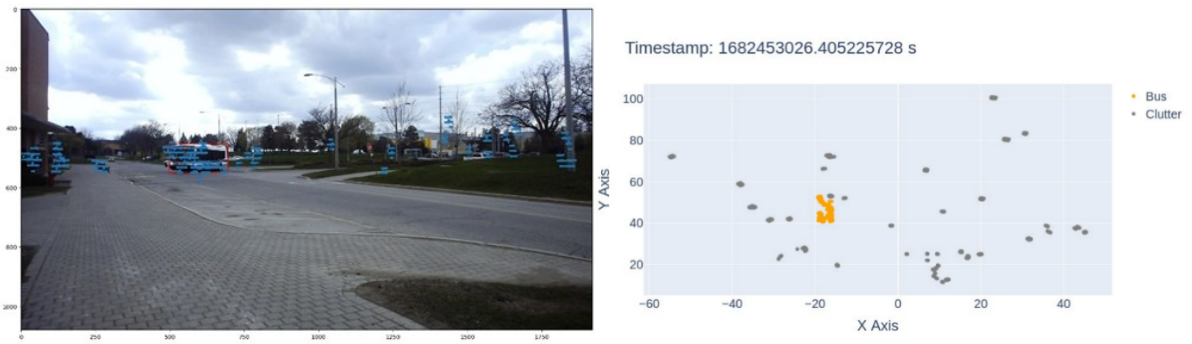


Figure 9. Bus in scene 1. (left) 3D Point cloud projection onto the 2D image. (right) X-Y axis scatter plot for point cloud dataset with target class.

https://doi.org/10.31436/iiumej.v26i1.3268

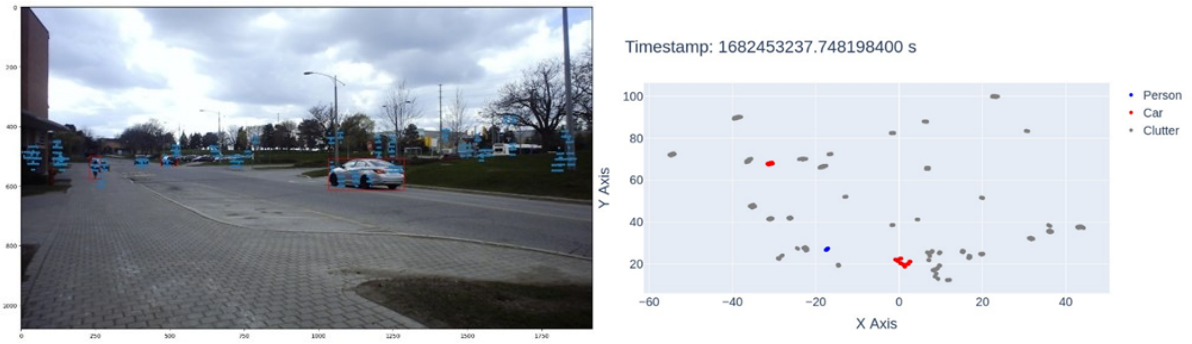


Figure 10. Car in scene 1. (left) 3D Point cloud projection onto the 2D image. (right) X-Y axis scatter plot for point cloud dataset with target class.

Figure 11. Pedestrian in scene 1. (left) 3D Point cloud projection onto the 2D image. (right) X-Y axis scatter plot for point cloud dataset with target class.

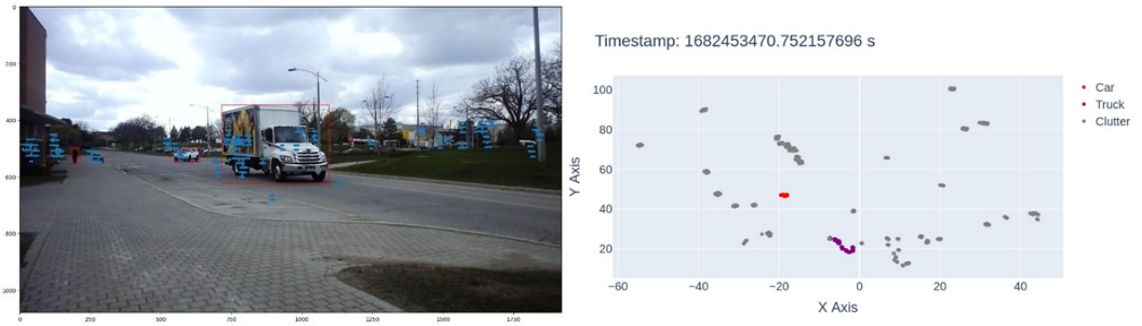


Figure 12. Truck in scene 1. (left) 3D Point cloud projection onto the 2D image. (right) X-Y axis scatter plot for point cloud dataset with target class.

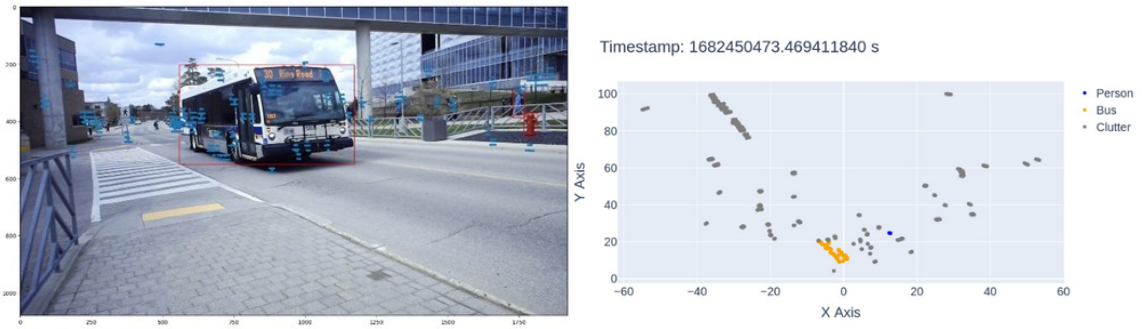


Figure 13. Bus in scene 2. (left) 3D Point cloud projection onto the 2D image. (right) X-Y axis scatter plot for point cloud dataset with target class.

https://doi.org/10.31436/iiumej.v26i1.3268

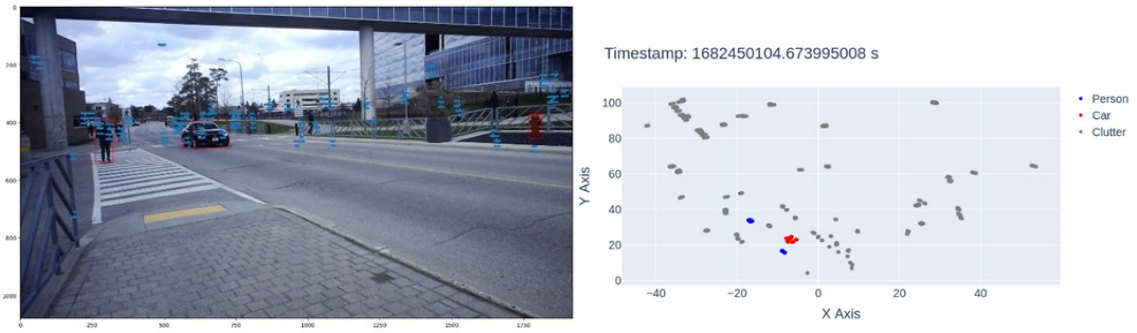


Figure 14. Car in scene 2. (left) 3D Point cloud projection onto the 2D image. (right) X-Y axis scatter plot for point cloud dataset with target class.

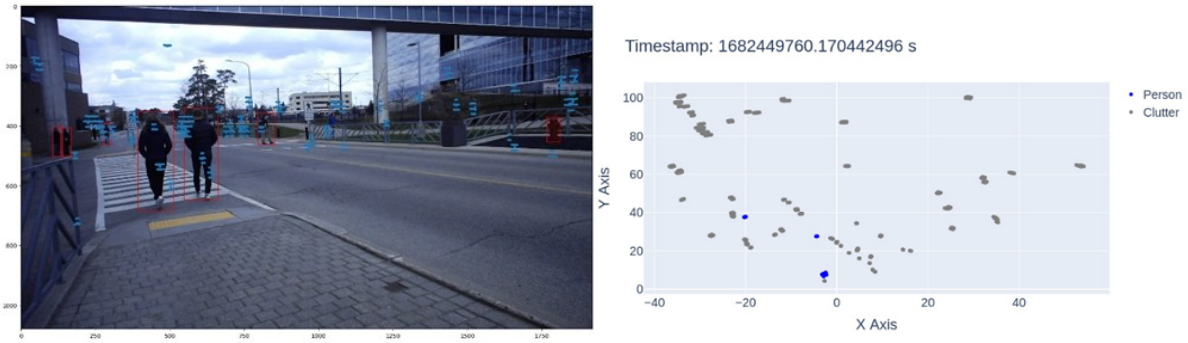


Figure 15. Pedestrian in scene 2. (left) 3D Point cloud projection onto 2D image. (right) X-Y axis scatter plot for point cloud dataset with target class.

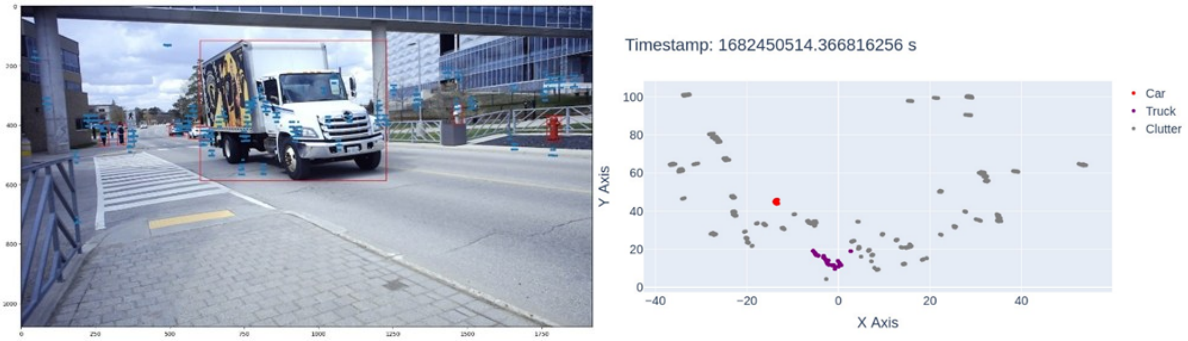


Figure 16. Truck in scene 2. (left) 3D Point cloud projection onto the 2D image. (right) X-Y axis scatter plot for point cloud dataset with target class.

This work aims to classify 4D point cloud data using a deep learning method to monitor road crossings. Following data fusion and the subsequent generation of a customized dataset, the next step involves training and testing the deep neural network. The model performed training with different numbers of layers for 10 epochs using a training dataset consisting of over 10,000 frames of point cloud data. Using 10 epochs is due to the computational resource hardware limitation. 1 epoch has taken an average of 307 seconds, making training deep neural networks with a large dataset require too much time. Subsequently, predictions were made on the radar point cloud using the training set.

https://doi.org/10.31436/iiumej.v26i1.3268

In this work, we construct 4 neural network layers to classify the object into respective classes. Figure 17 displays the confusion matrix, which provides an overview of the model's predictions for classifying point cloud clusters as either a person, car, or big vehicle. Based on an analysis of the confusion matrix, it can be observed that the model successfully predicts point cloud clusters of pedestrians as persons with an accuracy of 98.09%. However, there is still a notable misclassification rate of approximately 1.91 % in which the pedestrian cluster is erroneously identified as other objects. Next, the 4 layers model illustrated high accuracy, predicting the point cloud cluster of cars as cars with a precision of 94.79%. Despite the misclassification of person and car class within the corresponding class, its impact does not greatly affect the model's performance.

In addition, in the classification of large vehicles, which consists of bus and truck class types, a significant amount of misclassification is still observed. The model for the large vehicle class type demonstrates a predictive accuracy of 78.41 %. Nevertheless, a significant proportion of instances involve the incorrect classification of big vehicles as cars, up to 21.08 %.

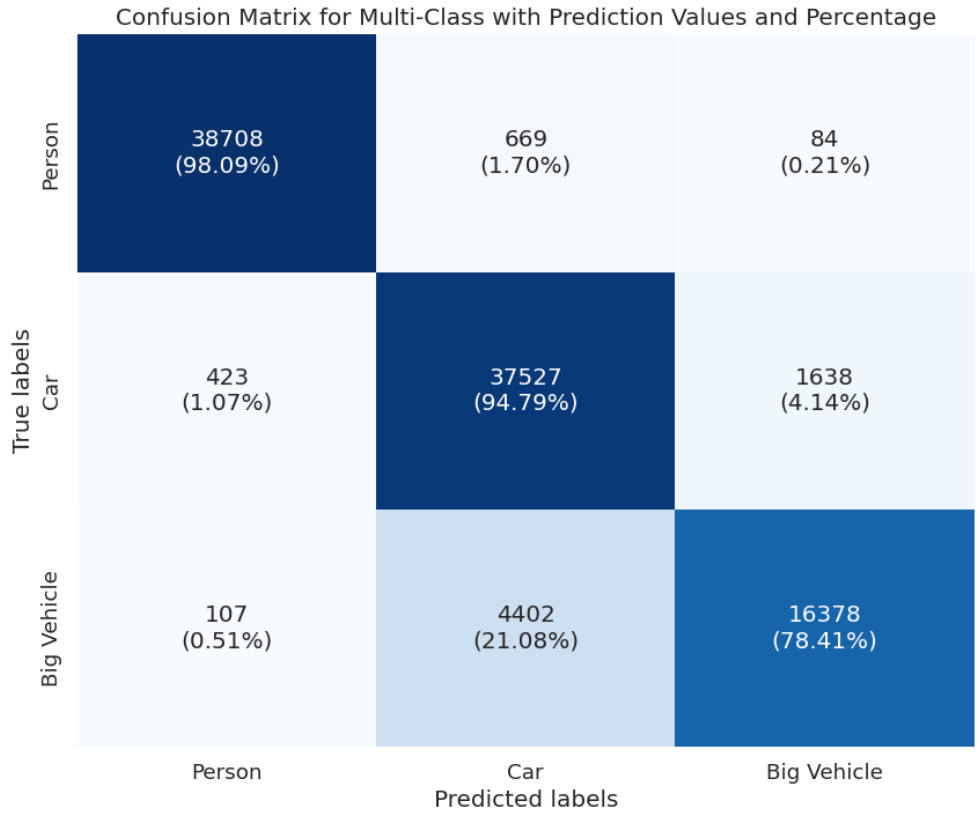


Figure 17. Confusion Matrix of 4 Layers Neural Network Model

Evaluating a deep learning model is facilitated using a confusion matrix, which is crucial for gaining valuable insights into the model's predictive capabilities. The confusion matrix provides essential information for assessing the success of a model. It allows us to calculate important metrics such as precision, accuracy, and F1 score, which comprehensively evaluate the model's performance. Additionally, in the context of multi-class classifications, it is

https://doi.org/10.31436/iiumej.v26i1.3268

important to consider the average metric that provides a comprehensive understanding of the performance exhibited by a neural network model designed to classify multiple classes.

Firstly, as a quantitative measure, it evaluates the model's ability to identify true positives among all positive predictions accurately. The attribute of high precision indicates that the model has a low rate of misclassifying negative instances as positive ones. This characteristic is significant in situations where the occurrence of false positives is undesirable. Next, recall is a metric that measures the model's ability to correctly detect all instances that truly belong to a specific category. High recall is crucial when recording many true positive instances, even at the cost of accepting some false positive instances. Lastly, the F1-score is a measurement that effectively balances precision and recall. The metric offers a comprehensive evaluation of a model's effectiveness, which is particularly advantageous in scenarios with imbalanced datasets or where there is a requirement to achieve a balance between precision and recall. F1-score is computed by taking the harmonic mean of precision and recall, providing a unified measure that reflects the balance between these two crucial elements of model efficacy.

Furthermore, based on the model evaluation shown in Table 3, the micro-average, macro-average, and weighted-average F1 scores are present. These findings imply a considerable level of proficiency exhibited by the model in its entirety. The micro-average score measures the model's effectiveness in producing accurate predictions for all categories without exhibiting bias towards any specific class. In this context, the micro-average represents the accuracy of the model's performance. The macro-average F1 score is calculated by determining the F1 score for each class and then taking the average. This metric provides evidence that the model demonstrates consistent performance across different classes. The calculation of the weighted average score addresses the issue of class imbalance by assigning a higher weight to classes with a larger number of occurrences.

Table 3. Model Evaluation Report (4 layers)

| | **Precision** | **Recall** | **F1-Score** |
|---|---|---|---|
| Person | 0.99 | 0.76 | 0.86 |
| Car | 0.88 | 0.82 | 0.85 |
| Big Vehicle | 0.90 | 0.70 | 0.79 |
| Micro avg | 0.93 | 0.77 | 0.84 |
| Macro avg | 0.92 | 0.76 | 0.83 |
| Weighted avg | 0.93 | 0.77 | 0.84 |

The 4-layer model, which consists of layers with 64, 32, 16, and 4 neurons, respectively, shows a significant improvement with a micro-average F1-score of 0.84. The additional layer in this model helps enhance its representational capacity, allowing it to capture more intricate features and relationships in the data. This higher score suggests that the model's increased depth enables better learning and generalization. The balance achieved in this model between complexity and performance indicates that it is well-suited for the given task, effectively leveraging the additional layer to improve predictive accuracy without introducing substantial overfitting.

The 4-layer model's superior performance with a micro-average F1-score of 0.84 suggests it strikes the right balance between model complexity and performance. The additional layer allows it to learn more sophisticated features without overcomplicating the training process or leading to overfitting. The 3-layer model, while simpler, performs reasonably well with a

micro-average F1-score of 0.81, indicating that it is effective but might benefit from a slight increase in complexity to improve performance further. On the other hand, the 5-layer model's performance, with a micro-average F1-score of 0.80, suggests that its added complexity does not translate into better performance, possibly due to overfitting and optimization difficulties.

Comparing our study with related work from [35], it becomes evident that our approach has several notable differences and improvements. The work aims to evaluate the performance of radar-based object categorization in real-world traffic monitoring, demonstrating the efficacy of Gaussian Mixture Models (GMM) in processing radar point cloud data despite the difficulties caused by noise and clutter.

The benchmark study and this research contrast notably regarding the radar devices utilized. The benchmark study used the Texas Instrument AWR1843BOOST radar chipboard, but this study employed the TI AWR2243. This differentiation suggests that each research may gain advantages from varied capabilities and performance criteria inherent to their corresponding radar evaluation boards. In terms of measurement resolutions, the benchmark study achieved a range resolution of 9 cm, a Doppler resolution of 0.8 m/s, an azimuth angle resolution of 15°, and an elevation angle resolution of 28°. Conversely, this study proposed using radar with a coarser range resolution of 50 cm but a significantly finer Doppler resolution of 0.06 m/s, an azimuth angle resolution of 2°, and an elevation angle resolution of 4.7°. In addition, the types of objects considered in each study also vary. The benchmark study focused on pedestrians and cars, while this study expanded the scope to include buses and trucks. This study's broader range of transportation modes indicates a more complex and challenging classification task, which could lead to more robust and versatile detection capabilities.

In terms of data collection, the benchmark study collected 8035 frames of training data over 13 minutes and 1222 frames of testing data over 2 minutes. However, in this study, the data is collected over 10,000 frames with a total measurement time of 2.5 hours, indicating a more extensive data collection process. This larger dataset could contribute to more robust training and testing, potentially leading to more reliable classification outcomes. Data processing tools and methods also varied between the studies. The benchmark study utilized Scikit-learn APIs to fit GMM for classification, an unsupervised learning method. In contrast, in this work, DBSCAN is used for clustering radar point cloud data and YOLOv7 for image processing and labeling, combining sensor fusion for data association. This approach will likely lead to more accurate and reliable classifications, combining unsupervised clustering with supervised labeling. Moreover, the classification methods employed were different. The benchmark study used GMM, which, as an unsupervised learning method, does not necessarily align predicted labels with ground truth. In this work, we applied supervised learning using KERAS and TensorFlow for deep neural network models. Given the nature of supervised learning, this approach likely results in more accurate classifications.

The confusion matrix from the benchmark study in Figure 20 presents the classification accuracy for three categories: clutter, car, and pedestrian. The true positive rates for clutter, car, and pedestrian are 89%, 61%, and 93%, respectively. The matrix reveals several key points. Firstly, the benchmark study accurately detects clutter, with 89% of true clutter instances correctly classified. This high detection rate indicates that the model distinguishes irrelevant data points from actual objects. Secondly, the car detection accuracy is moderate at 61%. This lower accuracy suggests that the model has difficulty distinguishing cars from pedestrians, as evidenced by 34% of cars being misclassified as pedestrians. Lastly, pedestrian detection shows a high accuracy of 93%, indicating that the model performs well in identifying pedestrians within the radar point cloud data. Overall, the benchmark study's results indicate

https://doi.org/10.31436/iiumej.v26i1.3268

that while the model is proficient in identifying pedestrians and clutter, it struggles with accurately classifying cars, often confusing them with pedestrians.

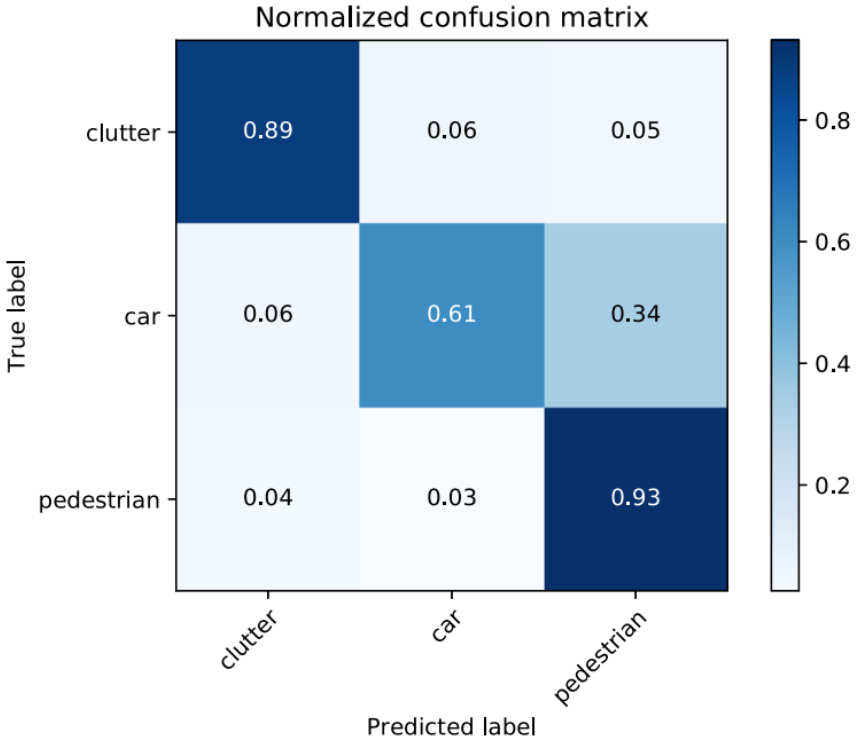


Figure 20. Confusion Matrix [35]

In contrast, this study's confusion matrix includes three categories: person, car, and big vehicle. The true positive rates for a person, car, and big vehicle are 98.09%, 94.79%, and 78.41%, respectively. Several critical points emerge from this matrix. Firstly, the person detection rate is exceptionally high at 98.09%, demonstrating that the model is highly effective at identifying individuals within the radar data. Secondly, the car detection accuracy is also high at 94.79%, significantly improving over the benchmark study. This improvement suggests that using YOLOv7 for image processing, DBSCAN for clustering, and sensor fusion has enhanced the model's capability to classify cars accurately. Lastly, detecting big vehicles (buses and trucks) shows a lower accuracy of 78.41%. This lower accuracy indicates that while the model performs well, there is still room for improvement in distinguishing between large vehicles and other categories.

In terms of performance and results, the confusion matrix in this study shows marked improvements in the detection of cars and persons compared to the benchmark study. Specifically, the car detection rate of 94.79% is significantly higher than the benchmark study's 61%, highlighting the effectiveness of this work model's approach. The person detection accuracy in this study (98.09%) also surpasses the pedestrian detection accuracy in the benchmark study (93%), indicating superior performance in this category. Although there is an additional challenge of detecting big vehicles in this work, the accuracy rate of 78.41% suggests that while effective, there is still potential for further refinement in distinguishing large vehicles from other categories.

In the benchmark study, the precision, recall, and F1-score for detecting persons were 0.85, 0.93, and 0.89, respectively, as shown in Table 4. This indicates a high recall, suggesting that the benchmark model was effective at identifying most instances of persons, but the precision

https://doi.org/10.31436/iiumej.v26i1.3268

was slightly lower, meaning there were some false positives. For car detection, the precision was 0.88, the recall was 0.61, and the F1-score was 0.72, showing a significant drop in recall compared to precision. This suggests that the benchmark model struggled more with correctly identifying cars, possibly confusing them with other categories. Clutter detection had a precision of 0.71, recall of 0.89, and an F1-score of 0.79, indicating a higher tendency to identify clutter correctly but with a relatively lower precision, reflecting a notable number of false positives.

In comparison, this work demonstrated improved performance metrics across all categories. The precision, recall, and F1-score for person detection were 0.99, 0.76, and 0.86, respectively, as shown in Table 3. While the recall is lower than the benchmark study, the precision is significantly higher, suggesting the model produces fewer false positives when detecting persons. For car detection, the model achieved a precision of 0.88, recall of 0.82, and F1-score of 0.85, showing a balanced and robust performance. This represents a substantial improvement in recall over the benchmark study, indicating the model's enhanced capability to identify cars correctly. For big vehicle detection, the precision was 0.90, the recall was 0.70, and the F1-score was 0.79. Although this category was not included in the benchmark study, the metrics indicate a solid performance in identifying large vehicles, albeit with a lower recall than precision.

Table 4. Model Evaluation Report [35]

| | **Recall** | **F1-Score** |
|---|---|---|
| Person | 0.93 | 0.89 |
| Car | 0.61 | 0.72 |
| Clutter | 0.89 | 0.79 |

This study also reports micro, macro, and weighted averages for the classification performance. The micro average precision, recall, and F1-score are 0.93, 0.77, and 0.84, respectively. These metrics provide an overall performance evaluation considering all instances across categories, showing a strong general performance with high precision and good recall. The macro averages, which consider the performance across categories equally, were 0.92, 0.76, and 0.83 for precision, recall, and F1-score, respectively. These averages reflect the model's balanced performance across different categories. The weighted averages, which take into account the proportion of each category, were 0.93, 0.77, and 0.84, respectively, indicating that the model maintains high performance even when the category distribution is considered.

In summary, the comparative analysis shows that this study's classification model demonstrates superior precision across all categories compared to the benchmark study. This indicates that the model in this work produces fewer false positives, particularly for person and car detection. The recall for car detection in this work is significantly improved, highlighting the model's enhanced capability to identify cars correctly. While the recall for person detection is lower than the benchmark, the higher precision compensates for this by reducing false positives. Including big vehicle detection in this study adds a layer of complexity, with good performance metrics indicating the model's capability to handle more diverse categories. The overall averages further underscore the robustness and effectiveness of this work classification model, showing high precision and balanced performance across all categories.

## 6. CONCLUSION

With the rigorous technical improvement of the presented approach on radar-powered intelligent infrastructure, diverse application domains, from autonomous navigation to microclimate monitoring, can benefit from enhanced environmental awareness.

This work demonstrates a target detection and classification approach by fusing 4D radar imaging with deep neural networks. This work is highly motivated to solve challenges relating to point cloud classification using a deep neural network as part of a monitoring system. With the presence of high-resolution radar imaging in the automotive market, given its advantages, there is a trend in research work toward developing a radar-based monitoring system with object classification capability. However, researchers face the challenges of object classification using radar imaging due to the sparsity characteristic of the point. This work proposes a method to solve this challenge through sensor data fusion. We integrate radar imaging and cameras to create a customized dataset of point clouds and use it to train a deep neural network. In this dataset, all the spatial relationships and information of the radar point cloud data are preserved. Hence, the deep neural network employed in this work could learn the complex relationships of the point cloud data and make predictions.

The results show 84% classification accuracy on three common roadway objects, indicating feasibility but also room for improvement. First, the custom dataset can be expanded to improve generalizability. Additional data capture in varied weather conditions, times of day, and geographic locales will reduce overfitting and aid robustness. Second, augmenting the radar point cloud with multi-perspective views from a lidar sensor could provide complementary geometric cues to resolve ambiguities. Third, modifying the deep network architecture itself may boost accuracy. Attention mechanisms could help focus feature extraction on more discriminative spatial regions of the point cloud. Also, transformer networks have shown value in processing unordered point sets and may outperform convolutional architectures. Lastly, implementing the deep network on dedicated hardware like GPUs or FPGAs would enable real-time inference critical for practical systems. The framework developed here establishes a baseline—further optimization of the sensor fusion, data representations, and neural network design provides an exciting path toward deployable 4D radar perception systems.

## REFERENCES

[1] “Road traffic injuries,” World Health Organization, 20-Jun-2022. [Online]. Available: https://www.who.int/news-room/fact-sheets/detail/road-traffic-injuries. [Accessed: 25-Aug-2022].
[2] C. Waldschmidt, J. Hasch and W. Menzel, "Automotive Radar — From First Efforts to Future Systems," in IEEE Journal of Microwaves, vol. 1, no. 1, pp. 135-148, Jan. 2021.
[3] X. Gao, G. Xing, S. Roy and H. Liu, "Experiments with mmWave Automotive Radar Test-bed," 2019 53rd Asilomar Conference on Signals, Systems, and Computers, 2019, pp. 1-6.
[4] I. Bilik, O. Longman, S. Villeval and J. Tabrikian, "The Rise of Radar for Autonomous Vehicles: Signal Processing Solutions and Future Research Directions," in IEEE Signal Processing Magazine, vol. 36, no. 5, pp. 20-31, Sept. 2019.
[5] E. Ragonese, G. Papotto, C. Nocera, A. Cavarra and G. Palmisano, "CMOS Automotive Radar Sensors: mm-Wave Circuit Design Challenges," in IEEE Transactions on Circuits and Systems II: Express Briefs, vol. 69, no. 6, pp. 2610-2616, June 2022.
[6] I. Bilik et al., "Automotive multi-mode cascaded radar data processing embedded system," 2018 IEEE Radar Conference (RadarConf18), 2018, pp. 0372-0376.

[7] Y. Cheng, J. Su, H. Chen and Y. Liu, "A New Automotive Radar 4D Point Clouds Detector by Using Deep Learning," ICASSP 2021 - 2021 IEEE International Conference on Acoustics, Speech and Signal Processing (ICASSP), 2021, pp. 8398-8402.
[8] S. Sun and Y. D. Zhang, "4D Automotive Radar Sensing for Autonomous Vehicles: A Sparsity-Oriented Approach," in IEEE Journal of Selected Topics in Signal Processing, vol. 15, no. 4, pp. 879-891, June 2021.
[9] M. Stolz, M. Wolf, F. Meinl, M. Kunert and W. Menzel, "A New Antenna Array and Signal Processing Concept for an Automotive 4D Radar," 2018 15th European Radar Conference (EuRAD), 2018.
[10] J. Martínez García, D. Zoeke and M. Vossiek, "MIMO-FMCW Radar-Based Parking Monitoring Application With a Modified Convolutional Neural Network With Spatial Priors," in IEEE Access, vol. 6, pp. 41391-41398, 2018.
[11] G. Li et al., "Novel 4D 79 GHz Radar Concept for Object Detection and Active Safety Applications," 2019 12th German Microwave Conference (GeMiC), 2019, pp. 87-90.
[12] X. Gao, S. Roy, G. Xing and S. Jin, "Perception Through 2D-MIMO FMCW Automotive Radar Under Adverse Weather," 2021 IEEE International Conference on Autonomous Systems (ICAS), 2021, pp. 1-5.
[13] J. Wu, Z. Zhu and H. Wang, "Human Detection and Action Classification Based on Millimeter Wave Radar Point Cloud Imaging Technology," 2021 Signal Processing Symposium (SPSympo), LODZ, Poland, 2021, pp. 294-299.
[14] Y. Kim, I. Alnujaim and D. Oh, "Human Activity Classification Based on Point Clouds Measured by Millimeter Wave MIMO Radar With Deep Recurrent Neural Networks," in IEEE Sensors Journal, vol. 21, no. 12, pp. 13522-13529, 15 June15, 2021.
[15] I. Alujaim, I. Park and Y. Kim, "Human Motion Detection Using Planar Array FMCW Radar Through 3D Point Clouds," 2020 14th European Conference on Antennas and Propagation (EuCAP), Copenhagen, Denmark, 2020, pp. 1-3.
[16] Z. Yu et al., "A Radar-Based Human Activity Recognition Using a Novel 3-D Point Cloud Classifier," in IEEE Sensors Journal, vol. 22, no. 19, pp. 18218-18227, 1 Oct.1, 2022.
[17] R. Girshick, J. Donahue, T. Darrell, and J. Malik, “Rich feature hierarchies for accurate object detection and semantic segmentation,” in Proc IEEE Comput. Soc. Conf. Comput. Vis. Pattern Recognit., 2014, pp. 580–587.
[18] X. Cai, M. Giallorenzo and K. Sarabandi, "Machine Learning-Based Target Classification for MMW Radar in Autonomous Driving," in IEEE Transactions on Intelligent Vehicles, vol. 6, no. 4, pp. 678-689, Dec. 2021.
[19] “Smart Radar System,” srs.ai. https://www.smartradarsystem.com/kr/index.html (accessed Mar. 02, 2021).
[20] S. Lim, J. Jung, B. -h. Lee, J. Choi and S. -C. Kim, "Radar Sensor Based Estimation of Vehicle Orientation for Autonomous Driving," in IEEE Sensors Journal, 2022.
[21] X. Gao, G. Xing, S. Roy and H. Liu, "Experiments with mmWave Automotive Radar Test-bed," 2019 53rd Asilomar Conference on Signals, Systems, and Computers, Pacific Grove, CA, USA, 2019, pp. 1-6.
[22] Nabati, R., & Qi, H. (2021). Centerfusion: Center-based radar and camera fusion for 3d object detection. In *Proceedings of the IEEE/CVF Winter Conference on Applications of Computer Vision* (pp. 1527-1536).
[23] M. Abdalwohab, W. Zhang, A. M. S. Abdelgader and I. Abdelazeem, "Deep learning based camera and radar fusion for object detection and classification," 2021 IEEE 4th International Conference on Automation, Electronics and Electrical Engineering (AUTEEE), Shenyang, China, 2021, pp. 322-326.
[24] A. Sengupta, L. Cheng and S. Cao, "Robust Multiobject Tracking Using Mmwave Radar-Camera Sensor Fusion," in IEEE Sensors Letters, vol. 6, no. 10, pp. 1-4, Oct. 2022.
[25] J S. Guo, P. Wang, J. Ding and H. Liu, "Deep Model Based Road User Classification Using mm-Wave Radar," 2021 CIE International Conference on Radar (Radar), Haikou, Hainan, China, 2021, pp. 2843-2846.

[26] F. Jin, A. Sengupta, S. Cao and Y. -J. Wu, "MmWave Radar Point Cloud Segmentation using GMM in Multimodal Traffic Monitoring," 2020 IEEE International Radar Conference (RADAR), Washington, DC, USA, 2020, pp. 732-737.
[27] A. P. Rangari, A. R. Chouthmol, C. Kadadas, P. Pal and S. Kumar Singh, "Deep Learning based smart traffic light system using Image Processing with YOLO v7," 2022 4th International Conference on Circuits, Control, Communication and Computing (I4C), Bangalore, India, 2022, pp. 129-132.
[28] C. Wang, A. Bochkovskiy and H. Liao, "YOLOv7: Trainable Bag-of-Freebies Sets New State-of-the-Art for Real-Time Object Detectors," in 2023 IEEE/CVF Conference on Computer Vision and Pattern Recognition (CVPR), Vancouver, BC, Canada, 2023 pp. 7464-7475.
[29] Y. A. Khan, S. Imaduddin, A. Ahmad and Y. Rafat, "Image-based Foreign Object Detection using YOLO v7 Algorithm for Electric Vehicle Wireless Charging Applications," 2023 5th International Conference on Power, Control & Embedded Systems (ICPCES), Allahabad, India, 2023, pp. 1-6.
[30] J. Oh, K. -S. Kim, M. Park and S. Kim, "A Comparative Study on Camera-Radar Calibration Methods," 2018 15th International Conference on Control, Automation, Robotics and Vision (ICARCV), Singapore, 2018, pp. 1057-1062.
[31] S. D. Boncolmo, E. V. Calaquian and M. V. C. Caya, "Gender Identification Using Keras Model Through Detection of Face," 2021 IEEE 13th International Conference on Humanoid, Nanotechnology, Information Technology, Communication and Control, Environment, and Management (HNICEM), Manila, Philippines, 2021, pp. 1-6.
[32] M. Si, T. J. Tarnoczi, B. M. Wiens and K. Du, "Development of Predictive Emissions Monitoring System Using Open Source Machine Learning Library – Keras: A Case Study on a Cogeneration Unit," in IEEE Access, vol. 7, pp. 113463-113475.
[33] S. -H. Chen, C. -S. Hung, J. -Y. Wang, C. -H. Chen and K. -C. Hsu, "The Implementation of Hybrid Electric Vehicle Battery Fault and Abnormal Early Warning System Using Keras Neural Network Technology," 2021 9th International Conference on Orange Technology (ICOT), Tainan, Taiwan, 2021, pp. 1-6.
[34] Wang, Y., Li, Y., Song, Y., & Rong, X. (2020). The influence of the activation function in a convolution neural network model of facial expression recognition. *Applied Sciences*, *10*(5), 1897.as
[35] Jin, F., Sengupta, A., Cao, S., & Wu, Y. J. (2020, April). Mmwave radar point cloud segmentation using gmm in multimodal traffic monitoring. In 2020 IEEE International Radar Conference (RADAR) (pp. 732-737). IEEE.

https://doi.org/10.31436/iiumej.v26i1.3328

# OPTIMIZING FPGA RESOURCE ALLOCATION FOR SHA-3 USING DSP48 AND PIPELINING TECHNIQUES

**AGFIANTO EKO PUTRA*, OSKAR NATAN, JAZI EKO ISTIYANTO**

*Department of Computer Science and Electronics, Faculty of Mathematics and Natural Sciences, Universitas Gadjah Mada, Yogyakarta - Indonesia*

**Corresponding author: agfi@ugm.ac.id*

*(Received: 13 June 2024; Accepted: 29 October 2024; Published online: 10 January 2025)*

***ABSTRACT:*** Deploying SHA-3 on FPGA devices requires significant resource allocation; however, the resulting throughput still needs improvement. This study employs the DSP48 module on the Xilinx FPGA to address this issue and implements an eight-stage pipeline methodology to minimize latency. The implementation design comprises a datapath and controller module, utilizing a Xilinx Artix-7-100T series FPGA as the hardware. This method makes use of FPGA resources like Look-Up Tables (LUT), Look-Up Table Random Access Memory (LUTRAM), Flip-Flops (FF), Block RAM (BRAM), Digital Signal Processing (DSP), Input/Output (IO), and Buffer (BUFG). The system's highest frequency is 107.979 MHz, achieving different throughputs for cryptographic hash functions. Specifically, it performs a throughput of 5.183 Gbps for SHA3-224, 4.895 Gbps for SHA3-256, 3.743 Gbps for SHA3-384, and 2.591 Gbps for SHA3-512.

***ABSTRAK:*** Menggunakan SHA-3 pada peranti FPGA memerlukan peruntukan sumber yang ketara, walaupun daya pengeluaran yang terhasil adalah terhad. Untuk menangani isu ini, kajian ini menggunakan modul DSP48 yang disertakan pada Xilinx FPGA dan melaksanakan metodologi saluran paip lapan peringkat untuk meminimumkan kependaman. Reka bentuk pelaksanaan terdiri daripada laluan data dan modul pengawal, menggunakan siri FPGA Xilinx Artix-7-100T sebagai perkakasan. Kaedah ini menggunakan sumber FPGA seperti Look-Up Tables (LUT), Look-Up Table Random Access Memory (LUTRAM), Flip-Flops (FF), Block RAM (BRAM), Digital Signal Processing (DSP), Input/Output (IO), dan Penampan (BUFG). Kekerapan tertinggi sistem ialah 107.979 MHz, dan ia mencapai daya pemprosesan yang berbeza untuk fungsi cincang kriptografi yang berbeza. Secara khususnya, ia mencapai daya pemprosesan 5.183 Gbps untuk SHA3-224, 4.895 Gbps untuk SHA3-256, 3.743 Gbps untuk SHA3-384 dan 2.591 Gbps untuk SHA3-512.

***KEYWORDS:*** *SHA-3, FPGA, DSP48, pipeline*

## 1. INTRODUCTION

NIST released SHA-3, the most recent cryptographic standard within the Secure Hash Algorithm family, on August 5, 2015. The algorithm aims to generate secure hash codes for use within computer and network security applications. SHA-3 compresses unlimited data into limited data by employing its functions. SHA-3 is designed based on permutation and has various versions, including SHA3-224, SHA3-256, SHA3-384, and SHA3-512, each with distinct security levels. The core component of SHA-3 is the permutation function that converts input data into SHA-3 hash. To generate a hash, a state register of 1,600 bits arranged in a three-dimensional matrix of 5x5*64 bits is necessary [1].

https://doi.org/10.31436/iiumej.v26i1.3328

An FPGA was used to test the throughput and slices required to implement SHA-3. Direct implementation of SHA-3 on an FPGA involves extensive and complex wiring demanding significant resources despite low throughput [2, 3]. The algorithm is optimized by merging all the compression functions into one, thereby eliminating intermediate states. The resulting compact version is implemented using LUT on the FPGA. Rao et al. found this implementation to increase throughput, although it still significantly utilizes many resources [4]. While SHA-3 provides robust security, its real-world application on FPGA devices presents significant challenges, particularly regarding resource allocation and throughput. Addressing these challenges is crucial for enabling efficient and scalable cryptographic implementations.

The look-up table (LUT) is a critical logic block in FPGA architecture, widely used for implementing specific logic functions. LUT_6, with six inputs and one output, is vital in realizing complex operations like 6-input logic functions or 64-bit asynchronous ROM. Permutation functions are fundamental in cryptographic applications like SHA-3, requiring extensive data manipulations between 64-bit blocks. As a result, 64 LUTs are often needed to execute such operations. While utilizing LUT_6 helps improve the performance and throughput of systems, it also demands significant hardware resources, especially in high-performance designs that aim to minimize area usage and maximize speed. For instance, optimizing SHA-3's round constants generator shows that a more efficient structure can reduce resource consumption while maintaining high throughput [5]. Pipelined architecture can be implemented at the loop level in FPGA designs to reduce idle time and improve efficiency. Simultaneously executing different stages, such as candidate generation and fitness function evaluation, the architecture ensures that multiple data sets are processed in parallel across iterations. This approach enhances resource utilization and allows for faster execution without increasing latency. In the BB-BC algorithm, this pipelining helps minimize resource usage while maintaining high throughput, making it particularly effective for real-time optimization problems and reducing overall computational time [6, 7].

Despite these efforts, a significant gap must be in optimizing resource allocation and power consumption when implementing SHA-3 on FPGAs. While LUT-based methods enhance throughput, they consume substantial resources and power. Previous research has yet to fully address the efficiency challenges in cryptographic implementations, particularly in balancing high throughput with reduced hardware complexity. To address this gap, this study explores using DSP48 blocks for XOR computations and pipeline techniques to minimize resource usage, aiming to improve FPGA efficiency without compromising performance. Consequently, implementing SHA-3 on FPGA demands significant power and offers limited throughput, while optimizing the SHA-3 algorithm on FPGA necessitates compromising resource usage to increase throughput. This article outlines a solution to this issue by incorporating DSP48 to compute XOR and using a pipeline to handle the system, allowing for implementing SHA-3 on FPGA.

## 2. RESEARCH METHOD

The DSP48 is a resource employed for carrying out specialized operations, specifically those related to the computational chain in DSP48 containing add/subtract units linked to multipliers. It is also connected to the final add/remove/accumulate engine. When used on FPGAs, it leads to high throughput and power efficiency [8]. DSP48 can also optimize complex operations like 2D convolution. Additionally, DSP48 can handle multiplication and accumulation within the block itself, reducing the need for extra logic, such as adders [9]. In this research, DSP48 enables more efficient resource allocation on the FPGA by reducing the need for additional logic components like LUTs and external adders [10, 11]. In this research,

https://doi.org/10.31436/iiumej.v26i1.3328

CascadeDSP will be used for the implementation. CascadeDSP is a technique in which multiple DSP blocks are connected in a cascading configuration, allowing them to work together to handle more complex operations that require higher bit-width or multiple stages of computation. Furthermore, DSP48 blocks are integrated into the pipeline architecture designed to minimize latency while maintaining high throughput, ensuring that operations are executed parallel to enhance overall system performance. Using the DSP48 slices, the system optimizes the processing of large data blocks required by the SHA-3 algorithm, achieving both efficiency and high performance in the cryptographic function's FPGA implementation.

A pipeline architecture can be utilized to reduce the delay time in SHA-3 implementation. The pipeline functions so that various execution stages can be conducted simultaneously on different data. The pipeline architecture is expected to enhance the utilization of FPGA resources without compromising computational speed [6]. In this system, the pipeline architecture is employed to reduce the latency of implementing the SHA-3 cryptographic algorithm. The pipeline operates by dividing the SHA-3 permutation function into several stages, such as Theta, Chi, and Iota, and allowing different operations to be executed in parallel across multiple stages [12, 13]. This design ensures that while one stage processes a data block, the next stage can begin processing the subsequent block, optimizing the data flow and reducing idle time. Specifically, the system utilizes an eight-stage pipeline, which includes internal registers within the DSP48 slices at critical points in the Theta and Chi stages to synchronize data and ensure efficient processing [14]. The Theta stage uses external serial registers to ensure data arrives promptly. In contrast, the Rho and Pi stages do not require pipelining as they perform more straightforward rotation and permutation operations. Implementing this pipeline structure achieves higher throughput without compromising execution speed, making it ideal for high-performance applications like SHA-3.

The system design incorporates three modules: input, processing, and output, which are depicted in Figure 1. The input module receives data serially and transmits it in parallel to the next module. This module receives data from a PC through a USB-UART interface. The GUI on the PC sends serial data to the FPGA, which the input module receives and then converts from serial to parallel format. This parallel data is crucial because it is easier to process in the subsequent stages of the system, especially in high-throughput cryptographic operations like SHA-3. The processing module comprises a data storage unit for temporarily holding data from the input module and the results generated by the SHA-3 permutation function. In the data storage unit, input data is stored before processing by the SHA-3 permutation function, which handles the system's core cryptographic operations. The SHA-3 permutation function unit performs crucial stages of the SHA-3 algorithm, including Theta, Rho, Pi, Chi, and Iota, which collectively transform the input data into its final cryptographic hash.

The controller unit plays a vital role in governing the overall flow of operations within the system. It ensures proper timing and coordination of data movement between the input, processing, and output modules, allowing smooth and efficient operation. After the data has been processed, the output from the processing module is transferred to the output module, which then transmits the serialized data back to the PC. The input and output modules communicate at 115,200 bits per second, ensuring fast and reliable data transmission between the FPGA and the external system. This high-speed communication enables efficient real-time processing and transmission of cryptographic data, optimizing system performance for practical applications.

https://doi.org/10.31436/iiumej.v26i1.3328

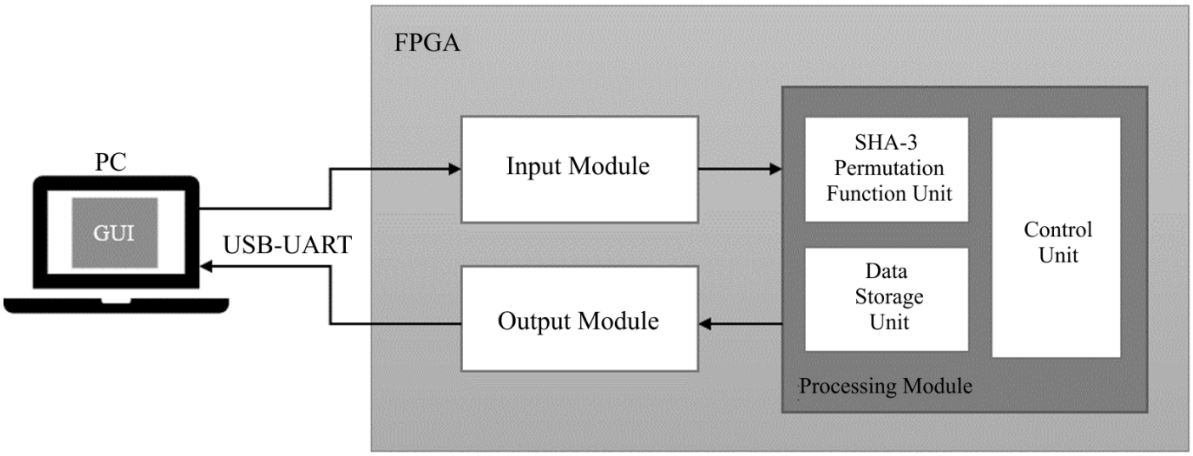


Figure 1. System block diagram

### 2.1. Design of the Top Layer System (Top Level Design)

The top-level design is the highest-level module in the hierarchy of all the designed modules. This design comprises four main components: UART_RX and UART_TX act as data receivers and senders to the PC via the UART serial port; the datapath is the system's core that performs SHA-3 operations, and the controller unit maintains regulation of system operations. Figure 2 shows the top-level block diagram. The top-level design features input and output ports. The input port comprises 'CLK100MHZ' linked to the FPGA clock generation pin and 'UART_TXD' connected to the serial communication pin for receiving data from the PC. The output port, 'UART_RXD,' transmits serial data to the PC via the relevant pin.

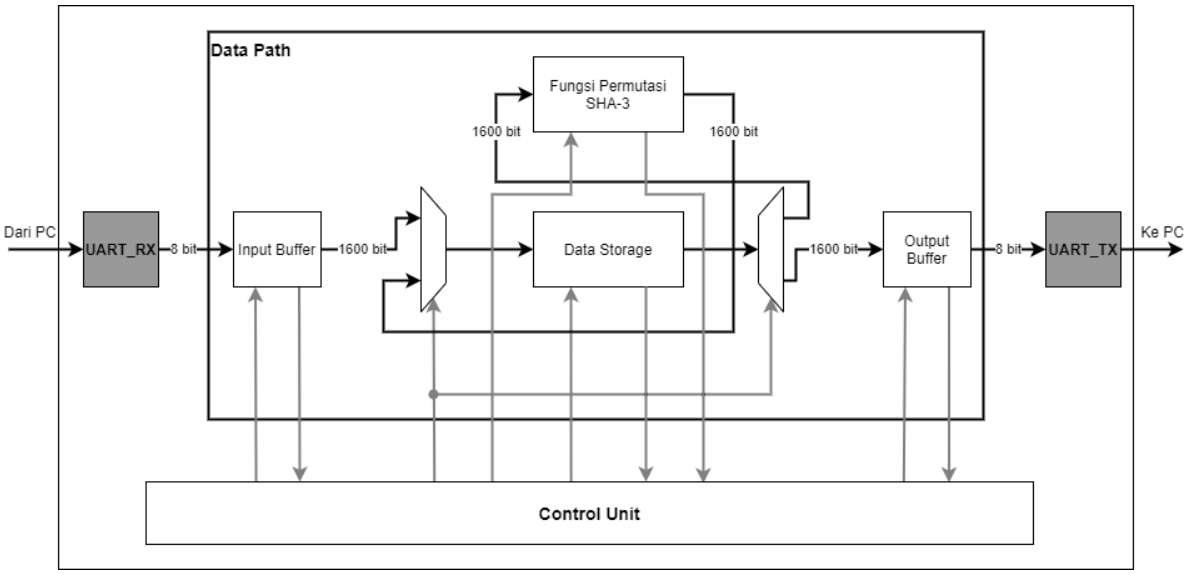


Figure 2. Top-level design block diagram

### 2.2. Datapath Module Design

The datapath module processes input data from the PC to generate new data via the SHA-3 permutation function operation. It comprises the input buffer, output buffer, data storage, and SHA-3 permutation function modules. The SHA-3 permutation function module, depicted in Figure 3, shall consist of five SHA-3 permutation function stages [1].

a. "Theta Step (θ): ($0 \leq x,y \leq 4$,)"

https://doi.org/10.31436/iiumej.v26i1.3328

$$C[x]=A[x,0]\oplus A[x,1]\oplus A[x,2]\oplus A[x,3]\oplus A[x,4]; \quad (1)$$

$$D[x]=C[(x-1)]\oplus ROT(C[(x+1),1]); \quad (2)$$

$$A[x,y]=A[x,y]\oplus D[x]; \quad (3)$$

b. "Rho Step" ("ρ" )": $(0 \le x,y \le 4)$"

$$A[x,y]=ROT(A[x,y,],r[x,y]); \quad (4)$$

c. "Pi Step " ("π" )": $(0 \le x,y \le 4)$"

$$B[y,(2x+3y)]=A[x,y]; \quad (5)$$

d. "Chi Step " ("χ" )": $(0 \le x,y \le 4)$"

$$A[x,y]=B[x,y]\oplus(NOT(B[(x+1),y])AND(B[(x+2),y])); \quad (6)$$

e. "Iota Step " ("ι" )":"

$$A[0,0]=A[0,0,z]\oplus RC[i]; \quad (7)$$

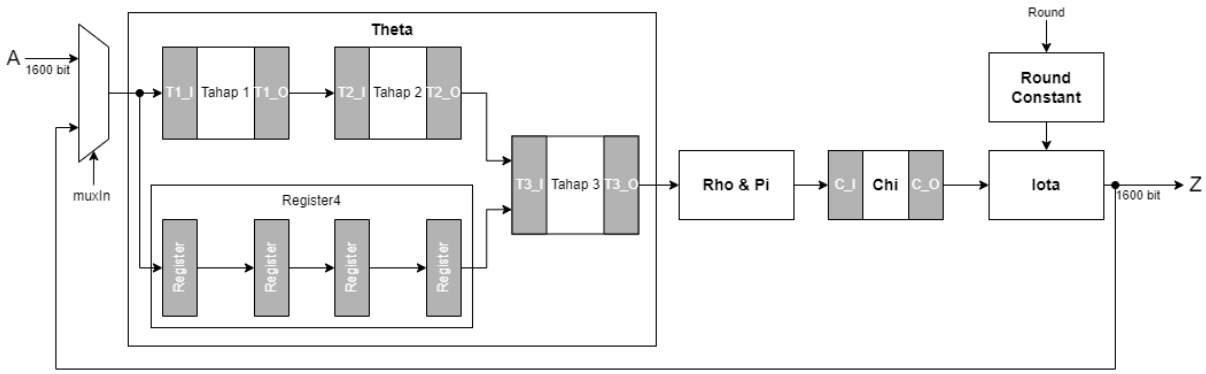


Figure 3. Block diagram of the SHA-3 permutation function

The DSP48 module executes logical equation operations through three stages - Theta, Chi, and Iota. The Theta stage comprises three sub-stages - the first sub-stage processes equation (1), the second sub-stage processes equation (2), and the third sub-stage processes equation (3). Notably, for equations involving more than two inputs for a single output, including equation (1) in the Theta stage and equation (6) in the Chi stage, the DSP48 employs a cascading method for connectivity. The methodology involves linking the output pin 'PCOUT' (Figure 4) of one DSP48 to the input pin 'PCIN' of another DSP48. The functionality of the 'PCOUT' pin is identical to that of the 'P' output pin on the DSP48, which has been explicitly configured for this cascading technique. This method was chosen due to the unique pins and pathways on the Xilinx FPGA DSP48, which allow for more efficient and rapid interconnection between DSPs in a single column compared to ordinary output pins [8].

The pipeline implementation in this research comprises eight stages that employ DSP48 internal registers at every input and output of stages 1, 2, and 3 Theta and Chi stages, as presented by the blue block in Figure 3. In the Theta module, we added four serial external registers that equalize the data arrival upon entering the Theta stage. The Rho and Pi modules lack pipelining because their sole purpose is rotation operations, which do not necessitate a DSP48. Similarly, the Iota module lacks pipelining as it merely executes an XOR operation on the A[0,0] matrix. This implementation mandates eight input data; each cycle inputs one data per module. One of these input data constitutes the complete data for SHA-3, which is 1,600 bits in size.

https://doi.org/10.31436/iiumej.v26i1.3328

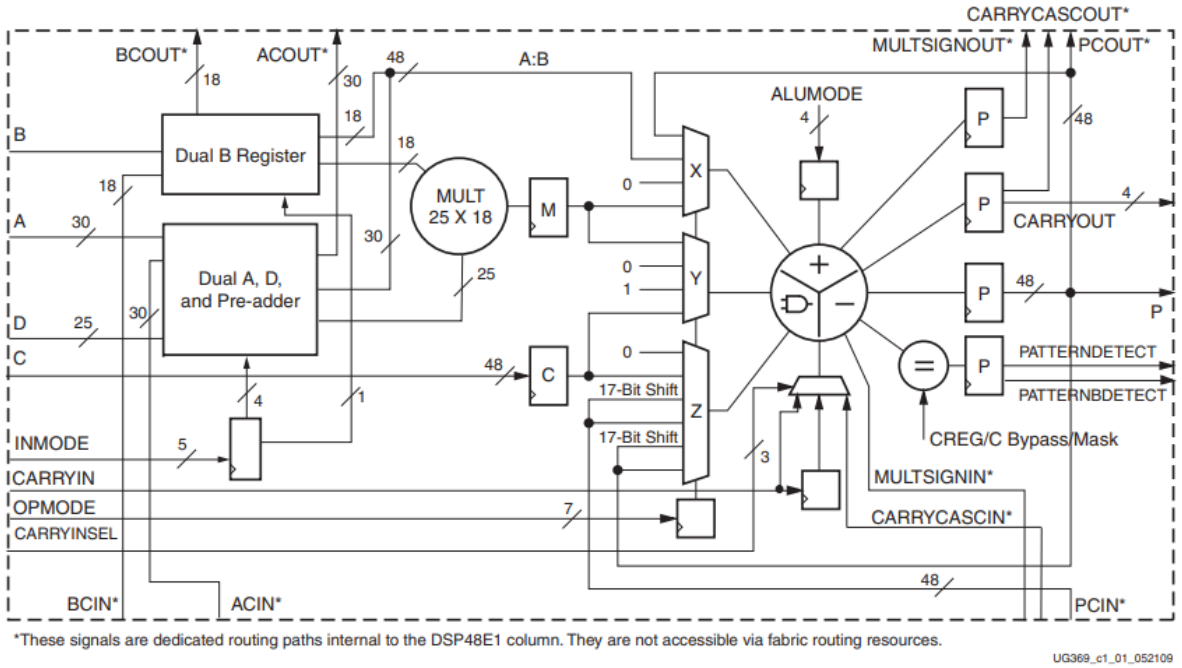


Figure 4. DSP48 block (Xilinx, 2018)

### 2.3. Controller module design

The controller module is implemented using a Finite State Machine (FSM), as depicted in Figure 5. Every condition in the FSM triggers the modules along with the MUX and DEMUX included in the data path module with the corresponding commands mentioned in Table 1.

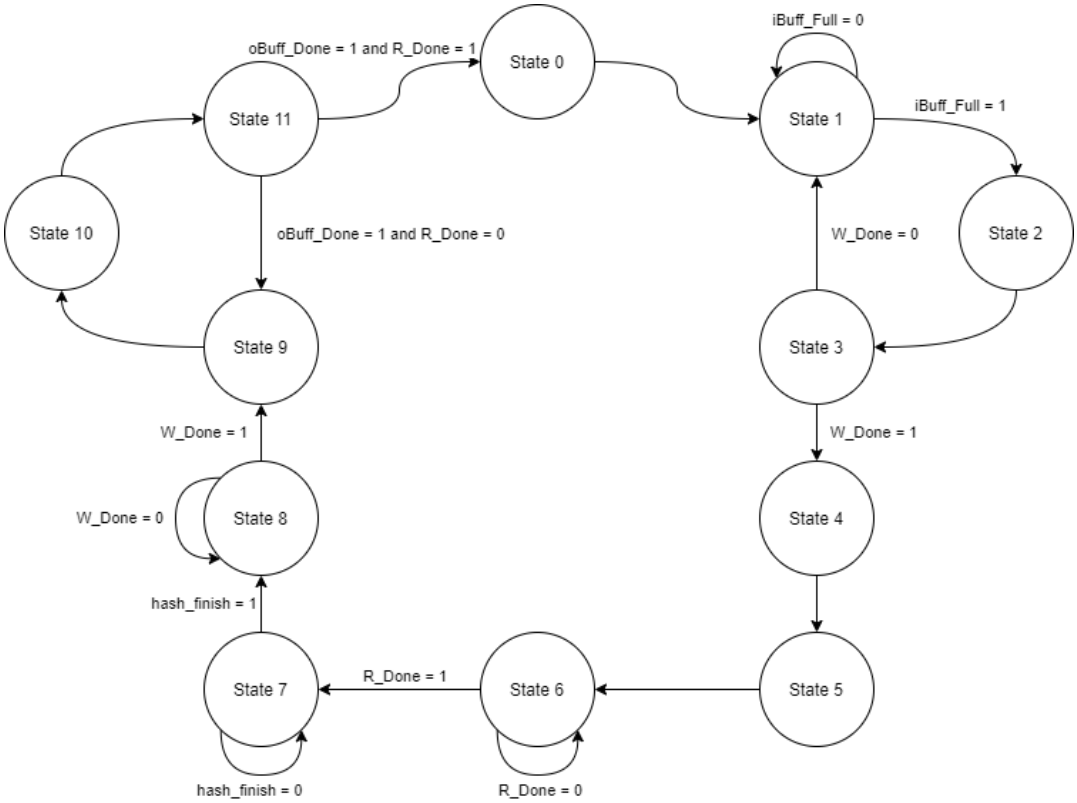


Figure 5. Controller module state diagram

https://doi.org/10.31436/iiumej.v26i1.3328

Table 1. Condition of control signals in each state

| Signal/State | Reset_I | Reset_DS | Reset_FP | Reset_O | W_EN | R_EN | muxData |
|---|---|---|---|---|---|---|---|
| **0** | 1 | 1 | 1 | 1 | 0 | 0 | 0 |
| **1** | 0 | 0 | 1 | 1 | 0 | 0 | 0 |
| **2** | 0 | 0 | 1 | 1 | 1 | 0 | 0 |
| **3** | 1 | 0 | 1 | 1 | 0 | 0 | 0 |
| **4** | 0 | 0 | 1 | 1 | 0 | 1 | 0 |
| **5** | 0 | 0 | 1 | 1 | 0 | 1 | 0 |
| **6** | 0 | 0 | 0 | 1 | 0 | 1 | 0 |
| **7** | 1 | 1 | 0 | 1 | 0 | 0 | 0 |
| **8** | 1 | 0 | 0 | 1 | 1 | 0 | 1 |
| **9** | 1 | 0 | 0 | 1 | 0 | 1 | 1 |
| **10** | 1 | 0 | 0 | 1 | 0 | 0 | 1 |
| **11** | 1 | 0 | 0 | 0 | 0 | 0 | 1 |

The control signals in Table 1 have the following functions:

1. Reset_I: Reset the input buffer module
2. Reset_DS: Reset the data storage module
3. Reset_FP : Reset SHA-3 permutation function module
4. Reset_O: Reset the output buffer module
5. W_EN: Store data in the data storage module
6. R_EN: Read data from the data storage module
7. muxData: Set MUX and DEMUX to determine the data to be stored in the storage module, whether from the PC input data or the SHA-3 process results.

The explanation of the state conditions in Table 1 are:

1. State 0: Reset all modules
2. State 1: Waiting for data input from PC.
3. State 2: Stores one SHA-3 data (1,600 bits) in the data storage module
4. State 3: Proceed to the next state if it has received 8 SHA-3 data; otherwise, it will return to state 1.
5. State 4 and 5: Initiate the data reading from the data storage module.
6. State 6: Initiate SHA-3 algorithm operation
7. State 7: Waiting for the SHA-3 process to complete
8. State 8: Save the SHA-3 result data to the data storage module
9. State 9 and 10: Initiate reading of one data from the data storage module
10. State 11: Returns to state 0 if all the SHA-3 output data has been sent to the PC; otherwise, it will return to state 9.

https://doi.org/10.31436/iiumej.v26i1.3328

### 2.4. GUI (Graphical User Interface) Design

The user interface displays the data sent to the FPGA and verifies whether the FPGA output matches the reference result (refer to Figure 6). To input the data for transmission, users select a text file containing eight datasets, with each dataset comprising three components: the first indicates the SHA-3 hash size of the input data under testing (224, 256, 384, or 512 bits); the second denotes the SHA-3 data to be dispatched to the FPGA; and the third represents the hash reference for comparison with the hash output from the FPGA. After the file has been successfully read, the second piece of information is merged and transmitted to the FPGA via the UART serial terminal. Once the program receives the hash result from the FPGA, it will be displayed through the interface.

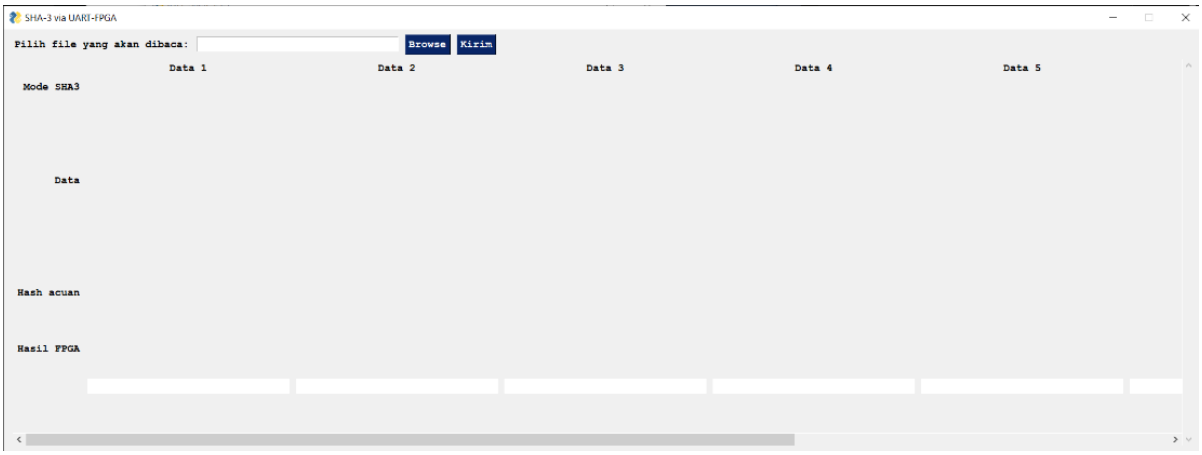


Figure 6. The GUI (Graphical User Interface) Design

## 3. RESULTS AND DISCUSSION

### 3.1. Testing the SHA-3 Permutation Module

The first step in testing the core of this research, the permutation function module, is a simulation using Xilinx Vivado software to ensure that the SHA-3 process and pipeline are functioning correctly and producing output following the reference data. We entered SHA-3 data for each clock eight times (eight data) to test. The SHA-3 mode determines the output data size. The module's outcomes are evaluated against the reference results to determine if it operates correctly. The input and reference data are sourced from the CSRC's sample SHA-3 data website [15].

### 3.2. Synthesis and Implementation Results for Top-Level Design

The top level is created through VHDL design, followed by synthesis and implementation without resource and area optimization. This process generates RTL schematics on an FPGA and reports detailing timing, resource, and power estimations. The resources employed by the top-level design are LookUp Table (LUT), accounting for 8.11% (5,140 out of 63,400), LUTRAM, accounting for 4.21% (800 out of 19,000), and Flip-flop (FF), accounting for 2%. 72% of the total 126,800 components were successful, with 16.67% (22.5 out of 135) of the BRAM, 59.17% (142 out of 240) of the DSP, 1.43% (3 out of 210) of the IO, and 9.38% (3 out of 32) of the BUFG not functioning correctly. The system requires 0.446 W power, as per the timing report. The system's Worst Negative Slack (WNS) value is 0.739 ns, the Worst Hold Slack (WHS) value is 0.026 ns, and the Worst Pulse Width Slack (WPWS) value is 4.020 ns.

https://doi.org/10.31436/iiumej.v26i1.3328

The system's maximum beat frequency can be determined by subtracting the designed clock period value from WNS [16], resulting in a maximum frequency of 107.979 MHz. To calculate throughput, the quantity of input SHA-3 data must be multiplied by the system's maximum frequency and then divided by the total cycles required to complete the SHA-3 hash process [17]. The input data quantity is calculated based on r bitrate, as it is the fundamental input of SHA-3. The bit rate for each SHA-3 mode differs, with SHA3-224 having a bit rate of 1,152 bits, SHA3-256 with 1,088 bits, SHA3-384 with 832 bits, and SHA3-512 with 576 bits. In this system, performing SHA-3 operations requires 192 cycles with eight input data. The throughput value for each SHA-3 mode in this system is 5.183 Gbps for SHA3-224, 4.895 Gbps for SHA3-256, 3.743 Gbps for SHA3-384, and 2.591 Gbps for SHA3-512.

### 3.3. Controller module synthesis and implementation results

After the synthesis and implementation process is carried out at the top-level design, the controller module as a system work control module produces a circuit that uses units such as FDRE and LUT. FDRE is a D Flip-flop with a clock enabled [18, 19].

### 3.4. Results of synthesis and implementation of the Datapath module

After synthesizing and implementing the top-level design, the data path module as a data processing module produces a circuit that uses units such as Output_Buffer, DEMUX, FunctionPermutation_SHA3, Input_Buffer, and Data_Storage. In this circuit, two LUTs are connected to the input of the Output_Buffer and Input_Buffer modules.

### 3.5. Synthesis and implementation results of the permutation function module

The SHA-3 operation module includes the SHA-3 permutation function stages modules Module_Chi, Module_Theta, Module_Iota, and Module RoundConstant. Module_RhoPi is not included in this circuit because the module is only a data transfer process, so the circuit implementation must change the data path between Module_Theta and Module_Chi without requiring any resources. This module also has a clock counter circuit and uses blocks such as CARRY4, LUT, and FDCE. CARRY4 is usually used to create an enumerator circuit [20].

The implementation of the DSP48 module, which is the core of this research, consists of DSPCascade4, DSPCascade2, and DSP48 modules. The DSPCascade4 module consists of four DSP48s, as shown in Figure 7; the DSPCascade2 module consists of two DSP48s, as shown in Figure 8, and the DSP48 Module consists of one DSP48, as shown in Figure 9. These modules are then arranged to be able to perform SHA-3 operations. The details of DSP48 usage in the SHA-3 permutation function stage modules are shown in Table 2.

Table 2. Details of DSP48 usage

| Step | Total modules used | DSP48 content in one module | DSP48 Total |
|---|---|---|---|
| Step 1 | 7 * DSPCascade4 | 4 | 28 |
| Step 2 | 7 * ModulDSP48 | 1 | 7 |
| Step 3 | 35 * ModulDSP48 | 1 | 35 |
| Chi | 35 * DSPCascade2 | 2 | 70 |
| | | Total | 142 |

https://doi.org/10.31436/iiumej.v26i1.3328

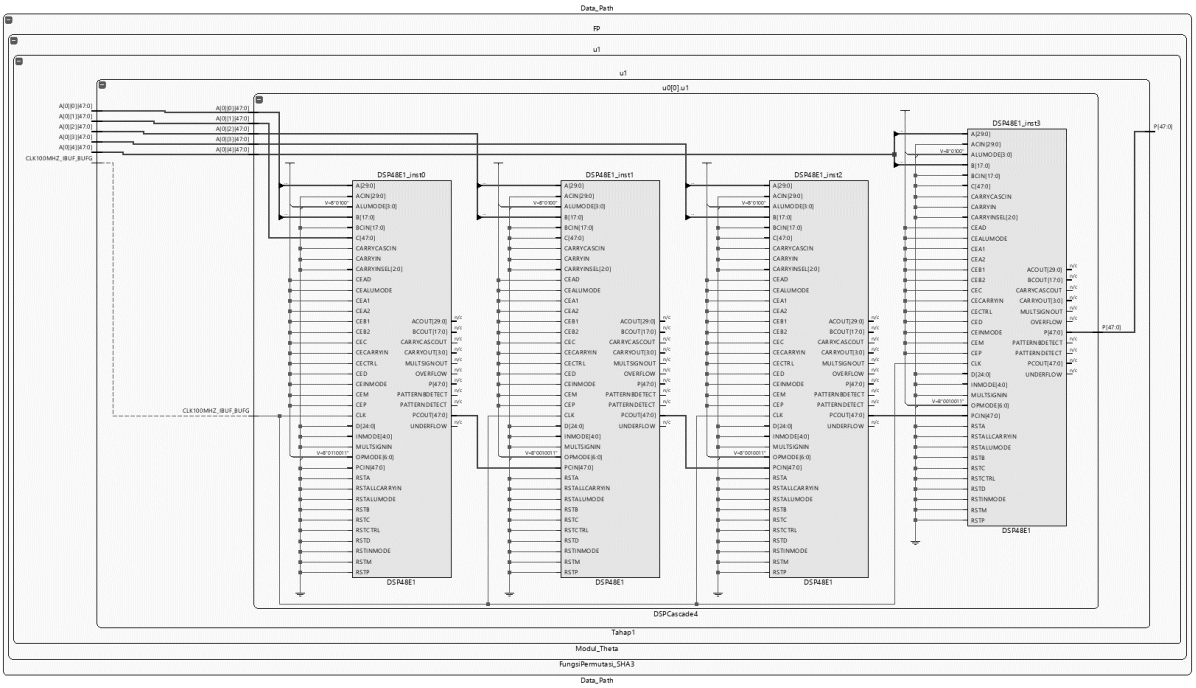


Figure 7. The DSPCascade4 implementation

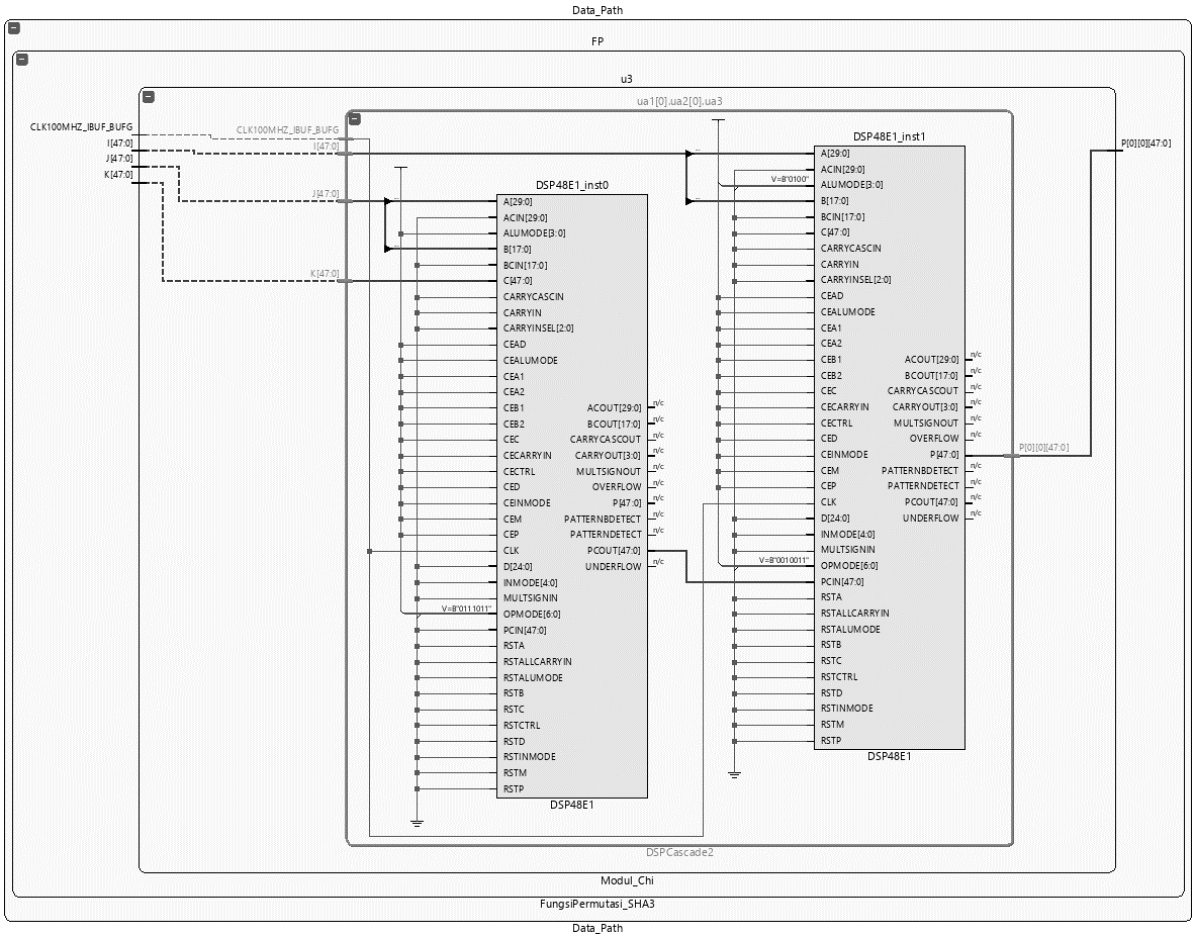


Figure 8. The DSPCascade2 implementation

https://doi.org/10.31436/iiumej.v26i1.3328

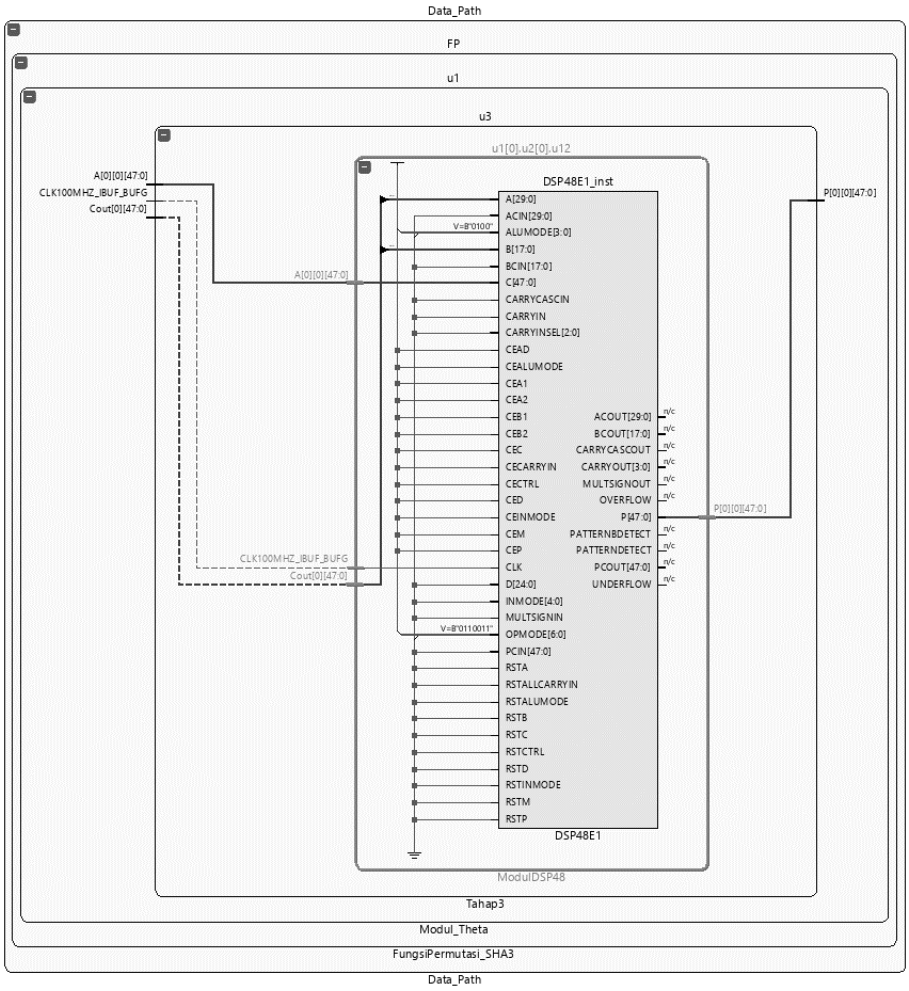


Figure 9. The implementation of the DSP48 Module.

### 3.6. Testing implementation results on FPGA

FPGA implementation testing occurs after all modules have successfully functioned. The GUI program was designed to enable easy monitoring of input data and output results generated by the FPGA, allowing for comparison with previously established reference results, especially in SHA-3 256, as shown in Table 3.

Table 3. Comparison Throughput between previous research

| **References** | **FPGA** | **Throughput (Gbps)** |
|---|---|---|
| F. Kahri et al.[21] | Virtex 2 | 0,73 |
| | Virtex 4 | 1,06 |
| | Virtex 5 | 2,30 |
| | Virtex 6 | 3,81 |
| | Virtex 7 | 4,2 |
| B. Jungk [22] | Virtex 5 | 0,86 |
| | Virtex 6 | 1,07 |
| **References** | **FPGA** | **Throughput (Gbps)** |
| I. San and N. At [23] | Virtex 5 | 0,501 |
| J.-P. Kaps et. al. [24] | Virtex 5 | 0,075 |
| | Virtex 6 | 0,136 |
| This Research | Artix-7-100T | 4,895 |

https://doi.org/10.31436/iiumej.v26i1.3328

Based on Table 3, this research demonstrates a significant improvement in throughput compared to previous studies using Virtex FPGAs, achieving 4.895 Gbps with the Artix-7-100T, a low-cost and moderate-performance FPGA. Notably, this throughput surpasses even the highest reported in Kahri's study with Virtex 7 (4.2 Gbps). It significantly outperforms Jungk's Virtex 6 (1.07 Gbps) and San and J.P Kaps' results by an even more substantial margin. Despite being a cost-effective FPGA, the Artix-7-100T performs better than the higher-cost and high-performance Virtex devices, showcasing the efficiency of this research's design and the potential to deliver high throughput in budget-sensitive applications.

(a)

(b)

Figure 10. FPGA implementation test results with data 1 - 5 (a) and 6 - 8 (b)

Test data is uploaded into the program using an eight-piece file containing three elements: SHA-3 mode, input data, and reference hash. The data that has been successfully read is transmitted to the FPGA by pressing the 'Send' button. Following the output data transmission by the FPGA through UART, as demonstrated in Figure 10, the outcomes will be promptly shown. Testing was conducted twice with eight different test data for each test, and the results verified the accurate execution of this system.

## 4. CONCLUSION

The SHA-3 algorithm was successfully implemented on the Artix-7-100T FPGA using the DSP48 unit and eight pipeline stages. Resources, including LUTs (equivalent to 8.11% of 63,400), LUTRAM (equivalent to 4.21% of 19,000), FF (equal to 2.72% of 126,800), BRAM (equivalent to 16.67% of 135), DSP48 (equivalent to 59.17% of 240), IO (equivalent to 1.43% of 210), and BUFG (equivalent to 9.38% of 32) were utilized for the implementation. The system's overall power requirement is 0.446 W, while the maximum frequency that can be applied to the system is 107.979 MHz. Additionally, the system produces a throughput of 5.183 Gbps for SHA3-224, 4.895 Gbps for SHA3-256, 3.743 Gbps for SHA3-384, and 2.591 Gbps for SHA3-512.

## ACKNOWLEDGEMENT

This work was partially supported by the Department of Computer Science and Electronics, Universitas Gadjah Mada, under the 2024 publication funding year.

## REFERENCES

[1] Paar, C. dan Pelzl, J., 2010, "SHA-3 and The Hash Function Keccak", Understanding Cryptography — A Textbook for Students and Practitioners, Available: http://www.crypto-textbook.com/.

[2] Honda, T., Guntur, H. dan Satoh, A., 2014, "FPGA implementation of new standard hash function Keccak," 2014 IEEE 3rd Global Conference on Consumer Electronics, GCCE 2014, Available: DOI:10.1109/GCCE.2014.7031105.

[3] Ahmad, I, and Das, A.S., 2005, Hardware implementation analysis of SHA-256 and SHA-512 algorithms on FPGAs, Computers and Electrical Engineering 31 (2005) 345–360.

[4] Rao, M., Newe, T. dan Grout, I., 2014, "Efficient high-speed implementation of secure hash algorithm-3 on Virtex-5 FPGA", Proceedings - 2014 17th Euromicro Conference on Digital System Design, DSD 2014, Available: DOI:10.1109/DSD.2014.24.

[5] Sideris, A.; Dasygenis, M., 2023, Enhancing the Hardware Pipelining Optimization Technique of the SHA-3 via FPGA. Computation 2023, 11, 152. https://doi.org/10.3390/computation11080152.

[6] Augoestien, N.G. dan Putra, A.E., 2015, "Purwarupa Perangkat Keras untuk Eksekusi Algoritma AES Berbasis FPGA", IJEIS (Indonesian Journal of Electronics and Instrumentation Systems), [Online] Available: DOI:10.22146/ijeis.7644.

[7] M. Psarakis, A. Dounis, A. Almabrok, S. Stavrinidis, and G. Gkekas, "An FPGA-Based Accelerated Optimization Algorithm for Real-Time Applications," Journal of Signal Processing Systems, vol. 92, no. 10, pp. 1155-1176, Oct. 2020. doi: 10.1007/s11265-020-01522-5.

[8] Kundi, D. e. S. dan Aziz, A., 2016, "A low-power SHA-3 designs using embedded digital signal processing slice on FPGA", Computers and Electrical Engineering, Available: DOI:10.1016/j.compeleceng.2016.04.004.

[9] W. Wang and G. Sun, "A DSP48-Based Reconfigurable 2-D Convolver on FPGA," 2019 International Conference on Virtual Reality and Intelligent Systems (ICVRIS), Jishou, China, 2019, pp. 342-345. doi: 10.1109/ICVRIS.2019.00089.

[10] E. Walters, "Array Multipliers for High Throughput in Xilinx FPGAs with 6-Input LUTs," Computers, vol. 5, no. 4, p. 20, Sep. 2016. doi: 10.3390/computers5040020.

[11] I. M. Alexandru, A. Grama, L. Viman, and D. Pitica, "FFT Radix2 Core Implemented on FPGA with DSP48 Slices," 2018 IEEE 24th International Symposium for Design and Technology in Electronic Packaging (SIITME), Iasi, 2018, pp. 109-113. doi: 10.1109/SIITME.2018.8599234.
[12] A. Sideris, T. Sanida, and M. Dasygenis, "Hardware acceleration design of the SHA-3 for high throughput and low area on FPGA," Journal of Cryptographic Engineering, vol. 14, no. 2, pp. 193-205, Jun. 2024. doi: 10.1007/s13389-023-00334-0.
[13] Z. Han, J. Jiang, J. Xu, P. Zhang, X. Zhao, D. Wen, and Y. Dou, "A high-throughput scalable BNN accelerator with fully pipelined architecture," CCF Transactions on High Performance Computing, vol. 3, no. 1, pp. 17-30, Mar. 2021. doi: 10.1007/s42514-020-00059-0.
[14] Sundal, M. dan Chaves, R., 2017, "Efficient FPGA Implementation of the SHA-3 Hash Function", Proceedings of IEEE Computer Society Annual Symposium on VLSI, ISVLSI, [Online] Available: DOI:10.1109/ISVLSI.2017.24.
[15] CENTER, CSR, 2021, "Cryptographic Standards and Guidelines," Available: https://csrc.nist.gov/projects/cryptographic-standards-and-guidelines/example-values,
[16] Xilinx, 2020, "UltraFast Design Methodology Guide for the Vivado Design Suite," Xilinx, Available: https://www.xilinx.com/content/dam/xilinx/support/documentation/sw_manuals/xilinx2020_1/ug949-vivado-design-methodology.pdf.
[17] Athanasiou, G.S., Makkas, G.P. dan Theodoridis, G., 2014, "High throughput pipelined FPGA implementation of the new SHA-3 cryptographic hash algorithm", ISCCSP 2014 - 2014 6th International Symposium on Communications, Control and Signal Processing, Proceedings, Available: DOI:10.1109/ISCCSP.2014.6877931.
[18] A. E. Putra, O. Natan, and J. E. Istiyanto, "Enhancing CNN Deployment Efficiency on Mobile Devices with FPGA-based Accelerators: Memory-based Convolution and Resource Optimization," ICIC Express Letters Part B: Applications, vol. 15, no. 10, pp. 989-997, Oct. 2024.
[19] Xilinx Inc., 2020, "Vivado Design Suite 7 Series FPGA and Zynq-7000 SoC Libraries Guide", Xilinx,. Available: https://www.xilinx.com/support/documentation/sw_manuals/xilinx2020_2/ug953-vivado-7series-libraries.pdf.
[20] Z. Hakim, O. Natan, R. H. Sari, J. T. Amael, A. Dharmawan and J. E. Istiyanto, "6-DOF Arm Robot Control Using Open-Source FPGA," 2024 9th International Conference on Control and Robotics Engineering (ICCRE), Osaka, Japan, 2024, pp. 157-161
[21] F. Kahri, B. Bouallegue, M. Machhout, R. Tourki, "An FPGA Implementation and Comparison of the SHA-256 and Blake-256", 14th international conference on Sciences and Techniques of Automatic control, & computer engineering, Sousse, Tunisia 2013, pp 152-157.
[22] B. Jungk, "Evaluation Of Compact FPGA Implementations For All SHA-3 Finalists", Third SHA-3 Candidate Conference, March, 2012.
[23] I. San, N. At, "Compact Keccak Hardware Architecture for Data Integrity and Authentication on FPGAs", Information Security Journal: A Global Perspective, Taylor & Francis, 21:5, 231-242, 2012.
[24] J.-P. Kaps, P. Yalla, K.K. Surapathi, B. Habib, S. Vadlamudi, S. Gurung, "Lightweight Implementations of SHA-3 Finalists on FPGAs", SHA-3 Conference, March 2012.

https://doi.org/10.31436/iiumej.v26i1.3337

# DESIGN OF INTELLIGENT FEATURE SELECTION TECHNIQUE FOR PHISHING DETECTION

**SHARVARI SAGAR PATIL*, NARENDRA M. SHEKOKAR, SRIDHAR CHANDRAMOHAN IYER**

*Department of Computer Engineering,*
*SVKM's Dwarkadas J. Sanghvi College of Engineering, Mumbai, India.*

**Corresponding author: sharvarichorghe@gmail.com*

*(Received: 23 June 2024; Accepted: 21 September 2024; Published online: 10 January 2025)*

***ABSTRACT:*** Phishing attacks lead to significant threats to individuals and organizations by gaining unauthorized access. The attackers redirect the users to fake websites and steal their credentials and other confidential data. Various techniques are employed to detect phishing using machine learning algorithms or static detection techniques that use blacklisting of web URLs. The attackers tend to change their approach to launch an attack, making it difficult for traditional phishing detection techniques to safeguard the user. The performance of conventional detection methods relies on exhaustive data and features selected for classification. Features selected for designing detection systems majorly contribute to the performance of the detection system. Phishing detection techniques rely mainly on static features that are selected based on traditional feature selection or ranking techniques. This paper proposes an innovative approach to phishing detection by designing a feature selection technique using reinforcement learning. A novel reinforcement learning agent is designed that uses a dynamic, adaptive, and data-driven approach to improve classifier performance in phishing detection. The technique is designed to select the features using the RL agent dynamically. We have evaluated our technique using the real-world phishing dataset and compared its performance with the existing techniques. Based on the evaluation, our proposed methodology of dynamic feature selection gives the best accuracy of 99.07 % with the random forest classifier model. Our work contributes to advancing phishing detection methodology by developing a dynamic feature selection technique.

***ABSTRAK:*** Serangan pancing data membawa ancaman besar kepada individu dan organisasi dengan mendapatkan akses tanpa kebenaran. Penyerang akan mengalihkan pengguna ke laman web palsu dan mencuri maklumat log masuk serta data sulit yang lain. Pelbagai teknik digunakan bagi mengesan pancing data menggunakan algoritma pembelajaran mesin atau teknik pengesanan statik yang menggunakan URL laman web yang disenarai hitam. Penyerang cenderung mengubah pendekatan mereka untuk melancarkan serangan, menjadikan teknik pengesanan pancing data tradisional sukar bagi melindungi pengguna. Prestasi kaedah pengesanan konvensional bergantung kepada data menyeluruh dan ciri-ciri yang dipilih untuk pengelasan. Teknik pengesanan pancing data kebanyakannya bergantung pada ciri-ciri statik yang dipilih berdasarkan kaedah pemilihan atau penarafan ciri tradisional. Kajian ini mencadangkan pendekatan inovatif bagi pengesanan pancing data dengan mereka bentuk teknik pemilihan ciri menggunakan pembelajaran peneguhan. Ejen pembelajaran peneguhan baru, direka menggunakan pendekatan yang dinamik, adaptif, dan berasaskan data bagi memperbaiki prestasi pengelas dalam pengesanan pancing data. Teknik ini direka untuk memilih ciri-ciri secara dinamik menggunakan ejen RL. Teknik ini dinilai menggunakan dataset pancing data sebenar dan dibanding prestasinya dengan teknik sedia ada. Berdasarkan penilaian, metodologi pemilihan ciri dinamik ini memberikan ketepatan terbaik sebanyak

99.07% dengan model pengelasan rawak. Kerja ini merupakan sumbangan kepada kemajuan metodologi pengesanan pancing data dengan membangunkan teknik pemilihan ciri dinamik.

***KEYWORDS:*** *Reinforcement Learning; Feature Selection; Phishing Detection; Machine Learning*

# 1. INTRODUCTION

Phishing is an attack where the attacker pretends to be a trusted entity to gain access to confidential information from internet users. The attackers generate genuine-looking URLs and send them to the victim through various channels like emails, messages, and other communication mediums. Based on The State of Phishing 2024 report, there is a 341% increase in malicious phishing links [1]. The launch of Chat GPT has also led to the rise of phishing attacks. The reports suggest that since the launch of ChatGPT in November 2022, there has been a surge of 4151% in phishing messages. In the Internet crime report published by the Federal Bureau of Investigation, phishing is among the top 5 cybercrimes reported in 2023 [2]. Multiple detection strategies have been designed that rely on static blacklisted datasets and other machine learning-based techniques. These techniques depend on the dataset and the features used while developing the detection model.

The technology for detecting phishing web pages has evolved continuously over the period. Various conventional methods for phishing detection include the blacklist method, heuristic feature method, visual similarity features based, and machine learning approaches [3]. Researchers have also employed advanced detection methods like deep learning. Traditional methods mainly depend on analyzing and modeling manually extracted features from various sources, including URL features, page content, and webpage structure. Recently, deep learning has been investigated and utilized for phishing webpage detection because of its strong ability to extract features automatically. Bio-inspired optimization algorithms like Particle Swarm Optimization have been used for feature selection [4]. Feature selection using ranking methods like omitting redundant features and filtering methods have been proposed by researchers on the phishing dataset [5]. However, as phishing webpages become more evasive and rapidly updated, these traditional methods require increasingly detailed analyses and the extraction of more features. This results in many feature dimensions and possible correlations between features.

To address the aforementioned issue, the proposed Intelligent Feature Selection Technique (IFST) utilizes artificial intelligence and machine learning to identify and prioritize features most indicative of phishing behavior dynamically. IFST aims to provide a robust defense against known and emerging phishing threats by intelligently adapting to evolving attack strategies and patterns.

Most relevant and informative features are selected using feature selection techniques. The features contribute to the accurate classification of the test cases. These techniques aim to improve model performance and decrease computational complexity. Various methods are used to select beneficial features, such as filtering, wrapping, and embedding techniques [4]. The significance of features is calculated using formulas like correlation between the variables, information gain calculated for each feature, and chi-square metrics. In developing embedded systems, feature selection is not done in a separate stage. It is an integral part of model building. Other advanced techniques the researchers use are genetic algorithms, particle swarm optimization, and recursive feature elimination. Despite the advantages of feature selection techniques, filter methods are formula-based, resulting in data loss. Wrapper and embedded methods might result in the computational complexity of the resulting model. Apart from this,

https://doi.org/10.31436/iiumej.v26i1.3337

these techniques generate dataset-dependent results that might not work optimally in real-world applications.

This paper introduces a novel idea of using reinforcement learning (RL) to select feature subsets. Reinforcement learning is an agent and environment-based approach. An agent learns to interact with the environment based on the action it takes and the rewards received based on the policy. One of the benefits of using RL is that balance can be achieved between exploration and exploitation strategy by adjusting the value of parameter epsilon. The idea of an agent taking action is considered a random selection of feature subsets. The agent gets a reward based on the accuracy of the classifier for a given feature subset. At the end of the episode, the reward is calculated for each feature subset selected randomly by the agent. In summary, we have developed a dynamic subset selection reinforcement learning agent that selects the subset of features and learns based on the rewards it gets after each episode. The objectives of this research are as follows:

- To evaluate the performance of the traditional feature selection techniques on the phishing dataset and compare their performance with the proposed methodology.
- To develop a novel reinforcement learning agent that dynamically selects the subset of features.
- To analyze the performance of the classification models with correlated features and the change in performance after eliminating the correlated features.

## 2. RELATED WORKS

Feature selection is a significant data preprocessing technique that aids in developing effective and efficient classification models. Various researchers have previously proposed different feature selection and ranking techniques. This section discusses the various methodologies proposed by the researchers in feature selection techniques for phishing detection.

In [7], the researchers introduce a sophisticated hybrid feature selection mechanism methodology using boosting algorithms to detect phishing websites. A multilayer learning algorithm based on Boosting was developed using hybrid feature selection technology to select relevant features. Extreme Gradient Boosting method (XGB), Classification Boosting (CatB), Light Gradient Boosting Machine method (LGBM), and average values are calculated to select the final feature subset. Datasets generated after excluding the irrelevant features are given as input to the classifiers at different levels. There are four models in the first layer: XGBoost, LGBM, CatBoost, and AdaBoost. The next layer includes three models: XGBoost, CatBoost, and AdaBoost. Finally, XGBoost implements the last meta-learner method. Phishing detection is done by taking input from the lower layer. The test results show that the model's accuracy increases from 96.16% to 98.95% without special options. Accuracy with custom selection is between 96.18% and 98.80%.

In [8], the authors highlight the challenges associated with phishing website classification. The major challenges the researchers have focused on are the evolving tendency of phishing attacks and the huge number of features used for classification. Filter and wrapper methods are evaluated based on the performance of a specific classifier. Two approaches are used in this research. The first approach is based on removing redundant features. In the second approach, the author selects features using the filter method. The dataset used in this research is from the University of California. The two approaches were evaluated by performing classification using algorithms like Random Forest, Multilayer Perceptron, and Naïve Bayes.

In [9], the author uses the Uni-variate feature selection (UFS) technique. Using this technique, features were selected and given as input to an ensemble learning classifier. This classifier was developed by combining Cat Boost, Gradient Boost, and Random Forest. It was observed that the accuracy was improved using this methodology. The accuracy without feature selection ranges from 96.16% to 98.95%, and with relevant features ranges from 96.18% to 98.80%. The study highlights the significance of ensemble learning and Uni-variate feature selection in optimizing the performance of phishing detection schemes. The authors suggest that the Uni-variate feature selection methodology is used to improve the response time. The research suggests that the features were selected based on their statistical significance level.

In [10], the researchers have proposed an explainable machine learning model. This model is responsible for the prediction of phishing websites and also explains. After the classification is done, this model explains the results. A novel multidimensional extension of the Gini Coefficient, Lorenz Zonoids, is proposed in this literature for feature selection. Initially, the features were selected based on a statistical formula-based method. The contribution of features in detection was also considered based on explainable model results. Validation of features was done in two stages: Exploratory analysis followed by Gini Index calculation.

The major motive of the research in [11] is to reduce the data dimensionality. The authors have proposed a technique that is a combination of filter methods. In the next stage, wrapper methods are used to build a model to detect websites. The results have shown improvement in the accuracy of the model. This methodology of selecting features from fewer features has improved computational time. The filter methods used in this research are Heatmap Correlation, ANOVA test, and Chi-square test. The top 12 features using all three formulas were considered. Researchers have used this approach in the view that the values obtained are independent of ML classifiers. In the last step, the researchers combined the three subsets obtained and applied them to the heuristic-based wrapper method using Logistic Regression, Random Forest, and Naïve Bayes models.

In [12], the authors have proposed a technique that selects features based on majority voting and consensus. The author proposes using random forest, gradient boosting, and LGBM for feature selection. These three techniques vote for each feature in the dataset, and based on the majority voting, the feature is either selected or rejected. These selected features are given as input to the detection model. The detection model is developed by combining Adaboost and LightGBM. It was observed that there was a drop in the detection time of the URLs.

In [13], the author analyzes the traditional feature selection algorithms and performance evaluation using ML algorithms. The performance of filter, wrapper, and embedded methods is compared. This survey paper has done a detailed analysis of how feature selection and dimensionality reduction algorithms affect the performance of the detection mechanisms. The metrics used for calculating the performance were Precision, Recall, K-fold Cross-validation, AUC-ROC, and execution time.

The research in [14] has focused on improvement of the recall values and reducing the number of false negatives. The authors have proposed a technique that classifies the URLs by combining deep learning and a genetic algorithm for searching the best feature subset. The deep learning algorithm used in this approach is a convolutional recurrent network. It was observed that combining a convolutional recurrent network with a genetic algorithm for feature selection improved the accuracy and recall. The results using a convolutional recurrent network without feature selection were used for performance comparison.

In [15], the authors proposed a technique for selecting relevant features that combined the correlation and recursive feature elimination techniques to identify features based on URL

characteristics. The authors combine recursive feature elimination with correlation, information coefficient correlation, and Spearman correlation coefficient. In this study, two datasets with 48 and 87 features were used. It was observed that it works effectively with small feature subsets. These techniques were evaluated based on the performance of Decision Tree, Random Forest, Support Vector Machine, and AdaBoost algorithms.

In [16], researchers proposed a model that recognizes relevant features using recursive feature elimination. The author has proposed a system consisting of five modules. In the first module, the author focuses on pre-processing the dataset, wherein missing and inconsistent data points are removed. The second module is related to finding the relation between the features using correlation and principal component analysis. The next stage involves automatically selecting several features using the Extra Tree Classifier. Different ensemble algorithms are compared to generate the best set of features.

In [17], authors have considered the use of psychological manipulation to trap users into phishing to design a multi-stage detection model that effectively detects fake websites in the real world. This research work covers the features of "Counterfeiting," "Affiliation," "Stealing," and "Evaluation." The technique focuses more on fast filtering and accurate detection. The legitimate websites are removed during the filtering stage, followed by a supervised detection model. The multistage model consists of several stages, each focusing on different aspects of phishing website detection. Initially, the model extracts features from web pages using the CASE framework, capturing diverse characteristics indicative of phishing behavior. Subsequently, these features are processed through multiple classifiers, each specializing in different aspects of phishing detection. Initially, whitelist-based filtering is done to remove the top-ranked websites. This filtering is based on the traffic of the DNS recursive server. In the second stage, the researchers used only a section of falsifying information on the web page, known as fast counterfeit filtering. In the final stage, classification is done based on the multiscale CASE features. Various algorithms are used in the experiments, including AdaBoost, sequential minimal optimization (SMO), and random forest.

In [18], the researchers used the optimization algorithm to extract important features. The authors claim that using Particle Swarm Optimization (PSO) for relevant feature selection improves the performance of the phishing recognition model. The feature weights are adjusted iteratively in PSO based on their contribution to identifying the phishing webpage as genuine. The research asserts that machine learning models are improved by employing a feature weighting technique based on Particle Swarm Optimization (PSO). The irrelevant features were removed based on their weights, ranging from 7 to 57%. The remaining features were used to perform classification operations. The study evaluated the proposed technique by comparing it with the performances of the Backpropagation neural network, SVM, k-nearest neighbor, random forest, naïve Bayes classifier, and decision tree. In Table 1, we summarize the methodology used, the features selected, and the performance of the methodologies discussed in the above literature.

The survey suggests that different approaches have been utilized to optimize the performance of the phishing detection methods. The approaches focus on combining traditional feature selection techniques or using metaheuristic optimization algorithms. The literature suggests that the feature selection improves the model accuracy. The research also highlights the importance of combining machine learning models with effective feature selection and optimization strategies to develop highly accurate, reliable, and interpretable phishing detection systems. The methods used by the researchers, like boosting-based hybrid selection mechanisms, filter and wrapper methods, and univariate feature selection, identify the important features from the dataset for correct classification. Dynamically evolving attack

https://doi.org/10.31436/iiumej.v26i1.3337

strategies may bypass the detection model trained using features selected based on a fixed strategy and classification algorithm.

Table 1. A Comparative Study of Research Papers: Methodology, Features, and Performance

| Paper Reference | Methodology | Total Features Selected | Performance (Accuracy) | Research Gaps |
|---|---|---|---|---|
| L.R. Kalabarige [7] | Feature importance is calculated using XGB, CatB, and LGBM, and an average of feature importance is computed to select the final feature subset. | 33 | 98.80 | Further investigation into hybrid and evolutionary-based feature selection methods could lead to more optimized feature subsets. |
| Shabudin et al. [8] | Feature Selection by Omitting Redundant Features(FSOR)and Feature Selection by Filtering Method (FSFM) | FSOR: 22<br>FSFM: 9 | FSOR: RF 97.1, MLP 96.5<br><br>FSFM: RF 95.3, MLP 95.0 | Explore optimizing these methods or developing new techniques to enhance performance further. |
| K Adane et al. [9] | Uni-variate feature selection (UFS) technique on each ensemble learning classifier | DS-1: 69 of 87<br>DS-2: 27 of 31<br>DS-3: All 48 | DS-1: 97.24<br>DS-2: 96.83<br>DS-3: 98.51 | Hybrid approaches could further improve model accuracy and reduce computational time. |
| Calzarossa et al. [10] | Lorenz Zonoids, the multi-dimensional extension of Gini coefficient | 6 | AUC: 0.96 | Testing is based on multiple classification models other than Random Forest. |
| Abulfaz Hajizada et al. [11] | Combination of multiple filter and wrapper methods for feature selections | 12 | Logistic Regression<br>Random Forest<br>Naïve Bayes | Investigation of the reasoning behind the choice of feature selection methods. |
| B Alotaibi et al. [12] | Voting-based Feature Selection. | 23 | 98.63% | Investigation of other feature selection techniques or combinations to reduce detection time and improve accuracy. |
| Amit Singh et al. [13] | Filter, wrapper, and embedded feature selection method | 23 | Random forest gives the best accuracy of 98.067% and a precision of 0.982. | Explore additional feature selection and dimensionality reduction methods to enhance phishing detection systems. |
| Moedjahedy, J et al. [15] | Combination correlation and recursive feature elimination | 10 | Dataset 1: 97.06<br>Dataset 2: 95.88 | Exercising the new evidence by providing the latest dataset. |
| Goud et al. [16] | Recursive feature elimination | 29 | 93% | Other Feature selection techniques can be implemented. |
| Liu, D. J. et al [17] | CASE feature framework | "Counterfeiting," "Affiliation," "Stealing," and "Evaluation" features. | Recall /TPR: 0.8923<br>FPR: 0.0005<br>Precision: 0.9886<br>F1-Measure: 0.9380 | Comprehensive utilization of multi-scale features. |

| | | | | |
|---|---|---|---|---|
| WALEED ALI et. al[18] | Particle swarm optimization-based feature weighting | PSO-based feature weighting omitted between 7% and 57% of irrelevant features. | BPNN (95.88%), kNN (94.79%), RF (94.3%), and C4.5(94.033%). | An improved version of PSO can enhance performance and reduce the time required for feature evaluation and weighting. |

Based on the studies, it was observed that feature selection impacts model accuracy. The researchers have used diverse methods like boosting-based hybrid selection mechanisms, filter and wrapper methods, and univariate feature selection to identify relevant features for accurate classification. The literature also showcases the use of ensemble learning approaches for phishing detection. Multi-layer stacked ensemble models, combining classifiers like XG-Boost, Cat-Boost, and Ada-Boost, are utilized to leverage the strengths of classifiers and improve overall performance. These ensemble models demonstrate high accuracy rates, ranging from 96.16% to 98.95% across different datasets.

It was observed that the models are trained on historical data that may not work with evolving phishing strategies. Studies have focused on specific feature selection techniques and machine learning models that might not adapt to constantly changing attack strategies. Since the technique is specific to a particular feature selection strategy and an ML model, it is easy for the attacker to bypass the security mechanism. To address these challenges, it is crucial to develop an effective feature selection method to dynamically select the features from the dataset and perform the classification.

## 3. PROPOSED METHODOLOGY

Previous research has applied different feature selection methods to improve the classification algorithm's effectiveness. These methods range from boosting-based hybrid mechanisms to filter and wrapper methods, aiming to select relevant features efficiently. Studies also explore the use of explainable machine learning models, where features are selected based on their contribution to the classification of fake web pages. Novel feature selection models have been proposed, highlighting the significant improvement in the performance of phishing detection systems.

The proposed system is based on reinforcement learning to select the feature subset. The idea behind reinforcement learning is the dynamic selection of feature subsets and learning based on the outcome and rewards. Reinforcement Learning is used for feature selection with the motive of automating the selection of features and developing a model that can decide the best feature subset dynamically. In addition, reinforcement learning is adaptive, and it continuously learns from the rewards and penalties it receives from the environment. Thus, reinforcement learning can systematically and effectively identify the most relevant features, improving model performance and efficiency.

To achieve this objective, a custom reinforcement learning environment was created. Fig. 1 represents the proposed system for feature selection using reinforcement learning. In the first stage of the proposed system, the data is balanced using hybrid data balancing algorithms, such as the Adaptive Synthetic Sampling Approach for Imbalanced Learning (ADASYN) and one-sided selection (OSS). Data balancing is an essential data preprocessing stage to get an unbiased model. ADASYN generates synthetic data points of the minority class based on the density distribution of the data points. OSS focuses on removing noisy and borderline data

https://doi.org/10.31436/iiumej.v26i1.3337

samples. The balanced dataset is pre-processed to remove the missing values and duplicated data.

In the next phase of the proposed system, the dataset is given as input to the RL environment for training the agent. RL environment consists of the agent, action space, observation space, and classifier training component. Initializing the environment involves loading the dataset. In the next stage, action space is defined using Gym's discrete space where each action corresponds to selecting a feature from the dataset. The number of features available in the dataset determines the size of the action space. Gym's Discrete space represents a discrete set of integers. It is used to define action spaces in reinforcement learning environments. In the context of a phishing detection environment, the discrete space represents the set of possible actions an agent can take, where each action corresponds to selecting a feature from the dataset. For example, if our dataset contains 111 features, the Discrete action space has 111 possible actions, each representing the selection of a different feature. The details of the RL Environment are as follows:

- Agent: The "agent" is a decision-making entity that interacts with the environment to learn an optimal strategy for selecting features that maximize the performance of a phishing detection model. The agent's role is crucial in reinforcement learning, where it learns through interaction with the environment to maximize some notion of cumulative reward. The agent interacts with the environment based on its current policy, which could be exploratory or exploitative. In each interaction, the agent observes the current state of the environment. After observation, it selects an action by choosing a feature. It receives feedback from the environment as a reward based on the model's accuracy when using the selected feature. Later, it transitions to a new state, the next feature subset. The agent is a function program that generates subsets with a selected feature. The agent aims to figure out a policy that maximizes total rewards. ε-greedy policy is used for this purpose. The agent uses Q-learning to develop a policy that chooses the best characteristics to optimize accuracy.
- Q-Learning Algorithm- The agent first determines learning parameters, including the exploration rate (ε), learning rate (α), discount factor (γ), and epsilon decay parameters, then sets up a Q-table to hold probable rewards for each state-action combination. The agent employs an ε-greedy policy to balance random action selection for exploration and best-known action selection for exploitation. This tactic uses the agent's current knowledge to help it discover new, possibly lucrative activities. Every episode starts with the environment being reset to its initial state. From then on, the agent keeps choosing actions based on the current state, gets rewarded, and watches the next state until the episode ends. Following the Q-learning update rule, the agent adjusts its Q-values after every action based on the reward received and the anticipated future rewards.

$$Q(s,a) = Q(s,a) + \alpha[r + \gamma\, maxQ(s',a') - Q(s,a)] \quad (1)$$

where $s$ is the current state, $a$ is the action taken, $r$ is the reward received, $s'$ is the next state, $a'$ is the action that would be taken in the next state, $\alpha$ is the learning rate, controlling how much the new information overrides the old, $\gamma$ is the discount factor, which balances immediate and future rewards. This update helps the agent to gradually improve its estimates of the value of actions in different states, leading to a better policy over time. Over multiple episodes, the agent's policy improves as it accumulates more information about which actions lead to higher rewards. The gradual reduction of epsilon over time ensures that the agent transitions from exploration to exploitation, utilizing its learned policy to maximize rewards. The agent undergoes training for 100 episodes.

The dataset has 111 features; at each step, the agent selects a feature from it and then combines it with 9 random features. The agent performs this action. This subset of size 10 is then used to train the classifier. The Q-learning algorithm is used to help an agent select the most important features for classification by learning from the outcomes of its previous actions. The agent aims to find feature subsets that maximize the classification accuracy. The Q-table of 111x111 is generated where rows represent different states. The agent's current state is the feature that has been selected so far, and columns represent the possible actions. Actions included which feature to select next. The agent can take 111 actions to choose any of the 111 features. The agent starts with a Q-table initialized to zeros, meaning it does not know which useful features. The working of the Q-learning algorithm for an episode is as follows:

*Episode 1*: The agent is in the initial state. It picks an action randomly due to high epsilon. Assume it selects feature f3. Now, the agent trains a Classifier using f3 and 9 other random features (for a subset of 10 features). Assume the randomly selected subset is [f3, f10, f22, f45, f67, f81, f89, f97, f102, f110]. The classifier is trained on this subset and tested. Let's say the accuracy is 75%. The accuracy (0.75) is the reward for selecting $f_3$. The agent updates the Q-value for selecting $f_3$ based on this reward. The Q-table is updated as follows:

$$Q(s,a) = Q(s,a) + \alpha[r + \gamma\, maxQ(s',a') - Q(s,a)] \quad (2)$$

$$Q(s,f_3) = 0 + 0.1 \times (0.75 + 0.99 \times 0 - 0) = 0.075 \quad (3)$$

*Episode 2*: In this, another feature is selected randomly. The current state is after selecting f3. Let us assume feature 45 is selected at random. The selected subset is [f45, f3, f22, f67, f81, f89, f97, f102, f110, f10]. Assume the accuracy is 80%, so the reward is 0.80. The agent moves to the next feature selection step $s'$.The q-table value is updated for feature 45.

$$Q(s,f_{45}) = 0 + 0.1 \times (0.80 + 0.99 \times 0 - 0) = 0.08 \quad (4)$$

As episodes continue, more Q-values are updated. The agent selects features based on experience. The Q-values will be further refined based on both the immediate and future rewards that are discounted by gamma.

- Action Space: Agents interact with the environment by selecting actions from this discrete set, and the environment responds accordingly based on the chosen action. This discrete action space structure allows reinforcement learning algorithms to operate efficiently, especially when actions can be represented as simple integers. There are as many actions in the action space as features in the dataset.
- Observation Space: Another crucial component of the environment is the observation space, defined using Gym's Box space. This space represents a vector of values ranging from 0 to 1, with each value corresponding to a feature. This vector provides the agent with information about the current state of the environment. The shape of the Box space matches the number of features.
- Reward Function: The Reinforcement Learning environment relies significantly on this function, which gives the agent feedback depending on its actions. It guides the agent's training process. This reward function is embedded within the step method. The accuracy of the environment's classification serves as the reward for the agent's action. Higher accuracy indicates better performance, resulting in a higher reward for the agent. The reward function evaluates the agent's selected actions (feature selections) and provides a numerical reward signal indicating the quality of those actions. The purpose of the reward function is to quantify how well the agent's selected features contribute to accurately classifying phishing instances in the dataset. In the proposed system environment, the

https://doi.org/10.31436/iiumej.v26i1.3337

classification accuracy performed using the selected features is the basis for computing the reward. Higher accuracy implies better performance and, therefore, yields a higher reward, while lower accuracy results in a lower reward.

- Classifier Training: This step enables the environment to evaluate the actions taken by the agent and provide feedback on the same. The classification models are trained using a subset of the features from the dataset. The environment uses This classifier internally to classify the dataset based on the agent's selected features. The classifier's accuracy is the reward signal for the agent's actions, guiding its learning process. The trained classifier is a proxy for evaluating the quality of the agent's actions (feature selections) by assessing their impact on classification accuracy.

At the start of each episode, the reset function is initiated so that the environment is reset to its initial state, a random binary vector of feature values. These elements are initialized so that the environment may give the agent relevant feedback and help determine the best feature selection policy for phishing detection. The epsilon-greedy policy determines the action the agent chooses. Selecting a feature index to ascertain the features that have been chosen is an action. The feature subset is then created by the environment as a result of the activity. This feature subset is used to train the classifier, and the accuracy is determined. Accuracy is rewarded, and the chosen features advance to the next stage. Using the reward and the projected future rewards, the Q-value for the state-action pairs is updated in the next stage of the process. The agent transitions to the next state and accumulates the total reward. After the episode ends, all the features are selected at least once.

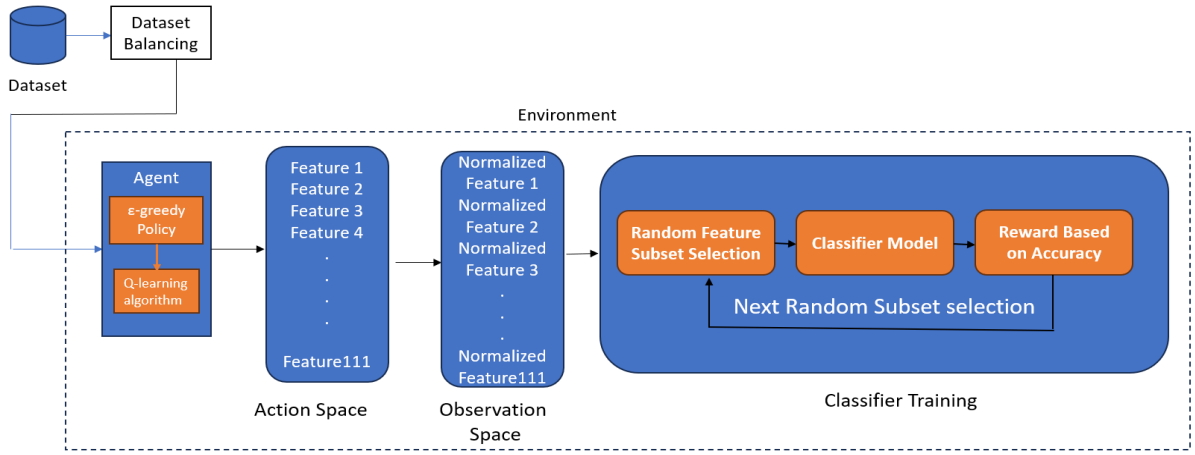


Figure 1. Feature Selection Using Reinforcement Learning

Traditional feature selection methods like the filter method and wrapper approach are also examined in the study. Fig. 2 depicts the methodology applied for analysis of feature selection techniques wherein the dataset is balanced using hybrid dataset balancing techniques followed by preprocessing of the dataset. Feature selection is done using ANOVA, Mutual Information, and Chi-square. Feature importances are also calculated using the SHAP explainable AI algorithm. Fig. 2 depicts the diagrammatic representation of the proposed system for feature selection using traditional feature selection techniques. Before applying the feature importance calculation techniques, redundant and quasi-constant features are removed from the dataset.

https://doi.org/10.31436/iiumej.v26i1.3337

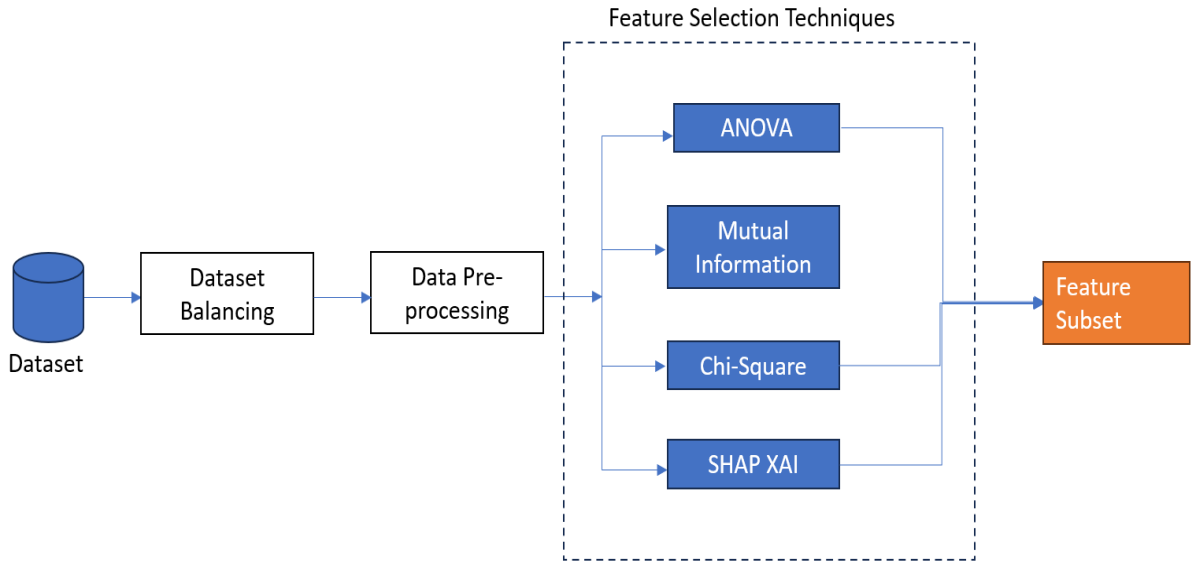


Figure 2. Feature selection using traditional methods

## 4. RESULTS AND DISCUSSION

This section will cover the evaluation of feature selection methods on phishing datasets. We will also discuss the study of comparative results of the proposed system and the traditional methodology using filter and wrapper methods.

### 4.1. Dataset Description

The dataset used for the experiments is accessible to the general public on Mendeley [16]. The features reported in the datasets were taken from publicly available lists of legitimate and phishing websites from which the data was obtained. 88,647 instances in total, of which 58,000 are genuine website instances (labeled as 0) and 30,647 are phishing website instances (labeled as 1). A total of 111 features are present. Fig. 3 gives an overview of the distribution of samples in the dataset.

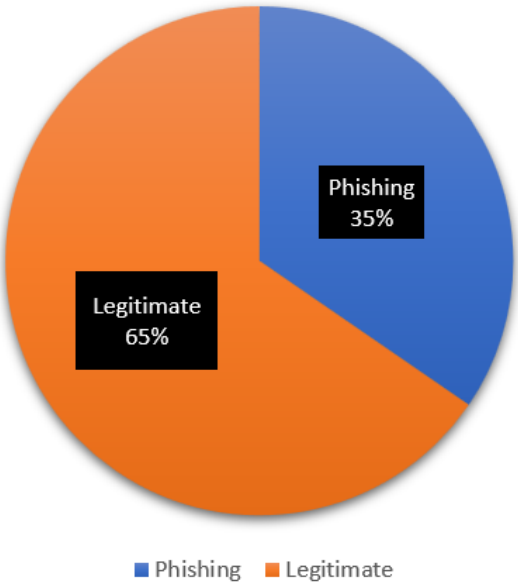


Figure 3. Dataset Distribution

### 4.2. Evaluation Metrics

The evaluation metrics Accuracy, Precision, Recall, and F-measure demonstrate the efficacy of the proposed approach. The metric used to assess the system's overall performance is accuracy. It is a ratio of the number of accurate predictions to the total number of predictions. [20].

$$Accuracy = \frac{TP+TN}{TP+TN+FP+FN} \quad (5)$$

True positives are denoted as TP. True Positives are those predictions that specify phishing URLs correctly identified as phishing. False positives, or FPs, are the number of actual URLs the model identified as fake, while false negatives, or FNs, are the number of fake URLs identified as genuine. TN stands for true negatives, which are equivalent to URLs that are legitimate and predicted as phishing. The measure of precision evaluates the proportion of accurate identifications [18]. The ratio of True Positive samples to all predicted positive samples can be used to describe it. When the costs of False Positives are large, precision is a useful metric to assess [20]. Precision can be calculated using the given formula,

$$Precision = \frac{TP}{TP+FP} \quad (6)$$

Recall is the measure of our system correctly identifying True Positives [20]. Whenever the cost of the fake samples getting unidentified is high, recall is used to select the best model. Thus, recall tells us URLs that are actually phishing and correctly identified as phishing. The formula gives it,

$$Recall = \frac{TP}{TP+FN} \quad (7)$$

It is important to select the performance metric for the classification model. Precision can be used when the cost of False Positives is High, that is, when the true URL is classified as fake. Recall is equally important for predicting phishing URLs since Recall calculates how many of the Actual Positives (Fake URLs) our model captured by labeling them as Fake. In the model, precision and recall are equally important. F1-score is the Harmonic mean of Precision and Recall [18].

$$F1\ score = 2 \times \frac{Precision \times Recall}{Precision+Recall} \quad (8)$$

### 4.3. Baseline Algorithms

We compare the performance of the proposed feature selection using baseline algorithms like K-best selection, Recursive Feature Elimination, Feature selection using the SHAP algorithm, Mutual Information, and Chi-square.

#### *4.3.1. K-best Selection*

K-Best ranks the top 'k' attributes according to a grading system. This scoring method was developed based on statistical tests that measure the degree of correlation between each feature and the target variable. Every aspect is assessed separately using a predefined scoring system. Common scoring functions include ANOVA F-value, mutual information, and chi-squared. These scoring functions evaluate each feature's significance to the target variable—the proposed methodology used K-best Selection with ANOVA as a scoring function.

#### *4.3.2. Recursive Feature Elimination (RFE).*

This algorithm works in a recursive, wherein the least significant features are removed from the data until the target feature count is attained. RFE works in the following steps: Model Training, Feature Importance Ranking, Feature Elimination, and Model Retraining. First, the ML model is trained using all the features. The significance of every feature is calculated once the model has been trained. Depending on the approach utilized, this can be accomplished using alternative metrics or coefficients in linear models or feature importances in tree-based models. Next, the features that aren't as crucial are eliminated from the feature set. Using the smaller feature set, the model is retrained. Recursively, the stages of feature elimination, model retraining, and feature importance ranking are carried out until the required number of features is attained.

#### *4.3.3. Feature selection using the SHAP algorithm*

The SHAP (SHapley Additive exPlanations) algorithm is a feature selection technique that uses game theory to give each feature a score determined by how much it contributes to the prediction of a machine learning model. A unifying indicator of feature relevance, SHAP values consider the strength and direction of each feature's influence on predictions. SHAP values are first calculated for every feature in the dataset. The influence of each feature on the model's predictions for specific data points is represented by SHAP values. By assigning each feature the difference between the actual and expected predictions, they offer a local explanation for the predictions made by the model. The total relevance of every feature can be determined by averaging the computed SHAP values. Several summary statistics can be used for this aggregation, including mean absolute SHAP values, mean SHAP values, and variation of SHAP values throughout the dataset. Next, features are arranged according to their importance scores obtained from SHAP values. Retaining the top-ranked features for additional analysis or model training depends on the number of features to choose from. The most significant features are chosen, and only those are used to train a machine learning model.

#### *4.3.4. Mutual Information-based Feature Selection*

A technique for choosing features is called mutual information-based feature selection, and it involves calculating the mutual information or dependency between each feature and the target variable. Mutual information is a measure of the amount of information obtained about one variable through the other variable.

#### *4.3.5. Chi-square-based Feature selection*

Using a measure of each feature's dependence on a categorical target variable, this feature selection method helps to find the most relevant features for classification problems. The chi-square statistic is computed for every feature, which shows how strongly the feature is associated with the target. This information is used to rank the features, with the highest-ranked features being chosen for model training.

### 4.4. Performance

We compare our feature selection method using reinforcement learning regarding accuracy, precision, recall, and F1-measure on the phishing dataset. In an initial stage where feature selection was made using baseline algorithms, the constant features were removed from the dataset. It was observed that among 111 features, 14 features were constant. Table No. 2 gives the list of constant features identified. Constant features have the same value for all observations, whereas duplicate features contain redundant information with other features.

https://doi.org/10.31436/iiumej.v26i1.3337

Removing these redundant features is crucial for improving the efficiency and effectiveness of the machine learning model. In the next step, duplicate features were removed from the dataset.

Table 2. Constant Features

| Sr. No | Feature Name |
|---|---|
| 1 | qty_slash_domain |
| 2 | qty_questionmark_domain |
| 3 | qty_equal_domain |
| 4 | qty_at_domain |
| 5 | qty_and_domain |
| 6 | qty_exclamation_domain |
| 7 | qty_space_domain |
| 8 | qty_tilde_domain |
| 9 | qty_comma_domain |
| 10 | qty_plus_domain |
| 11 | qty_asterisk_domain |
| 12 | qty_hashtag_domain |
| 13 | qty_dollar_domain |
| 14 | qty_percent_domain |

Table 3. Quasi-constant Features

| Sr.No | Feature Name | URL Variance |
|---|---|---|
| 1 | qty_exclamation_ | 0.00762844964915398 |
| 2 | qty_space_ | 0.005278395261483356 |
| 3 | qty_tilde_ | 0.00610379807390346 |
| 4 | qty_comma_ | 0.005771091175729697 |
| 5 | qty_hashtag_ | 0.003801380283231768 |
| 6 | qty_dollar_ | 0.009946095859835575 |
| 7 | qty_underline_domain | 0.010148545461142985 |
| 8 | qty_slash_domain | 0.0 |
| 9 | qty_questionmark_domain | 0.0 |
| 10 | qty_equal_domain | 0.0 |
| 11 | qty_at_domain | 1.1280697598339478e-05 |
| 12 | qty_and_domain | 0.0 |
| 13 | qty_exclamation_domain | 0.0 |
| 14 | qty_space_domain | 0.0 |
| 15 | qty_tilde_domain | 0.0 |
| 16 | qty_comma_domain | 0.0 |
| 17 | qty_plus_domain | 0.0 |
| 18 | qty_asterisk_domain | 0.0 |
| 19 | qty_hashtag_domain | 0.0 |
| 20 | qty_dollar_domain | 0.0 |
| 21 | qty_percent_domain | 0.0 |
| 22 | domain_in_ip | 0.0022623045431979945 |
| 23 | server_client_domain | 0.004480789902101015 |
| 24 | url_google_index | 0.003438663212102363 |
| 25 | domain_google_index | 0.004000615427297923 |
| 26 | url_shortened | 0.00545242362148391 |

A total of 26 features were identified as Quasi-constant features. The features with very low variance are known as Quasi-constant features. These features may provide little to no discriminatory information for predictive modeling and can potentially lead to overfitting. Identifying and handling quasi-constant features is an important step in data preprocessing to

https://doi.org/10.31436/iiumej.v26i1.3337

improve the performance and interpretability of the machine learning model. Table 3 shows the list of quasi-constant features from the phishing dataset. Table No. 4 gives a list of duplicate features in the dataset.

Table 4. List of duplicate features

| Sr. No | Feature Name |
|---|---|
| 1 | qty_hashtag_directory |
| 2 | qty_slash_file |
| 3 | qty_questionmark_file |
| 4 | qty_hashtag_file |
| 5 | qty_dollar_file |
| 6 | qty_slash_file |
| 7 | qty_questionmark_file |
| 8 | qty_hashtag_file |
| 9 | qty_dollar_file |
| 10 | qty_questionmark_file |
| 11 | qty_hashtag_file |
| 12 | qty_dollar_file |
| 13 | qty_hashtag_file |
| 14 | qty_dollar_file |
| 15 | qty_dollar_file |

In the next stage, we have focused on correlated features. Correlated features are pairs of features in a dataset that exhibit some degree of linear relationship with each other. This relationship can be positive (both features increase or decrease together) or negative (one feature increases while the other decreases). Identifying correlated features is important in data preprocessing as highly correlated features can introduce redundancy and potentially lead to overfitting in predictive modeling. Removing correlated features in the context of phishing detection can positively and negatively affect performance, depending on factors such as the dataset, the algorithm used, and the specific features being removed. Eliminating correlated features may lead to loss of information, and removing them may overly simplify the model, leading to underfitting. The total correlated features identified were 42. The system performance was tested with correlated features and by removing correlated features.

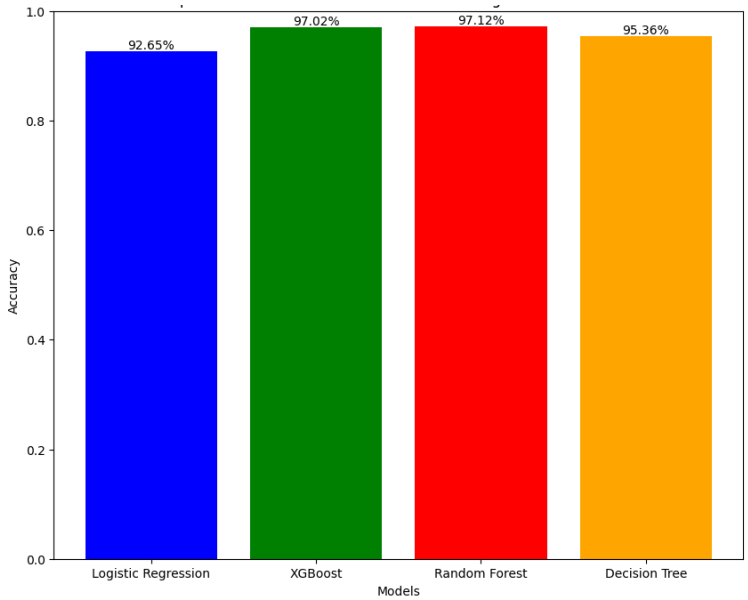


Figure 4. Comparison of Accuracy after removing Correlated Features.

https://doi.org/10.31436/iiumej.v26i1.3337

Fig. 5 shows the accuracy of the models with the correlated features, and Fig. 4 shows the accuracy of the models after removing the correlated features. For XG-Boost, Random Forest, and Decision Tree, accuracy was lower than that of correlated features. Accuracy was better in Logistic Regression for the dataset with correlated features.

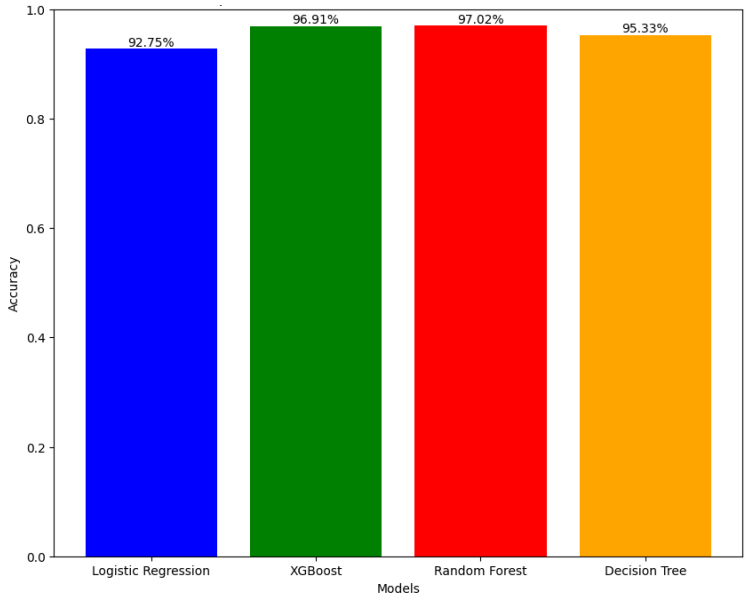


Figure 5. Comparison of Accuracy with Correlated Features.

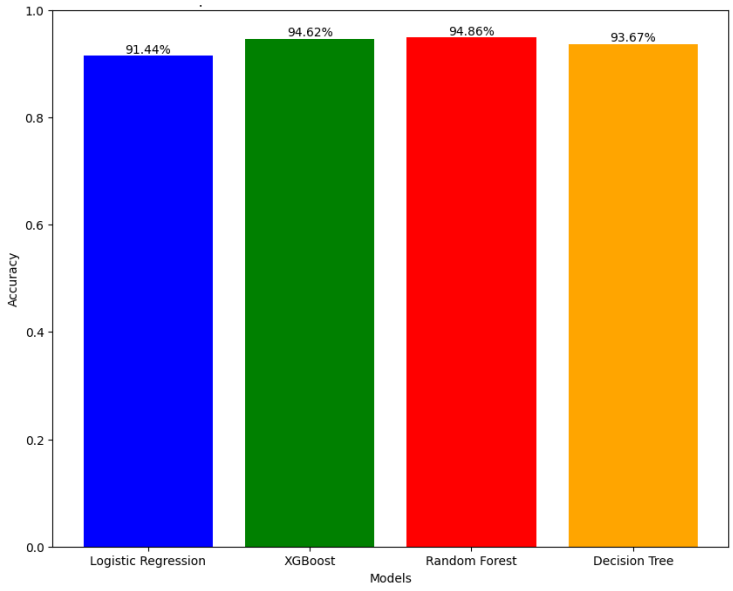


Figure 6. Comparison of Accuracy with ANOVA Feature Selection

While testing the K-best algorithm for feature selection, a total of 10 features were selected. The system utilizes the ANOVA F-value method via SelectKBest to select the top 10 features from the training dataset (X_train) based on their importance for classification. It then transforms the training and test datasets to contain only the selected features, maintaining consistency across the datasets. The selected feature names are captured and used to label the columns of the transformed datasets. ANOVA (Analysis of Variance) is a statistical technique that determines whether there are statistically significant differences between the means of three or more groups. In the context of feature selection, f_classif calculates the F-value for

https://doi.org/10.31436/iiumej.v26i1.3337

each feature by considering the variance between the classes (or groups) and the variance within the classes. 'qty_slash_url', 'qty_equal_url', 'length_url', 'qty_dot_domain', 'qty_dot_directory', 'qty_hyphen_directory', 'qty_underline_directory', 'directory_length', 'qty_questionmark_params', 'time_domain_activation' these features were selected using K-best Algorithm.

Feature selection using mutual information was done on the dataset by calculating the mutual information score for each feature. Fig. 7 depicts the score for mutual information of the features in the dataset. Based on this score top 10 features were selected using mutual information. These features were 'qty_slash_url', 'length_url', 'qty_dot_directory', 'qty_hyphen_directory', 'qty_underline_directory', 'directory_length', 'qty_hyphen_file', 'file_length', 'asn_ip', 'time_domain_activation'.

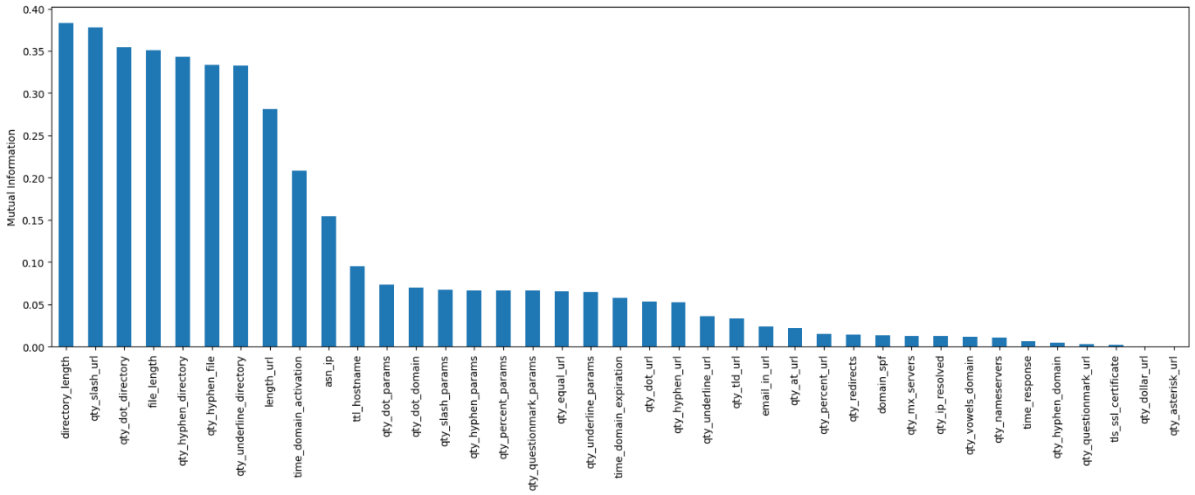


Figure 7. Mutual Information Scores

The dataset with features selected using mutual information was tested on different classification models. Fig. 8 gives an overview of the accuracy achieved after performing feature selection.

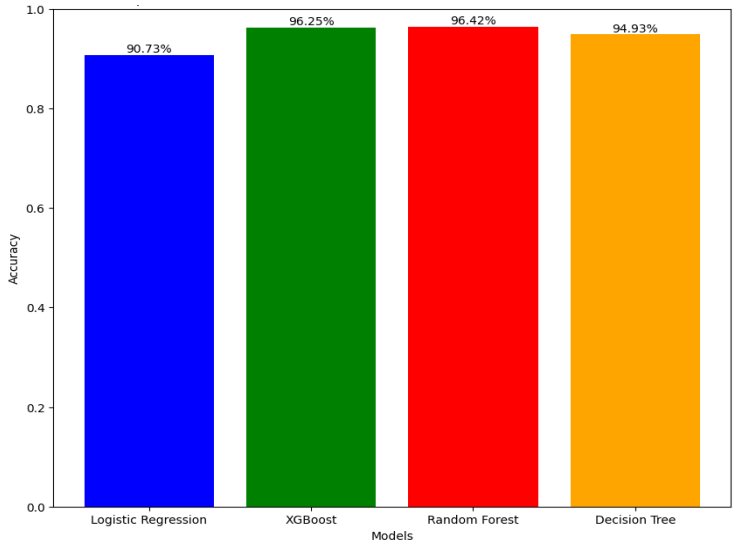


Figure 8. Comparison of Model Accuracies with Mutual Information-based select Features.

https://doi.org/10.31436/iiumej.v26i1.3337

The next baseline algorithm that was applied is Recursive Feature Elimination. In this approach, Recursive Feature Elimination (RFE) with a Random Forest classifier and Logistic Regression is done to select the top 10 features from the dataset. This approach offers a systematic way to identify the most relevant features for modelling tasks, aiding in dimensionality reduction and improving model interpretability. Table 5 shows the list of features selected by the RFE algorithm using Logistic Regression and Random Forest. Fig. 9 shows the comparison of accuracies obtained for RFE with logistic regression and RFE with Random Forest.

Table 5. Features Selected using RFE

| Sr.No | Logistic Regression | Random Forest |
|---|---|---|
| 1 | 'qty_hyphen_url' | 'qty_slash_url' |
| 2 | 'qty_slash_url' | 'length_url' |
| 3 | 'qty_at_url' | 'qty_hyphen_directory' |
| 4 | 'qty_asterisk_url' | 'qty_underline_directory' |
| 5 | 'qty_hyphen_domain' | 'directory_length' |
| 6 | 'qty_dot_directory' | 'qty_hyphen_file' |
| 7 | 'qty_hyphen_directory' | 'file_length' |
| 8 | 'qty_hyphen_params' | 'asn_ip' |
| 9 | 'qty_questionmark_params' | 'time_domain_activation' |
| 10 | 'email_in_url' | 'ttl_hostname' |

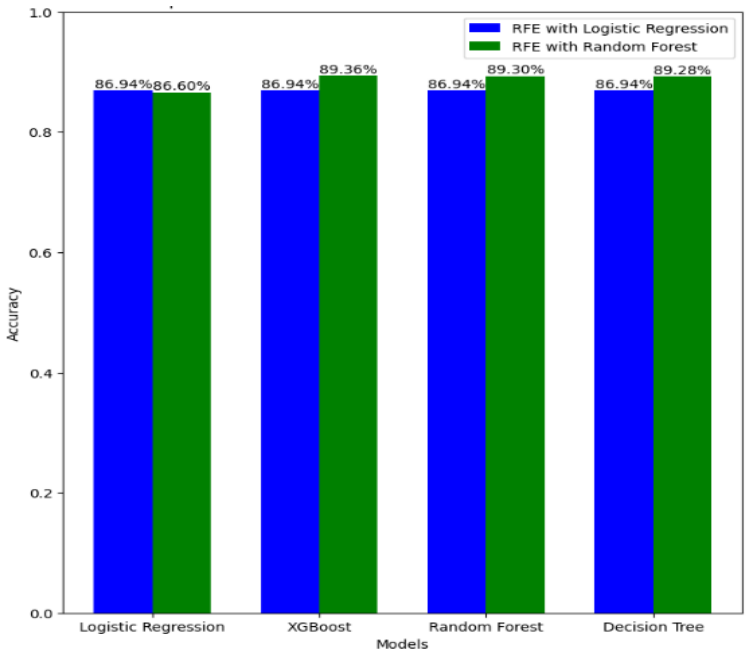


Figure 9. Comparison of Model Accuracies with RFE-Selected Features

The study uses the SHAP (SHapley Additive exPlanations) algorithm to explain the XG-Boost Classifier's output. It computes SHAP values for every feature after training the XG-Boost Classifier model on the training set. Machine learning models can be interpreted using SHAP (SHapley Additive exPlanations) values, which relate the model's output to its input features. They offer a single, Shapley-value-based way to quantify the significance of features. The SHAP values indicate the impact of each feature on the models' predictions. Understanding the importance of each feature to a particular prediction is aided by the explanation provided by SHAP values for individual predictions. The visualization for the XG-Boost Classifier is

https://doi.org/10.31436/iiumej.v26i1.3337

shown in Fig.10. The summarization of accuracies using the SHAP algorithm is depicted in Fig. 11.

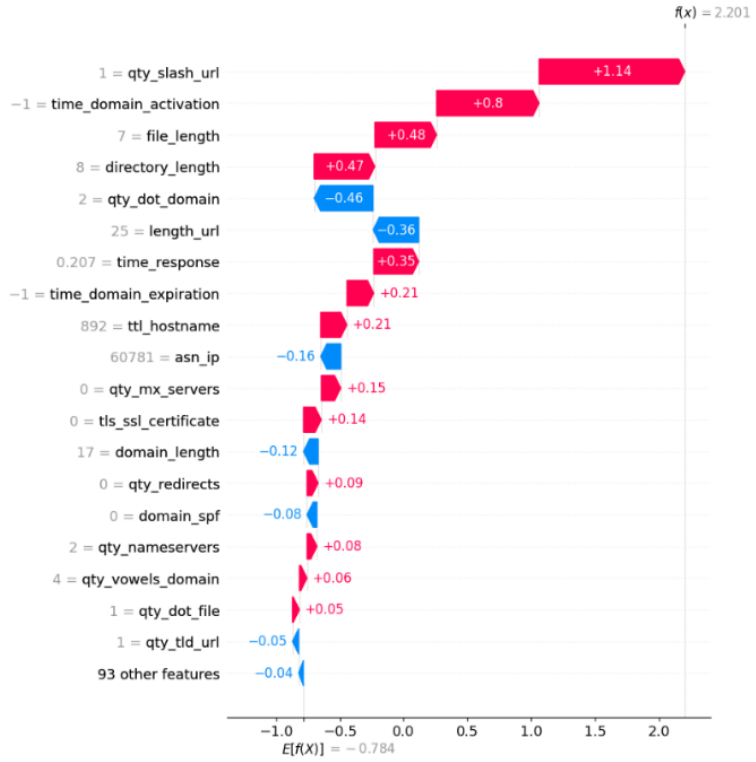


Figure 10. SHAP Values.

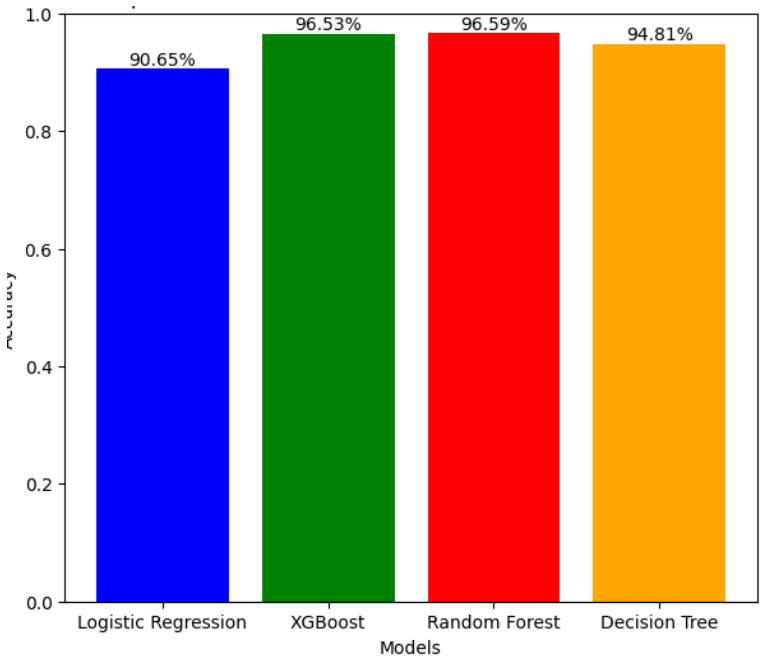


Figure 11. Comparison of Model Accuracies with SHAP-Selected Features

Fig. 13 shows the features selected based on the chi2 scoring function. It also shows the accuracy of the models using the selected features based on chi-square. Chi-square selects the features that are most relevant to the target phishing variable. The features selected using chi-square are shown in Fig. 12.

https://doi.org/10.31436/iiumej.v26i1.3337

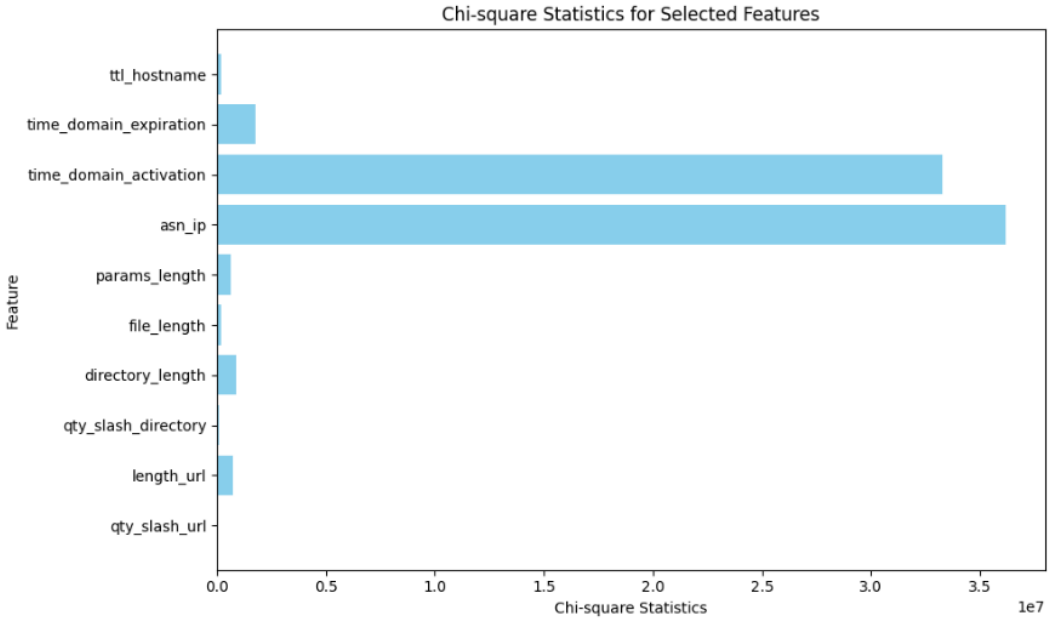


Figure 12. Chi-square values for top 10 features.

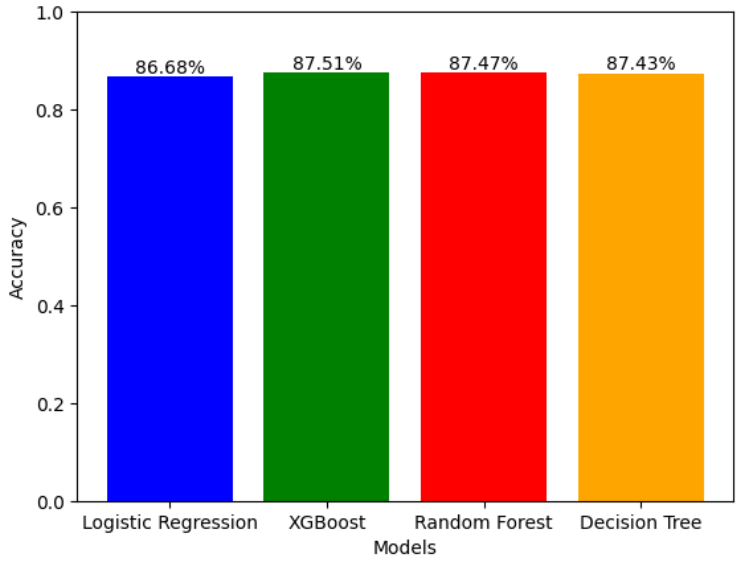


Figure 13. Accuracy of Models using feature selection with chi-square.

XG Boost algorithm gave an accuracy of 96.42 after 100 episodes of training. The selected features were 'time_domain_activation', 'qty_dot_domain', 'directory_length', 'params_length', 'qty_space_directory', 'tls_ssl_certificate', 'asn_ip', 'qty_asterisk_params', 'qty_dot_file', 'qty_tilde_directory'. The selected feature subset using Random Forest Algorithm was 'qty_redirects', 'asn_ip', 'qty_asterisk_params', 'qty_slash_url', 'file_length', 'qty_and_url', 'qty_equal_directory', 'qty_slash_directory', 'time_domain_activation', 'time_response' with best accuracy of 99.07 %. The selected feature subset using decision tree is 'qty_dot_params', 'time_response', 'qty_comma_file', 'qty_ip_resolved', 'domain_length', 'qty_comma_url', 'directory_length', 'qty_percent_params', 'time_domain_activation', 'qty_equal_params'. The accuracy achieved is 98.69%. Fig. 14 shows the comparison of accuracy for the algorithms.

https://doi.org/10.31436/iiumej.v26i1.3337

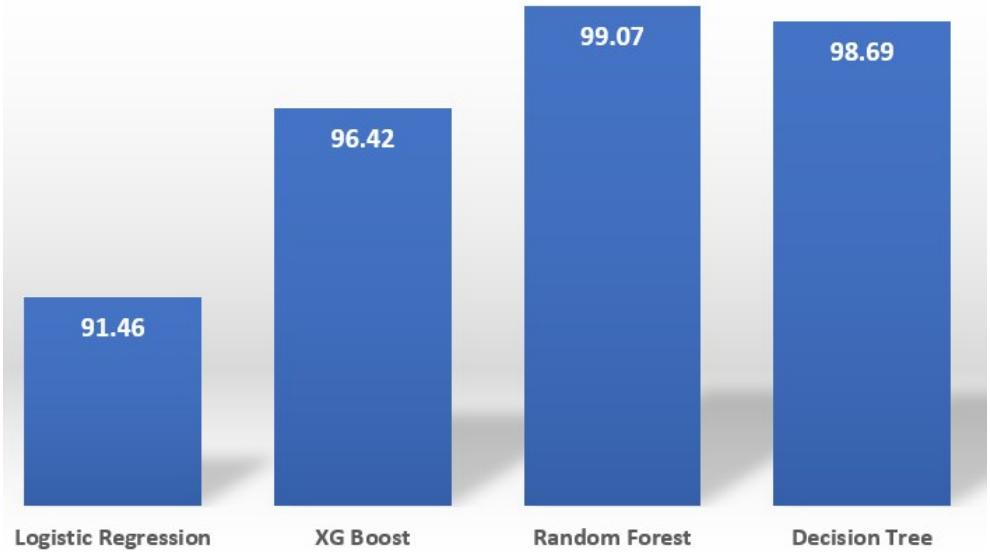


Figure 14. Cumulative Results

The proposed methodology was also evaluated based on other performance metrics like precision, recall, and f1-score. Table 6 shows the cumulative results obtained while testing the system. It compares the accuracy obtained for different feature selection techniques and the classification algorithms considered in this study. The proposed methodology significantly improves the accuracy of the Random Forest and Decision Tree, reaching near-perfect levels. This indicates that the methodology effectively enhances these models' ability to classify phishing websites, making them exceptionally reliable correctly. The proposed methodology consistently outperforms other feature selection techniques in terms of accuracy, particularly for ensemble methods like Random Forest and Decision Tree, which achieve near-perfect accuracy.

Table 6. Cumulative Results for Accuracy

| Accuracy | Logistic Regression | XG-Boost | Random Forest | Decision Tree |
|---|---|---|---|---|
| **With Correlated Features** | 92.65% | 97.02% | 97.12% | 95.36% |
| **After the removal of Correlated Features** | 92.75% | 96.91% | 97.02% | 95.33% |
| **K-best (ANOVA)** | 91.44% | 94.62% | 94.86% | 93.67% |
| **Mutual Information** | 90.73% | 96.25% | 96.42% | 94.93% |
| **Chi-square** | 86.68% | 87.51% | 87.47% | 87.43% |
| **RFE** | 90.96% | 91.94% | 91.87% | 91.86% |
| **SHAP** | 90.62% | 96.53% | 96.59% | 94.81% |
| **Proposed Methodology** | 91.39% | 92.45% | 99.07% | 95.49% |

Table 7 shows the proposed system's comparative results based on the precision performance metrics. The proposed methodology has outperformed all the other approaches to feature selection for Random Forest and Decision Tree Classifiers. The high Precision suggests that the feature selection process in the proposed methodology is very effective at isolating the most relevant features for these ensemble methods, allowing them to make highly accurate positive predictions. For Logistic Regression, the precision value decreased. This reduction in Precision suggests that the proposed feature selection may include some features that introduce

https://doi.org/10.31436/iiumej.v26i1.3337

noise or are less compatible with the linear nature of Logistic Regression, leading to more false positives. With 94% accuracy in positive predictions, XG-Boost performs reliably, though slightly less so than Random Forest and Decision Tree. The proposed methodology excels in Precision for ensemble models but may introduce challenges for linear models like Logistic Regression, which could lead to a higher rate of false positives.

Table 7. Cumulative Results for Precision

| Precision | Logistic Regression | XG-Boost | Random Forest | Decision Tree |
|---|---|---|---|---|
| **With correlated features.** | 0.93 | 0.97 | 0.97 | 0.95 |
| **After the removal of Correlated Features** | 0.93 | 0.97 | 0.97 | 0.95 |
| **K-best (ANOVA)** | 0.91 | 0.95 | 0.95 | 0.94 |
| **Mutual Information** | 0.91 | 0.96 | 0.96 | 0.95 |
| **Chi-square** | 0.90 | 0.89 | 0.89 | 0.89 |
| **RFE** | 0.87 | 0.87 | 0.87 | 0.87 |
| **SHAP** | 0.91 | 0.97 | 0.97 | 0.95 |
| **Proposed Methodology** | 0.85 | 0.94 | 0.98 | 0.98 |

The Recall performance metric is critical in evaluating how well your models identify all phishing websites. Random Forest and Decision Tree both achieve the highest Recall with the proposed methodology. A Recall of 0.98 means these models successfully identify 98% of all phishing websites. This is particularly valuable in security applications, where failing to detect a phishing threat (false negatives) can have serious consequences. The high Recall indicates that the proposed methodology is highly effective at selecting features that help these ensemble models capture nearly all relevant phishing cases, making them robust and reliable. With a Recall of 0.95, XG-Boost detects 95% of all phishing sites. While slightly lower than Random Forest and Decision Tree, it still performs strongly. While still performing reasonably well, Logistic Regression might miss more phishing sites compared to the ensemble methods, which could be a concern in highly sensitive applications.

Table 8. Cumulative Results for Recall

| Recall | Logistic Regression | XG-Boost | Random Forest | Decision Tree |
|---|---|---|---|---|
| **With correlated features.** | 0.93 | 0.97 | 0.97 | 0.95 |
| **After the removal of Correlated Features** | 0.93 | 0.97 | 0.97 | 0.95 |
| **K-best (ANOVA)** | 0.91 | 0.95 | 0.95 | 0.94 |
| **Mutual Information** | 0.91 | 0.96 | 0.96 | 0.95 |
| **Chi-square** | 0.87 | 0.88 | 0.87 | 0.87 |
| **RFE** | 0.87 | 0.89 | 0.89 | 0.89 |
| **SHAP** | 0.91 | 0.97 | 0.97 | 0.95 |
| **Proposed Methodology** | 0.91 | 0.95 | 0.98 | 0.97 |

Random Forest and Decision Tree both achieve the highest F1-Score (0.98) with the proposed methodology. The F1-Score of 0.98 indicates that these models are accurate in predicting phishing websites (high Precision) and very effective at identifying nearly all actual phishing sites (high Recall). An F1-Score of 0.95 demonstrates that XG-Boost maintains a strong balance between Precision and Recall, though slightly less than the ensemble models. The F1-Score of 0.88 indicates a more noticeable trade-off between Precision and Recall for

Logistic Regression under the proposed methodology. While it balances these metrics reasonably well, it does not perform as strongly as the ensemble methods.

Table 9. Cumulative Results for F1-Score

| F1-Score | Logistic Regression | XG-Boost | Random Forest | Decision Tree |
|---|---|---|---|---|
| **With correlated features.** | 0.93 | 0.97 | 0.97 | 0.95 |
| **After the removal of Correlated Features** | 0.93 | 0.97 | 0.97 | 0.95 |
| **K-best (ANOVA)** | 0.91 | 0.95 | 0.95 | 0.94 |
| **Mutual Information** | 0.91 | 0.96 | 0.96 | 0.95 |
| **Chi-square** | 0.87 | 0.88 | 0.88 | 0.88 |
| **RFE** | 0.86 | 0.89 | 0.89 | 0.89 |
| **SHAP** | 0.91 | 0.97 | 0.97 | 0.95 |
| **Proposed Methodology** | 0.88 | 0.95 | 0.98 | 0.98 |

Based on the results obtained in the study, the proposed methodology works better than most traditional techniques. The results show that the proposed feature selection methodology using reinforcement learning outperforms all the traditional feature selection algorithms for decision tree and Random Forest classifier with an accuracy of 98.69% and 99.007%. For logistic regression, it was observed that it worked better than mutual information, K-best, Chi-square, RFE, and SHAP-based feature selection. The proposed feature selection algorithm showed better results than ANOVA, Chi-square, and RFE for the Random Forest Algorithm. The results show that the proposed methodology gave the best accuracy compared to all the other techniques with the Random Forest Classifier. It was also observed that removing correlated features might not always improve the system's performance.

## 5. CONCLUSION

This paper proposes a novel system that selects the features using a reinforcement learning algorithm. The methodology focuses primarily on the phishing dataset. Using the proposed method, we can achieve dynamic feature selection at each episode and improve accuracy based on the rewards the agent receives. We have studied the traditional feature selection algorithms and then analyzed their performance. The research analyzed the effect of correlated features in the dataset. It was observed that there was an improvement in the accuracies of XG-Boost, Random Forest, and Decision Tree models after the removal of the correlated features. The proposed methodology is tested using logistic regression, XG-Boost, random forest, and decision tree classification algorithms. We have tested the results using the accuracy gained for each classification algorithm. We have considered the feature subset size to be 10 and the number of episodes to be 100. Based on the above parameters, we have 91.46,96.42,99.07, and 98.69 accuracies for Logistic Regression, XGBoost, Random Forest, and Decision Tree, respectively. Considering the evaluation parameters' accuracy, precision, recall, and F1 score, the results show that the random forest classifier algorithm gives the best results. In the future, the system can be extended to different feature subsets by increasing the number of episodes. Also, multiple phishing datasets can be studied to get an appropriate feature subset and an optimal feature subset size.

## REFERENCES

[1] Infosecurity Magazine, "341% Rise in Advanced Phishing Attacks," [Online]. Available: https://www.infosecurity-magazine.com/news/341-rise-advanced-phishing-attacks/.
[2] [Internet Crime Complaint Center (IC3), "2023 Internet Crime Report," [Online]. Available: https://www.ic3.gov/media/pdf/annualreport/2023_ic3report.pdf.
[3] Fredj, Ouissem Ben, et al. "An OWASP top ten driven survey on web application protection

methods." Risks and Security of Internet and Systems: 15th International Conference, CRiSIS 2020, Paris, France, November 4–6, 2020, Revised Selected Papers 15. Springer International Publishing, 2021.

[4] Alsenani, Theyab R., et al. "Intelligent feature selection model based on particle swarm optimization to detect phishing websites." *Multimedia Tools and Applications* 82.29 (2023): 44943-44975.

[5] Shabudin, Shafaizal, et al. "Feature selection for phishing website classification." International Journal of Advanced Computer Science and Applications 11.4 (2020).

[6] Hamim, Mohammed, et al. "A novel dimensionality reduction approach to improve microarray data classification." *IIUM Engineering Journal* 22.1 (2021): 1-22.

[7] Kalabarige, L. R., Rao, R. S., Pais, A. R., & Gabralla, L. A. (2023). A Boosting-based Hybrid Feature Selection and Multi-layer Stacked Ensemble Learning Model to detect phishing websites. IEEE Access.

[8] Shabudin, S., Sani, N. S., Ariffin, K. A. Z., & Aliff, M. (2020). Feature selection for phishing website classification. International Journal of Advanced Computer Science and Applications, 11(4).

[9] Adane, K., Beyene, B., & Abebe, M. (2023). Single and hybrid-ensemble learning-based phishing website detection: examining impacts of varied nature datasets and informative feature selection technique. Digital Threats: Research and Practice, 4(3), 1-27.

[10] Calzarossa, M. C., Giudici, P., & Zieni, R. (2024). Explainable machine learning for phishing feature detection. Quality and Reliability Engineering International, 40(1), 362-373.

[11] Abulfaz Hajizada and Sharmin Jahan. 2023. Feature Selections for Phishing URL Detection Using Combination of Multiple Feature Selection Methods. In 2023 15th International Conference on Machine Learning and Computing (ICMLC 2023), February 17–20, 2023, Zhuhai, China. ACM, New York, NY, USA, 7 pages. https://doi.org/10.1145/3587716.3587790

[12] Alotaibi, Bandar, and Munif Alotaibi. "Consensus and majority vote feature selection methods and a detection technique for web phishing." Journal of Ambient Intelligence and Humanized Computing 12 (2021): 717-727.

[13] Singh, Amit, and Abhishek Tiwari. "A study of feature selection and dimensionality reduction methods for classification-based phishing detection system." International Journal of Information Retrieval Research (IJIRR) 11.1 (2021): 1-35.

[14] Bu, S. J., & Kim, H. J. (2022). Optimized URL feature selection based on genetic-algorithm-embedded deep learning for phishing website detection. Electronics, 11(7), 1090.

[15] Moedjahedy, J., Setyanto, A., Alarfaj, F. K., & Alreshoodi, M. (2022). CCrFS: combine correlation features selection for detecting phishing websites using machine learning. Future Internet, 14(8), 229.

[16] Goud, N. Swapna, and Anjali Mathur. "Feature Engineering Framework to detect Phishing Websites using URL Analysis." International Journal of Advanced Computer Science and Applications 12.7 (2021).

[17] Liu, D. J., Geng, G. G., Jin, X. B., & Wang, W. (2021). An efficient multistage phishing website detection model based on the CASE feature framework: Aiming at the real web environment. Computers & Security, 110, 102421.

[18] Ali, Waleed, and Sharaf Malebary. "Particle swarm optimization-based feature weighting for improving intelligent phishing website detection." IEEE Access 8 (2020): 116766-116780.

[19] Vrbančič, Grega, Iztok Fister Jr, and Vili Podgorelec. "Datasets for phishing websites detection." Data in Brief 33 (2020): 106438.

[20] Foundational Courses. Google for Developers Online. Available: https://developers.google.com/machine-learning/crash-course/classification

https://doi.org/10.31436/iiumej.v26i1.3386

# GLOBAL-LOCAL SELF-ATTENTION BASED LONG SHORT-TERM MEMORY WITH OPTIMIZATION ALGORITHM FOR SPEAKER IDENTIFICATION

**PRAVIN MAROTRAO GHATE[1*], BHAGVAT D. JADHAV[1], SHRIRAM SADASHIV KULKARNI[2], PRAVIN BALASO CHOPADE[3], PRABHAKAR N. KOTA[3]**

[1]*Department of Electronics & Telecommunication, JSPM's Rajarshi Shahu College of Engineering, Tathawade, Pune, India*

[2]*Department of Information Technology, Sinhgad Academy of Engineering, Pune, India*

[3]*Department of Electronics & Telecommunication, M.E.S College of Engineering, Pune, India*

**Corresponding author: pmghate@gmail.com*

*(Received: 30 July 2024; Accepted: 8 October 2024; Published online: 10 January 2025)*

***ABSTRACT:*** Speaker identification (SI) involves recognizing a speaker from a group of unknown speakers, while speaker verification (SV) determines if a given voice sample belongs to a particular person. The main drawbacks of SI are session variability, noise in the background, and insufficient information. To mitigate the limitations mentioned above, this research proposes Global Local Self-Attention (GLSA) based Long Short-Term Memory (LSTM) with Exponential Neighborhood – Grey Wolf Optimization (EN-GWO) method for effective speaker identification using TIMIT and VoxCeleb 1 datasets. The GLSA is incorporated in LSTM, which focuses on the required data, and the hyperparameters are tuned using the EN-GWO, which enhances speaker identification performance. The GLSA-LSTM with EN-GWO method acquires an accuracy of 99.36% on the TIMIT dataset, and an accuracy of 93.45% on the VoxCeleb 1 datasets, while compared to SincNet and Generative Adversarial Network (SincGAN) and Hybrid Neural Network – Support Vector Machine (NN-SVM).

***ABSTRAK:*** Pengenalpastian pembicara (Speaker Identification, SI) melibatkan pengenalan pembicara daripada kumpulan pembicara yang tidak dikenali, manakala pengesahan pembicara (Speaker Verification, SV) menentukan sama ada sampel suara tertentu milik seseorang individu. Kekurangan utama dalam SI ialah variasi sesi, bunyi latar belakang, dan maklumat yang tidak mencukupi. Untuk mengatasi kekangan tersebut, kajian ini mencadangkan kaedah Global Local Self-Attention (GLSA) berasaskan Long Short-Term Memory (LSTM) dengan Pengoptimuman Grey Wolf Jiranan Eksponen (EN-GWO) bagi pengenalpastian pembicara yang berkesan menggunakan set data TIMIT dan VoxCeleb 1. GLSA digabungkan dalam LSTM yang memberi tumpuan pada data yang diperlukan, manakala parameter hiper ditala menggunakan EN-GWO untuk meningkatkan prestasi pengenalpastian pembicara. Kaedah GLSA-LSTM dengan EN-GWO mencapai ketepatan 99.36% pada dataset TIMIT dan ketepatan 93.45% pada dataset VoxCeleb 1, berbanding dengan SincNet dan Generative Adversarial Network (SincGAN) serta Hybrid Neural Network – Support Vector Machine (NN-SVM).

***KEYWORDS:*** *Exponential Neighborhood – Grey Wolf Optimization, Global-Local Self-Attention, Long Short-Term Memory, Mel-frequency Cepstral Coefficients, Speaker Identification.*

https://doi.org/10.31436/iiumej.v26i1.3386

# 1. INTRODUCTION

Recently, a wide variety of speech-related applications have been introduced, and many of the applications are highly convenient for communication with human-human and human-machine [1]. Every human has a unique voiceprint that reflects the specific acoustics of its voice-producing organs and their patterns of speaking [2-4]. The speech recognition technique is classified into two types: speaker identification (SI), which identifies the speaker from a set of known speakers, and speaker verification (SV), which determines whether a given speaker matches a particular identity of a person [5, 6]. Both verification and identification need a fixed phrase or sentence of agnostic to be attained through the speaker [7]. When the speakers and the text are predetermined, it is called a text-dependent system. Conversely, when speakers can speak freely without fixed constraints, it is a text-independent system [8]. Utilizing the voice-recognition technique effectively enhances the effectiveness of the minutes-development task. The ability to automatically identify speakers in transcripts greatly enhance the overall effectiveness of the minute process [9].

The performance degradation of SI in extra speech is caused by variance among emotion classes in enrolling data that represents training and test information for every speaker in the SI method [10, 11]. The SI method enhances its performance by utilizing speech data that belongs to the same emotional phase in both training and testing [12]. However, gathering balanced speech data that covers different emotional states for every speaker is difficult due to huge costs and consumption of time [13-15]. The main drawbacks of SI are session variability, noise in the background, and lack of enough information [16]. Significant differences often occur between training and testing sessions when training is performed in a clean environment, whereas testing is performed in a noisy environment. The noise in the background is another drawback that affects the accuracy of SI. Recently, deep learning methods like spatially dependent CNN have been utilized for audio and image classification fields for their capacity to extract robust features. The main drawbacks of SI are session variability, noise in the background, and insufficient information. The attention mechanism is incorporated in the DL-based algorithm, which focuses much on required data, and the hyperparameters are tuned by using the optimization algorithm that enhances speaker identification performance. The main contributions of the research are given as follows:

- Mel-frequency Cepstral Coefficients (MFCC) and Zero Crossing Rate (ZCR) techniques are utilized for feature extraction to differentiate the features for enhancing the classification.
- The Global Local Attention mechanism is utilized in LSTM to concentrate on essential features for speaker identification that enhance classification performance.
- Then, the hyperparameters of LSTM are tuned using the Exponential Neighborhood—Grey Wolf Optimization (EN-GWO) algorithm, which enhances classification performance.

This research is organized as follows: Section 2 provides a literature review, Section 3 provides details of the proposed methodology, Section 4 provides results and a discussion of the proposed method, and the conclusion is in Section 5.

# 2. LITERATURE REVIEW

Wei et al. [17] suggested SincNet and Generative Adversarial Network (SincGAN) methods for speaker identification using speech signals. Unlike other techniques, the implemented method utilized feature recognition of standard hand-crafted. The generator in GAN was used to reconstruct input samples to improve the count of training samples, while the discriminator was used for SI classification. The multiple-scale SincNet layer, depending

on 3 bespoke filter banks, was updated to capture low-level speech representation. The implemented method recognized the raw waveform of the input and allowed speaker identification by a smaller number of training utterances. However, the implemented method obtained speech data from users to extract sufficient data represented by speaker features, which was difficult because of the constraints of the practical environment. However, the implemented method was more time-consuming.

Karthikeyan et al. [18] introduced a Hybrid Neural Network–Support Vector Machine (NN-SVM) method for speaker identification using speech signals. Integrating the NNSVM structure involved passing the output of the Artificial Neural Network (ANN) to an SVM classifier to obtain the results. The introduced method integrated NN-SVM to classify multiple class imbalanced speech information, which obtained the respective advantages of machine learning and SVM structure with a reduced loss function. However, the introduced method had additional costs for the server.

Shahamiri [19] presented an Enhanced Multi-Active Learner (EMAL) method for speaker identification using speech signals. The presented method distributed the difficulty of the learning task between a learner's array with an effective SI technique in speakers, which were found to depend on one sound segment of voice biometrics. The datasets used for evaluation were VoxCeleb 1 and TIMIT. However, the presented method was too limited for lower frequency parts, unable to capture resonant peaks.

Barhoush et al. [20] suggested two parts of techniques, Fully Connected – Deep Neural Network (FC-DNN) and MFCC, depending on the features of Shuffled MFCC (SHMFCC), along with their Difference Shuffled MFCC (DSHMFCC) methods for speaker identification using speech signals. The FC-DNN method effectively localized and identified active speakers separately with huge accuracy. However, the suggested method was vulnerable to security issues.

Gaurav et al. [21] implemented Mask Region-based CNN (Mask R-CNN) technique parameter optimization using the Hosted Cuckoo Optimization (HCO) method for speaker identification using speech signals. From the input speech signal, four kinds of features were extracted: MF Differential Power (MFDPCC), Gamma tone Frequency (GFCC), Power Normalized (PNCC), and Spectral entropy to enhance signal strength. Next, the speaker's ID was classified through Mask R-CNN, with its parameters undergoing optimization through the HCO algorithm.

Al Dulaimi et al. [22] introduced a two-dimensional discrete Multi-Wavelet Transform (2D-DMWT) with deep learning neural network methods for speaker identification using speech signals. The introduced method was dependent on essential sampling pre-processing, which utilized a filter through Geronimo, Hardian, and Massopust, known as GHM. The 2D-DMWT was assigned to acquire discriminant features from the speech signal with minimized dimensions of the speech signal during the feature selection phase. Finally, CNN was utilized to classify SI.

## 3. PROPOSED METHODOLOGY

This research proposes a Global-Local Self-Attention (GLSA) based Long Short-Term Memory (LSTM) with EN-GWO for speaker identification using speech signals. The datasets utilized for research are TIMIT and VoxCeleb 1, alongside the pre-processing techniques, namely, median filter, pre-emphasis, and de-emphasis. Feature extraction is performed by MFCC, ZCR, and pitch extraction, while LSGA-based LSTM identifies the speaker with EGWO. Figure 1. illustrates the overall process of the proposed algorithm.

https://doi.org/10.31436/iiumej.v26i1.3386

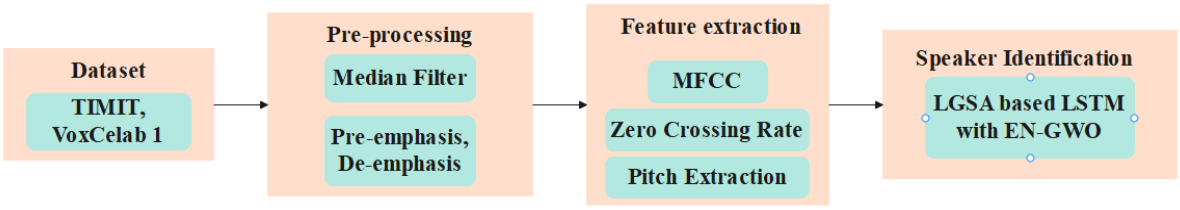


Figure 1. Overall Process of Proposed Algorithm

### 3.1. Dataset

The datasets used for research are TIMIT [23] and VoxCeleb 1 [24], which are audio signal datasets. These audio signal datasets are used for speaker identification. The brief details of these datasets are described below.

#### *3.1.1. TIMIT dataset*

The TIMIT is an Acoustic-Phonetic Continuous Speech Corpus that has 6300 speech data of quality, clean speech samples acquired from 630 speakers, and 10 speeches from each speaker are generated. Of 630 speakers, 192 are females, and 438 are males from 8 main areas of the USA.

#### *3.1.2. VoxCeleb 1 dataset*

The VoxCeleb 1 dataset has 153K gender-balanced utterances from 1251 speakers taken from videos on YouTube. This dataset includes 352 hours of speech and 55% of male samples of speech gathered from speakers of a varied range of ethnicities, professions, and ages. There is an average value of 116 speeches for every speaker, and the mean length of every sample is 8.2 seconds. These two datasets are used in the pre-processing techniques to reduce noise and boost the frequency phase of signals.

### 3.2. Pre-processing

Pre-processing is a vital phase in speaker identification. The methods utilized are median filter, pre-emphasis, and de-emphasis. The median filter reduces noise in the dataset, with pre-emphasis boosting the high-frequency phase while de-emphasis cutting the signal's low-frequency phase.

#### *3.2.1. Median Filter*

The median filter is a non-linear digital filtering method utilized for removing noise from dataset signals. Reducing noise in the pre-processing phase enhances the signals for feature extraction. The median filter eliminates the impact of input noise values with excessively high magnitudes. The median filter maintains the edge integrity, which is mainly used in speaker identification, where the boundary data are essential. The mathematical formula for reducing noise using a median filter is given in Eq. (1),

$$y[i] = \frac{1}{M}\sum_{j=0}^{M-1} x[i+j] \tag{1}$$

where, $x[]$ represents input signal, $y[]$ represents output signal, and $M$ represents the number of signals used in the median. The median filter eliminates the effect of input noise with large magnitudes.

https://doi.org/10.31436/iiumej.v26i1.3386

### *3.2.2. Pre-emphasis and De-emphasis*

The pre-emphasis is processed by boosting the signal's high-frequency phase, compensating for a high-frequency loss in the cable. The de-emphasis is processed by cutting the less-frequency phase in a signal coupled with maximized transmit voltage. Pre-emphasis is used in speech processing to increase high-frequency elements of speech signals and minimize fewer frequency elements. De-emphasis is utilized in speech processing to minimize the magnitude of specific (high) frequencies concerning other (less) frequencies and enhance the signal-to-noise ratio. The Pre-emphasis and De-emphasis balance the signal's frequency spectrum, enhance Signal Noise Ratio (SNR), and make it essential for high-frequency features. The pre-processed signal is given as input to the feature extraction phase to extract the features required for speaker identification.

## 3.2. Feature Extraction

Feature extraction is a process of identifying a compact and meaningful set of features from raw data that improves the classifier's efficiency. In this research, feature extraction is utilized to extract features from pre-processed signals for effective speaker identification. MFCC, ZCR, and pitch extraction techniques are utilized for feature extraction in pre-processed signals.

### *3.3.1. Mel-frequency Cepstral Coefficients*

The MFCC gives spectral speech data and characterizes a perception of human hearing. MFCC has characteristics of huge accuracy and stable recognition. At a similar time, the benefits of MFCC included their ability to provide high-fidelity representations, making them a potential candidate in the speech recognition field. The MFCC gives a meaningful representation of the audio signal and captures significant data about the timbre and speech sounds. The cepstral coefficients extracted by MFCC are efficient in recognizing the speaker, captured content, and individual characteristics of the speaker's voice. Figure 2. provides the flow of MFCC.

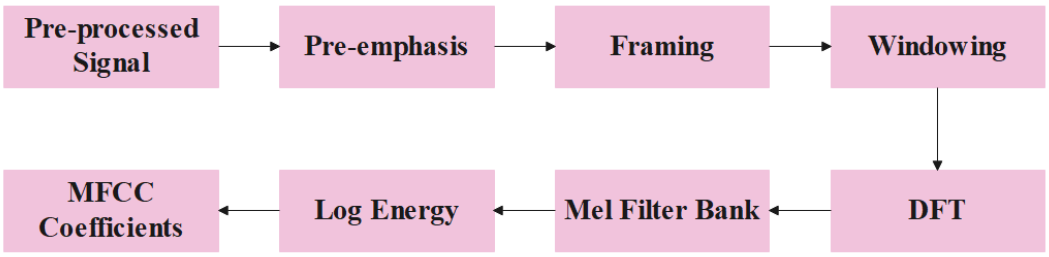


Figure 2. Provides the flow of MFCC

In the MFCC extraction procedure, pre-emphasis is utilized on normalized speech signals to reduce noise in the raw speech signals. The filtered signal is separated into 40ms frames with a 50% of frameshift. For 4s speech signals, the whole 199 frames are produced as a 40ms frame width. The hamming window with $\alpha = 0.46$ and $N$ represents the count of samples for each frame length of 30ms collected nearest to the frequency elements together, and the mathematical formula is given as Eq. (2),

$$H(n) = (1 - \alpha) - \alpha \times cos\left(\frac{2\pi n}{(N-1)}\right),\ 0 \leq n \leq N - 1 \quad (2)$$

https://doi.org/10.31436/iiumej.v26i1.3386

Next, the Discrete Fourier Transform (DFT) is utilized for converting speech signal time-domain to frequency domain ($X(k)$), and the mathematical formula is given as Eq. (3). Eq. (4) represents the power spectrum of DFT that represents characteristics of the vocal tract. Next, the signal is processed by triangular filter banks of Mel-frequency ($\nabla_m(k)$) the mathematical formula of Eq. (5) generates the conversion from linear to mel frequency to give speech-hearing perceptual data.

$$X(k) = \sum_{n=0}^{N-1} x(n) \times H(n) \times e^{-j2\pi nk/N}, 0 \leq n, k \leq N-1 \quad (3)$$

$$X_k = \frac{1}{N}|X(k)|^2 \quad (4)$$

$$ET_m = \sum_{k=0}^{k=1} \nabla_m(k) \times X_k; \quad m = 1,2,\dots,M \quad (5)$$

Next, the Discrete Cosine Transform (DCT) of the log-filter bank energy signal gives $L$ count of cepstral coefficients with its numerical formula is given as Eq. (6)

$$MFCC_i = \sum_{m=1}^{M} log_{10}(ET_m) \times cosj\left((m+0.5)\frac{\pi}{m}\right), j = 1,2,\dots,L \quad (6)$$

The extracted features significantly characterize the transition in speaker identification. The MFCC provides energy, MFCC coefficients, and significant derivative features for characterizing speech signals.

### *3.3.2. Zero Crossing Rate*

The ZCR generates a transition signal over a zero line, representing the speech signal's noise metrics. The ZCR is an effective feature extraction technique that supports the differentiation between various types of sounds or energy variations in audio. The sign function gives a value of 1 for positive and 0 for negative sample amplitudes across the time frame ($t$). The mathematical Eq. (7) generates the execution of ZCR in the time domain.

$$ZCR_t = \frac{1}{2}(\sum_{n=1}^{N} sign(x[n]) - sign(x[n-1])) \quad (7)$$

where, $sign(x[n])$ represents the sign function and $t$ represents the time frame. The ZCR counts how many times the speech signal crosses the zero axis, indicating modifications or occurrences in some sounds. The ZCR method produces less noise during the switching process.

### *3.3.3. Pitch Extraction by Synthesis based method*

In synthesis-based pitch extraction, the speech signal is considered a result of an all-pole filter $H(z)$ that is excited through the period impulse train or random noise. This method captures the essential signal frequency essential to identify the intonation patterns. Therefore, $S(f)$ power spectrum of the input speech segment is acquired through DFT, and the mathematical formula for decomposed is given in Eq. (8),

$$S(f) = H(f)E(f) \quad (8)$$

where, $E(f)$ represents the power spectrum in the excited signal. To synthesize the power spectrum, the input speech segment is considered as voice, and their frequency is hypothesized $\check{F}_o$. Transfer function H(z) of every-pole filter is evaluated from the input speech segment through linear prediction analysis. The numerical formula for the synthesized power spectrum is given in Eqs. (9) and (10).

$$S(f, \bar{F}_o) = H(f)E(f, \bar{F}_o) \quad (9)$$

https://doi.org/10.31436/iiumej.v26i1.3386

where,

$$\bar{E}(f,\bar{F}_o) = \begin{cases} 1, & for\ f = \bar{F}_o, 2\bar{F}_o, 3\bar{F}_o \\ 0, & otherwise \end{cases} \quad (10)$$

The amount of power spectra is synthesized for various scores of $\bar{F}_o$ with hypothesized frequency compared to S(f). The dissimilarity among Average Magnitude (AM) is compared to measure the variance between the input and synthesized power spectrum. The mathematical expression is in Eq. (11).

To compare the dissimilarity between the two spectra, the Average Magnitude (AM) variance between the input power spectrum and the synthesized power spectrum is calculated. This helps quantify differences in spectral characteristics.

$$D(\bar{F}_o) = \frac{1}{F_f}\int_0^{F_f} |d(f,\bar{F}_o)|\, df \quad (11)$$

where, $F_f$ represents the folding frequency and $d(f,\bar{F}_o)$ represents variance among two spectra at $f$ frequency and its mathematical formula is given as Eq. (12),

$$d(f,\bar{F}_o) = logS(f) - log\,\bar{S}(f,\bar{F}_o) \quad (12)$$

Rather than using power spectra $S(f)$ and $\bar{S}(f,\bar{F}_o)$, log power is utilized in the above equation for defining variance $d(f,\bar{F}_o)$. The value of fundamental frequency, which provides less AM variance among the synthesized spectrum and input spectrum, is selected as an evaluated score of significant frequency. This is performed to remove the effect of format architecture on pitch estimation. The extracted features are significant in speaker identification and are given as input to LSTM for identifying speakers. Finally, seven features of mean, median, standard deviation, variance, and so on are extracted. Various features give spectral modifications in speech signals because of modifications in metrics and intonation in speech signals. The extracted features are given as input to the neural network for identifying speakers.

### 3.3. Speaker Identification using GLSA-LSTM with EN-GWO

The extracted features are given as input to Long-Short-Term Memory (LSTM), which utilizes Global-Local Self-Attention (GLSA) to concentrate on the significant parts of the feature. The weight of LSTM is updated using the proposed Exponential Neighborhood—Grey Wolf Optimization (EN-GWO). Below are detailed explanations of LSTM, GLSA, and the proposed EN-GWO algorithms.

#### *3.3.1. Long Short-Term Memory (LSTM)*

The architecture of LSTM is represented in Figure 3, where the controlled state of information is considered at every moment in the whole LSTM using a structure known as the gate for attaining the learning effect. $C_t$ represents state information of the LSTM unit at the time $t$, $f_t$ represents forget gate at the time $t$, $i_t$ represents the input gate at the time $t$, $\tilde{C}_t$ represents present-moment information, $o_t$ represents the output gate at the time $t$, $tanh$ represents tangent activation function and $\sigma$ represents the sigmoid activation function.

https://doi.org/10.31436/iiumej.v26i1.3386

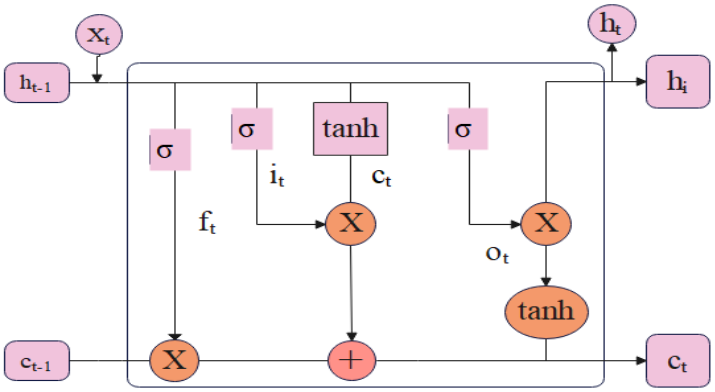


Figure 3. Architecture of LSTM

The mathematical formula for every gate is given from Eqs. (13) – (18),

$$i_t = \sigma(W_i \cdot [h_{t-1}, x_t] + b_i) \tag{13}$$

$$f_t = \sigma\left(W_f \cdot [h_{t-1}, x_t] + b_f\right) \tag{14}$$

$$\tilde{C}_t = tanh\ (W_{\tilde{c}} \cdot [h_{t-1}, x_t] + b_{\tilde{c}} \tag{15}$$

$$C_t = f_t \cdot C_{t-1} + i_t \cdot \tilde{C}_t \tag{16}$$

$$o_t = \sigma(W_o \cdot [h_{t-1}, x_t] + b_o) \tag{17}$$

$$h_t = o_t \cdot tanh C_t \tag{18}$$

where, $W_f, W_i, W_{\tilde{c}}\ and\ W_0$ represent weight matrices respective to every module, $b_f, b_i, b_{\tilde{c}}\ and\ b_o$ represent bias and mathematical formulas for tanh( ) and $\sigma$ is given as in Eqs. (19) and (20),

$$tanhx = (e^x - e^{-x})/(e^x + e^{-x}), \tag{19}$$

$$\sigma(x) = 1/(1 + e^{-x}) \tag{20}$$

At last, the output layer is dependent on $h_t$ by a fully connected layer for obtaining the predicted value $y_t$, given as Eq. (21),

$$y_t = \sigma\left(W_y \cdot h_t + b_y\right) \tag{21}$$

where, $W_y$ represents the weight matrix and $b_y$ represents bias term. The LSTM network provides much more accurate prediction using the features of past time points of time series. The initial position of the past phase is called currently, representing a phase of the familiar signal.

### *3.3.2. Global-Local Self Attention*

The self-attention mechanism has global dependencies but struggles to capture local data for utterances. This research utilizes a global-local self-attention mechanism, which enhances the ability to capture local features while retaining the ability of the method's long-term dependencies. Figure 4 represents the flow of Global-Local Self Attention.

https://doi.org/10.31436/iiumej.v26i1.3386

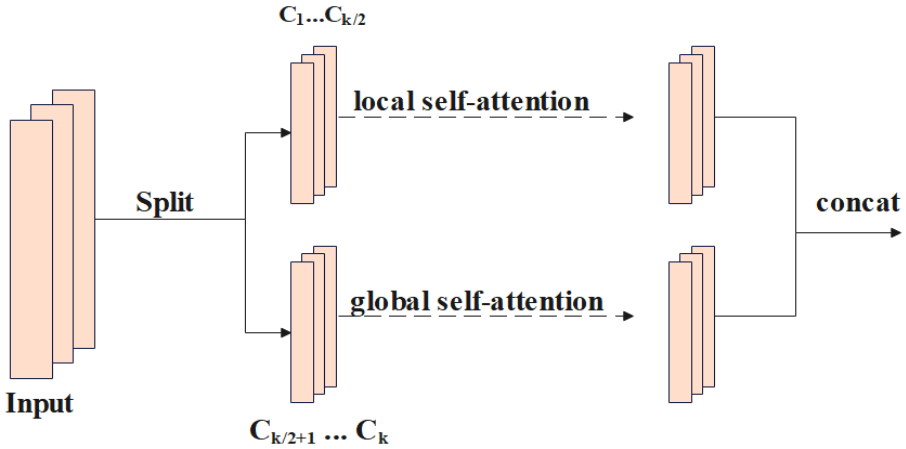


Figure 4. The Flow of Global-Local Self-Attention Mechanism

The SA mechanism was initially introduced with LSA, where every attention head included a sliding window of a specified size. As the next half channel is introduced, GSA is utilized without a sliding window. Similar to the actual SA mechanism, input features $X \in R^{C\times T}$ are linearly converted to $K$ attention head, and next, every attention head processes local and global SA. In GLSA, the non-overlapping sliding window partitions $X$ into $[X_1, \dots, X_N]$ and each segment has the same window size $w$. It is considered that matrices of query, key, and value of $kth$ attention head contains dimension $d_k$. The mathematical formula for LSA for $kth$ head are given in Eqs. (22) – (24),

$$X = [X_1, X_2, \dots, X_N],\ N = \frac{T}{w} \tag{22}$$

$$Y_i^k = Attention\left(X_i W_k^Q, X_i W_k^K, X_i W_k^V\right) \tag{23}$$

$$LocalAttention_k(X) = \left[Y_1^k, Y_2^k, \dots, Y_i^k\right] \tag{24}$$

where, $W_k^Q, W_k^K, W_k^V \in R^{C\times d_k}$ represents linear projection parameter matrix of query, key, and value in $kth$ attention head, $d_k$ represents set to $C/K$. $K$ attention head is divided correspondingly into two distinct sets. The $K$ is generally an even number, with the attention head equally separated into two sets. The initial set of attention heads performs LSA, and the next set of attention heads process global self-attention. The mathematical formula for output $kth$ head is given in Eq. (25),

$$head_k = \begin{cases} LocalAttention_k(X), & k = 1, \dots, \frac{K}{2} \\ GlobalAttention_k(X) & k = \frac{K}{2} + 1, \dots, K \end{cases} \tag{25}$$

At last, the outcomes of two attention mechanisms are combined as input of LSTM and represented as GL – Attention(X), with the mathematical formula given as Eq. (26).

$$GL - Attention(X) = cat(head_1, \dots, head_k)W \tag{26}$$

where, $W \in R^{C\times C}$ represents a projection matrix projecting self-attention output to the target result dimension. The main plan is to separate attention heads into 2 various sets and process GLSA in parallel. That enables local attention within the global attention process, allowing global data to interact with local data in a structured manner.

https://doi.org/10.31436/iiumej.v26i1.3386

### *3.3.3. Exponential Neighborhood Grey Wolf Optimization*

Exponential Neighborhood Grey Wolf Optimization (EN-GWO) emulates grey wolves' group hunting behavior and leadership hierarchy. This mathematical method models the prey's location as the optimal solution in the search space, while the wolf's current position represents a potential solution. In this approach, the positions of the alpha, beta, and delta wolves are denoted as $\alpha$, $\beta$, and $\gamma$, respectively. The EN-GWO algorithm involves four significant phases: encircling, hunting, attacking, and seeking prey. During the hunting phase, the wolves encircle their prey, which is mathematically modeled using the equations provided in Eqs. (27)–(30).

$$D = \left|C - X_p(t) - X_i(t)\right| \tag{27}$$

$$X_i(t+1) = X_p(t) - AD \tag{28}$$

$$C = 2a \times rand_1 - a \tag{29}$$

$$A = 2rand_2 \tag{30}$$

where, $X_i(t)$, $X_p(t)$ represents $ith$ grey wolf position vector and prey at $t$ iteration, $A\ and\ C$ represents coefficient vectors, $rand_1$ and $rand_2$ represents random vectors in [0,1], $a$ represents the vector whose values are minimized from iteration 2 – 0. In the hunting process, all wolves are the same with probable prey positions, and from that, three good agents are developed with their mathematical formula given in Eqs. (31) – (37).

$$D_\alpha = |C_1 X_\alpha - X_i| \tag{31}$$

$$D_\beta = \left|C_2 X_\beta - X_i\right| \tag{32}$$

$$D_\gamma = \left|C_3 X_\gamma - X_i\right| \tag{33}$$

$$X_1 = X_\alpha - A_1 . D_\alpha \tag{34}$$

$$X_2 = X_\beta - A_2 . D_\beta \tag{35}$$

$$X_3 = X_\gamma - A_3 . D_\gamma \tag{36}$$

$$X_{iGWO}(t+1) = \frac{X_1 + X_2 + X_3}{3} \tag{37}$$

Linear minimization in adaptive feature $a$ across iterations helps balance the exploitation and exploration of attacking methods. Another adaptive parameter manages exploitation and exploration $A$ that considers random values ranging from $[-2r, -2r]$. The exploitation develops the local optimum, which yields an optimum and lower quality. The default GWO represents half of their cycles for exploitation and the next half for exploitation. The diversity, lack of population, and premature convergence are other difficult factors of traditional GWO. To overcome this limitation, the research proposes an Exponential Neighborhood Grey Wolf Optimization by enhancing two phases of default GWO. The mathematical formula for introducing the exponential decline function for managing adaptive parameter $\vec{a}$ value is given in Eq. (38). Linear minimization in adaptive feature selection across iterations helps balance between exploitation and exploration in the attacking methods.

$$a = 2\left(1 - \frac{t^2}{T^2}\right) \tag{38}$$

where, $t$ represents the present iteration and $T$ represents the whole iteration. The neighborhood-based searching process is introduced by combining an individual wolf-hunting strategy with a global hunting strategy. Multi-neighbors are utilized to expand the search space. The initially updated location of the present wolf $X_{iGWrewrO}(t)$ is measured by Eq. (33). Next,

$R_i(t)$ is executed by Euclidean distance among the present location $X_i(t)$ and $X_{iGWO}(t)$ is given as Eq. (39).

$$R_i(t) = X_i(t) - X_{iGWO}(t) \tag{39}$$

Respective to the radius, the neighbors of the present wolf $X_i(t)$ are measured using below Eq. (40) with wolf $X_j(t)$ distance from the present wolf from the radius value.

$$N_i(t) = \left\{X_j(t) | D_i\left(X_j(t), X_i(t)\right) \leq R_i(t)\right\} \tag{40}$$

The next new position $X_{NL}(t)$ depends on the position of neighbors, as developed by Eq. (41),

$$X_{NL}(t) = X_i(t) + rand \times \left(X_n(t) - X_r(t)\right) \tag{41}$$

where, $X_n(t)$ represents the randomly chosen neighbor N(t) and $X_r(t)$ represents the randomly chosen wolves through the population. At last, good location within $X_{iGWO}$ and $X_{NL}$ with respect to its fitness value for further iteration is given as Eq. (42),

$$X_i(t+1) = \begin{cases} X_{iGWO}, iff(X_{iGWO}) > f(X_{NL}) \\ X_{NL}, \qquad\qquad otherwise \end{cases} \tag{42}$$

While utilizing a global-local self-attention mechanism at various gates, LSTM gives enhanced outcomes. When utilizing the EN-GWO algorithm for LSTM, every position vector of the wolf represents the weight of LSTM. After completing a set of iterations, the position vector of a wolf with the least cost in the EN-GWO algorithm is selected as the final weight for the trained network. At last, the robustness and accuracy are enhanced with the speaker's identity.

## 4. EXPERIMENTAL RESULTS

The GLSA-LSTM with EN-GWO algorithm is simulated on a Python environment with system configurations of an i5 processor and 16GB RAM. The performance metrics used for evaluating the GLSA-LSTM with the EN-GWO method are accuracy, precision, recall, and f1-score. The numerical expression for performance metrics is given in Eqs. (43) – (46).

$$Accuracy = \frac{TP+TN}{TP+TN+FP+FN} \tag{43}$$

$$Precision = \frac{TP}{TP+FP} \tag{44}$$

$$Recall = \frac{TP}{TP+FN} \tag{45}$$

$$F1 - score = 2 \times \frac{Precision \times Recall}{Precision + Recall} \tag{46}$$

where, the $TP$ – True Positive, $FP$ – False Positive, $TN$ – True Negative and $FN$ – False Negative.

### 4.1. Quantitative and Qualitative Analysis

The performance of the GLSA-LSTM with the EN-GWO technique is analyzed using performance measures of accuracy, precision, recall, and f1-score. Different tables and graphs show the proposed algorithm's performance.

https://doi.org/10.31436/iiumej.v26i1.3386

Table 1. Performance of proposed algorithm with 2 datasets

| Dataset | Accuracy (%) | Precision (%) | Recall (%) | F1-score (%) |
|---|---|---|---|---|
| TIMIT | 99.36 | 99.12 | 97.62 | 98.47 |
| VoxCeleb 1 | 93.45 | 92.78 | 92.04 | 91.58 |
| Average | 96.40 | 95.95 | 94.83 | 95.02 |

Table 1 represents the performance of the proposed method with two datasets. The developed method attains an accuracy of 99.36%, precision of 99.12%, recall of 97.62%, and f1-score of 98.47% on the TIMIT dataset. The GLSA attains an accuracy of 93.45%, precision of 92.78%, recall of 92.04, and f1-score of 91.58%, with the mean of the two datasets represented.

Table 2. Performance of Global-Local Self-Attention Mechanism with 2 datasets

| Attention Mechanism | Accuracy (%) | Precision (%) | Recall (%) | F1-Score (%) |
|---|---|---|---|---|
| SE | 90.40 | 90.77 | 89.83 | 86.18 |
| CAM | 91.39 | 91.02 | 90.17 | 87.27 |
| SAM | 92.24 | 91.82 | 90.94 | 88.72 |
| SA | 93.58 | 92.36 | 91.72 | 89.37 |
| GLSA | 95.67 | 93.29 | 92.15 | 90.48 |

Table 2 describes the performance of the GLSA mechanism with two datasets. The existing attention mechanisms considered for evaluation are Squeeze and Excitation (SE), Channel Attention Module (CAM), Spatial Attention Module (SAM), and Self Attention (SA). Compared to existing mechanisms, the utilized attention mechanism attains an accuracy of 95.67%, precision of 93.29%, recall of 92.15%, and F1-score of 90.48%.

Table 3. Performance of Proposed EN-GWO algorithm with 2 datasets

| Optimization algorithm | Accuracy (%) | Precision (%) | Recall (%) | F1-score (%) |
|---|---|---|---|---|
| CSO | 92.25 | 92.48 | 90.88 | 89.57 |
| GOA | 93.17 | 93.01 | 91.03 | 90.63 |
| WOA | 93.99 | 93.82 | 92.37 | 91.03 |
| GWO | 95.29 | 94.61 | 93.72 | 92.25 |
| EN-GWO | 96.72 | 95.34 | 94.28 | 93.66 |

Table 3 describes the performance of EN-GWO with 2 datasets. The existing optimization algorithms utilized for evaluation are Cat Swarm Optimization (CSO), Grasshopper Optimization Algorithm (GOA), Whale Optimization Algorithm (WOA), and Grey Wolf Optimization (GWO). The utilized optimization algorithm attains an accuracy of 96.72%, precision of 95.34%, recall of 94.28%, and F1-score of 93.66%, which is better than the existing algorithms.

Table 4. Performance of LSTM neural network with 2 datasets

| Methods | Accuracy (%) | Precision (%) | Recall (%) | F1-score (%) |
|---|---|---|---|---|
| MLP | 93.06 | 92.73 | 91.63 | 90.52 |
| ANN | 94.16 | 93.66 | 92.84 | 91.03 |
| CNN | 95.37 | 94.25 | 93.74 | 92.39 |
| RNN | 96.29 | 95.48 | 94.21 | 93.47 |
| LSTM | 97.48 | 96.26 | 95.37 | 94.28 |

https://doi.org/10.31436/iiumej.v26i1.3386

Table 4 describes the performance of LSTM with 2 datasets. The existing Neural networks utilized for evaluation are Multi-Layer Perceptron (MLP), Artificial Neural Network (ANN), Convolutional Neural Network (CNN), and Recurrent Neural Network (RNN). The utilized neural network attains an accuracy of 97.48%, precision of 96.26%, recall of 95.37%, and F1-score of 94.28%, which is better than existing classifiers.

Table 5. Performance of Proposed GLSA-based LSTM with EN-GWO with 2 datasets

| Methods | Accuracy (%) | Precision (%) | Recall (%) | F1-score (%) |
|---|---|---|---|---|
| GLSA based MLP | 91.38 | 90.37 | 89.73 | 90.63 |
| GLSA based ANN | 92.17 | 91.05 | 90.04 | 91.85 |
| GLSA based CNN | 93.49 | 92.71 | 91.74 | 92.94 |
| GLSA based RNN | 94.63 | 93.84 | 92.28 | 93.74 |
| GLSA-based LSTM with EN-GWO | 96.40 | 95.95 | 94.83 | 95.02 |

Table 5 describes the performance of the proposed GLSA-based LSTM with EN-GWO algorithm on two datasets. The existing attention mechanisms utilized for evaluation are GLSA-based MLP, GLSA-based ANN, GLSA-based CNN, and GLSA-based RNN. The utilized optimization algorithm attains an accuracy of 96.72%, precision of 95.34%, recall of 94.28%, and f1-score of 93.66%, outperforming the existing methods.

### 4.2. Comparative Analysis

The GLSA-LSTM with EN-GWO method is compared to the existing methods: SincGAN [17], Hybrid NN-SVM [18] and EMAL [19]. The GLSA-LSTM with EN-GWO method attains an accuracy of 99.36%, precision of 99.12%, recall of 97.62%, and f1-score of 98.47% on the TIMIT dataset. The attained accuracy of 93.45%, the precision of 92.78%, the recall of 92.04, and the f1-score of 91.58% are all more effective than the existing methods. Combining GLSA, LSTM, and EN-GWO introduces the computational overhead because of the quadratic complexity in GLSA and the sequence nature of LSTM in terms of memory usage and processing power. Table 6 describes the comparative analysis of GLSA-LSTM with the EN-GWO method.

Table 6. Comparative Analysis of GLSA-LSTM with EN-GWO method

| Method | Dataset | Accuracy (%) | Precision (%) | Recall (%) | F1-Score (%) |
|---|---|---|---|---|---|
| SincGAN [17] | TIMIT | 98.98 | NA | NA | NA |
| | LIBRISPEECH | 99.27 | NA | NA | NA |
| Hybrid NN-SVM [18] | TIMIT | 96.72 | 99.05 | 79.75 | 88.35 |
| | ELSDSR | 96.91 | 98.38 | 64.88 | 78.19 |
| EMAL [19] | TIMIT | 98.61 | NA | NA | NA |
| | VoxCeleb 1 | 82.93 | NA | NA | NA |
| Proposed GLSA-based LSTM with EN-GWO | TIMIT | 99.36 | 99.12 | 97.62 | 98.47 |
| | VoxCeleb 1 | 93.45 | 92.78 | 92.04 | 91.58 |

## 5. CONCLUSION

The main drawbacks of SI are session variability, noise in the background, and lack of enough information. To mitigate the limitations, this research proposes a GLSA-based LSTM with EN-GWO algorithm for effective speaker identification using TIMIT and VoxCeleb 1 dataset. The Median filter and pre-emphasis and de-emphasis techniques are employed for pre-processing. At the same time, the MFCC and ZCR methods are deployed for feature extraction

to extract the significant features. Next, the speaker identification is performed using GLSA-based LSTM with the EN-GWO algorithm. The proposed method acquires an accuracy of 99.36% on the TIMIT dataset and an accuracy of 93.45% on the VoxCeleb 1 datasets, which is superior to existing methods, SincGAN and NN-SVM. Combining GLSA, LSTM, and EN-GWO introduces the computational overhead because of the quadratic complexity in GLSA and the sequence nature of LSTM in terms of memory usage and processing power. In future work, we will apply the model to real-time applications and work on minimizing the computational overhead.

## REFERENCES

[1] Shah SM, Moinuddin M, Khan RA. (2022) A Robust Approach for Speaker Identification Using Dialect Information. Appl. Comput. Intell. Soft Comput., 2022(1):4980920. https://doi.org/10.1155/2022/4980920

[2] Nassif AB, Alnazzawi N, Shahin I, Salloum SA, Hindawi N, Lataifeh M, Elnagar A. (2022) A Novel RBFNN-CNN Model for Speaker Identification in Stressful Talking Environments. Applied Sciences,12(10):4841. https://doi.org/10.3390/app12104841

[3] Dua S, Kumar SS, Albagory Y, Ramalingam R, Dumka A, Singh R, Rashid M, Gehlot A, Alshamrani SS, AlGhamdi AS. (2022) Developing a Speech Recognition System for Recognizing Tonal Speech Signals Using a Convolutional Neural Network. Applied Sciences, 12(12):6223. https://doi.org/10.3390/app12126223

[4] Monir M, Kareem M, El-Dolil SM, Saleeb A, El-Fishawy AS, Nassar MAE, Eldin MZA, Abd El-Samie FE. (2022) Cancelable speaker identification based on cepstral coefficients and comb filters. Int. J. Speech Technol., 25(2):471-492. https://doi.org/10.1007/s10772-021-09804-4

[5] Chen YW, Hung KH, Li YJ, Kang ACF, Lai YH, Liu KC, Fu SW, Wang SS, Tsao Y. (2022) CITISEN: A Deep Learning-Based Speech Signal-Processing Mobile Application. IEEE Access, 10:46082-46099. doi: 10.1109/ACCESS.2022.3153469

[6] Noh K, Jeong H. (2023) Emotion-Aware Speaker Identification with Transfer Learning. IEEE Access, 11:77292-77306. doi: 10.1109/ACCESS.2023.3297715.

[7] Nakamura E, Kageyama Y, Hirose S. (2022) LSTM-based japanese speaker identification using an omnidirectional camera and voice information. IEEJ Trans. Electr. Electron. Eng., 17(5):674-684. https://doi.org/10.1002/tee.23555

[8] De Lima TA, Abreu MCD. (2022) Phoneme analysis for multiple languages with fuzzy-based speaker identification. IET Biom., 11(6):614-624. https://doi.org/10.1049/bme2.12078

[9] Saritha B, Laskar MA, Kirupakaran AM, Laskar RH, Choudhury M, Shome N. (2024) Deep Learning-Based End-to-End Speaker Identification Using Time–Frequency Representation of Speech Signal. Circuits Syst. Signal Process., 43(3):1839-1861. https://doi.org/10.1007/s00034-023-02542-9

[10] Shome N, Saritha B, Kashyap R, Laskar RH. (2023) A robust DNN model for text-independent speaker identification using non-speaker embeddings in diverse data conditions. Neural Comput. Appl., 35(26):18933-18947. https://doi.org/10.1007/s00521-023-08736-1

[11] Al-Karawi KA, Mohammed DY. (2023) Using combined features to improve speaker verification in the face of limited reverberant data. Int. J. Speech Technol., 26:789-799. https://doi.org/10.1007/s10772-023-10048-7

[12] Kuppusamy K, Eswaran C. (2022) Convolutional and Deep Neural Networks based techniques for extracting the age-relevant features of the speaker. J. Ambient Intell. Hum. Comput., 13(12):5655-5667. https://doi.org/10.1007/s12652-021-03238-1

[13] Radha K, Bansal M. (2023) Closed-set automatic speaker identification using multi-scale recurrent networks in non-native children. Int. J. Inf. Technol., 15(3):1375-1385. https://doi.org/10.1007/s41870-023-01224-8

[14] Malek J, Jansky J, Koldovsky Z, Kounovsky T, Cmejla J, Zdansky J. (2022) Target speech extraction: Independent vector extraction guided by supervised speaker identification. IEEE/ACM Trans. Audio Speech Lang. Process., 30:2295-2309.

[15] El Shafai W, Elsayed MA, Rashwan MA, Dessouky MI, El-Fishawy AS, Soliman NF, Alhussan

AA, Abd El-Samie FE. (2023) Optical Ciphering Scheme for Cancellable Speaker Identification System. Computer Systems Science and Engineering, 45(1):563-578. https://doi.org/10.32604/csse.2023.024375

[16] El-Gazar S, El Shafai W, El Banby G, Hamed HFA, Salama GM, Abd-Elnaby M, Abd El-Samie FE. (2022) Cancelable Speaker Identification System Based on Optical-Like Encryption Algorithms. Computer Systems Science and Engineering, 43(1):87-102. DOI:10.32604/csse.2022.022722

[17] Wei G, Zhang Y, Min H, Xu Y. (2023) End-to-end speaker identification research based on multi-scale SincNet and CGAN. Neural Comput. Appl., 35(30):22209-22222. https://doi.org/10.1007/s00521-023-08906-1

[18] Karthikeyan V, Priyadharsini SS, Balamurugan K, Ramasamy M. (2022) Speaker identification using hybrid neural network support vector machine classifier. Int. J. Speech Technol., 25(4):1041-1053. https://doi.org/10.1007/s10772-021-09902-3

[19] Shahamiri SR. (2023) An optimized enhanced-multi learner approach towards speaker identification based on single-sound segments. Multimedia Tools Appl,, 83:24541-24562. https://doi.org/10.1007/s11042-023-16507-2

[20] Barhoush M, Hallawa A, Schmeink A. (2023) Speaker identification and localization using shuffled MFCC features and deep learning. Int. J. Speech Technol., 26(1):185-196. https://doi.org/10.1007/s10772-023-10023-2

[21] Gaurav, Bhardwaj S, Agarwal R. (2023) An efficient speaker identification framework based on Mask R-CNN classifier parameter optimized using hosted cuckoo optimization (HCO). J. Ambient Intell. Hum. Comput., 14(10):13613-13625. https://doi.org/10.1007/s12652-022-03828-7

[22] Al-Dulaimi HW, Aldhahab A, Al Abboodi HM. (2023) Speaker Identification System Employing Multi-resolution Analysis in Conjunction with CNN. International Journal of Intelligent Engineering & Systems, 16(5):350-363. DOI: 10.22266/ijies2023.1031.30

[23] Dataset TIMIT: https://www.kaggle.com/datasets/nltkdata/timitcorpus.

[24] Dataset VoxCeleb 1: https://www.robots.ox.ac.uk/~vgg/data/voxceleb/vox1.html.

https://doi.org/10.31436/iiumej.v26i1.3392

# ELECTROCHEMICAL SENSING OF NICOTINE USING LASER-INDUCED GRAPHENE SCREEN PRINTED ELECTRODE

**BALQIS NURNADIA BADROL HISHAM[1], ROSMINAZUIN AB RAHIM[1], ANIS NURASHIKIN NORDIN[1], ALIZA AINI MD RALIB[1], NOR FARAHIDAH ZA'BAH[1], LUN HAO TUNG[2], ZAINIHARYATI MOHD ZAIN[3]**

*[1]Department of Electrical and Computer Engineering, Kulliyyah of Engineering, International Islamic University Malaysia, IIUM, Kuala Lumpur, Malaysia*
*[2]Manufacturing Technology Innovation, Jabil Circuit Sdn. Bhd., Penang, Malaysia*
*[3]Faculty of Applied Science, University Teknologi MARA, UiTM, Selangor, Malaysia*

**Corresponding author: rosmi@iium.edu.my*

*(Received: 5 August 2024; Accepted: 29 August 2024; Published online: 10 January 2025)*

***ABSTRACT:*** Nicotine is one of the major addictive substances in tobacco plants, which caused a global pandemic. Rapid detection of nicotine is crucial to allow quick identification of harmful substances that will cause significant health risks, especially with the recent rise in electronic cigarettes. Since smoking cessation programs are typically limited to screening, awareness, consultation, medication, and follow-up activities, there is a need for a device to check the nicotine level in former smokers at the end of the programs. However, most of the current nicotine detection is based on chromatography technology, which involves complicated sample pre-treatment and bulky and expensive instruments. Thus, screen-printing technology employing electrochemical detection is a promising solution as it offers a simple and portable setup for nicotine detection. Yet, conventional screen-printed electrodes (SPE) have relatively low sensitivity and need modification to improve the electrode material. Therefore, this work aims to investigate the performance of laser-induced graphene (LIG) as SPE-modified electrodes to detect the presence of nicotine through electrochemical measurements. A finite element simulation was conducted to investigate laser power's effect on the induced graphene's quality. The $CO_2$ laser with 3W laser power, Dots per inch (DPI) of 1200, and a laser speed of 13% was used to fabricate the LIG sensor on a Kapton substrate. Material characterizations such as SEM, EDX, and Raman spectra were performed on the fabricated LIG-SPE to confirm the presence of LIG. Cyclic voltammetry (CV) measurement was done using 0.1M $[Fe(CN)_6]^{3-/4-}$ and 0.1M KCL to find the suitable scan rates. At a fixed scan rate of 50 mV/s, the sensor's performance was analyzed using 0.1M of nicotine with 3 different phosphate buffer solutions (PBS) of pH 5, pH 7, and pH 9 at different nicotine concentrations. Nicotine with PBS pH 5 solution was found to be the optimum measured solution, with the value obtained for $R^2$ having the highest value of 0.9988 and the lowest LOD of 4.2183 μM. The proposed electrochemical sensing of nicotine using a laser-induced graphene screen printed electrode can detect nicotine with high linearity at different pH levels of PBS buffer solution.

***ABSTRAK:*** Nikotin adalah salah satu bahan ketagihan utama dalam tumbuhan tembakau yang menyebabkan pandemik global. Pengesanan cepat nikotin adalah penting bagi membolehkan pengecaman cepat bahan merbahaya yang menyebabkan risiko kesihatan ketara terutamanya dengan peningkatan rokok elektronik pada masa sekarang. Memandangkan program berhenti merokok biasanya terhad kepada pemeriksaan, kesedaran, perundingan, ubat-ubatan dan aktiviti susulan, terdapat keperluan bagi peranti memeriksa tahap nikotin dalam bekas perokok pada akhir program. Walau bagaimanapun, kebanyakan

https://doi.org/10.31436/iiumej.v26i1.3392

pengesanan nikotin semasa adalah berdasarkan teknologi kromatografi, di mana melibatkan sampel pra-rawatan rumit, instrumen besar dan mahal. Oleh itu, teknologi percetakan skrin yang menggunakan pengesanan eletrokimia adalah penyelesaian bermakna kerana ia menawarkan persediaan mudah dan mudah alih bagi mengesan nikotin. Namun, skrin-cetakan elektrod konvensional (SPE) mempunyai sensitiviti rendah dan memerlukan pengubahsuaian bagi menambah baik bahan elektrod. Oleh itu, kajian ini adalah untuk menyiasat prestasi laser graphen teraruh (LIG) sebagai elektrod SPE yang diubah suai bagi mengesan kehadiran nikotin melalui pengukuran elektrokimia. Simulasi unsur terhingga telah dijalankan bagi melihat kesan kuasa laser ke atas kualiti graphen teraruh. Laser $CO_2$ dengan kuasa laser 3W, dot per inci (DPI) sebanyak 1200, dan kelajuan laser sehingga 13% telah digunakan bagi mengfabrikasi pengimbas LIG pada substrat Kapton. Pencirian bahan sperti SEM, EDX, dan spektrum Raman dilakukan pada LIG-SPE yang direka bagi mengesahkan kehadiran LIG. Pengukuran voltametri kitaran (CV) dilakukan menggunakan 0.1M $[Fe(CN)_6]^{3-/4-}$ dan 0.1M KCL bagi mencari kadar imbasan yang sesuai. Pada kadar imbasan tetap 50 mV/s, prestasi pengimbas dianalisa menggunakan 0.1M nikotin dengan 3 larutan penimbal fosfat (PBS) berbeza pH 5, pH 7, dan pH 9 pada kepekatan nikotin berbeza. Nikotin dengan larutan PBS pH 5 didapati sebagai larutan optimum, dengan nilai $R^2$ tertinggi 0.9988 dan LOD terendah 4.2183 µM. Kesimpulannya, pengimbas elektrokimia nikotin menggunakan laser elektrod skrin bercetak graphen teraruh dapat mengesan nikotin dengan pemalaran tinggi pada pH larutan penimbal PBS yang berbeza.

***KEYWORDS:*** *laser-induced graphene, screen-printed electrode, nicotine, shrimp virus, electrochemical.*

# 1. INTRODUCTION

Nicotine, a highly addictive substance in tobacco plants, contributes to a global health crisis through smoking addictions. Nicotine poses serious health effects, including respiratory problems, cardiovascular system, and increased risk of lung cancer [1]. Gas chromatography/mass spectrometry (GC-MS), electro-chemiluminescent/flow injection analysis, and high-performance liquid absorption spectrometry (AAS) are among several analytical methods typically used to detect nicotine [2]. Despite providing accurate measurement results, these methods have some drawbacks, such as the need for skilled personnel to conduct the instrument and the fact that they are not portable, making them unsuitable for healthcare monitoring. Hence, there is an urgent need to develop a rapid and portable sensor to detect nicotine in various body fluids such as saliva, sweat, and urine. Electrochemical-based screen-printed electrode (SPE) sensor is regarded as a more suitable sensor for nicotine detection because of its ease of use, cost-effectiveness, and portability [3], [4]. [5]. However, SPE has limitations for electrochemical sensing applications, such as low robustness and limited electrochemical performance compared to conventional electrodes like glassy carbon or golden disk electrodes [1]. One of the drawbacks of glassy carbon electrodes is that they can exhibit a lack of electrochemical inertness under certain conditions, which can lead to the formation of an insulating layer on the surface, particularly when exposed to an oxidative environment; this later significantly reduces the current density and can compromise the electrode's performance over time. On the other hand, gold disk electrodes are susceptible to surface oxidation and can be affected by surface contamination, which may block active sites and hinder the electrochemical reactions [6], [7], [8]. Meanwhile, LIG offers a lot of advantages, where the formation of the porous network structure of LIG results in high conductivity and high specific surface area [9]. Because of its porous nature, the material has more accessibility to chemical processes [10]. Therefore, a laser-induced graphene (LIG) screen-printed electrode is proposed for nicotine detection.

https://doi.org/10.31436/iiumej.v26i1.3392

Graphene structure formation provides the basis for the construction of LIG, a three-dimensional porous carbon-based material constructed on a polyimide substrate [10], [11], [12]. A CO2 infrared laser is utilized to convert polyimide into LIG, which requires high temperatures and pressures. The formation of LIG leads to high electrical conductivity [9] because of graphene's large surface area and inherent superior chemical, physical, and electronic qualities [10]. LIG-based biosensors have been reported to be used in many applications, including glucose detection [13], neurotransmitter detection such as dopamine and serotonin [14], as well as protein and biomarker sensing, including cancer biomarkers, folic acids, and DNA methylation [15]. LIG electrochemical sensors can also be used to detect heavy metal ions, such as aluminum, in soil and water samples [16]. LIG's mechanical flexibility and conformity make it a promising material for fabricating wearable and flexible biosensors, which can be integrated into smart textiles or directly applied to the skin for continuous health monitoring. Recent advancements in nicotine detection have focused on the development of electrochemical sensors, particularly using SPE. However, a modification of SPE is needed to enhance the electrochemical sensing capabilities for nicotine detection. However, there are limited studies on nicotine detection using LIG-SPE sensors. Hence, this work aims to investigate the performance of LIG-SPE sensors in nicotine detection at different pH levels. The paper's organization is as follows: Section 2 explains the design concept of a laser-induced graphene screen-printed electrode. Section 3 discusses the materials and methods for simulating and fabricating laser-induced graphene screen-printed electrodes. Section 4 presents the simulation results, measurements, and performance analysis of electrochemical-based laser-induced graphene screen-printed electrodes for nicotine detection. Finally, the conclusion and future work are discussed in Section 5.

## 2. DESIGN CONCEPT OF ELECTROCHEMICAL-BASED LASER-INDUCED GRAPHENE SCREEN PRINTED ELECTRODE

Graphene is a widely used material in various technologies and is typically synthesized through chemical reduction methods like Hummer's method, which involves oxidizing graphite to graphene oxide before converting it to graphene [17]. Traditional methods like chemical vapor deposition (CVD) are surface-based coating techniques commonly used to produce graphene. However, they can be energy-intensive and have environmental concerns due to chemical treatments and toxic by-products [17]. Meanwhile, a single step of direct laser scribing carbonaceous precursors yields LIG, a three-dimensional carbon-based nanomaterial [18]. LIG offers advantages over traditional graphene synthesis methods as it is cost-effective, swift, and environmentally friendly. It does not require aggressive chemical conditions, extreme temperatures, or vacuum, making it sustainable and efficient [18]. Because it can be molded into numerous 3D forms with high surface-to-volume ratios, LIG may be created from various carbon-containing precursors, such as polyimide, wood, or even food. This makes it appropriate for applications like supercapacitors and sensors. [19]. However, the most common substrate used for LIG formation is polyimide substrate [11], [12], [20]. To obtain a 3D porous graphene structure, photochemical and thermal conversion processes from laser irradiation of a polymeric precursor should occur [12]. Thus, a CO2 infrared laser is used for this purpose [9], [21].

The LIG-SPE sensor consists of four layers, starting from the polyimide substrate, followed by LIG electrodes in Layer 1, Ag electric lines in Layer 2, an AgCl reference electrode in Layer 3, and the final layer, the encapsulation layer, as illustrated in Figure 1. Figure 2 (a) shows the cross-sectional view of the LIG-SPE sensor, while Figure 2 (b) shows the detailed dimensions

https://doi.org/10.31436/iiumej.v26i1.3392

of the design in mm. The working electrode and counter electrode were made using LIG fabrication.

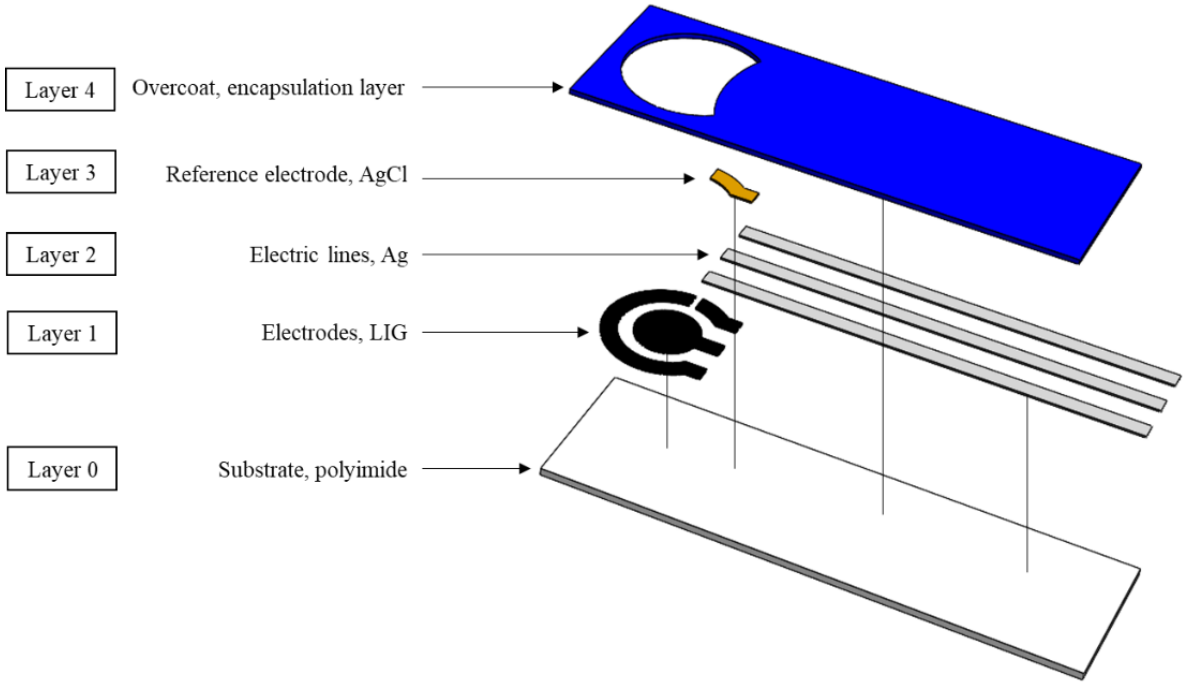


Figure 1. The exploded views of the LIG-SPE design by layers where the working electrode and counter electrode (Layer 1) of the screen-printed electrode were made using LIG fabrication

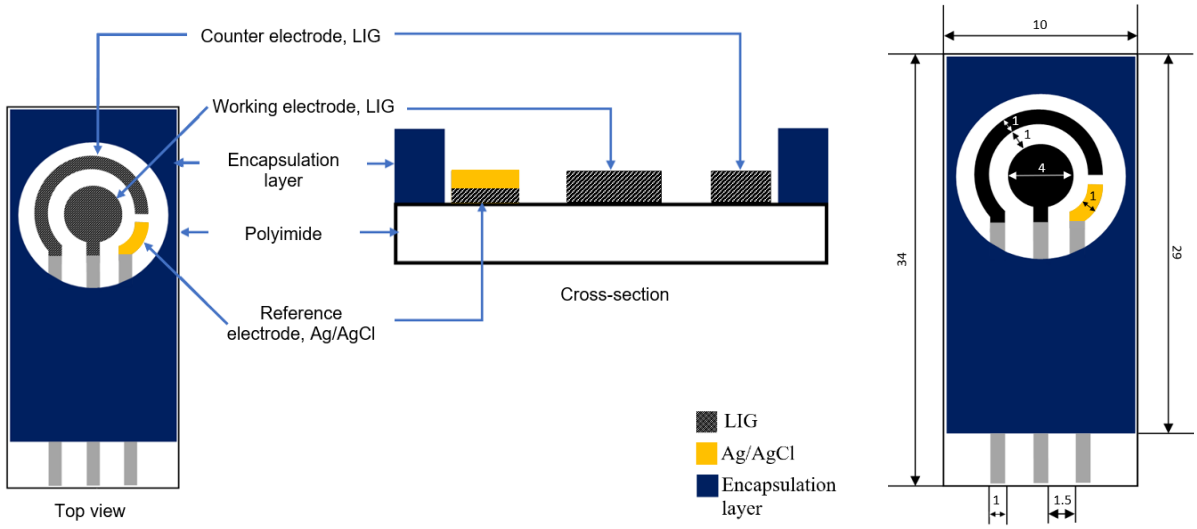


(a) (b)

Figure 2. (a) The cross-section of LIG-SPE showing all layers (b) The dimensions of LIG-SPE in mm

https://doi.org/10.31436/iiumej.v26i1.3392

# 3. MATERIAL AND METHODS

The optimization of laser parameters is vital for LIG fabrication because it determines the quality and properties of the produced graphene. Hence, a finite element simulation was conducted to investigate the effect of laser power on polyimide temperature. The fabrication of LIG-SPE using $CO_2$ laser was later performed with optimal laser parameters.

## 3.1. Finite Element Simulation of Laser Parameters

Numerous variables, including the kind of precursor material, the desired characteristics of the final graphene, and the particular application, contribute to the optimization of laser power. The power required for the LIG process depends on parameters like the material type, the desired graphene quality, the process speed, the laser setup and parameters, and the scale of production [22]. Typically, for the fabrication of LIG, a $CO_2$ laser with powers ranging from a few watts to tens or hundreds of watts is used [23]. The best analytical electrodes were obtained using a 1000 x 1000 CO2 pulse density with a modest, frequent energy input (low laser power) and speed setting. Too much energy input of laser power and laser speed can result in brittle electrodes that would peel off the substrate easily [24]. In the meantime, the substrate was either not carbonized at all or only partially carbonized at high power and speed levels [24].

A finite element simulation is carried out to examine the impact of laser power on the polyimide's temperature. The simulation examined the effect of varying laser power on the polyimide's temperature. The laser strength is adjusted in 1-percent increments between 1% and 5% of 30 W, and the mesh used is in a finer size. Figure 3 (a) shows a circular structure representing the working electrode (WE) of LIG-SPE, while Figure 3(b) shows the mesh of the working electrode with the thickness of the polyimide, 0.1mm.

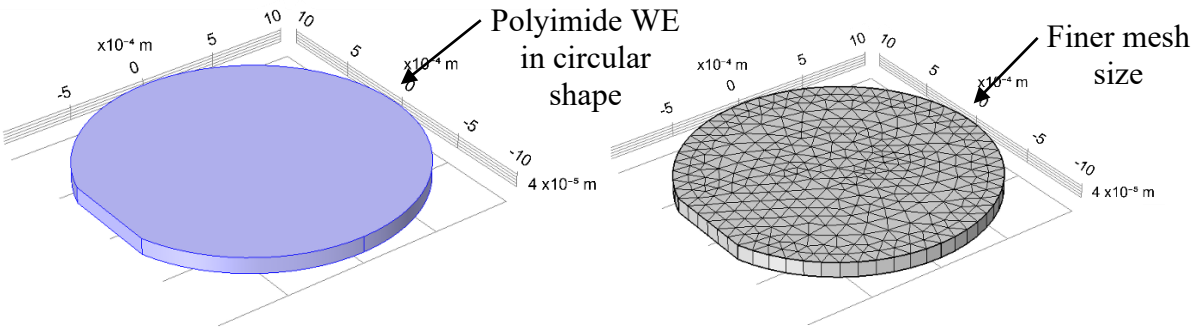


Figure 3. (a) The working electrode (WE) of LIG-SPE
(b) The mesh design of WE uses a finer mesh size

## 3.2. Fabrication of LIG

A $CO_2$ laser is used to fabricate the LIG-SPE sensor because it is good at producing flexible, affordable electrodes on various sustainable and recyclable materials [23]. The $CO_2$ lasers emit infrared light at a wavelength of around 10.6 µm and are known for their high-power output [23]. A CO2 laser's high-power output can produce localized heating on a suitable carbonaceous substrate, like polyimide, which can develop a structure like graphene on the surface of the material [25]. LIG-SPE was fabricated using $CO_2$ laser with laser power parameters 3 W, speed of 13%, and DPI of 1200. The substrate used to produce the LIG-SPE is Kapton or PET. The LIG-SPE consists of four separate layers: LIG serves as the counter and

https://doi.org/10.31436/iiumej.v26i1.3392

working electrode, silver (Ag) serves as a trace, silver-silver chloride (AgCl) serves as the reference electrode, and an encapsulating layer is the last layer. Figure 4(a) depicts the cross-section of the four layers, and Figure 4(b) shows the fabricated LIG-SPE, which was carried out at Jabil Circuit Sdn. Bhd.

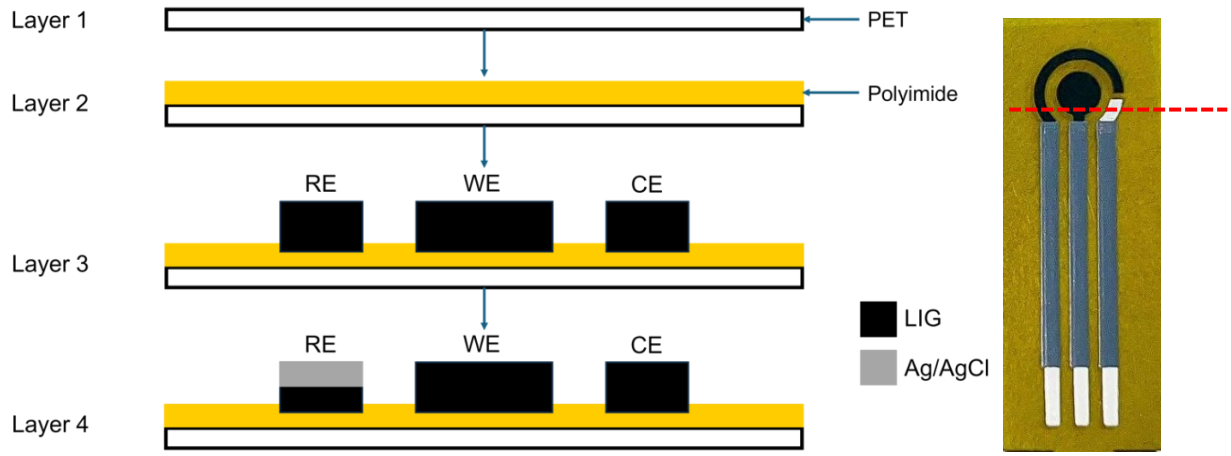


Figure 4. (a) The cross-section view of each layer in the fabrication process of LIG-SPE (b) The fabricated electrode of LIG-SPE

### 3.3. Material Characterization of LIG

Scanning electron microscopy (SEM) was performed to observe the surface morphology of LIG using SEM JEOL JSM-IT100 with an accelerating voltage of 8kV. Energy dispersive X-ray (EDX) integrated with SEM was utilized to provide elemental analysis and chemical characterization of LIG. Raman spectra were analyzed to see the characterization of LIG using the parameters setup of laser power, 1.7 mV, and Raman shift range from 80 $cm^{-1}$ to 3100 $cm^{-1}$.

### 3.4. Experimental Setup for Electrochemical Analysis Performance

Electrochemical testing is carried out to measure the LIG-SPE sensor's performance. Figure 5 illustrates the experimental setup of electrochemical-based LIG-SPE. The LIG-SPE sensor is connected to the PalmSens Emstat Pico Development Kit potentiostat, and electrochemical measurement is analyzed by connecting the potentiostats to the PSTrace software. The measurement set used for the electrochemical analysis performance is a cyclic voltammetry (CV) measurement, starting with the measurement from ferricyanide, [Fe(CN)6]3-/4- and potassium chloride (KCl) solutions to obtain valuable information about the electrochemical behavior of the redox system. A 100 mL of 0.01 M Ferricyanide solution, with 0.1 M of potassium chloride, KCL was prepared for CV measurements at various scan rates from 10 mV/s to 200 mV/s. Once a significant redox peak was shown, the LIG-SPE sensor performance was then tested at various concentrations of nicotine from 20 µM to 100 µM with 3 different phosphate buffer solutions (PBS) of pH-5, pH-7, and pH-9, using CV measurements with scan rate fixed at 50 mV/s.

## 4. RESULTS AND DISCUSSION

This section presents the results and analysis of the simulation and fabrication of LIG-SPE. It also discusses the CV measurements of the fabricated LIG-SPE sensor at various nicotine pH values.

https://doi.org/10.31436/iiumej.v26i1.3392

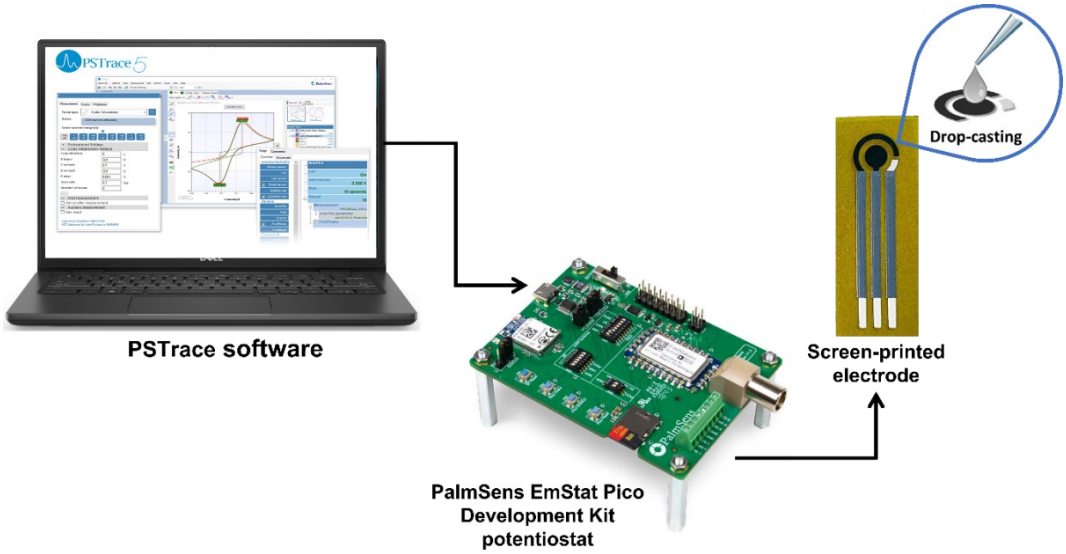


Figure 5. The experimental setup comprises the PalmSens Emstat Pico Development Kit potentiostat, PSTrace software, and a screen-printed electrode.

### 4.1. Simulation Results on the Effect of Laser Parameters for LIG

A laser power in the range of 1% to 5% of 30 W was studied using finite element simulation to investigate its effects on the temperature of polyimide substrate. Figure 6 shows the graph of the polyimide's temperature against time when a laser is fired onto the substrate. The graph shows that the laser power of 1% is the most stable, as the temperature is steadily rising, unlike the other laser powers, which are increasing rapidly. When the laser power increases, the temperature of polyimide also increases. However, a temperature that is too high can destroy the polyimide's surface, affecting the quality of the LIG electrode. A brittle electrode would readily peel off the substrate when the temperature is too high and when there is excessive energy input [26]. Figure 7 (a) shows the temperature of the polyimide substrate when the laser beam was irradiated onto the substrate, showing the heating profile on the surface with the highest temperature observed at the center. Figure 7 (b) shows the thermal contour of the polyimide when the laser beam was irradiated, indicating the temperature was distributed through the substrate thickness. This shows the laser's capability to heat the polyimide substrate to induce graphene at a laser power of 1%.

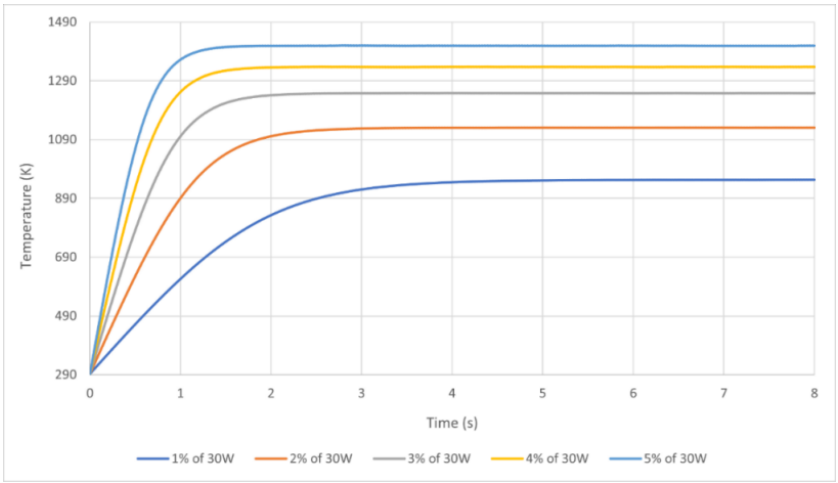


Figure 6. Graph of temperature of polyimide versus time based on the different laser powers (1%, 2%, 3%, 4%, and 5% of 30 W)

https://doi.org/10.31436/iiumej.v26i1.3392

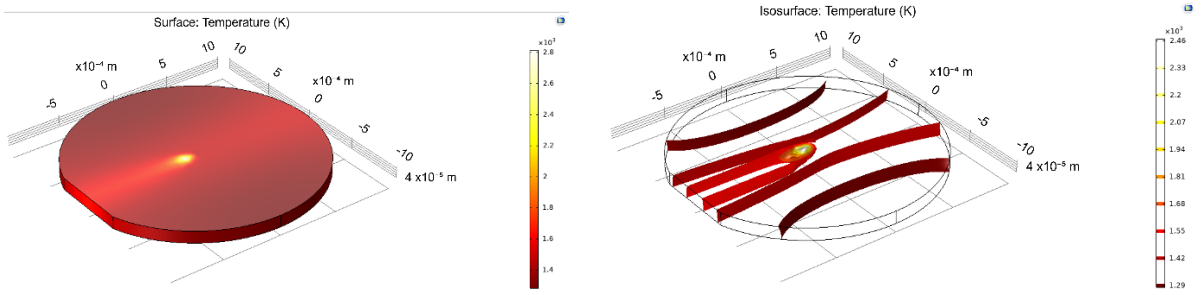


(a) (b)

Figure 7. (a) The temperature of the polyimide (b) The thermal contour of the polyimide

### 4.2. Material Characterization of LIG

After LIG-SPE was fabricated, material characterizations were carried out to confirm the formation of LIG on the polyimide substrate. Figure 8 (a) shows the SEM image of the LIG-SPE cross-section displaying two distinct layers of LIG (thickness of 176.018 µm) and polyimide (thickness of 142.004 µm). Figures 8 (b) and (c) display the SEM images of LIG-SPE with a porous structure, which can be clearly visible at 1k and 3k magnifications, respectively.

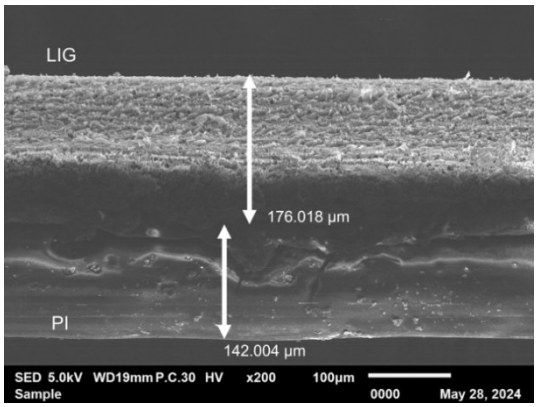


(a)

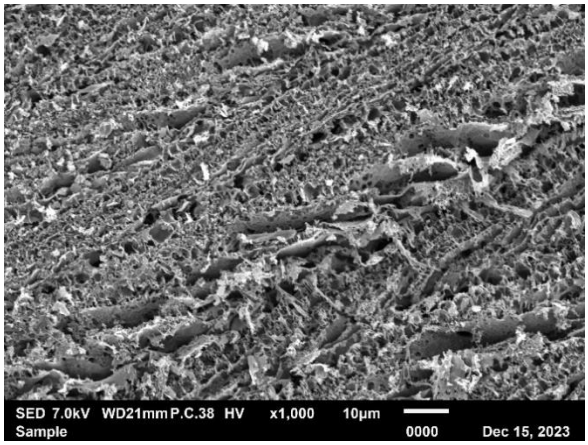


(b)

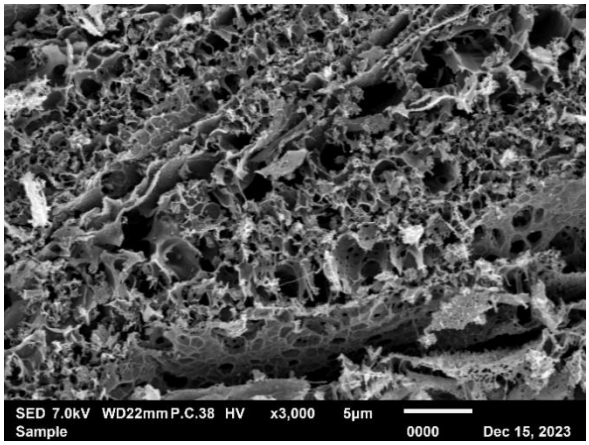


(c)

Figure 8. (a) SEM image of LIG-SPE cross-section (b) SEM images of LIG-SPE showing the porous structure at 1k magnification (c) at 3k magnification

https://doi.org/10.31436/iiumej.v26i1.3392

The LIG porous structure is similar to the surface morphology results reported by Kim et al. [27]. Due to a carbon network resembling graphene, LIG's porous structure allows for an extremely large surface area-to-volume ratio [16]. This property renders LIG electrically conductive [9]. EDX spectra of LIG that can be seen in Figure 9 show strong peaks corresponding to carbon (C) and oxygen (O), indicating the presence of graphene-based structure via laser irradiation. Table 1 presents the map sum spectrum of C and O weight percentage values for LIG, which conforms to the compositions described in [32], [33].

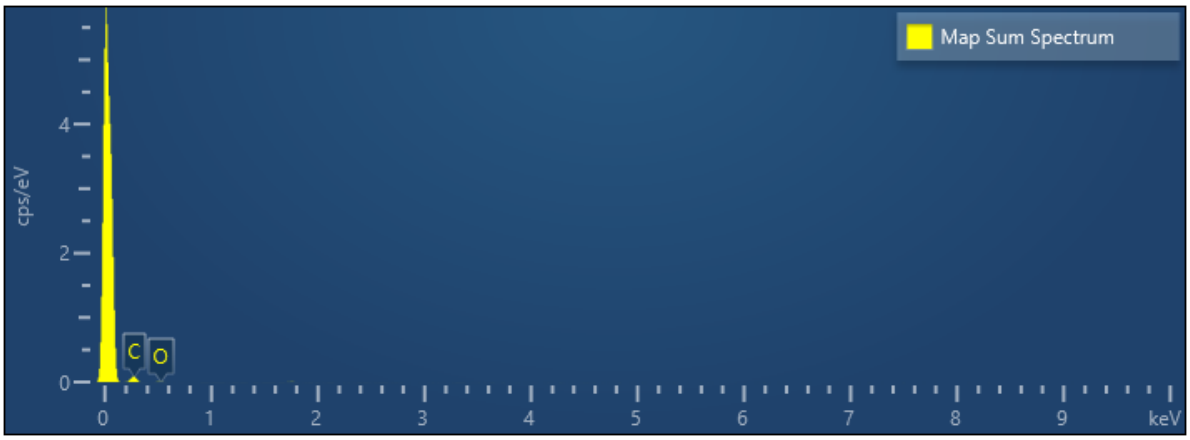


Figure 9. The map sum spectrum of LIG showing carbon (C) and oxygen (O) peaks

Table 1. Map sum spectrum of LIG-SPE

| Element | Line Type | Weight % | Weight % Sigma | Atomic % |
|---|---|---|---|---|
| **C** | K series | 90.31 | 2.78 | 92.55 |
| **O** | K series | 9.69 | 2.78 | 7.45 |
| **Total** | | 100.00 | | 100.00 |

The analysis of Raman spectra is important to analyze the presence of graphene in LIG-SPE. Three principal peaks are typically observed for graphene: the D peak at 1308 $cm^{-1}$, the G peak at 1595 $cm^{-1}$, and the 2D peak at 2612 $cm^{-1}$, as shown in Figure 10. These peaks correspond well with the peaks of ~1330 $cm^{-1}$ (D peak), ~1580 $cm^{-1}$ (G peak), and ~2660 $cm^{-1}$ (2D peak) as reported in [28].

### 4.3. Electrochemical Measurement

The electrochemical measurement was conducted to evaluate the LIG-SPE sensor's performance in nicotine detection. A CV measurement of 0.01 M [Fe(CN)6]3-/4- with 0.1 M KCL at various scan rates from 10 mV/s to 200 mV/s was carried out to observe the redox peak on the LIG-SPE sensor. The CV measurement was then continued to check the sensor's performance by using various nicotine concentrations from 20 µM to 100 µM with 3 different phosphate buffer solutions (PBS) of pH 5, pH 7, and pH 9 at a fixed scan rate of 50 mV/s.

https://doi.org/10.31436/iiumej.v26i1.3392

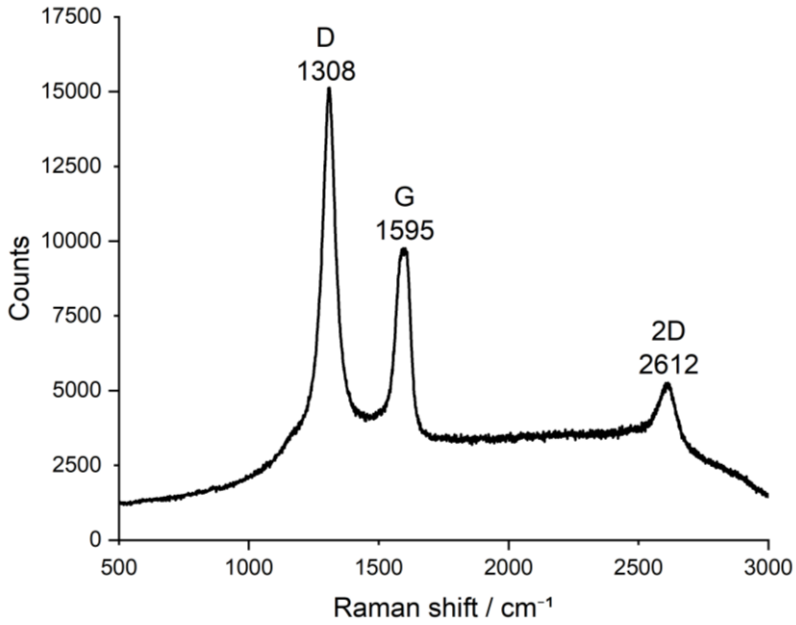


Figure 10. Raman spectroscopy of the LIG-SPE displaying the graphene D, G, and 2D peaks

### *4.3.1. Effect of Different Scan Rates*

Cyclic voltammetry (CV) is an electroanalytical technique used to study the electrochemical properties of a system by applying a linearly varying potential to an electrode immersed in an electrolyte solution and measuring the resulting current [29]. Increasing the scan rate can make an irreversible system appear more reversible by competing with the timescale of the follow-up chemical reaction [29]. At very slow scan rates, an irreversible system may show no peaks at all, while at faster scan rates, the peaks become more pronounced [29]. The CV measurements of LIG-SPE were performed using 0.1 M ferricyanide and 0.1 M KCL at various scan rates from 10 mV/s to 200 mV/s. The values from the LIG-SPE sensor at different scan rates are displayed in Figure 11. The graph shows distinct oxidation and reduction peaks, indicating that the anodic and cathodic currents increase with the scan rates.

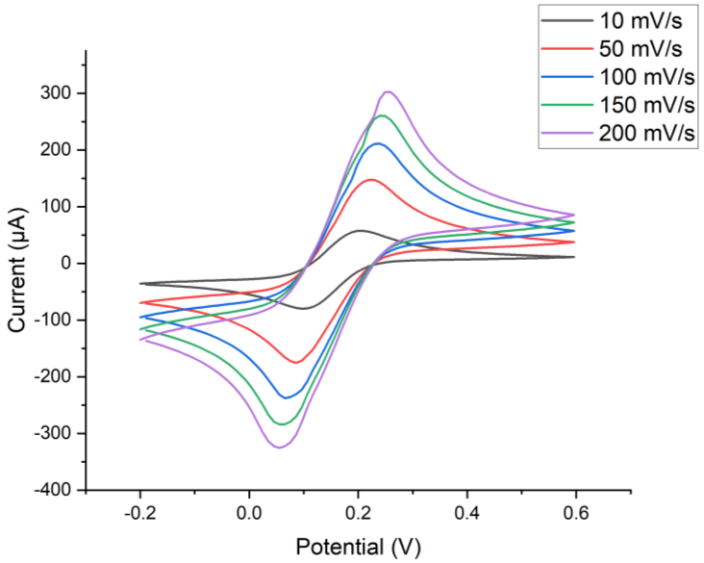


Figure 11. CV measurements for LIG-SPE at various scan rates from 10 mV/s to 200 mV/s

https://doi.org/10.31436/iiumej.v26i1.3392

### *4.3.2. Effect of Different pH Values on Nicotine Detection*

CV measurements were performed using different nicotine concentrations ranging from 20 µM to 100 µM with three different PBS pH values: pH 5, pH 7, and pH 9 at a fixed scan rate of 50 mV/s. Figure 16 displays the CV readings obtained by the LIG-SPE sensor at different nicotine concentrations for PBS pH 5, pH 7, and pH 9. In general, it can be observed that LIG-SPE can effectively detect nicotine in a PBS solution with the maximum oxidation peak at the highest concentration of 100 µM. Figure 12 shows the graph of the oxidation peak versus nicotine concentration for PBS at pH 5, pH 7, and pH 9. The calibration curve, $R^2$, and limit of detection, LOD for pH 5 are 0.9988 and 4.2183 µM. For pH 7, the values are 0.9912 and 11.3892 µM; for pH 9, the R2 and LOD values are 0.998 and 5.43399 µM, respectively. To determine how well the calibration curve value, $R^2$ was established, $R^2$ values above 0.990 generally indicate that calculated unknown values will be close to accurate across the calibration curve [30]. These values are summarized in Table 2.

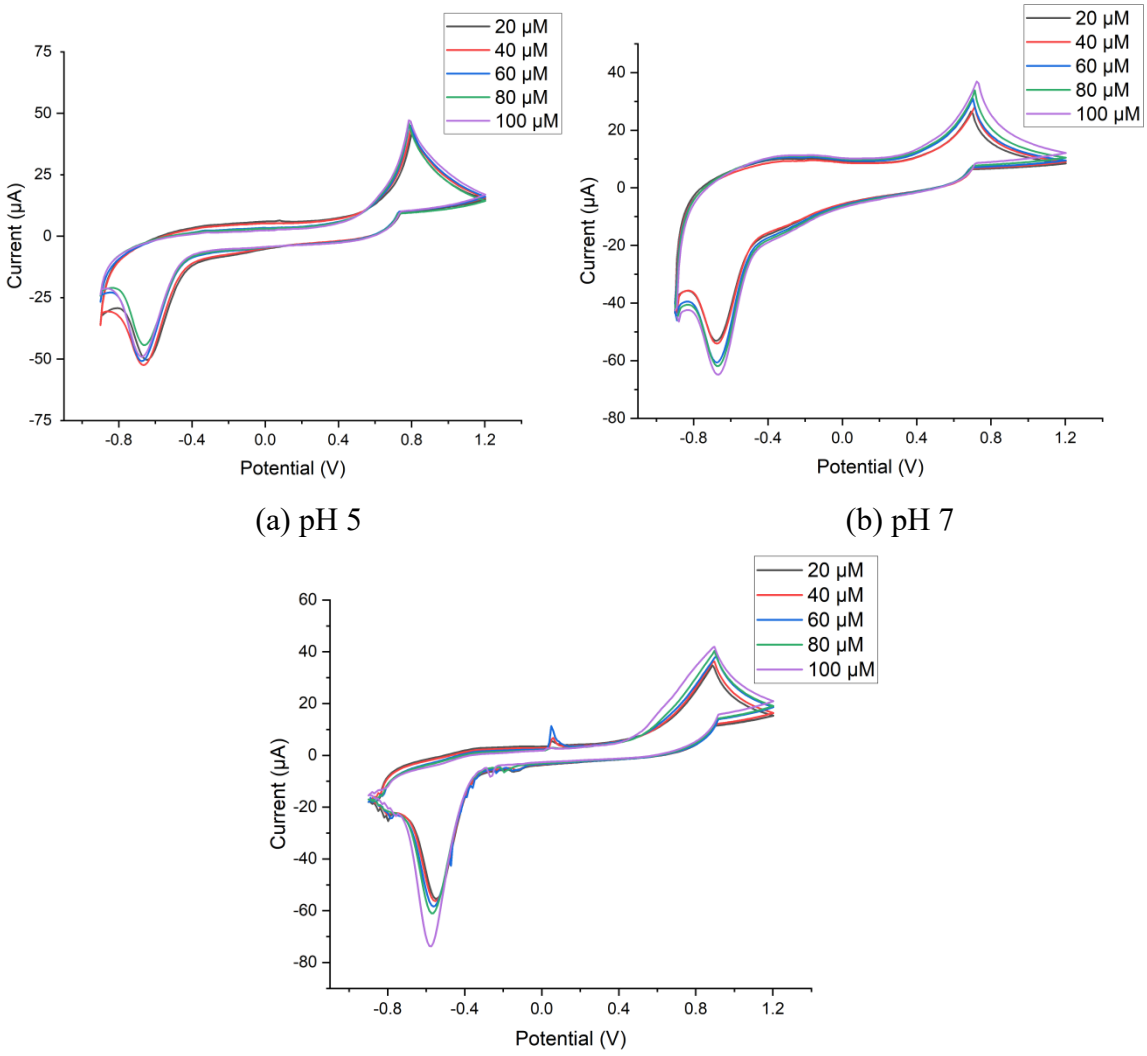


(a) pH 5

(b) pH 7

(c) pH 9

Figure 12. Current vs. potential graph of different concentrations of nicotine for (a) PBS pH 5, (b) pH 7, and (c) pH 9

https://doi.org/10.31436/iiumej.v26i1.3392

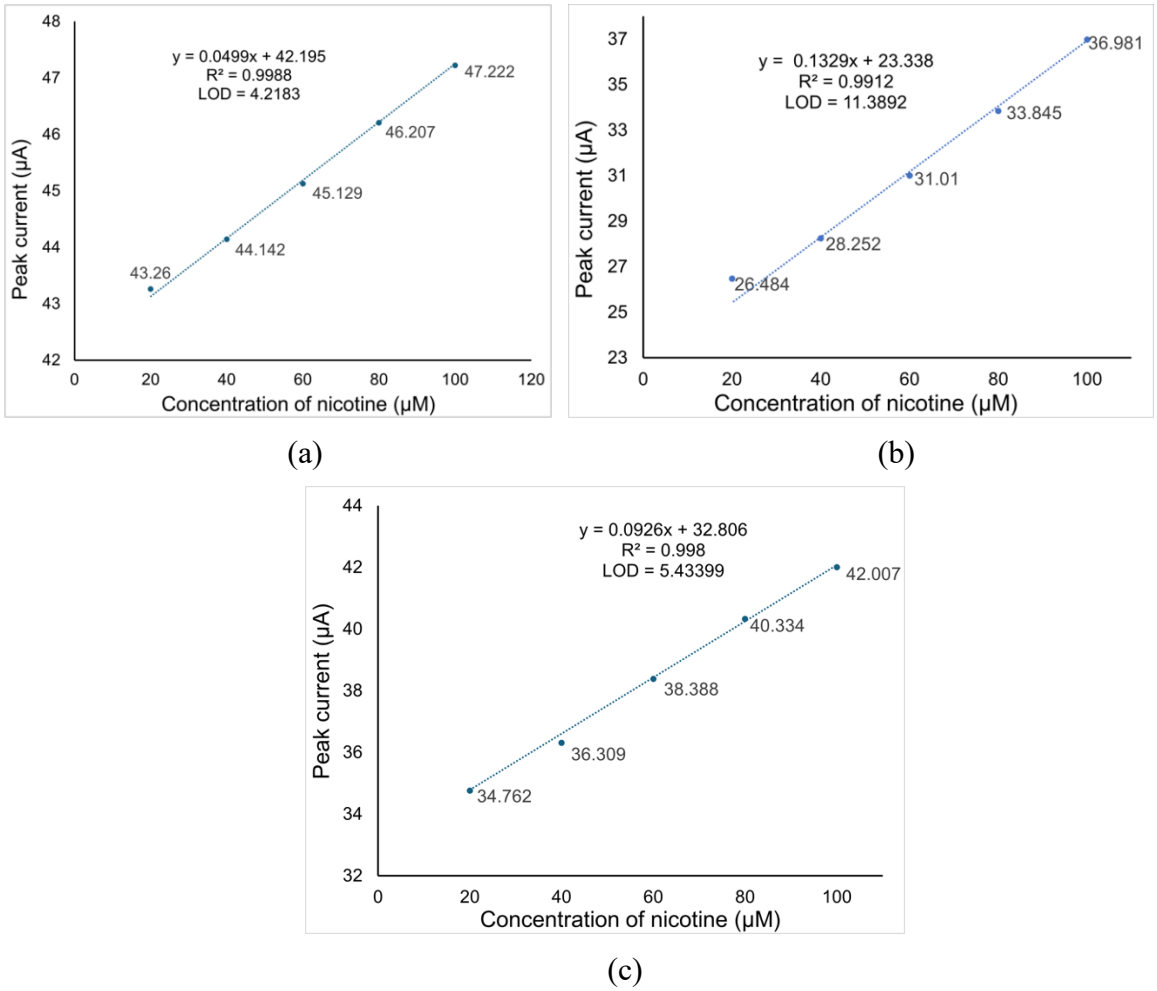


Figure 13. Oxidation peak vs. concentration of nicotine for PBS at (a) pH 5, (b) pH 7, and (c) pH 9

Table 2. Value of $R^2$ and LOD at different pH values

| pH value for PBS | $R^2$ | LOD (μM) |
|---|---|---|
| pH 5 | 0.9988 | 4.2183 |
| pH 7 | 0.9912 | 11.3892 |
| pH 9 | 0.9980 | 5.43399 |

Table 2 shows the values of the LIG-SPE's calibration curve, $R^2$, and LOD on detecting nicotine at different pH values. Based on the table shows that nicotine at pH 5 has the highest $R^2$ value of 0.9988 and the lowest LOD of 4.22 μM. This observation can be explained by considering that most sensors efficiently detect the predominant species of monoprotonated nicotine ions. Because nicotine is a weak base, its presence in the environment might cause it to ionize or non-ionize [31], [32]. Nicotine is mainly ionized in acidic environments and predominantly in its unionized form in alkaline environments [33]. At pH levels below 3, the predominant species is the diprotonated nicotinium ion ($NicH^{2+}$), where nicotine has gained 2 extra protons, resulting in doubly positively charged species [33]. The sensor does not efficiently sense diprotonated nicotine, as the potential decreases due to the formation of the species at low pH levels. However, at pH levels between 3.5 and 6.5, the predominant species is the monoprotonated nicotine ion ($NicH^{+}$), where nicotine has gained one extra proton,

resulting in a positively charged species efficiently sensed by most sensors [33]. Hence, sensors display optimal sensitivity within this pH range. As for the above pH 7, the predominant species is the non-protonated nicotine base, which is not associated with any additional protons, making it electrically neutral [33]. Nicotine is not ionized and does not carry a charge. Consequently, the LIG-SPE sensor shows lower sensitivity at higher pH levels. Table 3 summarizes the performance of LIG-SPE for nicotine sensors and comparison with previous works. This work contributes to the LIG-SPE's ability to detect nicotine without surface modification with good linearity and low detection limits.

Table 3. Summary of the performance of LIG-SPE for nicotine sensor and comparison with other previous works

| Type of sensor | Surface modification | $R^2$ | LOD | Ref |
|---|---|---|---|---|
| **SPCE** | β-CB grafted | * | 50.80 µM | [34] |
| | FC-MWCNTs | * | 4.25 µM | [35] |
| | AuNPs | 0.9920 | 8.30 mM | [36] |
| **LIG-SPE** | - | 0.9988 | 4.22 µM | This work (at pH 5 PBS solution) |

* Not specified

## 5. CONCLUSION

In summary, we have demonstrated the simulation and fabrication of laser-induced graphene screen-printed electrodes for nicotine detection. The finite element simulation result shows that the laser power of 1% is the most stable, as the temperature is steadily rising, unlike the other laser powers, which are increasing rapidly. When the laser power increases, the temperature of polyimide also increases. LIG fabrication was performed at the working and counter electrode of LIG-SPE using the optimum laser power based on the simulation results. Based on the electrochemical measurements, nicotine with PBS pH 5 solution was found to yield the optimum result, with the value obtained for the calibration curve. The $R^2$ value was the highest at 0.9988, and the LOD value of 4.2183 among all. Therefore, laser-induced graphene (LIG) electrochemical sensors show great potential for detecting nicotine.

## ACKNOWLEDGEMENT

This work is fully supported by the Ministry of Higher Education (MOHE) Fundamental Research Grant Scheme FRGS21-239-0848 (FRGS/1/2021/TK0/UIAM/02/9).

## REFERENCES

[1] A. García-Miranda Ferrari, S. J. Rowley-Neale, and C. E. Banks, "Screen-printed electrodes: Transitioning the laboratory in-to-the field," Aug. 01, 2021, *Elsevier B.V.* doi: 10.1016/j.talo.2021.100032.

[2] E. Mehmeti, T. Kilic, C. Laur, and S. Carrara, "Electrochemical determination of nicotine in smokers' sweat," *Microchemical Journal*, vol. 158, p. 105155, Nov. 2020, doi: 10.1016/J.MICROC.2020.105155.

[3] A. Hayat and J. L. Marty, "Disposable screen printed electrochemical sensors: Tools for environmental monitoring," Jun. 13, 2014, *MDPI AG*. doi: 10.3390/s140610432.

[4] Z. Taleat, A. Khoshroo, and M. Mazloum-Ardakani, "Screen-printed electrodes for biosensing: A review (2008-2013)," 2014, *Springer-Verlag Wien*. doi: 10.1007/s00604-014-1181-1.
[5] A. V. Shokurov and C. Menon, "Laser-Induced Graphene Electrodes for Electrochemistry Education and Research," *J Chem Educ*, Jun. 2022, doi: 10.1021/acs.jchemed.2c01237.
[6] S. Michalkiewicz, A. Skorupa, and M. Jakubczyk, "Carbon Materials in Electroanalysis of Preservatives: A Review.," *Materials (Basel)*, vol. 14, no. 24, Dec. 2021, doi: 10.3390/ma14247630.
[7] M. Zamani, C. M. Klapperich, and A. L. Furst, "Recent advances in gold electrode fabrication for low-resource setting biosensing.," *Lab Chip*, vol. 23, no. 5, pp. 1410–1419, Mar. 2023, doi: 10.1039/d2lc00552b.
[8] J. Edgington, A. Deberghes, and L. C. Seitz, "Glassy Carbon Substrate Oxidation Effects on Electrode Stability for Oxygen Evolution Reaction Catalysis Stability Benchmarking," *ACS Appl Energy Mater*, vol. 5, no. 10, pp. 12206–12218, Oct. 2022, doi: 10.1021/acsaem.2c01690.
[9] J. Lin *et al.*, "Laser-induced porous graphene films from commercial polymers," *Nat Commun*, vol. 5, 2014, doi: 10.1038/ncomms6714.
[10] L. Huang, J. Su, Y. Song, and R. Ye, "Laser-Induced Graphene: En Route to Smart Sensing," Aug. 01, 2020, *Springer*. doi: 10.1007/s40820-020-00496-0.
[11] A. R. Cardoso *et al.*, "Molecularly-imprinted chloramphenicol sensor with laser-induced graphene electrodes," *Biosens Bioelectron*, vol. 124–125, pp. 167–175, Jan. 2019, doi: 10.1016/j.bios.2018.10.015.
[12] F. M. Vivaldi *et al.*, "Three-Dimensional (3D) Laser-Induced Graphene: Structure, Properties, and Application to Chemical Sensing," Jul. 07, 2021, *American Chemical Society*. doi: 10.1021/acsami.1c05614.
[13] K. Y. Lau and J. Qiu, "Broad applications of sensors based on laser-scribed graphene," *Light Sci Appl*, vol. 12, no. 1, p. 168, Jul. 2023, doi: 10.1038/s41377-023-01210-6.
[14] Y. Guo, C. Zhang, Y. Chen, and Z. Nie, "Research Progress on the Preparation and Applications of Laser-Induced Graphene Technology.," *Nanomaterials (Basel)*, vol. 12, no. 14, Jul. 2022, doi: 10.3390/nano12142336.
[15] G. Bhattacharya *et al.*, "Disposable Paper-Based Biosensors: Optimizing the Electrochemical Properties of Laser-Induced Graphene," *ACS Appl Mater Interfaces*, vol. 14, no. 27, pp. 31109–31120, Jul. 2022, doi: 10.1021/acsami.2c06350.
[16] Z. Wan, N. T. Nguyen, Y. Gao, and Q. Li, "Laser induced graphene for biosensors," Sep. 01, 2020, *Elsevier B.V.* doi: 10.1016/j.susmat.2020.e00205.
[17] N. Dixit and S. P. Singh, "Laser-Induced Graphene (LIG) as a Smart and Sustainable Material to Restrain Pandemics and Endemics: A Perspective," *ACS Omega*, vol. 7, no. 6, pp. 5112–5130, Feb. 2022, doi: 10.1021/acsomega.1c06093.
[18] A. Velasco, Y. K. Ryu, A. Hamada, A. de Andrés, F. Calle, and J. Martinez, "Laser-Induced Graphene Microsupercapacitors: Structure, Quality, and Performance," *Nanomaterials*, vol. 13, no. 5, Mar. 2023, doi: 10.3390/nano13050788.
[19] W. Ma, J. Zhu, Z. Wang, W. Song, and G. Cao, "Recent advances in preparation and application of laser-induced graphene in energy storage devices," Dec. 01, 2020, *Elsevier Ltd*. doi: 10.1016/j.mtener.2020.100569.
[20] R. Ye, D. K. James, and J. M. Tour, "Laser-Induced Graphene: From Discovery to Translation," Jan. 04, 2019, *Wiley-VCH Verlag*. doi: 10.1002/adma.201803621.
[21] R. Ye, D. K. James, and J. M. Tour, "Laser-Induced Graphene," *Acc Chem Res*, vol. 51, no. 7, pp. 1609–1620, Jul. 2018, doi: 10.1021/acs.accounts.8b00084.
[22] M. Fan *et al.*, "CO2 Laser-Induced Graphene with an Appropriate Oxygen Species as an Efficient Electrocatalyst for Hydrogen Peroxide Synthesis," *Chemistry*, vol. 28, no. 60, Oct. 2022, doi: 10.1002/CHEM.202201996.
[23] T. Pinheiro *et al.*, "Influence of CO2 laser beam modelling on electronic and electrochemical properties of paper-based laser-induced graphene for disposable pH electrochemical sensors," *Carbon Trends*, vol. 11, Jun. 2023, doi: 10.1016/j.cartre.2023.100271.

[24] A. Behrent, C. Griesche, P. Sippel, and A. J. Baeumner, "Process-property correlations in laser-induced graphene electrodes for electrochemical sensing," *Microchimica Acta*, vol. 188, no. 5, May 2021, doi: 10.1007/s00604-021-04792-3.
[25] M. Liu, J. N. Wu, and H. Y. Cheng, "Effects of laser processing parameters on properties of laser-induced graphene by irradiating CO2 laser on polyimide," *Sci China Technol Sci*, vol. 65, no. 1, pp. 41–52, Jan. 2022, doi: 10.1007/s11431-021-1918-8.
[26] A. Behrent, C. Griesche, P. Sippel, and A. J. Baeumner, "Process-property correlations in laser-induced graphene electrodes for electrochemical sensing," *Microchimica Acta*, vol. 188, no. 5, May 2021, doi: 10.1007/s00604-021-04792-3.
[27] Y. Il Kim, M. K. Ro, U. Y. Paek, M. K. Sok, and H. Pak, "Maximum Temperature Determination for Stable Operation of Direct-Write Laser-Induced Graphene Heater on Exposed Polyimide Substrate through Numerical Simulation." [Online]. Available: https://ssrn.com/abstract=4254595
[28] J. H. Han, S. Hyun Park, S. Kim, and J. Jungho Pak, "A performance improvement of enzyme-based electrochemical lactate sensor fabricated by electroplating novel PdCu mediator on a laser induced graphene electrode," *Bioelectrochemistry*, vol. 148, Dec. 2022, doi: 10.1016/j.bioelechem.2022.108259.
[29] N. Elgrishi, K. J. Rountree, B. D. McCarthy, E. S. Rountree, T. T. Eisenhart, and J. L. Dempsey, "A Practical Beginner's Guide to Cyclic Voltammetry," *J Chem Educ*, vol. 95, no. 2, pp. 197–206, Feb. 2018, doi: 10.1021/acs.jchemed.7b00361.
[30] "Calibration Part II – Evaluating Your Curves - Cannabis Industry Journal." Accessed: Jun. 22, 2023. [Online]. Available: https://cannabisindustryjournal.com/column/calibration-part-ii-evaluating-your-curves/
[31] S. L. Tomar and J. E. Henningfield, "Review of the evidence that pH is a determinant of nicotine dosage from oral use of smokeless tobacco.," *Tob Control*, vol. 6, no. 3, pp. 219–25, Sep. 1997, doi: 10.1136/tc.6.3.219.
[32] O. Alharbi, Y. Xu, and R. Goodacre, "Simultaneous multiplexed quantification of nicotine and its metabolites using surface enhanced Raman scattering," *Analyst*, vol. 139, no. 19, pp. 4820–4827, Aug. 2014, doi: 10.1039/C4AN00879K.
[33] A. E. G. E. Amr, A. H. Kamel, A. A. Almehizia, A. Y. A. Sayed, E. A. Elsayed, and H. S. M. Abd-Rabboh, "Paper-Based Potentiometric Sensors for Nicotine Determination in Smokers' Sweat," *ACS Omega*, vol. 6, no. 17, pp. 11340–11347, May 2021, doi: 10.1021/acsomega.1c00301.
[34] S. K. Ali *et al.*, "Determination of Caffeic acid in Cigarette Smoke and Urine by Electrochemical Methods Using Supramolecular Electroactive Materials grafted in Screen Printed Carbon Electrode," *Oriental Journal Of Chemistry*, vol. 39, no. 6, pp. 1461–1468, Dec. 2023, doi: 10.13005/ojc/390606.
[35] Z. Su *et al.*, "A smart portable electrochemical sensor based on electrodeposited ferrocene-functionalized multiwalled carbon nanotubes for *in vitro* and *in vivo* detection of nicotine in tobacco samples," *New Journal of Chemistry*, vol. 48, no. 8, pp. 3370–3380, Feb. 2024, doi: 10.1039/D3NJ05035A.
[36] A. Aiman Ali Amran *et al.*, "Gold Nanoparticle Deposited on Screen-Printed Carbon Electrode for Electrochemical Detection of Nicotine in E-cigarette," 2023.

https://doi.org/10.31436/iiumej.v26i1.3407

# DEVELOPMENT OF 3D PRINTED SERPENTINE FLUIDIC CHANNEL INTEGRATED WITH HEATING ELEMENT FOR LOOP-MEDIATED ISOTHERMAL AMPLIFICATION (LAMP) PROCESS

**MUHAMMAD KHAIRUL FAISAL MUHAMAD ATAN[1], ROSMINAZUIN AB RAHIM[1*], ANIS NURASHIKIN NORDIN[1], ALIZA AINI MD RALIB[1], TEDDY SURYA GUNAWAN[2], ZAINIHARYATI MOHD ZAIN[3]**

*[1]VLSI-MEMS Research Unit, Department of Electrical and Computer Engineering, Engineering Faculty, International Islamic University Malaysia (IIUM), Kuala Lumpur 53100, Malaysia*

*[2]Electrical and Computer Engineering Department, International Islamic University Malaysia (IIUM), Kuala Lumpur 53100, Federal Territory of Kuala Lumpur, Malaysia*

*[3]Electrochemical Material and Sensor (EMaS), Faculty of Applied Sciences, Universiti Teknologi MARA (UiTM), 40450 Shah Alam, Selangor, Malaysia*

**Corresponding author: rosmi@iium.edu.my*

*(Received: 17 August 2024; Accepted: 24 Sep 2024; Published online: 10 January 2025)*

***ABSTRACT:*** DNA-based point-of-care (POC) diagnostics require rapid, accurate, and portable platforms for detection of infectious diseases. This can be achieved by incorporating a loop-mediated isothermal amplification (LAMP) process for DNA amplification into the system. LAMP offers a promising in-situ solution, but maintaining consistent reaction conditions, such as a constant temperature, specifically at 65°C for 35 minutes to complete the LAMP process, remains a critical challenge. Therefore, this work presents the development of a 3D-printed serpentine fluidic channel integrated with a heating element for DNA amplification through the LAMP process. To assess their heating capabilities, heating testing was initially performed on several commercially available heating elements (Heater Cartridge, PTC 140, and PTC 230). PTC 230 heating element was chosen for its rapid heating performance (reaching 65°C in 54.78 seconds). Later, three serpentine fluidic channels of different diameters (1.6 mm, 1.7 mm, and 1.8 mm) were fabricated using a Masked Stereolithography Apparatus (MSLA) 3D printer. The developed portable LAMP device consisting of a fabricated serpentine fluidic channel on a PTC 230 heating element allows the sample to be heated at 65°C for 35 minutes. Sample flow inside each serpentine fluidic channel was measured and compared with the expected flow time of 35 minutes. It was observed that the fluidic channel with a 1.6 mm diameter shows the closest value of 34.33 minutes (percentage deviation of 1.91%) as compared to the other two channels. The optimized fluidic channel design (channel diameter of 1.6 mm) coupled with the rapid heating performance of the PTC 230 element (reaching 65°C in 54.78 seconds) for a portable LAMP device represents a significant step towards developing rapid, accurate, and portable POC diagnostic tools.

***ABSTRAK*:** Diagnostik point-of-care (POC) berasaskan DNA memerlukan platform yang pantas, tepat, dan mudah alih untuk mengesan penyakit berjangkit. Ini boleh dicapai dengan menggabungkan proses penguatan isoterma bersandar gelung (LAMP) ke dalam sistem untuk penguatan DNA. LAMP menawarkan penyelesaian in-situ yang menjanjikan, tetapi mengekalkan keadaan reaksi yang konsisten, seperti suhu tetap pada 65°C selama 35 minit untuk menyelesaikan proses LAMP, kekal sebagai cabaran kritikal. Oleh itu, kajian ini membentangkan pembangunan saluran bendalir berlingkar 3D yang dicetak dengan integrasi

elemen pemanas untuk penguatan DNA melalui proses LAMP. Untuk menilai keupayaan pemanasannya, ujian pemanasan dijalankan pada beberapa elemen pemanas komersial yang tersedia (Heater Cartridge, PTC 140, dan PTC 230). Elemen pemanas PTC 230 dipilih kerana prestasi pemanasannya yang pantas (mencapai 65°C dalam 54.78 saat). Selepas itu, tiga saluran bendalir berlingkar dengan diameter berbeza (1.6 mm, 1.7 mm, dan 1.8 mm) telah dihasilkan menggunakan pencetak 3D Masked Stereolithography Apparatus (MSLA). Peranti LAMP mudah alih yang dibangunkan, terdiri daripada saluran bendalir berlingkar yang dihasilkan di atas elemen pemanas PTC 230, membolehkan sampel dipanaskan pada suhu 65°C selama 35 minit. Aliran sampel di dalam setiap saluran bendalir berlingkar diukur dan dibandingkan dengan masa aliran yang dijangkakan selama 35 minit. Didapati bahawa saluran bendalir dengan diameter 1.6 mm menunjukkan nilai yang paling hampir iaitu 34.33 minit (peratusan sisihan 1.91%) berbanding dua saluran lain. Reka bentuk saluran bendalir yang dioptimumkan (diameter saluran 1.6 mm) digabungkan dengan prestasi pemanasan pantas elemen PTC 230 (mencapai 65°C dalam 54.78 saat) untuk peranti LAMP mudah alih mewakili langkah signifikan ke arah pembangunan alat diagnostik POC yang pantas, tepat, dan mudah alih.

***KEYWORDS:*** *3D printing, fluidic channel, heating element, loop-mediated isothermal amplification (LAMP)*

# 1. INTRODUCTION

Rapid and accurate DNA-based point-of-care diagnostics are essential for effectively managing infectious diseases. Isothermal nucleic acid amplification techniques, such as loop-mediated isothermal amplification (LAMP), are frequently used to detect various molecules, including RNA, DNA, and proteins in infectious diseases [1]. Unlike the gold-standard polymerase chain reaction (PCR), LAMP provides faster and simpler alternatives, making them well-suited for use in resource-limited settings [2, 3]. Although LAMP holds promise for portable diagnostics, challenges persist in fulfilling its requirements, such as managing small liquid volumes and maintaining a consistent heating temperature. For example, to detect the COVID-19 virus, the LAMP process must maintain a constant temperature of 65°C for 35 minutes to amplify the DNA [4]. The virus can be detected using a portable potentiostat by amplifying the targeted genetic material of DNA in a fluidic sample [4].

Fluidics are crucial in analytical chemistry because they offer advantages in reagent consumption, waste reduction, process integration, and cost efficiency. Previous researchers have developed a microfluidic-based nucleic acid detection platform that uses circular reaction chambers for the LAMP process [5–8]. Lin et al. developed a chip that can perform multiplex testing with three microchannels and 18 circular chambers and is powered by capillary force, eliminating the need for valves or pumps [5]. In another work, Ma et al. presented a self-driven microfluidic chip using digital LAMP for rapid and automated DNA quantification, achieving a 30-minute amplification with an 11-copy limit of detection [6]. Yu et al. introduce a self-partitioning SlipChip (sp-SlipChip) microfluidic device for a robust droplet generation in digital LAMP, enabling point-of-care quantitative analysis of human papillomavirus (HPV) DNA [7]. Another work reported by Sun et al. demonstrated a smartphone-integrated point-of-care system for rapid and specific detection of live viruses in nasal swab samples using LAMP on a microfluidic chip, achieving accurate diagnoses with a limit of detection comparable to traditional PCR tests in about 30 minutes [8]. The mentioned research works have demonstrated the integration of microfluidic devices for the LAMP process. However, most developed microfluidic devices utilize complex fabrication methods, limited design flexibility, and material constraints [9].

https://doi.org/10.31436/iiumej.v26i1.3407

There is growing interest in exploring alternative fabrication techniques to address these limitations. 3D printing is identified as a promising alternative to developing microfluidic devices due to its simpler fabrication method, cost-effectiveness, and customizable fluidic channels [10]. In addition, testing-based optimization is feasible with 3D printing because designs can be easily modified and reprinted [11]. Furthermore, 3D printed devices can be produced without a cleanroom environment, and most importantly, 3D printing is inexpensive because the only consumables required is the filament [12]. Lastly, 3D printing fully utilizes all three dimensions in device architecture, enabling the development of innovative and unique capabilities [13]. 3D printing is a method of fabricating layer by layer consisting of three main stages. The first stage involves designing the structure using computer-aided design (CAD) software and exporting the design in stereolithography (STL) format. The second stage involves using slicer software to convert the STL file into G-code, which is tailored to the specific settings of the 3D printer. The third stage is the actual 3D printing process, where the printer uses the G-code to construct the object layer by layer according to its resolution. Various 3D printing methods are available, which include fused deposition modeling (FDM), stereolithography (SLA), digital light processing (DLP), and selective laser sintering (SLS).

Therefore, this work presents the development of a 3D-printed serpentine fluidic channel integrated with a heating element for DNA amplification through the LAMP process. Integrating a 3D-printed fluidic channel offers advantages in terms of design flexibility, rapid prototyping, and potential cost reduction compared to traditional microfabrication techniques [14]. The combination of a heating element and a fluidic channel system in a portable LAMP device allows all the necessary processes (DNA amplification, detection, and quantification) to be done in a single POC device. This paper is organized as follows: The design of the fluidic device is addressed in Section 2, where the design specifications required for LAMP and the calculation of dimension and flow rate are described. Section 3 discusses the experimental work, the fabrication process, and the functional testing of the fluidic device. Section 4 discusses the result of this work. Finally, the summary of this study is presented in Section 5.

## 2. DESIGN CONCEPT OF PORTABLE LAMP DEVICE

The design of the portable LAMP device, as illustrated in Figure 1, is meticulously engineered to ensure efficiency, accuracy, and portability. Figure 1(a) presents an exploded view of the connector lid, which houses several crucial components: the fluidic device, the PTC heating element, and the sensor holder. The PTC heating element maintains the temperature required for the LAMP process, while the fluidic device ensures proper sample flow. The sensor holder securely positions the sensor, facilitating accurate data acquisition. This modular arrangement enables easy assembly and maintenance, improving overall usability. Figure 1(b) depicts the fully assembled portable LAMP device, which integrates the connector lid assembly and the sensor holder assembly into a compact unit. Four strategically placed magnets on the connector lid reinforce the connection between these two assemblies. These magnets ensure secure attachment and enable seamless connectivity between the wire and the connector. The wire and connector link the sensor's electrodes to the potentiostat board, essential for processing the electrochemical signals generated during the LAMP process. This streamlined connection enhances the device's performance and minimizes potential signal loss. Figure 1(c) provides an exploded view of the sensor holder, which consists of the sensor, the sensor holder itself, and the PDMS sample well. The PDMS sample well is critical, as it channels the fluidic sample toward the sensor’s electrodes while preventing leakage. This precise flow control ensures that the sample remains intact and accurately reaches the sensor. Furthermore, the sensor holder assembly firmly secures the sensor and the sample well, preventing displacement

https://doi.org/10.31436/iiumej.v26i1.3407

during the LAMP process. This cohesive design highlights the device's reliability, ensuring precise operation, efficient heat distribution, and secure sample handling, making it a significant advancement in portable diagnostic tools.

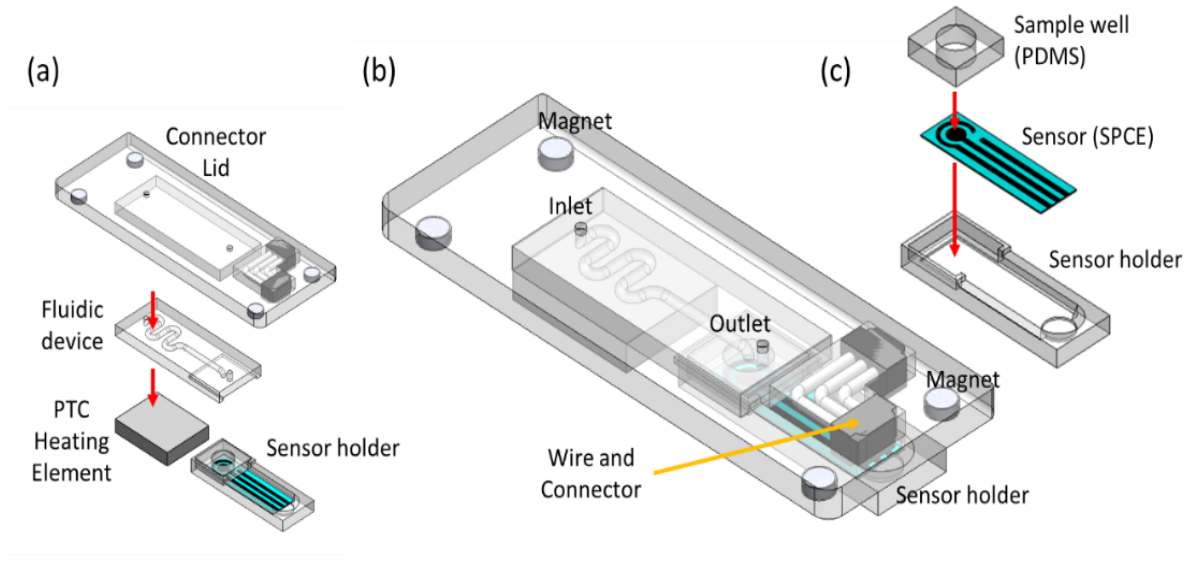


Figure 1. Design of portable LAMP device. (a) An expanded view of the assembly within the connector lid: PTC heating element, fluidic device, and connector lid. (b) Complete design of portable LAMP device consisting of the assembly within the connector lid and the assembly within the sensor holder (c) Exploded view of the assembly within the sensor holder: sensor holder, sensor, and sample well.

### 2.1. LAMP Specification

To complete the LAMP reaction for DNA amplification, a constant temperature of 65°C must be maintained for 35 minutes to optimize the amplification process [4]. A fluidic device was designed to transport fluidic samples to the screen-printed carbon electrode (SPCE) sensor while maintaining the temperature required for the LAMP reaction to complete. Optimizing the fluidic channel specifications is crucial for optimal fluid flow. The selection of the heating element is vital for accurate temperature regulation. Although the LAMP process typically utilizes sample volumes of 10 to 20 µL [15–17], the circular detection area of the SPCE requires a larger sample volume of 50 to 200 µL for sufficient coverage and measurement [18–20]. The volume range of 50 to 200 µL will be used for our design to ensure adequate signal detection and complete LAMP amplification results.

The fluidic channels, chambers, and structures are designed based on the fundamental principles of fluid dynamics and heat transfer. The serpentine configuration of the channel on top of the heater creates an extended fluid-path length, maximizing the thermal interaction between the sample and the heater surface. This design promotes efficient and uniform sample heating throughout the 35-minute heating process. The dimensions of the channels are carefully selected to control the sample volume to ensure accurate fluid handling. The outlet of the serpentine channel, strategically positioned above the sensor, enables rapid and direct delivery of the heated sample to the sensor area, facilitating real-time analysis and detection.

https://doi.org/10.31436/iiumej.v26i1.3407

### 2.2. Design of Fluidic Channels

The fluidic channels of various diameters were designed to test the MSLA 3D printer's capabilities in fabricating small-sized structures. A test design consisting of a linear arrangement of seven channels, each with a diameter ranging from 1.1 to 1.7 mm with 5 mm spacing, is shown in Figure 2. The channels, measuring 55 mm in length and 3 mm in thickness, were designed to facilitate sufficient heat transfer during the LAMP process while achieving printable dimensions of fluidic channels.

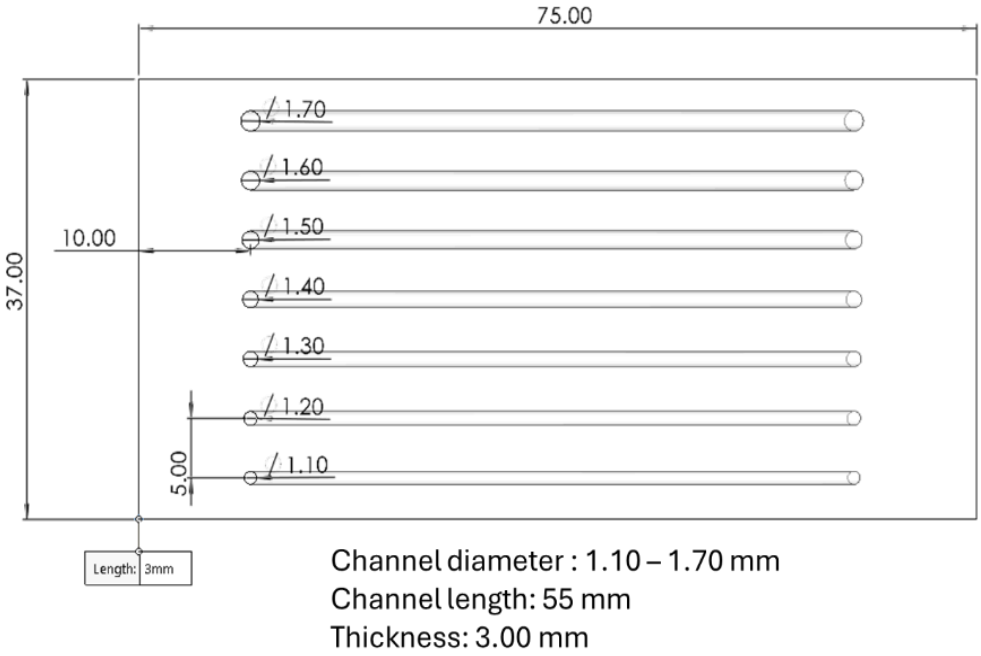


Figure 2. The test design consists of 7 channels with varying diameters (1.10 - 1.70 mm) and 55 mm channel length.

### 2.3. Fluidic Volume Calculation

The following equation was used to determine the sample volume flowing in the channel,

$$V = \frac{\pi D^2 l}{4} \quad (1)$$

where $D$ is the diameter and $l$ is the length of the channel (both in mm). This equation assumes that the fluidic channel has a circular cross-sectional area. The volume is calculated as the product of the cross-sectional area ($\frac{\pi D^2}{4}$) and the channel length ($l$). The calculated volumes of the serpentine channels are 93.61 ml to 118.48 ml, as shown in Table 1 in Section 3.2, together with the measured values.

## 3. EXPERIMENTAL WORKS

This section discusses the experimental works on fluidic channel fabrication, volume measurements, and heat distribution measurements. The fabricated fluidic devices will be tested with red-colored fluid (representing sample fluid) to observe fluid flow time within the serpentine channel. Heating elements will be tested with an Arduino microcontroller to determine the time required to reach the desired temperature.

https://doi.org/10.31436/iiumej.v26i1.3407

### 3.1. Fabrication of Fluidic Channels

The fluidic channel was fabricated using mask stereolithography (MSLA) with a Phrozen Sonic Mini 8K 3D printer. This high-resolution 3D printing technique uses UV light to cure a liquid photopolymer resin, resulting in exceptional detail and precision, making it ideal for crafting intricate fluidic devices. The printer's 8K resolution LCD panel contributes to improved accuracy and speed at an affordable cost. PMMA-like resin, selected for its fluid visualization capabilities, smooth surface properties, and biocompatibility, served as the primary material for the fluidic channel.

To achieve optimal fluidic channel formation, the exposure time for the MSLA process was determined through experimentation. The fluidic design file was uploaded to the printer, followed by resin being loaded into the printer's tank. The printer then initiated the curing process, solidifying the resin layer by layer according to the uploaded design. Upon completion, the printed part was immersed in isopropyl alcohol (IPA) for 4 minutes to remove excess resin. Afterward, it was exposed to UV light for 5 minutes to improve its mechanical properties and stability.

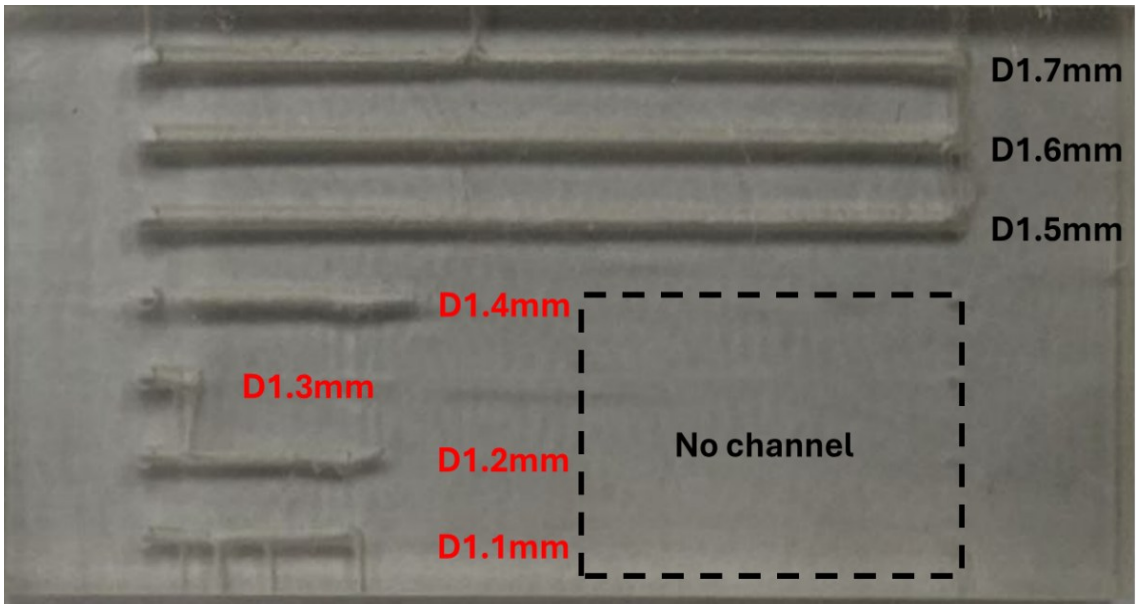


Figure 3. The fabricated fluidic channels of the test designs (channel length 55 mm) with a 5 mm gap between the channels for channel diameters ranging from 1.1 mm to 1.7 mm.

Figure 3 shows the fabricated fluidic channels of 55 mm length for channel diameters ranging from 1.1 mm to 1.7 mm. It was observed that the fluidic channels with diameters smaller than 1.5 mm were not fully formed, which indicates that the minimum printable channel diameter for this test design is 1.5 mm. Therefore, for subsequent fabrication, the smallest channel diameter was set at 1.6 mm to ensure full formation of channels can be achieved. Considering the printer's printing capability, the design of the fluidic channel is set as 50 mm x 20 mm x 4 mm (L × W × H), as shown in Figure 4(a). The heater area is where the heating element was placed (exactly below the fluidic device) to ensure uniform heating. An isometric view of the fluidic channel in Figure 4(b) shows the three-dimensional structure of the serpentine-shaped channel. Three-channel diameters of 1.6 mm, 1.7 mm, and 1.8 mm were chosen for performance comparison. To achieve a complete LAMP process, the channels were

https://doi.org/10.31436/iiumej.v26i1.3407

designed in a serpentine shape above the heater area to allow the sample volume to flow and stay on top of the heater while being heated at 65° for 35 minutes. As shown in Figure 4(c), the fluidic channel with a channel diameter of 1.7 mm was successfully fabricated using an MSLA printer. The length of the serpentine channel inside the heater area (from A to B) is 46.82 mm. The details of the fabricated fluidic channels' dimensions will be discussed in Section 4.1.

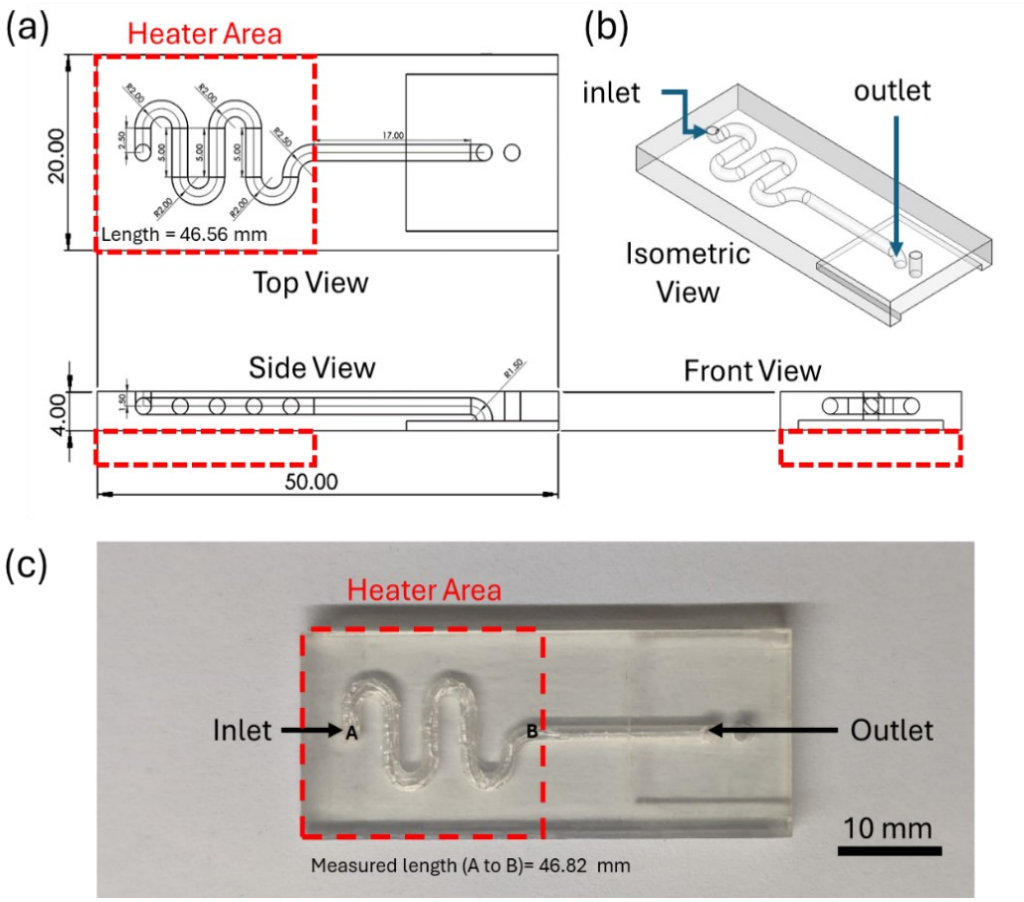


Figure 4(a) The fluidic device design uses SolidWorks 2022 (dimensions are millimeters). (b) Isometric view showing the three-dimensional structure of the serpentine-shaped channel. (c) Fabricated fluidic channel using an MSLA 3D printer with a measured channel length of 46.82 mm.

### 3.2. Experimental Setup for Fluidic Device

The experimental setup shown in Figure 5 was used to test the fabricated fluidic device's functionality and measure the channel's flow time. The setup comprises a syringe pump (NE-300, New Era Pump Systems, Inc), a small tube, the fabricated fluidic device, red-colored fluid to represent the fluidic samples, a heating element, and a digital microscope (Dino-Lite). The syringe pump was connected to the inlet of the fabricated channels via a small tube. The syringe pump was utilized to control the flow rate of the red-colored fluid into the fluidic channels. The Dino-Lite Digital Microscope was employed to track the flow time of the fluidic sample reaching the outlet. As depicted in Figure 5, the inset shows the flow of red-colored fluid inside the fabricated serpentine fluidic channel. The time for the fluid to flow from A to B was recorded on a computer for analysis.

https://doi.org/10.31436/iiumej.v26i1.3407

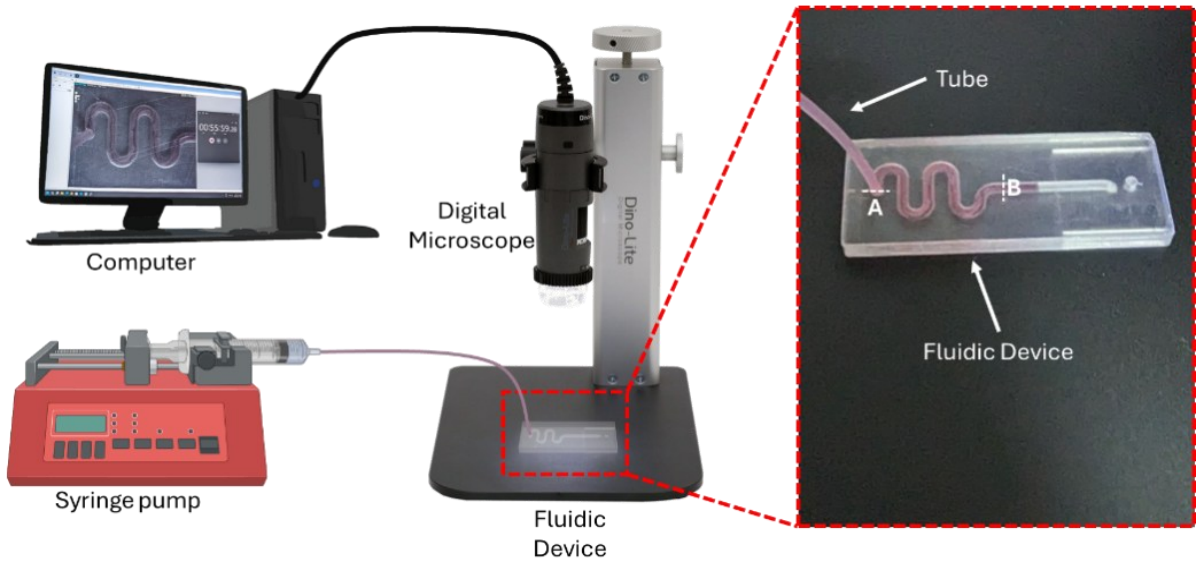


Figure 5. An experimental setup for fluid flow analysis consists of a fluidic device, a syringe pump, and a digital microscope connected to a computer.

Fluidic channels of varying diameters were configured with different flow rates to guarantee a 35-minute fluidic flow from point A to point B for all channels. For channel diameters of 1.6 mm, 1.7 mm, and 1.8 mm, the initial flow rates were established at 2.67 µl/min, 3.02 µl/min, and 3.39 µl/min, correspondingly. The video recording of the fluidic flow commenced immediately after the syringe pump was initiated to pump the fluid. The time interval between the fluid reaching point A and point B determines the flow time.

Table 1 shows the calculated volumes for each channel diameter are 1.6 mm, 1.7 mm, and 1.8 mm. The volume of the device's fluidic sample is 93.61 mm³ for the 1.6 mm diameter channel, 105.68 mm³ for the 1.7 mm diameter channel, and 118.48 mm³ for the 1.8 mm diameter channel. As previously mentioned, these values align with the standard range of 50 to 200 mm³ for fluidic sample volumes utilized with SPCE sensors [16–18].

Table 1. Calculated volume within the serpentine fluidic channel for each channel diameter

| Channel diameter [mm] | Channel Length [mm] | Calculated Volume [mm$^3$] (Eq. 1) |
|---|---|---|
| 1.6 | 46.56 | 93.61 |
| 1.7 | 46.56 | 105.68 |
| 1.8 | 46.56 | 118.48 |

### 3.3. Heat Distribution Measurements

Measuring the heating elements' temperatures is crucial to achieve a constant temperature of 65°C. Figure 6(a) shows the experimental setup that evaluated the heaters' capabilities by testing the heating elements using a 5V power supply derived from a USB C module. An Arduino microcontroller is connected to a MAX6675 thermocouple to measure the temperature of the heating elements powered by a 5 V USB-C module. The chosen heating elements are a heater cartridge (HC) and two positive temperature coefficient (PTC) heaters, as shown in Figure 6(b). The comparison was done by observing the time taken for each heating element

https://doi.org/10.31436/iiumej.v26i1.3407

to reach 65°C. PTC 230 was chosen as it took the least amount of time of 54.78 s compared to the other heating elements. The specifications of each heating element are listed in Table 2.

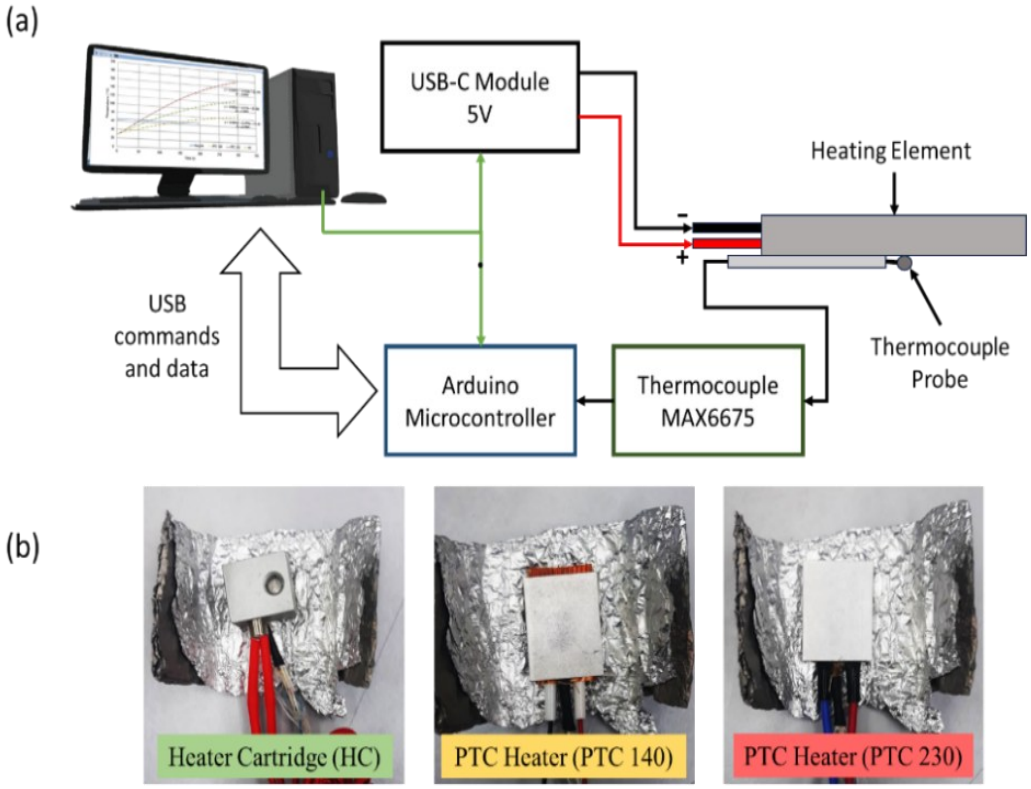


Figure 6(a) Block diagram of the experimental setup used to validate the functionality of the heating elements. (b) The different heating elements tested in the experiment: Heater Cartridge (HC), PTC Heater (PTC 140), and PTC Heater (PTC 230).

Table 2. Specification of heating elements

| Heating Element | Max Temperature [°C] | Voltage [V] | Power [W] | Heater size [mm] |
|---|---|---|---|---|
| Heater Cartridge | 300 | 12 | 40 | 20 x 11.5 x 16 |
| PTC heater 140 | 140 | 12 | 12 | 20 x 20 x 5 |
| PTC heater 230 | 230 | 12 | 12 | 20 x 20 x 5 |

The comparison was done by observing each heating element's time to reach 65°C. PTC 230 was selected for its shortest time of 54.78 seconds compared to the other heating elements. Details of the results will be discussed in Section 4.2. After the suitable heating element based on the rapid heating profile, the uniformity of heat distribution was analyzed using an infrared thermal imaging analyzing camera, Super Cam X (QianLi, China). The thermal camera was positioned directly on top of the heating element, and the heat distribution was observed from room temperature to a maximum temperature of 65°C. The thermal camera was connected to a computer, and the images were captured and analyzed using QianLi IR software. The heat distribution results are discussed in Section 4.2.

https://doi.org/10.31436/iiumej.v26i1.3407

# 4. RESULTS AND DISCUSSION

This section discusses the results of flow time measurement and heat distribution testing for selected heating elements.

## 4.1. Measurement Results for the Flow Time of the Fluidic Sample

Figure 7(a) shows the inset of the fluidic sample flowing inside the channel (from A to B) in 34 minutes 30 seconds ((Time at B) minus (Time at A)). Figure 7(b) shows the red-colored fluid flowing from the fluidic device into the PDMS sample well in the sensor holder. No leakage was observed during the measurement of the flow time of the fluidic sample.

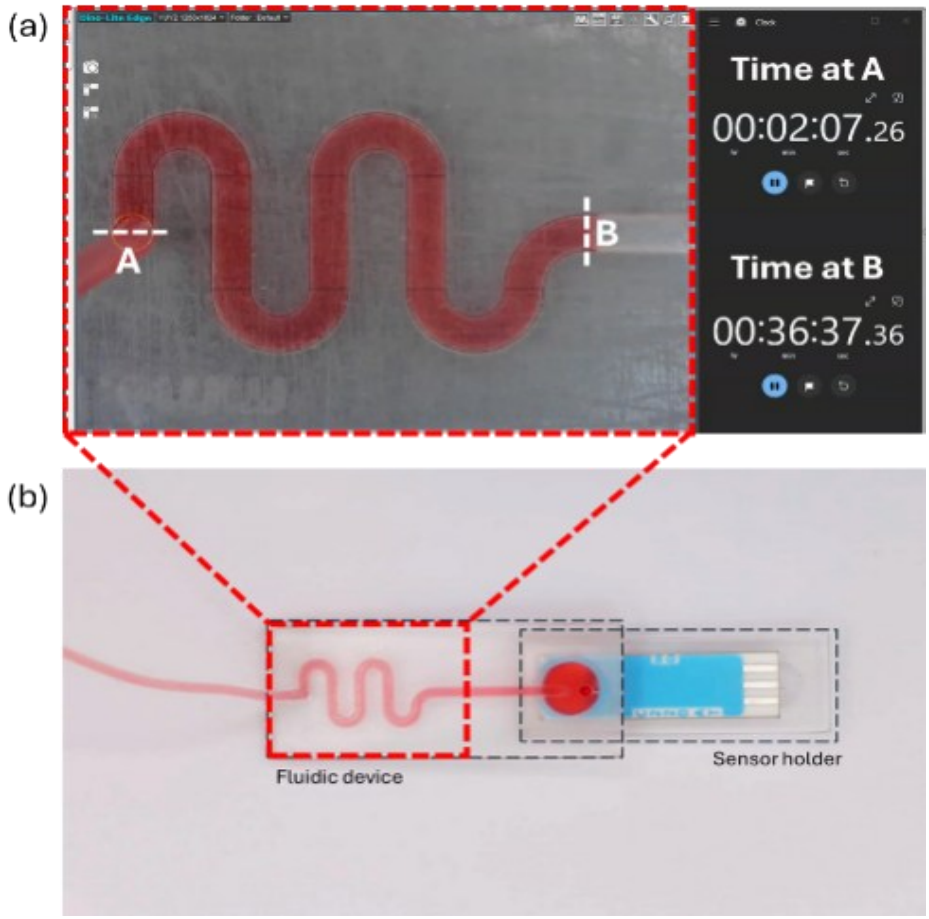


Figure 7(a) The inset of red-colored fluid flows within the channel without leakage and takes 35 minutes to complete its flow. (b) The flow of red-colored fluid in the fluidic channel into the PDMS sample well in the sensor holder.

Three fluidic channels of varying channel diameters (1.6 mm, 1.7 mm, and 1.8 mm) with the same channel length of 46.56 mm (from A to B) were 3D printed using an MSLA printer, as shown in Figure 8. The length and diameter of 3D-printed fluidic channels were measured by DinoCapture software.

https://doi.org/10.31436/iiumej.v26i1.3407

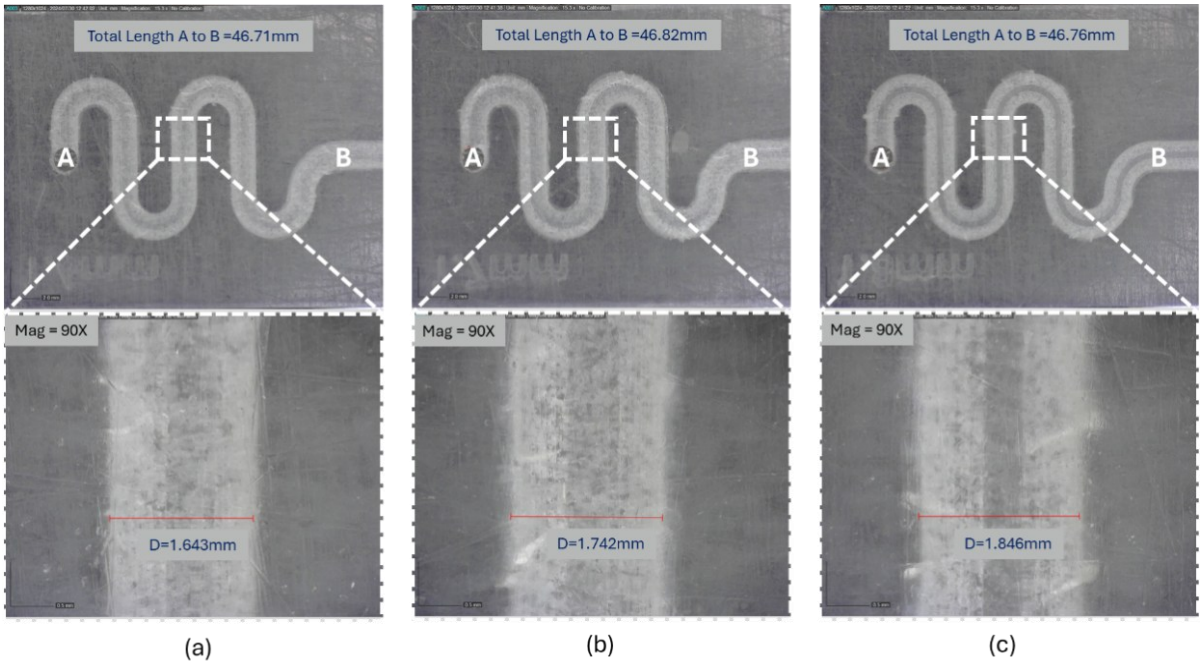


Figure 8. 3D-printed fluidic channels with three different channel diameters: (a) 1.6 mm channel diameter (b) 1.7 mm channel diameter c) 1.8 mm channel diameter.

Table 3 shows the summary of the flow time of the red-colored fluid from A to B, as well as the expected and measured values for all three channels. The measured dimension of the fabricated fluidic channels in terms of channel diameter and length is also shown in Table 3. It can be observed that the actual channel lengths of 46.71 mm (diameter 1.6 mm), 46.82 mm (diameter 1.7 mm), and 46.76 mm (diameter 1.8 mm) were slightly larger than the expected value (46.56 mm) due to fabrication tolerances. As a result, the measured flow times for all channel diameters were slightly different from the expected 35 minutes. The fluidic channel with a 1.6 mm diameter shows the closest flow time of 34.33 min to the expected value (35 minutes) with a percentage deviation of 1.91% compared to the other channels. Subsequently, the overall flow rate of the fluidic channel with a 1.6 mm channel diameter shows the most optimum value from the others with a percentage deviation of 7.87%.

Table 3. Summary of the flow time of the red-colored fluid from A to B and the measured dimensions for all channel diameters

| **Channel diameter [mm]** | | **Channel Length from A to B [mm]** | | **Flow time A to B [min]** | | | **Overall Flow Rate [mm$^3$/min]** | | |
|---|---|---|---|---|---|---|---|---|---|
| Expected | Measured | Expected | Measured | Expected | Measured | Percentage deviation [%] | Expected | Measured | Percentage deviation [%] |
| **1.60** | 1.64 | 46.56 | 46.71 | 35.00 | 34.33 | 1.91 | 2.67 | 2.88 | 7.87 |
| **1.70** | 1.74 | 46.56 | 46.82 | 35.00 | 30.14 | 13.89 | 3.02 | 3.68 | 21.85 |
| **1.80** | 1.85 | 46.56 | 46.76 | 35.00 | 30.09 | 14.03 | 3.39 | 4.17 | 23.00 |

### 4.2. Results of Measurements for Heating Elements

Selecting the appropriate heating elements is crucial to attain the optimal temperature for the LAMP process quickly. The experiment compared three distinct heating elements: PTC heater 230, PTC heater 140, and heater cartridge. The heater's temperature was measured using

https://doi.org/10.31436/iiumej.v26i1.3407

a thermocouple and microcontroller. The temperature profiles for each heating element's heating process over five minutes are shown in Figure 9(a). The durations for the heating elements to achieve 65°C were as follows: PTC heater 230 (54.78 seconds), Heater Cartridge (78.41 seconds), and PTC heater 140 (149.07 seconds). PTC 230 heating element was chosen for its rapid heating performance (reaching 65°C in 54.78 seconds). As shown in Figure 9(a), the R2 values obtained are close to 1, which indicates the accuracy of the time value obtained at 65°C for all heaters.

The PTC 230 was further tested under an infrared thermal imaging camera to observe the uniformity of heat distribution of the heating element when it reaches 65°C, as shown in Figure 9(b) and Figure 9(c). The images clearly demonstrate a consistent and minimal temperature gradient across the heating element surface when it reaches 65°C. The highest temperature is observed at the center, gradually decreasing towards the edges. This indicates a uniform heat distribution pattern. Given that the temperature variation between the center and edges is only 1°C, or ±0.5°C from the center temperature, it can be concluded that the tolerance for the expected temperature value of 65°C for the LAMP process is within an acceptable range. The calculated tolerance of ±0.5°C accurately reflects this minimal temperature variation and ensures that the heating element operates within the specified temperature limits for the LAMP process. These experiments show that the fluidic channel system can be placed on top of the heating element, allowing the simultaneous flow and heating of the fluidic sample for 35 minutes at 65°C. It is also suitable for portable LAMP devices.

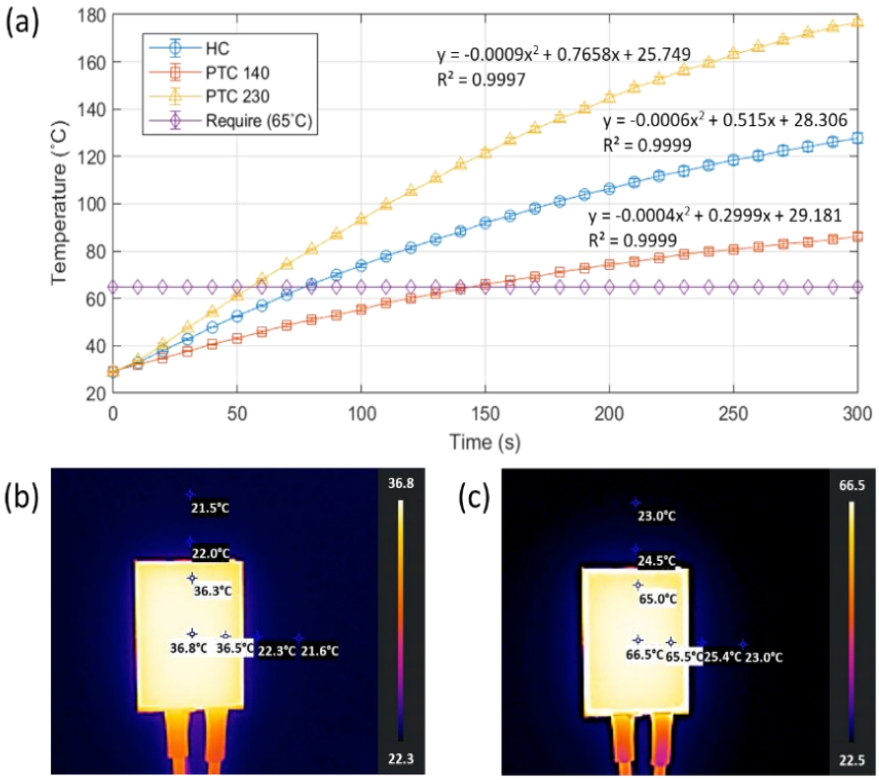


Figure 9(a) Temperature versus heating time for HC, PTC 140, and PTC 230 heating elements. (b) Thermal imaging of PTC 230 after 10 seconds of heating. (c) Thermal imaging of PTC 230 after 55 seconds of heating (reaching 65°C LAMP temperature).

The developed portable LAMP device, which consists of the PTC 230 heater and the fluidic channel, was used for DNA amplification of COVID-19 samples (74 positive, 74

negative) for COVID-19 detection using gold nanoparticle SPCE (AuNP-SPCE) electrochemical measurement, as reported in [4].

Table 4. Comparison of existing LAMP microfluidic devices with our work

| Technology | Material used for microfluidic device | Fabrication Method | Sealing method | Remarks | Ref |
|---|---|---|---|---|---|
| **Self-driven microfluidic chip** | PDMS with hydrophilic UV-cured glue | Photolithography, spin-coating, oxygen plasma treatment, and bonding | Closed the channel with an air-control channel via a vacuum system | Complex fabrication. LAMP process of 56°C for 30 minutes for fluorescent detection of vancomycin-resistant enterococcus strain (VRE). | [6] |
| **SlipChip / sp-SlipChip** | Two layers of glass plate | Photolithography and thin-film deposition | Lubricating oils were placed between two plates | Complex fabrication. LAMP process of 65°C for 60 minutes for fluorescent detection of human papillomavirus (HPV-16 and HPV-18). | [7] |
| **Smartphone-based multiplex test** | Silicon wafer with SiO2 film | Photolithography, etching (Bosch process), thermal oxidation and dicing | Sealed with a double side adhesive layer and covered with glass on top | Complex fabrication. LAMP process of 65°C for 30 minutes to detect live virus from nasal swab extract. | [8] |
| **Mask Stereolithography Fluidic** | PMMA-like Resin | 3D printing (MSLA) | Magnet Lid and PDMS sample well | Simpler method of 3D printed fabrication. LAMP process of 65°C for 35 minutes of COVID-19 detection using electrochemical measurement. | This work |

Table 4 provides a detailed comparison of various LAMP microfluidic devices and highlights the advantages of our work. Existing technologies, such as self-driven microfluidic chips, SlipChip, and smartphone-based multiplex tests, demonstrate complex fabrication methods that rely on photolithography, spin-coating, thin-film deposition, and chemical etching processes. These methods involve multiple steps, such as thermal oxidation, vacuum systems, and lubricating oils for sealing. While these approaches have enabled precise control over the LAMP process, such as maintaining temperatures between 56°C and 65°C for 30–60 minutes, they are often labor-intensive, require specialized equipment, and lack the accessibility needed for widespread deployment, especially in low-resource settings. Additionally, these devices primarily focus on fluorescence detection, which can be cost-prohibitive and requires trained personnel for analysis.

In contrast, our work introduces a 3D-printed LAMP microfluidic device fabricated using a Mask Stereolithography Apparatus (MSLA). Utilizing PMMA-like resin and a simple magnet-lid sealing mechanism with a PDMS sample well significantly simplifies the fabrication process. Unlike conventional methods, our device eliminates the need for

photolithography and bonding techniques, reducing fabrication complexity and costs. The magnet lid and PDMS sample will also provide an innovative sealing solution that ensures leak-proof operation and facilitates fluidic sample flow directly to the sensor electrodes without manual intervention. This design simplifies the user experience and ensures compatibility with the LAMP process, which is maintained at 65°C for 35 minutes for COVID-19 detection using electrochemical measurement.

Furthermore, the performance of our device demonstrates that simplification in fabrication and operation does not compromise the sensor's accuracy or efficiency. Compared to existing devices, our system offers a seamless integration of the LAMP process with electrochemical detection, eliminating manual pipetting between steps. This reduces the risk of contamination while enhancing the device's usability in point-of-care settings. Our 3D-printed LAMP device thus represents a significant step forward in developing accessible and portable diagnostic tools, bridging the gap between complex laboratory-grade systems and practical, low-cost alternatives suitable for real-world applications.

## 5. CONCLUSION

This study successfully developed a 3D-printed serpentine fluidic channel integrated with a heating element. Leveraging the precision of MSLA 3D printing, a PMMA-like resin was used to fabricate a channel with an optimized diameter of 1.6 mm due to its minimal deviations in channel length (0.32%), flow time (1.91%) and overall flow rate (7.87%) as compared to 1.7 mm and 1.8 mm channels. Fluidic performance testing demonstrated fluidic flow at 2.88 µL/min flow rate without any leakage. Integrating a PTC 230 heating element has enabled rapid temperature control, reaching 65°C in 54.78 seconds. These results demonstrate the feasibility of producing a compact and efficient fluidic device suitable for portable applications. Future research will focus on enhancing the precision and reliability of the fluidic channel device and exploring different heating element options for improved performance. Implementing a flow rate sensor and pressure-driven system could contribute to a more consistent fluid flow within the device. Additionally, exploring fabrication techniques with different materials may enable the production of channels with more precise diameters, thereby improving the overall device performance.

## ACKNOWLEDGEMENT

This research project was funded by the Ministry of Science, Technology, and Innovation (MOSTI) under the Combating COVID-19 Fund (project number: CV 02211032) grant and Ministry of Higher Education (MOHE) Fundamental Research Grant Scheme FRGS21-239-0848 (FRGS/1/2021/TK0/UIAM/02/9).

## REFERENCES

[1] NAKAYAMA T, SOGA K (2023) Simple and quick detection of extended-spectrum $\beta$-lactamase and carbapenemase-encoding genes using isothermal nucleic acid amplification techniques. Journal of Microorganism Control 28:145–152. https://doi.org/10.4265/jmc.28.4_145

[2] Rahman MT, Uddin MS, Sultana R, Moue A, Setu M (2013) Polymerase Chain Reaction (PCR): A Short Review. Anwer Khan Modern Medical College Journal 4:30–36. https://doi.org/10.3329/AKMMCJ.V4I1.13682

[3] Kumar A, Venkatesan G (2018) Isothermal Nucleic Acid Amplification System: An Update on Methods and Applications Evaluation of immunogenicity and diagnostic potential of

recombinant proteins of Buffalopox virus View project Genetic characterization of virulence genes of orf virus isolates from sheep and goats View project. J Genet Genom 2:

[4] Zulhairee M, Zain RM, Nor ACM, Jafar NF, Noh MFM, Noorden MSA, Nordin AN, Rahim RA, Gunawan TS, Chin LY, Mohd Y, Azman NA, Zain ZM (2023) Clinical Performance of Reverse Transcription Loop-mediated Isothermal Amplification COVID-19 Assay on Gold-nanoparticle-modified Screen-printed Carbon Electrode Using Differential Pulse Voltammetry. Sensors and Materials 35:4731–4750. https://doi.org/10.18494/SAM4430

[5] Lin PH, Li BR (2021) Passively driven microfluidic device with simple operation in the development of nanolitre droplet assay in nucleic acid detection. Scientific Reports 2021 11:1 11:1–11. https://doi.org/10.1038/s41598-021-00470-9

[6] Ma YD, Chang WH, Luo K, Wang CH, Liu SY, Yen WH, Lee G Bin (2018) Digital quantification of DNA via isothermal amplification on a self-driven microfluidic chip featuring hydrophilic film-coated polydimethylsiloxane. Biosens Bioelectron 99:547–554. https://doi.org/10.1016/J.BIOS.2017.08.026

[7] Yu Z, Lyu W, Yu M, Wang Q, Qu H, Ismagilov RF, Han X, Lai D, Shen F (2020) Self-partitioning SlipChip for slip-induced droplet formation and human papillomavirus viral load quantification with digital LAMP. Biosens Bioelectron 155:112107. https://doi.org/10.1016/J.BIOS.2020.112107

[8] Sun F, Ganguli A, Nguyen J, Brisbin R, Shanmugam K, Hirschberg DL, Wheeler MB, Bashir R, Nash DM, Cunningham BT (2020) Smartphone-based multiplex 30-minute nucleic acid test of live virus from nasal swab extract. Lab Chip 20:1621–1627. https://doi.org/10.1039/D0LC00304B

[9] Nielsen A V., Beauchamp MJ, Nordin GP, Woolley AT (2020) 3D Printed Microfluidics. Annu Rev Anal Chem (Palo Alto Calif) 13:45. https://doi.org/10.1146/ANNUREV-ANCHEM-091619-102649

[10] Gale BK, Jafek AR, Lambert CJ, Goenner BL, Moghimifam H, Nze UC, Kamarapu SK (2018) A review of current methods in microfluidic device fabrication and future commercialization prospects. Inventions 3:. https://doi.org/10.3390/inventions3030060

[11] Luo F, Lei L, Cheng Z, Wan L, Zhao C, Niu K, Li C, Chen Q, Liu L, Wang N (2022) Magnet-actuated microfluidic reactors with controllable Fe-based amorphous microspheres for tetracycline degradation. J Flow Chem 12:297–305. https://doi.org/10.1007/S41981-022-00227-Z/METRICS

[12] Price AJN, Capel AJ, Lee RJ, Pradel P, Christie SDR (2021) An open source toolkit for 3D printed fluidics. J Flow Chem 11:37–51. https://doi.org/10.1007/S41981-020-00117-2/FigureURES/10

[13] Enders A, Siller IG, Urmann K, Hoffmann MR, Bahnemann J (2019) 3D Printed Microfluidic Mixers—A Comparative Study on Mixing Unit Performances. Small 15:1–9. https://doi.org/10.1002/smll.201804326

[14] Chen C, Mehl BT, Munshi AS, Townsend AD, Spence DM, Martin RS (2016) 3D-printed microfluidic devices: fabrication, advantages and limitations - a mini review. Analytical Methods 8:6005–6012

[15] Donia A, Furqan Shahid M, Hassan S ul, Shahid R, Ahmad A, Javed A, Nawaz M, Yaqub T, Bokhari H (2022) Integration of RT-LAMP and Microfluidic Technology for Detection of SARS-CoV-2 in Wastewater as an Advanced Point-of-Care Platform. Food Environ Virol 14:364–373. https://doi.org/10.1007/S12560-022-09522-3/FigureURES/1

[16] Lim J, Stavins R, Kindratenko V, Baek J, Wang L, White K, Kumar J, Valera E, King WP, Bashir R (2022) Microfluidic point-of-care device for detection of early strains and B.1.1.7 variant of SARS-CoV-2 virus. Lab Chip 22:1297–1309. https://doi.org/10.1039/D2LC00021K

[17] Lu S, Duplat D, Benitez-Bolivar P, León C, Villota SD, Veloz-Villavicencio E, Arévalo V, Jaenes K, Guo Y, Cicek S, Robinson L, Peidis P, Pearson JD, Woodgett J, Mazzulli T, Ponce P, Restrepo S, González JM, Bernal A, Guevara-Suarez M, Pardee K, Cevallos VE, González C, Bremner R (2022) Multicenter international assessment of a SARS-CoV-2 RT-LAMP test for point of care clinical application. PLoS One 17:. https://doi.org/10.1371/JOURNAL.PONE.0268340

[18] Ramírez-Chavarría RG, Castillo-Villanueva E, Alvarez-Serna BE, Carrillo-Reyes J, Ramírez-Zamora RM, Buitrón G, Alvarez-Icaza L (2022) Loop-mediated isothermal amplification-based electrochemical sensor for detecting SARS-CoV-2 in wastewater samples. J Environ Chem Eng 10:. https://doi.org/10.1016/j.jece.2022.107488

[19] Rocha RG, Silva ICOF, Arantes LC, Stefano JS, Lima CD, Melo LMA, Munoz RAA, dos Santos WTP, Richter EM (2021) Simple and rapid electrochemical detection of 1-benzylpiperazine on carbon screen-printed electrode. Microchemical Journal 167:1–7. https://doi.org/10.1016/j.microc.2021.106282

[20] Boselli E, Wu Z, Haynes EN, Papautsky I (2024) Screen-Printed Sensors Modified with Nafion and Mesoporous Carbon for Electrochemical Detection of Lead in Blood. J Electrochem Soc 171:027513. https://doi.org/10.1149/1945-7111/ad2397

https://doi.org/10.31436/iiumej.v26i1.3411

# UTILIZING MFCCS AND TEO-MFCCS TO CLASSIFY STRESS IN FEMALES USING SSNNA

**NUR AISHAH ZAINAL[1], ANI LIZA ASNAWI[1*], SITI NOORJANNAH IBRAHIM[1], NOR FADHILLAH MOHAMED AZMIN[1], NORHARYATI HARUM[2], NORA MAT ZIN[3]**

*[1] Department of Electrical and Computer Engineering, Kulliyyah of Engineering, International Islamic University Malaysia, 53100, Kuala Lumpur, Malaysia*
*[2] Fakulti Teknologi Maklumat dan Komunikasi, Universiti Teknikal Malaysia Melaka, Durian Tunggal, Melaka, Malaysia*
*[3] Department of Psychiatry, Kulliyyah of Medicine, International Islamic University Malaysia, Jalan Sultan Ahmad Shah, Bandar Indera Mahkota, 25200 Kuantan, Pahang, Malaysia*

**Corresponding author: aniliza@iium.edu.my*

*(Received: 29 August 2024; Accepted: 4 December 2024; Published online: 10 January 2025)*

***ABSTRACT:*** All individuals are susceptible to experiencing stress in their everyday lives. Nevertheless, stress has a greater influence on females due to both biological and environmental factors. This study utilized female speeches to detect and classify stress and no stress in women. Using speech, composed of non-invasive and non-intrusive approaches, helps to identify stress better in females. A comparative analysis was conducted between Mel-frequency Cepstral Coefficients (MFCCs) and Teager Energy Operator- MFCCs (TEO-MFCCs) to determine the best speech feature for classifying emotions associated with stress and no-stress conditions for female voices. With the assistance of the Stress Speech Neural Network Architecture (SSNNA), an improved accuracy of 93.9% was achieved. This research showed that MFCCs enhanced higher-frequency components in stressed speech, distinguishing between stress and no-stress classes. This study shows that SSNNA achieved high accuracy with 14 female voices, confirming its ability to function independently of speaker identity.

***ABSTRAK:*** Semua individu terdedah kepada stres dalam kehidupan seharian mereka. Walau bagaimanapun, stres memberi pengaruh yang lebih besar terhadap wanita akibat faktor biologi dan persekitaran. Kajian ini menggunakan ucapan untuk mengesan dan mengklasifikasikan stres dan tiada stres dalam kalangan wanita. Penggunaan ucapan, yang merupakan pendekatan tidak invasif dan tidak mengganggu, membantu mengenal pasti tekanan dengan lebih baik dalam kalangan wanita. Analisis perbandingan telah dijalankan antara Mel-frequency Cepstral Coefficients (MFCCs) dan Teager Energy Operator-MFCCs (TEO-MFCCs). Tujuannya adalah untuk menentukan ciri ucapan terbaik bagi mengklasifikasikan emosi yang berkaitan dengan keadaan stres dan tiada stres bagi suara wanita. Dengan bantuan Stress Speech Neural Network Architecture (SSNNA), metrik prestasi yang lebih tinggi dengan ketepatan 93.9% telah dicapai. Penyelidikan ini menunjukkan bahawa MFCCs meningkatkan komponen frekuensi tinggi dalam ucapan yang stres, secara efektif membezakan antara kelas stres dan tiada stres. Kajian ini menunjukkan bahawa SSNNA mencapai ketepatan tinggi dengan 14 suara wanita, mengesahkan ia berfungsi secara bebas daripada identiti penutur.

***KEYWORDS:*** *stress detection via speech, stress classification for females, MFCCs, CNN*

https://doi.org/10.31436/iiumej.v26i1.3411

# 1. INTRODUCTION

Both females and males can experience stress in their daily lives. Stress can arise from various aspects of human life. However, when exposed to the same stressors, females tend to perceive higher stress levels than males. According to a 2023 survey report conducted by a human resources business in the United States, 43% of female workers rated their mental health as poor, compared to 15% of male workers [1]. Also, a study conducted by Costa et al. [2] on unemployment issues in 2021 found that 22.7% of females reported higher stress levels than 11% of males.

According to a report by the Sinar Harian newspaper in 2019, females experienced depression (a result of long-term stress) more frequently than males due to the hormonal transition [2]. Moreover, in 2019, Dr Elinda Tunan, a psychiatrist at a government hospital, concurred that there was a strong correlation between depression in females and hormonal fluctuations, particularly during pregnancy and childbirth [2]. These alterations facilitated a greater tendency for emotional expression. According to her, individuals were likelier to exhibit heightened moodiness, increased anger, and experience several other undesirable emotions [2].

Therefore, it is crucial to detect stress in females early to address its underlying causes and promote a healthy physical and mental lifestyle. Early detection of stress can help prevent physical and emotional disorders, which may lead to serious mental health problems if left unaddressed.

Speech for stress prediction presents an advantage to females by reducing unnecessary stress arising from equipment setup, particularly in healthcare settings where biological markers are used to measure stress levels [3]. Two examples of invasive and intrusive stress detection approaches include the utilization of an electroencephalogram (EEG) to measure brain electrical activity and collect blood samples [3]. These techniques have several drawbacks, including time-consuming procedures, the need for specialized skills, significant financial expenses, and the limitation of being exclusively conducted within healthcare facilities [3]. Therefore, to avoid unnecessary stress caused by these methods, our study uses speech to detect stress from female voices. This approach reduces the potential discomfort linked to invasive methods, as it solely requires participants to provide vocal samples without involving any invasive physical activities.

This study incorporated speech features such as Mel-frequency Cepstral Coefficients (MFCCs) and the fusion of MFCCs with the Teager Energy Operator (TEO)—the comparison aimed to identify the most suitable features that demonstrated significant performance metrics. Our study was motivated by a previous study that compared MFCCs and TEO-MFCCs in distinguishing emotions, which found that MFCCs performed better for female voices [3]. In our study, a binary classification task (e.g., stress and no stress) was performed with the assistance of deep learning technologies developed, known as Stress Speech Neural Network Architecture (SSNNA). This study utilized SSNNA to classify a combined dataset sourced from the Toronto Emotional Speech Set (TESS) [4] and the Ryerson Audio-Visual Database of Emotional Speech and Song (RAVDESS) [5]. Our study aimed to contribute by developing a stress detection model capable of classifying scripted datasets, specifically focusing on identifying stress and non-stress in female voices.

The subsequent sections of this work were structured in the following manner: Section 2 provided an assessment of prior research studies that had focused on detecting speech stress, specifically targeting females, and reviewed the speech features and the classifiers used. The

methodology employed in this study, elaborated in Section 3, encompassed the processes of data acquisition, data preprocessing, feature extraction, data organization into stress and no-stress classes, as well as the classification architecture (SSNNA). The findings and interpretation presented in Section 4 were examined and discussed. The paper's final section presented the conclusion and potential avenues for future research.

## 2. RELATED WORKS

The trend in this research work could be divided into several key areas, including stress classification using speech features on females, MFCCs and TEO-MFCCs speech features, and the current study utilizing neural network architecture in stress speech classification. The following sub-sections elaborate on each area.

### 2.1. Stress Classification Using Speech Features on Female

Stress detection is crucial for maintaining good mental health. Prolonged, untreated stress can lead to significant breakdowns in well-being and severe mental health issues. Detecting and classifying stress through speech offers an alternative to traditional methods. While traditional methods can effectively detect and classify stress, they have several drawbacks, such as being invasive and intrusive. For example, inserting a medical instrument into the body to perform a cortisol test is not a favorable technique for some patients, as it is considered invasive. Moreover, it likely increased the patient's stress due to unfamiliar procedures.

Speech-based stress detection and classification have brought significant changes in the medical field. It helped detect and classify stress more favorably, as it was considered a non-invasive and contactless approach. The differences in the speech signals produced during stress and non-stress became an important tool for differentiating between these two conditions. For instance, a stressed person exhibited several symptoms while speaking, including a shaky voice and slurred speech, whereas a stress-free person did not [6]. The similarity of speech produced during stress and the differences between these two conditions helped create a better stress classification tool for healthcare providers. This innovation undoubtedly contributed to society.

Speech signals and vocal characteristics produced from one's utterances offered insights into one's emotional state, facilitating stress identification. In this research context, using speech to classify stress in females provided advantages, as it avoided the discomfort associated with invasive and intrusive clinical procedures. Females typically expressed themselves verbally, which enhanced the comfort and engagement of this method [7]. This approach reduced the unnecessary stress that traditional measurements might have induced. Moreover, it was cost-effective and could be conducted at home, promoting broader participation and accessibility.

### 2.2. MFCCs and TEO-MFCCs Speech Features

MFCCs were widely used in the image and audio signal processing fields due to their ability to represent the power spectrum of audio signals compactly [8]. Based on findings from previous researchers, MFCCs effectively highlighted the energies of higher-frequency components in speech signals produced by female speakers [3], [8]. Their studies accurately classified several emotions associated with stress, especially female voices. However, their study focused on classifying individual emotions (emotion classification). It did not combine stress and no-stress emotions into the same classes, despite the title referencing speech stress detection. This approach differed from the objective of speech stress classification, which aimed to identify stress and no-stress classes.

Another speech feature often compared with MFCCs was the fusion of TEO-MFCCs. Under stress, muscle tension in the speaker's vocal tract influences the airflow that generates sound. Consequently, non-linear speech characteristics were crucial for accurately detecting stress in speech, which was the essence of the TEO feature [8]. Previous studies found that combining these two features further improved accuracy for both male and female speakers [3], [8]. The studies agreed that TEO enhanced the energies of the emotional contents of speech—nevertheless, the classification focused on individual emotions rather than combining stress and no-stress emotions.

### 2.3. Current Study Utilizing Neural Network Architecture in Stress Speech Classification

Based on previous works, the usage of neural network architecture in research increased due to the rapid development of the artificial intelligence field [9], [10]. A previous study utilizing an unscripted dataset of 363 recorded call center service interactions [9] employed the Long Short-Term Memory (LSTM) model with an attention layer for the classification task. Their study achieved an accuracy rate of 80% in generating binary classifications for stress and no-stress classes. The authors concluded that the unsatisfactory accuracy was due to the type of dataset used. Further work needed to be done to determine whether the classifier was robust and adaptable to any type of dataset related to the study field.

Another prior study conducted a subsequent investigation utilizing the SUSAS dataset [10]. The study employed deep neural networks (DNNs) operating within an ensemble one-vs-one classification framework. The binary classification achieved the highest level of accuracy, with a single DNN classifier having an accuracy rate of 78%. According to this result, combining many neural networks did not inherently yield favorable performance outcomes. This observation demonstrated that as an algorithm's complexity increased, its accuracy level decreased.

Several key distinctions existed between our work and prior studies. First, our study analysis was limited to the stress prediction of the female class exclusively, with no inclusion of male remarks. To our knowledge, there was a lack of literature on developing classification models for identifying stress in females. Furthermore, our study adhered to the research cycle by replicating a previous study that compared two speech features: MFCCs and the fusion of TEO-MFCCs. This decision was based on the observation that these features could yield good performance metrics, especially for female voices. Finally, our study merged two speech datasets that contained identical emotion classes but with different female speakers to examine the robustness of our model. The subsequent methodology section provides a more detailed explanation of this matter.

## 3. METHODOLOGY

This section provided an overview of every step undertaken to accomplish the main goal. The following subsections give a detailed description of each step. The TESS and RAVDESS datasets were used for this study, and these two datasets were combined. Subsequently, the acquired data underwent preprocessing procedures. Speech features were extracted from the preprocessed data, and the extracted features were organized with stress and no-stress labels. Finally, the workflow of the deep learning algorithm was established. The schematic representation of our research methodology is depicted in Figure 1.

https://doi.org/10.31436/iiumej.v26i1.3411

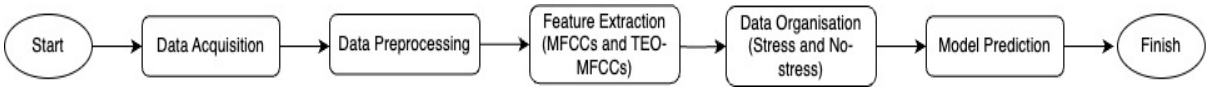


Figure 1. Study flow.

### 3.1. Data Acquisition

This section details each dataset used in the present investigation. Sections 3.1.1 and 3.1.2 detail the TEST and RAVDESS datasets, respectively.

#### *3.1.1. TESS Dataset*

The dataset consisted of female subjects. A total of 200 targeted English phrases were uttered by two actresses, aged 26 and 64, respectively. Recordings were captured for each of the seven emotions: anger, disgust, fear, happiness, neutrality, pleasant surprise, and sadness. In total, a collection of 2800 data points with a duration of 1-2 seconds in each snippet was created.

In the context of deep learning, achieving optimal outcomes necessitated using a balanced dataset across all classes. Consequently, our study decided to use a subset of six emotions instead of incorporating all seven to ensure balanced classes, omitting the disgust emotion. The emotional responses employed to measure stress encompassed anger, fear, and sadness, yielding a cumulative dataset of 1,200 data points. Furthermore, three other emotions were employed to represent the no-stress class: happiness, neutrality, and pleasant surprise. The dataset comprised 600 snippets representing the vocal expressions of young females, along with another 600 snippets representing the vocal expressions of elderly females.

#### *3.1.2. RAVDESS Dataset*

An additional dataset was introduced into the system to assess the reliability of our deep learning algorithm in distinguishing between stress and no-stress classes [11]. It was crucial to ensure that both datasets included identical types of emotion classes to achieve dependable and accurate results [11]. In the second dataset, a total of 24 actors and actresses were included, evenly distributed between 12 females and 12 males. These individuals were recorded vocalizing two English phrases. The speech encompassed a range of emotional expressions, including calmness, happiness, sadness, anger, fear, surprise, and disgust.

To achieve the desired outcome, twelve female speeches were selected, encompassing a variety of emotional states. The emotional states associated with stress included sadness, anger, fear, and disgust, totaling 384 instances. Conversely, emotions characterized by no-stress included neutral, calmness, happiness, and surprise, amounting to 336 instances. In total, there were 720 snippets, each lasting 3 seconds.

#### *3.1.3. Summary of the Combined Datasets*

Based on the elaboration in Sections 3.1.1 and 3.1.2, Table 1 presents a summary of the combined dataset used in this study. The total number of data points used in this study was 3120 snippets consisting of stress and no-stress speeches spoken by female speakers.

Table 1. Summary of the combined datasets

| Classes | TESS dataset | RAVDESS dataset | Total |
|---|---|---|---|
| Stress | 1200 | 384 | 1584 |
| No-stress | 1200 | 336 | 1536 |
| | | **Total** | **3120** |

### 3.2. Data Preprocessing

The data was imported into the IDE with the Torchaudio library, with a sample rate 48k and a total of 140k samples. Subsequently, the signals underwent a normalization process using the mean and standard deviation. Finally, the feature vectors were adjusted to have the same length to ensure that the deep learning process could be applied uniformly. This was achieved by padding the shorter signals with zeros. From our observations, RAVDESS had a longer duration of 2 seconds than the TESS dataset. Thus, all the speech signals from the TESS dataset were zero-padded to ensure the same length. The data was not subjected to filtration, as it was collected in a calm environment without external interference.

### 3.3. Feature Extraction

It was crucial to comprehend that speech involved the filtration of sounds generated by humans through the configuration of the vocal tract, encompassing the tongue, teeth, and other anatomical components. According to previous research [12], when the shape was accurately defined, it accurately represented the phoneme. The selection of the following speech features for this study was based on the promising findings demonstrated in earlier studies [3], [8], [13].

As previously indicated, this research focused on comparing the spectral and TEO speech properties. The first set of speech features employed MFCCs, consisting of 13 coefficients. The second set of speech features combined TEO and MFCCs, consisting of 13 coefficients. Sections 3.3.1 and 3.3.2 provide further details regarding the speech elements employed.

#### *3.3.1. MFCCs*

The compact representation known as MFCCs was obtained by expressing a waveform as the summation of a nearly limitless number of sinusoids. Fluctuations in the MFCC coefficients were detected across different spectrum bands. The predominant portion of the spectrum energy was primarily localized within the low-frequency regions, characterized by positive cepstral coefficients. Conversely, a significant portion of the spectrum energy was concentrated at higher frequencies, corresponding to negative values of the cepstral coefficient. A concise explanation of each sequential process involved in the computation of MFCCs was provided, as stated by previous research [8].

i. **Pre-emphasis:** The utilization of pre-emphasis facilitated the amplification of the higher frequencies within the signal.
ii. **Framing:** Using the Fast Fourier Transform (FFT) resulted in errors due to the non-stationary nature of audio processing. To address this, it was assumed that the audio could be considered a transient stationary process. Consequently, the signal was partitioned into tiny frames. To establish connections between frames, each frame overlapped with one another.
iii. **Windowing:** The conversion from the time domain to the frequency domain was achieved by utilizing the FFT technology. To preserve the quality of the audio resumes,

a window function was employed for each frame. Consequently, high-frequency distortions, known as spectral leakage, were mitigated.

iv. **Discrete Fourier Transform for acquiring the Power Spectrum**: The power spectrum, which is a representation of the frequency spectrum, was obtained by calculating the Short-Time Fourier Transform (STFT) using N iterations (N= 512) of the FFT on each frame.

v. **Filter banks**: The ultimate step in computing filter banks involved extracting frequency bands from the power spectrum by utilizing triangle filters on a Mel scale.

vi. **Discrete Cosine Transform**: The interdependence of the filter bank coefficients computed in the preceding step posed challenges in certain deep learning approaches. To achieve decorrelation to the filter bank coefficients and provide a compressed representation of the filter banks, the Discrete Cosine Transform (DCT) was employed.

### *3.3.2. TEO-MFCCs*

The subsequent technique employed in this study involved the integration of TEO with MFCCs. The signal derived from the pre-processing stage was incorporated into the TEO feature. The process of speech production included both linear and nonlinear components. Previous research has revealed that emotional speech, particularly under stress, exhibited significant alterations in its nonlinear components compared to regular speech [14]. An energy measurement was designed to accurately represent the instantaneous energy of nonlinear components as a direct outcome of the speech inquiry founded by Teager, with the initial form of the energy operator being defined by Kaiser [15]. To obtain the TEO-MFCC features, the signals were first retrieved from the pre-processing stage, then TEO features were applied to the signal, and finally, MFCC features were applied.

## 3.4. Data Organization

The Pandas library was used to differentiate the processed signals generated into stress and no-stress classes, as shown in Figure 2.

| | feature | class |
|---|---|---|
| 0 | [[[tensor(-121.2283), tensor(-121.2283), tenso... | 0 |
| 1 | [[[tensor(-137.1273), tensor(-137.1273), tenso... | 1 |
| 2 | [[[tensor(-125.5066), tensor(-125.5066), tenso... | 0 |
| 3 | [[[tensor(-117.8783), tensor(-117.8783), tenso... | 1 |
| 4 | [[[tensor(-115.4972), tensor(-115.4972), tenso... | 0 |
| ... | ... | ... |
| 3115 | [[[tensor(-18.1040), tensor(0.7011), tensor(9.... | 1 |
| 3116 | [[[tensor(-25.5897), tensor(-15.8098), tensor(... | 1 |
| 3117 | [[[tensor(-30.6487), tensor(-24.4433), tensor(... | 1 |
| 3118 | [[[tensor(-52.5320), tensor(-49.4062), tensor(... | 1 |
| 3119 | [[[tensor(-47.3476), tensor(-35.6632), tensor(... | 1 |

3120 rows × 2 columns

| | feature | class |
|---|---|---|
| 0 | [[[tensor(-139.3613), tensor(-139.3613), tenso... | 0 |
| 1 | [[[tensor(-157.3328), tensor(-157.3328), tenso... | 1 |
| 2 | [[[tensor(-145.3053), tensor(-145.3053), tenso... | 0 |
| 3 | [[[tensor(-132.0546), tensor(-132.0546), tenso... | 1 |
| 4 | [[[tensor(-143.7691), tensor(-143.7691), tenso... | 0 |
| ... | ... | ... |
| 3115 | [[[tensor(-169.3116), tensor(-169.3116), tenso... | 1 |
| 3116 | [[[tensor(-188.7097), tensor(-188.7097), tenso... | 1 |
| 3117 | [[[tensor(-178.7599), tensor(-178.7599), tenso... | 1 |
| 3118 | [[[tensor(-184.0467), tensor(-184.0467), tenso... | 1 |
| 3119 | [[[tensor(-178.6420), tensor(-178.6420), tenso... | 1 |

3120 rows × 2 columns

Figure 2. Features of MFCCs (left side) and TEO-MFCCs (right side) that have been put into classes. 0 means "no stress," and 1 means "stress".

https://doi.org/10.31436/iiumej.v26i1.3411

### 3.5. Model Prediction – Stress Speech Neural Network Architecture (SSNNA)

The PyTorch library performed a binary classification problem: stress and no-stress. This study employed the SSNNA, a CNN architecture developed by this study. Table 2 provides the best possible hyperparameter settings for the SSNNA architecture.

Table 2. Hyperparameter settings for SSNNA

| Settings | Total |
|---|---|
| **Batch size** | 12 |
| **Epoch no.** | 450 |
| **Loss Function** | Cross-Entropy Loss |
| **Optimizer** | Stochastic Gradient Descent |
| **Learning Rate** | 0.00001 |
| **Momentum** | 0.7 |

The SSNNA comprised successive convolutional layers implemented using the PyTorch toolkit, as shown in Figure 3. It consisted of six 2-dimensional convolutional layers (Conv2d) connected with Rectified Linear Unit (ReLU) layers, each followed by a 2-dimensional Max-pooling (MaxPoold2d) layer. After these Conv2d layers, flattened layers were appended, leading to three additional linear layers. The first linear layer begins with a ReLU activation and connects to the output layer, which is categorized into two classes: stress and no stress.

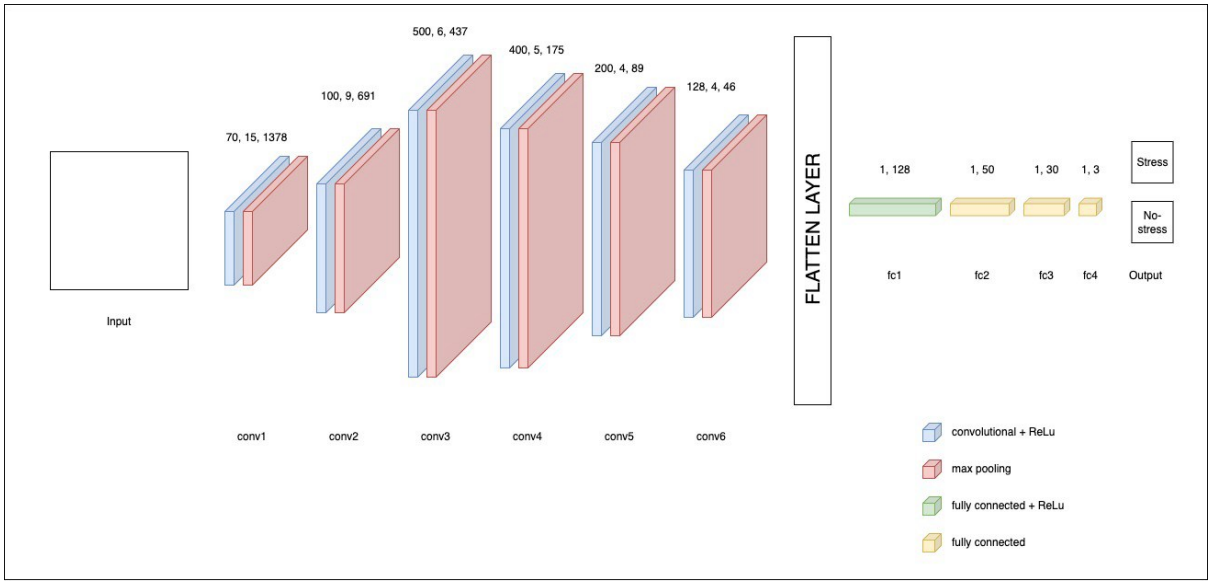


Figure 3. SSNNA architecture.

To ensure the reliability of the results, the data was partitioned into three sets: training, validation, and testing. The training set comprised 80% shuffled data, the validation set comprised 10% non-shuffled data, and the test set comprised 10% non-shuffled data. The model's training was halted once the testing accuracy stabilized, ensuring the prevention of overfitting across all three datasets.

## 4. RESULT AND DISCUSSION

This section presents the results and outcomes of this study. The dataset used for testing purposes encompassed 312 data points. The subsequent discussion relied on the findings

https://doi.org/10.31436/iiumej.v26i1.3411

derived from the testing set. The study employed a set of performance metrics: F1 score, accuracy, the area under the receiver operating characteristic curve (ROC-AUC curve), and confusion matrix. The confusion matrix comprised four components: True Negative (TN), False Positive (FP), False Negative (FN), and True Positive (TP). The confusion matrix results were based on the labeling shown in Table 3. Sections 4.1 and 4.2 provide the results for MFCCs and TEO-MFCCs.

Table 3. Relationship between the confusion matrix and classes

| Classes | No-stress | Stress |
|---|---|---|
| **No-stress** | TN | FP |
| **Stress** | FN | TP |

### 4.1. Performance Metrics Based on the MFCC's Speech Feature

This subsection presents the performance metrics for MFCCs. A confusion matrix is constructed based on the categorization of stress and no-stress to visually represent and summarize the overall performance of the model's predictive outputs, as shown in. Figure 4. The presented confusion matrix shows that the model achieves good accuracy for both stress and no-stress female speeches, with fewer than 10 misclassified data points in each class. The achieved outcomes for the F1 score and accuracy are deemed satisfactory, with values of 0.94 and 93.9%, respectively. Additionally, based on the classes, the stress and no-stress classes achieved 94.2% and 93.7% scores, respectively. The accuracy surpassed the average outcomes for the scripted dataset and approached 100%.

The accuracy scores for the training, validation, and testing sets were 94.9%, 91.7%, and 94.2%, respectively. The score difference between these sets was rather small, indicating that the algorithm was not affected by underfitting or overfitting problems. Furthermore, the ROC curve achieved an AUC value of 0.94, indicating a good outcome [18]. The model demonstrated better accuracy, indicates that the use of MFCCs as a speech feature is an effective approach for identifying stress emotions in female speakers.

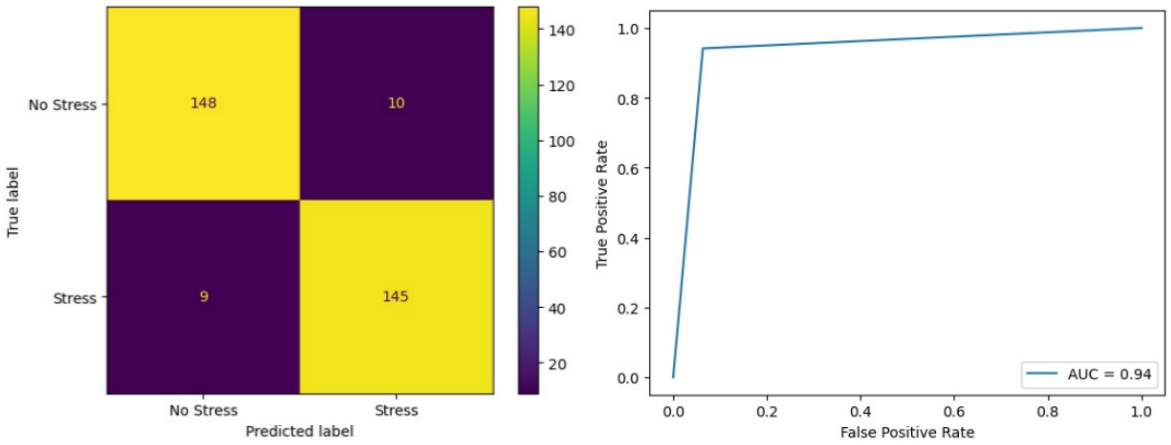


Figure 4. Confusion matrix (left side) and AUC curve (right side) of MFCCs.

### 4.2. Performance Metrics Based on the TEO-MFCC's Speech Feature

Based on the confusion matrix depicted in Figure 5, the model has achieved good accuracy for both stressful and no-stress classes, with less than 19 instances of misclassification in each class. The obtained results for the F1 score and accuracy were satisfactory, with respective

https://doi.org/10.31436/iiumej.v26i1.3411

values of 0.90 and 90.7%. Furthermore, the classes categorized as stress and no stress demonstrated accuracy rates of 93.6% and 87.7%, respectively. The no-stress class achieved good accuracy, while the stress class achieved almost a fair level of accuracy.

Furthermore, the accuracy scores for the training, validation, and testing sets were 93.7%, 89.4%, and 90.7%, respectively. The observed disparity in scores between the sets was also rather small, suggesting that the algorithm remained unaffected by issues related to underfitting or overfitting. In addition, the ROC curve depicted in Figure 5 acquired an AUC value of 0.91. The model has shown satisfactory performance, suggesting that utilizing TEO-MFCC features is another effective technique for recognizing stressed emotions in female speakers. Nevertheless, it could not surpass the superior performance of the MFCCs' speech feature alone. Based on our observation, this was mainly due to the disruption of the signal when it was padded with zeros, which likely led to inaccurate TEO value results. Those values might not have produced useful information distinguishing between stress and no-stress speeches.

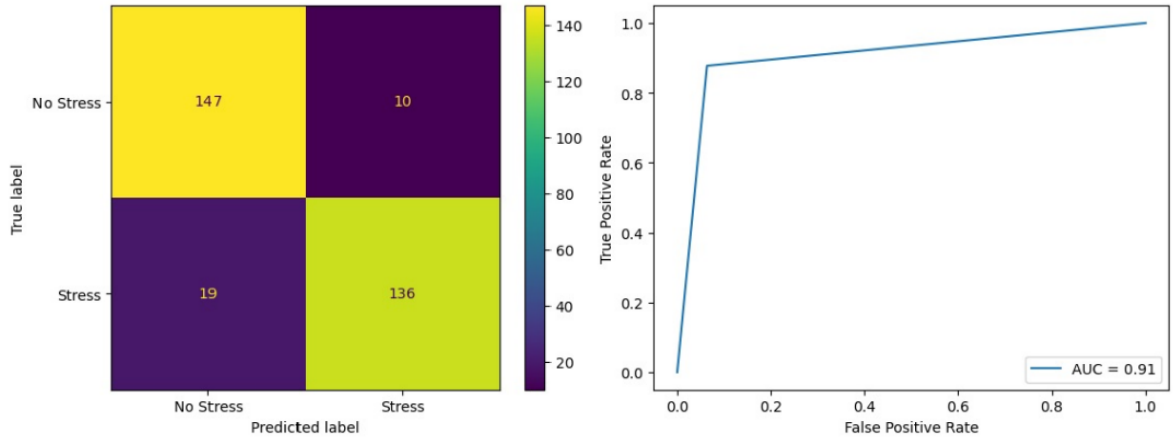


Figure 5. Confusion matrix (left side) and AUC curve (right side) of TEO-MFCCs.

Moreover, based on the analysis of the performance metrics presented in Table 4, it was observed that the speech characteristics derived from MFCCs exhibited favorable performance in stress and no-stress classifications in the female's voice. This was attributed to the characteristics of MFCCs, which were designed to enhance the amplitudes of higher-frequency components in speech signals. The frequencies produced by female vocalizations tend to be naturally higher in intensity compared to males. Besides, this assertion aligned with the results of a prior study [3], wherein the researchers observed that MFCCs yielded highly satisfactory outcomes in female subjects. On another note, the study discovered that the TEO-MFCCs also produced remarkable outcomes in discerning stress in female speakers based on their speech patterns.

Table 4. Relationship between the confusion matrix and classes

| Features | MFCCs | TEO-MFCCs |
|---|---|---|
| **Training Accuracy (%)** | 93.9 | 90.7 |
| **Accuracy based on classes (%)** | Stress: 94.2; No-stress: 93.7 | Stress: 87.7; No-stress: 93.6 |
| **F1-score (0 – 1)** | 0.94 | 0.90 |
| **AUC (0 – 1)** | 0.94 | 0.91 |

Additional components that contributed to the overall better outcomes were increased training data and a considerable balance of data between the classes (achieved by omitting

disgust emotion from the TESS dataset). This enhanced the model's learning capabilities and produced unbiased stress classification outcomes. In addition, based on our research, no study had been conducted that integrates several datasets while utilizing only females' speeches. Therefore, in this paper, we opted to exclude a comparative analysis with other studies due to their lack of direct comparability.

## 5. CONCLUSION AND FUTURE WORKS

The impact of stress on females was a prevalent concern that warranted attention since females were more stressed than males. This was attributed to differences in stress perception, hormonal transitions, and other factors. Efforts were made to mitigate the long-term persistence of this issue, as it could potentially lead to adverse consequences for affected individuals. Speech stress detection and classification provided several advantages, especially for females, as they were non-invasive and non-intrusive approaches. This method also comforted females as they were naturally verbally expressing their thoughts and feelings, adding another positive aspect to this approach. MFCCs demonstrated their effectiveness as speech features by providing valuable information in both stress and no-stress female speech datasets. MFCCs improved the energies of the higher-frequency components of the female speech signals, which could distinguish between these two classes. MFCCs achieved 93.9% accuracy, accompanied by an F1-score of 0.94 and an ROC-AUC of 0.94. Meanwhile, TEO-MFCCs also produced satisfactory results, but they could not surpass the results of MFCCs due to the disruptions of the speech signals during the feature extraction stage. Hence, care needs to be taken if the researchers intend to use TEO-MFCCs as the speech feature where manipulation of speech signals is involved.

The combination of SSNNA and MFCCs could distinguish between the two classes using 14 different female speeches expressing eight emotions. This demonstrated that the classifier was speaker-independent, indicating that the system was more scalable and user-friendly. Additionally, this made it easier for real-world applications since it did not require speaker-specific data collection for adaptation. It improved data efficiency by enabling diverse training datasets, which enhanced the algorithm's generalization and robustness and reduced bias. In conclusion, the combination of MFCCs and SSNNA helped accurately classify stress and no-stress classes, especially in female speeches. For future works, increasing the number of speakers in the dataset was suggested to enhance generalizability, reduce bias, and improve model performance. Additionally, expanding the classification from two to three categories—low, medium, and high stress—would allow a more effective assessment of an individual's stress levels.

## ACKNOWLEDGEMENT

The study was financially supported by the Fundamental Research Grant Scheme (FRGS) administered by the Ministry of Higher Education (MoHE), with the reference code FRGS/1/2021/TK0/UIAM/02/29.

## REFERENCES

[1] K. Monesson, "Why Are Women More Stressed Out Than Men? | UKG." Accessed: Sep. 11, 2023. [Online]. Available: https://www.ukg.com/blog/life-work-trends/why-are-women-more-stressed-out-men

[2] A. Ghazali, "Wanita tidak tahan tekanan - Sinar Harian," Sinar Harian Newspaper. Accessed: Sep. 04, 2023. [Online]. Available: https://www.sinarharian.com.my/article/10527/sinar-aktif/murung

[3] M. S. Nordin *et al.*, "Stress Detection based on TEO and MFCC speech features using Convolutional Neural Networks (CNN)," in *2022 IEEE International Conference on Computing (ICOCO)*, IEEE, Nov. 2022, pp. 84–89. doi: 10.1109/ICOCO56118.2022.10031771.

[4] M. K. Pichora-Fuller and K. Dupuis, "Toronto emotional speech set (TESS)," 2020, *Borealis*. doi: doi/10.5683/SP2/E8H2MF.

[5] S. R. Livingstone and F. A. Russo, "The Ryerson Audio-Visual Database of Emotional Speech and Song (RAVDESS): A dynamic, multimodal set of facial and vocal expressions in North American English," 2018, doi: 10.5281/zenodo.1188976.

[6] "Great Speech." Accessed: Jul. 11, 2024. [Online]. Available: https://www.greatspeech.com/can-emotional-stress-cause-speech-problems/

[7] B. Sağlam Topal and A. E. Yavuz Sever, "I love you but I can't say: adaptation of the Measure of Verbally Expressed Emotion (MoVEE) to Turkish and investigation of psychometric properties," *Current Psychology*, vol. 43, no. 24, pp. 20881–20890, Jun. 2024, doi: 10.1007/s12144-024-05861-5.

[8] S. R. Bandela and T. K. Kumar, "Stressed speech emotion recognition using feature fusion of teager energy operator and MFCC," in *2017 8th International Conference on Computing, Communication and Networking Technologies (ICCCNT)*, IEEE, Jul. 2017, pp. 1–5. doi: 10.1109/ICCCNT.2017.8204149.

[9] S. Bromuri, A. P. Henkel, D. Iren, and V. Urovi, "Using AI to predict service agent stress from emotion patterns in service interactions," *Journal of Service Management*, vol. 32, no. 4, pp. 581–611, 2020, doi: 10.1108/JOSM-06-2019-0163.

[10] S. Mihalache, D. Burileanu, and C. Burileanu, "Detecting Psychological Stress from Speech using Deep Neural Networks and Ensemble Classifiers," Institute of Electrical and Electronics Engineers (IEEE), Nov. 2021, pp. 74–79. doi: 10.1109/sped53181.2021.9587430.

[11] A. De Arriba, M. Oriol, and X. Franch, "Merging Datasets for Emotion Analysis," in *2021 36th IEEE/ACM International Conference on Automated Software Engineering Workshops (ASEW)*, IEEE, Nov. 2021, pp. 227–231. doi: 10.1109/ASEW52652.2021.00051.

[12] X. Huang, A. Acero, H.-W. Hon, and R. Reddy, *Spoken Language Processing: A Guide to Theory, Algorithm, and System Development*, 1st ed. USA: Prentice Hall PTR, 2001.

[13] M. S. Hafiy Hilmy *et al.*, "Stress Classification based on Speech Analysis of MFCC Feature via Machine Learning," in *2021 8th International Conference on Computer and Communication Engineering (ICCCE)*, IEEE, Jun. 2021, pp. 339–343. doi: 10.1109/ICCCE50029.2021.9467176.

[14] H. Gao, S. Chen, P. An, and G. Su, "Emotion recognition of mandarin speech for different speech corpora based on nonlinear features," in *2012 IEEE 11th International Conference on Signal Processing*, IEEE, Oct. 2012, pp. 567–570. doi: 10.1109/ICoSP.2012.6491552.

[15] M. El Ayadi, M. S. Kamel, and F. Karray, "Survey on speech emotion recognition: Features, classification schemes, and databases," *Pattern Recognit*, vol. 44, no. 3, pp. 572–587, Mar. 2011, doi: 10.1016/j.patcog.2010.09.020.

https://doi.org/10.31436/iiumej.v26i1.3446

# MODIFIED COST-235 EMPIRICAL PATHLOSS MODEL FOR AGRICULTURAL-WSN USING PARTICLE-SWARM-OPTIMIZATION

**SYAHFRIZAL TAHCFULLOH[1,4*], ETTY WAHYUNI[2,4], DWI SANTOSO[3,4], RIZKYANDI JULIANNANDA[1]**

[1]*Department of Electrical Engineering, Universitas Borneo Tarakan, Tarakan, Indonesia*
[2]*Department of Agribusiness, Universitas Borneo Tarakan, Tarakan, Indonesia*
[3]*Department of Agrotechnology, Universitas Borneo Tarakan, Tarakan, Indonesia*
[4]*Research Center for Natural Resources and Tropical Waters in Border Areas, Tarakan, Indonesia*

**Corresponding author: syahfrizal@borneo.ac.id*

*(Received: 13 September 2024; Accepted: 22 October 2024; Published online: 10 January 2025)*

***ABSTRACT:*** The increasing demand for agricultural products yearly encourages farmers to seek solutions to migrate from conventional farming to smart and precise farming by utilizing technological advances such as implementing wireless sensor networks (WSN). Unlike conventional farming, this technology is believed to provide many advantages, including low cost, high efficiency, optimized land use, and high productivity results. However, this system is highly dependent on the availability of network interconnection where the bottleneck is the instability of signal strength and path loss, especially for radio wave propagation from the transmitter (Tx) in the form of sensors to the receiver (Rx) in the form of data processors where its performance depends on the distance, agricultural, environmental conditions, and surrounding vegetation. This paper explicitly examines and analyzes radio wave propagation modeling for measuring radio frequency (RF) signal strength in local agriculture's 2.4 GHz WSN system, such as Adan rice, corn, and peanuts. The particle-swarm-optimization (PSO) method is used to modify empirical path loss models such as Weissberger, ITU-vegetation, COST-235, Egli, and FITU-R, which also involve the influence of rain attenuation. Several other factors are also considered in the evaluation and analysis, i.e., the planting period of agricultural crops (seedlings, growth, and maturity), vegetation depth, and the height of the Tx-Rx antenna from the ground. The results of the experimental evaluation show that the PL COST-235 model continues to be optimized using the PSO method because it has the lowest RMSE both in conditions without and with rain attenuation, which are 23.30 and 9.33, respectively. Meanwhile, after the selected model is optimized using the PSO method, the RMSE for both conditions becomes 2.49 and 5.29.

***ABSTRAK:*** Permintaan yang semakin meningkat terhadap produk pertanian setiap tahun mendorong para petani untuk mencari penyelesaian bagi beralih daripada pertanian konvensional kepada pertanian pintar dan tepat dengan memanfaatkan kemajuan teknologi seperti penggunaan rangkaian sensor tanpa wayar (WSN). Berbeza dengan pertanian konvensional, teknologi ini dipercayai memberikan banyak kelebihan, termasuk kos yang rendah, kecekapan yang tinggi, pengoptimuman penggunaan tanah, dan hasil produktiviti yang tinggi. Namun begitu, sistem ini sangat bergantung kepada ketersediaan rangkaian interkoneksi di mana kelemahan utamanya adalah ketidakstabilan kekuatan isyarat dan kehilangan laluan (path loss), terutamanya bagi penyebaran gelombang radio dari pemancar (Tx) berbentuk sensor ke penerima (Rx) berbentuk pemproses data, yang prestasinya bergantung kepada jarak, keadaan persekitaran pertanian, dan tumbuh-tumbuhan di sekeliling. Kajian ini secara khusus meneliti dan menganalisis pemodelan penyebaran gelombang radio untuk mengukur kekuatan isyarat frekuensi radio (RF) dalam sistem WSN

2.4 GHz di pertanian tempatan seperti padi Adan, jagung, dan kacang tanah. Kaedah pengoptimuman kawanan zarah (particle-swarm-optimization, PSO) digunakan untuk mengubah suai model kehilangan laluan empirikal seperti Weissberger, ITU-vegetation, COST-235, Egli, dan FITU-R, yang turut melibatkan pengaruh pelemahan hujan. Beberapa faktor lain juga dipertimbangkan dalam penilaian dan analisis ini, seperti tempoh penanaman tanaman pertanian (anak benih, pertumbuhan, dan kematangan), kedalaman tumbuh-tumbuhan, dan ketinggian antena Tx-Rx dari permukaan tanah. Hasil penilaian eksperimen menunjukkan bahawa model PL COST-235 terus dioptimumkan menggunakan kaedah PSO kerana ia mempunyai nilai RMSE paling rendah dalam kedua-dua keadaan tanpa dan dengan pelemahan hujan, iaitu masing-masing 23.30 dan 9.33. Sementara itu, selepas model yang dipilih dioptimumkan menggunakan kaedah PSO, nilai RMSE bagi kedua-dua keadaan menjadi 2.49 dan 5.29.

***KEYWORDS:*** *Agriculture-WSN, FITU-R, Pathloss, Particle-Swarm-Optimization, Root-Mean-Square-Error.*

# 1. INTRODUCTION

FAO stated that global supply and demand for agricultural products as food such as rice, wheat, corn, peanuts, etc., increased above 2,846 million tons per harvest season in 2024-2025 [1]. Several other factors also triggered a significant increase in agricultural output to be more effective, smart, precise, and operate efficiently, reduce farm labor costs, and support environmental sustainability [2], precise control over plant placement, soil conditions, to the use of chemicals, and minimize waste and costs [3], including the ability to monitor plant growth and development precisely in the presence of diseases or pests, nutrient provision, yield estimation, and production levels [4, 5]. One of these smart and precise agricultural technologies can be a combination of the implementation of a wireless sensor network (WSN) with the Internet of Things (IoT) architecture as a general monitoring system [6] and a smart agricultural management system such as that applied in Bangladesh agriculture [7], agricultural irrigation in greenhouses [8], and the application of certain network protocols [9].

One of the focuses of the study on the WSN system, especially related to radio wave propagation, is the measurement of radio frequency (RF) in the form of signal strength from sensors that carry information such as temperature, humidity, soil nutrient content, etc. to the node so that this paper is made to describe it. The availability of interconnection dictates the connection from sensors to nodes in the WSN system. One of the main obstacles in the WSN is the path loss (PL), namely the loss of the radio wave propagation path from the transmitter (Tx) to the receiver (Rx), which depends on the distance, the condition of the type of agricultural environment including weather, and the surrounding vegetation so that it can reduce the quality of the connection. The path passed through the farmland by the radio wave propagation signal reduces the signal strength due to attenuation, absorption, reflection, refraction, and scattering by trees, leaves, vegetation, and other environmental conditions. Several studies have examined PL in the agricultural sector, such as a study by [10] for agricultural products in the form of corn, rice, and peanuts, a study by [11] for corn growth variations, and a study by [12] for fruit farming. PL methods investigated in studies [10]-[12] include: in [10] using models such as ITU-vegetation, Weissberger, and COST-235 with a WSN system frequency of 2.4GHz, in [11] using the Log-normal distribution method for the 2.4GHz WSN system, and in a study by [12] where the PL calculation involves the effect of rain attenuation with a wireless system with a frequency of 433MHz and 2.4GHz. From this description, it is apparent that it is necessary to study in more depth how radio wave propagation from the WSN system, especially PL, can be applied to several agricultural

products at once, which may have different environmental and vegetation characteristics so that it is hoped that a general formulation of radio wave propagation modeling can be found that can represent all agricultural products.

This paper evaluates and analyzes the propagation of radio waves from RF measurements in the form of signal strength using a 2.4 GHz WSN system. The particle-swarm-optimization (PSO) method is still rarely applied to PL modeling, especially in agriculture, as reported in [13]. This method is used to obtain an accurate PL model that fits the surrounding environmental conditions. In the study [13], the PSO method was applied to grass farming, such as the alfalfa plant, to model exponential and polynomial PL. There is also a PSO method to determine PL, but it is applied to cellular networks, such as studies by [14] and [15]. PSO in this paper is used to modify empirical PL models such as Weissberger (W), ITU-vegetation (ITU), COST-235, Egli, and FITU-R by involving the influence of rain attenuation, which is then compared with PL results from RF measurements on local agricultural yields and lands such as Adan rice, peanuts, and corn. Adan rice, especially, needs little water in its growing land. It is a rice variant that grows in the highlands of the interior of North Kalimantan, Indonesia, i.e., the Krayan Area, Nunukan [16]. Therefore, this rice is known as highland rice, a major commodity in areas bordering neighboring countries, such as Malaysia. For these various reasons, the PL study of local Adan rice vegetation is worthy of study.

Evaluation of PL was conducted by considering several factors such as distance, Tx-Rx height, planting period of agricultural crops, and especially the influence of environmental characteristics as reported by [17]. What makes this paper more valuable is the additional contribution to the study of PL related to vegetation that influences it when compared to several previous related studies, including the study by [18] where the measurement location was in a tropical area which is known to have very high rainfall or wetlands as reported by [19], and the type of rice planted was not common because it could grow in land with less water or dry land. Thus, this research can increase technical knowledge in wireless radio wave propagation and its planning, which is influenced by relatively extreme environmental conditions.

This paper is organized as follows: Section 2 explains the methods used, such as research stages, including research materials, reviews of empirical models of PL, and the PSO method. Section 3 presents all study results and is followed by a discussion, including signal strength measurements, PL calculations, and performance modifications of PL. The paper ends with Section 4, which contains the conclusions of this study.

## 2. METHOD

This section describes how to collect measurement data, including the area, descriptions of empirical PL models, and the PSO method for determining modified PL.

### 2.1. Measurement Area and Data Collection

In this study, the strength of the RF signal was measured in the form of a received signal strength indicator (RSSI, $P_r$) on three types of local agricultural crops, such as Adan rice, corn, and peanuts, at their respective planting locations as shown in Fig. 1. This RF measurement considers three growth conditions of the three types of plants, i.e., the seedling period, growth period, and maturity period. According to a study [20], Adan rice in Krayan, Nunukan, Indonesia, has a maximum height of up to 1.5 m with an average planting period of 6.5 months. According to a study by [21], local corn in the same area has a maximum height of around 1.8m with a planting period of 3 months. Meanwhile, according to a study by [22], peanuts has an average height of 0.45m with a planting period of up to 2 months.

https://doi.org/10.31436/iiumej.v26i1.3446

Measurements were carried out at the planting location of the three types of plants to obtain RSSI values. RF signal strength measurements were taken when each plant had the three conditions mentioned previously, i.e., seedling, growth, and maturity periods, where the time and height of the three plants adjusted to the height and planting period based on studies [20]-[21] for Adan rice, corn, and peanuts. For Adan rice, the height of the plant during the seedling, growth, and maturity periods was 0.2m, 1.2m, and 1.4m, respectively. In corn plants, measurement data was taken with the height of the three planting periods, respectively around 0.2m, 1.4m, and 1.8m. In peanut plants, data was taken when the height in the three planting periods was around 0.1m, 0.2m, and 0.4m. The size of the three plants determines the height of the Tx and Rx installation. Fig. 2 shows the location of Tx and Rx during the measurement where there are wet and dry rice fields of Adan rice in Krayan, Nunukan, Indonesia. The location of Tx is conditioned to be fixed while the location of Rx is varied moving forward and up 20m along the size of the rice field, which is 40m × 500m. In contrast, corn and peanut plants have areas measuring 30m × 250m and 25m × 150m, respectively.

(a) Adan rice (b) Corn (c) Peanuts

Figure 1. Measurement environment for the three crop locations.

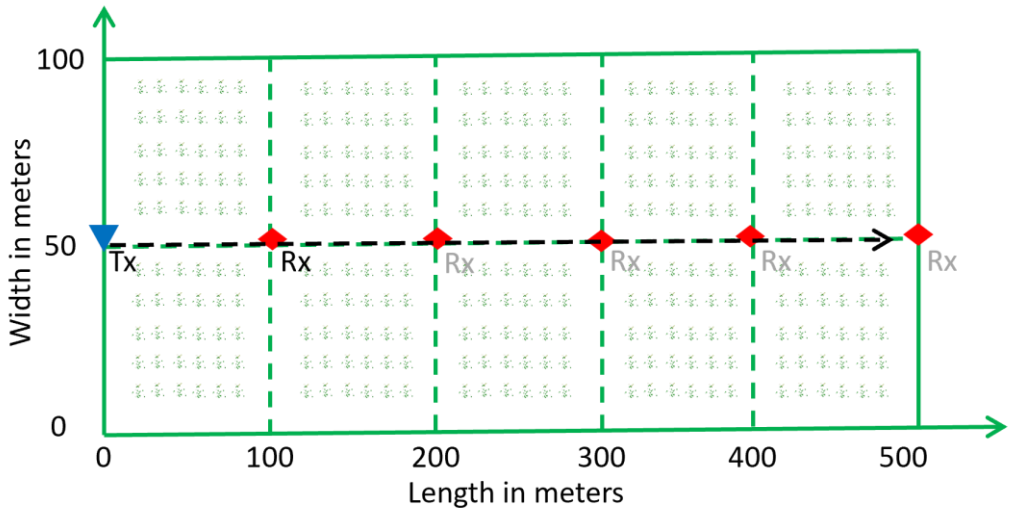


Figure 2. Setting the signal strength measurement area in rice fields, especially in the case of Adan rice.

Fig. 3 shows how to determine signal strength data (in dB) for signals received at the receiver antenna (Rx) in the form of RSSI. This RSSI comes from 2.4GHz RF measurements

https://doi.org/10.31436/iiumej.v26i1.3446

from the vector signal analyzer (VNA) to the Rx as a spectrum signal analyzer (SSA). Both devices use omnidirectional antennas with a gain of 0dBi ($G_t$ and $G_r$) and have a transmit power ($P_t$) of around 10dBm (≈ 0.01watt). A personal computer (PC) or laptop is used to calculate PL from measurement data in RSSI and PL from empirical models. The data of transmit power, working frequency, and antenna gain in the RF measurement system are summarized in Table 1. The placement of both equipment during measurements from the ground is adjusted to the condition of the plant height in 3 conditions, i.e., the seedling, growth, and maturity periods, which also determines the height of the Tx and Rx antennas as $h_t$ and $h_r$. From the measurement data of signal strength ($P_r$), transmit power ($P_t$), and the gain of both antennas. PL can be determined as $PL_m$ with the formula

$$PL_m = P_t + G_t + G_r - P_r \quad (1)$$

where the units for $P_t$, $P_r$, $G_t$, and $G_r$ are dBm, dBm, dBi, and dBi, respectively.

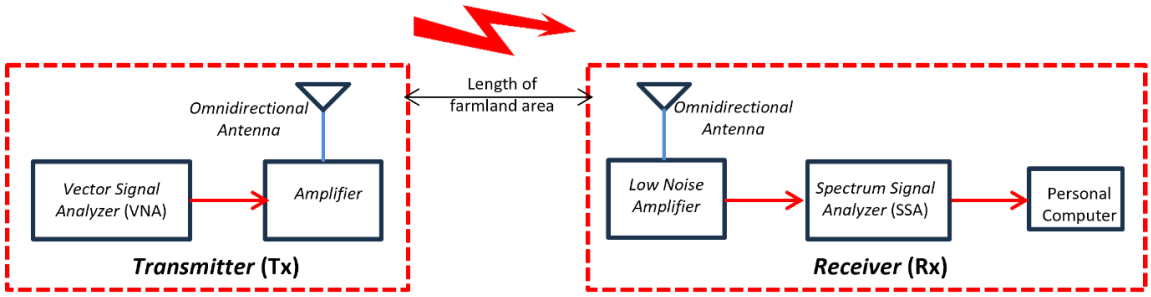


Figure 3. RF measurement configuration on farmland.

Table 1. Parameter settings for RF measurements

| System Parameters | Value |
|---|---|
| Frequency (GHz), $f$ | 2.4 |
| Transmit power (dBm), $P_t$ | 10 |
| Antenna type | Omnidirectional |
| Tx and Rx antenna gain (dBi), $G_t$ and $G_r$ | 0 |
| Measurement parameter (dBm), $P_r$ | RSSI |

Pathloss in Eq. (1) is calculated by involving aspects such as the height of the crop, the distance between Tx-Rx, the planting period of the crop, and the type of environmental vegetation. North Kalimantan, Indonesia, has a fairly high average rainfall. According to a study reported by [19], rainfall has a significant effect on the propagation of high-frequency radio waves, especially in Indonesia, which generally has a tropical climate with high rainfall and the location of the research area which is, in fact, an area on the equator so that rain attenuation also increases the high PL. In the study reported by [12], rain attenuation contributes positively to increasing the PL of the empirical model, which increases the attenuation described in Section 2.2. Rain attenuation in dB is expressed by [12]

$$A_r = kr^{\alpha} \quad (2)$$

where $r$ denotes the rain rate in mm/h, and both $k$ and $\alpha$ depend on the frequency distribution of rainfall size. Suppose it is assumed to use horizontally polarized antenna propagation at a frequency of 2.4GHz. In that case, the $k$ and $\alpha$ values are respectively 0.0001321 and 1.1209 [12], so by using Eq. (2) for a rain rate of 140mm/h, a rain attenuation of 14.73dB is obtained. However, if using statistical data from BPS North Kalimantan 2023 [26], the average rain rate is around 243.78 mm/h, so the rain attenuation is around 12.04dB. After the $PL_m$ determination

https://doi.org/10.31436/iiumej.v26i1.3446

process, it is continued by comparing it with the PL from theoretical calculations using models commonly used in the environment with the influence of vegetation, leaves, and trees, including Weissberger (W), ITU-vegetation (ITU), COST-235, Egli, and FITU-R, whose expressions are given in Section 2.2.

To test and validate the PL obtained from measurement results ($PL_m$) and empirical calculation results ($PL_e$) based on existing models, the root-mean-square-error (RMSE) and coefficient-of-determination ($R^2$) parameters are used to test statistically, which are respectively given by the expression [10].

$$RMSE = \sqrt{\frac{1}{n}\sum_{n=1}^{N}(PL_e - PL_m)^2} \tag{3}$$

and

$$R^2 = \frac{\sum_{n=1}^{N}(PL_e - \widehat{PL_m})^2}{\sum_{n=1}^{N}(PL_m - \widehat{PL_m})^2} \tag{4}$$

where $n$ indicates the amount of measurement data and $\widehat{PL_e}$ as the average of PL. Suppose the calculation result in Eq. (3) has a small value, in that case, it indicates a PL model that can be used as a reference to predict and estimate PL as a characteristic that matches the propagation of radio waves in the vegetation, likewise with $R^2$ in Eq. (4) where if the value is close to or equal to 1, the empirical PL model can be used as PL to predict the characteristics of radio wave propagation through WSN applications in the planting environment of the agricultural crops. This happens because the empirical PL model is said to have variations that are almost similar to PL from the measurement data.

## 2.2. Empirical Pathloss Models

Here are some empirical models of PL, and if the calculation result of RMSE is small and R2 is close to one, then the model will be used and agreed upon as a PL model to predict the characteristics of radio wave propagation in the vegetation. Furthermore, the PL model will also be optimized with the PSO method to become the best modified PL model for the type of plant and its vegetation. In this paper, several empirical models are applied specifically for PL involving trees, vegetation, and soil conditions, such as Weissberger (W), ITU-vegetation (ITU), COST-235, Egli, and FITU-R. These empirical models have been recommended for calculating PL by studies [12], [23]-[25] in the agricultural field.

### *2.2.1. Free Space (FS) Pathloss*

This PL model in dB is a simple model of the working frequency of the wireless system ($f$) in Hz and the distance ($d$) in meters between Tx and Rx, which is formulated with [10].

$$PL_F = 20log_{10}(f) + 20log_{10}(d) - 147.56 \tag{5}$$

### *2.2.2. Two-ray (TR) Pathloss*

This model includes the influence and reflection of two rays, i.e., the ground ray and the line-of-sight (LOS) ray, which are expressed by the expression [25].

$$PL_{TR} = 40log_{10}(d) - 20log_{10}(h_t) - 20log_{10}(h_r) \tag{6}$$

https://doi.org/10.31436/iiumej.v26i1.3446

#### *2.2.3. Weissberger Pathloss*

This model is used for paths with signals with a frequency ($f$) in GHz whose propagation is obstructed by dense, leafy, and dry trees in dB with a vegetation depth of $d$ in meters, which is stated by [10].

$$PL_W = \begin{cases} 0.45f^{0.284}d \text{ for } 0m < d \leq 14m \\ 1.33f^{0.284}d^{0.588} \text{ for } 14m < d \leq 400m \end{cases} \quad (7)$$

#### *2.2.4. ITU-Vegetation Pathloss*

This PL model is intended for Tx or Rx close to a small group of trees so that the signal propagates through the trees with a depth ($d$) in meters expressed by [10].

$$PL_{ITU} = 0.2f^{0.3}d^{0.6} \quad (8)$$

with the condition $d < 400$m.

#### *2.2.5. COST-235 Pathloss*

This PL model is for trees with a depth of $d$ in meters expressed in dB with [10].

$$PL_C = 15.6f^{-0.009}d^{0.26} \quad (9)$$

#### *2.2.6. Egli Pathloss*

This PL model is expressed in dB for the working frequency $f$ in MHz and involves the presence of the surrounding terrain factor with the expression [24].

$$PL_E = PL_F + 20log_{10}\left(\frac{f}{40}\right) \quad (10)$$

#### *2.2.7. FITU-R Pathloss*

This PL model applies to VHF signals with a maximum short foliage depth of around 400m with a depth $d$ in meters expressed in dB with [23], [25].

$$PL_{FITU} = 0.39f^{0.39}d^{0.25} \quad (11)$$

### 2.3. Particle-Swarm-Optimization Method for Pathloss

According to [13], PSO is a heuristic approach to solving optimization problems. Some particles, called swarms, can regulate the speed of optimization calculations that provide the best results. To determine the optimal solution, particle modifications are carried out involving parameters such as the best position ($p_b$) *and the best global position* ($g_b$) *where the position of the ith particle (pi) and the velocity of the ith* particle ($v_i$) for $i$ = 1, 2, ..., $I$. The iterative equation of the PSO method for iteration index $n$ = 1, 2, ..., $N$, which determines the solution by setting $v_i$ and $p_i$ is expressed as

$$v_i^{n+1} = wv_i^n + c_1r_1(p_b - p_i) + c_2r_2(g_b - p_i) \quad (12)$$

with

$$p_i^{n+1} = p_i + v_i^{n+1} \quad (13)$$

where $w$ is the inertia weight, $c_1$ and $c_2$ denote the scaling constants, and $r_1$ and $r_2$ are random vectors with values between 0-1. The formulation in Eqs. (12)-(13) is used to estimate the PL from the empirical model with the smallest RMSE value of all empirical PLs against the PL of the measurement data.

https://doi.org/10.31436/iiumej.v26i1.3446

Before PSO optimization is carried out on the PL model that has the smallest RMSE, first determine the empirical PL model from Eqs. (5)-(11), which has a trend close to the PL of measurement data as indicated by the smallest RMSE value. Furthermore, the PL model is optimized using the PSO method, which aims to generate coefficients from the PL model so that it has a trend close to the measurement PL, which is indicated by a smaller RMSE or R2 approaching 1. This adopts the steps of PL model optimization by [14], which is carried out for mobile communication systems. The basic process of the PSO method consists of initialization, constraint assignment, fitness evaluation of all particles, and selection, as in Fig. 4.

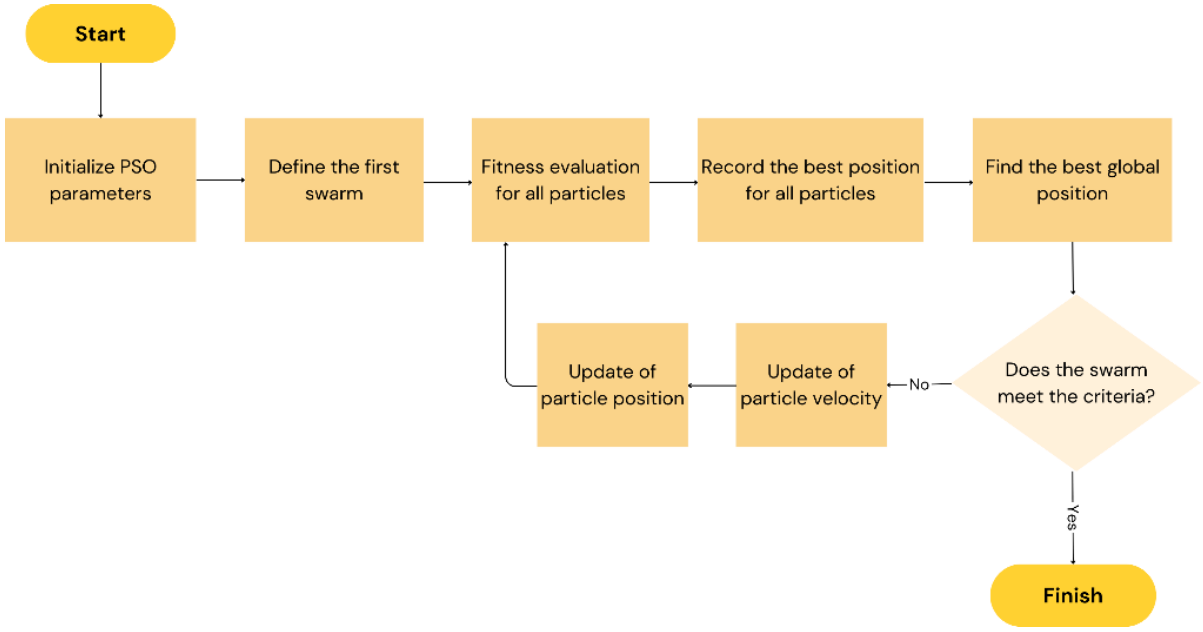


Figure 4. Flowchart of PSO method.

## 3. RESULTS AND DISCUSSION

This section presents the results of experimental measurements along with their analysis and discussion, which include (a) the results of signal strength measurements in the form of RSSI for the three types of plants during the seedling, growth, and maturity stages, (b) determining the $PL_m$ from measurements using Eq. (1) with the data in Table 1 and RSSI ($P_r$) obtained from the RF measurement results in point (a), (c) then the $PL_m$ is compared with theoretical calculations for the $PL_e$ models in Eqs. (5)-(11) with and without involving rain attenuation in Eq. (2), and (d) determining the empirical PL model that has the smallest RMSE and $R^2$ against the PL data from RF measurements with Eqs. (3)-(4) will be used as a modified PL model using the PSO method. It can then be recommended as a PL model for agricultural WSN systems at the research location and its surroundings.

### 3.1. Signal Strength Measurement in Agricultural Plants

Fig. 5 shows the results of RSSI measurements with the RF system for agricultural crops in three planting conditions for Adan rice, corn, and peanuts in Figs. 5(a), 5(b), and 5(c), respectively. All RSSI values decrease with increasing vegetation depth, which is proportional to the distance between the Tx and Rx antennas. In Fig. 5(a), the RSSI measurement data on Adan rice plants, the receiver sensitivity during the seedling, growth, and maturity periods is -82dBm, -89dBm, and -95dBm, respectively. RF measurements can still be done with vegetation depths up to 500m. RSSI at maturity is lower because rice plants at that age already have many dense leaves when compared to RSSI at seedling and growth periods. According to

https://doi.org/10.31436/iiumej.v26i1.3446

[20], the number of leaves at maturity is 108, more than the growth period where the number of leaves is 9. This happens because the signal emitted by the sensor node at Tx is mostly absorbed by vegetation, such as leaves from Adan rice. In the seedling period, the RSSI is measured relatively high compared to other planting periods because the depth of the plants is still sparse, and the trees are still relatively small. However, during the seedling period, there is still a reduction in the transmitted signal from the sensor node originating from the land surface where the conditions are wet and watery so that it reflects the transmitted signal. These results strengthen the study [10], which only measured the RSSI of agricultural crops such as corn, rice, and peanuts in two planting conditions, namely the growth and maturity periods only, and the results showed that the growth period had a relatively high RSSI compared to the maturity period.

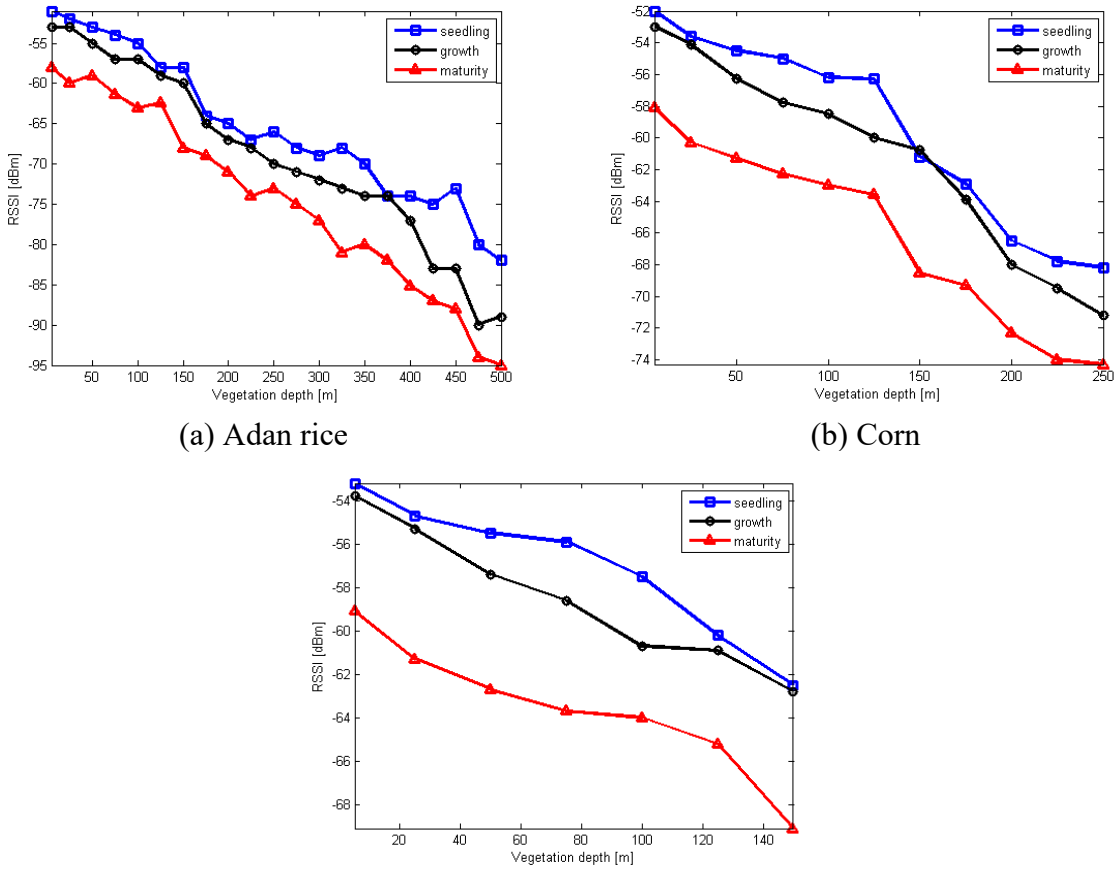


(a) Adan rice (b) Corn

(c) Peanuts

Figure 5. RSSI measurements during seedling, growth, and maturity periods for agricultural crops.

The RSSI measurement results on corn plants in Fig. 5(b) have a similar phenomenon to the RSSI measurement on Adan rice plants. However, because the length of the plant field is lower than the length of the Adan rice field, which is only 250m, the receiver sensitivity obtained successively at the seedling, growth, and maturity periods are -68.2dBm, -71.2dBm, and -74.3dBm. Compared to Adan rice plants at a vegetation depth of 250m, the RSSI of the three planting conditions is -66dBm, -70dBm, and -73dBm, respectively. This indicates that corn plants have denser and thicker vegetation than Adan rice, so signal absorption by vegetation, i.e., from trees and leaves, is relatively greater than that in Adan rice. This result has also been proven previously in a study by [10]. According to a study [21] on corn, the

https://doi.org/10.31436/iiumej.v26i1.3446

number of leaves is 3 strands per tree during the seedling period, and the stem diameter is around 0.29 cm. During the maturity period, the number of leaves is 25 strands more than during the seedling period, and the stem diameter is, on average, 3 cm.

RF measurements in peanut plants (see Fig. 5(c)) also have an RSSI level phenomenon as in RSSI measurements in Adan rice and corn. Receiver sensitivity obtained successively at seedling, growth, and maturity periods are -62.5dBm, -62.8dBm, and -69.1dBm, respectively, where the depth of plant vegetation is around 150m. For RSSI values on Adan rice with the same vegetation depth in the three measured planting conditions, around -64dBm, -65dBm, and -69dBm, respectively. It can be seen that during the maturity period, the RSSI received by the Rx node of the peanut plant is weaker than that of the rice plant because it is influenced by the depth of the peanut plant, which has dense leaves, and the reflection from the soil surface where the maximum planting height of peanuts is lower by around 45cm [22] compared to Adan rice up to 150cm.

### 3.2. Pathloss in Agricultural Crops

Based on Eq. (1), the PL of RF measurement results can be calculated through the RSSI signal strength obtained in Fig. 5 for all agricultural crops. In Fig. 6 for Adan rice plants, the PL of measurement data and PL from empirical models have been presented. In contrast, Fig. 6(a) shows the PL of measurements and PL of empirical models without the addition of PL from the Free-Space (PLF) model and PL from the Two-ray (PLTR) model, Fig. 6(b) shows the PL of measurements and PL of empirical models with the addition of PLF. Fig. 6(c) shows the PL of measurements and PL of empirical models with the addition of $PL_{TR}$. The three empirical PL determination conditions are used to calculate the empirical PL model that matches the PL measurement data in agricultural plants. This method has been investigated by [25] for tomato agricultural plants in greenhouses, and the aim is to determine the PL model that approaches the measurement PL model because the signal from the Tx node comes from various signal propagation paths.

At a glance, it can be seen in Fig. 6(a) that the empirical PL model that is closest to the trend of the RF measurement PL is the COST-235 PL model, where this empirical model is very close to the measurement PL data. At the same time, other empirical models have a range far below the measurement data, such as PL from ITU (PLITU), Weissberger PL (PLW), and PL from FITU (PLFITU), and above the measurement data, such as Egli PL ($P_{LE}$). In addition to PL from PLF, the PLE model that approaches the three conditions of measurement PL and other empirical PL is below the measurement PL, as shown in Fig. 6(b). In addition to path losses with PLTR, all empirical model PLs are above the measurement PL shown in Fig. 6(c). Thus, for the next PL calculation, to optimize the PL model with the PSO method, the COST-235 PL model in Fig. 6(a) is selected. As described in the last paragraph in Section 2.3, the PL model that has the smallest RMSE against the PL measurement is optimized by the PSO method. This is also supported by the study reported by [14]. To strengthen the determination of a suitable model for optimization, the RMSE value of the empirical PL model ($PL_e$) and the measured PL ($PL_m$) is calculated, and the one with the smallest RMSE value is selected, as was done by [14]. Based on the same approach to Adan rice plants in Fig. 6(a), the results of PL calculations from measurement data and empirical models are presented in corn and peanut plants, as in Fig. 7(a) for corn and Fig. 7(b) for peanut plants. It can be seen from Figs. 7(a)-(b) that the empirical PL model that approaches the trend of RF measurement PL is the COST-235 PL model.

https://doi.org/10.31436/iiumej.v26i1.3446

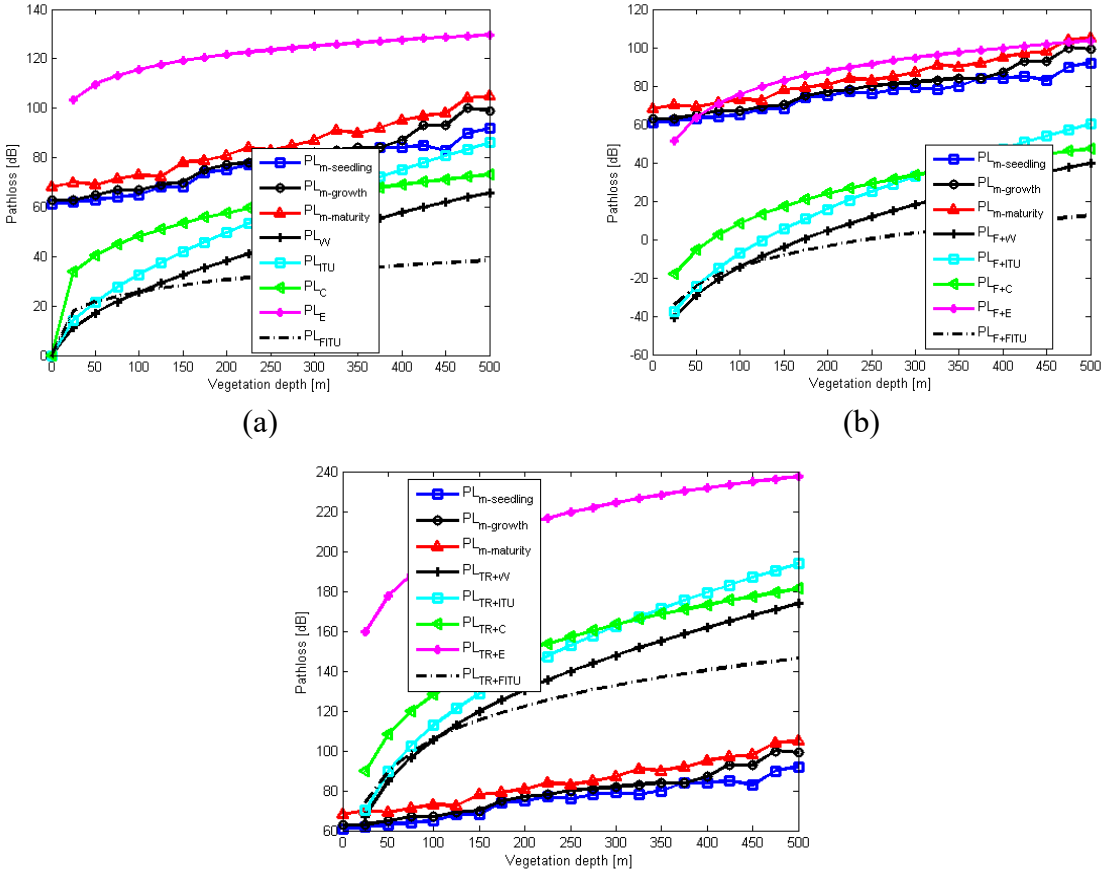


(a) (b)

(c)

Figure 6. Calculation of PL measurements and empirical PL models of Adan rice plants for (a) without adding $PL_F$ and $PL_T$, (b) adding $PT_F$, and (c) adding $PL_T$.

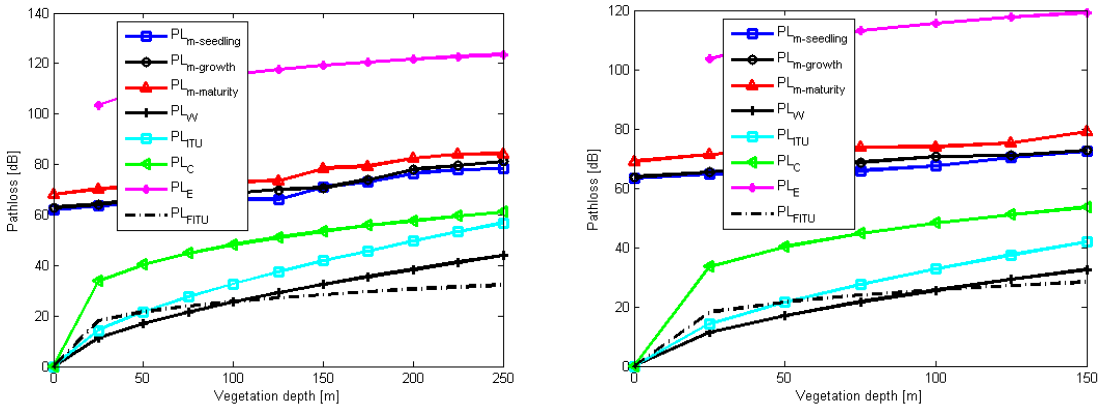


(a) (b)

Figure 7. Calculation of PL measurements and empirical PL models of crops: (a) corn and (b) peanuts.

To find an accurate PL model of the type of agricultural crops, land, and its environment, it is also advisable to consider the influence of weather, especially the presence of rain attenuation, because it is known that the research location is an area with high average rainfall as reported by [26] with an average of around 243.78 mm/h. A study that has reported the

https://doi.org/10.31436/iiumej.v26i1.3446

involvement of rain attenuation is [12], where rain attenuation influences fruit farming land on the propagation of 2.4GHz frequency radio waves.

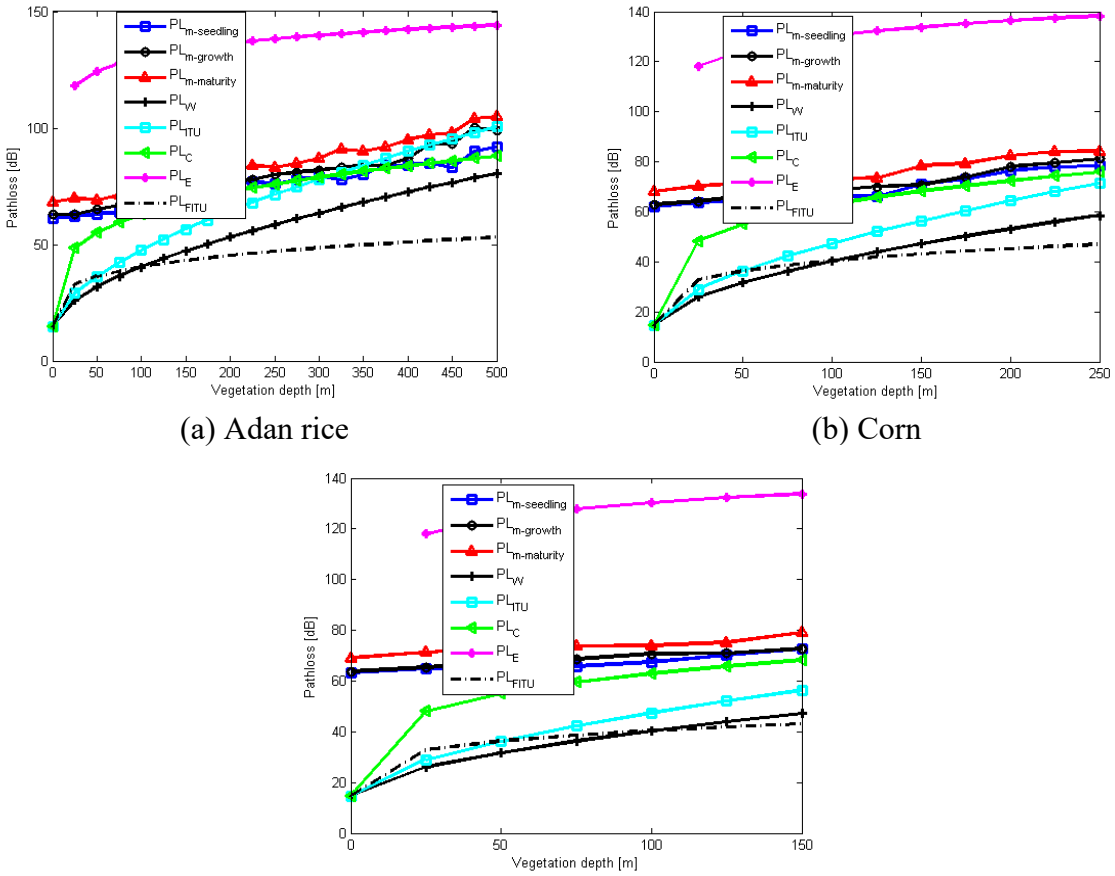


(a) Adan rice (b) Corn

(c) Peanuts

Figure 8. Calculation of PL measurement and PL empirical model of agricultural crops with the influence of rain for (a) Adan rice, (b) corn, and (c) peanuts.

It can be seen in Fig. 8 that the involvement of rain attenuation is also applied to the calculation of the empirical model PL. Rain attenuation at a location with a certain rainfall is calculated using Eq. (2), and then the results are added to the existing empirical model PL. Without involving the influence of the Free-space model PL and Two-ray PL and only with the PL shown in Fig. 6(a) and Fig. 7, the results of the PL calculation with rain attenuation are completely shown in Fig. 8, where there is an increase of around 14.7dB. It can be seen from these results that the COST-235 model PL is a strong candidate for continued optimization with the PSO method for the three types of plants that cover the three planting seasons.

### 3.3. Performance of RMSE and Pathloss Determination Coefficient with PL Measurement Results

The performance of PL, which is no less important for comparing PL measurement results, proposed PL, and PL results from empirical model calculations, is determining the accuracy of data predictions from both PL determinations, i.e., by determining RMSE [10], [12], [14], [23]. RMSE is one of the statistical parameters in modeling data, which is calculated using Eq. (3). Table 2 shows the results of the RMSE calculation of the PL of all empirical models, the proposed model against the PL of measurement data from the three plants presented in Figs.

6(a) and 7 previously. The model indicated as appropriate and suitable for estimating measurement data is the theoretical model with the lowest RMSE value [10], [18].

It can be seen from Table 2 that the PL model COST-235 is the right model to be used as a basis for estimating PL measurement data in wireless wave propagation systems, such as WSN systems, from three types of plants, including their planting conditions. This is based on the model's RMSE value, which is the lowest value compared to other models of PL measurement results. When compared with the RMSE value on corn and peanut plants, the RMSE on Adan rice plants is lower because the observation data is more, so the variation of empirical model prediction errors with measurement data shows a small value. By involving the influence of weather, such as rain attenuation, the RMSE value is presented in Table 3 for the three types of plants where the PL results have been shown in Fig. 8. The RMSE results in Table 3 show that the PL COST-235 model the smallest RMSE value of the PL models, so this result strengthens that this model continues to be optimized with the PSO method. Both results in Tables 2 and 3 show that the effect of rain attenuation for tropical areas such as those experienced by this data collection location is appropriate and appropriate to be included in the calculation and modeling of radio wave propagation.

Table 2. Comparison of RMSE in PL measurements and empirical models for agricultural crops

| Type | Planting period | RMSE | | | | |
|---|---|---|---|---|---|---|
| | | W | ITU | COST | E | FITU |
| Adan rice | Seedling | 34.06 | 23.99 | **17.24** | 45.83 | 45.03 |
| | Growth | 37.29 | 26.37 | **20.79** | 42.45 | 48.82 |
| | Maturity | 42.59 | 31.29 | **26.12** | 37.13 | 54.19 |
| Corn | Seedling | 40.95 | 33.19 | **20.13** | 46.56 | 43.43 |
| | Growth | 42.69 | 34.88 | **21.83** | 44.75 | 45.21 |
| | Maturity | 47.59 | 39.73 | **26.69** | 39.89 | 50.07 |
| Peanuts | Seedling | 45.11 | 39.09 | **22.94** | 45.48 | 43.61 |
| | Growth | 46.67 | 40.65 | **24.46** | 43.90 | 45.16 |
| | Maturity | 51.73 | 45.68 | **29.51** | 38.91 | 50.23 |

Table 3. Comparison of RMSE in PL measurements and empirical models for agricultural crops with rain attenuation

| Type | Planting period | RMSE | | | | |
|---|---|---|---|---|---|---|
| | | W | ITU | COST | E | FITU |
| Adan rice | Seedling | 20.01 | 13.79 | **4.22** | 60.49 | 30.40 |
| | Growth | 22.92 | 14.28 | **6.87** | 57.06 | 34.27 |
| | Maturity | 28.10 | 18.15 | **11.76** | 51.71 | 39.61 |
| Corn | Seedling | 26.43 | 19.31 | **6.48** | 61.23 | 28.76 |
| | Growth | 28.15 | 20.86 | **7.79** | 59.43 | 30.53 |
| | Maturity | 33.03 | 25.57 | **12.39** | 54.56 | 35.39 |
| Peanuts | Seedling | 30.53 | 24.75 | **8.97** | 60.16 | 28.93 |
| | Growth | 32.08 | 27.28 | **10.32** | 58.57 | 30.47 |
| | Maturity | 37.12 | 31.24 | **15.18** | 53.56 | 35.54 |

### 3.4. PSO Modified Pathloss Performance

After seeing the RMSE data in Tables 2 and 3, the optimization process with PSO was applied to the COST-235 PL model, which had the lowest RMSE compared to other empirical PL models. This procedure has been carried out by [13] and [14] by determining the values of

https://doi.org/10.31436/iiumej.v26i1.3446

the coefficients of a PL formulation based on the PSO method against Eq. (9), which is a candidate for modification, and the formulation is rewritten as

$$PL_{C-PSO} = \gamma_1 f^{\gamma_2} d^{\gamma_3} \tag{14}$$

and if we take into account rain attenuation, then it becomes

$$PL_{C-PSO} = \gamma_1 f^{\gamma_2} d^{\gamma_3} + \gamma_4 \tag{15}$$

where $\gamma_1$, $\gamma_2$, $\gamma_3$, and $\gamma_4$ are the coefficients of the PL model of COST-235 optimized by the PSO method.

In Eqs. (14)-(15), the complete coefficients before the PSO method is applied can be seen in Table 4. For the application of PSO using Eqs. (12)-(13) then the values of $w$, $c_1$, and $c_2$ are given as 0.5, 1.5, and 1.5, respectively. These numbers control the performance of PSO during the iteration process to produce a modified formulation of PL COST-235 with the latest RMSE value, which is smaller than before this method was applied. After conducting simulations and evaluations of the PSO method with PL measurement data and PL model COST-235 from the three types of plants and their planting periods, the results were obtained in Tables 5 and 6, respectively, for PSO performance without and with rain attenuation.

Table 4. Coefficients of the COST-235 path loss model without the PSO method

| COST-235 PL Parameters | COST-235 PL coefficient without PSO | COST-235 PL coefficient with rain attenuation and without PSO |
|---|---|---|
| $\gamma_1$ | 15.6 | 15.6 |
| $\gamma_2$ | -0.009 | -0.009 |
| $\gamma_3$ | 0.26 | 0.26 |
| $\gamma_4$ | 0 | 14.7 |

Table 5. Coefficients, RMSE, and $R^2$ of the COST-235 path loss model with the PSO method

| Type | Planting period | Coefficient | | | RMSE | | $R^2$ | |
|---|---|---|---|---|---|---|---|---|
| | | $\gamma_1$ | $\gamma_2$ | $\gamma_3$ | Without | With | Without | With |
| Adan rice | Seedling | 19.5 | -0.015 | 0.27 | 17.24 | 3.61 | 0.18 | 0.94 |
| | Growth | 19.3 | -0.014 | 0.28 | 20.79 | 3.34 | 0.21 | 0.95 |
| | Maturity | 19.1 | -0.013 | 0.29 | 26.12 | 3.24 | 0.15 | 0.96 |
| Corn | Seedling | 22.1 | -0.028 | 0.29 | 20.13 | 2.07 | 0.05 | 0.67 |
| | Growth | 21.8 | -0.028 | 0.28 | 21.83 | 2.02 | 0.06 | 0.68 |
| | Maturity | 21.2 | -0.023 | 0.28 | 26.69 | 2.01 | 0.06 | 0.71 |
| Peanuts | Seedling | 22.8 | -0.028 | 0.29 | 22.94 | 2.07 | 0.07 | 0.69 |
| | Growth | 22.4 | -0.028 | 0.28 | 24.46 | 2.02 | 0.08 | 0.71 |
| | Maturity | 22.2 | -0.023 | 0.28 | 29.51 | 2.01 | 0.08 | 0.75 |

Table 5 shows the application of the PSO method on the COST-235 PL model, where, in general, there are changes in the coefficients of the COST-235 PL model in Table 4. It also appears that by applying this method, it can be seen that the RMSE performance of all types of plants and their planting periods has decreased drastically in the RMSE value of around 11%, where the details for Adan rice, corn, and peanuts are 16%, 10%, and 8%, respectively. Meanwhile, the performance of the determination coefficient ($R^2$) of all types of plants and their planting periods has increased quite significantly by around 8.98 times, with the details for Adan rice, corn, and peanuts being 5.38, 12.18, and 9.37 times, respectively. Indeed, the results of the increase in RMSE and $R^2$ performance are not like those in the study reported by [13], where $R^2$ reached a perfect value of 1 because the PL model before optimization already

https://doi.org/10.31436/iiumej.v26i1.3446

had an $R^2$ above 0.90. In this research case, the previously optimized model has a very small $R^2$ below 0.5. This is because the COST-235 PL model starts from 0 and then approaches the PL value, which is very much determined by the working frequency of the WSN system and the distance between Tx and Rx. Furthermore, the factor of a lot of data can affect the performance of the PL optimization model. This is supported by evaluating the RMSE and $R^2$ performance for Adan rice, whose values are relatively better than those of corn and peanut plants.

The results of the performance of RMSE, coefficients, and $R^2$ in Table 6 with the PSO method involving rain attenuation show the same phenomenon as the condition without rain attenuation in Table 5, i.e., an increase in RMSE, changes in the values of the coefficients, and approaching the value of 1 for $R^2$. Due to the involvement of the rain attenuation factor, the RMSE value of the measurement data and the empirical PL model is smaller than without rain attenuation. The RMSE results with the PSO method involving rain attenuation from all types of plants and their planting periods showed a very drastic decrease in the RMSE value of around 61%, where the details for Adan rice, corn, and peanuts were 60%, 66%, and 58%, respectively. Meanwhile, for the performance of the determination coefficient ($R^2$) of all types of plants and their planting periods, there was a significant increase of around 10.5 times, with the details for Adan rice, corn, and peanuts being 1.28, 4.2, and 26.05 times, respectively.

Table 6. Coefficients, RMSE, and $R^2$ of the COST-235 pathloss model with the influence of rain and the PSO method

| Type | Planting period | Coefficient | | | RMSE | | $R^2$ | |
|---|---|---|---|---|---|---|---|---|
| | | $\gamma_1$ | $\gamma_2$ | $\gamma_3$ | Without | With | Without | With |
| Adan rice | Seedling | 18.1 | -0.014 | 0.25 | 4.22 | 4.08 | 0.60 | 0.90 |
| | Growth | 18.4 | -0.015 | 0.26 | 6.87 | 4.38 | 0.75 | 0.91 |
| | Maturity | 19.3 | -0.015 | 0.26 | 11.76 | 2.30 | 0.85 | 0.97 |
| Corn | Seedling | 17.8 | -0.019 | 0.26 | 6.48 | 5.02 | 0.31 | 0.81 |
| | Growth | 17.5 | -0.019 | 0.27 | 7.79 | 5.29 | 0.26 | 0.84 |
| | Maturity | 18.2 | -0.019 | 0.28 | 12.39 | 6.62 | 0.13 | 0.88 |
| Peanuts | Seedling | 20.5 | -0.010 | 0.22 | 8.97 | 5.38 | 0.07 | 0.83 |
| | Growth | 20.5 | -0.010 | 0.23 | 10.32 | 5.31 | 0.05 | 0.94 |
| | Maturity | 16.6 | -0.013 | 0.29 | 15.18 | 9.28 | 0.02 | 0.95 |

Based on the analysis related to the role of the PSO method in optimizing PL in the COST-235 model, there is an increase in the performance of both RMSE and R2 for conditions without and with rain attenuation. In general, it can be said that the PSO method works well and effectively in optimizing this PL, so several modification models of the COST-235 PL can be obtained for the three types of plants covering the planting period, both during the seedling period, growth, and maturity. If associated with a similar radio wave propagation study in agriculture by [13] with alfalfa plants, this PSO method seems to apply to any plant and any location, but by also considering vegetation factors, the surrounding environment, weather conditions, and the selection of empirical models that are appropriate for these conditions.

## 4. CONCLUSION

This paper presents calculations, evaluations, and analyses related to radio wave propagation, especially signal strength and path loss measured on Adan rice, corn, and peanuts agricultural land for 2.4GHz agriculture-WSN applications in North Kalimantan, Indonesia. Several empirical models are provided to find candidate models optimized by the PSO method, including Weissberger (W), ITU-vegetation (ITU), COST-235, Egli, and FITU-R. Various factors are taken into consideration in determining the appropriate PL model in the study,

including the planting period of the three types of agricultural crops (seedling, growth, and maturity periods), the depth of vegetation between Tx and Rx, the height of the Tx and Rx antennas from the ground according to the planting period of the three types of crops, environmental conditions, and the effect of rain attenuation. Based on the results of the RMSE calculation without and with rain attenuation, the COST-235 PL model provides the lowest RMSE of the other empirical PL models. Thus, this model continues to be optimized with the PSO method, which produces changes in the exact coefficients of the parameters in the COST-235 PL model. As a result, the modified COST-235 PL model with PSO significantly improves the RMSE value, which is very low, and the coefficient of determination (R2), which is almost 1. In the future, it is expected that farmers can implement and plan this WSN application for local plant cultivation and replace conventional and manual plant growth monitoring systems so that the agricultural process becomes more effective and efficient and also helps preserve the environment. Further studies of this wave propagation modeling by considering other empirical models, including hybrid methods involving numerical optimization, and considering the effects of seasonal and weather variations involving real-time and long measurement times, different observation and measurement locations, and practical implications for farmers.

## ACKNOWLEDGEMENT

The authors would like to thank the Institute for Research and Community Service at UBT for supporting and funding this research through the 2024 Thematic Research grant program.

## REFERENCES

[1] FAO. (2024) Food Outlook, Biannual Report on Global Food Markets.
[2] Jin T, Han X. (2024) Robotic arms in precision agriculture: a comprehensive review of the technologies, applications, challenges, and future prospects. Computers and Electronics in Agriculture, 221. https://doi.org/10.1016/j.compag.2024.108938
[3] Petrović B, Bumbálek R, Zoubek T, Kuneš R, Smutný L, Bartoš P. (2024) Application of precision agriculture technologies in central europe-review. Journal of Agriculture and Food Research, 15. https://doi.org/10.1016/j.jafr.2024.101048
[4] Ram BG, Oduor P, Igathinathane C, Howatt K, Sun X. (2024) A systematic review of hyperspectral imaging in precision agriculture: Analysis of its current state and future prospects. Computers and Electronics in Agriculture, 222. https://doi.org/10.1016/j.compag.2024.109037
[5] Atmaja FTS, Mandala S. (2023) Motion detection and pest prevention system in rice plants using deep learning. International Conference on Data Science and Its Applications, Bandung, Indonesia, 248-253. https://doi.org/10.1109/ICoDSA58501.2023.10276784
[6] Khasanov D, Khujamatov K, Fayzullaev B, Reypnazarov E. (2021) WSN-based monitoring systems for the solar power stations of the telecommunication devices. IIUM Engineering Journal, 22(2):98-118. https://doi.org/10.31436/iiumej.v22i2.1464
[7] Pandiyaraju V, Ganapathy S, Mohith N, Kannan A. (2023) An optimal energy utilization model for precision agriculture in WSNs using multi-objective clustering and deep learning. Journal of King Saud University-Computer and Information Sciences, 35(10). https://doi.org/10.1016/j.jksuci.2023.101803
[8] Benyezza H, Bouhedda M, Kara R, Rebouh S. (2023) Smart platform based on IoT and WSN for monitoring and control of a greenhouse in the context of precision agriculture. Internet of Things, 23. https://doi.org/10.1016/j.iot.2023.100830
[9] Suryady Z, Shaharil MHM, Bakar KA, Khoshdelniat R, Sinniah GR, Sarwar U. (2011) Performance evaluation of 6LoWPAN-based precision agriculture. The International Conference on Information Networking, Kuala Lumpur, Malaysia, 171-176. https://doi.org/10.1109/ICOIN.2011.5723173
[10] Balachander D, Rao TR, Mahesh G. (2013) RF propagation experiments in agricultural fields

and gardens for wireless sensor communications. Progress in Electromagnetics Research C, 39:103-118. https://doi.org/10.2528/PIERC13030710

[11] Li F, Wu H, Miao Y, Zhu L. (2013) A research on the radio signal propagation characteristics in corn field. BioTechnology: An Indian Journal, 8(10):1347-1352.

[12] Xu X, Zhang Z, Xu Y, Yang Z, Chen Y, Liang Z, Zhou J, Zheng J. (2018) Measurement and analysis of wireless propagative model of 433MHz and 2.4GHz frequency in southern china orchards. IFAC-PapersOnLine, 51(17):695-699. https://doi.org/10.1016/j.ifacol.2018.08.115

[13] Jawad HM, Jawad AM, Nordin R, Gharghan SK, Abdullah NF, Ismail M, Shaeer MJAA. (2019). Accurate empirical path-loss model based on particle swarm optimization for wireless sensor networks in smart agriculture. IEEE Sensors Journal, 20(1):552-561. https://doi.org/10.1109/jsen.2019.2940186

[14] Garah M, Oudira H, Djouane L, Hamdiken N. (2017). Particle swarm optimization for the path loss reduction in suburban and rural area. International Journal of Electrical and Computer Engineering, 7(4):2125-2131. http://doi.org/10.11591/ijece.v7i4.pp2125-2131

[15] Omasheye OR, Azi S, Isabona J, Imoize AL, Li CT, Lee CC. (2022). Joint random forest and particle swarm optimization for predictive pathloss modeling of wireless signals from cellular networks. Future Internet, 14(12):1-26. https://doi.org/10.3390/fi14120373

[16] Khaerunnisa, Wahyuni-MS E, Rukmana D, Egra S, Masitah, Fitriani R, Wulandary A. (2023) Is agricultural institutions affect the sustainability of local adan rice farming?. Indigenous Agriculture, 1(1):18-28. https://doi.org/10.20956/ia.v1i1.25785

[17] Popoola JJ, Ponnle AA, Olasoji YO, Oyetunji SA. (2018). Investigation on need for specific propagation model for specific environment based on different terrain characteristics. IIUM Engineering Journal, 19(2):90-104. https://doi.org/10.31436/iiumej.v19i2.886

[18] Tahcfulloh S, Riskayadi E. (2015) Optimized suitable propagation model for GSM 900 path loss prediction. TELKOMNIKA Indonesian Journal of Electrical Engineering, 14(1):154-162. http://dx.doi.org/10.11591/telkomnika.v14i1.7470

[19] Tahcfulloh S. (2010) The effects of rain attenuation and interference to BFWA system performance using site diversity-adaptive coded modulation in Indonesia area. Asia-Pacific Conference on Applied Electromagnetics, Port Dickson, Malaysia, 1-5. https://doi.org/10.1109/APACE.2010.5719774

[20] Fauziah F, Rizal M. (2022) Potensi pengembangan padi adan di kabupaten nunukan. Proceedings Series on Physical & Formal Sciences, 4:83–87. https://doi.org/10.30595/pspfs.v4i.488

[21] Ramayana S, Idris SD, Rusdiansyah R, Madjid KF. (2021) Pertumbuhan dan hasil tanaman jagung (zea mays l.) terhadap pemberian beberapa komposisi pupuk majemuk pada lahan pasca tambang batubara. Agrifor, 20(1):35-46. https://doi.org/10.31293/agrifor.v20i1.4877

[22] Idawanni I, Haiqal M. (2023) Pertumbuhan dan hasil kacang tanah pada lahan kering masam dengan teknologi pemupukan. Agriflora, 7(2):8-17. https://doi.org/10.3061/unayaded.v7i2.4652

[23] Hakim GPN, Habaebi MH, Toha SF, Islam MR, Yusoff SHB, Adesta EYT, Anzum R. (2022) Near ground pathloss propagation model using adaptive neuro fuzzy inference system for wireless sensor network communication in forest, jungle and open dirt road environments. Sensors, 22:3267. https://doi.org/10.3390/s22093267

[24] Joshi GG, Dietrich CB, Anderson CR, Newhall WG, Davis WA, Isaacs J, Barnett G. (2005) Near-ground channel measurements over line-of-sight and forested paths. IEE Proceedings - Microwaves, Antennas and Propagation, 152(6):589-596. https://doi.org/10.1049/ip-map:20050013

[25] Cama-Pinto D, Damas M, Holgado-Terriza JA, Gómez-Mula F, Cama-Pinto A. (2019) Path loss determination using linear and cubic regression inside a classic tomato greenhouse. Int. J. Environ Res Public Health, 16(10). https://doi.org/10.3390/ijerph16101744

[26] Badan Pusat Statistik Provinsi Kalimantan Utara. Available: https://kaltara.bps.go.id/id/statistics-table/2/MzQjMg==/jumlah-curah-hujan-menurut-bulan-dan-stasiun.html

https://doi.org/10.31436/iiumej.v26i1.3455

# DESIGN AND IMPLEMENTATION OF A DEEP LEARNING BASED HAND GESTURE RECOGNITION SYSTEM FOR REHABILITATION INTERNET-OF-THINGS (RIOT) ENVIRONMENTS USING MEDIAPIPE

**NURUL HANIS MOHD DHUZUKI[1], AHMAD ANWAR ZAINUDDIN[1*], NUR ANIS SOFEA KAMARUL ZAMAN[2], ALIN NUR MAISARAH AHMAD RAZMI[2], WONDERFUL SHAMMAH KAITANE[3], ASMARANI AHMAD PUZI[1], MOHD NAQIUDDIN JOHAR[4], MASLINA YAZID[5], NOR AZLIN MOHD NORDIN[6], SHAHRUL NAIM SIDEK[7], HASAN FIRDAUS MOHD ZAKI[7]**

[1]*Department of Computer Science, Kulliyyah of Information & Communication Technology, International Islamic University Malaysia, Gombak, Malaysia*
[2]*Department of Information System, Kulliyyah of Information & Communication Technology, International Islamic University Malaysia, Gombak, Malaysia*
[3]*MILA University, Putra Nilai, Nilai, Malaysia*
[4]*Physiotheraphy Unit, Rehabilitation Department, Hospital Putrajaya, Malaysia*
[5]*Department of Rehabilitation Medicine, Hospital Shah Alam, Malaysia*
[6]*Faculty of Health Sciences, Universiti Kebangsaan Malaysia, Malaysia*
[7]*Department of Mechatronics Engineering, Kulliyyah of Engineering, International Islamic University Malaysia, Gombak, Malaysia*

**Corresponding author: anwarzain@iium.edu.my*

*(Received: 1 October 2024; Accepted: 25 December 2024; Published online: 10 January 2025)*

***ABSTRACT:*** Frequent hospital visits for hand rehabilitation exercises, such as strengthening and opposition exercises, present significant challenges, especially for patients in remote areas. This paper addresses this problem by developing a Rehabilitation Internet-of-Things (RIOT) system that utilizes MediaPipe with its pre-trained Deep Learning (DL) to deliver real-time feedback during hand rehabilitation exercises alongside Web Assembly (WASM) for efficient processing. The system's objective is to provide precise, real-time tracking of hand movements, enabling patients to perform exercises at home by maintaining an optimal distance between the camera and hand placement, ensuring ideal room lighting conditions across IoT devices such as mobile phones' front cameras and webcams, while healthcare professionals remotely monitor their progress. The methodology involves the integration of MediaPipe for detecting hand landmarks and adaptive sensitivity algorithms to ensure reliable recognition across different environments, such as varying lighting and hand positions. Future work could incorporate additional deep-learning models like CNNs and RNNs to enhance gesture classification accuracy. Several limitations, including latency and distance sensitivity, are addressed in this system with edge computing alongside adaptive algorithms. The key contributions of this research are as follows: First, developing a real-time and cost-effective solution for remote stroke rehabilitation. Second, accuracy is improved by integrating MediaPipe with deep learning techniques. Lastly, latency issues and accuracy challenges at extended distances are alleviated by employing innovative calibration methods and adaptive adjustments. Initial trials demonstrate promising results, though further testing is required under real-world conditions to validate the system's effectiveness fully.

***ABSTRAK:*** Perjalanan yang kerap ke hospital untuk latihan pemulihan tangan, seperti latihan rawatan fisioterapi telah memberikan cabaran yang besar bagi pesakit yang tinggal di pedalaman. Sistem Pemulihan Internet Benda (RIOT) menggunakan MediaPipe bersama

https://doi.org/10.31436/iiumej.v26i1.3455

Deep Learning (DL) yang telah dilatih untuk memberikan maklum balas masa nyata semasa latihan pemulihan tangan, serta Web Assembly (WASM) untuk pemprosesan yang cekap, sebagai penyelesaian. Tujuan sistem ini adalah untuk menyediakan penjejakan pergerakan tangan yang tepat dalam masa nyata, yang mampu dijalankan latihan di rumah dengan pemantauan pegawai perubatan untuk meneliti kemajuan mereka dari jarak jauh. Metodologi melibatkan penyatuan MediaPipe untuk mengesan titik penting pada tangan dan algoritma kepekaan suaian untuk memastikan pengiktirafan yang boleh dipercayai dalam pelbagai persekitaran, seperti pencahayaan dan kedudukan tangan. Lonjakan bagi kajian in adalah dapat menggabungkan model DL seperti CNNs dan RNNs untuk meningkatkan ketepatan dan penyusunan isyarat. Sistem ini juga dapat mengurangkan masalah masa pendam dan perubahab jara dengan melaksanakan edge computing dan penyesuaian algoritma. Sumbangan utama kajian ini termasuklah sistem masa nyata yang kos efektif untuk pemulihan strok jarak jauh, peningkatan ketepatan melalui gabungan MediaPipe dan model DL, dan pengurangan masalah masa pendam dan ketepatan jarak yang lebih jauh melalui tentuukur dan suaian algoritma. Percubaan awal telah menunjukkan hasil yang bagus. Walau bagaimanapun, ujian lanjut masih perlu dibuat dalam dunia sebenar untuk menjamin keberkesanan sistem secara keseluruhan.

***KEYWORDS:*** *Rehabilitation Internet-of-Things (RIOT), MediaPipe, Deep Learning (DL), hand gesture recognition, Artificial Intelligence (AI).*

# 1. INTRODUCTION

Deep Learning (DL), a transformative branch of artificial intelligence (AI), has significantly advanced various domains by enabling machines to learn from vast datasets and make autonomous decisions. From a healthcare perspective, DL can analyze patient data to tailor personalized treatment plans and monitor progress effectively. For example, studies have demonstrated that DL algorithms can enhance the accuracy of gesture recognition systems, which are necessary for rehabilitation exercises, by processing and interpreting visual data in real-time [1]. The ability of DL to handle large datasets makes it particularly suitable for applications in medical imaging and patient monitoring using the Internet of Things (IoT), where it can uncover insights that traditional methods may overlook [2].

For stroke patients who require continuous exercise, IoT and DL combinations such as gesture recognition systems have emerged as tools for providing real-time feedback on patient movements. This is essential for effective therapy, and the accuracy of these systems is further enhanced through a robust calibration process, which adjusts for varying conditions such as lighting, hand positioning, and distance from the camera [3]. This shows that the integration of IoT and DL techniques has significantly improved the accuracy and reliability of gesture recognition systems, allowing for the detection of subtle movements that may indicate progress or areas needing improvement [2].

In addition, MediaPipe is an innovative framework developed by Google that facilitates real-time analysis and feedback and simplifies the implementation of complex machine-learning tasks, enabling developers to create applications that can detect and interpret human gestures with high accuracy and practicality. The combination of MediaPipe and its pre-trained DL models into rehabilitation technologies allows the development of user-friendly interfaces, thereby enhancing engagement and motivation during therapy sessions at home [4]. The system also uses Web Assembly (WASM) to ensure efficient processing, enabling it to run on various devices, including low-power edge devices.

RIOT utilizes IoT and AI to enable interactions between patients and healthcare professionals during remote therapy procedures to showcase advancements in modern technologies. This connectivity enables healthcare professionals to monitor patient progress with prescribed exercises and make data-driven decisions to enhance treatment outcomes [4]. The gathered data can be analyzed to create personalized rehabilitation plans tailored to each patient's specific needs, which can then be verified by healthcare providers based on rehabilitation scoring, ultimately enhancing overall treatment efficacy [5]. Rehabilitation scoring will assist the therapists in tracking the patient's progress records.

However, a study by Kelly et al. [6] the system addresses challenges such as latency and accuracy by incorporating a robust calibration process and proposing solutions like edge computing and adaptive sensitivity algorithms. The current work has focused on calibrating the system based on environmental factors, latency, and accuracy. Through the investigation, it has been shown that accuracy is influenced by latency and other environmental factors related to recognition and tracking. As the field of smart healthcare advances, RIOT is positioned to play a role in bridging the gap between patients and healthcare providers, ensuring that rehabilitation services are accessible and effective. To align with the efficacy and accuracy in RIOT development, the system's decision-making can be elevated by focusing on tuning the Convolutional Neural Networks (CNNs) for enhanced spatial analysis and Recurrent Neural Networks (RNNs) for dynamic gesture sequence recognition, which allows the system to adapt more effectively to the user's progress.

By offering a real-time, cost-effective, and adaptive solution for remote stroke rehabilitation, the RIOT system aims to greatly enhance the accessibility and quality of rehabilitation services for patients in remote areas. Initial trials demonstrate promising results in terms of recognition accuracy and real-time feedback, though further testing is required to validate the system fully under real-world conditions. Initial explorations of this work were already reported in [7], [8].

The design and implementation of the solution were delivered in this paper as arranged as follows: After this introduction, Section 2 will elaborate on the study of related and previous research, while the ML and DL elaboration in Section 3 entails how the system is developed. Next, Section 4 further explains the software used and shows the experimental results after testing the system. Section 5 breaks down the system's plans, as this paper concludes.

## 2. LITERATURE REVIEW

This section will elaborate on the role of Artificial Intelligence (AI), Machine Learning (ML), and Deep Learning (DL) in the RIOT system for hand gesture recognition by exploring the integration of those technologies within the system, their significance in improving patient rehabilitation results, and recent advancements in gesture recognition. Also, MediaPipe's role as a pre-trained model uses deep learning while leaving the possibility of future CNN/RNN integrations. Since MediaPipe handles gesture detection, it is important to be clarified, and CNNs/RNNs could be added in future work.

### 2.1. Introduction of Machine Learning and Deep Learning: An Overview of AI, ML, and DL in RIOT System

Artificial Intelligence (AI), Machine Learning (ML), and Deep Learning (DL) are integral components of the RIOT system for hand gesture recognition, automating the detection process, and delivering real-time feedback for stroke rehabilitation. MediaPipe, a framework developed by Google, plays a pivotal role in this system, leveraging a pre-trained deep-learning

https://doi.org/10.31436/iiumej.v26i1.3455

model to detect hand landmarks accurately and efficiently in real time. This pre-trained model enables the RIOT system to conduct gesture recognition without requiring additional ML or DL frameworks during deployment.

While MediaPipe serves as the primary tool for hand gesture recognition, the system's future enhancements may include advanced deep learning models such as Convolutional Neural Networks (CNNs) and Recurrent Neural Networks (RNNs) to improve the detection of more complex movements. Integrating these DL techniques would further enhance the system's ability to adapt to patient-specific needs during rehabilitation exercises.

### *2.1.1. Machine Learning and Deep Learning in Hand Gesture Recognition*

Machine Learning (ML) and Deep Learning (DL) play a crucial role in contemporary gesture recognition systems, particularly in the realm of rehabilitation. MediaPipe uses deep neural networks to recognize hand gestures in real-time [9]. This framework ensures high accuracy in detecting hand landmarks and movements, which is essential for rehabilitation exercises.

Firstly, in Machine Learning (ML), according to Figure 1, feature extraction is a process that requires manual intervention from domain experts who identify and design relevant features from structured data. This manual feature engineering is essential because the performance of ML models, like Support Vector Machines (SVM) and Decision Trees, heavily depends on the quality of these features [10]. Research suggests that effective feature engineering can greatly improve model accuracy and efficiency, highlighting its significance in traditional ML workflows [11].

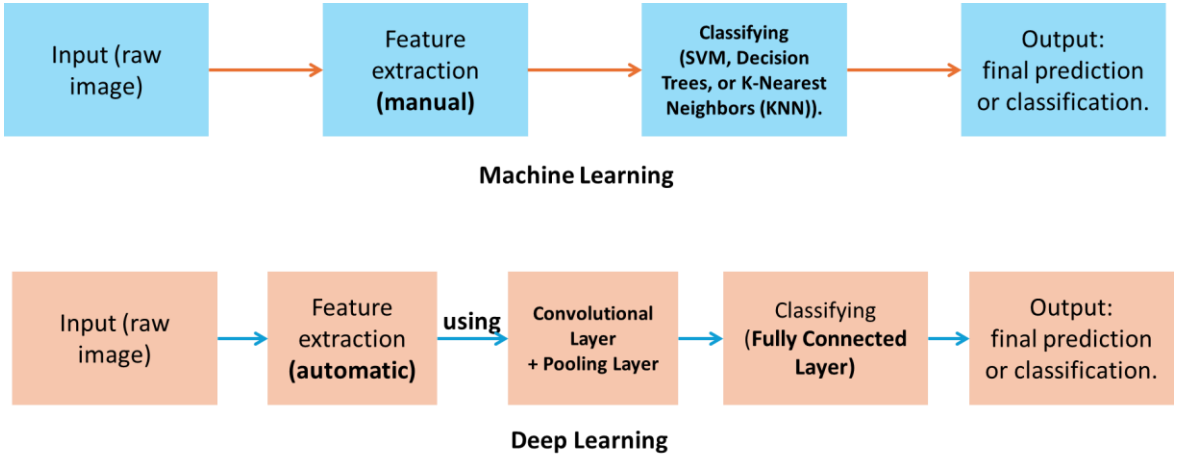


Figure 1. Key differences between ML and DL were presented in their flows and architecture before their final output.

In contrast, Deep Learning (DL) automates the feature extraction process, allowing models to learn directly from raw, unstructured data without the requirement for manual feature design (see Figure 1). This is accomplished through deep architectures that utilize layers such as Convolutional and Pooling layers to identify patterns automatically. The automatic nature of feature learning in DL enables it to excel in complex tasks, such as image and audio processing, where manual feature extraction would be impractical [12]. Thus, the fundamental distinction between ML and DL lies in their approach to feature handling, with ML depending on human expertise and DL leveraging automated learning processes. Figure 2 shows the visualization of machine learning and deep learning model architecture. Each model has its own structure for producing the output. For example, the architecture of CNN and RNN displays more layers

before reaching the output layer than SVM and Decision Tree. Here, it is evident that deep learning models are more complex than machine learning models.

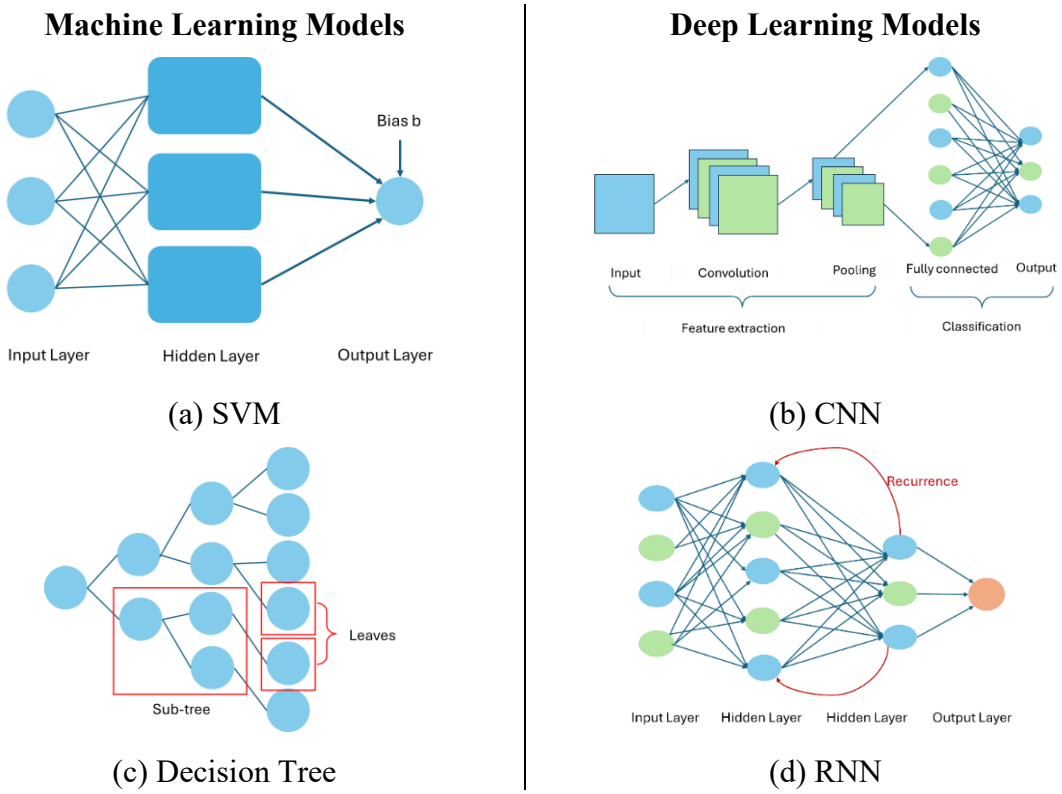


Figure 2 Examples of architecture diagrams of ML and DL models.

In addition, Figure 3 shows a step-by-step process of hand gesture recognition using the MediaPipe framework, which relies on CNN for accurate detection and classification [13]. The process begins with a video stream input, where each frame is analyzed for the presence of a hand. The model accurately locates the hand by extracting features like edges and contours. Subsequently, pooling layers are employed to decrease the dimensionality of the data while retaining information.

As a result, ML models are typically shallow and involve simpler algorithms. In contrast, DL models rely on multiple layers (deep architectures) to process and classify the data, making them better suited for more complex tasks.

### *2.1.2. Gesture Recognition Algorithm in Existing Products*

Accurate and real-time gesture detection is essential for hand rehabilitation systems. MediaPipe's pre-trained deep learning model currently serves as the backbone of the RIOT system, detecting and analyzing hand gestures in real-time. However, AI-based algorithms, such as LDA (Linear Discriminant Analysis), SVM, CNN, and LSTM, are often employed to recognize dynamic hand gestures. Researchers have developed systems that combine these techniques to achieve high accuracy in recognizing hand movements. For example, a researcher at Qingdao University of Science and Technology [15]. The LDA approach was used to create a wrist rehabilitation robot that recognizes five different types of movements with an accuracy rate of over 90% [20]. Other successful researchers from Nanchang University's SVM model were able to identify four distinct types of hand motions with an average success rate of 99.3%.

https://doi.org/10.31436/iiumej.v26i1.3455

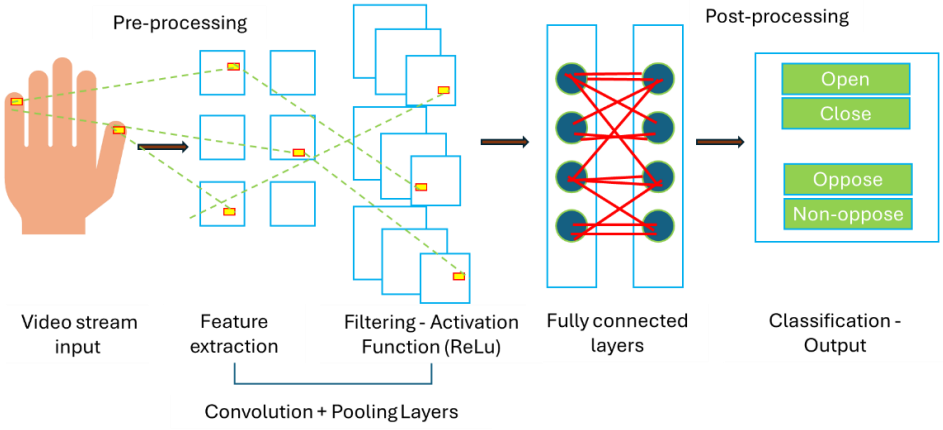


Figure 3. Hand gesture recognition process using MediaPipe framework, which integrates CNN for effective hand detection and classification.

By integrating CNNs and LSTMs as the future version of RIOT, the system could recognize more complex movements and provide real-time feedback to patients during therapy sessions. These studies demonstrate the effectiveness of combining different AI techniques for improved gesture recognition in rehabilitation. Lastly, in a study regarding combining RNN and LSTM algorithms, Zhang Jianxi has created a hand rehabilitation robot that recognizes nine movements with an average accuracy of 91.44% [16].

### 2.2. Significance and Contribution of Deep Learning in the RIOT System

Deep learning can contribute to real-time feedback in gesture recognition, especially for RIOT environments. Currently, in the environment, MediaPipe processes hand gesture data in real-time, ensuring that patients receive immediate feedback during rehabilitation exercises. The real-time feedback loop improves patient engagement and therapeutic outcomes during remote therapy sessions. It is a continuous adaptive support by DL models to eliminate the delays often associated with traditional rehabilitation methods, thereby creating an interactive environment that is necessary for effective therapy [17]. Moreover, RIOT could implement CNNs to process visual data in the future. At the same time, LTSMs handle sequential data, making these systems instantaneously recognize gestures and adapt to changing patterns in rehabilitation exercises.

Besides the algorithms themselves, it is believed that reducing latency in gesture recognition is key to maintaining a smoother feedback process within the rehabilitation tool and improving the user experience. Delays may cause interruptions and adversely affect the session and patients' progress. By refining advanced algorithms that learn from user interactions, such systems can tailor their responses according to the needs of patients and enable a better rehabilitation process. With the further development and refinement of DL architectures, including attention mechanisms and transformer models, additional gains in the responsiveness of the recognizing system can be expected. These advancements will enable more intricate interpretations of gestures, expanding the range of rehabilitation exercises that can be efficiently monitored and adjusted in real-time [18-19]. In short, DL's contribution to real-time feedback mechanisms is not only significant but also central to the future of rehabilitation technologies.

### 2.3. Latest Development in Gesture Recognition Technology

Gesture recognition has become immensely popular for rehabilitation based on its improvement in accuracy and adaptability. Traditional models, such as transformer-based

architecture, were replaced by more advanced models aiming to enhance gesture recognition performance. This includes the hybrid of CNN and LSTM for spatial and temporal dimensions in hand gesture study, which are essential for accurately interpreting complex gestures [14,17]. However, MediaPipe remains a highly practical framework for real-time gesture recognition, offering superior performance to older methods like Microsoft Kinect and Leap Motion.

Recent breakthroughs within hardware technologies like edge computing and low-latency networks have further made it possible to deploy these improved models for real-time rehabilitation. For example, technological advances such as these have allowed gesture recognition systems to perform seamlessly with no interruptions in remote environments and provide immediate feedback, thereby supporting users [21]In this feature, AI in gesture recognition not only enhances the accuracy of the systems but also makes them adaptable to the various needs of different patients under rehabilitation. Given AI-driven gesture recognition systems' ability to respond dynamically to patient progress, this feature will become one of the most important ways of creating personalized rehabilitation. As AI-driven rehabilitation tools evolve, MediaPipe's integration with more advanced models could improve system adaptability, providing patients with real-time feedback tailored to their needs.

Furthermore, the research was carried out to develop new AI architectures and learning paradigms that continue pushing gesture recognition's limits beyond what was previously possible. For instance, exploring multi-modal data input, such as the combination of visual and inertial sensor data, provides perspectives for developing more robust recognition systems capable of functioning in diverse environments. This ongoing research and development in AI signals bright prospects for gesture recognition technologies, particularly in the enhancement of rehabilitation practices [22].

### 2.4. AI-Driven Smart Healthcare System

RIOT system represents a significant advancement in smart healthcare. By imposing AI-driven gesture recognition, healthcare providers can achieve continuous monitoring and develop adaptive rehabilitation tools that are both efficient and accessible [21]. This connectivity allows therapists to track patient progress remotely, monitor therapy exercises in real time, and ensure adherence to therapeutic guidelines, thus enhancing the overall effectiveness of rehabilitation programs [17].

Additionally, the system incorporates edge computing to reduce latency and ensure smooth therapy sessions. This low-latency system allows for seamless interaction between the patient and the rehabilitation tool, eliminating delays that could negatively impact patient progress. Advanced adaptive sensitivity algorithms could further enhance the system's ability to recognize gestures in varying environmental conditions to make it more robust.

Here, the data collected through RIOT systems can be collected to be recorded for healthcare providers' rehabilitation scoring assessment on the patient's progress, which improves patient outcomes but also facilitates a more proactive approach to rehabilitation, where guidance can be made based on provided instructions for an immediate patient response [23].

### 2.5. Evaluation Metrics and Latency Measurement

Metrics such as accuracy, precision, recall, F1-score, and latency were used to calculate the implementation of the hand gesture recognition system developed in RIOT. During the simulated rehabilitation sessions, the effectiveness of identifying gestures and providing real-time feedback was investigated.

https://doi.org/10.31436/iiumej.v26i1.3455

First, accuracy was measured of how well the system correctly recognizes gestures [24] and was calculated in Eq. (1). Where TP (True Positive) and FP (False Positives) are represented as correctly detected gestures, incorrectly detected gestures, and missed gestures, respectively. Meanwhile, Precision Eq. (2) measures the proportion of correctly identified gestures out of all detected gestures to understand the accuracy of the system in prediction [25]. Moreover, Recall Eq. (3), which is also known as sensitivity, identifies true gestures out of all possible gestures [26]. Next, the balance between precision and recall was defined in Eq. (4) as the harmonic mean of the two metrics that can spot uneven class distribution during evaluation.

Besides the metrics mentioned above, latency is also an essential factor in real-time gesture recognition systems, particularly in rehabilitation contexts where immediate feedback is essential for the user [27]. Latency is measured in milliseconds (ms) and can be defined in two ways depending on the application, and Eq. (5) displays the time taken by the system to provide feedback and gesture inputs. Subsequently, in the experiment, the console window of the RIOT website inspection browser was used to retrieve timestamps and perform latency calculations [28] for every test, as displayed in Figure 4.

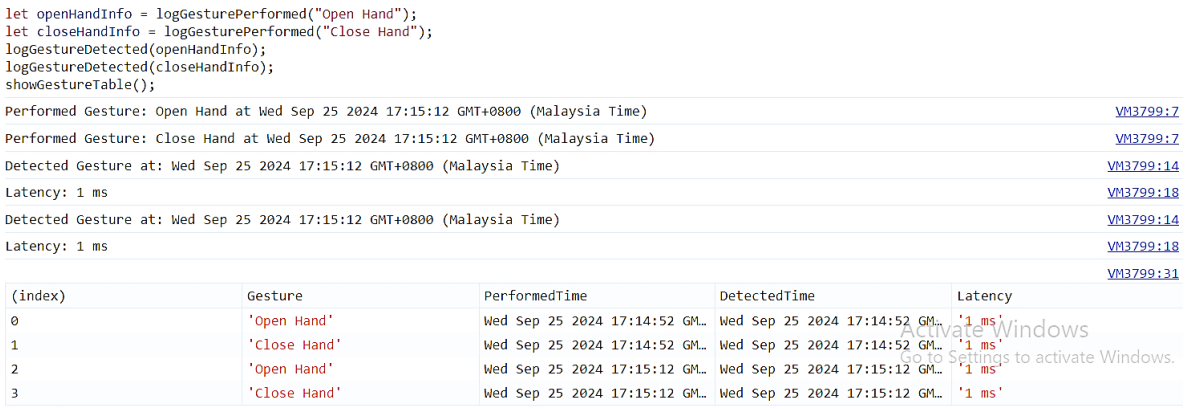


Figure 4. The real-time time taken was displayed in a table from the console window as outputs to calculate the gesture's latency.

In this experiment, latency was examined as one of the factors measuring the delay between executed gestures and gesture detection time. As illustrated below, Eq. (1), Eq. (2), Eq. (3), Eq. (4), and Eq. (5) represent the formulas for the measurements.

$$\text{Accuracy} = \frac{\text{TP}}{\text{TP+FP+FN}} \tag{1}$$

$$\text{Precision} = \frac{\text{TP}}{\text{TP+FP}} \tag{2}$$

$$\text{Recall (or Sensitivity)} = \frac{\text{TP}}{\text{TP+FN}} \tag{3}$$

$$\text{F1Score} = 2 \times \frac{\text{Precision} \times \text{Recall}}{\text{Precision+Recall}} \tag{4}$$

$$\text{Latency (ms)} = \text{Response Time} - \text{Input Time} \tag{5}$$

$$\text{Latency (ms)} = \text{Gesture Detected Time} - \text{Gesture Performed Time} \tag{6}$$

All these equations were implemented to observe the Design-of-Experiment factors' outcomes, which will be discussed in the next section.

https://doi.org/10.31436/iiumej.v26i1.3455

# 3. METHODOLOGY

The methodology for this investigation focuses on integrating MediaPipe, Web Assembly, and Deep Learning technologies to achieve real-time hand gesture recognition in the RIOT system. This chapter elaborates on the theoretical and practical implementation of these technologies, including the post-calibration process and experimental design factors that affect system accuracy.

## 3.1. System Design Overview

The RIOT system utilizes MediaPipe, a real-time framework for hand landmark detection and deep learning models to facilitate hand gesture recognition for rehabilitation. The system's design incorporates WASM for web-based operation, enabling lightweight execution of complex models without requiring significant computational resources from the client side.

MediaPipe captures real-time hand gestures through a camera device, such as a webcam, and detects 21 key points. MediaPipe Hands uses pre-trained machine learning models, likely developed using deep learning techniques. However, the MediaPipe framework itself does not require external deep learning frameworks such as TensorFlow or PyTorch during its deployment, as its models are pre-optimized for real-time performance [9].

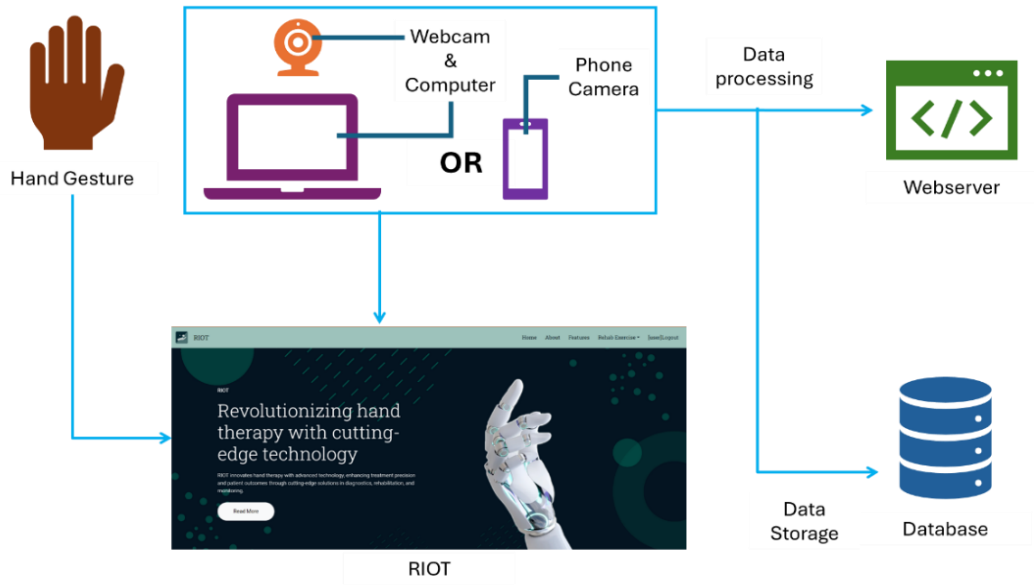


Figure 5. The RIOT system utilizes MediaPipe and WASM with IoT devices to detect and recognize exercise gestures in real time while efficiently managing data.

The website's interactivity was created for two types of users: the patient's guardian or the patient themselves and the administrators. Both users were required to sign up and log in before gaining full access to RIOT features. Since product was successfully built, the next step of the research is optimizing and tuning the system to ensure the optimal conditions for the exercises included in RIOT.

## 3.2. Calibration of Hand Gesture Recognition

Calibration is crucial to ensure precise hand gesture recognition in the RIOT system. The following section outlines the calibration process and the post-calibration adjustments.

https://doi.org/10.31436/iiumej.v26i1.3455

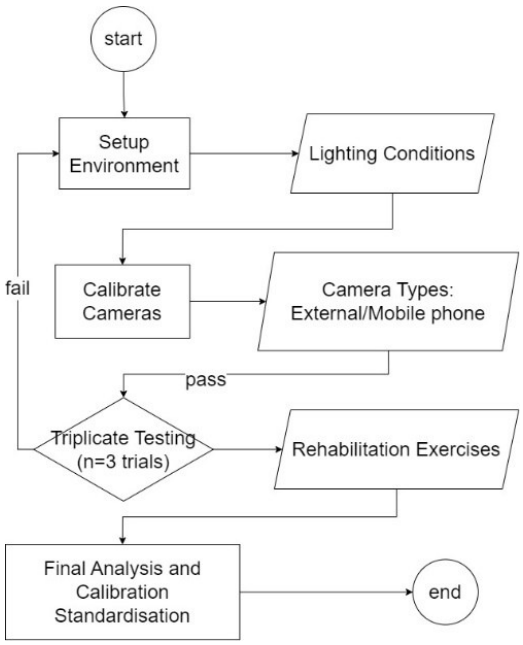


Figure 5. Flowchart of the post-calibration research displaying the process of testing the RIOT website.

Figure 5 reveals the flow of the calibration process, where the user's gestures are captured at various hand positions and distances at the setup, followed by factor adjustments to ensure accurate tracking. The study was repeated three times to ensure thorough analysis. The process began with setting up environmental factors, followed by adjusting camera variables for testing.

### *3.2.1. Post-Calibration Adjustment*

The initial calibration (pre-calibration) phase was focusing on setting up the system to ensure precise hand gesture recognition. This involves utilizing a Design of Experiment (DoE) methodology to test and optimize various factors like camera type, distance, and lighting conditions. Pre-calibration ensures that the gesture recognition system functions reliably, laying the groundwork for more precise rehabilitation assessments in stroke patients, as conducted in prior research [7]. The current focus is on post-calibration adjustments, which ensure that the system maintains high accuracy during real-time rehabilitation sessions. These adjustments involve compensating for varying environmental conditions, such as lighting, hand position, and distance from the camera.

The adaptive sensitivity algorithms implemented in the post-calibration phase dynamically adjust the system's recognition thresholds in response to changes in the user's environment. For example, if the user moves farther from the camera or if the lighting conditions change, the system recalibrates its detection sensitivity to maintain consistent accuracy. This ensures that the hand gestures are recognized effectively throughout the rehabilitation session.

The system setup for the calibration process involves laptop webcams. Meanwhile, post-calibration, an external webcam, and a mobile phone camera were experimented with, and the laptop ran the RIOT software. The specified distance to position the hand is 20.00 cm to 70.00 cm away from the camera because this range ensures optimal focus and clarity of the hand movements, which is accurate for gesture recognition [29]. When movements are precisely tracked in rehabilitation settings, the feedback can significantly enhance patient performance

https://doi.org/10.31436/iiumej.v26i1.3455

and confidence. Also, by emphasizing that real-time feedback during exercises can simulate the presence of a physical therapist, thereby improving adherence and outcomes.

This distance is a primary factor that influences the accuracy of gesture recognition when the camera captures hand movements, and the system processes this data to provide real-time feedback during rehabilitation exercises.

### 3.3. Design of Experiment (DoE) Factors for Post-Calibration

Following the initial calibration process described in the previous study, this paper focuses on post-calibration adjustments to enhance the hand gesture recognition system across various devices, including external webcam and mobile phone cameras. These adjustments are necessary to maintain accuracy in real-world environments where lighting, camera angles, and distances vary significantly.

To ensure the system's robustness, a Design of Experiments (DoE) methodology was implemented to systematically evaluate and optimize the performance of the gesture recognition system. The following factors were analyzed in Table 1. Data was collected from both external webcams and mobile phone cameras under the mentioned conditions.

Table 1. DoE Factors affecting the accuracy of hand gesture recognition during data collection and analysis.

| Factor | Levels/SI Unit | Objectives |
|---|---|---|
| **Distance** | 5.0 cm increment from 20.00 cm to 70.00 cm. | To determine the optimal distance at which the camera accurately captures hand gestures. This factor was tested by placing the hand at different distances from the webcam and observing the system's recognition accuracy. |
| **Types of Cameras** | • External webcam.<br>• Smartphone front camera. | To compare gesture recognition performance between a mobile phone camera and an external webcam. |
| **Lighting conditions** | Indoor under artificial light settings:<br>• Dim.<br>• Bright. | To assess how different ambient lighting conditions impact the accuracy of hand gesture detection. |
| **Latency** | Milliseconds (ms). | To measure the time delay (latency) between when a hand gesture is made and when the system recognizes it. This helps determine system responsiveness. |

The DoE framework determined the optimal setup for each device type. The results were analyzed to identify the most reliable combinations of camera type, distance, lighting, and hand positioning for both mobile and desktop environments. During this stage, JavaScript was used to conduct part of the investigation, as shown in Figure 7.

https://doi.org/10.31436/iiumej.v26i1.3455

```
// Create an array to store the data for gestures
let gestureData = [];

// Function to log when the gesture is performed
function logGesturePerformed(gestureType) {
    let gesturePerformedTime = new Date();
    console.log("Performed Gesture: " + gestureType + " at " + gesturePerforme
    return {gestureType, gesturePerformedTime};
}
// Function to log when the gesture is detected by the system
function logGestureDetected(gestureInfo) {
    let gestureDetectedTime = new Date();
    console.log("Detected Gesture at: " + gestureDetectedTime);
    // Calculate latency in milliseconds
    let latency = gestureDetectedTime - gestureInfo.gesturePerformedTime;
    console.log("Latency: " + latency + " ms");
    // Add the data to the array
    gestureData.push({
        Gesture: gestureInfo.gestureType,
        PerformedTime: gestureInfo.gesturePerformedTime,
        DetectedTime: gestureDetectedTime,
        Latency: latency + " ms"
    });
}
// Function to display the data in a table format
function showGestureTable() {
    console.table(gestureData);
}
let openHandInfo = logGesturePerformed("Open/Oppose Hand");
let closeHandInfo = logGesturePerformed("Close/Non-Oppose Hand");
logGestureDetected(openHandInfo);
logGestureDetected(closeHandInfo);
showGestureTable();
```

Figure 6. The snippet source code for retrieving the time taken for the gesture actions for latency data from live simulated rehabilitation sessions was written in the console window to perform the calculation.

#### *3.3.1. Potential for Future Deep Learning Integration*

Future iterations of the RIOT system will explore the integration of CNNs and RNNs (LSTMs) to improve gesture recognition and enhance the rehabilitation experience. CNNs can provide more refined spatial analysis of hand gestures, while LSTMs can manage dynamic movement sequences, offering users more personalized and accurate feedback.

## 4. RESULTS AND DISCUSSION

This section evaluates the RIOT system, highlighting its performance across different test environments. This chapter is structured to cover the experimental setup, performance benchmarking results, and comparison with existing systems.

### 4.1. Experimental Setup

The experimental setup was designed to evaluate the performance of the RIOT system under various environmental conditions and with different camera types, including external webcams and mobile phone cameras. The system was tested with hands positioned between 20.0 cm and 70.0 cm from the camera, as shown in Figs 8(a) and 8(b), to simulate real-world rehabilitation exercises. Key variables such as lighting conditions (dim and bright) and camera type were systematically controlled to ensure a comprehensive performance evaluation.

https://doi.org/10.31436/iiumej.v26i1.3455

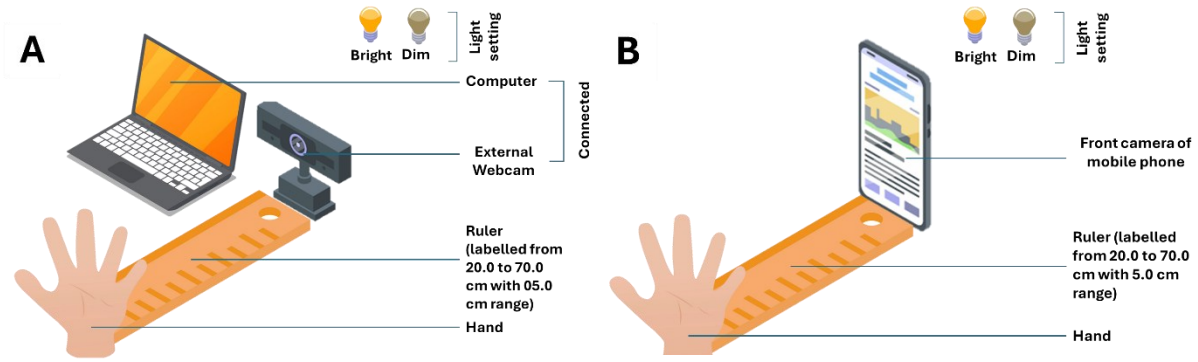


Figure 7. Setup for post-calibration was organized according to the discussed DoE elements.

All experiments were conducted in a controlled environment, ensuring consistency in lighting and camera placement. For example, the brightness of the light bulb and the distance are labeled every 5.0 cm increment gap. Finally, MediaPipe processed these data and integrated them into the RIOT system for gesture recognition. Then, the output of the experiments was analyzed for further assessment.

### 4.2. Results of Post-Calibration Adjustments

The results are categorized based on key factors that affect the system's performance. These factors include distance, camera type, and lighting conditions, which were systematically tested to assess the system's accuracy, precision, recall, F1 score, and latency. Table 2, Table 3, Table 4, and Table 5 were demonstrated as the brief findings of the experiment based on DoE factors.

#### *4.2.1. Performance by Distance*

The distance between the camera and the subject's hand significantly impacted the system's accuracy and latency. As the distance increased from 20 cm to 70 cm, there was a noticeable improvement in accuracy, precision, and F1 score. However, latency also increased at these distances, reflecting longer processing times. However, the trade-off is acceptable considering the significant gains in accuracy and F1 score. At 20 cm, the accuracy was 0.40, but at 60.00 cm, the accuracy increased to 0.97. The F1-score also increased from 0.43 at 20.00 cm to 1.00 at 60.00 cm, indicating an improved balance between precision and recall at greater distances. This trend aligns with the findings of a demonstration of gesture recognition accuracy improving with distance by achieving an average accuracy of 96.64% in their optimized model to reduce interference from background noise. Table 2 indicates results showing that the system performs optimally at 50.00 to 60.00 cm, where accuracy and F1-score reach their highest levels despite the increase in latency.

Similarly, the importance of distance in their real-time gesture recognition system is also noted in improved performance metrics at greater distances. The increase in latency with distance, while a drawback, is acceptable due to the significant gains in accuracy and F1 score, resulting in the notion that distance is a crucial factor in gesture recognition systems.

https://doi.org/10.31436/iiumej.v26i1.3455

Table 2. Comparison of all evaluation metrics and latency for gesture recognition by distances between the camera and patients' hand.

| Distance (cm) | Mean Accuracy (%) | | Mean Precision (%) | | Mean Recall (%) | | Mean F1-score (%) | | Mean Latency (ms) | |
|---|---|---|---|---|---|---|---|---|---|---|
| | Average | Standard Deviation | Average | Standard Deviation | Average | Standard Deviation | Average | Standard Deviation | Average | Standard Deviation |
| **20.0** | 0.40 | 0.32 | 0.33 | 0.47 | 1.14 | 0.58 | 0.43 | 0.37 | 0.54 | 0.42 |
| **25.0** | 0.44 | 0.37 | 0.67 | 0.36 | 1.74 | 1.21 | 0.51 | 0.45 | 0.61 | 0.50 |
| **30.0** | 0.50 | 0.36 | 0.58 | 0.24 | 0.93 | 0.35 | 0.57 | 0.42 | 0.64 | 0.41 |
| **35.0** | 0.53 | 0.37 | 0.58 | 0.30 | 1.14 | 0.63 | 0.60 | 0.41 | 0.68 | 0.44 |
| **40.0** | 0.59 | 0.32 | 0.63 | 0.42 | 1.59 | 1.36 | 0.65 | 0.38 | 0.74 | 0.40 |
| **45.0** | 0.75 | 0.30 | 0.46 | 0.40 | 1.98 | 1.39 | 0.80 | 0.32 | 0.91 | 0.36 |
| **50.0** | 0.82 | 0.19 | 0.71 | 0.21 | 1.69 | 1.06 | 0.93 | 0.18 | 1.01 | 0.18 |
| **55.0** | 0.86 | 0.13 | 0.63 | 0.28 | 2.03 | 1.35 | 0.98 | 0.03 | 1.05 | 0.08 |
| **60.0** | 0.97 | 0.03 | 0.67 | 0.36 | 1.34 | 1.06 | 1.00 | 0.00 | 1.02 | 0.10 |
| **65.0** | 0.89 | 0.10 | 0.50 | 0.44 | 1.99 | 1.25 | 1.00 | 0.01 | 1.08 | 0.12 |
| **70.0** | 0.89 | 0.10 | 0.54 | 0.50 | 1.27 | 0.43 | 0.98 | 0.07 | 1.03 | 0.07 |

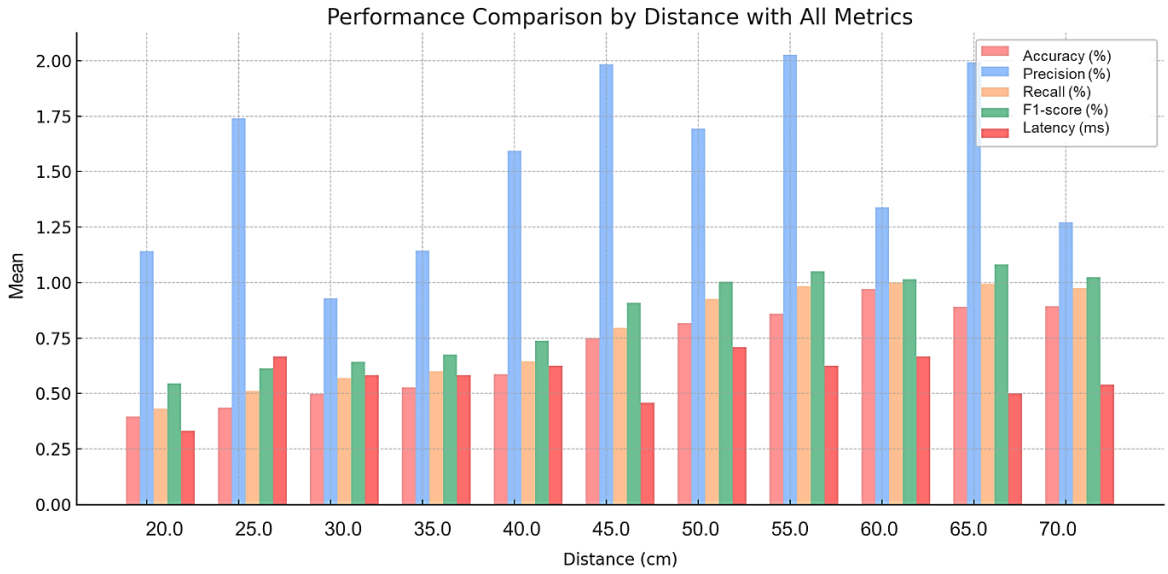


Figure 8. Various distances were determined in relation to the structure of the environmental factors of the post-calibration period. The bar chart effectively summarizes the findings across the metrics.

Accuracy and F1-score improved significantly at distances between 50.00 cm and 60.00 cm, where the system achieved the highest level of gesture recognition accuracy. The accuracy at this range is attributed to the effective capture of hand features and gestures, which diminishes at greater distances due to increased latency and reduced resolution.

Several scientific factors support the optimal distance of 60.00 cm for hand gesture recognition systems. At this distance, the system achieves high accuracy and F1-score, critical metrics for evaluating the performance of gesture recognition algorithms. As shown in Figure 8, the latency increases as distance increases, but it remains within an acceptable range, making the system responsive and practical for real-time hand gesture recognition. This is particularly true in the context of image recognition. As the distance increases, larger images must be processed, which can lead to increased computational demands and longer processing times.

https://doi.org/10.31436/iiumej.v26i1.3455

### *4.2.2. Performance by Camera Types*

An external webcam and a mobile phone camera have performed some tests on gesture recognition for both exercises to assess their impact on accuracy and latency. Table 3 shows that both cameras were tested and exhibited certain patterns. The comparative analysis of camera types reveals that while the mobile phone camera provides slightly better accuracy (0.70) compared to the external camera (0.68), the external camera outperforms in terms of precision, recall, and F1-score and it is clear that precision and low latency are dominant, according to Figure 9.

Table 3. Evaluation metrics and latency are based on the types of cameras used to capture hand gestures for both stroke rehabilitation exercises.

| Camera Type | Mean Accuracy (%) | | Mean Precision (%) | | Mean Recall (%) | | Mean F1-score (%) | | Mean Latency (ms) | |
|---|---|---|---|---|---|---|---|---|---|---|
| | Average | Standard Deviation | Average | Standard Deviation | Average | Standard Deviation | Average | Standard Deviation | Average | Standard Deviation |
| **External camera** | 0.68 | 0.31 | 0.47 | 0.35 | 1.59 | 1.08 | 0.79 | 0.35 | 0.85 | 0.36 |
| **Mobile phone camera** | 0.70 | 0.33 | 0.67 | 0.36 | 1.47 | 1.02 | 0.75 | 0.35 | 0.84 | 0.36 |

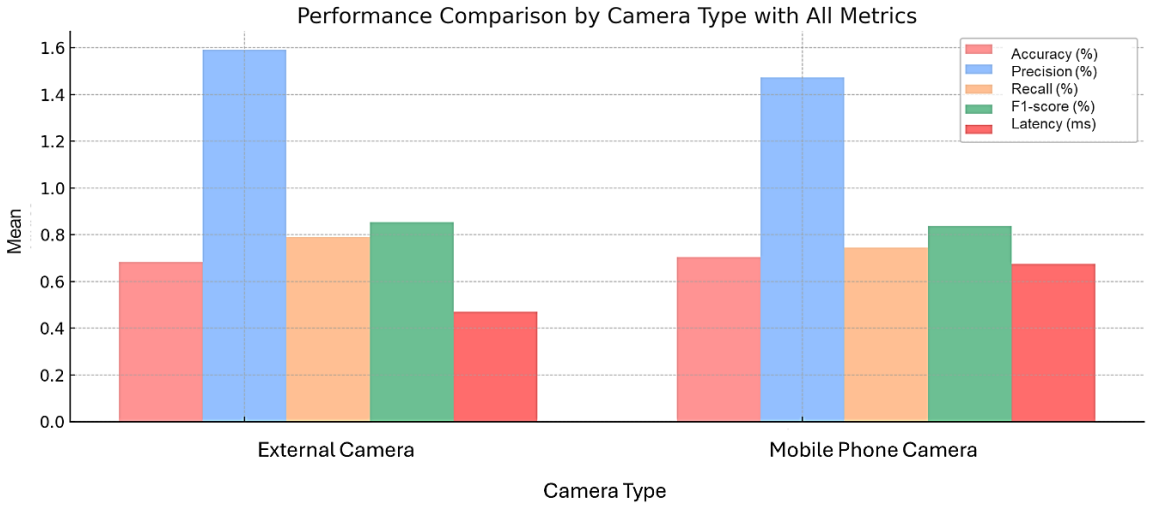


Figure 9. External camera and Mobile Phone Camera front camera present slight differences during the evaluation

These results specify that while the mobile phone camera provides marginally better accuracy, the external camera offers faster processing with higher precision, making it more efficient in real-time rehabilitation scenarios.

The system must respond promptly and prevent false positives, making it evident that an external camera is more suitable for this application. The findings align with research on the importance of camera quality in gesture recognition systems, highlighting that superior cameras result in improved recognition rates. Therefore, although both camera types are effective, the external camera's enhanced precision and reduced latency make it better suited for real-time rehabilitation scenarios.

https://doi.org/10.31436/iiumej.v26i1.3455

### *4.2.3. Performance by Lighting Conditions*

The lighting conditions during the experiment played a role in determining the system's performance. Investigations were conducted under both bright and dim lighting to evaluate how ambient light affects accuracy, precision, and latency, as shown in Table 4.

Table 4. The simplified version of average mean percentages of metrics under lighting settings.

| Lighting Condition | Mean Accuracy (%) | | Mean Precision (%) | | Mean Recall (%) | | Mean F1-score (%) | | Mean Latency (ms) | |
|---|---|---|---|---|---|---|---|---|---|---|
| | Average | Standard Deviation | Average | Standard Deviation | Average | Standard Deviation | Average | Standard Deviation | Average | Standard Deviation |
| **Bright** | 0.72 | 0.30 | 1.84 | 1.20 | 0.81 | 0.33 | 0.91 | 0.35 | 0.67 | 0.38 |
| **Dim** | 0.67 | 0.34 | 1.23 | 0.77 | 0.73 | 0.37 | 0.78 | 0.37 | 0.47 | 0.32 |

Referring to Figure 10, the system performed much better in bright lighting, with an accuracy of 0.72 and a precision of 1.84, compared to dim lighting, where accuracy dropped to 0.67 and a precision of 1.23. While dim lighting provided a slight speed advantage with lower latency (0.47 ms vs. 0.67 ms), this was not enough to compensate for the lower performance. Therefore, bright lighting is better for more accurate and precise gesture recognition. In addition to lighting, other factors, such as reinforcing what has already been found in other research, highlight how important it is to fine-tune these conditions for better real-world performance [30].

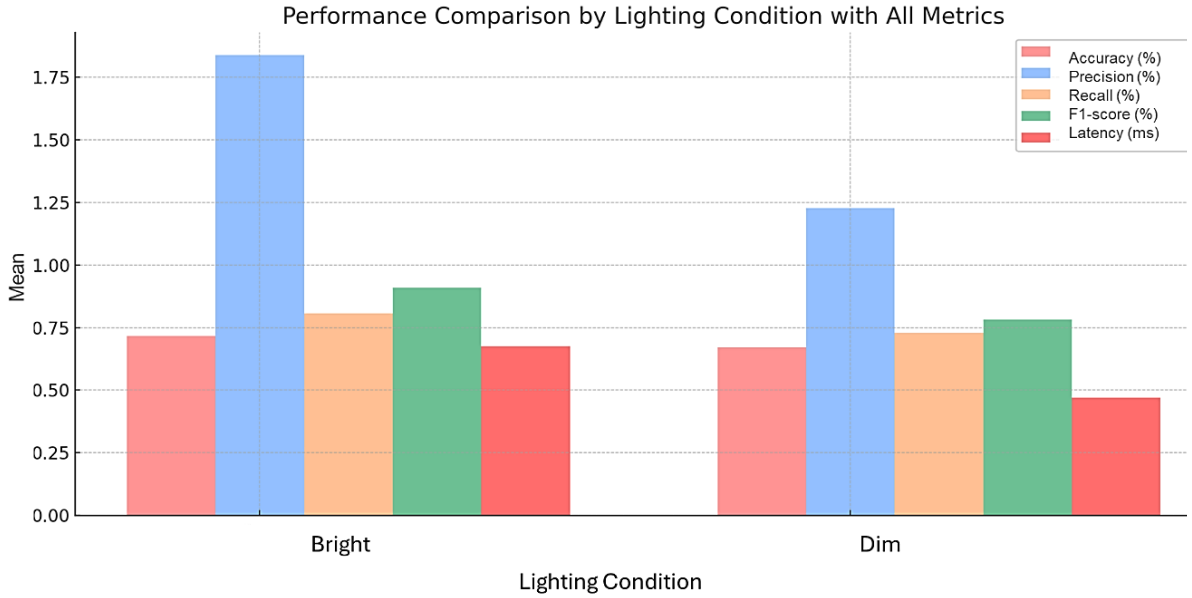


Figure 10. The chart illustrates the impact of bright and dim lighting conditions on the system.

### *4.2.4. Outline of Post-Calibration Outcomes*

Post-calibration adjustments were necessary to optimize the hand gesture recognition system within the RIOT framework. The calibration process focused on refining the system's accuracy, precision, recall, F1-score, and latency across varying distances, camera types, and lighting conditions. In this segment, Figure 11 and Table 5 provide insights into the post-calibration effects. The results showed that distance and camera accuracies averaged 0.69, with

https://doi.org/10.31436/iiumej.v26i1.3455

precision at 1.53. However, recall and F1-score were lower with distance, and latency increased to 1.62 ms, reflecting longer processing times.

Table 5. The finalized average means of factors and their evaluations in hand gesture recognition through the RIOT website.

| Factors | Accuracy (%) | Precision (%) | Recall (%) | F1-Score (%) | Latency (ms) |
|---|---|---|---|---|---|
| Distances | 0.69 | 1.53 | 0.59 | 0.36 | 1.62 |
| Camera | 0.69 | 1.53 | 0.77 | 0.85 | 0.57 |
| Lighting | 0.70 | 1.54 | 0.77 | 0.85 | 0.57 |

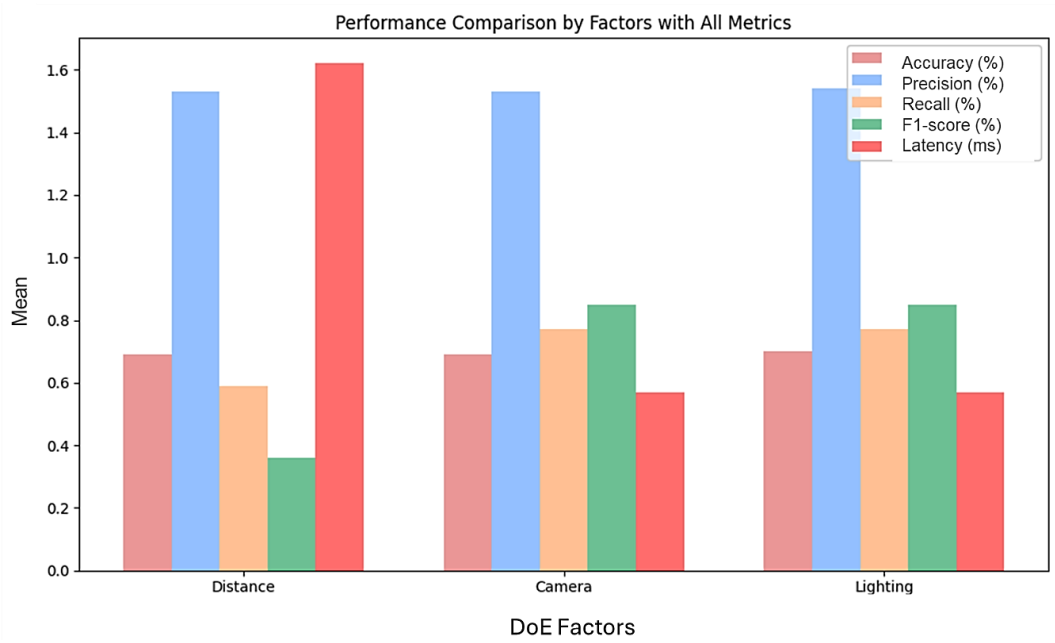


Figure 11. The grouped bar chart concluded the system's execution across three factors—distance, camera type, and lighting—evaluating metrics such as accuracy, precision, recall, F1-score, and latency.

Briefly, the optimal distance is 60.00 cm; the preference for external cameras due to their precision where it can avoid false positives, lower latency from the external camera, and the necessity of bright lighting conditions collectively enhance the system's reliability and effectiveness in real-world rehabilitation applications. These findings align with existing literature, confirming the validity of the post-calibration adjustments made to the system.

## 5. CONCLUSION

In conclusion, the RIOT system presents an innovative real-time, remote rehabilitation solution using pre-trained deep learning models like MediaPipe, recognizing CNNs and LSTMs to accurately detect hand gestures that can be considered for RIOT improvement in the future. Consequently, post-calibration adjustments have enhanced its performance across various conditions, making it suitable for at-home therapy. However, the system's effectiveness in real-world scenarios remains to be validated through clinical trials. Future work will focus on integrating adaptive learning and wearable technology and conducting broader testing to fully realize the system's potential in improving patient outcomes. As research advances in this

area, the potential for hand gesture recognition to transform rehabilitation practices and improve patient outcomes is immense. An edge computing approach can also impact healthcare, the environment, and scientific involvement in the computing world.

## ACKNOWLEDGEMENT

This work is funded by the Ministry of Higher Education (MOHE) Malaysia under FUNDAMENTAL RESEARCH GRANT SCHEME (FRGS): FRGS23-307-0916; FRGS/1/2023/TK07/UIAM/02/2; Formulation of Associating 4D Skeletal-based Hand Gesture Recognition with Hand Rehabilitation Scoring of Stroke Patient for Rehabilitation Internet-of-things (RIOT). The assistance and resources provided by the National Medical Research Register (NMRR), particularly under NMRR ID-24-02136-NJQ, were instrumental in successfully completing this paper.

## REFERENCES

[1] Y. J. Choo and M. C. Chang, "Use of Machine Learning in Stroke Rehabilitation: A Narrative Review," *Brain Neurorehabilitation*, vol. 15, no. 3, Nov. 2022, doi: 10.12786/bn.2022.15.e26.

[2] W. Zhang, C. Su, and C. He, "Rehabilitation Exercise Recognition and Evaluation Based on Smart Sensors With Deep Learning Framework," *IEEE Access*, vol. 8, pp. 77561–77571, 2020, doi: 10.1109/ACCESS.2020.2989128.

[3] X. Li and J. Zhong, "Upper Limb Rehabilitation Robot System Based on Internet of Things Remote Control," *IEEE Access*, vol. 8, pp. 154461–154470, 2020, doi: 10.1109/ACCESS.2020.3014378.

[4] S. H. Chae, Y. Kim, K.-S. Lee, and H.-S. Park, "Development and Clinical Evaluation of a Web-Based Upper Limb Home Rehabilitation System Using a Smartwatch and Machine Learning Model for Chronic Stroke Survivors: Prospective Comparative Study," *JMIR MHealth UHealth*, vol. 8, no. 7, p. e17216, Jul. 2020, doi: 10.2196/17216.

[5] on behalf of the Writing Expert Group of Expert Consensus on Clinical Application of IOT Medical Technology in the Rehabilitation of Chronic Obstructive Pulmonary Disease, the Respiratory Disease Rehabilitation Professional Committee of China Medical Education Association *et al.*, "Clinical guidelines on the application of Internet of Things (IOT) medical technology in the rehabilitation of chronic obstructive pulmonary disease," *J. Thorac. Dis.*, vol. 13, no. 8, pp. 4629–4637, Aug. 2021, doi: 10.21037/jtd-21-670.

[6] J. T. Kelly, K. L. Campbell, E. Gong, and P. Scuffham, "The Internet of Things: Impact and Implications for Health Care Delivery," *J. Med. Internet Res.*, vol. 22, no. 11, p. e20135, Nov. 2020, doi: 10.2196/20135.

[7] A. A. Zainuddin, N. H. M. Dhuzuki, A. A. Puzi, M. N. Johar, and M. Yazid, "Calibrating Hand Gesture Recognition for Stroke Rehabilitation Internet-of-Things (RIOT) Using MediaPipe in Smart Healthcare Systems," *Int. J. Adv. Comput. Sci. Appl.*, vol. 15, no. 7, 2024, doi: 10.14569/IJACSA.2024.0150756.

[8] N. H. Mohd Dhuzuki, A. A. Zainuddin, S. I. Kamarudin, D. Handayani, K. Subramaniam, and Mohd. I. Mohd. Tamrin, "Web-Based Medical Information System for Stroke Rehabilitation Intemet-of-Things (RIOT) Patients: A Prototype," in *2024 IEEE International Conference on Artificial Intelligence in Engineering and Technology (IICAIET)*, Kota Kinabalu, Malaysia: IEEE, Aug. 2024, pp. 326–330. doi: 10.1109/IICAIET62352.2024.10729958.

[9] "MediaPipe Solutions guide | Google AI Edge," Google AI for Developers. Accessed: Sep. 20, 2024. [Online]. Available: https://ai.google.dev/edge/mediapipe/solutions/guide

[10] B. Saravi *et al.*, "Clinical and radiomics feature-based outcome analysis in lumbar disc herniation surgery," *BMC Musculoskelet. Disord.*, vol. 24, no. 1, p. 791, Oct. 2023, doi: 10.1186/s12891-023-06911-y.

[11] S. Rajayyan and S. M. M. Mustafa, "Prediction of dementia using machine learning model and performance improvement with cuckoo algorithm," *Int. J. Electr. Comput. Eng. IJECE*, vol. 13, no. 4, 2023, doi: 10.11591/ijece.v13i4.pp4623-4632.

[12] R. Magar, L. Ghule, J. Li, Y. Zhao, and A. B. Farimani, "FaultNet: A Deep Convolutional Neural Network for Bearing Fault Classification," *IEEE Access*, vol. 9, 2021, doi: 10.1109/access.2021.3056944.

[13] C. Lugaresi *et al.*, "MediaPipe: A Framework for Perceiving and Processing Reality".

[14] D. Parashar, "A Deep Learning-Based Approach for Hand Sign Recognition Using CNN Architecture," *Rev. Intell. Artif.*, 2023, doi: 10.18280/ria.370414.

[15] J. A. Díez, A. Blanco, J. M. Catalán, F. J. Badesa, L. D. Lledó, and N. García-Aracil, "Hand exoskeleton for rehabilitation therapies with integrated optical force sensor," *Adv. Mech. Eng.*, vol. 10, no. 2, p. 168781401775388, Feb. 2018, doi: 10.1177/1687814017753881.

[16] W. Zhang, T. Zhao, J. Zhang, and Y. Wang, "LST-EMG-Net: Long Short-Term Transformer Feature Fusion Network for sEMG Gesture Recognition," *Front. Neurorobotics*, 2023, doi: 10.3389/fnbot.2023.1127338.

[17] Z. Slimane, K. Lakhdari, and D. Souhila Korti, "Enhancing Dynamic Hand Gesture Recognition using Feature Concatenation via Multi-Input Hybrid Model," *Int. J. Electr. Comput. Eng. Syst.*, vol. 14, no. 5, pp. 535–546, Jun. 2023, doi: 10.32985/ijeces.14.5.5.

[18] I.-J. Ding and N. Zheng, "RGB-D Depth-Sensor-Based Hand Gesture Recognition Using Deep Learning of Depth Images With Shadow Effect Removal for Smart Gesture Communication," *Sens. Mater.*, 2022, doi: 10.18494/sam3557.

[19] Y. Huo, J. Shen, X. Chen, and K. Yu, "A dynamic gesture recognition method based on R(2+1)D-transformer network," in *Third International Conference on Computer Graphics, Image, and Virtualization (ICCGIV 2023)*, Y. Wang and A. J. Moshayedi, Eds., Nanjing, China: SPIE, Nov. 2023, p. 57. doi: 10.1117/12.3008203.

[20] T. Bao, S. A. R. Zaidi, S. Xie, P. Yang, and Z.-Q. Zhang, "A CNN-LSTM Hybrid Model for Wrist Kinematics Estimation Using Surface Electromyography," *IEEE Trans. Instrum. Meas.*, vol. 70, pp. 1–9, 2021, doi: 10.1109/TIM.2020.3036654.

[21] M. Jaén-Vargas *et al.*, "A Deep Learning Approach to Recognize Human Activity Using Inertial Sensors and Motion Capture Systems," in *Frontiers in Artificial Intelligence and Applications*, A. J. Tallón-Ballesteros, Ed., IOS Press, 2021. doi: 10.3233/FAIA210196.

[22] J.-S. Kim, M.-G. Kim, and S.-B. Pan, "Two-Step Biometrics Using Electromyogram Signal Based on Convolutional Neural Network-Long Short-Term Memory Networks," *Appl. Sci.*, vol. 11, no. 15, p. 6824, Jul. 2021, doi: 10.3390/app11156824.

[23] G. Palanisamy and S. S. Thangaswamy, "An Efficient Hand Gesture Recognition Based on Optimal Deep Embedded Hybrid Convolutional Neural Network-long Short Term Memory Network Model," *Concurr. Comput. Pract. Exp.*, 2022, doi: 10.1002/cpe.7109.

[24] D. Copaci, J. Arias, M. Gómez-Tomé, L. Moreno, and D. Blanco, "sEMG-Based Gesture Classifier for a Rehabilitation Glove," *Front. Neurorobotics*, vol. 16, May 2022, doi: 10.3389/fnbot.2022.750482.

[25] C. Bagath Basha, "Enhancing Healthcare Data Security Using Quantum Cryptography for Efficient and Robust Encryption," *J. Electr. Syst.*, vol. 20, no. 5s, pp. 2070–2077, Apr. 2024, doi: 10.52783/jes.2544.

[26] A. Cisnal, J. Pérez-Turiel, J. Fraile, D. Sierra, and E. de la Fuente, "RobHand: A Hand Exoskeleton With Real-Time EMG-Driven Embedded Control. Quantifying Hand Gesture Recognition Delays for Bilateral Rehabilitation," *IEEE Access*, vol. 9, pp. 137809–137823, 2021, doi: 10.1109/ACCESS.2021.3118281.

[27] A. K. Panda, R. Chakravarty, and S. Moulik, "Hand Gesture Recognition using Flex Sensor and Machine Learning Algorithms," *2020 IEEE-EMBS Conf. Biomed. Eng. Sci. IECBES*, pp. 449–453, 2021, doi: 10.1109/IECBES48179.2021.9398789.

[28] S. Zhang *et al.*, "Real-Time and Accurate Gesture Recognition With Commercial RFID Devices," *IEEE Trans. Mob. Comput.*, vol. 22, pp. 7327–7342, 2023, doi: 10.1109/TMC.2022.3211324.

[29] K. Bell *et al.*, "Verification of a Portable Motion Tracking System for Remote Management of Physical Rehabilitation of the Knee," *Sensors*, vol. 19, no. 5, 2019, doi: 10.3390/s19051021.

[30] P. Lin, R. Zhuo, S. Wang, Z. Wu, and J. Huangfu, "LED Screen-Based Intelligent Hand Gesture Recognition System," *IEEE Sens. J.*, vol. 22, pp. 24439–24448, 2022, doi: 10.1109/JSEN.2022.3219645.

https://doi.org/10.31436/iiumej.v26i1.3531

# INTEGRATION OF LORA IOT WITH CLOUD PLATFORM IN STINGLESS BEEHIVE REMOTE MONITORING SYSTEM

**YASSER ARUL AHMAD[1*], NURUL SALSHABILA MUSTAPA[1], ANIS HANNANI RAZAMAN[1], MUHAMMAD NASRIN AQIL ABDUL HAMID[1], NOREHA ABDUL MALIK[1], MOHD FAIZAL JAMLOS[2,3]**

*[1]Department of Electrical and Computer Engineering, Kulliyyah of Engineering, International Islamic University of Malaysia, Kuala Lumpur, Malaysia*
*[2]Faculty of Electrical and Electronics Engineering Technology, Universiti Malaysia Pahang Al-Sultan Abdullah, Pekan, Malaysia*
*[3]Centre for Automotive Engineering, Universiti Malaysia Pahang Al-Sultan Abdullah,Pekan, Malaysia*

**Corresponding author: yasser@iium.edu.my*

*(Received: 14 November 2024; Accepted: 17 December 2024; Published online: 10 January 2025)*

***ABSTRACT:*** Stingless bee colonies require constant monitoring to ensure hive health and optimal honey production. However, conventional monitoring practices are time-consuming and labor-intensive, especially for beekeepers in rural or remote areas. Without access to real-time hive data, beekeepers may struggle to detect changes in temperature, humidity, and other vital conditions that could impact bee health and productivity. Most studies rely on Wi-Fi modules for communication between local and cloud servers. However, using Wi-Fi for bee monitoring requires that the stingless bee hives be located near buildings with Wi-Fi access. To address this issue, a prototype of a remote monitoring system for a stingless bee colony was developed using Long Range (LoRa) technologies due to the low data rate, low power, and operability in an outdoor environment. This system aims to help beekeepers monitor the beehives remotely. The prototype comprises two nodes: a beehive sensor node and a LoRa gateway node. The beehive monitoring sensor node is equipped with the ESP32 as a microcontroller, LoRa SX1278, BME680, and KY-037. The LoRa gateway comprises ESP32 and LoRa SX1278 and is interfaced with Ubidots through Node-Red. The developed prototype was tested at four locations at varying distances in the Mahallah Ruqayyah Kelulut farm. The result shows that LoRa is feasible for remote monitoring because it can reliably transmit data up to 58 meters despite a higher data rate. The Ubidots dashboard displays the temperature, humidity percentage, air quality, pressure, sound levels, and RSSI value for thorough insights into the bee's condition, as it can be accessed using web and mobile applications. Overall, the stingless bee remote monitoring system using LoRa communication is a promising solution for outdoor applications between the sender and receiver for data transmission in remote areas.

***ABSTRAK:*** Koloni lebah kelulut memerlukan pemantauan berterusan untuk memastikan kesihatan sarang dan pengeluaran madu yang optimum. Walau bagaimanapun, amalan pemantauan konvensional memerlukan banyak masa dan tenaga, terutamanya bagi penternak lebah di kawasan pedalaman atau terpencil. Tanpa akses kepada data sarang secara masa nyata, penternak lebah mungkin menghadapi kesukaran untuk mengesan perubahan suhu, kelembapan, dan keadaan penting lain yang boleh menjejaskan kesihatan serta produktiviti lebah. Kebanyakan kajian menggunakan modul Wi-Fi untuk komunikasi antara pelayan tempatan dan awan. Walau bagaimanapun, penggunaan Wi-Fi untuk pemantauan lebah memerlukan sarang lebah kelulut diletakkan berhampiran bangunan dengan akses Wi-Fi. Bagi mengatasi isu ini, satu prototaip sistem pemantauan jauh untuk koloni lebah kelulut telah dibangunkan menggunakan teknologi Long Range (LoRa) yang mempunyai kadar data

rendah, penggunaan tenaga yang rendah, serta sesuai untuk persekitaran luar. Sistem ini bertujuan membantu penternak lebah memantau sarang lebah dari jauh. Prototaip ini terdiri daripada dua nod: nod sensor sarang lebah dan nod pintu gerbang LoRa. Nod sensor pemantauan sarang lebah dilengkapi dengan ESP32 sebagai mikropengawal, LoRa SX1278, BME680, dan KY-037. Pintu gerbang LoRa pula menggunakan ESP32 dan LoRa SX1278 yang dihubungkan dengan Ubidots melalui Node-Red. Prototaip ini telah diuji di empat lokasi berbeza pada jarak yang berbeza di ladang Kelulut Mahallah Ruqayyah. Hasil menunjukkan bahawa LoRa adalah sesuai untuk pemantauan jarak jauh kerana, walaupun pada kadar data yang lebih tinggi, ia boleh menghantar data dengan baik sehingga jarak 58 meter. Papan pemuka Ubidots memaparkan suhu, peratusan kelembapan, kualiti udara, tekanan, tahap bunyi, dan nilai RSSI untuk memberikan gambaran lengkap mengenai keadaan lebah, yang boleh diakses melalui aplikasi web dan mudah alih. Secara keseluruhan, sistem pemantauan jauh lebah kelulut menggunakan komunikasi LoRa adalah penyelesaian yang menjanjikan untuk aplikasi luar di kawasan terpencil antara penghantar dan penerima bagi penghantaran data.

***KEYWORDS:*** *LoRa SX1278, ESP32, Remote Monitoring, BME680, Ubidots.*

# 1. INTRODUCTION

Stingless beekeeping has gained prominence in recent years due to the valuable role these bees play in pollination and the unique qualities of their honey, particularly in tropical regions. Stingless bee honey is known for its sour taste compared to honeybees because it sustains biodiversity and acts as an important pollination agent in forests full of different kinds of plants. Stingless bees are defined as small to medium-sized bees with short stingers originating from tropical regions of the world, such as Australia, Africa, and Southeast Asia [1]. Unusual behaviors that are less likely to be understood are especially the intense conflicts between the colonies, in which one of the conflicts may lead to high mortality rates of the stingless bees when their colonies and stored resources are stolen [2]. The inter-colony attacks will give advantages to the attackers, allowing them to gain benefits such as the hive, honey, and propolis from the attacked colonies [3]. Therefore, the monitoring system for the stingless bee colony is needed because many external factors, such as temperature and humidity, may cause the stingless bees to become extinct [4].

Traditional monitoring methods often require physical presence and can be labor-intensive, making it challenging to track real-time hive conditions, especially in remote areas. As the demand for stingless bee honey and its related products rises, so does the need for effective management and monitoring systems to maintain healthy bee colonies. The existing monitoring system for stingless bee colonies is not well suited for stingless beehives placed in a remote area. A problem faced by the beekeepers when they started to monitor the hive remotely is that most of the monitoring system uses a Wi-Fi module as a medium to connect the sensor node at the beehives directly to the internet. Most stingless beehives are placed remotely, far from the buildings, without access to a Wi-Fi router. When this happens, the beekeepers encounter a hard time sustaining the well-being of the stingless bees and later find out about the health problems faced by the stingless bees, thus restricting the beekeepers from monitoring the stingless bees. This might be caused by the transmission delay from the sensor node into the cloud server due to poor internet connection. A GSM-based stingless bee monitoring system could solve this problem, but GSM systems are getting outdated and being phased out of the market. Therefore, this research aims to develop a small, simple, and reliable monitoring system for stingless bees based on current IoT technology and Long Range (LoRa) radio technology. LoRa offers long-range, low-power wireless communication, making it ideal

https://doi.org/10.31436/iiumej.v26i1.3531

for IoT applications in remote and energy-constrained environments. The system aims to provide beekeepers with real-time information about the environmental parameters of the beehive, hence contributing to the colony's health and helping to optimize the stingless bee conditions to increase honey production.

## 2. RELATED WORKS

Heterotrigona itama and Geniotrigona thoracica, illustrated in Figure 1 (a) and (b), respectively, are stingless bee species found in Southeast Asia, particularly in countries like Malaysia, Indonesia, and Thailand [5]. These bees belong to the Apidae family and are highly valued for their pollination capabilities and honey production, especially in traditional and medicinal contexts. Malaysia's stingless bee industry has grown in demand in recent years. Rising in numbers, the agricultural community started their careers as stingless beekeepers. These beekeepers were guided to manage their hives, given information about the stingless bee, and acquired all techniques to cut down resources while having the same volume of honey production [6]. Stingless bee honey is known for its high quality, but it is expensive because of the limited quantity produced by the bees [7].

Figure 1. Stingless bee species: (a) Heterotrigona Itama, (b) Geniotrigona Thoracica [5].

Trigona Itama and Trigona Thoracica are the most frequently employed in Malaysia's stingless bee industry [4], and most beekeepers monitor the health of the stingless bees by observing them and examining their environment for any concerns [8]. The manual method has a record of success in beekeeping, but as time progresses, the number of stingless beehives has increased, and therefore, this method has become less efficient.

https://doi.org/10.31436/iiumej.v26i1.3531

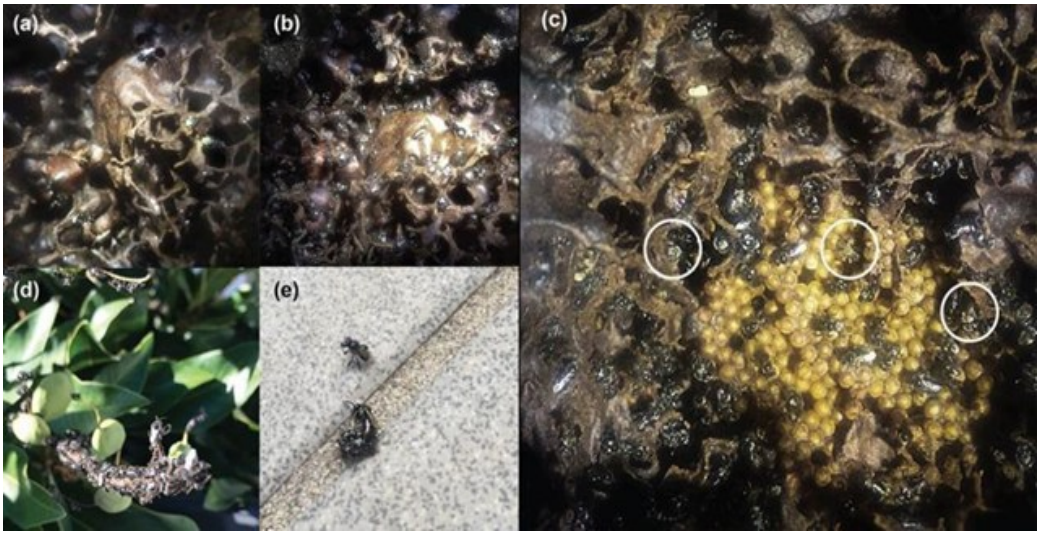


Figure 2. (a) Stingless beehive before the invasion, (b) Stingless beehive after the invasion, (c) New callows are present in the hive brood area, (d) Male stingless bee aggregates outside the hive, (e) Male stingless bee attempts to mate with the queen [2].

The stingless bee is a eusocial insect known for its exceedingly efficient foraging and resource-seeking behaviors facilitated by their complex social organization [2]. Although some unusual behaviors are less likely to be understood, especially the intense conflicts between the colonies, one of the conflicts may lead to high mortality rates of the stingless bees when their colonies and stored resources are stolen [2]. Figure 2 illustrates behaviors related to inter-colony fighting of stingless bees. When stingless bees attacked other colonies, they focused on two things: first, the stored supplies, and second, the hive. These attacks will give the attackers an advantage in benefiting from the attacked colonies [3].

Various crucial factors limit the volume of honey retrieved from the stingless beehive. Most of the factors come from the collapse of a stingless bee colony or a non-productive hive [4]. Stingless beehives should be placed near a food supply so that the stingless bee colony is healthy and can produce over 50% of propolis inside their hive. Also, stingless bees need a monitoring system because many external factors, such as temperature and humidity, may cause the stingless bees to become extinct [4].

A dependable beehive monitoring system should be created to collect high-quality data for processing. The technology involved in the design of the monitoring system should be affordable and capable of surviving the external climate of the beehives, which will constantly be in contact with rain, sun, wind, and other factors that are harmful to most electronic components [8].

A monitoring system must endure the hive's humidity and temperature variations both inside and outside, as well as potential disruptions or assaults from other colonies. The system must also ensure proper positioning of components within the hive to prevent harm to the bees and minimize disturbances to the stingless beehive environment. Additionally, high-quality video and audio recording capabilities are recommended to enhance the accuracy of the data collected for analysis [8].

https://doi.org/10.31436/iiumej.v26i1.3531

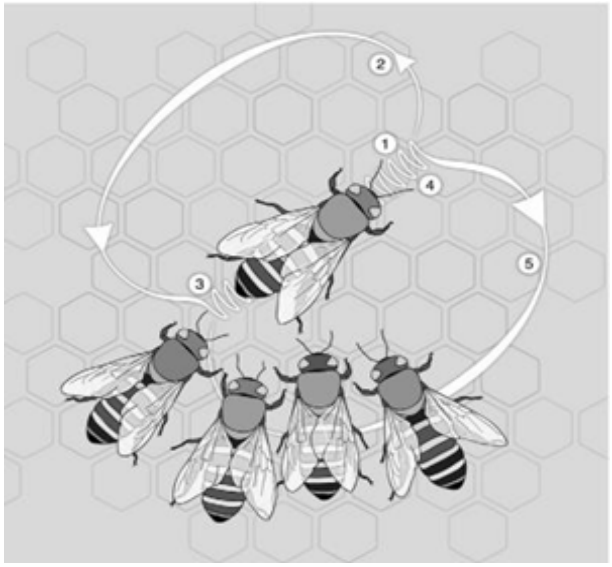


Figure 3. Waggle dance [3].

The waggle dance illustrated in Figure 3 produces a sound when the swarming bees want to send a message about a food discovery [3]. An audio monitoring system was invented to forecast bee swarming, where the audio data is captured at a sampling rate of 2 kHz [9]. This project involved 270 hours of sound recording in bee hives and recordings of temperature and humidity. Figure 4 shows the placement of the microphone and data logger inside the beehives.

Figure 4. The microphone and Hobo placement inside the beehives [9].

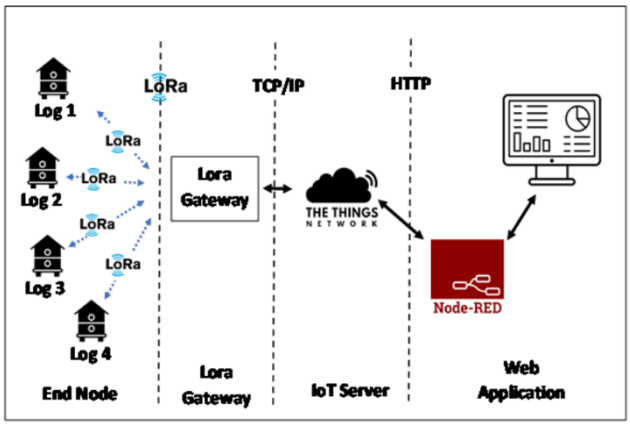


Figure 5. Lora-based test bed for stingless bee monitoring [4].

https://doi.org/10.31436/iiumej.v26i1.3531

The Lora-based testbed for monitoring stingless beehives in Figure 5 was created to gather accurate data stored in the MySQL database and visualize it in a web-based dashboard. This allows beekeepers to monitor closely and avoid any possible chances of losing a stingless bee colony [4].

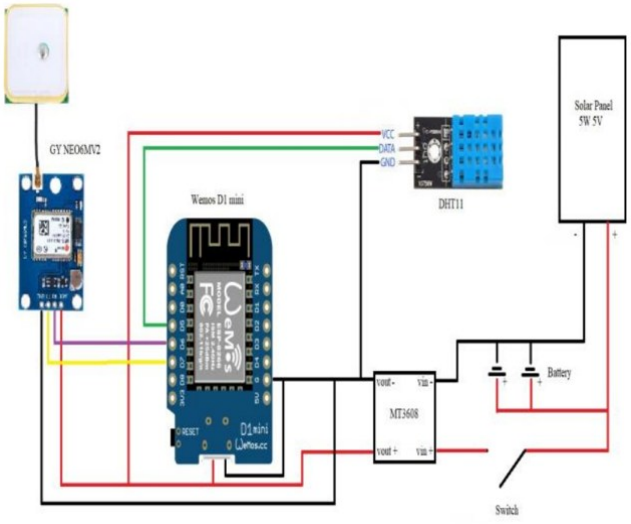


Figure 6. Wi-Fi-based iBees system [7].

The intelligent stingless beehive system (iBees) shown in Figure 6 was specifically crafted for beekeepers to keep track of the bees and monitor the hives [7]. iBees was built with a Global Positioning System (GPS) and sensors for temperature and humidity using DHT11 with a WeMo's D1 mini microcontroller. The purpose of iBees is to prevent the stingless bee colonies from being robbed.

Figure 7. Arnia remote hive monitoring system [10].

The developed iBees system was compared with other monitoring systems, such as Arnia, shown in Figure 7 [7]. Arnia is a remote honeybee hive monitoring system that allows its users to supervise the bee's health conditions at any time and provides information about the hive temperature and humidity [10]. This monitoring system starts by gathering data from the hive monitor and sending it to the gateway for analysis, which is later displayed to the users. However, the Arnia beehive monitoring system is designed for honeybee colonies.

https://doi.org/10.31436/iiumej.v26i1.3531

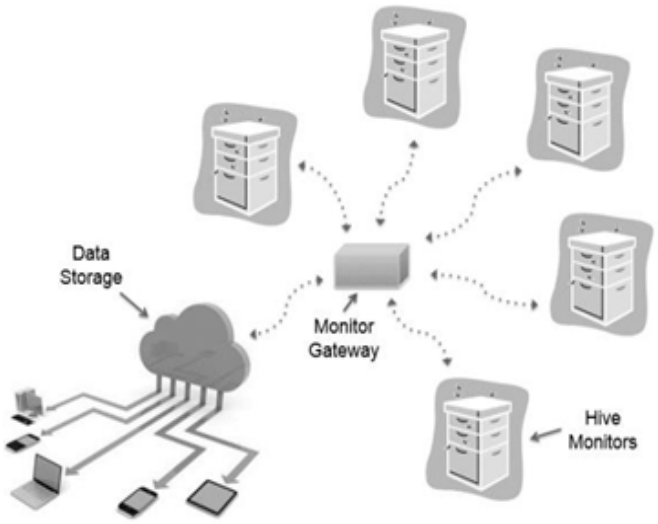


Figure 8. Arnia honeybee system configuration [10].

The Arnia electronic beehive monitoring system in Figure 8 includes temperature measurement with humidity sensors and a weight monitoring system for the honeybee hive. The sound of the bees is recorded to monitor and understand the colonies' behavior and health [10].

Another honeybee beehive monitoring system based on IoT, the Beemon system, as a comparison, is illustrated in Figure 9 [8]. The system focused more on analyzing the honeybee colony from the sound of bees, as this is a crucial component of bees' communication. They believed that research made from exploring bee noises is a growing field, where microphones and accelerometers must be positioned inside and outside the stingless beehives. Additionally, [8] highlighted existing research based on sound vibration in honeybee monitoring systems, noting that when a scouting bee discovers a food source and returns to the hive, it sends messages through the waggle dance upon returning.

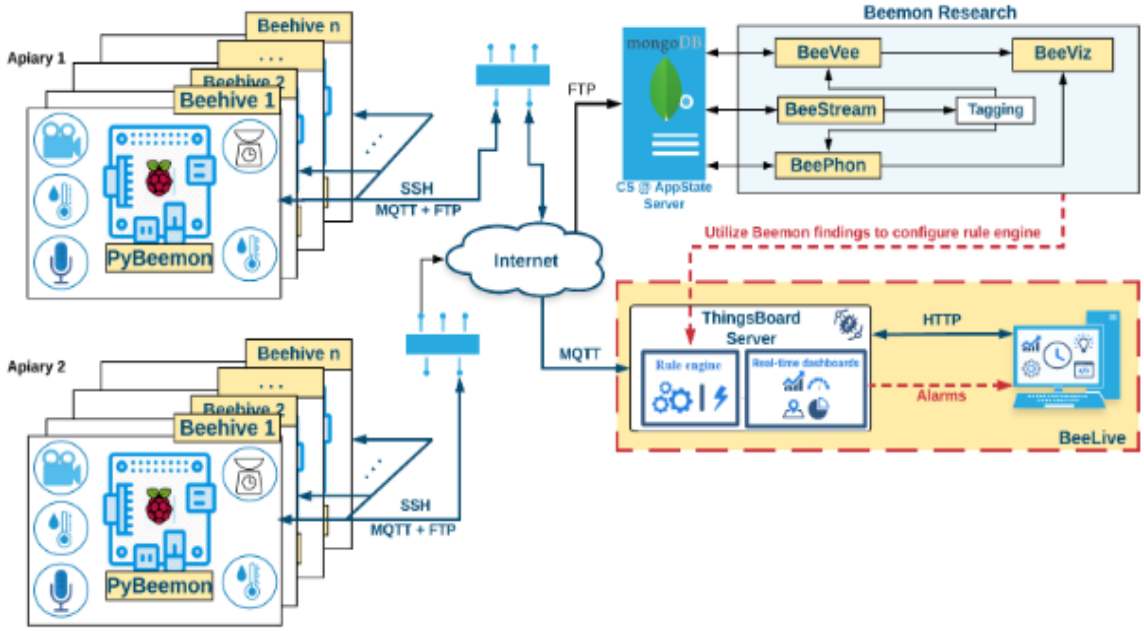


Figure 9. Beemon system for honeybee [8].

https://doi.org/10.31436/iiumej.v26i1.3531

The Beemon system utilizes Raspberry Pi along with a collection of sensors and capturing devices to collect data from multiple beehives simultaneously and transmit it to a central server for further analysis. The Beemon system consists of Beemon hardware, "PyBeemon", "BeeVee", "BeePhon", "BeesStream", "BeeViz" and "BeeLive". Beemon hardware includes the sensors that are placed inside and outside the hive. "PyBeemon" is a software developed by [8] that operates on Raspberry Pi. "BeeVee" is a video and image processing tool, while "BeePhon" is an analysis component used to monitor audio recordings. "BeeStream" is a tool that allows beekeepers to observe their bees, and it can be useful for data mining, whereas "BeeViz" is a web tool for data analytics, and "BeeLive" is a platform for the end user to monitor the analysis results.

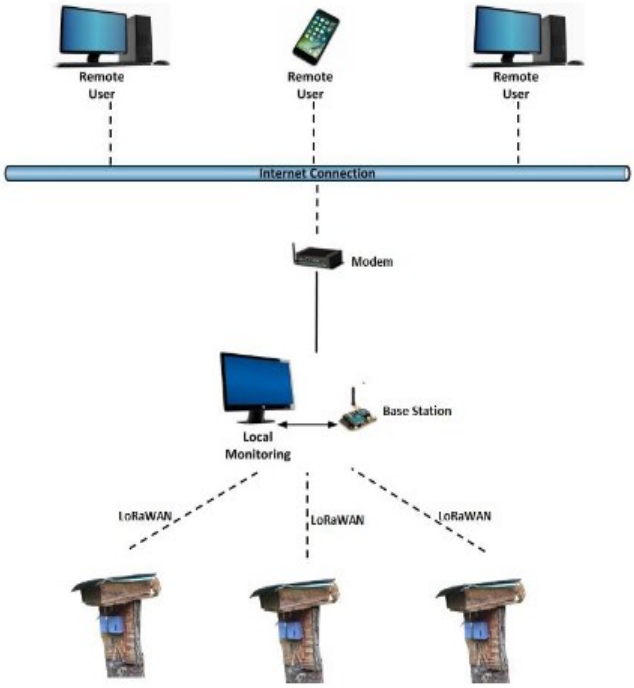


Figure 10. Air pollutant monitoring for stingless beehives [6].

Figure 10 shows a stingless beehive air pollutant monitoring system that is environmentally friendly, stable, robust, has real-time data monitoring, and consumes low power [6]. The system has a three-level stingless beehive monitoring system based on the chosen wireless communication, LoRa, with a simple architecture using Arduino Uno, DHT11, and MQ135 sensors to be sustained in any geographical conditions.

The fundamental criterion of a stingless bee monitoring system is low power [11]. The proposed system in Figure 11 is designed for low power and can remotely monitor the stingless bee colonies using a Wi-Fi connection. The system gathers all data and stores it in Google Firebase cloud storage, accessible anytime. The proposed system in Figure 11 uses two sensors: HX711 and DHT22. Both sensors were used with a buzzer as an alarm for the beekeepers to act when intruders are near the beehives.

https://doi.org/10.31436/iiumej.v26i1.3531

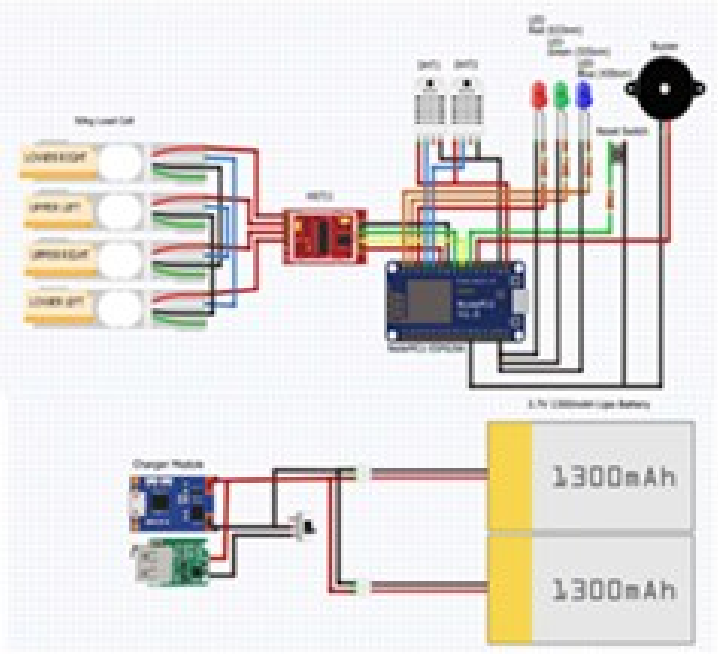


Figure 11. Wi-Fi-based low-powered stingless bee monitoring system [11].

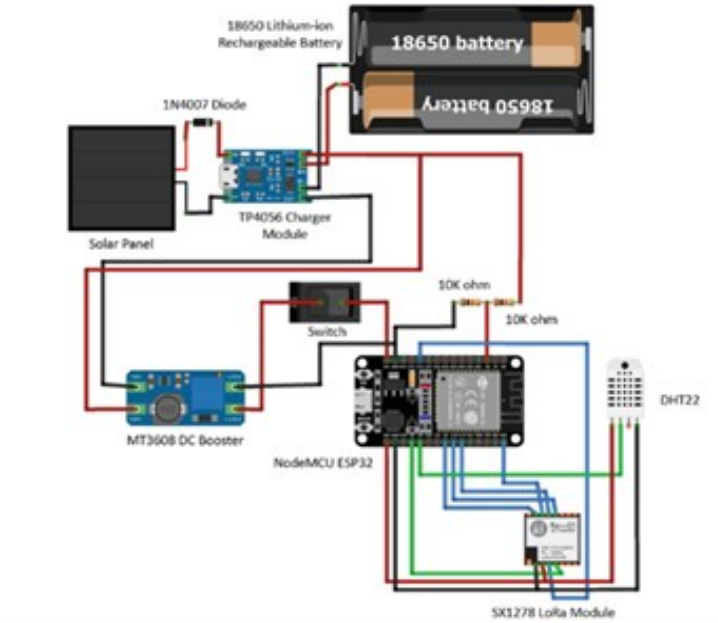


Figure 12. Temperature and Humidity IoT monitoring for stingless bees [12].

Figure 12 indicates a prospective stingless bee monitoring system that focused solely on the stingless beehive's temperature and humidity. The system includes three main parts: a single DHT22 sensor for temperature and humidity monitoring, LoRa Ra-01 as the gateway, and the Blynk app as a dashboard for the end user [12]. The DHT22 is placed inside the hives and is used to measure the hive's temperature and humidity. The DHT22 data were wirelessly sent to a centralized system using LoRa Ra-01. The centralized system, the gateway component, is the second part of the system. This component was tested under two main conditions: line-of-sight (LOS) at -60 dBm and non-line-of-sight (NLOS) at -88 dBm. Under these conditions, only three data packets were successfully received over a distance of 200 meters. The beekeepers, the end users, can view the processed data displayed on the Blynk app.

https://doi.org/10.31436/iiumej.v26i1.3531

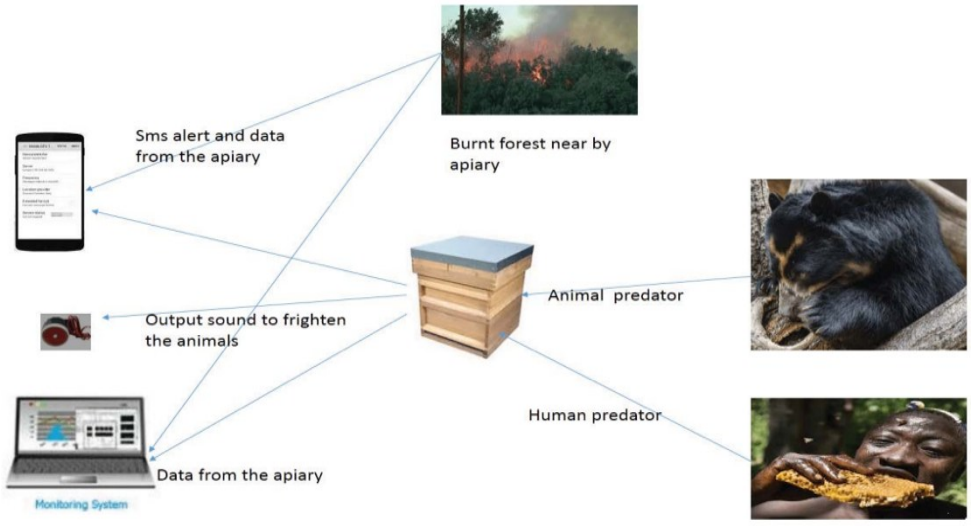


Figure 13. GSM-based honeybee monitoring system [13]

Figure 13 shows three levels of a hierarchical model: a wireless node, a local data server, and a cloud data server. These were proposed when designing the beehive monitoring system for honeybees in Rwanda, Africa. The system gathers and adjusts information in real time to monitor the bees using Arduino and a GSM module [13]. The system has three main parts: an Arduino Uno integrated with RFID for control, sensors for measuring the temperature and humidity, and a local cloud server to upload data. The system's main goal is to protect the beehive, using a flame sensor, air quality sensor, and digital siren [13].

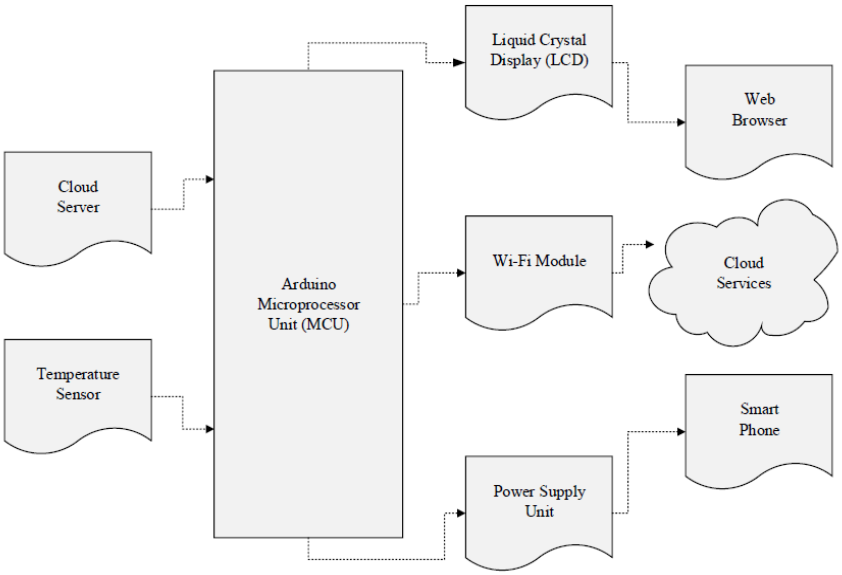


Figure 14. GSM-based honeybee beehive monitoring system [14].

Figure 14 illustrates a proposed monitoring system of wireless sensors configured with an Arduino microprocessor unit and Universal Asynchronous Receiver-Transmitter (UART) communication and GSM module in Lagos, Africa. Information is extracted from all sensors at the beehive in a Transmission Control Protocol (TCP) database [14]. The research aims to design and develop an affordable monitoring system for beekeepers to monitor temperature (°C) and sound levels (dB).

https://doi.org/10.31436/iiumej.v26i1.3531

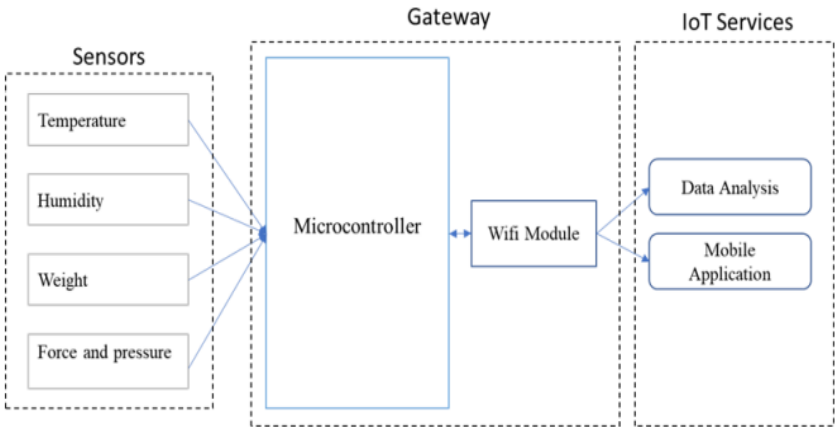


Figure 15. IoT-based monitoring system for stingless bee colonies in IIUM [15].

An IoT-based monitoring system was developed for stingless bee colonies in International Islamic University Malaysia (IIUM) with the system architecture as shown in Figure 15 [15]. The system aims to monitor the honey production of the stingless bee by measuring the hive's weight before and after honey harvesting and the bee colony parameters such as temperature, humidity, and intruder detection. The monitoring system compromises three main components: the sensors, gateway, and IoT services based on Wi-Fi. The monitoring system measured the hive's temperature, humidity, weight, force, and pressure using sensors interfacing with an Arduino Uno microcontroller board. The ESP 8266 was used to access the internet for data transfer. The Wi-Fi router inside the building is too far away from the stingless beehive, and it was replaced with a mobile hotspot for internet connectivity [15].

In summary, all authors highlight the importance of monitoring stingless beehive monitoring with various factors, such as the health of the stingless bees and the possibility of inter-colony fighting. The majority of research in this review monitors the temperature and humidity of the beehive. A stingless beehive's right temperature and humidity are vital for the bee colony's health and honey production. In addition, it is helpful to monitor the bee sound to check for signs of inter-colony fights.

This review highlights the three major sections of the stingless beehive monitoring systems: sensors, wireless communication methods, and gateways. Most studies rely on Wi-Fi modules for communication between local and cloud servers. However, using Wi-Fi for bee monitoring requires that the stingless bee hives be located near buildings with Wi-Fi access. Notably, some studies are showing the potential of adopting LoRa for communication. Building on these findings, this research is focused on advancing the application of LoRa-based technology for enhancing stingless bee colony remote monitoring systems, particularly for stingless bee hives in secluded areas without the reach of Wi-Fi. In addition, a more straightforward and reliable single-unit BME680 environmental sensor, a KY-037 sound sensor, and implementation with ESP32 are explored. The ESP32, KY-037, and BME680 modules are small and will have minimal interference with the stingless beehives. The Ubidots platform is explored as the IoT platform for this project as it offers a user-friendly interface, seamless data integration, real-time data monitoring, scalability, and data analytics capability suitable for stingless bee farmers.

https://doi.org/10.31436/iiumej.v26i1.3531

# 3. METHODOLOGY

The methodology discussed encompasses the system architecture, hardware development, data collection, and data visualization, each designed to enhance the reliability of a prototype system for remote monitoring of stingless bee colonies using LoRa-based technology. LoRa technology is the communication protocol for this system, which was selected for its low power consumption. This research intends to enable and improve remote monitoring for stingless bee colonies in a location with limited Wi-Fi connectivity [15]. The previous system was restructured according to the current situation of the IIUM Kelulut (stingless bee) farm, where the beehive's logs are screwed to the stands, which eliminates the possibility of measuring the weight of the beehive before and after honey harvesting. The communication protocol of the previous system, which relied on a Wi-Fi module, was replaced with a LoRa SX1278 module due to the limited range of Wi-Fi connectivity.

## 3.1. System Architecture

The system can be divided into four main parts: the LoRa sensor node (transmitter), LoRa gateway node (receiver), Node-RED as an IoT tool, and Ubidots as the cloud platform and database, as shown in Figure 16. The system can provide essential parameters, including the Received Signal Strength Indicator (RSSI), temperature, humidity, pressure, and gas resistance.

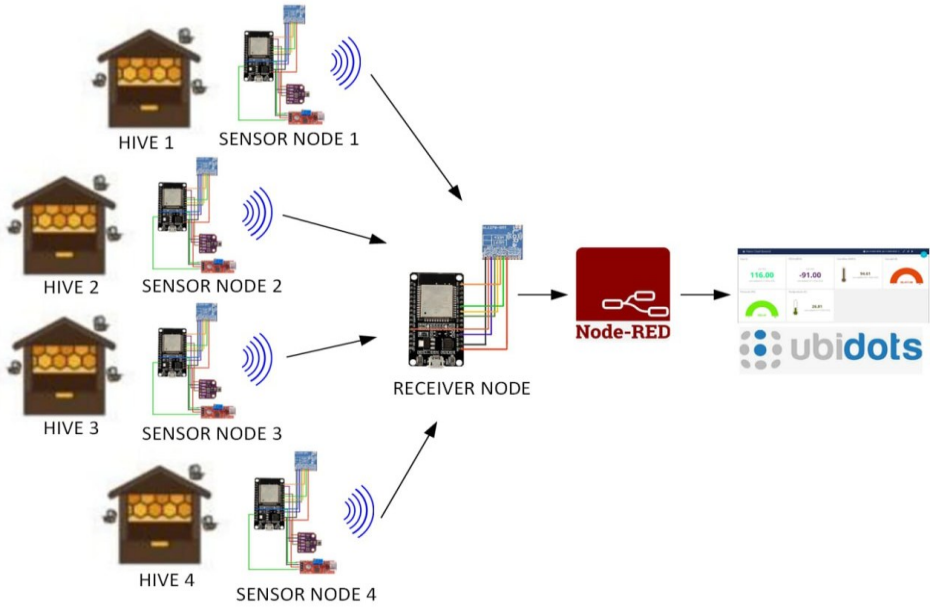


Figure 16. The system architecture for stingless bee remote monitoring system.

Figure 17 presents a flowchart of the monitoring system designed for stingless bee colonies, comprising two primary nodes: the beehive sensor node and the LoRa gateway node. The sensor node and LoRa gateway node were initialized to initiate the data transmission and establish a stable communication framework. Following this, Node-Red was launched using Node.js, providing the necessary platform for data processing within the system. Upon activation of Node-Red, the BME680 environmental sensor and KY037 sound sensor were engaged to commence data acquisition, capturing relevant environmental and sound data. It is essential at this stage to confirm the connection of the Com port and the link to the Ubidots server to ensure seamless data flow. With these components in place, Node-Red was configured to receive real-time data from the beehive sensor node. The incoming data was subsequently

https://doi.org/10.31436/iiumej.v26i1.3531

stored locally and published to the Ubidots cloud server, enabling visualization and further analysis. This sequence operates in a continuous loop, where data acquisition resumes cyclically to maintain an uninterrupted monitoring system.

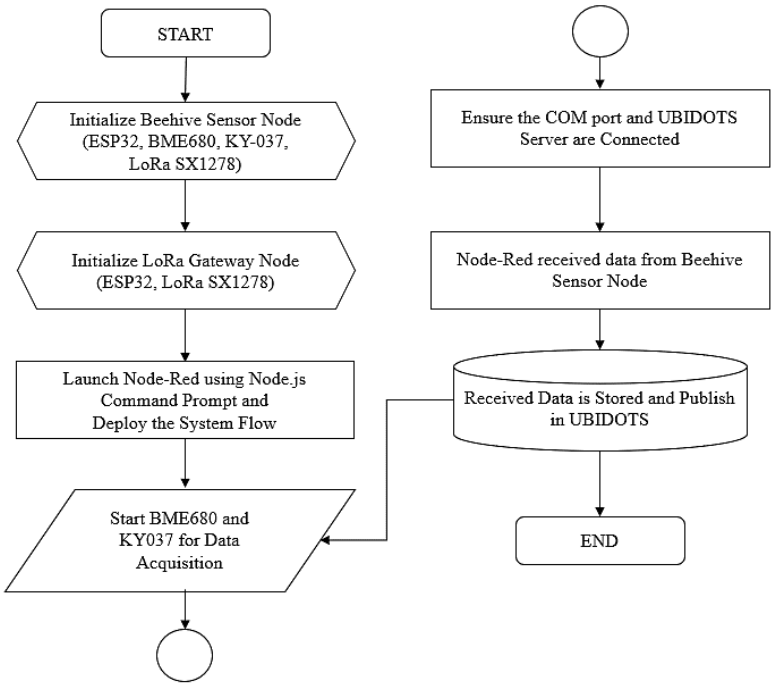


Figure 17. Flowchart diagram for stingless bee colony remote monitoring system using LoRa.

### 3.2. Hardware Development

Hardware development was initiated by selecting appropriate components and drawing a circuit diagram for pin connection for the sensor and receiver nodes. The sensor node was designed to have three main components: NodeMCU-ESP32 as the microcontroller, BME680 and KY-037 as the sensors, and LoRa SX1278 as the communication gateway (act as the transmitter). NodeMCU-ESP32 was chosen as it is cost-effective and compatible with the Arduino Integrated Development Environment (IDE) software application. The receiver node was built with NodeMCU-ESP32 and LoRa SX1278 (act as the receiver). The circuit diagram and the pin connection for the sensor node and receiver node are shown in Figures 18 and 19, respectively.

The LoRa SX1278 is a long-range radio transceiver commonly employed in developing prototype systems. In this research, the LoRa module serves a crucial function within the beehive sensor node by enabling extended-range communication, which is essential for the remote monitoring of beehive colonies. The SX1278 provides access to Serial Peripheral Interface (SPI) and D1O-0 pins that support LoRa mode only [13]. Operating at a frequency of 433 MHz, the SX1278 aligns with regulatory requirements for use in many Asian countries. To integrate the SX1278 transceiver with both the beehive sensor node and the LoRa gateway, an additional library, "LoRa" by Sandeep Mistry, was installed in the Arduino IDE. LoRa technology, which facilitates long-range data transmission, is fundamental to the Internet of Things (IoT); thus, the use of the SX1278 module underscores its pivotal role in the successful implementation of this project. The same pin connection between ESP32 and SX1278 was

https://doi.org/10.31436/iiumej.v26i1.3531

implemented for the LoRa gateway node, as shown in Figure 18 (d), while the circuit diagram is illustrated in Figure 19.

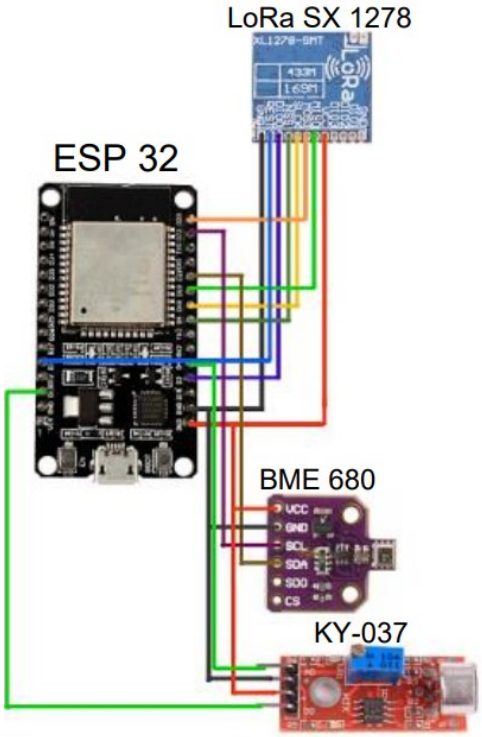


(a)

| BME680 | ESP32 |
|---|---|
| VCC | 3V3 |
| GND | GND |
| SCL | D22 |
| SDA | D21 |

(b)

| KY-037 | ESP32 |
|---|---|
| + | 3V3 |
| G | GND |
| A0 | D4 |
| D0 | D13 |

(c)

| LoRa SX1278 | ESP32 |
|---|---|
| SCK | D18 |
| MISO | D19 |
| MOSI | D23 |
| NSS | D5 |
| RST | D14 |
| DI0 | D2 |

(d)

Figure 18. Circuit drawing for (a) beehive sensor mode and pin connection between ESP32 and (b) BME680, (c) KY-037, and (d) SX1278.

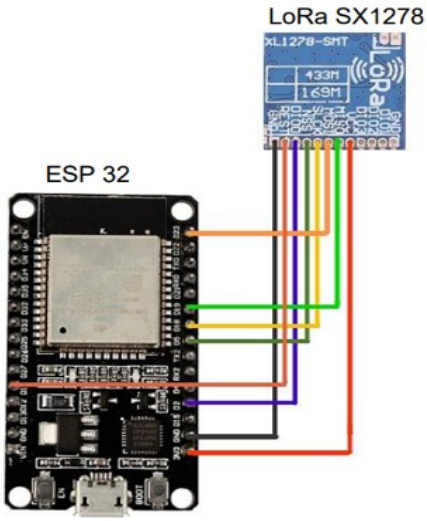


Figure 19. Circuit drawing for LoRa gateway node.

The sensors at the sensor node measure the parameters needed to monitor the stingless bee colony and the beehive, such as temperature, humidity, pressure, and gas resistance. BME680 has two communication protocols: Inter-Integrated Circuit (I2C) and SPI. The Adafruit_BME680 library and Adafruit_Sensor_Library were installed in Arduino IDE as required by the BME680 sensor. The sensor was placed near the top of the stingless beehive to measure environmental parameters such as temperature and humidity near the bee workspace.

https://doi.org/10.31436/iiumej.v26i1.3531

The KY-037 sensor is a high-sensitivity sound detection module that detects sound intensity through a built-in microphone, commonly used in projects for audio-based triggering and monitoring applications. The module is equipped with a potentiometer that allows users to adjust the sensitivity of the microphone, enabling control over the sound threshold level required to trigger the sensor's output signal. It has four pins, which are A0 (Analog input), G (Ground), + (3.3V), and D0 (Digital input). No specific library is required for this module. Both pins of the sensor, digital and analog, were declared in the Arduino IDE code to employ it in the system. The microphone on the module was placed near the entrance of the stingless beehive to detect the sound level, which indicates the bee's productivity.

Figure 20 shows the output of the Arduino IDE serial monitor during the verification of the LoRa SX1278 module. This verification was done at a shorter distance, within 1 meter, to verify that both LoRa modules can send and receive data packets. The serial monitor in Arduino IDE also shows the output of the successful LoRa point-to-point communication without packet loss. All verification tests for the hardware have been done before data collection at site locations.

```
Sending packet: 1
Sending packet: 2
Sending packet: 3
Sending packet: 4
Sending packet: 5
Sending packet: 6
Sending packet: 7
Sending packet: 8
Sending packet: 9
Sending packet: 10
```

(a)

```
Received packet 'hello 1' with RSSI -69
Received packet 'hello 2' with RSSI -70
Received packet 'hello 3' with RSSI -66
Received packet 'hello 4' with RSSI -71
Received packet 'hello 5' with RSSI -71
Received packet 'hello 6' with RSSI -71
Received packet 'hello 7' with RSSI -64
Received packet 'hello 8' with RSSI -71
Received packet 'hello 9' with RSSI -71
Received packet 'hello 10' with RSSI -66
```

(b)

Figure 20. Output displayed at the serial monitor for LoRa SX1278
(a) sender (b) receiver node

### 3.3. Data Collection and Data Visualization using Ubidots

Inside IIUM are known to be a few stingless bee species located in Mahallah Ruqayyah and Kulliyyah of Engineering. Currently, the stingless bee colony in IIUM is monitored manually by IIUM Union of Support Staff One (*Kesatuan Kakitangan Sokongan Satu*) (KESATU) members. The stingless bee species Heterotrigona Itama and Homotrigona Binghami, available at the IIUM Kelulut farm, were chosen for data collection in this research. These species were selected because they thrive on the Mahallah Ruqayyah Kelulut farm, which is located near a secluded area. This research aims to monitor the stingless bee colony in four different beehive locations at varying distances from the LoRa gateway node (located at a building with a Wi-Fi connection). The parameters such as the Received Signal Strength Indicator (RSSI), temperature, humidity, pressure, and gas resistance were measured using the developed monitoring system. The measured parameters were transferred to the cloud via Node-RED.

Node-RED is a flow-based development tool primarily for integrating and automating IoT, web, and cloud application data flows. In this research, the data flow is shown in Figure 21, and the process begins with a COM port, designated "COM6," which facilitates the connection between Node-Red flows and the ESP32 module with the LoRa gateway to upload incoming data. A debug node labeled "msg.payload" relays the data to subsequent nodes for each instance that data was loaded into the system. This flow includes two primary functions: the first transforms data from the beehive sensor node for the Ubidots platform, while the second refines

https://doi.org/10.31436/iiumej.v26i1.3531

the payload for storage in a .csv file, serving as a backup. Upon receipt at the gateway, data is directed to the Ubidots server by configuring the settings of the API token and the device name. Additionally, data converted at the "JSON to string object" node was saved locally as a .csv file to provide a backup, as Ubidots retains data for a maximum period of 24 months.

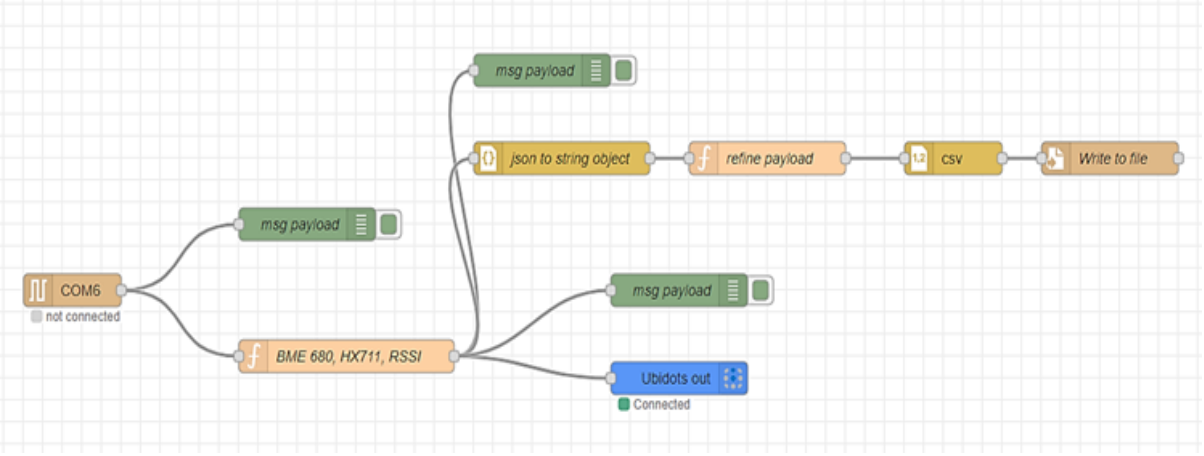


Figure 21. Node-Red flow for stingless bee remote monitoring system

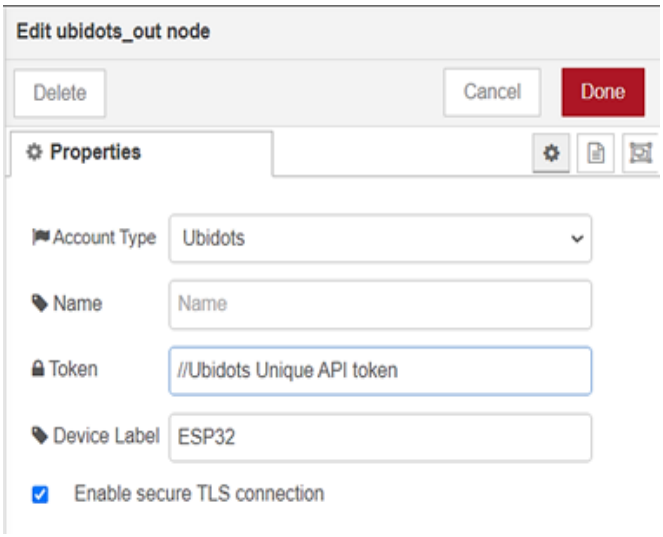


Figure 22. Ubidots settings in Node-Red

A platform called Ubidots is cloud-based and provides a range of features, including cloud functionality, dashboard visualization, and data analytics. Ubidots simplifies the integration of LoRa devices, providing a user-friendly platform to visualize and analyze data for beekeepers and accelerating IoT project development and deployment. Figure 22 shows the settings to connect the "Ubidots out node" in Node-Red flow by inserting the API token from Ubidots into Node-Red. In this research, the monitoring system is real-time based on data visualization and access to the Ubidots server. After deploying the flow in Node-Red, the Ubidots server attempted to connect with the flow. The message "Ubidots publisher connected" appeared in the Node.js command prompt when the connection was established. In the Ubidots devices section, the ESP32 device instantly appeared, allowing navigation through the dashboards to display real-time data from the beehive sensor node. Navigating through it, the parameters of the sensors in real-time data can be observed in the dashboard, as shown in Figure 23.

https://doi.org/10.31436/iiumej.v26i1.3531

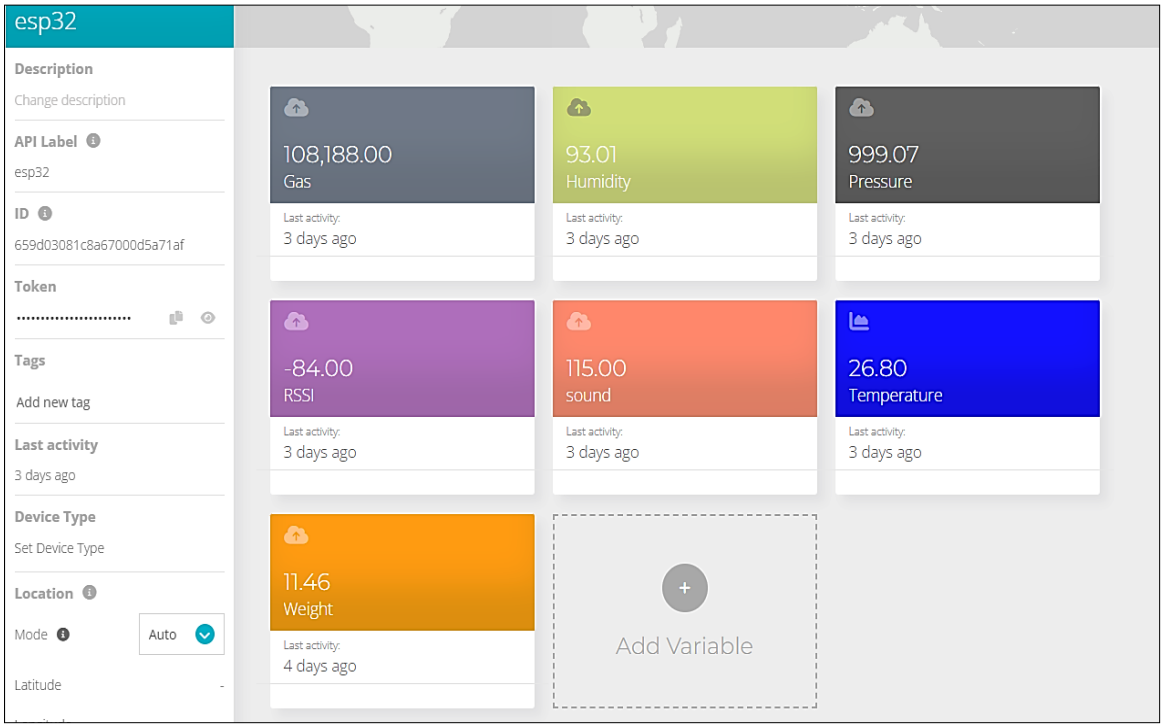


Figure 23. ESP32 device raw.

## 4. RESULTS AND DISCUSSION

LoRa-based technologies promote long-range with low-power wireless communications, specifically in a remote environment. The Received Signal Strength Indicator (RSSI) value was used to evaluate the LoRa communication, highlighting the system's performance and reliability in data transmission. The relationship between RSSI value over distances between the beehive sensor node and LoRa gateway is depicted in Figure 24. Four beehive locations were involved in the data collection, as shown in Figure 25 (a) to (d).

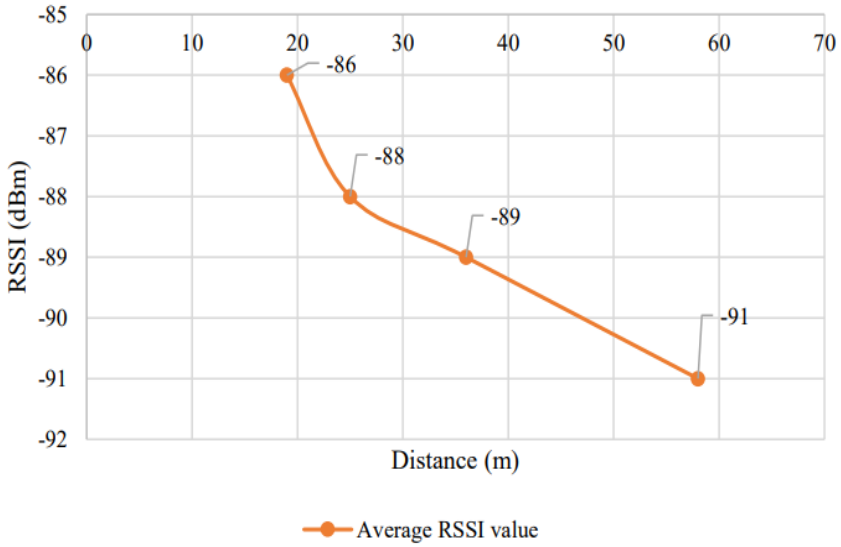


Figure 24. RSSI value (dBm) vs distance (m).

https://doi.org/10.31436/iiumej.v26i1.3531

Figure 25. Hive located at (a) 19 meters, (b) 25 meters, (c) 36 meters, and (d) 58 meters elevated from the LoRa gateway node.

The distances vary from the nearest beehive located 19 meters from the gateway, and the farthest distance from the gateway is 58 meters. For the hive positioned 19 meters from the gateway, the measured RSSI values range from -84 dBm to -87 dBm, with an average of -86 dBm. As shown in Figure 24, the data transmission reflects moderate signal strength. The hive situated 25 meters away exhibits slightly reduced signal strength compared to the 19-meter hive. The LoRa transmission from the 58-meter hive shows a further decrease in RSSI, which impacts the data upload process to Ubidots, causing a brief delay in data visualization on the dashboard. The hive positioned at 36 meters, which is elevated higher than the others, displays the weakest signal among all the beehives.

The following section analyzes and discusses the results obtained from the remote monitoring system. The system uses data from the BME680 sensor and KY-037 sound module to monitor the stingless bee condition in IIUM Kelulut farm. The parameters measured in this research include temperature, humidity percentage, pressure, air quality control, and sound levels of the stingless bees. All parameters were measured and transmitted through the LoRa network and uploaded to the Ubidots cloud for data visualization.

The sensor measurement throughout the day shows that the afternoon temperature fits in the ideal range, with an average of 31.61°C, while the average temperatures during the evening and night are below the ideal range, at 28.01°C and 26.63°C, respectively. The temperature value of the hives for H. Itama dropped under the range because of weather changes since the data was taken after the rain.

The humidity levels at night, ranging from 93.01% to 92.81%, represent the peak of the humidity curve and could potentially lead to mold growth inside the beehive. This is expected as the temperature drops to its lowest point, 24.65°C, due to changing weather conditions, which impacts the humidity. Persistent conditions maintaining 90% humidity throughout the

https://doi.org/10.31436/iiumej.v26i1.3531

day could concern beekeepers, causing Ubidots to send alert messages to their registered phone numbers. In summary, Figure 27 indicates an inverse relationship where an increase in temperature corresponds to a decrease in humidity.

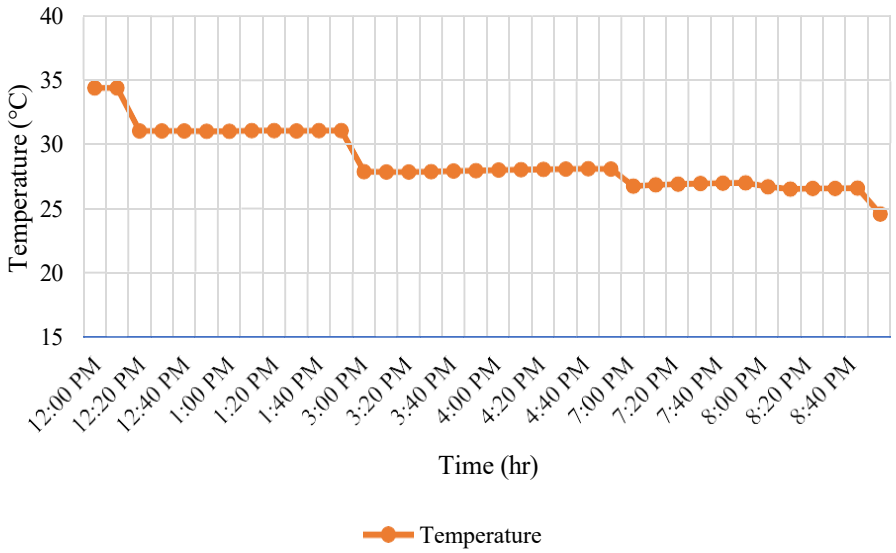


Figure 26. Beehive of H. Itama Temperature vs Time.

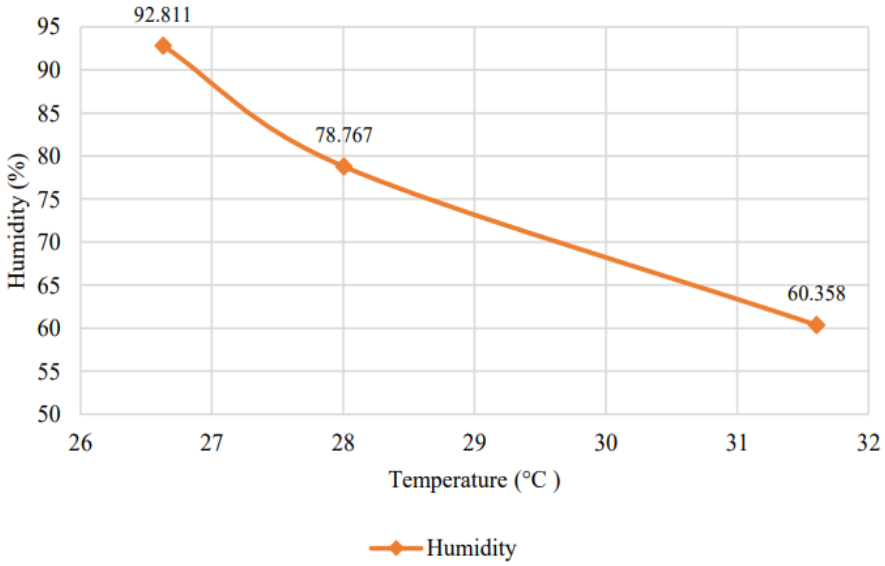


Figure 27. Humidity vs temperature of the beehive.

https://doi.org/10.31436/iiumej.v26i1.3531

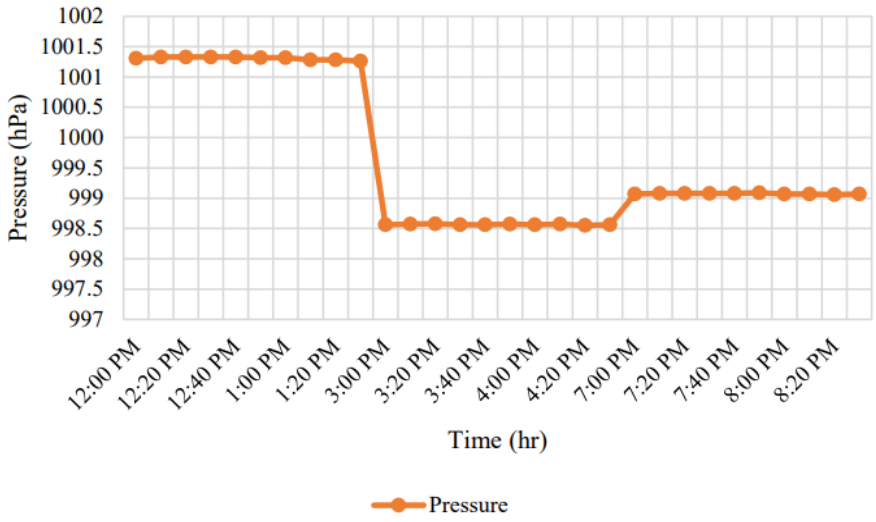


Figure 28. Pressure comparison of Heterotrigona Itama species in three different times.

The BME680 sensor provides pressure data, measured in hPa, and can help assess bee behavior, foraging activities, and hive ventilation both inside and outside. As shown in Figure 28, the highest pressure was recorded in the afternoon with an average of 1001.31 hPa, followed by 999.10 hPa at night, and the lowest pressure of 998.56 hPa occurred in the evening. In the afternoon, the stingless bees were most active, increasing their foraging as they searched for propolis and bee bread. The pressure drop in the evening may be linked to the bees' activities, such as swarming the hive before potential rainfall. The pressure then gradually increased at night, stabilizing at an ideal level.

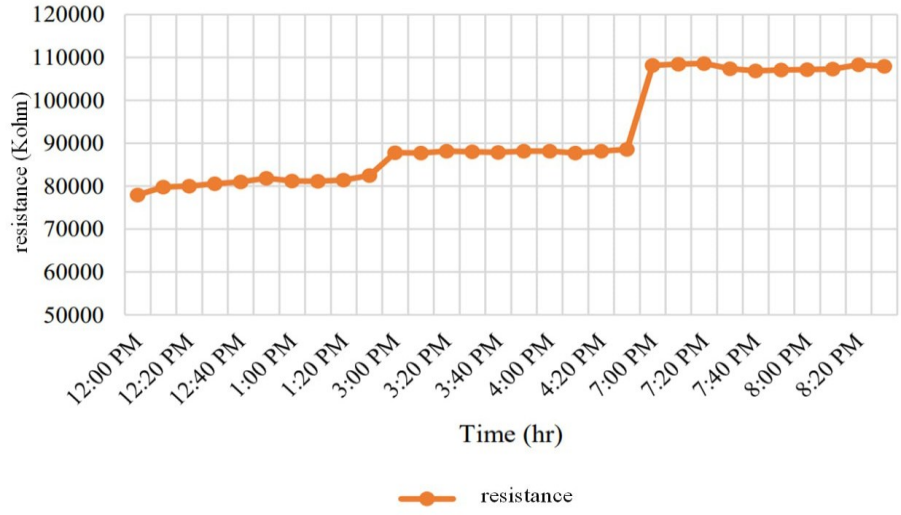


Figure 29. Air quality measurement of H. Itama vs Time

Air quality surrounding the beehives is determined using BME680 by measuring the changes in conductivity and a heater, which detects the volatile organic compounds (VOCs) by absorption of oxygen molecules on its sensitive layer and gives output in terms of resistance values. In Figure 29, during the night, the air quality around the beehives is better than during the day as it has a higher resistance value with an average of 107000 Kohm, while in the afternoon, the average value is 80740 Kohm, and in the evening, is 88050 Kohm. The beehives are located at IIUM Kelulut farm in Mahallah Ruqayyah, which is near the road. The presence

https://doi.org/10.31436/iiumej.v26i1.3531

of buses and cars contributes to the low resistance value, indicating poor air quality during the day.

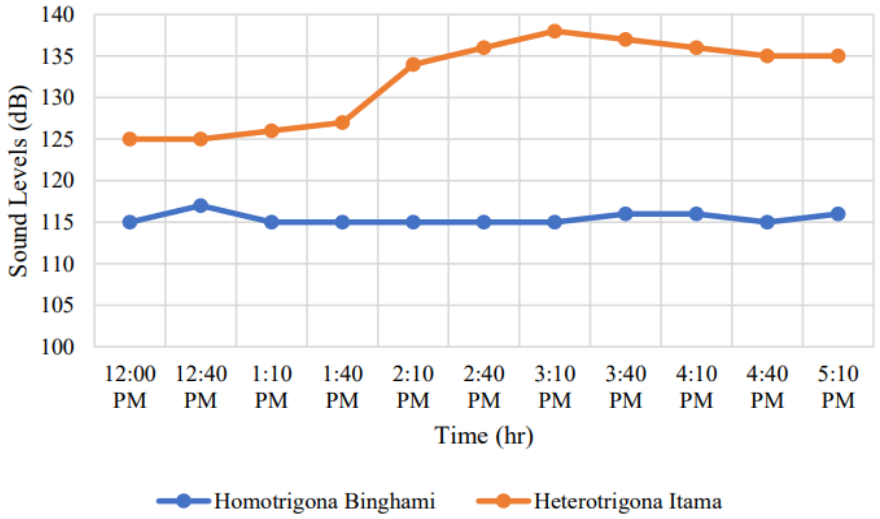


Figure 30. Sound level comparison for H. Itama and H. Binghami vs. Time

Homotrigona Binghami (H. Binghami) species are known to be less active than Heterotrigona Itama (H. Itama) as they forage in just a short period rather than H. Itama [16]. Figure 30 shows that the H. Itama species, with average sound levels of 132 dB in IIUM Kelulut farm, is more active than H. Binghami, with an average sound level of 115 dB. Lower sound levels prove that H. Binghami is less active as it generally produces honey in smaller amounts than H. Itama.

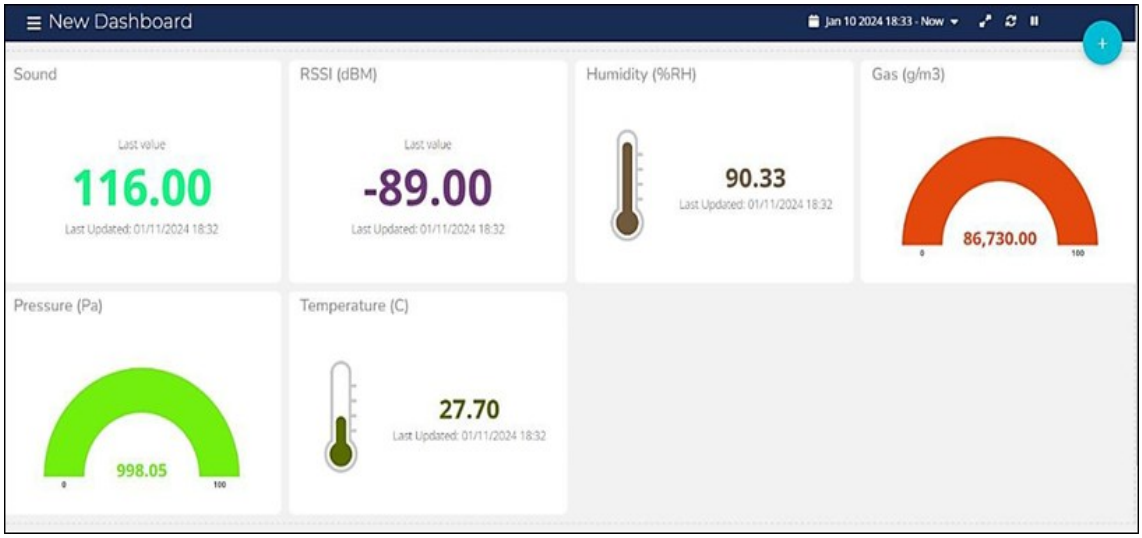


Figure 31. H. Binghami (19 meters from LoRa gateway).

https://doi.org/10.31436/iiumej.v26i1.3531

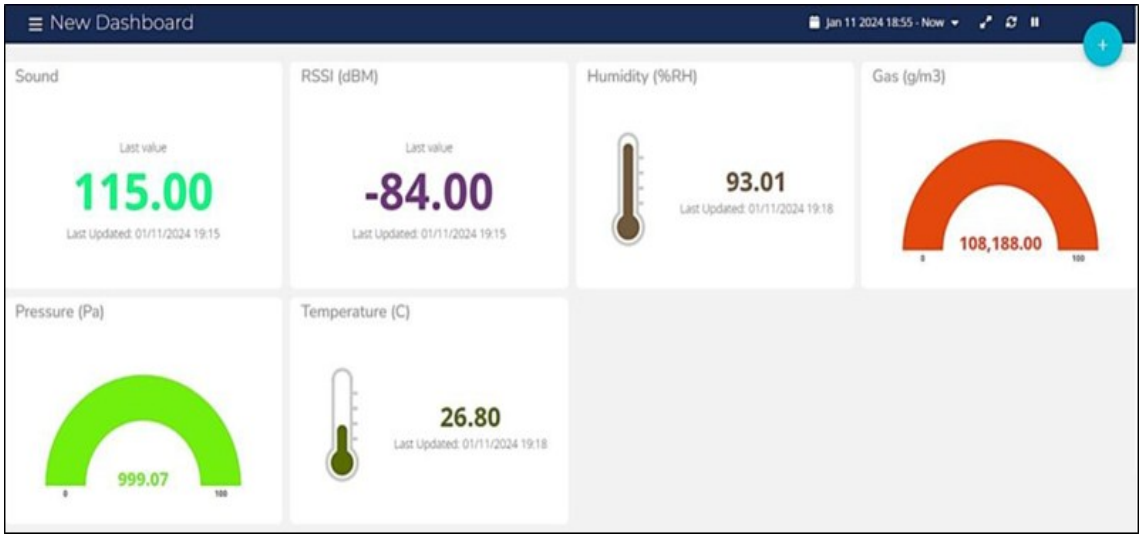


Figure 32. H. Itama (25 meters from LoRa gateway).

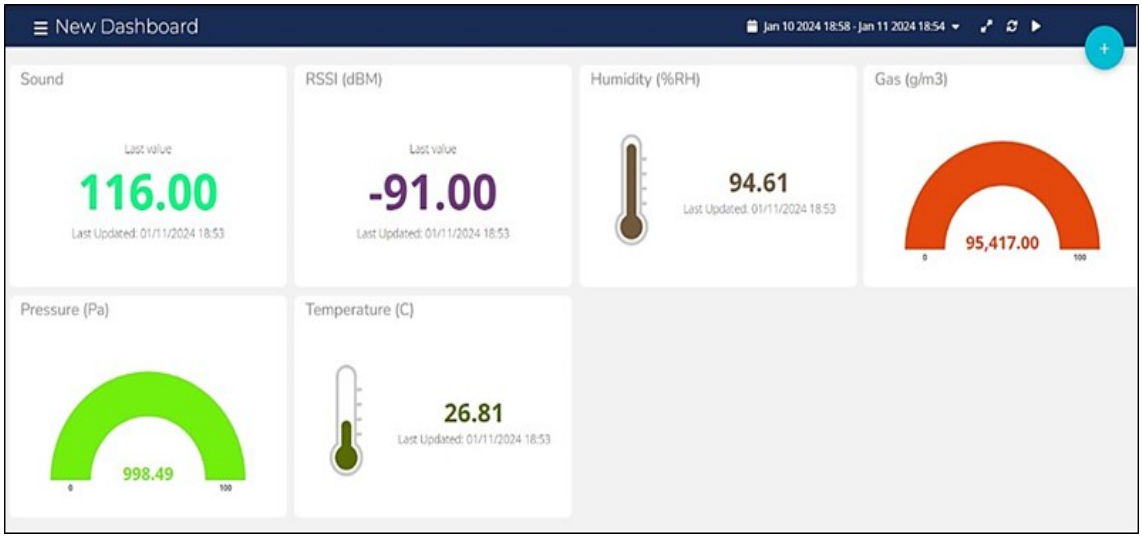


Figure 33. H. Itama (38 meters from LoRa gateway).

Data visualization using the Ubidots dashboard, portrayed in Figures 31 to 33, can be customized to represent it to the end user. All parameters transmitted using LoRa, which are temperature, humidity, gas resistance, pressure, sound levels, and RSSI value, are displayed in the dashboard. To access the dashboard, beekeepers must have Ubidots ID and password. Other than that, Ubidots also has a mobile app for Android and Apple users, named "Ubidots IoT," which is user-friendly and caters to the same information of data in Ubidots website dashboard, as shown in Figure 34.

https://doi.org/10.31436/iiumej.v26i1.3531

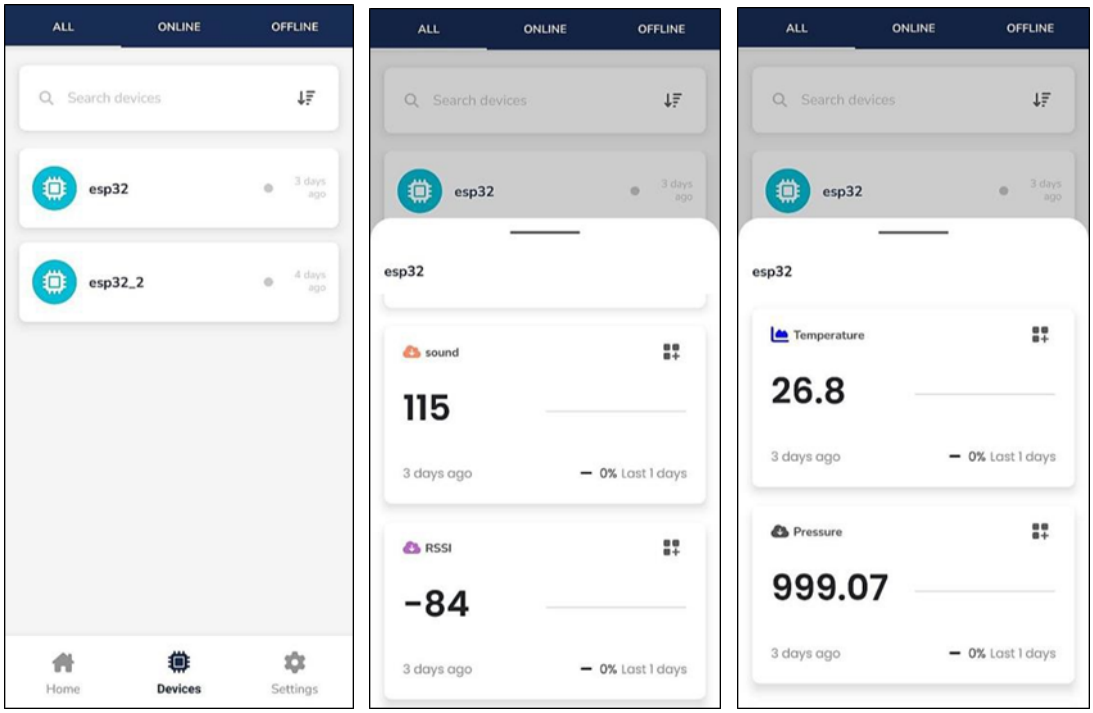


Figure 34. Ubidots IoT application.

The integration of LoRa IoT and the Ubidots platform in the system has demonstrated that remote monitoring of stingless beehives is feasible. The performance of LoRa in terms of RSSI is shown in Figure 25. The previous method [15] was unable to collect data such as temperature, humidity, and sound due to the lack of a WIFI connection in the Mahallah Ruqayyah Kelulut farm. Therefore, a comparison with the previous method is not possible.

## 5. CONCLUSION

In summary, this research successfully met its objective of developing a prototype for a remote stingless bee monitoring system, utilizing LoRa technology to monitor beehive conditions and establish reliable LoRa communication for data transmission in remote areas.

Compared to previous stingless bee monitoring systems using Arduino boards, this study employs the ESP32 microcontroller, which offers 4 MB of flash memory, significantly more than the Arduino Uno's 32 KB. Additionally, the ESP32 includes a built-in interface for USB, Wi-Fi, and Bluetooth, allowing seamless data uploads to the cloud via LoRa transmission. Upgrading from the DHT11 and DHT22 sensors to the BME680 sensor improves measurement accuracy, and the 4-in-1 sensor supports both I2C and SPI communication, making it compatible with the ESP32. New parameters like pressure and air quality monitoring further enhance this monitoring system.

The data collection approach involved using Node-Red and Ubidots, which offer a range of configuration options through MQTT, Serial Port, and HTTP protocols. Unlike other systems using Blynk and MySQL, Ubidots was selected for its user-friendly interface, offering data visualization on both the Ubidots website and its mobile application, "Ubidots IoT."

## 6. FUTURE WORKS

Enhancing real-world applications could involve improving the LoRa SX1278 module setup. This includes exploring different spreading factors to increase the range between sender and receiver nodes. Implementing LoRaMesh and LoRaWAN topologies could further expand the system's applicability. Additionally, parameters measured can be refined, and novel hive designs using materials like Styrofoam may replace traditional wood logs, promoting more accurate parameter measurements and advancing remote monitoring practices for beekeepers.

To further enhance the reliability and applicability of the system, additional data collection is necessary to accurately compute averages for temperature, pressure, and air quality. Expanding testing to diverse settings and collecting data over varied timeframes, hive setups, and environmental conditions will improve the system's generalizability. Incorporating statistical analyses, such as standard deviations and error margins, will validate the system's reliability. In addition, battery performance data will be collected. By understanding the energy requirements and battery life, the system can be optimized for remote deployments in isolated locations for a longer-term duration, such as one year. Upon longer-term data collection, a comparative analysis of the collected data against baseline values from traditional monitoring systems will be able to highlight the system's added value and its potential to provide more accurate and timely environmental insights.

## ACKNOWLEDGMENT

This project's funding comes from the University Malaysia Pahang (UMP) and International Islamic University Malaysia (IIUM) sustainable research collaboration 2022 grant scheme no. IUMP-SRCG22-001-0001.

## REFERENCES

[1] Heard, T. A. (1999). The role of stingless bees in crop pollination. In Annual Review of Entomology (Vol. 44, pp. 183–206). https://doi.org/10.1146/annurev.ento.44.1.183

[2] Lau, I. H., Hereward, J. P., Smith, T. J., Heard, T. A., & Walter, G. H. (2022). Inter-colony fights in Tetragonula stingless bees result in temporary mixed-species worker cohorts. Apidologie, 53(4). https://doi.org/10.1007/s13592-022-00936-3

[3] Grüter, C., von Zuben, L. G., Segers, F. H. I. D., & Cunningham, J. P. (2016). Warfare in stingless bees. In Insectes Sociaux (Vol. 63, Issue 2, pp. 223–236). Birkhauser Verlag AG. https://doi.org/10.1007/s00040-016-0468-0

[4] Miskon, M. T., Razak, M. A. A., Jaafar, H., Hassan, N., & Mahmood, R. (2022). A Lora-based Testbed Development for Stingless Bee Monitoring System. TEM Journal, 11(2), 712–718. https://doi.org/10.18421/TEM112-26

[5] Shamsudin, S., Selamat, J., Sanny, M., Abd. Razak, S. B., Jambari, N. N., Mian, Z., & Khatib, A. (2019). Influence of origins and bee species on physicochemical, antioxidant properties and botanical discrimination of stingless bee honey. International Journal of Food Properties, 22(1), 239-264.

[6] Ramli, M. F., Harun, A., Ismail, R. C., Ndzi, D. L., Turner, J. S. C., Farook, R. S. M., Isa, M., & Murad, S. A. Z. (2021). Design and development of stingless beehive air pollutant monitoring system. International Journal of Nanoelectronics and Materials (Vol. 14, Issue SI)

[7] Mustafa & Wan Abu Bakar, Wan Aezwani & Razak, Muhammad. (2019). An Intelligent Stingless Bee System with Embedded IoT Technology. International Journal of Recent Technology and Engineering (IJRTE). 8. 264-269. 10.35940/ijrte.C4124.098319.

[8] Tashakkori, R., Hamza, A. S., & Crawford, M. B. (2021). Beemon: An IoT-based beehive monitoring system. Computers and Electronics in Agriculture, 190. https://doi.org/10.1016/j.compag.2021.106427

[9] Ferrari, S., Silva, M., Guarino, M., & Berckmans, D. (2008). Monitoring of swarming sounds in bee hives for early detection of the swarming period. Computers and electronics in agriculture, 64(1), 72-77.

[10] Evans, S.K, (2015) Electronic beehive monitoring-applications to research. 12th International Symposium of the ICP-PR Bee Protection Group, Ghent, Belgium, 2014, pp. 121-129,

[11] N. H. Khairul Anuar et al., "IoT Platform for Precision Stingless Bee Farming," 2019 IEEE International Conference on Automatic Control and Intelligent Systems (I2CACIS), Selangor, Malaysia, 2019, pp. 225-229, doi: 10.1109/I2CACIS.2019.8825089.

[12] (pp. 334–342). Atlantis Press International BV. https://doi.org/10.2991/978-94- 6463-082-4_29

[13] E. Ntawuzumunsi and S. Kumaran, "Design and Implementation of Smart Bees Hiving & Monitoring System," 2019 IST-Africa Week Conference (IST-Africa), Nairobi, Kenya, 2019, pp. 1-9, doi: 10.23919/ISTAFRICA.2019.8764856.

[14] Imoize, A. L., Odeyemi, S. D., & Adebisi, J. A. (2020). Development of a low-cost wireless beehive temperature and sound monitoring system. Indonesian Journal of Electrical Engineering and Informatics, 8(3), 476–485. https://doi.org/10.11591/ijeei.v8i3.2268

[15] Rosli, H. A., Malik, N. A., & Ahmad, Y. A. (2022, August). IoT based monitoring system for stingless bees colony in IIUM. In Journal of Physics: Conference Series (Vol. 2312, No. 1, p. 012088). IOP Publishing.

[16] Syed Salleh, S. N. A., Mohd Hanapiah, N. A., Ahmad, H., Wan Johari, W. L., Osman, N. H., & Mamat, M. R. (2021). Determination of Total Phenolics, Flavonoids, and Antioxidant Activity and GC-MS Analysis of Malaysian Stingless Bee Propolis Water Extracts. Scientifica, 2021. https://doi.org/10.1155/2021/3789351

https://doi.org/10.31436/iiumej.v26i1.3537

# OPTIMIZING N-1 CONTINGENCY RANKINGS USING A NATURE-INSPIRED MODIFIED SINE COSINE ALGORITHM

**IRNANDA PRIYADI[1*], NOVALIO DARATHA[2], TEDDY SURYA GUNAWAN[3], KALAMULLAH RAMLI[1], FEBRIAN JALISTIO[2], HAZLIE BIN MOKHLIS[4]**

*[1]Electrical Engineering Department, Universitas Indonesia, Depok, Indonesia*
*[2]Electrical Engineering Department, Universitas Bengkulu, Bengkulu, Indonesia*
*[3]Electrical and Computer Engineering Department, International Islamic University Malaysia, Kuala Lumpur, Malaysia*
*[4]Electrical Engineering Department, Universiti Malaya, Kuala Lumpur, Malaysia*

**Corresponding author: irnanda.priyadi@ui.ac.id*

*(Received: 11 November 2024; Accepted: 22 December 2024; Published online: 10 January 2025)*

***ABSTRACT:*** Ensuring the reliability and sustainability of power systems is essential for maintaining efficient and uninterrupted operations, especially under varying load conditions and potential faults. This study tackles the critical task of contingency ranking by evaluating the severity of disturbances caused by transmission line disconnections. Such evaluations enable power system operators to make informed and strategic decisions during real-time scenarios. A novel approach utilizing the Modified Sine Cosine Algorithm (MSCA), a nature-inspired metaheuristic optimization technique, is proposed to resolve (N-1) contingency rankings efficiently. The MSCA method is validated using the IEEE 30-bus test case, focusing on optimal parameter tuning for population size, iterations, and key variables. Results demonstrate that MSCA achieves a high capture ratio of 96.67%, explores only $8.33 \times 10^{-7}$% of the search space, and requires a processing time of 3.69 seconds. Compared with established methods such as Ant Colony Optimization (ACO) and Genetic Algorithm (GA), MSCA exhibits superior computational efficiency while maintaining competitive accuracy. These findings underline the potential of MSCA in real-time applications where speed and precision are critical. By closely matching manual contingency rankings, the proposed method integrates reliability assessment and optimization techniques, offering practical value for improving system resilience and reducing risks associated with disruptions. This research advances state-of-the-art power system reliability assessment and optimization approaches, providing operators and planners with a robust tool for addressing complex contingency challenges.

***ABSTRAK:*** Memastikan keandalan dan kelestarian sistem tenaga elektrik adalah penting untuk mengekalkan operasi yang cekap dan tidak terganggu, terutamanya dalam menghadapi keadaan beban yang berubah-ubah dan kemungkinan kerosakan. Kajian ini menangani tugas kritikal dalam perangkingan kontingensi dengan menilai tahap keparahan gangguan yang disebabkan oleh pemutusan talian penghantaran. Penilaian sebegini membolehkan pengendali sistem tenaga membuat keputusan yang berinformasi dan strategik dalam senario masa nyata. Pendekatan baharu yang menggunakan Modified Sine Cosine Algorithm (MSCA), satu teknik pengoptimuman metaheuristik yang diilhamkan oleh alam, dicadangkan untuk menyelesaikan perangkingan kontingensi (N-1) dengan cekap. Kaedah MSCA ini disahkan menggunakan kes ujian IEEE 30-bus dengan memberi tumpuan kepada penalaan parameter optimum untuk saiz populasi, iterasi, dan pemboleh ubah utama. Keputusan menunjukkan bahawa MSCA mencapai nisbah tangkapan yang tinggi sebanyak 96.67%, hanya meneroka $8.33 \times 10^{-7}$% daripada ruang pencarian, dan memerlukan masa pemprosesan sebanyak 3.69 saat.

https://doi.org/10.31436/iiumej.v26i1.3537

Berbanding dengan kaedah sedia ada seperti Ant Colony Optimization (ACO) dan Genetic Algorithm (GA), MSCA menunjukkan kecekapan pengiraan yang unggul sambil mengekalkan ketepatan yang kompetitif. Penemuan ini menekankan potensi MSCA dalam aplikasi masa nyata di mana kelajuan dan ketepatan adalah kritikal. Dengan hasil yang hampir menyamai perangkingan kontingensi manual, kaedah yang dicadangkan ini mengintegrasikan penilaian keandalan dan teknik pengoptimuman, memberikan nilai praktikal untuk meningkatkan daya tahan sistem dan mengurangkan risiko yang berkaitan dengan gangguan. Penyelidikan ini memajukan pendekatan terkini dalam penilaian keandalan sistem tenaga dan pengoptimuman, menyediakan pengendali dan perancang dengan alat yang kukuh untuk menangani cabaran kontingensi yang kompleks.

***KEYWORDS:*** *contingency analysis, contingency ranking, sin cos algorithm, metaheuristic technique, nature-inspired.*

# 1. INTRODUCTION

Contingency analysis plays a vital role in ensuring the reliability and security of electrical power systems. It involves assessing potential disruptions to critical system components and evaluating their impacts on power flow and bus voltage. These disruptions can significantly change power flow patterns and voltage profiles throughout the network, requiring proactive measures to uphold system stability and operational reliability [1-3].

Contingency analysis is vital for simulating adverse power flow scenarios and triggering appropriate alarm systems to prevent operational violations. Identifying vulnerable nodes and high-risk transmission paths is essential for implementing effective preventive measures and managing risks in power systems [4, 5]. Traditionally, computational methods have been utilized to evaluate power networks' resilience. Various optimization techniques, including nature-inspired algorithms like Ant Colony Optimization (ACO) [6] and Genetic Algorithm (GA) [7], have been applied to enhance the effectiveness of contingency analysis. Additionally, machine learning approaches such as Artificial Neural Networks and Deep Learning models, encompassing Convolutional and Recurrent Neural Networks, have demonstrated their utility in enhancing prediction and classification tasks in power systems [8-11].

Despite these advancements, optimizing contingency ranking remains challenging due to computational complexity, scalability for large-scale systems, and the need to balance accuracy with efficiency [12-14]. Innovative approaches that efficiently prioritize critical contingencies while maintaining computational feasibility are crucial. Advanced metaheuristic optimization algorithms like the Modified Sin Cos Algorithm (MSCA) have shown promise in addressing such challenges by leveraging mathematical trigonometric functions for optimization [15-17]. The MSCA builds upon the foundational principles of the Sine Cosine Algorithm (SCA), addressing its limitations and extending its applicability to complex optimization challenges. The SCA employs mathematical models based on sine and cosine functions to dynamically balance exploration and exploitation, generating candidate solutions that converge toward the global optimum. While SCA effectively maintains this balance, its dependency on uniform sinusoidal movements can lead to premature convergence in highly nonlinear or unstructured search spaces. Similar challenges were highlighted in population-based optimization algorithms in [17], emphasizing the importance of adaptive mechanisms for step size and solution interactions to enhance global search capabilities. In response to these insights, MSCA integrates advanced modifications such as probabilistic selection, mutation strategies, and enhanced parameter tuning to overcome local optima entrapment, improve computational efficiency, and ensure robustness across diverse problem domains. These enhancements make

MSCA a superior alternative for addressing complex, large-scale optimization tasks in power system contingency analysis.

This study proposes using MSCA to optimize (N-1) contingency rankings, providing a reliable and computationally efficient solution for real-time decision-making. The methodology is validated using the IEEE 30-bus test case. MSCA achieves competitive performance in key metrics such as accuracy, processing time, and search space efficiency compared to ACO and other state-of-the-art methods [18, 19]. By demonstrating the robustness and scalability of MSCA, this research contributes to advancing power system reliability assessment and optimization techniques, offering practical value for utility providers in minimizing risks and improving network resilience.

## 2. SINE COSINE OPTIMIZATION ALGORITHM

Optimization is finding an effective and reliable approach based on performance within given constraints. Mathematically, optimization involves determining the minimum or maximum of a function subject to constraints. A set of values that satisfies all constraints constitutes a viable solution. Optimization problems are found across all fields of study, making the development of optimization techniques highly significant and a compelling research direction for many scholars. Due to limitations of conventional optimization paradigms, such as local optima stagnation and reliance on derivatives of the search space, interest in stochastic optimization approaches has grown over the last two decades.

In contingency ranking optimization, algorithms are required to explore the search space for the best solution to the problem at hand. The best value of the global optimum is retained as a reference throughout the optimization process. This process consistently updates the positions of solutions, tending to move toward the most promising regions of the search space. In this context, the Sine Cosine Algorithm (SCA) is a flexible and versatile algorithm applicable to various optimization problems [15, 16].

The SCA is a population-based metaheuristic algorithm inspired by sine and cosine functions. Unlike other population-based algorithms, SCA divides optimization into exploration and exploitation phases. It uses pure sine and cosine functions to control the steps in these phases [20]. During exploration, SCA searches widely across the solution space to identify promising areas. In contrast, exploitation refines solutions by focusing on specific areas near optimal points to improve accuracy and proximity to the global optimum.

SCA achieves exploration by leveraging sine and cosine functions, which create significant positional changes in candidate solutions. Exploitation reduces the amplitude of sine and cosine functions, resulting in smaller, more directed positional changes. This mechanism enables SCA to balance exploration and exploitation, although its dependency on sinusoidal functions sometimes makes it prone to local optima trapping due to its uniform search patterns.

Mathematically, SCA updates candidate solutions using a single mathematical expression and random numbers, as shown in Eq. 1, as follows [16]:

$$X_i^{t+1} = \begin{cases} X_i^t + r_1 \cdot \sin(r_2) \cdot |r_3 \cdot P_i^t - X_i^t|, & if\ r_4 < 0.5 \\ X_i^t + r_1 \cdot \cos(r_2) \cdot |r_3 \cdot P_i^t - X_i^t| & if\ r_4 \geq 0.5 \end{cases} \quad (1)$$

where $X_i^{t+1}$ is the new position of the solution, a scaling factor or step size multiplier, $r_2$ is a random number used within the sine and cosine functions in radians, $r_3$ acts as a scaling factor or weight that adjusts the magnitude of the difference between $P_i^t$ and $X_i^t$, $r_4$ is a random number used for probabilistic decision-making and $P_i^t$ is the best-known position at iteration

https://doi.org/10.31436/iiumej.v26i1.3537

$t$. The balance between exploration and exploitation is achieved by automatically adjusting the range of sine and cosine functions through Eq. (2):

$$r_1 = a - \frac{t \cdot a}{T} \tag{2}$$

where $T$ is the maximum number of iterations, $t$ is the current iteration, and $a$ is a constant.

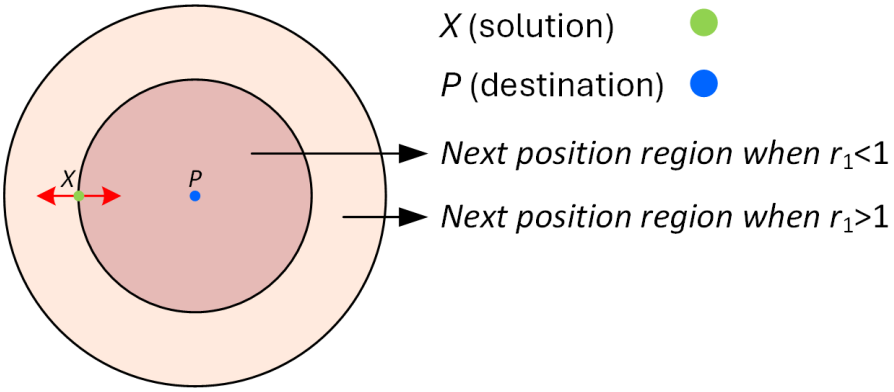


Figure 1. Position Determination using the SCA Algorithm

Figure 1 illustrates the Sin Cos Algorithm (SCA) mechanism for determining the next position of a candidate solution ($X$) in the search space relative to the global best solution ($P$). The figure highlights two key regions in the search space: the *inner region*, which represents potential positions when the random parameter $r_1 < 1$, and the *outer region* shows potential positions when $r_1 > 1$. Using sine and cosine functions, SCA adjusts the movement of $X$ toward or away from $P$, ensuring broad exploration and precise exploitation of the search space. In the *exploration phase*, $r_1$ is set to values outside the range of -1 to 1, enabling the algorithm to search widely for promising areas. During the *exploitation phase*, $r_1$ is restricted to values between -1 and 1, focusing on refining solutions around the most promising regions to approach the global optimum.

This mechanism enables SCA to balance exploration and exploitation, reducing the risk of premature convergence to local optima. The algorithm dynamically transitions between these phases by adapting each iteration's sine and cosine functions range. While SCA is effective for many optimization problems, its reliance on absolute values and sinusoidal patterns may limit performance in highly nonlinear or unstructured difficulties, particularly in high-dimensional spaces. Enhancements such as hybrid approaches and empirical adjustments to the search process have been proposed to address these limitations, ensuring effective global searches and faster convergence. Figure 1 visually encapsulates these dynamics, emphasizing SCA's adaptability and potential for solving complex optimization problems.

While the Sine Cosine Algorithm is a promising optimization approach, it faces limitations when dealing with highly nonlinear and unstructured problems. The reliance on absolute values in traditional SCA for position updates can lead to premature convergence, causing the algorithm to become trapped in local optima and fail to identify the global optimum. Additionally, the search path employed by the SCA needs to be more directed to guide the algorithm effectively toward the optimal solution. As problem dimensionality increases, the convergence speed of the SCA tends to decline, further limiting its effectiveness. Recent studies have highlighted the need for linear search paths and empirical parameter adjustments to enhance SCA performance in challenging scenarios [21].

https://doi.org/10.31436/iiumej.v26i1.3537

Research efforts to address these challenges have evolved along three primary directions: improving existing SCA techniques, developing entirely new algorithms, and hybridizing SCA with other optimization methods. SCA enhancement integrates stochastic and mathematical operators to improve convergence and search efficiency [22]. On the other hand, novel algorithms aim to introduce entirely new frameworks to overcome SCA's inherent limitations. Hybrid metaheuristic approaches, such as PSO-GA, PSO-ACO, and GA-DE, represent the most popular research avenue, combining SCA with other optimization techniques to balance exploration and exploitation effectively [23, 24]. By adopting linear search paths and empirically tuned parameters, researchers have proposed ways to improve the global search capabilities of SCA, resulting in more stable solutions and reduced risks of local optima trapping [25].

## 3. MODIFIED SINE COSINE ALGORITHM FOR POWER SYSTEM STATIC SECURITY ANALYSIS

The Modified Sine Cosine Algorithm (MSCA) represents a significant enhancement over the traditional Sin Cos Algorithm (SCA), aimed at improving efficiency and accuracy in identifying optimal solutions. In the context of static security analysis for power systems, particularly for N-1 contingency analysis, MSCA provides a robust framework for optimizing resource allocation and improving network stability. This algorithm addresses the limitations of the traditional SCA by integrating advanced mechanisms such as mutation, probabilistic selection, and more potent population-based strategies to overcome local optima trapping, a common challenge in SCA applications [26, 27].

The MSCA enhances the original SCA, as shown in Eq. (1), by replacing the scaling factor $r_1$ with a dynamic parameter $a$, which controls the amplitude. Additionally, the MCSCA introduces the $d$ parameter, which regulates the distance between candidate solutions and the global best position, adding an extra layer of adaptability to improve search efficiency. MSCA can be formulated as follows:

$$X_i^{t+1} = \begin{cases} X_i^t + a \cdot \sin(r_2) \cdot |r_3 \cdot P_i^t - X_i^t|, & if\ r_4 < 0.5 \\ X_i^t + a \cdot \cos(r_2) \cdot |r_3 \cdot P_i^t - X_i^t| & if\ r_4 \geq 0.5 \end{cases} \quad (3)$$

where $X_i^{t+1}$ is the new position of the solution, $a$ is a dynamic amplitude control parameter replacing $r_1$ in the original SCA, updated as

$$a = a_{max}\left(1 - \frac{t}{t_{max}}\right) \quad (4)$$

where $t$ is the current iteration $t_{max}$ is the maximum number of iterations, and $a_{max}$ is a predefined constant that depends on the problem domain and the desired balance between exploration and exploitation. In this paper, $a_{max}$ was set to 1 to provide more conservative exploration. The $d$ parameter is a distance regulation parameter integrated into $|r_3 \cdot P_i^t - X_i^t|$, modifying the search direction and step size. It can be expressed as:

$$d = |P_i^t - X_i^t| \cdot \left(1 - \frac{t}{t_{max}}\right) \quad (5)$$

This modification ensures that that $a$ decreases over iterations to prioritize local exploitation in later stages, while $d$ dynamically scales the search steps based on proximity to the global best position. Together, these parameters improve the algorithm's capability to explore the search space broadly during the initial stages and converge efficiently as the optimization progresses. The integration of $a$ and $d$ is further analyzed in Section 5.4, where

https://doi.org/10.31436/iiumej.v26i1.3537

their impact on the performance metrics, including Capture Ratio, Processing Time, and Search Scan Space Percentage, is evaluated. The three critical metrics will be discussed subsequently.

### 3.1. Capture Ratio

The capture ratio quantifies the algorithm's ability to identify optimal or near-optimal solutions across multiple iterations consistently. For MSCA, a high capture ratio signifies its effectiveness in converging to optimal solutions across diverse test functions. In the context of power system security, the capture ratio measures the algorithm's accuracy in identifying the most critical contingencies that could affect the system. This ratio is calculated using Eq. (6):

$$T_{cr} = \frac{k_p}{Q} \times 100 \tag{6}$$

where $T_{cr}$ is the capture ratio, $k_p$ is the number of the most severe contingencies captured in the top $p$ positions of the list and $Q$ is the total number of severe contingencies evaluated. A higher capture ratio indicates the algorithm's superior ability to rank contingencies accurately, ensuring the reliability of the contingency analysis framework.

### 3.2. Processing Time

Processing time measures the algorithm's total duration to complete the optimization process, from initialization to reaching an optimal solution or termination criteria. For MSCA, processing time is critical in assessing its suitability for real-time applications, particularly in scenarios requiring rapid analysis of contingencies. Efficient algorithms with shorter processing times are preferable for time-sensitive applications in power systems. In this study, the processing time of MSCA is compared against established methods such as Ant Colony Optimization (ACO) and Genetic Algorithms (GA) under identical conditions (number of iterations and computational resources).

### 3.3. Search Scan Space Percentage

Search Scan Space Percentage evaluates the extent of the search space the algorithm explores during optimization. This metric is crucial for understanding the balance between exploration (searching broadly across the solution space) and exploitation (focusing on refining the most promising areas). Search Scan Space Percentage is calculated using Eq. (7):

$$peb_i = \frac{qia_i}{C_k^r} \tag{7}$$

where $peb_i$ is the percentage of the search space explored at iteration $i$, $qia_i$ is the number of contingencies evaluated up to iteration $i$, and $C_k^r$ is the total possible combinations of contingencies. Lower Search Scan Space Percentage values indicate higher efficiency, as fewer power flow calculations are required to achieve the desired optimization level. MSCA leverages its enhanced exploration and exploitation mechanisms to minimize Search Scan Space Percentage, making it a more computationally efficient algorithm.

The MSCA provides clear advantages over traditional algorithms by addressing the key limitations of SCA. Its probabilistic selection and mutation strategies reduce the risk of premature convergence, ensuring a more thorough search space exploration. Its improved processing efficiency makes it suitable for real-time power system contingency analysis applications, where rapid and accurate decision-making is critical. Including advanced metrics such as Capture Ratio, Processing Time, and Search Scan Space Percentage ensures that the algorithm's performance can be rigorously assessed, demonstrating its potential to set new benchmarks in power system optimization. MSCA establishes itself as a reliable tool for static

https://doi.org/10.31436/iiumej.v26i1.3537

security analysis in modern power systems by offering a balanced trade-off between accuracy, efficiency, and robustness.

## 4. SECURITY INDEX ANALYSIS

The Security Index ($SI$) is a critical parameter used to quantify the impact of contingency scenarios on the overall performance of a power system. It provides a numerical representation of the severity of disruptions caused by the disconnection of transmission lines or other contingencies, enabling the prioritization of ranking for mitigation strategies. While $SI$ does not explicitly describe the type of violations or disturbances, it captures the magnitude of their impact on system performance. Higher $SI$ values correspond to more significant risks, indicating more severe contingencies. To calculate $SI$, contingencies are ranked based on performance indices, enabling practical risk assessment and prioritization.

This study leverages the MSCA to optimize the ranking of contingencies using $SI$, improving upon traditional approaches. After simulating the outage of specific lines, voltage performance indices are calculated using Matlab. These indices then rank the contingencies based on their respective $SI$ values. By integrating MSCA, a nature-inspired optimization algorithm, this research addresses limitations in traditional methods and compares the results against other nature-inspired algorithms. The enhanced optimization capabilities of MSCA ensure a more accurate and efficient ranking of critical contingencies, offering significant improvements in static security analysis for power systems.

The $SI$ used in this study is formulated to normalize and quantify upper and lower voltage and power flow limit violations. It is calculated using Eq. (8):

$$SI = \left[\sum_i \left(\frac{d_{v,i}^u}{g_{v,i}^u}\right)^{2n} + \sum_i \left(\frac{d_{v,i}^l}{g_{v,i}^l}\right)^{2n} + \sum_i \left(\frac{d_{p,j}}{g_{p,j}}\right)^{2n}\right]^{\frac{1}{2n}} \tag{8}$$

Here, $d_{v,i}^u$ and $d_{v,i}^l$ represent normalized upper and lower voltage limit violations beyond alarm thresholds while $d_{p,j}$ represents normalized power flow limit violations. Normalization factors ($g_{v,i}^u$, $g_{v,i}^l$, and $g_{p,j}$) ensure that the $SI$ values are dimensionless and comparable across different contingencies.

The normalized voltage limit violations are calculated as follows:

$$d_{v,i}^u = \begin{cases} \frac{V_i - F_i^u}{V_i^d}, & if\ V_i > F_i^u \\ 0, & if\ V_i \le F_i^u \end{cases} \tag{9}$$

$$d_{v,i}^l = \begin{cases} \frac{F_i^l - V_i}{V_i^d}, & if\ V_i < F_i^l \\ 0, & if\ V_i \ge F_i^l \end{cases} \tag{10}$$

where $V_i$ is the voltage magnitude at a bus, $F_i^u, F_i^l$ is the upper and lower alarm limits, and $V_i^d$ is the desired bus voltage. The corresponding normalization factors for voltage are given as:

$$g_{v,i}^u = \frac{V_i - F_i^u}{V_i^d},\ g_{v,i}^l = \frac{F_i^l - V_i}{V_i^d} \tag{11}$$

Power flow limit violations are calculated using:

https://doi.org/10.31436/iiumej.v26i1.3537

$$d_{p,j} = \begin{cases} \frac{|P_j| - P_{F_j}}{Base\ MVA}, & if\ |P_j| > P_{F_j} \\ 0, & if\ |P_j| \leq P_{F_j} \end{cases} \quad (12)$$

$$g_{pj} = \frac{P_{P_j} - P_{F_j}}{Based\ MVA} \quad (13)$$

where $P_j$ is the actual power flow, $P_{F_j}$ is the alarm limit for power flow, and $Base\ MVA$ is the base power for normalization.

By incorporating these detailed normalization factors, the Security Index accounts for voltage and power flow violations in a dimensionless and comparable manner. It ensures consistency and reliability in ranking contingencies. Using MSCA, this study optimizes the process of ranking these contingencies, improving computational efficiency and accuracy. MSCA's ability to avoid local optima and explore the solution space thoroughly ensures that critical contingencies with the highest SI values are identified accurately. This approach not only enhances the reliability of the power system but also enables real-time decision-making, making MSCA a valuable tool for static security analysis.

## 5. RESULTS AND DISCUSSION

This section presents the proposed Modified Sin Cos Algorithm (MSCA) results and analysis for contingency ranking in the IEEE 30-bus power system. The experimental setup, including the dataset, software, and hardware, is detailed to ensure reproducibility. Comparative simulations using manual contingency ranking, Ant Colony Optimization (ACO), and the original Sin Cos Algorithm (SCA) are conducted to evaluate the performance of MSCA. Key metrics such as capture ratio, search space scan percentage, and processing time are analyzed to assess the effectiveness and efficiency of each method. A benchmarking analysis highlights the advantages of MSCA against state-of-the-art algorithms, providing insights into its potential for real-world applications.

### 5.1. Simulation Setup

The IEEE 30-bus system, depicted in Figure 2, serves as the dataset for this study. It is a standard benchmark for power system analysis and contingency ranking, consisting of 30 buses, 41 lines, and detailed data for transmission lines, generation, and loads. The system includes:

- *One slack bus* is located at bus 1.
- *Five generator buses* are located at buses 2, 5, 8, 11, and 13.
- *Twenty-four load buses* represent the demand points across the network.

The network's connectivity is illustrated in Figure 2, where the red numbers represent the line indices, and the black numbers represent the bus indices. This structure captures the operational complexity of modern power grids, making it ideal for evaluating contingency ranking methods such as manual ranking, ACO, SCA, and the proposed MSCA.

The experiments were conducted using MATPOWER within the Matlab/Octave environment [28], a reliable tool known for its robustness and accuracy in solving power system optimization problems, particularly for $N-1$ contingency analysis. The computational hardware used was a Dell Inspiron 15 Laptop equipped with a 12th Gen Intel Core i5-1235U processor for efficient computation, 16 GB DDR4 RAM to handle memory-intensive

https://doi.org/10.31436/iiumej.v26i1.3537

simulations, and a 512 GB SSD for fast data access and storage. This combination of hardware and software ensured the smooth execution of simulations, enabling a comprehensive analysis of the IEEE 30-bus system and an accurate evaluation of the performance of the optimization algorithms tested.

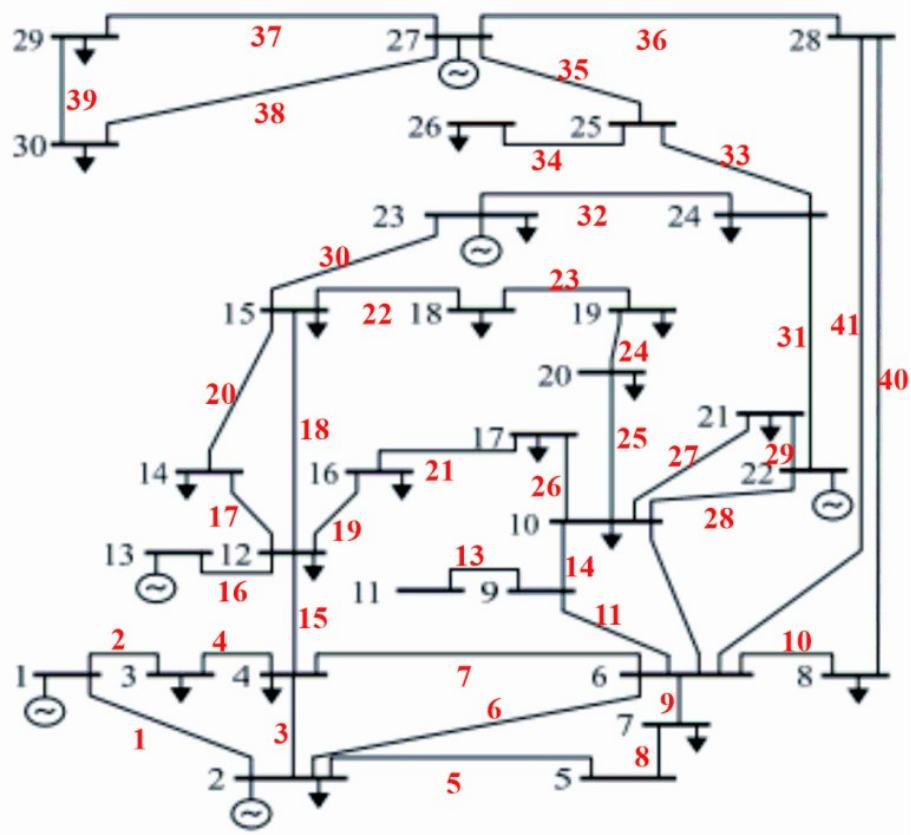


Figure 2. Line Diagram of IEEE 30-Bus System

The experimental setup involves simulating N-1 contingency scenarios on the IEEE 30-bus power system to compare the performance of three methods: manual ranking, Ant Colony Optimization (ACO), and the Sin Cos Algorithm (SCA). These simulations aim to evaluate the effectiveness of the proposed Modified Sin Cos Algorithm (MSCA). The IEEE 30-bus system, a widely used benchmark model, consists of 30 buses, 41 transmission lines, 5 generator buses, and 24 load buses. Manual ranking calculates the voltage performance index for each transmission line for each scenario sequentially using MATPOWER. At the same time, ACO and SCA automate the ranking process with various parameters, such as population size, iterations, and algorithm-specific variables (e.g., Alpha and Beta for ACO; $a$ and $d$ for SCA). Each method's performance is analyzed using three key metrics: capture ratio, processing time, and search space scan percentage.

This simulation scenario provides a comprehensive framework for analyzing contingency ranking methods. The study addresses real-world operational challenges using the IEEE 30-bus system and N-1 contingencies, ensuring practical relevance. Comparing manual and automated methods (ACO and SCA) highlights the benefits of optimization techniques in improving efficiency and accuracy. Additionally, the scenario allows for the benchmarking of MSCA against established methods, validating its capability as a superior tool for contingency analysis in power systems. These results demonstrate the potential of MSCA to enhance contingency ranking with better computational efficiency and accuracy, making it an effective solution for modern power systems.

https://doi.org/10.31436/iiumej.v26i1.3537

### 5.2. Manual Contingency Ranking As Simulation Baseline

Manual contingency ranking was conducted by disconnecting individual transmission lines in the IEEE 30-bus system ($N-1$ contingency analysis). Each line was removed one by one, starting from the first to the last, and the voltage performance index for each scenario was calculated using MATPOWER in the Matlab/Octave software environment. The results were then ranked in descending order, from the highest to the lowest voltage performance index, to identify the most critical contingencies. The transmission line associated with the highest performance index represents the most severe contingency scenario. The results of this manual ranking process are presented in Table 1.

Table 1. Manual Contingency Ranking Results for IEEE 30-Bus System

| Ranking | Line Number | From Bus | To Bus | Security Index |
|---|---|---|---|---|
| 1 | 36 | 28 | 27 | 56.5915 |
| 2 | 37 | 27 | 29 | 56.5443 |
| 3 | 38 | 27 | 30 | 56.5441 |
| 4 | 34 | 25 | 26 | 56.5434 |
| 5 | 9 | 6 | 7 | 56.5430 |
| 6 | 33 | 24 | 25 | 56.5416 |
| 7 | 39 | 29 | 30 | 56.5411 |
| 8 | 11 | 6 | 9 | 56.5409 |
| 9 | 29 | 21 | 22 | 56.5407 |
| 10 | 32 | 23 | 24 | 56.5407 |
| 11 | 10 | 6 | 8 | 56.5405 |
| 12 | 20 | 14 | 15 | 56.5405 |
| 13 | 23 | 18 | 19 | 56.5404 |
| 14 | 31 | 22 | 24 | 56.5404 |
| 15 | 21 | 16 | 17 | 56.5402 |
| 16 | 8 | 5 | 7 | 56.5399 |
| 17 | 41 | 6 | 28 | 56.5399 |
| 18 | 4 | 3 | 4 | 56.5398 |
| 19 | 24 | 19 | 20 | 56.5398 |
| 20 | 40 | 8 | 28 | 56.5398 |
| 21 | 28 | 10 | 22 | 56.5395 |
| 22 | 26 | 10 | 17 | 56.5394 |
| 23 | 30 | 15 | 23 | 56.5393 |
| 24 | 35 | 25 | 27 | 56.5392 |
| 25 | 12 | 6 | 10 | 56.5391 |
| 26 | 22 | 15 | 18 | 56.5387 |
| 27 | 25 | 10 | 20 | 56.5378 |
| 28 | 7 | 4 | 6 | 56.5374 |
| 29 | 17 | 12 | 14 | 56.5374 |
| 30 | 27 | 10 | 21 | 56.5374 |
| 31 | 19 | 12 | 16 | 56.5371 |
| 32 | 3 | 2 | 4 | 56.5369 |
| 33 | 5 | 2 | 5 | 56.5365 |
| 34 | 6 | 2 | 6 | 56.5365 |
| 35 | 2 | 1 | 3 | 56.5361 |
| 36 | 15 | 4 | 12 | 56.5330 |
| 37 | 18 | 12 | 15 | 56.5325 |
| 38 | 1 | 1 | 2 | 56.5309 |
| 39 | 13 | 9 | 11 | 56.5309 |
| 40 | 16 | 12 | 13 | 56.5308 |
| 41 | 14 | 9 | 10 | 56.5300 |

https://doi.org/10.31436/iiumej.v26i1.3537

Table 1 indicates that the most critical contingency occurs on line 36, which connects bus 28 to bus 27. Its security index of 56.5915 earns it the top ranking. On the other hand, the least critical contingency occurs on line 14, which connects bus 9 to bus 10, with the lowest voltage performance index of 56.53. These rankings provide a clear picture of the relative severity of each contingency scenario within the IEEE 30-bus system.

The manual ranking results also serve as a baseline for comparing the performance of optimization methods used for contingency ranking. The primary focus of this study is to evaluate the effectiveness of different optimization methods, such as Ant Colony Optimization (ACO) and the Modified Sin Cos Algorithm (MSCA), in identifying the top 20 most critical contingencies. For simplicity, the top 20 rankings in Table 1, highlighted in grey, represent the actual severity levels of the contingencies. These rankings are used as a reference for validating the accuracy of the capture ratio calculated by the optimization algorithms. This process ensures that the proposed methods are rigorously evaluated against a reliable benchmark.

### 5.3. Contingency Ranking Simulation Using the Ant Colony Optimization Method

The Ant Colony Optimization (ACO) method was applied to the IEEE 30-bus system to evaluate its performance in contingency ranking. ACO relies on ants' probabilistic selection of solutions (paths) based on pheromone trails and heuristic factors. During the iterative process, pheromones are updated to reflect the quality of the solutions, guiding ants toward better paths over time. Key parameters influencing ACO's performance include Alpha (pheromone influence), Beta (heuristic influence), population size (number of ants), and the number of iterations. This study conducted ACO simulations 50 times for each parameter variation, and the average capture ratio was calculated as the primary performance metric.

#### *5.3.1. Ranking Based on Alpha and Beta Variations*

The justification for testing the performance of ACO by simultaneously varying both Alpha and Beta lies in the fundamental role these parameters play in balancing exploration and exploitation during the search process. Alpha determines the influence of pheromone trails, guiding ants based on the solutions discovered in prior iterations. At the same time, Beta controls the weight given to heuristic factors, encouraging ants to explore promising solutions based on their immediate value. Simultaneous variation of these parameters enables a comprehensive assessment of how their interplay affects the algorithm's ability to discover high-quality solutions effectively.

Using 41 ants ensures a diverse population of solution candidates, which promotes broad exploration of the search space and reduces the likelihood of premature convergence to local optima. Similarly, setting the number of iterations to 82 allows the algorithm to refine its exploration and exploitation balance over multiple cycles, giving it sufficient opportunity to converge toward optimal solutions. This configuration evaluates the algorithm's robustness across various parameter settings, ensuring the findings are generalizable and informative for real-world applications.

The results in Table 2 demonstrate that the ACO algorithm achieves its best capture ratio of 98.80% when both Alpha and Beta are set to 2. It indicates that at moderate values, the balance between pheromone influence (Alpha) and heuristic influence (Beta) is optimized, enabling the ants to explore the solution space effectively while focusing on promising areas. This balanced interplay ensures that pheromone trails guide the algorithm efficiently without overemphasizing the influence of heuristic factors. Such a result underscores the importance of carefully tuning these parameters to achieve optimal performance in contingency ranking.

https://doi.org/10.31436/iiumej.v26i1.3537

Table 2. Processing Time, Search Space Scan Percentage, and Capture Ratio for ACO with Simultaneous Alpha and Beta Variations

| Alpha and Beta | Processing Time (seconds) | Search Space Scan Percentage (%) | Capture Ratio (%) |
|---|---|---|---|
| 1 | 100.23 | $1.25 \times 10^{-6}$ | 87.30 |
| **2** | **101.00** | **$1.25 \times 10^{-6}$** | **98.80** |
| 3 | 109.02 | $1.25 \times 10^{-6}$ | 93.43 |
| 4 | 111.32 | $1.25 \times 10^{-6}$ | 92.56 |
| 5 | 113.42 | $1.25 \times 10^{-6}$ | 93.30 |

As Alpha and Beta values increase beyond 2, the capture ratio declines. For instance, at Alpha and Beta set to 3, the capture ratio decreases to 93.43%, and further reductions are observed at values of 4 and 5, where the capture ratios are 92.56% and 93.30%, respectively. These declines suggest that excessive pheromone and heuristic influence can disrupt the balance between exploration and exploitation. When both factors are overemphasized, the algorithm may focus too narrowly on certain paths, leading to premature convergence on suboptimal solutions and an inability to explore new, potentially better solutions in the search space.

The processing time exhibits a linear increase as Alpha and Beta values rise. Starting at 100.23 seconds for Alpha and Beta set to 1, the processing time grows to 113.42 seconds when these parameters are set to 5. This increase in computational cost reflects the additional effort required for the ants to process pheromone trails and heuristic factors under high Alpha and Beta settings. Notably, the marginal increase in capture ratio from 93.43% to 93.30% (Alpha and Beta values of 3 to 5) does not justify the significantly higher processing time. It highlights the trade-off between accuracy and efficiency, where over-tuning parameters leads to diminishing returns in performance at the cost of greater computational resources.

Interestingly, the search space scan percentage remains constant at $1.25 \times 10^{-6}$ % across all Alpha and Beta variations. This consistency suggests that the algorithm explores a fixed proportion of the solution space regardless of parameter changes. While this uniformity ensures that a comparable scope of the search space is analyzed, it also highlights a limitation in ACO's adaptability, where the extent of exploration is not directly influenced by Alpha and Beta variations. It may contribute to the decline in capture ratio at higher parameter values, as the algorithm becomes less capable of compensating for over-concentration on specific areas of the search space.

Table 2 highlights the critical importance of parameter tuning in ACO. The optimal balance achieved at Alpha and Beta values of 2 demonstrates the algorithm's ability to navigate the trade-offs between exploration and exploitation effectively. However, the decline in capture ratio at higher parameter values underscores the risk of overemphasizing pheromones or heuristic factors, limiting the algorithm's ability to generalize effectively. Additionally, the linear increase in processing time at higher parameter values reveals the computational cost of over-tuning, emphasizing the need for careful consideration of efficiency in real-time applications. Finally, the static search space scan percentage indicates that while ACO maintains consistent exploration across the solution space, its adaptability could be improved to better respond to parameter variations.

### *5.3.2. Ranking with One Parameter Constant*

This section evaluates the performance of the ACO algorithm by varying one parameter—either Alpha or Beta—while keeping the other constant at 1. Alpha represents the influence of

https://doi.org/10.31436/iiumej.v26i1.3537

pheromones in guiding the ants toward promising solutions, while Beta represents the influence of heuristic factors in the decision-making process. The experiments utilized 41 ants and 82 iterations to ensure sufficient exploration and exploitation of the search space. The results, shown in Table 3, provide insights into how Alpha and Beta individually affect the algorithm's performance metrics: processing time, search space scan percentage, and capture ratio.

Table 3. Processing Time, Search Space Scan Percentage, and Capture Ratio for ACO with One Parameter Constant

| Alpha | Beta | Processing Time (seconds) | Search Space Scan Percentage (%) | Capture Ratio (%) |
|---|---|---|---|---|
| 1 | 1 | 109.30 | $1.25 \times 10^{-6}$ | 87.30 |
| **2** | **1** | **110.40** | **$1.25 \times 10^{-6}$** | **95.50** |
| 3 | 1 | 111.10 | $1.25 \times 10^{-6}$ | 94.46 |
| 4 | 1 | 111.98 | $1.25 \times 10^{-6}$ | 94.32 |
| 5 | 1 | 112.50 | $1.25 \times 10^{-6}$ | 95.40 |
| 1 | 2 | 110.39 | $1.25 \times 10^{-6}$ | 90.30 |
| 1 | 3 | 111.12 | $1.25 \times 10^{-6}$ | 89.40 |
| 1 | 4 | 111.94 | $1.25 \times 10^{-6}$ | 90.12 |
| 1 | 5 | 112.52 | $1.25 \times 10^{-6}$ | 91.20 |

When Alpha was varied while Beta was kept constant at 1, the capture ratio improved as Alpha increased, reaching a peak of 95.5% at Alpha = 2. Beyond this value, the capture ratio exhibited slight fluctuations, indicating diminishing returns. Similarly, when Beta was varied while Alpha was kept constant at 1, the highest capture ratio of 91.2% occurred at Beta = 5. It suggests that both pheromones and heuristic factors are critical in guiding the algorithm, but their contributions reach an optimal balance when Alpha and Beta are moderately increased. The values of Alpha ($\alpha$) and Beta ($\beta$) influence the ACO algorithm's balance between pheromone intensity and heuristic factors. A high Alpha value makes the ants overly reliant on pheromone trails, which can lead to premature convergence in local optima. Conversely, a high Beta value causes the ants to focus excessively on heuristic factors, neglecting pheromone trails. These extremes disrupt the balance necessary for effective exploration and exploitation, limiting the algorithm's ability to find optimal solutions. This behavior is evident in the results, where moderate increases in Alpha and Beta produce the best performance metrics.

The processing time for each scenario increased with larger Alpha or Beta values. It can be attributed to the additional computational effort required to process larger pheromone trails or more detailed heuristic evaluations. For example, the processing time rose from 109.3 seconds at Alpha = 1 to 112.5 seconds at Alpha = 5. A similar trend was observed when the Beta was varied. These findings highlight a trade-off between accuracy (capture ratio) and computational efficiency (processing time), emphasizing the need for careful parameter tuning in real-world applications where computational resources are limited.

The search space scan percentage remained constant across all tested Alpha and Beta values, demonstrating that the algorithm maintained a consistent level of exploration in the solution space. This consistency suggests that variations in Alpha and Beta primarily affect how ants prioritize pheromone trails and heuristic factors rather than the overall breadth of the search. However, the diminishing improvements in capture ratio at higher parameter values indicate that the algorithm may overemphasize one factor while underutilizing the other, leading to inefficiencies in solution refinement.

https://doi.org/10.31436/iiumej.v26i1.3537

Critically, these results underline the importance of balancing pheromone and heuristic influences in ACO. When Alpha or Beta values are set too high, the algorithm risks overfitting to certain paths, potentially converging prematurely on suboptimal solutions. Conversely, when these parameters are too low, the algorithm may fail to exploit high-quality solutions effectively, leading to lower capture ratios. Therefore, the optimal settings for Alpha and Beta—identified here as 2—strike a balance between exploration and exploitation, ensuring robust and efficient contingency ranking.

The experiments demonstrate that ACO's performance is highly sensitive to the balance between Alpha and Beta. While both parameters independently contribute to the algorithm's effectiveness, their interplay determines the overall quality of the solutions. The findings emphasize the need for adaptive parameter tuning for optimal performance in dynamic and resource-constrained environments, such as real-time power system contingency ranking. In subsequent analyses, these results provide a strong foundation for comparing ACO to alternative algorithms, such as the MSCA.

### *5.3.3. Ranking with Iteration and Population Variations*

The third experiment investigates the performance of the ACO algorithm by varying the population size (number of ants) and the number of iterations. These parameters significantly impact the algorithm's ability to explore the solution space and converge to optimal solutions. The experiments were conducted with Alpha and Beta fixed at 2, as these values provided the best balance of pheromone and heuristic influence in prior tests. The results, summarized in Tables 4 and 5, demonstrate the interplay between population size, iterations, processing time, search space scan percentage, and capture ratio.

Table 4. Processing Time, Search Space Scan Percentage, and Capture Ratio for ACO with Varying Population Sizes at 100 Iterations

| Alpha and Beta | Population Size | Processing Time (seconds) | Search Space Scan Percentage (%) | Capture Ratio (%) |
|---|---|---|---|---|
| 2 | 5 | 16.38 | $1.867 \times 10^{-7}$ | 83.4 |
| 2 | 10 | 37.78 | $3.72 \times 10^{-7}$ | 87.4 |
| 2 | 20 | 59.19 | $7.43 \times 10^{-7}$ | 89.2 |
| **2** | **40** | **80.60** | $\mathbf{1.49 \times 10^{-6}}$ | **92.3** |
| 2 | 80 | 102.00 | $2.97 \times 10^{-6}$ | 91.9 |

As shown in Table 4, when the number of ants (population size) was increased from 5 to 80 while keeping the number of iterations constant at 100, the capture ratio improved significantly, reaching a maximum of 92.3% at a population size of 40. Beyond this value, the capture ratio slightly declined to 91.9% at a population size of 80. It indicates an optimal population size exists, where the algorithm balances sufficient exploration and efficient pheromone reinforcement. However, larger populations require more pheromone updates and solution evaluations, leading to a proportional increase in processing time, which rose from 16.38 seconds at a population size of 5 to 102 seconds at 80 ants. This trade-off highlights the need to carefully tune the population size for efficient operation in time-sensitive applications.

As shown in Table 4, when the number of ants (population size) was increased from 5 to 80 while keeping the number of iterations constant at 100, the capture ratio improved significantly, reaching a maximum of 92.3% at a population size of 40. Beyond this value, the capture ratio slightly declined to 91.9% at a population size of 80. It indicates an optimal population size exists, where the algorithm balances sufficient exploration and efficient

https://doi.org/10.31436/iiumej.v26i1.3537

pheromone reinforcement. However, larger populations require more pheromone updates and solution evaluations, leading to a proportional increase in processing time, which rose from 16.38 seconds at a population size of 5 to 102 seconds at 80 ants. This trade-off highlights the need to carefully tune the population size for efficient operation in time-sensitive applications.

Table 5. Processing Time, Search Space Scan Percentage, and Capture Ratio for ACO with Varying Iterations at 10 Population Size

| Alpha | Iterations | Processing Time (seconds) | Search Space Scan Percentage (%) | Capture Ratio (%) |
|---|---|---|---|---|
| 2 | 10 | 3.34 | $13.72 \times 10^{-8}$ | 60.40 |
| 2 | 40 | 12.00 | $22.30 \times 10^{-8}$ | 65.83 |
| 2 | 70 | 20.67 | $30.80 \times 10^{-8}$ | 82.60 |
| **2** | **100** | **29.30** | **$3.940 \times 10^{-7}$** | **89.90** |
| 2 | 130 | 38.00 | $4.80 \times 10^{-7}$ | 89.80 |

For iterations, the results showed that increasing the number from 10 to 130 while keeping the population size constant at 10 led to a steady improvement in the capture ratio, peaking at 89.9% at 100 iterations. Beyond this point, the capture ratio plateaued, indicating diminishing returns with further increases in iterations. Processing time increased proportionally with iterations, rising from 3.34 seconds at 10 to 38 seconds at 130 iterations. Similarly, the search space scan percentage grew consistently, reflecting the algorithm's broader solution space exploration. These findings suggest that increasing iterations enhances solution quality up to a certain point, beyond which additional computational effort yields minimal benefits.

The experiments highlight a critical trade-off between population size and iterations. Larger populations improve the algorithm's ability to explore diverse regions of the solution space in parallel but at the cost of increased processing time. On the other hand, more iterations allow the ants to refine their solutions and converge to better optima, but the incremental improvements diminish as the solution space becomes saturated. Balancing these two parameters is essential to achieve high capture ratios without excessive computational overhead.

The search space scan percentage provides valuable insights into the algorithm's exploration efficiency. When either population size or iterations increased, the search space scan percentage rose significantly, indicating thorough coverage of potential solutions. For instance, at 100 iterations with a population size of 10, the scan percentage reached $3.94 \times 10^{-7}$%. However, this exhaustive exploration also increases computational demands. The challenge lies in ensuring that the algorithm explores the search space sufficiently to avoid local optima while maintaining computational efficiency. The diminishing improvements in capture ratio at higher parameter values suggest that the algorithm reached an effective saturation point, beyond which additional exploration yielded negligible gains.

The results underscore the importance of parameter tuning in ACO. For real-time applications, such as contingency ranking in power systems, selecting the optimal combination of population size and iterations is crucial. While higher values improve solution quality, the associated increase in processing time may render the algorithm unsuitable for time-sensitive tasks. This study's population size of 40 and 100 iterations emerged as a practical balance, achieving a high capture ratio of 92.3% with reasonable computational effort. These findings establish a solid benchmark for evaluating alternative optimization methods in contingency ranking scenarios, such as the Modified Sin Cos Algorithm (MSCA).

https://doi.org/10.31436/iiumej.v26i1.3537

### 5.4. Contingency Ranking Simulation Using Modified Sine Cosine Algorithm

The Modified Sine Cosine Algorithm (MSCA) was employed to simulate contingency ranking in the IEEE 30-bus system, focusing on its effectiveness under varying parameter configurations. MSCA builds upon the Sine Cosine Algorithm (SCA) by leveraging sinusoidal functions to explore and exploit the solution space. Key parameters influencing the algorithm's performance include $a$ and $d$ (amplitude and distance control parameters), population size, and the number of iterations. Each configuration was tested 50 times, and the most frequently observed capture ratio in the iterations was selected for evaluation.

Optimization algorithms like MSCA aim to strike a balance between exploration, which involves searching broadly across the solution space, and exploitation, which refines solutions around promising areas. The sinusoidal functions in MSCA enable this balance, but their efficiency depends significantly on the values of $a$ (denoted as $r_1$) and $d$ (denoted as $r_3$). Selecting appropriate parameter values ensures the algorithm's robustness, minimizing the risk of premature convergence or suboptimal performance.

The parameter $a$ regulates the amplitude of sinusoidal movements in the solution space. Higher values of $a$ increase the range of individual position changes during iterations, enhancing the algorithm's exploratory capacity. However, excessively high values of $a$ can introduce randomness, causing the population to drift away from optimal solutions. It underscores the necessity of carefully tuning $a$ to balance broad exploration with precise exploitation. Optimal values allow the algorithm to explore widely without losing focus on high-quality solutions, which is crucial in complex systems like the IEEE 30-bus power grid.

Similarly, $d$ affects the distance individuals move relative to the current best position during iterations. Higher values encourage broader exploration but may also lead to instability, with individuals deviating significantly from optimal regions. Conversely, excessively low values of $d$ can result in limited exploration, trapping the algorithm in local optima. It highlights the importance of tuning $d$ to achieve a dynamic balance between moving towards global optima and thoroughly exploring the search space.

By varying $a$ and $d$ systematically, the MSCA can adapt its search behavior to the complexities of contingency ranking in power systems. Properly calibrated, the algorithm comprehensively explores potential contingencies while focusing computational resources on the most critical scenarios. MSCA is particularly suited for optimizing large-scale, nonlinear systems like power grids, where balancing exploration and exploitation is essential for accurate and efficient contingency ranking.

#### *5.4.1. Ranking with MSCA by Varying the Amplitude and Distance Control Parameters*

The MSCA was evaluated under varying configurations of the amplitude control parameter ($a$) and the distance control parameter ($d$). These parameters are critical in determining the algorithm's ability to balance exploration and exploitation of the solution space. A total of 50 trials were conducted for each parameter variation, with the most frequently observed capture ratio used as the primary evaluation metric. The population size was set to 250, and the number of iterations was fixed at 500 to allow sufficient search space exploration. The results are summarized in Table 6, highlighting the interplay between parameter values and the algorithm's performance metrics, including processing time, search space scan percentage, and capture ratio.

https://doi.org/10.31436/iiumej.v26i1.3537

Table 6. Processing Time, Search Space Scan Percentage, and Capture Ratio for MSCA for Variations in $a$ and $d$

| $a$ | $d$ | Processing Time (seconds) | Search Space Scan Percentage (%) | Capture Ratio (%) | Number of Identified Lines |
|---|---|---|---|---|---|
| 1 | 0.1 | 18.06 | 0.0028736 | 93.3 | 28 |
| 2 | 0.1 | 17.82 | 100.0 | 100.0 | 30 |
| 3 | 0.1 | 17.95 | 100.0 | 100.0 | 30 |
| 4 | 0.1 | 17.89 | 0.0028736 | 93.3 | 28 |
| 5 | 0.1 | 18.65 | 100.0 | 100.0 | 30 |
| 1 | 0.2 | 18.18 | 100.0 | 100.0 | 30 |
| 1 | 0.3 | 18.12 | 100.0 | 100.0 | 30 |
| 1 | 0.4 | 18.67 | 100.0 | 100.0 | 30 |
| 1 | 0.5 | 18.67 | 100.0 | 100.0 | 30 |

The amplitude parameter ($a$) influences the scale of sinusoidal movements in the algorithm, directly impacting its exploratory capabilities. Higher values of $a$ enable broader exploration by allowing larger positional changes during iterations, reducing the risk of getting trapped in local optima. However, excessively high values can result in random movements, inefficiently exploiting promising areas in the search space. The results in Table 6 demonstrate that when $a = 2,3,5$, the algorithm achieved a 100% capture ratio and search space scan percentage, indicating that these values provide an optimal balance for contingency ranking tasks.

The distance control parameter ($d$) regulates the magnitude of individual movements relative to the best-known solution, thereby influencing local exploitation. Smaller $d$ values focus the search on refining solutions within a narrow region, while larger values promote more exploratory movements. The results indicate that values of $d = 0.1$ consistently achieved 100% search space coverage for $a = 2,3,5$, demonstrating the parameter's effectiveness in balancing localized refinement with broader exploration. In contrast, when $d = 0.1$ for $a = 1$, the search space scan percentage dropped significantly to 0.0028%, highlighting the algorithm's sensitivity to suboptimal parameter combinations.

Interestingly, despite achieving 100% capture ratio and search space coverage in several configurations, the algorithm exhibited stable processing times between 17.8 and 18.6 seconds. This consistency indicates that MSCA can efficiently explore the solution space without incurring excessive computational overhead, even when varying the amplitude and distance control parameters. However, low search space coverage was observed for specific configurations (e.g., $a = 1, d = 0.1$), suggesting that suboptimal parameter tuning may lead to reduced algorithmic efficiency and potentially overlooked solutions.

A notable difference between MSCA and previously tested algorithms, such as Ant Colony Optimization (ACO), lies in the comprehensive search space coverage achieved by MSCA. While ACO exhibited extremely low search space percentages in earlier tests, MSCA consistently covered the complete solution space under optimal configurations. It underscores the robustness of the sinusoidal-based exploration mechanisms in MSCA, which allow it to effectively navigate complex, nonlinear solution spaces such as those encountered in power system contingency ranking.

The experiments highlight the importance of carefully tuning the amplitude ($a$) and distance control ($d$) parameters to optimize MSCA's performance. The findings demonstrate that MSCA can identify all critical contingencies in the IEEE 30-bus system while maintaining efficient computational performance. By achieving a 100% capture ratio and search space scan

percentage in several configurations, MSCA establishes itself as a reliable tool for contingency ranking. Future work could explore adaptive parameter tuning to adjust dynamically $a$ and $d$ during execution, further enhancing MSCA's robustness and applicability across diverse optimization problems.

### *5.4.2. Ranking with MSCA by Varying the Number of Iterations and Population Size*

This section evaluates the performance of the MSCA by systematically varying the number of iterations and population size. These parameters are critical in determining the algorithm's ability to balance computational efficiency with optimization accuracy. Iterations define the number of updates made during the search process, while population size represents the number of candidate solutions explored simultaneously. The experiments used fixed parameter values of $a = 1$ and $d = 0.1$ to isolate the impact of iterations and population size. The results are summarized in Tables 7 and 8.

Table 7. Processing Time, Search Space Scan Percentage, and Capture Ratio for MSCA for Variations in Population Size at 250 Iterations.

| Population Size | Processing Time (seconds) | Search Space Scan Percentage (%) | Capture Ratio (%) | Number of Identified Lines |
|---|---|---|---|---|
| 50 | 1.82 | $2.87\times10^{-8}$ | 93.33 | 28 |
| 100 | 3.70 | $8.33\times10^{-7}$ | 96.67 | 29 |
| 150 | 5.53 | $1.25\times10^{-6}$ | 96.67 | 28 |
| 200 | 7.37 | 100.00 | 100.00 | 30 |
| 250 | 8.98 | 1.47 | 93.33 | 28 |

Table 7 demonstrates a clear trend where increasing population size improves the capture ratio and search space coverage but at the expense of processing time. For a fixed number of iterations (250), the capture ratio increased from 93.33% with a population size of 50 to 100% with a population size of 200. It indicates that larger populations enhance the algorithm's ability to explore diverse areas of the search space and identify critical contingencies accurately. However, processing time increased proportionally with population size, reflecting the higher computational demands of managing and evaluating a larger number of candidate solutions.

Table 8. Processing Time, Search Space Scan Percentage, and Capture Ratio for MSCA for Variations in Iterations at 500 Population Size.

| Iterations | Processing Time (seconds) | Search Space Scan Percentage (%) | Capture Ratio (%) | Number of Identified Lines |
|---|---|---|---|---|
| 25 | 2.20 | $8.77\times10^{-7}$ | 83.33 | 25 |
| 50 | 8.85 | $8.33\times10^{-7}$ | 96.67 | 29 |
| 100 | 7.98 | 100 | 100 | 30 |
| 250 | 20.61 | 100 | 100 | 30 |

Table 8 highlights the impact of varying the number of iterations while keeping the population size constant at 500. As the number of iterations increased, the capture ratio and search space coverage improved, reaching 100% with 100 or more iterations. This result underscores the importance of sufficient iterations to refine the search process and identify all critical contingencies. However, the processing time increased significantly, particularly for 250 iterations, indicating the trade-off between optimization accuracy and computational efficiency.

https://doi.org/10.31436/iiumej.v26i1.3537

The findings reveal that population size and iterations contribute significantly to MSCA's performance, but their effects differ. Larger populations enhance diversity and prevent premature convergence, while more iterations allow deeper exploration and refinement of candidate solutions. Notably, the configuration with 500 iterations and a population size of 200 achieved a 100% capture ratio and search space coverage with a processing time of 20.61 seconds, representing an optimal balance for this dataset.

MSCA demonstrates superior adaptability and robustness in balancing exploration and exploitation compared to other algorithms, such as ACO. When carefully tuned parameters, the results show that MSCA can achieve comprehensive search space coverage with fewer computational resources. The ability to scale performance with increasing population size and iterations highlights its potential for handling complex optimization problems in power systems.

The study confirms that fine-tuning population size and iterations are essential for optimizing MSCA's performance in real-world applications. The trade-offs observed between computational efficiency and optimization accuracy suggest that parameter selection should be guided by the problem's specific requirements, such as the search space size and the criticality of timely results. Future work could explore adaptive parameter adjustment strategies to dynamically balance these trade-offs, further enhancing MSCA's applicability in contingency ranking tasks.

### 5.5. Comparative Analysis

Contingency ranking is a critical component of power system reliability analysis, requiring algorithms that can efficiently prioritize system vulnerabilities during N-1 contingency scenarios. Nature-inspired algorithms like Ant Colony Optimization (ACO) and Modified Sine Cosine Algorithm (MSCA) have addressed this complex optimization task. ACO leverages pheromone-based heuristics to guide its search process, while MSCA employs sinusoidal dynamics with added modifications to balance exploration and exploitation. Table 9 compares these algorithms, focusing on key metrics: processing time, search space scan percentage, and capture ratio.

Table 9. Comparison of Nature-Inspired Algorithms for Contingency Ranking.

| Algorithm Type | Simulation Parameters | Processing Time (seconds) | Search Space Scan Percentage (%) | Capture Ratio (%) |
|---|---|---|---|---|
| ACO | Iterations = 82, Population = 41, Alpha = 2, Beta = 2 | 101.00 | $1.25 \times 10^{-6}$ | 98.8 |
| MSCA | Iterations = 250, Population = 100, $a = 1$, $d = 0.1$ | 3.70 | $8.33 \times 10^{-7}$ | 96.7 |

The metrics in Table 9 are carefully selected to capture the performance characteristics of the algorithms. Processing Time measures computational efficiency, a crucial factor for real-time applications. At the same time, the Search Space Scan Percentage quantifies the extent of solution space exploration, reflecting the algorithm's robustness against local optima. Capture Ratio assesses the accuracy of identifying high-impact contingencies, showcasing the algorithm's effectiveness in prioritization. These metrics comprehensively evaluate each algorithm's strengths and limitations, enabling informed decisions on their application in power system optimization tasks.

https://doi.org/10.31436/iiumej.v26i1.3537

ACO and MSCA exhibit distinct performance characteristics across key metrics. Processing Time highlights the computational efficiency of MSCA, which completes in 3.7 seconds compared to ACO's 101 seconds. MSCA's reliance on straightforward sinusoidal equations ensures minimal computational overhead, making it ideal for real-time applications, unlike ACO, whose iterative pheromone updates and probabilistic path selection result in significant processing delays. Regarding Search Space Scan Percentage, ACO demonstrates a narrower exploration focus ($1.25 \times 10^{-6}$ %) compared to MSCA's broader search coverage ($8.33 \times 10^{-7}$ %). While ACO's focused search improves accuracy in identifying critical contingencies, it may reduce robustness in high-dimensional or irregular solution spaces, where MSCA's adaptability becomes an advantage. Capture Ratio, a measure of accuracy, sees ACO slightly outperforming MSCA (98.8% vs. 96.7%), attributed to its pheromone-guided optimization. However, the marginal accuracy gain does not offset ACO's significantly higher computational cost, positioning MSCA as a more balanced and efficient option, especially for time-sensitive applications. These comparisons underscore the trade-offs between accuracy, computational efficiency, and robustness in applying nature-inspired algorithms for contingency ranking.

The MSCA enhances the standard SCA through targeted modifications that significantly improve its performance. By integrating sinusoidal dynamics with adjustable parameters ($a$=1, $d$=0.1), MSCA achieves a balanced trade-off between exploration and exploitation, effectively mitigating the risk of entrapment in local optima. Its reliance on simple mathematical functions ensures computational simplicity, enabling scalability to larger power system models while maintaining efficiency. Additionally, its broader search space coverage enhances robustness, making it well-suited for diverse optimization problems, including those with irregular or high-dimensional solution spaces. Comparative results underscore MSCA's computational efficiency and robust exploration as key advantages for contingency ranking tasks. In real-world applications, such as large-scale power systems with stringent computational constraints, MSCA provides a practical and efficient solution without significant accuracy trade-offs. While ACO's slightly higher accuracy may be advantageous in scenarios demanding precision and abundant computational resources, MSCA strikes a compelling balance between performance and practicality.

## 6. CONCLUSIONS

The study highlights the Modified Sine Cosine Algorithm (MSCA) as an efficient and robust tool for contingency ranking in power system reliability assessment. Leveraging simple sinusoidal dynamics and carefully adjusted parameters ($a$=1, $d$=0.1), MSCA achieves a notable balance between exploration and exploitation. The algorithm demonstrates superior computational efficiency, achieving a significantly faster processing time of only 3.7 seconds compared to 101 seconds for Ant Colony Optimization (ACO), making it particularly advantageous for real-time applications. Furthermore, MSCA demonstrates broader search space coverage ($8.33\times10^{-7}$ %) compared to ACO's narrower exploration focus ($1.25\times10^{-6}$ %), indicating its superior robustness in navigating irregular or high-dimensional solution spaces. While ACO achieves a marginally higher capture ratio (98.8% vs. 96.7% for MSCA), this improvement comes at a significantly higher computational cost, rendering ACO less practical for scenarios with strict time constraints or large-scale systems. MSCA's near-equivalent accuracy, faster computation, and scalability underscore its viability for modern power systems requiring efficient and adaptable solutions. These results solidify MSCA's position as a competitive alternative to ACO, addressing critical challenges such as local optima entrapment and the computational burden often faced in optimization problems. The comparative analysis

confirms that MSCA's strengths lie in its ability to deliver rapid, accurate, and scalable solutions, making it suitable for diverse power system applications. Its adaptability and computational simplicity make it an attractive choice for dynamic and high-stakes environments where real-time decision-making is paramount. Future research will enhance MSCA's capabilities by integrating hybrid optimization techniques, potentially combining MSCA with other metaheuristic methods to improve accuracy and adaptability in handling large-scale and dynamic power system challenges. Additionally, future studies could explore translating algorithmic performance into economic terms, such as the cost of increased processing time, providing a broader perspective on the real-world trade-offs associated with optimization techniques. This extension would offer valuable insights into the cost-benefit analysis of deploying MSCA in practical scenarios.

## REFERENCES

[1] M. R. Narimani *et al.*, "Generalized contingency analysis based on graph theory and line outage distribution factor," *IEEE Systems Journal,* vol. 16, no. 1, pp. 626-636, 2021.

[2] R. Patel, A. Nimje, S. Godwal, and S. Kanojia, "Contingency analysis: A tool to improve power system security," in *Smart Technologies for Power and Green Energy: Proceedings of STPGE 2022*: Springer, 2022, pp. 79-92.

[3] I. Priyadi, K. Ramli, N. Daratha, E. Fathoni, T. S. Gunawan, and E. Ihsanto, "Completion of Contingency Ranking Selection (N-1) Using Ant Colony Optimization Algorithm on 500 kV JAMALI System," in *2022 IEEE 18th International Colloquium on Signal Processing & Applications (CSPA)*, 2022: IEEE, pp. 144-149.

[4] S. Yang, B. Vaagensmith, and D. Patra, "Power grid contingency analysis with machine learning: A brief survey and prospects," *2020 Resilience Week (RWS),* pp. 119-125, 2020.

[5] Y. Zhao, Y. Li, Y. Cao, and M. Yan, "Risk-based contingency analysis for power systems considering a combination of different types of cyber-attacks," *Applied Energy,* vol. 348, p. 121551, 2023.

[6] K. Pal, S. Sachan, F. Gholian-Jouybari, and M. Hajiaghaei-Keshteli, "An analysis of the security of multi-area power transmission lines using fuzzy-ACO," *Expert Systems with Applications,* vol. 224, p. 120070, 2023.

[7] M. A. Majeed, S. Phichaisawat, F. Asghar, and U. Hussan, "Optimal energy management system for grid-tied microgrid: An improved adaptive genetic algorithm," *IEEE access,* vol. 11, pp. 117351-117361, 2023.

[8] Y. Du, F. Li, J. Li, and T. Zheng, "Achieving 100x acceleration for N-1 contingency screening with uncertain scenarios using deep convolutional neural network," *IEEE Transactions on Power Systems,* vol. 34, no. 4, pp. 3303-3305, 2019.

[9] C. Udhaya Shankar, S. Ram Inkollu, and N. Nithyadevi, "Deep Learning Based Effective Technique for Smart Grid Contingency Analysis Using RNN with LSTM," *Electric Power Components and Systems,* pp. 1-18, 2023.

[10] A. G. Rameshrao, E. Koley, and S. Ghosh, "A LSTM-based approach for detection of high impedance faults in hybrid microgrid with immunity against weather intermittency and N-1 contingency," *Renewable Energy,* vol. 198, pp. 75-90, 2022.

[11] F. Li and Y. Du, "Deep Convolutional Neural Network for Power System N-1 Contingency Screening and Cascading Outage Screening," in *Deep Learning for Power System Applications: Case Studies Linking Artificial Intelligence and Power Systems*: Springer, 2023, pp. 41-70.

[12] S. Mokred, Y. Wang, and T. Chen, "A novel collapse prediction index for voltage stability analysis and contingency ranking in power systems," *Protection and Control of Modern Power Systems,* vol. 8, no. 1, pp. 1-27, 2023.

[13] H. Bulat, D. Franković, and S. Vlahinić, "Enhanced contingency analysis—a power system operator tool," *Energies,* vol. 14, no. 4, p. 923, 2021.

[14] A. M. Al-Shaalan, "Contingency selection and ranking for composite power system reliability evaluation," *Journal of King Saud University-Engineering Sciences,* vol. 32, no. 2, pp. 141-147, 2020.

[15] A. B. Gabis, Y. Meraihi, S. Mirjalili, and A. Ramdane-Cherif, "A comprehensive survey of sine cosine algorithm: variants and applications," *Artificial Intelligence Review,* vol. 54, no. 7, pp. 5469-5540, 2021.

[16] S. Mirjalili, "SCA: a sine cosine algorithm for solving optimization problems," *Knowledge-based systems,* vol. 96, pp. 120-133, 2016.

[17] M. Noroozi, H. Mohammadi, E. Efatinasab, A. Lashgari, M. Eslami, and B. Khan, "Golden search optimization algorithm," *IEEE Access,* vol. 10, pp. 37515-37532, 2022.

[18] Y. Xie, Z. Liu, Y. Pan, F. Li, T. Jiao, and X. Li, "Minimum reactive power loss optimization of power grid systems based on improved differential evolution algorithm," in *IOP Conference Series: Earth and Environmental Science*, 2021, vol. 675, no. 1: IOP Publishing, p. 012159.

[19] Q. Yin, X. Du, A. Zhang, and H. Yang, "FAST computing model for multi-objective reactive power optimization," in *2010 Asia-Pacific Power and Energy Engineering Conference*, 2010: IEEE, pp. 1-4.

[20] E. H. Houssein, M. K. Saeed, G. Hu, and M. M. Al-Sayed, "Metaheuristics for solving global and engineering optimization problems: Review, applications, open issues and challenges," *Archives of Computational Methods in Engineering,* pp. 1-35, 2024.

[21] A. Faramarzi, M. Heidarinejad, B. Stephens, and S. Mirjalili, "Equilibrium optimizer: A novel optimization algorithm," *Knowledge-based systems,* vol. 191, p. 105190, 2020.

[22] L. Velasco, H. Guerrero, and A. Hospitaler, "A literature review and critical analysis of metaheuristics recently developed," *Archives of Computational Methods in Engineering,* vol. 31, no. 1, pp. 125-146, 2024.

[23] L. Lei, C. Ju, J. Chen, and M. I. Jordan, "Non-convex finite-sum optimization via scsg methods," *Advances in Neural Information Processing Systems,* vol. 30, 2017.

[24] X. Yu and D. Tao, "Variance-Reduced Proximal Stochastic Gradient Descent for Non-convex Composite optimization," *arXiv preprint arXiv:1606.00602,* 2016.

[25] G. Gantner, A. Haberl, D. Praetorius, and S. Schimanko, "Rate optimality of adaptive finite element methods with respect to overall computational costs," *Mathematics of Computation,* vol. 90, no. 331, pp. 2011-2040, 2021.

[26] M. Wang and G. Lu, "A modified sine cosine algorithm for solving optimization problems," *IEEE Access,* vol. 9, pp. 27434-27450, 2021.

[27] Y. Luo, W. Dai, and Y.-W. Ti, "Improved sine algorithm for global optimization," *Expert Systems with Applications,* vol. 213, p. 118831, 2023.

[28] R. D. Zimmerman, C. E. Murillo-Sánchez, and R. J. Thomas, "MATPOWER: Steady-state operations, planning, and analysis tools for power systems research and education," *IEEE Transactions on power systems,* vol. 26, no. 1, pp. 12-19, 2010.

https://doi.org/10.31436/iiumej.v26i1.3547

# IMPROVING MODEL PERFORMANCE FOR PREDICTING EXFILTRATION ATTACKS THROUGH RESAMPLING STRATEGIES

**ARIF RAHMAN HAKIM, KALAMULLAH RAMLI*, MUHAMMAD SALMAN, ESTI RAHMAWATI AGUSTINA**

*Department of Electrical Engineering, Faculty of Engineering, Universitas Indonesia, Depok, Indonesia*

**Corresponding author: kalamullah.ramli@ui.ac.id*

*(Received: 17 November 2024; Accepted: 1 January 2025; Published online: 10 January 2025)*

***ABSTRACT:*** Addressing class imbalance is critical in cybersecurity applications, particularly in scenarios like exfiltration detection, where skewed datasets lead to biased predictions and poor generalization for minority classes. This study investigates five Synthetic Minority Oversampling Technique (SMOTE) variants, including BorderlineSMOTE, KMeansSMOTE, SMOTEENC, SMOTEENN, and SMOTETomek, to mitigate severe imbalance in our customized tactic-labeled dataset with dominant majority class influence and weak class separability class imbalance. We use seven imbalance metrics to assess each SMOTE variant's impact on class distribution stability and separability. Furthermore, we evaluate model performance across five classifiers: Logistic Regression, Naïve Bayes, Support Vector Machine, Random Forest, and XGBoost. Findings reveal that SMOTEENN consistently enhances performance metrics (accuracy, precision, recall, F1-score, and geometric mean) on an average of 99% across most classifiers, establishing itself as the most adaptable variant for handling imbalance. This study provides a comprehensive framework for selecting resampling strategies to enhance classification efficacy in cybersecurity tasks with imbalanced data.

***ABSTRAK:*** Menangani ketidakseimbangan kelas adalah penting dalam aplikasi keselamatan siber, terutama dalam senario seperti pengesanan eksfiltrasi, di mana set data yang condong membawa kepada ramalan yang berat sebelah dan generalisasi yang lemah untuk kelas minoriti. Kajian ini menyiasat lima varian Teknik Sintetik Pencontohan Lebihan Minoriti (SMOTE), termasuk BorderlineSMOTE, KMeansSMOTE, SMOTEENC, SMOTEENN, dan SMOTETomek, untuk mengurangkan ketidakseimbangan teruk dalam set data berlabel taktik yang disesuaikan dengan pengaruh kelas majoriti dominan dan ketidakcerahan kelas yang lemah. Kami menggunakan tujuh metrik ketidakseimbangan untuk menilai kesan setiap varian SMOTE terhadap kestabilan dan ketidakcerahan taburan kelas. Selain itu, kami menilai prestasi model merentasi lima pengelas: Regresi Logistik, Naïf Bayes, Mesin Vektor Sokongan, Hutan Rawak, dan XGBoost. Penemuan menunjukkan bahawa SMOTEENN secara konsisten meningkatkan metrik prestasi (ketepatan, ketepatan, pengingatan, skor F1, dan purata geometri) sebanyak 99% secara purata merentasi kebanyakan pengelas, menegaskan dirinya sebagai varian yang paling boleh disesuaikan untuk menangani ketidakseimbangan. Kajian ini menyediakan rangka kerja komprehensif untuk memilih strategi pencontohan semula bagi meningkatkan keberkesanan klasifikasi dalam tugas keselamatan siber dengan data yang tidak seimbang.

***KEYWORDS:*** *Machine Learning, Imbalance Data, SMOTE, and Exfiltration*

https://doi.org/10.31436/iiumej.v26i1.3547

# 1. INTRODUCTION

Cybersecurity has become a critical issue across various sectors, affecting businesses, government entities, and individuals. The rapid advancement of technology has created new opportunities but also facilitated increasingly sophisticated cyber threats. The frequency of cyber-attacks has surged, with a notable rise in global incidents. Projections estimate that cybercrime will cost USD 9.5 trillion by 2024, growing at an annual rate of about 15%, reaching USD 10.5 trillion by 2025 [1].

The evolution of cyber threats requires organizations to assess their cybersecurity posture and adapt strategies accordingly and proactively. Common Vulnerabilities and Exposures (CVEs) are vital for identifying and responding to potential cyber incidents. CVEs provide a structured framework for categorizing vulnerabilities, aiding effective threat management and incident response. Integrating CVEs with frameworks like MITRE ATT&CK helps organizations understand adversary tactics and prioritize vulnerabilities based on their impact. Automated tools for vulnerability detection and remediation can reduce the time and resources required for effective cybersecurity management. Machine Learning (ML) also plays a crucial role in combating sophisticated cyber threats. ML algorithms improve accuracy by learning from new data and adapting to evolving threats. Additionally, ML is essential for incident response, automating threat mitigation to reduce the attack window and limit damage.

However, implementing ML in cybersecurity faces challenges from imbalanced datasets, which impact classification model performance. Imbalanced datasets occur when one class (usually the majority) outnumbers the other (minority) class. This imbalance can lead to biased predictions, poor generalization, and higher error rates for the minority class, which is often critical in cybersecurity, such as fraud or intrusion detection systems [2]. Several resampling methods have been developed to address class imbalance and improve classifier performance. These methods include undersampling, oversampling, and hybrid techniques. Our study focuses on addressing the class imbalance in a custom dataset designed to classify whether a sequence of tactics indicates exfiltration. We used a tactic-labeled dataset from CVE descriptions, which shows severe imbalance, with the minority class comprising less than 1%.

This paper examines the dataset's imbalance characteristics in detail and investigates oversampling-based solutions to address this issue. Oversampling was chosen for its ease of implementation and wide applicability. The most popular oversampling technique, SMOTE [3], is commonly used to balance class distribution and has proven effective in many studies and real-world applications. We investigate how five SMOTE variants affect imbalance characteristics: BorderlineSMOTE [4], KMeansSMOTE [5], SMOTEENC [6], SMOTEENN [7], and SMOTETomek [8]. We evaluate each dataset's imbalance using seven metrics: class distribution, imbalance ratio, minority class percentage, Coefficient of Variation (CV), Gini index, entropy, and Fischer's ratio. These metrics are applied to both the original and resampled datasets to assess the impact of each SMOTE variant.

The datasets from the five SMOTE variants are also used to assess model performance across five classifiers: Logistic Regression (LR) [9], Naïve Bayes (NB) [10], Support Vector Machine (SVM) [11], Random Forest (RF) [12], and Extreme Gradient Boosting (XGBoost) [13]. Performance is measured using six metrics: accuracy, precision, recall, specificity, F1-score, and geometric mean. These metrics facilitate a comparative analysis across models. The evaluation of imbalance characteristics is enhanced by including both seven imbalance metrics and six classifier performance metrics.

https://doi.org/10.31436/iiumej.v26i1.3547

Our study provides the following contributions:

- *A customized tactic-labeled dataset for exfiltration classification and measuring its imbalance characteristics*: Developed a new dataset specifically for classifying the Exfiltration tactic from ten other tactics. This dataset was derived from the originally used for mapping CVE description into MITRE Tactics and Techniques. Additionally, a focused analysis is conducted to identify and understand imbalance characteristics within a dataset using seven metrics (class distribution, imbalance ratio, minority class percentage, Coefficient of Variation, Gini index, entropy, and Fischer's ratio).
- *Investigation of SMOTE Variants*: Five SMOTE variants (BorderlineSMOTE, KMeansSMOTE, SMOTEENC, SMOTEENN, and SMOTETomek) are applied, and their impact on dataset characteristics is systematically assessed.
- *Multi-Metric Evaluation of Imbalance*: The imbalance of the original and resampled datasets is evaluated using the seven imbalanced metrics, providing an in-depth view of resampling effects.
- *Cross-Classifier Performance Comparison*: The impact of SMOTE resampling on model performance is assessed across five classifiers (LR, NB, SVM, RF, and XGBoost) using six classifier performance metrics (accuracy, precision, recall, specificity, F1-score, geometric mean) to establish a benchmark on how resampling strategies influence model efficacy.

This paper is divided into the following five sections. Section 2 reviews existing studies, focusing on existing studies that utilized the CVE dataset. Section 3 outlines the creation of our dataset and analysis of its imbalance characteristics. Section 4 investigates SMOTE variants by providing an in-depth view of resampling effects on imbalanced characteristics. In addition, we provide cross-classifier performance comparisons to establish a benchmark on how resampling strategies influence model efficacy. Lastly, conclusions are presented in Section 5.

## 2. RELATED WORKS

This section provides a review of existing methods or models that leverage the mapping of tactics from CVEs. Our review focuses on the aims, method used, how CVEs play a role in the method, and key findings, as provided in Table 1.

Table 1. Tactics distribution in the created dataset

| Study | Aims & Methods | Role of CVEs | Key Findings |
|---|---|---|---|
| [14] | Systematic mapping of CVEs to ATT&CK techniques using neural networks and unsupervised labeling. | CVEs are systematically connected to techniques for efficient threat mitigation. | Enhanced prioritization and threat management. |
| [15] | ML and DL approach for multi-label classification of CVEs to ATT&CK techniques. | CVEs form the basis for linking vulnerabilities to adversarial approaches. | Improved accuracy and reliability in mapping. |
| [16] | Transformer-based models (e.g., SecRoBERTa) for mapping CVEs to ATT&CK techniques. | CVEs are utilized for improving cybersecurity measures. | SecRoBERTa achieves 78.88% weighted F1; improved cybersecurity understanding. |
| [17] | BERT-based models with TextAttack for data augmentation to map CVEs to ATT&CK techniques. | CVEs are used to create a tagged corpus for ATT&CK Enterprise Matrix strategies. | F1-score of 47.84%; improved training set balance with augmentation. |

A study in [14] developed a systematic approach for mapping CVEs to MITRE ATT&CK techniques to enhance the understanding and management of cybersecurity threats. CVEs are crucial to the paper's investigation of how vulnerabilities might be systematically connected to attack strategies, improving defenders' ability to prioritize and mitigate threats efficiently. The research method combines advanced neural network modeling, unsupervised labeling, and enriched data representation to effectively map CVEs to ATT&CK techniques, enhancing cybersecurity threat management. Here are some research limitations: reproducibility and inconsistencies, concept drift, limited coverage of techniques, lack of granular categories, and dependence on unsupervised labeling.

Authors in [15] enhanced the process of linking CVEs to MITRE ATT&CK techniques using ML and deep learning (DL) approaches. They highlight the role of CVE as a foundational piece for linking vulnerabilities to adversarial approaches, hence improving organizations' ability to defend against cyber-attacks effectively. They employed multi-label classifications, Multi-Layer Perceptron (MLP), data augmentation, cross-validating techniques, hyperparameter tuning, reproduction, and comparison to enhance accuracy and reliability. The research limitations include dataset limitations, reproducibility issues, framework updates, limited technique coverage, and model comparison challenges.

Transformer-based models are used to automatically map CVEs to MITRE ATT&CK techniques to better cybersecurity understanding and protection measures [16]. An extended dataset of 9985 entries, security auditing tools, and MITRE ATT&CK methods are included in the study. The top models were SecRoBERTa, SecBERT, CyBERT, and TARS, with SecRoBERTa scoring 78.88% in weighted F1. Their study's main shortcoming is that conceptual linkages between tactics make it difficult to deduce a technique sequence from textual descriptions for specific vulnerabilities. Likewise, BERT-based language models are used to match 1813 MITRE ATT&CK-annotated CVEs to approaches in the study [17]. TextAttack-based data augmentation algorithms correct the training set imbalance, achieving an F1-score of 47.84%. The methodology creates a tagged corpus by manually mapping CVEs to MITRE ATT&CK Enterprise Matrix strategies and procedures, while the F1-score measures model performance.

Table 1 highlights that prior research has predominantly leveraged CVEs as a critical source for mapping MITRE ATT&CK tactics or techniques. However, these studies have largely overlooked the potential of analyzing sequences of tactics derived from CVEs to predict attacker objectives. To address this gap, our work focuses on processing CVE data into actionable sequences that predict specific attack goals, such as exfiltration. Moreover, existing literature emphasizes the lack of consensus on the optimal approach to handle data imbalance [18]. This variability underscores the pressing need for standardized evaluation frameworks to ensure consistency and comparability across datasets.

## 3. DATASET CREATION FOR EXFILTRATION CLASSIFICATION AND IMBALANCE CHARACTERISTICS

This section explains the dataset processing steps we employed and details the imbalance characteristics of the dataset. Additionally, we introduce the seven metrics used to measure the imbalance characteristics of the initial dataset in this section and the various datasets generated by the resampling methods discussed in the subsequent section. Furthermore, we present the measurement results of the imbalanced characteristics of the initial dataset using these seven metrics. These results serve as a baseline for analyzing the impact of resampling methods on imbalance characteristics by examining changes in the measured metrics.

https://doi.org/10.31436/iiumej.v26i1.3547

### 3.1. Modifying Tactics Mapping Dataset Based on CVE Description

The dataset source used in this study is created by the study [19] aimed to automatically map CVEs to the 14 MITRE ATT&CK tactics using transformer-based models and is publicly available in [20]. The data cleaning phase involved filtering out rows with missing tactic labels. In this research, two tactics, Reconnaissance, and Resources, were excluded as they predominantly occur on the attacker's side. We retained the tactic Initial Access to represent how attackers infiltrate the target environment. Consequently, ten tactics were chosen as features for this study: (1) Initial Access, (2) Execution, (3) Persistence, (4) Privilege Escalation, (5) Defense Evasion, (6) Credential Access, (7) Discovery, (8) Lateral Movement, (9) Collection, and (10) Command and Control. We also excluded the impact since we focused on exfiltration as the adversarial objective and designated exfiltration as the target variable. This custom-built dataset was selected to capture patterns within these ten tactics and assess whether their presence leads to exfiltration tactics. Fig. 1 shows 14 tactics derived from MITRE ATT&CK, where in this study, ten tactics were used as features, one tactic as a target feature, and three tactics were excluded.

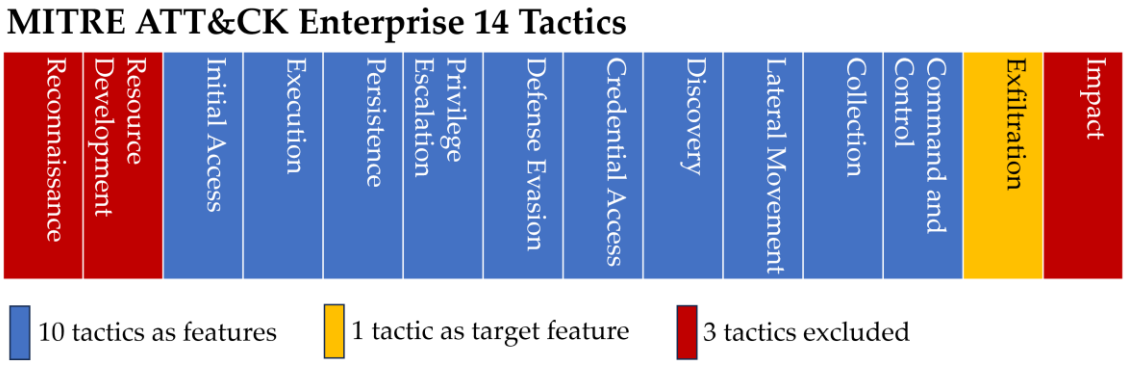


Figure 1. Adversarial tactics and features mapping in our modified dataset.

Table 2. Tactics distribution in the created dataset

| Features | Tactics | Number of 1 |
|---|---|---|
| **Feature_1** | Initial Access | 722 |
| **Feature_2** | Execution | 264 |
| **Feature_3** | Persistence | 3016 |
| **Feature_4** | Privilege Escalation | 3218 |
| **Feature_5** | Defense Evasion | 7552 |
| **Feature_6** | Credential Access | 614 |
| **Feature_7** | Discovery | 2369 |
| **Feature_8** | Lateral Movement | 1932 |
| **Feature_9** | Collection | 663 |
| **Feature_10** | Command and Control | 427 |
| **Target** | **Exfiltration** | **51** |

On the other hand, Table 2 shows the distribution of the ten tactics used as features, with the Exfiltration Tactic serving as the target feature in our 9602-row dataset. The table shows that "Defense Evasion" is the most frequently occurring tactic among the features, while "Command and Control" is the least frequent tactic in the dataset. On the other hand, "Exfiltration," as the target feature, appears only 51 times. The created dataset is referred to as the initial dataset, particularly in comparative analyses with datasets produced by various resampling methods to provide a sense of the initial state versus the post-resampling conditions.

https://doi.org/10.31436/iiumej.v26i1.3547

## 3.2. Imbalance Characteristics of the Initial Dataset

This section explains the characteristics of the initial dataset as measured by seven commonly used metrics to illustrate dataset imbalance. Each metric explains its purpose, accompanied by its calculation formula. Additionally, we provide an interpretation of the calculation results for each metric as applied to the initial dataset.

### *3.2.1. The Imbalance Metrics*

The class distribution indicates the number of instances present in each dataset class. In a balanced dataset, the instances across classes are generally equal, while an imbalanced dataset exhibits a noticeable difference in instance counts. Recognizing the class distribution is critical for choosing the appropriate modeling techniques and evaluation metrics, as standard metrics like accuracy may not provide a reliable assessment in imbalanced situations. Meanwhile, the imbalance ratio is a quantitative measure to represent the imbalance between the majority and minority classes. This ratio is determined by dividing the count of instances in the majority class by that in the minority class. A higher imbalance ratio suggests a more pronounced disparity between classes, which can create additional challenges for classifiers. This metric is essential for assessing the imbalance's severity and informing the selection of techniques to address it effectively. In addition, the minority class percentage is a significant metric representing the proportion of instances in the minority class relative to the total dataset size. When the minority class percentage is low, models tend to favor the majority class, potentially causing reduced recall for the minority class.

The CV quantifies the ratio of the standard deviation to the mean, offering insight into the variability within class distributions in imbalanced datasets. A high CV suggests significant variability relative to the mean, indicating an imbalance and inconsistent distribution within classes. The Gini index, commonly used to measure inequality, assesses class distribution disparity in imbalanced datasets. With values ranging from 0 (complete equality) to 1 (maximum inequality), a higher Gini index reveals a more significant disparity between majority and minority classes. This metric is beneficial for evaluating sampling strategies or model adjustments aimed at reducing class imbalance.

Entropy, measuring uncertainty or disorder, assesses the impurity of a dataset's class distribution. High entropy indicates a more balanced class distribution, while low entropy suggests dominance by a single class. When an excessive number of majority samples fall within the overlapping region, the probability for the majority class nears 1. In contrast, the minority class approaches 0, driving entropy toward its minimum value of 0. Conversely, as the count of majority samples approaches that of minority samples, entropy tends towards its maximum value of 1. Fischer's ratio, also known as Fischer's discriminant ratio [21], assesses class separability by comparing between-class variance to within-class variance. Higher Fischer's ratios indicate clearer class separability, an advantage in classification tasks. However, achieving high Fischer's ratios is more difficult with imbalanced datasets, as minority classes may be underrepresented

### *3.2.2. The Initial Dataset*

The calculation results for the seven imbalance metrics of the initial dataset are presented in Table 3. Overall, the measurements indicate that the initial dataset exhibits severe imbalance characteristics. The class distribution is highly skewed, with 9,551 instances in the majority class and only 51 in the minority class. An imbalance ratio of 187 means that the majority class is 187 times larger than the minority class, accompanied by a minority class percentage of merely 0.53%. Additionally, a relatively high CV of 2.44 reflects a significant disparity

between the majority and minority classes. Likewise, the entropy value of only 0.05 shows a strong dominance by the majority class. Furthermore, a very low Fisher's ratio of 0.05 indicates poor class separability, which could result in an even more significant underrepresentation of the minority class.

Table 3. Imbalance characteristics of the initial dataset

| Metrics | Result |
|---|---|
| **Class Distribution** | 955:51 |
| **Imbalance Ratio** | 187.27 |
| **Minority Class Percentage** | 0.53 |
| **Coefficient of Variation** | 2.44 |
| **Gini Index** | 0.01 |
| **Entropy** | 0.05 |
| **Fischer's Ratio** | 0.05 |

## 4. INVESTIGATION OF SMOTE VARIANTS

This study employed five SMOTE variants: BorderlineSMOTE, KMeansSMOTE, SMOTEENC, SMOTEENN, and SMOTETomek. This section provides a detailed description of each SMOTE variant utilized, along with the post-resampling dataset size and the feature distribution within each resulting dataset. We then present the imbalance characteristics of each dataset, which are evaluated using seven metrics consistent with those applied to the initial dataset. Based on the values derived from these metrics, we conduct a comparative analysis between the initial and resampled datasets. Furthermore, we compare these metric values across the five SMOTE variants to determine the most suitable variant for our dataset.

Additionally, we present a comprehensive evaluation of model performance across each of the five SMOTE variants using five commonly adopted classifiers: LR, NB, SVM, RF, and XGBoost. Model performance is assessed using six metrics: accuracy, precision, recall, specificity, F1-score, and geometric mean. By comparing model performance across the five SMOTE variants, we aim to identify the most effective resampling strategy for enhancing the model's efficacy with SMOTE techniques. Fig. 2 illustrates the block diagram of our study's investigation of SMOTE variants.

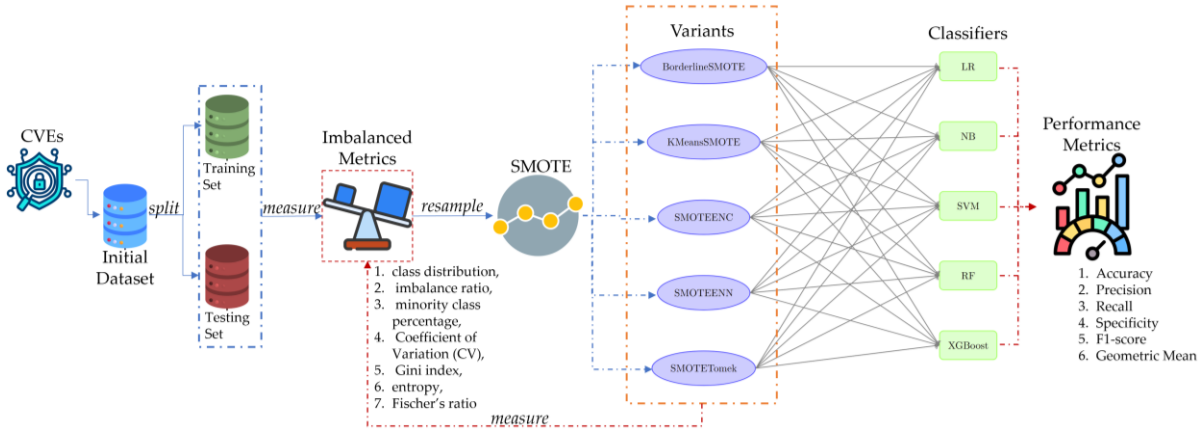


Figure 2. Block diagram of our investigation on SMOTE variants.

### 4.1. Resampled Datasets using SMOTE Variants

The cleaned dataset from the previous stage is clearly imbalanced, with the majority class outnumbering the minority class by 93%:7%. Table 4 compares the initial dataset

characteristics without resampling and the five datasets generated from each SMOTE Variants. The table displays the number of rows for each dataset and the ratio of majority to minority class in percentages.

Table 4. Comparison of dataset size and class distribution ratios after resampling

| Resampling | # Rows | *Ratio (%) |
|---|---|---|
| **Initial (without resampling)** | 9602 | 99.47:0.53 |
| **BorderlineSMOTE** | 19102 | 50:50 |
| **KMeansSMOTE** | 19104 | 50.1:49.9 |
| **SMOTEENC** | 19102 | 50:50 |
| **SMOTEENN** | 9520 | 74.61:25.39 |
| **SMOTETomek** | 19102 | 50:50 |

*Ratio between majority class and minority class

Notably, BorderlineSMOTE, SMOTEENC, and SMOTETomek datasets have the same number of rows and a precisely balanced ratio. Meanwhile, the KMeansSMOTE dataset has the most significant number of rows and has an almost balanced ratio. On the other hand, the SMOTEENN dataset has the lowest number of rows, with the majority class 3 times more rows than the minority class. However, this does not guarantee optimal model performance.

Additionally, to assess the number of features present, we provide each dataset's distribution of features (tactics), including the initial dataset and the five resampled datasets generated using SMOTE variants in Table 5. The table illustrates a significant variation in the effectiveness of different SMOTE techniques in balancing class distributions across features (tactics), with "Exfiltration" as the target feature. For several tactics, such as "Initial Access," "Execution," and "Defense Evasion," most SMOTE variants, especially SMOTENC, KMeansSMOTE, and BorderlineSMOTE, demonstrate substantial increases in sample counts. This increase indicates the strategy of these techniques in addressing class imbalance across non-target tactics.

Table 5. Comparison of features (tactics) distribution across the initial dataset and SMOTE variants

| Tactic | Initial | SMOTE Variants (Oversampling) | | | | |
|---|---|---|---|---|---|---|
| | | B-SMOTE[1] | K-SMOTE[1] | SMOTEENC | SMOTENN | SMOTE-T[1] |
| Initial Access | 722 | 2367 | 3831 | 5451 | 1241 | 1453 |
| Execution | 2642 | 8096 | 8721 | 7385 | 1366 | 4970 |
| Persistence | 3016 | 5445 | 3016 | 4209 | 2206 | 4192 |
| Privilege Escalation | 3218 | 6103 | 3218 | 4411 | 2404 | 4556 |
| Defense Evasion | 7552 | 10085 | 7553 | 14238 | 7008 | 13925 |
| Credential Access | 614 | 614 | 614 | 614 | 609 | 614 |
| Discovery | 2369 | 3312 | 3150 | 6890 | 4284 | 6669 |
| Lateral Movement | 1932 | 3737 | 1932 | 2717 | 840 | 2717 |
| Collection | 663 | 3824 | 3578 | 2232 | 1163 | 2030 |
| Command and Control | 427 | 627 | 427 | 553 | 498 | 505 |
| **Exfiltration[2]** | **51** | **9551** | **9553** | **9551** | **7103** | **9551** |

[1] B-SMOTE (BordelineSMOTE), K-SMOTE (KMeansSMOTE), SMOTE-T (SMOTETomek)
[2] Target feature

Notably, SMOTENC achieves the highest augmentation for "Defense Evasion," a tactic with high initial counts, while "Execution" also sees a marked rise under KMeansSMOTE and BorderlineSMOTE, reflecting these methods' responsiveness to the initial dataset's imbalance patterns. Interestingly, "Exfiltration," the target feature and the rarest class in the initial dataset (with only 51 samples), is consistently upsampled across all SMOTE variants. The substantial upsampling of "Exfiltration" by each SMOTE variant highlights the importance of this target

https://doi.org/10.31436/iiumej.v26i1.3547

class in the resampling process. Fig. 3 shows the tactics count comparison across SMOTE variants datasets and the initial dataset.

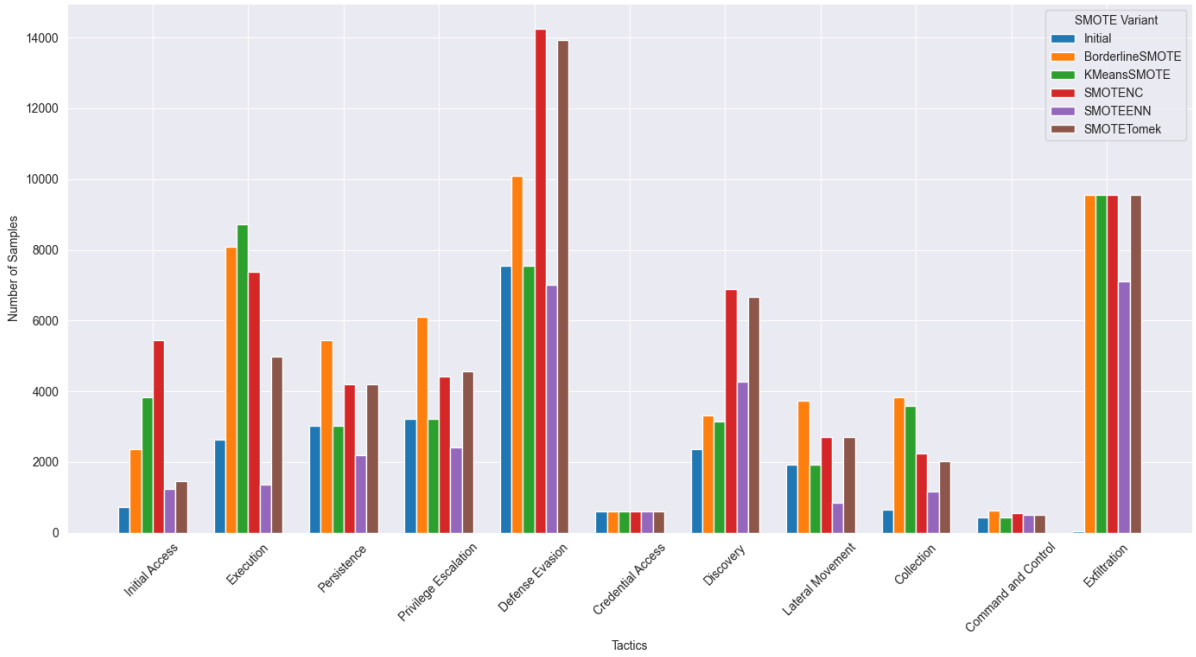


Figure 3. Tactics count comparison across SMOTE variants datasets and the initial dataset.

## 4.2. Imbalanced Metrics Value Across All Datasets

In this section, we employed a multi-metric evaluation of dataset imbalance characteristics. The imbalance of the original and resampled datasets is evaluated using the seven imbalanced metrics, including class distribution, imbalance ratio, minority class percentage, Coefficient of Variation, Gini index, entropy, and Fischer's ratio. This investigation provides an in-depth view of the resampling effects.

### *4.2.1. Comparison of Imbalance Metric Values*

We present the imbalance metric measurements for the initial dataset and the five SMOTE variant datasets in Table 6. The table shows that the initial dataset exhibits a severe imbalance, with a class distribution ratio of 9551:51, resulting in a high imbalance ratio of 99.47:0.53. This leads to a minority class percentage of only 0.53%, indicating the rarity of the "Exfiltration" feature. Consequently, the metrics of the Gini Index and Entropy are shallow at 0.01 and 0.05, respectively, reflecting the minimal uncertainty and high predictability due to the overwhelming presence of the majority class. The low Fischer's Ratio (0.05) suggests limited separability between the majority and minority classes in the initial dataset.

Substantial changes are observed in the class distribution and associated metrics after applying different SMOTE variants. BorderlineSMOTE, SMOTENC, and SMOTETomek successfully achieve a balanced class distribution with a 1:1 imbalance ratio and a 50% minority class percentage. These methods also show uniform Gini Index and Entropy values (0.5 and 1, respectively), representing increased class uncertainty and balance. However, variations in the CV indicate that SMOTETomek has a higher variability in class distribution at 2.77, compared to SMOTENC (2.49) and BorderlineSMOTE (2.49), suggesting differing impacts on the distribution's stability across these techniques. Fischer's ratio is slightly higher for BorderlineSMOTE (0.14), indicating better class separability than SMOTETomek (0.05).

https://doi.org/10.31436/iiumej.v26i1.3547

Table 6. Imbalances metric values

| Dataset | CD* | IR* | MCP* | CV* | GI* | E* | FR* |
|---|---|---|---|---|---|---|---|
| **Initial (without resampling)** | 9551:51 | 99.47 : 0.53 | 0.53 | 2.44 | 0.01 | 0.05 | 0.05 |
| **BorderlineSMOTE** | 9551:9551 | 50 : 50 | 50 | 2.49 | 0.50 | 1 | 0.14 |
| **KMeansSMOTE** | 9551:9553 | 50.1 : 49.9 | 49.99 | 2.82 | 0.50 | 1 | 0.57 |
| **SMOTENC** | 2417:7103 | 50 : 50 | 25.39 | 2.42 | 0.38 | 0.82 | 0.32 |
| **SMOTEENN** | 9551:9551 | 74.61 : 25.39 | 50 | 2.49 | 0.50 | 1 | 0.12 |
| **SMOTETomek** | 9551:9551 | 50 : 50 | 50 | 2.77 | 0.50 | 1 | 0.05 |

*CD (class distribution), IR (imbalance ratio), MCP (minority class percentage), CV (Coefficient of Variation), GI (Gini index), E (entropy), FR (Fischer's ratio)

In contrast, KMeansSMOTE and SMOTEENN result in distinct class distributions. KMeansSMOTE achieves a near-perfect 1:1 class distribution with a slight minority deviation, yielding a high Fischer's Ratio of 0.57, suggesting strong class separability. Meanwhile, SMOTEENN produces an imbalance ratio of 2.94 with a minority class percentage of 25.39%, positioning it as a less balanced but potentially more stable approach for specific models. The Entropy (0.82) and Gini Index (0.38) values for SMOTEENN indicate a moderate increase in class uncertainty and separability, highlighting its unique impact on dataset structure compared to other SMOTE techniques.

#### *4.2.2. Best Strategy Based on Imblalance Metric Values Across SMOTE Variants*

This section focuses on identifying the most effective SMOTE variant based on the results of the imbalance metrics measurements. Based on the comparison metrics presented in Table 5, KMeansSMOTE demonstrates the most effective performance in balancing the target class, "Exfiltration." This method nearly achieves a 1:1 distribution with a class ratio of 9551:9553, yielding an Imbalance Ratio close to 1. Additionally, the Minority Class Percentage reaches 49.99%, closely approximating 50%, indicating an almost perfect balance between the majority and minority classes. This balance is essential for enhancing the quality of training data, enabling the model to better recognize patterns within the minority "Exfiltration" class.

Moreover, KMeansSMOTE achieves the highest CV at 2.82, reflecting consistent distribution across classes after rebalancing. Its Gini Index and Entropy values are near optimal at 0.5 and 1, respectively, indicating a balanced level of uncertainty between classes. With the highest Fischer's Ratio (0.57), this method also exhibits superior separability between majority and minority classes, which is critical for improving the model's ability to distinguish between them. Based on these metrics, KMeansSMOTE provides an optimal balance of distribution consistency, separability, and class uncertainty, making it the preferred choice for addressing the imbalance in the target class, "Exfiltration." We further examine cross-classifier performance comparison using model performance metrics to investigate resampling strategies and their impact on model efficacy.

### 4.3. Cross-Classifier Performance Comparison

In this section, we investigate the impact of SMOTE resampling on model performance assessed across five classifiers (LR, NB, SVM, RF, and XGBoost) using six classifier performance metrics (accuracy, precision, recall, specificity, F1-score, geometric mean) to establish a benchmark on how resampling strategies influence model efficacy. We present each classifier's model performance individually, then compare SMOTE variant performance based on six performance metrics within each classifier. This approach focuses on comparing the performance of the five SMOTE variants rather than identifying the best classifier among the five used. This way, we can further determine which SMOTE variant performs most effectively for these models.

https://doi.org/10.31436/iiumej.v26i1.3547

### *4.3.1. Logistic Regression Classifier*

Based on the performance metrics across different resampling methods using LR in Fig. 4, several insights emerge regarding the efficacy of each SMOTE variant. The initial dataset without resampling exhibits high accuracy (0.995) and specificity (1) but has zero values for precision, recall, F1 score, and geometric mean, indicating that it fails to detect minority class instances. This outcome underscores the limitations of unbalanced data in handling minority classes effectively. Among the resampling methods, KMeansSMOTE and SMOTEENN stand out, as they yield superior metrics across the board, with KMeansSMOTE achieving a balanced performance across accuracy (0.962), precision (0.933), recall (0.996), and specificity (0.929). Meanwhile, SMOTEENN produces the highest F1 score (0.979) and an impressive recall (0.989), suggesting a robust ability to detect minority instances effectively while maintaining good overall accuracy.

Figure 4. Model performance of SMOTE variants using LR classifier.

When examining the overall effectiveness of each SMOTE variant, SMOTEENN emerges as the most effective method for this classifier model. It balances detection performance across metrics with high precision, recall, and F1 score values while achieving a notable geometric mean of 0.946, indicating balanced performance across both classes. KMeansSMOTE, with a slightly lower F1 score and geometric mean, still performs admirably and may be a suitable alternative depending on specific goals. In contrast, BorderlineSMOTE, SMOTENC, and SMOTETomek exhibit lower values in several metrics, particularly in recall and F1 score, suggesting they are less effective for minority class detection in this context. Consequently, SMOTEENN and KMeansSMOTE are recommended for optimizing this model's performance across balanced metrics.

### *4.3.2. Naïve Bayes Classifier*

Fig. 5 shows that the NB classifier yields varying results across resampling methods, with KMeansSMOTE and SMOTEENN demonstrating substantial improvements compared to others. Without resampling, the classifier achieves high specificity (0.945) but performs poorly in terms of recall (0.067), precision (0.006), and F1 score (0.012), highlighting its ineffectiveness in capturing the minority class. Among the resampling techniques, KMeansSMOTE shows the most balanced performance, with high scores across accuracy (0.950), precision (0.912), recall (0.996), and F1 score (0.952). This balanced metric profile

https://doi.org/10.31436/iiumej.v26i1.3547

reflects its ability to handle class imbalance effectively in NB. SMOTEENN also performs well, particularly in recall (0.989) and F1 score (0.907), but its lower specificity (0.436) suggests some trade-offs in its balance between classes.

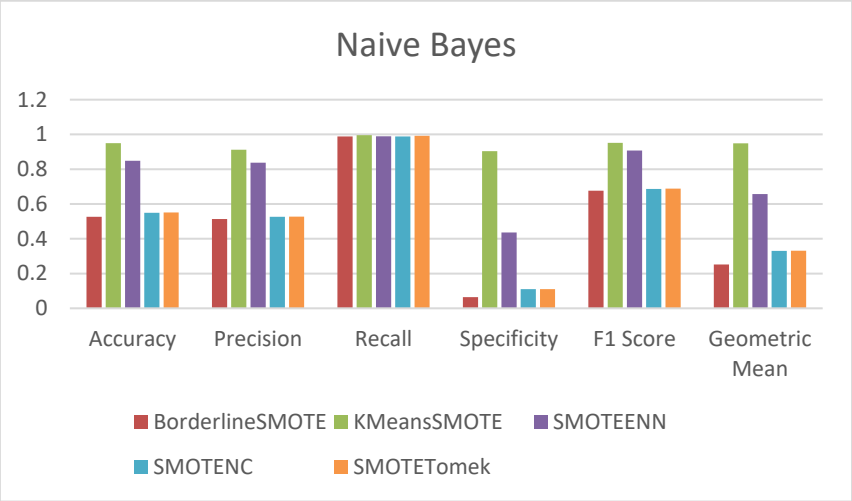


Figure 5. Model performance of SMOTE variants using NB classifier.

Considering the overall metrics, KMeansSMOTE is the best-performing variant for the NB classifier. It maintains high precision, recall, F1-score, and geometric mean (0.949), indicating stable and reliable performance across different metrics. While SMOTEENN also shows strong recall and F1-score, its reduced specificity could impact performance in specific applications. BorderlineSMOTE, SMOTENC, and SMOTETomek display lower accuracy and specificity values, making them less effective for NB in this context. KMeansSMOTE is recommended for optimal model efficacy with NB, as it provides balanced detection across both minority and majority classes.

### *4.3.3. Random Forest Classifier*

The RF classifier shows substantial improvement across various metrics when combined with resampling methods, particularly in recall and F1-score. Without resampling, RF achieves perfect specificity (1.0) but fails to identify any instances of the minority class, resulting in zero values for precision, recall, F1 score, and geometric mean. This demonstrates that the model is highly imbalanced and fails to generalize to the minority class. When resampling methods are applied, metrics like precision, recall, and F1 score improve significantly, with SMOTEENN and KMeansSMOTE showing the most robust results, as illustrated in Fig. 6.

Among the resampling methods, SMOTEENN provides the best performance across all metrics, achieving near-perfect values for accuracy (0.997), precision (1.0), recall (0.996), specificity (1.0), F1 score (0.999), and geometric mean (0.999). This indicates that SMOTEENN allows RF to balance minority and majority classes exceptionally well. KMeansSMOTE also performs well, with high scores in precision (0.944), recall (0.995), F1 score (0.969), and geometric mean (0.968), showing a solid balance across metrics, though slightly lower than SMOTEENN. Other methods, like BorderlineSMOTE and SMOTENC, show good but comparatively lower performance, particularly in recall and F1 score, while SMOTETomek lags with a lower overall balance. Therefore, SMOTEENN is the most effective resampling technique for the RF classifier, followed closely by KMeansSMOTE for robust, balanced performance across metrics.

https://doi.org/10.31436/iiumej.v26i1.3547

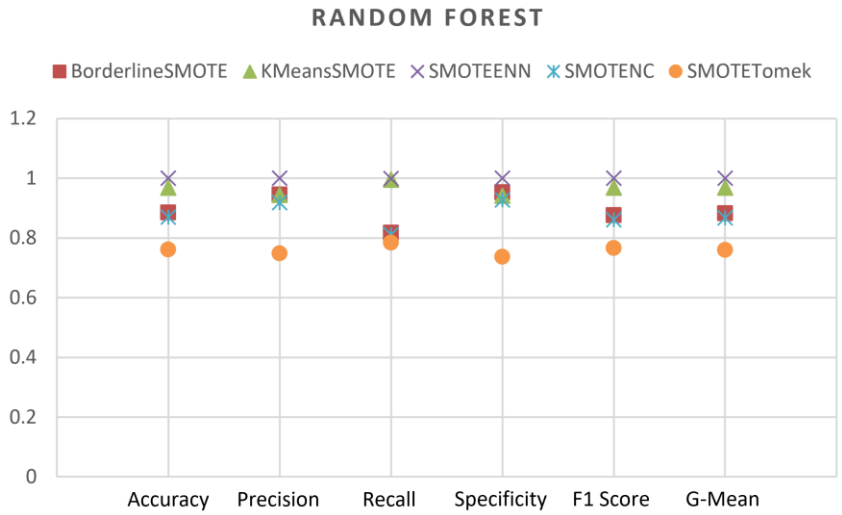


Figure 6. Model performance of SMOTE variants using RF classifier.

### *4.3.4. Support Vector Machine Classifier*

Using the SVM classifier, we can see in Fig. 7 that the performance metrics improve considerably when resampling methods are applied, particularly regarding recall and F1 score. Without resampling, the classifier achieves a high specificity (1.0) but ultimately fails to detect the minority class, resulting in zero values for precision, recall, F1 score, and geometric mean. This highlights that the model is severely biased toward the majority class. However, applying resampling techniques will significantly enhance the classifier's ability to capture the minority class, reflected by notable improvements in recall and F1 score across most methods.

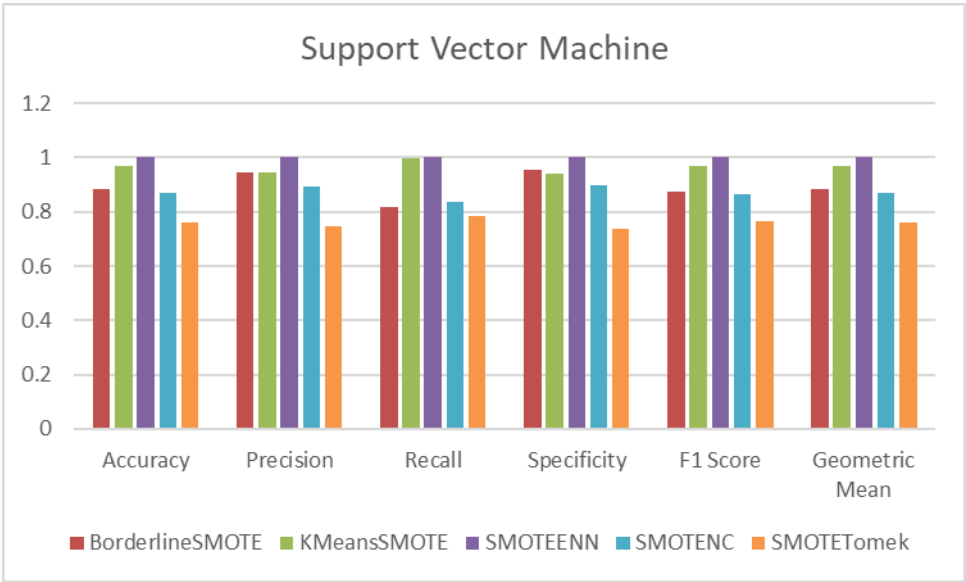


Figure 7. Model performance of SMOTE variants using SVM classifier.

Among the resampling techniques, SMOTEENN yields the best results, with near-perfect scores in accuracy (0.999), precision (1.0), recall (0.999), specificity (1.0), F1 score (0.999), and geometric mean (0.999). This indicates that SMOTEENN provides the SVM classifier an exceptional balance between both classes. KMeansSMOTE also performs well, showing high precision (0.944), recall (0.995), F1 score (0.969), and geometric mean (0.967), though slightly lower than SMOTEENN across these metrics. BorderlineSMOTE and SMOTENC offer

https://doi.org/10.31436/iiumej.v26i1.3547

moderate performance, with BorderlineSMOTE achieving a good balance (e.g., precision of 0.945 and F1 score of 0.876) but still falling short of SMOTEENN and KMeansSMOTE. SMOTETomek has the lowest performance across metrics, indicating a relatively weaker balance in addressing class imbalance. Overall, SMOTEENN stands out as the optimal resampling technique for SVM, followed closely by KMeansSMOTE for strong and balanced results across metrics.

### *4.3.5. XGBoost Classifier*

Using the XGBoost classifier and applying resampling techniques will significantly improve capturing the minority class compared to the baseline model (without resampling). Without resampling, XGBoost performs similarly to the SVM classifier, achieving perfect specificity (1.0) but with zero values for precision, recall, F1 score, and geometric mean, indicating that the model is heavily biased toward the majority class. This result highlights the necessity of resampling methods to enable XGBoost to recognize and classify instances from the minority class effectively.

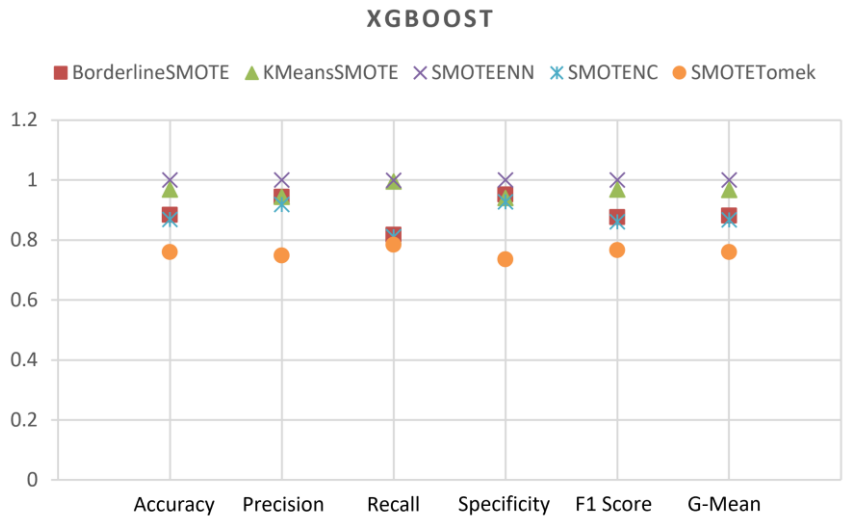


Figure 8. Model performance of SMOTE variants using XGBoost classifier.

Based on Fig. 8, we can see that among the resampling techniques, SMOTEENN again emerges as the best-performing method, achieving near-perfect metrics across the board with an accuracy of 0.9996, precision of 1.0, recall of 0.9995, specificity of 1.0, F1 score of 0.9998, and geometric mean of 0.9998. This suggests that SMOTEENN provides XGBoost with an optimal balance, allowing it to perform exceptionally well in both classes. KMeansSMOTE also performs strongly, with high values across precision (0.9434), recall (0.9951), F1 score (0.9686), and geometric mean (0.9673), making it a close alternative to SMOTEENN. BorderlineSMOTE and SMOTENC yield moderate performance, with BorderlineSMOTE achieving a good balance between metrics (e.g., F1 score of 0.8761), though lower than SMOTEENN and KMeansSMOTE. SMOTETomek shows the lowest performance, with lower scores across all metrics, indicating it may be less effective for balancing the dataset in this context. Overall, SMOTEENN is the optimal resampling technique for XGBoost, followed by KMeansSMOTE, as these two methods provide the most balanced and robust performance across all metrics.

https://doi.org/10.31436/iiumej.v26i1.3547

### *4.3.6. Results Across Different Classifiers*

Based on the analysis results across different classifiers in Section 4.4.1. to 4.4.5, SMOTEENN consistently outperforms other SMOTE variants across four classifiers, demonstrating its strong effectiveness in handling class imbalance across different model types. SMOTEENN achieved near-perfect accuracy, precision, recall, F1 score, and geometric mean for most classifiers, demonstrating its ability to create a balanced representation of majority and minority classes. KMeansSMOTE, although not consistently dominant, excels in one classifier and provides a reliable alternative with high performance in most metrics, especially in recall and F1 scores. The comparison in Table 7 highlights SMOTEENN as the most versatile and reliable variant of SMOTE across a wide range of classifiers, making it the preferred choice for unbalanced data sets in various machine-learning models.

Table 7. The six model performance metrics of five SMOTE variants across five classifiers

| Classifiers | SMOTE variants | Accuracy | Precision | Recall | Specificity | F1-score | G-Mean |
|---|---|---|---|---|---|---|---|
| **LR** | Initial | 0.995 | 0.000 | 0.000 | 1.000 | 0.000 | 0.000 |
| | BorderlineSMOTE | 0.823 | 0.895 | 0.732 | 0.914 | 0.806 | 0.818 |
| | KMeansSMOTE | 0.962 | 0.933 | 0.995 | 0.928 | 0.963 | 0.961 |
| | SMOTEENN | 0.968 | 0.968 | 0.989 | 0.905 | 0.979 | 0.946 |
| | SMOTENC | 0.814 | 0.897 | 0.710 | 0.919 | 0.793 | 0.808 |
| | SMOTETomek | 0.720 | 0.720 | 0.720 | 0.720 | 0.720 | 0.720 |
| **NB** | Initial | 0.941 | 0.006 | 0.067 | 0.945 | 0.012 | 0.251 |
| | BorderlineSMOTE | 0.526 | 0.514 | 0.989 | 0.064 | 0.676 | 0.252 |
| | KMeansSMOTE | 0.950 | 0.912 | 0.995 | 0.904 | 0.952 | 0.949 |
| | SMOTEENN | 0.849 | 0.838 | 0.989 | 0.436 | 0.907 | 0.657 |
| | SMOTENC | 0.549 | 0.526 | 0.988 | 0.111 | 0.687 | 0.331 |
| | SMOTETomek | 0.551 | 0.527 | 0.992 | 0.111 | 0.688 | 0.331 |
| **RF** | Initial | 0.995 | 0.000 | 0.000 | 1.000 | 0.000 | 0.000 |
| | BorderlineSMOTE | 0.885 | 0.945 | 0.817 | 0.953 | 0.877 | 0.882 |
| | KMeansSMOTE | 0.968 | 0.944 | 0.995 | 0.941 | 0.969 | 0.968 |
| | SMOTEENN | 0.997 | 1.000 | 0.996 | 1.000 | 0.999 | 0.999 |
| | SMOTENC | 0.869 | 0.918 | 0.811 | 0.928 | 0.861 | 0.868 |
| | SMOTETomek | 0.761 | 0.749 | 0.785 | 0.737 | 0.766 | 0.760 |
| **SVM** | Initial | 0.995 | 0.000 | 0.000 | 1.000 | 0.000 | 0.000 |
| | BorderlineSMOTE | 0.885 | 0.945 | 0.817 | 0.953 | 0.876 | 0.882 |
| | KMeansSMOTE | 0.968 | 0.944 | 0.995 | 0.941 | 0.969 | 0.968 |
| | SMOTEENN | 0.999 | 1.000 | 0.999 | 1.000 | 0.999 | 0.999 |
| | SMOTENC | 0.869 | 0.893 | 0.838 | 0.900 | 0.865 | 0.868 |
| | SMOTETomek | 0.760 | 0.748 | 0.785 | 0.736 | 0.766 | 0.760 |
| **XGBoost** | Initial | 0.995 | 0.000 | 0.000 | 1.000 | 0.000 | 0.000 |
| | BorderlineSMOTE | 0.884 | 0.944 | 0.817 | 0.952 | 0.876 | 0.882 |
| | KMeansSMOTE | 0.968 | 0.943 | 0.995 | 0.940 | 0.969 | 0.967 |
| | SMOTEENN | 1.000 | 1.000 | 1.000 | 1.000 | 1.000 | 1.000 |
| | SMOTENC | 0.869 | 0.918 | 0.811 | 0.927 | 0.861 | 0.867 |
| | SMOTETomek | 0.760 | 0.748 | 0.785 | 0.736 | 0.766 | 0.760 |

In terms of F1-scores the very low initial results are primarily due to severe class imbalance in the dataset, where the minority class is vastly underrepresented. This imbalance causes classifiers to prioritize the majority class, resulting in high specificity (1.000) but near-zero recall and precision, leading to F1-scores of 0.000. The classifiers struggle to learn patterns for the minority class without sufficient examples, highlighting their limitations when applied to imbalanced datasets without preprocessing. The marked improvement in F1-scores after applying resampling strategies, such as SMOTEENN and KMeansSMOTE, underscores the critical role of addressing class imbalance to enhance model performance.

# 5. CONCLUSION

This study addresses the class imbalance problem in datasets labeled with tactics derived from CVE descriptions for exfiltration classification. Our analysis highlights the severe imbalance in the initial dataset, marked by skewed class distribution, dominant majority classes, and poor separability between classes. By applying five SMOTE variants and evaluating their impact on imbalance characteristics and model performance, we identify SMOTEENN as the most effective method for achieving consistent, near-perfect performance across multiple classifiers. SMOTEENN's ability to maintain balance while enhancing accuracy, precision, recall, and F1 scores demonstrates its adaptability to diverse model types.

Among alternative approaches, KMeansSMOTE also shows potential, particularly for scenarios requiring high recall and class separability. These findings underline the importance of selecting appropriate resampling techniques based on specific use cases. Moreover, our study contributes to addressing the lack of consensus on the best imbalance handling method by providing a multi-metric evaluation framework that reveals the strengths and weaknesses of each technique across different classifiers. This framework establishes a foundation for standardized evaluation metrics, promoting comparability and reproducibility across datasets.

While resampling strategies offer a promising solution to address data imbalance, several challenges remain. These include computational overhead and training time, the sequence and proportion of oversampling and undersampling steps that can significantly influence classification outcomes, and the scalability and generalizability of methods across varying datasets and attack types. Additionally, the handling of sensitive data and the development of privacy-preserving approaches for imbalanced datasets are critical challenges that warrant further research. Future work will focus on integrating these techniques into real-world enterprise environments and advancing privacy-preserving SMOTE methods for sensitive data, ensuring both accuracy and privacy. By addressing these challenges, this research contributes to the development of more robust machine learning models capable of handling imbalanced datasets effectively.

# ACKNOWLEDGEMENT

The work of Arif Rahman Hakim was supported by the Lembaga Pengelola Dana Pendidikan (LPDP), Ministry of Finance of the Republic of Indonesia. Universitas Indonesia supported this work through the Hibah Publikasi Terindeks Internasional (PUTI) Kolaborasi Internasional (Q2) 2023 Scheme under Contract NKB-820/UN2.RST/HKP.05.00/2023.

# REFERENCES

[1] Cybersecurity ventures, "Cybercrime to cost the world $9,5 Trillion USD Annually in 2024," 2024. [Online]. Available: https://www.esentire.com/resources/library/2023-official-cybercrime-report

[2] P. Verma, J. G. Breslin, D. O'Shea, N. Mehta, N. Bharot, and A. Vidyarthi, "Leveraging Gametic Heredity in Oversampling Techniques to Handle Class Imbalance for Efficient Cyberthreat Detection in IIoT," *IEEE Trans. Consum. Electron.*, vol. 70, no. 1, pp. 1940–1951, 2024, doi: 10.1109/TCE.2023.3319439.

[3] W. P. Chawla, Nitesh V and Bowyer, Kevin W and Hall, Lawrence O and Kegelmeyer, "SMOTE: synthetic minority over-sampling technique," *J. Artif. Intell. Res.*, vol. 16, pp. 321–357, 2002.

[4] H. Han, W. Wang, and B. Mao, "Borderline-SMOTE : A New Over-Sampling Method in Imbalanced Data Sets Learning," pp. 878–879, 2005.

[5] G. Douzas, F. Bacao, and F. Last, "Improving imbalanced learning through a heuristic oversampling method based on k-means and SMOTE," *Inf. Sci. (Ny).*, vol. 465, pp. 1–20, 2018, doi: 10.1016/j.ins.2018.06.056.

[6] M. Mukherjee and M. Khushi, "Smote-enc: A novel smote-based method to generate synthetic data for nominal and continuous features," *Appl. Syst. Innov.*, vol. 4, no. 1, 2021, doi: 10.3390/asi4010018.
[7] G. E. A. P. A. Batista, R. C. Prati, and M. C. Monard, "A study of the behavior of several methods for balancing machine learning training data," *ACM SIGKDD Explor. Newsl.*, vol. 6, no. 1, pp. 20–29, 2004, doi: 10.1145/1007730.1007735.
[8] G. E. a P. a Batista, a L. C. Bazzan, and M. C. Monard, "Balancing Training Data for Automated Annotation of Keywords: a Case Study," *Rev. Tecnol. da Informação*, vol. 3, no. 2, pp. 15–20, 2004.
[9] N. H. N. B. M. Shahri, S. B. S. Lai, M. B. Mohamad, H. A. B. A. Rahman, and A. Bin Rambli, "Comparing the performance of adaboost, xgboost, and logistic regression for imbalanced data," *Math. Stat.*, vol. 9, no. 3, pp. 379–385, 2021, doi: 10.13189/ms.2021.090320.
[10] C. K. Aridas, S. Karlos, V. G. Kanas, N. Fazakis, and S. B. Kotsiantis, "Uncertainty Based Under-Sampling for Learning Naive Bayes Classifiers under Imbalanced Data Sets," *IEEE Access*, vol. 8, pp. 2122–2133, 2020, doi: 10.1109/ACCESS.2019.2961784.
[11] V. Ganganwar, "An overview of classification algorithms for imbalanced datasets," *Int. J. Emerg. Technol. Adv. Eng.*, vol. 2, no. 4, pp. 42–47, 2012, [Online]. Available: http://www.ijetae.com/files/Volume2Issue4/IJETAE_0412_07.pdf
[12] B. Pes, "Learning from high-dimensional and class-imbalanced datasets using random forests," *Information*, vol. 12, no. 8, p. 286, 2021.
[13] S. He, B. Li, H. Peng, J. Xin, and E. Zhang, "An Effective Cost-Sensitive XGBoost Method for Malicious URLs Detection in Imbalanced Dataset," *IEEE Access*, vol. 9, pp. 93089–93096, 2021, doi: 10.1109/ACCESS.2021.3093094.
[14] A. Kuppa, L. Aouad, and N. A. Le-Khac, "Linking CVE's to MITRE ATT and CK Techniques," *ACM Int. Conf. Proceeding Ser.*, 2021, doi: 10.1145/3465481.3465758.
[15] S. EL JAOUHARI, N. TAMANI, and R. I. JACOB, "Improving ML-based Solutions for Linking of CVE to MITRE ATT &CK Techniques," *2024 IEEE 48th Annu. Comput. Software, Appl. Conf.*, pp. 2442–2447, 2024, doi: 10.1109/compsac61105.2024.00392.
[16] I. Branescu, O. Grigorescu, and M. Dascalu, "Automated Mapping of Common Vulnerabilities and Exposures to MITRE ATT&CK Tactics," *Inf.*, vol. 15, no. 4, pp. 1–20, 2024, doi: 10.3390/info15040214.
[17] M. D. and R. R. Octavian Grigorescu , Andreea Nica, "CVE2ATT & CK : BERT-Based Mapping of CVEs to MITRE," *Algorithms*, pp. 1–22, 2022.
[18] T. Al-Shehari and R. A. Alsowail, "Random resampling algorithms for addressing the imbalanced dataset classes in insider threat detection," *Int. J. Inf. Secur.*, vol. 22, no. 3, pp. 611–629, 2023, doi: 10.1007/s10207-022-00651-1.
[19] I. Branescu, O. Grigorescu, and M. Dascalu, "Automated Mapping of Common Vulnerabilities and Exposures to MITRE ATT&CK Tactics," *Inf.*, vol. 15, no. 4, pp. 1–19, 2024, doi: 10.3390/info15040214.
[20] I. Branescu, "Open source the dataset and the code used for Automated Mapping CVE to ATT&CK," Github. Accessed: Oct. 16, 2024. [Online]. Available: https://github.com/readerbench/CVE2ATT-CK-tactics
[21] T. K. Ho and M. Basu, "Complexity measures of supervised classification problems," *IEEE Trans. Pattern Anal. Mach. Intell.*, vol. 24, no. 3, pp. 289–300, 2002, doi: 10.1109/34.990132.

https://doi.org/10.31436/iiumej.v26i1.3259

# ANALYSIS OF BRAIN TISSUE POROELASTIC PROPERTIES USING MULTISCALE MODELLING

**ABBAS SHABUDIN[1], MOHD JAMIL MOHAMED MOKHTARUDIN[1*], NIK ABDULLAH NIK MOHAMED[2], MOHD AKRAMIN MOHD ROMLAY[3]**

[1]*Faculty of Manufacturing and Mechatronic Engineering Technology, Universiti Malaysia Pahang Al-Sultan Abdullah, Pekan, Malaysia*

[2]*Faculty of Engineering, Technology and Built Environment, UCSI University Kuala Lumpur, Kuala Lumpur, Malaysia*

[3]*Faculty of Mechanical and Automotive Engineering Technology, Universiti Malaysia Pahang Al-Sultan Abdullah, Pekan, Malaysia*

**Corresponding author: mohdjamil@umpsa.edu.my*

*(Received: 15 April 2024; Accepted: 21 October 2024; Published online: 10 January 2025)*

***ABSTRACT:*** Mathematical models are developed to understand ischaemic stroke formation further and achieve treatment effectiveness. The existing poroelastic model of the brain assumed the brain as a homogenized structure with uniform capillary distribution. This paper describes using a multiscale modeling technique known as asymptotic expansion homogenization (AEH) to derive a new poroelastic model of brain tissue. The model consists of a homogenized governing macroscale model with the effective parameters determined from the microscale cell equations. The microscale cell equations are solved on a representative volume element (RVE) comprising brain tissue embedded with a capillary. Here, the effect of capillary tortuosity and radius on the effective parameters, which are the hydraulic conductivity of the capillary and interstitial space ($\boldsymbol{K}$ and $\boldsymbol{G}$), homogenous Biot's coefficient of the blood and interstitial space ($\alpha_c$ and $\alpha_t$), Young's modulus ($\bar{E}$) and Poisson's ratio ($\bar{\nu}$), are investigated. From the results, it is found that the percentage difference of $\boldsymbol{K}$ is 97.98% with increasing tortuosity, which suggests that $\boldsymbol{K}$ is significantly influenced by the shape of the capillary. Whereas the percentage difference of $\boldsymbol{G}$ is only 0.25%, which shows that it is unaffected by the shape of the capillary. Meanwhile, $\alpha_c$ and $\alpha_t$ decreases and increases with increasing tortuosity, respectively. Both $\bar{E}$ and $\bar{\nu}$ are not significantly affected by tortuosity, as the percentage difference for each is just 0.14% and 0.03%, respectively. In terms of capillary radius, it is found that $\boldsymbol{K}$ increases and $\boldsymbol{G}$ decreases with the increase of radius. Meanwhile, $\alpha_c$ increases with increasing radius while $\alpha_t$ instead shows the opposite trend. The percentage differences of 18.26% and 14.55% are observed for $\bar{E}$ and $\bar{\nu}$, respectively, implying that both parameters are significantly affected by the capillary radius. In conclusion, including capillary in the brain model significantly affects the effective parameters. Hence, important properties of the capillary, including shape and size, should be carefully emphasized so that accurate findings can be obtained when solving the poroelastic model of the brain.

***ABSTRAK:*** Model matematik dibangunkan untuk mendapatkan pemahaman lanjut tentang pembentukan strok iskemia supaya keberkesanan rawatan dapat dicapai. Model poroelastik otak yang sedia ada menganggap otak sebagai struktur homogen dengan taburan kapilari yang seragam. Makalah ini menerangkan penggunaan teknik pemodelan multiskala yang dikenali sebagai penghomogenan pengembangan asimtotik (PPA) untuk memperoleh model poroelastik baharu untuk tisu otak. Model ini terdiri daripada satu set model skala makro pentadbir homogen dengan parameter berkesan ditentukan daripada persamaan sel skala mikro. Persamaan sel skala mikro diselesaikan pada satu unsur isipadu perwakilan (RVE)

yang terdiri daripada tisu otak dengan kapilari yang tertanam. Di sini, kesan kelikuan dan jejari kapilari pada parameter berkesan, iaitu kekonduksian hidraulik ruang kapilari dan celahan ($\boldsymbol{K}$ dan $\boldsymbol{G}$), pekali Biot homogen bagi darah dan ruang celahan ($\alpha_c$ dan $\alpha_t$), modulus Young ($\bar{E}$) dan nisbah Poisson ($\bar{v}$), akan diselidiki. Daripada keputusan yang diperoleh, didapati perbezaan peratusan $\boldsymbol{K}$ ialah 97.98% dengan peningkatan kelikuan, yang menunjukkan bahawa $\boldsymbol{K}$ dipengaruhi oleh bentuk kapilari secara signifikan. Manakala peratusan perbezaan $\boldsymbol{G}$ hanyalah 0.25% menunjukkan bahawa ia tidak dipengaruhi oleh kelikuan. Sementara itu, $\alpha_c$ dan $\alpha_t$ masing-masing menurun dan meningkat dengan peningkatan kelikuan. Kedua-dua $\bar{E}$ dan $\bar{v}$ tidak terjejas dengan ketara oleh kelikuan kerana perbezaan peratusan bagi setiap satu ialah masing-masing hanya 0.14% dan 0.03%. Dari segi jejari kapilari pula, didapati $\boldsymbol{K}$ bertambah dan $\boldsymbol{G}$ berkurangan dengan pertambahan jejari. Sementara itu, $\alpha_c$ meningkat dengan peningkatan jejari, manakala $\alpha_t$ sebaliknya. Peratusan perbezaan 18.26% dan 14.55% diperhatikan untuk $\bar{E}$ dan $\bar{v}$ menunjukan bahawa kedua-dua parameter dipengaruhi dengan ketara oleh jejari kapilari. Kesimpulannya, kemasukan kapilari dalam model otak mempunyai kesan yang ketara terhadap parameter berkesan. Oleh itu, sifat penting kapilari termasuk bentuk dan saiz harus ditekankan dengan teliti supaya penemuan yang tepat boleh diperolehi apabila menyelesaikan model poroelastik otak.

***KEYWORDS:*** *Brain Tissue, Poroelastic Properties, Asymptotic Expansion Homogenization, Multiscale Modelling*

# 1. INTRODUCTION

The brain is a highly vascularized organ, making any computational modeling approach to include all the microvessels difficult [1]. The main problem is the computational cost, which can drastically increase with the number of microvessels in the model. According to Linninger et al., recent computational work can perform computation for 25,000 microvessels within a 30 $mm^3$ cube, and this, however, still does not represent a complete human brain [2]. Computer simulation of a brain with capillary networks is also time-consuming, so the model must be simplified.

Poroelastic model is an example of a modeling technique that models the interaction between these different phases in the brain tissue, such as the interstitial fluid, blood, and brain cells, and it has been used to study various brain diseases, such as hydrocephalus [3], head injury [4], and brain edema [5, 6]. The brain cell is modeled as a homogeneous linear elastic material. Meanwhile, the interstitial fluid and blood are modeled using Darcy's law, which usually has homogeneous permeabilities. However, this model assumed a homogeneous distribution of pores. This can be revised by considering the complex capillary network in the brain that has various sizes and shapes distributed unevenly in the brain [7]. This inhomogeneity may affect the poroelastic properties of the brain tissue.

To overcome this limitation, the multiscale modeling technique can include the inhomogeneity. Asymptotic expansion homogenization (AEH) is one of the multiscale modeling techniques that has been applied for homogenizing mechanical models of biological tissues and tumors [8-12]. Generally, the technique separates the governing model into homogenized macroscale equations of the brain. The effective parameters of the governing model can be obtained by solving a set of microscale cell equations on a representative volume element (RVE), in which, in the case of the brain, the RVE consists of solid cells and capillaries. The arrangement and dimension of the content of RVE may then affect the effective parameters of the homogenized macroscale equations.

https://doi.org/10.31436/iiumej.v26i1.3259

This article investigates the effect of capillary tortuosity and radius using the AEH technique. Applying the AEH technique will produce a new set of homogenized macroscale equations with the respective effective parameters to be determined by solving the microscale cell equations [13] on an RVE. The RVE used in this article will have a capillary with various radius and tortuosity levels, so its effect on the effective parameters can be investigated.

## 2. METHODOLOGY

This section discusses the process for obtaining the homogenized macroscale and respective microscale cell equations using the AEH technique. Then, the RVE used will be described.

### 2.1. Homogenized Governing Macroscale Equation

Assumed that the volume of brain tissue, $\Omega = \Omega_t \cup \Omega_c$, is made up of the poroelastic brain tissue, $\Omega_t$ and blood compartment, $\Omega_c$, respectively. The interface between these phases is represented by $\Gamma$. Figure 1 illustrates a portion of the brain that is made up of poroelastic tissue and capillary phases. The brain tissue and blood are originally governed by the poroelastic model and Navier-Stokes equations, respectively.

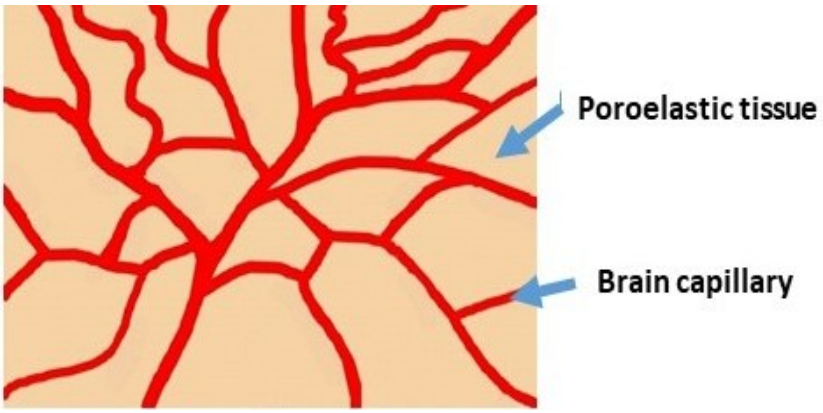


Figure 1. 2D representation of poroelastic brain tissue with capillary.

Assumed that the relationship of the distance between adjacent capillaries $d$ and the normal tissue length, $L$ follows the ratio $\epsilon$ as given by Equation (1):

$$\epsilon = \frac{d}{L} \tag{1}$$

which implies that $d$ is much smaller than $L$. Thus, the length separation between these is very large, allowing for the AEH technique to be applied. Then, two spatial variables $y$ and $x$ for microscale and macroscale, respectively, are defined as:

$$x = \epsilon y \tag{2}$$

Figure 2 illustrates a small portion of the brain consisting of repeating units of brain tissue. Applying the AEH can determine the effective parameters by solving the microscale cell equations on a single RVE without solving the overall brain model. This technique can significantly reduce the computational cost and time.

https://doi.org/10.31436/iiumej.v26i1.3259

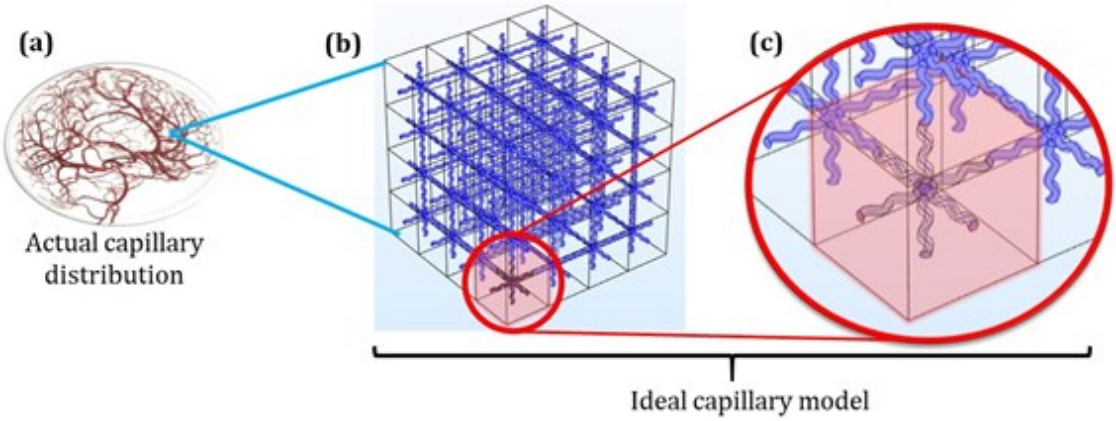


Figure 2. Illustration of repeating units of brain tissue.

### 2.2. Homogenized Macroscale Equations

The homogenized macroscale stress balance equation is given as:

$$\nabla_{\mathrm{x}} \cdot \sigma_H = 0 \tag{3}$$

Here, the effective stress, $\sigma_H$ is defined as:

$$\sigma_H = \bar{C} : \nabla_{\mathrm{x}} \boldsymbol{u} - \alpha_c P_c - \alpha_t P_t \tag{4}$$

Here, $\boldsymbol{u}$ is the tissue displacement, $P_c$ is the blood pressure within capillary and $P_t$ is interstitial fluid pressure. Moreover, $\alpha_c$, and $\alpha_t$ are the Biot's coefficient for blood and interstitial fluid, respectively, and $\bar{C} = \bar{C}(\bar{E}, \bar{\nu})$ is the effective elasticity tensor defined using the effective Young's modulus, $\bar{E}$ and Poisson's ratio, $\bar{\nu}$. These are effective parameters, which can be determined as follows:

$$\bar{C} = \langle (C\boldsymbol{L}C + C) \rangle_{\mathrm{t}} \tag{5}$$

$$\alpha_c = (\phi_c \mathbf{I} - \langle C : \boldsymbol{Q} \rangle_{\mathrm{t}}) \tag{6}$$

$$\alpha_t = (\langle C : \boldsymbol{Q} \rangle_{\mathrm{t}} + \phi_t \mathbf{I}) \tag{7}$$

where $\phi_c$ and $\phi_t$ represent the volume ratio for the blood and interstitial fluid, respectively and $\mathbf{I}$ is the identity tensor. Meanwhile, the tensors $\boldsymbol{L}$ and $\boldsymbol{Q}$ can be obtained from the microscale cell equations.

On the other hand, the two fluid pressures are governed by the pressure balance equations as follows:

$$0 = -\nabla_{\mathrm{x}} \cdot \langle \boldsymbol{w}_{\mathrm{c}} \rangle_{\mathrm{c}} 0 + \frac{|\Gamma|}{|\Omega|} \bar{L}_p \Phi_{c \to t} \tag{8}$$

$$0 = -\nabla_{\mathrm{x}} \cdot \langle \boldsymbol{w}_{\mathrm{t}} \rangle_{\mathrm{t}} 0 - \frac{|\Gamma|}{|\Omega|} \bar{L}_p \Phi_{c \to t} \tag{9}$$

where $|\Gamma|$, $|\Omega|$, and $\bar{L}_p$ are the surface area of Γ, the volume of RVE, and the hydraulic conductivity through capillary walls, respectively. Meanwhile, the term $\Phi_{c \to t}$ is defined as follows:

$$\Phi_{c \to t} = P_c - P_t \tag{10}$$

The average fluid velocities $\langle \boldsymbol{w}_c \rangle_c$ and $\langle \boldsymbol{w}_t \rangle_t$ are defined using the respective Darcy's law:

$$\langle \boldsymbol{w}_c \rangle_{\mathrm{c}} = -\boldsymbol{K} \nabla_{\mathrm{x}} P_c \tag{11}$$

https://doi.org/10.31436/iiumej.v26i1.3259

$$\langle \boldsymbol{w}_t \rangle_{\mathrm{t}} = -\bar{k}\boldsymbol{G}\nabla_{\mathrm{x}} P_t \tag{12}$$

Here, the terms $\boldsymbol{K}$ and $\boldsymbol{G}$ the effective parameters can also be obtained from the microscale cell equations. These are the effective hydraulic conductivity for the blood and interstitial fluid. Meanwhile, $\bar{k}$ is the original brain interstitial fluid hydraulic conductivity.

## 2.3. Microscale Cell Equations

There are four microscale cell equations to be solved on an RVE.

### *2.3.1 Laplace Cell Equations*

The tensor $\boldsymbol{G}$ can be calculated using Eq. (13):

$$\boldsymbol{G} = \phi_t \mathbf{I} - \langle \left(\nabla_{\mathrm{y}} P_t\right)^{\mathrm{T}} \rangle_{\mathrm{t}} \tag{13}$$

where $P_t$ can be determined as follows:

$$\nabla_{\mathrm{y}}^2 P_t = 0 \text{ in } \Omega_{\mathrm{t}} \tag{14}$$

$$\left(\nabla_y \boldsymbol{P}_t\right)\boldsymbol{n} = \boldsymbol{n} \text{ on } \Gamma \tag{15}$$

$$\langle \boldsymbol{P}_t \rangle_t = 0 \text{ in } \Omega_{\mathrm{t}} \tag{16}$$

### *2.3.2 Stoke's Cell Equations*

The tensor $\boldsymbol{K}$ can be calculated using Eq. (17):

$$\boldsymbol{K} = \langle \boldsymbol{W} \rangle_{\mathrm{c}} \tag{17}$$

where $\boldsymbol{W}$ and $P_c$ are obtained as follows:

$$\nabla_{\mathrm{y}}^2 \boldsymbol{W}^{\mathrm{T}} - \nabla_{\mathrm{y}} P_c + \mathbf{I} = 0 \text{ in } \Omega_{\mathrm{c}} \tag{18}$$

$$\nabla_{\mathrm{y}} \cdot \boldsymbol{W}^{\mathrm{T}} = 0 \text{ in } \Omega_{\mathrm{c}} \tag{19}$$

$$\boldsymbol{W}^{\mathrm{T}} = 0 \text{ on } \Gamma \tag{20}$$

$$\langle P_c \rangle_{\mathrm{c}} = 0 \text{ in } \Omega_c \tag{21}$$

### *2.3.3 One-elastic Cell Equations*

The tensor $\boldsymbol{Q}$ can be calculated using Eq. (22):

$$\boldsymbol{Q} = \langle \nabla_{\mathrm{y}} \boldsymbol{a} \rangle \tag{22}$$

where $\boldsymbol{a}$ can be determined as follows:

$$\nabla_{\mathrm{y}} \cdot \left(C \nabla_{\mathrm{y}} \boldsymbol{a}\right) = 0 \text{ in } \Omega_t \tag{23}$$

$$\left(C \nabla_{\mathrm{y}} \boldsymbol{a}\right)\boldsymbol{n} = -\boldsymbol{n} \text{ on } \Gamma \tag{24}$$

$$\langle \boldsymbol{a} \rangle_{\mathrm{t}} = 0 \tag{25}$$

where $\boldsymbol{n}$ is the normal vector to the surface $\Gamma$, and $C = C(E, v)$, where $E$ and $v$ are the original brain tissue Young's modulus and Poisson's ratio, respectively.

### *2.3.4 Six-elastic Cell Equations*

The tensor $\boldsymbol{L}$, is defined using Equation (26):

https://doi.org/10.31436/iiumej.v26i1.3259

$$\boldsymbol{L} = \langle \nabla_{\mathbf{y}} A \rangle \tag{26}$$

where $A$ can be calculated as follows:

$$\frac{\partial}{\partial y_j} \cdot \left( \mathbb{C} \frac{\partial A_{kmn}}{\partial y_l} \right) = 0 \text{ in } \Omega_t \tag{27}$$

$$\mathbb{C} \frac{\partial A_{kmn}}{\partial y_l} n_j = -\delta_{im} \delta_{jn} n_j \text{ on } \Gamma \tag{28}$$

$$\langle A \rangle_{\mathrm{t}} = 0 \tag{29}$$

### 2.4. Capillary RVE

In this study, the RVE used is shown in Figure 3, which is made of a cube and an intersection of cylinders, representing the brain tissue and capillary, respectively. The tortuosity level is determined using the function, $f(s) = Asin(2\pi\omega s/l)$, where $\omega$ and $A$ are the capillary tortuosity frequency and amplitude, respectively. Furthermore, Figure 4 shows examples of microstructure with different radius variations. All the analyses performed in this study are dimensionless and solved using the finite element software COMSOL Multiphysics 5.6a.

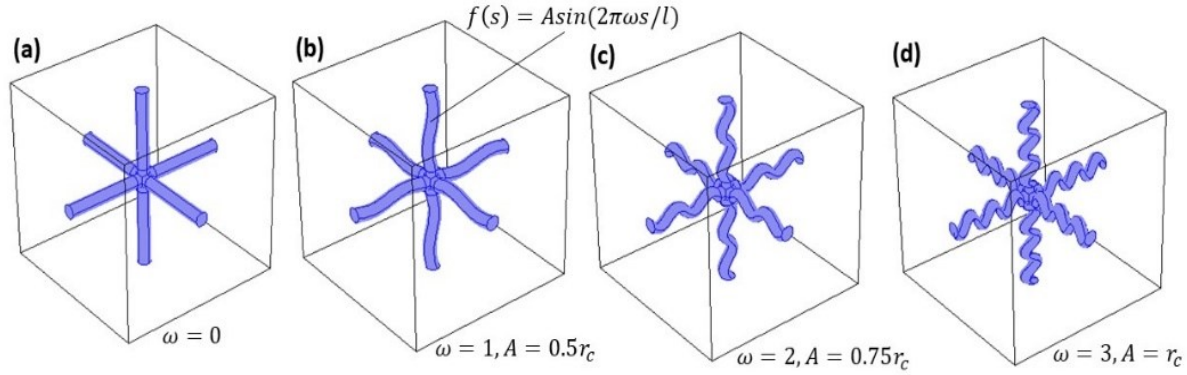


Figure 3. 4 different capillary shapes where (a) consists of straight capillary without tortuosity and (d) represents the most tortuous capillary.

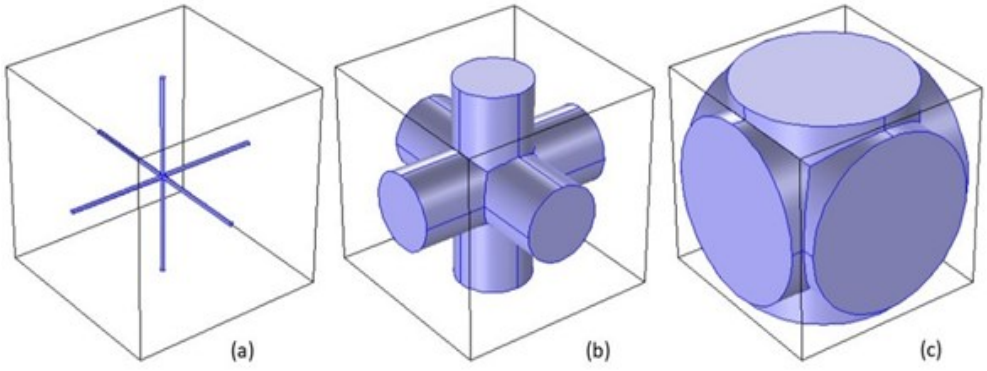


Figure 4. Example of 3 different capillary sizes used for the simulation.

## 3. RESULTS

The results section will discuss the variations of all the effective parameters with capillary tortuosity in the microstructure RVE.

https://doi.org/10.31436/iiumej.v26i1.3259

### 3.1. Examples of Microscale Cell Equations Results

Figures 5 and 6 show the example field variables distributions for the four cell equations for microstructure with $\omega = 0$. The results are then used to determine the tensors $\boldsymbol{G}$, $\boldsymbol{K}$, $\boldsymbol{Q}$ and $\boldsymbol{L}$ based on Eqs. (13), (17), (22), and (26).

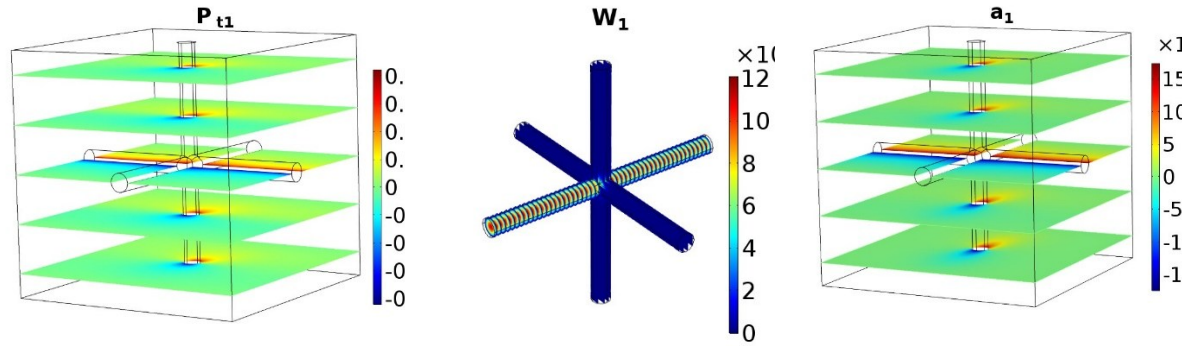


(a) (b) (c)

Figure 5. Example of field variable distribution for (a) Laplace's cell equation, (b) Stokes' cell equation, and (c) One-elastic cell equation.

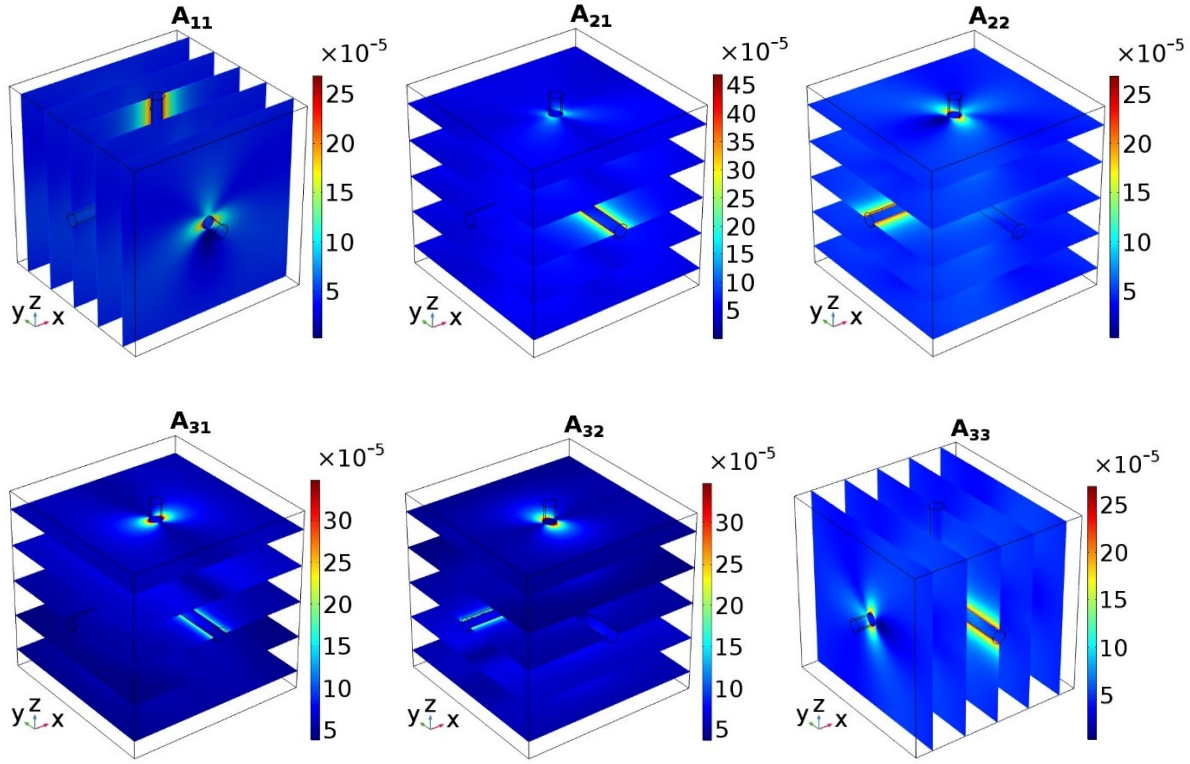


Figure 6. Example of field variable distribution for Six-elastic cell equation.

Figure 7 shows the volume changes in (a) capillary and (b) interstitial space with capillary tortuosity. As the tortuosity increases, the capillary volume decreases. This is because when the capillary is bent at the curve, the space at the curve becomes narrower, as shown in Figure 3(d). Since the volume of a cube is fixed, a smaller volume of capillary results in a larger volume of the interstitial space, as shown in Figure 7(b).

https://doi.org/10.31436/iiumej.v26i1.3259

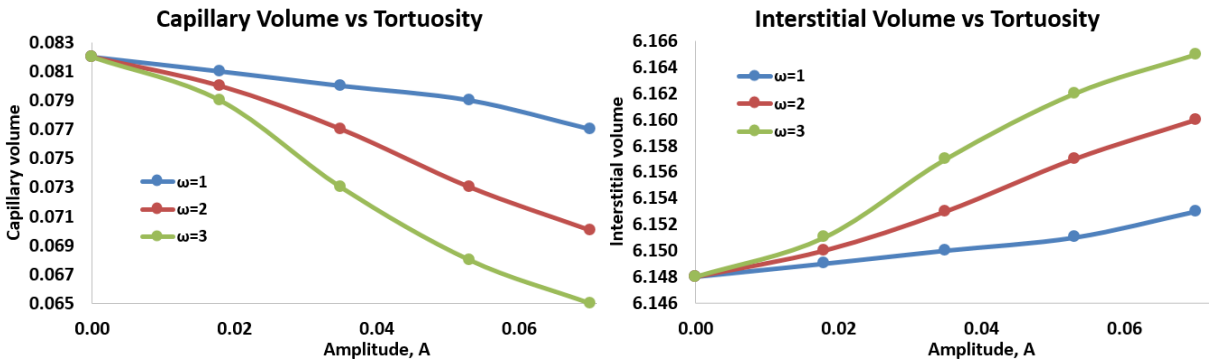


(a) (b)

Figure 7: Capillary and interstitial volume variation for each capillary tortuosity setting.

### 3.2. Effective Blood Conductivity Tensor, $\boldsymbol{K}$

Figure 8(a) shows that $\boldsymbol{K}$ decreases as the tortuosity increases for $\omega = 1$ to $\omega = 3$. The percentage difference in $\boldsymbol{K}$ between $\omega = 1$ and $\omega = 3$ is 97.98%, and this shows that $\boldsymbol{K}$ is significantly affected by capillary tortuosity. Meanwhile, Figure 8(b) shows that $\boldsymbol{K}$ changes exponentially with increasing microstructure capillary radius. This means that bigger capillaries allow for smoother blood flow due to lower flow resistance [14].

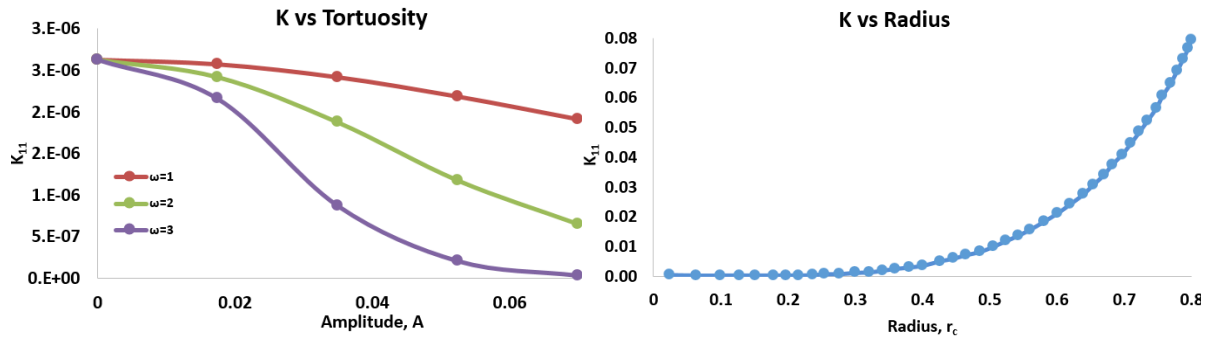


(a) (b)

Figure 8. Graph of $\boldsymbol{K}$ against (a) tortuosity and (b) radius.

### 3.3. Effective Interstitial Fluid Conductivity Tensor, $\boldsymbol{G}$

Figure 9(a) shows that $\boldsymbol{G}$ increases when tortuosity increases. The percentage difference of $\boldsymbol{G}$ is only about 0.25% between $\omega = 1$ and $\omega = 3$. This shows that $\boldsymbol{G}$ is not affected by capillary tortuosity. Whereas Figure 9(b) shows $\boldsymbol{G}$ decreases with increasing capillary radius. This is because bigger capillary minimizes the interstitial fluid volume and hinders the interstitial fluid flow.

https://doi.org/10.31436/iiumej.v26i1.3259

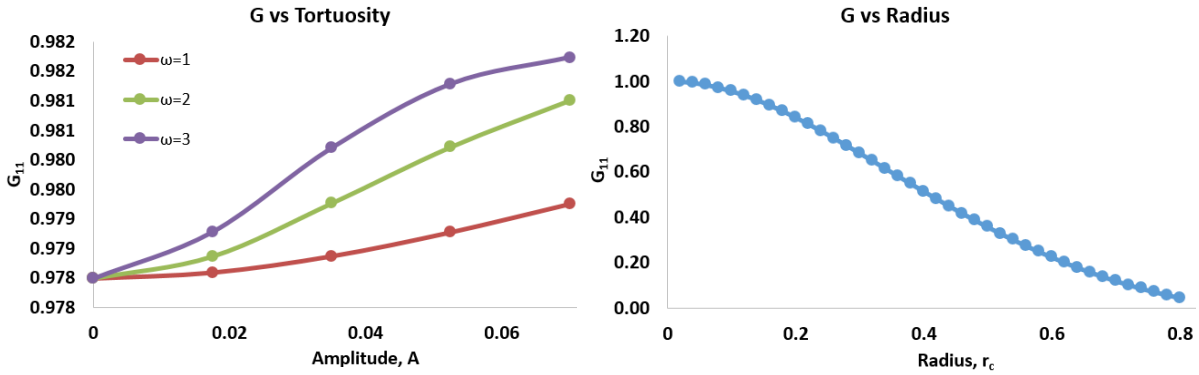


(a) (b)

Figure 9. Effective parameter $\boldsymbol{G}$ against (a) tortuosity and (b) radius.

### 3.4. Effective Biot's Coefficients, $\alpha_c$ and $\alpha_t$

In Figure 10(a), the effective blood Biot's coefficient, $\alpha_c$ decreases as the tortuosity increases from $\omega_1$ to $\omega_3$. Modification of capillary tortuosity, which involves changes in capillary volume, will affect $\alpha_c$ because this parameter is dependent on volume changes [11]. Meanwhile, Figure 10(b) shows the effective interstitial fluid Biot's coefficient, $\alpha_t$, which increases with increasing capillary tortuosity. This implies that more interstitial fluid can be removed from the tissue interstitial by increasing the capillary tortuosity [11].

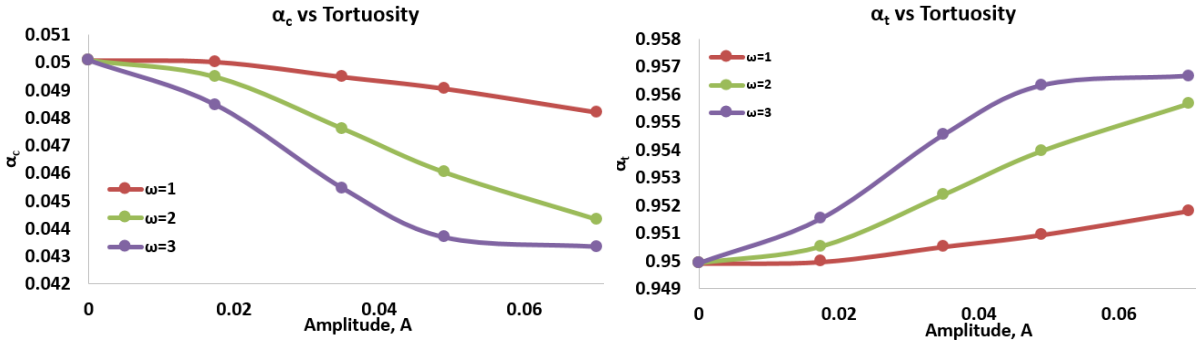


(a) (b)

Figure 10. Graphs of (a) $\alpha_c$ and (b) $\alpha_t$ against tortuosity.

Figure 11 shows the changes of $\alpha_c$ and $\alpha_t$ against radius. As the radius increases, $\alpha_c$ also increases because a bigger capillary volume allows for more blood to be removed from the blood compartment. Meanwhile, $\alpha_t$ decreases as the radius increases. This is because there is a lesser volume of interstitial fluid in the microstructure with a large capillary radius.

https://doi.org/10.31436/iiumej.v26i1.3259

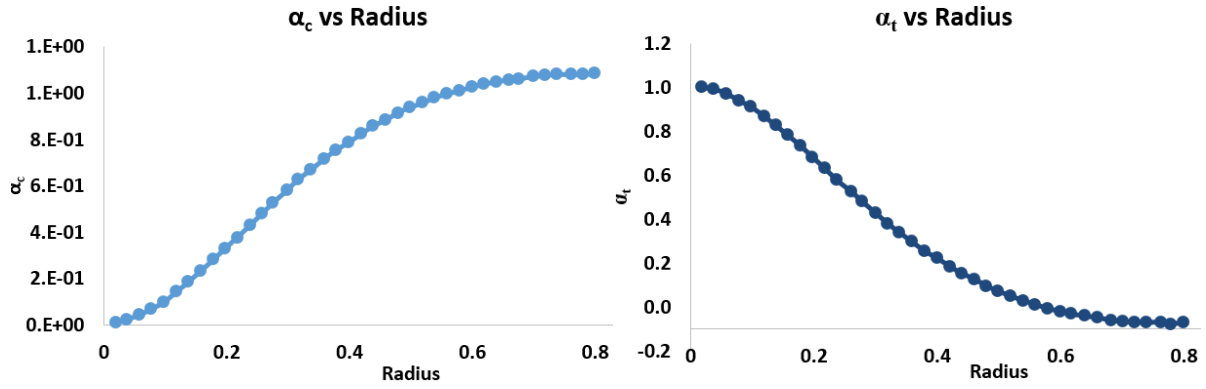


(a) (b)

Figure 11. Graphs of (a) $\alpha_c$ and (b) $\alpha_t$ against radius.

### 3.5. Effective Moduli

Figure 12 shows the changes in effective moduli with tortuosity. The percentage difference for both $\bar{E}$ and $\bar{\nu}$ are only 0.14% and 0.03%, respectively. The small percentage difference indicates that the tortuosity does not affect the effective elastic moduli. Figure 13 shows the changes in effective moduli with radius. The values of $\bar{E}$ and $\bar{\nu}$ reduce for up to the radius of about 0.4. Then, the values increase as the radius increases up to 0.8. The percentage changes of $\bar{E}$ and $\bar{\nu}$ from the maximum to the minimum values are 18.26% and 14.55%, respectively.

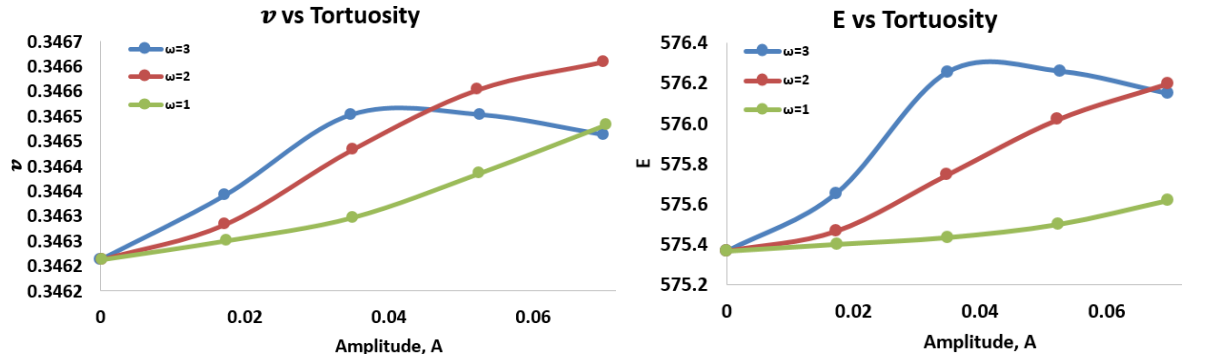


(a) (b)

Figure 12. Graphs of (a) $\bar{\nu}$ and (b) $\bar{E}$ against tortuosity.

As shown in Figure 13, both $\bar{E}$ and $\bar{\nu}$ increase when the capillary tortuosity increases. As mentioned earlier, geometry with high capillary tortuosity has low vascular volume with bigger interstitial tissue volume. Thus, it becomes stiffer (high $E$) as compared to the geometry with low capillary tortuosity. However, the percentage difference of both $\bar{E}$ and $\bar{\nu}$ from the results are very small, which implies that the tortuosity is insignificantly affecting $\bar{E}$ and $\bar{\nu}$. When varying the radius, it is expected that both $\bar{E}$ and $\bar{\nu}$ decrease as the radius increases since the geometry becomes more porous. However, the simulation outcome only meets our expectations for a radius smaller than 0.4. After 0.4, $\bar{E}$ and $\bar{\nu}$ increase with the capillary radius. For capillary radius bigger than 0.4, both $\bar{E}$ and $\bar{\nu}$ are only influenced by the volume of the capillary. Therefore, as the capillary volume is made larger, $\bar{E}$ and $\bar{\nu}$ obtained are also larger.

https://doi.org/10.31436/iiumej.v26i1.3259

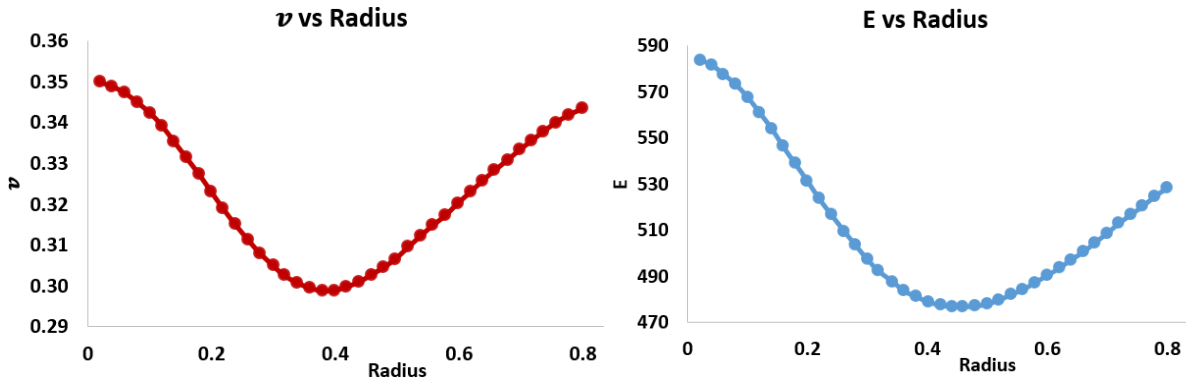


(a) (b)

Figure 13. Graphs of (a) $\bar{v}$ and (b) $\bar{E}$ against radius.

## 4. DISCUSSION

In this study, the AEH technique was used to derive the microscale cell equations to determine effective parameters for the homogenized macroscale governing equations of the brain. The effective blood hydraulic conductivity, $\boldsymbol{K}$ describes the ability of blood to move through the capillaries [15], in which it depends on several factors, such as the particle size, surface roughness, dimension, structure, and the interconnection between capillaries [16]. The value $\boldsymbol{K}$ obtained here shows a decreasing trend against the capillary tortuosity. The blood flow within a highly tortuous capillary becomes more difficult due to higher flow resistance compared to a less tortuous capillary, resulting in a lower $\boldsymbol{K}$. A similar argument applies to the capillary radius, as can be seen from the results that a bigger capillary has a higher $\boldsymbol{K}$ due to lower flow resistance. Furthermore, the flow resistance is inversely proportional to the radius, following Poiseuille's law [17]. Both tortuous and capillary with small radii have significantly low $\boldsymbol{K}$. These conditions can be used to model blood flow disruption at the macroscale level, representing an ischaemic condition.

Meanwhile, the effective interstitial fluid hydraulic conductivity, $\boldsymbol{G}$ explains the ability of the interstitial fluid to move through interstitial space. This parameter is also highly dependent on the interstitial volume. As the capillary tortuosity increases, the changes in $\boldsymbol{G}$ are very small. This shows that the tortuosity does not affect the interstitial fluid flow. However, $\boldsymbol{G}$ decreases with increasing capillary radius, implying that $\boldsymbol{G}$ is affected by the capillary lumen size. This situation can be explained by the fixed volume of our geometry used in the simulation. As the size of the capillary increases, it occupies more space in the microstructure RVE and reduces the volume of the interstitial fluid. This causes the interstitial fluid flow to become more difficult, hence lowering the hydraulic conductivity [11].

The tensors $\boldsymbol{Q}$ and $\boldsymbol{L}$ have no physical meaning, but it is required in determining the parameters $\alpha_c$ and $\alpha_t$ as well as the effective elastic moduli. Biot's coefficient is a parameter that measures the ratio of the fluid volume squeezed out to the volume change in the poroelastic medium under compression while allowing the fluid to escape [18]. This means that the coefficient depends on the microstructure RVE and capillary volumes. High tortuosity creates a smaller volume of capillary compared to a straight one [8]. This validates our findings whereby $\alpha_c$ decreases and $\alpha_t$ increases with increasing capillary tortuosity. Similarly, for varying radii, a capillary with a bigger radius has greater vascular volume, and hence, $\alpha_c$ and $\alpha_t$ increases and decreases, respectively.

Meanwhile, the effective elastic moduli calculated here are the effective Young's modulus, $\bar{E}$ and Poisson's ratio, $\bar{\nu}$. Young's modulus is defined as the ratio of the applied axial stress to the induced local axial strain in a solid material [19], whereas Poisson's ratio provides a measure of tissue compressibility [20]. Our findings show that the effective elastic moduli changes with the capillary tortuosity and radius. Changes in $\bar{E}$ and $\bar{\nu}$ in biological tissues may be used to indicate the initiation of brain pathological conditions [20]. Hence, sufficient information on these parameters could be used to diagnose a particular brain disease better.

## 5. CONCLUSION

Application of AEH technique has produced the homogenized macroscale equations with respective microscale cell problems, which are then solved a brain geometry with embedded capillary inside to obtain parameter $\boldsymbol{K}$, $\boldsymbol{G}$, $\alpha_c$, $\alpha_t$, $\bar{E}$ and $\bar{\nu}$. The relationship between each parameter and the shapes and sizes of capillaries has been investigated and analyzed. It is found that the value of $\boldsymbol{K}$ is affected by the shape (tortuosity), meanwhile $\boldsymbol{G}$, $\bar{E}$, and $\bar{\nu}$ are affected by the size of the capillary. Only $\alpha_c$ and $\alpha_t$ are influenced by both shape and size. In short, the addition of capillaries greatly impacts the outcome of the simulation of the human brain. Since stroke formation involves the reduction of blood flow in the capillary, all important properties of the capillary should be precisely emphasized so that the simulation outcomes can be improved and used to solve the macroscale equations in a bigger brain geometry.

## ACKNOWLEDGEMENT

This research is supported by the UMP Fundamental Research Grant (RDU220367) and the UMP International Publication Grant (RDU203302).

## REFERENCES

[1] Peyrounette, M., et al., Multiscale modelling of blood flow in cerebral microcirculation: Details at capillary scale control accuracy at the level of the cortex. PloS one, 2018. 13(1): p. e0189474.

[2] Linninger, A., et al., Cerebral microcirculation and oxygen tension in the human secondary cortex. Annals of biomedical engineering, 2013. 41(11): p. 2264-2284.

[3] Tully, B. and Y. Ventikos, Cerebral water transport using multiple-network poroelastic theory: application to normal pressure hydrocephalus. Journal of Fluid Mechanics, 2011. 667: p. 188-215.

[4] Lambride, C., et al., Decompressive craniectomy of post-traumatic brain injury: an in silico modelling approach for intracranial hypertension management. Scientific Reports, 2020. 10(1): p. 18673.

[5] Mohamed Mokhtarudin, M.J. and S. Payne, Mathematical model of the effect of ischemia–reperfusion on brain capillary collapse and tissue swelling. Mathematical Biosciences, 2015. 263: p. 111-120.

[6] Mohamed Mokhtarudin, M.J., A. Shabudin, and S.J. Payne. Effects of Brain Tissue Mechanical and Fluid Transport Properties during Ischaemic Brain Oedema: A Poroelastic Finite Element Analysis. in 2018 IEEE-EMBS Conference on Biomedical Engineering and Sciences (IECBES). 2018.

[7] Cassot, F., et al., A novel three-dimensional computer-assisted method for a quantitative study of microvascular networks of the human cerebral cortex. Microcirculation, 2006. 13(1): p. 1-18.

[8] Penta, R. and D. Ambrosi, The role of the microvascular tortuosity in tumor transport phenomena. Journal of theoretical biology, 2015. 364: p. 80-97.

[9] Mascheroni, P. and R. Penta, The role of the microvascular network structure on diffusion and consumption of anticancer drugs. International Journal for Numerical Methods in Biomedical Engineering, 2017. 33(10): p. e2857.

[10] Shabudin, A., M.H. Jasni, and M.J.M. Mokhtarudin. Brain capillary geometry development for multiscale modelling study. in Engineering Technology International Conference (ETIC 2022). 2022.

[11] Mohamed Mokhtarudin, M.J., et al., Multiscale modelling of brain tissue oxygen and glucose dynamics in tortuous capillary during ischaemia-reperfusion. Applied Mathematical Modelling, 2022. 109: p. 358-373.

[12] Shabudin, A., et al. Multiscale Modelling of 3-Dimensional Brain Tissue with Capillary Distribution. in 2020 IEEE-EMBS Conference on Biomedical Engineering and Sciences (IECBES). 2021.

[13] Penta, R. and J. Merodio, Homogenized modeling for vascularized poroelastic materials. Meccanica, 2017. 52(14): p. 3321-3343.

[14] Davis, H. and D. Attwell, A tight squeeze: how do we make sense of small changes in microvascular diameter? The Journal of physiology, 2023.

15] Ray, L.A. and J.J. Heys, Fluid flow and mass transport in brain tissue. Fluids, 2019. 4(4): p. 196.

[16] Papadopol, C., Determination of soil hydraulic conductivity in nurseries and plantations. Tree planters' notes, 2005.

[17] Agarwal, N. and R.O. Carare, Cerebral Vessels: An Overview of Anatomy, Physiology, and Role in the Drainage of Fluids and Solutes. Frontiers in Neurology, 2021. 11.

[18] Biot, M.A., General theory of three-dimensional consolidation. Journal of applied physics, 1941. 12(2): p. 155-164.

[19] Majumder, S., M.T. Islam, and R. Righetti, Estimation of Mechanical and Transport Parameters in Cancers Using Short Time Poroelastography. IEEE Journal of Translational Engineering in Health and Medicine, 2022. 10: p. 1-11.

[20] Islam, M.T., et al., Non-invasive imaging of Young's modulus and Poisson's ratio in cancers in vivo. Scientific Reports, 2020. 10(1): p. 7266.

https://doi.org/10.31436/iiumej.v62i1.3236

# SOLAR-DRIVEN WATER PURIFICATION: ADVANCING PVA-CHITOSAN/PANI HYDROGEL TO ENHANCE SOLAR VAPOR GENERATION FOR FRESHWATER TREATMENT

**FLORA SERATI[1], SYAZWANI MOHD ZAKI[2*], AHMAD AKID ZULKIFLI[2], SITI RABIZAH MAKHSIN[3]**

[1]*Department of Electrical and Computer Engineering, Kulliyah of Engineering, International Islamic University Malaysia, PO Box 50728 Kuala Lumpur, Malaysia.*
[2]*Department of Manufacturing and Materials Engineering, Kulliyah of Engineering, International Islamic University Malaysia, PO Box 50728 Kuala Lumpur, Malaysia.*
[3]*Micro-Nano ElectroMechanical System Lab (MiNEMS Lab), School of Mechanical Engineering, College of Engineering, University Technology MARA, 40450, Shah Alam, Selangor, Malaysia.*

**Corresponding author: syazwani_mohdzaki@iium.edu.my*

*(Received: 26 March 2024; Accepted: 18 June 2024; Published online: 10 January 2025)*

***ABSTRACT:*** Water scarcity is a global issue that affects human beings' ability to live healthily, and immediate action must be taken to alleviate this issue. Despite advances in water purification, current technologies exhibit pronounced deficiencies. Existing filtration systems and other conventional methods remain energy-intensive, with escalating maintenance costs at large-scale production. The advancement of innovative materials holds significant potential to revolutionize the landscape of solar water purification. While conventional solar vapor generation (SVG) technology has faced challenges in achieving high water yields under natural sunlight conditions, innovating new materials can substantially reduce the energy requirements for water vaporization. Herein, we introduce our outstanding light-absorbing hydrogel consisting of polyvinyl alcohol (PVA) and chitosan (CS) as the substrate with the addition of polyaniline (PANi) as the light absorber for water evaporation via SVG technique. In this study, PVA-CS/PANi hydrogels were prepared with distinct concentrations of PVA and denoted as PVA-CS/PANi/1.3 mol.%, PVA-CS/PANi/2.7 mol.% and PVA-CS/PANi/3.9 mol.%. Copolymerization of PVA-CS hydrogels with PANi was conducted via solution polymerization to incorporate PANi into the hydrogel network structure. Incorporating light-absorbing materials, such as PANi, into the hydrogel network structure is expected to enhance the absorption properties. The morphological structure of the obtained hydrogels was analyzed by scanning electron microscopy (SEM). In contrast, the physicochemical and mechanical properties of the hydrogels were evaluated by dynamic light scattering (DLS), FTIR, swelling test and rheology. From the analysis demonstrated in this work, the structure of PVA-CS/PANi hydrogels is significantly influenced by the concentration of PVA. The hydrogels' diameter and polydispersity index (PDI) were 146 nm and 0.331, respectively. The storage modulus (G') of PVA-CS/PANi/3.9 mol.% depicted the highest value of 2356 Pa compared to PVA-PVA-CS/PANi/1.3 mol.%, which depicted the G' value of 1173 Pa. From FTIR analysis, the absorption band was found between 3600 to 3000 $cm^{-1}$, attributed to O-H and N-H groups of PVA and PANi, while the PVA-CS with the presence of PANi shows characteristic bands at 1620 $cm^{-1}$, 1508 $cm^{-1}$, and 1298 $cm^{-1}$. The microporous structure of PVA-Chitosan/PANi hydrogels increases with a higher concentration of PVA, demonstrating the degree of cross-linking of PANi, which contributes to the rigid structure of porous hydrogel. The influence of PVA concentration on the hydrogel's porous structure and surface area allows for greater dye adsorption. As demonstrated by PVA-CS/PANi/3.9 mol.%, it shows higher absorption of Methylene Blue (MB) into the structure. The performance of SVG using PVA-CS/PANi/3.9 mol.% hydrogels

was measured, and the efficiency was found to be 69.8% under 1 sun with efficient temperature distribution on the surface. This finding indicates the capability of PVA-Chitosan/PANi/3.9 mol.% hydrogels in generating multi-scattering effects of natural sunlight for high-efficiency light-to-heat conversion via SVG.

***ABSTRAK:*** Kekurangan air adalah isu global yang menjejaskan kehidupan manusia untuk hidup sihat, dan tindakan drastik perlu diambil bagi mengatasi masalah ini. Walaupun terdapat kemajuan dalam pembersihan air, kelemahan ketara masih wujud dalam teknologi semasa. Sistem penapisan sedia ada dan kaedah konvensional lain kekal menggunakan tenaga dengan intensif, di tambah kos penyelenggaraan yang tinggi pada pengeluaran berskala besar. Pembangunan bahan inovatif mempunyai potensi besar bagi merevolusi pembersihan air dengan suria. Walaupun teknologi penjanaan wap suria konvensional (SVG) sedang menghadapi cabaran dalam mencapai hasil air yang tinggi di bawah keadaan cahaya matahari semula jadi, inovasi menggunakan bahan baharu dapat mengurangkan keperluan tenaga dengan berkesan bagi tujuan pengewapan air. Di sini, kami memperkenalkan hidrogel penyerap cahaya yang terdiri daripada polivinil alkohol (PVA) dan kitosan (CS) sebagai substrat dan dengan penambahan polianilin (PANi) sebagai penyerap cahaya bagi penyejatan air melalui teknik SVG. Kajian ini mensintesis hidrogel PVA-CS dengan penambahan PANi dengan kepekatan PVA berbeza; Hidrogel PVA-CS dengan PANi ditandakan sebagai PVA-CS/PANi/1.3 mol.%, PVA-CS/PANi/2.7 mol.%, dan PVA-CS/PANi/3.9 mol.%. Hidrogel PVA-CS dengan kopolimer PANi telah disintesis dengan pempolimeran larutan bagi meresapi PANi ke dalam struktur rangkaian hidrogel. Dengan mengadaptasi material penyerap cahaya seperti PANi ke dalam struktur rangkaian hidrogel, diharapkan dapat membantu dalam penyerapan. Struktur hidrogel yang diperolehi telah dicuba dari segi morfologi (SEM), sifat fisiokimia dan mekanikal (DLS, FTIR, ujian bengkak dan reologi). Melalui analisis ini, kepekatan PVA mempengaruhi struktur hidrogel PVA-CS/PANi dengan ketara. Diameter hidrodinamik hidrogel PVA-Chitosan yang dihasilkan ditentukan oleh DLS. Diameter dan indeks polidispersi (PDI) didapati masing-masing 146 nm dan 0.331. Modulus penyimpanan hidrogel PVA-CS untuk semua sistem ditentukan oleh reologi. Modulus penyimpanan (G') PVA-CS/PANi/3.9 mol.% mempunyai nilai tertinggi 2356 Pa berbanding PVA-PVA-CS/PANi/1.3 mol.% sebanyak G' 1173 Pa. Melalui Analisis FTIR, jalur serapan didapati antara 3600 hingga 3000 cm-1, dikaitkan dengan kumpulan O-H dan N-H PVA dan PANi manakala PVA-CS dengan kehadiran PANi menunjukkan jalur ciri pada 1620 cm-1, 1508 cm-1, dan 1298 cm-1. Struktur liang mikro hidrogel PVA-Chitosan/PANi meningkat dengan kepekatan PVA tertinggi menunjukkan bahawa tahap pengikatan silang PANi memberikan struktur hidrogel berliang lebih tegar. Pengaruh kepekatan PVA pada struktur berliang hidrogel dan luas permukaan membolehkan penyerapan pewarna lebih tinggi seperti ditunjukkan oleh PVA-CS/PANi/3.9 mol.%, menunjukkan penyerapan Metilena biru (MB) lebih tinggi ke dalam strukturnya. Penggabungan bahan penyerap cahaya, seperti PANi kepada formulasi hidrogel boleh meningkatkan sifat penyerapannya. Prestasi SVG menggunakan hidrogel PVA-CS/PANi/3.9 mol.% diukur, didapati sebanyak 69.8% di bawah 1 matahari dengan taburan suhu yang cekap pada permukaan hidrogel. Dapatan kajian ini menunjukkan keupayaan hidrogel PVA-Chitosan/PANi/3.9 mol.% dalam menjana pelbagai taburan cahaya matahari semula jadi bagi menukar cahaya kepada haba yang cekap melalui SVG.

***KEYWORDS:*** *Hydrogel, solar vapor generation, polyaniline, polymer colloids*

# 1. INTRODUCTION

Water is an essential element in maintaining life and is needed for the survival of all organisms. Water resources are critical assets, so water conservation is imperative since the global water crisis has become a common phenomenon. According to the United Nations Development, more than 40% of people are affected by water scarcity, an alarming number

https://doi.org/10.31436/iiumej.v62i1.3236

expected to increase as temperatures rise. Since 1990, 2.1 billion people have improved their water sanitation, yet depletion of drinking water resources remains across all continents. Many nations suffer from water scarcity, and rising drought and desertification aggravate these circumstances. It is predicted that by 2050, at least one in four individuals will experience recurring water shortages [1]. The difficulty of maintaining sustainable levels of water use is expected to increase because of rising population pressure, changing water consumption habits, and climate change. This is followed by the rising number of heavy metals in natural resources resulting from industrialization and the improper discharge of wastewater into freshwater. Solar energy is the most abundant and renewable energy on earth. Therefore, it is vital to maximize the use of solar energy for sustainable future development to protect the planet. One of the technologies that can efficiently utilize solar energy is Solar Vapor Generation (SVG). SVG is a technology for purifying polluted water through solar energy evaporation by separating water from impurities and, similar to the natural hydrological cycle, replenishing freshwater on land [2]. It is a famous alternative to producing water for living things to survive. In SVG, two main components require improvement to facilitate more efficient water evaporation. These two main components are the light absorber material and the substrate. The light absorber material is essential to improve the light-to-heat conversion during the SVG process, and it is also known as photothermal-conversion material. Ideally, black materials with low transmittances, such as carbon nanomaterials, are ideal light absorbers for incident light with a broad range of wavelengths. For high-efficiency SVG design, the substrate material, such as the light absorber, is important. In contrast, the substrate material must perform two basic things: water transport/evaporation and thermal insulation. Other factors, such as good wetting properties and continuous pathways, are important for water to flow and evaporate efficiently. Besides, for SVG, low thermal conductivity and porous structures are needed to achieve better thermal insulation. The ratio of the thermal energy contained in the generated vapor to the incoming solar flux can be used to calculate the evaporation efficiency [3].

$$\eta = \frac{\dot{m}\, h_{LV}}{P_{in}} \tag{1}$$

where $\dot{m}$ is denotes the mass flux, $h_{LV}$ is the total enthalpy of liquid-vapor transformation, and $P_{in}$ is the rate of solar energy incident. The marking point as an ideal number to achieve highly efficient SVG is $1 kWm^{-2}$ (typically ~50% to higher than 80%) under 1 sun or even weaker natural daylight.

In recent years, there has been an increasing interest in SVG involving distinct hydrogels owing to the network structure that can absorb a significant amount of water. Hydrogels are hydrophilic polymer chains that form networks, have specific water states, and are swollen by dispersion mediums such as water. The floatable composite hydrogel possesses these characteristics, permitting the gels to effectively heat the water's surface while it undergoes evaporation, resulting in a higher efficiency of water evaporation. Hydrogel has become a trend in SVG technology and is still in its early stages. Owing to outstanding properties such as water-transporting material due to its strong hydrophilicity and ability to bond with water easily, the hydrogel is the best selection for the SVG platform. In comparison to natural polymers, the biological activity of the hydrogel produced by synthetic polymers is diminished [4]. Natural and synthetic polymers can be combined during manufacturing to produce hydrogels with the desired physical and chemical properties. In the previous study conducted by Khurma et al.[5], he developed semi-interpenetrating chitosan and PVA-crosslinked Genipin hydrogels. In that work, the study was conducted at various pH levels, temperatures, and swelling behaviours to investigate the properties of the hydrogels. According to the results obtained in our study, the correlation between PVA concentration and swelling capacity is

interesting, as the concentration of PVA must be greater than the concentration of chitosan to enhance the swelling capacity of PVA-CS hydrogel. The most remarkable result from this study is that at the maximum concentration of PVA, the PVA-CS hydrogel has demonstrated a higher ratio of OH groups to $NH_2$ groups. This finding suggests that some OH groups not involved in hydrogen bonding can attract more water, resulting in higher swelling ability. However, in a similar swelling investigation by Khan et al. on PVA-CS hydrogels crosslinked by UV light, the opposite trend was observed regarding swelling behaviour [6]. That research observed greater swelling ability in the hydrogels containing more chitosan. This difference in swelling trajectory may be attributed to the method used to crosslink the hydrogels. Khan's group utilized UV radiation crosslinking, resulting in a complete chitosan and PVA hydrogel network. Due to the temperature sensitivity of the hydrogel, the difference between these two results is owing to the percentage hydrolysis of PVA used by Khurma et al. The increase in frozen water is attributed to the increased hydrophilicity of the hydrogels, which was induced by the addition of PVA. Another study conducted by Guo et al. [2] on in situ gelation of PVA with uniform nanoparticles of titanium sesquioxide ($Ti_2O_3$) exhibited high photothermal conversion efficiency of up to 90%. They conducted experiments with various concentrations of PVA, which resulted in different evaporation rates depending on the concentration of PVA. However, the optimal results are independent either on the highest concentrations of PVA or the lowest concentration; instead, they are connected to other factors such as light absorber materials. The SVG system can be improved by adding light absorber materials to the substrate, as demonstrated in a study conducted by Yin et al.[7]. In that work, a novel porous double-network hydrogel (p-PEGDA-PANi) reportedly achieves a maximum solar thermal efficiency of 91.5%. The pristine hydrogel by itself has poor thermal conductivity. Still, when combined with PANi as a composite and given the porous structure, it can effectively confine heat transfer to the evaporating surface and reduce heat loss to bulk water. Moreover, after PANi cross-linking took place, the porous hydrogel sample exhibited a broader and stronger absorption (98.5%) juxtaposition to the pure PEGDA samples, especially in the visible and near-infrared (NIR) regions, confirming the strong absorption capacity of PANi for SVG application.

In this work, PVA-CS/PANi hydrogels were prepared with distinct concentrations of PVA and denoted as PVA-CS/PANi/1.3 mol. %, PVA-CS/PANi/2.7 mol.% and PVA-CS/PANi/3.9 mol.%. Copolymerization of PVA-CS hydrogels with PANi was conducted via solution polymerization to incorporate PANi into the hydrogel network structure. Incorporating light-absorbing materials, such as PANi, into the hydrogel network structure is expected to enhance the absorption properties. The morphological structure of the obtained hydrogels was analyzed by scanning electron microscopy (SEM). In contrast, the physicochemical and mechanical properties of the hydrogels were evaluated by dynamic light scattering (DLS), FTIR, swelling test, and rheology. From the analysis demonstrated in this work, the structure of PVA-CS/PANi hydrogels is significantly influenced by the concentration of PVA and the ability of the hydrogels to generate multi-scattering effects of natural sunlight for high-efficiency light-to-heat conversion via SVG.

## 2. MATERIALS AND METHODS

### 2.1. Materials

Materials used for this experiment are 0.32 M aniline monomers, 0.08 M ammonium persulfate (APS), hydrochloric acid (HCl,1M), deionized water (DI), polyvinyl alcohol (PVA) powder, 0.44 mol% of chitosan (CS) powder, Acetic acid (glacial), calcium carbonate powder ($CaCO_3$), glutaraldehyde [GA, 50 wt% in deionized water], 150 ml distilled water, and 50 ml

https://doi.org/10.31436/iiumej.v62i1.3236

N-Methyl-2-Pyrrolidone (NMP). The chemicals were purchased from Sigma-Aldrich and R& M Chemicals.

### 2.2. Method

The water bath was heated up to a constant temperature of 80°C. The PVA powder (1.3 mol.%, 2.7 mol.%, 3.9 mol. %) was gradually added to the heated reactor containing 150 ml of DI water, followed by CaCO3 powder added to the mixture. Subsequently, the solution was stirred vigorously for 2 hours. Then, 1.5 g of CS powder was dissolved in 0.4M acetic acid and stirred for 5 hours at 70°C. The CS solution was gradually added to the PVA solution and vigorously stirred for another 6 hours. After 6 hours, the solution was transferred to another beaker and cooled to room temperature. The milky-white PVA-CS solution was formed. Subsequently, 1M HCl was added to the solution, and the milky-white solution turned into a transparent solution, which was left for another 2 hours. The prepared polyaniline (PANi) powder was mixed with 50 ml N-Methyl-2-pyrrolidone (NMP) to dissolve the PANi powder. The mixture was then stirred for 1 hour. Next, the PANi-NMP solution was added to the PVA-CS/HCl solution, resulting in a mixture ready for hydrogel gelation. Glutaraldehyde (GA) [50 wt.% in DI water] 0.48 wt.% was added to 3 ml of the PVA-CS/PANi hydrogel solution, and the gelation process was left to occur for 24 hours.

### 2.3. Characterizations

The hydrodynamic diameter measurements were carried out using dynamic light scattering (DLS) (Zetasizer Nano S, Malvern Instruments, Malvern, UK). The PVA-CS solution sample was diluted to 0.1% w/w, and data were averaged over three consecutive runs at 25°C. The total solid content (TSC) was determined after the fabrication of PVA-CS solutions. To measure the TSC percentage, the mass of the boat dish and three different masses of the solution were recorded and labeled accordingly before allowing the prepared solutions to dry for 24 hours at 60°C. Fourier-transform infrared spectroscopy (FTIR) characterizations were performed using the Bruker Invenio. The FTIR spectra were measured within a spectrum range of 4000 – 700 cm-1 over 32 scans with a resolution of 4 cm-1. The PVA-CS/PANi hydrogel was freeze-dried for 72 hours before observation. Scanning Electron Microscope (SEM) (JEOL JSM5600) was utilized to observe the morphology and microstructure of the samples. The PVA-CS/PANi hydrogels were freeze-dried for 72 hours before observation. The mechanical properties of PVA-CS/PANi hydrogels were determined using a rheological experiment (Rheometer Anton Paar MCR) using a parallel plate in the amplitude and frequency sweep mode. The swelling capacity of PVA-CS/PANi hydrogels was determined using a swelling test. The PVA-CS/PANi hydrogels were immersed in a buffer solution (pH 4, pH 7, pH 10) and allowed them to swell until they reached equilibrium at regular time intervals for 24 hours. The absorption spectra of the Methylene Blue (MB) solution were measured by observing the absorption of contaminants by the PVA-CS hydrogels. The measurements were conducted at $\lambda$=665 nm using a spectrophotometer (SHIMADZU UV-1900, Tokyo, Japan), with the blank as a reference. The solar simulator lamp (Ossila Solar Simulator) in the laboratory setting simulates one sun illumination (100 mW/cm2) for the PVA-CS/PANi hydrogel and PVA-CS hydrogel efficiency test. The infrared thermal camera was employed to record the sample's heating process under a solar simulator lamp to investigate the maximum temperature distribution on the top surface of the sample.

https://doi.org/10.31436/iiumej.v62i1.3236

# 3. RESULTS AND DISCUSSION

## 3.1. DLS Size Distribution

DLS measurement of PVA-CS hydrogels is depicted in Figure 1, which shows PVA hydrogels with a bimodal distribution of average particle diameter. This graph showed that the z-average diameter measured was 146nm with slightly aggregated particles. The aggregation of particles in the PVA-CS solution is influenced by the presence of a small amount of chitosan due to flocculation. PDI value indicates the size distribution of particles in a sample. The PVA-CS hydrogel has a low PDI of 0.331, suggesting that the sample is homogeneous, with most of the particles being of similar size. The findings demonstrate that the PVA-CS solution possesses suitable characteristics for solar absorption capacity owing to its smaller particle size, good stability, and mechanical strength. The system will be evaluated further with various PVA concentrations. Homogeneous dispersion of PVA-CS hydrophilicity in water requires a small particle size (nanoparticle) to prevent aggregation from occurring.

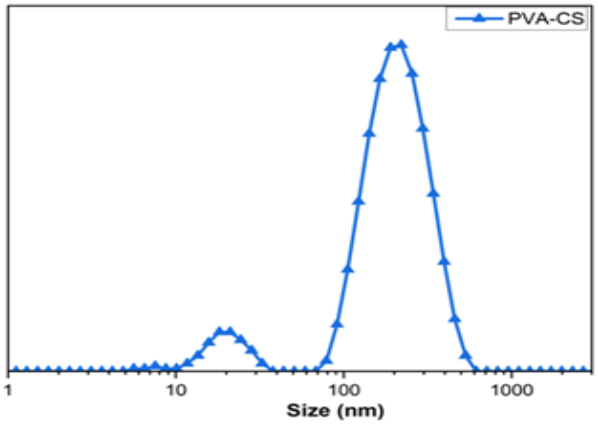


Figure 1. Particle size distribution of PVA-CS particles obtained from DLS analysis.

## 3.2. Total Solid Content (TSC) of PVA/Chitosan Solution

The total solid content (TSC) was conducted after the preparation of the PVA-CS solution. To measure the percentage of TSC, the mass of the boat dish and three different masses of the solution were recorded and dried in the oven for 24 hours at 60°C. The TSC data obtained is shown in Table 1. The TSC value of PVA-CS/PANi-3.9 mol.% was determined to be 87%, which is the highest percentage of all three observations. The magnitude of this value is sufficiently large to induce the polymerization of the solution into a hydrogel. Moreover, a low TSC value would result in an extended gelation period unfavorable for large-scale production. TSC influences the physical properties of hydrogel because hydrogel exhibits a denser microstructure when it has higher TSC values. Additionally, the TSC value would also impact the distribution of particles within the hydrogel. A previous study also found that an emulsion polymerization with a TSC value of 46% exhibited greater stability[8], and when the TSC value is below 20%, the hydrogel's overall strength may be diminished. Hence, a TSC value exceeding 46% is necessary and ideal for the synthesis of hydrogel[9].

Table 1. The total solid content of different concentrations of PVA-CS solution

| PVA concentrations | Total Solid Content (%) |
|---|---|
| 1.34 mol.% | 72.5 |
| 2.7 mol.% | 78 |
| 3.9 mol.% | 87 |

https://doi.org/10.31436/iiumej.v62i1.3236

### 3.3. Physical Observations of PVA-CS/PANi Hydrogels

The combination of PVA with chitosan results in a composite material that incorporates characteristics that impart mechanical robustness and stability, as well as tailoring the property of interest. PVA enhances the strength of the chitosan hydrogel and protects it against deterioration or degradation in aqueous environments. PVA is renowned for its exceptional characteristics that enhance the hydrogel matrix and its structural integrity. This characteristic is crucial for applications that necessitate the hydrogel's capacity in SVG applications that may be exposed to prolonged sunlight. Hence, this study presents the observation of PVA-CS hydrogels with different PVA concentrations, as depicted in Figure 2 (a-f). The appearance of the gel may be affected by the concentration of the PVA-CS hydrogel. In addition, the PVA-CS/1.3 mol.% exhibited a higher susceptibility to breakage upon contact, whereas higher concentrations of PVA-CS resulted in a stronger and more durable hydrogel. The polymer component ratio of PVA influenced these viscoelastic properties of PVA-CS hydrogel. Furthermore, Figure 2(d-f) shows the PVA-CS/PANi composite with varying concentrations of PVA. The color changes of PVA-CS/PANi are caused by the chemical reactions induced by the oxidation of PANi. The PANi concentrations are constant in this experiment. The hydrogel exhibited varying appearances depending on the concentrations of PVA, which consequently led to a more durable hydrogel. The presence of the dark hydrogel in PVA-CS/PANi/3.9 mol.% is necessary for the SVG application as a dark hydrogel has a higher capacity to absorb solar energy efficiently.

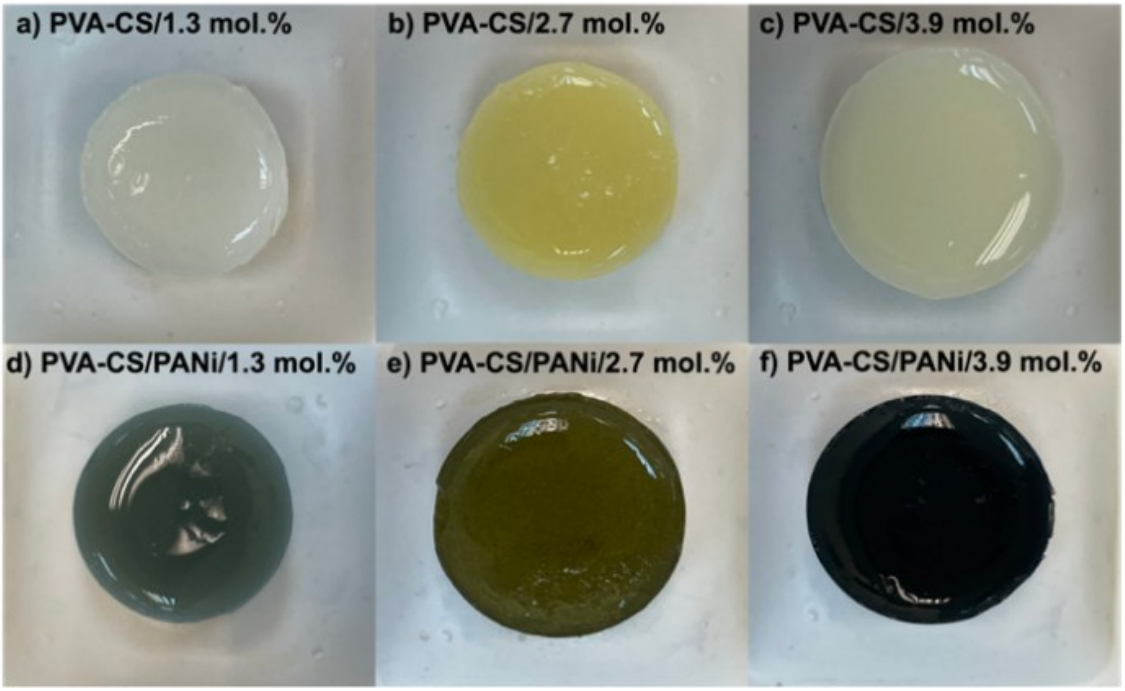


Figure 2. Gel images of PVA-CS hydrogel and PVA-CS/PANi hydrogel.

### 3.4. FTIR of PVA-Chitosan Hydrogel with Polyaniline

The FTIR spectra of PVA-CS hydrogel and PVA-CS/PANi hydrogel are depicted in Figure 3. It was observed that a broad peak at 3268 $cm^{-1}$ corresponds to hydrogen bonding in PVA-CS hydrogel. The peak at 1665 $cm^{-1}$ is typically associated with the carbonyl stretching vibration of the carboxylate group (-COO-) present in the chitosan structure. The PVA-CS with the presence of PANi exhibits peaks at 1620 $cm^{-1}$, 1508 $cm^{-1}$ and 1298 $cm^{-1}$. These bands correspond to the C=N and C=C stretch for the quinoid and benzenoid structures of PANi.

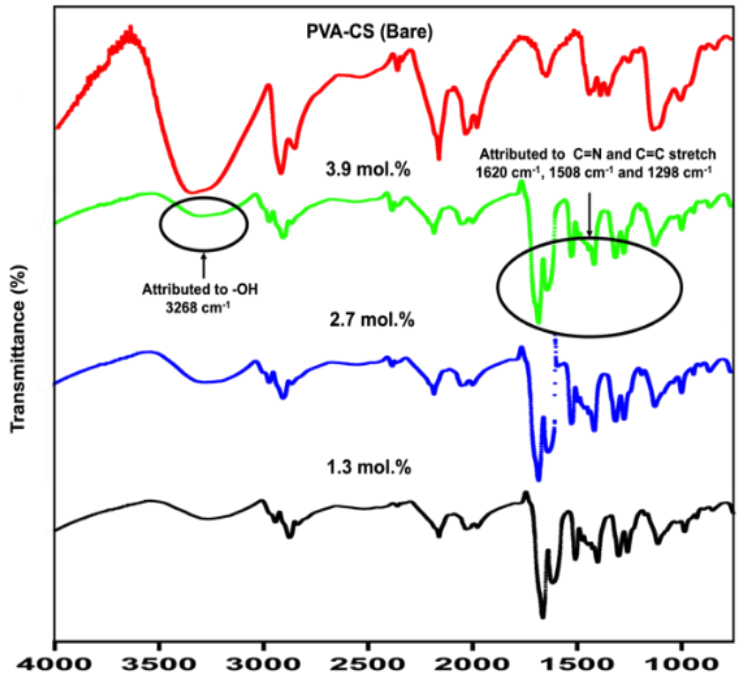


Figure 3. FTIR spectra of the chemical compositions of PVA-CS hydrogel and PVA-CS/PANi hydrogel

### 3.5. PVA-CS hydrogel and PVA-CS/PANi hydrogel SEM morphology

The SEM images were used to observe the cross-sectional morphology and microstructure of PVA-CS/PANi hydrogels with varying PVA concentrations (1.3 mol.%, 2.7 mol.%, 3.9 mol.%) and compared to PVA/Chitosan with PANI incorporation. Figure 4(a-f) displays the SEM morphology of the cross-section of the hydrogel at high magnification. Figure 4(a) illustrates the morphology of PVA-CS/1.3 mol.%, with fewer interconnected pores due to a lower polymer concentration. Fewer polymer concentrations may lead to a denser network, and PVA, being a hydrophilic polymer, is responsible for improving the hydrogel's viscosity. The PVA-CS solution decreased due to a lower PVA concentration. A decrease could induce restriction of polymer chain entanglement during the gelation process, thereby reducing the interconnected pores in the hydrogel. This can be seen in Figure 4(b-c), which displays a denser morphology with interconnected pores. The variation in PVA concentrations may lead to different hydrogel morphologies, and the presence of a denser morphology with interconnected pores may contribute to the mechanical strength of the hydrogel [10].

Furthermore, Figure 4(d-f) exhibits the SEM morphology of PVA-CS hydrogel incorporated under PANi with the influence of PVA concentrations. Adding PANi can impact the pore morphology and distribution within the hydrogel compared to pure PVA-CS hydrogels. Figure 4(d-f) demonstrates the distribution and dispersion of PANi within the PVA-CS hydrogel matrix, where particles or aggregates are visible as distinct features, and their distribution may enhance the homogeneity of the composite material. The microporous structure's pore size increases with the rise in PVA concentration, which is necessary for the PVA-CS/PANi hydrogel to provide a continuous water supply to the hydrogel's surface for SVG application. The pore distribution of the hydrogel indicates homogeneous gelation throughout the hydrogel matrix. The rich porous structure also enhances the multi-scattering of incident natural sunlight, enabling the incident light to be converted into heat at the evaporating surface[3].

https://doi.org/10.31436/iiumej.v62i1.3236

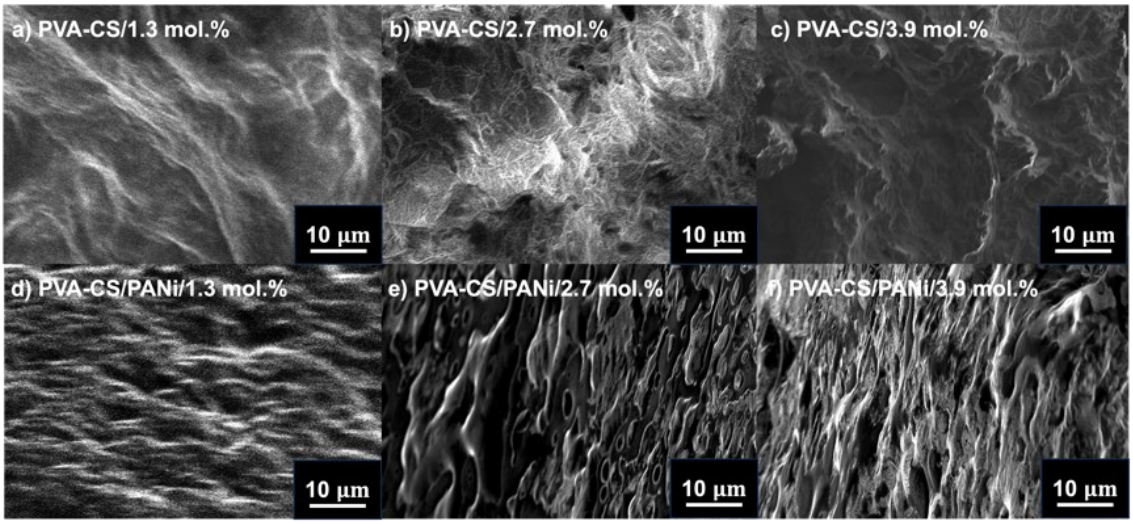


Figure 4. SEM images of PVA-CS hydrogel vs. PVA-CS/PANI with different PVA concentrations(a) PVA-CS hydrogel 1.3 mol.% (b) PVA-CS hydrogel 2.7 mol.% (c) PVA-CS hydrogel 3.9 mol.% (d) PVA-CS/PANi hydrogel 1.3 mol.% (e) PVA-CS/PANi hydrogel 2.7 mol.% (f) PVA-CS/PANi hydrogel 3.9 mol.%

### 3.6. Rheology Properties of PVA-Chitosan with Polyaniline

Dynamic rheological studies of gel samples were conducted to evaluate the PVA-CS/PANi hydrogels' mechanical properties with different concentrations of PVA. Each sample was tested in a rheometer at 1% constant strain and 1 Hz frequency corresponding to the linear viscoelastic range of the gel. G' and G" represent the elastic (storage modulus) and viscous (loss modulus) response, respectively. Based on Figure 5(a-b), it can be seen that the storage modulus was found to be larger than the loss modulus within a relatively smaller strain amplitude; this is an indicator that the rheological behavior in this region is dominated by an elastic, rather than a viscous property, which also indicates the reaction forming between polymer chains and crosslinkers as data shown in Table 2 and Table 3 [11]. Figure 5(a) shows the PVA-CS/PANi hydrogel with the increase of the storage modulus of reaction with the increased value of PVA concentrations (Table 2). The result demonstrates the ability of PVA-CS/PANi/3.9 mol.% hydrogel for SVG application as it shows the highest and greater value in both strain amplitude of 2356 Pa and frequency sweep of 3731 Pa. The increasing PVA concentration generally increases the viscosity and elastic modulus (storage modulus, G') of the hydrogel. This is because higher PVA concentrations result in a denser polymer network with more entanglements, which restricts the flow of the hydrogel and enhances its elastic behavior [12]. Moreover, when PANi is incorporated into hydrogels, its mechanical properties may be enhanced. Adding PANi into PVA-CS hydrogel can reinforce the hydrogel structure, leading to a higher elastic modulus and mechanical strength. PANi can act as physical cross-links within the hydrogel network, strengthening its overall structure [13].

https://doi.org/10.31436/iiumej.v62i1.3236

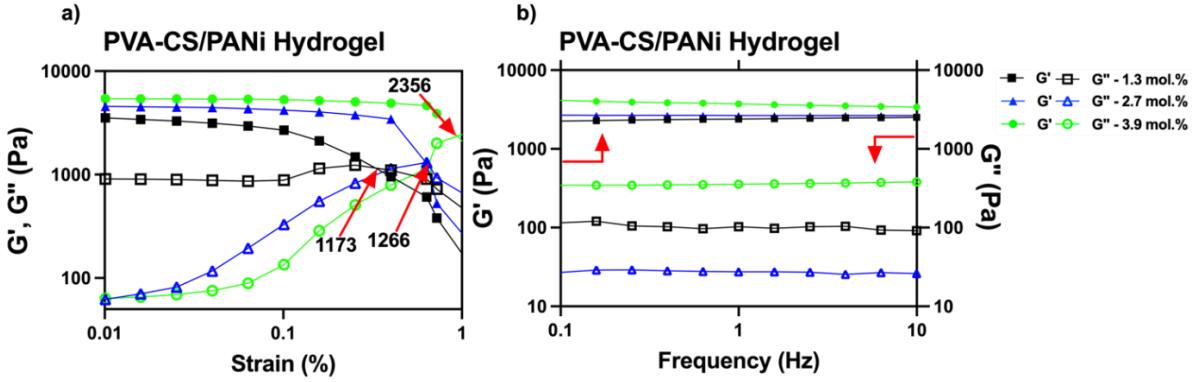


Figure 5. Rheology studies for PVA-CS/PANi with different concentrations of PVA (a) Strain amplitude of 1.3 mol.%, 2.7 mol.% and 3.9 mol.%; (b) Frequency-sweep of 1.3 mol.%, 2.7 mol.% and 3.9 mol.%

Table 2. Breaking point value of strain amplitude for PVA-CS/PANi with different PVA concentration

| PVA concentration | Breaking point (Pa) |
|---|---|
| **1.3 mol.%** | 1173 |
| **2.7 mol.%** | 1266 |
| **3.9 mol.%** | 2356 |

Table 3. Storage modulus and loss modulus value of frequency-sweep for PVA-CS/PANi with different PVA concentration

| PVA concentration | Storage Modulus (G´) (Pa) | Loss Modulus (G´´) (Pa) |
|---|---|---|
| **1.3 mol.%** | 2397.3 | 102.42 |
| **2.7 mol.%** | 2660 | 27.406 |
| **3.9 mol.%** | 3731 | 356.3 |

### 3.7. Swelling Test of PVA-CS/PANi hydrogel

Several factors influence a hydrogel's swelling capacity, including the concentration of the polymer used to form the hydrogel. As for PVA-CS hydrogels, the concentration of PVA can significantly affect their swelling behavior, as shown in Figure 6(a-d). Generally, as the PVA concentration increases, the hydrogel's swelling capacity decreases. This is because a larger PVA concentration increases the cross-links' density and results in a denser network structure, which restricts water uptake into the hydrogel. This explanation is supported by the research conducted by Ou et al., which states that a smaller concentration of PVA in the hydrogel resulted in a greater percentage of the degree of swelling hydrogel. In addition, the polymer chains in the hydrogel form physical crosslinks that impede the diffusion of water molecules, resulting in reduced swelling[14]. There's evidence shown in the equilibrium state of PVA-CS/PANi hydrogels with different PVA concentrations in Figure 6, where the water absorption of PVA-CS/PANi/1.3 mol.% was substantially higher compared to PVA-CS/PANi/3.9 mol.%. As a consequence of PANI's inherent hydrophobic nature, when incorporated into the PVA-CS hydrogel network, it can decrease the overall hydrophilicity of the hydrogel [15]. This hydrophobicity can impede the absorption of water by the hydrogel, resulting in a lower swelling capacity.

https://doi.org/10.31436/iiumej.v62i1.3236

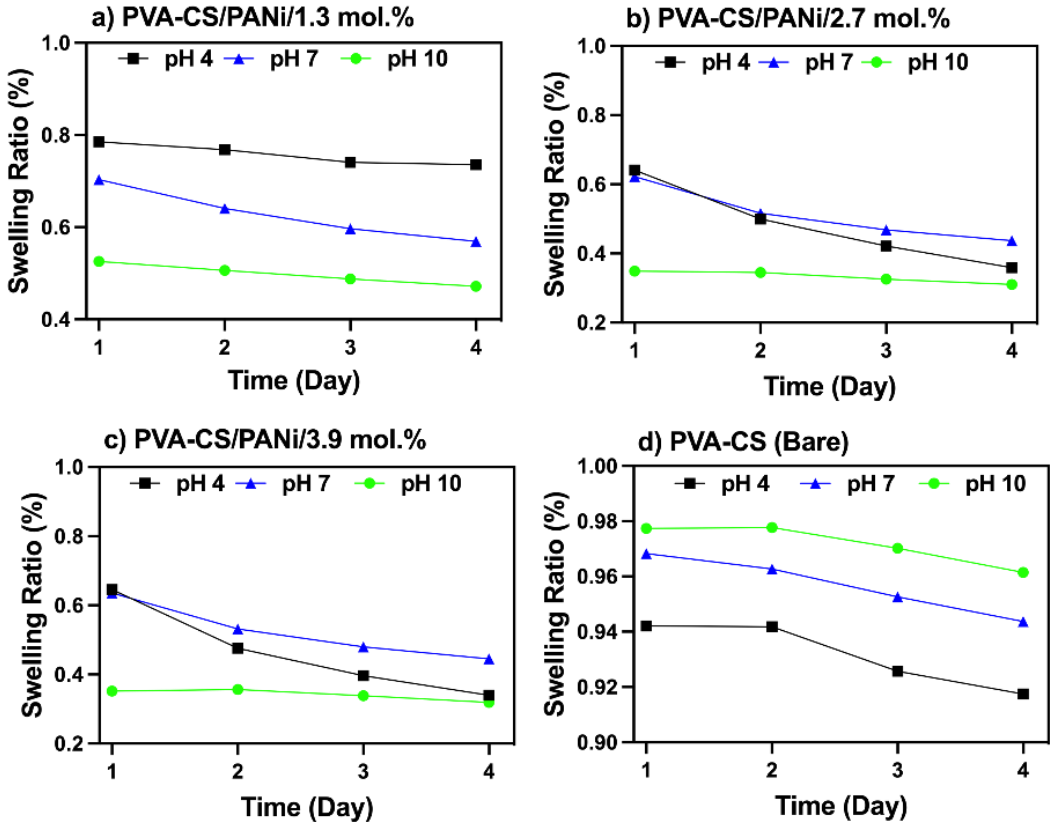


Figure 6. Swelling ratios of PVA-CS/PANi with different concentrations of PVA and PVA-CS hydrogel corresponding to pH (a) PVA-CS/PANi/1.3 mol.%; (b) PVA-CS/PANi/2.7 mol.%;(c) PVA-CS/PANi/3.9 mol.%;(d) bare PVA-CS

Figure 7 illustrates a noticeable difference between the PVA-CS hydrogel without PANi (Red) and the rest of PVA-CS/PANi hydrogel samples. PVA-based hydrogels' swelling behavior is often influenced by the pH of the medium [16]. A pH-sensitive hydrogels often exhibit significant changes in swelling or deswelling behavior in response to pH variations. This can be seen in Figure 7, which shows a different swelling capacity in PVA from low to high concentration; for instance, outside the optimal pH range, such as in highly alkaline conditions, the swelling capacity of the hydrogel can be significantly reduced. This phenomenon also explains the inconsistency between the morphology of these hydrogels (Figure 4) with swelling results (Figure 6), where the lowest PVA-CS/PANi inhibited the lower porosity but higher swelling absorption. However, the highest PVA-CS/PANi with greater porosity demonstrated the lowest swelling ability. Not only that, PANi as a conductive material may create an interaction between PVA-CS hydrogel with PANi in which when this hydrogel is immersed in acidic conditions, the presence of excess protons ($H^+$) leads to the protonation of PANi [17]. This protonation causes an increase in the hydrophilicity of the polymer, resulting in the absorption of water and subsequent swelling of the hydrogel (Figure 6(a)). The optimized PVA-CS/PANi hydrogel, despite its limited water absorption capacity, can still be leveraged effectively during the SVG process. By efficiently distributing the surface temperature of the hydrogel, it is possible to continuously and rapidly deliver water to the hydrogel's surface, thus enhancing its water intake and overall performance. This approach can be achieved by utilizing the hydrogel's dark property due to the incorporation of PANi.

https://doi.org/10.31436/iiumej.v62i1.3236

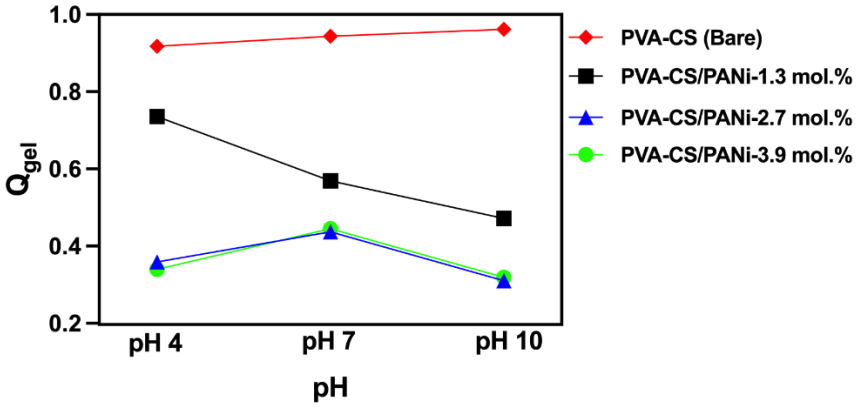


Figure 7. Equilibrium of PVA-CS/PANi with different concentrations of PVA and PVA-CS hydrogel corresponding to pH

Table 4. Equilibrium of PVA-CS/PANi with different concentrations of PVA and PVA-CS hydrogel corresponding to pH

| Abbreviations | pH 4 | pH 7 | pH 10 |
|---|---|---|---|
| **PVA-CS/PANi 1.3 mol.%** | 0.73588 | 0.56908 | 0.47152 |
| **PVA-CS/PANi 2.7 mol.%** | 0.35884 | 0.43732 | 0.31012 |
| **PVA-CS/PANi 3.9 mol.%** | 0.33988 | 0.445 | 0.319 |
| **PVA-CS (Bare)** | 0.91744 | 0.94372 | 0.96148 |

### 3.8. UV-VIS Methylene Blue Absorption with PVA-CS Hydrogel

Methylene Blue (MB) is a commonly used dye in analytical chemistry, including water quality testing. It can be used to measure the presence of reducing agents or monitor a solution's oxidation-reduction potential [18]. In the case of clean water, where the concentration of reducing agents is typically low, MB can be used as an indicator to detect any reducing substances that may be present. The ultraviolet-visible spectrophotometry (UV-Vis) absorption spectrum of MB was used to monitor changes in its concentration or oxidation state when the PVA-CS hydrogel with different concentrations of PVA was immersed for 24 hours in MB dye solution. Typically, MB exhibits a characteristic absorption peak around 665 nm when measured using UV-Vis spectroscopy, as depicted in Figure 8. The highest absorption is denoted as MB Sol (before) (Red), which is the solution before immersion with hydrogels. This peak corresponds to the maximum absorbance wavelength for MB in its oxidized form [19]. The reducing substances were present in the water, where they can react with the MB and cause a decrease in its absorbance at 665 nm, as shown in Figure 8 for PVA-CS/1.3 mol.% (Black), PVA-CS/2.7 mol.%(Blue) and PVA-CS/3.9 mol.% (Green). The decrease in the extent of the absorbance indicates the concentration or reactivity of the reducing substances in the water. In this experiment, the highest reduction can be witnessed in PVA-CS/3.9 mol.% (Green) hydrogel is shown in the physical visibility of the gel. The influence of PVA concentration can contribute to the hydrogel's porous structure and surface area, allowing for greater dye adsorption. The hydrogel's porous network provides a greater surface area for the dye molecules to interact [20]. Other than that, the PVA-CS hydrogels may have chemical interactions with MB due to the hydroxyl groups in PVA that can form hydrogen bonds with the dye molecules. Additionally, the chitosan functional groups, such as amino groups, can have chemical reactions with the MB, such as dye-chitosan complexation or covalent bonding.

https://doi.org/10.31436/iiumej.v62i1.3236

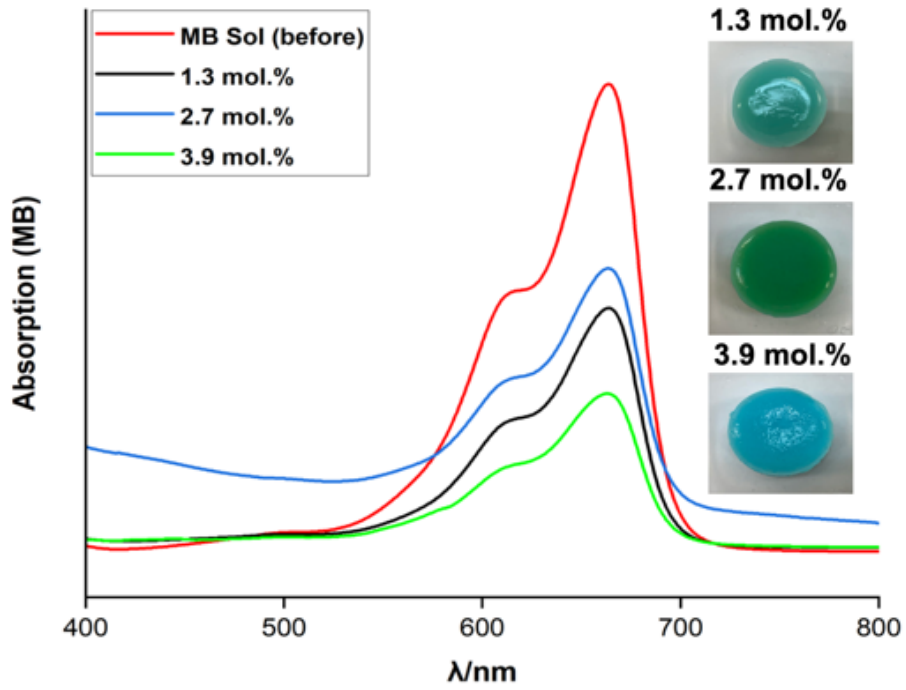


Figure 8. PVA-CS hydrogel UV-vis absorption of Methylene Blue (MB)

### 3.9. Solar Vapor Generation Efficiency

Enhancement of the SVG performance with hydrogel can be achieved by developing a dark hydrogel. A dark hydrogel absorbs more incident solar radiation, increasing heating and vapor generation. Also, selecting a polymer with a high absorption coefficient in the solar spectrum can be beneficial, such as PVA polymer, which allows for efficient light conversion into heat. Incorporating light-absorbing materials like PANi into the hydrogel formulation can enhance its absorption properties. PANi exhibits strong absorption in the visible and near-infrared regions of the solar spectrum. PANi can absorb a significant portion of the incident solar radiation when incorporated into PVA-CS hydrogel. This absorption is due to conjugated pi-electron systems within the PANi polymer backbone. Furthermore, upon absorption of solar radiation, PANi undergoes an electronic transition, generating excitons or charge carriers. These excitons or charge carriers undergo relaxation processes, during which they release excess energy as heat[21]. The heat generated within the PVA-CS/PANi raises the temperature of the surrounding environment, including the water within the hydrogel, increasing SVG efficiency (Figure 9). The absorbed heat from PVA-CS/PANi is transferred to the water present in the hydrogel, raising its temperature. As the water temperature increases, it can reach its boiling point, generating vapor. Based on the results in Figure 9, the PVA-CS/PANi shows greater efficiency than the PVA-CS hydrogel without incorporating PANi. The continuous water supply to the surface due to the porous structures of this hydrogel is proven, as previously discussed. Figure 10 shows the temperature distribution on the PVA-CS/PANi 3.9 mol.% surface increases due to the hydrogel's rich porosity and dark hydrogel's appearance. The PVA-CS hydrogel without PANi is physically white and causes reflection of the solar spectrum, making it less efficient when used alone for SVG. This observation may provide insight into how PANi influenced the performance to maximize the use of natural light incident and produce clean water. Moreover, as seen in Table 5, when compared to the earlier study

https://doi.org/10.31436/iiumej.v62i1.3236

conducted by Zhu and colleagues, the results showed a 4% improvement, which can be further enhanced through deliberate design in future studies [22].

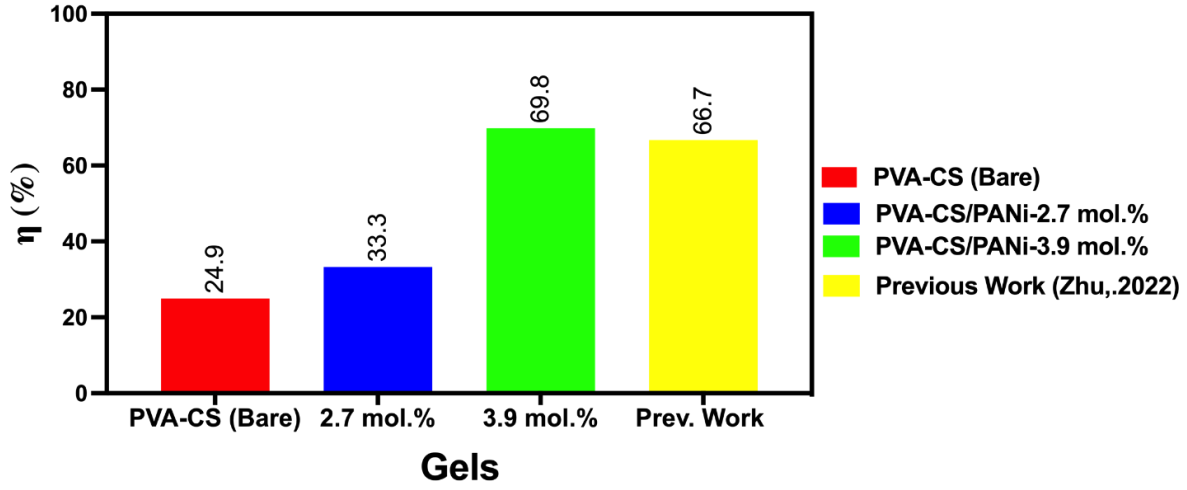


Figure 9. SVG efficiency of PVA-CS hydrogel and PVA-CS/PANi hydrogel

Table 5. The comparison of PVA-CS/PANi with previous work

| Previous Work | Zhu et al., 2022 | This work |
|---|---|---|
| **Substrate** | PVA-Chitosan | PVA-Chitosan |
| **Light absorber** | Carbon Nanoparticles (CNPs) | Polyaniline (PANi) |
| **SVG Efficiency** | 66.7% | 69.8% |

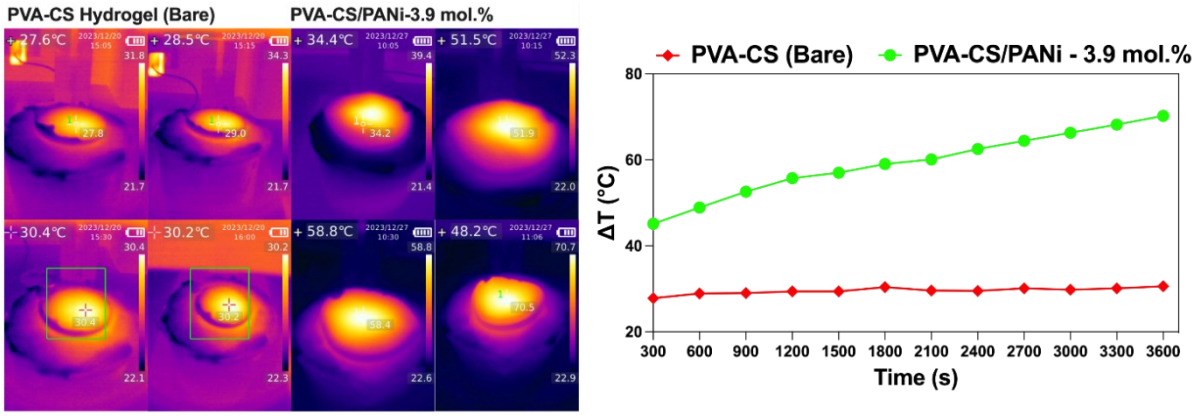


Figure 10. Water heating (ΔT- the temperature difference between the temperature before and after irradiation) was recorded in different illuminations over 1 hour period.

## 4. CONCLUSION

Based on the analysis of the results, the PVA-CS/PANi-3.9 mol.% hydrogel emerges as the most optimal choice. The findings highlight a significant improvement in the structure of the hydrogel's structure, the concentration of PVA concentration. The increase in concentration is essential to ensure a consistent water supply to the hydrogel's surface of the hydrogel during SVG. Furthermore, a higher hydrogel porosity signifies enhanced mechanical stability, as the increased storage modulus value observed in the rheology of PVA-CS/PANi 3.9 mol.%. The mechanical durability of the hydrogel is crucial for practical applications due to its continuous exposure to sunlight. Adding PANi to the PVA-CS hydrogel resulted in a darker appearance

and higher light absorption capacity. This enhanced light absorption capability is also reflected in the temperature distribution on the surface of the hydrogel. As a result, the construction of SVG becomes more efficient, making it easier to generate clean water. The efficiency of PVA-CS/PANi 3.9 mol.% can be further improved by surface modification and optimizing the PANi concentration.

## ACKNOWLEDGEMENT

This research was funded by UMP-IIUM-UiTM Sustainable Research Collaboration (SRCG) from Universiti Teknologi Mara and International Islamic University Malaysia, denoted as SRCG20-044-0044/ 100-TNCPI (1/1). The authors would also like to thank Majlis Amanah Rakyat (MARA) for their technical and financial support. The authors would like to acknowledge our collaborators, Dr. Wan Wardatul Amani Wan Salim, Dr. Nurul Sakinah Engliman, and Dr. Radhiyah Abd Aziz, for their invaluable input.

## REFERENCES

[1] Schewe, J., et al., *Multimodel assessment of water scarcity under climate change.* Proceedings of the National Academy of Sciences, 2014. **111**(9): p. 3245-3250.

[2] Guo, Y., et al., *Synergistic energy nanoconfinement and water activation in hydrogels for efficient solar water desalination.* ACS nano, 2019. **13**(7): p. 7913-7919.

[3] Chen, C., Y. Kuang, and L. Hu, *Challenges and opportunities for solar evaporation.* Joule, 2019. **3**(3): p. 683-718.

[4] Bashir, S., et al., *Fundamental concepts of hydrogels: Synthesis, properties, and their applications.* Polymers, 2020. **12**(11): p. 2702.

[5] Khurma, J.R., D.R. Rohindra, and A.V. Nand, *Synthesis and properties of hydrogels based on chitosan and poly (vinyl alcohol) crosslinked by genipin.* Journal of Macromolecular Science, Part A: Pure and Applied Chemistry, 2006. **43**(4-5): p. 749-758.

[6] Khan, S. and N.M. Ranjha, *Effect of degree of cross-linking on swelling and on drug release of low viscous chitosan/poly (vinyl alcohol) hydrogels.* Polymer bulletin, 2014. **71**: p. 2133-2158.

[7] Yin, X., et al., *Macroporous double-network hydrogel for high-efficiency solar steam generation under 1 sun illumination.* ACS applied materials & interfaces, 2018. **10**(13): p. 10998-11007.

[8] Zhu, Z., et al., *Preparation and properties of high solid content and low viscosity waterborne polyurethane—Acrylate emulsion with a reactive emulsifier.* Polymers, 2018. **10**(2): p. 154.

[9] Chen, J., et al., *An adhesive hydrogel with "Load-Sharing" effect as tissue bandages for drug and cell delivery.* Advanced Materials, 2020. **32**(43): p. 2001628.

[10] Chen, Y.-N., et al., *Self-assembled polyvinyl alcohol–tannic acid hydrogels with diverse microstructures and good mechanical properties.* ACS omega, 2018. **3**(9): p. 11788-11795.

[11] Kakadjian, S., O. Rauseo, and F. Mejias. *Dynamic rheology as a method for quantify gel strength of water shutoff systems*. in *SPE International Conference on Oilfield Chemistry?* 1999. SPE.

[12] Kjøniksen, A.-L. and B. Nyström, *Effects of polymer concentration and cross-linking density on rheology of chemically cross-linked poly (vinyl alcohol) near the gelation threshold.* Macromolecules, 1996. **29**(15): p. 5215-5222.

[13] Han, J., T. Lei, and Q. Wu, *High-water-content mouldable polyvinyl alcohol-borax hydrogels reinforced by well-dispersed cellulose nanoparticles: Dynamic rheological properties and hydrogel formation mechanism.* Carbohydrate polymers, 2014. **102**: p. 306-316.

[14] El Sayed, M.M., *Production of polymer hydrogel composites and their applications.* Journal of Polymers and the Environment, 2023. **31**(7): p. 2855-2879.

[15] Nawaz, H., et al., *Hybrid PVDF/PANI membrane for removal of dyes from textile wastewater.* Advanced Engineering Materials, 2022. **24**(5): p. 2100719.

[16] Shivakumara, L.R. and T. Demappa, *Synthesis and swelling behavior of sodium alginate/poly (vinyl alcohol) hydrogels.* Turkish journal of pharmaceutical sciences, 2019. **16**(3): p. 252.

[17] Golba, S., et al., *Impact of acidity profile on nascent polyaniline in the modified rapid mixing process—Material electrical conductivity and morphological study.* Materials, 2020. **13**(22): p. 5108.

[18] Khan, I., et al., *Review on methylene blue: Its properties, uses, toxicity and photodegradation.* Water, 2022. **14**(2): p. 242.

[19] Fernandez-Perez, A. and G. Marban, *Visible light spectroscopic analysis of methylene blue in water; what comes after dimer?* ACS omega, 2020. **5**(46): p. 29801-29815.

[20] Ghafelebashi, A., et al., *A novel fabricated polyvinyl alcohol/bentonite nanocomposite hydrogel generated into colloidal gas aphron.* Colloids and Surfaces A: Physicochemical and Engineering Aspects, 2022. **650**: p. 129580.

[21] Namsheer, K. and C.S. Rout, *Conducting polymers: a comprehensive review on recent advances in synthesis, properties and applications.* RSC advances, 2021. **11**(10): p. 5659-5697.

[22] Zhu, M., et al., *Dome-arrayed chitosan/PVA hydrogel-based solar evaporator for steam generation.* Scientific Reports, 2022. **12**(1): p. 4403.

https://doi.org/10.31436/iiumej.v26i1.3239

# APPLICATION OF KANSEI ENGINEERING IN VARIOUS TRAIN COMPARTMENT DESIGNS TO DETERMINE THE USER'S AFFECTIVE RESPONSE

**DINDA KARINA YOHANNY, LU'LU' PURWANINGRUM*, AMBAR MULYONO**

*Faculty of Art and Design, Sebelas Maret University, Surakarta, Indonesia*

**Corresponding author: lulu_purwaningrum@staff.uns.ac.id*

*(Received: 27 March 2024; Accepted: 10 September 2024; Published online: 10 January 2025)*

***ABSTRACT:*** Visual appearance (shapes, colors, materials, and surfaces) applied to product design can provide users with emotional and positive affective responses. The desire of such users will provide essential guidelines for companies to develop products, in this case, trains, in the form of private spaces called compartments. Trains are in great demand for long trips, so there is a need for market segmentation. However, current research only focuses on designs that examine functionality needs. Lack of study of design based on visual appearance, research on user preferences, and more scientific evaluation of design is needed. Therefore, this study aims to translate the user's affective response into the interior design specifications of train compartments with the *Kansei* Engineering method. This research consists of 5 steps: (1) Determining product semantics (*Kansei* Words assignment); (2) Define product properties (items and categories), as many as eight design samples; (3) Distributing questionnaires to 150 respondents (75 men and 75 women); (4) Data analysis with multivariate statistics, KMO, Barlett's Test, Principal Component Analysis, and clustering of respondents; (5) Evaluate the results of the most optimal design specifications. The results of this study obtained design recommendations: straight shape, studio green color, pine wood HPL material texture, and doff surface. In addition, several user clusters were formed based on gender, age, and monthly income to segment train compartments when commercialized. This research is expected to be helpful for the wider community and the development of the interior design of train compartments.

***ABSTRAK:*** Penampilan visual (bentuk, warna, bahan dan permukaan) yang digunakan pada reka bentuk produk dapat memberikan tindak balas emosi dan tindak balas afektif positif daripada pengguna. Keinginan pengguna akan memberikan garis panduan penting bagi syarikat untuk membangunkan produk, dalam kes ini kereta api dalam bentuk ruang peribadi yang dipanggil petak ruang kereta api. Kereta api mendapat permintaan yang tinggi bagi perjalanan jauh, jadi terdapat keperluan untuk pembahagian pasaran. Walau bagaimanapun, penyelidikan semasa hanya memberi tumpuan kepada reka bentuk yang mengkaji keperluan fungsi sahaja. Terdapat kekurangan kajian mengenai reka bentuk berdasarkan penampilan visual, penyelidikan mengenai keutamaan pengguna, dan penilaian reka bentuk yang lebih saintifik diperlukan. Oleh itu, kajian ini bertujuan untuk menterjemahkan tindak balas afektif pengguna ke dalam spesifikasi reka bentuk dalaman petak ruang kereta api menggunakan kaedah Kansei Engineering. Penyelidikan ini terdiri daripada 5 langkah: (1) Menentukan semantik produk (penentuan patah kata Kansei); (2) Tentukan sifat produk (item dan kategori), sebanyak lapan sampel reka bentuk; (3) Mengagihkan soal selidik kepada 150 responden (75 lelaki dan 75 perempuan); (4) Analisis data dengan statistik multivarian, KMO, Ujian Bartlett, analisis komponen utama, dan kelompok responden; (5) Penilaian keputusan spesifikasi reka bentuk paling optimum. Hasil kajian mencadangkan reka bentuk: bentuk lurus, warna hijau studio, tekstur bahan HPL kayu pain, dan permukaan doff. Di samping itu, beberapa kluster pengguna dibentuk berdasarkan jantina, umur dan pendapatan bulanan bagi

memudahkan pembahagian petak ruang kereta api apabila dikomersialkan. Kajian ini dijangka berguna kepada masyarakat yang lebih luas dan pembangunan reka bentuk dalaman petak ruang kereta api pada masa hadapan.

***KEYWORDS:*** *affective, interior design, Kansei engineering, railway, visual appearance*

# 1. INTRODUCTION

The visual appearance of a product can satisfy consumers in addition to ease of use. Trains must also consider visual impressions as one of the transportation products used for the public. One of the railway facilities currently being developed in Indonesia is a compartment that offers long trips with comfortable seating and more private beds with partitioned space [1]. Many developed countries already have similar trains that attract foreign tourists, such as the Shiki Shima Train Suite in Japan, the Caledonian Sleeper in England, and the Grand Express in Russia. Each train in the country applies a different visual appearance to its interior design and becomes a characteristic. This condition necessitates the existence of a compartment design that can create an emotional attachment with its users to attract tourists to travel by train in Indonesia. To create a memorable and pleasant experience for train passengers, the designer must consider the correlation with the users' emotions [2]. A person's emotional state results from an affective response when looking at a product. In this case, visual appearance becomes very important because it is the first stimulus captured by the five senses and attracts human attention [3]. Furthermore, the stimulus is processed in the brain and interpreted into perceptions assessing product design's advantages and disadvantages [4]. The visual display comprises shape, color, material, and surface [5].

This research applies *Kansei* Engineering as a method of emotion-based design for the interior design of railway compartments in Indonesia. *Kansei* Engineering is a powerful method for converting users' feelings and emotions into design specifications [6]. Kansei Engineering can also be used as a tool to develop the design of a product that generates innovative solutions [7]. This method is widely used behind the success of several well-known transportation product brands worldwide, such as Mazda, Hyundai, and Toyota. Other research on transportation is reported on the design of economic and business train seats in Indonesia [3] and the design of the product image of railway seats [8]. In the car design industry or interior design project, the *Kansei* Engineering method was used to evaluate respondents' preferences for car design [9]. At the same time, preliminary research on the design of luxury class train compartments resulted in selected design specifications by respondents [1].

To evaluate the design of train compartments with Kansei engineering, a semantic differential (SD) scale is needed to translate stimuli received by the five human senses [10]. The semantic differential scale consists of several Kansei words, which are adjectives that describe the product to be graded on a scale of 1-5. Furthermore, the results of respondents' assessments will be analyzed with multivariate statistics. Principal Component Analysis (PCA) determines the principal components and summarizes the variables into fewer [11]. At the same time, cluster analysis was used to classify the number of groups of respondents [12] in this study based on gender, age, and monthly income. User clustering proved helpful in identifying specific group responses to designs [13].

Considering the findings, this study proposes a specification of the interior design of the railway compartment based on visual appearance (color, shape, material, surface). It also considers three groups of respondents based on selected design and affective responses that best suit user preferences. This study's practical application is evident in its potential to serve

https://doi.org/10.31436/iiumej.v26i1.3239

as a reference for railway compartment design in Indonesia and around the world, making it a valuable resource for designers and professionals in the field.

# 2. METHODOLOGY

## 2.1. *Kansei* Engineering

*Kansei* Engineering includes the field of ergonomics (human factors), which focuses on human affective responses. Nagamachi, a professor from Japan who first developed this method, defines *Kansei* Engineering as a technology capable of translating user emotions into design specifications [11]. Currently, *Kansei* Engineering is applied to various disciplines (natural sciences, social sciences, and humanities) that integrate affective elements into the development stage of product design. In *Kansei* Engineering, users usually use adjectives that describe a product called *Kansei* Words. Here are the five main steps in *Kansei* Engineering:

### *2.1.1. Determine Product Semantics*

The first step is to choose a product domain by determining the object and subject of the research. Then, *Kansei* Words in adjectives and grammatical forms that describe the product are collected and obtained from various sources, such as journals, books, and magazines. These *Kansei* Words are crucial as they represent users' emotional and affective responses towards the product. Usually, the collection of *Kansei* Words is 50-600, so sorting is necessary [14]. The reduction process is carried out by grouping similar *Kansei* Words and selecting them until they obtain the most representative *Kansei* Words.

### *2.1.2. Determine Product Properties*

In the *Kansei* Engineering procedure, properties are divided into items and categories to be applied to design samples. An item is a particular characteristic used in the design, while the category is the division of groups within each item [1].

### *2.1.3. Data Collection*

This step prepares a questionnaire by combining product samples with Kansei Words. This study used the optimal 5-point semantic differential scale to assign values to each sample. The scale developed by Osgood can translate the stimulus received by the five human senses into numbers [10]. The data obtained from the questionnaire will be analyzed and used to build a relationship model.

### *2.1.4. Data Analysis*

After the data is collected, validity and reliability tests are conducted to ensure the research data is valid and reliable. Then, Kaiser-Meyer-Olkin (KMO) and Barletts's Test of Sphericity tested the feasibility of the data. Principal Component Analysis (PCA) summarizes variable dimensions so readers can understand the data structure [11]. In addition, it is also to find out the score and position of the product from the visualization of product aspect mapping. At the same time, cluster analysis aims to group respondents into clusters based on specific characteristics [15].

### *2.1.5. Evaluation of the Results of the Design Specification*

Decision-making for design specification recommendations is done by drawing conclusions based on the results of data analysis. Research results must be evaluated so that the product can provide an effective mechanism with the overall design expected by the user. As seen in Figure 1, the research framework adopts the procedures from *Kansei* Engineering described earlier.

https://doi.org/10.31436/iiumej.v26i1.3239

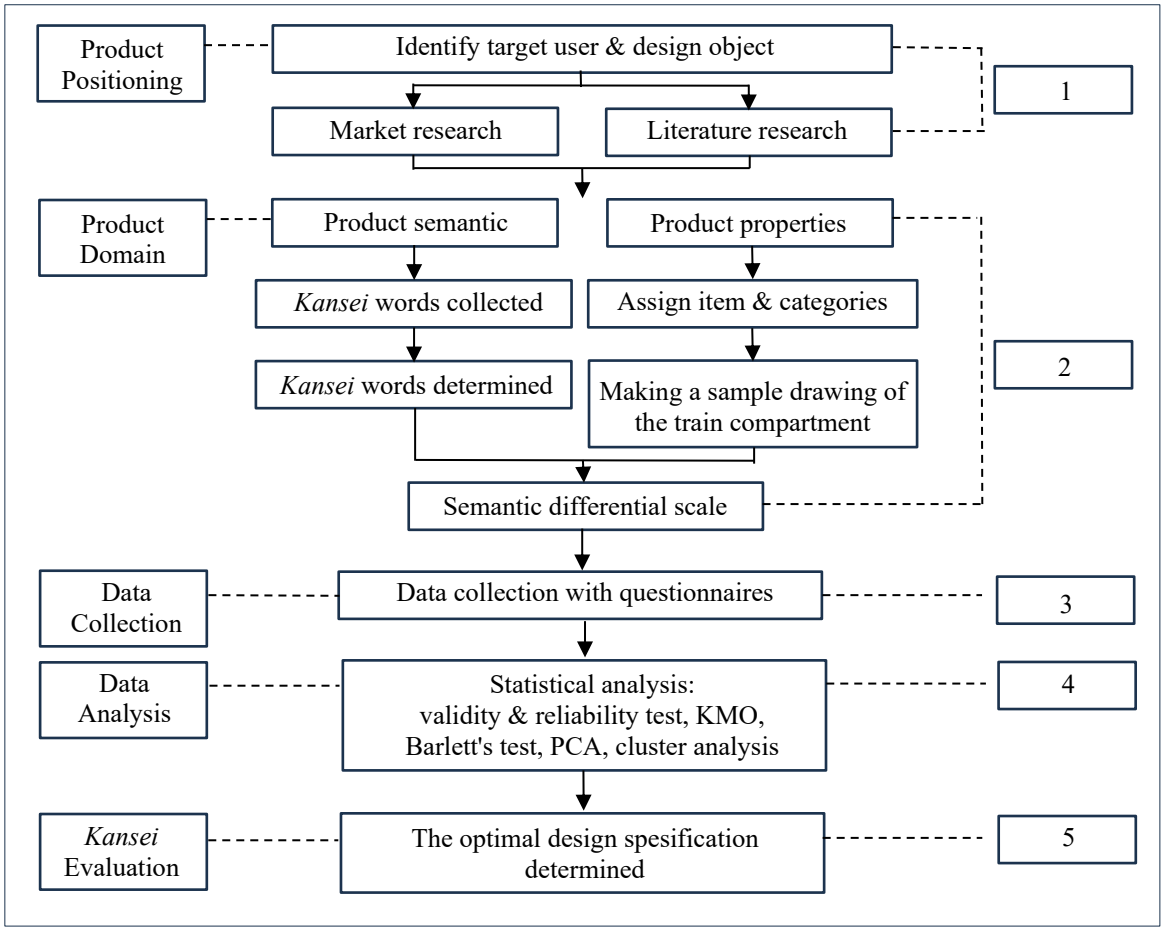


Figure 1. Flow diagram of the *Kansei* Engineering procedure.

### 2.2. Semantic Differential Method

A person's feelings and impressions of the product are complex structures that require measuring instruments. The semantic differential scale is one of the psychological measurement scales developed by Charles E. Osgood, an instrument to measure human affective responses to product development [7]. The SD scale consists of Kansei Words paired with their antonyms to be assigned point values in the number range 1-5. The 5-point scale is the easiest for respondents to use and understand [11].

### 2.3. Procedures

Most of Kansei's evaluations are user surveys that use semantic differential scales. This study distributed questionnaires to 150 respondents (75 men and 75 women) Indonesian people who had experience traveling by train. The questionnaire-filling stage begins with an explanation of the research and how to fill out the questionnaire. The respondent fills in their identity based on age, gender, and monthly income. After that, eight samples of train compartment designs appear on an SD scale. Respondents can also view the design display in 360o with AR (Augmented Reality) technology to see samples of train compartment designs. Respondents give scores by filling in the SD scale in the range of 1-5 according to their affective response when looking at the given designs.

https://doi.org/10.31436/iiumej.v26i1.3239

# 3. RESULT AND DISCUSSION

## 3.1. Collection and Determination of Kansei Words

One hundred twenty words describing the train compartment were collected from journals, books, magazines, and others. Then, a process of selecting Kansei Words was carried out with a focus group discussion (FGD) with the design team to summarize them into 40 Kansei Words. The 40 words were then verified with questionnaires to obtain objective results from respondents. The ranking of the Kansei Words reduction stage was carried out by a questionnaire with the results of 6 words with the top rank, namely 'comfortable,' 'luxurious,' 'unique,' 'enjoyable,' 'simple,' and 'modern,' for further use on an SD scale. Table 1 below is a questionnaire form with an SD scale with six selected Kansei Words.

Table 1. Questionnaire form for semantic differential analysis

| **Opposite Words** | **Scale** | | | | | ***Kansei* Words** |
|---|---|---|---|---|---|---|
| | **1** | **2** | **3** | **4** | **5** | |
| Uncomfortable | | | | | | Comfortable |
| Spartan | | | | | | Luxurious |
| Ordinary | | | | | | Unique |
| Boring | | | | | | Enjoyable |
| Complex | | | | | | Simple |
| Traditional | | | | | | Modern |

## 3.2. Determination of Specifications and Design Samples

The task in this step is to determine the design domain and specifications that can represent the target group and market needs. Then, prepare a comprehensive set of eight train compartment designs for the questionnaire. Design specifications are applied based on four visual display items (shape, color palette, surface, and material texture), and each is further divided into 2-3 categories. The shape items consist of curved and straight lines, the color palette consists of studio green, emerald green, and sage green, the surface appearance consists of glossy and doff, and the texture material of HPL (High-Pressure Laminate) consists of teak wood, mahogany wood, and pine wood. The design refers to the results of previous research [1] and the development of the compartment mock-up made by a railway company in Indonesia (PT. INKA). Table 2 shows eight interior designs of railway compartments as samples applied to the questionnaire.

Table 2. The samples of railway compartment interior design and specifications

| **Code** | **Design Sample** | **Specifications** |
|---|---|---|
| S1 | | • Shape: curved<br>• Color: studio green<br>• Surface: doff<br>• Texture: teak wood |

https://doi.org/10.31436/iiumej.v26i1.3239

| | | |
|---|---|---|
| S2 | | • Shape: curved<br>• Color: emerald green<br>• Surface: glossy<br>• Texture: mahogany wood |
| S3 | | • Shape: curved<br>• Color: sage green<br>• Surface: doff<br>• Texture: pine wood |
| S4 | 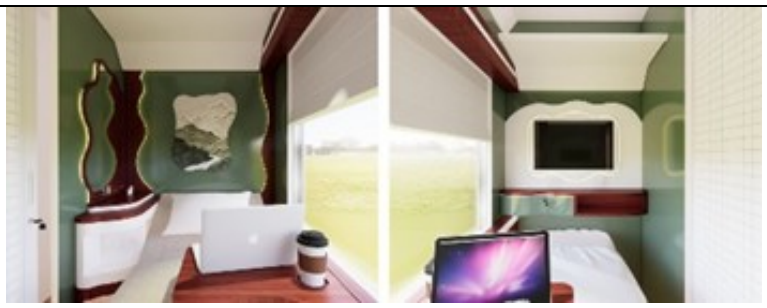 | • Shape: curved<br>• Color: studio green<br>• Surface: glossy<br>• Texture: mahogany wood |
| S5 | | • Shape: stright line<br>• Color: emerald green<br>• Surface: doff<br>• Texture: teak wood |
| S6 | | • Shape: stright line<br>• Color: sage green<br>• Surface: glossy<br>• Texture: mahogany wood |

https://doi.org/10.31436/iiumej.v26i1.3239

| | | |
|---|---|---|
| S7 | | • Shape: stright line<br>• Color: studio green<br>• Surface: doff<br>• Texture: pine wood |
| S8 | | • Shape: stright line<br>• Color: emerald green<br>• Surface: glossy<br>• Texture: mahogany wood |

Source: Design development from Indonesian Railway Company (PT. INKA)

### 3.3. Questionnaire Result

The respondents' identity or characteristics based on the questionnaire results include gender, age, and monthly income. The ratio of males and females is equal, with 50% each, totaling as many as 75 people. The age data of respondents can be seen in Figure 2, with the majority aged in the range of 20-30 years, as much as 70%, the age range of 30-40 years, as much as 16%, the age over 40 years as much as 11%, and the age range of 17-20 years as much as 3%. Then, based on monthly income in Figure 3, respondents were highest in the range of 1-5 million rupiah (IDR), as much as 53%, in the range of 5-10 million rupiah (IDR), as much as 22%, below 1 million rupiah (IDR), as much as 16%, and above 10 million rupiah (IDR) as much as 9%.

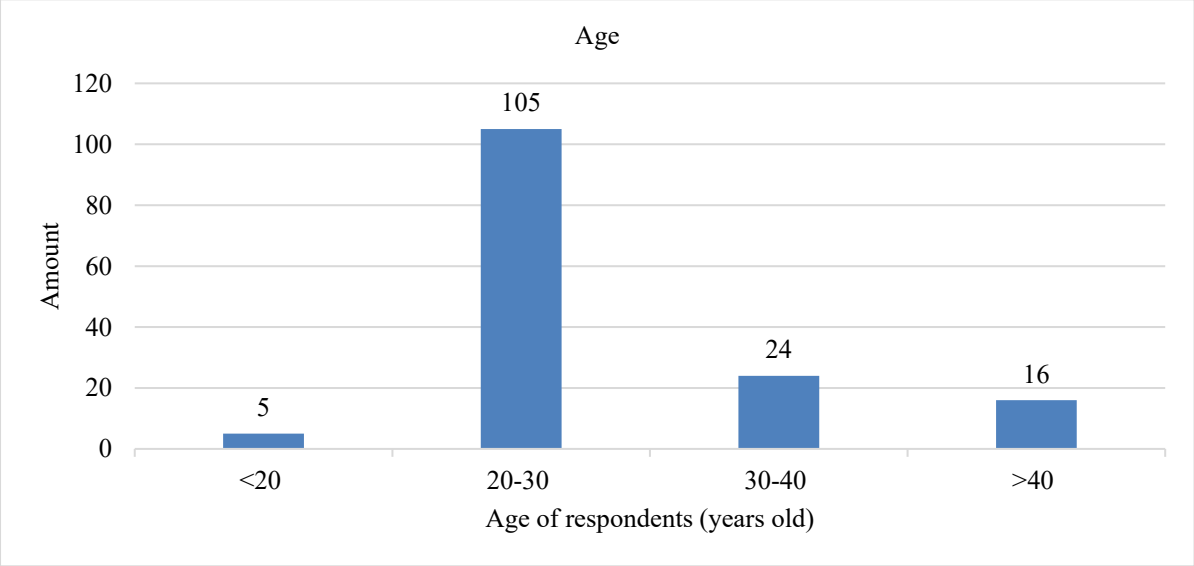


Figure 2. Respondent profile based on age.

https://doi.org/10.31436/iiumej.v26i1.3239

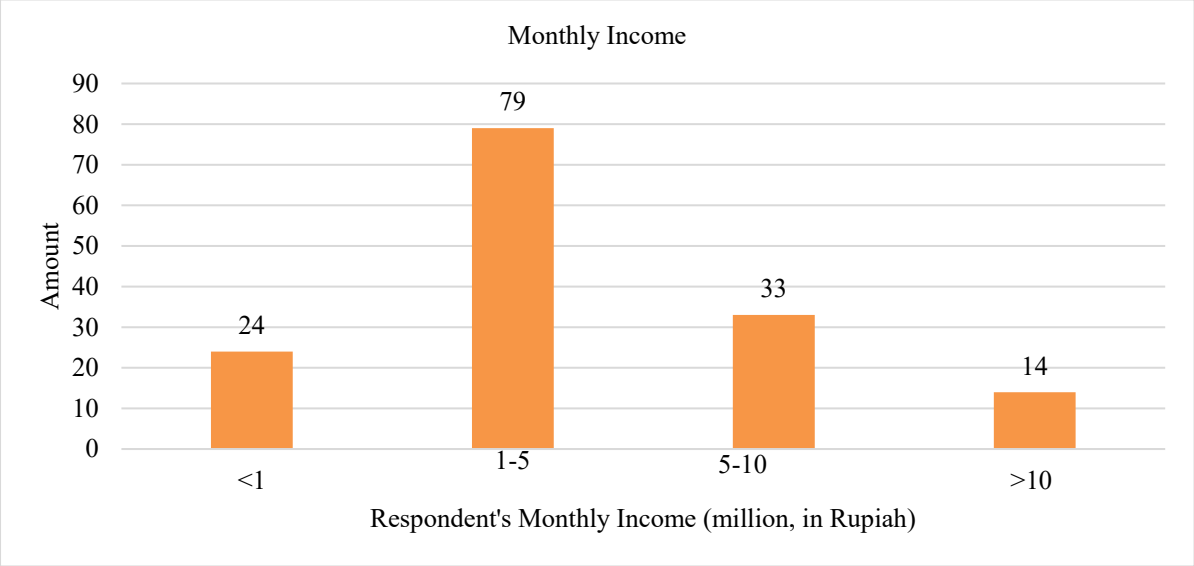


Figure 3. Respondent profile based on monthly income.

The clustering of respondents can be divided into geographic segmentation (city, province, country), demographic segmentation (age, gender, occupation), and psychographic segmentation (lifestyle). However, what is used in this study is only demographic segmentation [16]. Figures 2 and 3 show the cluster grouping for respondents determined based on demographic segmentation, namely gender, age, and monthly income of each respondent.

### 3.4. Data Analysis

#### *3.4.1. Validity and Reliability Test*

Testing the validity and reliability of the data is done with the help of SPSS 17.0 software. The value of the R table for 150 respondents with a significance level of 5% was 0.159, and for a significance level of 1%, it was 0.208. From the validity test results, all correlation values are more significant than the value of the R table, or it can also be called R calculate > R table so that the data is declared valid. Another requirement to report whether or not data other than correlation is to look at the significance value (Sig.). If the significance value < 0.05, then the data is declared valid. After being tested for validity, the next step is to test reliability. The reliability test results show that Cronbach's alpha value is 0.959 > 0.6, so the data is declared reliable.

#### *3.4.2. KMO and Barlett's Test*

KMO (Kaiser-Meyer-Olkin) and Barlett's Test of Sphericity to determine the feasibility of data before factor analysis or PCA (Principal Component Analysis). KMO aims to determine whether the variable is adequate and has a KMO value criterion of > 0.5. Then, the analysis can continue. While Barlett's Test seeks to assess the level of a significant relationship between variables with sig value criteria of < 0.05, it can be indicated that the variables are sufficiently correlated. The test results show that the KMO value for each design (S1-S8) is > 0.5, thus qualifying that the sample is adequate. The results also showed that all sig values were 0.000 < 0.05, and Barlett's Test produced a sufficient correlation between variables.

#### *3.4.3. Principal Component Analysis (PCA)*

Principal Component Analysis (PCA) was carried out in this study to reduce the initial variables that amounted to fewer without eliminating the information in the initial data. The

https://doi.org/10.31436/iiumej.v26i1.3239

new variable of reduction results is called the main component or factor. A variable can explain a factor with an extraction value of > 0.50. The analysis showed that all variables (comfortable, luxurious, unique, enjoyable, simple, modern) were valued at > 0.50.

The eigenvalue is the magnitude of the total variance that can be explained by the factor formed and is greater than 1. Table 3 illustrates that the eigenvalue of factor 1 is 4.611 > 1, thus explaining 76.852% of the variation. Meanwhile, the eigenvalue of factor 2 is 1.011, so it can explain 16.844% of the variation. Factor 1 and factor 2 can account for 93.696% of the variation. The values of factor 1 and factor 2 already represent data analysis or user preferences.

Table 3. PCA value for all respondents (total variance explained)

| **Component** | **1** | **2** | **3** | **4** | **5** | **6** |
|---|---|---|---|---|---|---|
| **Eigenvalue** | 4.611 | 1.011 | 0.265 | 0.087 | 0.024 | 0.001 |
| **Variability (%)** | 76.852 | 16.844 | 4.422 | 1.458 | 0.403 | 0.020 |
| **Cumulative (%)** | | | 98.119 | 99.577 | 99.980 | 100.000 |

From Table 4 of the Component Matrix, two factors influence user preferences for train compartment design based on Kansei Words: factor 1, consisting of 'comfortable,' 'luxurious,' 'unique,' 'enjoyable,' and 'modern,' and factor 2, consisting of 'simple' Kansei Words.

Table 4. Component matrix

| **Component** | **Comfortable** | **Luxurious** | **Unique** | **Enjoyable** | **Simple** | **Modern** |
|---|---|---|---|---|---|---|
| 1 | .866 | .959 | .967 | .949 | -.580 | .877 |
| 2 | .392 | -.159 | -.210 | .305 | .804 | .220 |

Biplot is the delivery of data information presented in a two-dimensional graph. Biplot analysis is descriptive and visually presents a cluster of objects and variables. This graph shows the proximity between objects with similar observed characteristics and correlated variables [17]. The biplot graph in Figure 4 presents information on the proximity between objects or variables with similar characteristics. The interpretation of biplot graphs based on the same quadrant, as below:

a. Quadrant I, S3, and S7 are the favorite designs because they are on the positive axis.
b. Quadrant II, namely S1, S2, and S4, has similar characteristics in design specifications and is closely related to the Kansei Words, which are 'comfortable,' 'modern,' 'unique,' 'luxurious,' and 'enjoyable.'
c. Quadrant III, namely S5, S6, and S8, has similar characteristics in the design specifications.
d. Quadrant IV is simple Kansei Words, but the distance is close to quadrant III, allowing a relationship to occur.

https://doi.org/10.31436/iiumej.v26i1.3239

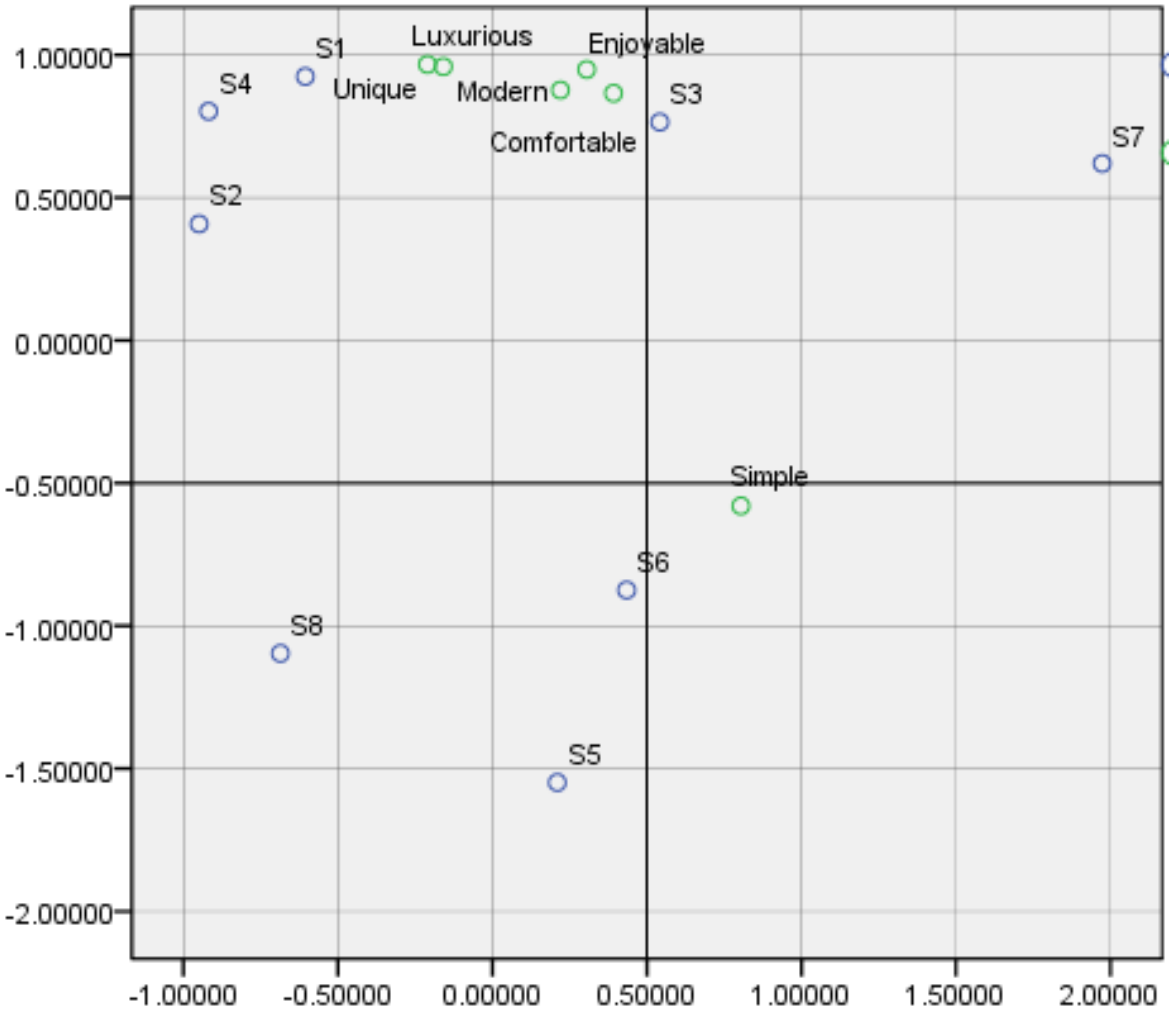


Figure 4. Biplot graph of a train compartment design samples.

### *3.4.4. Clustering of Respondents*

The output results in Table 5 refer to the z-score standardization provided that the data is above the total average if positive (+). Three clusters were formed: Cluster 1, consisting of 86 respondents who chose the S1 design the most; Cluster 2, composed of 8 respondents who chose the S7 design the most; and Cluster 3, consisting of 56 respondents who chose the S3 design the most. A total of 150 respondents were declared valid.

Table 5. Final cluster centers

| Design Samples | Cluster | | |
|---|---|---|---|
| | 1 | 2 | 3 |
| **S1** | 3.62 | 2.12 | 4.15 |
| **S2** | 3.40 | 1.96 | 4.21 |
| **S3** | 3.55 | 2.21 | 4.30 |
| **S4** | 3.55 | 2.07 | 4.14 |
| **S5** | 2.91 | 2.06 | 4.09 |
| **S6** | 3.10 | 2.42 | 4.21 |
| **S7** | 3.48 | 2.69 | 4.41 |
| **S8** | 2.99 | 2.38 | 4.09 |

https://doi.org/10.31436/iiumej.v26i1.3239

Cluster results based on the respondent‘s gender can be defined as follows:

a. *Cluster 1*: Consisting of 86 respondents, more female respondents amounted to 53% or 46, while males amounted to 47% or 40.
b. *Cluster 2*: Consists of 8 respondents; more male respondents are 75% or 6, while females are 25% or 2.
c. *Cluster 3*: There are 56 respondents, of which more respondents are male, 55% or 31, while females are 45% or 25.

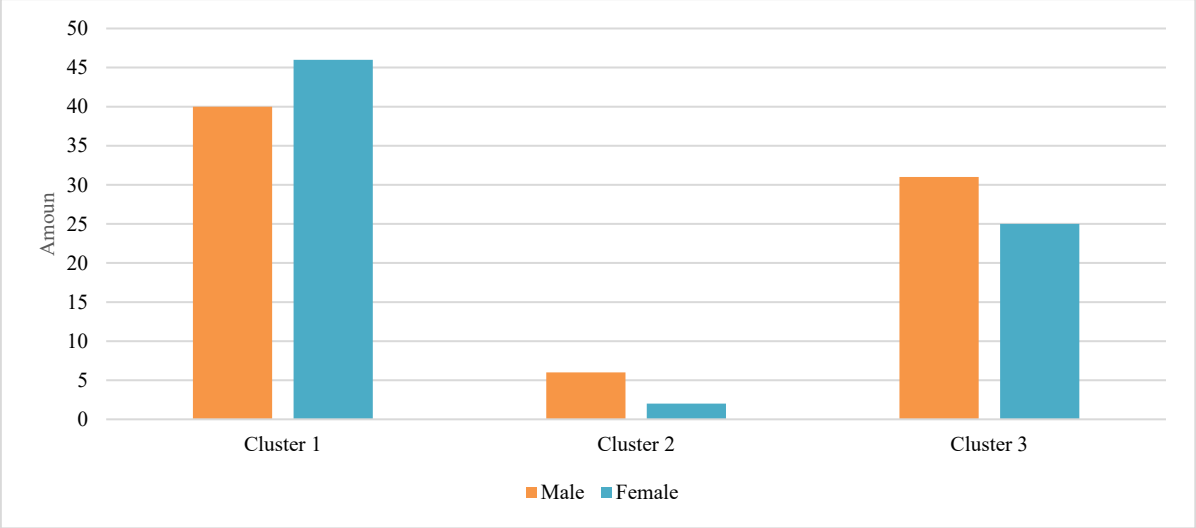


Figure 5. Clusters by the gender of respondents.

The results of cluster analysis based on respondents' age can be defined as follows:

a. *Cluster 1*: Consists of the most, namely, sixty-four people aged 20-30, twelve people aged 30-40, eight people over 40 years old, and two people less than 20 years old.
b. *Cluster 2*: Consists of the most, namely, seven people aged 30-40 and one person aged 20-30.
c. *Cluster 3*: Consists of the most, namely, forty people aged 20-30, eight people over 40, five people aged 30-40, and three people less than 20 years old.

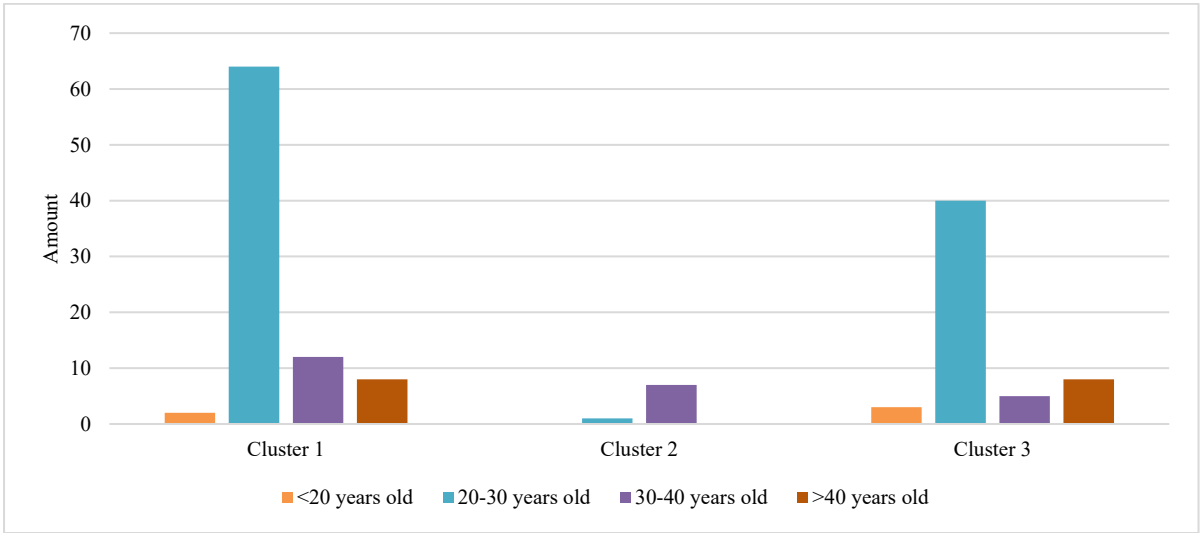


Figure 6. Clusters by the age of respondents.

https://doi.org/10.31436/iiumej.v26i1.3239

The results of the cluster analysis in terms of respondents' monthly income can be defined as follows:

a. *Cluster 1*: Dominated by the respondents with incomes of 1-5 million (in Rupiah), as many as 45 people, less than 1 million (in Rupiah), as many as 16 people, 5-10 million (in Rupiah) as many as 15 people, and more than 10 million (in Rupiah) as many as 10 people.
b. *Cluster 2*: Dominated by the respondents with an income of 5-10 million (in Rupiah), as many as 5 people, and more than 10 million (in Rupiah) as many as 3 people.
c. *Cluster 3*: Dominated by respondent groups with incomes of 1-5 million (in Rupiah), as many as 34 people, 5-10 million (in Rupiah), as many as 13 people, less than 1 million (in Rupiah) as many as eight people, and more than 10 million (in Rupiah) as many as one person.

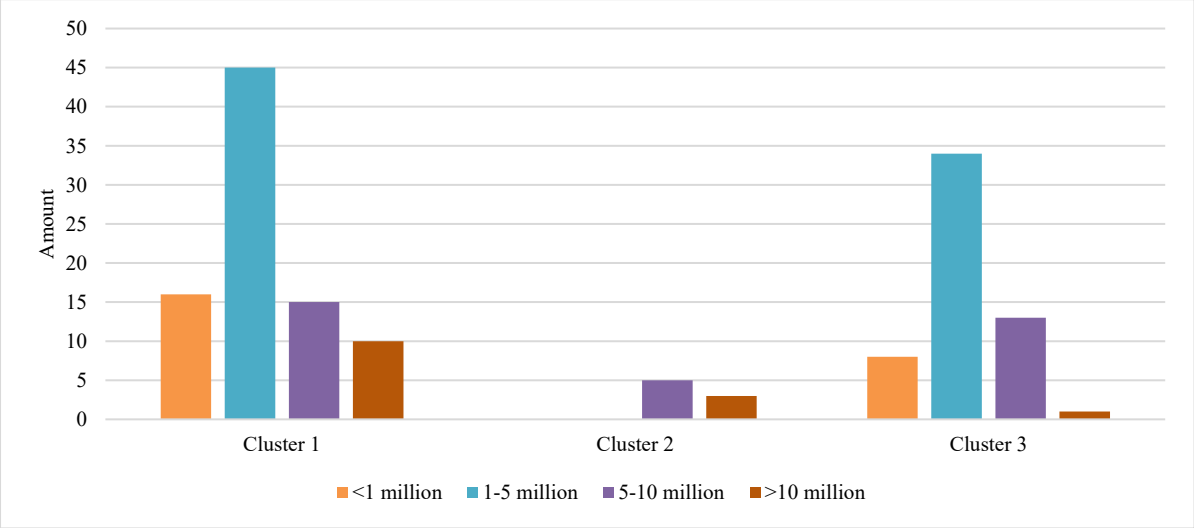


Figure 7. Clusters by the monthly income of respondents (in Rupiah).

### 3.5. Discussion

Discussion of the biplot graph of PCA output results places S3 and S7 in the first quadrant with positive axis values. The biplot graph displays the distribution points of the respondents' most and least selected items [18]. S3 and S7 emerged as the favored designs chosen by many respondents chose. The doff surface and texture of pine wood material are utilized in both favored designs due to pine wood's neutral and light color appearance [19], so it is in great demand by most respondents of various ages.

Based on the cluster analysis result based on design samples, respondents in cluster 1 opted for S1 with specifications: curved shape, studio green color palette, doff surface, and teak wood material texture. Females dominate this cluster with a productive adult age of 20-30 years and a monthly middle-class income ranging from 1-5 million (in Rupiah). Productive adults prefer dynamic design forms with curves that look dynamic, resembling human figures that were required to be efficient and adapt quickly following the times.

Many respondents in cluster 2 chose S7 with specifications: straight shape, studio green color palette, doff surface, and pine wood material texture. The characteristics of respondents in this cluster is characterized by males in their middle age of 30-40 years and the upper median income of 5-10 million (in Rupiah) per month. Middle-aged adults typically prefer simple shapes with straight lines and minimal ornamentation. The combination of studio green and light pine wood creates a serene and tranquil impression.

Many respondents in cluster 3 chose S3 with specifications: curved shape, sage green color palette, doff surface, and pine wood material texture. Cluster 3 respondents have characteristics dominated by males aged 20-30 years with a middle-class income ranging from 1-5 million (in Rupiah) per month. Bright green hues are often favored as design schemes with high-brightness colors provide better satisfaction [20]. The choice of design, according to the character of the respondents in this cluster, is quite dynamic with a combination of sage green, which is quite bright with pine wood.

# 4. CONCLUSION

This study concludes that six Kansei Words—'comfortable,' 'luxurious,' 'unique,' 'enjoyable,' 'simple,' and 'modern'—describe user preferences based on statistical analyses. Principal Component Analysis (PCA) identified two main components, Factor 1 and Factor 2, explaining 93.696% of the variation in user preferences. Factor 1, termed Variable A, includes 'comfortable,' 'luxurious,' 'unique,' 'enjoyable,' and 'modern,' while Factor 2, termed Variable B, consists of 'simple.' Biplot graphics revealed that respondents favored design S3, characterized by a curved shape, sage green color palette, doff surface, and pine wood texture, while S7, featuring a straight shape, studio green color palette, doff surface, and pine wood texture, also ranked highly. Clustering analysis further segmented respondents into three clusters: Cluster 1 (86 respondents, favoring S1), Cluster 2 (8 respondents, favoring S7), and Cluster 3 (56 respondents, favoring S3), categorized by gender, age, and monthly income. These findings highlight the role of specific clusters in shaping user preferences based on visual design features. The author is optimistic that this study's results will serve as a valuable resource for future research and applications in train compartment design, offering insights that could drive innovative solutions and enhance user experiences.

# REFERENCES

[1] D. K. Yohanny, L. Purwaningrum and A. Mulyono, "Analysis of User Preferences from the Visual Impression of New Generation Railway Compartment Interior Design with Kansei Engineering Method," 2022.

[2] M. Bergman, B.-G. Rosen and L. Eriksson, "Affective Surface Engineering for Total Appearence - Soft Metrology for Chrome Surface in Car Interior Design," *6th Kansei Engineering & Emotion Research,* August - September 2016.

[3] S. N. Hapsari, T. Sjafrizal and R. A. Anugraha, "Designing Train Passenger Seat by Kansei Engineering in Indonesia," Bandung, 2017.

[4] M. Trepayova, V. Kureykova, P. Zameynik and P. Yeazay, "Advantages and disadvantages of rail transportation as perceived by passengers: A qualitative and quantitative," *Transactions on Transport Sciences,* vol. 11, no. 3, pp. 52-62, 2020.

[5] R. Mono, Design for Product Understanding, Stockholm, Sweden: ISBN 9789147011056, 1977.

[6] M. Nagamachi and A. M. Lokman, "Innovations of Kansei Engineering," Tokyo, 2011.

[7] S. Schutte, Engineering Emotional Values in Product Design, Linkoping: UniTryck, 2005.

[8] L. Xue, X. Yi and Y. Zhang, "Research on Optimized Product Image Design Integrated Decision System Based on Kansei Engineering," *MDPI,* pp. 1-19, 2020.

[9] H. W.N, Y. S.H, S. H, S. M.S and A. A, "Customer Preferences in Car Design Using Kansei Engineering and Cubic Bezier Curve," *International Journal of Engineering and Technology,* vol. 7, no. 4, pp. 4170-4173, 2018.

[10] C. E. Osgood and J. G. Snider, Semantic Differential Technique, Chicago: Aldine Publishing Company, 1969.

[11] M. Nagamachi, Kansei Affective Engineering, CRC Press, 2010.

[12] R. A. Johnson and D. W. Wichern, Applied Multivariate Statistical Analysis, 6th ed., Upper Saddle River, New Jersey: Pearson Prentice Hall, 2007.

[13] P. H. Bloch, "Seeking the Ideal Form: Product Design and Consumer Response," *Journal of Marketing,* vol. 59, no. 3, p. 16, 1995.

[14] S. T. Schutte, J. Eklund, J. R. Axelsson and M. Nagamachi, "Concepts, Methods and Tools in Kansei Engineering," vol. 5, pp. 214-231, 2004.

[15] H. Medriosa, "Metode Cluster Analysis," *Jurnal Momentum,* vol. 16, no. 2, 2014.

[16] P. Kotler, Marketing Management, Jakarta: Erlangga, 1999.

[17] J. I. Principal Component Analysis, New York: Springer Verlag, 2022.

[18] A. Ginanjar and Y. Supendi, " Kansei Engineering's Implementation in Designing the Interface of the Mobile Website of the News Portal of Education and Children's Health Information," Jurnal Tiarsie, vol. 14, no. 1, 2017.

[19] D. K. Seftianingsih, " Introduction to Different Types of Solid Wood and Their Construction for Wooden Furniture," Interior Design Major, Universitas Sahid, Surakarta, 2018.

[20] X.-H. Xie, Y. Xu, S. Guo, H. Zhu and H. Yan, "Evaluation and Decision of a Seat Color Design Scheme for a High-Speed Train Based on the Practical Color Coordinate System and Hybrid Kansei Engineering," MDPI, vol. 12, p. 316, 2024.

https://doi.org/10.31436/iiumej.v26i1.3397

# SHEET METAL MANUAL HANDLING AIDS: EFFECTS OF DESIGN DIFFERENCES ON MUSCLE ACTIVITY AND SUBJECTIVE ASSESSMENT

**NADIAH AHMAD[1*], RADIN ZAID RADIN UMAR[1], ISA HALIM[1], DIAN MARDI SAFITRI[2]**

[1]*Fakulti Teknologi dan Kejuruteraan Industri dan Pembuatan, Universiti Teknikal Malaysia Melaka, Melaka, Malaysia*
[2]*Fakultas Teknologi Industri, Universitas Trisakti, Jakarta, Indonesia*

**Corresponding author: nadiaha@utem.edu.my*

*(Received: 7 August 2024; Accepted: 10 September 2024; Published online: 10 January 2025)*

***ABSTRACT:*** Manual material handling is a common task in various industries and has been linked to work-related musculoskeletal injuries. Handling heavy and bulky sheet metal manually can cause awkward postures and forceful exertion, leading to intense biomechanical load on the workers. A trolley lifter was designed and fabricated to address this issue and improve work postures during sheet metal transfer tasks. This study aimed to investigate the potential ergonomic benefits of the trolley lifter design compared to the traditional hydraulic table cart. The study aims to determine the effect of the design differences between the two devices on muscle activities during sheet metal handling operations and to compare subjective perceptions of the subjects on these devices. The independent variable in this study was the type of device used for sheet metal handling (i.e., trolley lifter vs. traditional hydraulic table cart) and types of sheet metals (vary by thickness). The dependent variables were muscle activities in four different muscles (biceps brachii, triceps brachii, erector spinae, and trapezius) and subjective perceptions of the devices. A randomized repeated-measure experimental design was employed, surface electromyography was used to measure muscle activities, and a subjective questionnaire was administered to gather data on the participant's perceptions of the devices. Participants were asked to perform separate sheet metal handling operations using both devices. The relationship between the dependent and independent variables was examined. The non-parametric test indicated that there were significant decreases in muscle activation levels in the biceps brachii, triceps brachii, erector spinae, and trapezius muscles when using the trolley lifter compared to the traditional hydraulic table cart. Moreover, participants rated the trolley lifter as more usable, useful, and desirable than the traditional hydraulic table cart. In conclusion, the trolley lifter was a more effective and ergonomically beneficial tool for handling large sheet metals than the traditional hydraulic table cart. This study highlights the importance of ergonomic interventions in manual material handling tasks, advocating for adopting tools and equipment that can enhance worker safety, reduce physical strain, and improve overall job satisfaction.

***ABSTRAK:*** Pengendalian bahan secara manual adalah tugas biasa dalam pelbagai industri dan telah dikaitkan dengan kecederaan muskuloskeletal yang berkaitan dengan kerja. Mengendalikan kepingan logam yang berat dan besar secara manual boleh menyebabkan postur yang janggal dan tenaga yang kuat yang membawa kepada beban biomekanikal yang kuat pada pekerja. Untuk menangani isu ini, pengangkat troli telah direka untuk memperbaiki postur kerja semasa tugas pemindahan kepingan logam. Kajian ini bertujuan untuk menyiasat lebih lanjut potensi faedah ergonomik reka bentuk pengangkat troli berbanding troli meja hidraulik tradisional. Objektif kajian ini adalah untuk menentukan kesan perbezaan reka bentuk antara kedua-dua peranti pada aktiviti otot semasa operasi pengendalian kepingan

logam dan untuk membandingkan persepsi subjektif subjek kepada peranti ini. Pembolehubah bebas dalam kajian ini ialah jenis peranti yang digunakan untuk pengendalian kepingan logam (iaitu, pengangkat troli berbanding troli meja hidraulik tradisional) dan jenis kepingan logam (berbeza mengikut ketebalan). Pembolehubah bersandar ialah aktiviti otot dalam empat otot yang berbeza (biceps brachii, triceps brachii, erector spinae, dan trapezius) dan persepsi subjektif pada peranti. Reka bentuk eksperimen ukuran berulang secara rawak telah digunakan dan elektromiografi permukaan digunakan untuk mengukur aktiviti otot, serta soal selidik subjektif telah diberikan untuk mengumpul data mengenai persepsi peserta kepada peranti. Peserta diminta melakukan operasi pengendalian kepingan logam menggunakan kedua-dua peranti pada masa yang berasingan. Hubungan antara pembolehubah bersandar dan tidak bersandar telah dikaji. Ujian bukan parametrik menunjukkan bahawa terdapat penurunan ketara dalam tahap pengaktifan otot dalam bisep brachii, triceps brachii, erector spinae, dan otot trapezius apabila menggunakan pengangkat troli berbanding dengan troli meja hidraulik tradisional. Selain itu, peserta menilai pengangkat troli sebagai lebih boleh digunakan, berguna dan diingini daripada troli meja hidraulik tradisional. Kesimpulannya, pengangkat troli telah terbukti sebagai alat yang lebih berkesan dan ergonomik untuk mengendalikan kepingan logam yang besar berbanding dengan kereta meja hidraulik tradisional. Kajian ini menyerlahkan kepentingan campur tangan ergonomik dalam tugas pengendalian bahan manual, menyokong penggunaan alatan dan peralatan yang boleh meningkatkan keselamatan pekerja, mengurangkan ketegangan fizikal, dan meningkatkan kepuasan kerja secara keseluruhan.

***KEYWORDS:*** *Ergonomics, manual material handling, trolleys, sheet metal, electromyography.*

# 1. INTRODUCTION

Manual material handling (MMH) is prevalent in industries and associated with work-related injuries such as musculoskeletal disorders. The International Labor Organization and the World Health Organization have raised concerns about the rise in work-related musculoskeletal disorders, which significantly impact productivity and have serious health implications. Injuries like overexertion may occur when workers perform MMH tasks that exceed their physical capabilities [1]. Workers' compensation claims associated with injuries due to MMH were found to represent a significant number of claims in Malaysia, with over 8000 cases reported in 2022 [2]. To mitigate these risks, several guidelines on MMH have been published by various agencies and regulatory bodies to guide proper handling techniques [3-5]. Improper handling techniques, especially for heavy and large items, can lead to low work efficiency and safety and health issues, such as back pain, sprains, strains, cuts, and bruises. These items can be challenging for human workers to handle due to their large dimensions and weight. As a result, mechanical aids are often used to facilitate safer and more efficient handling operations. Controlling hazards in material handling activities within the industry presents significant challenges, particularly in eliminating or substituting these hazards. Consequently, engineering controls are often the preferred approach. The design of material handling aids represents a form of engineering control aimed at minimizing ergonomic risks in material handling tasks.

There are two main types of mechanical aids available for handling large and heavy items: motorized and non-motorized. Motorized aids, including forklifts, vacuum lifting devices, and crane systems, enhance worker ergonomics and efficiency during heavy lifting tasks [6]. However, these devices can be expensive and bulky, require specific operational skills, and necessitate more space, making them less practical for small workshops. Non-motorized devices, such as industrial trolleys, hand trucks, hydraulic table carts, and tilt-top trolleys, offer

a more cost-effective and compact alternative for handling large items. In Malaysia's labor-intensive economy, with many foreign workers providing cheaper labor, non-motorized devices are still widely used, especially in small and medium-sized enterprises. However, these devices may be less efficient, and handling operations can still expose workers to health and safety risks, particularly when dealing with large or sharp-edged items like sheet metals, necessitating careful examination of more ergonomically designed devices.

When designing material handling equipment, it's essential to consider various ergonomic factors to ensure the well-being of workers. This includes minimizing the force required to operate equipment, avoiding awkward postures, reducing repetitive motions, considering the weight of objects being handled, optimizing workstation dimensions, and enhancing overall productivity. Considering these criteria, we can minimize the physical strain on workers' body mechanics and create a more efficient and healthy workplace design. Incorporating proper measures to control musculoskeletal hazards plays a crucial role in achieving Sustainable Development Goal (SDG) 3, which focuses on promoting good health and well-being. Furthermore, SDG 8, centered on promoting decent work and economic growth, emphasizes the importance of integrating occupational health and safety practices within the framework of decent work. Lastly, SDG 9 highlights the significance of industry, innovation, and infrastructure, emphasizing how effective ergonomic design can enhance efficiency and safety within operations.

Numerous ergonomic studies have explored manual handling aids to reduce work-related musculoskeletal disorders (WMSDs) [7-8]. For instance, Koppelaar et al. [9] examined the impact of ergonomic devices on the biomechanical load of nursing staff when handling patients. Greco et al. [10] proposed a method to analyze the design parameters of an industrial cart to assess ergonomic risks during pushing or pulling tasks. Kundu et al. [11] designed a trolley for mud transfer in brick-molding activities to reduce physical strain on workers by improving working postures. Additionally, using MMH aids for lifting has been shown to significantly lower the incidence rates of low-back injuries, physical work demands, and WMSD symptoms [12-14]. However, many studies have focused on the effects of various factors on human biomechanical load when using specific MMH aids [15-21]. Few studies have examined the efficiency of multiple non-motorized manual handling aids for large objects and compared their ergonomic impacts on users. These studies assessed changes in biomechanical workloads, such as when using modified table carts in production and warehouse lifting activities [22-23], hand trucks for agricultural products [24], assistive mechanisms for patient lateral transfers [25], auxiliary handling devices for construction work [26], and devices for carrying large water bottles [27].

For the manual handling of large sheet metals, the research team previously designed, developed and fabricated a trolley lifter to improve work postures [28]. The trolley lifter has shown early promise in improving work efficiency, occupational safety, and health conditions. In addition to reducing cycle time and manpower utilization, the device was found to enhance work postures and reduce exposure to physical contact with sharp edges, compared to traditional handling methods used by technicians. This study aims to further quantify the potential benefits of the trolley lifter design compared to traditional manual handling methods. Specifically, the study aims to investigate the impact of design differences between the trolley lifter and the traditional hydraulic table cart on muscle activity and subjective perceptions of subjects during sheet metal handling operations.

https://doi.org/10.31436/iiumej.v26i1.3397

# 2. METHODOLOGY

A randomized, two-way, repeated-measures experiment was conducted to determine the effect of material handling device design on muscle activities and subjects' subjective perceptions of using the devices during the sheet metal handling task. The experiment took place at a fabrication workshop involving a cutting machine for sheet metals.

## 2.1. Subjects

Twenty-five healthy, non-smoking male subjects, young adults, participated in the experiment. Only subjects free of any musculoskeletal disorders or injury history that might affect how they performed the experimental tasks were recruited. The subjects were fully informed and understood the study before beginning the experimental procedures, which included detailed information about the study's purpose, procedures, potential risks, and their right to withdraw at any time without consequence. Additionally, all data collected were anonymized and handled strictly to protect participants' privacy. Our study was designed following recognized ethical principles, including those outlined in the Declaration of Helsinki. Written informed consent was obtained from all participants aged between 20 and 25 years old, with a mean body weight of 75 kg (SD = 15) and a mean height of 175 cm (SD = 10).

## 2.2. Experimental Design

The experiment involved two independent variables: types of trolleys and types of sheet metals. Figure 1 shows the trolleys used in this experiment. The hydraulic lift table cart in Figure 1 (left) is the trolley commonly used in the operations of the fabrication workshop as a material handling tool. The authors designed the tilt-top trolley lifter in Figure 1 (right) to improve the handling of large sheet metals. Table 1 describes its basic structural elements. The details of the new trolley lifter have been described in a previous study [28].

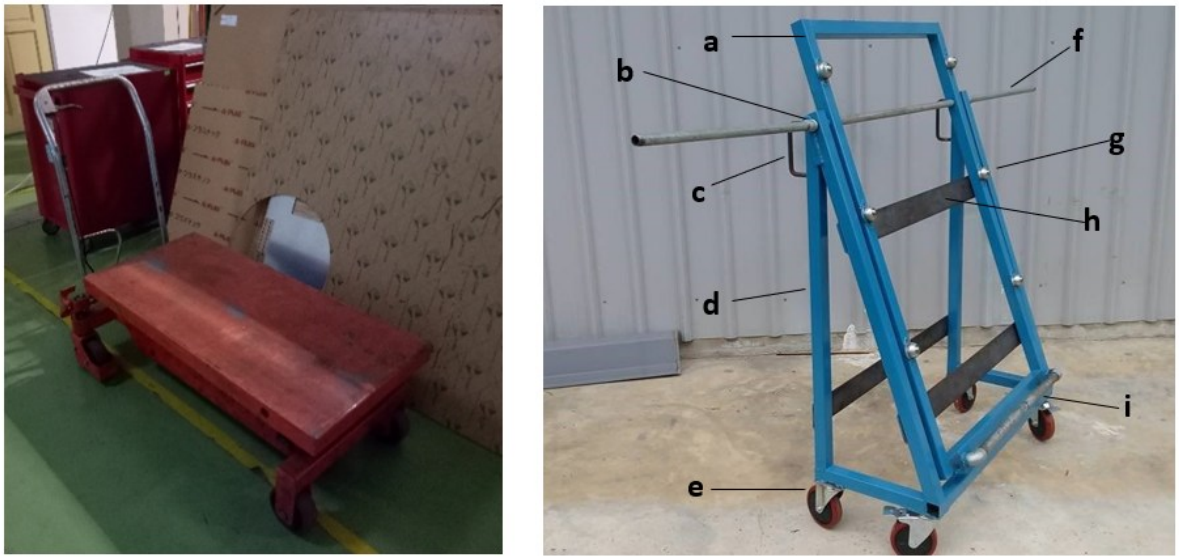


Figure 1. A hydraulic lift table cart (left) and tilt-top trolley lifter (right) were used in this study.

Three types of same-size sheet metals that differ by thickness were used in this study, representing various metal weights commonly handled by technicians in a local fabrication workshop. The sheet metals studied were 1mm galvanized iron sheet metal, 3 mm aluminum sheet metal, and 6mm aluminum sheet metal. The dependent variables were the subjects'

https://doi.org/10.31436/iiumej.v26i1.3397

normalized muscle activities (percent maximum voluntary contraction, %MVC) of four different muscles and subjective perceptions of the material handling devices' usability, usefulness, and desirability. The muscles involved in this study are the right side biceps brachii (BB), triceps brachii (TB), erector spinae (ES), and upper trapezius (TP), which were measured using surface electromyography (EMG). Additionally, subjective assessments were also conducted using a questionnaire specifically designed to gather the participants' perceptions of the two devices, focusing on the usability, usefulness, and desirability of the studied devices. A small pilot run was conducted with a few participants to ensure the questions were clear, understandable, and appropriate for the study context. Any feedback from the pilot was carefully incorporated into the final version of the questionnaire to enhance its relevance and clarity.

Table 1. Overview of trolley lifter components (as per Figure 1)

| Label | Part Element | Material |
|---|---|---|
| a | Rectangular frame | Hollow metal tube |
| b | Rotation socket | Galvanized iron |
| c | Handle for pushing/pulling | Iron rod |
| d | Triangular side frame | Hollow metal tube |
| e | Swivel caster wheel | Rubber wheel with galvanized steel |
| f | Support rod | Galvanized iron |
| g | Rollerball | Stainless steel |
| h | Plate support | Steel |
| i | Handle for tilting | Steel with rubber grip |

A randomized repeated measure experimental design was conducted such that each subject performed all the sheet metal and device combinations in a randomized order to prevent an order effect bias. Each combination was replicated twice for each subject. In each experimental task, the subject, with the help of an assigned helper, loaded a sheet metal onto the trolley from the storage rack and then transferred the metal to the specified location before unloading the metal onto a laser cutting machine (see Figure 2).

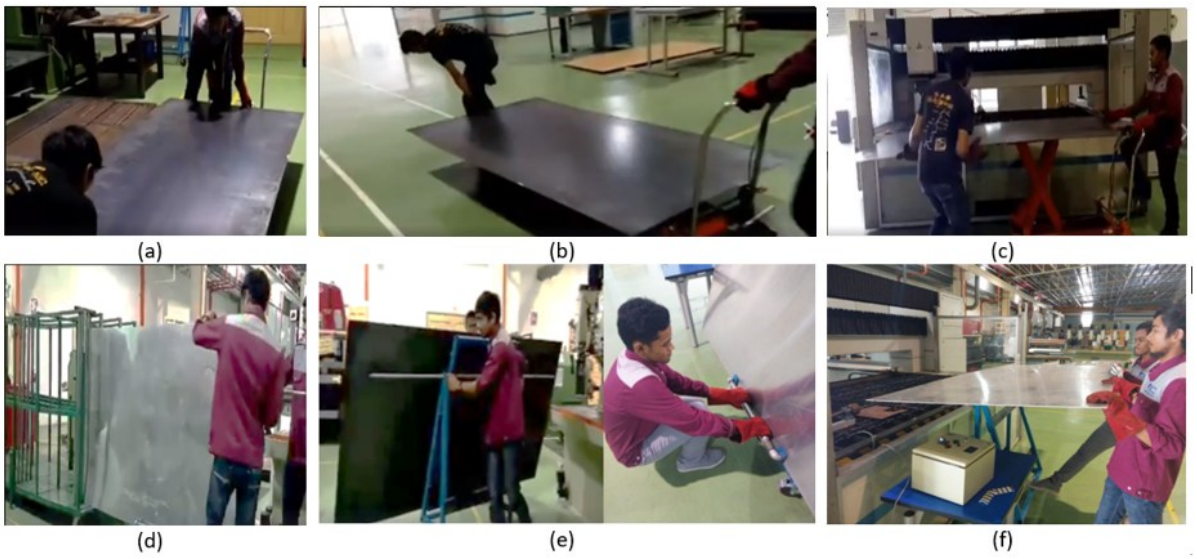


Figure 2. (a)-(c): The process of sheet metal handling with a table cart, (d)-(f): The process of sheet metal handling with a trolley lifter.

Before the subject performed the experimental tasks, skin preparation at the electrode sites was done as in [29] according to the sensor locations recommended by the standardization

https://doi.org/10.31436/iiumej.v26i1.3397

guideline "Surface electromyography (sEMG) for non-invasive assessments of muscles" (SENIAM) [30]. Figure 3 depicts the location of the sensors for the four muscles. A reference electrode was placed at the right lateral epicondyle of the humerus, approximately 1 inch from the olecranon elbow [31]. Maximum voluntary muscle contraction (MVC) value was recorded for each muscle three times. Each contraction lasted 3 seconds, and 30 seconds of rest was given between each successive MVC recording, as in [32].

In the experimental task, the subject was asked to perform sheet metal handling operations involving loading, transferring, and unloading from the storage location to the laser cutting machine. The subject must first load the sheet metal from the storage area onto the handling device and then transfer the metal to the cutting machine in the fabrication workshop. The metal was then unloaded from the trolley onto the cutting machine. Each subject performed the operations with the help of a helper, as the sheet metal needed to be handled by two people. The EMG amplitude data was recorded during the loading of the sheet metal onto the handling device and the unloading of the metal onto the cutting machine from the handling device. The subject will repeat the experiment for a different device and sheet metal weight. Each subject rested for two minutes between successive experiments as in [31].

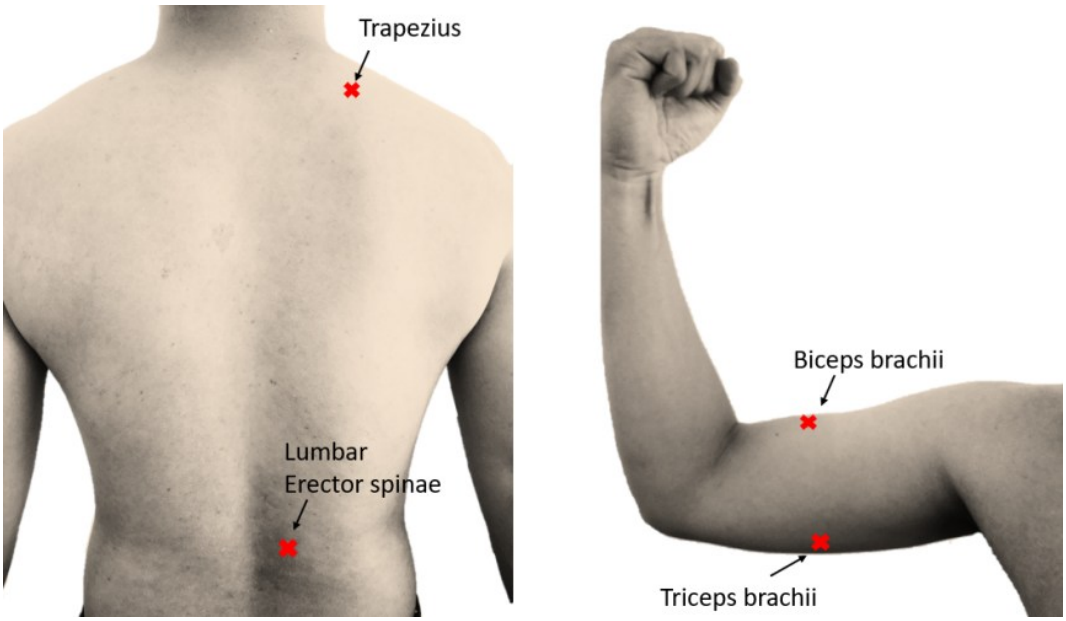


Figure 3. The placement of electrodes at lumbar erector spinae, upper trapezius, biceps brachii, and triceps brachii.

The EMG data was collected using sEMG TeleMyo 2400T G2 (Noraxon Inc., USA) device with Ag/AgCl electrodes. MyoResearch Master Edition software (Noraxon Inc., USA) was used to record and process the EMG signal data from each muscle studied. Each subject's resulting mean EMG amplitude data were normalized to the maximum voluntary contraction (MVC), a reference value for contraction.

After the subject completed all experimental task units, a questionnaire was given to obtain the subject's perception of the material handling devices concerning their usability, usefulness, and desirability. The subject was asked to indicate their level of agreement with the questions asked according to the 5-point Likert scale (1=strongly disagree, 2=disagree, 3=neutral, 4=agree, 5=strongly agree). Likert scale is a widely used questionnaire instrument to measure the degree of agreement with a set of questions in research [33].

https://doi.org/10.31436/iiumej.v26i1.3397

### 2.3. Statistical Analysis

Muscle activities in the biceps brachii, triceps brachii, erector spinae, and trapezius muscles were measured for both device types (trolley lifter and traditional hydraulic table cart) during loading and unloading tasks across three types of sheet metals (1mm, 3mm, and 6mm). Following data collection, comparisons of muscle activities were conducted between the two handling devices across the three sheet metal conditions for both tasks. The study analyzed differences in peak muscle activities using mean normalized EMG data (%MVC) at the 90th percentile [34].

We initially assessed the normality of the EMG data using the Shapiro-Wilk test. While most data sets yielded p-values above 0.05, indicating normality, some showed p-values below 0.05, suggesting deviations from normality. Given the sample size of 25 and mixed normality results, we applied non-parametric tests uniformly to ensure consistency and avoid selective bias in the analysis. Consequently, the Friedman test was employed to examine the effect of device types on peak muscle activities across the three types of sheet metal for both loading and unloading tasks. The significance level was set at $p < 0.05$, with effect sizes calculated using Kendall's W. Post hoc pairwise comparisons were performed using the Wilcoxon signed-rank test with Bonferroni correction to control for multiple comparisons. All statistical analyses were conducted using the SPSS statistics package [35]. Additionally, subjective perceptions were compared using descriptive statistics, with the median and interquartile range (IQR) reported as measures of central tendency to provide insights into participants' responses. The Wilcoxon signed-rank test was then utilized to examine the significant differences in participant response between the two devices.

## 3. RESULTS

### 3.1. Muscle Activities

Table 2 shows the means and standard deviations of normalized EMG (%MVC) data for each muscle from the loading and unloading tasks. The Friedman Test results, as shown in Table 3 on both loading and unloading tasks for each muscle, showed that there were significant differences in mean normalized EMG values between the related groups. Multiple pairwise Post Hoc comparisons were conducted to analyze the differences in peak muscle activity among the devices and the metal types using a Wilcoxon signed-rank test with a Bonferroni-corrected significance level of $p<0.0056$. Table 4 shows the results of the pairwise comparisons over nine combinations of levels. The Wilcoxon signed-rank test pairwise comparison revealed that the handling device significantly affected the peak muscle activity when compared over each type of sheet metal ($p<0.001$) for both loading and unloading tasks. The trolley lifter appeared to result in lower muscle activities, whereby the level of differences depended on the type of sheet metal. The types of sheet metals also affected the peak muscle activity for both devices in both tasks, such that higher muscle activities tend to correspond to heavier metal sheets. However, comparing the devices during the loading task with 6mm sheet metal, the differences in peak muscle activity were marginal for erector spinae and trapezius muscles. In addition, the results were also marginal for the trapezius muscle when comparing the handling devices over 3mm sheet metal in the unloading task. In the unloading task, an exception showed that handling the 3mm and 6mm sheet metals with a trolley lifter did not significantly affect the difference in the erector spinae peak muscle activity. These patterns can be observed in Figure 4-5. In short, the trolley lifter gives some advantages over the table cart in reducing biceps brachii, triceps brachii, lumbar, and trapezius muscles' activities depending on the types of sheet metal handled.

https://doi.org/10.31436/iiumej.v26i1.3397

### 3.2. Subjective Perception

Table 5 displays the results of the subjective assessment of the studied devices. The assessment showed more favorable results for the trolley lifter, including the subjects' perception of fatigue and muscle pain when operating the devices. Small IQR values indicate a relatively small spread in the central portion of your data, suggesting more consistent responses or agreement among participants regarding both devices. The Wilcoxon signed-rank test also showed that the differences in subjective perception between table cart and trolley lifter were significant for all questions with p<.001 and $W$=0 except for question 9 ($W$=210). In addition, through direct comparison, 60 percent of the subjects agreed to use the trolley lifter, while the rest remained neutral. In contrast, none of the subjects agreed that they preferred to use the lift table cart, but 64 percent remained neutral. Besides, 80 percent agreed that the trolley lifter was easy to use, while only 8 percent agreed that the lift table cart was easy. In short, the trolley lifter was more usable, practical, and desirable for handling large sheet metal manually than the lift table cart.

Table 2. Mean normalized EMG data (%MVC) and standard deviation at 90th percentile (n=25).

| **Loading Task** | | | | | | | | | |
|---|---|---|---|---|---|---|---|---|---|
| | | ***Biceps*** | | ***Triceps*** | | ***Erector Spinae*** | | ***Trapezius*** | |
| **Device** | **Metal** | **Mean** | **SD** | **Mean** | **SD** | **Mean** | **SD** | **Mean** | **SD** |
| **Table** | 1mm | 2.416 | 0.348 | 9.152 | 1.270 | 6.578 | 2.635 | 4.705 | 0.449 |
| | 3mm | 6.050 | 1.049 | 14.191 | 2.497 | 15.518 | 3.493 | 6.801 | 0.978 |
| | 6mm | 29.305 | 10.437 | 24.222 | 4.190 | 27.802 | 5.942 | 16.059 | 3.333 |
| **Trolley** | 1mm | 1.726 | 0.205 | 5.267 | 0.749 | 3.403 | 0.647 | 2.733 | 0.612 |
| | 3mm | 4.436 | 0.751 | 11.975 | 1.789 | 10.500 | 2.282 | 5.292 | 1.007 |
| | 6mm | 12.627 | 2.092 | 19.713 | 3.105 | 24.963 | 5.921 | 13.567 | 2.682 |
| **Unloading Task** | | | | | | | | | |
| | | ***Biceps*** | | ***Triceps*** | | ***Erector Spinae*** | | ***Trapezius*** | |
| **Device** | **Metal** | **Mean** | **SD** | **Mean** | **SD** | **Mean** | **SD** | **Mean** | **SD** |
| **Table** | 1mm | 3.403 | 0.656 | 12.970 | 1.646 | 10.445 | 2.552 | 6.569 | 1.792 |
| | 3mm | 8.730 | 1.314 | 18.296 | 3.055 | 21.404 | 4.683 | 7.120 | 1.674 |
| | 6mm | 16.254 | 3.087 | 27.650 | 5.223 | 24.060 | 5.507 | 16.686 | 2.481 |
| **Trolley** | 1mm | 2.048 | 0.297 | 7.834 | 1.216 | 6.619 | 1.229 | 3.477 | 0.744 |
| | 3mm | 6.041 | 0.825 | 12.064 | 1.992 | 17.943 | 4.099 | 6.646 | 1.282 |
| | 6mm | 13.930 | 1.958 | 16.845 | 2.287 | 17.926 | 3.451 | 10.611 | 1.368 |

Table 3. Friedman Test results

| **Task** | **Muscle** | **Chi-Squared** | **df** | **p** | **Kendall's W** |
|---|---|---|---|---|---|
| Loading | Biceps | 124.451 | 5 | < .001 | 0.996 |
| | Triceps | 121.069 | 5 | < .001 | 0.969 |
| | Erector Spinae | 118.463 | 5 | < .001 | 0.948 |
| | Trapezius | 120.017 | 5 | < .001 | 0.960 |
| Unloading | Biceps | 123.080 | 5 | < .001 | 0.985 |
| | Triceps | 114.371 | 5 | < .001 | 0.915 |
| | Erector Spinae | 115.400 | 5 | < .001 | 0.923 |
| | Trapezius | 112.794 | 5 | < .001 | 0.902 |

https://doi.org/10.31436/iiumej.v26i1.3397

# 4. DISCUSSIONS

This study revealed that the peak muscle activation levels were statistically significantly lower in the trolley lifter than in the lift table cart for both loading and unloading tasks (refer to Table 4 and Figures 4 to 5). This difference may be influenced by the types of sheet metal used. When using the table cart, the highest mean EMG value was recorded in the biceps brachii during the loading of a 6mm metal sheet (29.31). In contrast, when using the trolley lifter, the highest average load was observed in the erector spinae when loading a 6mm metal sheet (24.96). Further analysis of the data for both loading and unloading tasks indicated that the use of a trolley lifter had shown a reduction in muscular efforts, with an average maximum reduction of 57 percent in the biceps brachii, an average maximum reduction of 42 percent in the triceps brachii, an average maximum reduction of 48 percent in the erector spinae, and an average maximum reduction of 47 percent in the trapezius. For these muscles, the trolley lifter provided more advantages during the unloading task than the loading task. This conclusion outcome suggests that the trolley lifter can significantly decrease the muscular load when handling large sheet metals compared to the lift table cart. This is supported by the subjective perception assessment, which indicated more favorable results for the trolley lifter.

Table 4. Wilcoxon signed-rank test results on loading and unloading tasks

| Muscles / Group pair | Biceps | | Triceps | | Erector Spinae | | Trapezius | |
|---|---|---|---|---|---|---|---|---|
| | **Z** | **Asymp. Sig. (2-tailed)** | **Z** | **Asymp. Sig. (2-tailed)** | **Z** | **Asymp. Sig. (2-tailed)** | **Z** | **Asymp. Sig. (2-tailed)** |
| ***Loading Task*** | | | | | | | | |
| Tab,1mm - Tab,3mm | -4.372[b] | <.001 | -4.372[b] | <.001 | -4.372[b] | <.001 | -4.372[b] | <.001 |
| Tab,1mm - Tab,6mm | -4.372[b] | <.001 | -4.372[b] | <.001 | -4.372[b] | <.001 | -4.372[b] | <.001 |
| Tab,3mm - Tab,6mm | -4.372[b] | <.001 | -4.372[b] | <.001 | -4.345[b] | <.001 | -4.372[b] | <.001 |
| Tro,1mm - Tro,3mm | -4.372[b] | <.001 | -4.372[b] | <.001 | -4.372[b] | <.001 | -4.372[b] | <.001 |
| Tro,1mm - Tro,6mm | -4.372[b] | <.001 | -4.372[b] | <.001 | -4.372[b] | <.001 | -4.372[b] | <.001 |
| Tro,3mm - Tro,6mm | -4.372[b] | <.001 | -4.372[b] | <.001 | -4.372[b] | <.001 | -4.372[b] | <.001 |
| Tab,1mm - Tro,1mm | -4.372[c] | <.001 | -4.372[c] | <.001 | -4.372[c] | <.001 | -4.372[c] | <.001 |
| Tab,3mm - Tro,3mm | -4.345[c] | <.001 | -4.345[c] | <.001 | -4.049[c] | <.001 | -4.130[c] | <.001 |
| Tab,6mm - Tro,6mm | -4.372[c] | <.001 | -3.484[c] | <.001 | -2.731[c] | 0.006 | -2.973[c] | 0.003 |
| ***Unloading Task*** | | | | | | | | |
| Tab,1mm - Tab,3mm | -4.372[b] | <.001 | -4.292[b] | <.001 | -4.372[b] | <.001 | -1.601[b] | <.001 |
| Tab,1mm - Tab,6mm | -4.372[b] | <.001 | -4.372[b] | <.001 | -4.372[b] | <.001 | -4.372[b] | <.001 |
| Tab,3mm - Tab,6mm | -4.372[b] | <.001 | -4.345[b] | <.001 | -4.023[b] | <.001 | -4.372[b] | <.001 |
| Tro,1mm - Tro,3mm | -4.372[b] | <.001 | -4.372[b] | <.001 | -4.372[b] | <.001 | -4.372[b] | <.001 |
| Tro,1mm- Tro,6mm | -4.372[b] | <.001 | -4.372[b] | <.001 | -4.372[b] | <.001 | -4.372[b] | <.001 |
| Tro,3mm - Tro,6mm | -4.372[b] | <.001 | -4.372[b] | <.001 | -.040[c] | 0.968* | -4.372[b] | <.001 |
| Tab,1mm - Tro,1mm | -4.372[c] | <.001 | -4.372[c] | <.001 | -4.372[c] | <.001 | -4.372[c] | <.001 |
| Tab,3mm - Tro,3mm | -4.372[c] | <.001 | -4.372[c] | <.001 | -4.345[c] | <.001 | -2.812[c] | 0.005 |
| Tab,6mm - Tro,6mm | -3.646[c] | <.001 | -4.372[c] | <.001 | -4.372[c] | <.001 | -4.372[c] | <.001 |

a. Wilcoxon Signed ranks Test.
b. Based on positive ranks.
c. Based on negative ranks.
* non-significant result.

This study identified that the two devices—the table cart and trolley lifter—exhibited distinct muscle activation patterns as they handled heavier loads. Specifically, when comparing loading versus unloading tasks, the peak muscle loads on the biceps brachii, triceps brachii, erector spinae, and trapezius muscles were generally lower during loading tasks for both

https://doi.org/10.31436/iiumej.v26i1.3397

devices. However, exceptions emerged when handling 6mm metal sheets. With the table cart, the biceps, brachii, and erector spinae muscles showed higher activation levels during loading than unloading. Notably, the biceps brachii experienced a substantial increase in muscle load—nearly double—during the 6mm metal sheet loading. In contrast, when using the trolley lifter, higher muscle activation was observed in the triceps brachii, erector spinae, and trapezius during the loading task compared to unloading. These differences suggest that each device relies on distinct muscle recruitment strategies to manage the increased demands of heavier loads.

Additionally, during the loading tasks, the triceps brachii generally experienced higher peak loads than the biceps brachii across conditions. However, a notable exception was observed when using the table cart for loading the 6mm metal sheet, where the biceps brachii showed higher activation than the triceps brachii. This pattern indicates that the table cart may require more arm stabilization, possibly due to the positioning or grip required when handling heavier materials.

When comparing the two devices, all muscles showed an upward trend in activation levels as the metal sheet thickness increased, which aligns with previous findings [36]. However, the erector spinae muscle displayed a slight decrease in activation during the unloading of the 6mm sheet using the trolley lifter. This suggests that the trolley lifter might engage other muscle groups—such as the hips or legs—to assist in managing the load during unloading, thereby reducing the demand on the erector spinae.

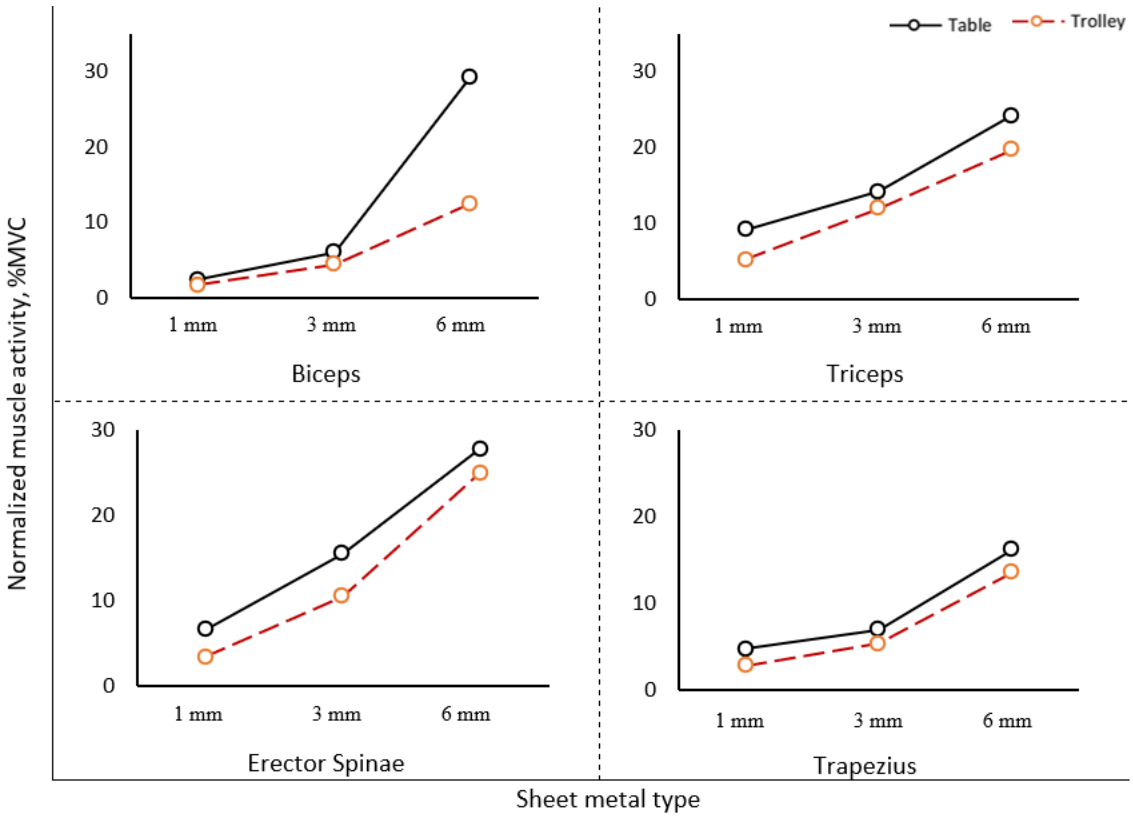


Figure 4. Mean normalized EMG values comparisons during the loading task against three different sheet metals for the four muscles.

https://doi.org/10.31436/iiumej.v26i1.3397

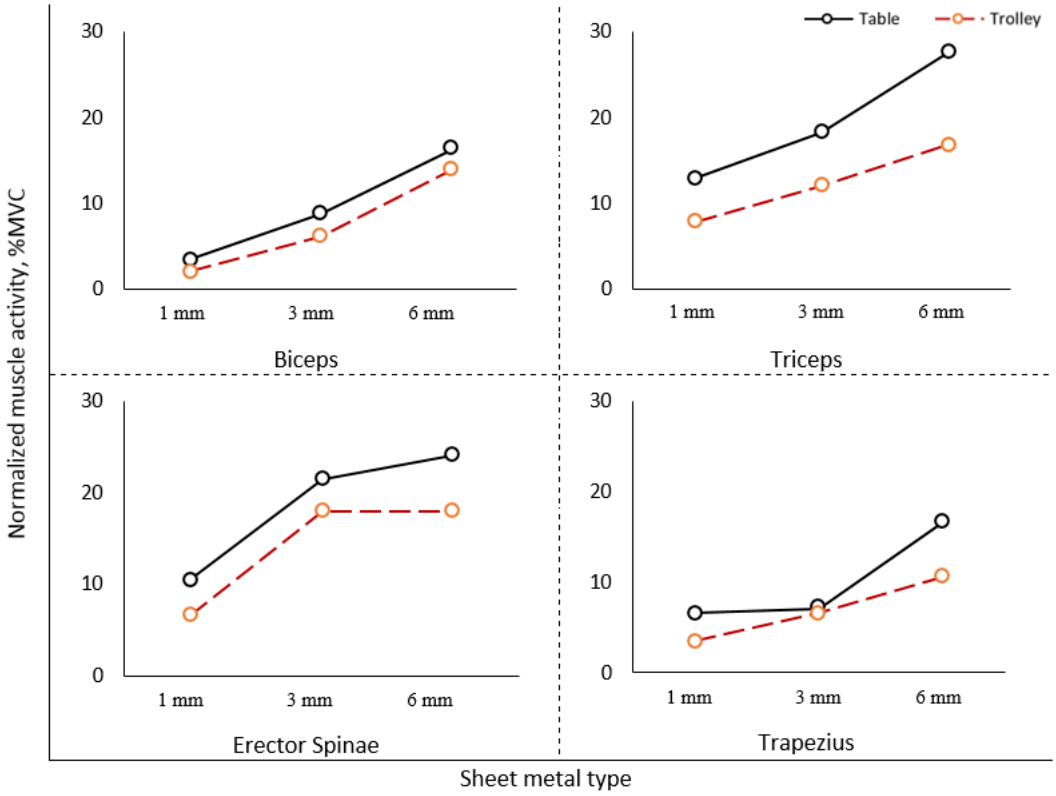


Figure 5. Mean normalized EMG values comparisons during the unloading task against three different sheet metals for the four muscles.

Table 5. Subjective assessment of the two devices.

| **Questions** | **Median (IQR) Score** | |
|---|---|---|
| | *Table cart* | *Trolley lifter* |
| 1. I can perform the task easier by using this device. | 3(1) | 4(0) |
| 2. I was able to complete the tasks quickly when using the device. | 2(1) | 4(0) |
| 3. I think that I would need the support of a person to be able to use the device. | 4(0) | 3(0) |
| 4. I found the device meets my needs. | 2(1) | 4(0) |
| 5. I am satisfied with the device. | 2(1) | 41) |
| 6. I felt the device was useful. | 3(1) | 4(1) |
| 7. I would like to use the device for the sheet metal transfer task. | 3(1) | 4(1) |
| 8. I think using the device can reduce fatigue at the end of the work day. | 3(1) | 4(1) |
| 9. I think I have muscle pain when performing the task using the device. | 4(1) | 2(1) |

Likert scale: 1=strongly disagree, 2=disagree, 3=neutral, 4=agree, 5=strongly agree.

As previously highlighted, the activation levels across the muscles generally followed a consistent trend across the devices and tasks, except when handling the heavier 6mm sheet metal. This exception likely reflects adaptive muscle recruitment strategies the body employs to maintain stability under increased mechanical demand [37]. Achieving this stability involves a coordinated activation pattern across multiple muscles, resulting in continuous adjustments depending on the task requirements [38]. For example, the biceps brachii exhibited higher EMG values when loading the 6mm sheet metal using the table cart, likely due to the need to hold the sheet horizontally in a bent posture before placing it on the cart. The weight of the sheet metal required greater activation from the biceps brachii to stabilize the arm and prevent extension while supporting the load.

The relationship between physical demand and spinal stability has been well-documented in previous studies, with stability quantified through lumbar spine compression force [39-40]. Higher physical demands trigger the co-activation of agonistic and antagonistic trunk muscles, enhancing lumbar stability and preventing injury. Research also emphasizes that mechanical stability requires co-activation across multiple antagonistic muscle groups [41-43]. In line with this, Lavender et al. [44] demonstrated that the co-activation of additional muscles can reduce the activation level of the erector spinae during physically demanding tasks.

In this study, the unloading task with the 6mm sheet metal using the trolley lifter potentially induced co-activation of other muscle groups, alleviating the load on the erector spinae. Interestingly, EMG data showed a slight reduction in erector spinae activation during this task (see Figure 5). This pattern may be attributed to the postural adjustments required for unloading, where the subject had to lift a tilted panel from a lower position and slide the metal using the trolley's roller wheels. In such scenarios, the subject likely relied more on hip and leg muscles to assist in the lifting motion, reducing the demand for the trunk muscles. Previous studies suggest that kinematic trade-offs between hip and trunk motion during lifting tasks influence muscle recruitment patterns [45-46]. Specifically, bending at the hips allows for a more upright trunk posture, reducing the load on the trunk muscles while lifting from lower positions [47]. Noe et al. [48] also reported that engaging the leg muscles is a common strategy to minimize the burden on the erector spinae during heavy lifting. However, the complex interactions between the trunk and other muscle groups remain insufficiently understood, especially in tasks with high mechanical demand [49].

This study was limited to the activation levels of a few muscles measured unilaterally and did not capture the full extent of co-activation among multiple muscles during the task. Future research should investigate neuromuscular control strategies across a broader range of muscles, particularly trunk and leg muscles, to enhance our understanding of how different muscle groups coordinate during material handling. Additionally, this study provides insights into how different non-motorized material-handling devices influence muscle recruitment strategies, which subsequently impact the load on specific muscles. Understanding these recruitment patterns can guide ergonomic design improvements, making handling devices more effective in reducing muscular strain and improving worker performance.

Our findings align with previous research, demonstrating the effectiveness of ergonomically designed handling in reducing work-related musculoskeletal disorders (WMSDs) and physical work demands. However, unlike many studies that focus on specific MMH aids in isolation, this research offers a comparative analysis between two different non-motorized devices—the trolley lifter and the table cart—providing valuable insights into their distinct impacts on worker health and safety. This comparative approach highlights the importance of evaluating device performance and how these devices influence muscle recruitment patterns under varying task demands.

## 5. CONCLUSION

The study investigated the effect of design differences between the trolley lifter and traditional hydraulic table carts on muscle activities with subjective assessment during the manual sheet metal handling task. The study showed that the trolley lifter reduces muscle activation levels in the biceps brachii, triceps brachii, erector spinae, and upper trapezius muscles. Additionally, participants rated the trolley lifter as more usable, useful, and desirable than the traditional hydraulic table cart. The findings of this study have important implications for the design and use of manual handling devices in various industries. The trolley lifter may offer a significant advantage over the traditional hydraulic table cart in reducing biomechanical

load and improving worker safety and comfort. However, the finding of this study is limited to the loading and unloading task of handling large sheet metals. Future research could investigate the effectiveness of the trolley lifter in other manual handling tasks and settings. It would also be valuable to explore the underlying mechanisms driving muscle activation changes and extend the analysis to additional muscles on both sides of the body for a more comprehensive understanding. In conclusion, this study contributes to the growing knowledge of the benefits of ergonomically designed manual handling devices. The trolley lifter can potentially improve work postures, reduce muscle activities, and enhance subjective experiences compared to the traditional hydraulic table cart. Further research and implementation of this device may help reduce the incidence of work-related musculoskeletal disorders associated with manual material handling tasks, promoting both worker well-being and operational efficiency.

## ACKNOWLEDGEMENT

The authors would like to thank the Malaysian government and Universiti Teknikal Malaysia Melaka (UTeM) for their support in this research. The authors would like to acknowledge Yap Peei Yong, Roslan Hassan, Tengku Ahmad Shauki, Lee Poh Yan, Zulaikah Sulaiman, and Nursyuhada Ismah for their contributions to this study.

## REFERENCES

[1] Dick RB, Hudock SD, Lu ML, Waters TR, Putz-Anderson V. Manual materials handling. In Physical and Biological Hazards of the Workplace. 3rd edition. Edited by Stave GM and Wald PH. New Jersey, Wiley; pp 33-52.

[2] Social Security Organization (2022). Annual Report.Malaysia: Ministry of Human Resource.

[3] Centers for Disease Control and Prevention (2007). Ergonomic guidelines for manual material handling (No. 2007-131). USA: National Institute of Occupational Safety and Health.

[4] Department of Occupational Safety and Health (2018). Guidelines for Manual Handling at Workplace. Malaysia: Ministry of Human Resources.

[5] Occupational Safety and Health Administration (2006). Materials Handling and Storage (OSHA 2236). USA: US Department of Labor.

[6] Colgate JE, Peshkin M, Klostermeyer SH. (2003) Intelligent assist devices in industrial applications: a review. In Proceedings of 2003 IEEE/RSJ International Conference on Intelligent Robots and Systems: 27-31 October 2003; Las Vegas. IEEE: pp 2516-2521.

[7] Muslim K, Nussbaum MA. (2016) Traditional posterior load carriage: Effects of load mass and size on torso kinematics, kinetics, muscle activity and movement stability. Ergonomics, 59(1): 99–111.

[8] Smallman C. (2012) Continuous relative phase variability of hand-held load carriage techniques: The effectiveness of a mover's assistive device. MSc Thesis. Queen's University, Kinesiology and Health Studies.

[9] Koppelaar E, Knibbe HJ, Miedema HS, Burdorf A. (2012) The influence of ergonomic devices on mechanical load during patient handling activities in nursing homes. Annals of Occupational Hygiene, 56(6): 708-718.

[10] Greco A, Sepe R, Caputo F. (2018) A numerical procedure for evaluating physical parameters of ergonomic assessment for cart pushing/pulling tasks. Procedia Structural Integrity, 12: 304–316.

[11] Kundu A, Bachwal L, Patle A, Rawal P, Ray GG. (2019) An Ergonomic assessment and design intervention on mud-transfer activity in brick-making industry, India. In Research Into Design for a Connected World, Smart Innovation, Systems and Technologies. Edited by Chakrabarti A. Singapore, Springer; pp 505–517.

[12] Marras WS, Allread WG, Burr DL, Fathallah FA. (2000) Prospective validation of a low-back disorder risk model and assessment of ergonomic interventions associated with manual materials handling tasks. Ergonomics, 43: 1866–1886.

[13] Garg A, Owen B, Beller D, Banaag J. (1991) A biomechanical and ergonomic evaluation of patient transferring tasks: Bed to wheelchair and wheelchair to bed. Ergonomics, 34 : 289-312.

[14] Van der Molen HF, Sluiter JK, Hulshof CTJ, Vink P, Frings-Dresen MHW. (2005) Effectiveness of measures and implementation strategies in reducing physical work demands due to manual handling at work. Scandinavian Journal of Work, Environment and Health, 31: 75–87.

[15] Nimbarte AD, Sun Y, Jaridi M, Hsiao H. (2013) Biomechanical loading of the shoulder complex and lumbosacral joints during dynamic cart pushing task. Applied Ergonomics, 44: 841–849.

[16] Argubi-Wollesen A, Wollesen B, Leitner M, Mattes K. (2017) Human body mechanics of pushing and pulling: analyzing the factors of task-related strain on the musculoskeletal system. Safety and Health at Work, 8(1): 11–8.

[17] Lachance CC, Korall AMB, Russell CM, Feldman F, Robinovitch SN, Mackey DC. (2016) External hand forces exerted by long-term care staff to push floor-based lifts: Effects of flooring system and resident weight. Human Factors, 58(6): 927–43.

[18] Lee SJ, Rempel D. (2019) Comparison of lift use, perceptions, and musculoskeletal symptoms between ceiling lifts and floor-based lifts in patient handling. Advances in Intelligent Systems and Computing, 820: 219–22.

[19] Resnick ML, Chaffin DB. (1995) An ergonomic evaluation of handle height and load in maximal and submaximal cart pushing. Applied Ergonomics, 26(3): 173–8.

[20] Botti L, Galizia FG, Mora C, Zecchi G. (2020) A thorough investigation on pushing activities in industry: The impact of the variation in the speed of motion and load conditions on initial and sustained forces. Applied Ergonomics, 85(1):103080.

[21] Kao HC, Lin CJ, Lee YH, Chen SH. (2015) The effects of direction of exertion, path, and load placement in nursing cart pushing and pulling tasks: an electromyographical study. PLoS ONE, 10(10):e0140792.

[22] Mohamed MSS, Halim I, Azani AH, Ling LY. (2018) Ergonomics intervention to improve plastic roll handling process at production area in plastic manufacturing industry. Human Factors and Ergonomics Journal, 3(1):12-21.

[23] Ramsey TR. (2013) The effects of load-positioning material handling equipment on spinal loading during manual handling of bulk bags. MSc Thesis. University of Cincinnati, Department of Environmental Health.

[24] Singh S, Sinwal N, Rathore H, Sinwal S. (2011) Assessment of physiological workload related to selected manual material handling tasks. The Anthropologist, 13(4): 293–8.

[25] Al-Qaisi SK, El Tannir A, Younan LA, Kaddoum RN. (2020) An ergonomic assessment of using laterally-tilting operating room tables and friction reducing devices for patient lateral transfers. Applied Ergonomics, 87(1): 103122.

[26] Sillanpää J, Lappalainen J, Kaukiainen A, Viljanen M, Laippala P. (1999) Decreasing the physical workload of construction work with the use of four auxiliary handling devices. International Journal of Industrial Ergonomics, 24(2): 211–22.

[27] Ramadan MZ, Alkahtani M. (2017) Development of a device to reduce the risk of injury in handling unstable loads. Work, 58(3): 349–59.

[28] Radin Umar RZ, Ahmad N, Halim I, Lee PY, Hamid M, Design and development of an ergonomic trolley-lifter for sheet metal handling task: A preliminary study. Safety and Health at Work, 10(3):327-35. https://doi.org/10.1016/j.shaw.2019.06.006.

[29] Konrad P. (2006) The ABC of EMG. Arizona, Noraxon U.S.A. Inc.

[30] Sensor location. SENIAM [http://www.seniam.org]

[31] Ahamed NU, Yusof Z, Alqahtani M, Altwijri O, Rahman SAMM, Sundaraj K. (2015) Gender effects in surface electromyographic activity of the biceps brachii muscle during prolonged isometric contraction. Procedia Computer Science, 61: 448–53.

[32] Ritchey P, Peres SC, Duffield TJ. (2012) Differences in muscle activity for 4 touch devices. In: Proceedings of the Human Factors and Ergonomics Society Annual Meeting, 56(1): 1594–8. https://doi.org/10.1177/107118131256131

[33] Jebb AT, Ng V, Tay L. (2021) A review of key Likert scale development advances: 1995–2019. Frontiers in Psychology, 12: 637547. doi: 10.3389/fpsyg.2021.637547

[34] Korak JA, Bruininks BD, Paquette MR. (2020) The influence of normalization technique on between-muscle activation during a back-squat. International Journal of Exercise Science, 13(1):1098-1107. PMID: 32922626; PMCID: PMC7449321.

[35] IBM Corp (2023). IBM SPSS Statistics for Windows, Version 29.0.0 Armonk, NY: IBM Corp [Computer software].

[36] Yoon J, Shiekhzadeh A, Nordin M. (2012) The effect of load weight vs. pace on muscle recruitment during lifting. Applied Ergonomics, 43(6): 1044–50.

[37] Butler HL, Hubley-Kozey CL, Kozey JW. (2009) Electromyographic assessment of trunk muscle activation amplitudes during a simulated lifting task using pattern recognition techniques. Journal of Electromyography and Kinesiology, 19(6): e505-e512.

[38] McGill SM, Grenier S, Kavcic N, Cholewicki J. (2003) Coordination of muscle activity to assure stability of the lumbar spine. Journal of Electromyography and Kinesiology, 13(4): 353-9.

[39] Cholewicki J, Simons AP, Radebold A. (2000) Effects of external trunk loads on lumbar spine stability. Journal of biomechanics, 33(11): 1377-1385.

[40] Cholewicki J, McGill SM. (1996) Mechanical stability of the in vivo lumbar spine: implications for injury and chronic low back pain. Clinical Biomechanics, 11(1): 1-15.

[41] Granata KP, Orishimo KF. Response of trunk muscle coactivation to changes in spinal stability. Journal of Biomechanics, 34(9): 1117-1123.

[42] Granata KP, Wilson SE. (2001) Trunk posture and spinal stability. Clinical Biomechanics, 16(8): 650-659.

[43] Vera-Garcia FJ, Elvira J L, Brown SH, McGill SM. (2007) Effects of abdominal stabilization maneuvers on the control of spine motion and stability against sudden trunk perturbations. Journal of Electromyography and Kinesiology, 17(5): 556-567.

[44] Lavender SA, Tsuang Y-H, Hafezi A, Anderson GBJ, Chaffin DB, Hughes RE. (1992) Coactivation of the trunk muscles during asymmetric loading of the torso. Human Factors: The Journal of the Human Factors and Ergonomics Society, 34(2): 239–47.

[45] Marras WS, Granata KP. (1997) Changes in trunk dynamics and spine loading during repeated trunk exertions. Spine, 22(21): 2564–70.

[46] Radin Umar RZ, Mohd Azli Lee FA, Khafiz MN, Ahmad N, & Abdullasim N. (2020) Space mapping of hip and wrists motions for different transfer distances in manual material handling task. IIUM Engineering Journal, 21(2), 164–176. https://doi.org/10.31436/iiumej.v21i2.1197

[47] Sreenivasa M, Millard M, Kingma I, Van Dieen JH, Mombaur K. (2018) Predicting the influence of hip and lumbar flexibility on lifting motions using optimal control. Journal of Biomechanic, 78: 118-125.

[48] Noe DA, Mostardi RA, Jackson ME, Porterfield JA, Askew MJ. (1992) Myoelectric activity and sequencing of selected trunk muscles during isokinetic lifting. Spine, 17(2): 225–9.

[49] Siu A, Schinkel-Ivy A, Drake JD. (2016) Arm position influences the activation patterns of trunk muscles during trunk range-of-motion movements. Human Movement Science, 49: 267–76.

https://doi.org/10.31436/iiumej.v26i1.3430

# DEVELOPMENT AND EVALUATION OF PASSIVE EXOSKELETON (SOLATEXO) FOR ASSISTING MUSLIMS WITH PHYSICAL DISABILITY IN SALAH

**ISA HALIM[1*], MUHAMMAD NADZIRUL IZZAT MAHADZIR[1], ZULKEFLEE ABDULLAH[1], MUHAMMAD HAIKAL SIDEK[1], MARIAM MD GHAZALY[2], ADI SAPTARI[3]**

*[1]Fakulti Teknologi dan Kejuruteraan Industri dan Pembuatan, Universiti Teknikal Malaysia Melaka, Hang Tuah Jaya, 76100 Durian Tunggal, Melaka, Malaysia*
*[2]Motion Control Research Laboratory (MCon Lab), Fakulti Teknologi dan Kejuruteraan Elektrik, Universiti Teknikal Malaysia Melaka, Malaysia*
*[3]Department of Industrial Engineering, President University, Jl. Ki Hajar Dewantara, Kota Jababeka, Cikarang Baru, Bekasi 17550, Indonesia*

**Corresponding author: isa@utem.edu.my*

*(Received: 30 August 2024; Accepted: 8 October 2024; Published online: 10 January 2025)*

***ABSTRACT:*** Performing Salah (Islamic prayer) is a fundamental practice for all Muslims worldwide, involving physical movements such as standing, bowing, and prostrating. However, these movements can be challenging for individuals with physical disabilities, who often rely on conventional chairs to support their bodies during Salah. Using conventional chairs presents limitations in mosques, disrupting congregation alignment and hindering mobility due to their bulky size and lack of portability. To address these challenges, this study aimed to design and develop SolatExo, a passive exoskeleton prototype tailored to assist Muslims with physical disabilities during Salah. The study evaluated SolatExo's impact on range of motion (ROM), muscle contraction using electromyography (EMG), usability, and user experience. Key findings indicated no significant reduction in ROM between wearing and not wearing SolatExo. The EMG analysis revealed reduced muscle contraction with SolatExo, suggesting its potential to alleviate muscular effort during Salah. Usability assessments yielded a moderate to good System Usability Scale (SUS) score of 68, although user feedback highlighted operational difficulties, particularly during transitions between Salah postures. This study underscores the importance of interdisciplinary collaboration between biomechanics, assistive technology design, and religious studies to develop inclusive solutions for enhancing Salah accessibility. Future research should focus on refining SolatExo's design to improve usability and user experience, addressing comfort issues and incorporating advanced ergonomics principles better to serve the diverse needs within the Muslim community.

***ABSTRAK:*** Mendirikan solat merupakan amalan wajib bagi semua umat Islam di seluruh dunia. Solat melibatkan pergerakan fizikal seperti berdiri, rukuk, dan sujud. Pergerakan ini sukar dilakukan oleh Muslim yang mempunyai kecederaan fizikal. Mereka akan menggunakan kerusi konvensional untuk solat. Walau bagaimanapun, kerusi konvensional akan mencetus beberapa kelemahan ketika solat di dalam masjid, seperti menjejaskan lurusnya saf jemaah, menghalang mobiliti dan mengganggu ruang jemaah lain kerana saiznya yang agak besar. Untuk menangani kelemahan ini, kajian ini bertujuan mereka bentuk dan membangunkan SolatExo, sebuah eksoskeleton pasif yang dicipta untuk membantu individu Muslim yang mempunyai kecederaan fizikal mendirikan solat. Kajian ini telah menilai kesan SolatExo terhadap julat pergerakan, penguncupan otot menggunakan elektromiografi, kebolehgunaan, dan pengalaman pengguna. Penemuan utama menunjukkan tiada perbezaan

https://doi.org/10.31436/iiumej.v26i1.3430

ketara dalam julat pergerakan di antara memakai dan tidak memakai SolatExo. Analisis elektromiografi menunjukkan pengurangan penguncupan otot ketika menggunakan SolatExo, bermakna ianya berpotensi mengurangkan usaha otot semasa solat. Penilaian kebolehgunaan menghasilkan skor Skala Kebolehgunaan Sistem yang sederhana tinggi iaitu 68. Dari aspek maklum balas pengguna, SolatExo memerlukan penambahbaikan terutamanya peralihan pergerakan solat yang lancar. Kajian ini menekankan kepentingan kerjasama pelbagai disiplin seperti biomekanik, reka bentuk teknologi bantuan, dan fiqh untuk membangunkan SolatExo yang berimpak tinggi. Penyelidikan masa depan perlu memberi tumpuan kepada memperhalusi reka bentuk SolatExo untuk meningkatkan kebolehgunaan dan pengalaman pengguna, aspek keselesaan dan menggabungkan prinsip ergonomik supaya memenuhi keperluan komuniti Muslim.

***KEYWORDS:*** *Human Factors Engineering, Exoskeleton Design, Muslim Prayer, User Testing*

# 1. INTRODUCTION

The Islamic prayer (also known as Salah, Solat, or Salat) holds a significant place in Islam as the performance of prayers. Exoskeletons, defined as mechanical devices designed to augment body motion, find applications in fields such as military, rehabilitation, industrial tasks, and sports, categorized into passive, active, and soft exoskeletons [1]. For instance, active exoskeletons have been developed for soldiers to reduce fatigue and increase endurance in carrying loads [2]. In rehabilitation, lower-limb exoskeletons aid patients with spinal cord injuries in regaining the ability to walk [3]. Passive exoskeletons are often used in industrial tasks to reduce musculoskeletal strain during repetitive activities [4], while soft exoskeletons are being explored in sports to improve athletic performance [5].

In the context of Salah, exoskeletons can play a crucial role in supporting the body weight of individuals, aiding in maintaining the postures required for the compulsory movement of Salah, and facilitating smooth transitions between these movements. The potential users include individuals falling into categories such as elderly individuals with limited physical strength, those with lower limb disabilities (e.g., injured legs, arthritis), and individuals who face challenges standing for extended periods, as pointed out by a past study [6]. The development of exoskeletons tailored for Salah aligns with the goal of inclusivity, enabling individuals with physical limitations to engage more actively in their religious practices.

Developing an exoskeleton to assist Muslims with physical disabilities in performing their Salah is a commendable and potentially impactful initiative. Such a device could enhance accessibility and inclusivity, allowing individuals with physical challenges to participate more fully in prayer practices. The exoskeleton could promote inclusivity by providing individuals with physical disabilities the means to actively engage in Salah actively, fostering a sense of belonging within the Muslim community. Enabling individuals with physical disabilities to perform their Salah without difficulty can contribute to their ability to fulfill prayer obligations, enhancing their spiritual well-being. The development of technology that supports individuals with disabilities can empower them to lead more independent and fulfilling lives, both within and beyond religious practices. This research may receive positive support from the Muslim community and beyond, as it aligns with values of compassion, empathy, and the promotion of equal opportunities.

The problem statement concerns the limitations of using conventional chairs or foldable stools during Salah, particularly in congregational prayers. These issues include challenges in straightening the row or *saf* when using chairs, difficulty in achieving a close row due to the

https://doi.org/10.31436/iiumej.v26i1.3430

bulkiness of prayer chairs, the troublesome process of bringing in and positioning conventional seating in crowded rows, and the potential for disrupting other Muslims, especially those in the rear rows. Addressing these challenges by developing exoskeletons tailored for Salah can significantly improve the experience for individuals with physical limitations, promoting inclusivity and facilitating a smoother congregational prayer environment.

The existing literature reveals a notable research gap concerning the application of exoskeletons in Muslim practices such as Salah and Hajj. Most research has focused on enhancing performance or rehabilitation in irreligious contexts, leaving a significant area unexplored - how exoskeletons can assist in performing religious practices such as Salah. This manuscript addresses this gap by developing the SolatExo, a passive exoskeleton designed to help Muslims with physical disabilities perform Salah. The design of SolatExo considers Salah's unique postural requirements, providing support and stability during transitions between standing, bowing, and prostration. Given the limited research in this area, this study contributes to the growing body of knowledge on applying exoskeleton technology in a religious context, offering a novel approach to improving the quality of life for Muslims with physical challenges.

### 1.1. The Needs of an Exoskeleton for Salah

The need for an exoskeleton for Salah arises from the challenges faced by Muslims with physical injuries, such as knee pain, who encounter difficulties in performing Salah like able-bodied individuals, particularly in standing up from a sitting position. While conventional chairs are often relied upon for support, they present various drawbacks. Firstly, their usage disrupts the alignment of worshippers in the row behind during congregation, impeding the harmonious flow of prayer (Fig. 1). Secondly, conventional chairs lack portability. They are cumbersome to carry, hindering ease of movement for users. Additionally, bringing in and passing through chairs amidst a congregation poses logistical challenges and disruptions. The design and development of an exoskeleton for Salah (called SolatExo, developed by this study) address these shortcomings by offering lightweight, discreet, and ergonomically designed support that facilitates seamless integration into the Salah environment while ensuring the dignity and inclusivity of all Muslims, regardless of physical abilities.

As depicted in Table 1, Muslim Salah chairs and foldable Salah chairs are commonly utilized by Muslims during Salah, particularly if they have physical disabilities. In addition to these chairs, plastic, and banquet chairs are frequently employed. Previous researchers [6], [7] have introduced new designs for chairs intended for Salah. However, these designs have yet to address alignment in the rows and issues of bulkiness adequately. Furthermore, Table 1 explains the uniqueness of SolatExo compared to the chairs mentioned above.

Figure 1. Muslims with physical disabilities such as knee pain use conventional chairs or stool to support their body during Salah.

https://doi.org/10.31436/iiumej.v26i1.3430

Table 1. Uniqueness of the SolatExo - a comparison with existing chairs

| Chair for Salah and exoskeleton | Design features |
|---|---|
| Muslim Salah Chair Sajda Chair Namaz Salah [8] | This chair facilitates people who do not have the ability to Salah. It has certain features, such as an armrest for placing both palms to suck in a sitting position, as well as a specially designed cushion to give comfort to the individual's back. The individual can also use the chair's armrests to counterbalance the downward lift-up force. Users will feel more at ease and comfortable in this situation because getting up from a sitting position is easier and more balanced. |
| Foldable Salah Chair [9] | This folding chair is a commercial one and is most commonly used in musolla and mosque. It is light, simple in design, easy to carry, and easily available in the market. These features make this product a priority for everyone who cannot stand when praying. This chair can support a weight of up to 130 kg. |
| [6] | This chair has features such as being lightweight, having a height regulator, being easy to fold, and being ergonomic for sitting. The height regulator adjusts according to the individual's height suitability. |
| 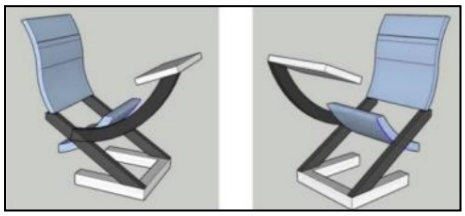 [7] | This chair has electronic components to help Muslims pray when they cannot stand. It has various features, such as a flexible design, a tool to help count the rakat during Salah, a sensor for the safety of the user's distance, and a tool to help recite and chant [7]. The main feature of this prototype is that the prostration panel and the seat are flexible to determine the degree to which the bowing and the act of prostration differ. |

https://doi.org/10.31436/iiumej.v26i1.3430

SolatExo (developed by this study)

A Muslim wearing SolatExo for walking and Salah

The SolatExo is an innovative exoskeleton designed to empower Muslim individuals with physical disabilities to perform Salah. Engineered as a wearable assistive technology, SolatExo seamlessly integrates with the wearer's trousers, boasting a lightweight and slim design for optimal comfort and discretion. Its advanced kinematic compatibility ensures natural movement, allowing users to effortlessly stand from a sitting position with the assistance of mechanical ratchets. One of SolatExo's key features is its ability to enable users to align their body positions with fellow worshippers in the row, fostering a sense of unity and inclusivity in congregational prayers. Moreover, its portable nature ensures minimal disruption to neighboring worshippers, making it an invaluable tool for individuals seeking to participate in their spiritual practices fully.

### 1.2. Research Questions and Objectives

In this study, the authors investigated the following research questions: (1) What essential features are needed by users for SolatExo? (2) To what extent does SolatExo reduce the range of motion of users during Salah? (3) How does SolatExo impact muscle contraction patterns in users while performing Salah? (4) What are users' perceptions of the usability of SolatExo in the context of aiding them during Salah? (5) What specific feedback do users provide after utilizing SolatExo in their Salah?

This study aims to design and develop a functional prototype of a passive exoskeleton named SolatExo, intended to assist Muslims with physical disabilities in performing Salah. Additionally, this study evaluated the effects of the SolatExo prototype on muscle contraction, ROM, and usability. The practical implications of SolatExo, explicitly designed for Salah, are profound and multifaceted. One of its primary objectives is to enhance Salah's perfection, emphasizing the congregation's alignment in a well-positioned and straight row, a fundamental requirement for congregational prayers. By supporting body motions and postures, SolatExo

not only aids users in performing Salah but also addresses challenges associated with conventional seating methods. Furthermore, the use of SolatExo aims to create a harmonious prayer environment. Unlike conventional chairs or foldable stools that may disrupt the alignment of the congregation or pose challenges in maintaining close distances between worshippers, SolatExo seamlessly integrates into the Salah experience. The technology ensures that users with exoskeletons do not interfere with others during Salah, fostering an atmosphere of tranquility and focus during congregational prayers. In this way, SolatExo goes beyond individual assistance; it actively contributes to the collective experience of worshippers, promoting a more inclusive and harmonized congregational prayer setting.

## 2. MATERIALS AND METHODS

The development of the SolatExo involved a systematic approach, incorporating both user-centered design principles and technical evaluations to ensure that the exoskeleton met the needs of individuals with physical disabilities performing Salah. This section outlines the key processes undertaken, starting with a survey of user requirements to identify functional needs (Section 2.1). The gathered insights were then translated into technical specifications during the design conceptualization phase (Section 2.2), followed by the creation of detailed three-dimensional computer models for precision and refinement (Section 2.3). The fabrication process (Section 2.4) brought the digital design into a physical prototype, which was subsequently tested through range of motion (ROM) assessments (Section 2.5) and muscle contraction analysis (Section 2.6) to evaluate its performance. Then, a usability study (Section 2.7) was conducted to evaluate the ease of use of the SolatExo. Finally, user experience testing (Section 2.8) assessed the overall effectiveness and user experience during Salah movements.

### 2.1. Survey of User's Requirements

The survey aimed to identify the design features of the SolatExo that potential users would need. A questionnaire was developed using Google Forms and distributed to various Muslims across Malaysia. Participants were selected through a purposive sampling, aiming to include individuals who could represent a broad range of perspectives based on their physical abilities, age, and gender. Inclusion criteria required respondents to be Muslim, aged 17 years old and above, and able to perform Salah independently or with assistance. No prior experience with exoskeletons was required. Exclusion criteria included individuals with severe cognitive impairments that could hinder their ability to complete the survey.

The questionnaire was written in both English and Bahasa Malaysia to ensure all respondents could fully comprehend the questions. The cover page outlined the survey's purpose, explained the SolatExo, and included pictures of the exoskeleton. The survey gathered demographic information, such as age and gender, and specific user insights. Respondents were asked about their willingness to use the SolatExo if needed, their acceptance of using it for Salah, and their intent to purchase the SolatExo. Additionally, factors influencing their decision to purchase the SolatExo, such as price, aesthetic value, functionality, usability, and durability, were rated on a Likert scale, ranging from "Strongly disagree" (score = 1) to "Strongly agree" (score = 5). The questionnaire also provided an open-ended section for respondents to suggest other design features based on their needs and preferences. This approach allowed for a comprehensive understanding of the potential users' requirements while ensuring a diverse sample, thus aiding in developing a user-centered design for SolatExo.

https://doi.org/10.31436/iiumej.v26i1.3430

### 2.2. Design Conceptualization

Once the user's requirements were gathered, these needs were translated into detailed technical specifications. The design conceptualization of the SolatExo began with translating the specific needs of users, primarily individuals with physical disabilities who face challenges in performing Salah. The primary objectives were to ensure that the SolatExo provided sufficient support during the main postures (e.g., standing, bowing, and prostration) while maintaining user comfort, ease of use, and alignment with the Salah perfection. Key performance criteria were established, including support for the knee, control of movement during sit-stand and standing-to-prostration transitions, and ensuring that the SolatExo would be lightweight and easy to wear. Anthropometric data from the target users were incorporated to ensure that the SolatExo would accommodate the 5th, 50th, and 95th percentile of the Malaysian population, especially focusing on lower limb dimensions for proper joint alignment and support.

Following this, initial design sketches were created to explore potential solutions. Various concepts were drafted, each offering different mechanisms of support and flexibility. These sketches focused on placing critical components, such as upper and lower structures, ratchets for controlled movement, and attachment systems for securing the SolatExo to the body. The sketches were also aimed at optimizing the ease of donning and doffing the exoskeleton to ensure that users could wear it with minimal assistance.

The design screening process then involved evaluating these sketches against the technical requirements and user needs. Multiple iteration cycles were carried out, wherein each concept was analyzed for its feasibility, practicality, and alignment with the Salah movements. This stage included reviewing the materials and mechanisms that could best serve the intended functions of the SolatExo, such as selecting lightweight materials like aluminum sheets for structural components and ensuring the durability of mechanical joints. Design alternatives were discussed, and those that showed potential for improving user experience, stability, and manufacturability were shortlisted for further development.

### 2.3. Three-Dimensional Computer Modeling

The outcome of the design conceptualization phase provided a clear foundation for the next step - the drafting of three-dimensional computer models. The finalized design concept transformed the sketches into detailed 3D representations using CAD software. This allowed for precise modeling of the SolatExo's components, enabling further refinement of dimensions, joint placements, and overall fit before moving on to the fabrication phase. Table 2 lists the components of the SolatExo that support the user's lower body. The upper and lower structures support the thighs and calves, respectively. The ratchet, hinge, and joint sheets assist with movement and stability at the knees and ankles. A foldable hinge is used for adaptability, bases offer foundational support, and isolated bolts and nuts ensure structural integrity.

https://doi.org/10.31436/iiumej.v26i1.3430

Table 2. List of components/ parts of SolatExo

| No. | Components / Parts | Quantity | Material Description |
|---|---|---|---|
| 1 | 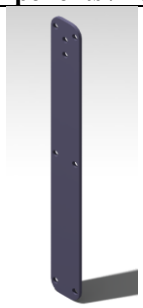 Upper structure | 2 | The upper structure of the SolatExo is aluminum sheet (270 mm x 30 mm x 3 mm), provides support to the user. It was attached to both thighs to provide stability in the knee-to-hip area. |
| 2 | 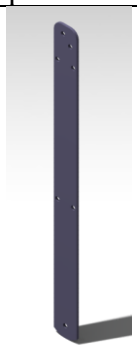 Lower structure | 2 | The lower structure of the SolatExo is aluminum sheet (380 mm x 30 mm x 3 mm), provides support to lower limb. It was attached to calves to provide stability in the knee-to-foot area. |
| 3 | Ratchet | 2 | This steel ratchet connects the upper structure and the lower structure. It facilitates controlled movement and stability during sit-to-stand transitions. This ratchet was attached close to the knees to replicate this joint. This is a reverse circular ratchet used to restrict movement in one direction. The toothed components engage with the circular track, preventing undesired rotation. This mechanism ensures stability in specific postures, enhancing safety and control during activities where reverse movement needs to be limited, such as sitting down from a standing position. |
| 4 | 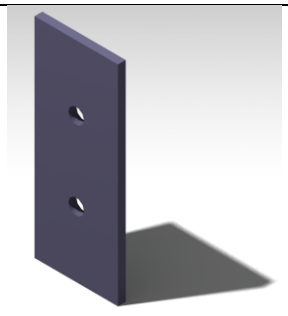 Joint sheet | 2 | The aluminum joint sheet (80 mm x 32 mm x 3 mm) supports the right ankle joint while maintaining flexibility. |

| | | | |
|---|---|---|---|
| 5 | 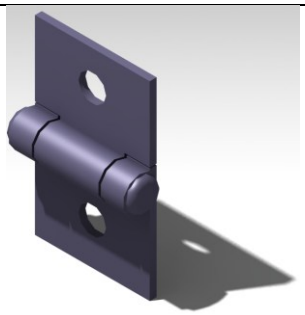 Hinge | 2 | Enables folding of the ankles, accommodating various movements. |
| 6 | 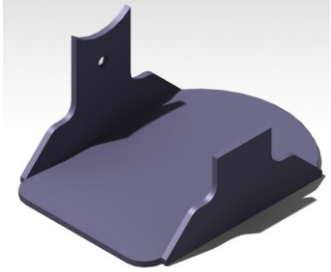 Right base | 1 | The right foot's base is an aluminum sheet (102 mm x 80 mm x 3 mm) connected to the hinge, joint sheet, and bottom frame. This component assists with body stability. |
| 7 | 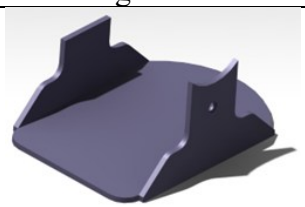 | 1 | The left foot's foundation is an aluminum sheet (102 mm x 80 mm x 3 mm) that mirrors the function of the right base. |
| 8 | M6 bolt | 12 | M6 bolts are used to fasten and secure components of the exoskeleton. |
| 9 | 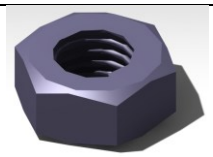 M6 nut | 12 | M6 nut secures the bolt in place, ensuring the stability of the connected components. |

The SolatExo was designed using Fusion 360, and ANSYS software was employed for mechanical stress analysis. Stress analysis helps identify regions of high stress or potential failure in the SolatExo components. It is useful for determining the suitability of materials, verifying design parameters, and ensuring that the SolatExo is both safe and reliable. Stress analysis significantly aids in optimizing the structural design and reducing the risk of mechanical failures. Fig. 2 shows the 3D CAD model of the SolatExo and the results of the mechanical stress analysis.

https://doi.org/10.31436/iiumej.v26i1.3430

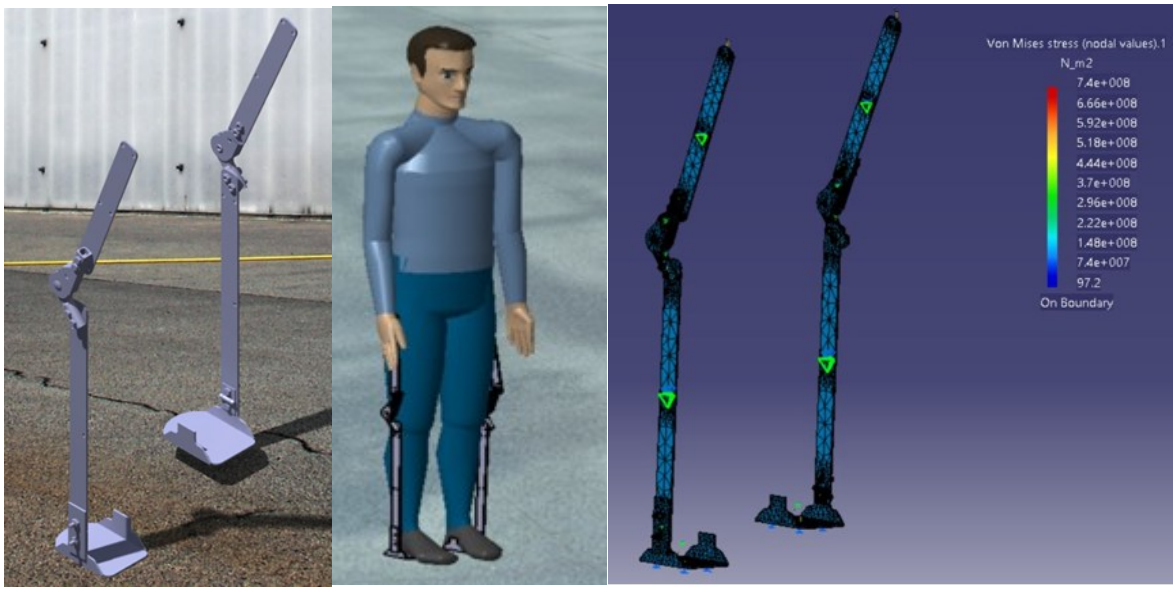


Figure 2. 3D CAD model of SolatExo and mechanical stress analysis

The overall height of the exoskeleton is 760 mm, the overall width is 50 mm, and the thickness is 3 mm. The weight of the exoskeleton is 2.55 kg. The SolatExo is designed to match the anthropometry of users at the 5$^{th}$, 50$^{th}$, and 95th percentile of the Malaysian population. A central focus of SolatExo design is its adaptability to accommodate anthropometry requirements, considering users at the 5$^{th}$ percentile for short users, the 50th percentile for medium-tall users, and the 95th percentile for tall users. The incorporation of six holes for height adjustability - three at the upper and three at the lower structures. Specifically, the hierarchical arrangement of these holes - level 1 for the 5th percentile, level 2 for the 50th percentile, and level 3 for the 95$^{th}$ percentile. This is to ensure optimal ergonomic support for users with diverse body dimensions.

The ratchet operating angle, or inclination angle, is also specified at 90, 72, 54, 36, and 18 degrees. These values likely indicate the range of angles or positions the exoskeleton can achieve, offering flexibility in supporting various movements or postures for users. The SolatExo was designed with adjustability to accommodate the 5th, 50th, and 95th of user anthropometrics. Table 3 presents the technical specifications of the SolatExo.

Table 3. Technical specifications of SolatExo

| **Item** | **Specification** |
|---|---|
| SolatExo dimensions | |
| Overall height | 760 mm |
| Overall width | 50 mm |
| Thickness | 3 mm |
| Weight (kg) | |
| SolatExo weight | 2.55 kg |
| Maximum weight of user | 80 kg |
| Anthropometry of user | |
| Percentiles | 5$^{th}$, 50$^{th}$, 95$^{th}$ |
| Body parts | Thighs, calves, feet |
| Ratchet operating angle | |
| Inclination angle (degree) | 90, 72, 54, 36, 18 |

https://doi.org/10.31436/iiumej.v26i1.3430

### 2.4. Fabrication Process

Once the three-dimensional computer models of the SolatExo were finalized, they provided detailed specifications for the fabrication phase. The profiles and dimensions of the SolatExo components, including length, width, hole diameter, and fillet edge, were sketched in CAD software. For prototyping purposes, the base material of the SolatExo was aluminum sheets with a thickness of 3 mm. The CAD file was then sent to a laser-cutting machine to cut the desired profile based on the dimensions. Angled shapes of the components were bent using a hydraulic bending machine.

To support weak knees, the SolatExo incorporated a mechanical ratchet (see Table 2, part no. 3), purchased rather than fabricated for cost efficiency. This steel ratchet connects the upper and lower structures, facilitating controlled movement and providing stability during sit-stand and stand-sit transitions. Positioned near the knees, the ratchet mimics the knee joint by limiting movement in one direction. This reverse circular ratchet engages its toothed components with a circular track to prevent undesired rotation, ensuring stability in specific postures. This is particularly useful during movements from standing to sitting, where control and safety are critical.

The components were connected using rivets, bolts, and nuts. After assembly, two fitted sleeves, similar to pockets, were stitched to the left and right sides of the trousers to securely attach the upper part of the SolatExo prototype to the thigh. Additionally, elastic straps are used to fasten the lower part of the exoskeleton to the ankles, reducing strain on the thighs and calves and improving overall comfort. Once the components were seamlessly integrated into the trousers, the researchers invited a volunteer to wear and experience the SolatExo. An iterative process was then undertaken to position the components and trousers to ensure that the SolatExo is comfortable to wear and does not disrupt the user's natural movements.

A SolatExo prototype was fabricated for Salah to demonstrate kinematic compatibility by seamlessly mirroring the natural movements of the human body during Salah, including standing upright (qiyam), bowing, prostration, and sitting during the last tashahhud, as shown in Fig. 3. This involves aligning the SolatExo's joints precisely to the user's hips, knees, and ankles, ensuring a harmonious interaction. The importance of kinematic compatibility in exoskeleton use for Salah lies in its ability to enhance the user's experience by providing support and alignment during the Salah movements. By accurately replicating the biomechanics of the lower limbs and incorporating anthropometric alignment with the user, the SolatExo promotes a fluid and comfortable prayer experience, allowing individuals to engage in their Salah with ease and confidence.

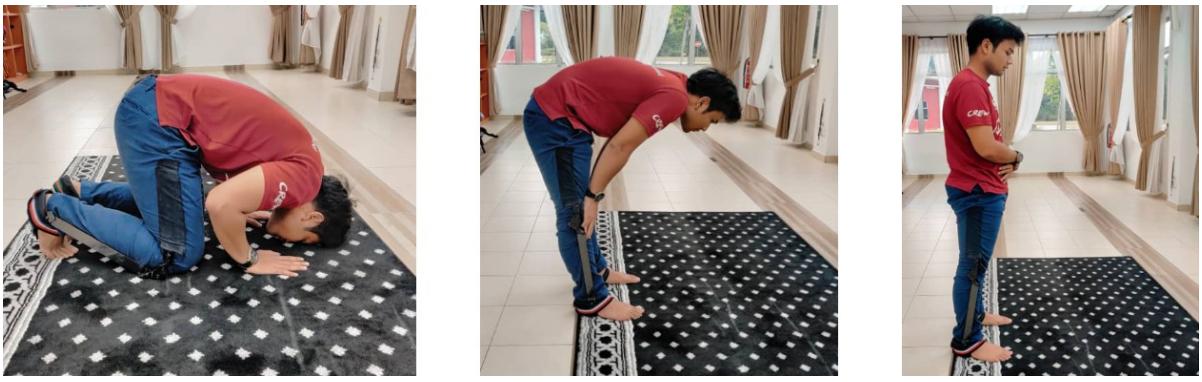

Figure 3. Prostration, bowing and standing using SolatExo prototype

https://doi.org/10.31436/iiumej.v26i1.3430

### 2.5. Range of Motion (ROM) Assessments

After the fabrication process was completed, the physical prototype of the SolatExo underwent thorough range of motion (ROM) assessments to determine its effectiveness in supporting and facilitating essential movements during Salah. These assessments utilized a Jamar goniometer (Sammons Preston, USA), as illustrated in Fig. 4, to ensure the SolatExo was properly configured and fitted for each user. The evaluations involved five healthy male participants aged 20 to 30 years, whose body dimensions were meticulously measured to customize the SolatExo's positioning for optimal alignment and movement during Salah. The focus of the assessment was on the main joint movements critical to the Salah sequences, including trunk flexion and abduction, knee flexion and extension, as well as ankle dorsiflexion, plantar flexion, and supination. The ROM measurements were adapted from the techniques described by Rabin and Kozol [10].

Figure 4. Range of motion assessments using a goniometer

### 2.5. Muscle Contraction Analysis

Following the ROM assessments, a detailed muscle contraction analysis was performed to quantify the muscle activity required using the SolatExo during various Salah movements. This analysis aimed to ensure that the exoskeleton provided adequate support without overexerting the user. Employing an electromyography (EMG) instrument (Delsys Trigno wireless EMG, USA) depicted in Fig. 5, the study analyzed muscle contractions of participants during Salah. The same five male subjects from the ROM assessments were recruited for consistency. The EMG experiment was structured into three phases for each participant: first, to establish the maximal voluntary contraction (MVC) as a baseline for maximal muscle activity; second, to measure muscle contractions without the use of the SolatExo; and finally, to evaluate muscle contractions while wearing the SolatExo during Salah. Targeted muscles included the vastus medialis, vastus lateralis, rectus femoris, tibialis anterior, and soleus on both legs. This methodical approach, repeated thrice for each participant, aimed to yield empirical insights into the SolatExo's influence on muscle contraction during Salah. The total duration of the EMG experiment was approximately 10 minutes, capturing complete movement cycles associated with Salah, thereby providing a comprehensive understanding of muscle engagement and exoskeleton efficacy. The EMG measurement protocols and signal processing techniques were adapted from the past study [11].

https://doi.org/10.31436/iiumej.v26i1.3430

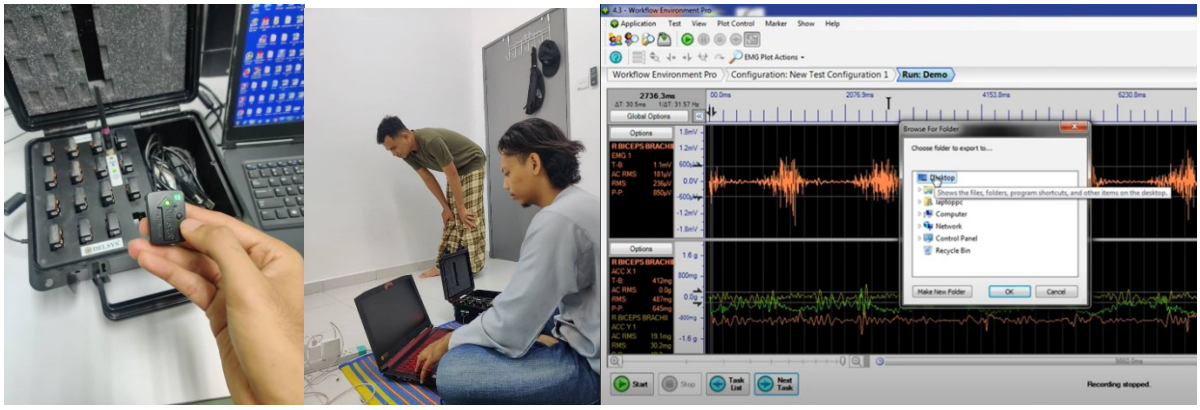

Figure 5. Muscle contraction analysis using EMG instrument

### 2.7. Usability Study

After completing the muscle contraction analysis, a usability study was conducted to gather user feedback on SolatExo's performance during real-world Salah scenarios. The system usability scale (SUS) was applied to assess SolatExo's ease of use, functionality, and user experience. The SUS consists of 10 statements that evaluate many facets of usability, including user pleasure, learnability, efficiency, and simplicity of use [12]. Users indicate how much they agree with each statement on a Likert scale (Strongly Disagree, Neutral, Agree, Strongly Agree). Statement 1: I would like to use this SolatExo to assist me in Salah. Statement 2: I found this SolatExo is complicated. Statement 3: I found the SolatExo to be simple to operate. Statement 4: I think I would need assistance to use this SolatExo. Statement 5: I noticed that this SolatExo has many useful functions. Statement 6: I think the design is too weird. Statement 7: I would expect that people who have a physical disability would quickly learn how to use this SolatExo to perform Salah. Statement 8: I found this SolatExo to be very difficult to operate. Statement 9: I feel comfortable when using this SolatExo. Statement 10: I need to learn many things before using this SolatExo. The usability of the SolatExo was assessed at before, during, and after wearing this exoskeleton.

### 2.8. User Experience Testing

Following the usability study, the researchers tested SolatExo's user experience. This testing involved two participants who had sustained knee injuries from road accidents, ensuring that the assessment focused on individuals who could benefit from the device. Each participant was equipped with the SolatExo while performing Salah, allowing for a practical evaluation of the exoskeleton's functionality and comfort during the Salah movements. The testing environment was structured to simulate a typical Salah setting, enabling participants to engage in the full range of movements, including standing, bowing, and prostration. Feedback was gathered through direct observation and interviews, focusing on comfort, ease of movement, and overall satisfaction with the SolatExo during the Salah experience. This methodology aimed to gain insights into how well the exoskeleton supported natural body movements and alleviated discomfort associated with knee injuries, ultimately informing further refinements to the design and functionality of the SolatExo.

### 2.9. Experimental Procedures Approval and Statistical Analysis

The experimental procedures were reviewed and approved by the Research Ethics Committee of UTeM. Both descriptive statistics and the inferential tests were conducted using Minitab software. Descriptive statistics were performed on the ROM angles and the root mean

square values of muscle contraction to summarize the central tendency and variability of the data. The minimum, mean, and maximum were calculated for each measure to provide an overall view of the data distribution and to facilitate comparison across conditions, i.e., with and without the SolatExo.

A paired sample t-test was applied to compare the trunk, knee, and ankle ROM between wearing and not wearing the SolatExo. This parametric test was chosen because it evaluates the differences in ROM across two related conditions (with and without the exoskeleton) and is appropriate when the data are normally distributed. The t-test determines whether the mean difference in ROM between the two conditions is statistically significant, thus enabling the assessment of the impact of the SolatExo on joint movement.

Before conducting the paired t-test, the normality of the data was assessed using the Shapiro-Wilk test. This test was selected due to its high power for detecting deviations from normality, especially with small to moderately sized datasets, ensuring that the parametric assumptions of the t-test were met. A significance level ($\alpha$) of 0.05 was used as the threshold for normality. When the p-value from the Shapiro-Wilk test exceeded 0.05, the data were considered normally distributed, justifying a parametric test.

## 3. RESULTS

### 3.1. User's Requirements

112 respondents took part in the questionnaire survey of user requirements. 59.8% and 40.2% for male and female, respectively. The age is 18 years and below (29.1%), 19 to 29 years (48.2%), 30 to 39 years (10.9%), and 40 and above (11.8%). Fig. 6 reveals the factors influencing the decision to deploy the SolatExo. The majority of respondents, comprising 87.5%, prioritize functionality, indicating a strong emphasis on the practical benefits and features of the SolatExo. To meet this demand, the SolatExo design focused on several technical elements. Lightweight materials, such as aluminum, were used to ensure the device was not cumbersome, making it easier for users to move during Salah. The SolatExo also features a slim design to allow natural body movements without restrictions. Adjustability was incorporated to accommodate users of various sizes and physical needs, enhancing comfort and usability. Additionally, the design ensured portability, aligning with users' need for a practical and convenient solution. These functional requirements gathered from the survey were integral to shaping the final design, ensuring it addressed the specific needs of its target users.

Price emerges as the second most influential factor, with 57.1% of participants highlighting its significance, suggesting that cost remains a substantial consideration in decision-making. Durability and lasting performance also hold weight, as indicated by 49.1% of respondents. Aesthetics and appearance appear in the provided data, with 47.3% of respondents expressing their influence on the decision, emphasizing the importance of the SolatExo visual appeal alongside its functional attributes. Usability, mentioned by 47.3%, complements the focus on functionality, indicating that ease of use is critical for potential buyers. Overall, these insights underscore the multifaceted nature of the decision-making process, incorporating aspects of cost, functionality, durability, and aesthetics into potential users' considerations.

https://doi.org/10.31436/iiumej.v26i1.3430

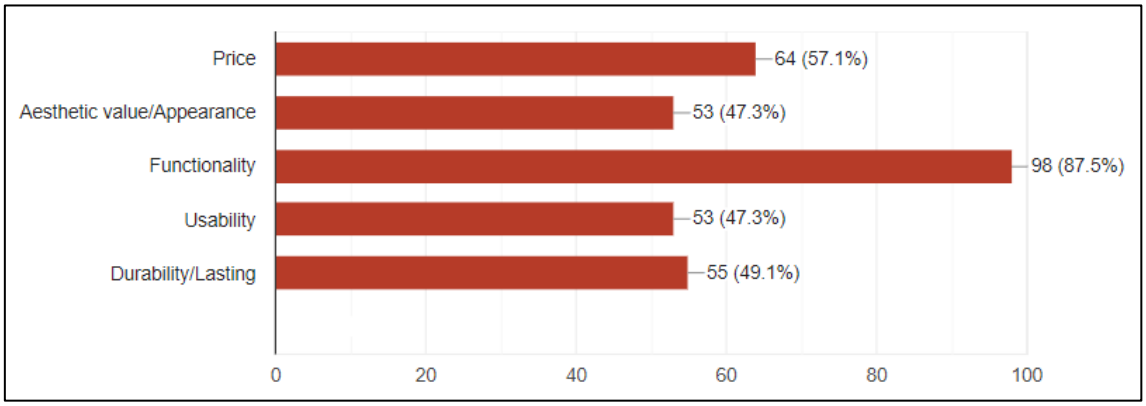


Figure 6. Factors influencing the decision to deploy the SolatExo

### 3.2. Range of Motion (ROM)

In this study, the ROM was analyzed to determine if there were any significant differences in joint movements while wearing and not wearing the SolatExo. Table 4 compares the ROM while wearing and not wearing the SolatExo. The p-values were obtained through a paired sample t-test, which compared the minimum and maximum joint angles between both conditions. The obtained p-values for minimum and maximum joint movements at a significance level of 0.05 reveal that, generally, there are no statistically significant differences in most of the examined parameters. Specifically, for minimum values, no significant differences are observed in trunk flexion, trunk abduction, knee flexion, ankle dorsiflexion, ankle plantar flexion, and ankle supination, with p-values ranging from 0.142 to 0.674. Similarly, for maximum values, trunk flexion, trunk abduction, knee flexion, and knee extension show no significant differences, with p-values ranging from 0.108 to 0.602.

However, significant differences were found in ankle plantar flexion ($p = 0.006$) and ankle supination ($p = 0.001$), indicating a potential restriction in movement for these joints. These results highlight that, although the SolatExo maintains standard movement patterns for most joints, improvements in ankle movement design could be beneficial. This limitation aligns with existing literature, where studies on passive exoskeletons often report restricted ankle movement due to the device's design. For instance, Chang [13] found that while exoskeletons are effective in recycling energy, they may limit ankle joint movement, especially during push-off phases. This restriction can impact the natural gait cycle and mobility, which is crucial for ensuring the exoskeleton does not hinder essential movements such as those in Salah. In light of these findings, improvements in ankle movement design for the SolatExo could enhance functionality, particularly in maintaining a natural ROM. The VS-AnkleExo, for example, highlights the significance of compliant actuators that adjust to user movements, which could alleviate some of the restrictions observed in traditional exoskeleton design [14]. By incorporating more adaptable components, the SolatExo could allow smoother transitions between standing, sitting, and prostration, which are vital movements in Salah.

Furthermore, optimizing ankle torque in exoskeletons has been shown to improve metabolic efficiency, particularly at varying speeds of movement, such as walking or transitioning between postures [15]. Applying these principles to the SolatExo could mitigate the current limitations in ankle movement and enhance user comfort and efficiency during key movements in Salah. Additionally, adjustable stiffness in the actuators could allow for more natural movement patterns, further enhancing user satisfaction and reducing discomfort during complex joint angles [14].

https://doi.org/10.31436/iiumej.v26i1.3430

In general, the results mentioned above collectively suggest that, at the 0.05 significance level, most observed variations in joint movements are not statistically significant, signifying overall consistency in the measured parameters. However, refining the ankle mechanism through these design improvements could significantly increase its overall effectiveness, particularly for users who need more flexibility and comfort in ankle-related movements during Salah.

Table 4. Comparisons of range of motion among five subjects while wearing and not wearing the SolatExo

| Joints | Movement | Without SolatExo (angle, °) | | With SolatExo (angle, °) | | Percentage Reduction of ROM | | P-value (significance level of 0.05) | |
|---|---|---|---|---|---|---|---|---|---|
| | | Min (°) | Max (°) | Min (°) | Max (°) | Min (%) | Max (%) | Min | Max |
| Trunk | Flexion | 7 | 90 | 6 | 87 | 14.29 | 3.33 | 0.574 | 0.526 |
| | Abduction | 4 | 18 | 4 | 16 | 0 | 11.11 | 0.577 | 0.108 |
| Knees | Flexion | 6 | 160 | 6 | 152 | 0 | 5 | 0.674 | 0.602 |
| | Abduction | 5 | 15 | 3 | 14 | 40 | 6.67 | 0.145 | 0.515 |
| Ankles | Dorsiflexion | 5 | 20 | 4 | 19 | 20 | 5 | 0.142 | 0.621 |
| | Plantar Flexion | 5 | 27 | 4 | 23 | 20 | 14.81 | 0.246 | 0.006 |
| | Supination | 3 | 32 | 3 | 27 | 0 | 15.63 | 0.621 | 0.001 |

### 3.3. Muscle Contraction

Results of EMG for Subject 1 in Fig. 7 varying impacts of SolatExo on different muscles during performing Salah movements. Notably, the rectus femoris muscles on both left and right show a higher percentage without wearing the SolatExo, suggesting an increased effort during those movements. With the SolatExo, these percentages decrease, indicating a positive effect in reducing muscle activity. Similarly, the tibialis anterior and soleus muscles, particularly on the left side, exhibit higher percentages without the SolatExo, implying increased muscle effort. However, with the SolatExo, these percentages decrease, suggesting potential support and alleviation of muscle load during the movements.

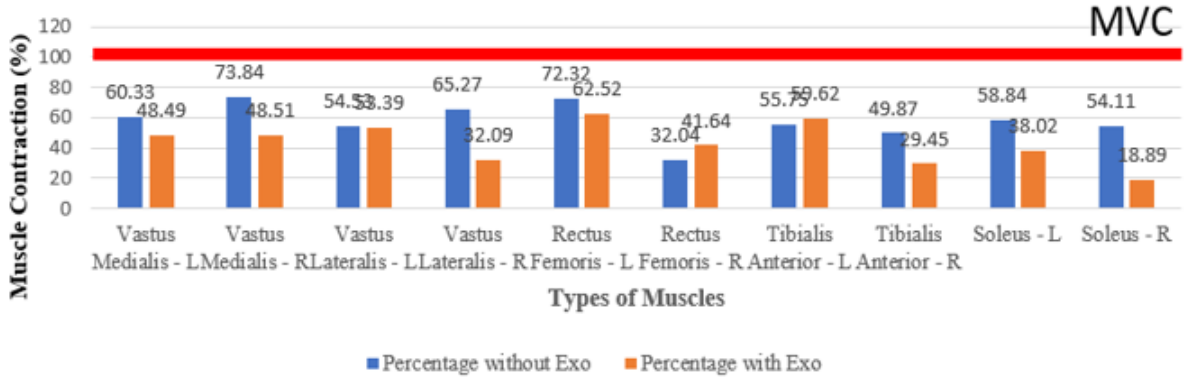


Figure 7. Percentage difference between the actual muscle contraction and the maximum voluntary contraction (MVC), with and without SolatExo, for subject 1

For Subject 2 as shown in Fig. 8, the EMG analysis reveals varied muscle activity with and without the SolatExo during Salah movements. The vastus medialis muscles on both sides exhibit higher percentages with the SolatExo, suggesting increased engagement during the movements. Similarly, the vastus lateralis muscles, particularly on the left, show higher percentages with the SolatExo, indicating elevated muscle activity. The rectus femoris muscles

https://doi.org/10.31436/iiumej.v26i1.3430

on both sides also display higher percentages with the SolatExo, suggesting increased effort. Conversely, the tibialis anterior and soleus muscles exhibit lower percentages with the SolatExo, implying a potentially positive impact on reducing muscle load. Overall, the findings suggest that while the SolatExo might increase engagement in specific muscles, it may contribute to alleviating the load on others, particularly the tibialis anterior and soleus muscles during the salah movements.

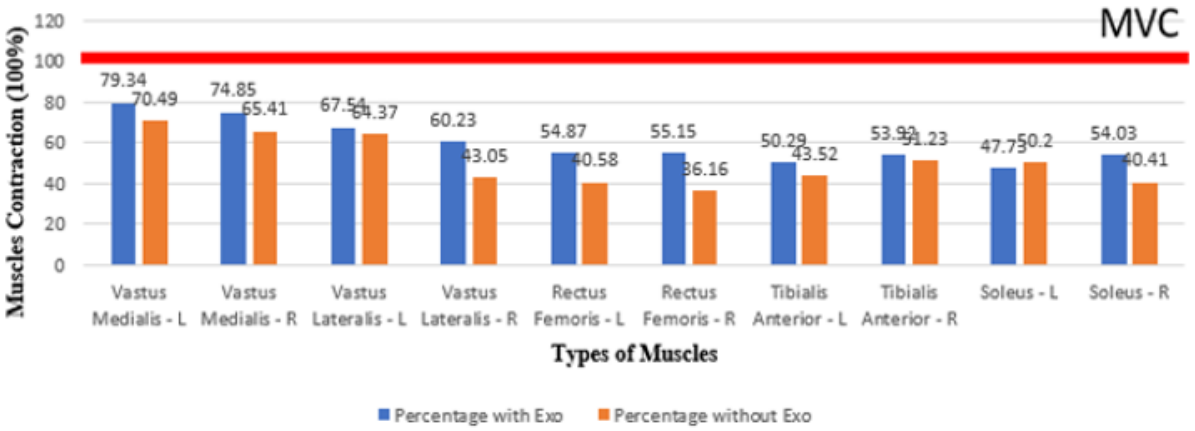


Figure 8. Percentage difference between the actual muscle contraction and the maximum voluntary contraction (MVC), with and without SolatExo, for subject 2

Subject 3's muscle activity assessment, both with and without the SolatExo during Salah movements, unveils distinctive patterns as shown in Fig. 9. The vastus medialis muscles present dissimilar responses, with the left exhibiting increased engagement when assisted by the exoskeleton, while the right experiences a reduction. Similarly, the vastus lateralis muscles, particularly on the left, display heightened contraction without the SolatExo, which diminishes with its use. The rectus femoris muscles on both sides show decreased activity with the exoskeleton, indicating potential relief. However, the tibialis anterior and soleus muscles manifest elevated percentages with the SolatExo, suggesting an augmented demand on these muscles during the movements.

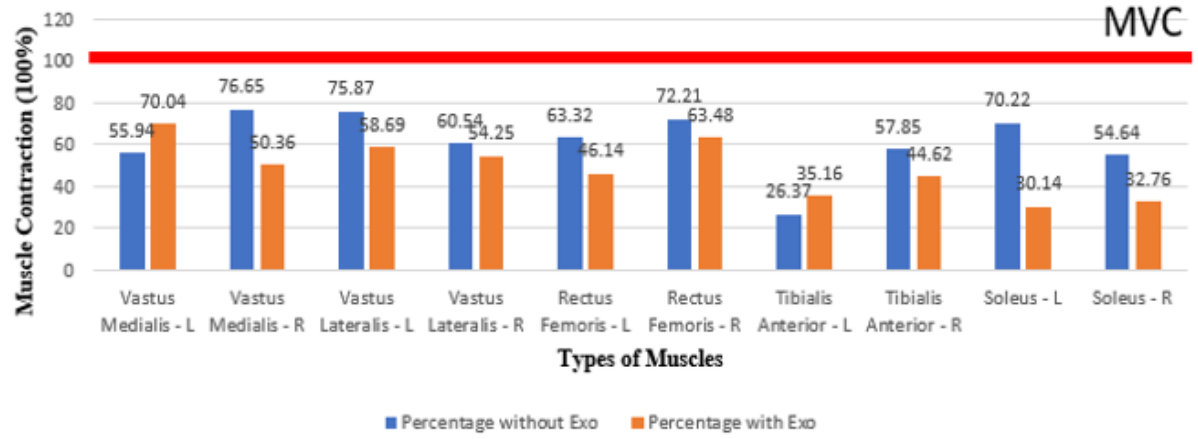


Figure 9. Percentage difference between the actual muscle contraction and the maximum voluntary contraction (MVC), with and without SolatExo, for subject 3

Subject 4's muscle activity analysis during Salah movements, with and without the SolatExo, suggests varied impacts. The rectus femoris muscles on both sides exhibit notably higher percentages with the SolatExo, indicating increased demand on these muscles when

https://doi.org/10.31436/iiumej.v26i1.3430

assisted, as illustrated in Fig. 10. Conversely, the vastus medialis and vastus lateralis muscles, particularly on the left side, show decreased contraction of the SolatExo, suggesting potential relief from muscular engagement. The tibialis anterior muscles demonstrate reduced activity with the exoskeleton, indicating potential support in minimizing muscle load. However, the soleus muscles on both sides manifest higher percentages with the SolatExo, implying increased engagement during the Salah movements.

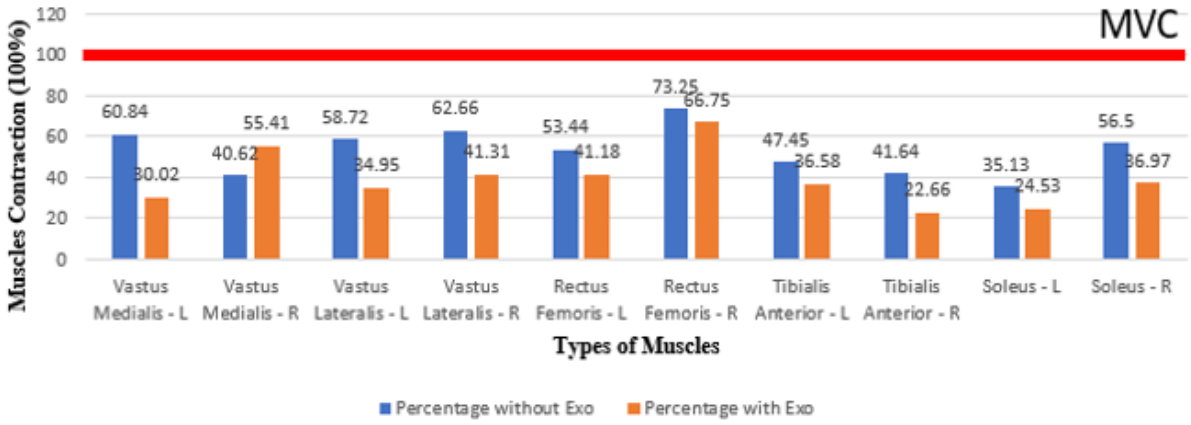


Figure 10. Percentage difference between the actual muscle contraction and the maximum voluntary contraction (MVC), with and without SolatExo, for subject 4

Subject 5's muscle activity comparison during Salah movements, with and without the SolatExo, reveals distinct patterns, as depicted in Fig. 11. The rectus femoris muscles on both sides display substantially higher percentages without the SolatExo, indicating increased engagement. In contrast, the vastus medialis and vastus lateralis muscles, particularly on the left side, demonstrate decreased activity with the SolatExo, suggesting potential relief from muscular strain. The tibialis anterior muscles exhibit relatively consistent percentages with and without the SolatExo. In contrast, the soleus muscles, particularly on the right side, show a notable reduction in contraction with the SolatExo.

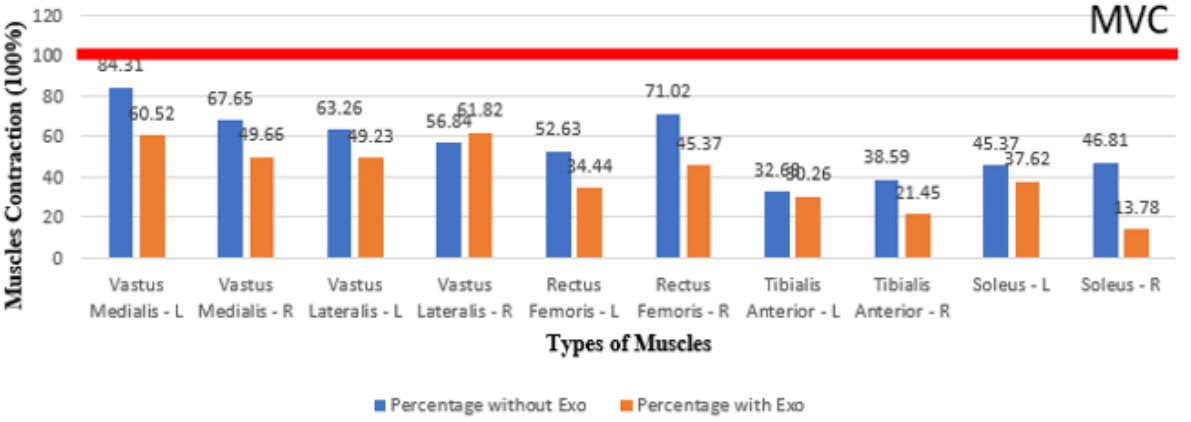


Figure 11. Percentage difference between the actual muscle contraction and the maximum voluntary contraction (MVC), with and without SolatExo, for subject 5

The high muscle contraction values observed during Salah (Fig. 7 till Fig. 11), particularly in the vastus medialis, vastus lateralis, rectus femoris, tibialis anterior, and soleus muscles, reaching 70%-80% of MVC, indicate significant muscle engagement in healthy individuals performing these movements. Since all participants in this study were healthy, their ability to

achieve such high activation levels can be attributed to their physical conditioning, enabling more efficient recruitment of muscle fibers during physical activity. These high contraction levels are not sustained throughout Salah but are concentrated during specific movements or postures that place increased demands on these muscle groups, such as transitioning from standing to prostration or rising from kneeling to standing.

The literature supports these findings. The vastus medialis and vastus lateralis, crucial for maintaining stability during standing and knee flexion, exhibit notable EMG activity during Salah (Rabbi et al., 2019) [16]. These muscles play a pivotal role in stabilizing the knee during flexion and extension, which is necessary for the smooth execution of Salah postures. Similarly, the rectus femoris shows significant activation during transitions between postures, such as kneeling or bowing during prayer [16]. These transitions require strong quadriceps engagement to support body weight and maintain posture.

Additionally, the tibialis anterior and soleus muscles are essential for maintaining ankle stability and control during Salah. These muscles, responsible for dorsiflexion and plantar flexion of the foot, help stabilize the ankles during various prayer positions, especially during movements like bowing and standing [17]. Their activation ensures balance and stability, particularly when transitioning between different postures.

Moreover, these muscle activation patterns are not unique to Salah but are also seen in similar physical activities, such as squatting. Studies show that the quadriceps muscles, including the rectus femoris, vastus lateralis, and vastus medialis, exhibit high EMG activity during squatting [18]. This suggests that Salah, particularly the transitions between its standing and kneeling postures, places similar biomechanical demands on the lower limbs, explaining the high contraction levels observed.

While the SolatExo users in this study demonstrated muscle contraction values reaching 70%-80% of MVC, such values are reasonable given Salah's physiological demands and parallels with other high-demand movements like squatting. These high activation levels highlight the importance of lower limb muscle strength and coordination during Salah, especially during critical moments of transition between postures. However, as these contraction levels are concentrated in specific phases of the prayer, future designs of assistive devices like SolatExo should focus on supporting these high-demand movements to reduce the physical effort required.

### 3.4. Usability of the SolatExo

In this study, the usability of the SolatExo was evaluated using the SUS, a widely accepted tool for measuring the usability of a system or product. The SUS score was calculated following the standard methodology described by the SUS's founder [12]. To derive the usability score, each participant's responses were processed as follows: for the odd-numbered questions (Q1, Q3, Q5, Q7, Q9), one point was subtracted from the participant's rating. The participant's rating was subtracted from five for the even-numbered questions (Q2, Q4, Q6, Q8, Q10). This adjustment aligns the scoring so that higher scores consistently reflect better usability. The adjusted scores for each question were then summed to obtain a total score for each participant. This total score was multiplied by 2.5 to convert it to a scale from 0 to 100, representing the individual SUS score.

The average score was computed after calculating the SUS scores for all participants. In this study, the final mean SUS score was 68, indicating a moderate to good level of usability for the SolatExo. According to the SUS interpretation scale, scores between 62.7 and 72.5

https://doi.org/10.31436/iiumej.v26i1.3430

reflect "Good" usability, while scores above 72.6 indicate "Excellent" usability. A score below 62.6 would indicate areas for improvement in usability.

### 3.5. User Experience

The user experience test involved two participants wearing the SolatExo while performing Salah. The outcomes of this test include feedback on usability, comfort, performance, safety, and overall user experience. Their feedback is summarized in Table 5. These user experience feedbacks provided important insights into both the strengths and challenges of the SolatExo. A key pattern that emerged from the two participants, who had knee injuries from road accidents, is that they found the SolatExo helpful but not without its difficulties. Both users reported that the SolatExo improved their ability to perform standing prayers, suggesting that the exoskeleton succeeded in providing the necessary physical support during this posture of Salah. However, they also both noted discomfort when sitting between prostrations and during the final tashahhud, which points to an area where the design could be improved. This discomfort likely stems from the structural rigidity of the SolatExo, which may not have adequately supported more nuanced, seated positions required during Salah.

Usability was another aspect that presented challenges. User 1 found the SolatExo "very difficult to operate," while User 2 needed more time to learn how to use the device. This feedback highlights that the ease of use could be improved through more intuitive design or better user instructions. Simplifying the adjustment mechanisms or enhancing the interface for adjusting the exoskeleton could make the device more user-friendly, especially for individuals who may not have extensive technical experience.

Both participants indicated that the SolatExo did not pose any safety risks, a positive outcome regarding the device's design integrity. Despite the challenges noted, the overall user experience was relatively positive. User 2 expressed delight in using the device, finding it unique and helpful. Although user 1 acknowledged that the device was challenging, still derived some pleasure from it. This indicates the value in the SolatExo, but refinements are needed to improve user comfort and ease of operation.

In future designs, these insights suggest a need to focus on improving the SolatExo's ergonomics features, particularly for seated positions in Salah, and on simplifying the usability of the device. A more flexible structure that can accommodate the dynamic shifts between standing, bowing, and sitting postures would enhance user comfort. Additionally, providing clearer instructions or developing a more intuitive design could improve user satisfaction and operational efficiency.

https://doi.org/10.31436/iiumej.v26i1.3430

Table 5. Feedback from the end users after using SolatExo

| End-user | Physical Injuries | Feedback after using SolatExo |
|---|---|---|
| User 1 | Knee injury due to road accident | Usability: I found the SolatExo to be very difficult to operate. Comfort: Sitting between the two prostrations and the final tashahhud is uncomfortable. Performance: I feel it helps me get up a bit. Safety: I do not feel that it can harm me when using it. Overall user experience: It's challenging to use, but I still find pleasure in using it. |
| User 2 | Knee injury due to road accident | Usability: I need time to learn how to use it. Comfort: It is a bit uncomfortable sitting during the two prostrations and the final tashahhud. Performance: It can help me to perform standing prayers without relying on a chair. Safety: It can help me to perform standing prayers without using a chair. Overall user experience: Overall user experience: I feel delighted using it because it is rarely found. |

# 4. DISCUSSION

## 4.1. Design Requirements

Table 6 outlines the essential design requirements for the SolatExo, tailored to enhance its usability and effectiveness during Salah. The specified physical dimensions and geometry of the main frame and ratchet ensure a lightweight, slim design that integrates seamlessly with the user's body, facilitating natural movements. Performance characteristics include a maximum sustained load capacity of 100 kg and adjustable operating angles (90°, 72°, 54°, 36°, 18°) to support dynamic postures during prayer. Materials such as lightweight aluminum, rubber for comfort, and flexible polyester and nylon contribute to durability and user comfort. User-centric considerations encompass price, aesthetics, functionality, usability, and durability, ensuring the exoskeleton meets diverse user needs effectively. Environmental requirements focus on corrosion resistance, recyclability of materials, and durability against wear and tear, promoting sustainability and long-term usability in various environments.

https://doi.org/10.31436/iiumej.v26i1.3430

Table 6. Design requirements of SolatExo

| Design Requirements | Specifications | Justification |
|---|---|---|
| Physical dimension/ geometry | Main structure:<br>• Length: 760 mm<br>• Width: 50 mm<br>• Thickness: 3 mm<br>Ratchet:<br>• Operating angle: 5 gears of adjustable level, maximum to 90°<br>• Length: 150 mm<br>• Width: 15 cm | The SolatExo is designed to match the anthropometry requirements, considering users at the 5th percentile for short users, the 50th percentile for medium-tall users, and the 95th percentile for tall users. |
| Performance characteristic | Maximum sustained load:<br>• 80 kg<br>Range of motion:<br>• 90°, 72°, 54°, 36°, 18° | These features directly impact SolatExo's ability to provide effective support during various activities, accommodating dynamic movements and sustaining loads without compromise. |
| Materials | • Aluminum sheet<br>• Rubber<br>• Polyester<br>• Nylon | The aluminum is lightweight and strong, providing necessary support without hindering mobility. Rubber ensures user comfort during movement. Polyester and nylon securely support various parts of the SolatExo while allowing for flexibility. |
| User needs | • Price<br>• Aesthetic<br>• Functionality<br>• Usability<br>• Durability | The user-centric aims to offer optimal support and comfort. By tailoring the technology to an individual's specific needs and lifestyle, the SolatExo enhances mobility, addressing unique considerations and empowering the user to move with greater ease and independence. |
| Environmental requirements | • Resistance to corrosion<br>• Material recyclability<br>• Wear and tear | These considerations ensure the device remains durable and reliable across different environments while adhering to sustainable practices. Incorporating these features results in an environmentally friendly, long-lasting solution tailored to individual needs, promoting enhanced mobility and an improved overall quality of life. |

## 4.2. Range of Motion

Body movements are crucial in prayer, as noted by [19]. The development of lower limb exoskeletons now includes multiple degrees of freedom to accommodate a range of motions guided by user intentions, such as transitions from sitting to standing, standing to sitting, and even walking [20]. Recent advancements in exoskeleton technology have improved joint mobility and range of motion, which has been beneficial for various applications such as therapeutic interventions and motion analysis [21]. Moreover, exoskeletons are now being engineered with innovative actuation techniques and variable stiffness actuators. This allows for natural joint movement and tailored support based on the user's level of impairment [22],

[23]. These design advancements enhance the functionality and adaptability of exoskeletons, supporting users with physical disabilities in their daily activities, including prayer.

Incorporating SolatExo into Salah presents unique challenges regarding ROM and physical dimensions. SolatExo, while intended to enhance mobility, may restrict crucial movements required for proper Salah postures, such as kneeling and prostration, potentially impacting the overall Salah experience. This is consistent with findings in exoskeleton-assisted gait training, where limitations in joint ROM [24] and altered gait patterns have been observed [25]. Additionally, the added weight and bulkiness of SolatExo may disrupt Salah's flexibility and tranquility. However, in this study, the SolatExo is designed to be adjustable to accommodate a wide range of physical dimensions, including users at the 5$^{th}$ percentile for short users, the 50$^{th}$ percentile for medium-tall users, and the 95$^{th}$ percentile for tall users. By prioritizing inclusivity and accessibility, these advancements aim to ensure that users can perform their Salah with dignity and ease despite physical limitations. Therefore, integrating exoskeletons into Salah contexts requires a careful balance between technological assistance and Salah movements to uphold the sanctity of these practices.

The analysis of ROM in this study revealed no significant differences in most joint movements when comparing participants wearing the SolatExo to those without it, except for ankle plantar flexion and supination, where significant restrictions were observed. These findings suggest that while the SolatExo maintains the normal movement patterns of key joints like the knees and trunk, its design may restrict ankle movements, particularly during dynamic phases of Salah. This is critical since ankle flexibility is vital in maintaining balance during postures such as standing and bowing. The restricted ROM in ankle plantar flexion and supination aligns with findings in similar passive exoskeletons, where ankle movement is often constrained due to the structural design of the device. For instance, Chang [13] reported limitations in ankle joint flexibility in passive exoskeletons designed for rehabilitation, where energy recycling mechanisms inadvertently limited natural movement. Passive devices often lack the adaptive mechanisms present in active exoskeletons, which can modulate joint stiffness and allow for more natural movement patterns [15].

Future iterations of SolatExo could integrate adjustable mechanisms that allow for a greater range of plantar flexion and supination without sacrificing structural support to improve ankle flexibility. As demonstrated in the VS-AnkleExo [14], adjustable stiffness components could provide the necessary balance between stability and freedom of movement, thus enhancing the overall functionality of the SolatExo for Salah performance. These improvements would allow for a more natural execution of postures that require full ankle mobility, such as during prostration and sitting between the two prostrations.

### 4.3. Muscle Contraction

Previous studies have applied EMG to analyze muscle contraction patterns during different Salah movements, such as standing, bowing, prostration, and sitting [26], [27], [28]. However, none of these studies involved participants wearing an exoskeleton. Investigating the impact of passive exoskeletons (e.g., SolatExo) on muscle contractions during the Salah movements reveals complex dynamics between technological assistance and physiological responses. While exoskeletons are engineered to assist users in their movements, their impact on muscle activity during Salah represents a crucial yet understudied aspect. A study focusing on the forward bending movement has shown that the passive Laevo exoskeleton alters muscle activation patterns, resulting in reduced contraction in the lumbar/back (erector spinae muscles); however, concerns arise regarding potential weakening of the lumbar musculature due to prolonged exoskeleton use [29]. Similarly, when applied to the context of Salah, the

exoskeletons may attenuate muscle contractions necessary for maintaining proper prayer postures, such as kneeling and prostration.

Previous studies have applied EMG to analyze muscle contraction patterns during different Salah movements, such as standing, bowing, prostration, and sitting [16], [17]. However, none of these studies involved participants wearing an exoskeleton. Investigating the impact of passive exoskeletons, like SolatExo, on muscle contractions during Salah reveals complex dynamics between technological assistance and physiological responses. While exoskeletons are designed to support users during movement, their influence on muscle activity during Salah represents a critical but understudied area.

The EMG experiments show that the SolatExo exerts varied effects on muscle activity during Salah movements. For instance, the vastus medialis reached up to 80% of MVC, which, while appearing elevated, is consistent with the demands placed on the lower limbs during Salah postures. This high activation level is particularly evident during movements requiring significant stabilization, such as rising from prostration, where the quadriceps and knee extensors are engaged to support the body [16]. Muscles like the rectus femoris showed decreased contraction while using the SolatExo, suggesting that the exoskeleton alleviates muscular effort in some areas. However, the tibialis anterior and soleus, responsible for ankle stability and control, exhibited greater contractions when using the SolatExo. These muscles are crucial for maintaining balance during standing, bowing, and transitions in Salah, where the ankle joints must compensate for any external support, potentially leading to increased activation [17].

The results indicate that while the SolatExo provides structural support to certain muscle groups, it also imposes additional demands on others, particularly those involved in ankle stability. This finding is comparable to studies in squatting and similar activities, where the quadriceps, including the vastus medialis and vastus lateralis, exhibited high EMG activity [18]. Thus, while elevated in some muscles, the observed muscle activation patterns during Salah are within reasonable ranges for physical activities that involve complex postural transitions.

Note that the high muscle contractions observed in specific muscles are not consistent throughout the entire prayer but are more prominent during particular movements, such as transitioning from standing to prostration. These findings underscore the complex interplay between the SolatExo mechanisms and the dynamic requirements of Salah movements, where some muscles experience reduced effort. In contrast, others may face increased demands due to the nature of passive exoskeleton assistance. While passive exoskeletons, including the SolatExo, aim to reduce muscular strain, they may not actively assist movements as powered exoskeletons do. The high activation levels observed in muscles like the tibialis anterior and soleus highlight the need for further design improvements in the SolatExo. Incorporating adjustable or semi-active mechanisms could alleviate excessive muscle activity, particularly in the ankle joints, thus enhancing the device's overall effectiveness for assisting Salah's movements, especially for individuals with physical disabilities. Further research is needed to optimize SolatExo for specific postures, ensuring personalized and effective assistance during Salah.

### 4.4. Usability

Examining the usability of SolatExo for Salah reveals multifaceted considerations at the intersection of technology and religious practice. While SolatExo aims to enhance mobility and support users' movements, their integration into the context of the Salah movement presents

unique challenges. Research on exoskeleton-assisted activities has highlighted usability concerns [30], such as comfort, ease of use, and adaptability to specific activities. When applied to Salah, users may encounter difficulties achieving the precise postures and movements required for prayer due to the constraints imposed by the SolatExo's structure. Additionally, the added weight and bulkiness of the device could hinder users' ability to seamlessly transition between Salah positions, potentially disrupting the flow and concentration essential for spiritual engagement. Optimizing the usability of SolatExo for Salah necessitates a holistic approach that considers both technological functionality and the user's cultural and religious practices. Emphasizing user-centered design principles is crucial to ensure a harmonious integration of technology into the ritualistic experience. Regarding technological design, kinematic compatibility [31] between the passive exoskeletons and users plays a significant role. For example, the mechanisms of gears and ratchets should allow smooth transitions of body postures. Furthermore, usability concerns include the ease of donning and doffing the exoskeletons, which requires careful study to ensure user comfort.

### 4.5. User Experience

Exploring the user experience of wearing SolatExo during Salah unveils intricate interactions between technology and religious devotion. While exoskeletons are engineered to enhance mobility and support users' movements, their integration into Salah practices introduces novel considerations. Research on user experience in assistive technology highlights the importance of comfort, usability, and perceived effectiveness [32], [33]. During Salah, users may perceive disruptions in the seamless flow of movements due to the exoskeleton's design, potentially impacting their overall satisfaction. Additionally, individual preferences and cultural sensitivities influence the acceptance and adoption of exoskeleton technology within Salah practices.

Extraordinary accessories for Salah can create social reluctance, as users might feel self-conscious or fear judgment from others when using visible or bulky exoskeletons. Therefore, inconspicuous and aesthetically pleasing designs are essential. The exoskeleton should be as unobtrusive as possible, utilizing slim structures, neutral colors, and materials that blend with traditional clothing. Incorporating traditional design elements, such as fabrics and patterns commonly found in traditional attire, can help the device integrate seamlessly into the user's Salah attire. Offering color, material, and fit customization options can further enhance user experience and confidence. Educating users and their communities about the benefits and functionalities of the exoskeleton, with endorsements from community leaders and religious scholars, can also help reduce social reluctance and normalize the use of such technology. These considerations highlight the importance of designing exoskeletons that are functionally effective, culturally, and socially acceptable to users.

### 4.6. Contribution of Study

The study's findings significantly contribute to understanding various factors related to SolatExo, an exoskeleton prototype designed to assist Muslims with physical disabilities during Salah. Firstly, this study identified the essential features required by users for SolatExo and revealed the specific functionalities and design elements crucial for its effectiveness in aiding Salah's performance. Secondly, this study investigated the extent to which SolatExo reduces users' range of motion during Salah, providing insights into its biomechanical implications and potential benefits for users with limited mobility. Thirdly, the authors examined how SolatExo influences muscle contraction patterns in users during Salah, offering valuable information about its impact on user physiology and comfort. Additionally, this study explored users'

perceptions of SolatExo's usability, considering its practicality and effectiveness in aiding Salah's performance. Lastly, the authors gathered specific feedback from users regarding SolatExo's functionality, comfort, and overall effectiveness in enhancing their Salah experience, contributing to the ongoing refinement and optimization of this innovative assistive technology.

## 5. CONCLUSION

This study addressed a critical challenge faced by Muslims with physical injuries, particularly in performing Salah, where conventional support methods like chairs present significant limitations. These include disrupting congregation alignment and impeding ease of movement and portability. The development of the SolatExo prototype aimed to overcome these challenges by offering a functional passive exoskeleton designed specifically for assisting in Salah. Evaluation of the SolatExo prototype revealed key findings; while range of motion (ROM) showed no significant difference between wearing and not wearing the exoskeleton, muscle contraction, as measured by EMG, indicated reduced effort with the SolatExo, suggesting potential benefits in muscle activity reduction during prayer movements. Usability testing yielded a moderate to good score (68 on SUS) across respondents, indicating favorable usability levels, although user feedback highlighted operational challenges during specific prayer postures.

Future research should focus on enhancing SolatExo's usability and user experience through iterative design improvements informed by user feedback. Addressing operational difficulties, such as comfort issues during transitions between prostration and sitting phases, is crucial. Additionally, integrating advanced ergonomics principles and materials to enhance comfort and ease of use could further optimize SolatExo's performance. Moreover, expanding the study to a larger and more diverse user group, including individuals with a broader range of physical abilities and preferences, would provide valuable insights for refining the SolatExo better to meet the diverse needs within the Muslim community. This interdisciplinary approach underscores the importance of collaborative efforts between biomechanics, assistive technology design, and religious studies to develop inclusive solutions that enhance accessibility and participation in religious practices for individuals with physical disabilities.

In terms of real-world implementation, future work should explore the integration of the SolatExo in mosques and religious spaces (e.g., muscle), where it could serve as a practical assistive device for Muslims with physical limitations. Collaborating with religious authorities (e.g. State Islamic Religious Council) and community leaders could facilitate the adoption of the SolatExo in these settings. Pilot programs in mosques could help test their usability in real-world conditions and gather further insights to inform design improvements.

Expanding this study to a larger and more diverse user group, including individuals with different physical abilities and preferences, will provide valuable data for refining the SolatExo to meet the diverse needs within the Muslim community. Ultimately, this interdisciplinary approach, combining biomechanics, assistive technology, and religious studies, aims to create inclusive solutions that enhance accessibility and participation in religious practices for individuals with physical disabilities.

## ACKNOWLEDGEMENT

This work was funded by the Ministry of Higher Education of Malaysia under grant number FRGS/1/2022/TK10/UTEM/02/4. The authors would like to express their gratitude to the Fakulti Teknologi dan Kejuruteraan Industri dan Pembuatan (FTKIP) and the Centre for

Research and Innovation Management (CRIM) for their invaluable support. We extend our special thanks to Muhammad Aminin for their crucial involvement in data collection.

## REFERENCES

[1] Zhou J, Yang S, Xue Q (2021). Lower limb rehabilitation exoskeleton robot: A review. Advances in Mechanical Engineering. 13(4). doi: 10.1177/16878140211011862/ASSET/IMAGES/LARGE/10.1177_16878140211011862-FIG2.JPEG

[2] Murugan, B. (2021). A review on exoskeleton for military purpose. I-Manager's Journal on Mechanical Engineering, 11(2):36–44. doi: https://doi.org/DOI:10.26634/jme.11.2.17924

[3] Plaza, A., Hernandez, M., Puyuelo, G., Garces, E., & Garcia, E. (2023). Lower-limb medical and rehabilitation exoskeletons: A review of the current designs. IEEE Reviews in Biomedical Engineering, 16:278–291. doi:https://doi.org/10.1109/RBME.2021.3078001

[4] Antwi-Afari, M. F., Li, H., Anwer, S., Li, D., Yu, Y., Mi, H. Y., & Wuni, I. Y. (2021). Assessment of a passive exoskeleton system on spinal biomechanics and subjective responses during manual repetitive handling tasks among construction workers. Safety Science, 142: 105382. doi:https://doi.org/10.1016/J.SSCI.2021.105382

[5] Wang, X. ; ;, Ji, X. ;, Zhou, Y. ;, Yang, J. ;, Wei, Y. ;, Zhang, W., Tang, X., Wang, X., Ji, X., Zhou, Y., Yang, J., Wei, Y., & Zhang, W. (2022). A wearable lower limb exoskeleton: reducing the energy cost of human movement. Micromachines, 13(6): 900. doi:https://doi.org/10.3390/MI13060900

[6] Shanat M, Kumalah MJ (2018). Universal design: Beyond usability and aesthetic studies for prayer chair. International Journal of Applied and Creative Arts, 1(1):13-21. doi: 10.33736/IJACA.835.2018

[7] Fauzi ASM, Sa'idan AAH Bin, Jamaludin J, Ismail WZW, Ismail I, Sahrim M (2020). The development of solah chair using electronic sensor to assist disabled Muslims in performing prayers. REKA ELKOMIKA: Jurnal Pengabdian kepada Masyarakat, 1(1):25-34. doi: 10.26760/REKAELKOMIKA.V1I1.25-34

[8] Salah Chair - Because Sujud Matters – Salahchair [https://salahchair.co.uk/]

[9] Foldable Chair [https://www.lazada.com.my/products/kerusi-solat-lipat-foldable-chair-kerusi-tongkat-kerusi-sakit-lutut-kerusi-umrahhaji-i3191236578-s16180394112.html?from_gmc=1&fl_tag=1&exlaz=d_1:mm_150050845_51350205_201035 0205::12:21486711976!!!!!c!!16180394112!5293769526&gad_source=1&gclid=CjwKCAjwl bu2BhA3EiwA3yXyu4uMxSnykufM3hzTFd5Y8VmpEq0SON4r0SpKoKPQxKu3-zNfqviCfBoC4Y0QAvD_BwE

[10] Rabin, A., & Kozol, Z. (2010). Measures of range of motion and strength among healthy women with differing quality of lower extremity movement during the lateral step-down test. Journal of Orthopaedic and Sports Physical Therapy, 40(12):792–800. doi:https://doi.org/10.2519/JOSPT.2010.3424/ASSET/IMAGES/LARGE/JOSPT-792-FIG006.JPEG

[11] Molina-Molina, A., Ruiz-Malagón, E. J., Carrillo-Pérez, F., Roche-Seruendo, L. E., Damas, M., Banos, O., & García-Pinillos, F. (2020). Validation of mDurance, a wearable surface electromyography system for muscle activity assessment. Frontiers in Physiology, 11: 606287. doi: https://doi.org/10.3389/FPHYS.2020.606287/BIBTEX

[12] Brooke, J. (2013). SUS: A retrospective. Journal of Usability Studies, 8(2): 29–40.

[13] Chang, Y., Wang, W., & Fu, C. (2020). A lower limb exoskeleton recycling energy from knee and ankle joints to assist push-off. Journal of Mechanisms and Robotics, 12(5). doi: https://doi.org/10.1115/1.4046835/1082341

[14] Baser, O., & Kizilhan, H. (2018). Mechanical design and preliminary tests of VS-AnkleExo. Journal of the Brazilian Society of Mechanical Sciences and Engineering, 40(9): 1–16. doi:https://doi.org/10.1007/S40430-018-1365-4/METRICS

[15] Bryan, G. M., Franks, P. W., Song, S., Voloshina, A. S., Reyes, R., O'Donovan, M. P.,

Gregorczyk, K. N., & Collins, S. H. (2021). Optimized hip–knee–ankle exoskeleton assistance at a range of walking speeds. Journal of NeuroEngineering and Rehabilitation, 18(1): 1–12. doi:https://doi.org/10.1186/S12984-021-00943-Y/TABLES/1

[16] Rabbi, M. F., Wahidah Arshad, N., Ghazali, K. H., Abdul Karim, R., Ibrahim, M. Z., & Sikandar, T. (2019). EMG activity of leg muscles with knee pain during Islamic prayer (Salat). Proceedings - 2019 IEEE 15th International Colloquium on Signal Processing and Its Applications, CSPA 2019: 213–216. doi:https://doi.org/10.1109/CSPA.2019.8696025

[17] Osama, M., & Malik, R. J. (2019). Activation of the trunk muscles during Salat (Muslim Prayer). Journal of the Pakistan Medical Association, 69(12): 1929

[18] Muyor, J. M., Martín-Fuentes, I., Rodríguez-Ridao, D., & Antequera-Vique, J. A. (2020). Electromyographic activity in the gluteus medius, gluteus maximus, biceps femoris, vastus lateralis, vastus medialis and rectus femoris during the Monopodal Squat, Forward Lunge and Lateral Step-Up exercises. PLOS ONE, 15(4), e0230841. doi:https://doi.org/10.1371/JOURNAL.PONE.0230841

[19] Aqlan F, Ahmed A, Cao W, Khasawneh MT (2017). An ergonomic study of body motions during Muslim prayer using digital human modelling. International Journal of Industrial and Systems Engineering, 25(3):279-296. doi: https://doi.org/10.1504/IJISE.2017.081914.

[20] Rosales-Luengas, Y., Espinosa-Espejel, K. I., Lopéz-Gutiérrez, R., Salazar, S., & Lozano, R. (2023). Lower limb exoskeleton for rehabilitation with flexible joints and movement routines commanded by electromyography and baropodometry sensors. Sensors , 23(11):5252. doi: https://doi.org/10.3390/S23115252.

[21] Meng, Q., Fei, C., Jiao, Z., Xie, Q., Dai, Y., Fan, Y., Shen, Z., & Yu, H. (2022). Design and kinematical performance analysis of the 7-DOF upper-limb exoskeleton toward improving human-robot interface in active and passive movement training. Technology and Health Care, 30(5):1167–1182. doi: https://doi.org/10.3233/THC-213573

[22] Mendoza, F., Durango, D., Pallo, G., & Merchan, E. (2023). Advances in exoskeletons for military use. Athenea Engineering Sciences Journal, 4(12):43–54. doi: https://doi.org/10.47460/ATHENEA.V4I12.57

[23] Liu, Y., Guo, S., Hirata, H., Ishihara, H., & Tamiya, T. (2018). Development of a powered variable-stiffness exoskeleton device for elbow rehabilitation. Biomedical Microdevices, 20(3):1–13. doi: https://doi.org/10.1007/S10544-018-0312-6/METRICS

[24] White, H., Hayes, S., & White, M. (2015). The effect of using a powered exoskeleton training programme on joint range of motion on spinal injured individuals: A pilot study. International Journal of Physical Therapy & Rehabilitation, 1(1). doi: https://doi.org/10.15344/2455-7498/2015/102

[25] Baud, R., Manzoori, A. R., Ijspeert, A., & Bouri, M. (2021). Review of control strategies for lower-limb exoskeletons to assist gait. Journal of NeuroEngineering and Rehabilitation, 18(1): 1–34. doi: https://doi.org/10.1186/S12984-021-00906-3

[26] Rabbi, M. F., Ghazali, K. H., Mohd, I. I., Alqahtani, M., Altwijri, O., & Ahamed, N. U. (2018). Investigation of the EMG activity of erector spinae and trapezius muscles during Islamic prayer (Salat). Journal of Back and Musculoskeletal Rehabilitation, 31(6):1097–1104. doi: https://doi.org/10.3233/BMR-170988

[27] Arshad, N. W., Rabbi, M. F., Ghazali, K. H., Karim, R. A., Ibrahim, M. Z., Ahamed, N., & Sikandar, T. (2018). Muscle activation pattern of upper and lower back muscles during Islamic prayer (Salat). Journal of Advanced Research in Applied Mechanics, 48(1):1–8. doi: https://www.akademiabaru.com/submit/index.php/aram/article/view/1820

[28] Khanam, F., Ahmad, M., & Rahman, M. A. (2018). Muscle activity and work done estimation: a semg analysis on salat muscle activity and work-done estimation: A sEMG analysis on Salat. doi: https://www.researchgate.net/publication/326988967

[29] Bosch, T., van Eck, J., Knitel, K., & de Looze, M. (2016). The effects of a passive exoskeleton on muscle activity, discomfort and endurance time in forward bending work. Applied Ergonomics, 54:212–217. doi:https://doi.org/10.1016/J.APERGO.2015.12.003

[30] La Bara, L. M. A., Meloni, L., Giusino, D., & Pietrantoni, L. (2021). Assessment methods of usability and cognitive workload of rehabilitative exoskeletons: A systematic review. Applied

Sciences, 11(15):7146. doi: https://doi.org/10.3390/APP11157146

[31] Halim, I., Mahadzir, M. N. I., Abdullah, Z., Abidin, M. Z. Z., Muhammad, M. N., & Saptari, A. (2023). A review on ergonomics factors determining working in harmony with exoskeletons. Malaysian Journal of Medicine and Health Sciences, 19(6). doi: https://doi.org/10.47836/mjmhs.19.6.41

[32] Baldassarre, A., Lulli, L. G., Cavallo, F., Fiorini, L., Mariniello, A., Mucci, N., & Arcangeli, G. (2022). Industrial exoskeletons from bench to field: Human-machine interface and user experience in occupational settings and tasks. Frontiers in Public Health, 10:1039680. doi: https://doi.org/10.3389/FPUBH.2022.1039680/BIBTEX

[33] Halim, I., Saptari, A., Abdullah, Z., Perumal, P. A., Abidin, M. Z. Z., Muhammad, M. N., & Abdullah, S. (2022). Critical factors influencing user experience on passive exoskeleton application: A review. International Journal of Integrated Engineering, 14(4):89–115. doi:https://doi.org/10.30880/ijie.2022.14.04.009

https://doi.org/10.31436/iiumej.v26i1.3379

# BILATERAL GROUND REACTION FORCE PREDICTION WITH DEEP LEARNING MODELS AND CUSTOM FORCE PLATE

**YING HENG YEO, MUHAMMAD FAUZINIZAM RAZALI*, ZAIDI MOHD RIPIN, NUR-AKASYAH J., MOHAMAD IKHWAN ZAINI RIDZWAN, ALEXANDER WAI TENG TAN, JIA YI TAY**

*Neurorehabilitation Engineering and Assistance Systems Research, School of Mechanical Engineering, Engineering Campus, Universiti Sains Malaysia, 14300 Nibong Tebal, Penang, Malaysia.*

**Corresponding author: mefauzinizam@usm.my*

*(Received: 24 July 2024; Accepted: 5 December 2024; Published online: 10 January 2025)*

***ABSTRACT:*** Several low-cost force plates have been proposed as alternatives for laboratory-grade force plates. Nevertheless, the inability to quantify bilateral ground reaction force (GRF) prevents these inexpensive force plates from being used for biomechanical analysis and certain clinical metric acquisition. This study developed deep-learning models, such as autoencoder and U-net, to predict bilateral GRF from vertical GRF measured using a low-cost custom force plate during sit-to-stand, gait initialization, and gait. Results indicated that the U-net model, which utilized STFT vertical GRF as input, performed the best. In addition to predicting the mediolateral GRF measured during sit-to-stand, the model accurately predicted the anterior-posterior and mediolateral GRF for sit-to-stand, gait initialization, and gait in the test dataset, achieving high Pearson's correlation coefficient, coefficient of determination, and intraclass correlation coefficient values of over 0.90, 0.79, and 0.89, respectively. The model demonstrated a higher Pearson's correlation coefficient compared to three related previous studies that utilized different methods to predict anterior-posterior GRF and six studies in inferring mediolateral GRF. The results demonstrated the potential of TFU and custom force plate as a GRF measurement tool to perform bio-mechanical analysis.

***ABSTRAK:*** Beberapa plat daya kos rendah telah dicadangkan sebagai alternatif kepada plat daya berkualiti makmal. Walau bagaimanapun, ketidakmampuan untuk mengukur daya reaksi tanah (GRF) secara bilateral menghalang plat daya yang murah ini daripada digunakan untuk analisis biomekanik dan pengambilan metrik klinikal tertentu. Kajian ini membangunkan model pembelajaran mendalam, seperti autoencoder dan U-net, untuk meramalkan GRF bilateral daripada GRF menegak yang diukur menggunakan plat daya khas kos rendah semasa pergerakan duduk-ke-berdiri, permulaan berjalan, dan berjalan. Hasil menunjukkan bahawa model U-net, yang menggunakan GRF menegak STFT sebagai input, memberikan prestasi terbaik. Selain meramalkan GRF mediolateral yang diukur semasa duduk-ke-berdiri, model ini juga meramalkan dengan tepat GRF anterior-posterior dan mediolateral untuk duduk-ke-berdiri, permulaan berjalan, dan berjalan dalam set data ujian, mencapai nilai koefisien korelasi Pearson, koefisien penentuan, dan koefisien korelasi intrakelas yang tinggi melebihi 0.90, 0.79, dan 0.89, masing-masing. Model ini menunjukkan koefisien korelasi Pearson yang lebih tinggi berbanding tiga kajian terdahulu yang berkaitan yang menggunakan kaedah berbeza untuk meramalkan GRF anterior-posterior dan enam kajian dalam menyimpulkan GRF mediolateral. Hasil kajian menunjukkan potensi TFU dan plat daya khas sebagai alat pengukuran GRF untuk melakukan analisis biomekanik.

***KEYWORDS:*** *Force plate; deep learning model; ground reaction force; prediction*

https://doi.org/10.31436/iiumej.v26i1.3379

# 1. INTRODUCTION

The force plate is the gold standard for measuring the ground reaction force (GRF) and the center of pressure (CoP) exerted by a person's movement, where the obtained data can be utilized for biomechanical analysis. The GRF represents external forces acting on the human body from the ground, while the CoP represents the position upon which the GRF works. A laboratory-grade force plate usually consists of a six-axis load cell enclosed in a flat rectangular case, which measures the three-dimensional GRF and moments. The CoP is then computed based on the recorded GRF and moments. Both GRF and CoP are necessary for determining the forces and torques withstood by various human body components in biomechanical analysis. In addition, the force plate is essential in acquiring various GRF- or CoP-derived metrics that assess the elderly or patients' health conditions in clinical settings. These applications demonstrate the importance of force plates in biomechanical and clinical domains.

In laboratory-grade force plates, the high production cost remains one of the concerns. For example, AMTI, Bertec, and Kistler force plates cost between USD 10,000 and 20,000. These prices restrict the availability of force plates in clinical or biomechanical fields, mainly when the budget is tight. The costing issue frequently occurs in clinical facilities worldwide, where the spending is directed towards other instruments with a higher return on investment than the force plate. In third-world countries, the affordability problem is even more severe, where less capital is invested in research. As a result, the clinical and biomechanical research that employs force plates is hampered in developing countries. On the other hand, the scalability of a force plate is infeasible due to the high cost. An example that demands force plate scalability involves a task under study, which must be performed over a long distance, requiring many force plates to provide sufficient coverage.

Several techniques that avoid the use of force plates have been introduced to address the concerns. This usage often involves inverse dynamic optimization and machine learning models. Accelerometers are also used instead of a complete inertial motion capture system to simplify the GRF prediction [6] further. However, when external pressures other than GRF are applied to the participants, the accuracy of these methods may be compromised [7]. Therefore, pressure-sensing insoles offer another alternative that can consider external forces [8-10]. However, these commercialized insoles are usually costly [8; 10]. Moreover, when fewer pressure sensors are used during movements (such as calf raises), the GRF prediction model applied with a low-cost customized insole may be unreliable [9].

Meanwhile, previous studies suggested low-cost force plates as alternatives to laboratory-grade force plates [11; 12]. A low-cost force plate typically consists of four single-axis load cells positioned vertically to measure the vertical GRF. However, no load cell faces the lateral direction to measure the bilateral GRF. When an individual performs tasks that generate perceivable bilateral GRF, the bilateral GRF will not be identified and analyzed.

The reaction of a single-axis load cell to off-axis loading may provide insight into addressing the issue of low-cost force plates. The load cell strain gauge generates values that depend on the force-induced strain. Generally, strain is highest in the direction of the primary applied force, while the off-axis loading creates minor strain. This minor strain is due to the Poisson effect, which influences the signals. The changes in readings can then determine the extent of off-axis loading. In other words, the vertical GRF readings from the four independent load cells on the inexpensive force plate estimate the off-axis bilateral GRF. To the authors' knowledge, no previous studies have investigated the algorithm for computing the bilateral GRF from the vertical GRF recorded using low-cost force plate load cells.

This study aimed to develop a low-cost custom force plate to acquire bilateral GRF, in which deep learning models were trained to predict bilateral GRF from vertical GRF. Considering the necessity of bilateral GRF in biomechanical analysis and clinical settings, the prediction of bilateral GRF for sit-to-stand, gait initialization, and gait was investigated. With the proposed method, the low-cost force plates, which previously were unable to measure bilateral GRF, could now be applied to predict bilateral GRF. The improved low-cost force plates, which were more affordable and easily accessible to clinicians and researchers with tight budgets, could potentially be used for biomechanical analysis with enhanced accuracy and acquisition of bilateral GRF-derived clinical assessment metrics. The scalability issue in biomechanical analysis could be overcome by acquiring multiple low-cost force plates at a reasonable price as compared to laboratory-grade force plates.

## 2. MATERIALS AND METHOD

### 2.1. Participants

As the intraclass correlation coefficient (ICC) was applied to evaluate the model accuracy in this study, as mentioned in Section "Statistical Analysis," the sample size to achieve an ICC precision of ±0.02 was calculated [13]. The expected ICC was set at 0.98 based on a study on low-cost force plates in measuring GRF during sit-to-stand [11]. The confidence interval was set as 95%, with two raters (laboratory-grade and custom force plates). The following criteria were used for participant selection:

- Being 18 years of age or older;
- Being able to stand for more than one hour;
- Being able to engage in physical activity without restriction;
- Not having a musculoskeletal or neurological disorder;
- Not taking medication that affects body balance;
- Not being pregnant;
- Being able to provide informed consent.

This study, with the protocol code USM/JEPeM/PP/23020164, was approved by the Ethics Committee of Universiti Sains Malaysia. Table 1 summarizes an overview of the participants' information.

Table 1. Summary of the information regarding the participants in this study

| Information | Value |
|---|---|
| Gender (male/female) | 10 / 10 |
| Age (year, mean ± standard deviation) | 30.65 ± 8.48 |
| Height (cm, mean ± standard deviation) | 165.05 ± 7.99 |
| Weight (kg, mean ± standard deviation) | 63.59 ± 10.68 |

### 2.2. Apparatus

The custom force plate with dimensions of 676 mm × 400 mm × 49 mm comprised a rectangular board, an ESP32, four HX711, and four half-bridge strain gauge single-axis load cells, which were used in typical digital bathroom scales. The cost of the custom force plate was less than USD$50, at least 200 times cheaper than a laboratory-grade force plate. The custom force plate has been granted an exemption from the registration of medical devices by the Medical Device Authority (MDA), Ministry of Health Malaysia, under protocol number

https://doi.org/10.31436/iiumej.v26i1.3379

CIU-20230226-11. Figure 1 exhibits the top and bottom views of a custom force plate. A 4060-05 Bertec (laboratory-grade force plate) was used as the gold standard to evaluate the accuracy of the model.

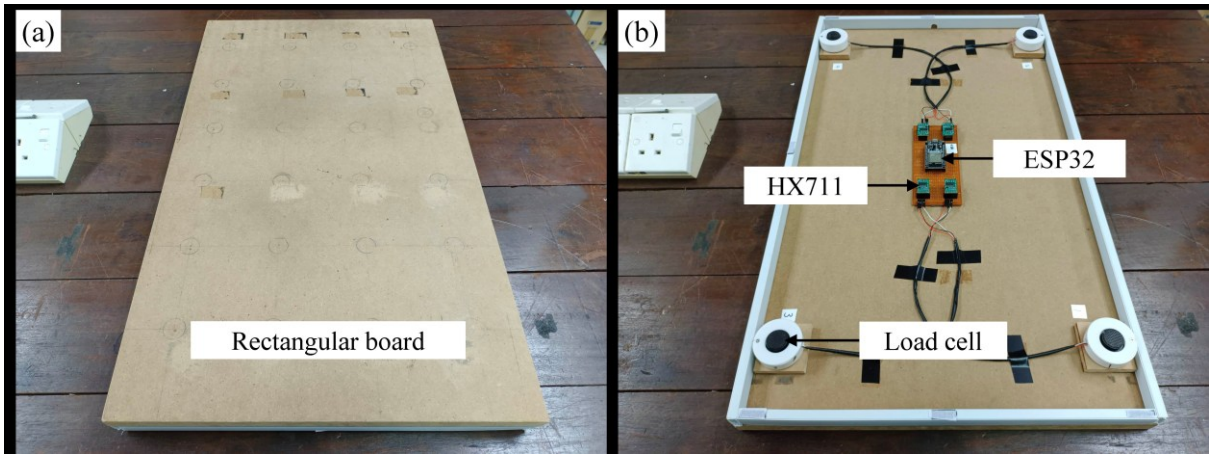


Figure 1. (a) The top view of the custom force plate. (b) The bottom view of the custom force plate.

### 2.3. Experimental Procedures

Before the experiment began, the custom force plate was placed on the Bertec force plate. The participants were asked to perform three tasks on the stacked force plates based on the procedures described in previous works: sit-to-stand [12], gait initialization [14], and gait [15]. When the participants conducted the tasks, forces were transmitted through the contact surfaces of the feet to the stacked force plates. Subsequently, vertical and bilateral GRF, which acted on the participants's feet, were generated according to the types of tasks. The three-dimensional GRF readings from the Bertec force plate and vertical GRF measurements from the custom force plate were then recorded at 500 Hz and 80 Hz sampling rates, respectively, and each task was repeated 10 times.

### 2.4. Data Preprocessing

A median filter with a window size of five was applied to custom force plate readings to remove outliers. Bertec force plate values were low-pass filtered using a zero-phase fourth-order low-pass Butterworth filter. The critical frequency was adjusted to half of the sampling rate of the custom force plate. The values measured with the Bertec force plate were then interpolated to match the sampling rate of the custom force plate.

### 2.5. Dataset Preparation

The complete dataset of 20 participants was randomly divided into training [fourteen participants (70 %)], validation [three participants (15 %)], and test datasets [three participants (15 %)], as shown in Figure 2. The dataset splitting ratio was applied according to previous research on gait cycle prediction models [16]. Each dataset included patches from the Bertec force plate's anterior-posterior and mediolateral GRF (model output) and the custom force plate's individual load cell vertical GRF (model input). To expand the dataset size, the readings were randomly cropped into smaller patches with a size of $ntt$. A total of 40 patches were cropped from each sit-to-stand trial recording, whereas 20 patches were generated from a recording of the gait initialization or a gait trial, as the sit-to-stand trial took longer. The training, validation, and test datasets comprised 16800, 3600, and 3600 patches, respectively.

https://doi.org/10.31436/iiumej.v26i1.3379

Following the rule of 10 events per variable [17], the minimum amount of data required was 10 times the amount of input required for the deep learning models. Considering the maximum length of model input, $ntt = 112$, as indicated in Table 2, and channel number 4 corresponding to the four load cell readings, the minimum number of training dataset readings was 4480 (10 × 112 × 4). Therefore, the number of training data utilized in this study, 16800, was deemed appropriate. The mean and standard deviation obtained from the training dataset were used to standardize the patches from all datasets.

The Short-Time Fourier Transform (STFT) was used to convert the patches into the time-frequency domain input and output to explore if representing the input in time-frequency form could enhance model accuracy. A Fourier transform window of 62 data points was employed to produce real and imaginary values, with 32 points on a frequency axis. The number of strides of the window sliding was set as 16, significantly less than the window size of 62, to generate a smooth output. An additional 62 subsequent data points from full trial readings were added to the patches to ensure enough data points were accommodated in the STFT window.

### 2.6. Model Architecture

Autoencoder [18] and U-net [19] were used in this study to predict bilateral GRF. The autoencoder was a neural network trained to compress input into a latent representation with a smaller dimension through an encoder. Later, a decoder was employed to reconstruct the output from the latent representation. Throughout the training process, the autoencoder acquired efficient representations, allowing for dimensionality reduction, feature extraction, anomaly detection, and even data generation through manipulation of the latent space. U-Net was similar in that it consisted of an encoder and a decoder. The difference was that the encoder's hidden layers were concatenated to the decoder's hidden layers with similar dimensions. This reduced the information loss, which may happen in an autoencoder [20], and allowed precise localization in generating the output [19].

https://doi.org/10.31436/iiumej.v26i1.3379

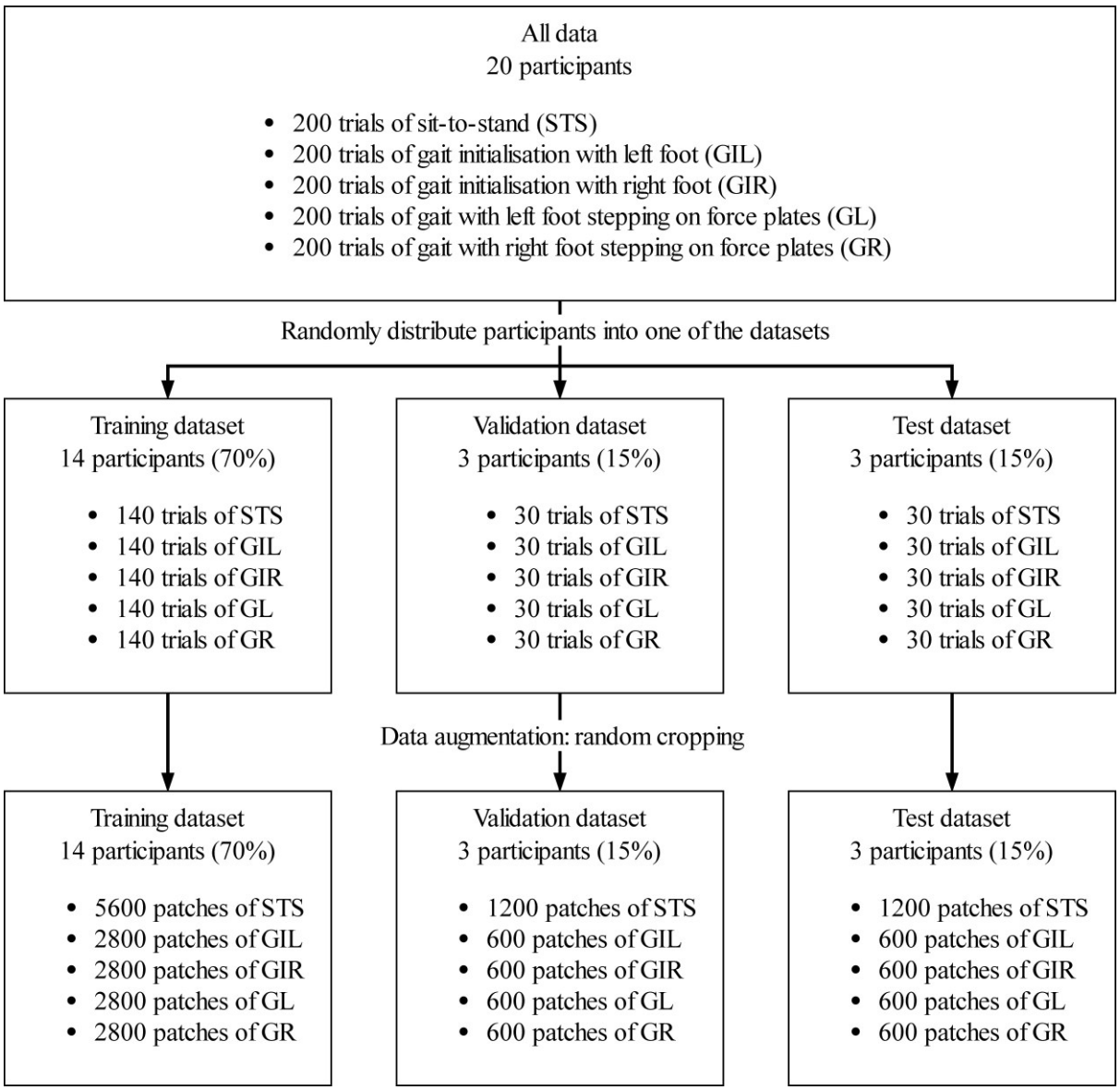


Figure 2. A flow chart shows the dataset preparation for model training.

Different model architectures were developed to receive input and produce output in the time and time-frequency domains (see Section "Data preparation"). Subsequently, four different model architectures, time domain autoencoder (TA), time domain U-Net (TU), time-frequency domain autoencoder (TFA), and time-frequency domain U-Net (TFU), were constructed. Several hyperparameters related to the model architectures were then modified in the hyperparameter optimization to acquire the optimal model architectures (see Section "Hyperparameter optimization"). Figures 3 and 4 depict the optimal architectures for the TA, TU, TFA, and TFU models determined through hyperparameter optimization. The following discussion of the model architecture and hyperparameter optimization was conducted using the figures.

https://doi.org/10.31436/iiumej.v26i1.3379

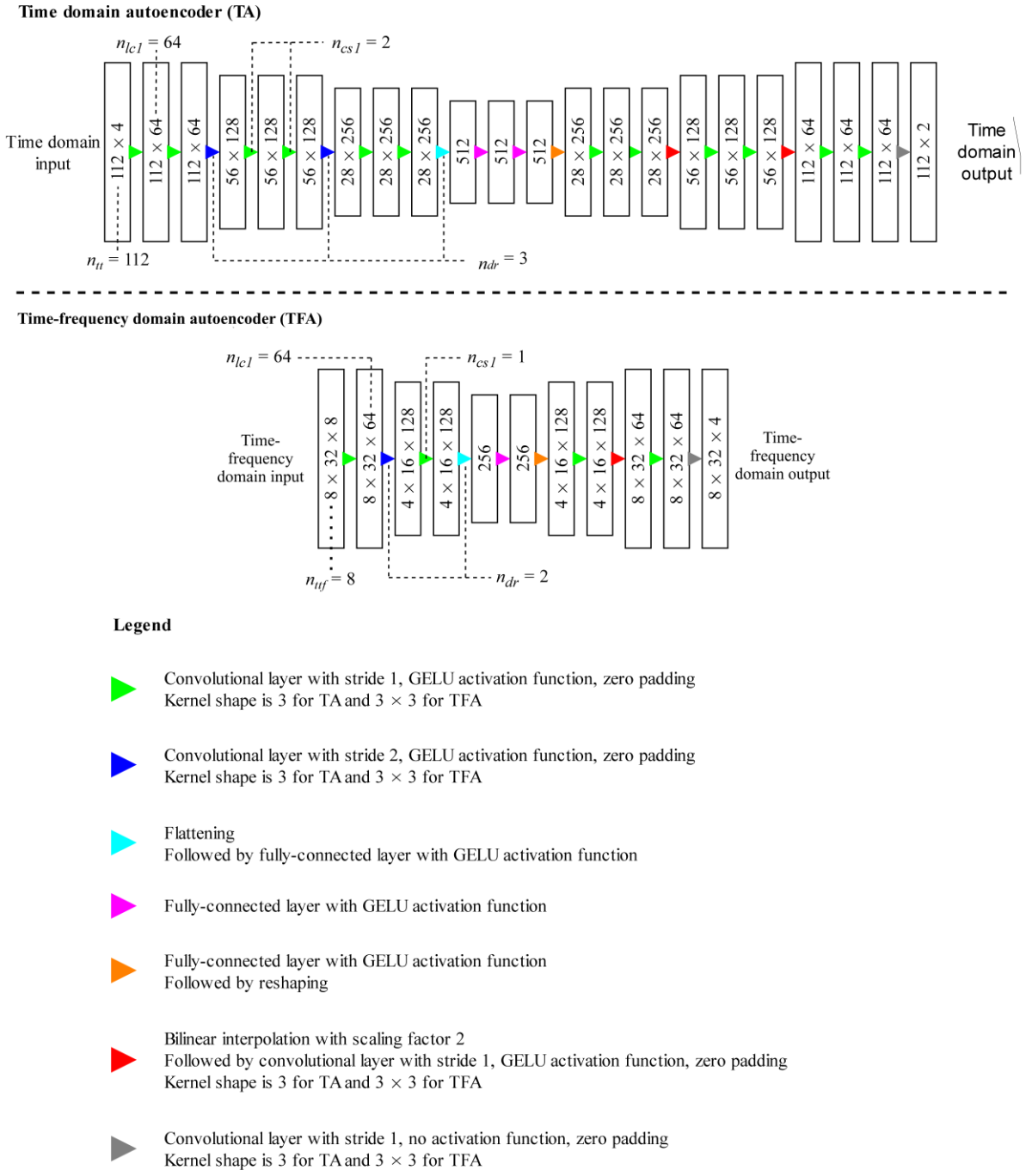


Figure 3. The optimal autoencoder model architectures are determined from hyperparameter optimization. The dotted lines are not part of the model architectures.

https://doi.org/10.31436/iiumej.v26i1.3379

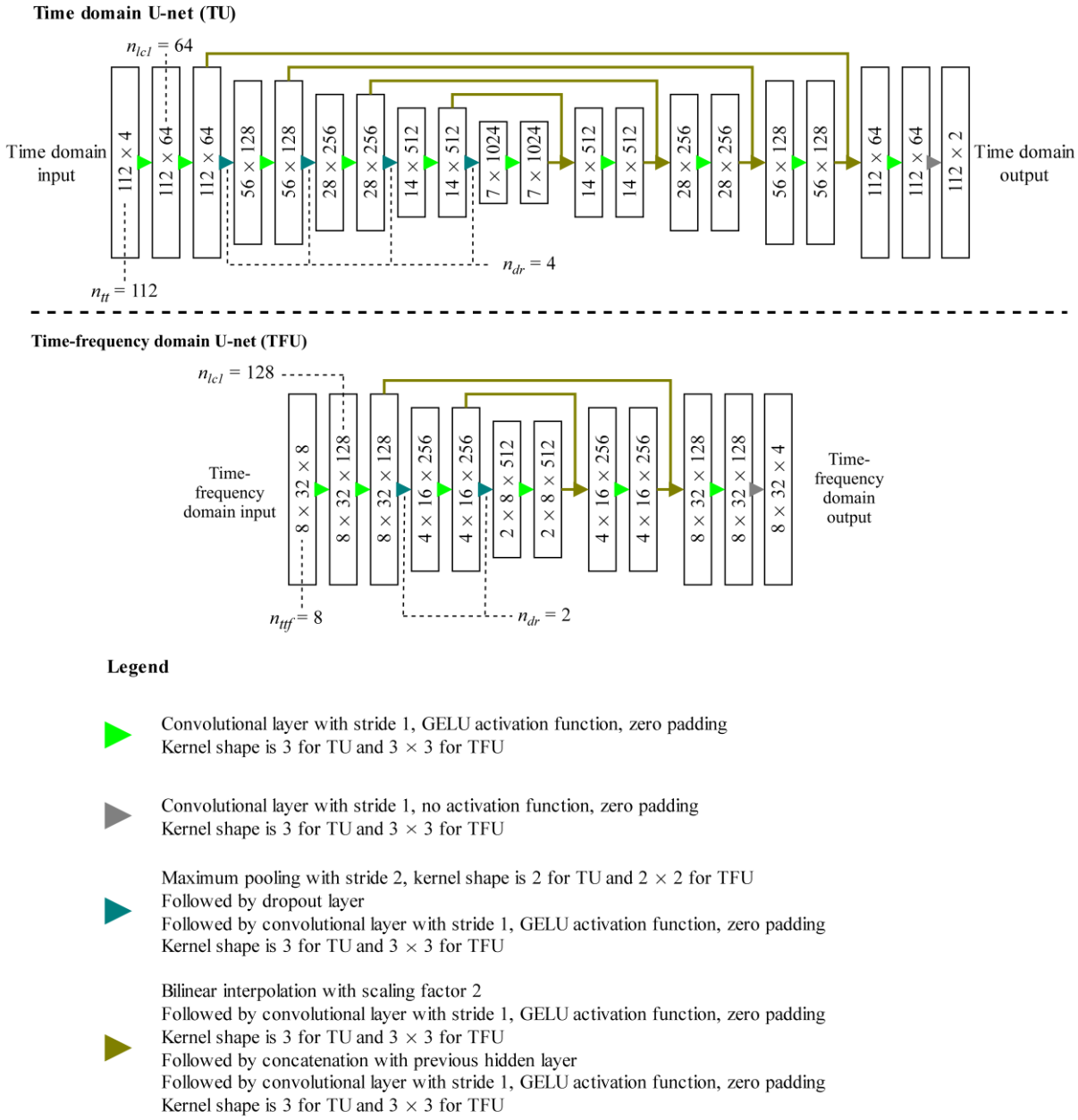


Figure 4. The optimal U-net model architectures are determined from the hyperparameter optimization. The dotted lines are not part of the model architectures.

The input for the time domain models (TA and TU) consisted of a two-dimensional patch with size $ntt \times 4$. Based on the random cropping operation described in Section "Data preparation," the first dimension represented the time axis with size $ntt$. The vertical GRF data points from the four custom force plate load cells were represented by the last dimension (channel having a size of four). The output was a two-dimensional patch with size $ntt \times 2$, where the anterior-posterior and mediolateral GRF of the models was predicted using the channel with size two. A three-dimensional $nttf \times 32 \times 8$ patch functioned as the input for the time-frequency domain models (TFA and TFU). The time and frequency axes were represented by the first (which had a size nttf) and the second dimensions (which had a size 32), respectively. Additionally, the real and imaginary values generated with STFT from the four custom force plate load cell measurements were stored in the eight channels. The output

was a three-dimensional patch with size $nttf \times 32 \times 4$. The four channels also represented the real and imaginary values of the model-predicted STFT-transformed anterior-posterior and mediolateral GRF. Different ntt and nttf were applied in hyperparameter optimization to investigate the optimal input receptive field.

In a typical convolutional layer, l, the value of the output feature, $y^{l}_{i,j,k}$ located at the *i*th row and jth column in the kth feature map was calculated with Eq. (1) [21],

$$y^{l}_{i,j,k} = \boldsymbol{w}^{l}_{k}{}^{T} \boldsymbol{x}^{l}_{i,j} + b^{l}_{k} \tag{1}$$

where $\boldsymbol{w}^{l}_{k}$ is the weight, $b^{l}_{k}$ is the bias of the $k^{th}$ filter, and $\boldsymbol{x}^{l}_{i,j}$ is the input value at the $i^{th}$ row and $j^{th}$ column of the $l^{th}$ layer. Gaussian error linear unit (GELU) activation function is shown in Eq. (2) [22], where $x$ is the function input while $y$ is the function output.

$$y = 0.5x\left(1 + \tanh\left(\sqrt{\frac{2}{\pi}}(x + 0.044715x^{3})\right)\right) \tag{2}$$

A fully-connected layer is the matrix multiplication between a one-dimensional input vector, $x$, and a two-dimensional weight matrix, $W$, as stated in Eq. (3) [23],

$$y = Wx + b \tag{3}$$

where $b$ is the scalar bias, and $\boldsymbol{y}$ is the one-dimensional output vector. Bilinear interpolation is described by Eq. (4) and (5) [24],

$$\omega(t) = \begin{cases} 1 - |t|, 0 \le |t| \le 1 \\ 0, others \end{cases} \tag{4}$$

$$y = \begin{bmatrix} \omega(\Delta i) & \omega(1 - \Delta i) \end{bmatrix} \begin{bmatrix} x_{00} & x_{01} \\ x_{10} & x_{11} \end{bmatrix} \begin{bmatrix} \omega(\Delta j) \\ \omega(1 - \Delta j) \end{bmatrix} \tag{5}$$

where $y$ is the interpolated value, x represents the values at the four adjacent corners of a square with coordinates (0, 0), (0, 1), (1, 0), (1, 1), Δi and Δj denote the positions of y in relative to x with coordinate (0, 0). The maximum pooling layer is defined by Eq. (6) [21],

$$y^{l}_{i,j,k} = \text{pool}\left(x^{l}_{m,n,k}\right), \forall (m, n) \in \mathcal{R}_{i,j} \tag{6}$$

where $y^{l}_{i,j,k}$ is the maximum value located at the ith row and jth column in the kth feature map of the lth layer obtained from $\mathcal{R}_{i,j}$, which is a group of adjacent values around the location (i, j).

In Figures 3 and 4, nlc1 represents the number of the first hidden layer channels. Following a dimensional reduction of the time or frequency axis, the number of channels in the subsequent encoder hidden layers was consistently doubled. In autoencoder models like TA and TFA, $ncs1$ signifies the number of convolutional layers with stride as one applies after each dimensionality reduction. The hyperparameters $nlc1$, $ndr$, and $ncs1$ are optimized in the hyperparameter optimization to achieve adequate model capacity and complexity [25]. The hyperparameter optimization was conducted on U-net models (TU and TFU) to identify the optimal dropout rate ($rd$) for reducing overfitting in the training dataset [19].

Autoencoder and U-net were selected as they performed effectively in the signal analysis. [26-28]. Even though there were several previous studies that applied machine learning models to predict GRF [3; 6; 8; 9; 29], these models were not used as they only accepted data points from a single time frame. It was doubted that a data point of vertical GRF recorded with the four load cells on a custom force plate could provide enough information to carry out bilateral

https://doi.org/10.31436/iiumej.v26i1.3379

GRF prediction. On the other hand, as compared to recurrent neural network (RNN)-based models, autoencoder and U-net models were relatively less computationally expensive to train, considering the backpropagation in the time dimension, especially when the RNN sequence was long [30].

### 2.7. Model Training

Google Jax and the NVIDIA RTX 2060 Super GPU were used to implement the model training. During each training iteration, a batch of inputs with a size of 64 was fed into the model to generate the expected outputs. A batch size of 64 was chosen for its positive impact on model accuracy and its compatibility with a higher learning rate, facilitating accelerated model training [31]. The loss was calculated using the mean square error. The weight decay rate (rwd) was implemented across all models to apply L2 norm regularization to the weights, reducing overfitting to the training dataset.

In the case of the autoencoder models (TA and TFA), L1 norm regularisation of hidden unit activations was conducted with a sparsity constant (ks) to explore whether a sparse autoencoder could generalize more effectively than one without sparse representation. Only the bottleneck hidden unit activations were considered in the L1 norm regularisation to prevent excessive regularization of the models. The values of rwd and ks were optimized using hyperparameter optimization. The losses of the autoencoder (lossA) and U-net (lossU) are obtained using Eq. (7) and (8), respectively, as follows:

$$\mathrm{loss_A} = \left\|\hat{\mathrm{Y}} - \mathrm{Y}\right\|_2 + \mathrm{r_{wd}} \cdot \|\mathrm{W}\|_2 + \mathrm{k_s} \cdot \|\mathrm{H}\|_1 \tag{7}$$

$$\mathrm{loss_U} = \left\|\hat{\mathrm{Y}} - \mathrm{Y}\right\|_2 + \mathrm{r_{wd}} \cdot \|\mathrm{W}\|_2 \tag{8}$$

where $\hat{\mathrm{Y}}$ is the predicted output; $Y$ is the actual output, $rwd$ is the weight decay rate; $W$ refers to all layer weights; $ks$ is the sparsity constant; $H$ refers to the bottleneck hidden unit activations.

The weights and biases were tuned using the Adam optimizer. The learning rate ($rl$) was optimized using hyperparameter optimization. Two phases constituted the model training, during which the models were trained for 100 epochs in the initial phase. Early stopping was performed using the epoch number determined in the first phase to reduce the overfitting of the training dataset.

### 2.8. Hyperparameter Optimization

Hyperparameter optimization was necessary to tune hyperparameters, which must be fixed before model training and could not be estimated through data learning [32]. The optimal hyperparameters for training models that produced good outcomes were obtained after employing hyperparameter optimization. Table 2 tabulates the list of hyperparameters that are optimized in this study. Remarkably, the range of $rl$ was determined based on the learning rate used in the previous work that analyzed signals with autoencoder, 10-4, 10-3, and 10-2 [33]. Apart from these values, smaller numbers such as 10-6 and 10-5 were used for $rl$ to avoid exploding gradient as the number of layers applied in the models could be more than that in the previous work [33]. The limited time and computational resources required to train the models led to the implementation of Bayesian optimization [34]. The training of 50 models was conducted for each architecture, including TA, TFA, TU, and TFU. The model with the lowest minimal validation loss score was then selected as the most effective model for the corresponding architecture. Minimal validation loss was used as the model selection metric because it accounted for overfitting to the training dataset compared to training loss [35]. Even though test loss exhibited a similar characteristic to minimal validation loss, test loss was not

applied in model selection to avoid train-test contamination in evaluating the performance of the selected models [36].

Table 2. Summary list of the hyperparameters to be optimized, description, targeted models, and the values.

| Hyperparameter | Description | Targeted Models | Values |
|---|---|---|---|
| $n_{tt}$ | Dimension of time axis for time-domain input and output | TA, TU | 16, 48, 112 |
| $n_{ttf}$ | Dimension of time axis for time-frequency domain input and output | TFA, TFU | 2, 4, 8 (corresponded to 16, 48, and 112 values of $n_{tt}$ after STFT) |
| $n_{lc1}$ | Number of channels of first hidden layer | TA, TFA, TU, TFU | 16, 32, 64, 128 |
| $n_{dr}$ | Number of dimensional reductions in time and frequency axis of encoder | TA, TFA, TU, TFU | 2, 3, 4, 5 |
| $n_{cs1}$ | Number of convolutional layers with stride as one after each dimensional reduction | TA, TFA | 1, 2, 3 |
| $r_d$ | Dropout rate | TU, TFU | 0, 0.25, 0.5, 0.75 |
| $r_{wd}$ | Weight decay rate | TA, TFA, TU, TFU | $10^{-8}$, $10^{-7}$, $10^{-6}$, $10^{-5}$, $10^{-4}$ |
| $k_s$ | Sparsity constant | TA, TFA | 0, $10^{-7}$, $10^{-6}$, $10^{-5}$, $10^{-4}$ |
| $r_l$ | Learning rate | TA, TFA, TU, TFU | $10^{-6}$, $10^{-5}$, $10^{-4}$, $10^{-3}$, $10^{-2}$ |

## 2.9. Model Deployment

The best model of each architecture was employed to predict the bilateral GRF readings of complete sit-to-stand, gait initialization, and gait trials in the training dataset (inclusive of the validation dataset) and test dataset. Initially, if a time-frequency domain model (such as TFA and TFU) was used, STFT was applied to the complete vertical GRF readings of the individual load cell. The trial readings were then cropped into patches with $ntt$ or $nttf$ input size and fed into the model. For the cropping operation, sliding windows with a stride of 50% of the input size were applied. Subsequently, the average of the overlapping outputs for the model was calculated. If the time-frequency domain model was implemented, inverse STFT was applied to the averaged output. Lastly, the expected time series bilateral GRF represented the model's output.

## 2.10. Statistical Analysis

Prior to the analysis, the bilateral GRF was normalized using the participant's weight to obtain a value expressed as a percentage of body weight (% BW). To determine the extent of the difference between predicted readings and their actual counterparts, the Root Mean Square Error (RMSE) and relative RMSE (rRMSE) between the actual and predicted bilateral GRF readings were computed [37]. The Pearson correlation coefficient (ρ) was also calculated to evaluate the linearity between predicted and actual readings. The value of ρ was important for assessing the accuracy of predicted readings. If predicted readings showed a strong linear correlation with actual readings, the model could infer the trend of actual readings with minimal residual noise. The equation of ρ is shown in Eq. (9) [38],

$$\rho = \frac{\sum(x_p - \bar{x}_p)(x_a - \bar{x}_a)}{\sqrt{(\sum(x_p - \bar{x}_p)^2 \sum(x_a - \bar{x}_a)^2)}} \quad (9)$$

https://doi.org/10.31436/iiumej.v26i1.3379

where $x_p$ is predicted reading, $\bar{x}_p$ is the mean of predicted readings, $x_a$ is actual reading, and $\bar{x}_a$ is the mean of actual readings. Based on the ranges of ρ, the strength of the correlation is considered [39] as follows:

- 0.9 is "very strong"
- 0.7–0.9 is "strong"
- 0.4–0.7 is "moderate"
- 0.2–0.4 is "weak"
- < 0.2 is "very weak"

The coefficient of determination (R2) was calculated to assess the fit of the predicted readings to the actual readings. A good fit between predicted and actual readings was suggested, with R2 exceeding 0.8 [40]. The agreement between predicted and actual readings was assessed using the intraclass correlation coefficient [ICC (2, 1)] through the application of the two-way mixed-effects model (single rater type and defining the definition as absolute agreement) [41]. The definition is relevant to measuring the model performance, where the actual and predicted readings acquired from the same tasks must be equal to achieve absolute agreement. ICC (2, 1) is calculated according to Eq. (10),

$$\mathrm{ICC}\,(2,1) = \frac{\mathrm{MS_R} - \mathrm{MS_E}}{\mathrm{MS_R} + (\mathrm{k_r}-1)\mathrm{MS_E} + \frac{\mathrm{kr}}{\mathrm{n}}(\mathrm{MS_C} - \mathrm{MS_E})} \tag{10}$$

where MSR is the mean square for trial, MSE is the mean square for error, MSC is the mean square for actual and predicted readings, kr is the number of raters (which is one since only actual readings are used as the gold standard), and n is the number of readings. The agreement is rated based on the ICC (2, 1) ranges [41] as follows:

- 0.9 is "excellent"
- 0.75–0.9 is "good"
- 0.5–0.75 is "moderate"
- < 0.5 is "poor"

## 3. RESULTS

The optimal hyperparameter sets were obtained via hyperparameter optimization, as tabulated in Table 3. Model training with these hyperparameters yielded TA, TFA, TU, and TFU models with the lowest minimal validation loss.

Table 3. Summary of the optimal hyperparameter sets for TA, TFA, TU, and TFU models

| Hyperparameter | Autoencoder | | U-net | |
|---|---|---|---|---|
| | TA | TFA | TU | TFU |
| $n_{tt}$ | 112 | - | 112 | - |
| $n_{ttf}$ | - | 8 | - | 8 |
| $n_{lc1}$ | 64 | 64 | 64 | 128 |
| $n_{dr}$ | 3 | 2 | 4 | 2 |
| $n_{cs1}$ | 2 | 1 | - | - |
| $r_d$ | - | - | 0 | 0.5 |
| $r_{wd}$ | $10^{-6}$ | $10^{-7}$ | $10^{-5}$ | $10^{-5}$ |
| $k_s$ | $10^{-5}$ | $10^{-5}$ | - | - |
| $r_l$ | $10^{-4}$ | $10^{-4}$ | $10^{-4}$ | $10^{-3}$ |

https://doi.org/10.31436/iiumej.v26i1.3379

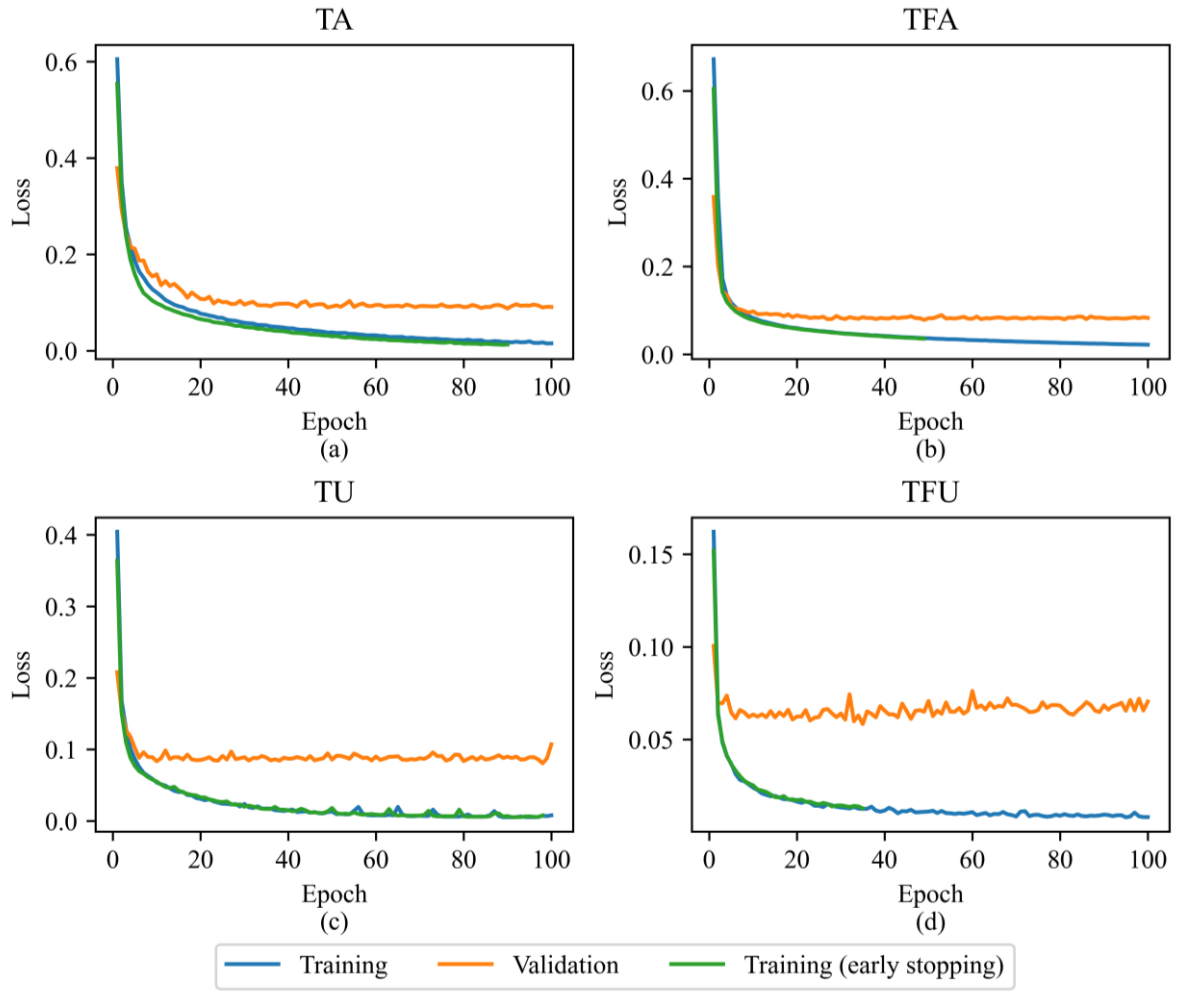


Figure 5. Graphs of loss versus epoch for training of different models.

The graphs of loss versus epoch are plotted in Figure 5 for the training of each model listed in Table 3. The training and validation losses during model training without and with early stopping, as highlighted in Section "Model training," are shown. For all models, the losses decreased and converged towards a horizontal level over training epochs, indicating that the configurations listed in Table 3 were suitable for conducting stable model training. Validation losses did not exhibit a clear U-shaped curve, indicating that overfitting to the training dataset did not occur to a significant extent. By implementing early stopping at the epoch when minimum validation loss was recorded, overfitting to the training dataset could be further reduced.

https://doi.org/10.31436/iiumej.v26i1.3379

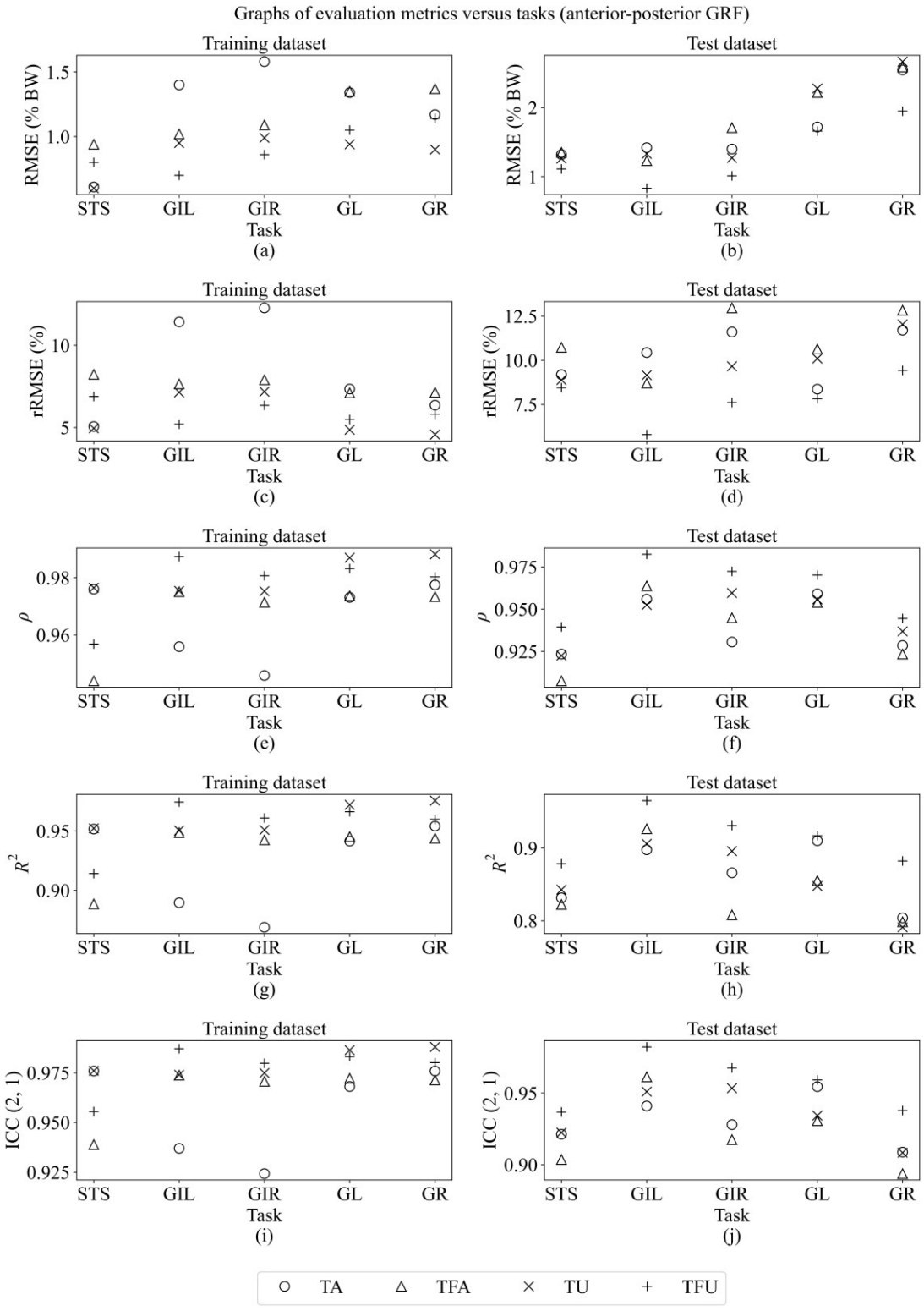


Figure 6. Graphs of RMSE, rRMSE, ρ, $R^2$, and ICC (2, 1) versus task in measuring anterior-posterior GRF. The tasks include sit-to-stand (STS), gait initialization with the left foot (GIL), gait initialization with the right foot (GIR), gait with the left foot stepping on a force plate (GL), and gait with the right foot stepping on a force plate (GR). The validation dataset was included in the training dataset.

https://doi.org/10.31436/iiumej.v26i1.3379

Figure 6 portrays the RMSE, rRMSE, ρ, R2, and ICC (2, 1) between the predicted and actual anterior-posterior GRF readings. According to the figure, the TFU model yielded the best results for the test dataset. The TFU model surpassed the TA, TFA, and TU models, achieving lower RMSE and rRMSE for anterior-posterior GRF in all tasks. The TFU model also attained the highest test dataset ρ, R2, and ICC (2, 1) for all tasks. According to the test dataset, the TFU model demonstrated excellent agreement (ICC > 0.9), good fitting (R2 > 0.8), and very strong linear correlation (ρ > 0.9) for all tasks in predicting anterior-posterior GRF.

According to Figure 7, the TFU model records the lowest RMSE and rRMSE in inferring the test dataset mediolateral GRF for all tasks, except the rRMSE obtained for sit-to-stand, where the TA model achieves the lowest value. Moreover, the TFU model obtained the highest values of ρ, R2, and ICC (2, 1) in the test dataset for all tasks. The TFU model demonstrated excellent agreement (ICC > 0.9), good fitting (R2 > 0.8), and very strong linear correlation (ρ > 0.9) in predicting the mediolateral GRF for gait initialization and gait with the right foot stepping on a force plate. A strong linear correlation ($0.7 < \rho \leq 0.9$) and moderate agreement ($0.5 < ICC \leq 0.75$) were also observed for the mediolateral GRF during sit-to-stand. In addition, the TFU model successfully predicted the mediolateral GRF during gait with the left foot stepping on a force plate, showing a strong linear correlation ($0.7 < \rho \leq 0.9$) and good agreement ($0.75 < ICC \leq 0.9$). The values of RMSE, rRMSE, ρ, R2, and ICC (2, 1) displayed in Figures 6 and 7 are listed in Supplementary File 1 in the form of tables.

Figure 8 presents examples of anterior-posterior GRF versus time graphs for sit-to-stand, gait initialization, and gait. The trial data for the graphs was randomly chosen from the test dataset. Each predicted curve fitting to the actual measurements was demonstrated with the $R^2$ values. The TFU model generated the highest $R^2$ values throughout all examined trials. Compared to other models, the TFU model fit more closely to the actual readings. The predicted measurements of the TFA model were obviously smoother than the actual equivalents. On the contrary, the prediction results of time domain models (TA and TU) suggested undesirable abrupt changes [see Figure 8(b) to 8(e)].

https://doi.org/10.31436/iiumej.v26i1.3379

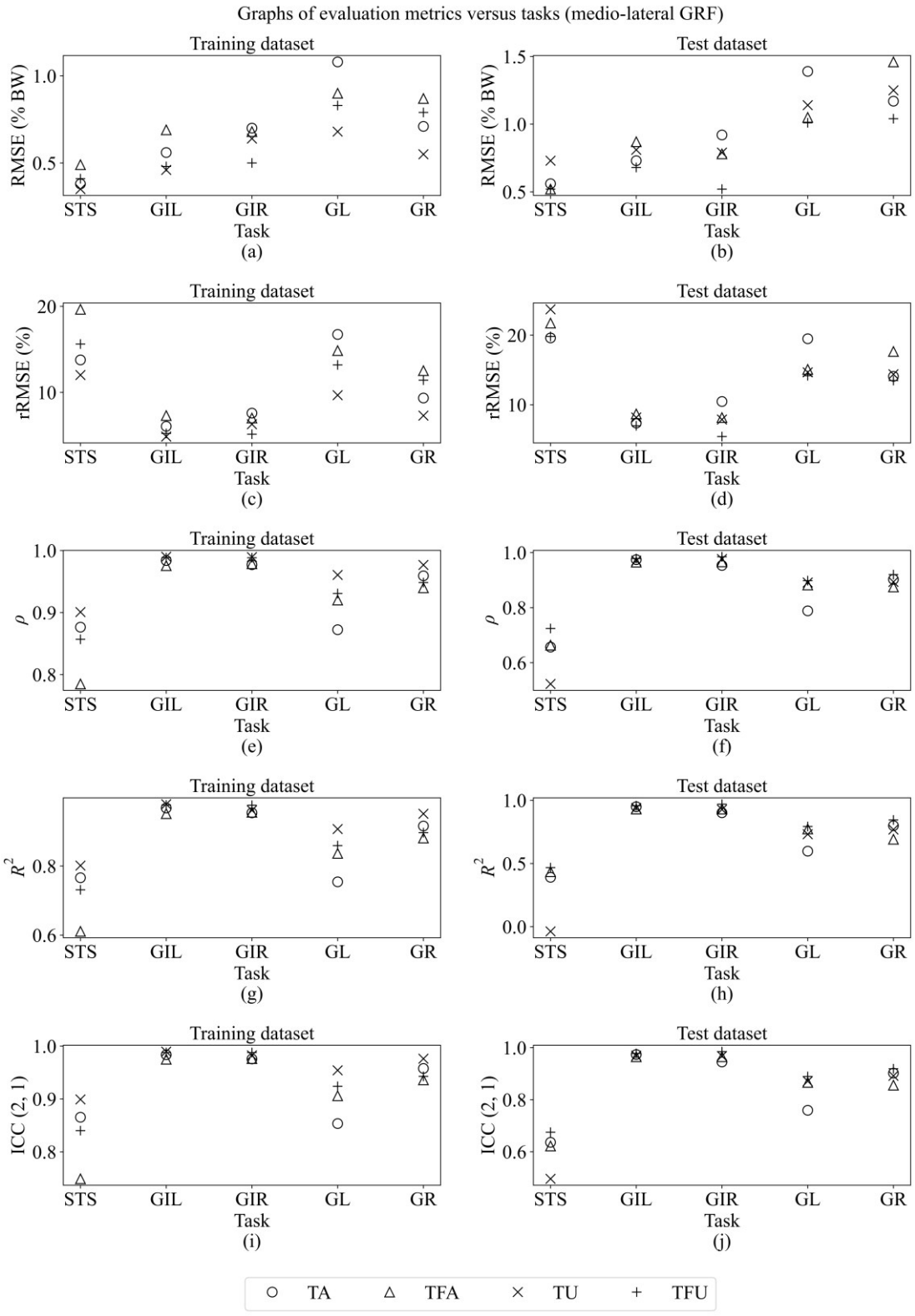


Figure 7. Graphs of RMSE, rRMSE, ρ, $R^2$, and ICC (2, 1) versus task in measuring mediolateral GRF. The tasks include sit-to-stand (STS), gait initialization with the left foot (GIL), gait initialization with the right foot (GIR), gait with the left foot stepping on a force plate (GL), and gait with the right foot stepping on a force plate (GR). The validation dataset was included in the training dataset.

https://doi.org/10.31436/iiumej.v26i1.3379

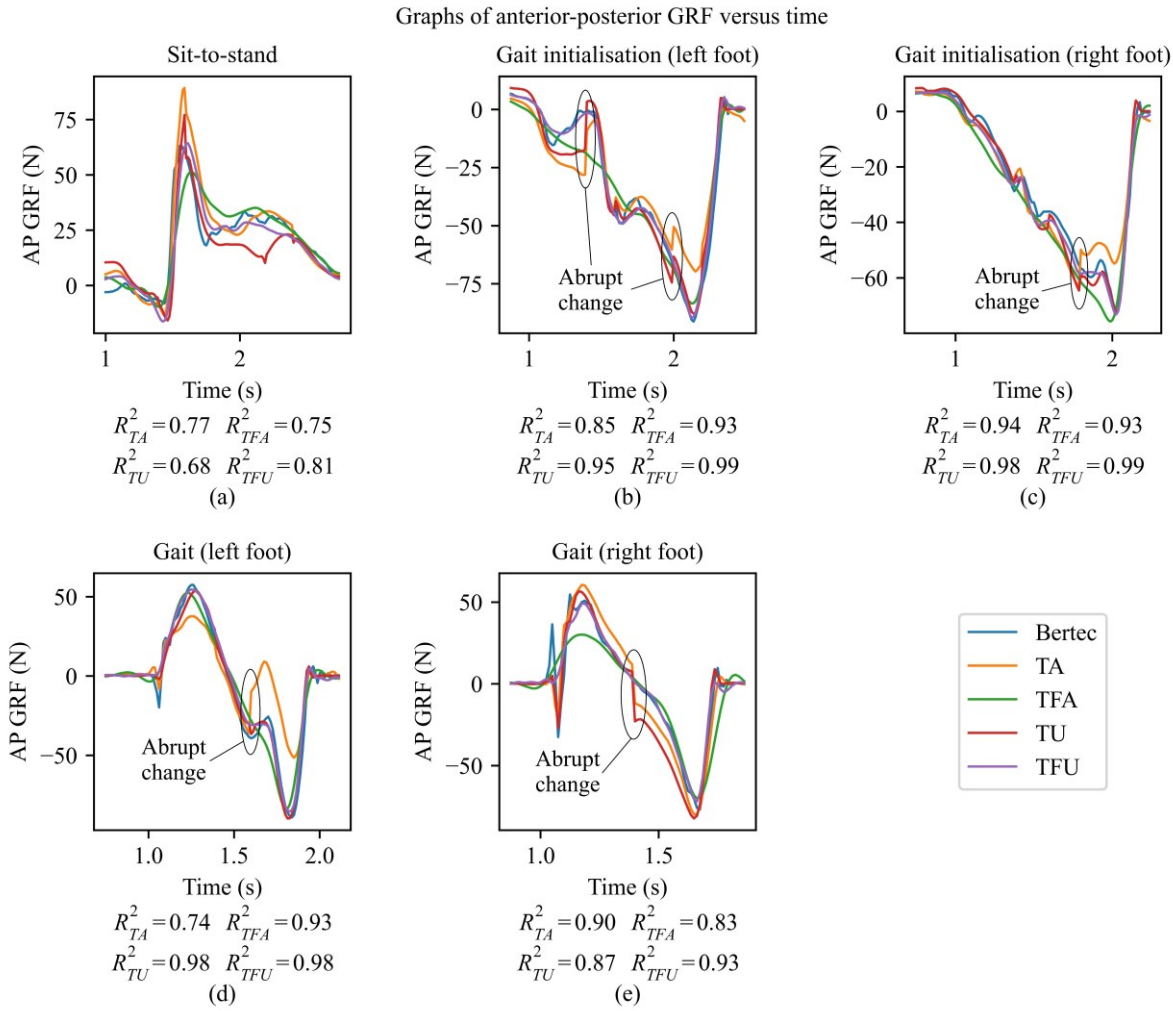


Figure 8. Graphs of anterior-posterior GRF versus time for various tasks. AP represents anterior-posterior.

The graphs of mediolateral GRF versus time plotted with randomly chosen trial data are shown in Figure 9. The TFU model achieved the highest R2 values for most of the selected trials, except in predicting the mediolateral GRF for gait where the right foot stepped on the force plate. Again, the TFA model-generated curves are the smoothest, while abrupt changes in TA and TU model readings can be observed based on Figures 9(b) and 9(d). The mediolateral GRF measured during sit-to-stand can barely be predicted by all the models based on Figure 9(a) and the corresponding R2 values.

https://doi.org/10.31436/iiumej.v26i1.3379

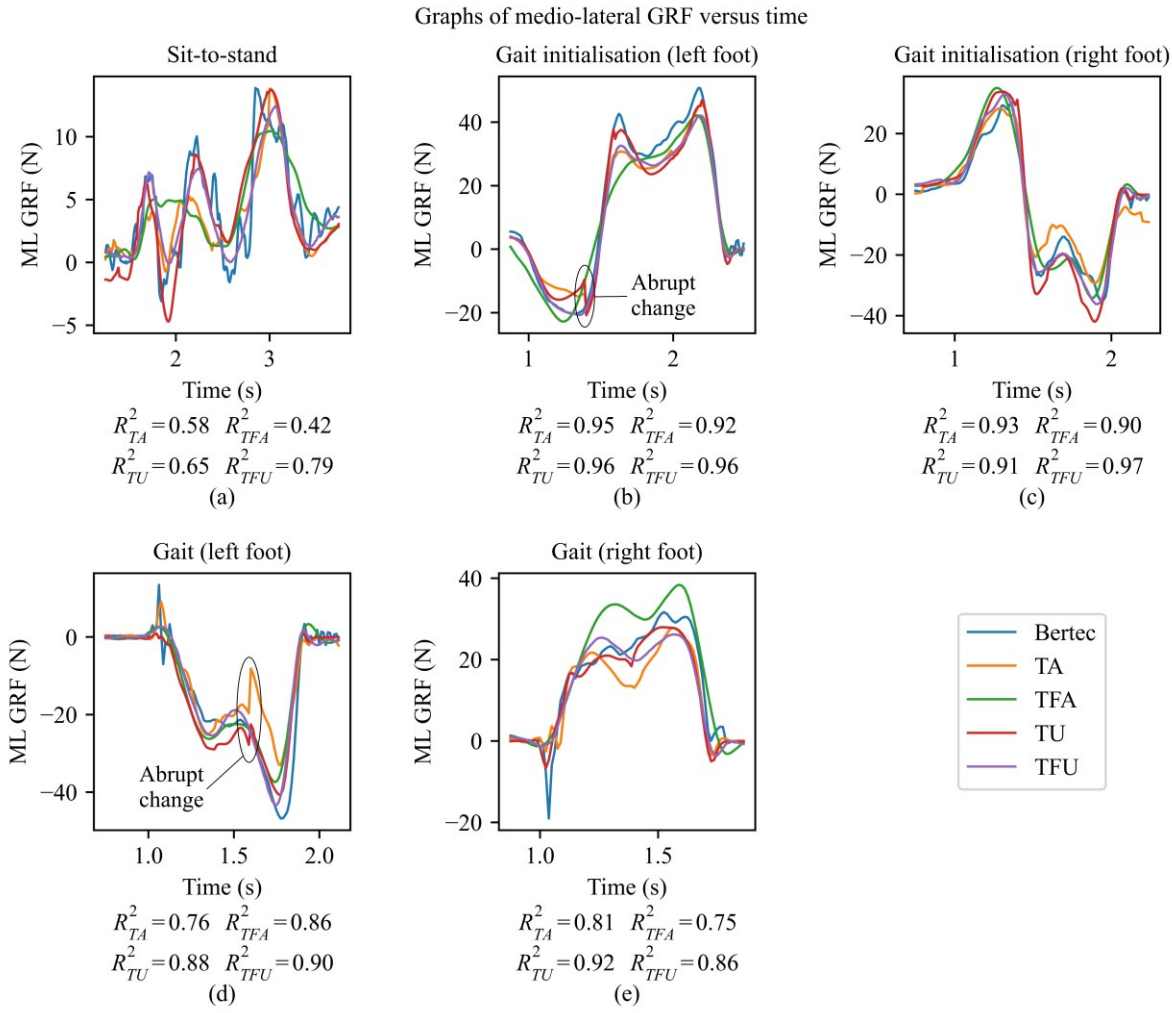


Figure 9. Graphs of mediolateral GRF versus time for various tasks. ML represents mediolateral.

## 4. DISCUSSION

Four deep learning models (TA, TFA, TU, and TFU) were developed in this study to predict the bilateral GRF from the vertical GRF measured using a cost-effective custom force plate. In Table 3, it was noted that inputs with the largest dimensions ($ntt$ and $nttf$) were selected to train the best models, suggesting that these models needed data from the majority of vertical GRF readings to predict the bilateral GRF accurately. This shows that the autoencoder bottleneck's sparsity helped extract features from the input to improve the output inference.

Figs. 6 and 7 highlight that the TFU model is the most accurate and demonstrates the most generalisability. Figs. 8 and 9 further indicated that, compared to other models, the prediction of the TFU model matched the actual readings to a closer extent. The absence of overshoot in TFU-predicted readings provided insight into the model architecture and hyperparameters applied, which helped mitigate overfitting through appropriate model complexity.

Compared to other tasks, the actual pattern of mediolateral GRF recorded during sit-to-stand was more amorphous. Thus, this observation explained the challenging prediction task for sit-to-stand movement. The satisfactory results indicated that the information extracted from four vertical GRF readings recorded using custom force plate load cells was insufficient

https://doi.org/10.31436/iiumej.v26i1.3379

to accurately predict the mediolateral GRF during sit-to-stand. A subject may produce multiple sit-to-stand vertical readings that are similar but exhibit inconsistent mediolateral GRF patterns due to minor variations in sit-to-stand movements. To enhance accuracy, prediction models may require additional sources of information, such as human body posture and kinematics.

The values predicted by the TFA were significantly smoother than the actual measurements, suggesting that the model could not capture the high-frequency components of the bilateral GRF. Conversely, the swift changes in outputs generated by the time-domain models (TA and TU) may have been due to distinct values at the boundaries of overlapping output that could not be smoothed out through the averaging process (refer to Section "Model deployment"). The absence of sudden changes in the time-frequency domain model, TFA, and TFU outputs may have been due to the extensive STFT sliding window overlap. The STFT sliding window size was 62, significantly larger than the number of strides of 16, resulting in a substantial overlap between consecutive sliding windows. This overlap prevented a decrease in reading magnitude at the window function's boundary, leading to smoother readings [42]. Reducing the undesirable quick changes in predicted readings allowed for a better fit between predicted and actual readings. This explained the accuracy improvement when STFT was applied.

Two explanations were proposed to justify the accurate prediction. The initial explanation (refer to Section 1) suggested that the model could have extracted features from the strain gauge elongation caused by off-axis bilateral GRF exertion to make the prediction. Secondly, prediction could possibly be conducted due to the consistent patterns of model inputs and outputs. The vertical GRF readings obtained by individual load cells of the custom force plate during various tasks followed several recognizable and consistent trends (see Figure 10). For example, the vertical GRF readings for sit-to-stand obtained by load cells began with a decrease, progressed through a peak and a local minimum, and finally ended with decreasing fluctuation. In contrast, the vertical GRF readings recorded during gait initialization started with fluctuation, followed by a peak, and a drop to zero. Clear patterns were observed in gait vertical GRF readings, with values increasing from zero to a peak and then decreasing back to zero at varying rates.

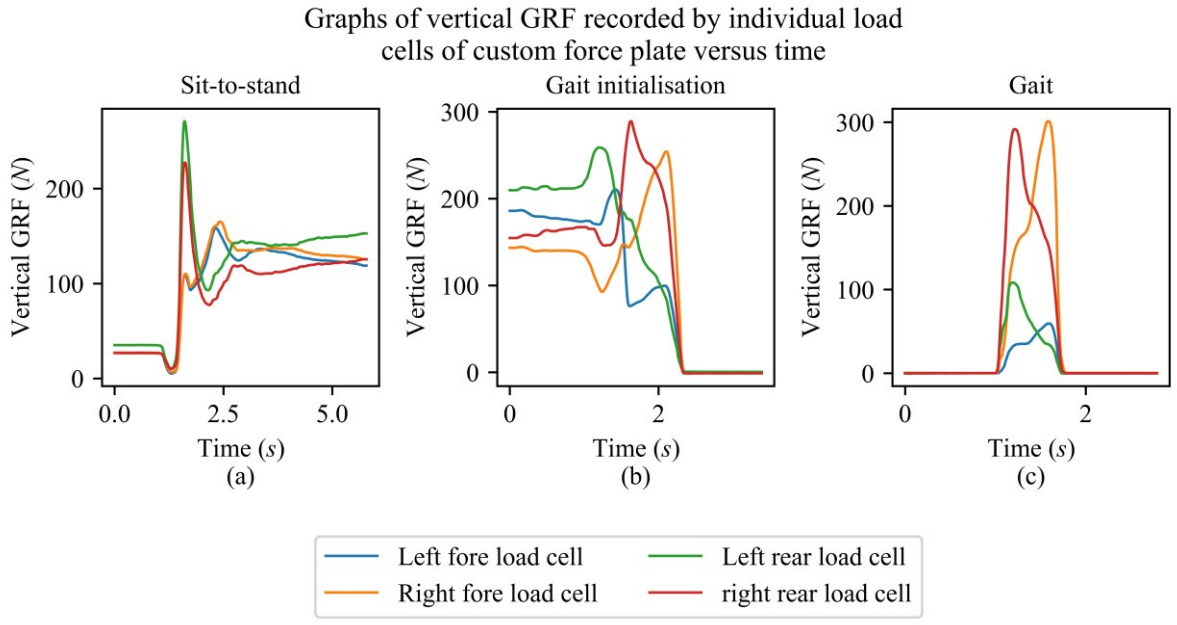


Figure 10. Graphs of vertical GRF recorded by individual load cells of custom force plate versus time for various tasks. The readings recorded exhibit perceivable patterns.

https://doi.org/10.31436/iiumej.v26i1.3379

On the other hand, the bilateral GRF recorded for most tasks also illustrated predictable patterns (see Figures 8 and 9). For instance, the anterior-posterior GRF measurements during gait initialization indicated a deep valley, showing the propulsive force exerted by the participant's feet as they moved forward. The anterior-posterior GRF during gait included a peak representing the peak braking force and a valley indicating the peak propulsive force. Distinct trends were noticeable in mediolateral GRF, particularly during gait initialization, where the readings started with a peak or valley, followed by an 'M' or 'W' pattern, depending on the foot used to start the gait. Thus, the model could have linked the input pattern to the corresponding output trend.

The findings of this study were compared with those of earlier studies. In previous studies, RMSE stated in the unit "N/kg" was transformed into % BW. Due to the limited information in previously published studies, the sit-to-stand findings were not compared. Only one previous study investigated the GRF prediction during gait initialization [1]. The RMSE of the anterior-posterior GRF (0.83–1.01 % BW) and mediolateral GRF (0.52–0.68 % BW) recorded in this study for gait initialization using the TFU model were lower than the previous study (1.63–2.96 % BW for anterior-posterior GRF and 1.73–1.94 % BW for mediolateral GRF) [1]. Consequently, the ρ values of gait initialization anterior-posterior GRF (0.97–0.98 versus 0.94–0.97) and mediolateral GRF (0.98 versus 0.84–0.90) values obtained in this study were greater than the earlier study [1]. Hence, the bilateral GRF prediction during gait initialization was improved in this work as compared to before.

Figure 11 reveals the comparison of the result for gait between this work and previous studies, in which the TFU model prediction results are concluded as follows when anterior-posterior GRF during gait is taken into consideration:

- Lower RMSE range than seven studies [1; 2; 4; 5; 9; 10; 29]
- Lower rRMSE range than three studies [5; 8; 29]
- Higher ρ range than the three studies [4; 5; 29]

https://doi.org/10.31436/iiumej.v26i1.3379

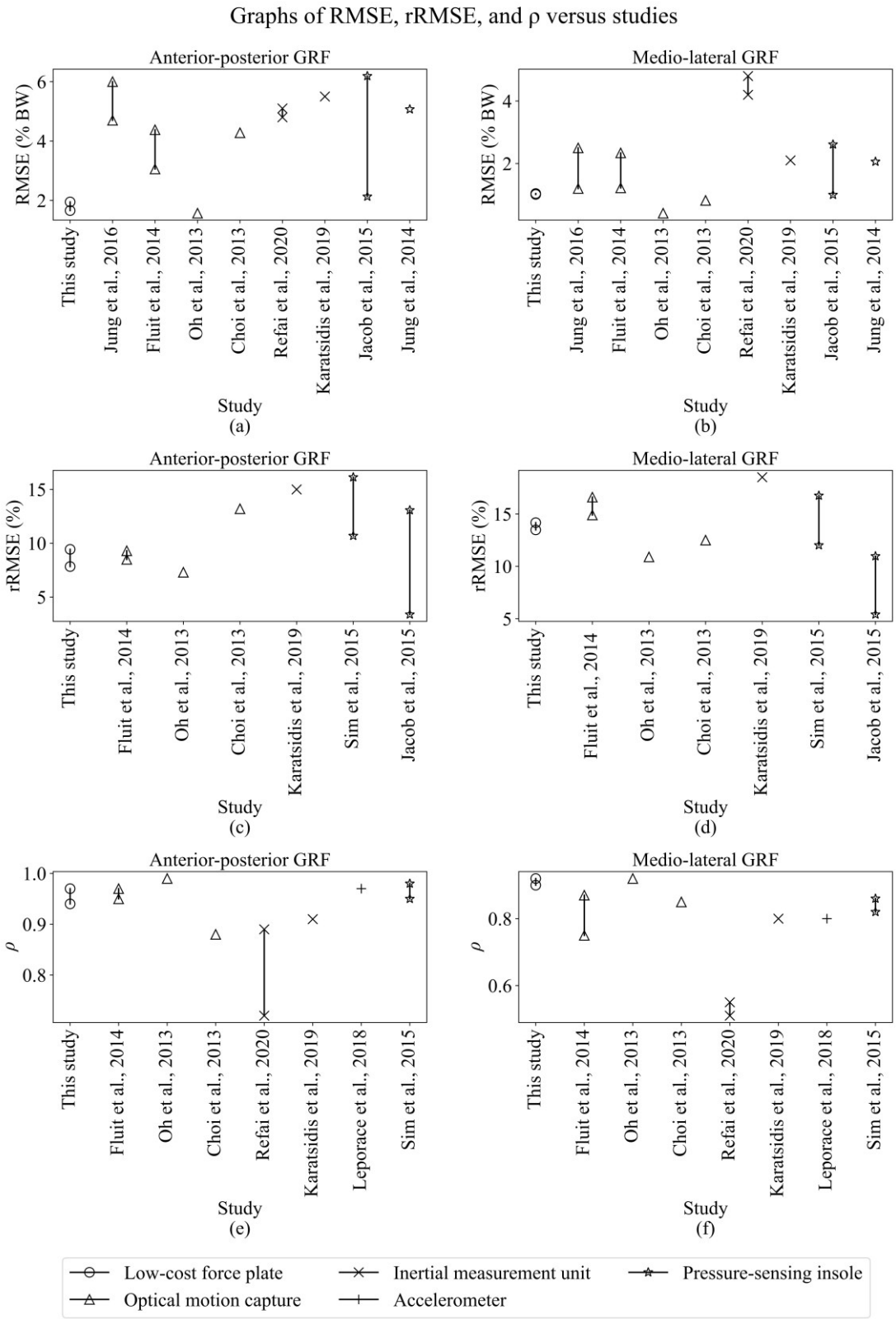


Figure 11. The RMSE, rRMSE, and ρ in this study and previous studies. The data investigates bilateral GRF prediction in gait. The results from this study are derived from the test dataset.

Furthermore, the mediolateral gait GRF results achieved in this study are observed to exhibit the following:

- Lower RMSE range than five studies [1; 2; 4; 5; 10]
- Lower rRMSE range than two studies [1; 5]
- Higher ρ range than six studies [1; 4-6; 8; 29]

Therefore, the comparison showed that the method in this study generated a relatively good prediction.

A larger dataset could be collected to improve the model performance and generalization in future work. By collecting more data from different individuals, the models could learn the various patterns of bilateral GRF that do not exist in the current dataset. This could potentially improve the prediction accuracy and generalization of data from different subjects, especially for the outputs that were challenging to infer, such as mediolateral GRF during sit-to-stand tasks. Furthermore, the larger dataset could include GRF recorded during other tasks, such as running and jumping. This enhanced the model's ability to generalize across a wider range of tasks, thereby improving its applicability in various research settings.

In dealing with noisy input, high-frequency noises, and outliers were suppressed with low-pass and medium filters, as highlighted in the Section "Data preprocessing." However, the application of external force on the subjects who performed tasks on the force plates could cause perturbation in GRF readings, which could not be reduced with low-pass and medium filters. In future studies, sensitivity analysis will be conducted to identify the effect of the noises due to the application of external forces. The model would be trained to generate the correct bilateral GRF readings under this condition.

## 5. CONCLUSION

The bilateral GRF predictions in this study were successfully implemented for sit-to-stand, gait initialization, and gait. The best model was determined to be the TFU model. Based on the test dataset readings for all tasks, apart from the mediolateral GRF readings for sit-to-stand, the model could generalize to a good extent with a high ICC (2, 1) of more than 0.88. The accuracy of the low-cost custom force plate and TFU model in bilateral GRF prediction was demonstrated to be comparable with and even higher than other previous alternatives. The results could encourage biomechanical studies even in budget-limited conditions by using a low-cost bilateral GRF sensing force plate. The proposed method could enhance the accuracy of force and torque acting on musculoskeletal models calculated during biomechanical analysis compared to any other low-cost force plate that cannot quantify bilateral GRF. Moreover, the bilateral GRF-based metrics used to assess health conditions may soon be obtained using a low-cost force plate.

## ACKNOWLEDGEMENT

This work was supported by Collaborative Research in Engineering, Science & Technology Center (CREST), School of Mechanical Engineering, Universiti Sains Malaysia, and SAS Institute Sdn. Bhd. under Grant 304.PMEKANIK.6050419.C121.

## REFERENCES

[1] Fluit, R., Andersen, M.S., Kolk, S., Verdonschot, N., Koopman, H.F. (2014). Prediction of ground reaction forces and moments during various activities of daily living. J Biomech, 47(10):2321-2329.10.1016/j.jbiomech.2014.04.030.

[2] Jung, Y., Jung, M., Ryu, J., Yoon, S., Park, S.K., Koo, S. (2016). Dynamically adjustable foot-ground contact model to estimate ground reaction force during walking and running. Gait Posture, 45:62-68.10.1016/j.gaitpost.2016.01.005.

[3] Oh, S.E., Choi, A., Mun, J.H. (2013). Prediction of ground reaction forces during gait based on kinematics and a neural network model. J Biomech, 46(14):2372-2380.10.1016/j.jbiomech.2013.07.036.

[4] Refai, M.I.M., Beijnum, B.J.F.v., Buurke, J.H., Veltink, P.H. (2020). Portable Gait Lab: Estimating 3D GRF Using a Pelvis IMU in a Foot IMU Defined Frame. IEEE Transactions on Neural Systems and Rehabilitation Engineering, 28(6):1308-1316.10.1109/TNSRE.2020.2984809.

[5] Karatsidis, A., Jung, M., Schepers, H.M., Bellusci, G., de Zee, M., Veltink, P.H., et al. (2019). Musculoskeletal model-based inverse dynamic analysis under ambulatory conditions using inertial motion capture. Med Eng Phys, 65:68-77.https://doi.org/10.1016/j.medengphy.2018.12.021.

[6] Leporace, G., Batista, L., Nadal, J. (2018). Prediction of 3D ground reaction forces during gait based on accelerometer data. Research on Biomedical Engineering, 34.10.1590/2446-4740.06817.

[7] Faber, G.S., Chang, C.C., Kingma, I., Dennerlein, J.T., van Dieën, J.H. (2016). Estimating 3D L5/S1 moments and ground reaction forces during trunk bending using a full-body ambulatory inertial motion capture system. J Biomech, 49(6):904-912.10.1016/j.jbiomech.2015.11.042.

[8] Sim, T., Kwon, H., Oh, S.E., Joo, S.B., Choi, A., Heo, H.M., et al. (2015). Predicting Complete Ground Reaction Forces and Moments During Gait With Insole Plantar Pressure Information Using a Wavelet Neural Network. J Biomech Eng, 137(9).10.1115/1.4030892.

[9] Jacobs, D.A., Ferris, D.P. (2015). Estimation of ground reaction forces and ankle moment with multiple, low-cost sensors. J Neuroeng Rehabil, 12:90.10.1186/s12984-015-0081-x.

[10] Jung, Y., Jung, M., Lee, K., Koo, S. (2014). Ground reaction force estimation using an insole-type pressure mat and joint kinematics during walking. J Biomech, 47(11):2693-2699.10.1016/j.jbiomech.2014.05.007.

[11] Abujaber, S., Gillispie, G., Marmon, A., Zeni, J., Jr. (2015). Validity of the Nintendo Wii Balance Board to assess weight bearing asymmetry during sit-to-stand and return-to-sit task. Gait Posture, 41(2):676-682.10.1016/j.gaitpost.2015.01.023.

[12] Yamako, G., Chosa, E., Totoribe, K., Fukao, Y., Deng, G. (2017). Quantification of the sit-to-stand movement for monitoring age-related motor deterioration using the Nintendo Wii Balance Board. PLoS One, 12(11):e0188165.10.1371/journal.pone.0188165.

[13] Arifin, W.N. (2018). A Web-based Sample Size Calculator for Reliability Studies. 10:67-76.10.21315/eimj2018.10.3.8.

[14] Onuma, R., Masuda, T., Hoshi, F., Matsuda, T., Sakai, T., Okawa, A., et al. (2021). Measurements of the centre of pressure of individual legs reveal new characteristics of reduced anticipatory postural adjustments during gait initiation in patients with post-stroke hemiplegia. J Rehabil Med, 53(7):jrm00211.10.2340/16501977-2856.

[15] Eltoukhy, M., Kuenze, C., Andersen, M.S., Oh, J., Signorile, J. (2017). Prediction of ground reaction forces for Parkinson's disease patients using a kinect-driven musculoskeletal gait analysis model. Med Eng Phys, 50:75-82.10.1016/j.medengphy.2017.10.004.

[16] Izhar, C., Zakaria, H., Maruzuki, M., Sulaiman, M., Rahim, A. (2021). Gait cycle prediction model based on gait kinematic using machine learning technique for assistive rehabilitation device. IAES International Journal of Artificial Intelligence (IJ-AI), 10:752.10.11591/ijai.v10.i3.pp752-763.

[17] Vittinghoff, E., McCulloch, C.E. (2007). Relaxing the rule of ten events per variable in logistic and Cox regression. Am J Epidemiol, 165(6):710-718.10.1093/aje/kwk052.

[18] Bank, D., Koenigstein, N., Giryes, R. (2020). Autoencoders. arXiv preprint arXiv:2003.05991.

[19] Ronneberger, O., Fischer, P., Brox, T. (2015). U-Net: Convolutional Networks for Biomedical Image Segmentation. In Proceedings of Medical Image Computing and Computer-Assisted Intervention – MICCAI 2015: 5-9 October 2015;Cham; pp 234-241.

[20] Yu, S., Príncipe, J.C. (2019). Understanding autoencoders with information theoretic concepts. Neural Networks, 117:104-123.https://doi.org/10.1016/j.neunet.2019.05.003.

[21] Gu, J., Wang, Z., Kuen, J., Ma, L., Shahroudy, A., Shuai, B., et al. (2018). Recent advances in convolutional neural networks. Pattern Recognition, 77:354-377.https://doi.org/10.1016/j.patcog.2017.10.013.

[22] Lee, M. (2023). Mathematical Analysis and Performance Evaluation of the GELU Activation Function in Deep Learning. Journal of Mathematics, 2023(1):4229924.https://doi.org/10.1155/2023/4229924.

[23] Mu, R., Zeng, X. (2019). A Review of Deep Learning Research. KSII Trans. Internet Inf. Syst., 13:1738-1764.

[24] Sun, N., Li, H. (2019). Super Resolution Reconstruction of Images Based on Interpolation and Full Convolutional Neural Network and Application in Medical Fields. IEEE Access, 7:186470-186479.10.1109/ACCESS.2019.2960828.

[25] Goodfellow, I., Yoshua, B., Courville, A. (2016). Capacity, overfitting and underfitting. In Deep Learning. MIT press; pp. 108 - 114.

[26] Zeghidour, N., Luebs, A., Omran, A., Skoglund, J., Tagliasacchi, M. (2021). Soundstream: An end-to-end neural audio codec. IEEE/ACM Transactions on Audio, Speech, and Language Processing, 30:495-507.

[27] Kristoffersen, M., Møller, M., Martinez Nuevo, P., Ostergaard, J. (2021). Deep Sound Field Reconstruction in Real Rooms: Introducing the ISOBEL Sound Field Dataset. ArXiv, abs/2102.06455.https://arxiv.org/abs/2102.06455.

[28] Li, Y., Tagliasacchi, M., Rybakov, O., Ungureanu, V., Roblek, D. (2021). Real-time speech frequency bandwidth extension. In Proceedings of ICASSP 2021-2021 IEEE International Conference on Acoustics, Speech and Signal Processing (ICASSP): 6-11 June 2021; pp 691-695.

[29] Choi, A., Lee, J.-M., Mun, J.H. (2013). Ground reaction forces predicted by using artificial neural network during asymmetric movements. International Journal of Precision Engineering and Manufacturing, 14(3):475-483.10.1007/s12541-013-0064-4.

[30] Orvieto, A., Smith, S.L., Gu, A., Fernando, A., Gulcehre, C., Pascanu, R., et al., (2023). Resurrecting Recurrent Neural Networks for Long Sequences, in: Andreas, K., Emma, B., Kyunghyun, C., Barbara, E., Sivan, S., Jonathan, S. (Eds.), Proceedings of the 40th International Conference on Machine Learning. PMLR, Proceedings of Machine Learning Research, pp. 26670--26698.

[31] Kandel, I., Castelli, M. (2020). The effect of batch size on the generalizability of the convolutional neural networks on a histopathology dataset. ICT Express, 6(4):312-315.https://doi.org/10.1016/j.icte.2020.04.010.

[32] Yang, L., Shami, A. (2020). On hyperparameter optimization of machine learning algorithms: Theory and practice. Neurocomputing, 415:295-316.https://doi.org/10.1016/j.neucom.2020.07.061.

[33] Nogales, A., Caracuel-Cayuela, J., García-Tejedor, Á.J., (2024). Analyzing the Influence of Diverse Background Noises on Voice Transmission: A Deep Learning Approach to Noise Suppression, Applied Sciences.

[34] Snoek, J., Larochelle, H., Adams, R.P. (2012). Practical bayesian optimization of machine learning algorithms. Advances in neural information processing systems, 25.

[35] Goodfellow, I., Yoshua, B., Courville, A. (2016). Early stopping. In Deep Learning. MIT press; pp. 241 - 249.

[36] Magar, I., Schwartz, R. (2022). Data Contamination: From Memorization to Exploitation. ArXiv, abs/2203.08242.

[37] Ren, L., Jones, R.K., Howard, D. (2008). Whole body inverse dynamics over a complete gait cycle based only on measured kinematics. J Biomech, 41(12):2750-2759.https://doi.org/10.1016/j.jbiomech.2008.06.001.

[38] Šverko, Z., Vrankić, M., Vlahinić, S., Rogelj, P., (2022). Complex Pearson Correlation Coefficient for EEG Connectivity Analysis, Sensors.

[39] Learner, J., Goodman, N.W. (1996). Descriptions of correlation. Lancet, 348(9021):199-200.10.1016/s0140-6736(05)66149-1.

[40] Chicco, D., Warrens, M.J., Jurman, G. (2021). The coefficient of determination R-squared is more informative than SMAPE, MAE, MAPE, MSE and RMSE in regression analysis evaluation. PeerJ Comput Sci, 7:e623.10.7717/peerj-cs.623.

[41] Koo, T.K., Li, M.Y. (2016). A Guideline of Selecting and Reporting Intraclass Correlation Coefficients for Reliability Research. J Chiropr Med, 15(2):155-163.10.1016/j.jcm.2016.02.012.

[42] Heinzel, G., Rüdiger, A.O., Schilling, R. (2002). Spectrum and spectral density estimation by the Discrete Fourier transform (DFT), including a comprehensive list of window functions and some new at-top windows.

https://doi.org/10.31436/iiumej.v26i1.3189

# FUZZY LOGIC-BASED ARRIVAL TIME ESTIMATION FOR INDOOR NAVIGATION USING AUGMENTED REALITY

**MUHAMMAD HIDAYAT MOHAMMED SOHIF, MUHAMMAD IMRAN MARDZUKI*, AZHAR MOHD IBRAHIM, AHMAD JAZLAN**

*Department of Mechatronics, International Islamic University Malaysia, Kuala Lumpur, Malaysia*

**Corresponding author: imran.mardzuki@live.iium.edu.my*

*(Received: 30 January 2024; Accepted: 19 March 2024; Published online: 10 January 2025)*

***ABSTRACT:*** In recent years, Augmented Reality (AR) has gained popularity in various industries due to its ability to enhance efficiency, provide real-time information and data, and maintain user awareness of their surroundings. One of the applications of AR is in navigation, but most existing systems primarily focus on outdoor environments, neglecting indoor spaces. Mobile applications designed for indoor navigation often rely on expensive and computationally demanding beacons or natural markers to track the user's location along a predetermined path. Furthermore, traditional navigation estimation methods based on GPS are ineffective for indoor navigation. This study proposes a mobile AR application for indoor navigation that uses an intelligent signage algorithm based on fuzzy logic to estimate arrival time. The algorithm takes phone acceleration in the x and z directions as inputs and employs triangular-shaped membership functions for input and output variables. The experimental results indicate the feasibility of using fuzzy logic to estimate arrival time for indoor navigation, with an average prediction error of 5.82%.

***ABSTRAK:*** Beberapa tahun ini, Realiti Terimbuh (AR) telah menjadi popular dalam pelbagai industri kerana keupayaannya meningkatkan kecekapan, menyediakan maklumat dan data secara masa nyata, dan mengekalkan kesedaran pengguna terhadap persekitaran sekeliling. Salah satu aplikasi AR adalah dalam navigasi, tetapi kebanyakan sistem sedia ada lebih menumpukan kepada persekitaran luar, mengabaikan ruang dalaman. Aplikasi mudah alih yang direka untuk navigasi dalaman sering bergantung pada bekon mahal dan memerlukan komputasi tinggi atau penanda semula jadi bagi menjejaki lokasi pengguna sepanjang laluan yang ditetapkan. Selain itu, kaedah anggaran navigasi tradisional berdasarkan GPS tidak berkesan bagi navigasi dalaman. Kajian ini mencadangkan aplikasi AR mudah alih bagi navigasi dalaman yang menggunakan algoritma papan tanda pintar berdasarkan logik kabur bagi menganggarkan masa ketibaan. Algoritma ini mengambil pecutan telefon dalam arah x dan z sebagai input dan menggunakan fungsi keahlian berbentuk segi tiga bagi pemboleh ubah masuk dan keluar. Dapatan eksperimen menunjukkan kebolehan menggunakan logik kabur bagi menganggarkan masa ketibaan bagi navigasi dalaman, dengan kesilapan anggaran purata sebanyak 5.82%.

***KEYWORDS:*** *Indoor Navigation, Path Planning, Estimated Time Arrival, Fuzzy Logic.*

## 1. INTRODUCTION

The purpose of a navigation system is to provide users with the necessary and relevant information to guide them to their desired destination while also tracking their location on pre-established maps. According to data from the Fire and Rescue Department of Malaysia, the Department of Statistics Malaysia has released statistics on fire incidents in Malaysia. The

https://doi.org/10.31436/iiumej.v26i1.3189

statistics revealed a significant increase in the number of deaths and injuries due to indoor fire outbreaks [1].

Various factors can contribute to a high number of deaths during a fire outbreak, such as inadequate signage, complex building layouts, and panicked crowds that can lead to stampedes. The high density of people in these situations often results in a significant number of injuries and fatalities due to difficulty in movement. This highlights the significance of a navigation system that can assist individuals by providing a safer route to their desired destination. In light of this, this research aims to propose a project that can help achieve this objective by identifying the most efficient route and estimating the arrival time at the targeted location. This will provide users with added reassurance, as they will better understand how long it will take them to reach their destination.

One of the most perilous aspects of evacuation is the potential for individuals to lose their bearings [2-3]. This is particularly true for those who are unfamiliar with the layout of a building, leading to prolonged escape times. Including a legend or map of the structure can aid in their navigation. However, during severe emergencies, such as earthquakes, fires, or smoke, natural disasters can obscure signs and paths, hindering and confounding evacuation directions.

Normally, the majority of the physical signage within indoor spaces has become worn and is not kept up to date, which can cause confusion among visitors and building occupants when trying to navigate the area. This is particularly the case when there is a need to quickly evacuate a building with a complex layout [4]. Therefore, there is a need to implement augmented reality indoor navigation in order to reduce the reliance on physical signage.

Several mobile applications have been created to assist individuals in navigating through buildings. Most of the indoor augmented reality navigation systems currently available utilize either beacons or natural markers to obtain and update the user's location along a predefined path. However, implementing this method often requires the installation of expensive beacon devices and can also be computationally demanding when using natural markers. Therefore, it would be beneficial to have an alternative that is more cost-effective and less taxing on mobile devices [5-9].

There are several methods for estimating arrival time for navigation purposes. However, many rely on GPS to determine the user's location, rendering them ineffective for indoor navigation [10]. Currently, limited research is being conducted on methods for estimating arrival time for indoor navigation. As a result, it is crucial to develop new methods for estimating arrival time for indoor navigation [11].

The main aim of this study is to create an augmented reality application that assists users in navigating indoor spaces. To achieve this, we introduced a Smart Augmented Reality application with embedded intelligent signage for the Kulliyyah of Engineering (KOE) indoor spaces. A significant focus of our work is on modeling an intelligent system to estimate the time required to reach the desired destination, with a particular emphasis on analyzing the prediction errors between the estimated and actual arrival times.

## 2. METHODOLOGY

In this research, we employ artificial markers in place of natural markers, as the latter necessitates a significant number of computational resources, which can lead to overheating of the device. To effectively integrate artificial markers into the environment, several factors must be considered. The marker should possess a unique image with a predefined visual pattern and dimensions, be easily identifiable based on its color or shape, and be of an appropriate size.

https://doi.org/10.31436/iiumej.v26i1.3189

Additionally, the marker should be visible in emergency situations. For the purpose of experimentation, we utilized QR codes as markers [12 - 13].

A single location will be selected to obtain test results for the simulation. The first floor of the E1 Kulliyyah of Engineering (KOE) building, International Islamic University Malaysia, has been chosen as it possesses an appropriate layout with appropriate movement flow and an adequate number of exit paths. The path from the Dean's Office to the Mechatronics Laboratory will be utilized for the simulation. Initially, the floor plan was obtained from the Technical Department of the Kulliyyah of Engineering. Next, the 3D floor plan was constructed using the Blender software, with the images of the floor plan serving as its foundation. It was then imported into Unity 3D in accordance with the real-world scale in meters, using the scale provided in the floor plan.

Figure 1. The original floor plan of E1 building level 1 KOE.

https://doi.org/10.31436/iiumej.v26i1.3189

Subsequently, objects must be created to represent the user and the target location in the environment. In this project, a blue sphere will be utilized to represent the user, and a green cube will be employed as the target location. Additionally, it is essential to create an empty game object to indicate the QR code in the environment. These objects must be positioned at the precise location on the map, where the blue sphere is located in front of the Dean's Office as the starting point, and the green cube is located in front of the Mechatronics Laboratory as the target destination.

For the QR code, it is not necessary to incorporate it into the Unity environment. However, the name of the empty game objects that represent the QR code must correspond to the name assigned to the physical QR code in order for it to match when decoding the QR code. It is also essential to ensure that the z-axis of the empty game object for the QR code always aligns with the phone's negative z-axis, as that is the direction the camera is facing.

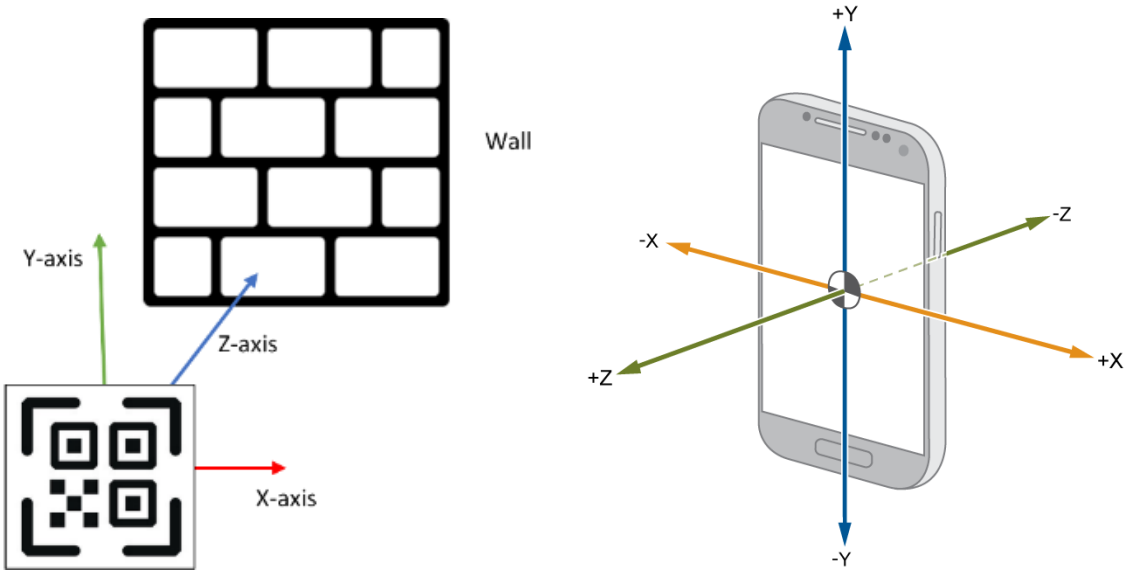


Figure 2. (a) Axis of QR code in Unity (b) Axis of mobile phone.

Unity 3D's Navigation Mesh is an inherent feature that aids developers in generating a pathfinding system within a complex environment for the simulation program. Also known as Navmesh, the Navigation Mesh facilitates the automatic programming of the agent to avoid collisions with surrounding objects. Navmesh is a two-dimensional polygon mesh that defines the area in which the selected agent can traverse. The agent is unable to walk or pass through the simulation outside of the Navmesh area.

The "bake" function will automatically generate a walkable surface for the agent, but the layer must be configured beforehand to distinguish which objects in the environment will be the surface and which will be obstacles. The bake function will result in a blue polygon that covers the surfaces that represent the walkable area. The Artificial Intelligence embedded within NavMesh will automatically compute the path to the target location utilizing the current position coordinates and target location coordinates.

In this research, we utilized an Artificial Intelligence algorithm [14] fuzzy logic to estimate the time of arrival (ETA) by utilizing acceleration as the input. Initially, we designed the membership function for the inputs and outputs. To design the membership function, it is necessary to determine the range of each membership, which can be achieved through experimentation. All experiments and simulations are conducted using a Xiaomi Mi 9T Pro Android phone, the specifications of which are detailed in Table 1.

https://doi.org/10.31436/iiumej.v26i1.3189

Table 1. Xiaomi MI 9T Pro specification

| CPU | RAM | OS | Battery |
|---|---|---|---|
| Qualcomm Snapdragon 855 | 8GB | Android 11, MIUI 12.5 | 4000mAh, Li-Po |

Based on the data, the fuzzy logic algorithm is designed to start by determining the universe of discourse and the range of each fuzzy set. Then, the Mamdani base fuzzy rule is constructed by observing the behavior of both accelerations with time. Mamdani fuzzy logic is suitable for complex problems requiring transparency and interpretability in decision-making, particularly when linguistic rules play a crucial role, and the relationships between inputs and outputs are not easily expressed mathematically or are subject to interpretation, distinguishing it from Takagi-Sugeno-Kang (TSK) and Adaptive Neuro-Fuzzy Inference System (ANFIS). Then, by referring to the fuzzy rules and membership function, we estimated the time of arrival after the fuzzification and defuzzification process.

The accuracy of fuzzy logic is determined by running field tests with five repetitions to get the average error by comparing estimated time with actual time using the same pathway. The next sections will go over the mathematical model of fuzzy logic, its theory and approach to navigation problems, and the experimental setup used in this project.

### 2.1. Mathematical Equations and Theory

In reference to the collected data, we will have the following membership function where the acceleration in the x and z directions are the inputs, while the estimated time of arrival is the output. The selection of acceleration in the x and z directions as inputs for the Mamdani fuzzy system, with estimated time as the output, is based on the understanding that acceleration data in different directions can provide comprehensive information about the movement dynamics, which in turn can be effectively utilized to estimate the time required to reach a destination accurately, as shown in Fig. 3.

Then, by observing the relationship of the data with reference to the membership function, the following rule has been developed, as shown in Table 2.

Table 2. Fuzzy Rule

| | | **Acceleration at Z-axis** | | |
|---|---|---|---|---|
| | | **Slow** | **Normal** | **Fast** |
| **Acceleration at X-axis** | **Slow** | Slow | Normal | Normal |
| | **Normal** | Normal | Normal | Normal |
| | **Fast** | Normal | Normal | Fast |

https://doi.org/10.31436/iiumej.v26i1.3189

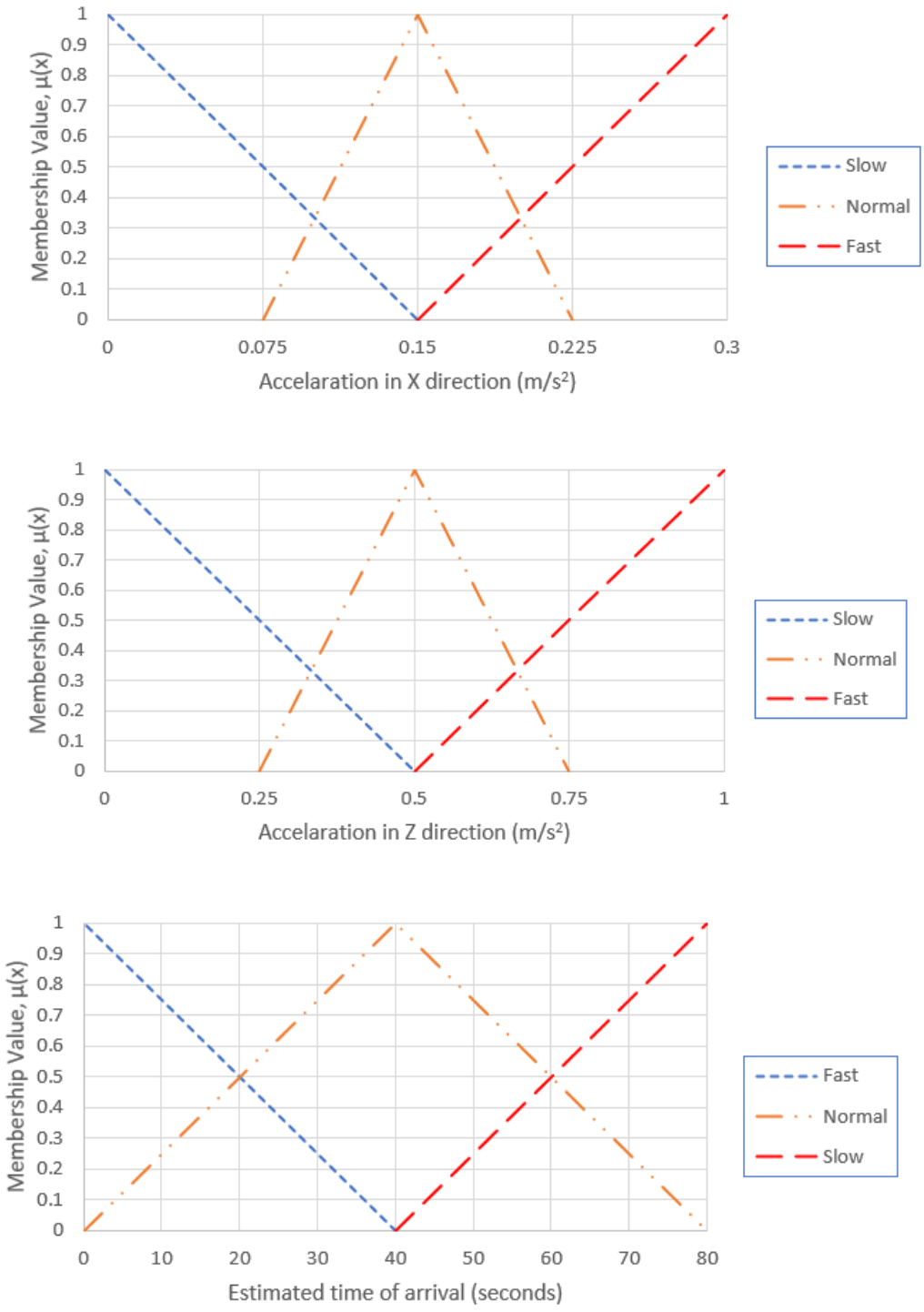


Figure 3. The membership function for the input and the output of the system.

According to the Mamdani Rule Base, the Fuzzy rule can be read as "If condition A AND condition B, then outcome C." Therefore, we can find the compound value of the membership by finding the minimum value between both conditions. However, the conditions of Normal are overlapping with multiple compound values. This situation can be represented by the OR operator, which can be defined as the maximum value among them in fuzzy logic. The membership value for the triangular function can be calculated using Eq. (1).

https://doi.org/10.31436/iiumej.v26i1.3189

$$\mu_A(x) = \begin{cases} 0 & x \leq a \\ \frac{x-a}{b-a} & a \leq x \leq b \\ \frac{c-x}{c-b} & b \leq x \leq c \\ 0 & x \geq c \end{cases} \quad (1)$$

where $a$ is the lower value, $b$ is the medium value, and $c$ is the higher value with the constraint of $a \leq b \leq c$, while $x$ refers to the current crisp input or output. For the fuzzy inference system, the equation for combining fuzzy propositions according to a fuzzy rule is as follows:

$$\mu_{C1} = \min(\mu_{A1}, \mu_{B1}) \quad (2)$$

$$\mu_C = \max(\mu_{C1}, \mu_{C2}) \quad (3)$$

Eq. (2) is for rule evaluation, where the $\mu_{A1}$ and $\mu_{B1}$ are the membership functions for condition A and condition B for rule 1 and $\mu_{C1}$ and $\mu_{C2}$ are the outcome C for rule 1 and rule 2. Eq. (3) is for aggregation, where $\mu_C$ is the overall fuzzified output as the output from the aggregation method.

The final crisp value can be found using Eq. (4), the Centre of Sum (CoS), by finding the value of each area and center of the area for each fuzzy set, where $x_i$ is the center of the area and $A_i$ is the area of the fuzzy set.

$$x^* = \frac{\sum_{i=1}^{n} x_i A_i}{\sum_{i=1}^{n} A_i} \quad (4)$$

The architecture of the fuzzy Mamdani for the system is shown in Figure 4.

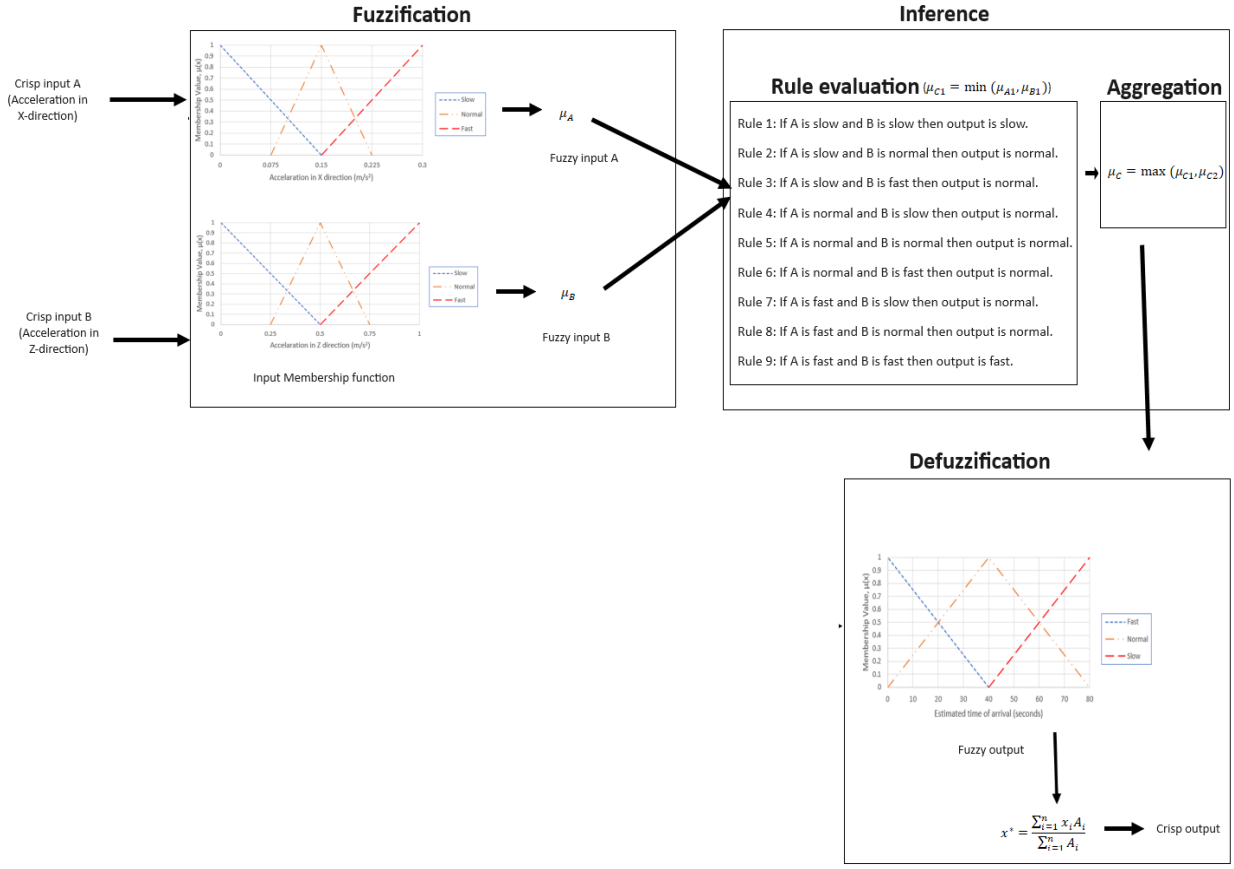


Figure 4. Architecture of fuzzy Mamdani system.

https://doi.org/10.31436/iiumej.v26i1.3189

### 2.2. Field Test Setup

The first assumption made in the test is that the value of acceleration in the z-direction is always positive as the user moves forward. Initially, the value will always be negative since the pointing direction of the camera is at the negative z-axis. However, since we are moving forward, we will assume it as a positive value. The second assumption is that the acceleration in the y direction does not affect the estimated time of arrival since we are not moving to different floor levels.

The field test is conducted using the same path which is from point A (Dean's Office) to point B (Mechatronics Lab). The time to walk from point A to point B will be recorded as the actual value, while the estimated arrival time is recorded every 2 seconds. Since people usually will not walk with constant acceleration, fluctuating output is expected.

Figure 5. The pathway from point A to point B.

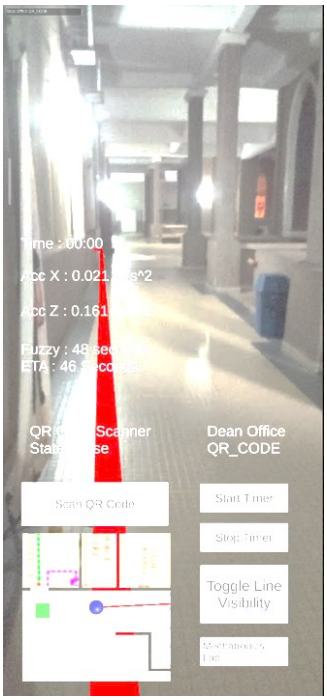


Figure 6. The application interface during a field test.

https://doi.org/10.31436/iiumej.v26i1.3189

## 3. RESULTS

The performance of the fuzzy logic from the test is evaluated and plotted for the results. The evaluation is mainly on the difference in time required to reach the goal within the estimated time. Figures 7 to 11 contain all the data for the first test and the fifth test. Based on the recorded data, fluctuations in the crisp value could be observed as we were not walking at a constant acceleration. The ETA should have decreased as time passed. However, the output from fuzzy logic does not reflect this behavior as it only predicts the time taken to travel from point A to point B. To ensure that the ETA decreased with time, certain conditions were established, as follows:

1. The starting ETA value will be the same as the crisp value.
2. If the difference between the crisp value and the previous ETA is between 0 and 3 seconds, the new ETA is the difference between the crisp value and the current time.
3. If the difference between the crisp value and the previous ETA is more than 3 seconds, the new ETA is the difference between the previous value and the current time.

For each set of results from Figure 7 to Figure 11, there are three graphs denoted as (a), (b), and (c). In subgraph (a), which displays the acceleration in the $x$ and $z$ directions over time, the movement is depicted in terms of the decomposed acceleration from the actual magnitude into the x and z directions recorded over time. In subgraph (b), which shows the fuzzy logic output over time, the estimated arrival time from the starting point to the goal is indicated over time. Even when in motion and not at the starting point, the fuzzy output will display the estimated arrival time from the starting point. Lastly, in subgraph (c), which presents the estimated time of arrival over time based on real-time data, the estimated time is derived from the current location rather than from the starting point.

The percentage error for each test and the average error are tabulated in Table 3. The error is calculated using Eq. (5), with the experimental value being the estimated time obtained from the fuzzy logic model and the actual value being the duration derived from real-time movement tracking.

$$\%Error = \left|\frac{Experimental\ value - Actual\ value}{Actual\ value}\right| \quad (5)$$

https://doi.org/10.31436/iiumej.v26i1.3189

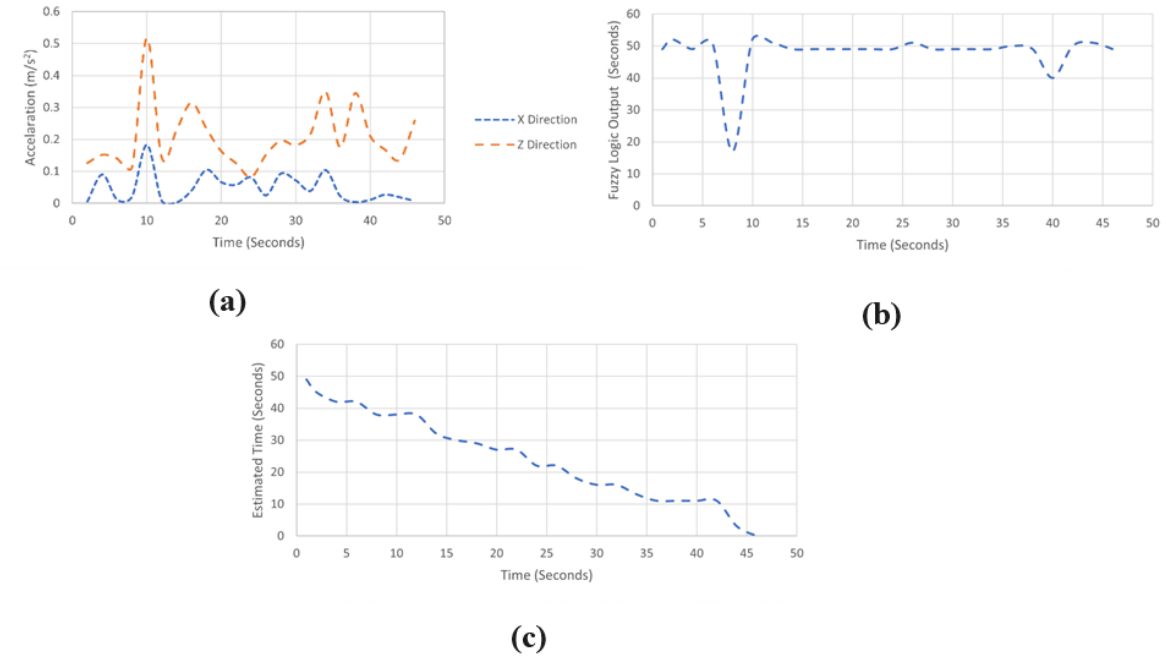


Figure 7. The result of the first test for (a) acceleration in x and z direction over time. (b) fuzzy logic output over time. (c) estimated time over time.

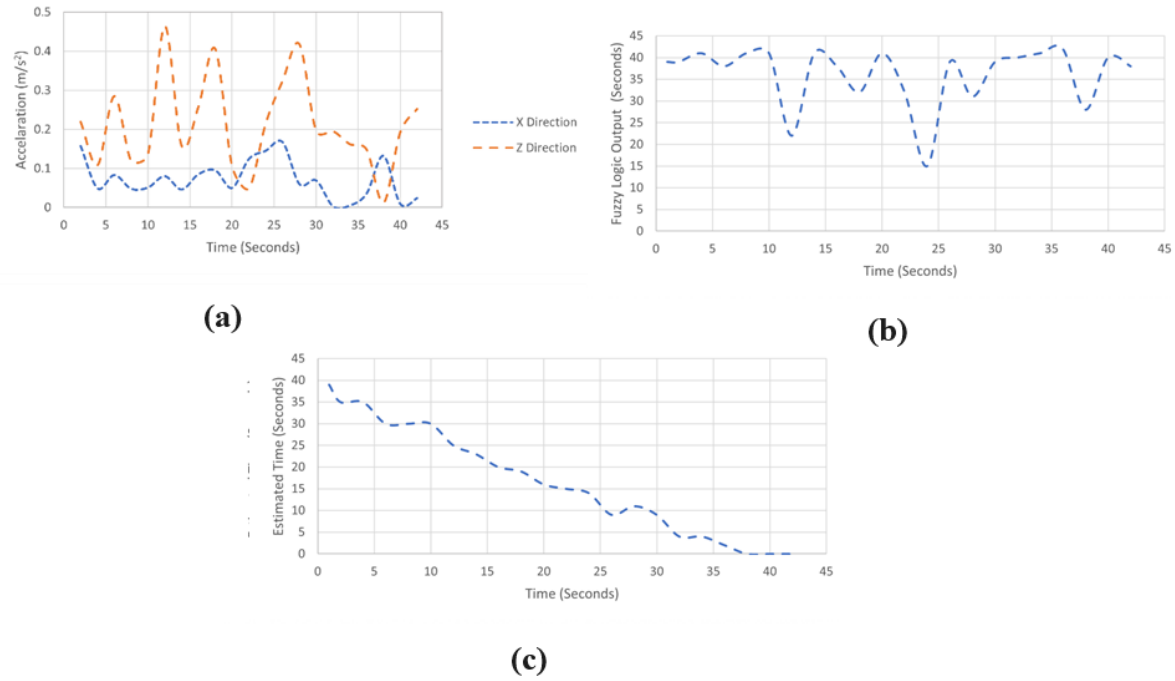


Figure 8. The result of the second test for (a) acceleration in x and z direction over time. (b) fuzzy logic output over time. (c) estimated time over time.

https://doi.org/10.31436/iiumej.v26i1.3189

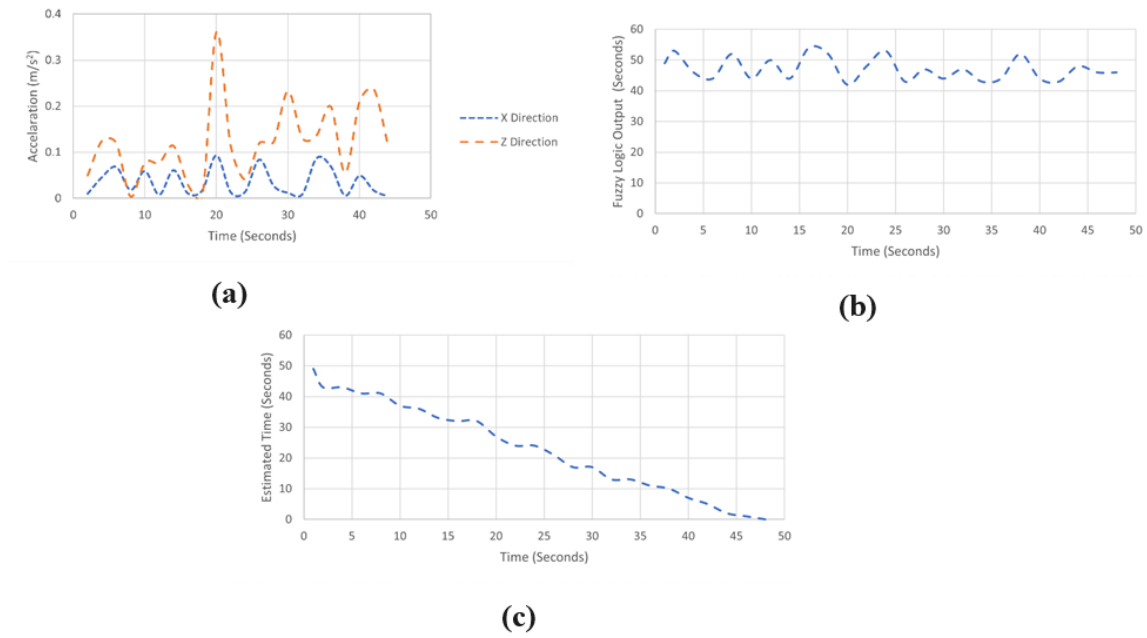


Figure 9. The result of the third test for (a) acceleration in x and z direction over time. (b) fuzzy logic output over time. (c) estimated time over time.

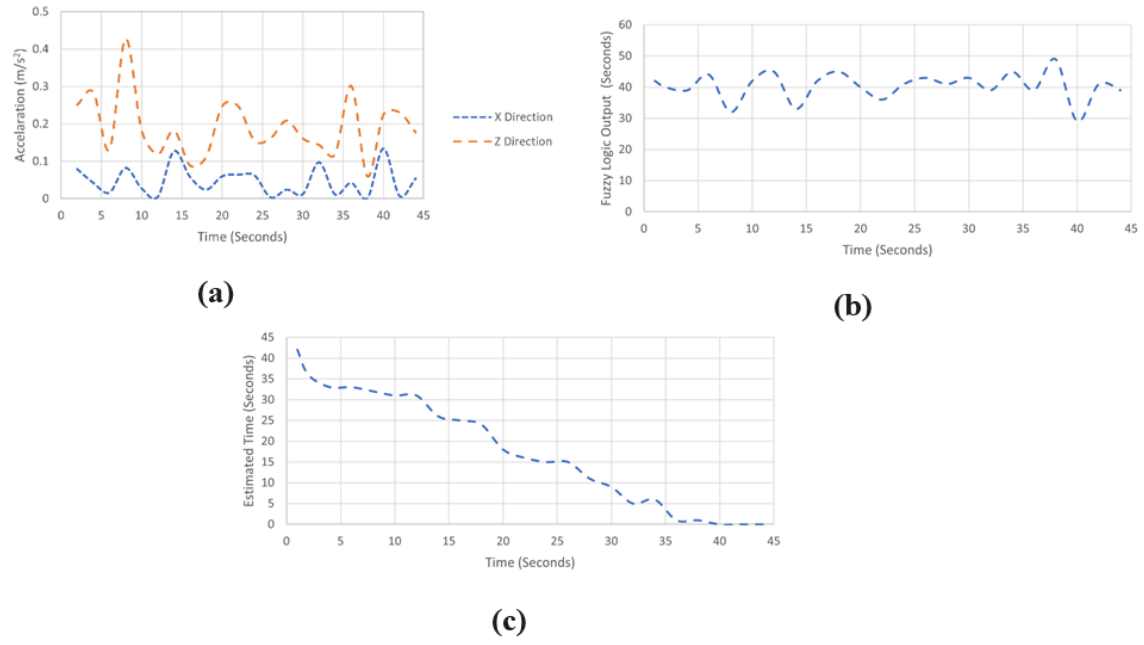


Figure 10. The result of the fourth test for (a) acceleration in x and z direction over time. (b) fuzzy logic output over time. (c) estimated time over time.

https://doi.org/10.31436/iiumej.v26i1.3189

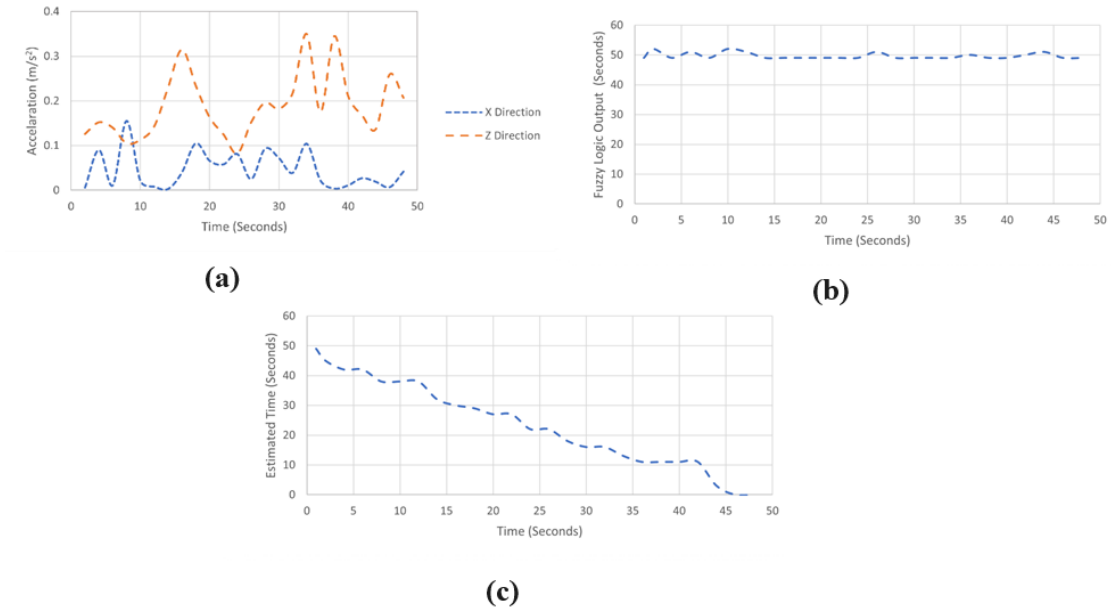


Figure 11. The result of the fifth test for (a) acceleration in x and z direction over time. (b) fuzzy logic output over time. (c) estimated time over time.

Table 3. Calculated percentage of error

| Test | Estimated Time(s) | Actual Time(s) | % Error |
|---|---|---|---|
| 1 | 49 | 46 | 6.25 |
| 2 | 39 | 42 | 7.14 |
| 3 | 40 | 44 | 9.09 |
| 4 | 42 | 44 | 4.55 |
| 5 | 49 | 48 | 2.08 |
| | | *Average Error* | **5.82** |

## 4. DISCUSSION

Based on the results, it is evident that the average error remains at 5.82%, comfortably below the designated maximum threshold of 10%. For accurate estimations in varied locations, constructing diverse membership functions may be imperative to meet specific conditions. Nevertheless, this limitation could be mitigated by integrating fuzzy logic with a neural network, forming a neuro-fuzzy system capable of learning, thereby refining estimations and reducing errors. However, it is important to note that data collection is necessary for training the system. Additionally, potential variation in error arises when different phone models with distinct specifications are employed. Moreover, while using identical phone models, discrepancies may occur due to variations in acceleration readings, particularly if the phone utilized was defective before the experiment commenced. Furthermore, the accuracy of the fuzzy rules may be compromised as the data collection process relies on manual recording, introducing the possibility of human error during data acquisition. While the study demonstrates promising results in arrival time estimation, acknowledging and addressing these limitations is imperative for enhancing the robustness and reliability of the proposed approach in real-world applications.

## 5. CONCLUSION

In conclusion, the use of intelligent signage in intelligent augmented reality applications has shown promising results in certain cases, highlighting the effectiveness of this approach. Given its use of augmented reality technology to enhance navigation, this method could serve as a viable option for security-related projects. Nonetheless, as the study progresses, researchers may identify some limitations and drawbacks to this approach. The current research mainly used ARCore, which has broader compatibility with different phone models. However, Unity, the platform used for the study, only offers two AR platforms, ARCore and Vuforia, and not all phones are compatible with these platforms, which can make experimentation more challenging. Consequently, this paper offers opportunities for future research. In conclusion, while the study demonstrates promising results in arrival time estimation, acknowledging and addressing these limitations is imperative for enhancing the robustness and reliability of the proposed approach in real-world applications.

## ACKNOWLEDGEMENT

This research is supported by the FRGS 2023 Grant: FRGS/1/2023/TK02/UIAM/02/1 awarded by the Ministry of Education Malaysia and also by International Islamic University Malaysia under the KOE Engineering Merit Scholarships 2023 (KOEiems2023).

## REFERENCES

[1] Fire and Rescue Department. (2020). Statistics On Fire Breakouts, *Statistics On Fire* Breakouts, Malaysia - Dataset - MAMPU. Department of Statistics Malaysia. Retrieved from https://www.data.gov.my/data/en_US/dataset/statistics-on-fire-breakouts-malaysia .

[2] Bahamid, A., Ibrahim, A. M., Ibrahim, A., Zahurin, I. Z., & Wahid, A. N. (2020, December). Intelligent robot-assisted evacuation: A review. In Journal of Physics: Conference Series (Vol. 1706, No. 1, p. 012159). IOP Publishing.

[3] Abir, I. M., Ibrahim, A. M., Toha, S. F., & Shafie, A. A. (2022). A review on the hospital evacuation simulation models. International Journal of Disaster Risk Reduction, 103083

[4] Ibrahim, A. M., Saifullah, M., Romlay, M. R. M., Venkat, I., & Ibrahim, I. (2019, October). Hybrid Social Force-Fuzzy Logic Evacuation Simulation Model For Multiple Exits. In 2019 7th International Conference on Mechatronics Engineering (ICOM) (pp. 1-5). IEEE

[5] Craig, A. B. (2013). Understanding augmented reality: Concepts and applications.

[6] De Oliveira, L. C., Andrade, A. O., De Oliveira, E. C., Soares, A., Cardoso, A., & Lamounier, E. (2017). Indoor navigation with mobile augmented reality and beacon technology for wheelchair users. 2017 IEEE EMBS International Conference on Biomedical and Health Informatics, BHI 2017, 37–40. https://doi.org/10.1109/BHI.2017.7897199

[7] Huang, B. C., Hsu, J., Chu, E. T. H., & Wu, H. M. (2020). Arbin: Augmented reality-based indoor navigation system. Sensors (Switzerland), 20(20), 1–20. https://doi.org/10.3390/s20205890

[8] Matuszka, T., Gombos, G., & Kiss, A. (2013). A new approach for indoor navigation using semantic web technologies and augmented reality. Lecture Notes in Computer Science (Including Subseries Lecture Notes in Artificial Intelligence and Lecture Notes in Bioinformatics), 8021 LNCS(PART 1), 202–210. https://doi.org/10.1007/978-3-642-39405-8_24

[9] Lo Valvo, A., Croce, D., Garlisi, D., Giuliano, F., Giarré, L., & Tinnirello, I. (2021). A Navigation and Augmented Reality System for Visually Impaired People. Sensors (Basel, Switzerland), 21(9), 1–15. https://doi.org/10.3390/s21093061

[10] Md Noor, R., Seong Yik, N., Kolandaisamy, R., Ahmedy, I., Hossain, M. A., Lim, K.-, Yau, A., Shah, W. M., & Nandy, T. (2020). Predict Arrival Time By Using Machine Learning Algorithm

To Promote Utilization of Urban Smart Bus. February. https://doi.org/10.20944/preprints202002.0197.v1

[11] Liu, Z., Chen, L., Zhou, X., Jiao, Z., Guo, G., & Chen, R. (2023). Machine Learning for Time-of-Arrival Estimation with 5G Signals in Indoor Positioning. 14(8). https://doi.org/10.1109/JIOT.2023.3234123

[12] Bhorkar, G. (2017). A Survey of Augmented Reality Navigation. Retrieved from http://arxiv.org/abs/1708.05006

[13] Koch, C., Neges, M., König, M., & Abramovici, M. (2014). Natural markers for augmented reality-based indoor navigation and facility maintenance. Automation in Construction, 48, 18–30. https://doi.org/10.1016/j.autcon.2014.08.009

[14] Romlay, M. R. M., Rashid, M. M., Toha, S. F., & Ibrahim, A. M. (2019). Rainfall-Runoff Model Based on ANN with LM, BR and PSO as Learning Algorithms. International Journal of Recent Technology and Engineering (IJRTE), 8(3), 971-979.

https://doi.org/10.31436/iiumej.v26i1.3436

# OPTIMIZED TYPE 2 FUZZY LOGIC CONTROL FOR LOW-SPEED VEHICLE PEDAL PRESSING AUTOMATION USING HYBRID SPIRAL SINE COSINE ALGORITHM

**AZRUL AZIM ABDULLAH HASHIM[1], NOR MANIHA ABDUL GHANI[1*], SALMIAH AHMAD[2,3], MOHD RUZAINI HASHIM[4], NOOR ZIRWATUL AHLAM NAHARUDDIN[1], ADDIE IRAWAN[1]**

*[1]Faculty of Electrical and Electronics Engineering Technology, Universiti Malaysia Pahang Al-Sultan Abdullah, Pahang, Malaysia*
*[2]College of Engineering and Technology, University of Doha for Science and Technology, Qatar*
*[3]Kulliyyah of Engineering, International Islamic University Malaysia, Malaysia*
*[4]Faculty of Electrical Technology and Engineering, Universiti Teknikal Malaysia Melaka, Melaka, Malaysia*

**Corresponding author: normaniha@umpsa.edu.my*

*(Received: 3 September 2024; Accepted: 6 October 2024; Published online: 10 January 2025)*

***ABSTRACT:*** This paper describes the systematic design and experimental analysis of a Fuzzy Logic Controller (FLC) to govern vehicle speed for low-speed driving by adjusting an attached linear actuator that governs the vehicle's pedal. The research investigates two FLC approaches: the standard Type 1 FLC and the advanced Type 2 FLC, both optimized using the Hybrid Spiral Sine Cosine Algorithm (SSCA). The integrated system linking the actuator to the dynamics model of the vehicle shows improved ability in the manner in which control is done. Physical modeling and simulation were done in Simscape MATLAB, which provides an opportunity for modeling and visual description of the actuator system's relationship with the dynamics of the car. The results presented in this paper prove the fact that the analyzed Type 2 FLC optimized by the SSCA method performs better than the traditional Type 1 FLC in terms of the key metrics, with improvements of 32.4242% in overshoot, 0.364 seconds in settling time, and a reduction of 0.002009 in steady-state error at 2 km/h reference speed. This superior performance highlights the potential of the SSCA-optimized Type 2 FLC to automate pedal pressing for vehicle speed control, effectively replacing repetitive pedal actions and reducing driver fatigue, as this mechanism proves capable of controlling vehicle speed with high precision.

***ABSTRAK:*** Kertas kerja ini menerangkan reka bentuk sistematik dan analisis eksperimen Pengawal Logik Kabur (FLC) untuk mengawal kelajuan kenderaan untuk pemanduan berkelajuan rendah dengan melaraskan penggerak linear yang dipasang yang mengawal pedal kenderaan. Penyelidikan ini menyiasat dua pendekatan FLC: FLC Jenis 1 standard dan FLC Jenis 2 lanjutan, kedua-duanya dioptimumkan menggunakan Algoritma Kosinus Sinus Lingkaran Hibrid (SSCA). Sistem bersepadu yang menghubungkan penggerak kepada model dinamik kenderaan menunjukkan keupayaan yang lebih baik dalam cara kawalan dilakukan. Pemodelan dan simulasi fizikal telah dilakukan dalam Simscape MATLAB di mana ia menyediakan peluang pemodelan dan penerangan visual tentang hubungan sistem penggerak dengan dinamik kereta. Keputusan yang dibentangkan dalam kertas kerja ini membuktikan fakta bahawa FLC Jenis 2 yang dianalisis yang dioptimumkan oleh kaedah SSCA menunjukkan prestasi yang lebih baik daripada FLC Jenis 1 tradisional dari segi metrik utama, dengan peningkatan sebanyak 32.4242% dalam overshoot, 0.364 saat dalam masa penyelesaian, dan pengurangan 0.002009 dalam ralat keadaan mantap pada kelajuan rujukan 2 km/j. Prestasi unggul ini menyerlahkan potensi Type 2 FLC yang dioptimumkan SSCA

https://doi.org/10.31436/iiumej.v26i1.3436

untuk mengautomasikan penekanan pedal untuk kawalan kelajuan kenderaan, menggantikan tindakan pedal berulang dengan berkesan dan mengurangkan keletihan pemandu, kerana mekanisme ini terbukti mampu mengawal kelajuan kenderaan dengan ketepatan tinggi.

***KEYWORDS:*** *Fuzzy Logic Controller Type 2, Hybrid Spiral Sine Cosine, Automate Pedal Pressing, Vehicle Speed Control.*

# 1. INTRODUCTION

Extensive progress in vehicle control technology has resulted in the production of advanced systems, such as adaptive cruise control, designed to perform automated speed control and provide higher driving comfort on highways. ACC systems, especially those supporting stop-and-go functionality, are intended to decrease the driver's workload by independently responding to traffic and even stopping with the following movement on congested roads [1,2]. Unfortunately, these sophisticated systems are generally supported in high-end car models [3] and, hence, not available to middle-end car owners.

In markets like Malaysia, where middle-end vehicles are more prevalent, such disparities hinder the use of such technologies and their advantages. However, there are issues in frequent acceleration and deceleration cases, such as in stop-and-go traffic. Current systems may not support dynamic traffic changes and rapid responses, leading to fatigue among drivers and discomfort [4,5]. For the optimal benefit of these technologies, more advancement is required to enable improved availability and performance of automated vehicle control, especially in the urban environment where a high level of control is desirable.

Several studies have been conducted to improve and create new developments in vehicle control systems. Specifically, several solutions for enhancing the performance and reliability of technologies, including adaptive cruise control, have been developed. For example, Idzham et al. [6] explored a deep learning technique for diagnosing the consequences of repetitive brake pedal pressing and leg positions during traffic jams. The authors employed LGBM to analyze leg position and brake pressure data. Subsequently, the authors ascertained that this model based on AI could achieve about 80% forecast of vehicle speed. It can be employed to fine-tune the adaptive cruise control systems and improve vehicle accident prevention. On the other hand, Isa et al. [7] attempt to develop a linear electromechanical actuator to simulate brake and accelerator pedal pressing needs during traffic congestion to reduce a driver's fatigue leading to accidents. The contrast between the actuator force and the force produced by the human leg was deemed acceptable, and the response time was measured to be less than a second. In general, the advancements in such technologies are mainly focused on their reliability and response characteristics. This is important for driving scenarios such as stop-and-go, where technologies such as adaptive cruise control should work quickly and consistently to provide the ability to brake or accelerate. In addition, they strive to introduce cost-effective solutions that can be implemented on mid-range vehicles.

The pivotal part of any advanced automated pedal pressing for a vehicle speed control system is the controller, which is adjusted to the system to reach desired performance outcomes. The controller aims to process input data from sensors and change the actuator's performance to control the vehicle's pedals effectively and smoothly. In some situations, changing the car's pedals may be desirable, but they will not change due to road conditions. This is when the given control system is designed to provide efficient ways to control the functionality. Since driving is a rather complex activity and vehicles move in a dynamic manner, the traffic situation and the driving environment may change rapidly. Many control

systems today are based on fuzzy logic control as it has proven to manage more complex and nonlinear systems than traditional controllers, which require precise mathematical models and continuous adjustments such as PID controllers [8]. Fuzzy logic controllers operate on linguistic rules and approximate reasoning to adjust the system's behavior [9]. Thus, they can be based on the fact that real-time data can be approximate and variable. The implications for real-time data uncertainty and variability are embedded in fuzzy logic controllers' rules and rough estimates [10]. They can change and react to ever-changing conditions due to data from precise models' algorithms. This means a rather powerful solution in such a system as an automated pedal adjusting system since the behavior of the system is rather flexible and not as rigid as with standard algorithm-based systems. The main benefit of using fuzzy logic in control systems is better adaptability for dealing with imprecise data.

One of the significant difficulties of fine-tuning automatic driving systems is the proper selection of the controller's parameters [11]. It is also noted that properly tuning the control parameters poses a challenge no matter the control technique used, such as a fuzzy logic controller or other conventional methods [12]. In this context, researchers have applied optimization methods to solve this problem. Genetic Algorithms (GA) [13,14], Spiral Dynamic Algorithm (SDA) [15], Artificial Bee Colony (ABC) [16,17], Firefly Algorithm (FA) [18,19], Cuckoo Search (CS) [20,21], and Particle Swarm Optimization (PSO) [22,23] have been used to explore and optimize the parameter space quickly. These algorithms explore the parameter space systematically and efficiently, imitating natural processes or based on mathematical equations to perform optimizations and come up with the best setting. Applying all these optimization techniques can enhance controller performance, reliability, and flexibility, leading to generally enhanced, reliable, and high-quality automated systems.

Advanced optimization, on the other hand, is a technique of combining many optimizations in a bid to enhance the results while reducing the challenges that affect single optimization techniques. Hybrid optimization, therefore, is a process where two or more optimization techniques are used to take advantage of the strengths while avoiding some difficulties like getting stuck in local optima, where instead of getting the best solution, the algorithms end up getting the worst one. For example,[24] ] one study integrated the spiral equation from SDA directly into the Bacterial Foraging Algorithm (BFA). It showed that it enhanced both the exploration and exploitation steps and the accuracy level. Another research work [25] employed the integration of SDA with GA to achieve greater accuracy using the mutation and crossover features of GA. These hybrid techniques have been observed to perform better in challenging optimization conditions.

Motivated by the latest developments and findings, this work aims to assess the hybrid optimization approaches for refining the parameters of advanced fuzzy logic type 2 controllers for self-controlled pedals. The study will particularly assess how SSCA can enhance the automated pedal pressing operation in low-traffic circumstances. This work aims to improve the fuzzy logic controller's performance by applying hybrid optimization to solve real-world and time-varying driving conditions more efficiently. The focus will be to improve the control system to ensure the driver is comfortable in traffic-sensitive conditions and address the practical issues identified in the low-traffic context.

This research introduces a novel integration of the Hybrid Spiral Sine Cosine Algorithm (SSCA) with a Type-2 Fuzzy Logic Controller (FLC) to optimize automated pedal pressing systems for low-speed driving conditions in a simulation environment. Unlike previous studies that focus on single optimization techniques or conventional controllers, this study utilizes the strengths of SSCA to improve the adaptability and precision of Type-2 FLC in handling dynamic and nonlinear traffic scenarios. This work enhances the performance and reliability

https://doi.org/10.31436/iiumej.v26i1.3436

of automated pedal systems in simulated environments by addressing challenges such as parameter tuning, imprecise data, and real-time response. Additionally, it contributes to the field of vehicle control by demonstrating how hybrid optimization techniques can refine controller parameters to achieve superior results under variable and time-sensitive driving conditions, offering insights into potential future applications for Advanced Driver Assistance Systems (ADAS).

## 2. METHODOLOGY

### 2.1. Design of Pedal Subsystem Prototype

The pedal subsystem was designed based on the brake pedal system commonly found in the Proton Saga, a popular sedan model in Malaysia. Figure 1 shows the process of measuring the available space in the car's footwell, a crucial step to ensure that the subsystem design fits the spatial limitations typical of sedan vehicles. By capturing accurate dimensions from the Proton Saga's pedal system, this design approach can be effectively applied to similar sedan models.

Figure 1. Measuring available space

After the measurements, key components were selected and integrated into the design. Figure 2 and Figure 3 illustrate the linear actuator model L16-P, chosen for its compact size and suitable force output for controlling the pedal. The Wilwood swing mount brake pedal, shown in Figure 4 and Figure 5, was selected to simulate realistic pedal movement. The complete pedal subsystem was then modeled in SolidWorks Figure 6, with each component positioned and scaled to match the measured dimensions.

Figure 2. Linear actuator L16-P

https://doi.org/10.31436/iiumej.v26i1.3436

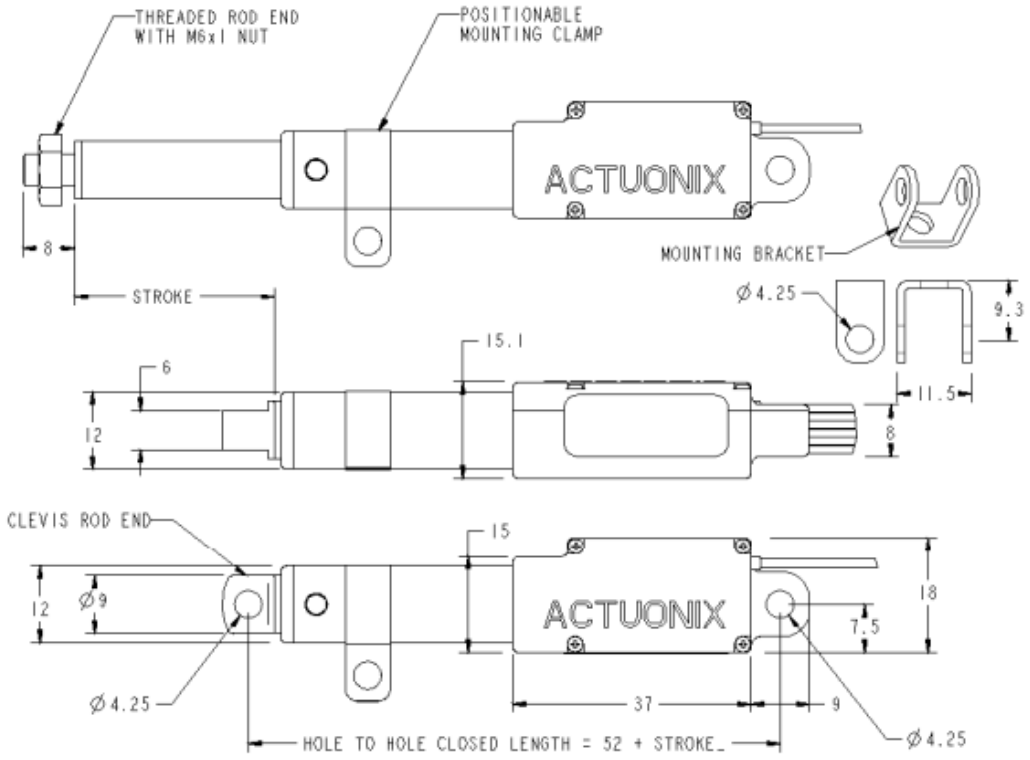


Figure 3. Dimension of linear actuator L-16P

Figure 4. Wilwood swing mount brake pedal

https://doi.org/10.31436/iiumej.v26i1.3436

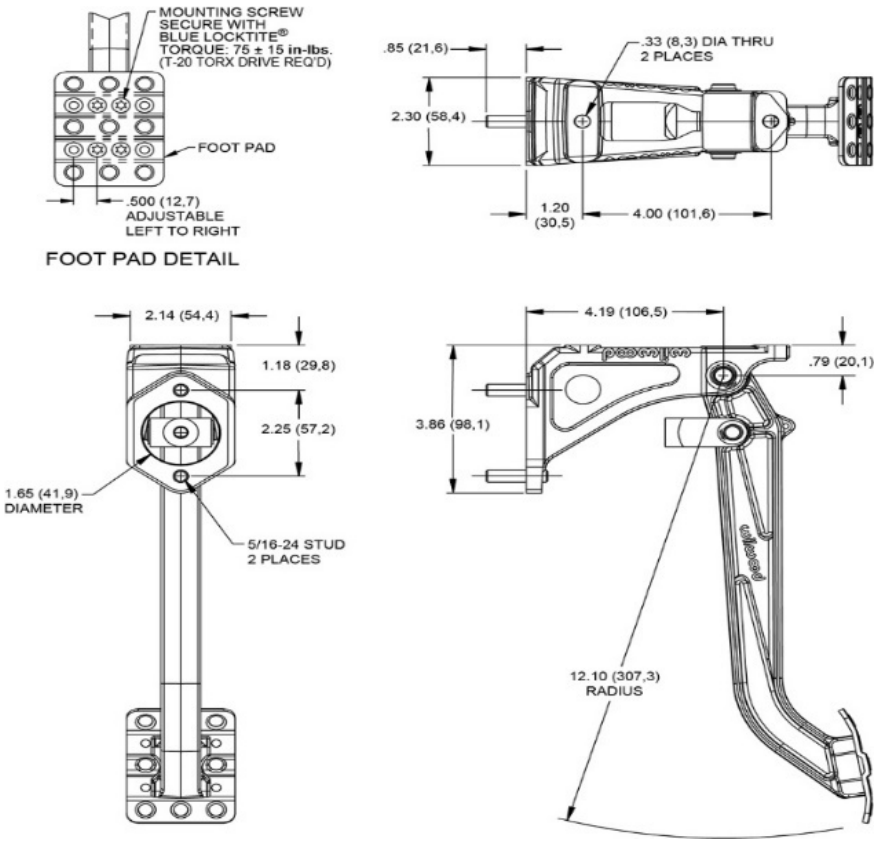


Figure 5. Dimension of Wilwood swing mount brake pedal

This CAD model is an efficient alternative to complex mathematical modeling before implementation on real hardware, as it requires a shorter time to derive accurate equations from complex variations [26,27]. Additionally, the 3D CAD model in SolidWorks brings the advantage of closely replicating the real system by incorporating essential factors such as nonlinearity, mass, gravity, and friction within the software environment. This enables more realistic simulations throughout the study, enhancing the model's practical applicability to real-world conditions.

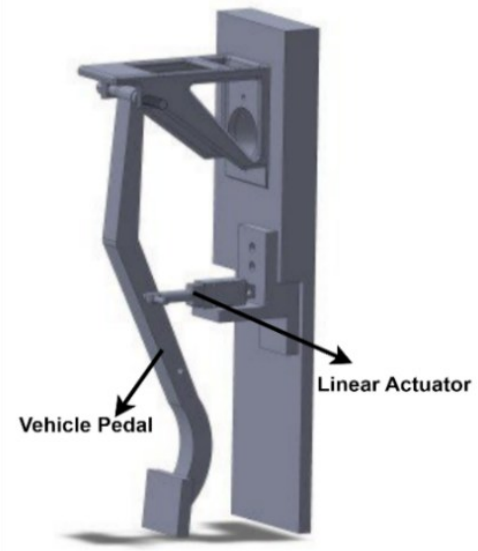


Figure 6. Automate Pedal Pressing Prototype design in 3D SolidWorks

https://doi.org/10.31436/iiumej.v26i1.3436

## 2.2. Physical Component Modeling of Linear Electromechanical Actuator in Simscape.

Figure 7, which employs Simscape component models for its systems representation, illustrates the physical components of this linear actuator. The lead screw, DC motor and gearbox transmission, force sensor, and voltage source are all components of this linear actuator. All of these components are essential for the actuation of responses, including the pressing and releasing of the accelerator. Thus, Table 2 presents the parameters of the chosen linear electromechanical actuator, with values that will be utilized in the modeling represented in Figure 2.

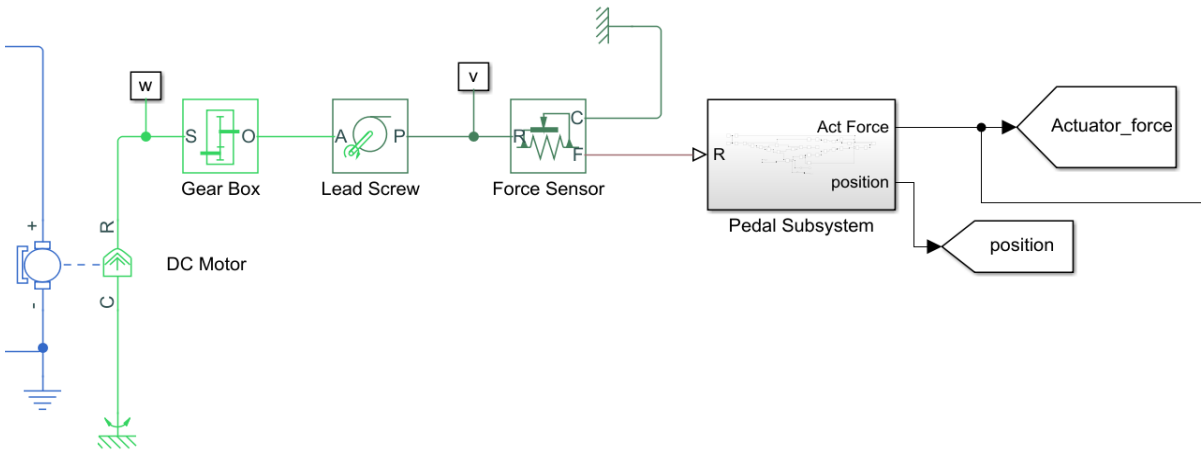


Figure 7. Modeling of Linear Actuator component in Simscape Matlab

In Figure 7, the system begins with the DC motor, which converts electrical energy into mechanical energy. The motor generates torque $T_{motor}(S)$ based on the input voltage $V(s)$, as described by the relationship in Eq. (1).

$$\frac{T_{motor}(S)}{V(s)} = \frac{K_{motor}}{sL+R} \tag{1}$$

where $K_{motor}$ is the motor constant, L is the winding inductance, and R is the winding resistance.

The gearbox then reduces or increases the angular speed and torque output of the motor. The angular speed of the shaft $W_{shaft}(S)$ is related to the input voltage $V(s)$ as shown in Eq. (2).

$$\frac{W_{shaft}(S)}{V(S)} = \frac{1/b}{s(J/b)+1} \tag{2}$$

where $b$ and $J$ are shaft's rotational friction constant and moment of inertia, respectively.

Then the lead screw converts rotational motion into linear motion. The relationship between the gear ratio G, input torque $\tau_{in}$, and output torque $\tau_o$ is given by Eq. (3).

$$G = \frac{\tau_o}{\tau_{in}} \tag{3}$$

The linear force, $F$, generated by the rotating lead screw can be calculated using Eq. (4)

$$F = G\,\frac{2\pi}{l} \tag{4}$$

where $l$ is the length of one pitch on the leadscrew. As for the linear position $X_{linear}$ of the leadscrew can be expressed by the following Eq. (5).

https://doi.org/10.31436/iiumej.v26i1.3436

$$X_{linear} = \theta_{linear} \frac{l}{2\pi} \quad (5)$$

Thus, Table 1 presents the parameters for the chosen linear electromechanical actuator, providing essential values for the system's performance.

Table 1. Parameter for the Chosen Linear Electromechanical Actuator

| No | Parameter | Value |
|---|---|---|
| 1 | Torque Constant | 0.4 N.m |
| 2 | Winding Resistance | 1 Ω |
| 3 | Winding Inductance | 0.05 H |
| 4 | Screw lead pitch | 0.008 m |
| 5 | Gearbox ratio | 2 |
| 6 | Lead screw efficiency | 40 % |
| 7 | Shaft moment of inertia | 0.01 Kg.m^2 |
| 8 | Rotational friction coefficient | 0.1 N.m. s |

## 2.3. Type-2 Fuzzy Logic Controller

Type 2 Fuzzy Logic Controllers (FLCs) offer a distinct advantage over Type 1 FLCs, particularly in handling uncertainty and variability in complex systems. While Type 1 FLCs use crisp membership functions, Type 2 FLCs employ fuzzy sets with fuzzy boundaries such as lower scale and lower lag, allowing them to manage the uncertainties inherent in real-world applications better. This capability improves performance, especially in systems with highly uncertain or dynamic input-output relationships.

Lower scale and lower lag are critical features of Type 2 FLCs. The lower scale refers to the finer granularity in the fuzzy membership functions, enabling the controller to respond more precisely to small variations in input data. This precision is particularly beneficial in systems requiring high accuracy and smooth control, such as in-vehicle speed control, where minor deviations must be corrected quickly.

Lower lag in a Type 2 FLC reduces the delay between the input signal and the system's response, leading to a more responsive control system. This is especially important in dynamic environments where the system must adapt rapidly to changes, such as sudden decelerations in a vehicle. Selecting lower scale and lower lag values typically involves tuning the fuzzy membership functions and rules to optimize the controller's performance. By including these values in the Type 2 FLC, engineers can test and validate whether the controller provides improved response time, stability, and accuracy compared to a Type 1 FLC. This comparison often reveals that Type 2 FLCs offer enhanced robustness and flexibility, making them more suitable for complex and uncertain control tasks.

Step 1: Specify the number of inputs and outputs and the number of Fuzzy sets. As shown in Figure 8, there are 2 inputs: Error of vehicle speed and Change of error of vehicle speed, 1 output: Voltage, and 5 number of fuzzy set: Negative Big (NB) and Negative Small (NK), Zero (Z), Positive Small (PK), and Positive Big (PB) are the five fuzzy sets with which each such input value is associated.

Step 2: Selecting the type of membership functions, such as Gaussian, trapezoidal, and others, for imprecise sets that include inputs (error and change of error) and outputs (voltage supply) is essential. Furthermore, applying lower scale and lower lag values, randomly specified within the range of 0 to 1, is crucial for Type 2 FLC.

https://doi.org/10.31436/iiumej.v26i1.3436

This approach enhances the quality of uncertainty handling by providing an ideal transition between membership categories.

Step 3: To determine the outputs, 25 fuzzy rules are implemented by combining the five fuzzy sets for each input. The rule foundation provided corresponds to the pedal control subsystem's specifications. It consists of a 5x5 matrix in which each cell corresponds to a specific pair of input fuzzy values and describes the amount of voltage that should be applied to the adjusting linear actuator.

Step 4: Transform the fuzzy output data into a precise voltage value. This technique transforms the fuzzy results from the rule application into a precise and accurate control value for the actuator, ensuring precise and appropriate pedal control. The defuzzification process, supported by the lowered scale and lower lag, effectively controls dynamic changes in the system.

In fuzzy logic controller (FLC) design, normalized values, typically ranging from -1 to 1, simplify the design process and ensure consistency across varying system conditions. This normalization allows for easier handling of inputs and outputs, making defining membership functions and process control actions straightforward without being influenced by the absolute scales of the parameters involved. However, the range of input and output values needs to be scaled according to the system's specific characteristics, as it may not naturally produce values within this normalized range.

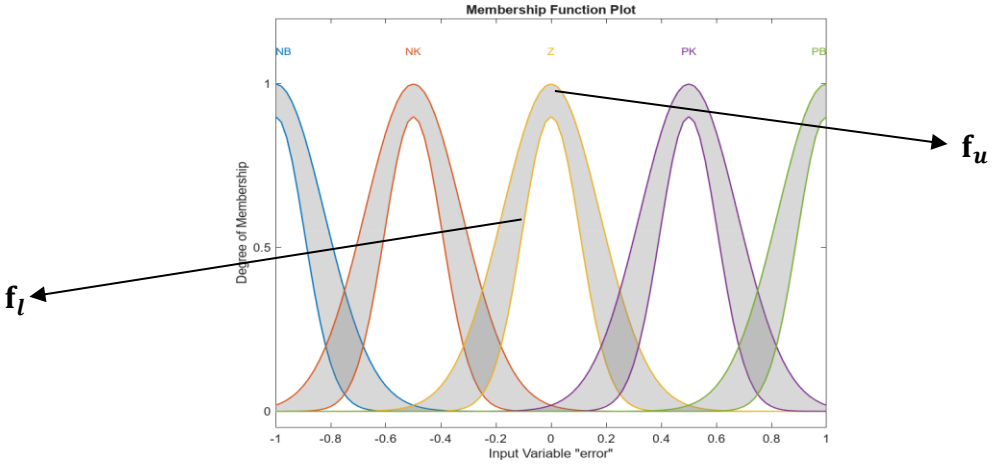


(a)

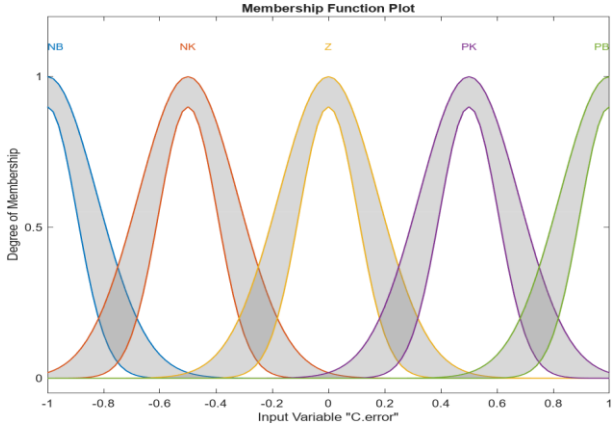


(b)

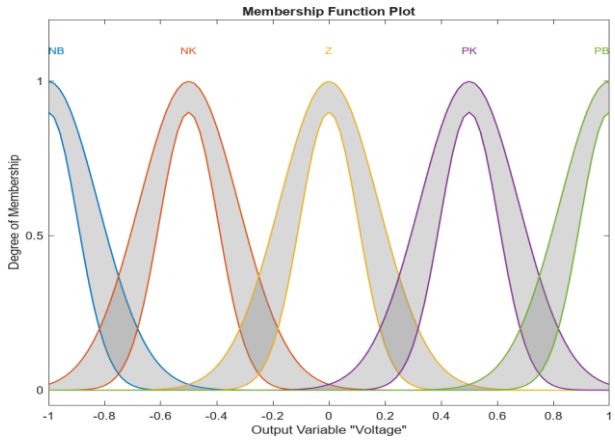


(c)

Figure 8. Design of Membership Function: (a). Error Input, (b). Change of error input and (c). Output (Voltage)

Table 2. Fuzzy Rules Table

| **Error** | **Change of Error** | | | | |
|---|---|---|---|---|---|
| | **NB** | **NK** | **Z** | **PK** | **PB** |
| **NB** | NB | NB | NB | NK | Z |
| **NK** | NB | NB | NK | Z | PK |
| **Z** | NB | NK | Z | PK | PB |
| **PK** | NK | Z | PK | PB | PB |
| **PB** | Z | PK | PB | PB | PB |

The block diagram in Figure 3 (a) illustrates the structure of a Type-2 Fuzzy Logic Controller (FLC) specifically designed to manage uncertainties through interval type-2 fuzzy sets. The system receives two input signals: the error (e) and the change of error (Δe), representing the difference between the desired and actual values. These inputs are fuzzified using interval type-2 membership functions, which consist of an upper membership function (UMF) and a lower membership function (LMF). This dual-layer approach forms the foundation of interval type-2 fuzzy sets, allowing for the representation of uncertainty through a footprint of uncertainty (FOU). During the fuzzification process, each input is assigned a degree of membership across both the UMF and LMF, represented by the functions.

$$f_u(x) \text{ and } f_l(x) \tag{6}$$

where $f_u(x)$ and $f_l(x)$ denote the upper and lower membership values, respectively, for a given input x.

Once fuzzified, the inputs are processed through a rule evaluation (inference) stage. Each input's membership values interact within a set of fuzzy rules to produce outputs. Each rule acts as a conditional statement linking the inputs to the control output, with the strength of each rule defined by a range of values due to the FOU. The firing strengths for each rule, represented as intervals, are calculated by applying the minimum operator to both UMF and LMF values. For a given rule i, the upper and lower firing strengths $w_{u,i}$ and $w_{l,i}$

$$w_{u,i} = min(f_u(e)\ , f_u(\Delta e)) \tag{7}$$

$$w_{l,i} = min(f_l(e)\ , f_l(\Delta e)) \tag{8}$$

https://doi.org/10.31436/iiumej.v26i1.3436

Here, $f_u(e)$ and $f_u(\Delta e)$ represent the upper membership values for the error and change of error while $f_l(e)$ and $f_l(\Delta e)$ denote the lower membership values.

The outputs from each rule are then aggregated to form an output fuzzy set, resulting in an interval type-2 fuzzy set. This aggregated output undergoes type reduction to yield an interval type-1 fuzzy set. Type reduction determines the limits of the resulting fuzzy set, typically computed using the left and right centroids, denoted as $c_L$ and $c_R$. These are calculated using the following equations.

$$c_L = \frac{\sum_{i=1}^{L} x_i \cdot f_{u,i} + \sum_{j=L+1}^{N} x_J \cdot f_{l,j}}{\sum_{i=1}^{L} f_{u,i} + \sum_{j=L+1}^{N} f_{l,j}} \tag{9}$$

$$c_R = \frac{\sum_{i=1}^{R} x_i \cdot f_{l,i} + \sum_{j=R+1}^{N} x_J \cdot f_{u,j}}{\sum_{i=1}^{R} f_{l,i} + \sum_{j=R+1}^{N} f_{u,j}} \tag{10}$$

In these expressions, $x_i$ represents the sampled values over the output universe of discourse, while $f_{u,i}$ and $f_{l,i}$ correspond to the UMF and LMF values within the output set.

Finally, the defuzzification process produces a crisp output by averaging the lower and upper centroid values, $c_L$ and $c_R$, to determine a single control action. The resulting control output y is expressed as:

$$y = \frac{c_L + c_R}{2} \tag{11}$$

This output $y$ is then connected to the integrator block and the gain K3 in the control system. The integration process allows the system to accumulate the effect of the control action over time, effectively enhancing the system's response. Given that the output can range from [-1,1], K3 amplifies the signal as needed until the system achieves the desired output. This configuration ensures that force control is appropriately managed in response to input conditions.

### 2.4. Spiral Sine Cosine Tuning Approach.

Problems such as getting stuck in local optima have always posed a great challenge for optimization algorithms, especially when numerous obstacles exist in the search space. This difficulty arises when one optimizes only for a specific region in the solution space rather than the entire space, leading the algorithm to take an optimal measure in that region but not the best one. In other words, the algorithm may converge to a 'solution' that does not prevent it from searching for a more optimal solution across the entire search space, a globally optimal solution for the problem.

The SSCA algorithm is another modern meta-heuristic optimization algorithm that addresses the issue of premature convergence. While the SCA is responsible for exploring the search space, the SCA overcomes the exploration capabilities of the Spiral Dynamic Algorithm to prevent the algorithm from falling into suboptimal solutions. The SCA component encourages a large exploration of the solution space and frees it from the local optimum by consistently updating the direction and amplitude of the search. In addition, the SDA part of the algorithm carries the burden of the detailed adjustment of the search in the promising regions, making the algorithm fast in converging to the best solutions.

https://doi.org/10.31436/iiumej.v26i1.3436

The SSCA starts by creating a population of agents in the search space, each representing a solution. The first step of the algorithm used, called "spiral movement," can be described in Eq. (12)

$$X(i)'' = (rz \times Rz \times X(i)') - \Big(\big((rz \times Rz) - I\big) \times xStar\Big) \tag{12}$$

where $xStar$ represents the center of the spiral, X(i)″the updated position of the searching agent, $rz$ is a spiral radius, $RZ$ is the rotational matrix, $I$ is $n \times n$ identity matrix, and X(i)′ is the current position of the searching agent. This equation ensures that agents move in a spiral trajectory toward the best solution, promoting global exploration.

After updating the positions using the spiral equation, SSCA performs another step to refine the updated position of the agents using sine and cosine functions, as shown in Eq. (13) and Eq. (14).

$$X(i)''' = X(i)'' + r1 + sin(r2) + |r3 \times (P(i) + X(i)'')| \tag{13}$$

$$X(i) = X(i)''' + r1 + cos(r2) + |r3 \times (P(i) + X(i)''')| \tag{14}$$

where X(i) is the updated position of the current agent, r1 is the adaptive step size that decreases over iteration, r2 is a random angle between 0 and 2π, r3 random factor, and P(i) is the best-known position. The r1 is defined as Eq. (15).

$$r1(t) = a + t\frac{a}{T} \tag{15}$$

where $a$ is a predefined constant, $t$ represents the current iteration index, and $T$ denotes the maximum number of iterations specified for the algorithm. The equation for $r1$ is structured to decrease as the iteration count increases. Equation $r2$ is formulated as follows in Eq. (16)

$$r2 = 2 \times \pi \times rand \tag{16}$$

where $rand$ is a random number defined between [0,1]. It depicts the algorithm's random behavior in deciding the agent's direction. Additionally, the parameter $r3$ is a separate random value applied to each agent, adding individual variability to each agent's behavior.

These equations ensure the local searches around the best-known positions, allowing the algorithm exploitative capability. Through these procedures, the cost function values are updated as the algorithm converges towards the optimal solution of the target problem, allowing SSCA to be suitable for solving complex optimization problems.

Figure 9 shows the overall block diagram of the automated pedal pressing for the vehicle speed control system. This system also incorporates Fuzzy Logic Control to control the vehicle pedal, where the FLC has been optimized by applying SSCA to fine-tune the control model. Figure 10 illustrates the design of this system in the Simulink MATLAB environment. This design mimics the block diagram of Figure 9, where the control logic, the sensors' input, and the actuators' output are performed in simulation.

Since the normalized values in the Type 2 FLC design range from (-1, 1) for both input and output, there is a need to scale these values to adapt to the system's requirements. The parameters K1, K2, and K3 are employed for this purpose. K1 adjusts the proportional response to the current error, while K2 accumulates the error over time to eliminate steady-state discrepancies. Additionally, K3 is associated with the integral aspect, facilitating the accumulation of past errors to ensure that any lingering steady-state error is effectively corrected. Optimization techniques are then utilized to fine-tune these parameters, ensuring they align with the system's specific dynamics and performance needs. This approach allows

https://doi.org/10.31436/iiumej.v26i1.3436

the FLC to adapt its control actions effectively, achieving robust and precise performance tailored to the unique operational conditions of the application.

Thus, Table 4 depicts the important parameters that should be defined within the Spiral Sine Cosine Algorithm (SSCA) for optimizing the values of K1, K2, and K3. These parameters play a critical role in ensuring that the Type 2 FLC can operate effectively within the normalized range while adapting to the system's specific requirements. By fine-tuning these parameters, the SSCA facilitates improved performance and stability of the FLC, enabling enhanced control actions that are responsive to varying operational conditions.

Figure 11 presents the flowchart of the SSCA implementation. The SSCA flowchart begins with the agent population being initialized at various locations in the solution space. Following initialization, the algorithm updates the agents' positions in a loop, where the direction of movement is determined by the spiral movement combined with sine-cosine formulas. During each iteration, the agents explore the problem space and leverage the most promising points to refine the solutions. This iterative process continues until a termination condition is met, at which point the best solution is identified.

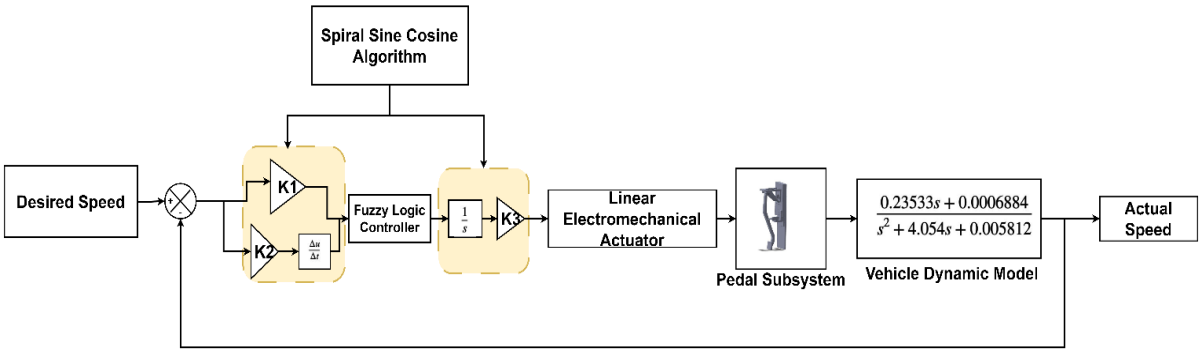


Figure 9. Block diagram structure of the Automated Pedal Pressing for Vehicle Speed Control

https://doi.org/10.31436/iiumej.v26i1.3436

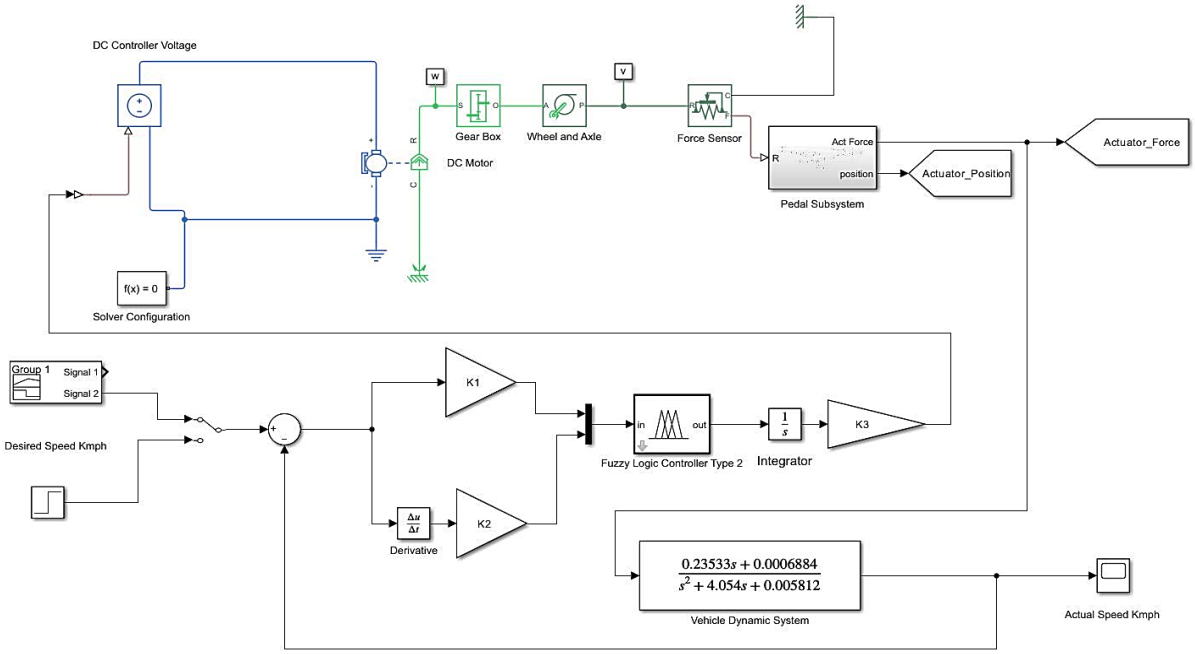


Figure 10. Detailed Simscape Model of the Automated Pedal Pressing for Vehicle Speed Control in MATLAB Simulink

Table 3. Parameters for the SSCA

| **Parameter** | **Value** | |
|---|---|---|
| Number Iteration | 30 | |
| Number of Agents | 10 | |
| Dimensions | 3 | |
| Boundaries | Min | Max |
| K1 | 0 | 1 |
| K2 | 0 | 1 |
| K3 | 0 | 30 |
| Spiral Parameter | | |
| rz | 0.96 | |
| θ | π/2 | |
| RZ | 1 | |

https://doi.org/10.31436/iiumej.v26i1.3436

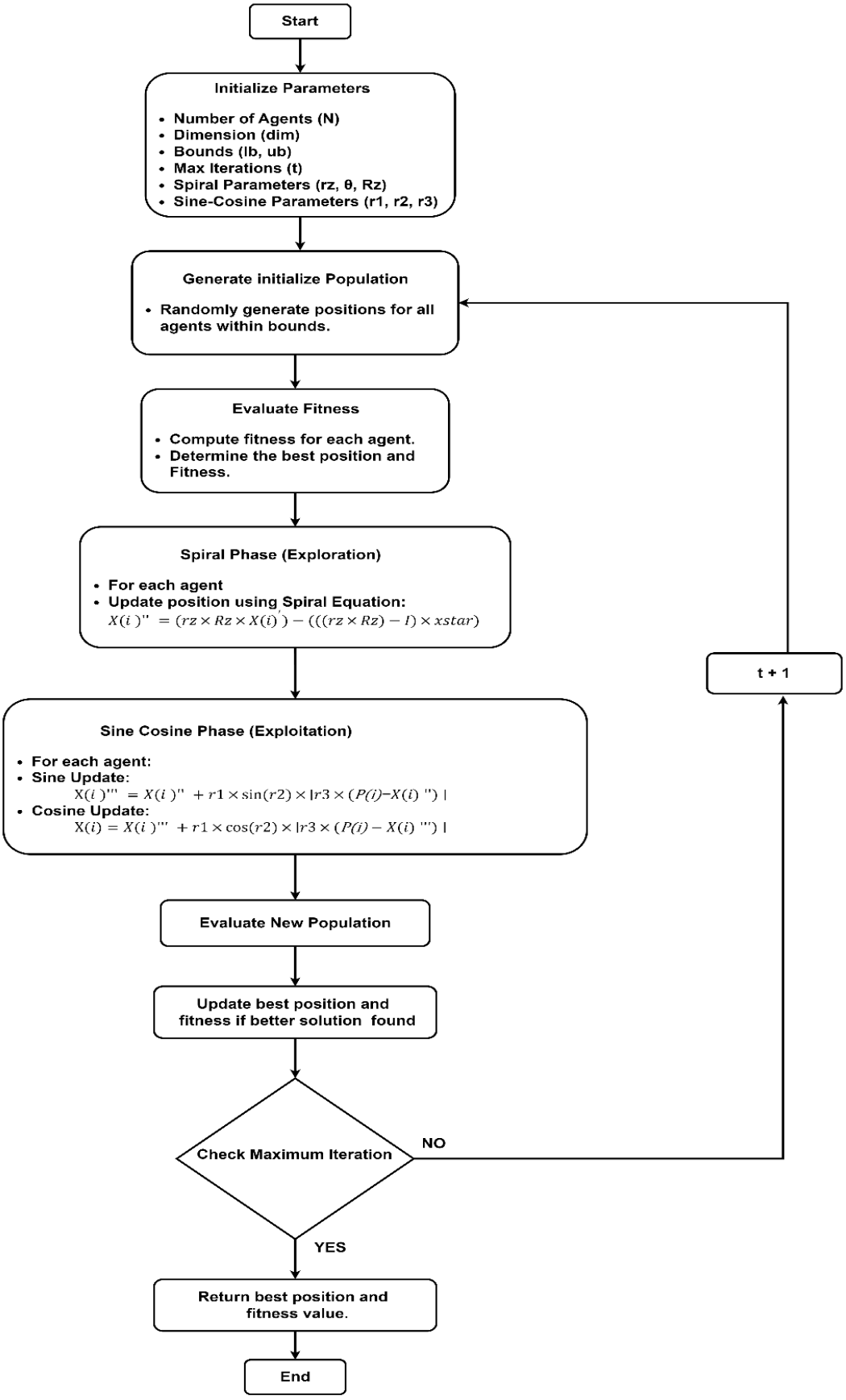


Figure 11. Flowchart of implementation Spiral Sine Cosine Algorithm

https://doi.org/10.31436/iiumej.v26i1.3436

# 3. RESULTS AND DISCUSSION

The following section provides the outcomes of the simulations on the automated pedal pressing for vehicle speed control using a linear actuator intended to control the vehicle's speed during low-speed driving situations. The system replaces leg activities by pressing and releasing the automobile's pedals. The research mainly focuses on testing a Type-2 FLC, tuned by the SSCA, to bring the actuator to stability and maintain the vehicle's speed of the vehicle constant. To demonstrate the efficiency of the Type-2 FLC, it is compared with a Type-1 FLC. The comparison of the Type-2 FLC design optimized using the SSCA with a conventional Type-1 FLC controller allows us to observe the benefits in the overshoot, settling time, rise time, and steady-state error that will give stability and accuracy of speed control, especially in low-speed driving.

## 3.1. Convergence Analysis of Spiral Sine Cosine Algorithm

The convergence plot of the spiral sine cosine algorithm with two fuzzy logic controllers, Type-2 and Type-1, was performed as shown. The parameters K1, K2, and K3 were optimized in the process. The tuning was done through 30 iterations with a Root Mean Square Error as a fitness function.

Figure 12 presents the convergence behavior of the Type-2 FLC, showing the results from 10 cycles of the SSCA optimization algorithm. As indicated in the figure, the best performance was achieved during the 8th cycle, with the RMSE initially stabilizing at 0.945 for the first 5 cycles. From cycle 6 onward, a significant improvement was observed, with the RMSE decreasing to 0.903, and this value was maintained consistently throughout cycle 30. This indicates that the SSCA effectively converged to an optimal solution, improving the control parameters of the Type-2 Fuzzy Logic Controller.

Conversely, the Type-1 FLC did not exhibit the same convergence properties. Throughout all 30 iterations, the RMSE value remained constant at 0.905, showing no further reduction. This lack of convergence suggests that the SSCA was less effective in optimizing the Type-1 FLC parameters, as it failed to achieve significant improvements throughout the iterations.

https://doi.org/10.31436/iiumej.v26i1.3436

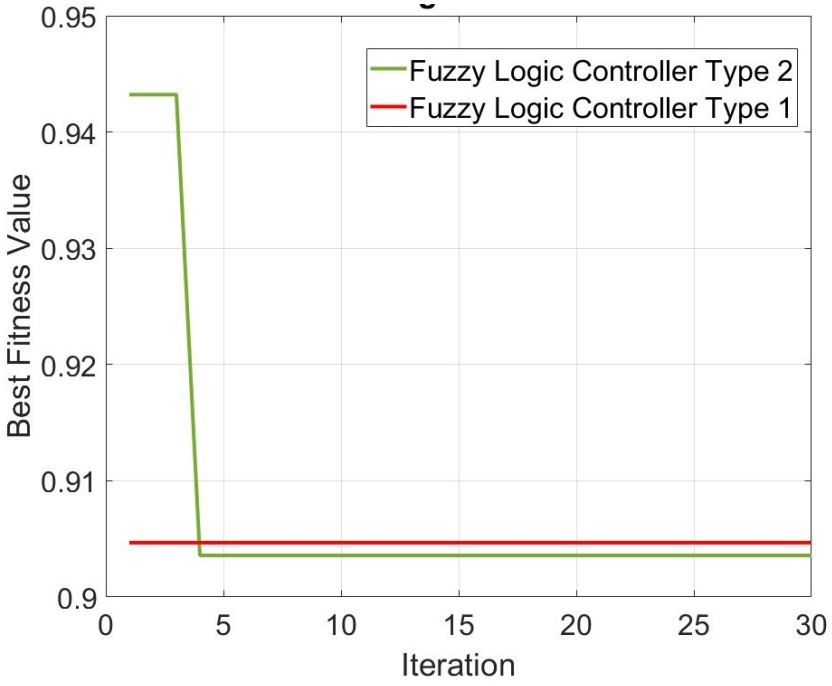


Figure 12. Comparison of Convergence Curve for both Type1 and Type 2 FLC

### 3.2. Performance Analysis with Different Speed

Table 5 shows some of the parameters tuned by the SSCA for both Type-1 and Type-2 Fuzzy Logic Controllers (FLC). Another point that distinguishes the Type-2 FLC is the existence of extra parameters, such as the lower lag and the lower scale value, which are randomly specified within the range of 0 to 1. In contrast, the Type-1 FLC does not include these parameters, contributing to the Type-2 FLC's improved performance and stability. Additionally, for both FLC types, the three constants designated as K1, K2, and K3, as shown in Figure 9, were adjusted by SSCA over defined boundaries, as depicted in Table 4.

Figure 13 illustrates the system's response in three key areas: vehicle speed (km/h), force applied by the actuator (N), and actuator position (mm). A comparative analysis of the two FLC types shows that FLC Type-1, even when tuned by SSCA, exhibits a certain level of oscillation with regard to system response. This oscillation is particularly evident when comparing the speed and actuator force graphs.

The presence of oscillations in the FLC Type-1 controller is significant due to its higher overshoot, which renders the speed control system unstable. The actuator force also fluctuates and follows a cycle, indicating consistent control. The Type-2 FLC, with parameters tuned by SSCA, offers a less oscillatory response compared to its basic counterpart.

A comparison between FLC Type 1 and FLC Type 2 has revealed improved performance in terms of the following indices, achieved using the Spiral Sine Cosine Algorithm (SSCA). Table 5 shows that at a speed of 2 Kmph, FLC Type 1 had an overshoot of 36.0198%. Meanwhile, (FLC Type 2) reduced the overshoot by 3.5956 %, improving about 32.4242%. Concerning rise time, FLC Type 1 was observed to be better than FLC Type 2 at certain speeds, exhibiting a shorter rise time. For instance, at 2 Kmph, FLC Type 1 reached a rise time of 0.2093 seconds compared to 0. 5573 seconds for FLC Type 2. However, one obvious disadvantage of the faster rise time in FLC Type 1 is that it exhibits a larger overshoot, causing the pedal and the actuator to oscillate and resulting in poor performance of vehicle speed control. The Simscape visual representation of the automated pedal-pressing vehicle speed

https://doi.org/10.31436/iiumej.v26i1.3436

control is depicted in Figure 14The figure illustrates how the actuator responds to various vehicle speeds. If the desired speed is 5 km/h, the actuator retracts, and the pedal attached to it extends, thereby releasing the pedal vehicle and increasing the speed.

In terms of settling time, FLC Type 2 was slightly better on average, especially at 2 Kmph, where settling time was reduced by 0.364 seconds compared with FLC Type 1. As such, it allows a steady state to be achieved faster and makes the overall structure more stable.

As for the steady-state error, FLC Type 2 had lower and constant results, providing a more accurate control. At 2 Kmph, the steady-state error was -0.0018, compared to -0.0038 for FLC Type 1, reflecting an improvement of 0.002009.

Table 4. Parameter Tune by Spiral Sine Cosine Algorithm for both Type FLC

| Controller | Parameter Tune By SSCA | | | Randomly Specified | |
|---|---|---|---|---|---|
| | K1 | K2 | K3 | Lower Scale | Lower Lag |
| FLC Type 1 | 0.1188 | 0.0099 | 21.9156 | - | - |
| FLC Type 2 | 0.0678 | 0.0100 | 30 | 1 | 0.2 |

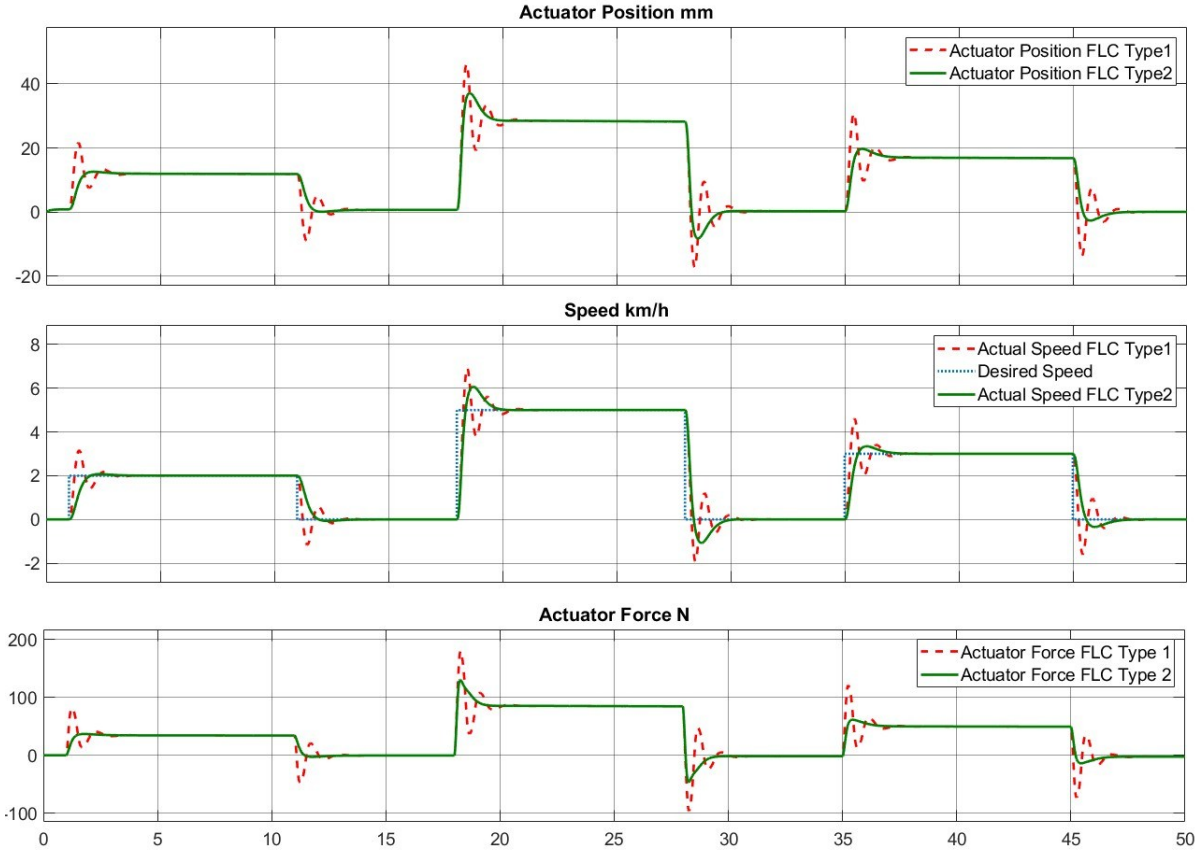


Figure 13. Vehicle Speed Response with Different Reference Speed

https://doi.org/10.31436/iiumej.v26i1.3436

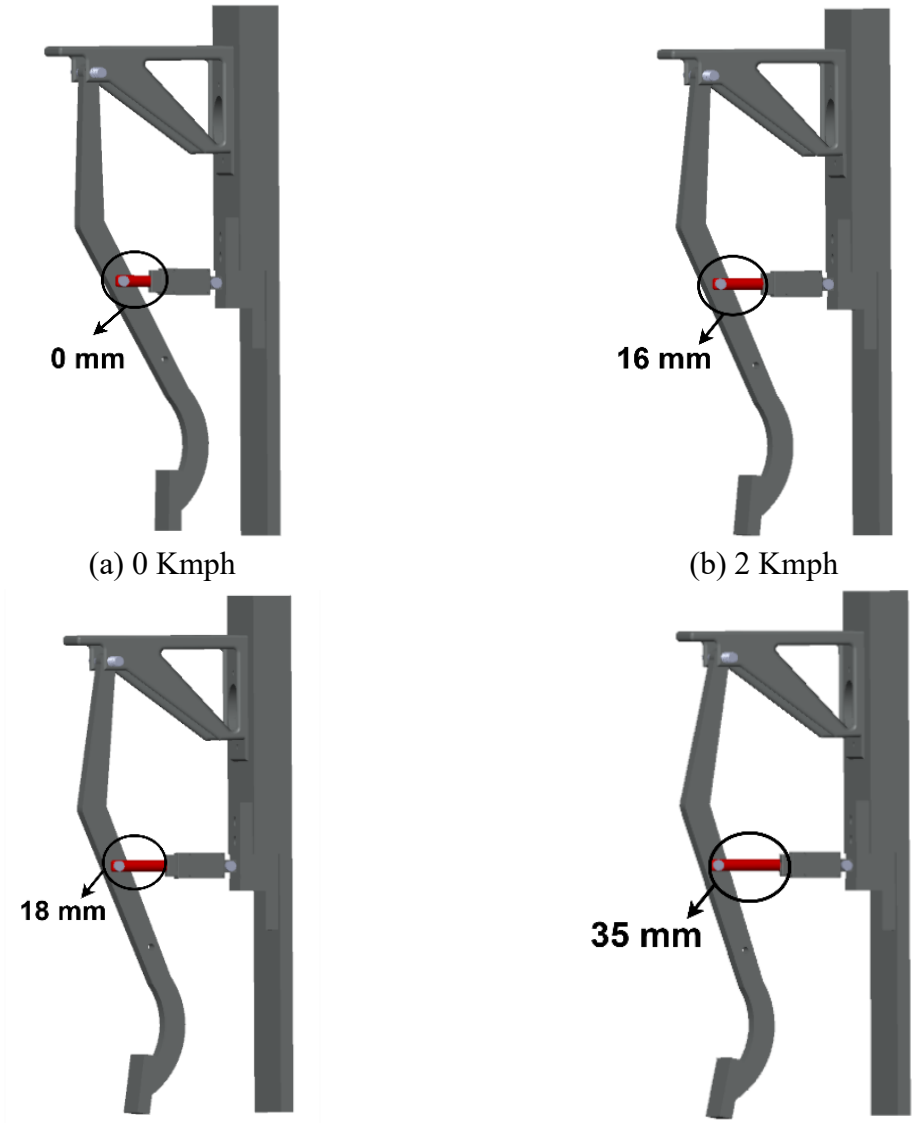


(a) 0 Kmph (b) 2 Kmph

(c) 3 Kmph (d) 5 Kmph

Figure 14. Visualization of Automate Pedal Pressing of Vehicle Response in Simscape

Table 5. System Performance Analysis tuned by SSCA for both Type FLC

| Reference Speed | System Performance Analysis | | | |
|---|---|---|---|---|
| | **Parameter** | **FLC Type 1** | **FLC Type 2** | **FLC Type 2 Improvement** |
| 2 Kmph | Overshoot (%) | 36.0198 | 3.5956 | 32.4242 |
| | Rise time (s) | 0.2093 | 0.5573 | Not reduced |
| | Settling time (s) | 3.2538 | 2.8894 | 0.3644 |
| | Steady-State Error | -0.0044 | -0.0020 | 0.0024 |
| 3 Kmph | Overshoot (%) | 41.6032 | 11.4938 | 30.1094 |
| | Rise time (s) | 0.1799 | 0.3641 | Not reduced |
| | Settling time (s) | 37.6442 | 36.9800 | 0.6642 |
| | Steady-State Error | -0.0011 | -0.0025 | Not reduced |
| | Steady-State Error | -0.003809 | -0.0018 | 0.002009 |
| 5 Kmph | Overshoot (%) | 33.2372 | 21.4962 | 11.741 |
| | Rise time (s) | 0.23740 | 0.2661 | Not reduced |
| | Settling time (s) | 19.6979 | 19.5361 | 0.1618 |

# 4. CONCLUSION

A new approach towards the development of controlling a linear actuator is presented in the study in the form of a Fuzzy Logic Controller (FLC), which is intended to impose control over vehicle speeds, especially during low-speed driving in heavy traffic conditions where frequent pressing and releasing of the brake pedal is required. Integrating the actuator with the vehicle dynamics model enables the control system to maintain optimal speed by applying the appropriate force on the pedal, alleviating the driver's need for repetitive pedal activities, and is especially beneficial in traffic congestion. The system's performance was evaluated using two different FLC approaches: the traditional FLC Type 1 and the more advanced FLC Type 2. The results obtained effectively demonstrate the concept proposed in this research and confirm that the FLC Type 2 optimized with the SSCA exhibits a significantly lower overshoot than the conventional FLC Type 1 algorithm and a significantly faster settling time while maintaining a considerably small steady-state error. However, the settling time is influenced by the presence of variation. This advancement suggests that it could be possible to substitute the tiresome procedure of the presses and releases of the pedal vehicle among drivers. This system's enabled combination of FLC Type 2 with SSCA improves the overall performance of a real hardware solution. However, transitioning from exercise to application poses many difficulties that can be outlined as follows. Thus, future research will focus on the hardware-in-the-loop testing of the presented system to ensure a comprehensive analysis of the system's behavior and efficiency in a realistic environment. Additionally, the current model is primarily tested for very low-speed scenarios, which is effective in simulating stop-and-go traffic but may limit its broader applicability. Future studies should consider testing the system across different terrains, including urban areas, rural environments, and highways, to evaluate its performance in various driving conditions. This approach aims to bridge the gap between simulation and the implementation of the system on the actual hardware to provide a more reliable and efficient subsystem for usage.

# ACKNOWLEDGMENT

This work has been financially supported by the Postgraduate Research Grant Scheme, PRGS, with a university reference number (PGRS230341), and the UMPSA Research Grant Scheme, with a university reference number (RDU220328). The Research and Innovation Department, Universiti Malaysia Pahang Al-Sultan Abdullah, has awarded both grants.

# REFERENCES

[1] Stanton NA, Dunoyer A, Leatherland A. Detection of new in-path targets by drivers using Stop & Go Adaptive Cruise Control. Appl Ergon 2011;42:592–601. https://doi.org/https://doi.org/10.1016/j.apergo.2010.08.016.

[2] Yu L, Wang R. Researches on Adaptive Cruise Control system: A state of the art review. Proceedings of the Institution of Mechanical Engineers, Part D: Journal of Automobile Engineering 2022;236:211–40. https://doi.org/10.1177/09544070211019254.

[3] Sankar V. REVIEW ON ADAPTIVE CRUISE CONTROL IN AUTOMOBILES. International Journal of Mechanical Engineering & Robotics Research 2014;3:404–9.

[4] Tjolleng A, Yang J, Jung K. Analysis of Leg Muscle Activities and Foot Angles while Pressing the Accelerator Pedal by Different Foot Postures. Applied Sciences (Switzerland) 2022;12:13025. https://doi.org/10.3390/app122413025.

[5] Jammes Y, Weber JP, Behr M. Consequences of Car Driving on Foot and Ankle Mobility and Reflexes. Clin Res Foot Ankle 2017;05. https://doi.org/10.4172/2329-910x.1000233.

[6] Idzham MK, Ahmad S, Abdullah M. Deep learning based prediction model of recurrent pedal pressing for low speed. 8th International Conference on Mechatronics Engineering (ICOM 2022), vol. 2022, 2022, p. 63–7. https://doi.org/10.1049/icp.2022.2266.

[7] Isa HM, Ahmad S, Abdullah M, Rahman A, Ghani N, Noor NMM. Modelling of Pedals Pressing Mechanisms for Low Speed Driving in Road Traffic Delay. IOP Conf Ser Mater Sci Eng 2022;1244:012010. https://doi.org/10.1088/1757-899x/1244/1/012010.

[8] Godjevac J. Comparison between PID and fuzzy control. Ecole Polytechnique Fédérale de Lausanne, Département d'Informatique, Laboratoire de Microinformatique, Internal Report 1993;93.

[9] Coleman CP, Godbole D. A comparison of robustness: fuzzy logic, PID, and sliding mode control. Proceedings of 1994 IEEE 3rd International Fuzzy Systems Conference, 1994, p. 1654–9 vol.3. https://doi.org/10.1109/FUZZY.1994.343945.

[10] Kaur A. Comparison between Conventional PID and Fuzzy Logic Controller for Liquid Flow Control: Performance Evaluation of Fuzzy Logic and PID Controller by Using MATLAB/Simulink. International Journal of Innovative Technology and Exploring Engineering (IJITEE) 2012:2278–3075.

[11] George T, Ganesan V. Optimal tuning of PID controller in time delay system: a review on various optimization techniques. Chemical Product and Process Modeling 2022;17:1–28. https://doi.org/doi:10.1515/cppm-2020-2001.

[12] Hashim AAA, Ghani NMA, Ahmad S, Nasir ANK. System Identification and Control of Linear Electromechanical Actuator Using PI Controller Based Metaheuristic Approach. Applications of Modelling and Simulation 2024;8:213–24.

[13] Wang H, Xu S, Hu H. PID Controller for PMSM Speed Control Based on Improved Quantum Genetic Algorithm Optimization. IEEE Access 2023;11:61091–102. https://doi.org/10.1109/ACCESS.2023.3284971.

[14] Dogruer T, Can MS. Design and robustness analysis of fuzzy PID controller for automatic voltage regulator system using genetic algorithm. Transactions of the Institute of Measurement and Control 2022;44:1862–73. https://doi.org/10.1177/01423312211066758.

[15] Ghani NMA, Nasir NM, Hashim AAA. Comparative Analysis of Spiral Dynamic Algorithm and Artificial Bee Colony Optimization for Position Control of Flexible Link Manipulators. Journal Europeen Des Systemes Automatises 2024;57:773–9. https://doi.org/10.18280/jesa.570315.

[16] Mahmoodabadi MJ, Shahangian MM. A New Multi-objective Artificial Bee Colony Algorithm for Optimal Adaptive Robust Controller Design. IETE J Res 2022;68:1251–64. https://doi.org/10.1080/03772063.2019.1644211.

[17] Yao LJ, Hashim MR, M. O. Tokhi. Artificial Bee Colony Optimization Algorithm with Flexible Manipulator System. International Journal of Electrical Engineering and Applied Sciences (IJEEAS) 2020;3.

[18] Huang M, Tian M, Liu Y, Zhang Y, Zhou J. Parameter optimization of PID controller for water and fertilizer control system based on partial attraction adaptive firefly algorithm. Sci Rep 2022;12. https://doi.org/10.1038/s41598-022-16425-7.

[19] Jamshidpour Ehsan and Parameshachari BD and SE and SC-L and RSH and SMH. Modeling and Optimal Control of Power System Frequency Load Controller by Applying Disturbance in the System by a Modified Version of Firefly Algorithm. In: Razmjooy Navid and Ghadimi N and RV, editor. Metaheuristics and Optimization in Computer and Electrical Engineering: Volume 2:

Hybrid and Improved Algorithms, Cham: Springer International Publishing; 2023, p. 199–240. https://doi.org/10.1007/978-3-031-42685-8_6.

[20] Dhal KG, Das A, Gálvez J. A Novel Fuzzy Logic-Based Improved Cuckoo Search Algorithm. International Journal of Applied Metaheuristic Computing 2022;13:1–29. https://doi.org/10.4018/ijamc.292516.

[21] Ou X, Wu M, Pu Y, Tu B, Zhang G, Xu Z. Cuckoo search algorithm with fuzzy logic and Gauss–Cauchy for minimizing localization error of WSN. Appl Soft Comput 2022;125:109211. https://doi.org/https://doi.org/10.1016/j.asoc.2022.109211.

[22] Pozna C, Precup R-E, Horváth E, Petriu EM. Hybrid Particle Filter–Particle Swarm Optimization Algorithm and Application to Fuzzy Controlled Servo Systems. IEEE Transactions on Fuzzy Systems 2022;30:4286–97. https://doi.org/10.1109/TFUZZ.2022.3146986.

[23] Sathish Kumar A, Naveen S, Vijayakumar R, Suresh V, Asary AR, Madhu S, et al. An intelligent fuzzy-particle swarm optimization supervisory-based control of robot manipulator for industrial welding applications. Sci Rep 2023;13:8253. https://doi.org/10.1038/s41598-023-35189-2.

[24] Kasruddin Nasir AN, Ahmad MA, Tokhi MO. Hybrid spiral-bacterial foraging algorithm for a fuzzy control design of a flexible manipulator. Journal of Low Frequency Noise Vibration and Active Control 2022;41:340–58. https://doi.org/10.1177/14613484211035646.

[25] Nasir ANK, Razak AAA, Ismail MTR, Ahmad MA. A Hybrid Spiral-Genetic Algorithm for Global Optimization. Journal of Telecommunication, Electronic and Computer Engineering (JTEC) 2018;10:93–7.

[26] Ghani NMA, Othman A, Hashim AAA, Nasir ANK. Comparative Analysis of PID and Fuzzy Logic Controllers for Position Control in Double-Link Robotic Manipulators. Journal of Intelligent Systems and Control 2023;2:183–96. https://doi.org/10.56578/jisc020401.

[27] Karim MI, Hashim AAA, Ghani NMA. Control of Double Link Flexible Robotic Manipulator System. Journal Europeen Des Systemes Automatises 2022;55:759–63. https://doi.org/10.18280/jesa.550607.